WILEY-VCH

Edited by Chunying Chen and Haifang Wang

Biomedical Applications and Toxicology of Carbon Nanomaterials

Edited by
Chunying Chen and
Haifang Wang

Biomedical Applications and Toxicology of Carbon Nanomaterials

Related Titles

Handbook of Systems Toxicology 2V Set

2011
Print ISBN: 978-0-470-68401-6

Syversen, T.T. (ed.)

General and Applied Toxicology 3e 6V set

2009
Print ISBN: 978-0-470-72327-2
ISBN: 978-0-470-74430-7

Nanotoxicity – From In Vivo and In Vitro Models to Health Risks

2009
Print ISBN: 978-0-470-74137-5
Adobe PDF ISBN: 978-0-470-74779-7
ISBN: 978-0-470-74780-3

Nanotoxicity – From In Vivo and In Vitro Models to Health Risks

2009
Print ISBN: 978-0-470-74780-3

Stanley, L.A.

Molecular and Cellular Toxicology - An Introduction

2013
Print ISBN: 978-1-119-95207-7
ePub ISBN: 978-1-118-52601-9
Adobe PDF ISBN: 978-1-118-52606-4
CourseSmart ISBN: 978-1-118-87137-9
Vital eBook PDF ISBN: 978-1-118-87152-2

Braithwaite, R.R. (ed.)

Applied Toxicology – Analytical Aspects of Forensic and Clinical Toxicology

2016
Print ISBN: 978-1-119-95232-9
ePub ISBN: 978-1-118-68353-8
WOL obook PDF ISBN: 978-1-118-68363-7
Adobe PDF ISBN: 978-1-118-68370-5

Environmental and Human Health Impacts of Nanotechnology

2009
Print ISBN: 978-1-444-30750-4

Vogel, V. (ed.)

Nanotechnology

Volume 5: Nanomedicine

2009
Print ISBN: 978-3-527-31736-3

Mumtaz, M. (ed.)

Principles and Practice of Mixtures Toxicology

2010
Print ISBN: 978-3-527-31992-3
ISBN: 978-3-527-63019-6
Adobe PDF ISBN: 978-3-527-63020-2
ePub ISBN: 978-3-527-63211-4
MobiPocket ISBN: 978-3-527-64039-3

Zhang, Z., Feng, W., Zhao, Y. (eds.)

Toxicology of Nanomaterials

2016
Print ISBN: 978-3-527-33797-2
WOL obook PDF ISBN: 978-3-527-68912-5
Adobe PDF ISBN: 978-3-527-68913-2
MobiPocket ISBN: 978-3-527-68914-9
ePub ISBN: 978-3-527-68915-6

Zhao, Y., Shen, Y. (eds.)

Biomedical Nanomaterials

2016
Print ISBN: 978-3-527-33798-9
WOL obook PDF ISBN: 978-3-527-69439-6
ePub ISBN: 978-3-527-69441-9
MobiPocket ISBN: 978-3-527-69442-6
Adobe PDF ISBN: 978-3-527-69443-3

Edited by Chunying Chen and Haifang Wang

Biomedical Applications and Toxicology of Carbon Nanomaterials

WILEY-VCH
Verlag GmbH & Co. KGaA

Editors

Prof. Dr. Chunying Chen
National Ctr. for Nanoscience & Techn.
No.11, Beiyitiao
Zhongguancun
100190 Beijing
China

Prof. Dr. Haifang Wang
Shanghai University
Inst. of Nanochemistry and Nanobiology
99 Shangda Rd
200444 Shanghai
China

Cover
getty Images; Alamy

Library of Congress Card No.: applied for

British Library Cataloguing-in-Publication Data
A catalogue record for this book is available from the British Library.

Bibliographic information published by the Deutsche Nationalbibliothek
The Deutsche Nationalbibliothek lists this publication in the Deutsche Nationalbibliografie; detailed bibliographic data are available on the Internet at <http://dnb.d-nb.de>.

Print ISBN: 978-3-527-33871-9
ePDF ISBN: 978-3-527-69285-9
ePub ISBN: 978-3-527-69287-3
Mobi ISBN: 978-3-527-69288-0
oBook ISBN: 978-3-527-69286-6

Typesetting SPi Global, Chennai, India

Printed on acid-free paper

Contents

List of Contributors

Harri Alenius
Finnish Institute of Occupational Health
Nanosafety Research Centre
Systems Toxicology Unit
Topeliuksenkatu 41aA
00250 Helsinki
Finland

Aoneng Cao
Shanghai University
Institute of Nanochemistry and Nanobiology
Shangda Rd
Shanghai 200444
China

Vincent Castranova
West Virginia University
Department of Pharmaceutical Sciences
One Medical Center Avenue
Morgantown WV 26506
USA

Chunying Chen
Chinese Academy of Sciences
National Center for Nanoscience and Technology (NCNST)
CAS Key Laboratory for Biomedical Effects of Nanomaterials and Nanosafety &
CAS Center for Excellence in Nanoscience
ZhongGuanCun Beiyitiao
Zhongguancun
Beijing 100190
China

Pan Chen
Shanghai University
School of Environmental and Chemical Engineering
Institute of Nanochemistry and Nanobiology
Shangda Rd
Shanghai 200444
China

Rui Chen
Chinese Academy of Sciences
National Center for Nanoscience and Technology of China
CAS Key Laboratory for Biomedical Effects of Nanomaterials and Nanosafety & CAS Center for Excellence in Nanoscience
Beiyitiao
Zhongguancun
Beijing 100190
China

Donna C. Davidson
National Institute for Occupational Safety and Health
Health Effects Laboratory Division
Allergy and Clinical Immunology Branch
Willowdale Road
Morgantown WV 26505
USA

Xiaoyong Deng
Shanghai University
School of Environmental and Chemical Engineering
Institute of Nanochemistry and Nanobiology
Shangda Rd
Shanghai 200444
China

Liangzhu Feng
Institute of Functional Nano & Soft Materials (FUNSOM)
Soochow University
Ren'ai Road
Suzhou
Jiangsu 215123
China

Cuicui Ge
School for Radiological and Interdisciplinary Sciences (RAD-X)
Collaborative Innovation Center of Radiological Medicine of Jiangsu Higher Education Institutions
Soochow University
Ren-Ai Road
Suzhou Industrial Park
Suzhou 215123
China

Yao He
Institute of Functional Nano & Soft Materials (FUNSOM) and Jiangsu Key Laboratory for Carbon-Based Functional Materials and Devices
Soochow University
Ren-ai Road
Suzhou Industrial Park
Suzhou
Jiangsu 215123
China

Marit Ilves
Finnish Institute of Occupational Health
Nanosafety Research Centre
Systems Toxicology Unit
Topeliuksenkatu 41aA
00250 Helsinki
Finland

Baowen Li
Center for Multidimensional Carbon Materials
Institute of Basic Sciences Center at UNIST Campus
UNIST-gil
Ulju-gun
Ulsan 689-798
Korea

Cheng Li
Shanghai University
School of Environmental and Chemical Engineering
Institute of Nanochemistry and Nanobiology
Shangda Rd
Shanghai 200444
China

Xiaojin Li
Chinese Academy of Medical Sciences and Peking Union Medical College
Institute of Basic Medical Sciences
Department of Biomedical Engineering
Dongdan Santiao
Beijing 100005
China

Xiaoyang Liu
Southwest University for Nationalities
College of Chemistry and Environment Protection Engineering
4th of the southern first loop
Wuhou district
Chengdu 610041
China

Ying Liu
Chinese Academy of Sciences
National Center for Nanoscience and Technology of China
CAS Key Laboratory for Biomedical Effects of Nanomaterials and Nanosafety &
CAS Center for Excellence in Nanoscience
ZhongGuanCun BeiYiTiao
Beijing 100190
China

Yuanfang Liu
Shanghai University
Institute of Nanochemistry and Nanobiology
Shangda Rd
Shanghai 200444
China

and

Peking University
College of Chemistry and Molecular Engineering
Department of Chemical Biology
Chengfu Rd
Beijing 100871
China

Zhuang Liu
Soochow University
Institute of Functional Nano & Soft Materials (FUNSOM)
Ren'ai Road
Suzhou
Jiangsu 215123
China

Xing Lu
Huazhong University of Science and Technology (HUST)
State Key Laboratory of Materials Processing and Die & Mould Technology
School of Materials Science and Engineering
Wuhan 430074
China

Qiang Ma
Chinese Academy of Medical Sciences and Peking Union Medical College
Institute of Basic Medical Sciences
Department of Biomedical Engineering
Dongdan Santiao
Beijing 100005
China

Jie Meng
Chinese Academy of Medical Sciences and Peking Union Medical College
Institute of Basic Medical Sciences
Department of Biomedical Engineering
Dongdan Santiao
Beijing 100005
China

Yon Rojanasakul
West Virginia University
Department of Pharmaceutical Sciences
One Medical Center Avenue
Morgantown WV 26506
USA

Linda Sargent
National Institute for Occupational Safety and Health
Toxicology and Molecular Biology Branch
Health Effects Laboratory Division
Willowdale Road
Morgantown WV 26505
USA

Zheng-Mei Song
Shanghai University
Institute of Nanochemistry and Nanobiology
Shangda Rd
Shanghai 200444
China

Todd A. Stueckle
National Institute for Occupational Safety and Health
Allergy and Clinical Immunology Branch
Health Effects Laboratory Division
Willowdale Road
Morgantown WV 26505
USA

Jian Tian
Soochow University
School for Radiological and Interdisciplinary Sciences (RAD-X)
Collaborative Innovation Center of Radiological Medicine of Jiangsu Higher Education Institutions
Ren-Ai Road
Suzhou Industrial Park
Suzhou 215123
China

Haifang Wang
Shanghai University
Institute of Nanochemistry and Nanobiology
Shangda Rd
Shanghai 200444
China

Jiajun Wang
Shanghai University
School of Environmental and Chemical Engineering
Institute of Nanochemistry and Nanobiology
Shangda Rd
Shanghai 200444
China

Jie Wang
Soochow University
Institute of Functional Nano & Soft Materials (FUNSOM) and Jiangsu Key Laboratory for Carbon-Based Functional Materials and Devices
Ren-ai Road
Suzhou Industrial Park
Suzhou
Jiangsu 215123
China

Liying Wang
National Institute for Occupational Safety and Health
Health Effects Laboratory Division
Allergy and Clinical Immunology Branch
Willowdale Road
Morgantown WV 26505
USA

Sheng-Tao Yang
Southwest University for Nationalities
College of Chemistry and Environment Protection Engineering
4th of the southern first loop
Wuhou district
Chengdu 610041
China

Jingru Xie
Southwest University for Nationalities
College of Chemistry and Environment Protection Engineering
4th of the southern first loop
Wuhou district
Chengdu 610041
China

Yi-Fan Yang
Shanghai University
Institute of Nanochemistry and Nanobiology
Shangda Rd
Shanghai 200444
China

Jia Yao
Food and Drug Administration
Office of Scientific Coordination
National Center for Toxicological Research
NCTR/ORA Nanotechnology Core Facility
Jefferson AR
USA

and

Food and Drug Administration
Office of Chief Scientist
Office of the Commissioner
FDA Commissioner's Fellowship Program
Silver Spring MD
USA

Haiyan Xu
Chinese Academy of Medical Sciences and Peking Union Medical College
Institute of Basic Medical Sciences
Department of Biomedical Engineering
Dongdan Santiao
Beijing 100005
China

Jianxun Xu
Chinese Academy of Sciences
National Center for Nanoscience and Technology
CAS Key Laboratory for Biomedical Effects of Nanomaterials and Nanosafety & CAS Center for Excellence in Nanoscience
Beiyitiao
Zhongguancun
Beijing 100190
China

Ligeng Xu
Soochow University
Institute of Functional Nano and Soft Materials (FUNSOM)
Ren-ai Road
Suzhou
Jiangsu 215123
China

Yingying Xu
Chinese Academy of Sciences
National Center for Nanoscience and Technology of China
CAS Key Laboratory for Biomedical Effects of Nanomaterials and Nanosafety & CAS Center for Excellence in Nanoscience
Beiyitiao
Zhongguancun
Beijing 100190
China

Yongbin Zhang
Food and Drug Administration
Office of Scientific Coordination
National Center for Toxicological Research
NCTR/ORA Nanotechnology Core Facility
Jefferson AR
USA

Preface

Carbon nanomaterials are a big family; its members include "superstars" like fullerene, carbon nanotubes, and graphene. They have been studied in depth, moved out of laboratories, produced in large scales, and used widely in various fields. Especially, carbon nanomaterials have many potential biomedical applications, including in imaging, biodevices, biosensors, anticancer drugs, drug delivery vehicles, and bioengineering. At the same time, their biosafety concerns have drawn increasing attention from the academia, public, businesses, and governments. After over 10 years of unremitting efforts of researchers all over the world, we not only have synthesized more novel carbon nanomaterials and developed many products incorporating them but also have acquired more knowledge on the biological effects of these nanomaterials to accelerate their bioapplications and assess accurately the risks involved in their use. This book focuses on the achieved knowledge on the main aspects of carbon nanomaterials in the biomedical field, providing a valuable reference source for a broad range of readers who want to understand the bioapplications and toxicology of carbon nanomaterials, ranging from undergraduate students and graduate students to carbon nanomaterial scientists and toxicologists in academia and industry.

This book comprises 16 chapters. After a brief introduction of the synthesis, functionalization, and characterization of carbon nanomaterials (Chapter 1), their detection methods in biosystems are given (Chapter 2), followed by the *in vivo* biodistribution/pharmacokinetic profiles of carbon nanomaterials via different administration routes (Chapter 3) and the interaction of carbon nanomaterials and biological systems (Chapter 4). These are the bases for bioapplications and toxicology studies of carbon nanomaterials. After that, the biomedical applications and toxicology involving carbon nanomaterials are addressed. Biomedical applications are presented in Chapters 5, 8, 13, and 14. As for toxicology, pulmonary toxicity, cardiovascular toxicity, hepatotoxicity, nephron toxicity, neurotoxic potential, genotoxicity, carcinogenesis potential, reproduction and development toxicity, toxicity to the gastrointestinal tract and skin are documented (Chapters 6–14). In addition, the fate and toxicity of carbon nanomaterials in the environment are included (Chapter 15). Finally, the exposure scenarios in the workplace and risk assessment are introduced (Chapter 16).

Of course, this book does not include all achievements and aspects of carbon nanomaterials. Yet, we hope that through this book the readers will not only gain profound insight into this fascinating research area but also be attracted to keep an eye on this field in the future, and even be inspired to join the search for new biomedical applications and toxicology of carbon nanomaterials.

We would like to thank all the contributors of this book wholeheartedly for their enthusiastic participation and the effort they have made in preparing such wonderful chapters. We are also grateful to Dr. Martin Preuss of John Wiley for his help in getting the book published.

Beijing, China — *Chunying Chen*
Shanghai, China — *Haifang Wang*

1
Synthesis, Functionalization, and Characterization

Jianxun Xu, Xing Lu, and Baowen Li

1.1
Introduction

Recent years have witnessed tremendous development in the studies of carbon nanomaterials, including fullerenes, carbon nanotubes (CNTs), and graphene. These carbon nanomaterials solely comprise sp^2 carbon atoms, which form conjugated six-membered rings fused together with various numbers of five-membered rings. These novel materials, which exhibit unique structures and properties, are expected to be useful in many fields.

To achieve the proposed applications, it is of primary importance to synthesize these nanomaterials with defined structures in reasonable production yield. At the same time, it is always required to further modify their surface properties to optimize the interface environment where they function. The fine structure and the surface properties are critical for their biological effects. And, it is actually important to identify the comprehensive structure parameters and surface modifications for their toxicological evaluations and understanding the related mechanisms. In this chapter, we present the basic concept and the latest achievements in the synthesis of carbon nanomaterials and their functionalization, especially related to biological purposes. The state-of-the-art characterization methods are also critically reviewed.

1.2
Fullerenes and Metallofullerenes

There have been a tremendous amount literature describing the synthesis, characterization, structures, and properties of empty fullerenes. As a result, we will only focus on the achievements in the recent studies of endohedral metallofullerenes (EMFs), which are hybrid molecules formed by the encapsulation of metallic species into the fullerene cages in the following contexts.

Biomedical Applications and Toxicology of Carbon Nanomaterials, First Edition.
Edited by Chunying Chen and Haifang Wang.

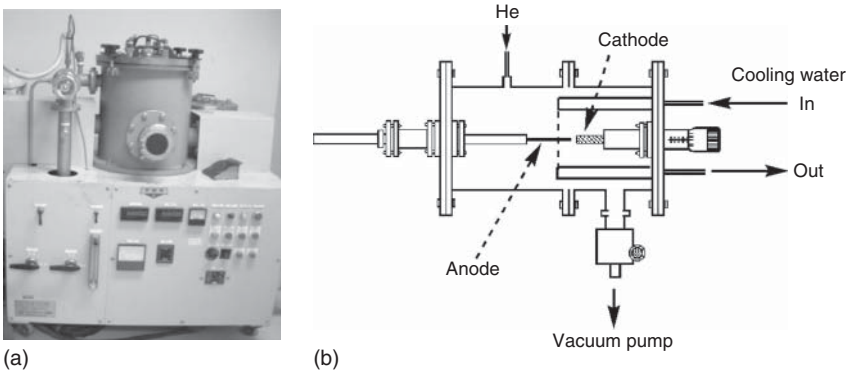

Figure 1.1 (a) An arc discharge reactor used to synthesize EMFs and (b) its schematic illustration.

1.2.1
Synthesis and Purification

1.2.1.1
Synthesis

The synthesis of empty fullerenes can be achieved rather easily via such methods as initial laser ablation, then arc discharge, and finally combustion of aromatic organic molecules even under ambient conditions. However, to produce EMFs, harsher conditions are always required to evaporate the metals into the gas phase. As such, only laser ablation and arc discharge approaches are effective.

Smalley and colleagues made the first attempt by using laser ablation equipment. A composite graphite disk doped with lanthanum oxide was irradiated with laser in a quartz tube under an inert atmosphere. The tube was heated to a temperature higher than 800 °C in order to ensure the formation of fullerenes and EMFs [1–3].

This is the most powerful and convenient method for EMF production (Figure 1.1). By allowing N_2 or NH_3 into the chamber, or by adding some nitrogen-containing compounds into the graphite rod, metal nitride cluster EMFs are readily obtained [4, 5]. EMFs containing a metal oxide cluster (Sc_4O_3) [6], a metal sulfide cluster (Sc_2S) [7], or even a metal cyanide cluster (Sc_3NC) have been synthesized by introducing the corresponding heterogeneous additives into the reactor.

1.2.1.2
Purification

Extraction Solvent extraction is the most common method and frequently used in the first step of fullerenes separation from soot. Generally, 1,2,4-trichlorobenzene (TCB) shows the highest affinity toward the fullerene species. Alternatively,

1,2-dichlorobenzene (ODCB), chlorobenzene, toluene (xylene, benzene), and CS_2 are also commonly used to extract fullerenes and EMFs [8–10].

On the other hand, electrochemical methods were also used for the extraction of insoluble EMFs. The insoluble species can be made soluble by altering the electronic properties of these insoluble species. Diener and Alford made the first attempt, and obtained a mixture of insoluble, small-bandgap fullerenes such as C_{74}, Gd@C_{60}, and Gd@C_{74} by electrochemical reduction of the sublimate of Gd-containing soot [11]. In addition, some insoluble EMFs were extracted after increasing the solubility via chemical derivatization. For example, upon extraction with 1,2,4-trichlorobenzene of La-containing soot, some insoluble species such as La@C_{2n} ($2n = 72–82$) were functionalized by the trace dichlorophenyl radicals generated during refluxing [12–16].

HPLC Separation Complete separation of EMFs has been accomplished only by high-performance liquid chromatography (HPLC) [17–19], which has proven to be the most powerful and frequently used technique for the separation of EMFs. The HPLC technique utilizing different modified HPLC columns can even afford the separation of structural cage isomers of various EMFs. Five complementary HPLC columns are available commercially: PYE, PBB, NEP, Buckyprep, and Buckyprep M.

Non-HPLC separation Electrochemical studies of EMFs have indicated that their redox potentials are quite different from those of empty fullerenes, so electrochemical methods can be efficiently used for separating EMFs from the latter. In 2003, Bolskar and Alford designed a separation protocol based on the electrochemical as well as chemical oxidation of EMF extracts by $AgPF_6$, $AgSbCl_6$, and tris(4-bromo-phenyl)aminium hexachloroantimonate [20].

Moreover, the "SAFA" (stir and filter approach) was proposed by Stevenson *et al.* [21, 22]. Without using any chromatography equipment, the authors used cyclopentadienyl and amino-functionalized silica to selectively bind contaminant fullerenes (empty fullerenes and non-nitride clusterfullerenes) and claimed to obtain the purified nitride clusterfullerenes under optimum conditions [21]. This method could also be used to separate Sc_3N@C_{80}-I_h and Sc_3N@C_{80}-D_{5h} isomers [22].

1.2.2
Chemical Functionalization

1.2.2.1
Carbene Reaction

Carbene reaction is used frequently to functionalize many different kinds of EMFs; this is mainly due to its highly selectivity. For example, through photoirradiation or even heating, reactions of M@C_{2v}-C_{82} (M = La, Y, Pr, Gd, etc.) with 2-adamantane-2,3-[3*H*]-diazirine (AdN_2) were conducted and two monoadducts of M@C_{2v}-C_{82} were obtained [23]. The single-crystal results

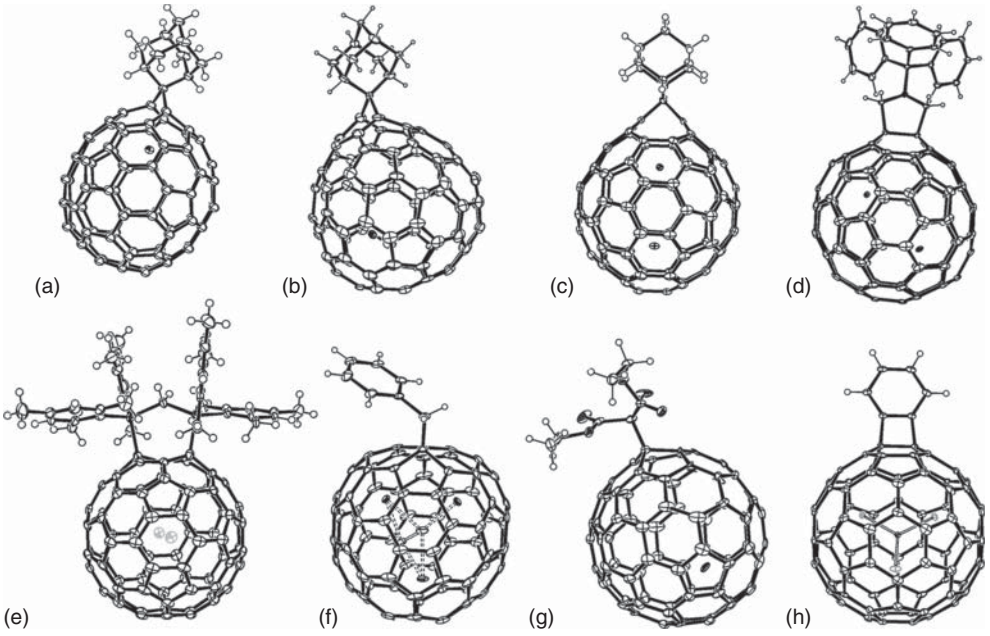

Figure 1.2 Ortep drawings of (a) $Y@C_{82}-Ad$, (b) $Yb@C_{84}Ad$, (c) $La_2@C_{80}-Ad$, (d) $La_2@C_{80}-NTrt$, (e) $Ce_2@I_h-C_{80}-(Mes_2Si)_2CH_2$, (f) $Sc_3C_2@C_{80}-CH_2C_6H_5$, (g) $La@C_{82}-CBr(COOC_2H_5)_2$, (h) $Sc_3N@C_{80}-C_6H_4$.

(Figure 1.2a) revealed that the addition always took place on those carbon atoms near the metal atom. Similar reaction of dimetallofullerenes $M_2@C_{80}$ (M = La, Ce) were carried out by Akasaka's group. The single-crystal X-ray structure (Figure 1.2c) analysis of monoadduct $La_2@C_{80}Ad$ confirmed that two La atoms were interestingly collinear with the spiro carbon of the Ad group and the distance between La atoms is increased [24]. Recently, the carbene reaction has been used to investigate the chemical properties of divalent EMFs. Reaction of $Yb@C_{80}$ with AdN_2 reported by Lu in 2013 resulted in the first derivative of a divalent metallofullerene. Only one isomer was obtained, indicating the high regioselectivity of this reaction [25]. $Yb@C_{84}$ (Figure 1.2b) was used to react with AdN_2 in the same year. Theoretical calculations suggest that the addition of divalent EMFs is mainly driven by the release of the local strains of cage carbons rather than by charge recombination, which is always prominent due to the affinity of typical trivalent EMFs [26].

1.2.2.2 Bingel–Hirsch Reaction

The Bingel–Hirsch reaction is one of the famous nuclophilic reactions in fullerene chemistry. The reactions of diethyl bromomalonate with metallofullerenes in the presence of 1,8-diazabicyclo[5.4.0]-undec-7ene (DBU) are extremely aggressive, so it is always used to synthesize various adducts. Surprisingly, Akasaka obtained

a singly bonded monoadduct of La@C_{82}(La@C_{82}CBr($COOC_2H_5$)$_2$) (Figure 1.2g) by means of the Bingel–Hirsch reaction [27].

1.2.2.3

Prato Reaction

Many investigations of Prato reaction of metallofullerenes indicate that changing the substituted group of aldehydes is a very efficient approach to obtain metallofulleropyrrolidines with different branched chains. This method is widely used to introduce functional groups for further photophysical studies. The first Prato reaction of EMFs was carried out by adding azomethine ylide into La@C_{82} solution. Two major endohedral metallofulleropyrrolidines, a monoadduct and a bisadduct of La@C_{82}, were isolated with HPLC, which suggested that the reaction is regioselective to some extent. A special Prato reaction of M_2@C_{80} (M = La, Ce) with 3-triphenylmethyl-5-oxazolidinone (NTrt) was reported by Akasaka's group; the [6,6]- and [5,6]-adducts resulted were and characterized. The X-ray crystallographic analysis of the [6,6]-adduct (Figure 1.2d) confirmed that the metal atoms are fixed, which is opposite of the random circulation in pristine La_2@C_{80} [28].

1.2.2.4

Bis-Silylation

Bis-silylation of La@C_{2v}–C_{82} reported by Akasaka *et al.* in 1995 was the first exohedral chemical functionalization of metallofullerenes [29]. Afterward, they succeeded likewise in the bis-silylation of M@C_{2v}–C_{82} (M = Gd, Y, Ce) and M@C_s-C_{82} with disilirane through a photochemical or thermal pathway [30]. Similar works of di-EMFs such as M_2@C_{80} (M = La, Ce) (Figure 1.2e) were conducted by Akasaka. In 2006, the reaction of trimetallic nitride-templated endohedral metallofullerene (TNT EMF) Sc_3N@C_{80} with 1,1,2,2-tetramesityl-1,2-disilirane under photoirradiation was carried out. Both 1,2- and 1,4-cycloadducts were successfully isolated and completely characterized by NMR measurement and single-crystal X-ray structure analysis.

1.2.2.5

Diels–Alder Reaction and Benzyne Reaction

Cyclopentadiene (Cp) and 1,2,3,4,5-pentamethylcyclopentadiene (Cp*) were used to participate in the [4 + 2] reaction of La@C_{82}. Interestingly, Diels–Alder reactions of La@C_{82} with Cp was reversible even at 298 K, which was proved through HPLC. X-ray analysis of La@C_{82}Cp* showed that 60% of the monoadduct formed a dimer in the solid state [31]. Benzyne reaction of La@C_{82} was undertaken by Lu in 2010, and the X-ray crystallographic structure analysis of the adduct showed that two benzyne moieties were attached to the highly pyramidized section and NO_2 was unexpectedly linked to cage [32]. Later on, two similar benzyne reactions of Sc_3N@C_{80} (Figure 1.2h) were reported by Echegoyen and Wang in 2011. Besides the typical cycloadditions above, some uncommon cycloadditions

of metallofullerenes such as radical malonate addition, azide addition, zwitterion addition, carbosilylation, so on, were investigated as well to some extent [30].

1.2.2.6 Singly Bonded Addition

The thermal reaction of La@C_{82} with 3-triphenylmethyl-5-oxazolidinone (NTrt) reported by Akasaka in toluene afforded the benzyl monoadducts La@C_{82}($CH_2C_6H_5$), Surprisingly, the same monoadducts were also obtained by the photoirradiation of La@C_{2v}–C_{82} in toluene without NTrt [33]. In 2008, Dorn obtained a dibenzyl adduct M_3N@C_{80}($CH_2C_6H_5$)$_2$ (M = Sc, Lu) by photochemical reactions of M_3N@C_{80} (M = Sc, Lu) with benzyl bromide, and confirmed the structure of 1,4-dibenzyl adduct of M_3N@C_{80} (M = Sc, Lu) by X-ray crystallographic analysis [34]. Recently, photochemical reaction of Sc_3C_2@C_{80} with benzyl bromide was undertaken by Lu, in 2014. X-ray structure analysis (Figure 1.2f) demonstrated that the cluster configuration in EMFs was highly sensitive to the electronic structure, which is tunable by exohedral modification [35]. Another typical singly bonded addition of EMFs is perfluoroalkylation. Perfluoroalkylation of metallofullerens, which is a special solid–solid reaction, prefers to afford various multiadducts. CH_3I and Ag(CF_3CO_2) are widely used as reagents for the perfluoroalkylations of EMFs. Reactions of Sc_3N@C_{80} were the most investigated because of the less selectivity of perfluoroalkylation and relatively large amount of Sc_3N@C_{80}. After persistent efforts, single crystals of the multiadduct Sc_3N@C_{80}(CF_3)$_n$ (n = 14, 16) were obtained by Yang and coworkers [30]

1.2.2.7 Supramolecular Complexes of EMFs

Supramolecular complexes based on metallofullerenes with macrocycles or organic donors have been investigated because of its attractive electron transfer behavior. In 2006, Akasaka and colleagues synthesized complexes of La@C_{82} with 1, 4, 7, 10, 13, 16-hexaazacycloctadecane. The complexes, which precipitate in toluene, are soluble in polar solvents. According to this phenomenon, they successfully separated metallofullerenes from soot extracts selectively [36]. Another organic donor, *N*,*N*,*N*′*N*′-tetramethyl-*p*-phenylenediamine (TMPD), was also used to form complexes with La@C_{82}; the characterization with spectroscopy and ESR confirmed the reversible intermolecular electron transfer system at complete equilibrium in solution and the formation of stable diamagnetic/paramagnetic anions of La@C_{82} and radical anions of the donor, respectively [37].

1.2.3 Characterization

1.2.3.1 Synchrotron Radiation Powder Diffraction (SRPD)/Rietveld/MEM

This method is the earliest to confirm EMFs [38]. In 1995, Takata *et al.* reported the MEM maps of Y@C_{82} and C_{82} and confirmed that the metal atom is indeed

encapsulated inside the fullerene cage [38]. Thereafter, the structures of numerous EMFs were determined similarly, such as those of $Sc@C_{82}$, $La@C_{82}$, and $Y_2C_2@C_{82}$ [39–41]. This experiential strategy is not always reliable because several erroneous structures have been assigned using this method [42, 43].

1.2.3.2

Nuclear Magnetic Resonance (NMR) Spectroscopy

NMR spectroscopy was also used to characterize structures. The cage structures of many trivalent EMFs have been established, especially those of $M@C_{82}$, showing that both $C_{2v}(9)$-C_{82} and $C_s(6)$-C_{82} cages are favorable, with the former being much more stable. Furthermore, using the two-dimensional incredible natural abundance double quantum transfer experiment (INADEQUATE), bond connectivities among nonequivalent cage carbons were also modeled in cases where the NMR spectrum was sufficiently clear [44, 45]. Recently, the signals from the internal C_2 unit of carbide cluster EMFs were detected with NMR spectrometry using ^{13}C-enriched samples. For the Sc_2C_2 cluster, which is frequently encountered in carbide cluster EMFs, peaks of the C_2 unit are observed between 220 and 260 ppm, but the corresponding signal of the C_2 motif in the $Sc_3C_2@I_h(7)$-C_{80} anion was shifted downfield to 328 ppm [46–49]. For divalent EMFs, di-EMFs, and cluster EMFs, which are all diamagnetic species, direct NMR measurements are valid for establishing their structures [50–52].

1.2.3.3

Theoretical Calculation

Calculations can predict the relative stabilities of EMF by considering the charge transfer from the encapsulated metals to the carbon cage [48, 53]. A "maximum pentagon separation rule" proposed by Poblet and coworkers stated that the pentagonal carbon rings on the fullerene cage tend to accumulate negative charges transferred from the internal metallic species. Consequently, they are separated to the greatest degree over the cage, engendering the maximum separation of the positively charged internal metal cations.

1.2.3.4

Single-Crystal X-ray Diffraction Crystallography

It is the most reliable solution to molecular structures. The EMF can form neat co-crystals with metal porphyrins: M^{II}(OEP) (M = Ni, Co etc., OEP = 2,3,7,8,12,13,17,18-octaethylporphyrin dianion) as the eight alkyl groups of M^{II}(OEP) wrap the spherical molecule. Balch and colleagues have also obtained the structure of $Kr@C_{60}$, indicating that the inert gas molecule is at the center of the cage [54]. In contrast, the single metal in mono-EMFs always departs from the center of the cage, either approaching closely to a hexagonal carbon ring for rare-earth metals or over a carbon bond for alkali metals, for example, $M@C_{3v}(134)$-C_{94}(M = Tm, Ca) [55]. In large cages, it is also possible for the single metal to move even at low temperatures (e.g., $Sm@C_{90}$ isomers) [56]. It is noteworthy that the crystal of $Li^+@C_{60}$ was obtained by co-crystallization with

its counter anion, $[SbCl_6]^-$, instead of metal porphyrin [57]. Furthermore, it was found in a recent study that the solvated $Sc_3N@C_{80}$ are nicely ordered in the crystal lattice, providing new insight into the structures of "pristine" EMFs [58].

1.2.3.5 Others

In addition to the methods that can be viewed as direct solutions to the molecular structure of EMFs, means such as infrared spectroscopy, Raman spectroscopy, absorption spectroscopy, electrochemical spectroscopy, and even high-resolution tunneling electronic microscopy (HRTEM) have all been used to characterize EMFs.

1.2.4 Questions and Future Directions

The development and structural recognition of fullerenes and metallofullerenes have a long way to go. The availability of EMFs is much less than sufficient for scientific research or practical application. Except for $Sc_3N@C_{80}$, other EMF species yielded less using the arc discharge method, and are more difficult to separate, because of the numerous structural isomers and low stability. As a result, more powerful synthetic methods and more efficient separation process are urgently needed to increase the availability of EMFs.

Practical applications of these fascinating materials also demand detailed exploration. Because of the presence of the metallic species, which are the mainstay of many novel electronic, magnetic, and optic applications, every detail of the functions of both the fullerene cage and the metallic core must be investigated.

1.3 Carbon Nanotubes

CNTs, including single-walled carbon nanotubes (SWCNTs) and multi-walled carbon nanotubes (MWCNTs), can be imagined as cylinders by rolling up hexagonal carbon sheets. The diameter and the chirality of a SWCNT can be defined in terms of its chiral vector (*m, n*), which determines the direction of rolling the carbon sheet, as illustrated in Figure 1.3. It is fantastic that SWCNTs with different (*m*, *n*) values exhibit different electrical (metallic or semiconducting) and optical properties in spite of the same chemical composition and bonding behaviors [59].

CNTs were probably observed for the first time using transmission electron microscopy (TEM) in the 1970s. But, only after Iijima *et al.*'s reports on their discovery and structural characterizations on MWCNTs in 1991 and SWCNTs in 1993, researchers around the world started to intensively study this kind of new materials, which have been proven to possess outstanding mechanical, thermal, optical, and electrical properties [59–61]. Various potential applications of CNTs

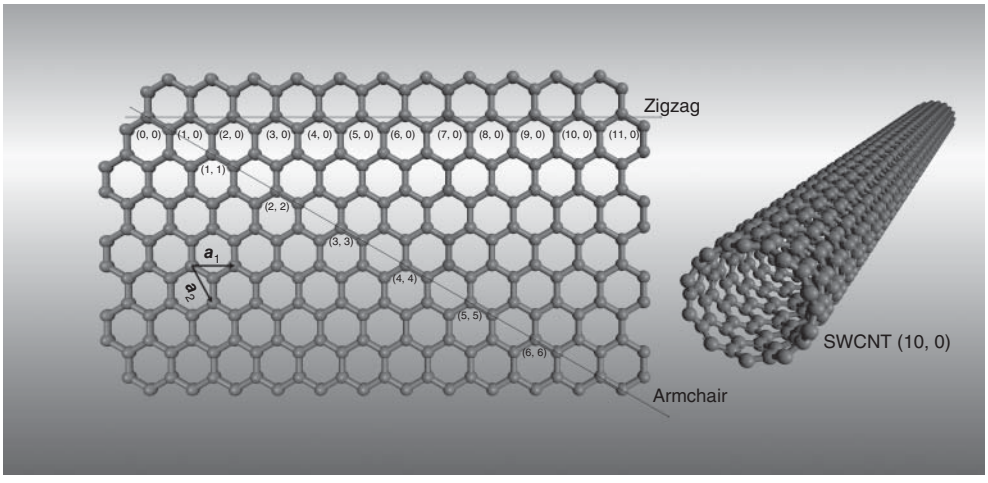

Figure 1.3 A carbon nanotube can be regarded as a cylinder obtained by rolling up a graphene sheet. The vector convention is used to define the points in the graphene lattice. The illustrated SWCNT (10, 0) is formed by superimposing the point (10, 0) with (0, 0) in the graphene sheet, which is a zigzag tube.

are expected for composites, flat panel displays, electronic nano-devices, sensors, functional probes, drug delivery systems, and so forth [62–67].

1.3.1 Synthesis

The widely used methods to synthesize CNTs are arc discharge, laser ablation, and chemical vapor deposition (CVD).

1.3.1.1 Arc Discharge Method

An arc discharge can be used to produce various carbon nanomaterials, including fullerenes, CNTs, and carbon nanohorns. It is an effective way to synthesize high-quality CNTs having different structural features. The SWCNTs and MWCNTs observed by Iijima in his pathbreaking work were actually obtained by means of arc discharge. The facility is very similar to that used to produce fullerenes described previously (Figure 1.1). Under optimal conditions of arcing between two high-purity graphite electrodes, MWCNTs can be synthesized. SWCNTs can be generated by arc discharge only when suitable metal catalysts are used, including Fe, Co, Ni, Pt, and Rh [61, 68, 69]. CNTs produced by arc discharge have few structural defects, which helps in preserving the unique properties of CNTs. Meanwhile, it also causes problems to handle these CNTs in wet processes. For example, it is difficult to disperse such CNT powders well in the aqueous phase when researchers aim to use CNTs for biological applications.

1.3.1.2

Laser Ablation Method

Laser ablation is another method developed for CNT synthesis at the early stage of studies on carbon nanomaterials. Carbon evaporated from high-purity graphite source under high-power YAG laser irradiation can form MWCNTs at 1200 °C in an Ar or a N_2 atmosphere [70]. When metal catalysts (Co–Ni) were mixed into the graphite target, SWCNT bundles were synthesized [71]. On the other hand, spherical aggregates of single-walled carbon nanohorns were obtained in the absence of any catalyst at room temperature [72, 73]. Currently, laser ablation method is not widely adopted for CNT synthesis because of the necessity of high-power lasers and high-purity graphite.

1.3.1.3

CVD Method

Many research groups and commercial manufacturers are using CVD for the synthesis of CNTs, which is a versatile and economic method to produce different types of CNTs and graphene (discussed below). In the CVD process, carbon sources in the gas phase flowing through a heating furnace decompose and dissolve on the surface of active catalyst nanoparticles, initiating the growth of CNTs. Since the successful CVD growth of SWCNTs in the late 1990s, a huge amount of work has been reported on growing CNTs by this technique [74–78]. It has been revealed that various CNTs with different morphologies and crystallinity can be generated by adjusting the parameters including the carbon feedstock, catalyst (composition, size, shape, density, and crystal structure), carrier gas, temperature, and even the direction of gas flow and tube furnace. Furthermore, aligned CNTs (vertical or horizontal) with designed patterns can also be obtained based on the CVD technique [79–81].

1.3.1.4

Synthesis of CNTs with a Defined Structure

Nowadays, it has been realized that the crucial point for practical applications of CNTs is to obtain sufficient amount of a single type of CNTs with defined diameter and chirality. Many research groups have contributed to this effort by optimizing the characteristics of the catalysts used in the CVD process. For example, Harutyunyan *et al.* increased the fraction of metallic SWCNTs up to 91% by optimizing the thermal annealing conditions of the Fe nanocatalyst [82]. Wang *et al.* reported their work on the growth a single type of SWCNTs (9, 8) with 51.7% abundance by using a sulfate-promoted $CoSO_4/SiO_2$ catalyst [83]. Most recently, Li and colleagues successfully obtained specific SWCNTs (12, 6) with an abundance over 92% in their CVD growth studies [84]. W_6Co_7 alloy nanoclusters with specific structural features were used as the catalyst and believed to be the key factor to initialize the SWCNT's specific growth. These works demonstrated the possibility to directly grow structure-controlled CNTs, which is of great importance to achieve CNT applications for nanoelectronics and biological purposes.

1.3.2 Functionalization

Before applying CNTs to a certain applications, it is usually required to modify the surface of CNTs for functionalization, better dispersion, and feasible manipulation. There have been a large number of reports on the surface modifications of CNTs, which can be generally classified as covalent chemistry and noncovalent modifications.

1.3.2.1 Covalent Chemical Reactions

There are usually some impurities (amorphous carbon, catalyst particles, etc.) in the raw soot of CNTs. During the purification processes using acid oxidation, oxygenated functional groups are induced onto CNTs, mainly carbonyl and carboxylic groups. The most widely used covalent chemical reactions of CNTs are through amidation based on the carboxylic groups on the surface or the open ends of the nanotubes. Many other chemical reactions, such as Prato reaction, halogenation, cycloaddition, necleophilic addition, and radical addition, among others, have also been reported. The related reaction route, mechanism, and characterizations have been reported in several reviews [85, 86].

1.3.2.2 Noncovalent Modifications

Wrapping the CNTs with surfactants, biomolecules, and various types of polymers is another effective way to disperse and functionalize CNTs. This approach takes advantage of the nonspecific interactions (mainly hydrophobic affinity and $\pi-\pi$ stacking) between the graphite surface of CNTs and hydrophobic moieties or aromatic rings of the reactants. A wide variety of surfactants (ionic and nonionic) have been used to wrap and disperse CNTs, such as sodium dodecyl sulfate, sodium cholate, sodium pyrenebutyrate, Tween, Triton, and so on. It has been found that bile salts are exceptionally effective for dispersing CNTs due to their unique structure comprising a steroid ring and facial amphiphiles [87, 88]. These types of surfactants were utilized to obtain stable, monodispersed SWCNTs suitable for diameter sorting using density gradient ultracentrifugation.

Modification Using Biomolecules Different types of biomolecules are used for the dispersion and functionalization of CNTs. Among them, DNA molecules have proven to be highly effective through helical wrapping onto the CNT surface [89]. On the basis of their outstanding dispersion efficiency, DNA sequences were able to further recognize and separate structure-specific CNTs [90]. Moreover, phosphate lipid-functionalized short CNTs can self-insert into lipid bilayers and live cell membranes to form biomimetic ion channels able to transport water, protons, small ions, and DNA [91]. Some proteins, such as bovine serum albumin and streptavidin, were also widely used for surface modification and possible further functionalization of CNTs, especially for biological applications.

Modification Using PEG-based Polymers The integration between CNTs and polymers has been extensively investigated. To fabricate high-performance CNT–polymer composites, CNTs were dispersed and bonded with various species of polymers, such as poly(acrylate), hydrocarbon polymers, and conjugated polymers, to name a few [85]. Meanwhile, for biological purposes, block copolymers comprising hydrophobic chains and hydrophilic poly(ethylene glycol) (PEG) are the most widely used reagents to modify and disperse CNTs in highly salted aqueous solutions and biofluids [92]. It is well known that the PEG moieties over the CNT surface can prevent nonspecific protein adsorption and increase the biocompatibility of CNTs. PEG chains with different lengths and branch structures have been attached to CNTs. Among them, phosphate–lipid conjugated PEG polymers were the most commonly used to form stable suspension of CNTs in solutions with high ionic strength [93]. A comb-shaped PEG branch was proven to have higher dispersion efficiency as a result of the higher density of PEG chains above the hydrophobic graphite surface [94]. It was also possible to further enhance the dispersion ability of PEG polymers by adjusting the linker structure between the hydrophobic and the PEG chains. For example, it was found that ceramide-conjugated PEG, which has a neutral linker group, possesses a higher dispersion potential than the corresponding charged phospholipid-conjugated PEG polymers [95].

1.3.3 Characterization

Different from real molecules, a CNT sample is actually a mixture containing CNTs with different diameters, lengths, and chirality. They cannot form real solutions or identical crystals. Therefore, many analysis methods commonly used in molecular chemistry, such as X-ray diffraction crystallography, NMR, and so on, are not effective for identifying the exact chemical composition and binding information of CNTs and the attached functional groups. Alternative methods are adopted to obtain the structural features of CNTs and functionalized derivatives to some extent, which include transmission electron microscopy (TEM), atomic force microscopy (AFM), Raman spectroscopy, ultraviolet–visible (UV–vis) absorbance spectroscopy, and near-infrared (NIR) fluorescence.

1.3.3.1 Microscopic Characterizations

Among these analysis tools, TEM is a widely used method to characterize CNTs with respect to their morphology and composition information. It is also a powerful tool to study *in situ* dynamic processes in the nanoscale. For example, Suenaga *et al.* [96] were able to directly image Stone–Wales defects in SWCNTs and their propagation under heating by means of high-resolution TEM with atomic resolution. The development of this technique in recent years has made it possible to achieve elemental analysis using electron energy loss spectroscopy to an

unprecedented sensitivity, even at the atomic level [97]. Compared to TEM, AFM is more versatile and nondestructive. The morphology and conformation of the attached soft materials on the surface of CNTs, such as DNA and proteins, were able to be analyzed by AFM observations [98]. Moreover, tip-enhanced Raman spectroscopy integrated with AFM is regarded as a fantastic tool for chemical analysis at the nano-scale [99]. It holds promise to detect single molecules on surfaces, although the current sensitivity is still limited by the use of conventional AFM tips. The newly developed multiple-probe AFM is a specialized method that allows researchers to manipulate up to four AFM probes at the same time [100]. It affords flexible and precise control of the tip location and tip–sample force when the tips are used as electrodes for probing the electrical properties of individual CNTs.

1.3.3.2 Spectroscopic Characterizations

Spectroscopic methods are also very useful in obtaining structural information of CNTs, which is especially important to identify the functionalized chemical species on CNTs. Raman spectroscopy is a versatile and sensitive tool that has been utilized from the very beginning of CNT studies [101, 102]. It is possible to identify a single CNT based on its resonance Raman spectrum, giving structural characteristics including the diameter, defect density, surface functionality, and much beyond. It has been a standard tool in the studies of nanocarbon materials. UV–vis absorbance and NIR fluorescence are commonly used to analyze CNT samples dispersed in solution [103]. Both methods are very sensitive to the dispersion state of functionalized CNTs in solution (individuals or bundles). Especially, UV–vis measurements are very easy to perform, and can give valuable information of CNTs on the dispersion state, preliminary chemical functional components, diameter, chirality, and even the length.

1.3.4 Questions and Future Directions

Based on their outstanding structural features and properties, CNTs are expected to be used in various applications, including electronic devices, sensors, and biological uses. However, to effect these practical applications, it is necessary to obtain the CNT samples having a defined structure. The diameter, chirality, and even the length of a CNT affect its electrical and biological properties. As mentioned above, researchers have been able to synthesize CNT samples with identical chirality. It is also possible to separate CNTs having a certain structural feature by density-gradient ultracentrifugation. But, until now, the amount of the pure CNTs produced is too small to be applied to practical applications. It is of critical importance to produce pure CNTs of a defined structure in a reproducible and economical way to achieve practical applications of this amazing material after over two decades of its discovery.

1.4 Graphene

Graphene, a single sp^2-bonding carbon layer of the graphite structure, is a basic building block for graphitic materials of all other dimensionalities. It can be wrapped up into 0D fullerenes, rolled into 1D nanotubes, and stacked into 3D graphite (Figure 1.4a) [104]. It has potential to exhibit a wide range of remarkable structural and transport properties, for example, specific surface area, high carrier mobility (>200 000 $cm^2 V^{-1} s^{-1}$) [108, 109], high Young's modulus (~1100 GPa) [110], excellent optical transparency [111], and high thermal conductivity (~5000 $W m^{-1} K^{-1}$) [112]. These peculiar properties arise from its unique electronic band structure, in which the conduction band overlaps with the valence band at two points (K and K′) in the Brillouin zone, and in the vicinity of these points the electron energy exhibits a linear relationship with the wave vector (Figure 1.4b) [105]. The experimental observations of the extraordinary transport properties have fueled extensive research on its chemical and physical properties [113, 114]. Although the experimentally observed values are substantially lower than theoretical predictions, research into graphene to date has highlighted the potential for applications in nanodevices, energy-storage materials, polymer composites, liquid crystal devices, and biomedicine [115, 116]. In this section, we aim to summarize the progress made on graphene, ranging from the synthesis and characterization to functionalization. Clearly, the development of various methods for producing graphene with controllable quality, quantity, and morphology might enable us to expand the graphene family with fascinating properties.

1.4.1 Synthesis and Characterization

In extensive studies to date, four different routes have been reported to produce graphene. The first was the micromechanical exfoliation of graphite, named as the "Scotch tape" or peel-off method [113]. This approach was inspired by earlier work on the micromechanical exfoliation from patterned graphite [117]. The second was CVD, such as the decomposition of a carbon source on metal substrates, for example, copper and nickel [118, 119]. The third was the epitaxial growth on electrically insulating surfaces, for example, SiC [120]. The fourth was the liquid-phase exfoliation of graphite into graphene nano-platelets [121].

The resulting graphene obtained by the above methods exhibit diversities in sample size and quality, implying their applicability for niche applications. Micromechanical exfoliation has, for example, yielded the highest quality but with small sample sizes ranging from few micrometers to ~1 mm, which are applicable only for fundamental studies on their transport properties. Large-area, uniform, and continuous graphene films are now achievable by CVD on Cu foil, but they exhibit moderate charge carrier mobility. A complete process requires the transfer from the Cu foil to a target substrate, and the production of square meters of graphene has already been achieved. The polymers used as a supporting

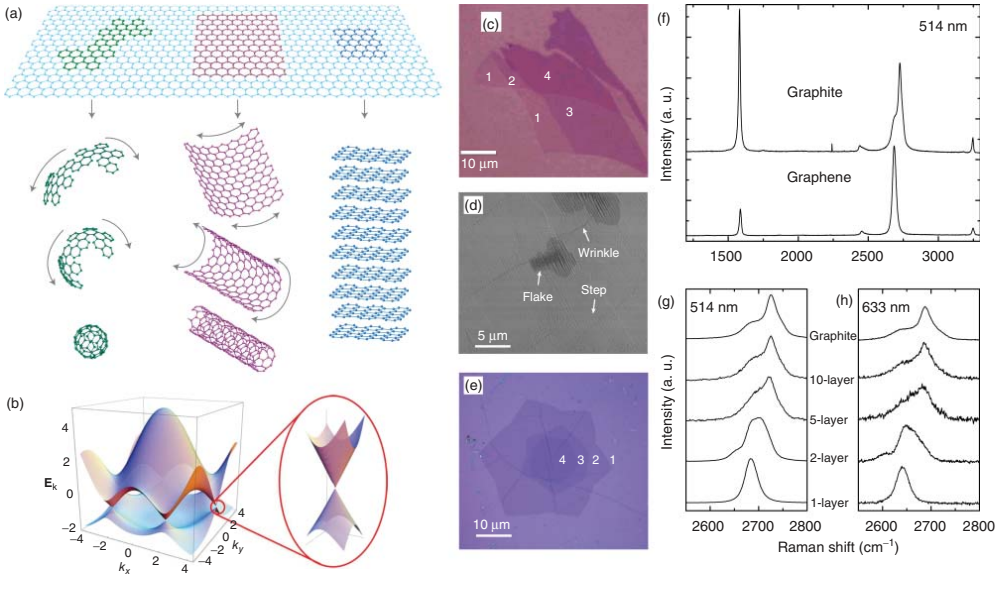

Figure 1.4 (a) Graphene is a 2D building material for carbon materials of all other dimensionalities. It can be wrapped up into 0D buckyballs, rolled into 1D nanotubes, or stacked into 3D graphite. (Reprinted with permission from [104]. ©2007 Nature Publishing Group.) (b) Electronic dispersion in the honeycomb lattice. Left: energy spectrum (in units of t) for finite values of t and t', with $t = 2.7$ eV and $t' = -0.2t$. Right: zoom-in of the energy bands close to one of the Dirac points. (Reprinted with permission from [105]. ©2009 American Physical Society.) Characterization of graphene. (c) Optical image of mechanically exfoliated graphene flakes with one, two, three, and four layers on a SiO_2(285 nm)-on-Si substrate. (Reprinted with permission from [106]. ©2007 American Chemical Society.) (d) High-resolution SEM and (e) optical images of CVD-grown graphene transferred on to a SiO_2(285 nm)-on-Si substrate, respectively. (f) Comparison of Raman spectra recorded at 514 nm for bulk graphite and graphene. The 2D peaks at 2700 cm^{-1} are scaled to have similar height; evolution of the spectra at (g) 514 nm (h) 633 nm with the number of layers. (Reprinted with permission from [107]. ©2006 American Physical Society.)

layer in the transferring procedure, however, are rather difficult to be completely removed from the graphene surface. The residual polymers are found to greatly influence the graphene's properties and thus make the materials properties less controllable in devices. CVD-grown graphene films are ready for use in transparent conductive coating applications, sensors, and nanoelectronics, although there are defects, grain boundaries, and thicker graphene that would result in variable device performance from one device to another. The quality of graphene grown on SiC can be very high, with crystallites approaching hundreds of micrometers in size. Thus, SiC-grown graphene may find application in high-frequency transistors. In the liquid exfoliation of graphite, intercalation of solvents into the gallery of graphite favors the interlayer expansion. With further aids of sonication and thermal or plasma processes, such graphite intercalated compounds can subsequently be delaminated into graphene nano-platelets, with a wide dispersion of thickness and lateral size, strongly depending on the treatment conditions [121]. The tone-scale synthesis of graphene via this method is currently being evaluated in numerous applications in printed electronics, electromagnetic shielding, barrier coatings, heat dissipation, supercapacitors, and so on [122].

The peculiar chemical and physical properties of graphene have demonstrated experimentally a strong dependence on the number of graphene layers, the quality of the material, the type of defects, and the substrates. In this context, it is of critical importance to perform various characterizations on graphene in order to explore the issues mentioned above. Optical microscopy is a quick and precise method to rapidly locate graphene and to determine the thickness of graphene nano-platelets in terms of their contrast spectrum. One can observe a contrast between the graphene layers and SiO_2(285 nm)/Si substrate in a reflection spectrum using a normal white-light illumination on samples supported on a substrate (Figure 1.4c) [106]. The graphene sample shows four different contrast regions, which are related to four different thicknesses. By fitting the experimental data to Fresnel's law, the experimental refractive index of a single-layer graphene $n = 2.0 - 1.1i$ differs from that of bulk graphite $n = 2.6 - 1.3i$ in the visible range. Such a large deviation was ascribed to the decrease of interlayer interaction in the ultrathin range. In similar cases, the thickness of few-layer graphene with less than 10 layers has clearly been discriminated. As to a continuous graphene film on a Cu foil by CVD, scanning electron microscopy (SEM) is an efficient method for the direct evaluation. Figure 1.4d depicts a higher resolution image of graphene on Cu with the presence of Cu surface steps, graphene "wrinkles," and the presence of nonuniform dark flakes. The wrinkles are caused by the thermal expansion coefficient difference between Cu and graphene. The CVD-grown graphene also exhibits a clear contrast between the graphene layers when it is transferred onto the SiO_2(285 nm)/Si substrate (Figure 1.4e).

Raman spectroscopy is another nondestructive and quick inspection method for evaluating the thickness and quality of graphene. In the Raman spectra of graphene, a G peak located at $\sim 1580\,cm^{-1}$ and a 2D peak at $\sim 2700\,cm^{-1}$ are observed, as shown in Figure 1.4f, corresponding to the in-plane optical vibration (degenerate zone-center E_{2g} mode) and second-order of zone-boundary phonons,

respectively [107]. The D peak, located at ~1350 cm^{-1} due to first-order zone boundary phonons, is absent from defect-free graphene. It will be activated by defects, vacancy, and structural disorder in graphene. The number of layers in graphene can be determined by the shape, width, and position of the 2D peak. Figure 1.4g and h shows that the 2D peak shifts to higher wavenumber values and becomes broader with an increase in the number of layers. For more than five layers, however, the Raman spectrum becomes hardly distinguishable from that of bulk graphite. Raman spectroscopy has also been useful in identifying the quality and types of edge, the effects of perturbations, such as electric and magnetic fields, strain, doping, disorder, and functional groups [123].

1.4.2 Functionalization of Graphene and Graphene Oxide

The chemical modification of graphene generally includes covalent attachment of organic molecules, hydrogen, and halogens to pristine graphene and/or its derivatives, noncovalent functionalization, and deposition of various nanoparticles on it [124].

Graphene and graphene oxide with large surface area, delocalized π electrons, and easy functionalization by various molecules provide opportunities for applications in nanodevices, energy-storage materials, and polymer composites [115]. In terms of the solid-state ^{13}C NMR spectroscopy analysis done to date (Figure 1.2a–c) [125, 126], the possible structural model of graphene oxide has been proposed in Figure 1.4d [126]. The carbon network is bonded to hydroxyl groups or epoxide groups as well as five- and six-membered lactols. Most of covalent functionalization methods rely on these groups that are active sites.

Covalent chemistry has proven to be an effective path to convert the sp^2-hybridized carbon atoms into sp^3-hybridized ones by forming a single bond with external groups. For example, the aryl radicals dissociated from diazonium salts upon heating broke the –C═C– double bonds and introduced aryl groups onto the graphene plane [127]. By use of photoinduced free radicals, one can also introduce aryl groups onto graphene scaffold from benzoyl peroxide. However, the free-radical reactions usually give rise to disordered crystal structures [128].

It would be ideal to control the crystal structure and chemical composition of graphene derivatives. Theoretical calculations predicted the existence of fully hydrogenated and fluorinated graphene from both sides, named as graphane and fluorographene, respectively [129–131]. Graphane and fluorographene are both thermodynamically stable with a C/H or C/F ratio of 1:1. Graphane has two stable configurations: a chair conformer and a boat conformer, the former being slightly more stable than the latter. The direct bandgap values at the K point are 3.5 and 3.7 eV for the former and latter, respectively. By exposing free-standing graphene to a hydrogen plasma, one can achieve the double-sided hydrogenation of graphene [132]. The electron diffraction (ED) pattern revealed that the graphane has a hexagonal symmetry with a lattice constant $d = 2.46 \pm 0.02$ Å, which is ~1% smaller than that of pristine graphene. This lattice shrinkage after exposure to H

radicals arises from the change of carbon configuration from sp^2 to sp^3, which generally results in longer C–C bonds. The unit cell of fluorographene is, in contrast, ~1% larger than that of graphene as a consequence of the corrugation [133], whereas the measured unit cell of C_2F chair, partially fluorinated graphene on one side, revealed a 2.4% expansion with respect to graphene, which is larger than corrugated fluorographene. The C_2F chair, one-sided fluorination of graphene, demonstrated a much higher degree of pristine long-range structural and morphological order than fluorographene [134]. The tetragonal "boat" form exhibits a short-range order.

Noncovalent functionalization involves the reactions with biocompatible polymers or biomolecules via hydrophobic interactions, $\pi-\pi$ stacking, or electrostatic interactions. Such modification greatly improves their stability in aqueous solutions. Since graphene oxide nanosheets are negatively charged, a positively charged polyelectrolyte (PEI) can effectively bind with them via electrostatic interactions. The resulting nano-graphene oxide (nGO)/PEI hybrids, for example, show much improved physiological stability compared to graphene oxide, reduced toxicity compared to bare PEI, and high gene transfection efficiency [135].

Deposition of nanoparticles, including those of metals (e.g., Au, Ag, Pd, Pt, Ni, and Cu) and metal oxides (TiO_2, ZnO, MnO_2, Co_3O_4, and Fe_3O_4), on graphene and nGO demonstrates the potential for their applications in biomedicine [136]. For example, graphene oxide/iron oxide nanoparticle composites have been investigated for magnetic targeted drug delivery and *in vivo* multimodal-imaging-guided photothermal therapy because of their interesting magnetic and optical properties.

Biofunctionalization of graphene and graphene oxide with biomolecules and cells have expanded their applications to a variety of biological platforms, biosensors, and biodevices. Until now, a number of biomolecules, for example, nucleic acids (NAs), peptides, proteins and cells, have been successfully employed in biological modification of graphene and graphene oxide (Figure 1.5a) [137]. One can also achieve its surface modification through reaction with various hydrophilic macromolecules, such as PEG (Figure 1.5b–f) [138], amine-modified dextran (DEX) [139], and poly(acrylic acid) (PAA) [140]. The modified graphene oxides have exhibited improved biocompatibility, reduced nonspecific binding to biological molecules and cells, and improved *in vivo* pharmacokinetics for better tumor targeting [138].

1.4.3
Prospects and Challenges

In more than 10 years of worldwide research, graphene and its derivatives with fascinating properties have shown potential for applications. Toward these applications, mass production techniques are required to produce uniform graphene nano-platelets. Low-temperature growth of large-area, uniform, high-quality bilayer and multilayer graphene films on arbitrary substrates need to be developed. The efficient, intact, and clean transfer from metal substrates

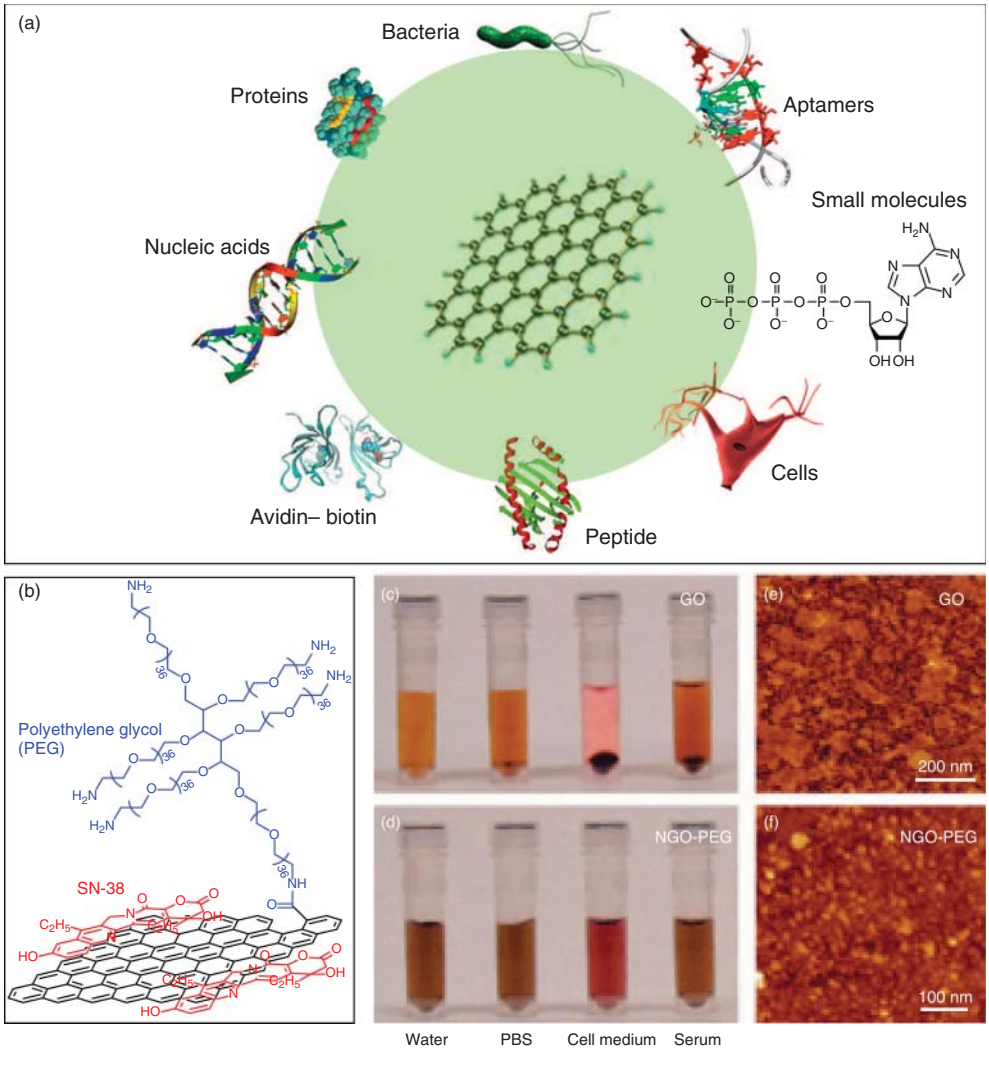

Figure 1.5 (a) Logo for biofunctionalization of graphene and its derivatives with avidin–biotin, peptides, nucleic acids, proteins, aptamers, small molecules, bacteria, and cells through physical adsorption or chemical conjugation. (Reprinted with permission from [137]. ©2011 Cell Press). Nano-graphene oxide (nGO)–PEG for drug loading and delivery. (b) Schematic structure of SN38 loading on nGO–PEG. PEGylation of graphene oxide: photos of (c) GO and (d) nGO–PEG in different solutions recorded after centrifugation at 10 000*g* for 5 min. GO crashed out slightly in PBS and completely in cell medium and serum (top panel). nGO–PEG was stable in all solutions. AFM images of (e) GO and (f) nGO–PEG. (Reprinted with permission from [138]. ©2008 American Society Chemistry.)

without etching the metals remains challenging. The combination of graphene and biotechnology is still in its infancy. There are many issues to be resolved before putting graphene to bioapplications. The potential long-term toxicity has been central to these issues. Whether and how graphene and its derivatives gradually degrade in biological system is essentially unclear. Its influence on the immune and reproductive systems of animals requires more research activities.

1.5 Summary and Outlook

In the past three decades, researchers all over the world have carried out extensive studies on carbon nanomaterials, especially fullerenes, CNTs, and graphene. Various methods to synthesize these nanomaterials with different morphology and structures have been reported. Diverse and attractive mechanical, chemical, and physical properties have also been investigated by means of state-of-the-art characterization tools. Based on these comprehensive studies, carbon nanomaterials are believed to have the potential for use in many exciting applications in many fields.

However, most of the proposed applications have not been realized. Till now, it is widely accepted that the biggest challenge to achieve these practical applications is obtaining enough amount of carbon nanomaterials having a designated structure. Researchers are now reconsidering ways to synthesize carbon nanomaterials.

The first thing is to set up effective methods to produce carbon nanomaterials with a precisely controlled structure and identical properties. The chirality, diameter, layer number, and even the assembly status of CNTs may change their optical, electrical, and biological behaviors dramatically. Similarly, the layer number, width, edge structure, and defect number of graphene determine its properties and feasible applications. Therefore, a uniform sample having the same structure is required for many real applications, especially in the electrical and biological fields.

The second consideration is the production yield. Now it is possible to synthesize or separate identical fullerene isomers and CNTs of a single chirality. Graphene ribbons in a narrow range of widths were also successfully engineered in the laboratory. The problem is that the obtained amount is far below that is needed for practical usage. It remains a big challenge to improve the yield of these materials with structural purity. On the other hand, researchers are currently able to produce CNTs and graphene on an industrial scale despite the precise control on their fine structures, which greatly promote the progress toward some applications such as films, composites, and surface coating. In this aspect, it will be very helpful to further decrease the production cost and keep a comparatively high structural quality at the same time.

In conclusion, to achieve practical applications, the primary goal and task is to scale up the production of carbon nanomaterials in a reproducible way, preferably with a precise control on their fine structures.

References

1. Heath, J.R., Zhang, Q., O'Brien, S.C., Curl, R.F., Kroto, H.W., and Smalley, R.E. (1987) The formation of long carbon chain molecules during laser vaporization of graphite. *J. Am. Chem. Soc.*, **109**, 359–363.
2. Heath, J.R., O'Brien, S.C., Zhang, Q., Liu, Y., Curl, R.F., Tittel, F.K., and Smalley, R.E. (1985) Lanthanum complexes of spheroidal carbon shells. *J. Am. Chem. Soc.*, **107**, 7779–7780.
3. Chai, Y., Guo, T., Jin, C., Haufler, R.E., Chibante, L.P.F., Fure, J., Wang, L., Alford, J.M., and Smalley, R.E. (1991) Fullerenes with metals inside. *J. Phys. Chem.*, **95**, 7564–7568.
4. Stevenson, S., Rice, G., Glass, T., Harich, K., Cromer, F., Jordan, M.R., Craft, J., Hadju, E., Bible, R., Olmstead, M.M., Maitra, K., Fisher, A.J., Balch, A.L., and Dorn, H.C. (1999) Small-bandgap endohedral metallofullerenes in high yield and purity. *Nature*, **401**, 55–57.
5. Yang, S., Zhang, L., Zhang, W., and Dunsch, L. (2010) A facile route to metal nitride clusterfullerenes by using guanidinium salts: a selective organic solid as the nitrogen source. *Chem. Eur. J.*, **16**, 12398–12405.
6. Mercado, B.Q., Olmstead, M.M., Beavers, C.M., Easterling, M.L., Stevenson, S., Mackey, M.A., Coumbe, C.E., Phillips, J.D., Phillips, J.P., Poblet, J.M., and Balch, A.L. (2010) A seven atom cluster in a carbon cage, the crystallographically determined structure of Sc4([small mu]3-O)3@Ih-C80. *Chem. Commun.*, **46**, 279–281.
7. Chen, N., Chaur, M.N., Moore, C., Pinzon, J.R., Valencia, R., Rodriguez-Fortea, A., Poblet, J.M., and Echegoyen, L. (2010) Synthesis of a new endohedral fullerene family, Sc2S@C2n (n = 40-50) by the introduction of SO2. *Chem. Commun.*, **46**, 4818–4820.
8. Lu, X., Shi, Z.J., Sun, B.Y., He, X.R., and Gu, Z.N. (2005) Isolation and spectroscopic study of a series of monogadolinium endohedral metallofullerenes. *Fullerenes Nanotubes Carbon Nanostruct.*, **13**, 13–20.
9. Feng, L., Sun, B.Y., He, X.R., and Gu, Z.N. (2002) Isolation and spectroscopic study of a series of monoterbium endohedral metallofullerenes. *Fullerenes Nanotubes Carbon Nanostruct.*, **10**, 353–361.
10. Akasaka, T., Okubo, S., Kondo, M., Maeda, Y., Wakahara, T., Kato, T., Suzuki, T., Yamamoto, K., Kobayashi, K., and Nagase, S. (2000) Isolation and characterization of two Pr@C82 isomers. *Chem. Phys. Lett.*, **319**, 153–156.
11. Diener, M.D. and Alford, J.M. (1998) Isolation and properties of small-bandgap fullerenes. *Nature*, **393**, 668–671.
12. Wakahara, T., Nikawa, H., Kikuchi, T., Nakahodo, T., Rahman, G.M.A., Tsuchiya, T., Maeda, Y., Akasaka, T., Yoza, K., Horn, E., Yamamoto, K., Mizorogi, N., Slanina, Z., and Nagase, S. (2006) La@C72 having a non-IPR carbon cage. *J. Am. Chem. Soc.*, **128**, 14228–14229.
13. Nikawa, H., Kikuchi, T., Wakahara, T., Nakahodo, T., Tsuchiya, T., Rahman, G.M.A., Akasaka, T., Maeda, Y., Yoza, K., Horn, E., Yamamoto, K., Mizorogi, N., and Nagase, S. (2005) Missing metallofullerene La@C74. *J. Am. Chem. Soc.*, **127**, 9684–9685.
14. Nikawa, H., Yamada, T., Cao, B.P., Mizorogi, N., Slanina, Z., Tsuchiya, T., Akasaka, T., Yoza, K., and Nagase, S. (2009) Missing metallofullerene with C80 cage. *J. Am. Chem. Soc.*, **131**, 10950–10954.
15. Akasaka, T., Lu, X., Kuga, H., Nikawa, H., Mizorogi, N., Slanina, Z., Tsuchiya, T., Yoza, K., and Nagase, S. (2010) Dichlorophenyl derivatives of La@C3v(7)-C82: endohedral metal induced localization of pyramidalization and spin on a triple-hexagon junction. *Angew. Chem. Int. Ed.*, **49**, 9715–9719.
16. Chaur, M.N., Melin, F., Ashby, J., Elliott, B., Kumbhar, A., Rao, A.M., and Echegoyen, L. (2008) Lanthanum nitride endohedral fullerenes

$La_3N@C_{2n}$ (43 <= n <= 55): preferential formation of $La_3N@C_{96}$. *Chem. Eur. J.*, **14**, 8213–8219.

17. Shinohara, H., Yamaguchi, H., Hayashi, N., Sato, H., Ohkohchi, M., Ando, Y., and Saito, Y. (1993) Isolation and spectroscopic properties of scandium fullerenes (Sc2@C74, Sc2@C82, and Sc2@C84). *J. Phys. Chem.*, **97**, 4259–4261.
18. Klute, R.C., Dorn, H.C., and McNair, H.M. (1992) HPLC separation of higher (C84+) fullerenes. *J. Chromatogr. Sci.*, **30**, 438–442.
19. Meier, M.S. and Selegue, J.P. (1992) Efficient preparative separation of C60 and C70. Gel permeation chromatography of fullerenes using 100% toluene as mobile phase. *J. Org. Chem.*, **57**, 1924–1926.
20. Bolskar, R.D. and Alford, J.M. (2003) Chemical oxidation of endohedral metallofullerenes: identification and separation of distinct classes. *Chem. Commun.*, 1292–1293.
21. Stevenson, S., Harich, K., Yu, H., Stephen, R.R., Heaps, D., Coumbe, C., and Phillips, J.P. (2006) Nonchromatographic "Stir and Filter Approach" (SAFA) for isolating Sc3N@C80 metallofullerenes. *J. Am. Chem. Soc.*, **128**, 8829–8835.
22. Stevenson, S., Mackey, M.A., Coumbe, C.E., Phillips, J.P., Elliott, B., and Echegoyen, L. (2007) Rapid removal of D5h isomer using the "stir and filter approach" and isolation of large quantities of isomerically pure Sc3N@C80 metallic nitride fullerenes. *J. Am. Chem. Soc.*, **129**, 6072–6073.
23. Lu, X., Feng, L., Akasaka, T., and Nagase, S. (2012) Current status and future developments of endohedral metallofullerenes. *Chem. Soc. Rev.*, **41**, 7723–7760.
24. Yamada, M., Someya, C., Wakahara, T., Tsuchiya, T., Maeda, Y., Akasaka, T., Yoza, K., Horn, E., Liu, M.T.H., Mizorogi, O.N., and Nagase, S. (2008) Metal atoms collinear with the spiro carbon of 6,6-open adducts, M2@C80(Ad) (M = La and Ce, Ad = adamantylidene). *J. Am. Chem. Soc.*, **130**, 1171–1176.
25. Xie, Y., Suzuki, M., Cai, W., Mizorogi, N., Nagase, S., Akasaka, T., and Lu, X. (2013) Highly regioselective addition of adamantylidene carbene to Yb@C2v(3)-C80 to afford the first derivative of divalent metallofullerenes. *Angew. Chem. Int. Ed.*, **52**, 5142–5145.
26. Zhang, W., Suzuki, M., Xie, Y., Bao, L., Cai, W., Slanina, Z., Nagase, S., Xu, M., Akasaka, T., and Lu, X. (2013) Molecular structure and chemical property of a divalent metallofullerene Yb@C2(13)-C84. *J. Am. Chem. Soc.*, **135**, 12730–12735.
27. Feng, L., Wakahara, T., Nakahodo, T., Tsuchiya, T., Piao, Q., Maeda, Y., Lian, Y., Akasaka, T., Horn, E., Yoza, K., Kato, T., Mizorogi, N., and Nagase, S. (2006) The Bingel monoadducts of La@C82: synthesis, characterization, and electrochemistry. *Chem. Eur. J.*, **12**, 5578–5586.
28. Yamada, M., Wakahara, T., Nakahodo, T., Tsuchiya, T., Maeda, Y., Akasaka, T., Yoza, K., Horn, E., Mizorogi, N., and Nagase, S. (2006) Synthesis and structural characterization of endohedral pyrrolidinodimetallofullerene: La2@C80(CH2)2NTrt. *J. Am. Chem. Soc.*, **128**, 1402–1403.
29. Akasaka, T., Kato, T., Kobayashi, K., Nagase, S., Yamamoto, K., Funasaka, H., and Takahashi, T. (1995) Exohedral adducts of La@C82. *Nature*, **374**, 600–601.
30. Popov, A.A., Yang, S., and Dunsch, L. (2013) Endohedral fullerenes. *Chem. Rev.*, **113**, 5989–6113.
31. Maeda, Y., Sato, S., Inada, K., Nikawa, H., Yamada, M., Mizorogi, N., Hasegawa, T., Tsuchiya, T., Akasaka, T., Kato, T., Slanina, Z., and Nagase, S. (2010) Regioselective exohedral functionalization of La@C82 and its 1,2,3,4,5-pentamethylcyclopentadiene and adamantylidene adducts. *Chem. Eur. J.*, **16**, 2193–2197.
32. Lu, X., Nikawa, H., Tsuchiya, T., Akasaka, T., Toki, M., Sawa, H., Mizorogi, N., and Nagase, S. (2010) Nitrated benzyne derivatives of La@C82: addition of NO2 and its

positional directing effect on the subsequent addition of benzynes. *Angew. Chem. Int. Ed.*, **49**, 594–597.

33. Takano, Y., Yomogida, A., Nikawa, H., Yamada, M., Wakahara, T., Tsuchiya, T., Ishitsuka, M.O., Maeda, Y., Akasaka, T., Kato, T., Slanina, Z., Mizorogi, N., and Nagase, S. (2008) Radical coupling reaction of paramagnetic endohedral metallofullerene La@C82. *J. Am. Chem. Soc.*, **130**, 16224–16230.

34. Shu, C., Slebodnick, C., Xu, L., Champion, H., Fuhrer, T., Cai, T., Reid, J.E., Fu, W., Harich, K., Dorn, H.C., and Gibson, H.W. (2008) Highly regioselective derivatization of trimetallic nitride templated endohedral metallofullerenes via a facile photochemical reaction. *J. Am. Chem. Soc.*, **130**, 17755–17760.

35. Fang, H., Cong, H., Suzuki, M., Bao, L., Yu, B., Xie, Y., Mizorogi, N., Olmstead, M.M., Balch, A.L., Nagase, S., Akasaka, T., and Lu, X. (2014) Regioselective benzyl radical addition to an open-shell cluster metallofullerene. Crystallographic studies of cocrystallized Sc3C2@Ih-C80 and its singly bonded derivative. *J. Am. Chem. Soc.*, **136**, 10534–10540.

36. Tsuchiya, T., Kurihara, H., Sato, K., Wakahara, T., Akasaka, T., Shimizu, T., Kamigata, N., Mizorogi, N., and Nagase, S. (2006) Supramolecular complexes of La@C82 with unsaturated thiacrown ethers. *Chem. Commun.*, 3585–3587.

37. Tsuchiya, T., Sato, K., Kurihara, H., Wakahara, T., Maeda, Y., Akasaka, T., Ohkubo, K., Fukuzumi, S., Kato, T., and Nagase, S. (2006) Spin-site exchange system constructed from endohedral metallofullerenes and organic donors. *J. Am. Chem. Soc.*, **128**, 14418–14419.

38. Takata, M., Umeda, B., Nishibori, E., Sakata, M., Saito, Y., Ohno, M., and Shinohara, H. (1995) Confirmation by X-ray diffraction of the endohedral nature of the metallofullerene Y@C_{82}. *Nature*, **377**, 46–49.

39. Nishibori, E., Ishihara, M., Takata, M., Sakata, M., Ito, Y., Inoue, T., and Shinohara, H. (2006) Bent (metal)2C2 clusters encapsulated in (Sc2C2)@C82(III) and (Y2C2)@C82(III) metallofullerenes. *Chem. Phys. Lett.*, **433**, 120–124.

40. Nishibori, E., Takata, M., Sakata, M., Inakuma, M., and Shinohara, H. (1998) Determination of the cage structure of Sc@C82 by synchrotron powder diffraction. *Chem. Phys. Lett.*, **298**, 79–84.

41. Nishibori, E., Takata, M., Sakata, M., Tanaka, H., Hasegawa, M., and Shinohara, H. (2000) Giant motion of La atom inside C82 cage. *Chem. Phys. Lett.*, **330**, 497–502.

42. Nishibori, E., Terauchi, I., Sakata, M., Takata, M., Ito, Y., Sugai, T., and Shinohara, H. (2006) High-resolution analysis of (Sc3C2)@C80 metallofullerene by third generation synchrotron radiation X-ray powder diffraction. *J. Phys. Chem. B*, **110**, 19215–19219.

43. Sun, B.Y., Sugai, T., Nishibori, E., Iwata, K., Sakata, M., Takata, M., and Shinohara, H. (2005) An anomalous endohedral structure of Eu@C82 metallofullerenes. *Angew. Chem. Int. Ed.*, **44**, 4568–4571.

44. Tsuchiya, T., Wakahara, T., Maeda, Y., Akasaka, T., Waelchli, M., Kato, T., Okubo, H., Mizorogi, N., Kobayashi, K., and Nagase, S. (2005) 2D NMR characterization of the La@C82 anion. *Angew. Chem. Int. Ed.*, **44**, 3282–3285.

45. Yamada, M., Wakahara, T., Lian, Y.F., Tsuchiya, T., Akasaka, T., Waelchli, M., Mizorogi, N., Nagase, S., and Kadish, K.M. (2006) Analysis of lanthanide-induced NMR shifts of the Ce@C82 anion. *J. Am. Chem. Soc.*, **128**, 1400–1401.

46. Kurihara, H., Lu, X., Iiduka, Y., Mizorogi, N., Slanina, Z., Tsuchiya, T., Akasaka, T., and Nagase, S. (2011) Sc_2C_2@C_{80} rather than Sc_2@C_{82}: templated formation of unexpected $C_{2v}(5)$-C_{80} and temperature-dependent dynamic motion of internal Sc_2C_2 cluster. *J. Am. Chem. Soc.*, **133**, 2382–2385.

47. Lu, X., Nakajima, K., Iiduka, Y., Nikawa, H., Mizorogi, N., Slanina, Z., Tsuchiya, T., Nagase, S., and Akasaka, T. (2011) Structural elucidation and regioselective functionalization of an unexplored carbide cluster metallofullerene

$Sc_2C_2@C_s(6)$-C_{82}. *J. Am. Chem. Soc.*, **133**, 19553–19558.

48. Lu, X., Nakajima, K., Iiduka, Y., Nikawa, H., Tsuchiya, T., Mizorogi, N., Slanina, Z., Nagase, S., and Akasaka, T. (2012) The long-believed $Sc_2@C_{2v}(17)$-C_{84} is actually $Sc_2C_2@C_{2v}(9)$-C_{82}: unambiguous structure assignment and chemical functionalization. *Angew. Chem. Int. Ed.*, **51**, 5889–5892.
49. Iiduka, Y., Wakahara, T., Nakajima, K., Tsuchiya, T., Nakahodo, T., Maeda, Y., Akasaka, T., Mizorogi, N., and Nagase, S. (2006) 13C NMR spectroscopic study of scandium dimetallofullerene, Sc2@C84 vs. Sc2C2@C82. *Chem. Commun. (Camb.)*, 2057–2059.
50. Akasaka, T., Nagase, S., Kobayashi, K., Walchli, M., Yamamoto, K., Funasaka, H., Kako, M., Hoshino, T., and Erata, T. (1997) ^{13}C and ^{139}La NMR studies of $La_2@C_{80}$: first evidence for circular motion of metal atoms in endohedral dimetallofullerenes. *Angew. Chem. Int. Ed. Engl.*, **36**, 1643–1645.
51. Lu, X., Akasaka, T., and Nagase, S. (2013) Carbide cluster metallofullerenes: structure, properties, and possible origin. *Acc. Chem. Res.*, **46**, 1627–1635.
52. Xu, W., Feng, L., Calvaresi, M., Liu, J., Liu, Y., Niu, B., Shi, Z., Lian, Y., and Zerbetto, F. (2013) An experimentally observed trimetallofullerene Sm-3@I-h-C-80: encapsulation of three metal atoms in a cage without a nonmetallic mediator. *J. Am. Chem. Soc.*, **135**, 4187–4190.
53. Kobayashi, K. and Nagase, S. (2002) A stable unconventional structure of Sc2@C66 found by density functional calculations. *Chem. Phys. Lett.*, **362**, 373–379.
54. Lee, H.M., Olmstead, M.M., Suetsuna, T., Shimotani, H., Dragoe, N., Cross, R.J., Kitazawa, K., and Balch, A.L. (2002) Crystallographic characterization of Kr@C60 in (0.09Kr@C60/0.91C60)·{NiII(OEP)}·2C6H6. *Chem. Commun.*, 1352–1353.
55. Che, Y., Yang, H., Wang, Z., Jin, H., Liu, Z., Lu, C., Zuo, T., Dorn, H.C., Beavers, C.M., Olmstead, M.M., and Balch, A.L. (2009) Isolation and structural characterization of two very large, and largely empty, endohedral fullerenes: Tm@C(3v)-C(94) and Ca@C(3v)-C(94). *Inorg. Chem.*, **48**, 6004–6010.
56. Yang, H., Jin, H., Zhen, H., Wang, Z., Liu, Z., Beavers, C.M., Mercado, B.Q., Olmstead, M.M., and Balch, A.L. (2011) Isolation and crystallographic identification of four isomers of Sm@C90. *J. Am. Chem. Soc.*, **133**, 6299–6306.
57. Aoyagi, S., Nishibori, E., Sawa, H., Sugimoto, K., Takata, M., Miyata, Y., Kitaura, R., Shinohara, H., Okada, H., Sakai, T., Ono, Y., Kawachi, K., Yokoo, K., Ono, S., Omote, K., Kasama, Y., Ishikawa, S., Komuro, T., and Tobita, H. (2010) A layered ionic crystal of polar Li@C60 superatoms. *Nat. Chem.*, **2**, 678–683.
58. Hernandez-Eguia, L.P., Escudero-Adan, E.C., Pinzon, J.R., Echegoyen, L., and Ballester, P. (2011) Complexation of Sc3N@C80 endohedral fullerene with cyclic Zn-bisporphyrins: solid state and solution studies. *J. Org. Chem.*, **76**, 3258–3265.
59. Dresselhaus, M.S., Dresselhaus, G., and Jorio, A. (2004) Unusual properties and structure of carbon nanotubes. *Annu. Rev. Mater. Res.*, **34**, 247–278.
60. Iijima, S. (1991) Helical microtubules of graphitic carbon. *Nature*, **354**, 56–58.
61. Iijima, S. and Ichihashi, T. (1993) Single-shell carbon nanotubes of 1-nm diameter. *Nature*, **363**, 603–605.
62. Byrne, M.T. and Gun'ko, Y.K. (2010) Recent advances in research on carbon nanotube-polymer composites. *Adv. Mater.*, **22**, 1672–1688.
63. Spitalsky, Z., Tasis, D., Papagelis, K., and Galiotis, C. (2010) Carbon nanotube-polymer composites: chemistry, processing, mechanical and electrical properties. *Prog. Polym. Sci.*, **35**, 357–401.
64. McCarthy, M.A., Liu, B., Donoghue, E.P., Kravchenko, I., Kim, D.Y., So, F., and Rinzler, A.G. (2011) Low-voltage, low-power, organic light-emitting transistors for active matrix displays. *Science*, **332**, 570–573.
65. Che, Y.C., Chen, H.T., Gui, H., Liu, J., Liu, B.L., and Zhou, C.W. (2014)

Review of carbon nanotube nanoelectronics and macroelectronics. *Semicond. Sci. Technol.*, **29**, 073001.

66. Wilson, N.R. and Macpherson, J.V. (2009) Carbon nanotube tips for atomic force microscopy. *Nat. Nanotechnol.*, **4**, 483–491.
67. Wang, J., Hu, Z., Xu, J.X., and Zhao, Y.L. (2014) Therapeutic applications of low-toxicity spherical nanocarbon materials. *NPG Asia Mater.*, **6**, e84.
68. Bethune, D.S., Kiang, C.H., Devries, M.S., Gorman, G., Savoy, R., Vazquez, J., and Beyers, R. (1993) Cobalt-catalyzed growth of carbon nanotubes with single-atomic-layerwalls. *Nature*, **363**, 605–607.
69. Journet, C., Maser, W.K., Bernier, P., Loiseau, A., de la Chapelle, M.L., Lefrant, S., Deniard, P., Lee, R., and Fischer, J.E. (1997) Large-scale production of single-walled carbon nanotubes by the electric-arc technique. *Nature*, **388**, 756–758.
70. Guo, T., Nikolaev, P., Rinzler, A.G., Tomanek, D., Colbert, D.T., and Smalley, R.E. (1995) Self-assembly of tubular fullerenes. *J. Phys. Chem.*, **99**, 10694–10697.
71. Thess, A., Lee, R., Nikolaev, P., Dai, H.J., Petit, P., Robert, J., Xu, C.H., Lee, Y.H., Kim, S.G., Rinzler, A.G., Colbert, D.T., Scuseria, G.E., Tomanek, D., Fischer, J.E., and Smalley, R.E. (1996) Crystalline ropes of metallic carbon nanotubes. *Science*, **273**, 483–487.
72. Iijima, S., Yudasaka, M., Yamada, R., Bandow, S., Suenaga, K., Kokai, F., and Takahashi, K. (1999) Nano-aggregates of single-walled graphitic carbon nanohorns. *Chem. Phys. Lett.*, **309**, 165–170.
73. Azami, T., Kasuya, D., Yuge, R., Yudasaka, M., Iijima, S., Yoshitake, T., and Kubo, Y. (2008) Large-scale production of single-wall carbon nanohorns with high purity. *J. Phys. Chem. C*, **112**, 1330–1334.
74. Dai, J.Y., Lauerhaas, J.M., Setlur, A.A., and Chang, R.P.H. (1996) Synthesis of carbon-encapsulated nanowires using polycyclic aromatic hydrocarbon precursors. *Chem. Phys. Lett.*, **258**, 547–553.
75. Kong, J., Cassell, A.M., and Dai, H.J. (1998) Chemical vapor deposition of methane for single-walled carbon nanotubes. *Chem. Phys. Lett.*, **292**, 567–574.
76. Li, Y., Liu, J., Wang, Y.Q., and Wang, Z.L. (2001) Preparation of monodispersed Fe-Mo nanoparticles as the catalyst for CVD synthesis of carbon nanotubes. *Chem. Mater.*, **13**, 1008–1014.
77. Zheng, B., Lu, C.G., Gu, G., Makarovski, A., Finkelstein, G., and Liu, J. (2002) Efficient CVD growth of single-walled carbon nanotubes on surfaces using carbon monoxide precursor. *Nano Lett.*, **2**, 895–898.
78. Huang, S.M., Cai, X.Y., and Liu, J. (2003) Growth of millimeter-long and horizontally aligned single-walled carbon nanotubes on flat substrates. *J. Am. Chem. Soc.*, **125**, 5636–5637.
79. Hata, K., Futaba, D.N., Mizuno, K., Namai, T., Yumura, M., and Iijima, S. (2004) Water-assisted highly efficient synthesis of impurity-free single-waited carbon nanotubes. *Science*, **306**, 1362–1364.
80. Liu, Z.F., Jiao, L.Y., Yao, Y.G., Xian, X.J., and Zhang, J. (2010) Aligned, ultralong single-walled carbon nanotubes: from synthesis, sorting, to electronic devices. *Adv. Mater.*, **22**, 2285–2310.
81. Jiang, K.L., Wang, J.P., Li, Q.Q., Liu, L.A., Liu, C.H., and Fan, S.S. (2011) Superaligned carbon nanotube arrays, films, and yarns: a road to applications. *Adv. Mater.*, **23**, 1154–1161.
82. Harutyunyan, A.R., Chen, G.G., Paronyan, T.M., Pigos, E.M., Kuznetsov, O.A., Hewaparakrama, K., Kim, S.M., Zakharov, D., Stach, E.A., and Sumanasekera, G.U. (2009) Preferential growth of single-walled carbon nanotubes with metallic conductivity. *Science*, **326**, 116–120.
83. Wang, H., Wei, L., Ren, F., Wang, Q., Pfefferle, L.D., Haller, G.L., and Chen, Y. (2013) Chiral-selective CoSO4/SiO2 catalyst for (9,8) single-walled carbon nanotube growth. *ACS Nano*, **7**, 614–626.
84. Yang, F., Wang, X., Zhang, D.Q., Yang, J., Luo, D., Xu, Z.W., Wei, J.K., Wang,

J.Q., Xu, Z., Peng, F., Li, X.M., Li, R.M., Li, Y.L., Li, M.H., Bai, X.D., Ding, F., and Li, Y. (2014) Chirality-specific growth of single-walled carbon nanotubes on solid alloy catalysts. *Nature*, **510**, 522524.

85. Tasis, D., Tagmatarchis, N., Bianco, A., and Prato, M. (2006) Chemistry of carbon nanotubes. *Chem. Rev.*, **106**, 1105–1136.
86. Niyogi, S., Hamon, M.A., Hu, H., Zhao, B., Bhowmik, P., Sen, R., Itkis, M.E., and Haddon, R.C. (2002) Chemistry of single-walled carbon nanotubes. *Acc. Chem. Res.*, **35**, 1105–1113.
87. Wenseleers, W., Vlasov, I.I., Goovaerts, E., Obraztsova, E.D., Lobach, A.S., and Bouwen, A. (2004) Efficient isolation and solubilization of pristine single-walled nanotubes in bile salt micelles. *Adv. Funct. Mater.*, **14**, 1105–1112.
88. Gubitosi, M., Trilo, J.V., Vargas, A.A., Pavel, N.V., Gazzoli, D., Sennato, S., Jover, A., Meijide, F., and Galantini, L. (2014) Characterization of carbon nanotube dispersions in solutions of bile salts and derivatives containing aromatic substituents. *J. Phys. Chem. B*, **118**, 1012–1021.
89. Zheng, M., Jagota, A., Semke, E.D., Diner, B.A., Mclean, R.S., Lustig, S.R., Richardson, R.E., and Tassi, N.G. (2003) DNA-assisted dispersion and separation of carbon nanotubes. *Nat. Mater.*, **2**, 338–342.
90. Tu, X.M., Manohar, S., Jagota, A., and Zheng, M. (2009) DNA sequence motifs for structure-specific recognition and separation of carbon nanotubes. *Nature*, **460**, 250–253.
91. Geng, J., Kim, K., Zhang, J.F., Escalada, A., Tunuguntla, R., Comolli, L.R., Allen, F.I., Shnyrova, A.V., Cho, K.R., Munoz, D., Wang, Y.M., Grigoropoulos, C.P., Ajo-Franklin, C.M., Frolov, V.A., and Noy, A. (2014) Stochastic transport through carbon nanotubes in lipid bilayers and live cell membranes. *Nature*, **514**, 612615.
92. Bottini, M., Rosato, N., and Bottini, N. (2011) PEG-modified carbon nanotubes in biomedicine: current status and challenges ahead. *Biomacromolecules*, **12**, 3381–3393.
93. Liu, Z., Tabakman, S.M., Chen, Z., and Dai, H.J. (2009) Preparation of carbon nanotube bioconjugates for biomedical applications. *Nat. Protoc.*, **4**, 1372–1382.
94. Matsumura, S., Sato, S., Yudasaka, M., Tomida, A., Tsruruo, T., Iijima, S., and Shiba, K. (2009) Prevention of carbon nanohorn agglomeration using a conjugate composed of comb-shaped polyethylene glycol and a peptide aptamer. *Mol. Pharmaceutics*, **6**, 441–447.
95. Xu, J.X., Iijima, S., and Yudasaka, M. (2010) Appropriate PEG compounds for dispersion of single wall carbon nanohorns in salted aqueous solution. *Appl. Phys. A*, **99**, 15–21.
96. Suenaga, K., Wakabayashi, H., Koshino, M., Sato, Y., Urita, K., and Iijima, S. (2007) Imaging active topological defects in carbon nanotubes. *Nat. Nanotechnol.*, **2**, 358–360.
97. Suenaga, K. and Koshino, M. (2010) Atom-by-atom spectroscopy at graphene edge. *Nature*, **468**, 1088–1090.
98. Ge, C.C., Du, J.F., Zhao, L.N., Wang, L.M., Liu, Y., Li, D.H., Yang, Y.L., Zhou, R.H., Zhao, Y.L., Chai, Z.F., and Chen, C.Y. (2011) Binding of blood proteins to carbon nanotubes reduces cytotoxicity. *Proc. Natl. Acad. Sci. U.S.A.*, **108**, 16968–16973.
99. Hartschuh, A. (2008) Tip-enhanced near-field optical microscopy. *Angew. Chem. Int. Ed.*, **47**, 8178–8191.
100. Nakayama, T., Kubo, O., Shingaya, Y., Higuchi, S., Hasegawa, T., Jiang, C.S., Okuda, T., Kuwahara, Y., Takami, K., and Aono, M. (2012) Development and application of multiple-probe scanning probe microscopes. *Adv. Mater.*, **24**, 1675–1692.
101. Dresselhaus, M.S., Jorio, A., Hofmann, M., Dresselhaus, G., and Saito, R. (2010) Perspectives on carbon nanotubes and graphene Raman spectroscopy. *Nano Lett.*, **10**, 751–758.
102. Dresselhaus, M.S., Jorio, A., and Saito, R. (2010) Characterizing graphene, graphite, and carbon nanotubes by Raman spectroscopy. *Annu. Rev. Condens. Matter Phys.*, **1**, 89–108.

103. Fagan, J.A., Bauer, B.J., Hobbie, E.K., Becker, M.L., Walker, A.R.H., Simpson, J.R., Chun, J., Obrzut, J., Bajpai, V., Phelan, F.R., Simien, D., Huh, J.Y., and Migler, K.B. (2011) Carbon nanotubes: measuring dispersion and length. *Adv. Mater.*, **23**, 338–348.

104. Geim, A.K. and Novoselov, K.S. (2007) The rise of graphene. *Nat. Mater.*, **6**, 183–191.

105. Castro Neto, A.H., Guinea, F., Peres, N.M.R., Novoselov, K.S., and Geim, A.K. (2009) The electronic properties of graphene. *Rev. Mod. Phys.*, **81**, 109–162.

106. Ni, Z.H., Wang, H.M., Kasim, J., Fan, H.M., Yu, T., Wu, Y.H., Feng, Y.P., and Shen, Z.X. (2007) Graphene thickness determination using reflection and contrast spectroscopy. *Nano Lett.*, **7**, 2758–2763.

107. Ferrari, A.C., Meyer, J.C., Scardaci, V., Casiraghi, C., Lazzeri, M., Mauri, F., Piscanec, S., Jiang, D., Novoselov, K.S., Roth, S., and Geim, A.K. (2006) Raman spectrum of graphene and graphene layers. *Phys. Rev. Lett.*, **97**, 187401.

108. Bolotin, K.I., Sikes, K.J., Jiang, Z., Klima, M., Fudenberg, G., Hone, J., Kim, P., and Stormer, H.L. (2008) Ultrahigh electron mobility in suspended graphene. *Solid State Commun.*, **146**, 351–355.

109. Morozov, S.V., Novoselov, K.S., Katsnelson, M.I., Schedin, F., Elias, D.C., Jaszczak, J.A., and Geim, A.K. (2008) Giant intrinsic carrier mobilities in graphene and its bilayer. *Phys. Rev. Lett.*, **100**, 016602.

110. Lee, C., Wei, X.D., Kysar, J.W., and Hone, J. (2008) Measurement of the elastic properties and intrinsic strength of monolayer graphene. *Science*, **321**, 385–388.

111. Nair, R.R., Blake, P., Grigorenko, A.N., Novoselov, K.S., Booth, T.J., Stauber, T., Peres, N.M.R., and Geim, A.K. (2008) Fine structure constant defines visual transparency of graphene. *Science*, **320**, 1308.

112. Balandin, A.A., Ghosh, S., Bao, W.Z., Calizo, I., Teweldebrhan, D., Miao, F., and Lau, C.N. (2008) Superior thermal conductivity of single-layer graphene. *Nano Lett.*, **8**, 902–907.

113. Novoselov, K.S., Geim, A.K., Morozov, S.V., Jiang, D., Zhang, Y., Dubonos, S.V., Grigorieva, I.V., and Firsov, A.A. (2004) Electric field effect in atomically thin carbon films. *Science*, **306**, 666–669.

114. Zhang, Y.B., Tan, Y.W., Stormer, H.L., and Kim, P. (2005) Experimental observation of the quantum Hall effect and Berry's phase in graphene. *Nature*, **438**, 201–204.

115. Dreyer, D.R., Park, S., Bielawski, C.W., and Ruoff, R.S. (2010) The chemistry of graphene oxide. *Chem. Soc. Rev.*, **39**, 228–240.

116. Zhu, Y.W., Murali, S., Cai, W.W., Li, X.S., Suk, J.W., Potts, J.R., and Ruoff, R.S. (2010) Graphene and graphene oxide: synthesis, properties, and applications. *Adv. Mater.*, **22**, 3906–3924.

117. Lu, X.K., Yu, M.F., Huang, H., and Ruoff, R.S. (1999) Tailoring graphite with the goal of achieving single sheets. *Nanotechnology*, **10**, 269–272.

118. Li, X.S., Cai, W.W., An, J.H., Kim, S., Nah, J., Yang, D.X., Piner, R., Velamakanni, A., Jung, I., Tutuc, E., Banerjee, S.K., Colombo, L., and Ruoff, R.S. (2009) Large-area synthesis of high-quality and uniform graphene films on copper foils. *Science*, **324**, 1312–1314.

119. Kim, K.S., Zhao, Y., Jang, H., Lee, S.Y., Kim, J.M., Kim, K.S., Ahn, J.H., Kim, P., Choi, J.Y., and Hong, B.H. (2009) Large-scale pattern growth of graphene films for stretchable transparent electrodes. *Nature*, **457**, 706–710.

120. Berger, C., Song, Z.M., Li, X.B., Wu, X.S., Brown, N., Naud, C., Mayou, D., Li, T.B., Hass, J., Marchenkov, A.N., Conrad, E.H., First, P.N., and de Heer, W.A. (2006) Electronic confinement and coherence in patterned epitaxial graphene. *Science*, **312**, 1191–1196.

121. Park, S. and Ruoff, R.S. (2009) Chemical methods for the production of graphenes. *Nat. Nanotechnol.*, **4**, 217–224.

122. Ren, W.C. and Cheng, H.M. (2014) The global growth of graphene. *Nat. Nanotechnol.*, **9**, 726–730.

123. Ferrari, A.C. and Basko, D.M. (2013) Raman spectroscopy as a versatile tool for studying the properties of graphene. *Nat. Nanotechnol.*, **8**, 235–246.
124. Georgakilas, V., Otyepka, M., Bourlinos, A.B., Chandra, V., Kim, N., Kemp, K.C., Hobza, P., Zboril, R., and Kim, K.S. (2012) Functionalization of graphene: covalent and non-covalent approaches, derivatives and applications. *Chem. Rev.*, **112**, 6156–6214.
125. Cai, W.W., Piner, R.D., Stadermann, F.J., Park, S., Shaibat, M.A., Ishii, Y., Yang, D.X., Velamakanni, A., An, S.J., Stoller, M., An, J.H., Chen, D.M., and Ruoff, R.S. (2008) Synthesis and solid-state NMR structural characterization of ^{13}C-labeled graphite oxide. *Science*, **321**, 1815–1817.
126. Gao, W., Alemany, L.B., Ci, L.J., and Ajayan, P.M. (2009) New insights into the structure and reduction of graphite oxide. *Nat. Chem.*, **1**, 403–408.
127. Bekyarova, E., Itkis, M.E., Ramesh, P., Berger, C., Sprinkle, M., de Heer, W.A., and Haddon, R.C. (2009) Chemical modification of epitaxial graphene: spontaneous grafting of aryl groups. *J. Am. Chem. Soc.*, **131**, 1336–1337.
128. Liu, H.T., Ryu, S.M., Chen, Z.Y., Steigerwald, M.L., Nuckolls, C., and Brus, L.E. (2009) Photochemical reactivity of graphene. *J. Am. Chem. Soc.*, **131**, 17099–17101.
129. Sofo, J.O., Chaudhari, A.S., and Barber, G.D. (2007) Graphane: a two-dimensional hydrocarbon. *Phys. Rev. B*, **75**, 153401.
130. Boukhvalov, D.W., Katsnelson, M.I., and Lichtenstein, A.I. (2008) Hydrogen on graphene: electronic structure, total energy, structural distortions and magnetism from first-principles calculations. *Phys. Rev. B*, **77**, 035427.
131. Sahin, H., Topsakal, M., and Ciraci, S. (2011) Structures of fluorinated graphene and their signatures. *Phys. Rev. B*, **83**, 115432.
132. Elias, D.C., Nair, R.R., Mohiuddin, T.M.G., Morozov, S.V., Blake, P., Halsall, M.P., Ferrari, A.C., Boukhvalov, D.W., Katsnelson, M.I., Geim, A.K., and Novoselov, K.S. (2009) Control of graphene's properties by reversible hydrogenation: evidence for graphane. *Science*, **323**, 610–613.
133. Nair, R.R., Ren, W.C., Jalil, R., Riaz, I., Kravets, V.G., Britnell, L., Blake, P., Schedin, F., Mayorov, A.S., Yuan, S.J., Katsnelson, M.I., Cheng, H.M., Strupinski, W., Bulusheva, L.G., Okotrub, A.V., Grigorieva, I.V., Grigorenko, A.N., Novoselov, K.S., and Geim, A.K. (2010) Fluorographene: a two-dimensional counterpart of teflon. *Small*, **6**, 2877–2884.
134. Kashtiban, R.J., Dyson, M.A., Nair, R.R., Zan, R., Wong, S.L., Ramasse, Q., Geim, A.K., Bangert, U., and Sloan, J. (2014) Atomically resolved imaging of highly ordered alternating fluorinated graphene. *Nat. Commun.*, **5**, 4902.
135. Zhang, L.M., Lu, Z.X., Zhao, Q.H., Huang, J., Shen, H., and Zhang, Z.J. (2011) Enhanced chemotherapy efficacy by sequential delivery of siRNA and anticancer drugs using PEI-grafted graphene oxide. *Small*, **7**, 460–464.
136. Yang, K., Feng, L.Z., Shi, X.Z., and Liu, Z. (2013) Nano-graphene in biomedicine: theranostic applications. *Chem. Soc. Rev.*, **42**, 530–547.
137. Wang, Y., Li, Z.H., Wang, J., Li, J.H., and Lin, Y.H. (2011) Graphene and graphene oxide: biofunctionalization and applications in biotechnology. *Trends Biotechnol.*, **29**, 205–212.
138. Liu, Z., Robinson, J.T., Sun, X.M., and Dai, H.J. (2008) PEGylated nanographene oxide for delivery of water-insoluble cancer drugs. *J. Am. Chem. Soc.*, **130**, 10876–10877.
139. Zhang, S.A., Yang, K., Feng, L.Z., and Liu, Z. (2011) In vitro and in vivo behaviors of dextran functionalized graphene. *Carbon*, **49**, 4040–4049.
140. Gollavelli, G. and Ling, Y.C. (2012) Multi-functional graphene as an in vitro and in vivo imaging probe. *Biomaterials*, **33**, 2532–2545.

2
Identification and Detection of Carbon Nanomaterials in Biological Systems

Haifang Wang, Zheng-Mei Song, Yi-Fan Yang, Aoneng Cao, and Yuanfang Liu

2.1
Introduction

Along with the discovery of fullerene, carbon nanotubes (CNTs), nanodiamond, and graphene, varied carbon nanomaterials (CNMs) have been extensively synthesized, studied, and produced in vast quantities because their gigantic application potentials in diverse areas such as materials, electronic, sensor, environmental, and biomedical areas [1–3]. For example, in the biomedical field, CNMs have been used as drug delivery carriers, anticancer agents, imaging probes, sensors, and tissue engineering materials [4, 5]. With their extensive applications, CNMs have widely entered our daily lives and been detected in our environments. Consequently, humans have been exposed to CNMs through different pathways, and there is a big chance for CNMs to enter human bodies. Thus, the safety issue of CNMs to humans and the environment has been raised and attracted serious concerns from the academia, government, and society [6–8].

To assess their biosafety, it is indispensable to determine the fate of CNMs in biological systems, that is, identify and quantify CNMs in the systems under different situations. In fact, it is a pretty difficult task because the carbon background in biosystems, especially organisms, is very high compared to the content of exotic CNMs. In addition, a characteristic detecting signal is lacking in many CNMs [9]. Therefore, the detection of CNMs in biosystems is limited by the available techniques. Luckily, several techniques have been developed thanks to the great efforts that have been made in the recent years.

These techniques, including optical microscopic observation, electron microscopic investigation, Raman spectroscopy, fluorescence analysis, and isotopic labeling, have been applied to qualitatively and quantitatively determine CNMs in biological systems. Each technique has its own advantages and disadvantages, and could be used for different purposes. Still, more reliable and sensitive quantification techniques in biosystems are highly demanded.

In this chapter, we introduce currently available techniques employed to investigate CNMs in biological systems. The advantages, applicable situations, and limits

Biomedical Applications and Toxicology of Carbon Nanomaterials, First Edition.
Edited by Chunying Chen and Haifang Wang.

of each technique are summarized and addressed. Finally, a suggested guideline for choosing suitable techniques is proposed.

2.2 Available Techniques for Qualitative and Quantitative Determination

Currently, optical microscopic observation, electron microscopic investigation, Raman spectroscopy, fluorescence analysis, and isotopic labeling are being widely used. All these techniques are suitable for qualitative identification and determination. For quantitative detection, Raman spectroscopy, fluorescence analysis, and isotopic labeling could be adopted. For different CNMs, there will be a most appropriate or best technique. For example, isotope (radioisotope or stable isotope) tracing technique is the most pivotal and efficient for CNTs, while chromatography is best for fullerene. Other methods such as flow cytometry are applicable in specific situations. Here, we provide the detailed information about the techniques one by one in the following sections.

2.2.1 Optical Microscopic Observation

Microscopic observation is widely used in identifying CNMs in biological systems, such as culture media, cells, histological sections, and organs, and is based on the brown to black color of CNMs directly or under the microscope. For example, the high accumulation and aggregation of intratracheally instilled multiwalled carbon nanotubes (MWCNTs) make the direct observation of MWCNTs in lung tissues possible (Figure 2.1a–f) [10]. After intravenous injection, graphene oxide aggregates could also be distinguished from tissues in the lungs and liver by their intrinsic brown to dark color under the optical microscope [11, 12]. At the cell tier, cells become black after exposure to C_{60} and CNTs, indicating the considerable adsorption and uptake of CNTs by the cells [13]. This color change of organs and cells could be easily observed even with naked eyes [10, 13]. Optical microscope also is used to investigate the suspension and aggregation states of CNMs in biological solutions, such as a culture medium (Figure 2.1g,h) [10, 14].

Optical investigation is a very convenient method to determine the entrapment of CNMs in cells, tissues, or organs, but its sensitivity and credibility are low. It works only when our naked eyes can distinguish the color of CNMs from the background. Therefore, it just plays an assistant role and becomes a part of histopathological investigation in most cases. It should be noted that, if in the case of well-dispersed, for example, functionalized single-walled carbon nanotubes (SWCNTs) and single layer graphene, CNMs are in light beige color, or in very low concentration, then optical observation is inapplicable.

In general, based on the color difference, this method is direct and easy for investigating all CNMs, especially for aggregated C_{60}, nanodiamond, CNT, and graphene. The disadvantage is its low sensitivity and reliability.

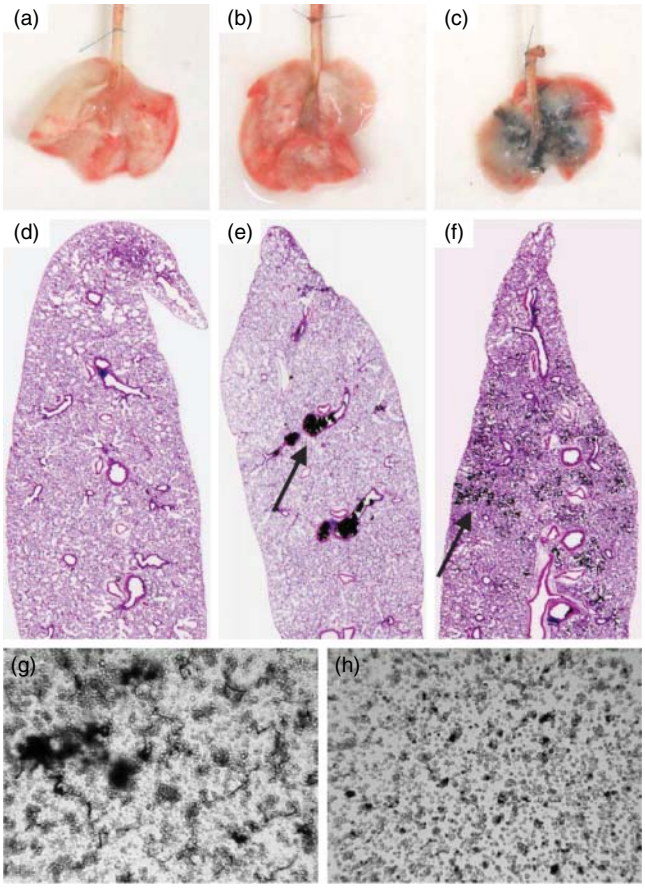

Figure 2.1 Distribution of CNTs in the lungs after intra-tracheal administration. Animals were sacrificed immediately after administration and the lungs were perfused with a saline solution by cannulating the right ventricle. The panels present macroscopic views and hematoxylin and eosin-stained lung sections from saline (a, d), CNT (b, e: 2 mg per rat), or ground CNT (c, f: 2 mg per rat) in rats after intra-tracheal instillation, (g, h) show the typical dispersion of CNT (g) or ground CNT (h) in peritoneal macrophages cultures. (Reproduced with permission from [10]. © 2005 Elsevier Ltd.)

2.2.2 Electron Microscopic (EM) Observation

EM observation is an essential technique in studies of CNMs in biological systems. Transmission electron microscopy (TEM) is a popular method to characterize all CNMs in cells and tissues. In the case of CNTs, they can be easily distinguished from normal biostructures in a TEM observation because of their special one-dimensional structure, no matter whether they are functionalized or not. So does graphene with the special two-dimensional structures. In fact, usually only

aggregates of CNMs in larger sizes can be distinguished under the low resolution of TEM. More intricate and detailed information about CNMs can be obtained with high-resolution TEM. Anyway, TEM is regarded as the most conventional visual method in investigating CNMs in biological systems.

There are two strategies for preparing TEM samples. The first one is to investigate the ultrathin tissue/cell section directly. After exposure to CNMs, cells or tissues are fixed, dehydrated, embedded in resin, sectioned into ultrathin slices, mounted on TEM grids, and then investigated under TEM. If CNTs are found in the ultrathin section, abundant location information will be acquired at the same time, such as the type of cells incorporating CNMs and the distribution pattern at the cellular level. For example, by observing ultrathin liver sections, Deng *et al.* found that MWCNTs were trapped in Kupffer cells and hepatic sinusoids (Figure 2.2b,c) [15]. By using TEM, Ronzani *et al.* revealed the presence of MWCNTs in the mucus layer covering ciliated airway epithelial cells, neutrophils infiltrated in the airway lumen, and type II alveolar epithelial cells [16]. Yuan *et al.* [17] found nanodiamonds in liver macrophage, that is, Kupffer cells, but not in hepatocytes. Kupffer cells phagocytosed nanodiamonds to a large extent, forming phagosomes.

TEM is more reliable and sensitive than optical microscopy. However, the sensitivity is still not high enough and the investigation area is very small. The low concentration of CNMs in tissue/cell and a micro-sized slice make it difficult to identify CNMs when their accumulation level is very low. In such cases, it is impossible to draw a conclusion as to whether any CNM is present in the tissue/cell if no CNM was observed under TEM. In animals, TEM observation of tissue slices is perfect for high accumulation organs such as liver and lungs. Usually, TEM investigation is combined with optical microscopy observations and other techniques to provide more abundant and accurate information.

Besides investigating the original biospecimens under TEM, we also can investigate cells, tissues, or other biological samples after chemical digestion (Figure 2.2d). Although the bioinformation of samples is lost during digestion, this method can enrich, defunctionalize, and aggregate CNMs in biosamples, making the observation of CNMs in much lower concentration or well-dispersed CNMs possible. Yang *et al.* observed PEGylated single-walled carbon nanotubes (PEG-SWCNTs) in the liver by digesting the samples in a $HClO_4/H_2O_2$ mixture in which PEG-SWCNTs are highly dispersed and with a low content [18]. Yuan *et al.* [17] digested liver, lungs, and spleen to confirm the presence of nanodiamond in mice at 28 days post exposure. Another merit of this method is its reliability for any biosamples, for example, blood, urine and feces samples, after proper separation (Figure 2.2e) [15, 19]. These samples contain ample amount of various proteins, salts, and so on, which may interfere with the direct observation. For example, Singh *et al.* [20] applied this method to identify the excretion of CNTs from urine. Detailed experiments for preparing TEM samples of urine and feces can be found in [19].

In general, the TEM technique is more sensitive and reliable than the optical microscopy technique. More information on CNMs in biosamples can be

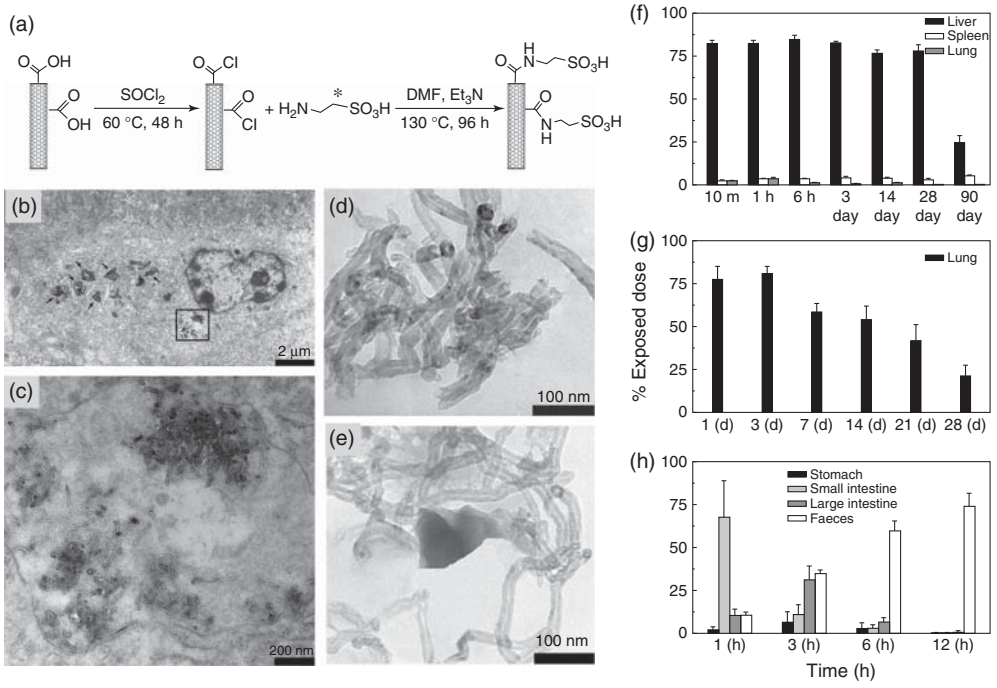

Figure 2.2 Distribution of tau-MWCNTs in mice. (a) synthesis process of ^{14}C-tau-MWCNTs. (b, c) TEM images of liver ultrathin sections from mice exposed to tau-MWCNTs, sacrificed at 7 days post intravenous injection. (b) MWCNTs are trapped in a Kuppfer cell. The black arrows point to the many phagosomes entrapping MWCNTs. (c) A zoom of the rectangular highlighted portion in (b). (d) TEM image of MWCNTs in the digested solution of lungs (d) and feces (e). (f–h) Histograms of distribution versus time post exposure to ^{14}C-tau-MWCNTs by intravenous injection (f), intra-tracheal administration (g), and gavage (h). (Reproduced with permission from [15]. ©2007 Elsevier Ltd.)

obtained, though the investigation area is limited. TEM sample preparation, which is important for getting good results, should be carefully selected and operated. Although this method is qualitative in nature, it is suitable for all CNMs and is a nice complement to quantitative measurements.

2.2.3
Raman Spectroscopic Measurement

The Raman G band is one of the characteristic features of CNTs and graphene. This G band at ~1590 cm^{-1} arises from stretching along the C–C bonds of CNTs and graphene. This intrinsic Raman peak is sensitive and stable, thus helps in identifying CNTs and graphene, generally in a qualitative/semiquantitative way (Figure 2.3a,b) [21, 22]. It does not disappear or quench, and will not diminish under prolonged excitation. In addition, it is relatively insensitive to the surface coating of CNMs and solution environments. Liu *et al.* [21] reported the detection

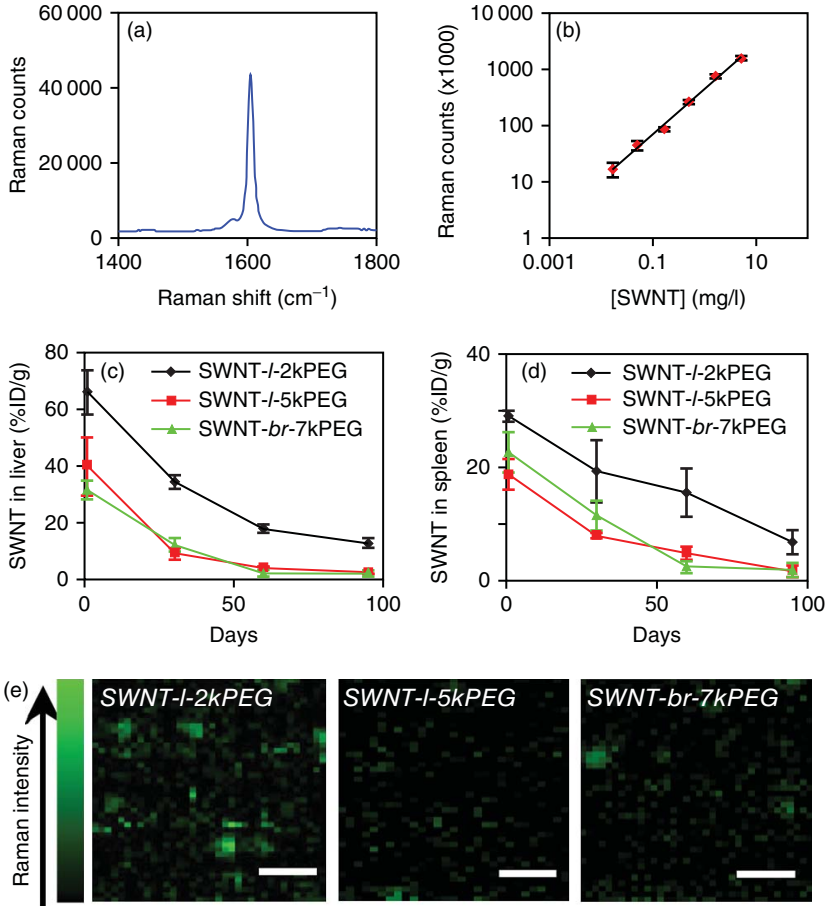

Figure 2.3 SWCNTs in tissues probed by Raman spectroscopy after injection into mice. (a) A Raman spectrum of a solution of SWCNTs-l-2kPEG. The G band peak at 1590 cm^{-1} was used for SWCNT detection. (b) Raman intensity versus SWCNTs concentration calibration curve. Linear dependence is from 0.02 µg per ml. (c and d) Evolution of the concentrations of SWCNTs retained in the liver (b) and spleen (c) of mice over a period of 3 months. (e) Raman mapping images of liver slices from mice treated with SWCNTs at 3 months post injection. l: linear; br: branched; 2k, 5k, and 7k: molecular weight of PEG is 2000, 5000, and 7000, respectively (Reproduced with permission from [21]. ©2008 The National Academy of Sciences, USA.)

of 0.2–0.4 µg g^{-1} wet tissue for SWCNTs in mice (Figure 2.3b). But the G band intensity of graphene oxide is lower by orders of magnitudes compared to that of SWCNTs. The Raman property of SWCNTs wrapped with DNA remains for a long time and has been used to trace SWCNTs (0.22 mg l^{-1}) for over 3 months in live cells [23]. However, the damage to the in-plane C=C bond of CNMs usually reduces the Raman intensity. For example, oxidized SWCNTs show weaker signals

than SWCNT due to damage to the skeletal carbon atom networks in sidewalls from the oxidation process [22]. The distribution, retention, and clearance pathways of SWCNTs in mice have been obtained by measuring SWCNT's specific Raman G band in the 1590–1600 cm^{-1} (Figure 2.3c,d) [21, 24, 25]. It has been used to detect tiny SWCNTs in the liver and spleen at 90 days after a single intravenous injection of 0.4 mg per mouse (Figure 2.3c,d) [21]. For the above Raman spectroscopic studies, the organs/tissues or other biological samples have to be homogenized and solubilized first in suitable buffer solutions.

In addition, the Raman mapping technique allows direct imaging CNTs and graphene in the cells/tissue slides/living animals by plotting the Raman G band intensity (Figure 2.3e) [21]. Raman mapping should be considered as a semiquantitative method because a lower signal can be due to lower levels of CNMs or to increased damage of the carbon hexagon structures [22]. Ladeira *et al.* [26] reported the SWCNT concentration inside the neonatal cardiomyocyte by this method. Schipper *et al.* [22] carried out the Raman mapping of CNTs in liver and spleen sections when they studied PEG-wrapped SWCNTs *in vivo*. Liu *et al.* [27] obtained graphene oxide distribution in lung tissue sections by Raman mapping. In addition, successful noninvasive Raman spectroscopic imaging of CNTs in living mice was tracked for several days [28, 29]. In a step further, Biris *et al.* [30] used time-resolved Raman spectroscopy for *in vivo* real-time detection of circulating CNTs or CNTs in cancer cells in the lymph, blood, and tissues of live animals with very short spectral acquisition times of a few milliseconds. This technique can be used for real-time monitoring of circulating CNTs with simultaneous presence of at least 60 individual CNTs or their small clusters in the laser focal volume.

Besides CNTs and graphene, nanodiamond also possesses a Raman signal. Yuan *et al.* revealed the presence of nanodiamonds in liver, lungs, and spleen with a Raman peak at 1332 cm^{-1} [17]. The sharp and intense peak at 1332 cm^{-1} of nanodiamond arises from the phonon mode of the sp^3-binding carbon. This Raman peak is not affected by the surrounding material and can be used as an indicator of diamond in different organs, but the intensity decreases with decreasing size [31]. Nanodiamond particle size of 50 nm and above can provide a peak clear enough for Raman detection. These indicate that the Raman method is a flexible identification method of CNMs from cell level to living animal level.

The Raman method can be promoted to a semiquantitative method with careful handling. Liu *et al.* measured the blood circulation time of intravenously injected SWCNTs and detected SWCNTs in various tissues of mice by measuring the intensity of the G band [21, 32]. The biosamples usually are homogenized and preseparated to achieve better results. The obtained Raman data were confirmed to be comparable with those by radioisotope labeling method [32].

The Raman spectroscopic method can be treated as a qualitative and semiquantitative label-free method for CNTs, graphene, and nanodiamond with great convenience. The detection limit is closely related to the Raman intensity of CNMs samples, which is affected by defects and by the functionalization of CNMs.

2.2.4 Fluorescence Analysis

2.2.4.1 Intrinsic Fluorescence Analysis

Besides their Raman feature, some CNMs possess intrinsic fluorescence. This can be used to identify and detect CNMs in biosystems.

Intrinsic near-infrared (NIR) fluorescence (900–1600 nm) is a simple and straightforward method for the detection and characterization of the pristine, individualized, semiconducting SWCNTs in biological samples, tissues, and organisms because of the low autofluorescence in the NIR range. Each type of semiconducting SWCNTs has a specific NIR fluorescence that arises only from the individual SWCNTs [33]. Using this method, Cherukuri *et al.* [34] studied the active digestion of SWCNTs by macrophage cells *in vitro*. Later, they observed the distribution of individualized, chemically pristine SWCNT in blood and various tissues of rabbits by measuring their NIR fluorescence intensity and/or mapping tissues (Figure 2.4b–d) [35]. The individualized SWCNTs wrapped with different molecules can be distinguished from the positions and widths of their NIR fluorescence feature (Figure 2.4a). In addition, accurate location of SWCNTs in cells and hepatic sections was displayed by intrinsic NIR fluorescence imaging [34, 35]. This method could also be used to track SWCNTs in living organisms. Leeuw *et al.* [36] first captured the optical images of SWCNTs in a living organism to show peristaltic movements of SWCNTs in the digestive system of *Drosophila* after oral exposure (Figure 2.4e). Welsher *et al.* [37] achieved the whole-animal NIR fluorescence imaging of SWCNTs noncovalently functionalized with phospholipid–polyethylene glycol (PL–PEG).

The NIR fluorescence method has very high sensitivity. It can detect even a single intracellular nanotube. The distribution of SWCNTs in organs of *Drosophila* larvae fed with food containing only 16 $\mu g\, g^{-1}$ SWCNTs was successfully obtained by counting the individual fluorescent nanotubes in selected organs [36]. The *in vivo* NIR fluorescence imaging of SWCNTs at a low dose of 3.4 μg per mouse was achieved after intravenous injection [37]. It should be mentioned again that metallic SWCNTs are invisible in NIR fluorescence. Therefore, to account for all SWCNTs, the obtained data should be corrected by multiplying an estimated factor of 1.5, considering that approximately two-thirds of SWCNTs are electronic semiconductors [36].

This label-free method guarantees that SWCNTs can be traced without worrying about the detachment of the labeling molecules. However, as mentioned previously, only the disaggregated semiconducting SWCNTs possess intrinsic NIR fluorescence. In addition, the conjugation of SWCNTs with other molecules, such as aromatic structured molecules, may quench their NIR fluorescence. Considering the complexity of Biosystems as well as the aggregation tendency of SWCNTs and the mixed types of SWCNTs, this method cannot detect all SWCNTs in biosystems.

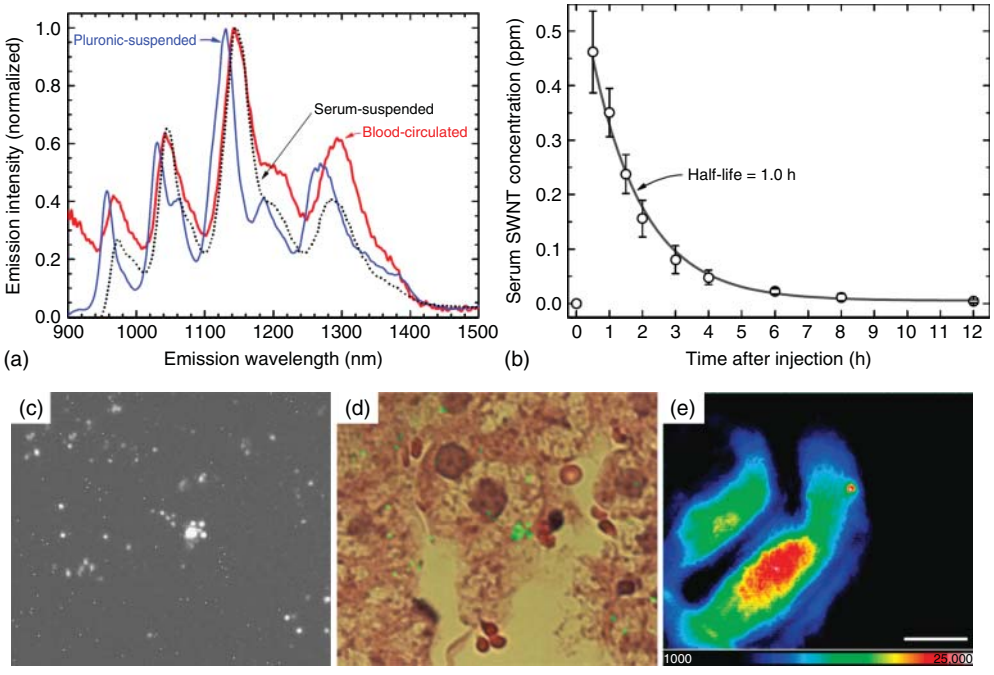

Figure 2.4 SWCNTs in organisms detected with the NIR fluorescence method. (a) Normalized emission spectra (using 658 nm excitation) of samples of SWCNTs prepared as suspensions in aqueous Pluoronic F108 in rabbit serum and in blood serum sampled 30 min after intravenous injection. (b) Time dependence of blood serum SWCNT concentration after injection, as measured for four rabbits. The solid curve is a first-order kinetic fit to the data. (c) NIR SWCNT fluorescence image (field widths of 83 μm) of a 3-μm thick liver specimen slice that had been stained with hematoxylin and eosin. Rabbits exposed to SWCNTs were killed 24 h after intravenous administration. (d) Overlap of (c) and bright-field image of the liver slice. (e) Boluses of food containing SWCNTs in a loop of the gut of a living larva. Scale bar is 100 μm. The larva was fed yeast paste containing 9 $\mu g\, l^{-1}$ SWCNTs. (Reproduced with permission from [35, 36]. ©2006 The National Academy of Sciences, USA and ©2007 American Chemical Society.)

Apart from SWCNTs, carbon dots, nanodiamonds, and graphene dots also possess intrinsic fluorescence property. Their fluorescence can also be used to detect CNMs in biosamples [38–40].

Ruan *et al.* synthesized 120 nm fluorescent carbon nanoparticles (CNPs) with strong blue fluorescence (emission at 424 nm) and a relative quantum yield of 34.2%. By imaging the fluorescence of CNPs, the authors identified the uptake of CNPs in heart cells and mouse heart [38].

Carbon dots usually show strong fluorescence with a quantum yield of 0–0.78 and are stable against photobleaching [39]. By checking their fluorescence, carbon dots could be detected and imaged in cells, tissues, and organisms (Figure 2.5) [41–43].

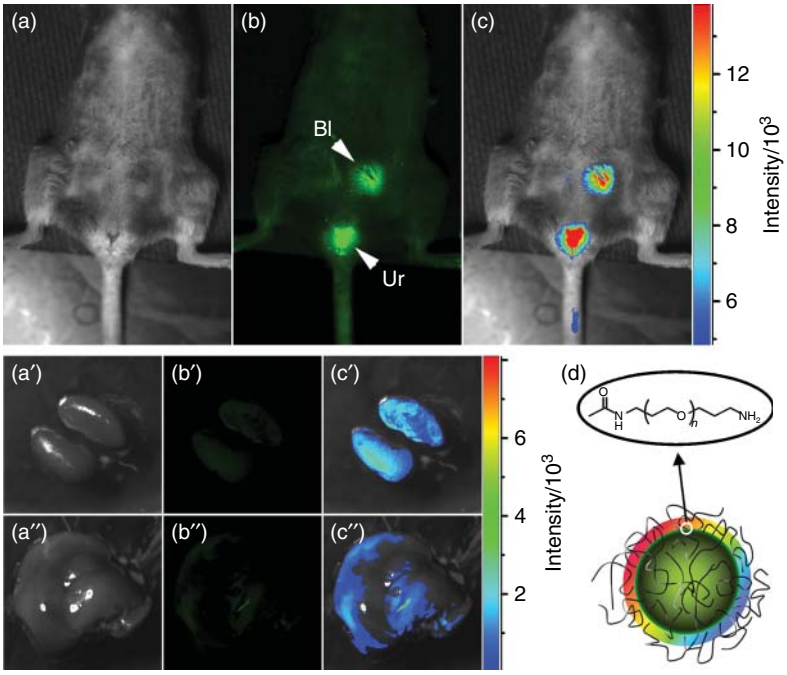

Figure 2.5 Intravenous injection of carbon dots: (a) bright field, (b) as-detected fluorescence (Bl, bladder; Ur, urine), and (c) color-coded images. The same order is used for the images of the dissected kidneys (a′–c′) and liver (a″–c″). (d) Illustration of carbon dots. (Reproduced with permission from [41]. ©2009 The American Chemical Society.)

Some types of nanodiamonds show strong fluorescence at ~700 nm because of point defects within the crystal lattice. The excellent photostability, high brightness, and insensitivity to the environment make long-term, three-dimensional tracking of a single nanodiamond possible [44]. By investigating the fluorescence of individual nanodiamonds for ~10 days after they entered the cells, Liu *et al.* [45] clearly observed the fate of nanodiamonds in the cells; that is, the entrapped nanodiamonds equally separated into two daughter cells during cell division. Moreover, the imaging of nanodiamonds in *Caenorhabditis elegans* was achieved [46]. Carboxylated nanodiamonds emitted green-blue fluorescence, which was strong enough for fluorescence detection of nanodiamonds in biosystems [39].

Nurunnabi *et al.* [47] achieved the quantitative analysis of biodistribution of graphene quantum dots (GQDs) (3–6 nm in diameter) in mice. GQDs have a fluorescence peak at 510 nm. The fluorescence stability of GQDs decreased in aqueous solution with time; therefore, only the short-term distribution of GQDs could be measured. Coating on GQDs may improve their fluorescence stability.

2.2.4.2

Labeled Fluorescence Analysis

For CNMs with weak or no fluorescence, conjugating a fluorophore to CNMs is a popular method for tracing CNMs in biological systems. Popular dyes, such as fluorescein isothiocyanate (FITC), Cy3, and Alexa Fluor, have been attached to SWCNTs or compounds complexed/bound with CNMs for the fluorescence spectrometric, confocal fluorescence microscopic, and flow cytometry measurements [48–50]. In order to trace CNMs *in vivo*, NIR dyes should be chosen such as to improve the emission ability. Huang *et al.* [51] labeled carbon dots with a NIR dye ZW800 to track their *in vivo* fates and tumor uptake after intravenous, subcutaneous, or intramuscular injection. Similarly, Cy7, a commonly used NIR fluorescent dye, was anchored on PEG-functionalized fluorescent graphene dots to reveal semiquantitatively the distribution of graphene dots *in vivo* [52]. Taking advantage of the higher quantum yield and sharper emission spectrum of quantum dots (QDs), Shi *et al.* [53] labeled carbon nanotubes with quantum dots (QD-CNTs). In their work, CdSe/ZnS QDs were covalently linked to the polymer coating functionalized on CNTs. The live *in vivo* images exhibited strong signals of QD-CNTs in the liver, kidneys, stomach, and the intestine in animals at up to 6 days post exposure, which was further confirmed by detecting the Cd content in tissues using inductively coupled plasma mass spectrometry (ICP-MS) [53, 54].

It should be noted that severe or even total fluorescent quenching usually occurs when fluorophores attach directly to the surface of CNTs or graphene, no matter whether they are noncovalently or covalently bound. In order to prevent this, PEG or other reagents have often been used as a spacer/bridge to connect fluorophores and CNMs [55, 56]. This might affect the measurement of CNMs. For example, PEGylation usually changes the pharmacokinetics of CNMs *in vivo*, making their circulation longer in blood. But Jia *et al.* [57] found that the fluorescence property of porphyrin remained after direct conjugation to CNTs. Then they tracked CNTs in animals for over 130 days by checking the fluorescence of the attached porphyrin.

Fluorescence methods are reliable, simple, and sensitive. However, they have disadvantages also. First, fluorescence is sensitive to the environment, including pH, other chemicals, and temperature; therefore, the fluorescence detected may not reflect the real situation of CNMs. Second, labeling with the dye may change the properties of CNMs, or the dye detach during the experiment. It is better to confirm the stability of the label and the properties of CNMs after labeling.

2.2.5

Isotope Labeling Method

Isotope tracing is an effective and indispensable technique in tracking exotic molecules in biological systems. So also it works well in the detection of CNMs; it is applicable for most CNMs. Both radioisotopes and stable isotopes are used.

2.2.5.1

Radioisotope Labeling

Radioisotopes, including ^{125}I, ^{131}I, ^{111}In, ^{86}Y, ^{64}Cu, ^{99m}Tc, ^{67}Ga, ^{188}Re, ^{165}Ho, ^{18}F, and ^{14}C, have been used in CNMs tracing [9, 15, 58–67].

The first strategy of attaching a radioisotope onto CNMs is linking the isotope (mostly I, H, and C) to the surface of CNMs by covalent bonds. For example, Wang *et al.* [9] labeled hydroxylated single-walled carbon nanotubes (SWCNTols) with ^{125}I and reported the distribution of SWCNTols in the organs through different exposure pathways. ^{125}I binds directly and covalently to C on SWCNTs. In addition, the atomic ratio of I to C is $\sim 9/10^{-7}$ or $\sim 9 \times 10^{-7}$, indicating that the high sensitivity and the effect of the label on the properties of SWCNTols is negligible. This I-labeling method can be a general adoptable technique for tracing various CNTs and graphene, for example, taurine covalently functionalized multiwalled carbon nanotubes (tau-MWCNTs), Tween-80 wrapped MWCNTs, nanodiamonds, and graphene oxide [12, 17, 58]. ^{125}I labeling method is simple, reliable, and effective, but suitable for the short-term tracking because the stability of the label is not good. The stability of ^{125}I-graphene oxide in culture media was found to decrease slowly after 6 h, and dropped to 88% after 18 h [12].

To improve the stability, ^{14}C/^{3}H was introduced to trace CNMs by covalently linking a molecule containing the radioisotope onto CNMs. Early in 1995, ^{14}C labeled fullerene had been prepared for *in vivo* distribution study [68]. In 2007, Deng *et al.* linked ^{14}C-taurine onto MWCNTs to study the distribution of soluble taurine-MWCNTs in mice (Figure 2.2a, f–h) [15]. The stability of ^{14}C-taurine-MWCNTs was evidenced by a dialysis experiment on a 6-month-old radioactive sample. ^{3}H-paclitaxel (PTX) was attached to branched PEG functionalized SWCNTs to study the delivery of PTX by SWCNTs in *in vivo* cancer treatment [32]. In comparison, ^{14}C/3H is sensitive and suitable for a long-term tracking.

Labeling CNMs with radioisotopes could also be achieved through chelation with CNMs or through ligands covalently or noncovalently bound to CNMs in advance.

^{99m}Tc, ^{188}Re, and ^{67}Ga have been complexed directly with CNMs. Guo *et al.* [59] reported the distribution of MWCNTs modified with glucosamine (MWCNTs-G) in mice, in which the MWCNTs were labeled with ^{99m}Tc. The authors found that ^{99m}Tc was directly linked to CNTs but the mechanism was not well defined. Similar studies have been performed by using ^{188}Re and ^{67}Ga to label fullerol [62], graphene oxide [65], and nanodiamond [66].

Singh *et al.* first reported the biodistribution of ammonium-functionalized SWCNTs and MWCNTs by ^{111}In tracing (Figure 2.6a). The chelating molecule, Diethylene triamine pentacetate acid (DTPA), was covalently anchored onto CNTs to chelate ^{111}In [20]. The complex reaction is extremely efficient because of the much higher stability constant between DTPA and ^{111}In; and CNTs did not cause any incomplete chelation of ^{111}I. Isotopes ^{111}In, ^{86}Y, and ^{64}Cu have been applied to the study of the biodistribution of CNTs, where the labels have proven very stable during the experimental period by the *in vitro* tests [20, 60, 61, 69, 70]. ^{64}Cu also was used to trace carbon dots *in vivo* by chelating with DOTA

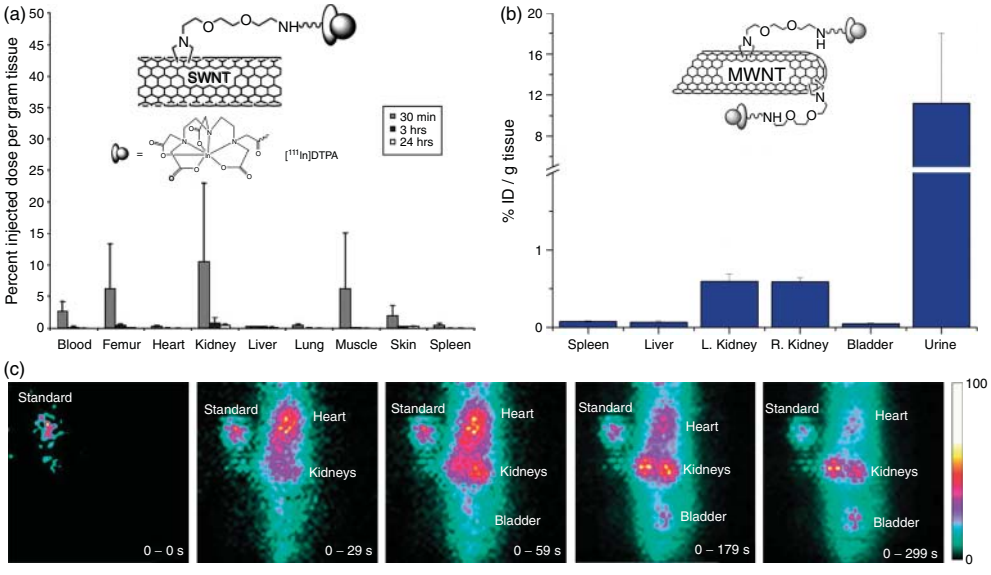

Figure 2.6 Biodistribution of CNTs in mice detected with the radiolabeling method. (a) Biodistribution per collected gram of tissue of [^{111}In]DTPA-SWCNTs after intravenous injection. (b) % ID radioactivity per gram tissue at 24 h after intravenous administration of [^{111}In]DTPA-MWCNTs quantified by gamma counting ($n = 3$). (c) Dynamic anterior planar images of whole-body distribution of [^{111}In]DTPA-MWCNTs within 5 min after intravenous administration in rats. Color scale for radioactivity levels is shown in arbitrary units. (Reproduced with permission from [20, 69]. ©2006 The National Academy of Sciences, USA and ©2008 The Wiley-VCH.)

(1,4,7,10-tetraazacyclododecane-N,N′,N,N′-tetraacetic acid) [51]. The results are comparable with those obtained by detecting fluorescence emitted from a dye (ZW800) attached to carbon dots. This method is flexible and easy to operate. The tracing period depends on the stability of the label.

The radiolabeling methods described above have some shortcomings. The labeling may change the properties of CNMs or detach during the experimental process. For example, PTX attached to PEG-SWCNTs changes the pharmacokinetics and biodistribution of PEG-SWCNTs and PTX may cleave from PEG-SWCNTs *in vivo* [32]. It is necessary to confirm whether the presence of the label changes the *in vivo* fate of CNMs. Valid tracking also relies on the *in vivo* stability of the linking structure.

Radioisotopes could be trapped inside the CNMs, for example, fullerene. Cagle *et al.* [67] using ^{166}Ho inside fullerene to trace the *in vivo* distribution of $C_{82}(OH)_x$. First, $^{165}Ho@C_{82}$ was prepared by arc discharge and was irradiated with a neutron beam to produce $^{166}Ho@C_{82}$. Then, radioactive $^{166}Ho@C_{82}$ was functionalized to $^{166}Ho@C_{82}(OH)_x$ and used for distribution and metabolism study. Application of this method is quite limited, because the synthesis and the following purification are not very easy. The labeling does not influence the surface properties of CNMs in biosystems.

The last method is to label the skeleton of CNMs. In 1996, Bullard-Dillard *et al.* [71] synthesized ^{14}C-labeled C_{60} and functionalized it to a more water-soluble quaternary ammonium salt-derivatized C_{60}. By measuring the activity of ^{14}C, the behaviors, including the distribution and metabolism of two C_{60} samples in cells and rats, were investigated and compared. Petersen *et al.* accurately traced the uptake of CNTs by the earthworms *Eisenia foetida*, *Daphnia magna*, and *Lumbriculus variegatus* using ^{14}C skeleton labeling [72–74]. ^{14}C-SWCNTs and ^{14}C-MWCNTs were synthesized from ^{14}C-labeled methane by a chemical vapor deposition process. The problem is that the whole procedure of synthesis, detection, and waste treatment is quite arduous and expensive. That is why such a good labeling method is not widely used in related studies.

The superiority of skeleton ^{14}C labeling are obvious. First, skeleton labeling keeps the original nature of CNTs intact because of the same chemical properties of ^{14}C and ^{12}C. Second, we need not worry about the detachment of labeled isotopes from CNMs during the experiments. Therefore, the results obtained from skeleton labels are more reliable than those from attaching radioisotopes to CNTs in long-term biodistribution studies. But, the big trouble is the synthesis, considering the requirement for the operation with radioactive material and radioactive waste disposal.

Based on the relationship between radioactivity and the CNM quality, we obtained the fate information of CNMs in the biological systems by measuring the radioactivity of the label. Generally, there are two methods for the detection of radiolabeled CNMs. One is the radioactivity measurement, and the other is radioimaging.

The main procedure is collecting biosamples to detect their radioactivity taken up by the cells/animals. ^{125}I, ^{111}In, ^{99m}Tc, ^{66}Ga, ^{188}Re, ^{166}Ho, and ^{64}Cu are all γ-emitting radioisotopes and can be measured by a γ-counter directly without complicated pretreatments. ^{14}C and ^{3}H emit β-rays and can be measured by a liquid scintillation counter with high sensitivity. However, biosamples have to go through a complicated digestion or combustion process according to the detection requirement. Eventually, quantitative values of the percentage injected dose (%ID) in tissue or percentage injected dose per gram wet tissue (%ID/g tissue) can be achieved.

Radiological imaging, including positron emission computed tomography (PECT or PET) and single-photon emission computerized tomography (SPECT), provides noninvasive and real-time images of the experimental objects.

PET is used to measure the positron (β^+)-emitting radionuclides. After the positron emitted is annihilated, a pair of gamma photons (0.511 MeV) is emitted and recorded by the PET system. Finally, a three-dimensional image is reconstructed on a series of two-dimensional tomographs of the radioisotope distribution *in vivo*. ^{64}Cu, ^{86}Y, ^{66}Ga, and ^{18}F have been used in PET for the measurement of CNTs [60, 70]. ^{64}Cu chelated to DOTA also was used to dynamically image C-dots *in vivo* [51] to confirm the distribution data obtained by the fluorescence method. ^{66}Ga coordinated to NOTA (1, 4, 7-triazacyclononane-N, N′, N′′triacetic acid) was attached to nanographene for PET measurement of

graphene in tumor vasculature, providing the quantitative data of the graphene uptake [75]. By means of scanning with SPECT, a panoramic image of radioisotope in body is achieved. Lacerda *et al.* [69] reported the dynamic accumulation of [^{111}In]DTPA-MWCNTs in a rat within 5 min after injection by micro-SPECT (Figure 2.6c), which supported that MWCNTs were eliminated through urine (Figure 2.6b). PET provides clearer and more quantitative images, while SPECT is more easily available and inexpensive in clinical and experimental studies.

2.2.5.2 Stable Isotope Labeling

The stable isotope ^{13}C has been used to label CNMs such as C_{60}, CNTs, and carbon particles. Usually, ^{13}C is introduced to CNMs during the preparation procedure of CNMs. After exposure to CNMs, the biosamples are collected, homogenized, and lyophilized for ^{13}C measurements (Figure 2.7a) [18, 76–78]. ^{13}C is quantified by measuring the stable isotopic abundance (^{13}C/^{12}C ratio) using isotope ratio mass spectrometry (IRMS). Yang *et al.* [18, 77] reported the biodistribution of pristine SWCNTs and PEGylated SWCNTs (PEG-SWCNTs) by using skeleton ^{13}C-labeling technique, where the experimental details were given. Using the ^{13}C-labeling technique, the biodistributions of carbon particle and of CNTs were compared [78]. Recently, Chang *et al.* [76] synthesized ^{13}C-enriched fullerene by the arc discharge method, purified it by high-performance liquid chromatography (HPLC), and then measured its distribution in mice after intravenous injection (Figure 2.7).

The distinct superiority of skeleton ^{13}C labeling is the same as that of skeleton ^{14}C labeling. In addition, compared with ^{14}C, ^{13}C is a stable isotope, thus avoiding the troublesome radioactivity operation and special radioactive waste disposal. It can be used in any common laboratory. The disadvantage is that its sensitivity is much lower than that of ^{14}C labeling, and therefore is not suitable for CNMs with very low concentrations in biosystems.

2.2.5.3 Tips for Isotopic Labeling

Selecting a suitable isotope is a key step to achieving a successful distribution study. The experiment time scale, sensitivity, and stability of the tracer, experimental conditions, and waste handling should be considered in advance. The pros and cons of various isotopic labeling methods for CNTs and gave suggestions have been summarized [79]. The suggested guidelines may be applied to all CNMs studies.

Briefly, for short-term (a few days) tracing, almost all isotopes are eligible. Considering the sensitivity and the ease of labeling and sampling, the isotopes with a short half-life and emitting γ-photon are first recommended, especially ^{125}I.

For the long-term tracing studies, the isotopes with longer half-life and higher labeling stability, that is, ^{13}C, ^{14}C, and ^{3}H, are needed. ^{14}C or ^{3}H labeling has a

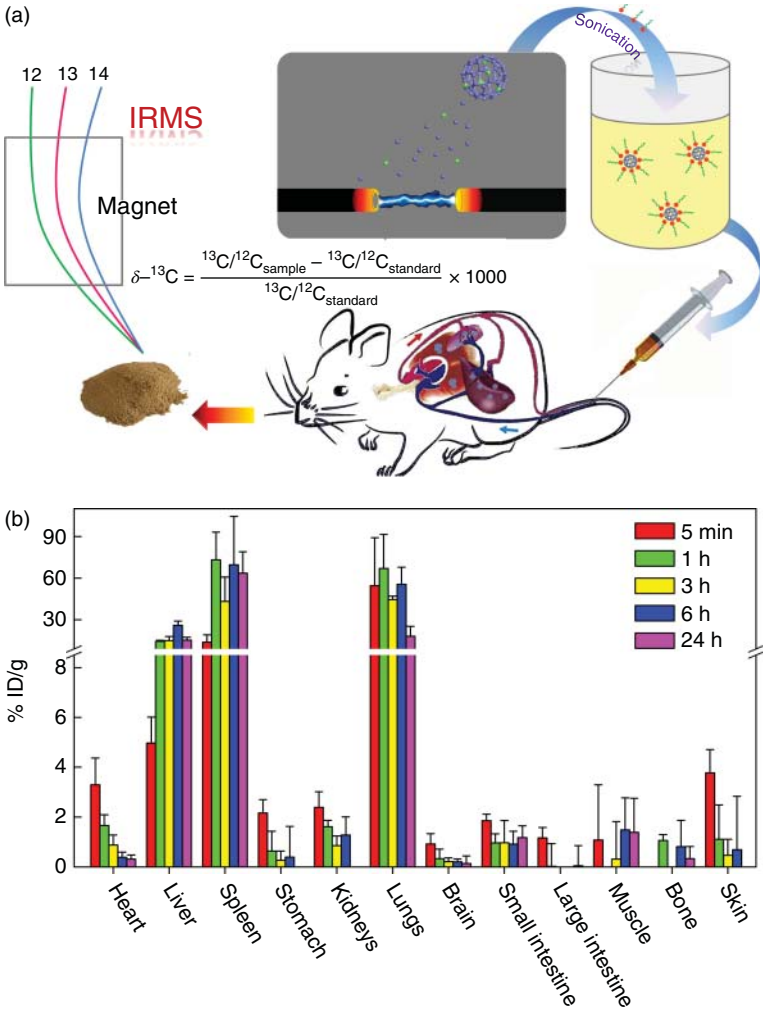

Figure 2.7 Detection of C_{60} *in vivo* by ^{13}C-labeling method. (a) Schematic illustration of experimental design. (b) Biodistribution of ^{13}C-enriched C_{60} in mice after intravenous administration ($n = 4$). (Reproduced with permission from [76]. ©2014, The Royal Society of Chemistry.)

high sensitivity, but sampling and radioactive waste handling are quite laborious; ^{13}C labeling is reliable and easy, but its detection sensitivity is low.

A combination of labeling with different isotopes is encouraged: for instance, labeling CNMs with both stable ^{13}C and radioactive ^{125}I for long-term and short-term studies, respectively. Skeleton and functional groups of CNMs could be double labeled with different isotopes for simultaneously tracing CNM derivatives.

2.2.6 Chromatographic Technique

Liquid chromatography-mass spectrometry (LC- MS) combined with toluene extraction has been used to quantify C_{60} in biological samples [80–82]. The determination limit of these methods is $1.1\,\mu g\,g^{-1}$ tissue [81], which is even better than with radioisotopic analysis. Shinohara *et al.* developed a highly sensitive method for the analysis of C_{60} in biological samples, with a detection limit of $8.9\,ng\,g^{-1}$ tissue [83]. They determined C_{60} in the organs of a rat with high-performance liquid chromatography (HPLC)-ultraviolet (UV) detection, combined with a procedure of extraction from tissue sample and concentration of C_{60} in the extracted solution [83]. In addition, $C_{60}O$, a metabolic product of C_{60}, was identified, indicating the method is applicable for studying the *in vivo* metabolism of C_{60}.

This method is very sensitive for C_{60}. However, the extraction process is very crucial to determine the recovery of C_{60} from the biosamples and the following chromatographic measurement. For example, the aggregation of C_{60} makes the low detectable content of C_{60} inaccurate and produces unknown peaks in the chromatogram. Chromatographic techniques are inapplicable for most CNMs because of the polydisperse nature of CNTs, graphenes, and other CNMs. Regardless of the synthesis procedure employed, nanotubes and graphenes vary widely in size.

2.2.7 Flow Cytometry Method

Flow cytometry is a technique widely used in the field of biology to detect cells by measuring their fluorescence. Besides, in a light-scatter analysis, when a laser beam illuminates each cell, it generates a forward scatter signal (FSC) and side scatter signal (SSC). SSC depends on the intracellular complexity of the cell such as the membrane roughness, the shape of the nucleus, and the amount of cytoplasmic granules, reflecting the inner density of cells. The presence of CNMs in cells and on cell membranes alters SSC, which could be quantitatively measured by flow cytometry. In 2007, Suzuki *et al.* first introduced cytometry to qualitatively analyze the incorporation of TiO_2 NPs into cells using the SSC intensity [84]. Later, this method was applied to measure the level of CNMs in cells, where the SSC level was proportional to the amount of CNTs in cells [85, 86]. In addition, this method could be used to measure CNM aggregates in biosystems. Changes of the suspension state of CNMs change the diffraction and scattering of laser light, thereby causing an altered population distribution in the FSC–SSC planes. Liu *et al.* [12] measured the size and number of graphene oxide aggregates in serum by this technique. They found that the size of graphene oxide in serum increased with increasing graphene oxide concentration.

2.2.8 Other Methods

In raw CNTs, there are always some metal impurities, such as Ni, Co, and Fe, which are introduced into CNTs during their production process. Taking advantage of their high stability, the metal impurities have been used to quantify purified CNTs in the animals. Muller *et al.* [10] determined the content of MWCNTs in tissues by measuring the Co content in the tissue digestion solution using an atomic absorption spectrometer. The results were reliable because only 5% Co was released during the 60 days of incubation of MWCNTs in the physiological saline in the *in vitro* culture. Later, Ge *et al.* [87] developed a quantification method for detecting metal impurities in CNTs by using ICP-MS and neutron activation analysis. By measuring Cd content in QDs attached to CNTs using ICP-MS, Guo *et al.* gave the *in vivo* distribution of CNT-QDs in various organs of live animals [54]. Wang *et al.* [88] obtained the distribution of $Gd@C_{82}(OH)_{22}$ in mice by measuring the Gd content in biosamples by ICP-MS. The detection limit of Gd was 1.47 pg ml^{-1}.

Determination of nanodiamond/CNT contents in tissues can be achieved by UV–vis spectrometry. Yuan *et al.* found that the absorbance of nanodiamonds at 350 nm in water was linear with concentration from 0 to 20 μg ml^{-1}. This provides a method for quantifying the concentration of nanodiamonds in tissues [17]. After careful digestion and dialysis, the absorbance of suspended NDs was measured and the content was calculated referring to the standard curve of absorbance versus CNM concentration for the animal samples. This method detected the distribution of nanodiamonds in the liver and lungs of mice at 28 days post exposure. This method was also used to detect taur-MWCNTs, and the results were well comparable to those obtained with the radiolabeling method [15]. Many CNMs well dispersed in solution could be detected using this method; however, the sensitivity is not satisfactory enough.

The photoacoustic signal from SWCNTs allows high spatial resolution and deep tissue imaging. Highly intense photoacoustic signals are acquired at the wavelength of 690 nm, at which the human tissues and biological fluids are practically transparent. La Zerda *et al.* [89] found that photoacoustic imaging of SWCNTs could offer better spatial resolution and sensitivity than optical imaging. Quantitatively, the photoacoustic signal of RGD-PEG_{5000}-PL/SWCNTs (RGD, cyclic Arg-Gly-Asp, a tumor-targeting peptide) was comparable to the results from the Raman imaging. Later, Chen *et al.* imaged the accumulation of poly(maleic anhydride-*alt*-1-octadecene-PEG)-modified SWCNTs in tumors in mice [90].

Optoacoustic tomography (OAT) is an emerging imaging technology that utilizes ultrasound generated by the absorption of nanosecond-scale laser pulses to re-create an image of the absorbing volume based on the spatial variation of optical absorption (intrinsic optical absorption and fluorescence for SWCNTs) coefficients [91]. This imaging modality is capable of revealing internal organs and vasculature in three dimensions at depths of several centimeters and resolutions

of 500 μm or less. OAT has been used to image SWCNTs in living mice [91]. By calculating the intensity of the OA signals, the quantitative distribution data of SWCNTs was obtained. This method is not particularly sensitive to nanotube aggregation and largely interfered by the SWCNT coating. The surface derivatization or structural damage results in strong quenching of SWCNT fluorescence but little change in SWCNT absorption.

Doudrick *et al.* [92] also reported that CNTs could be quantified in biosamples using programmed thermal analysis (PTA), an analytical method that relies on the unique thermal stability of CNTs. But the extraction of CNTs from biological matrices is a prerequisite for this method. The major challenge was dissolving the matrix carbon while keeping the CNTs intact; thus the authors could get the accurate CNT content in biological matrices. A final two-step extraction method was developed to keep the CNTs remain intact and to remove all interfering carbon. The extraction of 2.9 μg of CNTs from rat lungs was efficient, with a recovery of 98%. The PTA instrument detection limit for carbon mass is ~200 ng.

Bourdiol *et al.* [93] developed a quantitative detection method for CNTs in biological samples by an original method based on microwave permittivity measurements, taking advantage of the intrinsic high conductivity of CNTs at microwaves frequencies. They employed the developed technique and devices to examine the double-walled carbon nanotubes (DWCNTs) in amphibian *Xenopus laevis* larvae and validated the results by quantification of the impurities (Co and Mo) existing in DWCNTs with classical chemical analysis. They showed a detection threshold of 0.02 μg of DWCNTs in the sensing area, that is, 15 μg DWCNTs per milligram dry sample, which is the lowest threshold reported in the literature to date.

2.3 Summary and Outlook

The importance of the identification and detection of CNMs in biosystems goes without saying. And their accurate identification and detection rely on the related techniques. In this chapter, currently available techniques in identifying and detecting CNMs in biosystems were introduced and summarized. We listed the merits and demerits of each technique, as well as provided the application scope with examples.

Generally, no technique is perfect and solves the all detection problems. Each technique has its own advantages and can be used for proper objects. The identification and detection of CNMs in biosystems can be successful by combining different and suitable techniques together. In addition, the obtained information of CNMs in biosystems using one technique can be confirmed by another technique when more than one technique is applied for the same purpose [17, 25, 32].

Briefly, qualitative techniques, such as optical microscopic investigation and TEM observation, should be combined with quantitative techniques such as fluorescence analysis and isotopic labeling. Then, one can obtain a precise picture of CNMs in certain biosystems, from qualitative investigation to quantitative

measurement. The qualitative investigation is straightforward knowledge, and the quantitative measurement provides the accurate information.

To make sure that the quantitative measurement is correct, sometimes more than one technique should be adopted. For example, Huang *et al.* studied the distribution of carbon dots in mice by attaching an NIR dye onto carbon dots; meanwhile, they also labeled carbon dots with ^{64}Cu to visualize and quantify the distribution of carbon dots by PET [51]. Liu *et al.* [32] compared the distributions of ^{3}H-PTX-SWCNT in mice after intravenous injection by measuring SWCNT with Raman method and PTX with radioisotope labeling. It was found that the distribution profiles obtained by different methods were slightly different. The accumulation of PTX in most tissues was less than that of SWCNTs. They assumed that PTX was partially released from SWCNTs because of the cleavage of ester bond *in vivo*.

At present, accurate detection of CNMs in biosystems still is a challenge for most CNMs. First, the detection limit of the currently available analytical methods is not sufficiently high, considering CNM concentration in biosystems usually is extremely low and studies are often made after exposing to CNMs with environmental doses. Second, most detection techniques are not able to distinguish CNMs from background carbon. However, intrinsic properties of CNTs and graphene, such as Raman signal and NIR fluorescence signal, could be used to distinguish CNMs from the large background carbon. It is highly desirable to detect CNMs based on their intrinsic physical properties. Third, most techniques cannot detect CNMs *in situ* at real time, except by some imaging techniques. The changes in the properties of CNMs may alter with time and location in the bioenvironment, which consequently affect their final fate.

Therefore, we hope that the detection of CNMs will be performed specifically *in situ* and in real time with satisfactorily high sensitivity in the future. The development of such techniques certainly will accelerate our understanding of CNMs in biosystems.

Acknowledgments

We thank the National Basic Research Program of China (973 Program) (No. 2011CB933402) and the Chinese Natural Science Foundation (No. 21371117) for financial support.

References

1. Jariwala, D., Sangwan, V.K., Lauhon, L.J., Marks, T.J., and Hersam, M.C. (2013) Carbon nanomaterials for electronics, optoelectronics, photovoltaics, and sensing. *Chem. Soc. Rev.*, **42** (7), 2824–2860.
2. Mauter, M.S., and Elimelech, M. (2008) Environmental applications of carbon-based nanomaterials. *Environ. Sci. Technol.*, **42** (16), 5843–5859.
3. De Volder, M.F.L., Tawfick, S.H., Baughman, R.H., and John Hart, A.

(2013) Carbon nanotubes: present and future commercial applications. *Science*, **339** (6119), 535–539.
4. Kostarelos, K., Bianco, A., and Prato, M. (2009) Promises, facts and challenges for carbon nanotubes in imaging and therapeutics. *Nat. Nanotechnol.*, **4**, 627–633.
5. Fraczek-Szczypta, A. (2014) Carbon nanomaterials for nerve tissue stimulation and regeneration. *Mater. Sci. Eng., C*, **34**, 35–49.
6. Kipen, H.M., and Laskin, D.L. (2005) Smaller is not always better: nanotechnology yields nanotoxicology. *Am. J. Physiol. Lung Cell. Mol. Physiol.*, **289** (5), L696–L697.
7. Dreher, K.L. (2004) Health and environmental impact of nanotechnology: toxicological assessment of manufactured nanoparticles. *Toxicol. Sci.*, **77** (1), 3–5.
8. Hoet, P.H.M., Bruske-Hohlfeld, I., and Salata, O.V. (2004) Nanoparticles – known and unknown health risks. *J. Nanobiotechnol.*, **2**, 12 (15 pp).
9. Wang, H., Wang, J., Deng, X., Sun, H., Shi, Z., Gu, Z., Liu, Y., and Zhao, Y. (2004) Biodistribution of single-wall carbon nanotubes in mice. *J. Nanosci. Nanotechnol.*, **4** (8), 1019–1024.
10. Muller, J., Huaux, F., Moreau, N., Misson, P., Heilier, J.-F., Delos, M., Arras, M., Fonseca, A., Nagy, J.B., and Lison, D. (2005) Respiratory toxicity of multi-wall carbon nanotubes. *Toxicol. Appl. Pharmacol.*, **207** (3), 221–231.
11. Qu, G., Wang, X., Liu, Q., Liu, R., Yin, N., Ma, J., Chen, L., He, J., Liu, S., and Jiang, G. (2013) The ex vivo and *in vivo* biological performances of graphene oxide and the impact of surfactant on graphene oxide's biocompatibility. *J. Environ. Sci.-China*, **25** (5), 873–881.
12. Liu, J.-H., Yang, S.-T., Wang, H., Chang, Y., Cao, A., and Liu, Y. (2012) Effect of size and dose on the biodistribution of graphene oxide in mice. *Nanomedicine*, **7** (12), 1801–1812.
13. Jia, G., Wang, H., Yan, L., Wang, X., Pei, R., Yan, T., Zhao, Y., and Guo, X. (2005) Cytotoxicity of carbon nanomaterials: single-wall nanotube, multi-wall nanotube, and fullerene. *Environ. Sci. Technol.*, **39** (5), 1378–1383.
14. Wang, H., Gu, L., Lin, Y., Lu, F., Meziani, M.J., Luo, P.G., Wang, W., Cao, L., and Sun, Y.-P. (2006) Unique aggregation of anthrax (*Bacillus anthracis*) spores by sugar-coated single-walled carbon nanotubes. *J. Am. Chem. Soc.*, **128** (41), 13364–13365.
15. Deng, X., Jia, G., Wang, H., Sun, H., Wang, X., Yang, S., Wang, T., and Liu, Y. (2007) Translocation and fate of multi-walled carbon nanotubes *in vivo*. *Carbon*, **45** (7), 1419–1424.
16. Ronzani, C., Spiegelhalter, C., Vonesch, J.-L., Lebeau, L., and Pons, F. (2012) Lung deposition and toxicological responses evoked by multi-walled carbon nanotubes dispersed in a synthetic lung surfactant in the mouse. *Arch. Toxicol.*, **86** (1), 137–149.
17. Yuan, Y., Chen, Y., Liu, J.-H., Wang, H., and Liu, Y. (2009) Biodistribution and fate of nanodiamonds *in vivo*. *Diamond Relat. Mater.*, **18** (1), 95–100.
18. Yang, S.-T., Fernando, K.A.S., Liu, J.-H., Wang, J., Sun, H., Liu, Y., Chen, M., Huang, Y., Wang, X., Wang, H., and Sun, Y.-P. (2008) Covalently PEGylated carbon nanotubes with stealth character *in vivo*. *Small*, **4** (7), 940–944.
19. Kolosnjaj-Tabi, J., Hartman, K.B., Boudjemaa, S., Ananta, J.S., Morgant, G., Szwarc, H., Wilson, L.J., and Moussa, F. (2010) *In vivo* behavior of large doses of ultrashort and full-length single-walled carbon nanotubes after oral and intraperitoneal administration to Swiss mice. *ACS Nano*, **4** (3), 1481–1492.
20. Singh, R., Pantarotto, D., Lacerda, L., Pastorin, G., Klumpp, C., Prato, M., Bianco, A., and Kostarelos, K. (2006) Tissue biodistribution and blood clearance rates of intravenously administered carbon nanotube radiotracers. *Proc. Natl. Acad. Sci. U.S.A.*, **103** (9), 3357–3362.
21. Liu, Z., Davis, C., Cai, W., He, L., Chen, X., and Dai, H. (2008) Circulation and long-term fate of functionalized, biocompatible single-walled carbon nanotubes in mice probed by Raman spectroscopy. *Proc. Natl. Acad. Sci. U.S.A.*, **105** (5), 1410–1415.
22. Schipper, M.L., Nakayama-Ratchford, N., Davis, C.R., Kam, N.W.S., Chu, P.,

Liu, Z., Sun, X., Dai, H., and Gambhir, S.S. (2008) A pilot toxicology study of single-walled carbon nanotubes in a small sample of mice. *Nat. Nanotechnol.*, **3** (4), 216–221.

23. Heller, D.A., Baik, S., Eurell, T.E., and Strano, M.S. (2005) Single-walled carbon nanotube spectroscopy in live cells: towards long-term labels and optical sensors. *Adv. Mater.*, **17** (23), 2793–2799.
24. Bhirde, A.A., Patel, S., Sousa, A.A., Patel, V., Molinolo, A.A., Ji, Y., Leapman, R.D., Gutkind, J.S., and Rusling, J.F. (2010) Distribution and clearance of PEG-single-walled carbon nanotube cancer drug delivery vehicles in mice. *Nanomedicine*, **5** (10), 1535–1546.
25. Yang, S.-T., Wang, X., Jia, G., Gu, Y., Wang, T., Nie, H.-Y., Ge, C., Wang, H., and Liu, Y. (2008) Long-term accumulation and low toxicity of single-walled carbon nanotubes in intravenously exposed mice. *Toxicol. Lett.*, **181** (3), 182–189.
26. Ladeira, M.S., Andrade, V.A., Gomes, E.R.M., Aguiar, C.J., Moraes, E.R., Soares, J.S., Silva, E.E., Lacerda, R.G., Ladeira, L.O., Jorio, A., Lima, P., Fatima Leite, M., Resende, R.R., and Guatimosim, S. (2010) Highly efficient siRNA delivery system into human and murine cells using single-wall carbon nanotubes. *Nanotechnology*, **21** (38), 385101.
27. Liu, J.-H., Wang, T., Wang, H., Gu, Y., Xu, Y., Tang, H., Jia, G., and Liu, Y. (2015) Biocompatibility of graphene oxide post intravenously administrated in mice-effects of dose, size and exposure protocol. *Toxicol. Res.*, **4**, 83–91.
28. Keren, S., Zavaleta, C., Cheng, Z., de la Zerda, A., Gheysens, O., and Gambhir, S.S. (2008) Noninvasive molecular imaging of small living subjects using Raman spectroscopy. *Proc. Natl. Acad. Sci. U.S.A.*, **105** (15), 5844–5849.
29. Zavaleta, C., de la Zerda, A., Liu, Z., Keren, S., Cheng, Z., Schipper, M., Chen, X., Dai, H., and Gambhir, S.S. (2008) Noninvasive Raman spectroscopy in living mice for evaluation of tumor targeting with carbon nanotubes. *Nano Lett.*, **8** (9), 2800–2805.
30. Biris, A.S., Galanzha, E.I., Li, Z., Mahmood, M., Xu, Y., and Zharov, V.P. (2009) *In vivo* Raman flow cytometry for real-time detection of carbon nanotube kinetics in lymph, blood and, tissues. *J. Biomed. Opt.*, **14** (2), 021006.
31. Chao, J.-I., Perevedentseva, E., Chung, P.-H., Liu, K.-K., Cheng, C.-Y., Chang, C.-C., and Cheng, C.-L. (2007) Nanometer-sized diamond particle as a probe for biolabeling. *Biophys. J.*, **93** (6), 2199–2208.
32. Liu, Z., Chen, K., Davis, C., Sherlock, S., Cao, Q., Chen, X., and Dai, H. (2008) Drug delivery with carbon nanotubes for *in vivo* cancer treatment. *Cancer Res.*, **68** (16), 6652–6660.
33. Tsyboulski, D.A., Bachilo, S.M., and Weisman, R.B. (2005) Versatile visualization of individual single-walled carbon nanotubes with near-infrared fluorescence microscopy. *Nano Lett.*, **5** (5), 975–979.
34. Cherukuri, P., Bachilo, S.M., Litovsky, S.H., and Weisman, R.B. (2004) Near-infrared fluorescence microscopy of single-walled carbon nanotubes in phagocytic cells. *J. Am. Chem. Soc.*, **126** (48), 15638–15639.
35. Cherukuri, P., Gannon, C.J., Leeuw, T.K., Schmidt, H.K., Smalley, R.E., Curley, S.A., and Weisman, R.B. (2006) Mammalian pharmacokinetics of carbon nanotubes using intrinsic near-infrared fluorescence. *Proc. Natl. Acad. Sci. U.S.A.*, **103** (50), 18882–18886.
36. Leeuw, T.K., Reith, R.M., Simonette, R.A., Harden, M.E., Cherukuri, P., Tsyboulski, D.A., Beckingham, K.M., and Weisman, R.B. (2007) Single-walled carbon nanotubes in the intact organism: near-IR imaging and biocompatibility studies in Drosophila. *Nano Lett.*, **7** (9), 2650–2654.
37. Welsher, K., Liu, Z., Sherlock, S.P., Robinson, J.T., Chen, Z., Daranciang, D., and Dai, H. (2009) A route to brightly fluorescent carbon nanotubes for near-infrared imaging in mice. *Nat. Nanotechnol.*, **4** (11), 773–780.
38. Ruan, S., Wan, J., Fu, Y., Han, K., Li, X., Chen, J., Zhang, Q., Shen, S., He, Q., and Gao, H. (2014) PEGylated fluorescent carbon nanoparticles for noninvasive

heart imaging. *Bioconjugate Chem.*, **25** (6), 1061–1068.
39. Liu, J.-H., Yang, S.-T., Chen, X.-X., and Wang, H. (2012) Fluorescent carbon dots and nanodiamonds for biological imaging: preparation, application, pharmacokinetics and toxicity. *Curr. Drug Metab.*, **13** (8), 1046–1056.
40. Luo, P.G., Sahu, S., Yang, S.-T., Sonkar, S.K., Wang, J., Wang, H., LeCroy, G.E., Cao, L., and Sun, Y.-P. (2013) Carbon "quantum" dots for optical bioimaging. *J. Mater. Chem. B*, **1** (16), 2116–2127.
41. Yang, S.-T., Cao, L., Luo, P.G., Lu, F., Wang, X., Wang, H., Meziani, M.J., Liu, Y., Qi, G., and Sun, Y.-P. (2009) Carbon dots for optical imaging *in vivo*. *J. Am. Chem. Soc.*, **131** (32), 11308–11309.
42. Sun, Y.-P., Zhou, B., Lin, Y., Wang, W., Fernando, K.A.S., Pathak, P., Meziani, M.J., Harruff, B.A., Wang, X., Wang, H., Luo, P.G., Yang, H., Kose, M.E., Chen, B., Veca, L.M., and Xie, S.-Y. (2006) Quantum-sized carbon dots for bright and colorful photoluminescence. *J. Am. Chem. Soc.*, **128** (24), 7756–7757.
43. Yang, S.-T., Wang, X., Wang, H., Lu, F., Luo, P.G., Cao, L., Meziani, M.J., Liu, J.-H., Liu, Y., Chen, M., Huang, Y., and Sun, Y.-P. (2009) Carbon dots as nontoxic and high-performance fluorescence imaging agents. *J. Phys. Chem. C*, **113** (42), 18110–18114.
44. Chang, Y.-R., Lee, H.-Y., Chen, K., Chang, C.-C., Tsai, D.-S., Fu, C.-C., Lim, T.-S., Tzeng, Y.-K., Fang, C.-Y., Han, C.-C., Chang, H.-C., and Fann, W. (2008) Mass production and dynamic imaging of fluorescent nanodiamonds. *Nat. Nanotechnol.*, **3** (5), 284–288.
45. Liu, K.-K., Wang, C.-C., Cheng, C.-L., and Chao, J.-I. (2009) Endocytic carboxylated nanodiamond for the labeling and tracking of cell division and differentiation in cancer and stem cells. *Biomaterials*, **30** (26), 4249–4259.
46. Mohan, N., Chen, C.-S., Hsieh, H.-H., Wu, Y.-C., and Chang, H.-C. (2010) *In vivo* imaging and toxicity assessments of fluorescent nanodiamonds in *Caenorhabditis elegans*. *Nano Lett.*, **10** (9), 3692–3699.
47. Nurunnabi, M., Khatun, Z., Huh, K.M., Park, S.Y., Lee, D.Y., Cho, K.J., and Lee, Y.K. (2013) *In vivo* biodistribution and toxicology of carboxylated graphene quantum dots. *ACS Nano*, **7** (8), 6858–6867.
48. Donkor, D.A. and Tang, X.S. (2014) Tube length and cell type-dependent cellular responses to ultra-short single-walled carbon nanotube. *Biomaterials*, **35** (9), 3121–3131.
49. Kam, N.W.S., Liu, Z., and Dai, H. (2006) Carbon nanotubes as intracellular transporters for proteins and DNA: an investigation of the uptake mechanism and pathway. *Angew. Chem.*, **118** (4), 591–595.
50. Lao, F., Chen, L., Li, W., Ge, C., Qu, Y., Sun, Q., Zhao, Y., Han, D., and Chen, C. (2009) Fullerene nanoparticles selectively enter oxidation-damaged cerebral microvessel endothelial cells and inhibit JNK-related apoptosis. *ACS Nano*, **3** (11), 3358–3368.
51. Huang, X., Zhang, F., Zhu, L., Choi, K.Y., Guo, N., Guo, J., Tackett, K., Anilkumar, P., Liu, G., Quan, Q., Choi, H.S., Niu, G., Sun, Y.-P., Lee, S., and Chen, X. (2013) Effect of injection routes on the biodistribution, clearance, and tumor uptake of carbon dots. *ACS Nano*, **7** (7), 5684–5693.
52. Chong, Y., Ma, Y., Shen, H., Tu, X., Zhou, X., Xu, J., Dai, J., Fan, S., and Zhang, Z. (2014) The *in vitro* and *in vivo* toxicity of graphene quantum dots. *Biomaterials*, **35** (19), 5041–5048.
53. Shi, D., Guo, Y., Dong, Z., Lian, J., Wang, W., Liu, G., Wang, L., and Ewing, R.C. (2007) Quantum-dot-activated luminescent carbon nanotubes via a nano scale surface functionalization for *in vivo* imaging. *Adv. Mater.*, **19** (22), 4033–4037.
54. Guo, Y., Shi, D., Cho, H., Dong, Z., Kulkarni, A., Pauletti, G.M., Wang, W., Lian, J., Liu, W., Ren, L., Zhang, Q., Liu, G., Huth, C., Wang, L., and Ewing, R.C. (2008) *In vivo* imaging and drug storage by quantum-dot-conjugated carbon nanotubes. *Adv. Funct. Mater.*, **18** (17), 2489–2497.
55. Chen, M.-L., Liu, J.-W., Hu, B., Chen, M.-L., and Wang, J.-H. (2011) Conjugation of quantum dots with graphene

for fluorescence imaging of live cells. *Analyst*, **136** (20), 4277–4283.

56. Campagnolo, L., Massimiani, M., Palmieri, G., Bernardini, R., Sacchetti, C., Bergamaschi, A., Vecchione, L., Magrini, A., Bottini, M., and Pietroiusti, A. (2013) Biodistribution and toxicity of pegylated single wall carbon nanotubes in pregnant mice. *Part. Fibre Toxicol.*, **10** (1), 21.
57. Jia, F., Wu, L., Meng, J., Yang, M., Kong, H., Liu, T., and Xu, H. (2009) Preparation, characterization and fluorescent imaging of multi-walled carbon nanotube-porphyrin conjugate. *J. Mater. Chem.*, **19** (47), 8950–8957.
58. Deng, X., Yang, S.-T., Nie, H.-Y., Wang, H., and Liu, Y. (2008) A generally adoptable radiotracing method for tracking carbon nanotubes in animals. *Nanotechnology*, **19** (7), 075101.
59. Guo, J., Zhang, X., Li, Q., and Li, W. (2007) Biodistribution of functionalized multiwall carbon nanotubes in mice. *Nucl. Med. Biol.*, **34** (5), 579–583.
60. Liu, Z., Cai, W., He, L., Nakayama, N., Chen, K., Sun, X., Chen, X., and Dai, H. (2007) *In vivo* biodistribution and highly efficient tumour targeting of carbon nanotubes in mice. *Nat. Nanotechnol.*, **2** (1), 47–52.
61. McDevitt, M.R., Chattopadhyay, D., Jaggi, J.S., Finn, R.D., Zanzonico, P.B., Villa, C., Rey, D., Mendenhall, J., Batt, C.A., Njardarson, J.T., and Scheinberg, D.A. (2007) PET imaging of soluble yttrium-86-labeled carbon nanotubes in mice. *PLOS One*, **2** (9), e907.
62. Li, Y., Huang, X., Zhang, X., Liu, R., Zhang, Y., and Li, W. (2003) Biodistribution of ^{67}Ga-C_{60}(OH)x in mice. *Nucl. Technol.*, **26** (5), 394–396.
63. Rojas, S., Gispert, J.D., Martin, R., Abad, S., Menchon, C., Pareto, D., Victor, V.M., Alvaro, M., Garcia, H., Raul, and Herance, J. (2011) Biodistribution of amino-functionalized diamond nanoparticles. *in vivo* studies based on ^{18}F radionuclide emission. *ACS Nano*, **5** (7), 5552–5559.
64. Wang, J., Deng, X., Yang, S.-T., Wang, H., Zhao, Y., and Liu, Y. (2008) Rapid translocation and pharmacokinetics of hydroxylated single-walled carbon nanotubes in mice. *Nanotoxicology*, **2** (1), 28–32.
65. Zhang, X., Yin, J., Peng, C., Hu, W., Zhu, Z., Li, W., Fan, C., and Huang, Q. (2011) Distribution and biocompatibility studies of graphene oxide in mice after intravenous administration. *Carbon*, **49** (3), 986–995.
66. Zhang, X., Yin, J., Kang, C., Li, J., Zhu, Y., Li, W., Huang, Q., and Zhu, Z. (2010) Biodistribution and toxicity of nanodiamonds in mice after intratracheal instillation. *Toxicol. Lett.*, **198** (2), 237–243.
67. Cagle, D.W., Kennel, S.J., Mirzadeh, S., Alford, J.M., and Wilson, L.J. (1999) *In vivo* studies of fullerene-based materials using endohedral metallofullerene radiotracers. *Proc. Natl. Acad. Sci. U.S.A.*, **96** (9), 5182–5187.
68. Yamago, S., Tokuyama, H., Nakamura, E., Kikuchi, K., Kananishi, S., Sueki, K., Nakahara, H., Enomoto, S., and Ambe, F. (1995) *In vivo* biological behavior of a water-miscible fullerene: ^{14}C labeling, absorption, distribution, excretion and acute toxicity. *Chem. Biol.*, **2** (6), 385–389.
69. Lacerda, L., Soundararajan, A., Singh, R., Pastorin, G., Al-Jamal, K.T., Turton, J., Frederik, P., Herrero, M.A., Li, S., Bao, A., Emfietzoglou, D., Mather, S., Phillips, W.T., Prato, M., Bianco, A., Goins, B., and Kostarelos, K. (2008) Dynamic imaging of functionalized multi-walled carbon nanotube systemic circulation and urinary excretion. *Adv. Mater.*, **20** (2), 225–230.
70. McDevitt, M.R., Chattopadhyay, D., Kappel, B.J., Jaggi, J.S., Schiffman, S.R., Antczak, C., Njardarson, J.T., Brentjens, R., and Scheinberg, D.A. (2007) Tumor targeting with antibody-functionalized, radiolabeled carbon nanotubes. *J. Nucl. Med.*, **48** (7), 1180–1189.
71. Bullard-Dillard, R., Creek, K.E., Scrivens, W.A., and Tour, J.M. (1996) Tissue sites of uptake of ^{14}C-labeled C_{60}. *Bioorg. Chem.*, **24** (4), 376–385.
72. Petersen, E.J., Huang, Q., and Weber, Jr., W.J. (2008) Bioaccumulation of radiolabeled carbon nanotubes by *Eisenia*

foetida. *Environ. Sci. Technol.*, **42** (8), 3090–3095.

73. Petersen, E.J., Akkanen, J., Kukkonen, J.V.K., and Weber, Jr., W.J. (2009) Biological uptake and depuration of carbon nanotubes by *Daphnia magna*. *Environ. Sci. Technol.*, **43** (8), 2969–2975.
74. Petersen, E.J., Huang, Q., and Weber, Jr., W.J. (2008) Ecological uptake and depuration of carbon nanotubes by lumbriculus variegatus. *Environ. Health Perspect.*, **116** (4), 496–500.
75. Hong, H., Zhang, Y., Engle, J.W., Nayak, T.R., Theuer, C.P., Nickles, R.J., Barnhart, T.E., and Cai, W. (2012) *In vivo* targeting and positron emission tomography imaging of tumor vasculature with ^{66}Ga-labeled nano-graphene. *Biomaterials*, **33** (16), 4147–4156.
76. Chang, X.-L., Ruan, L., Yang, S.-T., Sun, B., Guo, C., Zhou, L., Dong, J., Yuan, H., Xing, G., Zhao, Y., and Yang, M. (2014) Quantification of carbon nanomaterials *in vivo*: direct stable isotope labeling on the skeleton of fullerene C_{60}. *Environ. Sci. Nano*, **1** (1), 64–70.
77. Yang, S.-T., Guo, W., Lin, Y., Deng, X., Wang, H., Sun, H., Liu, Y., Wang, X., Wang, W., Chen, M., Huang, Y., and Sun, Y.-P. (2007) Biodistribution of pristine single-walled carbon nanotubes *in vivo*. *J. Phys. Chem. C*, **111** (48), 17761–17764.
78. Liu, J.-H., Yang, S.-T., Wang, X., Wang, H., Liu, Y., Luo, P.G., Liu, Y., and Sun, Y.-P. (2014) Carbon nanoparticles trapped *in vivo*-similar to carbon nanotubes in time-dependent biodistribution. *ACS Appl. Mater. Interfaces*, **6** (16), 14672–14678.
79. Wang, H., Yang, S.-T., Cao, A., and Liu, Y. (2013) Quantification of carbon nanomaterials *in vivo*. *Acc. Chem. Res.*, **46** (3), 750–760.
80. Isaacson, C.W., Usenko, C.Y., Tanguay, R.L., and Field, J.A. (2007) Quantification of fullerenes by LC/ESI-MS and its application to *in vivo* toxicity assays. *Anal. Chem.*, **79** (23), 9091–9097.
81. Kubota, R., Tahara, M., Shimizu, K., Sugimoto, N., Hirose, A., and Nishimura, T. (2009) Development of a liquid chromatography-tandem mass spectrometry method for the determination of fullerene C60 and C70 in biological samples. *Bull. Natl. Inst. Health Sci.*, **127**, 65–68.
82. Moussa, F., Trivin, F., Ceolin, R., Hadchouel, M., Sizaret, P.Y., Greugny, V., Fabre, C., Rassat, A., and Szwarc, H. (1996) Early effects of C_{60} administration in Swiss mice: a preliminary account for *in vivo* C_{60} toxicity. *Fullerene Sci. Technol.*, **4** (1), 21–29.
83. Shinohara, N., Nakazato, T., Tamura, M., Endoh, S., Fukui, H., Morimoto, Y., Myojo, T., Shimada, M., Yamamoto, K., Tao, H., Yoshida, Y., and Nakanishi, J. (2010) Clearance kinetics of fullerene C_{60} nanoparticles from rat lungs after intratracheal C_{60} instillation and inhalation C_{60} exposure. *Toxicol. Sci.*, **118** (2), 564–573.
84. Suzuki, H., Toyooka, T., and Ibuki, Y. (2007) Simple and easy method to evaluate uptake potential of nanoparticles in mammalian cells using a flow cytometric light scatter analysis. *Environ. Sci. Technol.*, **41** (8), 3018–3024.
85. Wang, J., Sun, R., Zhang, N., Nie, H.-Y., Liu, J.-H., Wang, J., Wang, H., and Liu, Y. (2009) Multi-walled carbon nanotubes do not impair immune functions of dendritic cells. *Carbon*, **47** (7), 1752–1760.
86. Cai, D., Blair, D., Dufort, F.J., Gumina, M.R., Huang, Z.P., Hong, G., Wagner, D., Canahan, D., Kempa, K., Ren, Z.F., and Chiles, T.C. (2008) Interaction between carbon nanotubes and mammalian cells: characterization by flow cytometry and application. *Nanotechnology*, **19** (34), 345102.
87. Ge, C., Lao, F., Li, W., Li, Y., Chen, C., Qiu, Y., Mao, X., Li, B., Chai, Z., and Zhao, Y. (2008) Quantitative analysis of metal impurities in carbon nanotubes: efficacy of different pretreatment protocols for ICPMS spectroscopy. *Anal. Chem.*, **80** (24), 9426–9434.
88. Wang, J., Chen, C., Li, B., Yu, H., Zhao, Y., Sun, J., Li, Y., Xing, G., Yuan, H., Tang, J., Chen, Z., Meng, H., Gao, Y., Ye, C., Chai, Z., Zhu, C., Ma, B., Fang, X., and Wan, L. (2006) Antioxidative function and biodistribution of $[Gd@C_{82}(OH)_{22}]_n$ nanoparticles in

tumor-bearing mice. *Biochem. Pharmacol.*, **71** (6), 872–881.

89. De La Zerda, A., Zavaleta, C., Keren, S., Vaithilingam, S., Bodapati, S., Liu, Z., Levi, J., Smith, B.R., Ma, T.J., Oralkan, O., Cheng, Z., Chen, X., Dai, H., Khuri-Yakub, B.T., and Gambhir, S.S. (2008) Carbon nanotubes as photoacoustic molecular imaging agents in living mice. *Nat. Nanotechnol.*, **3** (9), 557–562.
90. Chen, D., Wang, C., Nie, X., Li, S., Li, R., Guan, M., Liu, Z., Chen, C., Wang, C., Shu, C., and Wan, L. (2014) Photoacoustic imaging guided near-infrared photothermal therapy using highly water-dispersible single-walled carbon nanohorns as theranostic agents. *Adv. Funct. Mater.*, **24** (42), 6621–6628.
91. Tsyboulski, D.A., Liopo, A.V., Su, R., Ermilov, S.A., Bachilo, S.M., Bruce Weisman, R., and Oraevsky, A.A. (2014) Enabling *in vivo* measurements of nanoparticle concentrations with three-dimensional optoacoustic tomography. *J. Biophotonics*, **7** (8), 581–588.
92. Doudrick, K., Corson, N., Oberdorster, G., Eder, A.C., Herckes, P., Halden, R.U., and Westerhoff, P. (2013) Extraction and quantification of carbon nanotubes in biological matrices with application to rat lung tisssue. *ACS Nano*, **7** (10), 8849–8856.
93. Bourdiol, F., Dubuc, D., Grenier, K., Mouchet, F., Gauthier, L., and Flahaut, E. (2015) Quantitative detection of carbon nanotubes in biological samples by an original method based on microwave permittivity measurements. *Carbon*, **81**, 535–545.

3
Biodistribution and Pharmacokinetics of Carbon Nanomaterials *In Vivo*

Sheng-Tao Yang, Xiaoyang Liu, and Jingru Xie

3.1
Introduction

Pharmacokinetics and biodistribution are essential information for biomedical applications and biosafety evaluations of carbon nanomaterials [1–5]. Pharmacokinetics is crucial for gaining knowledge on the retention in and clearance from blood of carbon nanomaterials [6]. The biodistribution of carbon nanomaterials directly points out their accumulation in organs and the related systems [7]. Thus, pharmacokinetics and biodistribution are the first issues to consider when measuring the *in vivo* bioeffects of carbon nanomaterials [1–5].

There are diverse carbon nanomaterials, such as ultrafine carbon particles, carbon nanoparticles (CNPs), carbon dots, fullerenes, carbon nanotubes (CNTs), graphene, and nanodiamonds (NDs). The structure and properties of these carbon nanomaterials are completely different. The clearance and distribution patterns from blood of these carbon nanomaterials depend on their shape, size, and functionalization [8]. The crossing of biological barriers of carbon nanomaterials is also of serious concern. Therefore, various quantification methods are applied in tracing these carbon nanomaterials [7].

By using isotopic labeling, Raman spectroscopy, fluorescence spectroscopy, and so on, many carbon nanomaterials were subjected to pharmacokinetic and biodistribution evaluations both quantitatively and qualitatively [1–8]. In this chapter, we summarize the available data on the pharmacokinetics and biodistribution of carbon nanomaterials. The guidelines for studying the pharmacokinetics and biodistribution of carbon nanomaterials are outlined in Figure 3.1.

3.2
Amorphous Carbon Nanoparticles

Amorphous carbon is one of the most common forms of carbon materials. When the size of amorphous carbon materials is in the range 1–100 nm, they are called CNPs. These amorphous CNPs are already smaller than the cut-off size of the

Biomedical Applications and Toxicology of Carbon Nanomaterials, First Edition.
Edited by Chunying Chen and Haifang Wang.

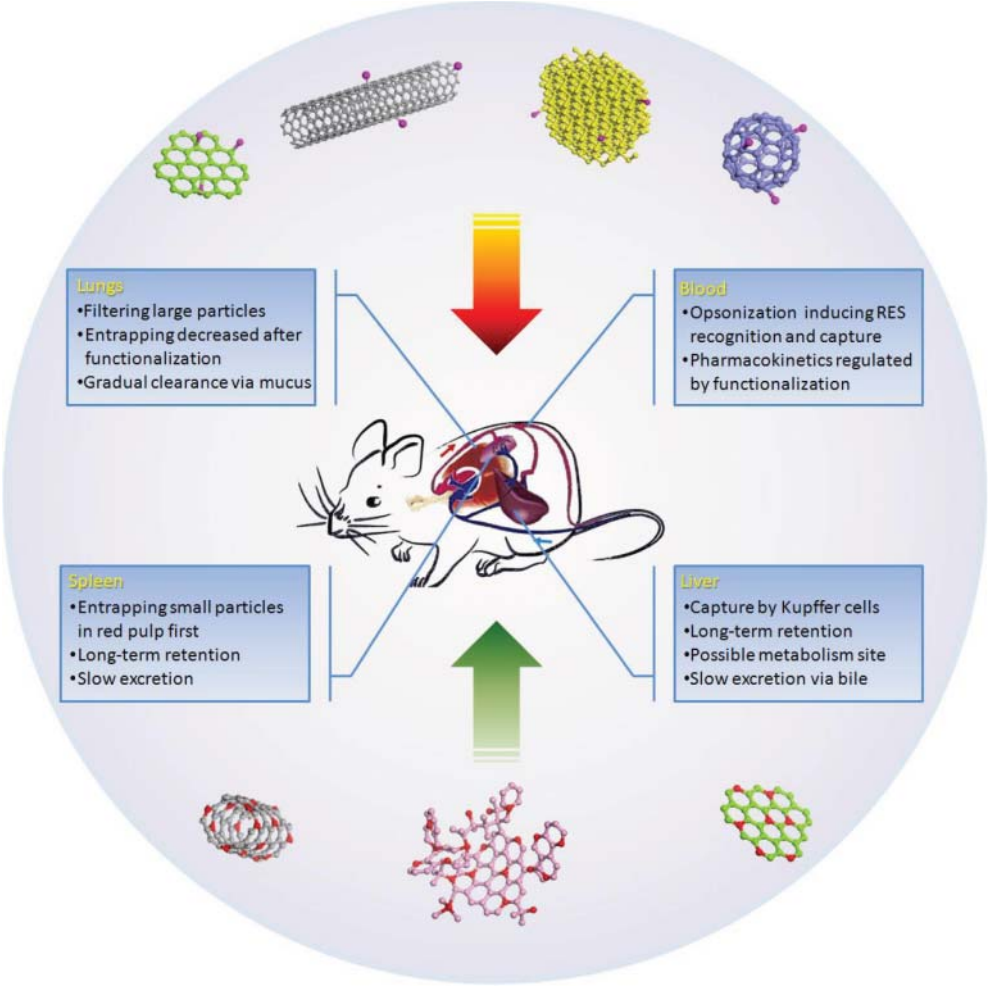

Figure 3.1 RES uptake of carbon nanomaterials after intravenous (i.v.) injection. (Adapted with permission from [7]. ©2012 American Chemical Society.)

pulmonary capillary and can cross many biological barriers. Therefore, the translocation and distribution of these CNPs are of great concern.

3.2.1 Ultrafine Carbon Particles

Ultrafine carbon particles were the first CNPs to be considered in translocation and distribution studies. The original purpose of such studies was to reveal the behavior of the ultrafine particles existing in the atmosphere and inhaled by humans. Thus, the available literature is only concerned with the pulmonary

exposure of ultrafine carbon particles. Beyond the limited exposure pathway, these ultrafine carbon particles are poorly characterized because these studies followed the common ways of ultrafine particles rather than the later developed nanoparticles (NP)s.

The representative results were reported by Oberdörster *et al.* [9, 10], who investigated the extrapulmonary translocation of ultrafine carbon particles in rats after inhalation exposure [9]. Ultrafine carbon particles were labeled by ^{13}C and detected using isotope ratio mass spectrometry (IRMS). At 0.5 h post a 6-h exposure to high and low concentrations, ultrafine carbon particles were found in the lungs. The lung accumulation levels did not change during the 24-h observation. For liver, at 0.5 h post the 6-h exposure to high concentration, ultrafine carbon particles were found in the organ and retained during the 24-h observation. For low concentration, the exposure induced significant ^{13}C increase only at 18 h post exposure. Although the accumulation concentrations in the lungs were much higher than in the liver, the total amounts in the liver were higher due to the higher weight of the liver. In their subsequent work, using ^{13}C-labeling technique, Oberdörster *et al.* specified the translocation of ultrafine carbon particles after pulmonary exposure to brain [10]. After a 6-h exposure, the rats were scarified at different time points. The accumulation in the lungs was $1.39\,\mu g\,g^{-1}$ at day 1 and decreased gradually to $0.59\,\mu g\,g^{-1}$ at day 7. The olfactory bulb had a slight increase from $0.35\,\mu g\,g^{-1}$ at day 1 to $0.43\,\mu g\,g^{-1}$ at day 7. Cerebrum had a nearly constant accumulation of $0.27\,\mu g\,g^{-1}$ at day 1 and $0.23\,\mu g\,g^{-1}$ at day 7. The cerebellum accumulation was $0.44\,\mu g\,g^{-1}$ at day 1 and decreased gradually to $0.21\,\mu g\,g^{-1}$ at day 7. Clearly, Oberdörster *et al.* could show that ultrafine carbon particles could translocate into blood circulation, cross biological barriers, for example, the blood–brain barrier, and distribute in the whole body. Thus, the biosafety of ultrafine carbon particle should consider the toxicity not only to the respiratory system but also to the cardiovascular system, brain, and digestive system.

Using ^{99m}Tc labeling, Nemmar *et al.* observed the translocation of ultrafine carbon particles in the blood circulation and liver after inhalation exposure [11]. The results indicated that the radioactivity of blood increased in the first 20 min and remained constant thereafter. Their thin-layer chromatography (TLC) results suggested that most ^{99m}Tc was bound to the carbon particle in the beginning but detached gradually. It should be noted that even at 60 min, about half of the radioactivity was found on the particles, suggesting that the blood concentration of ultrafine carbon particles was significant. In the contrast, the radioactivity in urine was large, but in the form of soluble, free ^{99m}Tc form. In the time range 5–45 min, about 8% of the radioactivity was detected in the liver, indicating the distribution of ultrafine carbon particles in that organ.

Other studies have found that the translocation of ultrafine carbon particles into the blood circulation was not significant. Moller *et al.* compared the shallow and deep bolus inhalation of ultrafine carbon particles in nonsmokers, smokers, and patients with chronic obstructive pulmonary disease [12]. The particle deposition was lower after shallow bolus inhalation (37–43%), and the difference

among nonsmokers, smokers, and patients was insignificant. The particle deposition was higher after deep bolus inhalation (50–64%). The nonsmokers had the lowest deposition (50%), while the smokers (64%) and patients (62%) showed significantly higher deposition. The exposure methods affected the distribution in the lung. Shallow bolus inhalation resulted in high central/peripheral (C/P) ratios. The C/P ratio of nonsmokers was higher (2.01) than that of smokers (1.42) and patients (1.22). Deep bolus inhalation led to low C/P ratios (0.83–0.84), indicating that more particles distributed into other regions of the lung. Air retention after shallow bolus inhalation was faster than that after deep bolus inhalation. The retention after deep bolus inhalation was not significantly different among nonsmokers, smokers, and patients. At 1.5 h, the retention was 0.98–0.99, which slightly decreased to 0.96–0.97 at 24 h and 0.95–0.96 at 48 h. After shallow bolus inhalation, the retention in patients was higher than that in smokers, and the nonsmokers had the lowest retention. At 1.5 h, the retention was 0.89 for nonsmokers, 0.97 for smokers, and 0.96 for patients. The clearance was fast in the first 24 h, after which the retention decreased to 0.75 for nonsmokers, 0.76 for smokers, and 0.84 for patients. In the following 24 h, the retention decreased more slowly (0.70 for nonsmokers, 0.76 for smokers, and 0.82 for patients). No significant radioactivity was detected in the liver, implying the negligible translocation of ultrafine carbon particles into the liver.

Overall, the translocation of ultrafine carbon particles after pulmonary exposure into blood circulation and other tissues might depend on the exposure methods and the physiochemical properties of ultrafine carbon particles. ^{13}C-labeling is more reliable than ^{99m}Tc-labeling in the quantification of ultrafine carbon particles because the detachment of ^{99m}Tc can be confirmed by TLC [11]. To verify the exact mechanism, separating the ultrafine carbon particles into individual components should be performed, and the investigations on those separated particles might shield light on the influencing factors and mechanisms.

3.2.2
Carbon Nanoparticles

As discussed in Section 3.2.1, the individual components of ultrafine carbon particles would help us to understand the regulating factors of the translocation and distribution behaviors. Upon separation, the ultrafine carbon particles are subjected to different carbon NPs. Therefore, the translocation and biodistribution of carbon NPs were investigated mainly following pulmonary exposure.

Wiebert *et al.* [13] reported that 35 nm CNPs did not translocate into the blood circulation after inhalation exposure by deep breath. The median diameter of carbon NPs was 37 nm. The deposition of CNPs was 51% for asthmatic subjects and 63% for healthy subjects. The retention of CNPs was 102% at 24 h, suggesting there was no translocation and excretion of CNPs after the exposure. Photography using the gamma camera indicated that low-leaching CNPs were strictly trapped in the lung and did not distribute into other areas of experimental subjects. Again, the

results suggested that ^{99m}Tc labeling was not very stable and that the leaching of ^{99m}Tc from CNPs should be fully considered in the quantification.

Unlike Wiebert *et al.*, Mills *et al.* [14] reported the translocation of CNPs from the lungs to the blood circulation. CNPs were also labeled by ^{99m}Tc. After the exposure, the blood radioactivity was detected within the first minute and it reached a maximum at 60 min. The activity gradually decreased thereafter. The lung activity lost 3.2% in the first 1 h, followed by 1.2% in the next 5 h. An increase in the bladder and gastrointestinal tract was observed, rather than in the liver and spleen. However, the radioactivity in urine should be attributed to the free ^{99m}Tc ions according to TLC analyses. The translocation of CNPs into the blood circulation here might be attributed to their small sizes. The CNPs were in the range of 4–20 nm in diameter, while two-thirds of them were smaller than 10 nm. The particles were much smaller than those in Wiebert *et al.*'s evaluation. This suggested that smaller carbon particles could translocate more freely in body.

Beyond the pulmonary exposure, very recently, Liu *et al.* [15] reported the distribution of CNPs after intravenous (i.v.) injection in mice. The purpose of this study was to reveal the biological behavior of "naked" carbon dots, which are fluorescent CNPs applied in whole-body imaging. The CNPs were labeled by ^{13}C on the skeleton and quantified by IRMS. The CNPs were all smaller than 10 nm. Upon i.v. injection, the blood clearance of CNPs was fast and the CNPs were totally removed at 6 h. The CNPs were found in the liver, spleen, lungs, and brain. At day 1, 26.2%ID (injected dose) was detected in the liver, 6.0%ID was detected in the spleen, and 13.7%ID was found in the lungs. This suggested the reticuloendothelial system (RES) capture of CNPs. The liver accumulation level increased to 40.5%ID at day 7 and remained nearly constant up to 28 days (37.5%ID). The spleen uptake did not largely change during the 28 days. The slow excretion of CNPs in the lungs led to the decrease of the accumulation level to 6.1%ID at 28 days. The brain uptake indicated that small CNPs might cross the blood–brain barrier. The results suggested that small CNPs could translocate more freely in body (Figure 3.2).

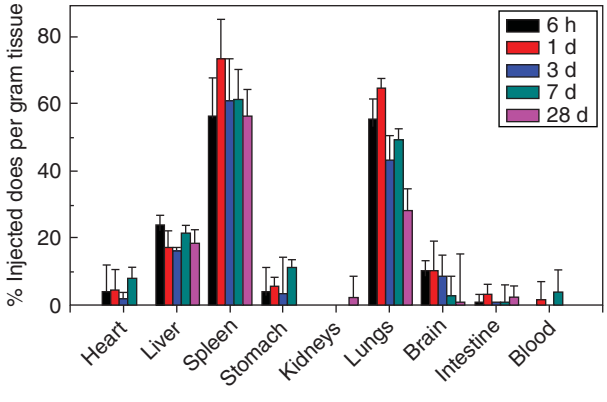

Figure 3.2 Biodistribution of carbon NPs after i.v. injection. (Adapted with permission from [15]. ©2014 American Chemical Society.)

Although the data on CNPs were few, the available data collectively suggest that the size of CNPs regulates the translocation and biodistribution behaviors. Such size-dependent biodistribution is widely observed in other carbon nanomaterials [7].

3.2.3 Carbon Dots

Carbon dots, also named as carbon quantum dots or C-dots, are generally small CNPs obtained with various surface passivation via modification or functionalization. C-dots are highly fluorescent and of low toxicity, and therefore are very useful in the bioimaging, drug delivery, bioanalysis, and related areas. Therefore, the biodistribution, which is the first issue to be considered in the biosafety studies of carbon dots, has been recognized and investigated.

The very first investigation on the biodistribution of carbon dots was reported by Yang *et al.* in 2009 [16, 17]. They combined ^{13}C labeling and whole-body imaging to reveal the translocation and biodistribution of carbon dots in mice. Carbon dots were found to distribute quickly into the whole body except the brain. The accumulation levels in the liver, spleen, and kidneys were moderate. The majority of injected carbon dots were rapidly accumulated in the bladder and excreted through urine [16]. Two-photon imaging of the sliced liver and spleen confirmed the presence of carbon dots in the liver and spleen, where the spectra and peak position were identical to carbon dots in solution [17]. In addition, they also found that carbon dots could migrate through the body after subcutaneous (s.c.) injection along lymph vessels. The biodistribution data guided their toxicity evaluations. They focused on the hepatic toxicity and renal toxicity of carbon dots, where the serum biochemistry and histopathology indicated the good biocompatibility of carbon dots.

Similar to Yang *et al.* [18], Tao *et al.* investigated the biodistribution and toxicity of carbon dots. Carbon dots were labeled by ^{125}I for quantification. The distribution half-life of carbon dots was 0.1 h, and the clearance half-life was 2.1 h in the pharmacokinetics analysis by the two-compartment model. Carbon dots were distributed throughout the body except the brain. The accumulation levels were relatively high in the liver, spleen, and kidneys. At 5 h, the hepatic uptake was near 12%ID g^{-1}, which decreased to 2%ID g^{-1} at 7 days. The high accumulation in the stomach and intestine was surprising, which might imply the detachment of ^{125}I, because free ^{125}I showed high accumulation in the stomach after i.v. injection (Figure 3.3).

Other studies also showed the distribution of carbon dots in the RES organs and the excretion into the urine. Li *et al.* investigated the biodistribution of carbon dots after i.v. injection in mice [19]. The organs were dissected, sliced, and imaged under 405 nm excitation and 500 nm emission. Blue fluorescence was observed in the heart, liver, spleen, kidneys, lungs, brain, and small intestine. More carbon dots were found in the spleen in particular. Srivastava *et al.* imaged iron oxide-doped carbogenic nanocomposite (IO-CNC) after i.v. injection in rats [20].

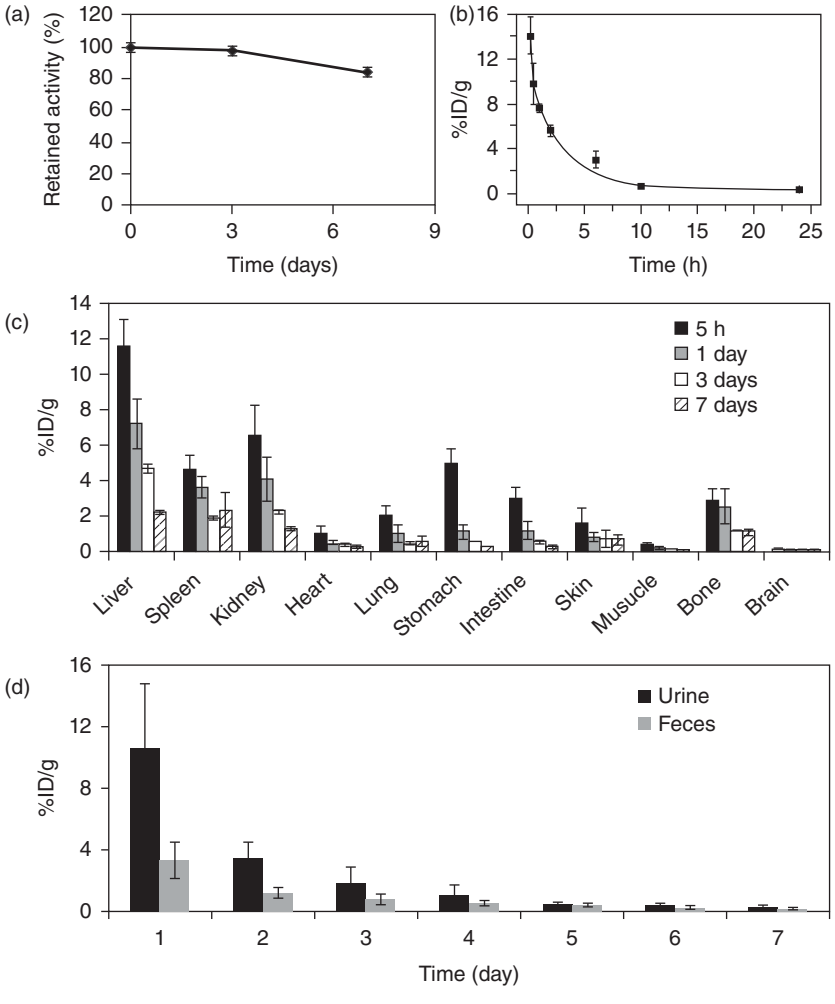

Figure 3.3 Pharmacokinetics and biodistribution of carbon dots after i.v. injection. (a) Radiolabeling stability in mouse plasma. (b) Blood circulation curve. (c) Time-dependent biodistribution. (d) Urine and feces concentrations. (Adapted with permission from [18]. ©1999–2015 John Wiley & Sons, Inc.)

IO-CNC was detected in the slides of spleen by fluorescence imaging. Magnetic resonance imaging (MRI) imaging showed enhanced signal in the brain blood vessel under both T1 and T2 models. Huang *et al.* [21] conjugated carbon dots to Ce6, and the fluorescence resonance energy transfer (FRET) property allowed excitation at 430 nm and emission at 668 nm. After i.v. injection, carbon dot-Ce6 complex was accumulated in the tumor. Fluorescence was detected in the liver, spleen, lung, kidneys, and heart. The kidney accumulation increased at 24 h, which implied the renal excretion of carbon dots.

In other exposure pathways, carbon dots showed free translocation in the body, which should be due to the very small size and high hydrophilicity. Xu *et al.* [22] reported the biodistribution of Gd-carbon quantum dots (Gd-CQDs) after intra-tracheal instillation (i.t.) exposure. The biodistribution of Gd-CQDs was measured by Gd^{3+} quantification. The results suggested that Gd-CQDs were trapped in the liver and spleen. Gd-CQDs were also detected in the kidneys, lungs, and heart. The distribution was similar in tumor-bearing mice, with about 10%ID g^{-1} accumulation in the tumor. The results suggested carbon dots could translocate from the lungs to the blood circulation and be distributed into other tissues. Huang *et al.* [23] reported the biodistribution of carbon dots after i.v., s.c., and intramuscular (i.m.) exposures to mice. After i.v. injection, the carbon dot concentration at 60 min decreased 17.3-fold compared to that at 1 min. In contrast, the carbon dot concentration at 60 min increased 4.4-fold after s.c. injection and 9.6-fold after i.m. injection. These increases suggested the translocation of carbon dots into the blood circulation. At 1 h, the accumulation of carbon dots in kidneys was obvious via three exposure pathways (i.v. < s.c. < i.m.). Low accumulations in the liver, spleen, and lungs were observed, and the exposure by s.c. had the lowest levels. At 24 h, the carbon dots were cleared to very low accumulation levels (lower than 0.7%ID g^{-1}), where the liver and kidneys had relative higher concentrations. The fluorescence intensity increased in the bladder with time (i.v. > i.m. > s.c.) in the first 30 min, consistent with the positron emission tomography (PET) results of ^{64}Cu-carbon dots. The initial slope was larger for i.v. injection. This indicated the urine excretion of carbon dots.

The aforementioned data collectively showed that carbon dots of small sizes could translocate and distribute in the body after different exposure pathways. Similar to other NPs, the RES uptakes of carbon dots in the short term were dominating. The hydrophilicity and small size allowed the renal excretion of carbon dots, so the RES retentions were not long.

3.3 sp^2 Carbon Nanomaterials

Among the carbon nanomaterials, sp^2 carbon nanomaterials have attracted most interest and are widely investigated. The discovery of fullerene and graphene won the Nobel Prizes in 1996 and 2010, respectively. As novel materials, their biological behaviors, including biodistribution and toxicity, have been investigated.

3.3.1 Fullerene

Fullerene is the first developed sp^2 carbon nanomaterials. The most studied fullerene is C_{60}. Other novel fullerenes are C_{70} and C_{82}. The rest have lower production yield, and are of less concern.

To understand the pharmacokinetics and distribution of fullerene, the first issue to address is the binding of fullerene with proteins. There are a number of papers documenting protein–fullerene interaction [24]. The influence of fullerene binding on the protein structure, the binding model, and the binding strength are widely reported, which allow us to figure out some guidelines. Generally, fullerene binds to proteins tightly via $\pi-\pi$ stacking. The functionalization with hydrophilic chains reduces the binding strength. Larger fullerene cages result in higher binding strength. After fullerene enters the blood circulation, it unavoidably binds to proteins to form protein–fullerene composites. The pharmacokinetics and distribution behaviors of fullerenes change completely upon protein binding. Keeping this information in mind helps us in understanding the currently available data on the pharmacokinetics and distribution of fullerene.

Pristine fullerene usually has the strongest binding strength with proteins [25], and tends to aggregate into larger particles. Thus, to some extent, pristine fullerene show similar behavior to CNPs. Bullard-Dillard *et al.* reported the biodistribution of ^{14}C-C_{60} and its derivative (^{14}C-C_{60}-*N*-dimethylpyrrolidine ammonium iodide derivative) after i.v. exposure [26]. ^{14}C-C_{60} was transferred from an organic solution to a water suspension by increasing the solvent polarity. The water suspension of C_{60} had a particle size of ~300 nm. Clearance of ^{14}C-C_{60} from the circulation was extremely rapid, with less than 1%ID remaining 1 min after the injection. The fast clearance of pristine C_{60} was reasonable because the hydrophobicity of C_{60} allowed strong interaction between C_{60} and proteins in the blood circulation. Upon binding with opsonin (opsonization-related proteins), C_{60} would be quickly cleared from blood circulation and captured by RES organs. C_{60} accumulated in RES organs at 2 h, including the liver (91.95%ID), lung (1.49%ID), and spleen (4.23%ID). In other tissues, except the brain, C_{60} was detected with very low contents. At 120 h, the hepatic accumulation reached 95.68%ID, while the rest all showed decreases. Similar to Bullard-Dillard *et al.*'s results, several other investigations confirmed the fast blood clearance and the high RES uptake of C_{60}. Nikolic *et al.* [27] reported the biodistribution of C_{60} aggregates after i.v. exposure. C_{60} was transferred from tetrahydrofuran (THF) solution into water. The average particle size was 217 nm. The blood concentration of C_{60} aggregates was about 3%ID g^{-1} at 15 min and slowly decreased thereafter. C_{60} aggregates were mainly distributed in the liver, spleen, intestine, and kidneys. The accumulations in bladder, bone, and lungs were also significant. All the accumulation levels were lower than 6%ID g^{-1}. It should be noted that the low accumulation levels were expressed in the form of %ID g^{-1}. The animals were rats in this study; thus when converting into %ID by pulsing the weight of organs, the accumulations would be very high. Kubota *et al.* [28] reported the biodistribution of C_{60}-liposome after i.v. exposure. Although it was capsulated in liposome, C_{60} was still recognized by RES and cleared totally from blood circulation within 1 day. The distribution showed a different pattern to Bullard-Dillard *et al.*'s results, where the lung accumulation became dominating. C_{60} was found in the lung (254.2 μg g^{-1}), spleen (53 μg g^{-1}), liver (25.6 μg g^{-1}), kidney (1.3 μg g^{-1}), and brain (0.078 μg g^{-1}) at day 1. The high lung accumulation indicated that the C_{60}-liposome was too large to pass the pulmonary capillary.

Dramatic decrease was found in the lung (about 50% in 14 days), similar to other carbon nanomaterials accumulating in the lung. Slow decreases were presented in the liver, kidneys, and brain. The accumulation in spleen increased to 70.5 $\mu g\, g^{-1}$ at 28 days, suggesting the translocation of C_{60} from other tissues to the spleen. Recently, Chang *et al.* [29] reported the biodistribution of Tween 80-suspended C_{60} in mice after i.v. injection. The blood clearance was fast with a half-life of 14 min. The distribution of C_{60} was detected in the liver, spleen, and lung. Low accumulations were seen in other tissues including the brain, heart, kidneys, stomach, intestine, muscle, bone, and skin. The highest hepatic accumulation (37%ID) was found at 6 h. The slow excretion made the hepatic accumulation decrease to 23.7%ID at 24 h. The spleen uptake slowly increased to 17.3%ID at 24 h. The lung uptake decreased from 14.7%ID at 5 min to 4.6%ID at 24 h.

The hydrophobicity and aggregation of C_{60} limit its translocation in the body. An example of intraperitoneal (i.p.) injection of C_{60} was reported by Moussa *et al.* [30], in which C_{60} showed longer circulation in blood but extremely low accumulation in other tissues after the injection. C_{60} was suspended with Tween 80 and carboxymethyl cellulose. The blood clearance of C_{60} was slow. The concentration in blood was 179 $mg\, l^{-1}$ at day 1, 87.5 $mg\, l^{-1}$ at day 2, and 1.1 $mg\, l^{-1}$ at day 6. Consistent with the low blood concentration, the RES uptakes of C_{60} were very small. C_{60} was detected in the liver (0.7%ID) and spleen (0.5%ID) at day 1 by high-performance liquid chromatography (HPLC). The accumulation in liver increased at day 2 (1.0%ID) and decreased thereafter to 0.4%ID at day 6. Transmission electron microscopy (TEM) investigations confirmed the presence of C_{60} aggregates in fat-storing cells, Kupffer cells, and hepatocytes of the liver. The spleen accumulation was 2.4%ID at both days 2 and 6. The slow increases and low accumulations indicated that it was hard for C_{60} to translocate from the abdominal cavity to the organs.

In addition, there have been two interesting investigations on pristine C_{60} that should be highlighted. The first one was concerned with the translocation of C_{60} from pregnant dam to fetuses and the possibility of the secretion of C_{60} into latex [31]. Sumner *et al.* reported the biodistribution of polyvinylpyrrolidone (PVP) dispersed ^{14}C-C_{60} after i.v. exposure to pregnant and lactating rats. In pregnant dams, liver was the main accumulation organ with 42.9%ID at 24 h. The other organs were the spleen (3.98%ID), lung (0.792%ID), uterus/vagina/cervix (3.05%ID), placenta (2.21%ID), fetuses pooled (0.872%ID), brain (0.036%ID), heart (0.23%ID), carcass digest (31.7%ID), residual carcass (5.8%ID), and total blood (18.8%ID). The results indicated the important fact that C_{60} could be passed to the second generation after i.v. exposure. In lactating dams, liver was the main accumulation organ with 34.5%ID at 24 h and 38.6%ID at 48 h. The others were spleen (4.09%ID), kidney (0.545%ID), lung (26.4%ID), uterus/vagina/cervix (0.222%ID), mammary glands (0.715%ID), total adipose (0.746%ID), brain (0.038%ID), heart (0.28%ID), pup gastrointestinal tract (2.75%ID), pup liver (0.0626%ID), carcass digest (24.7%ID), residual carcass (3.4%ID), and total blood (13.7%ID). At 48 h, the pup gastrointestinal tract C_{60} increased to 4.37%ID but that in the pup liver decreased slightly (0.0514%ID). The detection of C_{60} in pup indicates that C_{60}

could be excreted into latex and adsorbed by the pup. In addition, the excretion of C_{60} was observed via both the renal pathway and feces. Radioactivity was detected in urine (1.47%ID) and feces (2.15%ID) in pregnant dams after i.v. injection after 24 h. The second investigation was about the bioaccumulation of C_{60} in earthworm [32]. Li *et al.* reported the bioaccumulation of $^{14}C_{60}$ by the earthworm *Eisenia fetida*. The biota-sediment accumulation factor (BSAF) for earthworms in the high organic-carbon (OC) content in FD soil (soil collected from Ft. Drum) containing 100 mg-C_{60}/kg dry soil increased initially to a peak of 0.190 after 7 days and then decreased to 0.093 over the 28-day observation period. A similar bioaccumulation pattern with much higher values was observed for phenanthrene in GL soil (silty loam Grenada–Loring field soil), where the BSAF reached a maximum of 17.75 on day 7 and decreased to 7.93 during the remaining time. C_{60} bioaccumulation in the two soils with low OC content increased asymptotically over the incubation period to values similar to that of the FD soil (0.111 for GL and 0.179 for Lula soils). Therefore, higher OC content accelerated the accumulation only in the initial stage but did not affect the accumulation after 28 days exposure. Higher C_{60} dose resulted in lower BSAF values, which had the same trend for both GL and FD soils. In high-dose GL soils, the BSAF values were 0.126 for 60 mg kg^{-1}, 0.111 for 100 mg kg^{-1}, and 0.065 for 300 mg kg^{-1}. In FD soil, the final BSAF values were 0.093 at 100 mg kg^{-1} and 0.047 at 300 mg kg^{-1}. When very low soil concentration of C_{60} (0.25 mg kg^{-1}) was adopted, C_{60} might be in the molecular form (absorbed by soil constituents including OC). Higher BSAF values (0.22–0.79) were observed accordingly, suggesting that the sorbed/molecular C_{60} was more available for bioaccumulation than the larger aggregates. At very low soil concentration of C_{60} (0.25 mg kg^{-1}), BSAF decreased with increasing OC content in a statistically significant way ($p < 0.05$). This should be attributed to the lower bioavailability due to greater partitioning into soil with the higher OC content. ^{14}C elimination from worms exposed to FD soil with 100 and 300 mg kg^{-1} of C_{60} showed a rapid increase in the first 24 h.

Upon chemical modification, the protein–fullerene interaction would be weakened, thus showing prolonged blood circulation and different distribution patterns. Bullard-Dillard *et al.* reported the biodistribution of a fullerene derivative (^{14}C-C_{60}-*N*-dimethylpyrrolidine ammonium iodide derivative) after i.v. exposure [26]. The C_{60} derivative was quickly cleared from the circulation but the kinetics were slower than that observed for the C_{60}. About 9%ID of fullerene derivative remained after 1 min, 3% after 60 min, and only 1.5% remained after 120 min. The fast clearance of fullerene derivative should be due to the partial hydrophobicity (only with one small soluble chain). Because of the solubility, the distribution of fullerene derivative was more in other tissues. At 2 h, liver only had 52.43%ID. High accumulation was found in the lung (4.79%ID), skin (10.87%ID), fat (2.1%ID), muscle (12.01%ID), and spleen (1.61%ID). The functionalization of *N*-dimethylpyrrolidine ammonium iodide on C_{60} also enhanced the excretion. Renal excretion was indicated by the urine concentrations at 2 h for C_{60} (0.12%ID) and its derivative (0.15%ID). Rajagopalan *et al.* [33] reported the pharmacokinetics of bis(monosuccinimide) derivative of *p*,*p*′-bis(2-aminoethyl)-diphenyl-C_{60}

(MSAD-C_{60}) after i.v. exposure. The pharmacokinetic parameters of MSAD-C_{60} were as follows: AUC (area under the blood-concentration vs time curve) = 88.9 mg h l^{-1}, CL (total clearance) = 0.19 l h^{-1} kg^{-1}, V_{ss} (steady-state volume of distribution) = 2.1 l kg^{-1}, $t_{1/2}$ = 6.8 h, mean residence time (MRT in the body) = 11.4 h, MRT_c (mean residence time in the central compartment) = 1.1 h, and MRT_p (mean residence time in the peripheral compartment) = 10.3 h. The blood circulation half-life of 6.8 h was much longer than that of pristine C_{60}. However, a different functionalization has a completely different consequence. Yamago *et al.* [34] functionalized fullerene via cycloaddition with dipolar trimethylenemethane to get a water-soluble fullerene derivative. After i.v. injection, the blood clearance of the fullerene derivative was fast. At 1 h, only 1.6%ID was detected in blood circulation. The value decreased to 0.5%ID at 6 h. The fullerene derivative was retained in the body strongly. At 1 h, 72.9%ID was found in the liver already, which reached a maximum of 91.7%ID at 16 h and gradually decreased to 1.6%ID at 160 h. The distribution into other tissues, including the heart, spleen, lung, kidneys, brain, and testicles, was significant but much lower compared to that in liver. Feces excretion was observed after oral exposure. In the first 6–12 h, 47%ID of fullerene was detected in the feces. Most of it was excreted in the first 24 h. The feces excretion was much slower in the i.v. exposure. The excretion was all lower than 1.2%ID for each 6 h.

Hydroxylation is very useful method to reduce protein–fullerene interaction. After hydroxylation, fullerene was called fullerenol or fullerol. Fullerenol has been developed as anticancer drug [35], antioxidant [36], immunologic adjuvant [37], and so on. Thus, the pharmacokinetics and biodistribution of fullerenol have received intensive interest. Li *et al.* reported the biodistribution of ^{67}Ga-$C_{60}(OH)_x$ after i.v. exposure [38]. The blood concentration was 6.75%ID g^{-1} at 1 h and decreased to 0.62%ID g^{-1} at 24 h. It further decreased to 0.05%ID g^{-1} at 168 h. The distribution of ^{67}Ga-$C_{60}(OH)_x$ in the whole body was monitored. Accumulation in the brain was the lowest, 0.34%ID g^{-1} at 1 h and 0.1%ID g^{-1} at 24 h. Liver (12.42%ID g^{-1}), spleen (10.75%ID g^{-1}), skull (12.44%ID g^{-1}), and thighbone (9.23%ID g^{-1}) had higher accumulation levels at 1 h. Accumulation in the liver reached the maximum of 14.62%ID g^{-1} at 10 h. The spleen (17.09%ID g^{-1}), skull (23.72%ID g^{-1}), and thighbone (17.55%ID g^{-1}) reached the maximum values at 24 h. The accumulation levels decreased thereafter. The exposure dose affected the distribution of fullerenol. The liver, lung, spleen, and marrow showed higher accumulation at 1 h at higher dosages. The liver, lung, and spleen had higher accumulation at 24 h at higher dosages. Using another radioactive isotope, ^{99m}Tc, Li *et al.* [39] quantified the biodistribution of $C_{60}(OH)_x$ after i.v. exposure. At 1 h, the blood concentration was 2.59%ID g^{-1}. Half the distribution was lost at 3 h (1.22%ID g^{-1}). After 48 h, only 0.2%ID g^{-1} remained. ^{99m}Tc-$C_{60}(OH)_x$ was distributed in the liver, spleen, bone, lung, kidneys, intestine, and heart of mice. The accumulation in liver reached the maximum of 13.95%ID g^{-1} at 3 h. Spleen had the highest accumulation of 7.18%ID g^{-1} at 24 h. Bone accumulated 8.72%ID g^{-1} at 6 h. Decrease was observed in all organs at 48 h. Similar results were observed by using single-photon emission computed tomography (SPECT) of rats. It

was speculated that ^{99m}Tc-$C_{60}(OH)_x$ was excreted through urine and feces. Similarly, Song *et al.* [40] reported the biodistribution of $^{99m}Tc(CO)_3$-$C_{60}(OH)_{20}$ after i.v. exposure. The blood concentration decreased from 8%ID g^{-1} at 10 min to 3%ID g^{-1} at 3 h, and was totally cleared at 24 h. $^{99m}Tc(CO)_3$-$C_{60}(OH)_{20}$ got distributed in the whole body except the brain. All the organs showed a decrease in accumulation with time. Liver, lungs, spleen, and kidneys showed relatively high accumulations. At 24 h, the accumulation levels were all below 1%ID g^{-1}. The distribution pattern was confirmed by SPECT. In SPECT, the bladder had high accumulation, implying the renal excretion of $^{99m}Tc(CO)_3$-$C_{60}(OH)_{20}$. Maksin *et al.* reported the biodistribution of fullerenol, $C_{60}(OH)_{22}$, after i.v. exposure [41]. The blood content was 2.4%ID at 2 h, 0.5%ID at 4 h, and 0.1%ID at 24 h. Fullerenol got distributed into the lung (2.1%ID), liver (20.1%ID), kidney (5.3%ID), muscle (0.16%ID g^{-1}), bone (0.59%ID g^{-1}), thyroid (0.2%ID), spleen(0.66%ID), and intestine (16%ID) at 2 h. The muscle accumulation did not change during the 24 h. Bone had an increase after 4 h and reached 1.56%ID g^{-1} at 34 h. Accumulation in the intestine increased to 32%ID at 4 h and decreased to 5.1%ID at 24 h. The rest of the organs showed decreased accumulation with time. For instance, the liver accumulation decreased to 14.1%ID at 24 h. Li *et al.* reported the biodistribution of $C_{60}(OH)_x(O)_y$ after i.v. exposure [42]. The blood clearance of fullerenol was fast. At 1 h, 1.74%ID g^{-1} was found in blood, which decreased to 0.77%ID g^{-1} at 3 h. Fullerenol was distributed in the heart, lung, liver, spleen, kidney, muscle, bone, intestine, fur, and brain after i.v. injection. Relatively high accumulation levels were found in the liver (8.61%ID g^{-1}), spleen (3.34%ID g^{-1}), kidney (8.63%ID g^{-1}), and bone (10.67%ID g^{-1}) 1 h post exposure. Bone showed a continuous decrease thereafter. The liver (9.70%ID g^{-1}), spleen (3.78%ID g^{-1}), and kidney (9.43%ID g^{-1}) had the maximum accumulations at 6 h. For rabbits, SPECT results suggested accumulation in the heart, liver, kidney, bladder, coronal bone, backbone, extremities, and the honeycomb. Excretion through urine was implied by the high accumulation in kidneys and indicated more directly by the bladder accumulation at 1 and 5.5 h. The distribution of fullerenol in tumor-bearing mice was similar to that in normal mice. Ji *et al.* [43] labeled $C_{60}(OH)_x$ by ^{125}I and followed the translocation of ^{125}I-$C_{60}(OH)_x$ in tumor-bearing mice. The accumulation level of ^{125}I-$C_{60}(OH)_x$ was higher than that of free ^{125}I. ^{125}I-$C_{60}(OH)_x$ was found in the whole body except the brain. Higher accumulation levels were found in the liver, stomach, kidney, and bone. Interestingly, the tumor/normal tissue and tumor/blood ratios of ^{125}I-$C_{60}(OH)_x$ were higher than 1 at 24 and 72 h. The excretion of ^{125}I-$C_{60}(OH)_x$ was mainly detected in urine (52.3%ID) and slightly in feces (4%ID). The available data of fullerenol are slightly different, which might be due to the different samples and different quantification methods. Nevertheless, these data collectively indicated that fullerenol was cleared fast from the circulation and distributed into the whole body (Figure 3.4).

When the fullerene cage is larger, the protein binding strength would increase according to the docking results [25]. However, the accumulation and distribution of larger fullerenol were following the same pattern as C_{60} fullerenol. Cagle *et al.*

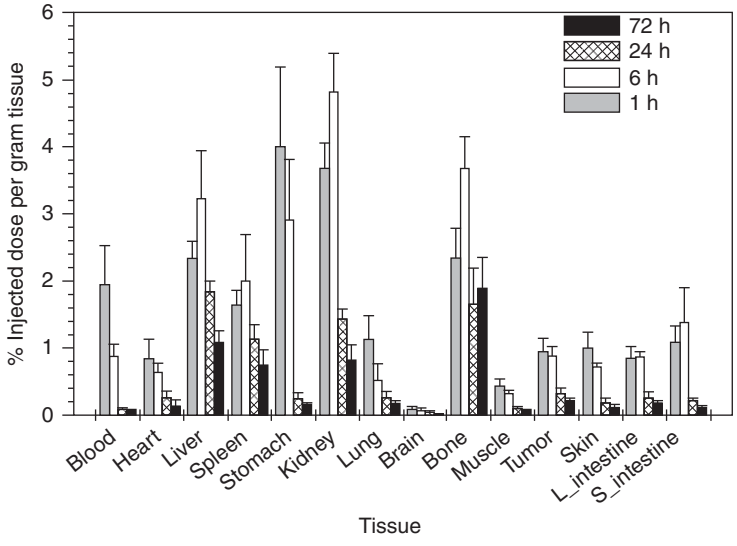

Figure 3.4 Biodistribution of fullerenol in tumor-bearing mice after i.v. injection. (Adapted with permission from [43]. ©Springer International Publishing AG.)

reported the biodistribution of $^{166}Ho_x@C_{82}(OH)_y$ in BALB/c mice after i.v. exposure [44]. The blood concentration of $^{166}Ho_x@C_{82}(OH)_y$ was 5%ID g^{-1} at 1 h and decreased to less than 1%ID g^{-1} at 24 h. $^{166}Ho_x@C_{82}(OH)_y$ accumulated in the liver, spleen, and bone. Accumulation in the liver was 24%ID g^{-1} at 4 h and decreased to 15%ID g^{-1} at 48 h. The accumulation in spleen was about 6%ID g^{-1} and decreased very slowly. The accumulation in bone increased slowly and reached 12%ID g^{-1} at 48 h. The rest of the organs showed similar decreasing trend as that of blood clearance.

Since fullerenol was mostly used for biomedical purposes, the other exposure pathways were of less concern. Xu *et al.* [45] reported the biodistribution of $^{99m}Tc\text{-}C_{60}(OH)_x$ after i.t. exposure. The translocation of $^{99m}Tc\text{-}C_{60}(OH)_x$ into blood circulation was confirmed. At 1 h, there was 0.24%ID g^{-1} in blood and was not detected after 6 h. $^{99m}Tc\text{-}C_{60}(OH)_x$ was mainly retained in lung after i.t. exposure. At 1 h, 40.06%ID g^{-1} was found in the lung, which decreased to 18.12%ID g^{-1} at 48 h. The distribution in the liver, spleen, stomach, kidney, and bone was also observed. The accumulation levels in the liver and bone were relatively stable. However, obvious clearance was seen in other tissues. In SPECT imaging, accumulation in the bladder was obvious at 3 min post exposure. The accumulation was still observed at 60 min. This implied excretion through urine of $^{99m}Tc\text{-}C_{60}(OH)_x$.

Overall, the pharmacokinetics and biodistribution of fullerene have been widely investigated, where the biological behaviors of fullerene depend more on the functionalization. The size of fullerene cage has less influence. However, current researches only focused on some fullerenes and their derivatives. We are

still far from reaching some solid conclusions regarding the regulating factors in the biological behaviors of fullerene. In particular, the most studied fullerene derivative, fullerenol, is usually a mixture. The results from different research groups show variations. In future studies, uniform samples and quantification methods are recommended to reveal the guidelines of fullerene distribution.

3.3.2 Carbon Nanotubes

CNTs are novel sp^2 carbon nanomaterials and hold many attractive properties and great potential in diverse areas. CNTs have found their applications in biomedical areas, and therefore animals and humans are likely to be exposed to them. There are a number of papers dedicated to the tracing and quantification of CNTs after their exposure via different pathways [7].

Yang *et al.* reported the distribution of pristine single-walled carbon nanotubes (SWCNTs) after i.v. injection in mice [46]. It should be noted that naked, pristine SWCNTs cannot be dispersed in aqueous systems. Thus, Tween 80 was used to disperse SWCNTs (Figure 3.5). ^{13}C-SWCNTs dispersed in Tween 80 were detected in the liver (21.1%ID), lungs (15.0%ID), and spleen (1.2%ID) with relatively high levels. ^{13}C was also detected in other tissues, including the brain. During the 28-day observation period, the hepatic accumulation did not change. Lung accumulation showed meaningful decrease to 9.4%ID at 28 days. Part of the SWCNTs might have translocated into the spleen and led to the final spleen uptake of 1.9%ID at 28 days. In their qualitative study, the authors could not detect SWCNTs in the liver, spleen, and lung at 90 days. This indicated the long-term retention of SWCNTs after i.v. injection. The accumulation in the lung of SWCNTs should be due to the large aggregates of SWCNTs in blood circulation. In the hematoxylin and eosin (H&E) staining of lung slides, micrometer-sized black particulates were observed. In another report, where SWCNTs were dispersed with Pluronic F108 and centrifuged to remove the large aggregates, Cherukuri *et al.* [47] found that SWCNTs were not trapped in the lung. The blood circulation half-life of SWCNTs dispersed in Pluronic F108 was 1 h. Pluronic F108 suspended SWCNTs were distributed only in the liver. The detection of SWCNTs was based on the near-infrared fluorescence of singly dispersed SWCNTs. There might be a possibility that SWCNTs were trapped in other organs as aggregates and could not be detected.

By improving the dispersing reagent, that is, using poly(ethylene glycol)–phospholipid (PEG–PL), the pharmacokinetics of CNTs could be improved largely. Dai and coworkers developed PEG–PL-dispersed CNTs for biomedical detection, imaging, thermal therapy, and drug delivery [5]. The pharmacokinetics and biodistribution of PEG–PL-dispersed SWCNTs were investigated. It is well known that PEG is very efficient in improving the pharmacokinetic behavior of exotic substances because it is protein resistant and could shield exotic substances from opsonin recognition [48]. In Liu *et al.*'s [49] studies, PEG chains (hydrophilic) were linked to PL molecules (hydrophobic) to form a hydrophilic–hydrophobic

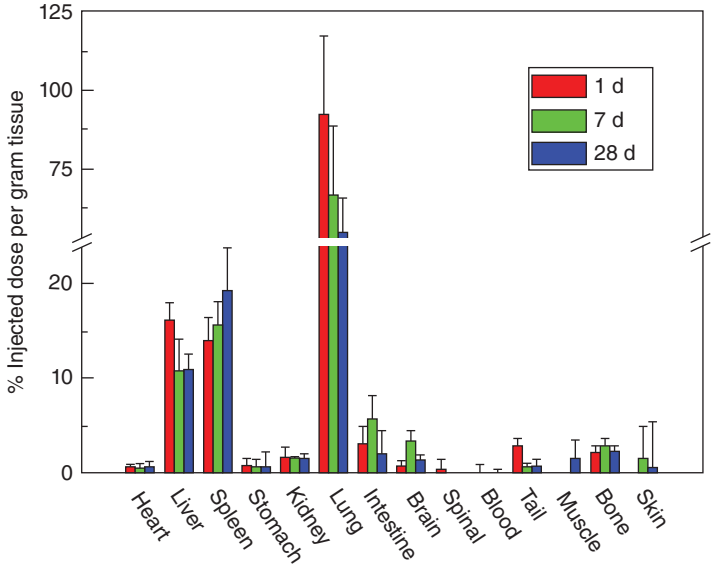

Figure 3.5 Biodistribution of Tween 80-dispersed SWCNTs in mice after i.v. injection. (Adapted with permission from [46]. ©2007 American Chemical Society.)

structure. PEG–PL suspended CNTs by the hydrophobic interaction between PL and CNTs. PEG–PL prolonged the circulation in blood and reduced the RES capture of SWCNTs *in vivo* after i.v. injection. PEG_{2000}–PL-suspended SWCNTs had a blood circulation half-life of 1.2 h [49]. Longer PEG chains protected the SWCNT surface better, thus providing a longer half-life. The circulation half-life of PEG_{5000}–PL-suspended SWCNTs increased to about 5 h. Using branched PEG chains, the half-life could be higher than 15 h [50] because the branched structure covered SWCNTs tightly and less hydrophobic SWCNT surface was exposed to proteins. Prencipe *et al* [51]. used γPGA–Py–mPEG [poly-(γ-glutamic acid)–pyrine(30%)–poly(ethylene glycol) methyl ethers) (70%)] to disperse SWCNTs and prolonged the circulation half-life of SWCNTs to 22.1 h. The RES uptakes showed a decrease when the blood circulation half-life was prolonged by using different PEG reagents. The hepatic uptake of PEG_{2000}–PL-suspended SWCNTs was 70%ID g^{-1}, which decreased to 40%ID g^{-1} for PEG_{5000}–PL-suspended SWCNTs [49]. The value was only 30%ID g^{-1} for br-PEG_{7000}–PL-dispersed SWCNTs (br: branched) [50].

Other PEG-suspended SWCNTs were investigated by Campagnolo *et al.* [52]. The biodistribution of PEG-dispersed SWCNTs was quantified by Seta750 labeling and fluorescence imaging after i.v. injection to pregnant female mice. The results suggested that the majority of PEG-dispersed SWCNTs was retained in the liver and brown fat after 10 min post exposure. Migration toward the bladder was observed at 1 h. The biodistribution of PEG-dispersed SWCNTs was nearly the same in pregnant and nonpregnant mice. After 24 h, the dissection of organs was

performed, and significant fluorescence was detected in the liver, spleen, brown fat, kidneys, and thymus. PEG-dispersed SWCNTs were found in the uterus and placenta. However, PEG-dispersed SWCNTs could not cross the fetal membrane, as shown by the absence of fluorescence in the fetuses. The strong fluorescence in bladder implied that PEG-dispersed SWCNTs were excreted via urine.

In addition to simple dispersal, another strategy for dispersing CNTs is to chemically functionalize them with hydrophilic moieties. The simplest method is to oxidize CNTs to attach oxygen-containing groups on the sidewall. Hydroxyl and carboxyl groups make CNTs dispersible in aqueous systems. Qi *et al.* reported the biodistribution of oxidized MWCNTs after i.v. exposure to pregnant mice [53]. MWCNTs were labeled by ^{99m}Tc for tracing. At 1 h, the blood concentration of MWCNTs was 1.5%ID g^{-1}, which decreased to about 0.2%ID g^{-1} at 24 h. MWCNTs were highly trapped in the lungs. Liver, spleen, kidneys, and stomach had significant accumulations. Clearance in the lungs, kidneys, and stomach was observed, and the contents in the liver and spleen were not changed in 24 h. The radioactivity increased in the amniotic fluid in 24 h. The contents in placenta and fetus increased in the first 6 h and decreased thereafter. The accumulation levels in fetus's lungs decreased in the first 2 h and then remained unchanged. Accumulation in the liver and heart remained unchanged in 24 h. The total accumulation level in the fetus decreased after 6 h. Consistently, Georgin *et al.* reported the biodistribution of oxidized MWCNTs after i.v. exposure [54]. Oxidized MWCNTs were chemically modified with ^{14}CN for quantification. Blood clearance was very fast. At 24 h, the blood concentration was lower than 2%ID. The lungs, spleen, and kidneys were the other targeted organs; no radioactivity was detected in the brain, heart, bones, stomach, and muscle. At day 1, about 42%ID was found in the liver, which decreased to 15%ID at day 14. A similar decrease in trend was observed for the other organs. Urine had a very high concentration of MWCNTs. At day 1, 10%ID was found in urine and more than 6%ID was found at day 14. It is very hard to believe such fast renal excretion of MWCNTs of 10 μm length. Deng *et al.* [55] combined oxidation and surfactant dispersal to suspend MWCNTs. Oxidized MWCNTs were further suspended with Tween 80. The blood content of Tween 80-suspended oxidized MWCNTs was 6.5%ID at 5 min, which decreased to 2.7%ID at 1 h. The half-life of MWCNTs was calculated to be 0.4 h. Unlike Tween 80-suspended pristine SWCNTs [45], Tween 80-suspended oxidized MWCNTs were not trapped in the lungs. At 1 h, only 2%ID of MWCNTs were detected in the lung. The main accumulation organ was liver, with ~60%ID of MWCNTs accumulation.

Hydroxylation can also be regarded as oxidation. In 2004, Wang *et al.* [56] performed the first biodistribution investigation of CNTs. Hydroxylated single-walled carbon nanotubes (SWCNTols) were administrated to mice via i.v., i.p., s.c., and gavage exposure. After i.v. injection, SWCNTols were found in the whole body except the brain. The accumulation levels in the tissues were all low. In their short-term evaluation, the blood circulation eliminative half-life of SWCNTols was calculated as 49.3 min after i.v. injection [57]. The pharmacokinetics parameters were also obtained.

More and more accumulation data implied that functionalization affects the pharmacokinetics of CNTs. In particular, the charges of the moieties should be carefully designed. In 2007, Deng *et al.* [58] reported that negatively charged, taurine-functionalized MWCNTs were trapped in the liver after i.v. injection: 80%ID of ^{14}C-taurine-MWCNTs was trapped in the liver until 28 days. At 90 days, the hepatic accumulation decreased to 20%ID. Only 5%ID was found in the spleen and lung. The rest of the organs showed no significant accumulation. By using ^{125}I labeling, Deng *et al.* [55] traced the short-term distribution of taurine-MWCNTs. Similar high liver accumulation was confirmed within a 6-h observation period. The spleen had 2.5%ID and lung trapped about 5%ID. Very low accumulation levels in blood, kidneys, intestine, and stomach were also observed. Compared to oxidized MWCNTs [55], taurine-MWCNTs had higher negative charge density because the sulfonic acid group deprotonated more. Highly charged MWCNTs seemed to bind opsonin easier, and thus had higher RES uptakes.

Tyrosine has a pI of 5.68, and therefore would be slightly negatively charged in neutral systems. Liang *et al.* [59] reported the biodistribution of tyrosine-functionalized MWCNTs after i.v. and gavage exposure. The half-life of ^{125}I-MWCNTs-Tyr was ~4.4 h. However, the initial concentration at 10 min was 3.79%ID. This suggested that most of MWCNTs-Tyr were cleared within 10 min. After gavage and i.p., the blood concentration was 1.03 and 3.88%ID at 10 min, suggesting the translocation of MWCNTs into blood circulation. Upon i.v. injection, MWCNTs-Tyr were trapped in the lungs at 10 min with 37.15%ID and further increased to 52.89%ID at 24 h. This indicated that MWCNTs-Tyr were not well dispersed and formed large aggregates in blood circulation. This should be due to the low charge density, which could not form strong electrostatic repulsion to avoid aggregation. The second accumulation organ was kidney, which had 12.07%ID at 10 min and gradually decreased to 2.96%ID at 24 h. The accumulations in other tissues were very low. No significant brain accumulation was observed.

Sugar is nearly neutral. When the functionalization density is not high, the short sugar moieties cannot effectively suspend CNTs because of the lack of electrostatic repulsion. Hong *et al.* reported the biodistribution of sugar-functionalized Na^{125}I@SWCNT after i.v. exposure [60]. Only 1%ID was detected in blood after 3 min, which decreased to 0.5%ID at 10 min. Na^{125}I@SWCNT was mainly trapped in the lungs (higher than 80%ID) and slightly distributed in the liver. With time, the pulmonary uptake decreased and the hepatic accumulation increased.

For positively charged CNTs, available data suggested low RES uptakes and fast excretion. Singh *et al.* reported the biodistribution of amino-CNTs after i.v. exposure [61]. Diethylenetriaminepentaacetic (DTPA)-CNTs had a blood circulation half-life of 3.5 h. And when the NH_2 was not fully linked to DTPA, the half-life was 3 h. DTPA-CNTs were cleared from blood circulation very fast and were found in the kidney, muscle, fur, and skin at 30 min. The accumulation became very low at 3 h. When the $-NH_2$ moiety was not fully linked with DTPA, the accumulation level was slightly lower. Excretion through urine was observed and confirmed by the TEM examination of urine samples, where the fiber of

SWCNTs and tube of MWCNTs were present. The same group performed the dynamic imaging of DTPA-MWCNTs in rats after i.v. injection [62]. The low RES uptakes and fast renal excretion were confirmed. According to the radioactivity, less than 0.1%ID g^{-1} of DTPA-MWCNTs were found in the liver, spleen and lung, which was equivalent to less than 0.6 μg DTPA-MWCNTs/g tissue. It might be argued that part of the ^{111}In atoms detached from MWCNTs and led to the lower accumulation levels than the actual situation, because MWCNTs were identified under optical microscopy after H&E staining. At such low (<0.6 μg g^{-1}) MWCNT concentration, optical recognition was nearly impossible. Wang *et al.* reported the biodistribution of DTPA-MCWNT conjugates after i.v. exposure [63]. DTPA-MWCNTs with higher aspect ratios displayed higher tissue affinity compared to wider MWCNTs. All the accumulation levels were much higher than in their previous reports. Another example also suggested that amino-CNTs might remain in the body longer than expected [64, 65]. Although using the same protocol to prepare amino-CNTs as Singh *et al.*, McDevitt *et al.* found that amino-CNTs retained in body for a longer period. Amino-SWCNTs were injected via i.v. and i.p. pathways. After 1 h, 2.7660%ID g^{-1} was still in the blood circulation and after 20 h it was only 0.4160%ID g^{-1} post i.v. exposure. Amino-SWCNTs remained in body for more than 24 h. At 3 h, amino-SWCNTs accumulated in the liver (17.8%ID g^{-1}), spleen (14.3%ID g^{-1}), kidneys (8.3%ID g^{-1}), and skin (2.3%ID g^{-1}). Except in kidneys, the amino-SWCNT content remained unchanged after 24 h. By i.p. injection, the liver and spleen accumulations were lower.

Lysine is a positively charged amino acid with a pI of 9.74. Mulvey *et al.* [66] functionalized SWCNTs with lysine and traced the biodistribution of lysine-SWCNTs after i.v. exposure. The blood concentration was less than 0.05%ID g^{-1} at 90 min. Lysine-SWCNTs were found mostly in the kidneys (1.2%ID g^{-1}) at 90 min. In the liver it was 0.2%ID g^{-1} and in other tissues even lower. About 91.4%ID of lysine-SWCNTs was in urine and 6.8%ID was in the carcass. The level in feces was very low (<1%ID). Such low hepatic accumulation and so fast excretion of positively charged SWCNTs are very strange. However, similar phenomena have been reported by other groups [61]. The underlying mechanism requires further investigations.

Others used inorganic components to functionalize CNTs. Wang *et al.* reported the biodistribution of superparamagnetic iron oxide nanoparticle (SPION)–MWCNT hybrids after i.v. exposure [67]. SPION–MWCNT hybrids were labeled by ^{99m}Tc and quantified by SPECT/computed tomography (CT) or gamma scintigraphy. SPION–MWCNT hybrids distributed in the lungs, liver, and spleen. The lung uptake was 175%ID g^{-1} at 1 h and decreased to 90%ID g^{-1} at 24 h. The liver and spleen had 20%ID g^{-1} or lower. The results were confirmed by liver, lung, and spleen staining, where black particulates were found. TEM investigations found SPION–MWCNT hybrids in hepatocytes, Kupffer cells, and spleen cells. Li *et al.* [68] reported the biodistribution of Pt-MWCNTs after i.v. exposure. Pt-MWCNTs accumulated in the liver, lung, spleen, and kidneys. The accumulation level followed the order Pt-MWCNTs < Pt-$MWCNT_{ox}$ < Pt-$MWCNT_{TEG}$. With time, the lung uptake decreased and the spleen uptake

increased. Pt-MWCNT$_{TEG}$ had very high lung uptake at 1 h (70%ID g^{-1}), which decreased to 32%ID g^{-1} at 24 h. The spleen uptake was 16%ID g^{-1} at 1 h and increased to 35%ID g^{-1} at 24 h. The concentrations in urine for all three samples were ~5%ID, as indicated the renal excretion of Pt-MWCNT.

Apart from small molecules, CNTs could be conjugated with larger molecules for i.v. injection. McDevitt *et al.* [64] reported the biodistribution of antibody–CNTs after i.v. exposure. Antibody–CNTs were labeled by ^{111}In, and were found to be distributed in the kidney (46%ID g^{-1}), liver (16%ID g^{-1}), and spleen (5%ID g^{-1}) at 1 h. The kidney accumulation decreased with time. For liver and spleen, the accumulation levels increased at 24 h and then decreased.

Covalent PEGylation has been regarded as more efficient than noncovalent PEGylation in improving the pharmacokinetics of nanomaterials [48]. Yang *et al.* [69] reported the blood clearance and biodistribution of PEG-SWCNTs. Using a short PEG$_{1500}$ chain, the blood circulation half-life was prolonged to 15.3 h. The value was much longer than that of PEG$_{2000}$–PL- and PEG$_{5000}$–PL-suspended SWCNTs, suggesting that covalent PEGylation was more efficient in improving the pharmacokinetic properties of CNTs. The RES uptakes of PEG$_{1500}$-SWCNTs (28%ID) were lower than those of Tween 80-suspended SWCNTs (37%ID). The hepatic accumulation was confirmed by TEM investigation of the digested liver. In addition, PEG$_{1500}$-SWCNTs suffered slow defunctionalization in the liver so that the PEG chains detached from the sidewalls of SWCNTs via hydrolysis and radical attack [70]. However, when covalent PEGylation was applied on MWCNTs, the improvement of blood circulation became small. PEG$_{4000}$-MWCNTs had a blood circulation half-life of 4.2 min [71]. The hepatic accumulation (7.9%ID) was very low at 24 h. The hepatic uptake could be further decreased to 2.45%ID when the PEG chain was longer (PEG$_{20000}$). The short half-life and low accumulation might be the result of the terminal change from –NH$_2$ (PEG$_{1500}$) to –OH (PEG$_{4000}$ and PEG$_{20000}$).

In addition, other exposure pathways were also considered in the biodistribution studies of CNTs. Because of the easy exposure, the i.p. route was widely adopted. SWCNTols were found in the kidney, stomach, and bone with relatively high accumulation levels after i.p. injection, which further increased from 1 to 3 h and then decreased. The rest of the organs, except the brain, had lower accumulation levels and the concentration decreased gradually. Other exposure pathways showed similar distribution patterns as that of i.p. injection. Separately, gavage exposure had higher stomach and lung accumulations; s.c. injection showed higher skin accumulations. Radioactivity was detected in urine and more weakly in feces, indicating the excretion of SWCNTols via urine and feces. The concentrations in urine and feces decreased with time. The results of SWCNTols indicated that hydroxylation made CNTs translocate freely in the body. Only the blood–brain barrier blocked the translocation of SWCNTols. In a short-term evaluation, the blood circulation eliminative half-life of SWCNTols was calculated as 54.7 min after i.p. injection [57]. After i.p. exposure, the blood concentration of MWCNTs-Tyr was 3.88%ID at 10 min, suggesting the translocation of MWCNTs into the blood circulation [59]. MWCNTs-Tyr were

detected in the kidney, lungs, stomach, intestine, skin, bone, muscle, liver, spleen, and heart. The spleen uptake increased within 24 h, while that in the rest of the organs showed a decreasing trend. Weber *et al.* [72] reported the biodistribution of PEG-SWCNTs after i.p. exposure to zebra fish. PEG-SWCNTs were not found in the brain and heart based on the Raman spectra. Guo *et al.* [73] reported the biodistribution of MWCNT-glucosamine (MWCNT-G) after i.p. exposure. The blood circulation half-life was 5.5 h. MWCNT-G largely was retained in the enterogastric area within the first 6 h. At 6 h, the accumulation level in the enterogastric area reached a maximum of 53.67%ID g^{-1}. The clearance was obvious at 24 h, and only 0.81%ID g^{-1} was found. The translocation of MWCNT-G into the blood circulation and other tissues was observed. At 3 h, the stomach accumulation reached 15.93%ID g^{-1} and the value was 2.28%ID g^{-1} for the liver. In the rest of the organs, the uptakes decreased with time. At 24 h, expect for the stomach (2.09%ID g^{-1}), the accumulations in other organs were less than 0.5%ID g^{-1}. In urine, about 5%ID g^{-1} of MWCNT-G was detected. In feces, the maximum was reached at 10 h, of 30.7%ID g^{-1}. The concentration was still very high at 24 h: 18.31%ID g^{-1}.

Pulmonary exposure was investigated since it is the most possible exposure pathway of humans to CNTs. Deng *et al.* compared the distribution of taurine-MWCNTs after i.t. exposure [58]. The pulmonary uptake of taurine-MWCNTs after i.t. injection was 78%ID at day 1, which decreased to 20%ID at day 28. No ^{14}C radioactivity was detected in blood or other tissue, indicating that taurine-MWCNTs could not translocate from the lung into the blood circulation. Lin *et al.* reported the biodistribution of SWCNTs after i.t. exposure [74]. The ^{125}I labeled SWCNTs mainly accumulated in the trachea (20–90%ID g^{-1}). The distribution in other organs was very low. Urine excretion was confirmed by the high radioactivity in urine. Czarny *et al.* [75] reported the biodistribution of MWCNTs after pulmonary exposure via oropharynx. MWCNTs were labeled on the skeleton by ^{14}C and quantified by a β-autoradiography imager. Radioactivity was not detected in the blood. MWCNTs were trapped in the lung at day 1 and decreased gradually during the 90-day observation time. Increases were observed in the spleen and liver during 7–360 days. Much weaker increases were also found in the kidneys and bone marrow. The MWCNTs were concentrated in the white pulp of the spleen and in the bone marrow. The organs were analyzed by the liquid scintillation counting, suggesting the clearance of MWCNTs from the lungs (50%ID at day 1 and less than 10%ID after 90 days, and an increase of MWCNT accumulation in the liver (0.4%ID at 360 days) and the spleen (0.1%ID at 360 days). The presence of MWCNTs in the lung, liver, and spleen was confirmed by high-resolution transmission electron microscopy (HRTEM) of the organ extracts. It was speculated that MWCNT clearance from the lung was by mucociliary transport, and most probably a significant proportion of the applied dose has been swallowed, ending up in the stomach/gastrointestinal tract (Figure 3.6).

In addition, gavage was also investigated to address the gastrointestinal absorption of CNTs. Deng *et al.* [58] found that after gavage exposure taurine-MWCNTs could not be absorbed in gastrointestinal tract. Taurine-MWCNTs were detected

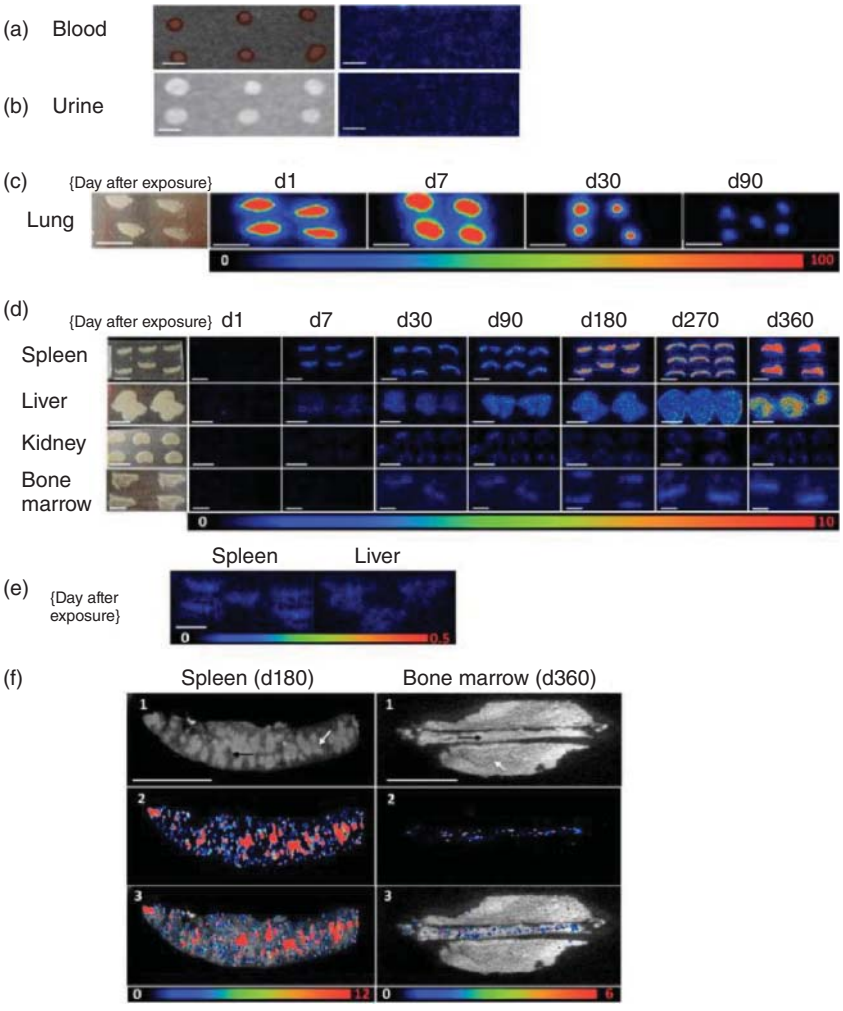

Figure 3.6 (a, b) Blood and urine samples one day after pulmonary exposure. (c, d) Optical images (left) and radioimaging (right) of tissue sections from mice. (e) Radioimaging of spleen and liver tissue sections one day post exposure. (f) High-resolution radioimaging of spleen and bone tissue sections 360 days post exposure. (Adapted with permission from [75]. ©2014 American Chemical Society.)

only in the stomach and intestine. About 74%ID of taurine-MWCNTs were detected in feces after 12 h. After gavage exposure, the blood concentration of MWCNTs-Tyr was 1.03%ID at 10 min [59], suggesting the absorption of MWCNTs into blood circulation. MWCNTs-Tyr could not translocate into the blood circulation and were only found in the stomach and intestine. At 10 min, the stomach had 49.14%ID and the intestine had 5.67%ID. All were cleared within 24 h.

Mover, similar to fullerene studies, there have been several reports on the ecological uptakes of CNTs. Petersen *et al.* reported the ecological uptake of MWCNTs. MWCNTs were labeled by ^{14}C for quantification [76–78]. For *Lumbriculus variegatus*, purified MWCNTs had a slightly higher bioaccumulation factor (BAF) than oxidized MWCNTs [77]. At day 14, the BAF of purified MWCNTs was 0.67 and that of oxidized MWCNTs was 0.39. With time, higher BAFs were achieved for both samples. For earthworm (*E. foetida*), the BAFs increased from day 1 and day 7, and remained constant thereafter [76]. There was no significant difference between purified and oxidized MWCNTs. The overall BAFs for earthworm was very low (smaller than 0.1). The body burden of oxidized MWCNTs was nearly constant during the 28 days, but slightly decreased in the first 1 day. In Petersen *et al.*'s another study, they reported the ecological uptake and depuration of CNTs. The BAFs of SWCNTs and MWCNTs were one order of magnitude lower than that of pyrene. SWCNTs and MWCNTs were not significantly different. At 28 days, the BAFs were 0.28 for SWCNTs, 0.40 for MWCNTs, and 3.6 for pyrene. About 80% of SWCNTs and MWCNTs were excreted after 3 days of exposure to water. The excretion was enhanced when clean sediment was added to the water. In the contrast, the excretion of pyrene was much slower. After 6 h, only 13% was purged. They also compared the uptake and depuration of CNTs in different soils [78]. The BAFs of pyrene were much higher than those of CNTs. SWCNTs had a BAF of 0.0061 in Chelsea soil at 0.03 mg g^{-1} and increased to 0.0078 at 0.1 mg g^{-1}. The BAF was higher in Ypsilanti soil, which was 0.022 at 0.03 mg g^{-1}. MWCNTs had BAF of 0.016 in Chelsea soil at 0.03 mg g^{-1} and increased to 0.023 at 0.3 mg g^{-1}. The BAF was lower in Ypsilanti soil, which was 0.014 at 0.3 mg g^{-1}. The clearance of both SWCNTs and MWCNTs was very slow compared to that of pyrene. Overall, the ecological uptake investigations suggested that the uptakes of CNTs were much lower than small molecules with much faster excretion. The low uptakes of CNTs were similar to those of fullerene.

In summary, the pharmacokinetics and biodistribution of CNTs are regulated by the exposure pathway, particle size, surface charge, and surface functionalization. By designing the surface functionalization, the *in vivo* behaviors of CNTs can be designed as one wishes. The work on CNTs accumulates valuable experience for other carbon nanomaterials. In future study of CNTs, the standardization of samples and quantification methods is highly demanded.

3.3.3 Carbon Nanohorns

Carbon nanohorns (CNHs) are horn-like sp^2 carbon nanomaterials. They can be regarded as sealed CNTs at one end. In most cases, CNHs aggregate to form spherical particles, where the open ends are stacked together and the closed ends are spread toward the outside. Although the structure of CNTs is similar to that of CNTs, CNH aggregates have a completely different morphology. Thus, the biological behaviors of CNHs are obviously different from those of CNTs.

There are two examples showing that PEGylation regulates the pharmacokinetics and distribution of CNHs. The first example was about Gd_2O_3@CNHs. Miyawaki *et al.* [79] reported the biodistribution of single-walled carbon nanohorns (SWCNHs) that were embedded with Gd_2O_3 after i.v. injection. The accumulation of Gd_2O_3@SWCNHs was clearly indicated by the black substances present in histopathological microscopic examination. The nanohorn structure in the liver slices was also observed under TEM, and the presence of Gd was confirmed by the energy dispersive X-ray (EDX) measurement. Qualitatively, about 90% of the injected Gd_2O_3@SWCNHs were detected by inductively coupled plasma atomic emission spectrometry (ICP-AES), with major accumulations in the liver and spleen. This should be attributed to the RES uptake, because the capture of Gd_2O_3@SWCNHs in Kupffer cells was shown in the TEM investigation. The accumulation levels in both the liver and spleen increased within day 1 and decreased thereafter. Small amounts of Gd_2O_3@SWCNHs were found in the lungs and stomach/intestine. The low accumulation in lungs was consistent with the high dispersibility of Gd_2O_3@SWCNHs and implied that Gd_2O_3@SWCNHs remained dispersible in the blood circulation. The excretion of Gd_2O_3@SWCNHs was not quantified, but the excretion pathways might be figured out on the basis of the accumulations in lungs and stomach/intestine. The accumulation in lungs decreased by 40% within 1 week, suggesting the export of Gd_2O_3@SWCNHs to other tissues and excretion via respiration. The increased stomach/intestine accumulation implied that Gd_2O_3@SWCNHs were excreted via the respiratory pathway, captured in sputum, and swallowed into the stomach followed by intestine. Another possibility was that Gd_2O_3@SWCNHs in the liver were exported to the stomach/intestine through the gall bladder. Zhang *et al.* [80] reported the biodistribution of Gd_2O_3@CNHs-PEG after i.v. exposure. Compared to Gd_2O_3@SWCNHs, PEG functionalization greatly prolonged the blood circulation of CNHs. The Gd_2O_3@CNHs-PEG concentration in the blood decreased gradually and the blood circulation half-life of Gd_2O_3@CNHs-PEG in blood was ~5–6 h. Gd_2O_3@CNHs-PEG were trapped in the liver and reached a maximum of ~70%ID at 24 h. The hepatic uptake decreased gradually to ~30%ID at 30 days. Thereafter, no further decrease in the liver was observed in the following 90 days. Gd_2O_3@CNHs-PEG in the spleen increased from 6% at 1 h to 10% at 7 days. The accumulation level in the spleen remained constant during 7–120 days. The decrease of Gd_2O_3@CNHs-PEG was observed in the kidney from ~3–5% at 24 h to 1% at 30 days. The existence of Gd_2O_3@CNHs-PEG in the liver, spleen, and kidneys was confirmed by histopathological examinations of black particulates. Separately, minor amounts of Gd_2O_3@CNHs-PEG were also detected in the intestine and skin. The excretion of Gd_2O_3@CNHs-PEG was faster in the first 30 days, and the excretion seemed to stop in the following 90 days. The total amount in the body decreased to 60%ID at 30 days. The 40%ID excretion was assigned to 15% in feces (confirmed by experiment) and 25% by degradation (speculated). It should be noted that CNTs and even C_{60}, which is much more reactive, could be stable for more than 30 days. It is unlikely that CNHs would be degraded in such a short time (Figure 3.7).

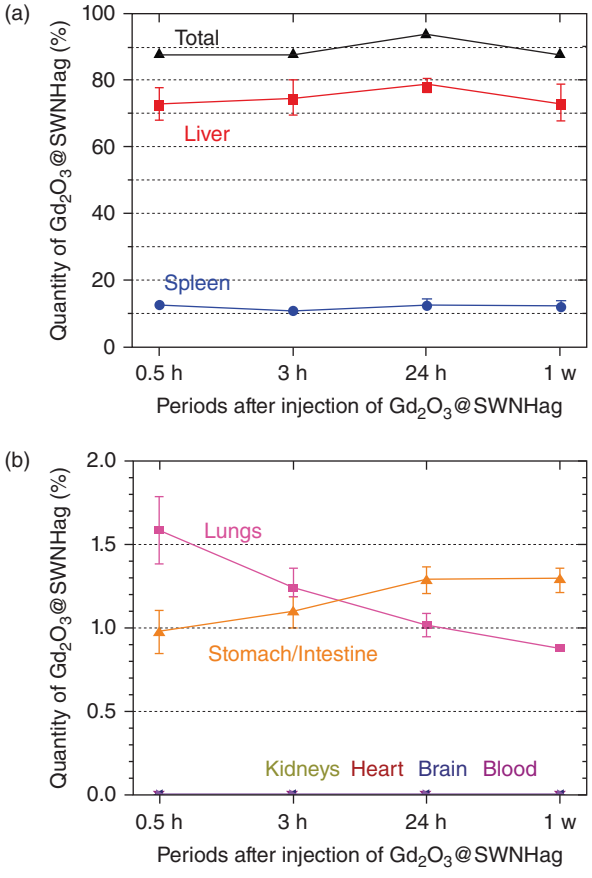

Figure 3.7 Biodistribution of Gd_2O_3@CNHs-PEG in mice. (Adapted with permission from [79]. ©2009 American Chemical Society.)

The same group reported the second example on CNHs. Matsumura *et al.* [81] reported the biodistribution of SWCNHs after i.v. exposure to tumor-bearing mice. Similar to CNTs, PEGylation could prolong the blood circulation of CNHs. With dispersion in DPEG [*N*-(carbonyl-methoxypolyethyleneglycol 5000)-1,2-distearoyl-*sn*-glycero-3-phosphoethanolamine], the SWCNH concentration was 38%ID g^{-1} at 0.5 h and the blood circulation half-life was ~2 h. In the contrast, bare SWCNHs were cleared in blood within 30 min. DPEG-suspended SWCNHs accumulated at 38%ID g^{-1} in liver at 21 h. In the spleen, the value was 18%ID g^{-1}. In stomach/intestine, ~5%ID g^{-1} of DPEG-SWCNH was detected; and 7%ID g^{-1} was found in the skin. Very small amounts were present in the lungs and kidneys. SWCNHs were not found in the brain and heart, suggesting that SWCNHs could not cross the blood–brain barrier. The tumor-targeting of SWCNHs was not ideal: only 3%ID g^{-1} was found in tumor, which was lower than that in blood (4%ID g^{-1}). According to TEM, SWCNHs were trapped in macrophages and

vascular endothelial cells. This was also similar to CNTs, where RES capture was the main reason for their retention.

Apart from PEGylation, size is another key factor that alters the biological behavior of CNHs. Zhang *et al.* [82] reported the size-dependent biodistribution of CNHs after i.v. exposure. CNHs were found in the spleen and liver. In the spleen, the maximum accumulation was reached at 2 days, and for the liver it was 7 days. Small CNHs had much lower accumulation levels in the spleen, while the number of large CNHs was already higher than that of small CNHs at 1 h and further increased in the first 48 h.

Using other exposure pathways, the uptake and distribution of CNHs are completely different. Nakamura *et al.* [83] reported the biodistribution of SWCNHs after oral exposure to mice. SWCNHs were not detected in blood circulation and were present only in the gastrointestinal tract. In normal mice, 6.5%ID was found in stomach after 4 h, which was totally cleared at 24 h. In the small intestine, 9.4%ID was found at 4 h, of which only 0.1%ID was retained at 24 h. In the cecum, 20.3%ID was detected at 4 h, which decreased to 0.9%ID at 24 h. For colon, the value was 15.4%ID at 4 h and 1.1%ID at 24 h. In the dextran sulfate sodium (DSS)-induced colitis models, 20.6%ID was detected in the stomach after 4 h and 4.4%ID at 24 h. In the small intestine, 32.9%ID was found at 4 h and only 5.6%ID was retained at 24 h. In the cecum, 8.4%ID of SWCNHs was found at 4 h, which decreased to 5.8%ID at 24 h. The colon accumulation was much lower (1.3%ID at 4 h and 0.7%ID at 24 h). The difference between normal mice and the colitis models suggested that patients might have different responses to CNHs, to which special attention should be paid. Such differences were also observed during the excretion of CNHs. The excretion of CNHs was faster in normal mice. In feces, 41.3%ID was found at 4 h and 94.7%ID at 24 h. In DSS-induced colitis models, 27.5%ID was detected in feces at 4 h and 91.1%ID at 24 h. In both normal and colitis models of mice, all CNHs were detected in feces after 48 h.

It should be noted that all distribution studies of CNHs were performed by Yudasaka and coworkers. They made solid contributions to the biological evaluation of CNHs. The investigation might be extended to other functionalizations and aggregate sizes of CNHs in future.

3.3.4 Graphene

Graphene is a single-layered graphite sheet. All the carbon atoms of graphene are sp^2 hybrids, and all of them are superficial atoms. Graphene shows great potential in bioimaging, drug delivery, bioanalysis, and so on. Based on the research experience on CNTs and other carbon nanomaterials, the pharmacokinetics and biodistribution of graphene are extensively studied in more efficient ways. The quantification methods for CNTs are nearly the same as for graphene because the two have extremely similar structure and properties. The explanation of graphene behaviors can also be extended to CNTs, such as RES uptakes and excretion pathways.

Graphene sheets (usually several micrometers) are generally larger than other carbon nanomaterials in diameter. Therefore, graphene sheets are cut into smaller sizes for i.v. injection. In the chemical preparation of graphene, graphite is oxidized to graphene oxide (GO) and then GO is reduced to produce reduced graphene oxide (rGO) [84]. GO is soluble in aqueous systems. Thus, it is very simple to administer GO into animals. The biodistribution of GO is widely investigated.

Liu *et al.* [85] labeled GO with ^{125}I and investigated the influence of GO size on the bidistribution behavior. Large graphene oxide (l-GO) was cleared from blood circulation faster than small graphene oxide (s-GO). The terminal elimination half-life of l-GO was 102 min and that of s-GO was 170 min. The distribution patterns of l-GO and s-GO were significantly different. Higher lung accumulation was found for l-GO (about 20%ID), as well as lower hepatic uptakes (around 2%ID). In the contrast, s-GO mainly accumulated in the liver (10–25%ID), and the lung uptakes were much lower (<7%ID). For s-GO, with the increase of the exposure dose, more of the material was trapped in the lungs. This implied that s-GO aggregated more at high doses. Therefore, Liu *et al.*'s results indicated that smaller sized GO should be administrated i.v. at a low dosage to avoid too much pulmonary trap. For biomedical uses, the avoidance of aggregation of GO in blood circulation is crucial. In addition, Zhang *et al.* [86] also reported the biodistribution of GO after i.v. exposure to mice. The diameters of GO were in the range 10–800 nm. The blood circulation half-life of GO was 5.3 h. At 1 h, the blood concentration was 0.4%ID g^{-1}. This indicated the fast clearance of GO in blood. Accumulation in the lung was a distinct character of GO. The GO concentration in lungs was 40%ID g^{-1} at 1 h, which decreased to 25%ID g^{-1} at 48 h. The liver and spleen uptakes increased in the beginning and decreased after 24 h. The stomach accumulation decreased after 3 h and became nearly zero at 48 h. GO was not detected in the brain. The excretion of GO was via urine. Relatively high concentration in urine was detected in the first 12 h (4–7%ID g^{-1}). The concentration was not detectable after 24 h (Figure 3.8).

To prolong the circulation in blood, escape of pulmonary capillary filtration, and reduce the RES uptakes, PEGylation has been widely adopted. In the case of GO, PEGylation strategy still works well just like for CNTs. Li *et al.* [87] compared the biodistribution of GO and PEG-GO after i.v. exposure. The half-life of GO was 5.35 h, which was prolonged to 6.29 h for PEG-GO. However, the blood concentrations were all lower than 4%ID g^{-1} after 10 min. GO distributed mainly in the liver with 55%ID at 10 min and 26%ID at 6 h. The second organ was the lung, with 10%ID at 10 min and 7%ID at 6 h. Other tissues had accumulations of <2%ID. The liver and lung accumulations were lower for PEG-GO: 25%ID of PEG-GO was found in the liver and 9%ID in the lung at 10 min. In the liver, 9%ID PEG-GO was found and in the lung 2.5%ID at 10 min. The presences of GO and PEG-GO in the liver, lung, and spleen were evidenced by H&E staining of the pathology. The lung accumulation of PEG-GO suggested that its particle size was too large for capillary vessels. PEG-GO in dynamic light scattering analysis showed a size of 314 nm, which was smaller than the diameter of the capillary vessels.

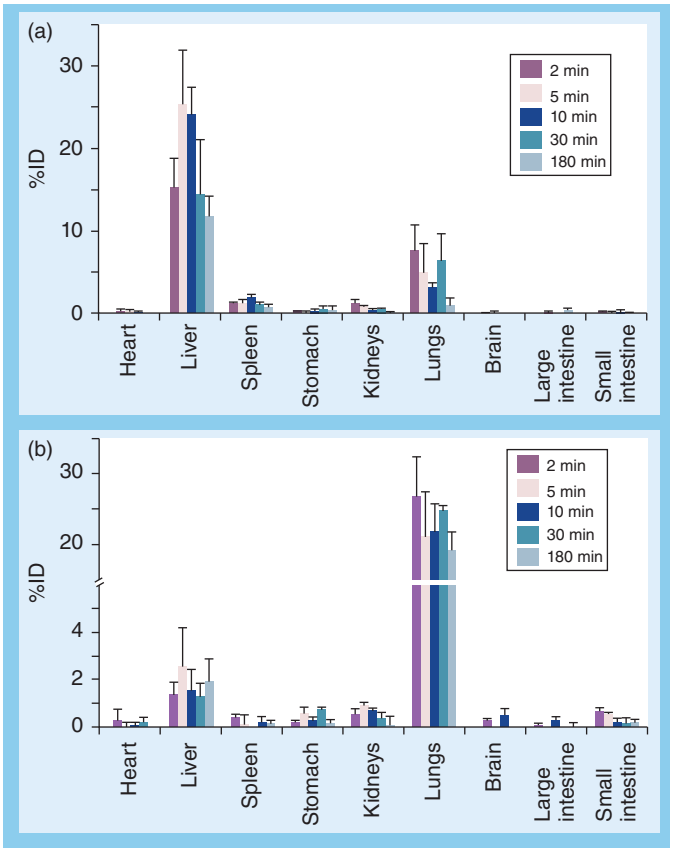

Figure 3.8 Biodistribution of s-GO (a) and l-GO (b) in mice. (Adapted with permission from [85]. ©2012 Future Medicine Ltd.)

Therefore, PEG-GO might aggregate or form protein composites in blood circulation. By cutting GO to even smaller size, the pulmonary uptakes could be reduced to very low levels. Such results were reported by Yang *et al.* [88]. The biodistribution of PEG-GO nanosheets (NGS-PEG) after i.v. exposure was detected upon ^{125}I labeling. The blood circulation curve showed that the pharmacokinetics of NGS-PEG followed a two-compartment model, with the first and second phase blood circulation half-lives of 0.39 and 6.97 h, respectively. The volume of distribution was measured to be 3.76 l, and the AUC was 4.64 mg min ml^{-1}. NGS-PEG mainly accumulated in the liver and spleen, but also distributed into other tissues with low accumulation levels. The liver level was 16%ID g^{-1} and the spleen uptake was 25%ID g^{-1} at 1 h. They were gradually cleared from body. They were also recognized in the liver sections in the histopathological observations during the 90-day investigation. NGS-PEG was excreted in urine and feces. At day 1, the urine level was 7.5%ID g^{-1} and the feces had 5%ID g^{-1}. With time, the urine and feces concentrations decreased. The low lung accumulation and fast excretion of

NGS-PEG should be due to its small size. According to atomic force microscopy (AFM) investigation, NGS-PEG was in the range of 10–30 nm in diameter, which is much smaller than the capillary vessels.

Unlike Li *et al.* and Yang *et al.*, Lu *et al.* [89] found that PEG-GO nanoribbon (PEG-GONR) was cleared from blood circulation quickly and mainly trapped in the liver after i.v. exposure. Whole-body autoradiography and SPECT/computerized tomography (CT) were used to detect PEG-GONR, which was labeled by ^{99m}Tc. Very low radioactivity was detected in blood (0.79%) after 0.5 h, which decreased to 0.26% at 24 h. Whole-body autoradiography suggested that PEG-GONR accumulated in the liver and spleen. SPECT/CT suggested that 84.7% of PEG-GONR accumulated in the liver at 30 min post exposure. The spleen caught 2.18% and lungs 0.37%. The liver accumulation decreased to 7.49%, and the spleen accumulation increased to 7.77% at 24 h. Meaningful but low accumulation occurred in kidneys (0.23%). SPECT/CT indicated the accumulation of PEG-GONR in the bladder and kidney. This suggested the renal excretion of PEG-GONR. This was confirmed by the TEM of urine samples, where GONR was identified.

Other functionalities were adopted in the GO modification for i.v. exposure. Hong *et al.* reported the biodistribution of NOTA-GO (NOTA: 1,4,7-triazacyclononane-1,4,7-triacetic acid) after i.v. exposure to tumor-bearing mice [60, 90]. NOTA-GO was labeled by ^{64}Cu or ^{66}Gd. The blood concentration was 12%ID g^{-1} at 0.5 h and decreased to ~4%ID g^{-1} at 48 h. Whether or not the antibody was linked or blocked, the biodistribution pattern was not influenced. NOTA-GO mainly distributed in the liver and spleen. The accumulation level in the liver was ~20%ID g^{-1} at 3 h and decreased to 15%ID g^{-1} at 48 h. The antibody TRC105 only resulted in higher tumor uptakes. Fazaeli *et al.* [91] reported the biodistribution of ^{98,199}Au-labeled, amino-functionalized GO (^{98,199}Au@AF-GO) after i.v. exposure. ^{98,199}Au@AF-GO mainly distributed in the liver, spleen, and kidneys. ^{98,199}Au@AF-GO also distributed in the lungs, intestine, stomach, and other tissues with low concentrations. The accumulation reached a maximum at 4 h for liver (65%ID g^{-1}), spleen (85%ID g^{-1}), and kidneys (80%ID g^{-1}). ^{98,199}Au@AF-GO was detected in the feces. The high kidney accumulation implied renal excretion. Kanakia *et al.* [92] reported the biodistribution of dextran-coated graphene oxide nanoplatelet (GNP-Dex) formulations after i.v. exposure. The blood concentration was 6% at 50 mg kg^{-1} body weight (bw), 1.5% at 250 mg g^{-1} bw, and 0.5% at 500 mg g^{-1} bw at 30 min. GNP-Dex distributed in the liver, heart, lungs, kidneys, and brain. At low dosage, liver and heart had higher accumulation. At medium and high dosages, heart and kidneys had higher accumulations. The overall accumulations were <4%ID g^{-1} at day 1. At 30 days, the accumulations decreased to <1.5%ID g^{-1}. Brain accumulation became obvious at low dosage. Liver accumulations were more dominating at medium and high dosages. The excretion was via both urine and feces. High dosage resulted in higher feces concentrations, and at 24 h the concentrations were higher than those at 8 h. High dosage induced lower urine concentration at 8 h, but at 24 h the high dosage resulted in higher urine level.

A very unusual study was performed by Li *et al.* [93], in which the biodistribution of MWCNTs and GO was monitored after i.v. co-exposure. The biodistribution of MWCNTs and GO was quantified by ^{99m}Tc labeling and measured by a gamma counter. The blood concentrations of MWCNTs and GO were lower than 1%ID g^{-1} after 1 h. In the co-exposure, MWCNTs were accumulated in the liver, but radioactivities were also found other tissues, including the lungs, spleen, and stomach. The activities were very low in the heart and kidneys. The accumulation reached a maximum at 16 h for liver, lungs, and spleen. The distribution patterns were similar for both co-exposure and individual exposure for MWCNTs, where the individual exposure showed much lower accumulation level and the time-dependent effect was different. For GO, the co-exposure and individual exposure gave completely different distribution patterns. In the individual exposure, GO accumulated in the liver, lungs, and spleen. Radioactivities were also detected in kidneys and stomach. The accumulation reached a maximum at 16 h. In the co-exposure, GO had the highest accumulation level in stomach, while the rest had similar low accumulations. The accumulation decreased after 1 h post exposure. Moreover, MWCNTs were found in the digested stomach and chime after individual exposure and co-exposure.

Like CNTs, pristine graphene cannot be dispersed in aqueous systems; thus, pristine graphene should be dispersed with surfactants for i.v. exposure. For example, Nahain *et al.* [94] reported the biodistribution of rGO/HA-SP (rGO functionalized by hyaluronic acid and spiropyran) after i.v. exposure. rGO/HA-SP distributed in the liver and kidneys but was not found in the spleen and lung.

In addition to i.v. exposure, graphene and its derivatives were administrated via other pathways also. Li *et al.* [95] reported the biodistribution of GO after i.t. exposure. The biodistribution of GO was quantified by ^{125}I labeling and measured by SPECT and a gamma counter. The blood concentration of GO was less than 2%ID at 10 min after the i.t. exposure and further decreased to <0.5%ID after 12 h. The blood concentration of ^{125}I-GO was less than that of free ^{125}I; thus, it is not possible to conclude the transport of GO from the lungs to blood circulation. The results suggested that the majority of GO retained in the lungs and was cleared with time. The accumulation level in the lungs was 70%ID at 10 min and decreased to less than 30%ID at 12 h. The pulmonary capture was directly confirmed by the blackening in the lungs after the dissection. Low accumulation levels in the thyroid, liver, kidneys, stomach, and intestine were observed. Although ^{125}I labeling results suggested the fast clearance of GO, the dissection photographs suggested a much slower clearance. A possible reason might be the detachment of ^{125}I; in particular, similar thyroid accumulation levels of ^{125}I-GO and free ^{125}I were reached at 6 h. GO was believed to be eliminated in the sputum from the body through mucociliary clearance or by other mechanisms. And the other pathway was the renal excretion, where the radioactivity was detected in the bladder and urine.

Another report concerned i.p. and oral exposure. Yang *et al.* [96] reported the biodistribution of NGO-PEG, rGO-PEG and NRGO-PEG after i.p. and oral exposure. After oral exposure, NGO-PEG was mainly retained in the stomach

(15%ID g^{-1}) and intestine (4%ID g^{-1}) at 4 h. Similarly, NRGO-PEG was also retained in the stomach (13%ID g^{-1}) and intestine (5%ID g^{-1}). rGO-PEG showed relatively low levels in the stomach (7%ID g^{-1}) and intestine (3%ID g^{-1}). The clearance of three samples in the gastrointestinal tract was achieved at day 1. The behavior of graphene after i.p. exposure was different. At day 1, NGO-PEG was mainly trapped in the liver (11%ID g^{-1}) and spleen (7%ID g^{-1}). The contents decreased to 8.5%ID g^{-1} for the liver and increased to 9%ID g^{-1} for the spleen at 7 days. NRGO-PEG was very similar to NGO-PEG, and the former was found in the liver (10%ID g^{-1}) and spleen (7%ID g^{-1}) at day 1. The contents decreased to 9.5%ID g^{-1} for the liver and increased to 10%ID g^{-1} for the spleen at 7 days. Again, rGO-PEG had lower accumulation levels in the liver (9%ID g^{-1}) and spleen (9%ID g^{-1}) compared to other two samples. The contents increased to 17%ID g^{-1} for the liver and increased to 23%ID g^{-1} for the spleen at 7 days. The i.p. injection led to the dark color of the liver and the particulates were recognized at 30 days in histopathological investigations for all three samples. The above data suggested that NGO-PEG and NRGO-PEG were very similar, and implied that, upon PEGylation, the oxidation degree of graphene did not influence the biological translocation. rGO-PEG showed lower accumulation levels than NRGO-PEG, indicating that the larger size hindered the translocation of graphene.

Unlike the studies of CNTs, the distribution studies of graphene concerned more on PEGylated ones. Other functionalizations are less investigated. This might due to the fact that scientists have learned lessons from CNTs that PEGylation can improve the pharmacokinetics of carbon nanomaterials more than other functionalizations [5]. Upon PEGylation, the size of graphene becomes the vital parameter regulating the biological behavior. Therefore, more elegant investigations to reveal the size-dependent behaviors and toxicity of graphene *in vivo* are needed.

3.3.5
Graphene Quantum Dots

Graphene quantum dots have similar size as that of carbon dots and nearly the same mechanism of luminescence. However, current graphene quantum dots emit blue or green fluorescence, and are therefore not ideal for *in vivo* imaging. There are only a few reports on the pharmacokinetics and biodistribution of graphene quantum dots.

Nurunnabi *et al.* reported the biodistribution of graphene nanoparticles (GNPs) after i.v. to nude mice [97]. It was very hard to distinguish the fluorescence in body during the *in vivo* imaging. *Ex vivo* imaging indicated the accumulation of GNPs in the liver, kidneys, and spleen at 4 h post exposure. Weak signals were detected in the heart and lung. At 16 h, the accumulation level decreased dramatically. The RES uptakes of graphene quantum dots were also reported by Nahain *et al.* [98]. They found that graphene quantum dots with/without

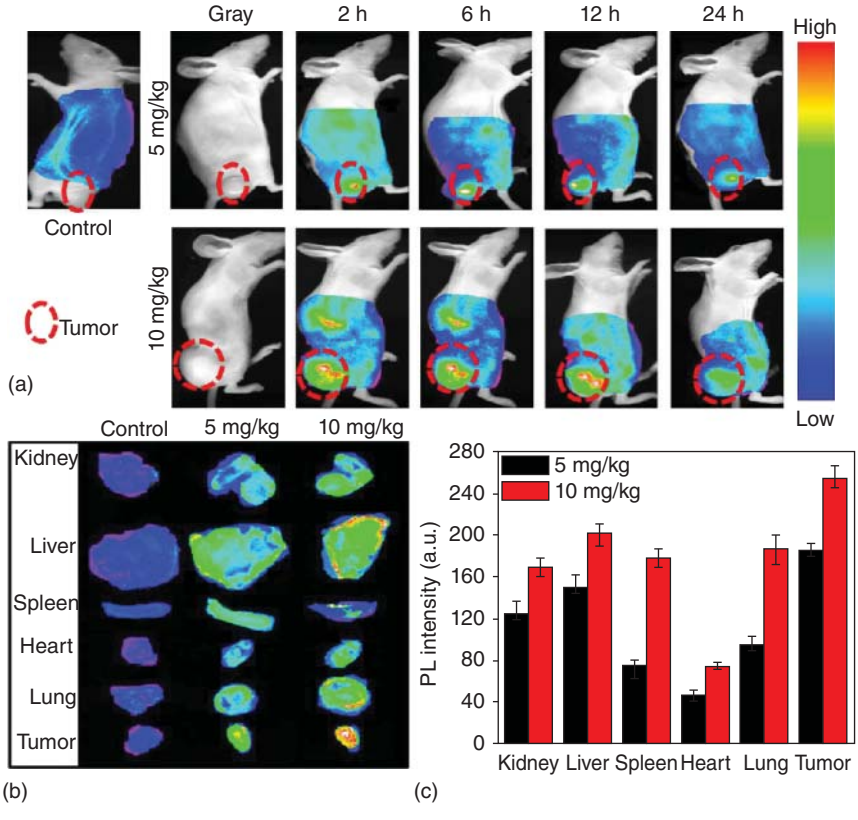

Figure 3.9 Biodistribution of GNPs in mice. (a) *In vivo* imaging. (b) *Ex vivo* imaging. (c) Fluorescence intensity of organs. (Adapted with permission from [99]. ©2013 American Chemical Society.)

hyaluronic acid functionalization distributed in the liver and kidneys. However, they were not detectable in the spleen and lung. Hyaluronic acid could reduce the liver and kidney accumulations, which benefited the tumor uptake of graphene quantum dots. Another strategy to enhance the tumor uptakes is PEGylation. Nurunnabi *et al.* functionalized graphene quantum dots with PEG, which led to longer blood circulation and higher enhanced permeability and retention (EPR) effect [99]. PEGylated graphene quantum dots were found in the liver, spleen, lung, kidneys, and heart. Tumor accumulation level was higher than in the aforementioned organs (Figure 3.9).

The results here suggested that the behaviors of graphene quantum dots were very similar to those of carbon dots. This implied that the hybrid state of carbon atoms did not affect the biodistribution much. The small size of graphene quantum dots made them different from large graphene sheets. Again, functionalization regulated the biodistribution of graphene quantum dots. By designing the functionalities carefully, lower RES uptakes could be achieved.

3.4 Nanodiamonds

ND is a category of fluorescent carbon nanomaterials. The majority of carbon atoms should be in the form of sp^3 hybrids. The fluorescence of NDs could be in the range of red to near-infrared; so NDs are ideal for *in vivo* imaging [100]. However, the generation of fluorescent NDs usually requires a high energy beam, which limits the investigation and applications of NDs. Alternatively, several studies used radioisotope labeling to trace NDs *in vivo*.

After i.v. injection, NDs, just like other carbon nanomaterials, are likely to be trapped in RES organs. In 2009, Yuan and coworkers reported the biodistribution of bovine serum albumin (BSA)-suspended NDs in mice after i.v. injection [101]. The blood concentration of NDs was 6%ID at 30 min after the i.v. injection, corresponding to a moderate blood clearance speed of NDs. Both ^{125}I labeling and UV–vis spectroscopy suggested that NDs accumulated in the liver and lungs. The accumulations in the spleen, kidneys, intestine, stomach, muscle, and skin were all below 2%ID at 30 min. The liver (60%ID) and lung (5%ID) accumulations did not change over the 28-day observation period. The hepatic accumulation should be due to the RES uptake, and the Kupffer cells were found to capture NDs, as shown by TEM. Rojas *et al.* quantified the biodistribution of NDs by ^{18}F-labeling and measured it by a gamma counter and PET [102]. After the injection, the hepatic and spleen uptakes showed increases in the first 10 min. The levels in lungs and kidneys remained unchanged. The radioactivity increased in the bladder. The accumulation levels in rats were all very low, targeting in the lungs, spleen, liver, and kidneys. The accumulation levels in mice were much higher. In particular, the pulmonary uptake became dominant in mice. The distribution patterns of ND, ND-Tween80, and ND-PEG_{8000} were very similar. The filtered NDs accumulated much less and were detected only in the liver and kidneys. This indicated that the lung accumulation should be assigned to the larger aggregates, which were trapped in the lung by pulmonary capillary filtration. The NDs were slowly cleared via urine after entering blood circulation because they were detected in bladder and urine. The filtered NDs showed much higher levels in urine. The excretion was influenced by the presence of a dispersing reagent, such as Tween 80 or PEG_{8000}. For rats, Tween 80 and PEG inhibited the excretion, resulting in lower urine levels. For mice, Tween 80 inhibited the excretion whereas PEG showed mild enhancement (Figure 3.10).

Separately, Zhang *et al.* reported the biodistribution of NDs after i.t. exposure [103]. The blood concentration of ^{188}Re-ND was 1%ID g^{-1} at 1 h after the i.t. exposure and decreased to 0.19%ID g^{-1} after 48 h. The blood circulation half-life was ~8 h. The detection of NDs in blood indicated that NDs could translocate from the lung into blood circulation. This was similar to ultrafine carbon particles and CNPs. A possible explanation could be that NDs here were very small, which were of several nanometers in diameter and aggregated into ~40 nm particles. The majority of NDs were retained in lungs and they were cleared with time. The

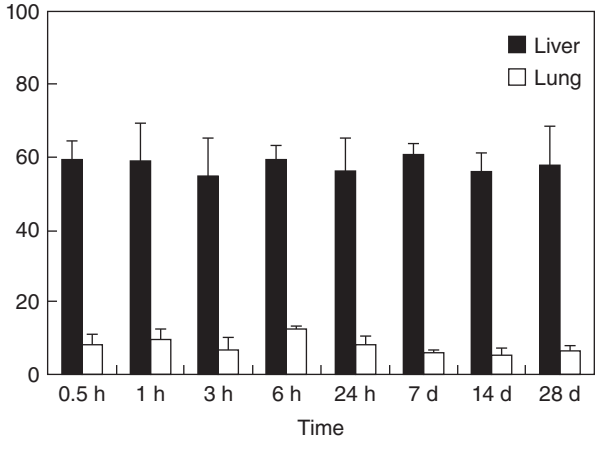

Figure 3.10 Biodistribution of NDs in mice. (Adapted with permission from [101]. ©2009 Elsevier B.V.)

accumulation level in the lungs was 192%ID g^{-1} at 1 h, which decreased to 69%ID g^{-1} at 48 h. The pulmonary capture was directly indicated by the particles in H&E staining. Low accumulation levels were observed in the spleen, bone, liver, kidneys, and stomach. NDs in blood circulation and other organs might be slowly cleared via urine, because NDs were detected in urine and reached a maximum of 4.6%ID g^{-1} at 24 h.

Another report of *Caenorhabditis elegans* was from Mohan *et al.* [104]. NDs were supplied as food to *C. elegans* and were found in the gut at 2 and 12 h. The excretion occurred only when *Escherichia coli* was supplied. Dextran-coated NDs and BSA-coated NDs were seen to be localized within in the intestinal cells, and a few remained in the lumen after the supply to *C. elegans*. After *E. coli* was supplied, NDs in the intestinal cells were retained while those in the lumen were excreted. Upon microinjection into the gonads of adult hermaphrodites, bare NDs were found in the progeny at early and late embryonic stages. NDs dispersed in the distal gonad and oocytes at 30 min. NDs were present in the cytoplasm of many cells in the early embryos, and became predominantly in the intestinal cells of the late embryo. This suggested that, although NDs could be passed to the progeny (second generation), NDs would be excreted into intestinal cells and might be finally excreted during the growth of *C. elegans*.

The distribution studies of NDs were seldom performed, where the surface chemistry and exposure pathway regulates the distribution and excretion of NDs. More investigations are required to reach more reliable conclusions in the future. Whole-body and *ex vivo* imaging of NDs in mice or other mammals are encouraged to solve the stability issue of radioisotope labeling.

3.5 Summary and Outlook

In summary, the pharmacokinetics and biodistribution behaviors of carbon nanomaterials have been extensively investigated, where multiple quantification techniques were adopted. Different properties of carbon nanomaterials were focused in the distribution studies. By comparing the different results of carbon nanomaterials, we could reach some general rules of the pharmacokinetics and biodistribution of carbon nanomaterials.

The first issue to consider is the exposure pathway. Intravenous injection has 100% bioavailability of carbon nanomaterials. The major issues for i.v. exposure are pulmonary capillary filtration and RES capture. Pulmonary exposure leads to high lung accumulation of carbon nanomaterials. After entering the lung, two things are crucial for carbon nanomaterials: the translocation into blood circulation and excretion through mucus (sputum). For gavage exposure, the absorption of carbon nanomaterials in the gastrointestinal tract and the translocation into blood circulation are important for biosafety studies. In intraperitoneal injection, carbon nanomaterials directly come into contact with the organs in the abdominal cavity. The translocation of carbon nanomaterials into the organs and blood circulation should be of concern.

The second issue is the size of carbon nanomaterials. If aggregation occurs, the size of the aggregates is more important than the size of an individual particle. Particle size is crucial for the translocation of carbon nanomaterials into blood circulation in exposure pathways, except in i.v. injection. Smaller particles translocate more freely than larger ones and have higher bioavailability. After entering the blood circulation, large particulates (>2 μm) will be filtered by pulmonary capillary vessels. The rest circulate and distribute into other tissues. Very small particles (<100 nm) might shift the distribution pattern to the spleen and marrow.

The third issue is the surface properties, including charge, hydrophilicity/hydrophobicity, length of the moiety, and density of functionalities. The surface properties determine the interaction between carbon nanomaterials and biological systems. There might be electrostatic, hydrogen-bonding, hydrophobic, π–π interaction, and so on, involved [25]. Too strong an interaction might hinder the translocation of carbon nanomaterials into the blood circulation. As discussed in the *sp^2 Carbon Nanomaterials* section, hydroxylated fullerene and CNTs showed free translocation into the blood circulation upon different exposure pathways [38–43, 56, 57]. In the blood circulation, opsonization is main reason for the RES uptake [48]. Reducing the interaction between carbon nanomaterials and opsonin inhibits the RES capture. Less charge and high hydrophilicity benefit the reduction of carbon nanomaterial–protein interaction, and therefore will significantly reduce the RES accumulation of carbon nanomaterials. The most powerful functionalization to get protein resistance is PEGylation [48]. The results collectively demonstrate that PEGylated carbon nanomaterials circulate longer and are captured less [49–52, 69, 87–89]. Moreover, to cross the blood–brain barrier, the lipid compatibility of carbon nanomaterials is important.

The fourth issue is the shape of carbon nanomaterials. Although lacking direct comparison, there are several groups of data that could be analyzed to reach this conclusion. Tween 80-dispersed fullerene (spherical) [29] and CNTs (tubular) [46] showed similar distribution pattern, but the RES accumulation levels were not identical. Oxidized MWCNTs (tubular) [54] and graphene oxide (planar) [85] had completely different biodistribution patterns although they shared similar surface functionalities. The shape-dependent pharmacokinetics and biodistribution of other nanomaterials were also acknowledged in the literature [105–107].

For future studies, some elegantly designed experiments are needed to verify the aforementioned conclusions. Sample standardization is essential to arrive at some definite conclusions. More importantly, the connection between distribution data and toxicological investigations should be strengthened. Toxicological evaluations of carbon nanomaterials should be performed under the guidance of pharmacokinetics and biodistribution data. The interpretation of toxicological data should take the pharmacokinetics and biodistribution of carbon nanomaterials into consideration.

Acknowledgments

The authors acknowledge the financial support from the National Natural Science Foundation of China (Grant No. 21307101).

References

1. Oberdörster, G., Oberdörster, E., and Oberdörster, J. (2005) An emerging discipline evolving from studies of ultrafine particles. *Environ. Health Perspect.*, **113**, 823–839.
2. Nel, A., Xia, T., Madler, L., and Li, N. (2006) Toxic potential of materials at the nanolevel. *Science*, **311**, 622–627.
3. Uo, M., Akasaka, M., Watari, F., Sato, Y., and Tohji, K. (2011) Toxicity evaluations of various carbon nanomaterials. *Dent. Mater. J.*, **30**, 245–263.
4. Liu, J.H., Yang, S.T., Wang, H., and Liu, Y. (2010) Advances in biodistribution study and tracing methodology of carbon nanotubes. *J. Nanosci. Nanotechnol.*, **10**, 8469–8481.
5. Yang, S.T., Luo, J., Zhou, Q., and Wang, H. (2012) Pharmacokinetics, metabolism and toxicity of carbon nanotubes for biomedical purposes. *Theranostics*, **2**, 271–282.
6. Riviere, J.E. (2009) Pharmacokinetics of nanomaterials: an overview of carbon nanotubes, fullerenes and quantum dots. *Wiley Interdiscip. Rev. Nanomed. Nanobiotechnol.*, **1**, 26–34.
7. Wang, H., Yang, S.T., Cao, A., and Liu, Y. (2012) Quantification of carbon nanomaterials in vitro. *Acc. Chem. Res.*, **46**, 750–760.
8. Wang, B., He, X., Zhang, Z., Zhao, Y., and Feng, W. (2012) Metabolism of nanomaterials in vivo: blood circulation and organ clearance. *Acc. Chem. Res.*, **46**, 761–769.
9. Oberdörster, G., Sharp, Z., Atudorei, V., Elder, A., Gelein, R., Lunts, A., Kreyling, W., and Cox, C. (2002) Extrapulmonary translocation of ultrafine carbon particles following whole-body inhalation exposure of rats. *J. Toxicol. Environ. Health, Part A*, **65**, 1531–1543.

10. Oberdörster, G., Sharp, Z., Atudorei, V., Elder, A., Gelein, R., Kreyling, W., and Cox, C. (2004) Translocation of inhaled ultrafine particles to the brain. *Inhalation Toxicol.*, **16**, 437–445.
11. Nemmar, A., Hoet, P.H.M., Vanquickenborne, B., Dinsdale, D., Thomeer, M., Hoylaerts, M.F., Vanbilloen, H., Mortelmans, L., and Nemery, B. (2015) Passage of inhaled particles into the blood circulation in humans. *Circulation*, **105**, 411–414.
12. Moller, W., Felten, K., Sommerer, K., Scheuch, G., Meyer, G., Meyer, P., Haussinger, K., and Kreyling, W.G. (2008) Deposition, retention, and translocation of ultrafine particles from the central airways and lung periphery. *Am. J. Respir. Crit. Care Med.*, **177**, 426–432.
13. Wiebert, P., Sanchez-Crespo, A., Falk, R., Philipson, K., Lundin, A., Larsson, S., Moller, W., Kreyling, W.G., and Svartengren, M. (2006) No significant translocation of inhaled 35-nm carbon particles to the circulation in humans. *Inhalation Toxicol.*, **18**, 741–747.
14. Mills, N.L., Amin, N., Robinson, S.D., Anand, A., Davies, J., Patel, D., Fuente, J.M., Cassee, F.R., Boon, N.A., MacNee, W., Millar, A.M., Donaldson, K., and Newby, D.E. (2006) Do inhaled carbon nanoparticles translocate directly into the circulation in humans? *Am. J. Respir. Crit. Care Med.*, **173**, 426–431.
15. Liu, J.H., Yang, S.T., Wang, X., Wang, H., Liu, Y., Luo, P.G., Liu, Y., and Sun, Y.P. (2014) Carbon nanoparticles trapped in vivo – similar to carbon nanotubes in time- dependent biodistribution. *ACS Appl. Mater. Interfaces*, **6**, 14672–14678.
16. Yang, S.T., Cao, L., Luo, P.G., Lu, F., Wang, X., Wang, H., Meziani, M.J., Liu, Y., Qi, G., and Sun, Y.P. (2009) Carbon dots for optical imaging in vivo. *J. Am. Chem. Soc.*, **131**, 11308–11309.
17. Yang, S.T., Wang, X., Wang, H., Lu, F., Luo, P.G., Cao, L., Meziani, M.J., Liu, J.H., Liu, Y., Chen, M., Huang, Y., and Sun, Y.P. (2009) Carbon dots as nontoxic and high performance fluorescence imaging agents. *J. Phys. Chem. C*, **113**, 18110–18114.
18. Tao, H., Yang, K., Zhen, M., Wan, J., Zhang, Y., Kang, Z., and Liu, Z. (2012) In vivo NIR fluorescence imaging, biodistribution, and toxicology of photoluminescent carbon dots produced from carbon nanotubes and graphite. *Small*, **8**, 281–290.
19. Li, N., Liang, X., Wang, L., Li, Z., Li, P., Zhu, Y., and Song, J. (2012) Biodistribution study of carbogenic dots in cells and in vivo for optical imaging. *J. Nanopart. Res.*, **14**, 1177.
20. Srivastava, S., Awasthi, R., Tripathi, D., Rai, M.K., Agarwal, V., Gajbhiye, N.S., and Gupta, R.K. (2012) Magnetic-nanoparticle-doped carbogenic nanocomposite: an effective magnetic resonance/fluorescence multimodal imaging probe. *Small*, **8**, 1099–1109.
21. Huang, P., Lin, J., Wang, X., Wang, Z., Zhang, C., He, M., Wang, K., Chen, F., Li, Z., Shen, G., Cui, D., and Chen, X. (2012) Light-triggered theranostics based on photosensitizer-conjugated carbondots for simultaneous enhanced-fluorescence imaging and photodynamic therapy. *Adv. Mater.*, **24**, 5104–5110.
22. Xu, Y., Jia, X.H., Yin, X.B., He, X.W., and Zhang, Y.K. (2014) Carbon quantum dot stabilized gadolinium nanoprobe prepared via a one-pot hydrothermal approach for magnetic resonance and fluorescence dual-modality bioimaging. *Anal. Chem.*, **86**, 12122–12129.
23. Huang, X.L., Zhang, F., Zhu, L., Choi, K.Y., Guo, N., Guo, J.X., Tackett, K., Anilkumar, P., Liu, G., Quan, Q.M., Choi, H.S., Niu, G., Sun, Y.P., Lee, S., and Chen, X.Y. (2013) Effect of injection routes on the biodistribution , clearance , and tum or uptake of carbon dots. *ACS Nano*, **7** (7), 5684–5693.
24. Yang, S.T., Liu, Y., Wang, Y., and Cao, A. (2013) Biosafety and bioapplication of nanomaterials by designing protein-nanoparticle interactions. *Small*, **9**, 1635–1653.
25. Wu, X., Yang, S.-T., Wang, H., Wang, L., Hu, W., Cao, A., and Liu, Y. (2010) Influences of the size and hydroxyl number of fullerenes/fullerenols on

their interactions with proteins. *J. Nanosci. Nanotechnol.*, **10**, 6298–6304.

26. Bullard-Dillard, R., Creek, K., Scrivens, W.A., and Tour, J.M. (1996) Tissue sites of uptake of ^{14}C-labeled C_{60}. *Bioorg. Chem.*, **24** (32), 376–385.
27. Nikolic, N., Đuric, S.V., Jankovic, D., Đokic, D., Mirkovic, M., Bibi, N., and Trajkovic, V. (2009) Preparation and biodistribution of radiolabeled fullerene C_{60} nanocrystals. *Nanotechnology*, **20**, 385102.
28. Kubota, R., Tahara, M., Shimizu, K., Sugimoto, N., Hirose, A., Nishimura, T. (2011) Time-dependent variation in the biodistribution of C_{60} in rats determined by liquid chromatography-tandem mass spectrometry. *Toxic. Lett.*, **206**, 172–177.
29. Chang, X., Ruan, L., Yang, S.T., Sun, B., Guo, C., Zhou, L., Dong, J., Yuan, H., Xing, G., Zhao, Y., and Yang, M. (2014) Quantification of carbon nanomaterials in vivo: direct stable isotope labeling on the skeleton of fullerene C_{60}. *Environ. Sci. Nano*, **1**, 64–70.
30. Moussa, F., Pressac, M., Genin, E., Roux, S., Trivin, F., Rassat, A., Ceolin, R., and Szwarc, H. (1997) Quantitative analysis of C_{60} fullerene in blood and tissues by high-60 performance liquid chromatography with photodiode-array and mass spectrometric detection. *J. Chromatogr. B*, **696**, 153–159.
31. Sumner, S.C.J., Fennell, T.R., Snyder, R.W., Taylor, G.F., and Lewin, A.H. (2010) Distribution of carbon-14 labeled C_{60} ($[^{14}C]C_{60}$) in the pregnant and in the lactating dam and the effect of C_{60} exposure on the biochemical prof le of urine. *J. Appl. Toxicol.*, **30**, 354–360.
32. Li, D., Fortner, G.D., Johnson, D.R., Chen, C., Li, Q.L., and Alvarez, P.J.J. (2010) Bioaccumulation of $^{14}C_{60}$ by the earthworm eisenia fetida. *Environ. Sci. Technol.*, **44** (23), 9170–9175.
33. Rajagopalan, P., Wudl, F., Schinazi, R.F., and Boudinot, F.D. (1996) Pharmacokinetics of a water-soluble fullerene in rats. *Antimicrob. Agents Chemother.*, **40** (10), 2262–2265.
34. Yamago, S., Tokuyama, H., Nakamuralr, E., Kikuchi, K., Kananishl, S., Sueki, K., Nakahara, H., Enomoto, S., and Ambe, F. (1995) In viva biological behavior of a water-miscible fullerene: ^{14}C labeling, absorption, distribution, excretion and acute toxicity. *Chem. Biol.*, **2** (6), 385–389.
35. Chen, C., Xing, G., Wang, J., Zhao, Y., Li, B., Tang, J., Jia, G., Wang, T., Sun, J., Xing, L., Yuan, H., Gao, Y., Meng, H., Chen, Z., Zhao, F., Chai, Z., and Fang, X. (2005) Multihydroxylated $[Gd@C_{82}(OH)_{22}]_n$ nanoparticles: antineoplastic activity of high efficiency and low toxicity. *Nano Lett.*, **5**, 2050–2057.
36. Injac, R., Boskovic, M., Perse, M., Koprivec-Furlan, E., Cerar, A., Djordjevic, A., and Strukelj, B. (2008) Acute doxorubicin nephrotoxicity in rats with malignant neoplasm can be successfully treated with fullerenol $C_{60}(OH)_{24}$ via suppression of oxidative stress. *Pharmacol. Rep.*, **60**, 742–749.
37. Zhu, J., Ji, Z., Wang, J., Sun, R., Zhang, X., Gao, Y., Sun, H., Liu, Y., Wang, Z., Li, A., Ma, J., Wang, T., Jia, G., and Gu, Y. (2008) Tumor-inhibitory effect and immunomodulatory activity of fullerol $C_{60}(OH)_x$. *Small*, **4**, 1168–1175.
38. Li, Y.G., Huang, X., Liu, R.L., Li, Q.N., Zhang, X.D., and Li, W.X. (2005) Preparation of ^{67}Ga-$C_{60}(OH)_x$ and its biodistribution. *J. Radioanal. Nucl. Chem.*, **265** (1), 127–131.
39. Li, Q.N., Xiu, Y., Zhang, X.D., Liu, R.L., Du, Q.Q., Shun, X.G., Chen, S.L., and Li, W.X. (2002) Preparation of ^{99m}Tc-$C_{60}(OH)_x$ and its biodistribution studies. *Nucl. Med. Biol.*, **29**, 707–710.
40. Song, H., Luo, S.Z., Wei, H.Y., Song, H.T., Yang, Y.Q., and Zhao, W.W. (2010) In vivo biological behavior of $^{99m}Tc(CO)_3$ labeled fullerol. *J. Radioanal. Nucl. Chem.*, **285**, 635–639.
41. Maksin, T., Djokic, D., Jankovic, D., Djordjevic, A., and Neskovic, O. (2007) Comparison of some physico-chemical parameters and biological behaviour of fullerenol labelled with technetium -99 m. *J. Optoelectron. Adv. Mater.*, **9** (8), 2571–2577.
42. Li, Q.N., Xiu, Y., Zhang, X.D., Liu, R.L., Du, Q.Q., Sun, X.G., Chen, S.L., and Li, W.X. (2001) Biodistribution of fullerene

derivative $C_{60}(OH)_x(O)_y$. *Chin. Sci. Bull.*, **46** (19), 1615–1618.
43. Ji, Z., Sun, H., Wang, H., Xie, Q., Liu, Y., and Wang, Z. (2006) Biodistribution and tumor uptake of $C_{60}(OH)_x$ in mice. *J. Nanopart. Res.*, **8**, 53–63.
44. Cagle, D.W., Kennel, S.J., Mirzadeh, S., Alford, J.M., and Wilson, L.J. (1999) In vivo studies of fullerene-based materials using endohedral metallofullerene radiotracers. *Proc. Natl. Acad. Sci. U.S.A.*, **96**, 5182–5187.
45. Xu, J.Y., Li, Q.N., Li, J.G., Ran, T.C., Wu, S.W., Song, W.M., Chen, S.L., and Li, W.X. (2007) Biodistribution of ^{99m}Tc-$C_{60}(OH)_x$ in Sprague–Dawley rats after intratracheal instillation. *Carbon*, **45**, 1865–1870.
46. Yang, S.T., Guo, W., Lin, Y., Deng, X.Y., Wang, H.F., Sun, H.F., Liu, Y.F., Wang, X., Wang, W., Chen, M., Huang, Y.P., and Sun, Y.P. (2007) Biodistribution of pristine single-walled carbon nanotubes in vivo. *J. Phys. Chem. C*, **111** (48), 17761–17764.
47. Cherukuri, P., Gannon, C.J., Leeuw, T.K., Schmidt, H.K., Smalley, R.E., Curley, S.A., and Weisman, R.B. (2006) Mammalian pharmacokinetics of carbon nanotubes using intrinsic near-infrared fluorescence. *Proc. Natl. Acad. Sci. U.S.A.*, **103** (50), 18882–18886.
48. Owens, D.E. and Peppas, N.A. (2006) Opsonization, biodistribution, and pharmacokinetics of polymeric nanoparticles. *Int. J. Pharm.*, **307**, 93–102.
49. Liu, Z., Cai, W.B., He, L.N., Nakayama, N., Chen, K., Sun, X.M., Chen, X.Y., and Dai, H.J. (2007) In vivo biodistribution and highly efficient tumour targeting of carbon nanotubes in mice. *Nat. Nanotechnol.*, **2**, 47–52.
50. Liu, Z., Davis, C., and Cai, W. (2008) Circulation and long-term fate of functionalized, biocompatible single-walled carbon nanotubes in mice probed by Raman spectroscopy. *Proc. Natl. Acad. Sci. U.S.A.*, **105**, 1410–1415.
51. Prencipe, G., Tabakman, S.M., and Welsher, K. (2009) PEG branched polymer for functionalization of nanomaterials with ultralong blood circulation. *J. Am. Chem. Soc.*, **131**, 4783–4787.
52. Campagnolo, L., Massimiani, M., Palmieri, G., Bernardini, R., Sacchetti, C., Bergamaschi, A., Vecchione, L., Magrini, A., Bottini, M., and Pietroius, A. (2013) Biodistribution and toxicity of pegylated single wall carbon nanotubes in pregnant mice. *Part. Fibre Toxicol.*, **10** (21), 1–13.
53. Qi, W., Bi, J.J., Zhang, X.Y., Wang, J., Wang, J.J., Liu, P., Li, Z., and Wu, W.S. (2014) Damaging effects of multi-walled carbon nanotubes on pregnant mice with different pregnancy times. *Sci. Rep.*, **4** (4252), 101038.
54. Georgin, D., Czarny, B., Botquin, M., Mayne-L'Hermite, M., Pinault, M., Bouchet-Fabre, B., Carriere, M., Poncy, J.L., Chau, Q., Maximilien, R., Dive, V., and Taran, F. (2009) Preparation of ^{14}C-labeled multiwalled carbon nanotubes for biodistribution investigations. *J. Am. Chem. Soc.*, **131**, 14658–14659.
55. Deng, X.Y., Yang, S.T., Nie, H.Y., Wang, H.F., and Liu, Y.F. (2008) A generally adoptable radiotracing method for tracking carbon nanotubes in animals. *Nanotechnology*, **19**, 075101.
56. Wang, H.F., Wang, J., Deng, X.Y., Sun, H.F., Shi, Z.J., Gu, Z.N., Liu, Y.F., and Zhao, Y.L. (2004) Biodistribution of carbon single-wall carbon nanotubes in mice. *J. Nanosci. Nanotechnol.*, **4** (8), 1019–1024.
57. Wang, J., Deng, X.Y., Yang, S.T., Wang, H.F., Zhao, Y.L., and Liu, Y.F. (2008) Rapid translocation and pharmacokinetics of hydroxylated single-walled carbon nanotubes in mice. *Nanotoxicology*, **2** (1), 28–32.
58. Deng, X., Jia, G., Wang, H., Sun, H., Wang, X., Yang, S., Wang, T., and Liu, Y. (2007) Translocation and fate of multi-walled carbon nanotubes in vivo. *Carbon*, **45**, 1419–1424.
59. Liang, G.Y., Zhang, T., Liu, R., Ye, B., Yin, L.H., and Pu, Y.P. (2010) Preparation and biodistribution of tyrosine modified multiwall carbon nanotubes. *J. Nanosci. Nanotechnol.*, **10**, 8508–8515.
60. Hong, S.Y., Tobias, G., Al-Jamal, K.T., Ballesteros, B., Ali-Boucetta, H.,

Lozano-Perez, S., Nellist, P.D., Sim, R.B., Finucane, C., Mather, S.J., Green, M.L.H., Kostarelos, K., Davis, B.G. (2010) Filled and glycosylated carbon nanotubes for in vivo radioemitter localization and imaging. *Nat. Mater*, **9**, 485–490.

61. Singh, R., Pantarotto, D., Lacerda, L., Pastorin, G., Klumpp, C., Prato, M., Bianco, A., and Kostarelos, K. (2006) Tissue biodistribution and blood clearance rates of intravenously administered carbon nanotube radiotracers. *Proc. Natl. Acad. Sci. U.S.A.*, **103** (9), 3357–3362.
62. Lacerda, L., Soundararajan, A., Singh, R., Pastorin, G., Al-Jamal, K.T., Turton, J., Frederik, P., Herrero, M.A., Li, S., Bao, A., Emfietzoglou, D., Mather, S., Phillips, W.T., Prato, M., Bianco, A., Goins, B., and Kostarelos, K. (2008) Dynamic imaging of functionalized multi-walled carbon nanotube systemic circulation and urinary excretion. *Adv. Mater.*, **20**, 225–230.
63. Wang, J.T.-W., Fabbro, C., Venturelli, E., Menard-Moyon, C., Chaloin, O., Ros, T.D., Methven, L., Nunes, A., Sosabowski, J.K., Mather, S.J., Robinson, M.K., Amadou, J., Prato, M., Bianco, A., Kostarelos, K., and Al-Jamal, K.T. (2014) The relationship between the diameter of chemic ally-functionalized multi-walled carbon nanotubes and their organ biodistribution profiles in vivo. *Biomaterials*, **35**, 9517–9528.
64. McDevitt, M.R., Chattopadhyay, D., Kappel, B.J., Jaggi, J.S., Schiffman, S.R., Antczak, C., Njardarson, J.T., Brentjens, R., and Scheinberg, D.A. (2007) Tumor targeting with antibody-functionalized, radiolabeled carbon nanotubes. *J. Nucl. Med.*, **48** (7), 1180–1189.
65. McDevitt, M.R., Chattopadhyay, D., Jaggi, J.S., Finn, R.D., Zanzonico, P.B., Villa, C., Rey, D., Mendenhall, J., Batt, C.A., Njardarson, J.T., and Scheinberg, D.A. (2007) PET Imaging of soluble yttrium-86-labeled carbon nanotubes in Mice. *PLoS One*, **9**, e907.
66. Mulvey, J.J., Feinberg, E.N., Alidori, S., McDevitt, M.R., Heller, D.A., and Scheinberg, D.A. (2014) Synthesis, pharmacokinetics, and biological use of lysine-modified single-walled carbon nanotubes. *Int. J. Nanomed.*, **9**, 4245–4255.
67. Wang, J.T., Cabana, L., Bourgognon, M., Kafa, H., Protti, A., Venner, K., Shah, A.M., Sosabowski, J.K., Mather, S.J., Roig, A., Ke, X.X., Tendeloo, G.V., Rosales, R.T.M., Tobias, G., and Al-Jamal, K.T. (2014) Magnetically decorated multiwalled carbon nanotubes as dual MRI and SPECT contrast agents. *Adv. Funct. Mater.*, **24**, 1880–1894.
68. Li, J., Panta, A., Chin, C.F., Ang, W.H., Menard-Moyon, C., Nayak, T.R., Gibson, D., Ramaprabhu, S., Panczyk, T., Bianco, A., and Pastorin, G. (2014) In vivo biodistribution of platinum-based drugs encapsulated into multi-walled carbon nanotubes. *Nanomed. Nanotechnol. Biol. Med.*, **10**, 1465–1475.
69. Yang, S.T., Shiral Fernando, K.A., Liu, Y.H., Wang, J., Sun, H.F., Liu, Y.F., Chen, M., Huang, Y.P., Wang, X., Wang, H.F., and Sun, Y.P. (2008) Covalently PEGylated carbon nanotubes with stealth character In vivo. *Small*, **4** (7), 940–944.
70. Yang, S.T., Wang, H.F., Meziani, M.J. *et al.* (2009) Biodefunctionalization of functionalized single-walled carbon nanotubes in mice. *Biomacromolecules*, **10**, 2009–2012.
71. Yang, S.T., Wang, Y., Liu, J., and Wang, H. (2013) Biodistribution of multi-walled carbon nanotubes functionalized by hydroxyl terminated poly(ethylene glycol) in mice. *J. Radioanal. Nucl. Chem.*, **295**, 1181–1186.
72. Weber, G.E.B., Bosco, L.D., Gonçalves, C.O.F., Santos, A.P., Fantini, C., Furtado, C.A., Parfitt, G.M., Peixoto, C., Romano, L.A., Vaz, B.S., and Barros, D.M. (2014) Biodistribution and toxicological study of PEGylated single-wall carbon nanotubes in the zebrafish (danio rerio) nervous system. *Toxicol. Appl. Pharmacol.*, **280**, 484–492.
73. Guo, J.X., Zhang, X., Li, Q.N., and Li, W.X. (2007) Biodistribution of functionalized multiwall carbon nanotubes in mice. *Nucl. Med. Biol.*, **34**, 579–583.

74. Lin, Z.Q., Zhang, H.S., Huang, J.H., Xi, Z.G., Liu, L.H., and Lin, B.C. (2014) Biodistribution of single-walled carbon nanotubes in rats. *Toxicol. Res.*, **3**, 497–502.
75. Czarny, B., Georgin, D., Berthon, F., Plastow, G., Pinault, M., Patriarche, G., Thuleau, A., L'Hermite, M.M., Taran, F., and Dive, V. (2014) Carbon nanotube translocation to distant organs after pulmonary exposure: insights from in situ 14C-radiolabeling and tissue radioimaging. *ACS Nano*, **8** (6), 5715–5724.
76. Petersen, E.J., Huang, Q.G., and Weber, W.J. Jr., (2008) Bioaccumulation of radio-labeled carbon nanotubes by Eisenia foetida. *Environ. Sci. Technol.*, **42** (8), 3090–3095.
77. Petersen, E.J., Huang, Q.G., and Weber, W.J. Jr., (2008) Ecological uptake and depuration of carbon nanotubes by lumbriculus variegatus. *Environ. Health Perspect.*, **116** (4), 496–500.
78. Petersen, E.J., Huang, Q.G., and Weber, W.J. Jr., (2010) Relevance of octanol–water distribution measurements to the potential ecological uptake of multi-walled carbon nanotubes. *Environ. Toxicol. Chem.*, **29** (5), 1106–1112.
79. Miyawaki, J., Matsumura, S., Yuge, R., Murakami, T., Sato, S., Tomida, A., Tsuruo, T., Ichihashi, T., Fujinami, T., Irie, H., Tsuchida, K., Iijima, S., Shiba, K., and Yudasaka, M. (2009) Biodistribution and ultrastructural localization of single-walled carbon nanohorns determined in vivo with embedded Gd_2O_3 labels. *ACS Nano*, **3** (6), 1399–1406.
80. Zhang, M.F., Tahara, Y., Yang, M., Zhou, X., Iijima, S., and Yudasaka, M. (2014) Quantifi cation of whole body and excreted carbon nanohorns intravenously injected into mice. *Adv. Healthcare Mater.*, **3**, 239–244.
81. Matsumura, S., Yuge, R., Sato, S., Tomida, A., Ichihashi, T., Irie, H., Iijima, S., Shiba, K., and Yudasaka, M. (2014) Ultrastructural localization of intravenously injected carbon nanohorns in tumor. *Int. J. Nanomed.*, **9**, 3499–3508.
82. Zhang, M.F., Yamaguchi, T., Iijimaa, S., and Yudasaka, M. (2013) Size-dependent biodistribution of carbon nanohorns in vivo. *Nanomed. Nanotechnol. Biol. Med.*, **9**, 657–664.
83. Nakamura, M., Tahara, Y., Murakami, T., Iijima, S., and Yudasaka, M. (2014) Gastrointestinal actions of orally-administered single-walled carbon nanohorns. *Carbon*, **69**, 409–416.
84. Hummers, W.S. and Offerman, R.E. (1958) Preparation of graphitic oxide. *J. Am. Chem. Soc.*, **80**, 1339–1346.
85. Liu, J.H., Yang, S.T., Wang, H., Chang, Y., Cao, A., and Liu, Y. (2012) Effect of size and dose on the biodistribution of graphene oxide in mice. *Nanomedicine*, **7**, 1801–1812.
86. Zhang, X.Y., Yin, J.L., Peng, C., Hu, W.Q., Zhu, Z.Y., Li, W.X., Fan, C.H., and Huang, Q. (2011) Distribution and biocompatibility studies of graphene oxide in mice after intravenous administration. *Carbon*, **49**, 986–995.
87. Li, B., Zhang, X.Y., Yang, J.Z., Zhang, Y.J., Li, W.X., Fan, C.H., and Huang, Q. (2014) Influence of polyethylene glycol coating on biodistribution and toxicity of nanoscale graphene oxide in mice after intravenous injection. *Int. J. Nanomed.*, **9**, 4697–4707.
88. Yang, K., Wan, J.M., Zhang, S., Zhang, Y.J., Lee, S.T., and Liu, Z. (2010) In vivo pharmacokinetics, long-term biodistribution, and toxicology of PEGylated graphene in mice. *ACS Nano*, **5** (1), 516–522.
89. Lu, Y.J., Lin, C.W., Yang, H.W., Lin, K.J., Wey, S.P., Sun, C.L., Wei, K.C., Yen, T.C., Lin, C.I., Ma, C.M., and Chen, J.P. (2014) Biodistribution of PEGylated graphene oxide nanoribbons and their application in cancer chemo-photothermal therapy. *Carbon*, **74**, 83–95.
90. Hong, H., Zhang, Y., Engle, J.W., Nayak, T.R., Theuer, C.P., Nickles, R.J., Barnhart, T.E., and Cai, W.B. (2012) In vivo targeting and positron emission tomography imaging of tumor vasculature with 66Ga-labeled nano-graphene. *Biomaterials*, **33**, 4147–4156.
91. Fazaeli, Y., Akhavan, O., Rahighi, R., Aboudzadeh, M.R., Karimi, E., and

Afarideh, H. (2014) In vivo SPECT imaging of tumors by 198,199Au-labeled graphene oxide nanostructures. *Mater. Sci. Eng., C*, **45**, 196–204.

92. Kanakia, S., Toussaint, J.D., Chowdhury, S.M., Tembulkar, T., Lee, S., Jiang, Y.P., Lin, R.Z., Shroyer, K.R., Moore, W., and Sitharaman, B. (2014) Dose ranging, expanded acute toxicity and safety pharmacology studies for intravenously administered functionalized graphene nanoparticle formulations. *Biomaterials*, **35**, 7022–7031.
93. Li, Z., Geng, Y.X., Zhang, X.Y., Qi, W., Fan, Q.H., Li, Y., Jiao, Z.X., Wang, J.J., Tang, Y.Q., Duan, X.J., and Wu, W.S. (2011) Biodistribution of co-exposure to multi-walled carbon nanotubes and graphene oxide nanoplatelets radiotracers. *J. Nanopart. Res.*, **13**, 2939–2947.
94. Nahain, A.A., Lee, J.E., Jeong, J.H., and Park, S.Y. (2013) Photoresponsive fluorescent reduced graphene oxide by spiropyran conjugated hyaluronic acid for in vivo imaging and target delivery. *J. Am. Chem. Soc.*, **14**, 4082–4090.
95. Li, B., Yang, J.Z., Huang, Q., Zhang, Y., Peng, C., Zhang, Y.J., He, Y., Shi, J.Y., Li, W.X., Hu, J., and Fan, C.H. (2013) Biodistribution and pulmonary toxicity of intratracheally instilled graphene oxide in mice. *NPG Asia Mater.*, **5**, e44.
96. Yang, K., Gong, H., Shi, X.Z., Wan, J.M., Zhang, Y.J., and Liu, Z. (2013) In vivo biodistribution and toxicology of functionalized nano-graphene oxide in mice after oral and intraperitoneal administration. *Biomaterials*, **34**, 2787–2795.
97. Nurunnabi, M., Khatun, Z., Reeck, G.R., Lee, D.Y., and Lee, Y.K. (2013) Near infra-red photoluminescent graphene nanoparticles greatly expand their use in noninvasive biomedical imaging. *Chem. Commun.*, **49**, 5079–5081.
98. Nahain, A.A., Lee, J.E., In, I., Lee, H., Lee, K.D., Jeong, J.H., and Park, S.Y. (2013) Target delivery and cell imaging using hyaluronic acid-functionalized graphene Quantum dots. *Mol. Pharmaceutics*, **10**, 3736–3744.
99. Nurunnabi, M., Khatun, Z., Huh, K.M., Park, S.Y., Lee, D.Y., Cho, K.J., and Lee, Y.K. (2013) In vivo biodistribution and toxicology of carboxylated graphene quantum dots. *ACS Nano*, **7** (8), 6858–6867.
100. Fu, C.C., Lee, H.Y., Chen, K., Lim, T.S., Wu, H.Y., Lin, P.K., Wei, P.K., Tsao, P.H., Chang, H.C., and Fann, W. (2007) Characterization and application of single fluorescent nanodiamonds as cellular biomarkers. *Proc. Natl. Acad. Sci. U.S.A.*, **104** (3), 727–732.
101. Yuan, Y., Chen, Y.W., Liu, J.H., Wang, H.F., and Liu, Y.F. (2009) Biodistribution and fate of nanodiamonds in vivo. *Diamond Relat. Mater.*, **18**, 95–100.
102. Rojas, S., Gispert, J.D., Martin, R., Abad, S., Menchon, C., Pareto, D., Victor, V.M., Alvaro, M., Garcia, H., and Herance, J.R. (2011) Biodistribution of amino-Functionalized diamond nanoparticles. In vivo studies based on 18 F radionuclide emission. *ACS Nano*, **5** (7), 5552–5559.
103. Zhang, X.Y., Yin, J.L., Kang, C., Li, J., Zhu, Y., Li, W.X., Huang, Q., and Zhu, Z.Y. (2010) Biodistribution and toxicity of nanodiamonds in mice after intratracheal instillation. *Toxicol. Lett.*, **198**, 237–243.
104. Mohan, N., Chen, C.S., Hsieh, H.H., Wu, Y.C., and Chang, H.C. (2010) In vivo imaging and toxicity assessments of fluorescent nanodiamonds in *Caenorhabditis elegans*. *Nano Lett.*, **10** (9), 3692–3699.
105. Geng, Y., Dalhaimer, P., Cai, S., Tsai, R., Tewari, M., Minko, T., and Discher, D.E. (2007) Shape effects of filaments versus spherical particles in flow and drug delivery. *Nat. Nanotechnol.*, **2**, 249–255.
106. Huang, X., Li, L., Liu, T., Hao, N., Liu, H., Chen, D., and Tang, F. (2011) The shape effect of mesoporous silica nanoparticles on biodistribution, clearance, and biocompatibility in vivo. *ACS Nano*, **5**, 5390–5399.
107. Akiyama, Y., Mori, T., Katayama, Y., and Niidome, T. (2012) Conversion of rod-shaped gold nanoparticles to spherical forms and their effect on biodistribution in tumor-bearing mice. *Nanoscale Res. Lett.*, **7**, 1–6.

4
Interaction of Carbon Nanomaterials and Components in Biological Systems

Jian Tian and Cuicui Ge

4.1
Introduction

Because of their superior electric, mechanical, and optical properties, carbon nanomaterials find a variety of potential applications, resulting in an increased chance of exposing carbon nanomaterials to biological systems simultaneously [1–15]. Exposure to carbon nanomaterials might induce adverse biological/physiological effects, which raise biosafety concerns during their practical applications, especially in biomedicine, such as diagnosis, therapy, and drug delivery. There have been numerous studies investigating the adverse biological effects of carbon nanomaterials. It has been demonstrated that carbon nanotubes (CNTs) cause oxidative stress through oxidation of cellular biomolecules, such as DNA, proteins, and lipids [16]. Graphene-layer numbers [17–21] can induce toxicity by inflammation, increasing the reactive oxygen species (ROS) level, or negative feedback of the immune response.

However, there is still controversy regarding the toxicity mechanism of carbon nanomaterials. The key point is to take into consideration the interaction of nanomaterials with biomolecules. It is known that, upon entry of carbon nanomaterials into the biological system, a large number of biological molecules rapidly get adsorbed onto the surfaces of these materials to reduce their surface energy. As a typical example, proteins adsorbed onto a nanomaterial are often called "protein corona," which have attracted intense interest in recent years [3, 5, 10, 22–36]. Such corona-like coating endows the nanomaterials with new biological identities [26, 37–39]. These new biological identities are very different from their original ones acquired during their synthesis, which are derived from the laboratory or engineered chemical reactions, including the chemical composition, shape, size, surface charge, hydrophobicity, and other application-orientated specific physiochemical properties [38, 40–42]. On the other hand, the

Biomedical Applications and Toxicology of Carbon Nanomaterials, First Edition.
Edited by Chunying Chen and Haifang Wang.

formation of the protein corona occurs within a complex physiological environment, showing reversible, dynamic, and complex features. Some viewpoints also consider such processes as a combination of nanomaterial–protein and outside protein–protein interactions [38, 43, 44]. Further, the nanomaterial–protein interaction induces conformational alteration of the protein, resulting in different (and unknown) biological responses [10, 37]. Therefore, investigating nanomaterial–protein interaction will provide a deep understanding of their toxicity mechanism and also suggest guidelines for the safe design of carbon nanomaterials, which will provide more opportunities and challenges in enriching innovative knowledge in nanotechnology, biology, and other interdisciplinary fields.

As a central element present in almost any organism on earth, carbon has unique physiochemical characteristics depending on its allotropic forms, such as graphite, diamond, and amorphous carbon for traditional ones, and CNTs, carbon nanospheres (nanodots or carbon black), graphene, fullerene, and so on [45–50]. Interestingly, most of these newly discovered carbon allotropes are composed of graphite layers. For example, graphene is a single layer of graphite, CNTs can be considered as a graphite layer rolled along a specific axis, and fullerene is the shortened version of CNTs. The similar elementary unit of the graphite layer is composited of sp^2 carbon atoms, showing in-layer and out-of-layer anisotropy. This unique property makes these novel carbon nanomaterials share similar performance and endow these materials with one of the largest nanomaterial groups with versatile applications in both academia and industry, for example, from nanotechnology, optics, electronics, and materials science to biology and medicine [51]. Although many biocompatible materials are carbon-based [12–15, 52], the stability and metabolization in complex biological environments is not yet known. Besides, long-term toxicology is still at an infant stage [53]. Therefore, deep understanding of the interacting behaviors between carbon nanomaterials and biological molecules is not only helpful in safe application of these materials but also in promoting knowledge innovation in biology, materials science, nanotechnology, and other related disciplines.

In this chapter, the interaction of carbon-based nanomaterials with components of the biological system, including biomolecules and cells, is reviewed. We will first discuss in general the interaction of carbon nanomaterials with the biological system and the corresponding characterization technologies. Then we review the latest advances in understanding the interaction of carbon nanomaterials with the biological components at the molecular and cellular levels, and also their specific interactions with typical biomolecules (including phospholipids, proteins, and DNA) and cells. In the last part, we give a brief summary and further prospects in this field. This chapter is by no means complete and is based on our (could-be-biased) views; other comprehensive reviews based on different viewpoints exist [2, 7, 26, 37, 38, 43, 44].

4.2
Factors Affecting Interaction

4.2.1
Characteristics of Carbon Nanomaterials

4.2.1.1
Size and Layer

CNTs are probably ideal materials because of their combination of superlative mechanical, thermal, and electronic properties [54, 55]. Besides, CNTs also exhibit excellent chemical stability, which ensures their long-term applications. However, this stability also raise biosafety and environmental concerns [56]. Typically, the single-walled carbon nanotubes (SWCNTs) can be categorized as armchair-like, zigzag, and chiral types, depending on the way of "rolling up" a single graphite layer [57, 58]. Further, multiwalled carbon nanotubes (MWCNTs) are larger and consist of many single-walled tubes stacked one inside another [59]. Based on these elemental types, CNTs also possess several shapes according to their different morphological tuning processes [60].

As CNTs are the typical one-dimensional nanomaterials, their characteristic parameter is their diameter, which influences the curvature and further binding behavior with biological molecules (e.g., proteins) [61–63]. For example, Yan and colleagues [64] revealed that the diameter of functionalized MWCNTs (f-MWCNTs) governed the binding behavior and the adsorption capacity of proteins. As shown in Figure 4.1, f-MWCNTs with distinct diameters exhibit different capacity and binding affinity of proteins. Besides, their curvature also influences the adsorption behavior of proteins on the surface of CNTs. Besides, the wall number of CNTs also influences their interaction with biomolecules. SWCNTs exhibit different physiochemical properties from those of double-walled carbon nanotubes (DWCNTs), which result in their differences in biological responses. Recently, Liu *et al.* revealed that DWCNTs may have higher affinity to proteins than SWCNTs [65]. According to this character, the subsequent biological

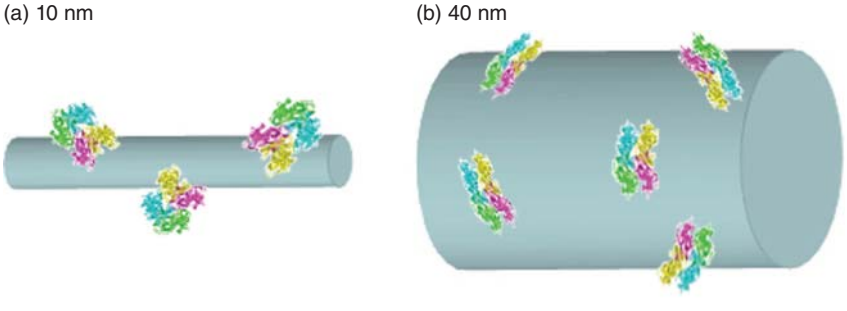

Figure 4.1 Schematic showing protein binding to f-MWNT with different diameters. (Reprinted with permission from [64]. © 2008 American Chemical Society.)

responses were different. For the activation of the pro-inflammatory cytokine interleukin-6 (IL-6) in A549 cells, SWCNT suspensions with bovine serum albumin (BSA) could result in a higher level of IL-6 than DWCNTs. Besides, the authors also found that DWCNTs showed a larger binding ability to the bronchoalveolar lavage fluid (BALF) protein than SWCNTs. By using the atomic force microscopy (AFM), the differences in their interaction with cells could be observed. Irrespective of the cell lines, SWCNTs tend to accumulate in the cell border and often be absent near the center regions, while the DWCNTs accumulate inside the cells [66, 67].

4.2.1.2

Surface Modification and Functionalization

As CNTs (and most nanomaterials) possess high surface energy, their surface modification is often required for their biological applications. This is also very important for their interaction with the biological systems [56, 68]. For example, Sacchetti *et al.* [68] revealed the effect of surface properties on the interaction of nanomaterials with protein (adsorption) and organ accumulation. In their study, poly(ethylene glycol) (PEG)-functionalized carbon nanotubes (f-CNTs) and PEG-coated carbon nanotubes (c-CNTs) were used (Figure 4.2). The results reveal that tuning the surface functionalization changes their surface hydrophobicity and surface charge, which then affects their binding capacity and affinity to different proteins. They also concluded that proteins tend to bind to elongated, unmodified CNTs through hydrophobic patches on their surface (aromatic residues) [69–72]. These binding processes can also subsequently induce conformational changes of the protein's secondary structure [73].

Chemical modification is often done for increasing the biocompatibility of nanomaterials [74, 75]. It is widely accepted that covalent modification of PEG or other biocompatible polymers (i.e., dextran) can reduce the cytotoxicity for a series of cell lines in certain doses [76, 77]. Recently, Choi and colleagues [78] systematically investigated the effect of surface functionalization of nano-graphene on its interaction with cells (Figure 4.3). By comparing graphene oxide (GO) with reduced graphene oxide (rGO), a possible toxicity mechanism was proposed regarding graphene with different surface functionalizations. For GO, transforming growth factor (TGF)-β1 plays the central role, which can induce DNA damage, apoptosis, inflammation, and other biological responses by increasing the ROS level or through other pathways. On the other hand, rGO with less degree of oxidation finally induces the host defense and innate immune responses. The differences are ascribed to the difference in their surface wettability (hydrophobic/hydrophilic properties).

As the other part of the surface properties, defects, which include the edges and in-plane nanoholes, can also result in different biological interactions. For graphene edges, two configurations are known: armchair and zigzag [79]. Owing to the difficulty in characterizing the dynamic structural properties

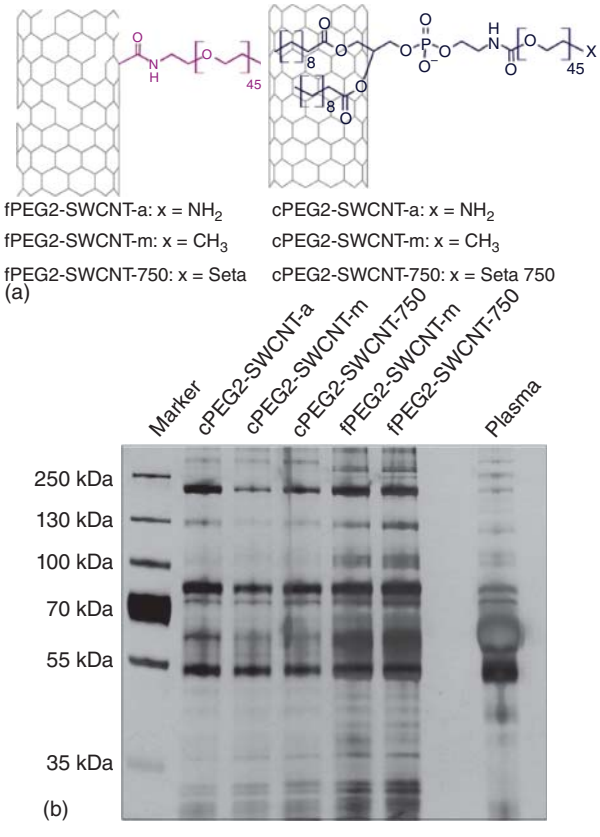

Figure 4.2 (a) Molecular schemes of PEG(2k)-functionalized CNTs (f-CNTs) and PEG(2k)-coated CNTs (c-CNTs). (b) Pattern of one-dimensional sodium dodecyl sulfate-polyacrylamide gel electrophoresis (1D SDS-PAGE) showing the relative abundance of human plasma proteins adsorbed onto PEG2-SWCNTs. The PEG2-SWCNTs were incubated with human plasma proteins at 37 °C and free plasma proteins were separated. (Reprinted with permission from [68]. © 2013 American Chemical Society.)

of defects, the effect of defects on the interaction of nanomaterials with biomolecules is still under debate [80]. Nevertheless, we can generally regard the edge of graphene as an active site owing to its sharpness and discontinuous/dangling bonds [81]. Recent reports also reveal that the sharp edge of graphene can induce direct rupture of the bacterial membrane [82, 83]. On the other hand, the in-plane nanoholes are formed by removing carbon atoms after reduction of graphene by intense chemical or mild biological methods, or even by solar irradiation [84, 85]. Graphene and its derivatives may exhibit distinct interaction with the biological system, from proteins to cell. Liu and colleagues [86] revealed that functionalized graphene oxides exhibit increased

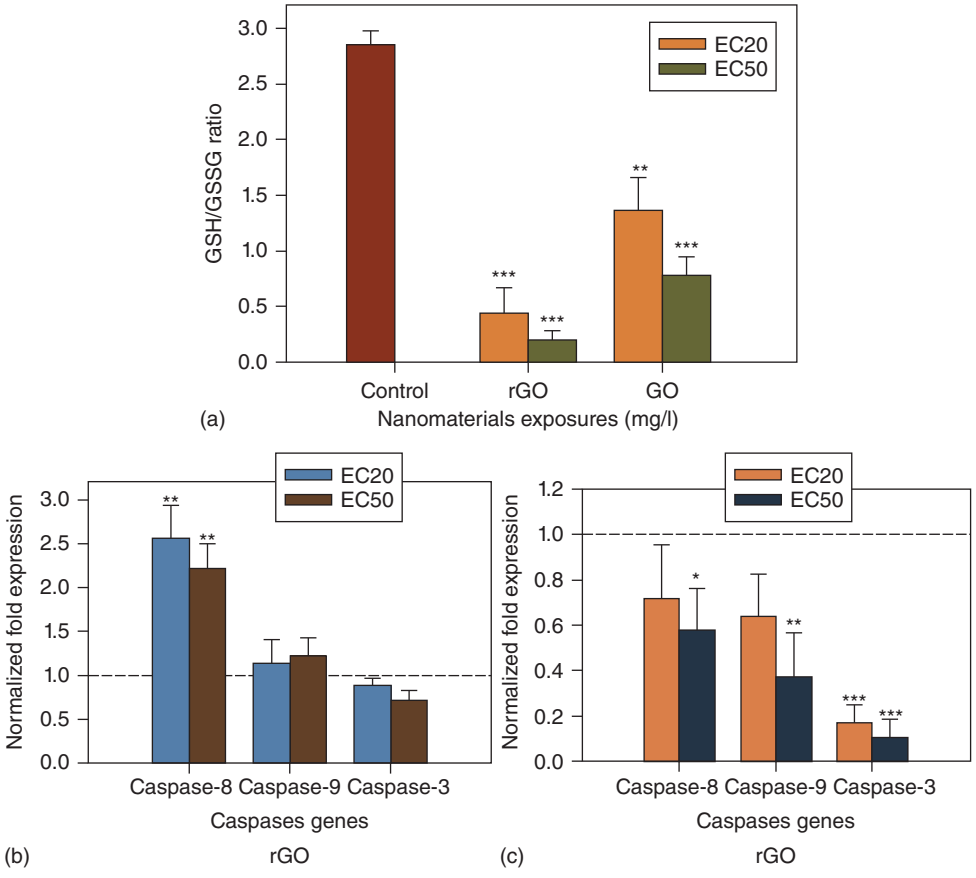

Figure 4.3 (a) Changes in GSH/GSSG ratio due to GO and rGO exposure for 24 h at the irrespective EC_{20} and EC_{50} doses. (b, c) Alteration of antioxidant genes (SOD1, SOD2, CAT, GSTA1, GSTA4) expressions due to rGO (b) and GO (c) exposure for 24 h at the respective EC_{20} and EC_{50} doses. (Reprinted with permission from [78]. © 2014 Elsevier B.V.)

binding of proteins (such as human sera and immune factors) with certain selectivity.

4.2.2
Biological Microenvironment

In the biological system, carbon nanomaterials often directly (bare nanomaterials) or indirectly (through their functionalized surface) interact with the biomolecules. The pH, charge, hydrophobicity, and other factors in biological environments will also affect the interaction of the carbon nanomaterials with biological entities. Taking into consideration these factors will enrich the understanding on the behavior and fate of carbon nanomaterials after entering into organisms as a whole associated, complex system.

4.2.2.1

pH

In general, the pH value of human blood is ~7.4, which is almost neutral environment. Therefore, the interaction of carbon nanomaterials with the biological system under normal conditions is similar to the *in vitro* case. However, the microenvironment near a tumor has a relatively low pH compared to the normal tissue [87, 88]. For carbon nanomaterials, this pH sensitivity is realized by grafting with polysaccharide materials [89] and lysozyme (LSZ) [90, 91]. For example, the dispersing ability of the SWCNTs in aqueous solution can be highly improved in the presence of LSZ, where accumulating and debundling of the formed lysozyme–single-walled carbon nanotube (L-SWCNT) complex can be influenced by the pH of the solution. Nine-month-stable solutions of L-SWCNT possess the original pH of ~6.5. By adjusting the pH of the solution to 8.5–11, L-SWCNTs are easily coagulated and can be separated from the aqueous phase. However, when slowly increasing the pH to a higher value (e.g., >11), the aggregates revert back to dispersions in the aqueous system, forming again a homogeneous phase (Figure 4.4, insets). The zeta potential of the complex shows that its isoelectric point (IEP) is at pH 10.02 (Figure 4.4), which is close to the IEP of pristine LSZ. This may be ascribed to the influence of the solution pH on both van der Waals attraction and electrostatic repulsion, according to the Derjaguin-Landau-Verwey-Overbeek (DLVO) theory of colloidal dispersions [92]. In the case of the solution around the IEP, Lysozyme (LSZ) becomes deficient in charge,

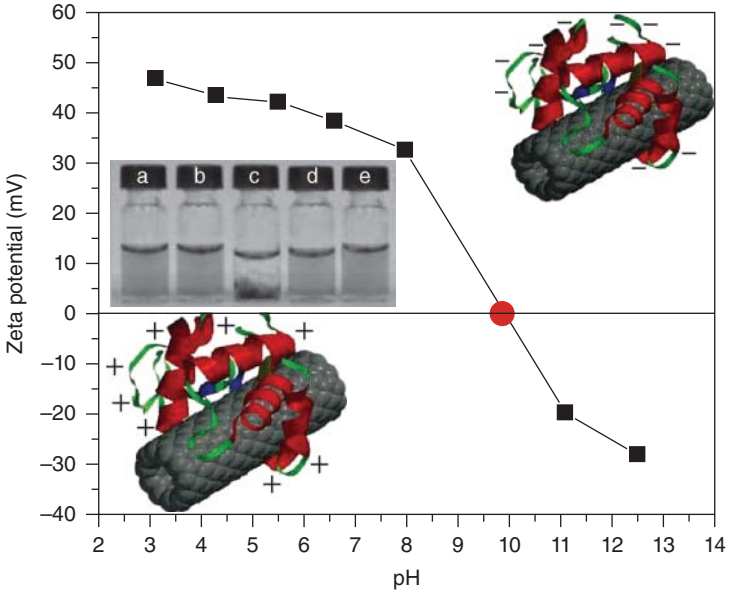

Figure 4.4 Zeta potential of L-SWNT at different pH values. The inset shows the vials containing the products at different pH values: (a) 2.95, (b) 6.5, (c) 9.0, (d) 11.15, and (e) 12.47. (Reprinted with permission from Ref. [90]. © 2006 John Wiley & Sons, Inc.)

which results in attraction between the LSZ-stabilized nanotubes (major in van der Waals attractions), and they become flocculated in the system. When pH value is below the IEP, the cationic charge density dominates as a result of the residues containing protonated amines, resulting in repulsion between SWCNTs and leading to good dispersion in the system. Similarly, by increasing the pH above the IEP, the anionic charge density becomes dominant due to carboxylate ions, which again induces the SWNT–SWNT repulsion, resulting in a fine dispersion.

4.2.2.2 Ionic Strength

In addition to the hydrogen and hydroxide ions in the biological environment (as characterized by pH), other ions (e.g., Ca^{2+}, Na^{+}, K^{+}, Cl^{-}, etc.) also influence the behavior of carbon nanomaterials in the biological microenvironment. The effect of ions on the interaction between nanomaterials and the biological system is related to the electrostatic attraction and charge transfer. During noncovalent interaction between CNT and a protein containing aromatic amino acid residues, the processes of electron donation and withdrawal occur [93], and such interaction induces both Raman band shifts and new additional features near the Fermi level. It was also revealed through a pioneering theoretical investigation that the adsorption of protein onto the surface of CNTs can induce the charge transfer between the aromatic amino acid residues and the amino group on the CNTs [94]. The presence of ions can influence the interaction of nanoparticles with proteins by changing the ionic strength of the medium (such as sodium chloride, NaCl). It is reported that the adsorption of BSA on Fe_3O_4 nanoparticles is affected by the ionic strength of the NaCl solution (Figure 4.5a) [95]. Chen and colleagues reported that the adsorption of LYZ and horseradish peroxidase (HRP) on the surface of silicon nanowire arrays (SiNWAs) was inhibited at high NaCl concentrations (Figure 4.5b, c) [96].

4.2.2.3 Weak Interactions

Apart from the relatively "strong" electrostatic interaction, which depends on the pH value and ionic strength of the medium, weak interactions, including hydrophobic, van der Waals, and $\pi-\pi$ stacking, also play important roles in the interaction of carbon nanomaterials with biological components. Through hydrophobic interaction, CNTs can plug into the binding pocket of calcium ions in calmodulin (CaM) [97], which then induces aberrant Ca^{2+} signaling in astrocytes, which is related to a variety of neurological diseases such as epilepsy and Alzheimer's disease [98]. Similarly, hydrophobic effect, hydrogen bond effect, and other stacking effects can also stabilize the insertion of fullerene into an antibody (a kind of immunoglobulin) [99]. As is shown in Figure 4.6b, some polypeptide chains that possess aromatic groups or carboxyl groups lie parallel to C_{60} molecule, such as tryptophan-47 (Trp-47) and asparagine-35 (Asn-35) in the heavy chain domain (V_H), and tryptophan-91 (Tyr-91), phenylalanine-96 (Phe-96), and glutamine-96 (Gln-89) in the light chain domain (V_L). We have

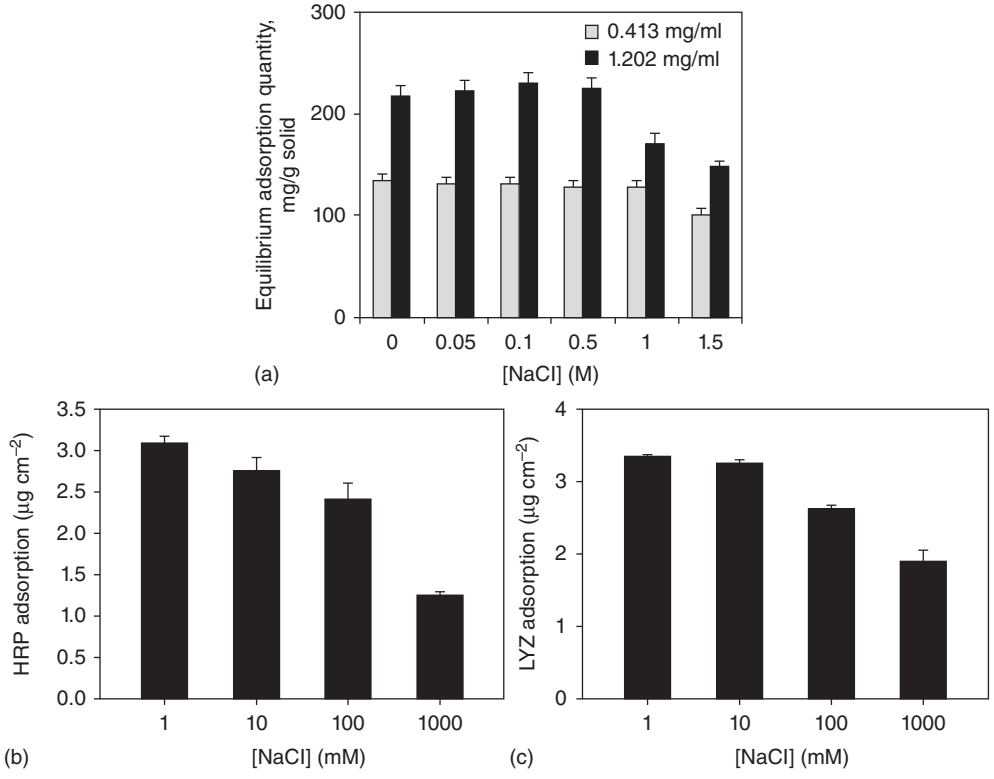

Figure 4.5 (a) Effect of salt (NaCl) concentration on BSA adsorption at pH 7.11 for two feed concentrations (0.413 and 1.202 mg ml^{-1}). (Reprinted with permission from [95]. © 2004 Elsevier B.V.) (b, c) Effect of NaCl on the adsorption of HRP (b) and LYZ (c) on PDMAEMA-modified SiNWAs at pH 7.0. (Reprinted with permission from [96]. © 2011 Royal Society of Chemistry.)

also reported that the π−π stacking effect occur between SWCNTs and the aromatic residues in four types of proteins, namely bovine fibrinogen (BFG), gamma globulin (Ig), transferrin (Tf), and BSA [1]. The exposed aromatic groups then determine the adsorption capacity of the proteins for the CNTs through a distinct degree of their π−π stacking effect.

4.2.2.4

Cell Selectivity

There are different types of cells showing very distinct functions and morphologies. Therefore, nanomaterials may exhibit distinct interactions with different cells lines. Ma and colleagues investigated the internalization of graphene oxides using a series of cell lines [100]. These cell lines include four types of nonphagocytic cells, that is, murine Lewis lung carcinoma (LLC) cells, human breast cancer (MCF-7) cells, human hepatocarcinoma cells (HepG2), and human umbilical vein endothelial cells (HUVEC), and two types of macrophages,

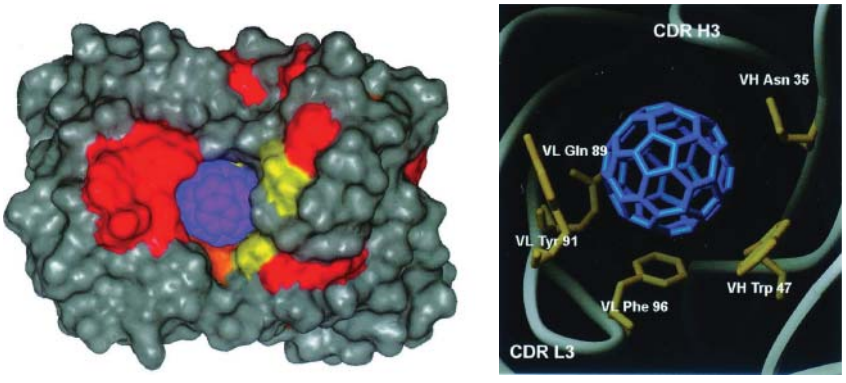

Figure 4.6 Model of C_{60} binding site. (a) Van der Waals surface representation of C_{60} bound to the anti-fullerene antibody. Surface is color-coded by amino acid: red, tyrosine; orange, phenylalanine; yellow, tryptophan. All other amino acids are colored gray; C_{60} is colored pink. (b) Residues involved in stacking interactions to modeled C_{60}. (Reprinted with permission from [99]. © 2000 National Academy of Sciences, USA.)

that is, peritoneal macrophage (PMØ) and murine macrophage (J774A.1). The planar feature of graphene also provides more chances for adsorbing amino acid residues with an aromatic ring through $\pi-\pi$ conjugation with little steric hindrance. Indeed, it is agreed that the cellular uptake behaviors of nanoparticles are obviously influenced by the type of cell lines [101, 102]. Some thermodynamic limitations, such as enthalpy and entropy, can determine these uptake processes [103]. For instance, enthalpy is an important driving force for the sharp transition from endocytosis to ligand-shortage vanishing (the vanishing of cellular uptake by the lack of ligands on the nanoparticles). In contrast, the gradual transition from endocytosis to receptor-shortage vanishing is driven by the upper limit of entropy when adhesion becomes insufficient to overcome the membrane deformation cost [103]. These distinct uptake behaviors can give some helpful insights into the interaction of carbon nanomaterials with the components in cell membranes such as lipids and transmembrane proteins, along with their corresponding driving forces.

Furthermore, the uptake also shows cellular selectivity based on the identities of the proteins that are adsorbed onto the surfaces of nanoparticles. For example, nanoparticles adsorbed with complement proteins or immunoglobulins are often taken up by phagocytes [104–106]. Precoating with fetuin can promote the cellular uptake of polystyrene nanoparticles by liver macrophages such as Kupffer cell [107, 108]. The uptake level of titanium oxide nanoparticles by A549 cells (in lung) can increase after adsorbing vitronectins onto the surface, which is regulated by a clathrin-mediated pathway [109]. These different uptake behaviors seem to be mediated by the acceptor–protein corona recognitions.

4.3
Interaction of Carbon Nanomaterials with Various Components in Biological Systems

In the biological environment, carbon nanomaterials will often interact with biological components, such as proteins, lipids, DNA, enzymes, and so on. As the relatively primary entities in most organisms, cells also often interact with carbon nanomaterials. Understanding these interactions and the corresponding characterization methods is of great importance in controlling (promoting or inhibiting) their biological consequences (e.g., unfolding of proteins) and ensuring their safety in practical applications.

4.3.1
Characterization and Methodology of Interaction of Carbon Nanomaterials with Components in the Biological System

As the formation of nanoparticle–protein corona is often accompanied by electron or energy transfer, the interaction between nanomaterials and biomolecules can be sensitively characterized by fluorescence spectroscopy. This method provides information such as the rotational motion of proteins, molecular binding, and the conformational changes of proteins [110]. Steady-state fluorescence spectroscopy can be used to detect the interaction of nanomaterials with proteins involved in various biological functions [111–115]. In addition, according to the classical Stern–Volmer equation [116], the relationship between the quenching of fluorescence and the concentration of the quencher can be expressed as $F_0/F = \tau_0/\tau = 1 + K_{sv}[Q]$, where F_0, F and τ_0, τ represent the initial or modified fluorescence intensity and lifetimes, respectively. This quantitative analysis provides further knowledge on the interactions. For example, by labeling with a kind of fluorescamine dye, the protein can be tagged with a specific fluorophore, which could be used as a high throughout platform in determining the binding behavior and detecting the unfolding of proteins after their interaction with nanoparticles (Figure 4.7) [117]. Besides, also there is a large number of spectrum-based and visual characterization strategies, such as mass spectroscopy, surface plasmon resonance, transmission electronic microscopy, scanning electronic microscopy, confocal laser microscopy, AFM, and so on [10].

At the cellular level, some well-established methods are utilized, including cell viability assays by 3-[4,5-dimethylthylthiazol-2-yl]-2,5 diphenyltetrazolium broide (MTT) or Cell Counting Kit-8 (CCK-8), membrane integrity assay, generation of ROS, cell adhesion and morphology, apoptosis assay, cytokine detection, and so on [118–121]. It was pointed out that MTT assay is problematic in the case of carbon nanomaterials; a possible alternative assay is WST-8 [119]. Besides, biological characterizations should also include gene-level assays because of their importance in DNA damage and the potential danger of cancer [122]. At the tissue level, one of the major *in vivo* methods is based on the evaluation of tissue distribution (bioaccumulation) and excretion of nanomaterials. By using zebrafish, the *in vivo* toxicity of graphene-related materials was evaluated [123].

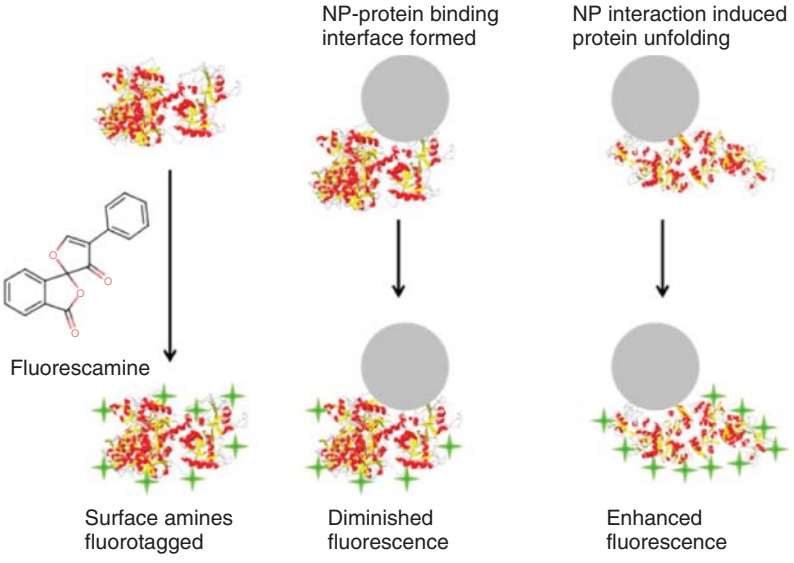

Figure 4.7 Schematic illustration of the fluorescamine labeling method for detecting the binding behavior of the proteins onto nanoparticle surfaces and the subsequent unfolding of proteins. (Reprinted with permission from [117]. © 2015 American Chemical Society.)

Besides, methods based on radiolabeling and nuclear detection by imaging or counting can also provide some information [9, 124, 125].

4.3.2 Carbon Nanomaterial–Phospholipid Interaction

As one of the most abundant and also important biological molecules, phospholipids cannot only form the cell membrane and other membrane-based organelles but also serve in a series of physiologic functions [126]. It is generally agreed that both the hydrophobic effect and electrostatic interaction drive the interaction of nanomaterials with phospholipids [43]. Molecular dynamics calculations by Ceulemans and colleagues have indicated that the hydrophobic tails of dipalmitoylphosphatidylcholine (DPPC) were bound to the surface of SWCNTs, while the hydrophilic top was directed toward the aqueous environment [127]. Their theoretical modeling results suggested that supramolecular multilayers wrapped around the CNT surface would be formed at a higher concentration of this lipid. Besides, Shiraki and colleagues also found that lysozyme-conjugated SWNTs could induce the leakage of the liposome through electrostatic interaction [128]. As shown in Figure 4.8a,b, a tilted orientation of the hydrophobic chain of 1,2-dipalmitoyl-*sn*-glycero-3-phosphocholine (DPPC) in the lowest energy conformation is observed with respect to the alignment of the lipids on the SWNT, while the hydrophobic chain is found to be aligned parallel to the SWNT axis. Other lipids, including phosphatidylglycerol (PG), phosphatidylserine (PS),

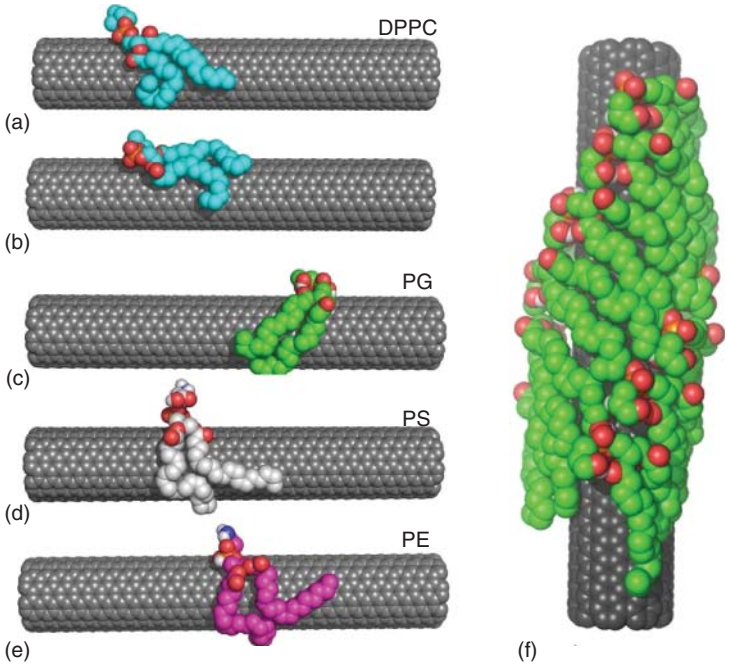

Figure 4.8 Computer modeling of SWCNTs binding with phospholipids and SP-D. The predicted binding pose of (a) the lowest energy conformation of DPPC, (b) DPPC) bound along the axis of SWCNT, lowest energy conformation of (c) PG, (d) PS, and (e) PE. (f) Lipid coating model generated using the PG-bound form of SWCNT shown in (c). The SWCNT is represented as spheres and colored in gray. The different phospholipids DPPC, PG, PS, and PE are rendered as spheres and colored in cyan, green, white, and magenta, respectively. In all cases, the N, O, and P atoms are colored in blue, red, and orange, respectively. (Reprinted with permission from [129]. © 2012 American Chemical Society.)

and phosphoethanolamine (PE), exhibit the tilted orientation on the surface of SWCNTs (Figure 4.8c–e). The alignment of lipids on the SWNTs and tilt in their orientation can be ascribed to the hydrogen bonding between the SWNTs and the lipid chain [129]. Using the lowest energy tilted conformation of PG, a model was generated to understand the progressive lipid coating on an SWCNT (Figure 4.8f).

As a consequence, these interactions can influence the transporting performance. For instance, Ma and colleagues [130] presented a theoretical investigation on the transportation of water molecules inside lipid-coated CNTs. As shown in Figure 4.9a, CNTs with different surface free energies, that is, from fully hydrophobic to fully hydrophilic (denoted as S0–S6), exhibit distinct behaviors of interaction with the lipid molecules. These lipid–CNT complexes result in difference in the water flow rate according to their surface hydrophobicity (Figure 4.9b). In addition, these complexes are also helpful in understanding and mimicking the transportation of ions across the cell membrane. Noy and

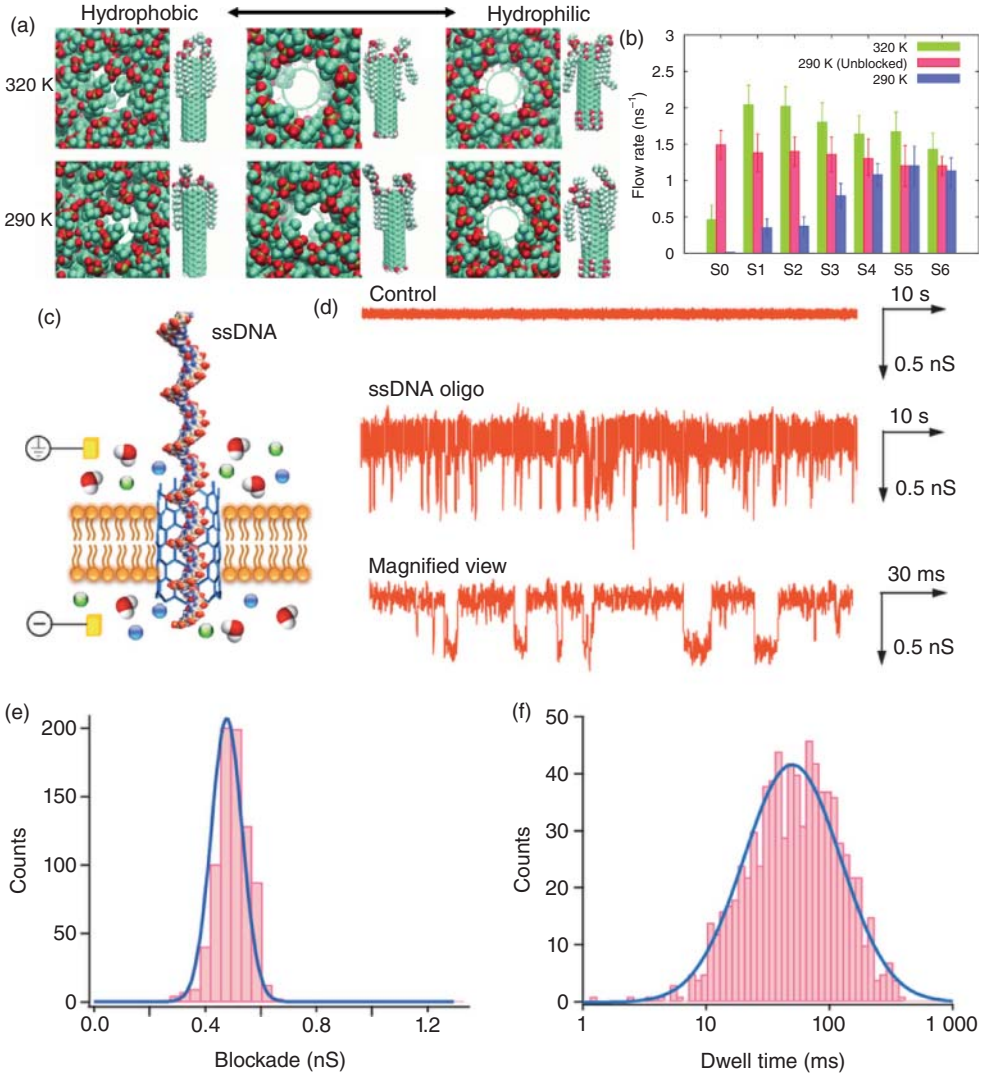

Figure 4.9 (a) Snapshots showing the CNT–membrane interactions at (top) 320 K and (bottom) at 290 K. (b) Water flow rates at 320 K (green), 290 K (blue), and 290 K with the CNT unblocked (red). These CNTs denoted as S0–S6 have different surface free energy, from fully hydrophobic to fully hydrophilic. (Reprinted with permission from [130]. © 2014 AIP Publishing LLC.) (C) Schematic showing the translocation of single-stranded DNA through a CNT porin in the lipid bilayer. Symbols in circles indicate ground electrode (top) and reference electrode (bottom). (d) Current trace showing multiple transient blockades caused by 81-nt ssDNA translocation through the CNT channel (middle) with magnified view (bottom). The top trace shows the control trace recorded in the absence of ssDNA. The applied voltage was −50 mV. (e, f) Histograms of conductance blockade levels (d) and dwell times (e) for 806 ssDNA translocation events. (Reprinted with permission from [131]. © 2014 Nature Publishing Group.)

colleagues showed that CNTs could act as "porins" after insertion into lipid-based cell membranes [131]. As shown in Figure 4.9c,d, rapid conductance blockades occur when the individual 81-nucleotide-long single-stranded DNA (81-nt ssDNA) passes through the CNT's pore. The conductance blockade values follow a normal distribution centered at 0.48 ± 0.08 nS (Figure 4.9e), while the DNA translocation dwell times follow a lognormal distribution (Figure 4.9f) centered around a value of 53 ms, which corresponds to an average DNA translocation speed of 1.5 nt ms^{-1}. These results on the electrophoretic translocation of macromolecules through individual nanotube porins provide an interesting mimic of functional proteins in cell membrane.

4.3.3
Carbon Nanomaterial–Protein Interaction

Proteins participate in almost all important biological process, from metabolism and immunity to enzymatic catalysis. Besides, the carbon nanomaterial–protein interactions are often accompanied by a change in the conformation of the protein's secondary structure, which further influences the operation of the biological system as a whole. As a polymeric arrangement of amino acids, the interaction of proteins with carbon nanomaterials can be first considered as the interaction between amino acids (and residues) and the functional groups in carbon nanomaterials. Recently, Zhou and colleagues [132] revealed the interaction of graphene with the C-terminal DNA-binding domain of human immunovirus-1 (HIV-1) integrase (Figure 4.10). Initially, the graphene sheet rotated and contacted one dimer of the protein after 2 ns, while one edge of the graphene sheet remained in the vicinity of the dimer interface. This process was driven by the favorable van der Waals interaction between the protein and the graphene sheet. Because the graphene surface is hydrophobic, the energy penalty due to the unfavorable graphene–water interaction outweighs that due to the graphene–protein interaction. After about 30 ns, the flexible graphene

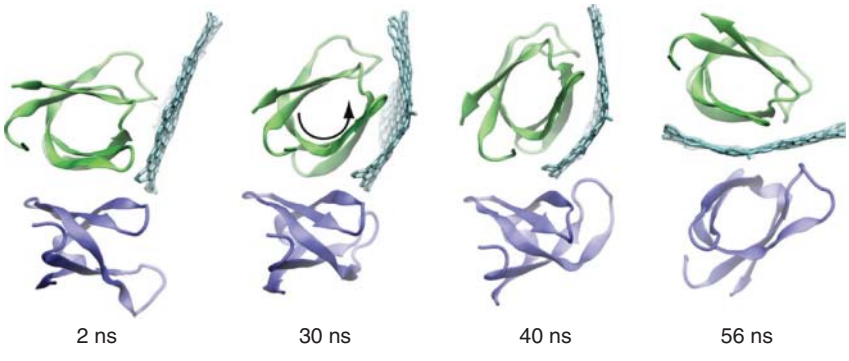

Figure 4.10 Snapshots of the insertion process of a graphene sheet into the dimer from the first simulation trajectory. (Reprinted with permission from [132]. © 2015 American Chemical Society.)

sheet contacted the protein conformally, that is, maximizing the contact area (or reducing the unfavorable graphene–water interaction). From 30 to 40 ns, the monomer began to rotate about its barrel axis as a result of the preferred hydrophobic interaction between the graphene surface and nonpolar residues at the dimer interface. Meanwhile, interfacial nonpolar residues of the other monomer began to interact with the other side of the graphene sheet, similarly driven by the graphene–protein interaction that is more hydrophobic than the one between the two protein monomers. At 56 ns, the graphene sheet was fully inserted and the dimer was separated. Because of the special $\pi-\pi$ conjugation effect from the sidewall of the CNTs, adsorption toward some biological molecules with aromatic ring is preferred, which is due to the strong affinity of the $\pi-\pi$ conjugation systems between the adsorbent and adsorbate (Figure 4.11) [133]. Besides, the structural distinctions of proteins also influence the adsorption behavior (and also the adsorbing capacity) of proteins.

We have recently found a competitive binding of various serum proteins on SWCNTs with different adsorption capacities and packing modes [1]. BFG was found to bind to SWCNTs in a more amorphous way when the initial adsorption process occurred (Figure 4.12a,b, top) and was prone to interwinding and forming aggregates on the SWCNT surface. This is probably due to their large molecular weight and cord-shaped structure with long and flexible helices. Obvious changes in the circular dichroism (CD) spectrum of BFG were also found when incubated for only 10 min (Figure 4.12g, top). Even by extending the incubation time, these changes in their secondary structures did not recover. The amorphous adsorption of the BFG protein may be due to the large contact surfaces of BFG available to the SWCNTs. After 5 h, BFG protein molecules tended to form some kind of blurred node shape with high thermodynamic stability (Figure 4.12b, top), which suggests

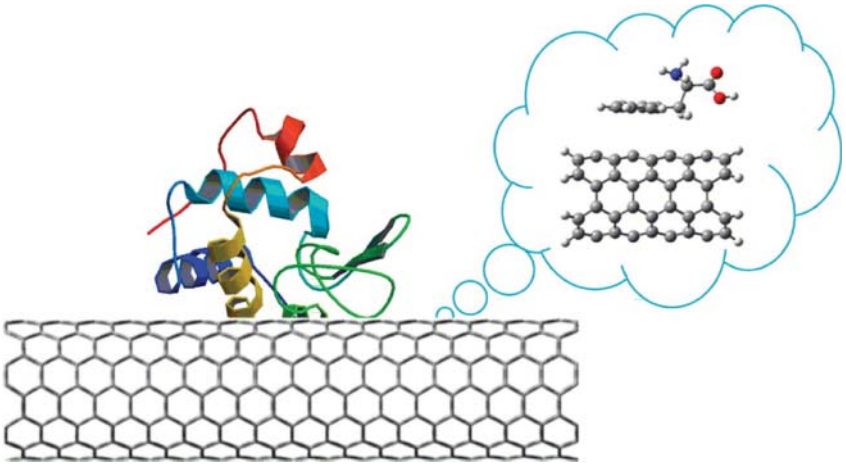

Figure 4.11 Schematic representation of the interaction between a CNT and a protein. The CNT and amino acid models used to mimic this interaction are shown in the inset. (Reprinted with permission from [133]. © 2014 American Chemical Society.)

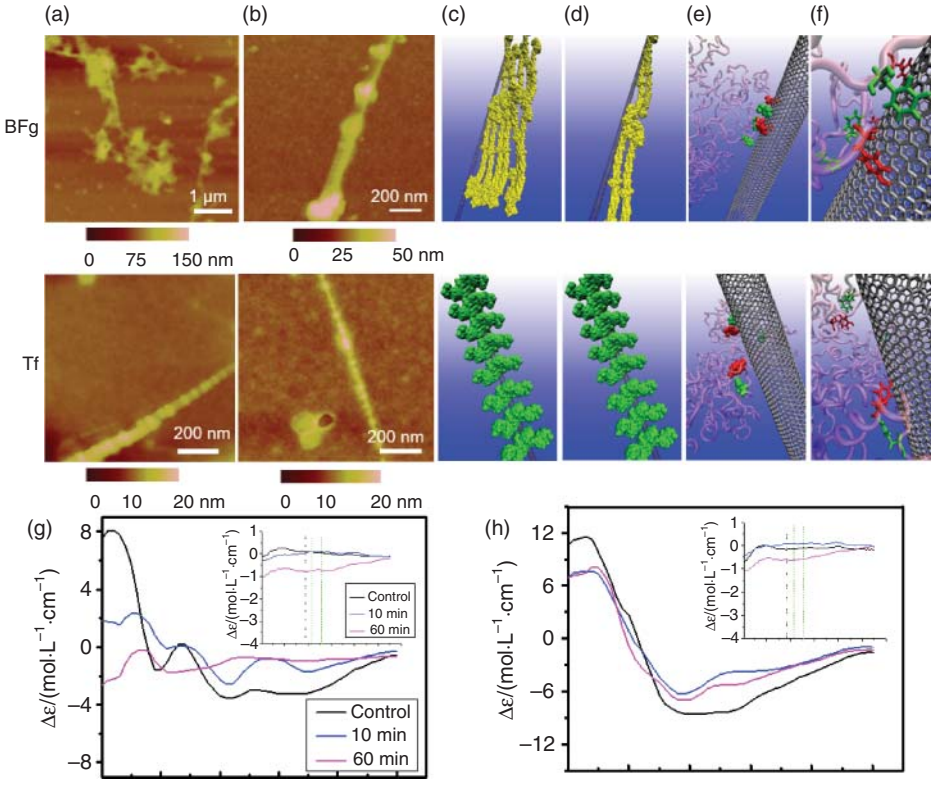

Figure 4.12 Interactions between bovine fibrinogen, transferrin, and SWNTs. AFM images of proteins after incubation with SWCNTs for 10 min (a) and 5 h (b). Molecular modeling illustrations for proteins (in beads representation) binding to SWCNTs (c). (d) Locations of the most preferred binding sites on proteins for SWCNTs. (e) Detailed orientations of aromatic rings of tyrosine and phenylalanine residues interacting with six-membered rings of SWCNTs colored in silver. The tyrosine residues are rendered as licorice representation and colored in red, and phenylalanine residues are in green. (f) The live and dead stains for THP-1 cells after treatment with SWCNT–protein complexes for 12 h. (g) The far-UV CD spectra of proteins after incubation with SWCNTs; (h) near-UV CD spectra of proteins incubated with SWCNTs. (Reprinted with permission from [1]. © 2011 National Academy of Sciences, USA.)

that the BFG chain tends to wrap along the surface of the SWCNTs with node-like shapes. In contrast, Tf was adsorbed on the SWCNT surface to form well-ordered node-like aggregates at the beginning, which uniformly bound to the surface of the SWCNTs (Figure 4.12a, low). By increasing the interaction time, the protein adsorption reached thermodynamic equilibrium, and the Tf–SWCNT binding model remained unchanged even after an extra time of 5 h (Figure 4.12b, low). These phenomena were confirmed by the CD spectra of Tf, without detectable changes in the subsequent incubation time (Figure 4.12g, low), indicating few changes in the secondary structure of Tf.

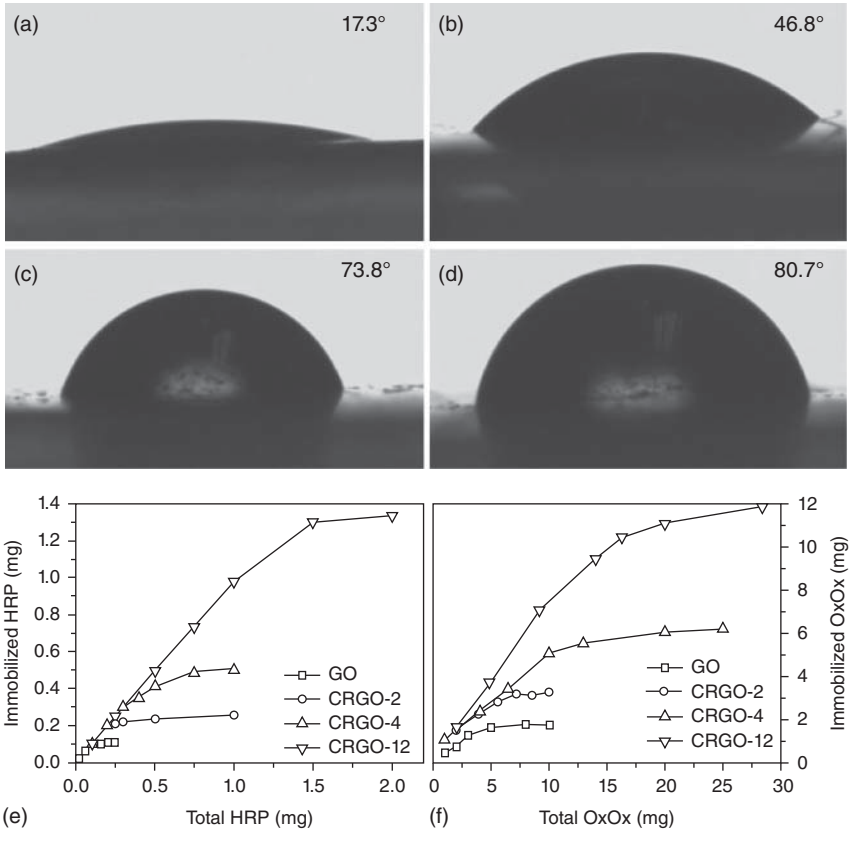

Figure 4.13 (a–d) Water contact angles of graphene oxide (GO) and chemically reduced graphene oxide (CRGO) thin films: (a) GO, (b) CRGO-2, (c) CRGO-4, and (d) CRGO-12. (e, f) Horseradish peroxidase (HRP) and oxalate oxidase (OxOx) loadings on GO and CRGO as a function of the total amount of enzyme. GO and CRGO weights are all 1 mg. (Reprinted with permission from [134]. © 2012 John Wiley & Sons, Inc.)

The hydrophobic effect is also important in the interaction of carbon nanomaterials with proteins, because most proteins possess nonpolar residues. For instance, the hydrophobic effect can regulate the immobilization of enzymes [134]. By chemical reduction using L-ascorbic acid, GO can be changed into chemically reduced graphene oxide (CRGO), which alters its hydrophobicity as demonstrated by measuring the value of the water contact angle (Figure 4.13a–d). It is clearly evident that the hydrophobicity is enhanced by increasing the reduction time. Along with this trend, it is found that the loading efficiency of both HRP and oxalate oxidase (OxOx) is enhanced. As shown in Figure 4.13e,f, the immobilizations were enhanced 13-fold for HRP and 7.5-fold for OxOx, respectively. Besides, it was also found that the hydrophobic effect also controlled the interaction of CNTs with a series of proteins [1, 135].

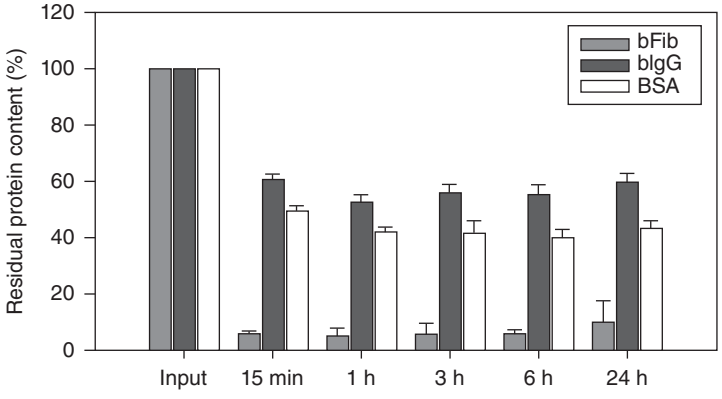

Figure 4.14 Quantification of time-dependent depletion of single proteins by carbon nanoparticles. Input = protein mixture without nanoparticles, not processed. (Reprinted with permission from [136]. © 2012 Elsevier B.V.)

Besides, the protein identities also show selectivity toward the same carbon nanoparticles. For instance, Weiss and colleagues investigated the binding capacity of proteins on various nanomaterials. Their results reveal that several types of proteins from bovine and human plasma show different binding ability toward carbon nanoparticles (14 nm in diameter and 300 $m^2 g^{-1}$ BET surface area). The qualification of proteins that were depleted by carbon nanoparticles was conducted through multistep separation and gel electrophoresis. As shown in Figure 4.14, carbon nanoparticles show obviously distinct adsorbing capacity of different coincubated proteins [136]. Interestingly, the results also show that the adsorbing capability seems to be constant after a prolonged time despite a very slight fluctuation. Besides, the obvious distinction in the residual content of different proteins indicated that BSA and bovine immunoglobulin G (bIgG) are less efficiently depleted by the carbon nanoparticles, which may be ascribed to the strong adsorption of fibrinogen (FBG). The result of the similar adsorption behavior between BSA and Ig is different from the case of CNTs [1].

Fullerenes, such as C_{60}, also show interesting interaction behavior with proteins. The structure of LSZ consists of two domains (α and β): the α domain contains four α helices and a short 3_{10} helix, while the β domain contains a triple-stranded antiparallel β sheet, a long loop, and a 3_{10} helix. It was found that C_{60} can be wedged in the cleft between the α and β domains (Figure 4.15), according to the theoretical calculation [138]. This interaction is very similar to the catalytic process with the yellow sites of the active site for the catalytic interaction.

4.3.4
Carbon Nanomaterial–DNA Interaction

As the most important hereditary material, DNA is a very important biomolecule to conserve and transcribe genetic messages. Because of the complex structural

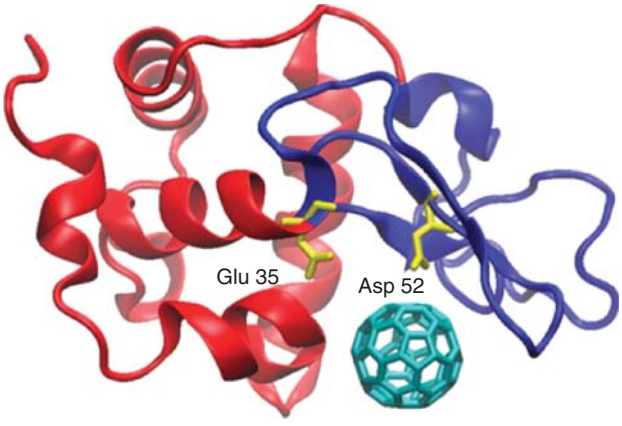

Figure 4.15 LSZ α (red) and β domains (blue). The active site residues (Glu 35 and Asp 52), which are critical for the catalytic activity of the enzyme, are shown in yellow. (Reprinted with permission from [137]. © 2014 American Chemical Society.)

features from nucleotide, double-helix structure, and high-level structures as well as the conjugated π−π systems from carbon nanomaterials, the interactions between carbon nanomaterials and DNA are governed by different types of forces. Quantum mechanical calculation is a powerful theoretical tool to understand the interaction between nucleobases and carbon nanomaterials. Figure 4.16 shows the first-principles calculation of the configuration of nucleobases on the surface of graphene and CNTs, which, respectively, represents two-dimensional and one-dimensional nanomaterials with a honeycomb network of carbon atoms [137, 139]. It is of interest that the nucleobase molecules tend to lie parallel to the carbon rings (either on the surface of graphene sheets or on the sidewall of CNT). In particular, the heterocyclic rings in the nucleobases possess some kinds of interactions, such as π−π conjugation effect, hydrogen bonding, and van der Waals force. Besides, it is also concluded that the theoretical binding energy between carbon nanomaterials and nucleobases can be ordered as $G > T \approx A > C > U$ for CNTs and $G > A > T > C > U$ for graphene, where G, T, A, C, U represent guanine, adenine, thymine, cytosine, and uracil, respectively [140].

In DNA strands, the nucleobases can be seen as a polymeric arrangement, where steric effects may hinder the interaction of nucleobases with carbon rings or induce changes of high-level structures of DNA [141]. As shown in Figure 4.17a, the electron energy levels of the carbon atoms often change after the interaction between DNA molecules and carbon nanomaterials (here, CNT as an example), which can be predicted by calculating the highest occupied molecular orbital (HOMO) and the lowest unoccupied molecular orbital (LUMO). Besides, owing to steric hindrance, these interactions also induce changes in the high-level structures of DNA molecules (Figure 4.17b).

In addition to the theoretical method for predicting the molecular behavior of small nucleobases and DNA on/along the surface of carbon nanomaterials,

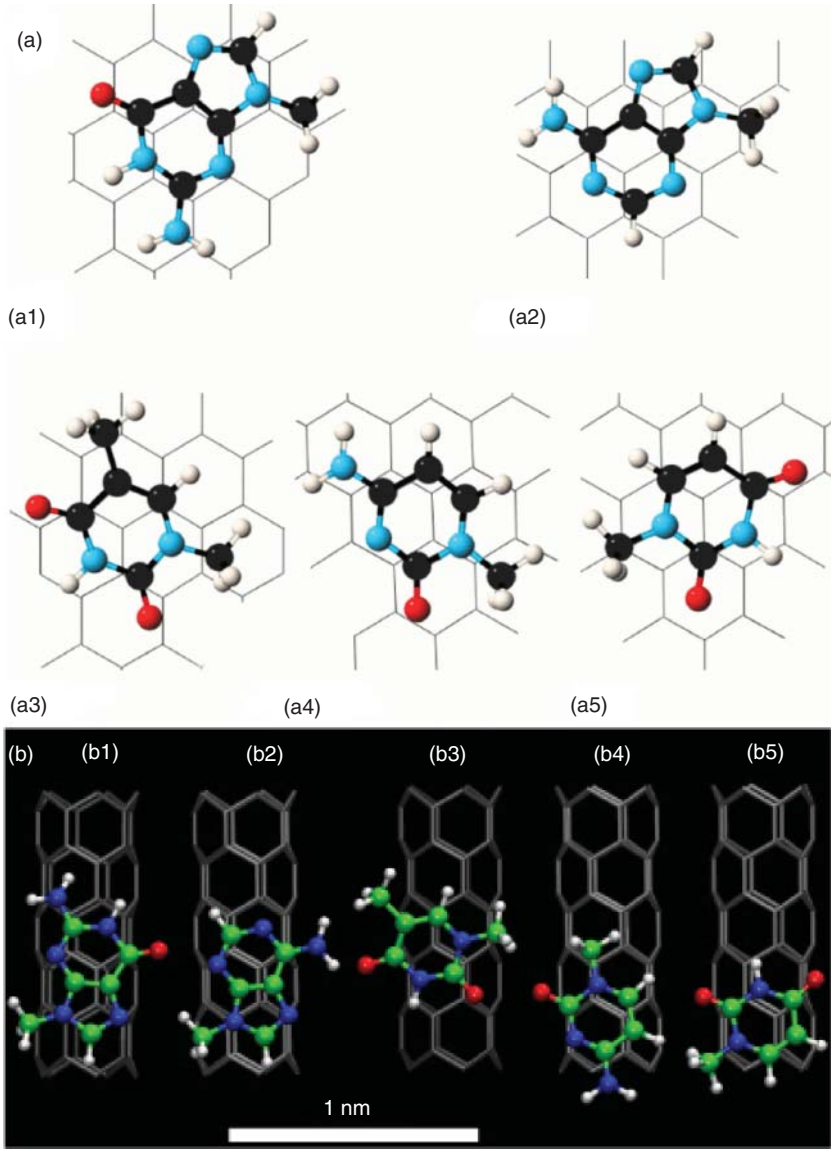

Figure 4.16 (a) Equilibrium geometry of nucleobases on top of graphene: (a1) guanine, (a2) adenine, (a3) thymine, (a4) cytosine, and (a5) uracil. (Reprinted with permission from [138]. © 2007 American Physical Society.) (b) Equilibrium geometry of nucleic acid bases on top of (5, 0) CNT: (b1) guanine, (b2) adenine, (b3) thymine, (b4) cytosine, and (b5) uracil. (Reprinted with permission from [139]. © 2008 IOP Publishing.)

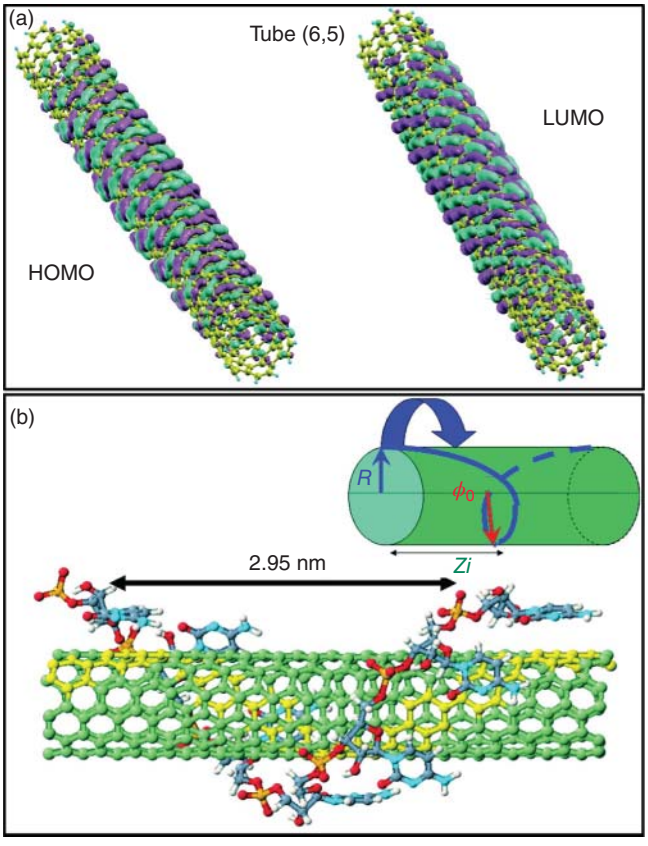

Figure 4.17 (a) Lowest unoccupied molecular orbitals (LUMO) of the (6,5) tube. The positive or the negative sign of the wave function is shown by red or blue color, respectively. The orbital charge density is aligned normal to the tube chiral vector, thus showing a strong orbital charge distribution dependence on the natural chiral coordinates of a tube. (b) Schematic representation of DNA wrapping around a CNT (inset) and an initial configuration of the C-oligomer wrapped along the (6,5) tube chirality. Here, red, orange, cyan, gray, and white colors represent oxygen, phosphor, nitrogen, carbon, and hydrogen atoms of cytosine, respectively. Green and yellow colors represent carbon atoms of the CNT. Carbon atoms marked by yellow indicate the direction of DNA wrapping with seven cytosine bases per helical turn, which lie parallel to the tube surface and nearly normal to the tube chiral vector, thus increasing $\pi-\pi$ overlap between the base and tube orbitals. (Reprinted with permission from [141]. © 2009 American Chemical Society.)

innovative visualization methods such as AFM can also provide some intuitive observations of their interacting behaviors. As shown in Figure 4.18, it is found by both theoretical and experimental methods that there are significant curvature features present in the optimized structures of the nucleobase – graphene complex as well as isolated graphene [142].

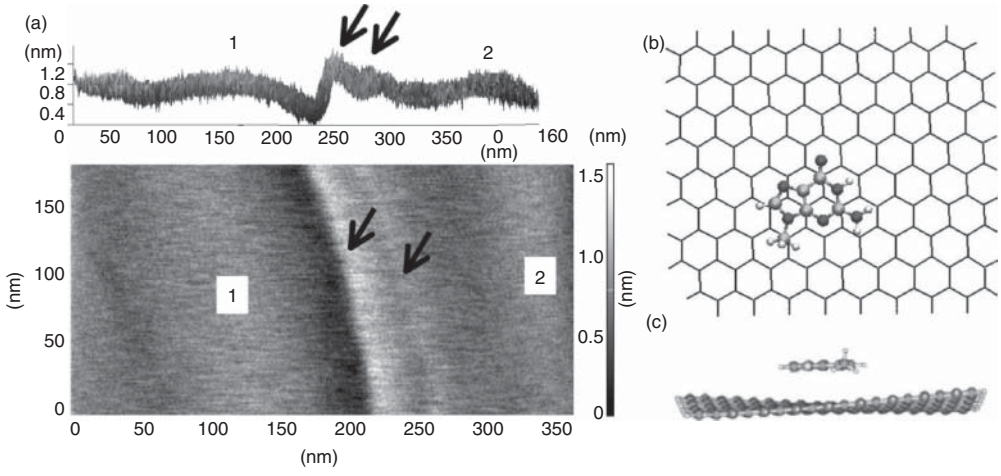

Figure 4.18 (a) Three-dimensional and two-dimensional AFM image showing ripple/wrinkle formation at the edge of the graphene sheet dislodged from the underlying highly oriented pyrolytic graphite (HOPG). The arrows indicate smaller wavelength ripples at the edges. Regions marked 1 and 2 are the large wavelength ripples. (b, c) Top and side views of the interaction of graphene (layer-like) with guanine (the bicyclic molecule). (Reprinted with permission from [142]. © 2012 American Chemical Society.)

4.3.5
Carbon Nanomaterial–Cell Interaction

The cell is the primary structural, functional, and biological unit of the living organism. In addition, there are different types of cells showing quite distinct functions and morphology. Therefore, it is more complex when carbon nanomaterials interact with cells. In the nanomaterial–cell interaction, the cellular uptake of the carbon nanomaterial is the critical step. In general, the cellular uptake involves the processes of recognition, internalization, and further intracellular trafficking and interactions. For instance, it is easily recognized that the dimensional parameter can influence the cellular uptake [100]. Under the same internalizing pathway, much stronger inflammation responses occur when the cells take up the micro-scale graphene oxide than nano-scale graphene oxide, showing a size-dependent effect. However, it has been shown that the size of graphene oxide results in different cellular internalizing pathways. Protein-coated graphene oxide with size of ~500 nm shows the clathrin-mediated endocytosis by mouse mesenchymal progenitor C2C12 cells, whereas larger graphene oxide sheets (~1 μm) exhibit phagocytosis-like uptake (Figure 4.19) [143].

When nanomaterials enter into the physiological environment, the surface of such materials will adsorb biomolecules, which not only endows them with a new biological identity but also influence their interaction with cells and cellular organelles. As shown in Figure 4.20, irreversible cell damage will be induced

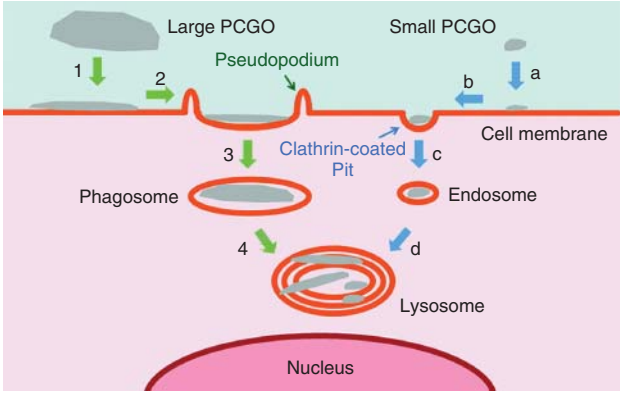

Figure 4.19 Schematics of the cellular uptake of small and large protein-coated graphene oxide nanosheets. Processes (1–4) and (a–d) denote the different internalization pathways of large and small nanosheets into cells, respectively. (Reprinted with permission from [143]. © 2012 American Chemical Society.)

by graphene oxide nanosheets taken up by the A549 cell. In contrast, when the nanosheets are incubated in fetal bovine serum at near-body temperature, the subsequently formed nanoparticle–protein corona complexes show less damage on the integrity of cell membranes [144]. This study reveals that the protein corona can protect the cell from destruction by nanoparticles. However, such protection also presents selectivity. For example, when CNTs are coated with FBG, the release of lactate dehydrogenase is the same as the control, which indicates that the FBG coating protects CNTs from destructing the platelet membranes. In contrast, CNTs coated with γ-globulins (IgG) or histone (H1) show fragmentation of cell membranes as the bare CNTs [23]. These results again partly support our previous results in understanding the effect of the adsorption behaviors of protein corona on cytotoxicity [1].

4.4 Conclusion and Perspectives

In this chapter, we summarized the recent progress in understanding the interaction of carbon nanomaterials with the components of biological systems, such as DNA, proteins, phospholipids, and cells. After a brief introduction on their background and general characterization methods, we reviewed the recent advances in the interaction between biological components and carbon nanomaterials, including CNTs, graphene, fullerene, carbon nanospheres, and nanodiamonds, with the biological system. These results not only provide us fresh knowledge in the understanding the nano/bio interactions but also promote further deep research on many uncovered fields, such as the dynamic aspect and/or electronic level of these interactions and the consideration of the individual distinction.

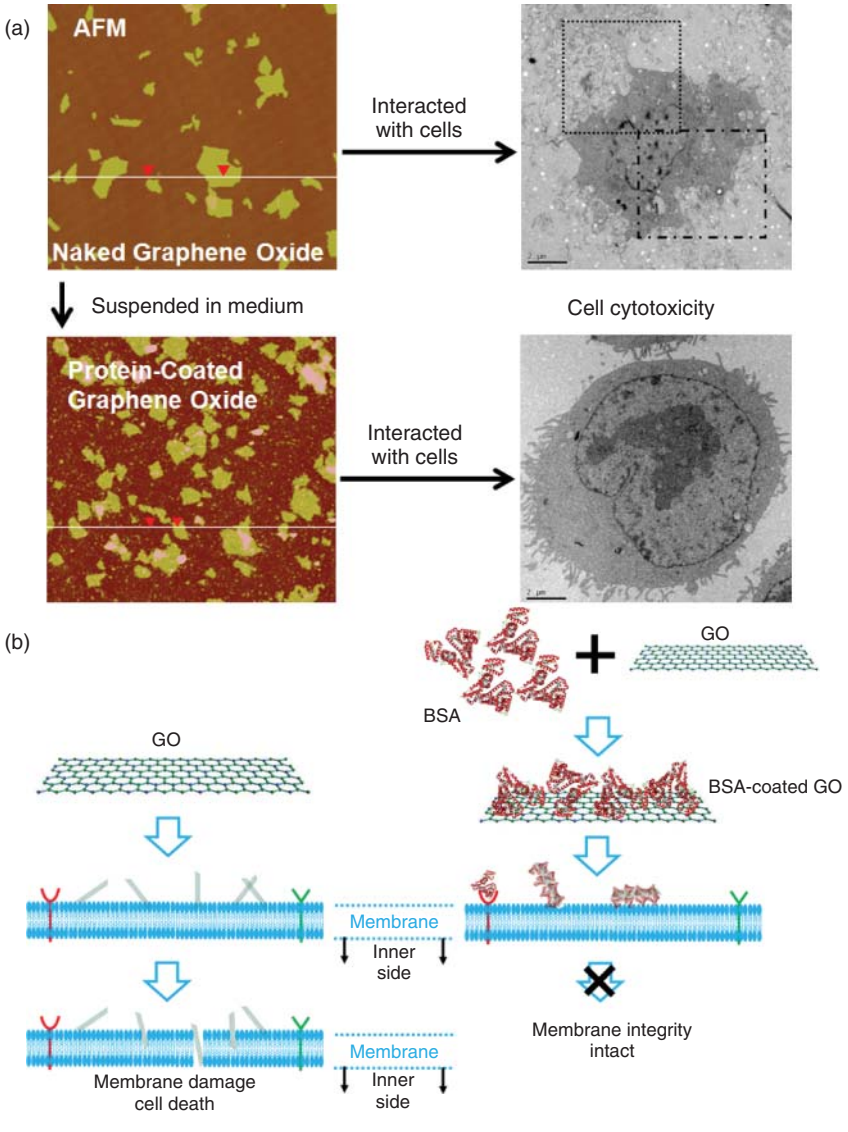

Figure 4.20 (a) Cytotoxicity of GO nanosheets against A549 cells in complete RPIM 1640 medium (10% v/v FBS). AFM images of GO (upper left) and FBS-coated GO nanosheets (lower left). TEM images of A549 cells treated with 100 μg ml^{-1} GO nanosheets (upper right) and FBS-coated GO nanosheets (lower right) at 37 °C for 2 h. (Reprinted with permission from [144]. © 2011 American Chemical Society.) (b) Role of BSA protein in eliminating the cell membrane integrity.

For obtaining further knowledge, detailed investigation and summarization on the pH, ionic strength and viscosity of the biological environment, the charger transfer process during the nano–bio interaction, conformational changes of biological macromolecules when interacting with nanoparticles, and other information may be taken into account. Besides, also novel characterization methods are needed for more precise and intuitional monitoring of the interaction process in detail, *in situ*, and in real time, some of which are listed below:

1) Tuning the biological interaction of the carbon nanomaterials and their toxicology during their syntheses, functionalization, *in vivo* trafficking, uptake, metabolization, and discharging process.
2) Constructing the mechanism framework of the interactions between carbon nanomaterials with biological molecules, cells, tissues, organs, and also other bio–nano interfaces.
3) Establishing the characterization standards and methodologies for nanotoxicology and biological interaction of nanomaterials by extending the current knowledge in nanotoxicology to the current toxicology.
4) *In situ*, real-time, and visual investigations of these interactions with regard to the specification of dose and individual differences, for example, species, patients, medical history, and symptoms.

References

1. Ge, C., Du, J., Zhao, L., Wang, L., Liu, Y., Li, D., Yang, Y., Zhou, R., Zhao, Y., Chai, Z., and Chen, C. (2011) Binding of blood proteins to carbon nanotubes reduces cytotoxicity. *Proc. Natl. Acad. Sci. U.S.A.*, **108** (41), 16968–16973.
2. Rivera-Gil, P., Jimenez De Aberasturi, D., Wulf, V., Pelaz, B., Del Pino, P., Zhao, Y., De La Fuente, J.M., Ruiz De Larramendi, I., Rojo, T., Liang, X.-J., and Parak, W.J. (2013) The challenge to relate the physicochemical properties of colloidal nanoparticles to their cytotoxicity. *Acc. Chem. Res.*, **46** (3), 743–749.
3. Laurent, S., Ng, E.P., Thirifays, C., Lakiss, L., Goupil, G.M., Mintova, S., Burtea, C., Oveisi, E., Hebert, C., de Vries, M., Motazacker, M.M., Rezaee, F., and Mahmoudi, M. (2013) Corona protein composition and cytotoxicity evaluation of ultra-small zeolites synthesized from template free precursor suspensions. *Toxicol. Res.*, **2** (4), 270–279.
4. Zhou, R. and Gao, H. (2014) Cytotoxicity of graphene: recent advances and future perspective. *Wiley Interdiscip. Rev. Nanomed. Nanobiotechnol.*, **6** (5), 452–474.
5. Mortensen, N.P., Hurst, G.B., Wang, W., Foster, C.M., Nallathamby, P.D., and Retterer, S.T. (2013) Dynamic development of the protein corona on silica nanoparticles: composition and role in toxicity. *Nanoscale*, **5** (14), 6372–6380.
6. Jimenez-Cruz, C.A., Kang, S.G., and Zhou, R. (2014) Large scale molecular simulations of nanotoxicity. *Wiley Interdiscip. Rev. Syst. Biol. Med.*, **6** (4), 329–343.
7. Zhao, Y., Xing, G., and Chai, Z. (2008) Nanotoxicology: are carbon nanotubes safe? *Nat. Nanotechnol.*, **3** (4), 191–192.
8. Ge, C., Li, W., Li, Y., Li, B., Du, J., Qiu, Y., Liu, Y., Gao, Y., Chai, Z., and Chen, C. (2011) Significance and systematic analysis of metallic impurities of carbon

nanotubes produced by different manufacturers. *J. Nanosci. Nanotechnol.*, **11** (3), 2389–2397.

9. Zhu, J., Zhang, B., Tian, J., Wang, J., Chong, Y., Wang, X., Deng, Y., Tang, M., Li, Y., Ge, C., Pan, Y., and Gu, H. (2015) Synthesis of heterodimer radionuclide nanoparticles for magnetic resonance and single-photon emission computed tomography dual-modality imaging. *Nanoscale*, **7** (8), 3392–3395.
10. Ge, C., Tian, J., Zhao, Y., Chen, C., Zhou, R., and Chai, Z. (2015) Towards understanding of nanoparticle–protein corona. *Arch. Toxicol.*, **89** (4), 519–539.
11. Pan, Y., Du, X., Zhao, F., and Xu, B. (2012) Magnetic nanoparticles for the manipulation of proteins and cells. *Chem. Soc. Rev.*, **41** (7), 2912–2942.
12. Wu, J. and Chu, C.-C. (2012) Block copolymer of poly(ester amide) and polyesters: synthesis, characterization, and in vitro cellular response. *Acta Biomater.*, **8** (12), 4314–4323.
13. Wu, J., Kamaly, N., Shi, J., Zhao, L., Xiao, Z., Hollett, G., John, R., Ray, S., Xu, X., Zhang, X., Kantoff, P.W., and Farokhzad, O.C. (2014) Development of multinuclear polymeric nanoparticles as robust protein nanocarriers. *Angew. Chem. Int. Ed.*, **53** (34), 8975–8979.
14. Wu, J., Wu, D., Mutschler, M.A., and Chu, C.-C. (2012) Cationic hybrid hydrogels from amino-acid-based poly(ester amide): fabrication, characterization, and biological properties. *Adv. Funct. Mater.*, **22** (18), 3815–3823.
15. Wu, J., Yamanouchi, D., Liu, B., and Chu, C.-C. (2012) Biodegradable arginine-based poly(ether ester amide)s as a non-viral DNA delivery vector and their structure-function study. *J. Mater. Chem.*, **22** (36), 18983–18991.
16. Liu, Y., Zhao, Y., Sun, B., and Chen, C. (2013) Understanding the toxicity of carbon nanotubes. *Acc. Chem. Res.*, **46** (3), 702–713.
17. Poland, C.A., Duffin, R., Kinloch, I., Maynard, A., Wallace, W.A.H., Seaton, A., Stone, V., Brown, S., MacNee, W., and Donaldson, K. (2008) Carbon nanotubes introduced into the abdominal cavity of mice show asbestos-like pathogenicity in a pilot study. *Nat. Nanotechnol.*, **3** (7), 423–428.
18. Sato, Y., Yokoyama, A., Shibata, K.-i., Akimoto, Y., Ogino, S.-i., Nodasaka, Y., Kohgo, T., Tamura, K., Akasaka, T., Uo, M., Motomiya, K., Jeyadevan, B., Ishiguro, M., Hatakeyama, R., Watari, F., and Tohji, K. (2005) Influence of length on cytotoxicity of multi-walled carbon nanotubes against human acute monocytic leukemia cell line THP-1 in vitro and subcutaneous tissue of rats in vivo. *Mol. Biosyst.*, **1** (2), 176–182.
19. Palomäki, J., Välimäki, E., Sund, J., Vippola, M., Clausen, P.A., Jensen, K.A., Savolainen, K., Matikainen, S., and Alenius, H. (2011) Long, needle-like carbon nanotubes and asbestos activate the NLRP3 inflammasome through a similar mechanism. *ACS Nano*, **5** (9), 6861–6870.
20. Zhou, H., Zhao, K., Li, W., Yang, N., Liu, Y., Chen, C., and Wei, T. (2012) The interactions between pristine graphene and macrophages and the production of cytokines/chemokines via TLR- and NF-κB-related signaling pathways. *Biomaterials*, **33** (29), 6933–6942.
21. Li, Y., Liu, Y., Fu, Y., Wei, T., Le Guyader, L., Gao, G., Liu, R.-S., Chang, Y.-Z., and Chen, C. (2012) The triggering of apoptosis in macrophages by pristine graphene through the MAPK and TGF-beta signaling pathways. *Biomaterials*, **33** (2), 402–411.
22. Cai, X., Ramalingam, R., Wong, H.S., Cheng, J., Ajuh, P., Cheng, S.H., and Lam, Y.W. (2013) Characterization of carbon nanotube protein corona by using quantitative proteomics. *Nanomed. Nanotechnol. Biol. Med.*, **9** (5), 583–593.
23. De Paoli, S.H., Diduch, L.L., Tegegn, T.Z., Orecna, M., Strader, M.B., Karnaukhova, E., Bonevich, J.E., Holada, K., and Simak, J. (2014) The effect of protein corona composition on the interaction of carbon nanotubes with human blood platelets. *Biomaterials*, **35** (24), 6182–6194.
24. Treuel, L., Brandholt, S., Maffre, P., Wiegele, S., Shang, L., and Nienhaus,

G.U. (2014) Impact of protein modification on the protein corona on nanoparticles and nanoparticle-cell interactions. *ACS Nano*, **8** (1), 503–513.

25. Yallapu, M.M., Chauhan, N., Othman, S.F., Khalilzad-Sharghi, V., Ebeling, M.C., Khan, S., Jaggi, M., and Chauhan, S.C. (2015) Implications of protein corona on physico-chemical and biological properties of magnetic nanoparticles. *Biomaterials*, **46**, 1–12.
26. Fleischer, C.C. and Payne, C.K. (2014) Nanoparticle-cell interactions: molecular structure of the protein corona and cellular outcomes. *Acc. Chem. Res.*, **47** (8), 2651–2659.
27. Dai, Q., Walkey, C., and Chan, W.C.W. (2014) Polyethylene glycol backfilling mitigates the negative impact of the protein corona on nanoparticle cell targeting. *Angew. Chem. Int. Ed.*, **53** (20), 5093–5096.
28. Soja, B., Heinkelmann, R., and Schuh, H. (2014) Probing the solar corona with very long baseline interferometry. *Nat. Commun.*, **5**, 4166.
29. Mirsadeghi, S., Dinarvand, R., Ghahremani, M.H., Hormozi-Nezhad, M.R., Mahmoudi, Z., Hajipour, M.J., Atyabi, F., Ghavami, M., and Mahmoudi, M. (2015) Protein corona composition of gold nanoparticles/nanorods affects amyloid beta fibrillation process. *Nanoscale*, **7** (11), 5004–5013.
30. Sakulkhu, U., Mahmoudi, M., Maurizi, L., Salaklang, J., and Hofmann, H. (2014) Protein corona composition of superparamagnetic iron oxide nanoparticles with various physico-chemical properties and coatings. *Sci. Rep.*, **4**, 5020.
31. Walkey, C.D., Olsen, J.B., Song, F., Liu, R., Guo, H., Olsen, D.W.H., Cohen, Y., Emili, A., and Chan, W.C.W. (2014) Protein corona fingerprinting predicts the cellular interaction of gold and silver nanoparticles. *ACS Nano*, **8** (3), 2439–2455.
32. Kah, J.C.Y., Grabinski, C., Untener, E., Garrett, C., Chen, J., Zhu, D., Hussain, S.M., and Hamad-Schifferli, K. (2014) Protein coronas on gold nanorods passivated with amphiphilic ligands affect cytotoxicity and cellular response to penicillin/streptomycin. *ACS Nano*, **8** (5), 4608–4620.
33. Docter, D., Distler, U., Storck, W., Kuharev, J., Wuensch, D., Hahlbrock, A., Knauer, S.K., Tenzer, S., and Stauber, R.H. (2014) Quantitative profiling of the protein coronas that form around nanoparticles. *Nat. Protoc.*, **9** (9), 2030–2044.
34. Ashby, J., Pan, S., and Zhong, W. (2014) Size and surface functionalization of iron oxide nanoparticles influence the composition and dynamic nature of their protein corona. *ACS Appl. Mater. Interfaces*, **6** (17), 15412–15419.
35. Miclaus, T., Bochenkov, V.E., Ogaki, R., Howard, K.A., and Sutherland, D.S. (2014) Spatial mapping and quantification of soft and hard protein coronas at silver nanocubes. *Nano Lett.*, **14** (4), 2086–2093.
36. Wan, S., Kelly, P.M., Mahon, E., Stockmann, H., Rudd, P.M., Caruso, F., Dawson, K.A., Yan, Y., and Monopoli, M.P. (2015) The "sweet" side of the protein corona: effects of glycosylation on nanoparticle-cell interactions. *ACS Nano*, **9** (2), 2157–2166.
37. Monopoli, M.P., Aberg, C., Salvati, A., and Dawson, K.A. (2012) Biomolecular coronas provide the biological identity of nanosized materials. *Nat. Nanotechnol.*, **7** (12), 779–786.
38. Lundqvist, M. (2013) Nanoparticles: tracking protein corona over time. *Nat. Nanotechnol.*, **8** (10), 701–702.
39. Mirshafiee, V., Mahmoudi, M., Lou, K., Cheng, J., and Kraft, M.L. (2013) Protein corona significantly reduces active targeting yield. *Chem. Commun.*, **49** (25), 2557–2559.
40. Euliss, L.E., DuPont, J.A., Gratton, S., and DeSimone, J. (2006) Imparting size, shape, and composition control of materials for nanomedicine. *Chem. Soc. Rev.*, **35** (11), 1095–1104.
41. Roduner, E. (2006) Size matters: why nanomaterials are different. *Chem. Soc. Rev.*, **35** (7), 583–592.

42. El-Sayed, M.A. (2004) Small is different: shape-, size-, and composition-dependent properties of some colloidal semiconductor nanocrystals. *Acc. Chem. Res.*, **37** (5), 326–333.
43. Mu, Q., Jiang, G., Chen, L., Zhou, H., Fourches, D., Tropsha, A., and Yan, B. (2014) Chemical basis of interactions between engineered nanoparticles and biological systems. *Chem. Rev.*, **114** (15), 7740–7781.
44. Walkey, C.D. and Chan, W.C.W. (2012) Understanding and controlling the interaction of nanomaterials with proteins in a physiological environment. *Chem. Soc. Rev.*, **41** (7), 2780–2799.
45. Stoddart, J.F. (1991) The 3rd allotropic form of carbon. *Angew. Chem. Int. Ed. Engl.*, **30** (1), 70–71.
46. Whittake, A.G. and Kintner, P.L. (1969) Carbon: observations of new allotropic form. *Science*, **165** (3893), 589–591.
47. Sokolov, V.I. and Stankevich, I.V. (1993) Fullerenes-new allotropic forms of carbon: molecular and eletronic-structures and chemical-properties. *Usp. Khim.*, **62** (5), 455–473.
48. Goresy, A.E. and Donnay, G. (1968) A new allotropic form of carbon from the ries crater. *Science*, **161** (3839), 363–364.
49. Konyashin, I., Khvostov, V., Babaev, V., Guseva, M., Mayer, J., and Sirenko, A. (2006) A new hard allotropic form of carbon: dream or reality? *Int. J. Refract. Met. Hard Mater.*, **24** (1–2), 17–23.
50. Pauly, N., Novak, M., and Tougaard, S. (2013) Surface excitation parameter for allotropic forms of carbon. *Surf. Interface Anal.*, **45** (4), 811–816.
51. Gorityala, B.K., Ma, J., Wang, X., Chen, P., and Liu, X.W. (2010) Carbohydrate functionalized carbon nanotubes and their applications. *Chem. Soc. Rev.*, **39** (8), 2925–2934.
52. Wang, L., Sun, Q., Wang, X., Wen, T., Yin, J.J., Wang, P., Bai, R., Zhang, X.Q., Zhang, L.H., Lu, A.H., and Chen, C. (2015) Using hollow carbon nanospheres as a light-induced free radical generator to overcome chemotherapy resistance. *J. Am. Chem. Soc.*, **137** (5), 1947–1955.
53. Chen, R., Zhang, L., Ge, C., Tseng, M.T., Bai, R., Qu, Y., Beer, C., Autrup, H., and Chen, C. (2015) Subchronic toxicity and cardiovascular responses in spontaneously hypertensive rats after exposure to multiwalled carbon nanotubes by intratracheal instillation. *Chem. Res. Toxicol.*, **28** (3), 440–450.
54. Yu, M.-F., Files, B.S., Arepalli, S., and Ruoff, R.S. (2000) Tensile loading of ropes of single wall carbon nanotubes and their mechanical properties. *Phys. Rev. Lett.*, **84** (24), 5552–5555.
55. Xie, S., Li, W., Pan, Z., Chang, B., and Sun, L. (2000) Mechanical and physical properties on carbon nanotube. *J. Phys. Chem. Solids*, **61** (7), 1153–1158.
56. Zhao, F., Meng, H., Yan, L., Wang, B., and Zhao, Y. (2015) Nanosurface chemistry and dose govern the bioaccumulation and toxicity of carbon nanotubes, metal nanomaterials and quantum dots in vivo. *Sci. Bull.*, **60** (1), 3–20.
57. Saifuddin, N., Raziah, A.Z., and Junizah, A.R. (2013) Carbon nanotubes: a review on structure and their interaction with proteins. *J. Chem.*, **2013**, 676815.
58. Saito, R., Dresselhaus, G., and Dresselhaus, M.S. (1998) *Physical Properties of Carbon Nanotubes*, vol. 4, World Scientific.
59. Donaldson, K., Aitken, R., Tran, L., Stone, V., Duffin, R., Forrest, G., and Alexander, A. (2006) Carbon nanotubes: a review of their properties in relation to pulmonary toxicology and workplace safety. *Toxicol. Sci.*, **92** (1), 5–22.
60. Zhang, M. and Li, J. (2009) Carbon nanotube in different shapes. *Mater. Today*, **12** (6), 12–18.
61. Lundqvist, M., Sethson, I., and Jonsson, B.-H. (2004) Protein adsorption onto silica nanoparticles: conformational changes depend on the particles' curvature and the protein stability. *Langmuir*, **20** (24), 10639–10647.
62. Vertegel, A.A., Siegel, R.W., and Dordick, J.S. (2004) Silica nanoparticle size influences the structure and enzymatic activity of adsorbed lysozyme. *Langmuir*, **20** (16), 6800–6807.

63. Shang, W., Nuffer, J.H., Dordick, J.S., and Siegel, R.W. (2007) Unfolding of ribonuclease a on silica nanoparticle surfaces. *Nano Lett.*, **7** (7), 1991–1995.
64. Mu, Q., Liu, W., Xing, Y., Zhou, H., Li, Z., Zhang, Y., Ji, L., Wang, F., Si, Z., Zhang, B., and Yan, B. (2008) Protein binding by functionalized multiwalled carbon nanotubes is governed by the surface chemistry of both parties and the nanotube diameter. *J. Phys. Chem. C*, **112** (9), 3300–3307.
65. Liu, W.T., Bien, M.Y., Chuang, K.J., Chang, T.Y., Jones, T., BeruBe, K., Lalev, G., Tsai, D.H., Chuang, H.C., Cheng, T.J., and Taiwan CardioPulmonary Research (T-CPR) Group (2014) Physicochemical and biological characterization of single-walled and double-walled carbon nanotubes in biological media. *J. Hazard. Mater.*, **280**, 216–225.
66. Lamprecht, C., Liashkovich, I., Neves, V., Danzberger, J., Heister, E., Rangl, M., Coley, H.M., McFadden, J., Flahaut, E., Gruber, H.J., Hinterdorfer, P., Kienberger, F., and Ebner, A. (2009) AFM imaging of functionalized carbon nanotubes on biological membranes. *Nanotechnology*, **20** (43), 434001.
67. Cheng, J., Flahaut, E., and Cheng, S.H. (2007) Effect of carbon nanotubes on developing zebrafish (Danio rerio) embryos. *Environ. Toxicol. Chem.*, **26**, 708–716.
68. Sacchetti, C., Motamedchaboki, K., Magrini, A., Palmieri, G., Mattei, M., Bernardini, S., Rosato, N., Bottini, N., and Bottini, M. (2013) Surface polyethylene glycol conformation influences the protein corona of polyethylene glycol-modified single-walled carbon nanotubes: potential implications on biological performance. *ACS Nano*, **7** (3), 1974–1989.
69. Li, L.L., Lin, R., He, H., Jiang, L., and Gao, M.M. (2013) Interaction of carboxylated single-walled carbon nanotubes with bovine serum albumin. *Spectrochim. Acta, Part A*, **105**, 45–51.
70. Chen, R.J., Zhang, Y., Wang, D., and Dai, H. (2001) Noncovalent sidewall functionalization of single-walled carbon nanotubes for protein immobilization. *J. Am. Chem. Soc.*, **123** (16), 3838–3839.
71. Li, X., Chen, W., Zhan, Q., Dai, L., Sowards, L., Pender, M., and Naik, R.R. (2006) Direct measurements of interactions between polypeptides and carbon nanotubes. *J. Phys. Chem. B*, **110** (25), 12621–12625.
72. Zorbas, V., Smith, A.L., Xie, H., Ortiz-Acevedo, A., Dalton, A.B., Dieckmann, G.R., Draper, R.K., Baughman, R.H., and Musselman, I.H. (2005) Importance of aromatic content for peptide/single-walled carbon nanotube interactions. *J. Am. Chem. Soc.*, **127** (35), 12323–12328.
73. Karajanagi, S.S., Vertegel, A.A., Kane, R.S., and Dordick, J.S. (2004) Structure and function of enzymes adsorbed onto single-walled carbon nanotubes. *Langmuir*, **20** (26), 11594–11599.
74. Yang, K., Feng, L., Shi, X., and Liu, Z. (2013) Nano-graphene in biomedicine: theranostic applications. *Chem. Soc. Rev.*, **42** (2), 530–547.
75. Zhang, Y., Nayak, T.R., Hong, H., and Cai, W. (2012) Graphene: a versatile nanoplatform for biomedical applications. *Nanoscale*, **4** (13), 3833–3842.
76. Liu, Z., Robinson, J.T., Sun, X., and Dai, H. (2008) PEGylated nanographene oxide for delivery of water-insoluble cancer drugs. *J. Am. Chem. Soc.*, **130** (33), 10876–10877.
77. Zhang, S., Yang, K., Feng, L., and Liu, Z. (2011) In vitro and in vivo behaviors of dextran functionalized graphene. *Carbon*, **49** (12), 4040–4049.
78. Chatterjee, N., Eom, H.J., and Choi, J. (2014) A systems toxicology approach to the surface functionality control of graphene-cell interactions. *Biomaterials*, **35** (4), 1109–1127.
79. Erickson, K., Erni, R., Lee, Z., Alem, N., Gannett, W., and Zettl, A. (2010) Determination of the local chemical structure of graphene oxide and reduced graphene oxide. *Adv. Mater.*, **22** (40), 4467–4472.
80. Hu, X. and Zhou, Q. (2013) Health and ecosystem risks of graphene. *Chem. Rev.*, **113** (5), 3815–3835.

81. Yan, L., Zheng, Y.B., Zhao, F., Li, S., Gao, X., Xu, B., Weiss, P.S., and Zhao, Y. (2012) Chemistry and physics of a single atomic layer: strategies and challenges for functionalization of graphene and graphene-based materials. *Chem. Soc. Rev.*, **41** (1), 97–114.
82. Akhavan, O. and Ghaderi, E. (2010) Toxicity of graphene and graphene oxide nanowalls against bacteria. *ACS Nano*, **4** (10), 5731–5736.
83. Tu, Y., Lv, M., Xiu, P., Huynh, T., Zhang, M., Castelli, M., Liu, Z., Huang, Q., Fan, C., Fang, H., and Zhou, R. (2013) Destructive extraction of phospholipids from Escherichia coli membranes by graphene nanosheets. *Nat. Nanotechnol.*, **8** (8), 594–601.
84. Jiao, Y., Qian, F., Li, Y., Wang, G., Saltikov, C.W., and Gralnick, J.A. (2011) Deciphering the electron transport pathway for graphene oxide reduction by Shewanella oneidensis MR-1. *J. Bacteriol.*, **193** (14), 3662–3665.
85. Kotchey, G.P., Allen, B.L., Vedala, H., Yanamala, N., Kapralov, A.A., Tyurina, Y.Y., Klein-Seetharaman, J., Kagan, V.E., and Star, A. (2011) The enzymatic oxidation of graphene oxide. *ACS Nano*, **5** (3), 2098–2108.
86. Tan, X., Feng, L., Zhang, J., Yang, K., Zhang, S., Liu, Z., and Peng, R. (2013) Functionalization of graphene oxide generates a unique interface for selective serum protein interactions. *ACS Appl. Mater. Interfaces*, **5** (4), 1370–1377.
87. Liu, J., Huang, Y.R., Kumar, A., Tan, A., Jin, S.B., Mozhi, A., and Liang, X.J. (2014) pH-sensitive nano-systems for drug delivery in cancer therapy. *Biotechnol. Adv.*, **32** (4), 693–710.
88. Wojtkowiak, J.W., Verduzco, D., Schramm, K.J., and Gillies, R.J. (2011) Drug resistance and cellular adaptation to tumor acidic pH microenvironment. *Mol. Pharmaceutics*, **8** (6), 2032–2038.
89. Zhang, X., Meng, L., Lu, Q., Fei, Z., and Dyson, P.J. (2009) Targeted delivery and controlled release of doxorubicin to cancer cells using modified single wall carbon nanotubes. *Biomaterials*, **30** (30), 6041–6047.
90. Nepal, D. and Geckeler, K.E. (2006) pH-sensitive dispersion and debundling of single-walled carbon nanotubes: lysozyme as a tool. *Small*, **2** (3), 406–412.
91. Zhu, J., Liao, L., Bian, X., Kong, J., Yang, P., and Liu, B. (2012) pH-Controlled delivery of doxorubicin to cancer cells, based on small mesoporous carbon nanospheres. *Small*, **8** (17), 2715–2720.
92. Hunter, R.J. (2001) *Foundations of Colloid Science*, Oxford University Press 2nd rev. edn.
93. Samarajeewa, D.R., Dieckmann, G.R., Nielsen, S.O., and Musselman, I.H. (2012) Modifying the electronic properties of single-walled carbon nanotubes using designed surfactant peptides. *Nanoscale*, **4** (15), 4544–4554.
94. Bradley, K., Briman, M., Star, A., and Grüner, G. (2004) Charge transfer from adsorbed proteins. *Nano Lett.*, **4** (2), 253–256.
95. Peng, Z.G., Hidajat, K., and Uddin, M.S. (2004) Adsorption of bovine serum albumin on nanosized magnetic particles. *J. Colloid Interface Sci.*, **271** (2), 277–283.
96. Wang, L., Wang, H., Yuan, L., Yang, W., Wu, Z., and Chen, H. (2011) Step-wise control of protein adsorption and bacterial attachment on a nanowire array surface: tuning surface wettability by salt concentration. *J. Mater. Chem.*, **21** (36), 13920–13925.
97. Gao, J., Wang, L., Kang, S.-g., Zhao, L., Ji, M., Chen, C., Zhao, Y., Zhou, R., and Li, J. (2014) Size-dependent impact of CNTs on dynamic properties of calmodulin. *Nanoscale*, **6** (21), 12828–12837.
98. Park, K.H., Chhowalla, M., Iqbal, Z., and Sesti, F. (2003) Single-walled carbon nanotubes are a new class of ion channel blockers. *J. Biol. Chem.*, **278** (50), 50212–50216.
99. Braden, B.C., Goldbaum, F.A., Chen, B.X., Kirschner, A.N., Wilson, S.R., and Erlanger, B.F. (2000) X-ray crystal structure of an anti-Buckminsterfullerene antibody Fab fragment: biomolecular recognition of

C_{60}. *Proc. Natl. Acad. Sci. U.S.A.*, **97** (22), 12193–12197.

100. Yue, H., Wei, W., Yue, Z., Wang, B., Luo, N., Gao, Y., Ma, D., Ma, G., and Su, Z. (2012) The role of the lateral dimension of graphene oxide in the regulation of cellular responses. *Biomaterials*, **33** (16), 4013–4021.
101. Jin, H., Heller, D.A., and Strano, M.S. (2008) Single-particle tracking of endocytosis and exocytosis of single-walled carbon nanotubes in NIH-3T3 cells. *Nano Lett.*, **8** (6), 1577–1585.
102. Salvati, A., Åberg, C., dos Santos, T., Varela, J., Pinto, P., Lynch, I., and Dawson, K.A. (2011) Experimental and theoretical comparison of intracellular import of polymeric nanoparticles and small molecules: toward models of uptake kinetics. *Nanomed. Nanotechnol. Biol. Med.*, **7** (6), 818–826.
103. Yuan, H., Li, J., Bao, G., and Zhang, S. (2010) Variable nanoparticle-cell adhesion strength regulates cellular uptake. *Phys. Rev. Lett.*, **105** (13), 138101.
104. Gaucher, G., Asahina, K., Wang, J., and Leroux, J.-C. (2009) Effect of poly(N-vinyl-pyrrolidone)-block-poly(d,l-lactide) as coating agent on the opsonization, phagocytosis, and pharmacokinetics of biodegradable nanoparticles. *Biomacromolecules*, **10** (2), 408–416.
105. Mosqueira, V.C.F., Legrand, P., Gulik, A., Bourdon, O., Gref, R., Labarre, D., and Barratt, G. (2001) Relationship between complement activation, cellular uptake and surface physicochemical aspects of novel PEG-modified nanocapsules. *Biomaterials*, **22** (22), 2967–2979.
106. Walkey, C.D., Olsen, J.B., Guo, H., Emili, A., and Chan, W.C.W. (2012) Nanoparticle size and surface chemistry determine serum protein adsorption and macrophage uptake. *J. Am. Chem. Soc.*, **134** (4), 2139–2147.
107. Nagayama, S., Ogawara, K.-i., Minato, K., Fukuoka, Y., Takakura, Y., Hashida, M., Higaki, K., and Kimura, T. (2007) Fetuin mediates hepatic uptake of negatively charged nanoparticles via scavenger receptor. *Int. J. Pharm.*, **329** (1–2), 192–198.
108. Nagayama, S., Ogawara, K.-i., Fukuoka, Y., Higaki, K., and Kimura, T. (2007) Time-dependent changes in opsonin amount associated on nanoparticles alter their hepatic uptake characteristics. *Int. J. Pharm.*, **342** (1–2), 215–221.
109. Tedja, R., Lim, M., Amal, R., and Marquis, C. (2012) Effects of serum adsorption on cellular uptake profile and consequent impact of titanium dioxide nanoparticles on human lung cell lines. *ACS Nano*, **6** (5), 4083–4093.
110. Gratton, E., Jameson, D.M., and Hall, R.D. (1984) Multifrequency phase and modulation fluorometry. *Annu. Rev. Biophys. Bioeng.*, **13**, 105–124.
111. Kim, C.-Y., Chang, J.S., Doyon, J.B., Baird, T.T., Fierke, C.A., Jain, A., and Christianson, D.W. (2000) Contribution of fluorine to protein-ligand affinity in the binding of fluoroaromatic inhibitors to carbonic anhydrase II. *J. Am. Chem. Soc.*, **122** (49), 12125–12134.
112. Paoli, M., Liddington, R., Tame, J., Wilkinson, A., and Dodson, G. (1996) Crystal structure of T state haemoglobin with oxygen bound at all four haems. *J. Mol. Biol.*, **256** (4), 775–792.
113. Stein, P.E., Leslie, A.G., Finch, J.T., and Carrell, R.W. (1991) Crystal structure of uncleaved ovalbumin at 1.95 A resolution. *J. Mol. Biol.*, **221** (3), 941–959.
114. Anderson, C.M., Stenkamp, R.E., and Steitz, T.A. (1978) Sequencing a protein by x-ray crystallography. II. Refinement of yeast hexokinase B co-ordinates and sequence at 2.1 A resolution. *J. Mol. Biol.*, **123** (1), 15–33.
115. Ghuman, J., Zunszain, P.A., Petitpas, I., Bhattacharya, A.A., Otagiri, M., and Curry, S. (2005) Structural basis of the drug-binding specificity of human serum albumin. *J. Mol. Biol.*, **353** (1), 38–52.
116. Lakowicz, J.R. (2007) *Principles of Fluorescence Spectroscopy*, Springer Science & Business Media.
117. Ashby, J., Duan, Y., Ligans, E., Tamsi, M., and Zhong, W. (2015) High-throughput profiling of nanoparticle-protein interactions by

fluorescamine labeling. *Anal. Chem.*, **87** (4), 2213–2219.

118. Zhang, Y., Ali, S.F., Dervishi, E., Xu, Y., Li, Z., Casciano, D., and Biris, A.S. (2010) Cytotoxicity effects of graphene and single-wall carbon nanotubes in neural phaeochromocytoma-derived PC12 cells. *ACS Nano*, **4** (6), 3181–3186.

119. Liao, K.-H., Lin, Y.-S., Macosko, C.W., and Haynes, C.L. (2011) Cytotoxicity of graphene oxide and graphene in human erythrocytes and skin fibroblasts. *ACS Appl. Mater. Interfaces*, **3** (7), 2607–2615.

120. Chang, Y., Yang, S.-T., Liu, J.-H., Dong, E., Wang, Y., Cao, A., Liu, Y., and Wang, H. (2011) In vitro toxicity evaluation of graphene oxide on A549 cells. *Toxicol. Lett.*, **200** (3), 201–210.

121. Bitounis, D., Ali-Boucetta, H., Hong, B.H., Min, D.H., and Kostarelos, K. (2013) Prospects and challenges of graphene in biomedical applications. *Adv. Mater.*, **25** (16), 2258–2268.

122. Zhang, Z., Niu, B., Chen, J., He, X., Bao, X., Zhu, J., Yu, H., and Li, Y. (2014) The use of lipid-coated nanodiamond to improve bioavailability and efficacy of sorafenib in resisting metastasis of gastric cancer. *Biomaterials*, **35** (15), 4565–4572.

123. Fako, V.E. and Furgeson, D.Y. (2009) Zebrafish as a correlative and predictive model for assessing biomaterial nanotoxicity. *Adv. Drug Delivery Rev.*, **61** (6), 478–486.

124. Avanasi, R., Jackson, W.A., Sherwin, B., Mudge, J.F., and Anderson, T.A. (2014) C_{60} fullerene soil sorption, biodegradation, and plant uptake. *Environ. Sci. Technol.*, **48** (5), 2792–2797.

125. Nadežda, N., Sanja, V.-D., Drina, J., Divna, Đ., Marija, M., Nataša, B., and Vladimir, T. (2009) Preparation and biodistribution of radiolabeled fullerene C_{60} nanocrystals. *Nanotechnology*, **20** (38), 385102.

126. Vance, D.E. (2014) Phospholipid methylation in mammals: from biochemistry to physiological function. *Biochim. Biophys. Acta, Biomembr.*, **1838** (6), 1477–1487.

127. Wang, H., Michielssens, S., Moors, S.C., and Ceulemans, A. (2009) Molecular dynamics study of dipalmitoylphosphatidylcholine lipid layer self-assembly onto a single-walled carbon nanotube. *Nano Res.*, **2** (12), 945–954.

128. Hirano, A., Uda, K., Maeda, Y., Akasaka, T., and Shiraki, K. (2010) One-dimensional protein-based nanoparticles induce lipid bilayer disruption: carbon nanotube conjugates and amyloid fibrils. *Langmuir*, **26** (22), 17256–17259.

129. Kapralov, A.A., Feng, W.H., Amoscato, A.A., Yanamala, N., Balasubramanian, K., Winnica, D.E., Kisin, E.R., Kotchey, G.P., Gou, P.P., Sparvero, L.J., Ray, P., Mallampalli, R.K., Klein-Seetharaman, J., Fadeel, B., Star, A., Shvedova, A.A., and Kagan, V.E. (2012) Adsorption of surfactant lipids by single-walled carbon nanotubes in mouse lung upon pharyngeal aspiration. *ACS Nano*, **6** (5), 4147–4156.

130. Feng, J.W., Ding, H.M., and Ma, Y.Q. (2014) Controlling water flow inside carbon nanotube with lipid membranes. *J. Chem. Phys.*, **141** (9), 7.

131. Geng, J., Kim, K., Zhang, J., Escalada, A., Tunuguntla, R., Comolli, L.R., Allen, F.I., Shnyrova, A.V., Cho, K.R., Munoz, D., Wang, Y.M., Grigoropoulos, C.P., Ajo-Franklin, C.M., Frolov, V.A., and Noy, A. (2014) Stochastic transport through carbon nanotubes in lipid bilayers and live cell membranes. *Nature*, **514** (7524), 612–615.

132. Luan, B.Q., Huynh, T., Zhao, L., and Zhou, R.H. (2015) Potential toxicity of graphene to cell functions via disrupting protein-protein interactions. *ACS Nano*, **9** (1), 663–669.

133. Umadevi, D., Panigrahi, S., and Sastry, G.N. (2014) Noncovalent interaction of carbon nanostructures. *Acc. Chem. Res.*, **47** (8), 2574–2581.

134. Zhang, Y., Zhang, J., Huang, X., Zhou, X., Wu, H., and Guo, S. (2012) Assembly of graphene oxide-enzyme conjugates through hydrophobic interaction. *Small*, **8** (1), 154–159.

135. Mayadunne, E. and El Rassi, Z. (2014) Facile preparation of octadecyl monoliths with incorporated carbon

nanotubes and neutral monoliths with coated carbon nanotubes stationary phases for HPLC of small and large molecules by hydrophobic and π–π interactions. *Talanta*, **129**, 565–574.

136. Ruh, H., Kuehl, B., Brenner-Weiss, G., Hopf, C., Diabate, S., and Weiss, C. (2012) Identification of serum proteins bound to industrial nanomaterials. *Toxicol. Lett.*, **208** (1), 41–50.

137. Calvaresi, M., Arnesano, F., Bonacchi, S., Bottoni, A., Calo, V., Conte, S., Falini, G., Fermani, S., Losacco, M., Montalti, M., Natile, G., Prodi, L., Sparla, F., and Zerbetto, F. (2014) C_{60}@lysozyme: direct observation by nuclear magnetic resonance of a 1:1 fullerene protein adduct. *ACS Nano*, **8** (2), 1871–1877.

138. Gowtham, S., Scheicher, R.H., Ahuja, R., Pandey, R., and Karna, S.P. (2007) Physisorption of nucleobases on graphene: density-functional calculations. *Phys. Rev. B*, **76** (3), 033401.

139. Gowtham, S., Scheicher, R.H., Pandey, R., Karna, S.P., and Ahuja, R. (2008) First-principles study of physisorption of nucleic acid bases on small-diameter carbon nanotubes. *Nanotechnology*, **19** (12), 125701.

140. Umadevi, D. and Sastry, G.N. (2011) Quantum mechanical study of physisorption of nucleobases on carbon materials: graphene versus carbon nanotubes. *J. Phys. Chem. Lett.*, **2** (13), 1572–1576.

141. Yarotski, D.A., Kilina, S.V., Talin, A.A., Tretiak, S., Prezhdo, O.V., Balatsky, A.V., and Taylor, A.J. (2009) Scanning tunneling microscopy of DNA-wrapped carbon nanotubes. *Nano Lett.*, **9** (1), 12–17.

142. Panigrahi, S., Bhattacharya, A., Banerjee, S., and Bhattacharyya, D. (2012) Interaction of nucleobases with wrinkled graphene surface: dispersion corrected DFT and AFM studies. *J. Phys. Chem. C*, **116** (7), 4374–4379.

143. Mu, Q., Su, G., Li, L., Gilbertson, B.O., Yu, L.H., Zhang, Q., Sun, Y.P., and Yan, B. (2012) Size-dependent cell uptake of protein-coated graphene oxide nanosheets. *ACS Appl. Mater. Interfaces*, **4** (4), 2259–2266.

144. Hu, W.B., Peng, C., Lv, M., Li, X.M., Zhang, Y.J., Chen, N., Fan, C.H., and Huang, Q. (2011) Protein corona-mediated mitigation of cytotoxicity of graphene oxide. *ACS Nano*, **5** (5), 3693–3700.

5
Biomedical Applications of Carbon Nanomaterials

Liangzhu Feng and Zhuang Liu

5.1
Introduction

In the past two decades, various nanomaterials with different compositions, shapes, and sizes have been synthesized and intensively explored for a great variety of biomedical applications [1, 2]. Among those intensively explored nanomaterials, carbon nanomaterials consisting of fullerenes, carbon nanotubes (CNTs), graphene, carbon nanohorns, carbon nanodots, nanodiamonds, and amorphous carbon nanospheres have found many possibilities for various biomedical applications by utilizing their unique intrinsic properties [3–6].

Taking advantage of their small size and unique structure, fullerene and its derivatives have shown excellent ability in free-radical scavenging, bioimaging, and tumor growth regression [3, 7]. Various carbon nanomaterials with reasonable surface modifications have also been demonstrated to be efficient in the delivery of small drug molecules and biomacromolecules [4, 5, 8]. Owning to the fact that biological tissues have less optical absorbance and scattering for near-infrared (NIR) light, several carbon nanomaterials (e.g., CNTs, graphene) with strong absorbance in this region can generate efficient heating to elevate the surrounding temperature under laser irradiation for photothermal ablation of tumors [2]. Moreover, many other unique properties such as NIR-II fluorescence, resonance Raman signal of single-walled carbon nanotubes (SWCNTs) have also made them promising probes for bioimaging and the detection of disease-related biomarkers [9]. In this chapter, we will focus primarily on the biomedical applications of fullerene, CNTs, graphene, and their relevant derivatives in three sections. Finally, we will make a brief mention of the biomedical applications of those carbon nanomaterials and discuss the challenges and perspectives for their further explorations.

Biomedical Applications and Toxicology of Carbon Nanomaterials, First Edition.
Edited by Chunying Chen and Haifang Wang.

5.2
Biomedical Applications of Fullerenes

Since its discovery, fullerene and its various derivatives have found great potential for applications in biomedicine owing to their unique geometry and excellent chemical, physical, and electronic properties [3]. However, because of their poor aqueous solubility, fullerenes showed only tardy progress in biomedical applications in the early stage of their development. After that, many different strategies, such as chemically modifying fullerenes with hydroxyl, carboxyl, and amine groups or physically entrapping hydrophobic fullerenes in cyclodextrins, calixarenes, and liposomes, have been developed to improve their aqueous solubility and physiological stability [10, 11]. These great improvements of fullerenes in solubility and physiological stability have dramatically promoted them to be explored as promising candidates for biomedical research.

To date, a wide range of applications of fullerenes in biomedicine have been intensively studied (Table 5.1) [17, 47]. Owing to their unique three-dimensional (3D) conjugated structure, fullerenes, well known as a "free radical sponge," have been confirmed to be effective antioxidants with superior capacity to treat reactive oxygen species (ROS)-related diseases [48]. Apart from their intrinsic antitumor effects via different mechanisms, fullerenes can also work as an effective drug and gene delivery carrier with promising potential for cancer treatments [7, 49]. Metallofullrenes, also known as endohedrals, have shown great possibility as radiotracers and magnetic resonance imaging (MRI) contrast agents with better biocompatibility than commercially available gadolinium (Gd)-based contrast agents [17]. Utilizing their strong interactions with various proteins, fullerenes have been demonstrated to have great possibilities for enzyme inhibition, showing good potential in treating ADIS by inhibiting the catalytic activity of HIV protease [42]. Besides, fullerenes have been shown as an effective antibacterial agent, immune adjuvant, and some others [3, 46]. In this section, we will give a brief summary of fullerene applications as effective antioxidants, neuroprotective agents, antitumor agents, MRI contrast agents, and some others.

5.2.1
Fullerenes as Antioxidants and Neuroprotective Agents

ROS and reactive nitrogen species (RNS), collectively called as free radicals, have been proven to play important roles in the process of biosynthesis, defense against bacterial infection, as well as cellular signaling pathway of cell proliferation and survival to keep homeostasis of the human body [50]. However, dysfunctional generation of ROS or other free radicals would induce a variety of diseases, such as neurodegenerative disorders and inflammatory diseases [51].

Considering their 3D conjugated structure with excellent capacity to adsorb unpaired electrons from various free radicals, fullerenes have been widely explored for their excellent performance in scavenging free radicals since the pioneering fundamental studies by Dugan *et al.* [12]. Since then, fullerenes

Table 5.1 Biomedical applications of fullerene.

Application	Example	References
Fullerene as free-radical scavenger		
Antioxidants and neuroprotective agents	Buckminsterfullerenes, tris-malonic acid fullerene derivatives, dendrofullerene, Baa	[12–16]
Anti-inflammation	Polyhydroxy C_{60}, *N*-ethyl-polyamino C_{60}, C_{70}-tetraglycolate, amphiphilic liposomal malonyl fullerene	[17–20]
Radioprotection	Dendrofullerene, $C_{60}(OH)_{24}$	[21, 22]
Fullerene as antitumor agent		
Photosensitizer	C_{60}-NVP copolymer, PEG-conjugated C_{60}, D-glucose residue pendant fullerene	[23–25]
Immunomodulator	$[Gd@C_{82}(OH)_{22}]_n$	[26, 27]
Anti-angiogenesis	$Gd@C_{82}(OH)_{22}$	[28]
Tumor metastasis inhibition	$C_{60}(OH)_{20}$, $[Gd@C_{82}(OH)_{22}]_n$	[29, 30]
MDR modulator	$[Gd@C_{82}(OH)_{22}]_n$	[31]
Fullerene as nano delivery carrier		
Antitumor drugs (e.g., PTX, DOX)	C_{60}-paclitaxel conjugate, methano-C_{60} Conjugated DOX	[32, 33]
Peptides (e.g., EPO)	Labrasol-suspended C_{60} fullerene	[34]
Nucleotides (e.g., pDNA)	Poly-*N*,*N*-dimethylfulleropyrrolidinium, aminofullerenes, tetra(piperazino)fullerene epoxide	[35–38]
Fullerene for other applications		
MRI	Gd-TMS, $Gd@C_{82}(OH)_x$, $Gd@C_{60}(OH)_x$, $Gd@C_{60}[C(COOH)_2]_{10}$	[39–41]
HIV protease inhibitor	Bis(phenethy1amincuccinate) C_{60}, 1,4-diamino C_{60}	[42]
Antibacterial agents	C_{60}-bis(*N*,*N*-dimethylpyrrolidinium iodide), C_{60}-NH_2	[43–45]
Nanoadjuvants	Fullerenol	[46]

with distinguished surface modifications have been reported to be efficient in protecting cells or animal models from oxidative stress. In 2006, Yang *et al.* [13] synthesized a peptide-decorated fullerene – also known as bulky amino acid (Baa) – and suggested that it could work as an efficient antioxidant, showing 10 times higher activity over Trolox, a widely used commercialized antioxidant. Moreover, Lotharius *et al.* [14] found that carboxyl group-modified C_{60} fullerene was effective in reducing the harmful effects of neurotoxin-induced oxidative stress on dopaminergic neurons. The aforementioned studies indicate fullerene as a promising antioxidant with great promise for the treatment of many free-radical-induced diseases.

Probably motivated by their excellent performance in free-radical scavenging, fullerenes have also found promising application as an anti-inflammatory agent.

In 2007, Ryan *et al.* [18] found that preincubation of human mast cells and peripheral blood basophils with C_{60} fullerene could effectively suppress Ag-driven type I hypersensitivity via inhibiting the release of the IgE-dependent mediator. This result indicated C_{60} fullerene as a promising candidate in the treatment of various mast-cell-dependent allergic inflammations including asthma, inflammatory arthritis, heart disease, and multiple sclerosis [17, 18]. Furthermore, a variety of studies have confirmed the potent activities of fullerenes in anti-inflammation via stabilizing mast cells and peripheral blood basophils with effective control over the release of allergic mediators [17].

Radiotherapy is effective in cancer treatment, but it often causes serious side effects to the patients attributable to radiation-induced production of free radicals [52]. Utilizing their powerful ability in scavenging free radicals, fullerenes have been demonstrated to be effective in radioprotection. By using a zebrafish embryo model, Daroczi *et al.* [21] demonstrated that preincubation of dendrofullerene would effectively protect zebrafish embryos from radiation-induced damage by significantly reducing the production of ROS. Moreover, even when administrated 15 min post irradiation, dendrofullerene also could effectively prevent the harmful effect in zebrafish embryos. Detailed comparison experiments have revealed that dendrofullerene could offer comparable radioprotection as the Food and Drug Administration (FDA)-approved radioprotector amifostine, indicating it to be a promising candidate for future clinical use.

5.2.2
Fullerenes as Antitumor Agents

In addition to their functioning as free-radical scavengers, fullerenes have been found to be able to generate cytotoxic free radicals under photoirradiation, showing promising possibility for treating cancer via photodynamic therapy (PDT) [11]. It is well documented that C_{60} can be photoexcited from the ground state to short-lived singlet state $^1C_{60}$, which subsequently relaxes to the long-lived triplet state $^3C_{60}$, which, in turn, will transfer energy to peripheral oxygen to form singlet oxygen. Moreover, $^1C_{60}$ and $^3C_{60}$ can be easily reduced to C_{60}^- via the electron transfer [11, 23]. Utilizing these free radicals with high affinity to various biomolecules (e.g., lipids, proteins, and nucleic acids), fullerenes have been shown to be effective in destroying cells via a reaction mechanism similar to that of classical PDT. In the pioneering study by Iwamoto *et al.* [23], the authors found that C_{60} solubilized by covalent conjugation of *N*-vinylpyrrolidone (NVP) showed remarkable $O_2^{\bullet-}$ generation and DNA cleavage under visible light irradiation, indicating its great potential for PDT. Stemming from this work, a large number of functionalized fullerenes have shown excellent ability in photoirradiation-induced toxicity to cells and mouse tumor xenografts, confirming the great possibility of using fullerenes for the PDT of tumors [3, 11].

Apart from suppressing tumor growth via PDT, a large number of studies have indicated that fullerene derivatives show superior activities in restricting the growth of tumors via several mechanisms (Figure 5.1) [7]. Several studies by Zhao

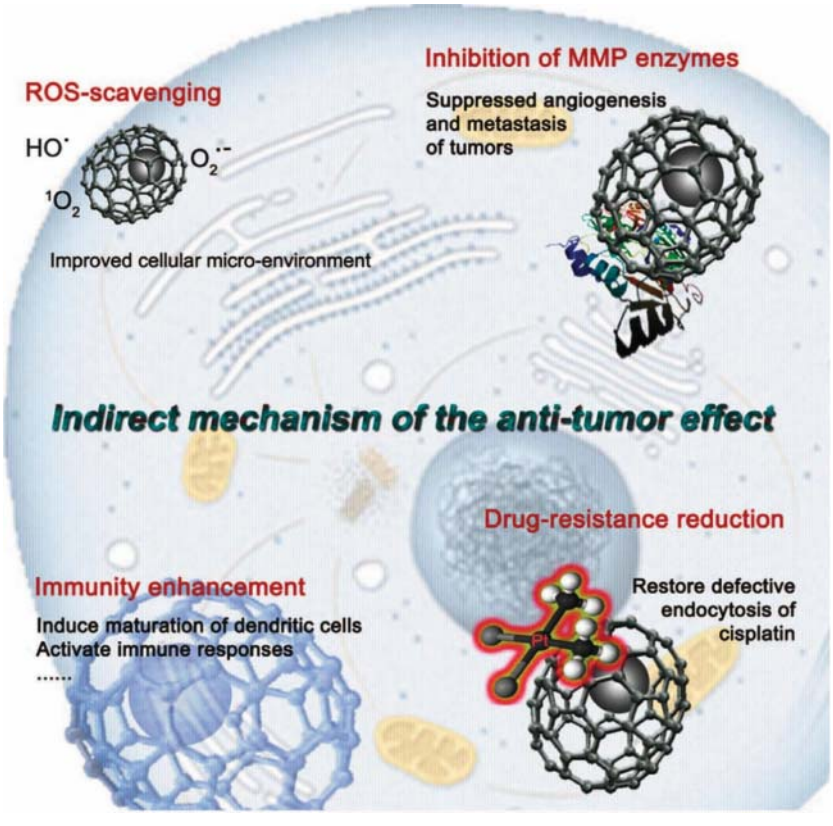

Figure 5.1 Scheme illustrating the several indirect mechanisms underlying the $Gd@C_{82}(OH)_{22}$ nanoparticle-induced antitumor effect [47]. (©2014 Nature Publishing Group.)

and colleagues and Chen *et al.* [26, 27] have demonstrated that $[Gd@C_{82}(OH)_{22}]_n$ nanoparticles could work as an strong immunomodulator for the activation of T cells and macrophages, initiating specific antitumor effects on tumor-bearing mice via promoting antigen presentation and inducing Th1-related cytokine secretion. Besides, in a work by the Zhao group, it was found that $Gd@C_{82}(OH)_{22}$ fullerene nanoparticles showed an obvious anti-angiogenesis effect in the tumor site, inducing over 40 % reduced microvessel density and about 40% lowered rate of blood supply [28]. Follow-up experiments revealed that $Gd@C_{82}(OH)_{22}$ fullerene nanoparticles were comparable to clinically used paclitaxel (PTX) in the terms of anti-tumor efficacy, but without inducing apparent side effects to the treated mice. Moreover, $[Gd@C_{82}(OH)_{22}]_n$ nanoparticles have shown great possibility in inhibiting tumor metastasis via suppressing the expression of matrix metalloproteinase (MMP), a major detrimental component in tumor metastasis [29]. Taken together, $[Gd@C_{82}(OH)_{22}]_n$ nanoparticles appear to be a novel antitumor agent, showing great possibilities for future use.

Apart from their intrinsic antitumor properties, fullerenes have also potential to be used as effective nanocarriers for drug and gene delivery, attributable to their desired sizes and hydrophobic surface that facilitate them to cross cell membranes [49]. Starting from 2005, several studies have indicated that clinically used antitumor drugs (e.g., PTX; doxorubicin, DOX) could be successfully conjugated to the surface of C_{60} [32, 33]. The as-prepared drug conjugates presented favorable release profiles and showed satisfactory antitumor effects as tested by *in vitro* experiments. Besides, Liang *et al.* [31] demonstrated that incubation of $[Gd@C_{82}(OH)_{22}]_n$ nanoparticles with cisplatin-resistant cells could effectively inhibit the cell growth both *in vitro* and *in vivo*. Such an exciting effect of $[Gd@C_{82}(OH)_{22}]_n$ nanoparticles in overcoming multidrug resistance (MDR) might be due to their excellent cell penetration ability, which subsequently promoted the cellular uptake of cisplatin. In addition, fullerenes have showed good capacity in improving the bioavailability of erythropoietin (EPO, a peptide hormone) in rats by means of intraperitoneal administration [34]. Moreover, a variety of studies have indicated that cationic fullerenes could effectively bind oligonucleotides, forming a compact complex that could shield oligonucleotides from nuclease digestion [35, 49]. Thanks to their superior membrane penetration ability, various cationic fullerene derivatives have showed good transfection efficiency as well as limited toxicity, demonstrating these cationic fullerene derivatives as promising candidates for gene therapy.

5.2.3
Metallofullerenes as MRI Contrast Agent

Metallofullerenes, which are also known as endohedrals, are prepared by encapsulating different metal atoms inside the carbon shells of fullerenes. Aside from being explored as antioxidants and antitumor agents as mentioned previously, several Gd-containing fullerene derivatives (e.g., $Gd@C_{82}(OH)_x$, $Gd@C_{60}(OH)_x$, $Gd@C_{60}[C(COOH)_2]_{10}$) have shown great potential as pronounced MRI contrast agent [17]. Compared to commercially available Gd-based MRI contrast agent, Gd-containing fullerene derivatives showed superior advantages in sensitivity, ease of decoration of the targeting moiety, and acceptable safety [17]. Utilizing the Gd Trimetaspheres® (Gd-TMS, one type of metallofullerene) encapsulated liposomes conjugated with CD36 (macrophage scavenger receptor) specific to oxidized phosphatidylcholine and oxidized low-density lipoprotein, Kolovou *et al.* [17, 39] successfully visualized atherosclerotic plaques in a mouse model. This work demonstrated Gd-TMS to be a promising candidate as an MRI contrast agent, indicating that Gd-containing fullerene derivatives can be useful in the development of novel theranostic platforms.

5.2.4
Fullerenes for Other Applications

In addition to their exploration as antioxidants, antitumor agents, and MRI contrast agents, fullerenes have also found a lot of potential applications in other

fields of biotechnology and biomedicine. Utilizing the strong hydrophobic or electrostatic interactions with proteins, various fullerenes have shown excellent ability in inhibiting the activities of several enzymes [3]. For example, C_{60} fullerene could tightly bind with the catalytic cavity of HIV protease, and thus dramatically inhibit the activity of the protease [42]. This excellent ability could effectively suppress the infection of HIV, showing their possibility for treating ADIS. Besides, to interpret the effective antibacterial activity of several fullerene derivatives, various mechanisms have been proposed including disturbing the membrane integrity, interfering with the respiratory chain, and producing free radicals by means of photoirradiation [43–45]. Moreover, the Chen group found that fullerenol could self-assemble into a virus-like nanoparticle and efficiently encapsulate the DNA antigen specific to HIV [46]. Those fullerenol nanoparticles could initiate strong immune response to the HIV DNA vaccine, less DNA antigen, and fewer immunizations via various immunization routes, indicating it as a promising nanoadjuvant for the treatment of AIDS.

As mentioned previously, fullerenes have found a great variety of possibilities for biomedical applications. Considering its excellent biocompatibility and inspiring intrinsic properties, fullerenes could serve as interesting building blocks for the construction of multifunctional theranostics platform. Therefore, much more effort should be devoted to promote the development of fullerene-based biomedicine.

5.3
Biomedical Applications of Carbon Nanotubes

CNTs, another allotrope of sp^2 carbon nanomaterials, were discovered by Iijima in 1991 [53]. With a seamless tube-like structure rolled up by graphene sheets, CNTs exhibit many unique chemical, physical, and electronic properties, and have found a great variety of possible applications in many different fields including biomedicine (Table 5.2) [4].

CNTs, including SWCNTs and multi-walled carbon nanotubes (MWCNTs), are water insoluble because of their hydrophobic surface. To enable the biomedical applications of CNTs, a large number of scientists have devoted great efforts to afford nanotubes with good solubility and stability, especially in physiological systems. It was found that covalent oxidation with condensed acids and noncovalent functionalization with amphiphiles are two effective strategies for the functionalization of CNTs (Figure 5.2) [4]. Utilizing their efficient intracellular shuttling ability, CNTs have been proven to be effective intracellular carriers for small drug molecules and several biomacromolecules loaded via the noncovalent attachment or covalent conjugation [92]. SWCNTs have been found to be photoluminescent and of high optical absorbance in the NIR region and confirmed to be efficient for bioimaging and tumor therapy, respectively. Exploiting their strong resonance Raman scattering property, SWCNTs have been shown to be interesting Raman probes for specific detection and multiplexed imaging [9]. In

Table 5.2 Biomedical applications of CNT.

Application	Example	References
CNT as nano delivery carrier		
Antitumor drugs (e.g., DOX, PTX, platinum(IV) complexes, HCPT)	PEGylated SWCNTs, amine-functionalized SWCNT, Pluronic F127-functionalized MWCNTs, diaminotriethylene glycol-functionalized MWCNTs	[54–59]
Nucleotides (e.g., siRNA, DNA)	PEGylated SWCNTs, siRNA-suspended SWCNTs, PEI-grafted MWCNTs	[60–64]
Proteins	Acid-oxidized SWCNTs	[60, 65]
CNT as photothermal agent		
Direct PTT of tumor	PEGylated SWCNTs, AuNP-decorated SWCNTs, DNA-coated MWCNTs	[66–68]
Tumor metastasis inhibition	PEGylated SWCNTs	[69]
Combined PTT with other therapeutics (e.g., chemotherapy, gene therapy and immunotherapy)	Mesoporous silica-coated SWCNTs, PEI-functionalized SWCNTs, PEGylated SWCNTs	[70–72]
CNT for bioimaging		
NIR-II fluorescence imaging	PEGylated SWCNT	[73–76]
Raman imaging	PEGylated SWCNTs, AuNP-decorated SWCNTs	[66, 77, 78]
PA imaging	PEGylated SWCNTs	[79, 80]
MR imaging	PEGylated SWCNTs, BSA-functionalized SWCNTs, amphiphilic gadolinium (III) chelate-functionalized MWCNTs, Pluronic F127-functionalized MWCNT	[9, 81–84]
Nuclear imaging (e.g., micro-SPECT, PET)	^{64}Cu-labeled PEGylated SWCNTs, ^{111}In-labeled amine-functionalized SWCNTs	[85, 86]
CNT for other applications		
CNT-based biosensing	CNT-based field effect transistor, SWCNT-based Raman tags	[4, 87, 88]
CNT-based tissue engineering scaffolds	Porous SWCNT-based nanocomposites	[89–91]

HCPT, 10-hydroxycamptothecin; BSA, bovine serum albumin.

this section, a brief overview of using CNTs as drug carriers, imaging probes, and photothermal agents will be given (Figure 5.3).

5.3.1 Carbon Nanotubes for Drug Delivery

Possibly owing to their different surface chemistry and sizes, CNTs are able to enter cells via either energy-independent diffusion/penetration or the energy-dependent endocytosis pathway [60, 65, 94]. With all atoms exposed on their surface, especially for SWCNTs, CNTs have a large, delocalized, π-conjugated

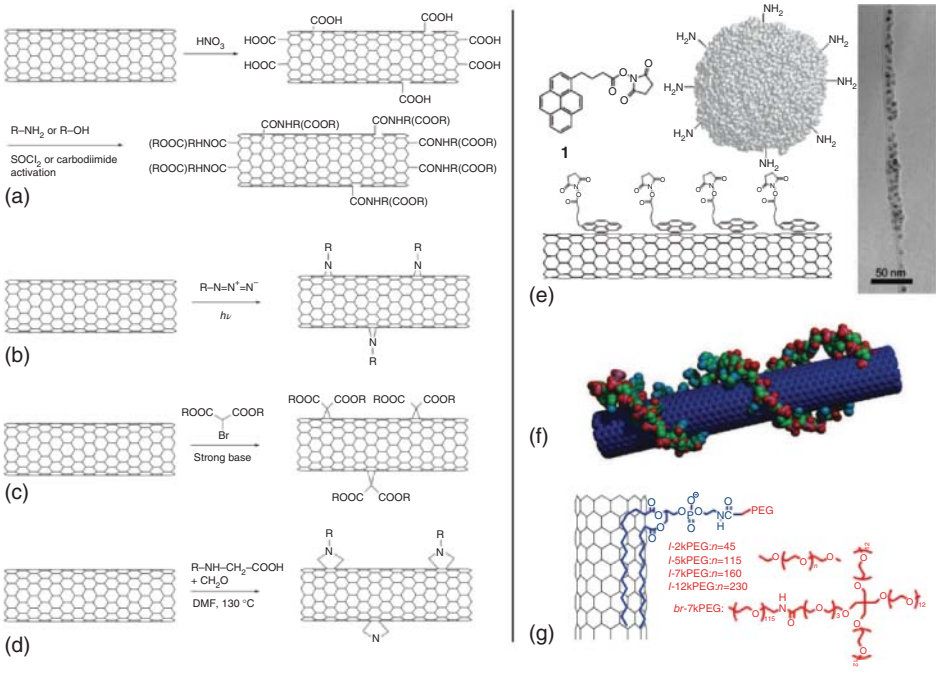

Figure 5.2 Schematic illustration of the surface functionalization of CNTs via various covalent (a–d) and noncovalent (e–g) methods. (a) CNTs were first oxidized by condensed acids and then conjugated with hydrophilic polymers (e.g., PEG) or other functional moieties; (b) photoinduced addition of azide compounds with CNTs; (c) Bingel reaction on CNTs; (d) 1,3-dipolar cycloaddition on CNTs. "R" in the figure (a–d) represents a hydrophilic domain rendering CNTs water soluble and physiologically stable for potential biomedical applications. SWCNTs were solubilized by the attachments of pyrene (e), single-stranded DNA (f) and PEGylated phospholipids (g) via the π–π stacking or hydrophobic interactions. In the right of Figure 5.3e is a transmission electron microscopy (TEM) image of an SWCNT conjugated with proteins [4]. (©2009 Springer-Verlag.)

surface, which can be utilized for efficient loading of aromatic drugs, proteins, and DNA via π–π stacking and hydrophobic interactions [54, 55]. Besides the noncovalent attachments, small drug molecules and biomacromolecules can also be loaded via some chemical bonds (e.g., ester bond, double sulfide bond), conferring them efficient stimuli-responsive release profiles for effective cancer treatments [56, 61].

5.3.1.1

Carbon Nanotubes for the Delivery of Small Drug Molecules

In 2007, Dai and colleagues found that DOX (a widely used antitumor drug) could be efficiently loaded onto the surface of phospholipid-poly(ethylene glycol) (PL-PEG)-functionalized SWCNTs via π–π stacking and hydrophobic interactions [55]. Their results revealed that as-prepared PEGylated SWCNTs had an

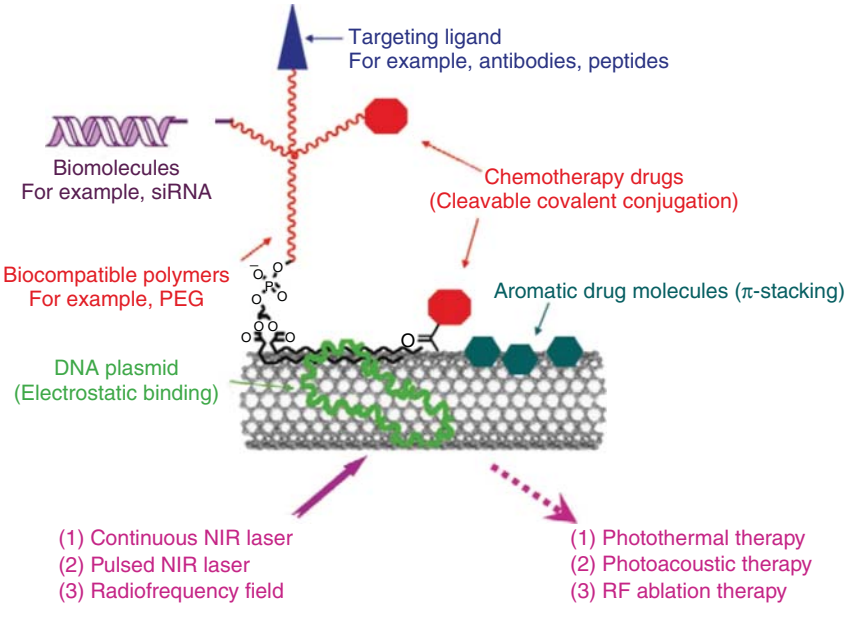

Figure 5.3 Schematic illustration of using CNTs for the fabrication of various theranostics platforms [93]. (©2011 Elsevier.)

ultrahigh drug loading capacity of up to 4 g DOX per gram of SWCNTs. The loaded DOX showed a pH-responsive release profile and could specifically kill cancer cells when conjugating a targeting moiety onto the surface of PEGylated SWCNTs. In a follow-up study by the same group, the authors found that PEGylated SWCNTs loaded with DOX would induce less toxicity to the mouse xenografts and realized a better antitumor effect when injected intravenously [54]. These two studies together demonstrated that SWCNT with a rational surface functionalization would be a promising candidate for drug delivery. Moreover, this effective drug loading strategy could be extended to other drug carriers with similar structures (e.g., MWCNT, graphene) and a variety of other aromatic drug molecules, realizing effective drug loading and cancer treatment [57].

On the other hand, many studies have found that drug molecules could be effectively conjugated to the functional groups on the surface of CNTs or to the polymer coating of CNTs via cleavable bonds. In 2008, Dai and colleagues demonstrated that PTX (another widely used anticancer drug) could be effectively conjugated to the branched PEG used for SWCNTs functionalization via a cleavable ester bond. *In vivo* treatment experiment indicated that PTX-conjugated SWCNTs showed a higher suppressing effect on tumor growth than clinical Taxol in murine 4T1 breast cancer xenografts [56]. In a later work, accomplished collaboratively by this group and Lippard group, the results revealed that platinum(IV) complexes (a prodrug of cisplatin) could be successfully anchored onto the surface of noncovalently PEGylated SWCNTs via a conjugating chemistry

similar to that of PTX [95]. It was found that the conjugated platinum(IV) complex could be easily reduced to cytotoxic cisplatin in the highly intracellular redox environment of cancer cells and specifically kill the cancer cells with help of folic acid conjugated on the surface of PEGylated SWCNTs. Besides the use of SWCNTs as intracellular drug molecule shuttles, MWCNTs have also been confirmed to be efficient for drug conjugation and showed potency in tumor treatment [58].

5.3.1.2

Carbon Nanotubes for the Delivery of Biomacromolecules

Intracellular translocation of biomacromolecules, including proteins and nucleic acids, by themselves are difficult [96]. However, efficient intracellular delivery of functional proteins or nucleic acids (e.g., ribonuclease, RNase, small interfering RNA, siRNA) has shown great potential for the treatment of many diseases [97]. Therefore, the development of such nanocarriers, which can improve the cellular uptake efficiency of various biomacromolecules and protect them from enzyme digestion, has attracted much attention. As efficient intracellular shuttles, CNTs with diverse surface functionalizations have been confirmed to be effective carriers for intracellular delivery of those biomacromolecules [60].

Many early studies have found that CNTs with different surface functionalization have strong interactions with proteins in specific or nonspecific manners [92]. Several early studies showed that proteins could be easily transported into cells when binding with CNTs via noncovalent adsorption or covalent conjugation [60]. Unfortunately, those proteins engulfed via the endocytosis would be difficult to escape from endosomes for those CNTs based vehicles lacking endosome disrupting ability, which limited the further application of using CNTs for protein delivery.

Efficient delivery of nucleic acids into cells are very important for the study of fundamental biological functions and the treatment of gene-related diseases [97]. In 2005, Dai and colleagues showed that siRNA could be conjugated to the surface of noncovalently PEGylated SWCNTs via a cleavable double sulfide bond [61]. The as-prepared siRNA-conjugated SWCNTs could be efficiently delivered into cells and specifically downregulate the expression of the targeted lamin A/C protein. In a follow-up study by the same group, the authors found that siRNA-conjugated SWCNTs prepared via a conjugation method similar to the aforementioned one could even efficiently deliver siRNA into several hard-to-transfect cell lines including human T cells and primary cells, which are difficult for the commercially available drug Lipofectamine [62]. Further investigations indicated that the tumor growth could be successfully suppressed by intratumoral injection of CNT–siRNA complexes, indicating the great potential of CNTs as effective siRNA transporters [98].

Apart from covalent conjugation, polyethylenimine (PEI), a widely utilized cationic polymer for gene delivery, and some other cationic polymers have been found to be able to functionalize the CNTs, obtaining positively charged CNT complexes for efficient nucleic acid loading and intracellular delivery [63]. Several

related studies demonstrated that the as-prepared CNT–PEI conjugates showed comparable transfection efficiency – if not better – and reduced cytotoxicity when compared with PEI itself or commercially available transfection reagents [64, 99]. These studies indicate the promising potential of CNTs as efficient carriers for gene delivery.

5.3.2 Carbon Nanotubes for Photothermal and Combined Therapies of Tumors

Photothermal therapy (PTT), which uses the heat generated by photoirradiation to elevate the surrounding temperature for cancer therapy, has been demonstrated to be effective for tumor ablations in the past decade. Currently, various nanomaterials with strong optical absorbance in the NIR region have been explored for the PTT of tumors, achieving excellent treatment outcomes, which should be attributed to the excellent deep tissue penetration ability of NIR light [2]. Moreover, many studies have shown that the mild photothermal effect could efficiently promote the intracellular delivery and lysosomal escaping of a variety of different molecules, realizing photothermally enhanced chemo, photodynamic, or gene therapies, indicating photothermal heating as a powerful strategy for the combination therapy of cancers [100–103].

5.3.2.1 Carbon Nanotubes for Photothermal Therapy of Tumors

Owning to their unique quasi-one-dimensional structure, CNTs exhibit strong optical absorbance in the NIR region and have been validated to be efficient in photothermal conversion [9]. Utilizing this excellent photothermal effect, PEGylated SWCNTs were first demonstrated to be able to efficiently ablate tumor cells using an 808-nm NIR laser irradiated at a power density of 2 W cm^{-2} [104]. In this work, the results showed that conjugating folic acid onto the surface of PEGylated SWCNTs could selectively kill the cells with overexpressed folic acid receptor. In a later work by Chakravarty *et al.* [105], antibody-conjugated SWCNTs were explored for selectively destroying tumor cells via photothermal ablation. Our group has found that gold nanoparticles (AuNPs) could be effectively anchored onto the surface of single-stranded DNA-suspended SWCNT via a seed-mediated growth process [66]. The obtained SWCNT-Au nanocomposite showed a greatly enhanced absorbance in the NIR range and excellent stability against laser irradiation compared to gold nanorods (another widely explored photothermal agent) and resulted in much more efficient killing of cancer cells in comparison with bare PEGylated SWCNT.

The *in vivo* antitumor effect of CNTs via the photothermal ablation has also been explored by many groups in recent years. Ghosh and coworkers demonstrated that PC3 tumor xenografts could be completely destroyed when receiving an intratumoral injection of DNA-coated MWCNTs at a dose of 50 μg MWCNT per mouse followed by irradiation with a 1064-nm laser at a power density of 2.5 W cm^{-2}

[67]. The growth of control tumors receiving single MWCNTs injection or laser irradiation was not obviously affected, indicating the superior selectivity of PTT. Afterward, successful treatments of tumors with intratumoral injection of CNTs and NIR light irradiation were demonstrated by several other groups [106, 107].

Given that the inability of intratumoral injection to reach deep-set and metastatic tumors, developing photothermal agents for systemic administration have inspired a variety of detailed explorations. In 2011, we found that SWCNTs with finely tuned surface PEGylation showed a desired blood circulation half-life of ~12 h and a high tumor accumulation via the enhanced permeability and retention (EPR) effect accompanied with relatively low accumulation in the reticuloendothelial system (RES) organs and the skin [108]. Utilizing this optimized PEGylated SWCNT, we successfully destroyed tumors that were irradiated with an 808-nm laser at 2 W cm^{-2} for 5 min following the intravenous injection of PEGylated SWCNT. In several later works, the authors demonstrated the complete ablation of tumors via SWCNT-induced photothermal effect with lower injection dosage of SWCNT and irradiation power density [109]. More interesting, a latest work by our group demonstrated that PEGylated SWCNTs after being injected into primary tumor could effectively translocate into the nearby sentinel lymph nodes, which could be clearly visualized by utilizing the intrinsic NIR-II fluorescence of SWCNT [69]. Under the guidance of NIR-II fluorescent imaging, both the primary tumor and the metastatic cancer cells in the sentinel lymph nodes were effectively eliminated via the SWCNT-induced photothermal ablation, which dramatically improved the survival rate and inhibited pulmonary metastasis. This work is the first one to demonstrate the successful inhibition of tumor metastasis via SWCNT-based photothermal ablation of primary tumors and metastatic cancer cells, indicating a promising strategy for cancer treatment.

5.3.2.2 Carbon Nanotubes for Combined Therapies of Tumors

Combined therapies, which involves applying more than one type of therapeutics simultaneously, are reported to be able to realize a synergistic treatment effect on tumors with lower drug injection dose when compared with those applied separately, obviously reducing drug-induced side effects [2]. CNTs have been shown to be effective for drug delivery in the successful treatment of tumors with a much lower drug dosage in comparison with the free drug dosage. However, high RES uptake of CNT-based carriers still makes those organs exposed to a relative high drug concentration, with great possibility to induce severe side effects in those normal organs. In recent years, a great deal of effort has been devoted to finding out effective strategies to treat tumors with much less drug injection, among which conjugating the drug carrier with the targeting moieties and combining multiple therapeutics together are shown to be two promising strategies.

Utilizing the excellent photothermal conversion ability of SWCNTs, our group recently demonstrated that SWCNTs coated with mesoporous silica could be used as an magnetic resonance (MR) and photoacoustic (PA) dual-mode imaging

contrast agent and as a therapeutic agent to effectively kill tumors after loading with DOX via combined chemo and photothermal therapies [70]. Besides, several reports by other groups have shown that rationally modified CNTs could effectively deliver therapeutic siRNA into the cancer cells, and then induce obvious synergistic inhibition effects on the tumor growth with the help of NIR light irradiation-induced photothermal effect [71]. In another work by our group, we found that PEGylated SWCNTs could effectively destroy the primary tumors via the 808-nm laser irradiation and promote the release of tumor-associated antigens, which subsequently initiated a strong immune response in mice via promoting maturation of dendritic cells (DCs) and production of antitumor cytokines [72]. In combination with anti-cytotoxic T-lymphocyte-associated protein 4 (CTLA-4) antibody therapy, successful suppression of the distant subcutaneous tumor model and a lung metastasis model was observed, demonstrating SWCNTs to be a promising candidate for combined photothermal and immuno therapies.

5.3.3
Carbon Nanotubes for Bioimaging

With their quasi-1D quantum-wire-like structure, SWCNTs have several unique optical properties, including NIR fluorescence, resonance Raman scattering, and high NIR absorbance, conferring them with superior ability in fluorescence, Raman, and PA imaging [9]. Besides, metal catalysts (e.g., Fe, Co), involved in the synthesis of CNTs, are always contained in the synthesized CNTs, making them promising candidates for T_2-weighted MRI [81]. Moreover, by conjugating external labels such as radioisotopes to their surface, CNTs have been found to be versatile probes for many other imaging modalities [85]. A detailed summary of the use of CNTs as the imaging contrast agents was given by our group in 2013 [9]. Here, we will give a brief summary on the latest developments of CNTs in the field of bioimaging.

5.3.3.1
Carbon Nanotubes for Fluorescence Imaging

Based on their intrinsic physical properties, semiconducting SWCNTs have been shown to be able to emit NIR-II (900–1600 nm) fluorescence under excitation at 550–850 nm, offering an ultrahigh sensitivity owing to the remarkably lowered autofluorescence of biological tissues during imaging [4]. A series of works by Dai group demonstrated that NIR-II imaging using the PEGylated SWCNTs with the help of principal component analysis (PCA) could efficiently distinguish organs, light up tumors, and indicate blood vessels with much increased resolution compared to commercial NIR-I dye (IRDye800) and micro-CT, respectively [73–76]. Moreover, we found that NIR-II fluorescence of PEGylated SWCNTs could be exploited to indicate metastatic cancer cells in the sentinel lymph nodes near the primary tumor, allowing precise removal of those sentinel lymph nodes via photothermal ablation [69].

5.3.3.2

Carbon Nanotubes for Raman Imaging

Unlike other molecules, SWCNTs give strong Raman signals through resonance Raman scattering, attributable to their intrinsic physical properties. SWCNTs have several different Raman peaks including the radical breathing mode (RBM, $100-300\,cm^{-1}$) and the tangential G band ($\sim 1580\,cm^{-1}$), making them much flexible for Raman imaging [9]. Since 2005, a great amount of work has demonstrated the successful use of SWCNTs as Raman probes. For example, by utilizing the ^{13}C isotope-doped SWCNTs conjugated with different targeting moieties, multiplexed Raman imaging of different types of cancer cells was realized [77, 78]. To further enhance the Raman signals of SWCNTs, we have successfully anchored different noble metal nanoparticles (e.g., Au nanoparticles, Ag nanoparticles) on the surface of SWCNTs, whose Raman signals were enhanced by over 20 times in the solution phase via the surface-enhanced Raman scattering (SERS) [66]. Utilizing the Au nanoparticle-decorated SWCNTs with the conjugation of folic acid, we successfully realized specific cell labeling and Raman imaging with greatly shortened imaging time, enabling fast mapping of biological samples.

5.3.3.3

Carbon Nanotubes for Photoacoustic Imaging

PA imaging is a newly developed hybrid bioimaging modality based on the photoacoustic effect. During PA imaging, a laser pulse illuminates biological tissues containing light-absorbing endogenous molecules or contrast agents to generate heat, which subsequently induces transient thermoelastic expansion and thus wideband ultrasonic emission, which is then detected by ultrasonic transducers to produce 2D or 3D images [110]. To obtain high-quality PA imaging, contrast agents with strong optical absorbance and then good photothermal conversion ability are desired. Because of the photothermal conversion ability of CNTs, their use as efficient PA contrast agents has also been explored by different groups in recent years [79, 80]. Several studies have indicated that the PA imaging is a promising bioimaging modality with high sensitivity and resolution.

5.3.3.4

Carbon Nanotubes for Other Bioimaging Modalities

In addition their use in optical imaging modalities, CNTs have been proven to be effective for some other techniques including MRI and radioimaging [9]. Metal residuals as nanoparticles formed during the synthesis of CNTs can be utilized for effective MRI because of their excellent capacity as T_2 contrast agents [111]. Moreover, CNTs with reasonable surface functionalization were explored for the labeling of mesenchymal stem cells (MSCs), whose *in vivo* behavior could be tracked by MRI [81].

Additionally, because of the good *in vivo* behavior of functionalized CNTs, they have been labeled with various radioisotopes for nuclear imaging, including micro single-photon emission computerized tomography (micro-SPECT) imaging and

position emission tomography (PET) [85, 86]. Such studies demonstrate the potential of using radioisotope-decorated CNTs for biomedical imaging with high sensitivity.

5.3.4 Carbon Nanotubes for Other Biomedical Applications

Apart from being explored for drug delivery, cancer treatment, and bioimaging, CNTs have also been intensively explored for the fabrication of a great variety of biosensors based on their unique structure, NIR-II fluorescence, and resonance Raman scattering. The relevant studies have been systemically summarized in several comprehensive review articles [4, 52, 56, 112]. Besides, CNTs have also been shown to be good substrates for the construction of tissue engineering scaffolds, with excellent ability in inducing the differentiation of stem cells [89, 90].

In this section, the up-to-date diverse biomedical applications of CNTs were briefly summarized. Though the wide range of the above-mentioned studies has indicated the great promise of using CNTs in biomedicine, several drawbacks, including relatively high RES uptake and potential toxicity of CNTs, are still present and need to be solved, particularly for further *in vivo* applications during clinical translation.

5.4 Biomedical Applications of Graphene

Graphene, a two-dimensional (2D) allotrope of sp^2-hybridized carbon nanomaterials, has been attracting tremendous attention in a great variety of fields since its discovery in 2004 [113]. Motivated by the inspiring possibilities of CNTs for various biomedical applications, graphene and its derivatives have been intensively explored and found to be promising nanomaterials for drug and gene delivery and cancer therapy [5, 114]. Besides, owing to their unique physiochemical and electrical properties, graphene and its derivatives have also shown promising potential in the fabrication of biosensors and tissue engineering scaffolds [8, 115]. With the decoration of inorganic nanoparticles (e.g., iron oxide nanoparticles) onto the surface of graphene oxide (GO), the obtained graphene-based nanocomposites have been demonstrated to be effective contrast agents for MRI and some other applications [5]. Moreover, to elucidate the possibility of graphene for further applications, a great deal of effort has been devoted by many a group to study the *in vivo* behavior of graphene and its potential toxic effects to the injected animals [116]. In this section, we will give a brief summary of the latest advances in the use of graphene for biomedical applications including drug delivery, cancer therapy, bioimaging, biosensing, and many others (Table 5.3).

Table 5.3 Biomedical applications of graphene.

Application	Example	References
Graphene as nano delivery carrier		
Antitumor drugs (e.g., DOX, SN38, CPT)	PEGylated GO, sulfonic acid-functionalized GO, PEGylated GO–IONP nanocomposites	[114, 117–120]
Photosensitizer (e.g., Ce6)	PEGylated GO	[101]
DNA and siRNA	GO-PEI, NGO-PEG-PEI, chitosan-functionalized GO	[100, 103, 121, 122]
Graphene as photothermal agent		
Direct PTT of tumor	PEGylated GO, rGO, and RGO–IONP nanocomposites	[108, 123, 124]
Combined PTT with other therapeutics (e.g., chemotherapy, gene therapy)	PEGylated GO, NGO-PEG-DA, NGO-PEG-PEI	[102, 103, 121, 125, 126]
Graphene for bioimaging		
Fluorescence imaging	Cy 7-conjugated PEGylated GO, QD-anchored GO	[123, 127]
MR imaging	PEGylated RGO–IONP nanocomposite	[124]
X-ray imaging	PEGylated RGO–IONP–AuNP nanocomposite	[128]
Graphene for other applications		
Graphene-based biosensing	Fluorescent biosensing, electrochemical biosensing, electronic device-based biosensing	[8, 129–132]
Graphene-based tissue engineering scaffolds	Guiding the differentiation of MSCs, iPSCs	[133, 134]
Antibacterial agent	Graphene paper	[135, 136]

5.4.1 Graphene for Drug Delivery

GO, a derivative of graphene, has many oxygen-containing functional groups on its surface, allowing it to be efficiently functionalized via different methods to achieve good stability in various physiological solutions [5]. Because of the existence of large delocalized π-conjugated structures on its surface, GO with suitable surface modification has shown superior capacity for the loading of various aromatic drugs [101, 117, 118]. Besides being utilized for the delivery of small drug molecules, GO, after being decorated with cationic polymers, has demonstrated effectiveness in the delivery of many biomacromolecules, such as plasmid DNA and siRNA, indicating it to be a promising gene delivery carrier for gene therapy [103, 121, 137].

5.4.1.1

Graphene for the Delivery of Small Drug Molecules

Utilizing the large delocalized π-conjugated surface on its surface, GO, like its sister material CNTs, has been found be effective in drug delivery. In 2008, Dai's group first reported that GO after PEGylation could effectively load aromatic anticancer drugs (e.g., DOX, SN38) and then deliver them into the cancer cells, showing superior anticancer effects especially when being attached with a targeting moiety [117, 118]. Since then, many studies have also confirmed the feasibility of using GO for the delivery of aromatic drugs, showing excellent *in vitro* anticancer effect [114]. Then, a piece of work by Zhang *et al.* [125] demonstrated that GO with PEGylation could effectively deliver DOX to the tumor site via the EPR effect after being intravenously injected, thus inhibiting the growth of tumors. More recently, we conjugated GO with PEG and poly(allylamine hydrochloride) (PAH), obtaining positively charged NGO-PEG-PAH, which was then modified with 2,3-dimethylmaleic anhydride (DA) via a pH-responsive amide bond, obtaining negatively charged NGO-PEG-DA with an excellent surface charge reversibility responsive to the tumor acid microenvironment. After being loaded with DOX, NGO-PEG-DA showed a pH-responsive cancer cell killing ability (Figure 5.4) [126] and was able to effectively overcome the MDR of cancer cells in combination with PTT.

Apart from being utilized for the delivery of anticancer drugs, GO has been found to be a promising candidate for the delivery of a photosensitizer, another type of small-molecule drug extensively explored for PDT. In 2011, we explored the possibility of using PEGylated GO for the intracellular delivery of Chlorin e6 (Ce6), a commonly used photosensitizer molecule for PDT [101]. Then, we realized superior cancer inhibition effect by exploiting the photothermal effect of GO under the NIR laser irradiation, which could dramatically enhance the cellular uptake of Ce6 delivered by GO–PEG. Since then, several groups have also utilized GO as an efficient intracellular delivery carrier for targeted PDT, achieving excellent therapeutic effects [138, 139].

5.4.1.2

Graphene for the Delivery of Biomacromolecules

In addition to being explored as carriers for the delivery of small drug molecules, GO with reasonable surface modifications has shown inspiring capacity in the delivery of several different biomacromolecules. In 2011, we modified GO with PEI via electrostatic interaction, obtaining GO-PEI complexes, which exhibited remarkably reduced cytotoxicity and comparable – if not better – plasmid DNA transfection efficiency in comparison with bare PEI molecules [137]. Almost at the same time, another report by Zhang *et al.* [121] demonstrated that GO-PEI prepared by covalently conjugating GO with PEI showed good ability in the intracellular delivery of siRNA, which could effectively downregulate the expression of the targeted gene and efficiently kill cancer cells in a synergistic manner by sequentially administering DOX. In another work by our group published in 2013, we prepared a physiologically stable NGO-PEG-PEI via covalent conjugation. More

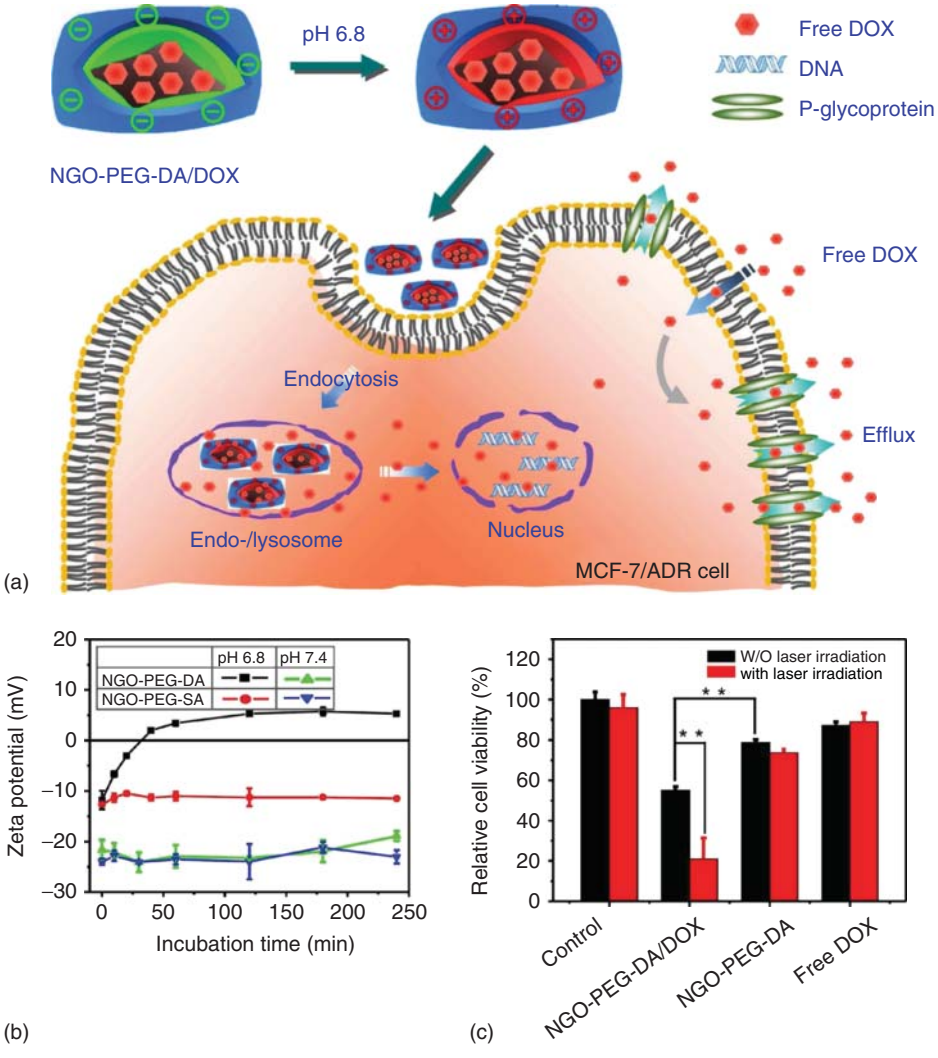

Figure 5.4 Preparation of a pH-responsive drug delivery carrier for the combination therapy of multidrug resistant (MDR) cancer cells. (a) A scheme showing the utility of surface charge reversible NGO-PEG-DA/DOX complexes responsive to the acid microenvironment of the tumor for overcoming multidrug resistance. (b) Time-dependent change of the surface charge of NGO-PEG-DA and NGO-PEG-SA incubated with PBS at pH 6.8 and 7.4. (c) Relative cell viabilities of MCF-7/ADR cells incubated with NGO-PEG-DA/DOX and free DOX at 20 μg ml^{-1} in terms of DOX and NGO-PEG-DA at an equivalent NGO concentration to NGO-PEG-DA/DOX, with or without an 808-nm laser irradiation for 5 min at 0.5 W cm^{-2} in the middle of the 48-h incubation [126]. (©2014 Wiley-VCH.)

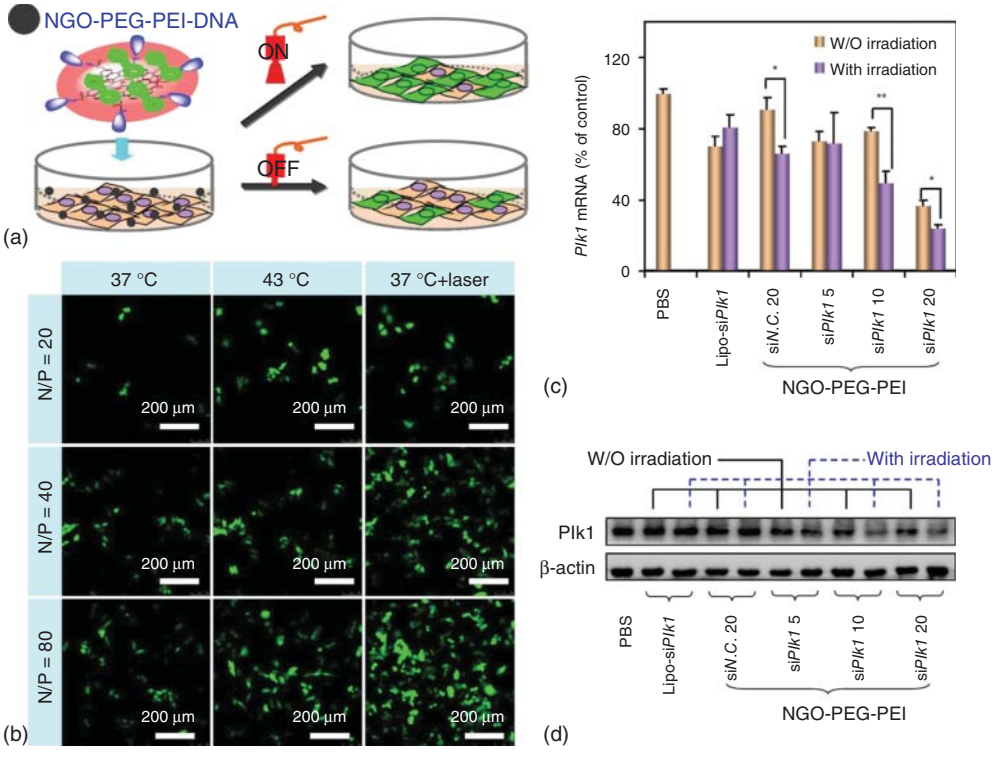

Figure 5.5 Photothermally enhanced gene delivery by NGO-PEG-PEI. (a) Scheme showing the photothermally enhanced gene delivery. (b) Confocal fluorescence images of EGFP transfected HeLa cells delivered by NGO-PEG-PEI at different N/P ratios and culture temperatures with or without 808-nm laser irradiation of 0.5 W cm^{-2}. The expression levels of Plk1 mRNA (c) and protein (d) detected by qRT-PCR and western blotting, respectively [103]. (©2013 Wiley-VCH.)

exciting, the as-prepared NGO-PEG-PEI showed superior gene transfection efficiency without the interference by serum albumin, while bare PEI molecule and GO-PEI without PEGylation showed limited transfection efficiency in the presence of serum albumin (Figure 5.5) [103]. Utilizing the photothermal effect of GO, we found that the mild temperature increase induced by NIR laser irradiation of NGO-PEG-PEI could dramatically enhance the intracellular delivery of plasmid DNA and siRNA, indicating it to be a promising photothermally controllable gene delivery carrier. After that, Kim and Kim found that NIR laser irradiation could promote the escape of PEG-bPEI-rGO nanocomposite from endosomes and lysosomes, realizing photothermally controllable gene delivery with high spatial and temporal selectivity [100].

Additionally, Zhang and workers demonstrated that PEGylated GO could effectively load several different protein molecules via noncovalent interactions [140]. Ribonuclease A (RNase A) and protein kinase A (PKA) could be separately

loaded onto the surface of GO-PEG and then efficiently delivered into the cells, inducing obvious cell death and growth, respectively. This work indicates that GO-PEG is a promising protein delivery carrier with high biocompatibility, good protein loading capacity, and superior protection ability against the enzyme degradation.

5.4.2 Graphene for Photothermal and Combined Therapies of Tumors

Like CNTs, graphene and its derivatives also have strong optical absorbance in the NIR region, which confers them with efficient photothermal conversion ability. In 2010, we were the first to explore the *in vivo* behavior of PEGylated GO and found that GO-PEG could efficiently accumulate at tumor site via the EPR effect after being intravenously injected into mice [123]. Utilizing the excellent photothermal conversion ability of GO, the tumors grown on mice were completely eliminated when irradiated with an 808-nm laser beam. However, owing to the presence of many oxygen-containing groups and defects on its surface, GO's optical absorbance in the NIR region is scarified to some degree. To further improve its NIR optical absorbance, reduced graphene oxide (rGO) was prepared from GO by treatment with reducing agents such as hydrazine hydrate [141, 142]. In another work by our group, we found that rGO functionalized with amphiphilic PEG could efficiently home to the tumor site in a size-dependent manner. Photothermal ablation of tumors was then realized by intravenous injection of PEGylated ultrasmall nano-rGO and NIR laser irradiation at a power density of ~0.15 W cm^{-2}, which is the lowest recorded dose compared to that achieved with other photothermal agents [141].

Though many successes have been achieved by utilizing the photothermal effect of various nanomaterials to directly inhibit tumor growth, single PTT would have only limited effects to deep-seated and metastatic tumors, which are hard to be exposed to the irradiating light. Because of this, PTT has been applied together with chemotherapy, photodynamic therapy, or gene therapy to achieve excellent synergistic therapeutic effects [2]. As mentioned above, the photothermal effect of GO under NIR laser irradiation has been exploited to promote the cellular uptake of photosensitizer and genes, indicating GO to be a promising delivery carrier for photothermally controllable PDT and gene therapy [101, 103]. Besides, PEGylated GO after loading DOX showed superior effect in inhibiting the *in vivo* tumor growth when combined with laser irradiation, in comparison to single chemotherapy or PTT [125]. Moreover, Yang *et al.* [143] constructed a GO-based triple-therapeutic by conjugating PEGylated GO with cetuximab and then loading with epirubicin for tumor targeting and tumor growth inhibition, respectively. Such a formulation was later demonstrated to be much more effective in inhibiting tumor growth in mice. In addition, many other studies have also confirmed GO to be effective in suppressing the tumor

growth by utilizing its excellent photothermal conversion ability combined with chemotherapy or other therapeutic modalities [102, 126].

5.4.3 Graphene for Bioimaging

Apart from being explored as drug delivery carriers and photothermal agents for cancer therapy, graphene and it derivatives have also been explored as bioimaging contrast agents by utilizing their intrinsic optical properties or being labeled with fluorescent probes or radionuclides. Though not as efficient as SWCNTs, GO also could emit NIR fluorescence, which was first utilized by Dai and colleagues for *in vitro* cell imaging with limited autofluorescence, indicating it as a potential candidate for future cell labeling [118]. Besides, PEGylated GO was labeled with different fluorescent dyes (e.g., FITC, Cy7) for *in vitro* cell labeling or *in vivo* tumor imaging by several groups [123]. However, several previous studies have indicated that fluorescent labeling is not quite suitable for quantitative analysis of the *in vivo* behavior of fluorescent substrates, because of the quenching and photobleaching of dyes. As an alternative, radioimaging has been shown to be a more accurate tool for quantitative study of the *in vivo* behaviors of radiolabeled substrates. In 2011, we studied the *in vivo* behaviors of PEGylated GO by utilizing the signal of ^{125}I that was anchored on the defects and edges of GO [144]. After that, in another work collaborated by us and the Cai group, it was found that PEGylated GO labeled with ^{64}Cu could efficiently home to the tumor site when conjugated with a tumor-targeting moiety (e.g., TRC105, a monoclonal antibody that binds to CD105), indicating it a promising candidate for *in vivo* PET imaging [145]. Moreover, utilizing its good photothermal conversion ability, several different groups demonstrated that GO or rGO with reasonable surface modifications could be used for *in vivo* PA imaging of tumors [142].

In addition to GO-based nanocomposites, another type of graphene derivative, obtained by anchoring inorganic nanoparticles (e.g., iron oxide nanoparticles, IONPs; quantum dots, QDs) onto the surface of GO, has acquired many other intriguing properties. In 2012, a novel imaging probe based on an RGO–IONP nanocomposite was prepared by our group from GO and iron chloride hexahydrate via the hydrothermal method. This nanocomposite was then utilized for *in vivo* triple-modal fluorescence, PA, and MRI after being decorated with an amphiphilic PEG polymer [124]. In a follow-up study by us, the as-prepared RGO–IONP nanocomposite was further decorated with a layer of gold via a seeded growth method, and then used for dual-modal MR and X-ray imaging [128]. Besides IONPs, semiconductor QDs were successfully anchored onto the surface of GO by Chen and colleagues, which then were demonstrated to be efficient for cell imaging [127]. Taken together, these studies indicate that GO is a versatile platform for the fabrication of various imaging probes.

5.4.4
Graphene for Other Biomedical Applications

Utilizing their unique physiochemical, optical, and electrical properties, graphene and its derivatives have been intensively explored and found to be versatile platforms for the fabrication of various biosensors [8]. Because of the existence of a large hydrophobic area on its surface, graphene has shown strong interaction with single-stranded DNA (ssDNA) via a $\pi-\pi$ interaction, while this interaction would be diminished when double-stranded DNA (dsDNA) was formed by adding a complementary ssDNA. Utilizing this interesting phenomenon, many different off/on fluorescent biosensors have been designed and constructed, showing great sensitivity and selectively for the detection of different targets in solutions or even of live cells [129, 130]. Besides, utilizing its excellent electrical properties, graphene has been exploited to fabricate electronic devices or modify electrodes of the electrochemical platforms, respectively, for the detection of various biomolecules, including glucose, DNA, and proteins [131, 132].

Moreover, many studies have demonstrated that GO-coated substrates could promote the adherence and proliferation of a variety of different cell lines and even selectively guide the differentiation of cultured MSCs and induce the formation of pluripotent stem cells (iPSCs), indicating GO's great promise as a scaffold material for regenerative medicine [133, 134]. Additionally, GO dispersed in solutions and in the form of a paper-like substrate prepared via vacuum filtration showed superior activity in inhibiting the growth of *Escherichia coli* bacteria, which was possibly attributed to the disturbance of membrane integrity caused by direct contact with GO [135, 136].

5.5
Conclusion and Perspectives

In this chapter, we summarized the latest advances in the use of fullerenes, CNTs, graphene, and their corresponding derivatives for biomedical applications during the past several years. Utilizing their excellent intrinsic properties, fullerenes and their derivatives have been found to be efficient in free-radical scavenging, ROS generation under light irradiation showing as efficient antioxidants, neuroprotective agents, and photosensitizers for PDT. Though these possibilities have been implied for many years, real application regarding these is limited. Therefore, more effort needs to be made to clarify the feasibility of using these fullerenes for treatment of diseases. Moreover, $[Gd@C_{82}(OH)_{22}]_n$ has also been indicated to be an effective antitumor agent apart from being explored for MRI. Up to now, several mechanisms have been proposed to interpret this exciting tumor inhibition effect, but to understand the exact molecular mechanism more intensive studies are needed.

SWCNT shows intriguing NIR-II fluorescence, which has been intensively explored for efficient *in vivo* imaging and *in vitro* detection of several

disease-related biomarkers with ultrahigh sensitivity because of the limited autofluorescence in this region. However, SWCNTs prepared by currently available methods contain mixed chiralities, and thus have rather low fluorescent quantum yield. To further improve its sensitivity for imaging and detection, more efforts should be devoted to preparing SWCNT with high purity. Moreover, SWCNTs have been demonstrated to be an efficient Raman probe because of their unique resonance Raman signal but the imaging process is still time consuming. Therefore, how to improve the Raman signal intensity of SWCNTs for fast Raman imaging would deserve more intensive studies. Besides, a series of studies have indicated that CNTs are a type of effective intracellular shuttles for the delivery of a large range of cargoes, showing their great potential for cancer therapy apart from being directly exploited for PTT of cancers. To improve the applicable value of CNTs for *in vivo* drug delivery and cancer PTT, a detailed screening of surface functionalization methods for CNTs to improve their tumor homing ability and reduce RES clearance is needed, which deserves more research interest.

Graphene and it derivatives have great potential for drug delivery, cancer PTT, and many other biomedical applications. Though the currently observed therapeutic effects of graphene-based nanomaterials are promising, further improvements are needed by enhancing their tumor homing ability via the attachment of targeting moieties or modifying them with smart polymers responsive to tumor microenvironments or external physical stimuli. Moreover, combining PTT with other therapeutic modalities based on graphene also represents as another reasonable way to enhance their therapeutic effect.

As mentioned before, by utilizing their tremendous intrinsic properties, fullerenes, CNTs, graphene, and their derivatives have been shown to be promising candidate materials for future biomedical applications. However, concerns about the biocompatibility of carbon nanomaterials, especially for those explored for biomedical applications, have been attracting a lot of attention from different communities because of their potential toxicities when exposed to humans. Therefore, much work has been devoted to explore the toxicology profiles of carbon nanomaterials using different cells and animal animals in the past several years. Though preliminary results have shown that these carbon materials with rational surface functionalization would not induce any obvious toxic effects to the tested cells and animals, more efforts are still needed to clarify their toxicology profiles as well as biodegradation behaviors in detail and more systemically.

Acknowledgments

This work was partially supported by the National Basic Research Programs of China (973 Program) (2012CB932600, 2011CB911002), the National Natural Science Foundation of China (51222203, 51132006, 51002100), and a Project Funded by the Priority Academic Program Development (PAPD) of Jiangsu Higher Education Institutions.

References

1. Gao, J., Gu, H., and Xu, B. (2009) Multifunctional magnetic nanoparticles: design, synthesis, and biomedical applications. *Acc. Chem. Res.*, **42** (8), 1097–1107.
2. Cheng, L., Wang, C., Feng, L. *et al.* (2014) Functional nanomaterials for phototherapies of cancer. *Chem. Rev.*, **114** (21), 10869–10939.
3. Da Ros, T. (2008) Twenty years of promises: fullerene in medicinal chemistry, in *Medicinal Chemistry and Pharmacological Potential of Fullerenes and Carbon Nanotubes*, vol. **1** (eds F. Cataldo and T. Da Ros), Springer.
4. Liu, Z., Tabakman, S., Welsher, K. *et al.* (2009) Carbon nanotubes in biology and medicine: In vitro and in vivo detection, imaging and drug delivery. *Nano Res.*, **2** (2), 85–120.
5. Yang, K., Feng, L., Shi, X. *et al.* (2013) Nano-graphene in biomedicine: theranostic applications. *Chem. Soc. Rev.*, **42** (2), 530–547.
6. Tao, H., Yang, K., Ma, Z. *et al.* (2012) In vivo NIR fluorescence imaging, biodistribution, and toxicology of photoluminescent carbon dots produced from carbon nanotubes and graphite. *Small*, **8** (2), 281–290.
7. Meng, J., Liang, X., Chen, X. *et al.* (2013) Biological characterizations of $[Gd@C_{82}(OH)_{22}]_n$ nanoparticles as fullerene derivatives for cancer therapy. *Integr. Biol.*, **5** (1), 43–47.
8. Feng, L. and Liu, Z. (2011) Graphene in biomedicine: opportunities and challenges. *Nanomedicine*, **6** (2), 317–324.
9. Gong, H., Peng, R., and Liu, Z. (2013) Carbon nanotubes for biomedical imaging: the recent advances. *Adv. Drug Delivery Rev.*, **65** (15), 1951–1963.
10. Bosi, S., Da Ros, T., Spalluto, G. *et al.* (2003) Fullerene derivatives: an attractive tool for biological applications. *Eur. J. Med. Chem.*, **38** (11–12), 913–923.
11. Markovic, Z. and Trajkovic, V. (2008) Biomedical potential of the reactive oxygen species generation and quenching by fullerenes (C_{60}). *Biomaterials*, **29** (26), 3561–3573.
12. Dugan, L.L., Gabrielsen, J.K., Yu, S.P. *et al.* (1996) Buckminsterfullerenol free radical scavengers reduce excitotoxic and apoptotic death of cultured cortical neurons. *Neurobiol. Dis.*, **3** (2), 129–135.
13. Yang, J., Wang, K., Driver, J. *et al.* (2007) The use of fullerene substituted phenylalanine amino acid as a passport for peptides through cell membranes. *Org. Biomol. Chem.*, **5** (2), 260–266.
14. Lotharius, J., Dugan, L.L., and O'Malley, K.L. (1999) Distinct mechanisms underlie neurotoxin-mediated cell death in cultured dopaminergic neurons. *J. Neurosci.*, **19** (4), 1284–1293.
15. Witte, P., Beuerle, F., Hartnagel, U. *et al.* (2007) Water solubility, antioxidant activity and cytochrome C binding of four families of exohedral adducts of C60 and C70. *Org. Biomol. Chem.*, **5** (22), 3599–3613.
16. Beuerle, F., Witte, P., Hartnagel, U. *et al.* (2007) Cytoprotective activities of water-soluble fullerenes in zebrafish models. *J. Exp. Nanosci.*, **2** (3), 147–170.
17. Dellinger, A., Zhou, Z., Connor, J. *et al.* (2013) Application of fullerenes in nanomedicine: an update. *Nanomedicine*, **8** (7), 1191–1208.
18. Ryan, J.J., Bateman, H.R., Stover, A. *et al.* (2007) Fullerene nanomaterials inhibit the allergic response. *J. Immunol.*, **179** (1), 665–672.
19. Norton, S.K., Wijesinghe, D.S., Dellinger, A. *et al.* (2012) Epoxyeicosatrienoic acids are involved in the C70 fullerene derivative- induced control of allergic asthma. *J. Allergy Clin. Immunol.*, **130** (3), 761–769.e2.
20. Lee, D.M., Friend, D.S., Gurish, M.F. *et al.* (2002) Mast cells: a cellular link between autoantibodies and inflammatory arthritis. *Science*, **297** (5587), 1689–1692.
21. Daroczi, B., Kari, G., McAleer, M.F. *et al.* (2006) In vivo radioprotection

by the fullerene nanoparticle DF-1 as assessed in a zebrafish model. *Clin. Cancer Res.*, **12** (23), 7086–7091.

22. Cai, X., Hao, J., Zhang, X. *et al.* (2010) The polyhydroxylated fullerene derivative C60(OH)24 protects mice from ionizing-radiation-induced immune and mitochondrial dysfunction. *Toxicol. Appl. Pharmacol.*, **243** (1), 27–34.
23. Iwamoto, Y. and Yamakoshi, Y. (2006) A highly water-soluble C_{60}-NVP copolymer: a potential material for photodynamic therapy. *Chem. Commun.*, (46), 4805–4807.
24. Liu, J., Ohta, S.-i., Sonoda, A. *et al.* (2007) Preparation of PEG-conjugated fullerene containing Gd^{3+} ions for photodynamic therapy. *J. Controlled Release*, **117** (1), 104–110.
25. Otake, E., Sakuma, S., Torii, K. *et al.* (2010) Effect and mechanism of a new photodynamic therapy with glycoconjugated fullerene. *Photochem. Photobiol.*, **86** (6), 1356–1363.
26. Liu, Y., Jiao, F., Qiu, Y. *et al.* (2009) The effect of $Gd@C_{82}(OH)_{22}$ nanoparticles on the release of Th1/Th2 cytokines and induction of TNF-α mediated cellular immunity. *Biomaterials*, **30** (23–24), 3934–3945.
27. Chen, C., Xing, G., Wang, J. *et al.* (2005) Multihydroxylated $[Gd@C_{82}(OH)_{22}]_n$ nanoparticles: antineoplastic activity of high efficiency and low toxicity. *Nano Lett.*, **5** (10), 2050–2057.
28. Meng, H., Xing, G., Sun, B. *et al.* (2010) Potent angiogenesis inhibition by the particulate form of fullerene derivatives. *ACS Nano*, **4** (5), 2773–2783.
29. Meng, H., Xing, G., Blanco, E. *et al.* (2012) Gadolinium metallofullerenol nanoparticles inhibit cancer metastasis through matrix metalloproteinase inhibition: imprisoning instead of poisoning cancer cells. *Nanomed. Nanotechnol. Biol. Med.*, **8** (2), 136–146.
30. Jiao, F., Liu, Y., Qu, Y. *et al.* (2010) Studies on anti-tumor and antimetastatic activities of fullerenol in a mouse breast cancer model. *Carbon*, **48** (8), 2231–2243.
31. Liang, X.-J., Meng, H., Wang, Y. *et al.* (2010) Metallofullerene nanoparticles circumvent tumor resistance to cisplatin by reactivating endocytosis. *Proc. Natl. Acad. Sci. U.S.A.*, **107** (16), 7449–7454.
32. Zakharian, T.Y., Seryshev, A., Sitharaman, B. *et al.* (2005) A fullerene-paclitaxel chemotherapeutic: synthesis, characterization, and study of biological activity in tissue culture. *J. Am. Chem. Soc.*, **127** (36), 12508–12509.
33. Liu, J.-H., Cao, L., Luo, P.G. *et al.* (2010) Fullerene-conjugated doxorubicin in cells. *ACS Appl. Mater. Interfaces*, **2** (5), 1384–1389.
34. Venkatesan, N., Yoshimitsu, J., Ito, Y. *et al.* (2005) Liquid filled nanoparticles as a drug delivery tool for protein therapeutics. *Biomaterials*, **26** (34), 7154–7163.
35. Maeda-Mamiya, R., Noiri, E., Isobe, H. *et al.* (2010) In vivo gene delivery by cationic tetraamino fullerene. *Proc. Natl. Acad. Sci. U.S.A.*, **107** (12), 5339–5344.
36. Isobe, H., Nakanishi, W., Tomita, N. *et al.* (2006) Gene delivery by aminofullerenes: structural requirements for efficient transfection. *Chem. Asian J.*, **1** (1–2), 167–175.
37. Klumpp, C., Lacerda, L., Chaloin, O. *et al.* (2007) Multifunctionalised cationic fullerene adducts for gene transfer: design, synthesis and DNA complexation. *Chem. Commun.*, (36), 3762–3764.
38. Bolskar, R.D. (2008) Gadofullerene MRI contrast agents. *Nanomedicine*, **3** (2), 201–213.
39. Kolovou, G., Anagnostopoulou, K., Mikhailidis, D.P. *et al.* (2008) Apolipoprotein E knockout models. *Curr. Pharm. Des.*, **14** (4), 338–351.
40. Bolskar, R.D., Benedetto, A.F., Husebo, L.O. *et al.* (2003) First soluble $M@C_{60}$ derivatives provide enhanced access to metallofullerenes and permit in vivo evaluation of $Gd@C_{60}[C(COOH)_2]_{10}$ as a MRI contrast agent. *J. Am. Chem. Soc.*, **125** (18), 5471–5478.
41. Tóth, É., Bolskar, R.D., Borel, A. *et al.* (2005) Water-soluble gadofullerenes: toward high-relaxivity, pH-responsive

MRI contrast agents. *J. Am. Chem. Soc.*, **127** (2), 799–805.
42. Friedman, S.H., DeCamp, D.L., Sijbesma, R.P. *et al.* (1993) Inhibition of the HIV-1 protease by fullerene derivatives: model building studies and experimental verification. *J. Am. Chem. Soc.*, **115** (15), 6506–6509.
43. Mashino, T., Usui, N., Okuda, K. *et al.* (2003) Respiratory chain inhibition by fullerene derivatives: hydrogen peroxide production caused by fullerene derivatives and a respiratory chain system. *Bioorg. Med. Chem.*, **11** (7), 1433–1438.
44. Tang, Y.J., Ashcroft, J.M., Chen, D. *et al.* (2007) Charge-associated effects of fullerene derivatives on microbial structural integrity and central metabolism. *Nano Lett.*, **7** (3), 754–760.
45. Tegos, G.P., Demidova, T.N., Arcila-Lopez, D. *et al.* (2005) Cationic fullerenes are effective and selective antimicrobial photosensitizers. *Chem. Biol.*, **12** (10), 1127–1135.
46. Xu, L., Liu, Y., Chen, Z. *et al.* (2013) Morphologically virus-like fullerenol nanoparticles act as the dual-functional nanoadjuvant for HIV-1 vaccine. *Adv. Mater.*, **25** (41), 5928–5936.
47. Wang, J., Hu, Z., Xu, J. *et al.* (2014) Therapeutic applications of low-toxicity spherical nanocarbon materials. *NPG Asia Mater.*, **6**, e84.
48. Tong, J., Zimmerman, M.C., Li, S. *et al.* (2011) Neuronal uptake and intracellular superoxide scavenging of a fullerene (C_{60})-poly(2-oxazoline)s nanoformulation. *Biomaterials*, **32** (14), 3654–3665.
49. Montellano, A., Da Ros, T., Bianco, A. *et al.* (2011) Fullerene C_{60} as a multifunctional system for drug and gene delivery. *Nanoscale*, **3** (10), 4035–4041.
50. Aitken, J. and Fisher, H. (1994) Reactive oxygen species generation and human spermatozoa: the balance of benefit and risk. *BioEssays*, **16** (4), 259–267.
51. Halliwell, B. (1991) Reactive oxygen species in living systems: source, biochemistry, and role in human disease. *Am. J. Med.*, **91** (3, Suppl. 3), S14–S22.
52. Bentzen, S.M. (2006) Preventing or reducing late side effects of radiation therapy: radiobiology meets molecular pathology. *Nat. Rev. Cancer*, **6** (9), 702–713.
53. Iijima, S. (1991) Helical microtubules of graphitic carbon. *Nature*, **354** (6348), 56–58.
54. Liu, Z., Fan, A.C., Rakhra, K. *et al.* (2009) Supramolecular stacking of doxorubicin on carbon nanotubes for in vivo cancer therapy. *Angew. Chem. Int. Ed.*, **48** (41), 7668–7672.
55. Liu, Z., Sun, X., Nakayama-Ratchford, N. *et al.* (2007) Supramolecular chemistry on water-soluble carbon nanotubes for drug loading and delivery. *ACS Nano*, **1** (1), 50–56.
56. Liu, Z., Chen, K., Davis, C. *et al.* (2008) Drug delivery with carbon nanotubes for in vivo cancer treatment. *Cancer Res.*, **68** (16), 6652–6660.
57. Ali-Boucetta, H., Al-Jamal, K.T., McCarthy, D. *et al.* (2008) Multiwalled carbon nanotube-doxorubicin supramolecular complexes for cancer therapeutics. *Chem. Commun.*, (4), 459–461.
58. Wu, W., Li, R., Bian, X. *et al.* (2009) Covalently combining carbon nanotubes with anticancer agent: preparation and antitumor activity. *ACS Nano*, **3** (9), 2740–2750.
59. Feazell, R.P., Nakayama-Ratchford, N., Dai, H. *et al.* (2007) Soluble single-walled carbon nanotubes as longboat delivery systems for platinum(IV) anticancer drug design. *J. Am. Chem. Soc.*, **129** (27), 8438–8439.
60. Kam, N.W.S., Liu, Z., and Dai, H. (2006) Carbon nanotubes as intracellular transporters for proteins and DNA: an investigation of the uptake mechanism and pathway. *Angew. Chem. Int. Ed.*, **118** (4), 591–595.
61. Kam, N.W.S., Liu, Z., and Dai, H. (2005) Functionalization of carbon nanotubes via cleavable disulfide bonds for efficient intracellular delivery of siRNA and potent gene silencing. *J. Am. Chem. Soc.*, **127** (36), 12492–12493.
62. Liu, Z., Winters, M., Holodniy, M. *et al.* (2007) siRNA delivery into human T cells and primary cells with carbon-nanotube transporters. *Angew. Chem. Int. Ed.*, **46** (12), 2023–2027.

63. Liu, Y., Wu, D.-C., Zhang, W.-D. *et al.* (2005) Polyethylenimine-grafted multiwalled carbon nanotubes for secure noncovalent immobilization and efficient delivery of DNA. *Angew. Chem. Int. Ed.*, **44** (30), 4782–4785.
64. Foillard, S., Zuber, G., and Doris, E. (2011) Polyethylenimine-carbon nanotube nanohybrids for siRNA-mediated gene silencing at cellular level. *Nanoscale*, **3** (4), 1461–1464.
65. Kam, N.W.S. and Dai, H. (2005) Carbon nanotubes as intracellular protein transporters: generality and biological functionality. *J. Am. Chem. Soc.*, **127** (16), 6021–6026.
66. Wang, X., Wang, C., Cheng, L. *et al.* (2012) Noble metal coated single-walled carbon nanotubes for applications in surface enhanced raman scattering imaging and photothermal therapy. *J. Am. Chem. Soc.*, **134** (17), 7414–7422.
67. Ghosh, S., Dutta, S., Gomes, E. *et al.* (2009) Increased heating efficiency and selective thermal ablation of alignant tissue with DNA-encased multiwalled carbon nanotubes. *ACS Nano*, **3** (9), 2667–2673.
68. Liu, X., Tao, H., Yang, K. *et al.* (2011) Optimization of surface chemistry on single-walled carbon nanotubes for in vivo photothermal ablation of tumors. *Biomaterials*, **32** (1), 144–151.
69. Liang, C., Diao, S., Wang, C. *et al.* (2014) Tumor metastasis inhibition by imaging-guided photothermal therapy with single-walled carbon nanotubes. *Adv. Mater.*, **26** (32), 5646–5652.
70. Liu, J., Wang, C., Wang, X. *et al.* (2015) Mesoporous silica coated single-walled carbon nanotubes as a multifunctional light-responsive platform for cancer combination therapy. *Adv. Funct. Mater.*, **25** (3), 384–392.
71. Wang, L., Shi, J., Zhang, H. *et al.* (2013) Synergistic anticancer effect of RNAi and photothermal therapy mediated by functionalized single-walled carbon nanotubes. *Biomaterials*, **34** (1), 262–274.
72. Wang, C., Xu, L., Liang, C. *et al.* (2014) Immunological responses triggered by photothermal therapy with carbon nanotubes in combination with anti-CTLA-4 therapy to inhibit cancer metastasis. *Adv. Mater.*, **26** (48), 8154–8162.
73. Welsher, K., Sherlock, S.P., and Dai, H. (2011) Deep-tissue anatomical imaging of mice using carbon nanotube fluorophores in the second near-infrared window. *Proc. Natl. Acad. Sci. U.S.A.*, **108** (22), 8943–8948.
74. Welsher, K., Liu, Z., Sherlock, S.P. *et al.* (2009) A route to brightly fluorescent carbon nanotubes for near-infrared imaging in mice. *Nat. Nanotechnol.*, **4** (11), 773–780.
75. Hong, G., Lee, J.C., Robinson, J.T. *et al.* (2012) Multifunctional in vivo vascular imaging using near-infrared II fluorescence. *Nat. Med.*, **18** (12), 1841–1846.
76. Robinson, J.T., Hong, G., Liang, Y. *et al.* (2012) In vivo fluorescence imaging in the second near-infrared window with long circulating carbon nanotubes capable of ultrahigh tumor uptake. *J. Am. Chem. Soc.*, **134** (25), 10664–10669.
77. Liu, Z., Tabakman, S., Sherlock, S. *et al.* (2010) Multiplexed five-color molecular imaging of cancer cells and tumor tissues with carbon nanotube Raman tags in the near-infrared. *Nano Res.*, **3** (3), 222–233.
78. Liu, Z., Li, X., Tabakman, S.M. *et al.* (2008) Multiplexed multicolor raman imaging of live cells with isotopically modified single walled carbon nanotubes. *J. Am. Chem. Soc.*, **130** (41), 13540–13541.
79. De La Zerda, A., Zavaleta, C., Keren, S. *et al.* (2008) Carbon nanotubes as photoacoustic molecular imaging agents in living mice. *Nat. Nanotechnol.*, **3** (9), 557–562.
80. Zerda, A.d.l., Liu, Z., Bodapati, S. *et al.* (2010) Ultrahigh sensitivity carbon nanotube agents for photoacoustic molecular imaging in living mice. *Nano Lett.*, **10** (6), 2168–2172.
81. Wang, C., Ma, X., Ye, S. *et al.* (2012) Protamine functionalized single-walled carbon nanotubes for stem cell labeling

and in vivo raman/magnetic resonance/photoacoustic triple-modal imaging. *Adv. Funct. Mater.*, **22** (11), 2363–2375.

82. Al Faraj, A., Fauvelle, F., Luciani, N. *et al.* (2011) In vivo biodistribution and biological impact of injected carbon nanotubes using magnetic resonance techniques. *Int. J. Nanomed.*, **6**, 351–361.

83. Richard, C., Doan, B.-T., Beloeil, J.-C. *et al.* (2008) Noncovalent functionalization of carbon nanotubes with amphiphilic Gd^{3+} chelates: toward powerful T1 and T2 MRI contrast agents. *Nano Lett.*, **8** (1), 232–236.

84. Vittorio, O., Duce, S.L., Pietrabissa, A. *et al.* (2011) Multiwall carbon nanotubes as MRI contrast agents for tracking stem cells. *Nanotechnology*, **22** (9), 095706.

85. Liu, Z., Cai, W., He, L. *et al.* (2007) In vivo biodistribution and highly efficient tumour targeting of carbon nanotubes in mice. *Nat. Nanotechnol.*, **2** (1), 47–52.

86. McDevitt, M.R., Chattopadhyay, D., Kappel, B.J. *et al.* (2007) Tumor targeting with antibody-functionalized, radiolabeled carbon nanotubes. *J. Nucl. Med.*, **48** (7), 1180–1189.

87. Chen, R.J., Bangsaruntip, S., Drouvalakis, K.A. *et al.* (2003) Noncovalent functionalization of carbon nanotubes for highly specific electronic biosensors. *Proc. Natl. Acad. Sci. U.S.A.*, **100** (9), 4984–4989.

88. Chen, Z., Tabakman, S.M., Goodwin, A.P. *et al.* (2008) Protein microarrays with carbon nanotubes as multicolor Raman labels. *Nat. Biotechnol.*, **26** (11), 1285–1292.

89. Harrison, B.S. and Atala, A. (2007) Carbon nanotube applications for tissue engineering. *Biomaterials*, **28** (2), 344–353.

90. Abarrategi, A., Gutiérrez, M.C., Moreno-Vicente, C. *et al.* (2008) Multiwall carbon nanotube scaffolds for tissue engineering purposes. *Biomaterials*, **29** (1), 94–102.

91. Shi, X., Sitharaman, B., Pham, Q.P. *et al.* (2007) Fabrication of porous ultra-short single-walled carbon nanotube nanocomposite scaffolds for bone tissue engineering. *Biomaterials*, **28** (28), 4078–4090.

92. Chen, B., Liu, M., Zhang, L. *et al.* (2011) Polyethylenimine-functionalized graphene oxide as an efficient gene delivery vector. *J. Mater. Chem.*, **21** (21), 7736–7741.

93. Liu, Z., Robinson, J.T., Tabakman, S.M. *et al.* (2011) Carbon materials for drug delivery & cancer therapy. *Mater. Today*, **14** (7–8), 316–323.

94. Kostarelos, K., Lacerda, L., Pastorin, G. *et al.* (2007) Cellular uptake of functionalized carbon nanotubes is independent of functional group and cell type. *Nat. Nanotechnol.*, **2** (2), 108–113.

95. Dhar, S., Liu, Z., Thomale, J. *et al.* (2008) Targeted single-wall carbon nanotube-mediated Pt(IV) prodrug delivery using folate as a homing device. *J. Am. Chem. Soc.*, **130** (34), 11467–11476.

96. Gupta, B., Levchenko, T.S., and Torchilin, V.P. (2005) Intracellular delivery of large molecules and small particles by cell-penetrating proteins and peptides. *Adv. Drug Delivery Rev.*, **57** (4), 637–651.

97. Oh, Y.-K. and Park, T.G. (2009) siRNA delivery systems for cancer treatment. *Adv. Drug Delivery Rev.*, **61** (10), 850–862.

98. Bartholomeusz, G., Cherukuri, P., Kingston, J. *et al.* (2009) In vivo therapeutic silencing of hypoxia-inducible factor 1 alpha (HIF-1α) using single-walled carbon nanotubes noncovalently coated with siRNA. *Nano Res.*, **2** (4), 279–291.

99. Ahmed, M., Deng, Z., Liu, S. *et al.* (2009) Cationic glyconanoparticles: their complexation with DNA, cellular uptake, and transfection efficiencies. *Bioconjugate Chem.*, **20** (11), 2169–2176.

100. Kim, H. and Kim, W.J. (2014) Photothermally controlled gene delivery by reduced graphene oxide-polyethylenimine nanocomposite. *Small*, **10** (1), 117–126.

101. Tian, B., Wang, C., Zhang, S. *et al.* (2011) Photothermally enhanced photodynamic therapy delivered by nano-graphene oxide. *ACS Nano*, **5** (9), 7000–7009.

102. Kim, H., Lee, D., Kim, J. *et al.* (2013) Photothermally triggered cytosolic drug delivery via endosome disruption using a functionalized reduced graphene oxide. *ACS Nano*, **7** (8), 6735–6746.

103. Feng, L., Yang, X., Shi, X. *et al.* (2013) Polyethylene glycol and polyethylenimine dual-functionalized nano-graphene oxide for photothermally enhanced gene delivery. *Small*, **9** (11), 1989–1997.

104. Kam, N.W.S., O'Connell, M., Wisdom, J.A. *et al.* (2005) Carbon nanotubes as multifunctional biological transporters and near-infrared agents for selective cancer cell destruction. *Proc. Natl. Acad. Sci. U.S.A.*, **102** (33), 11600–11605.

105. Chakravarty, P., Marches, R., Zimmerman, N.S. *et al.* (2008) Thermal ablation of tumor cells with antibody-functionalized single-walled carbon nanotubes. *Proc. Natl. Acad. Sci. U.S.A.*, **105** (25), 8697–8702.

106. Moon, H.K., Lee, S.H., and Choi, H.C. (2009) In vivo near-infrared mediated tumor destruction by photothermal effect of carbon nanotubes. *ACS Nano*, **3** (11), 3707–3713.

107. Burke, A., Ding, X., Singh, R. *et al.* (2009) Long-term survival following a single treatment of kidney tumors with multiwalled carbon nanotubes and near-infrared radiation. *Proc. Natl. Acad. Sci. U.S.A.*, **106** (31), 12897–12902.

108. Yang, K., Wan, J., Zhang, S. *et al.* (2012) The influence of surface chemistry and size of nanoscale graphene oxide on photothermal therapy of cancer using ultra-low laser power. *Biomaterials*, **33** (7), 2206–2214.

109. Robinson, J., Welsher, K., Tabakman, S. *et al.* (2010) High performance in vivo near-IR (>1 μm) imaging and photothermal cancer therapy with carbon nanotubes. *Nano Res.*, **3** (11), 779–793.

110. Xu, M. and Wang, L.V. (2006) Photoacoustic imaging in biomedicine. *Rev. Sci. Instrum.*, **77** (4), 041101.

111. Kostarelos, K., Bianco, A., and Prato, M. (2009) Promises, facts and challenges for carbon nanotubes in imaging and therapeutics. *Nat. Nanotechnol.*, **4** (10), 627–633.

112. Wang, J. (2005) Carbon-nanotube based electrochemical biosensors: a review. *Electroanalysis*, **17** (1), 7–14.

113. Geim, A.K. and Novoselov, K.S. (2007) The rise of graphene. *Nat. Mater.*, **6** (3), 183–191.

114. Yang, K., Feng, L., and Liu, Z. (2015) The advancing uses of nano-graphene in drug delivery. *Expert Opin. Drug Delivery*, **12** (4), 601–612.

115. Wang, Y., Li, Z., Wang, J. *et al.* (2011) Graphene and graphene oxide: biofunctionalization and applications in biotechnology. *Trends Biotechnol.*, **29** (5), 205–212.

116. Yang, K., Li, Y., Tan, X. *et al.* (2013) Behavior and toxicity of graphene and its functionalized derivatives in biological systems. *Small*, **9** (9–10), 1492–1503.

117. Liu, Z., Robinson, J.T., Sun, X.M. *et al.* (2008) PEGylated nanographene oxide for delivery of water-insoluble cancer drugs. *J. Am. Chem. Soc.*, **130** (33), 10876–10877.

118. Sun, X.M., Liu, Z., Welsher, K. *et al.* (2008) Nano-graphene oxide for cellular imaging and drug delivery. *Nano Res.*, **1** (3), 203–212.

119. Zhang, L.M., Xia, J.G., Zhao, Q.H. *et al.* (2010) Functional graphene oxide as a nanocarrier for controlled loading and targeted delivery of mixed anticancer drugs. *Small*, **6** (4), 537–544.

120. Ma, X., Tao, H., Yang, K. *et al.* (2012) A functionalized graphene oxide-iron oxide nanocomposite for magnetically targeted drug delivery, photothermal therapy, and magnetic resonance imaging. *Nano Res.*, **5** (3), 199–212.

121. Zhang, L., Lu, Z., Zhao, Q. *et al.* (2011) Enhanced chemotherapy efficacy by sequential delivery of siRNA and anticancer drugs using PEI-grafted graphene oxide. *Small*, **7** (4), 460–464.

122. Bao, H., Pan, Y., Ping, Y. *et al.* (2011) Chitosan-functionalized graphene oxide as a nanocarrier for drug and gene delivery. *Small*, **7** (11), 1569–1578.
123. Yang, K., Zhang, S., Zhang, G.,.X. *et al.* (2010) Graphene in mice: ultrahigh in vivo tumor uptake and efficient photothermal therapy. *Nano Lett.*, **10** (9), 3318–3323.
124. Yang, K., Hu, L., Ma, X. *et al.* (2012) Multimodal imaging guided photothermal therapy using functionalized graphene nanosheets anchored with magnetic nanoparticles. *Adv. Mater.*, **24** (14), 1868–1872.
125. Zhang, W., Guo, Z., Huang, D. *et al.* (2011) Synergistic effect of chemo-photothermal therapy using PEGylated graphene oxide. *Biomaterials*, **32** (33), 8555–8561.
126. Feng, L., Li, K., Shi, X. *et al.* (2014) Smart pH-responsive nanocarriers based on nano-graphene oxide for combined chemo- and photothermal therapy overcoming drug resistance. *Adv. Healthcare Mater.*, **3** (8), 1261–1271.
127. Hu, S.-H., Chen, Y.-W., Hung, W.-T. *et al.* (2012) Quantum-dot-tagged reduced graphene oxide nanocomposites for bright fluorescence bioimaging and photothermal therapy monitored in situ. *Adv. Mater.*, **24** (13), 1748–1754.
128. Shi, X., Gong, H., Li, Y. *et al.* (2013) Graphene-based magnetic plasmonic nanocomposite for dual bioimaging and photothermal therapy. *Biomaterials*, **34** (20), 4786–4793.
129. He, S., Song, B., Li, D. *et al.* (2010) A graphene nanoprobe for rapid, sensitive, and multicolor fluorescent DNA analysis. *Adv. Funct. Mater.*, **20** (3), 453–459.
130. Wang, Y., Li, Z.H., Hu, D.H. *et al.* (2010) Aptamer/graphene oxide nanocomplex for in situ molecular probing in living cells. *J. Am. Chem. Soc.*, **132** (27), 9274–9276.
131. Tang, L.,A.,L., Wang, J.,Z., and Loh, K.,.P. (2010) Graphene-based SELDI probe with ultrahigh extraction and sensitivity for DNA oligomer. *J. Am. Chem. Soc.*, **132** (32), 10976–10977.
132. Liu, Y., Yu, D.S., Zeng, C. *et al.* (2010) Biocompatible graphene oxide-based glucose biosensors. *Langmuir*, **26** (9), 6158–6160.
133. Lee, W.C., Lim, C.H.Y.X., Shi, H. *et al.* (2011) Origin of enhanced stem cell growth and differentiation on graphene and graphene oxide. *ACS Nano*, **5** (9), 7334–7341.
134. Chen, G.Y., Pang, D.W.P., Hwang, S.M. *et al.* (2012) A graphene-based platform for induced pluripotent stem cells culture and differentiation. *Biomaterials*, **33** (2), 418–427.
135. Hu, W., Peng, C., Luo, W. *et al.* (2010) Graphene-based antibacterial paper. *ACS Nano*, **4** (7), 4317–4323.
136. Liu, S., Zeng, T.H., Hofmann, M. *et al.* (2011) Antibacterial activity of graphite, graphite oxide, graphene oxide, and reduced graphene oxide: membrane and oxidative stress. *ACS Nano*, **5** (9), 6971–6980.
137. Feng, L., Zhang, S., and Liu, Z. (2011) Graphene based gene transfection. *Nanoscale*, **3** (3), 1252–1257.
138. Huang, P., Xu, C., Lin, J. *et al.* (2011) Folic acid-conjugated graphene oxide loaded with photosensitizers for targeting photodynamic therapy. *Theranostics*, **1**, 240–250.
139. Sahu, A., Choi, W.I., Lee, J.H. *et al.* (2013) Graphene oxide mediated delivery of methylene blue for combined photodynamic and photothermal therapy. *Biomaterials*, **34** (26), 6239–6248.
140. Shen, H., Liu, M., He, H. *et al.* (2012) PEGylated graphene oxide-mediated protein delivery for cell function regulation. *ACS Appl. Mater. Interfaces*, **4** (11), 6317–6323.
141. Yang, K., Wan, J., Zhang, S. *et al.* (2011) The influence of surface chemistry and size of nanoscale graphene oxide on photothermal therapy of cancer using ultra-low laser power. *Biomaterials*, **33** (7), 2206–2214.
142. Sheng, Z., Song, L., Zheng, J. *et al.* (2013) Protein-assisted fabrication of nano-reduced graphene oxide for combined in vivo photoacoustic imaging and photothermal therapy. *Biomaterials*, **34** (21), 5236–5243.

143. Yang, H.-W., Lu, Y.-J., Lin, K.-J. *et al.* (2013) EGRF conjugated PEGylated nanographene oxide for targeted chemotherapy and photothermal therapy. *Biomaterials*, **34** (29), 7204–7214.
144. Yang, K., Wan, J., Zhang, S. *et al.* (2011) In vivo pharmacokinetics, long-term biodistribution, and toxicology of PEGylated graphene in mice. *ACS Nano*, **5** (1), 516–522.
145. Hong, H., Yang, K., Zhang, Y. *et al.* (2012) In vivo targeting and imaging of tumor vasculature with radiolabeled, antibody-conjugated nanographene. *ACS Nano*, **6** (3), 2361–2370.

6
Pulmonary Effects of Carbon Nanomaterials

Liying Wang, Donna C. Davidson, Vincent Castranova, and Yon Rojanasakul

6.1
Introduction

Carbon nanomaterials, a class of small-scale (<100 nm) carbon-based materials formed by molecular-level engineering with unique mechanical, optical, and electrical properties, have increasingly been utilized for a wide range of applications in such as electronics, energy storage, structural materials, pharmaceuticals, cosmetics, agriculture, medical diagnostics, and drug delivery [1–3]. The chemistry of pure carbon particles is surprisingly uninteresting, since they are significantly unreactive. However, there are some types of carbon nanomaterials, such as carbon nanotubes (CNTs), which are more reactive than others because of the defects from missing carbon atoms and the more strained curved-end caps [4]. Additionally, nano-scale materials have a high surface area-to-volume ratio in comparison to their bulk counterparts, which leads to their high reactivity as well as biological activities following intended and unintended exposure to sensitive mammalian tissue.

Because of the small size and low density of carbon nanoparticles (NPs), aerosolization is likely during energetic processes such as vortexing, weighing, sonication, mixing, and blending [5–8]. Thus, human exposure via inhalation is anticipated during the production, usage, and disposal of nanoparticles [9]. As a result, the lung is the major target organ for aerosolized nanoparticle exposure. Consistently, the respiratory system represents a unique target for the potential toxicity of nanoparticles due to the fact that, in addition to being the portal of entry for inhaled particles, it also receives the entire cardiac output. As such, there is potential for exposure of the lungs to nanoparticles resulting in particle translocation to extrapulmonary organs via systemic circulation. Nanomaterials may also enter the lung via other exposure routes including dermal and gastrointestinal absorption or direct injection.

In response to inhaled airborne particles, biological defense of the lung occurs [10]. In general, alveolar macrophages and epithelial cells are the two major

Biomedical Applications and Toxicology of Carbon Nanomaterials, First Edition.
Edited by Chunying Chen and Haifang Wang.

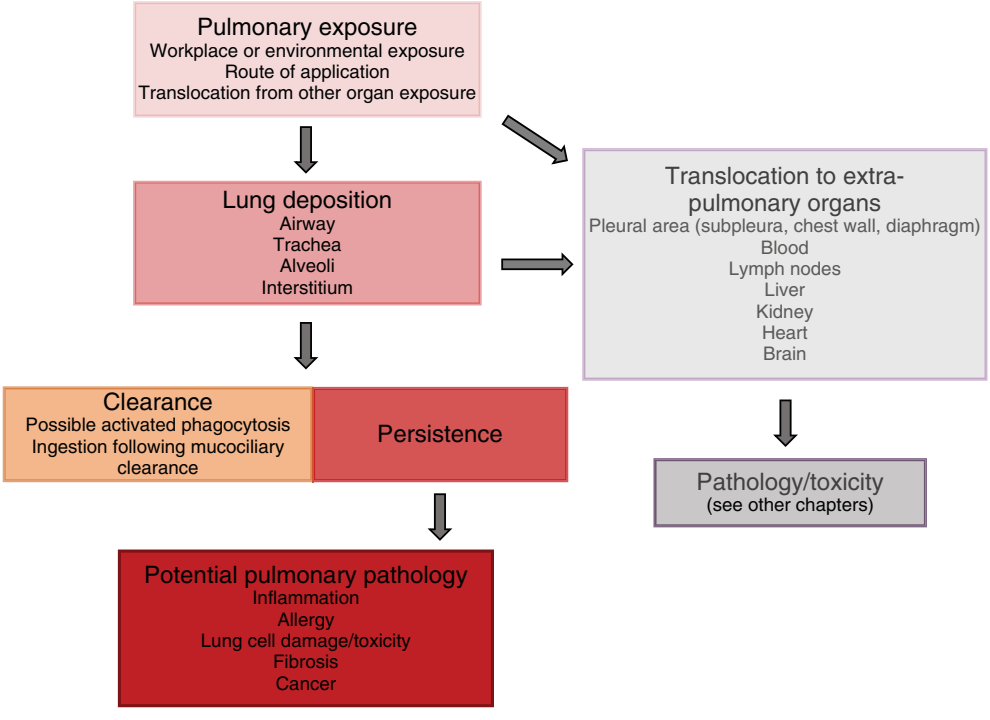

Figure 6.1 Overall fate and toxicity potential of pulmonary-exposed CNTs.

resident cells that interact with inhaled particles in the alveolar region of the lung. Classically, pulmonary responses to inhaled insoluble particles include physiological defense mechanisms, such as clearance, as well as pathological response mechanisms, such as inflammation, oxidative stress, cell damage, aberrant proliferation, and lung tissue remodeling, which may lead to the development of lung fibrosis. However, studies have found that nanomaterials deposited in the lungs, including carbon nanoparticles, show a different behavior compared to fine particles of the same chemical composition (Figure 6.1). In this chapter, the unique bioactivities of nanomaterials exposed to the lungs will be discussed.

6.2
Physicochemical Properties of Carbon Nanomaterials

Nanoparticles exhibit unique physicochemical properties and are likely to exhibit biological activities that are significantly different from those by fine or micrometer-sized particles of the same chemical composition. These properties, such as the particle size, shape, solubility, charge, and surface reactivity, are

believed to be important determinants of the biological responses [11, 12]. For example, a large body of literature suggests that the fiber-like CNTs may have unusual toxicity properties. In particular, CNTs seem to have a special ability to stimulate mesenchymal cell growth and cause granuloma formation and fibrogenesis, causing more adverse effects than the same mass of NP carbon and quartz, the latter a commonly used benchmark of particle toxicity [13]. In addition to the particle characteristics mentioned above, the bioactivities of NPs also depend on particle oxidant generation, surface functionalization, and the rate of dissolution. Changes in physicochemical reactivity of NPs also cause them to interact with circulatory and cellular proteins differentially, leading to their altered biokinetic profiles, including adsorption, distribution, translocation, transformation, and elimination [14].

When assessing the respiratory toxicity of nanomaterials through inhalation, intratracheal instillation, or pharyngeal aspiration, discrepancies observed among these administration routes can result from differences in the physiochemical properties of the nanomaterials themselves, such as agglomeration and dispersion. Therefore, it is essential that identification and characterization of the NPs' physicochemical properties be performed in all toxicity studies [15]. Examples of these physicochemical parameters and how they affect the bioactivities of carbon nanomaterials are discussed below.

6.2.1
Types of Carbon Nanomaterials

Commonly studied classes of carbon nanoparticles include fullerenes, graphene, CNTs, carbon nanofibers (CNFs), and ultrafine carbon black (UFCB). Fullerenes are hollow balls of carbon, while graphene consists of carbon that is arranged in flat sheets. In the case of CNTs, carbon is arranged in a cylindrical structure. CNTs are further subdivided based on the number of carbon layers that make up the nanotubes; that is, one ("single-walled carbon nanotube"; SWCNT), two ("double-walled carbon nanotube"; DWCNT), or several ("multi-walled carbon nanotube"; MWCNT) layers. CNTs range from one to several nanometers in width and up to several micrometers in length. This large length-to-width (aspect) ratio, a property shared with asbestos fibers, has led to concerns that inhaled CNTs may cause asbestos-like pathologies, such as pulmonary fibrosis and lung cancer [16]. CNFs differ from CNTs in that they are usually larger in diameter and noncontinuous, containing exposed graphene edge planes [17]. UFCB represents the nano-sized portion of carbon black (CB) materials, and is often used as surrogate for nano-scaled particulate matter found in ambient air.

6.2.2
Effects of Size

When the dimension of a solid material becomes very small, its physical and chemical properties can be very different from those of the same material in its

bulk form. A growing body of data indicates that particle size is an important factor in determining the biological response to particles. Accordingly, the bioactivity of MWCNTs has been shown to increase with both their diameter and length [18]. Xu *et al.* utilized an exposure period of 24 weeks to determine whether the size and shape of MWCNTs impact deposition and lesion development in the lung pleura [14]. Using two different types of MWCNT, namely a large, needle-like MWCNT (length = 8 μm, diameter = 150 nm) and a small MWCNT (length = 3 μm, diameter = 15 nm), administered to the lungs of rats once every 2 weeks for 24 weeks by transtracheal intrapulmonary spraying, the authors noted that the large MWCNTs – but not the small ones – translocated into the pleural cavity, deposited in the parietal pleura, and induced fibrosis with occasional parietal mesothelial proliferative lesions. In addition, the large MWCNTs induced a greater number of inflammatory cells in the pleural lavage, while the small MWCNTs induced stronger inflammation and higher 8-hydroxydeoxyguanosine level in the lung tissue. Collectively, these results suggest that the large MWCNTs may pose a greater risk of pleural lesions relevant to mesothelioma development, similar to asbestos [14].

In addition to affecting the distribution in tissue, the size of particles can influence their toxicity. In general, small particles exert harmful effects as a consequence of two factors that act together to contribute to their toxicity: surface area and the intrinsic reactivity or toxicity of that surface [19, 20]. The smaller the particles, the more their surface area per unit mass and, consequently, the more the enhancement in the intrinsic toxicity of the particle surface [21]. Therefore, as the particles become smaller, their likelihood of causing harm to the lung tissue increases.

Interestingly, Poulsen *et al.* [22] found that exposure of mice to small or large MWCNTs resulted in a similar global transcription pattern, with both MWCNTs eliciting strong acute-phase and inflammatory responses that peaked at day 3 and persisted up to 28 days and were characterized by a large number of inflammatory cells in the bronchoalveolar lavage fluid, interstitial pneumonia, and gene expression changes. However, exposure to large CNTs resulted in a faster onset of inflammation and DNA damage, and caused more fibrosis with a unique fibrotic gene signature at day 28, as compared to small CNTs [22].

6.2.3 Effects of Agglomeration State

Nanoparticles are often dispersed in aqueous media, the composition of which may differ substantially depending on their applications, in order to deliver the particles to the *in vitro* or *in vivo* systems of interest. However, nanoparticles may or may not disperse well in these media, and likewise may not disperse to the same extent in the same medium, depending on their physicochemical properties. Therefore, the particles may be delivered as agglomerates of various structures and sizes of the nanomaterial. Accordingly, the agglomeration state has been demonstrated to impact the bioactivities of nanomaterials as elaborated below.

Several studies have shown that exposure to well-dispersed CNTs can have different pathological outcomes as compared to agglomerated CNTs. For example, pulmonary aspiration of large agglomerates of SWCNTs (~15 μm in diameter) resulted in structures that remained in the alveolar airspaces and ultimately induced inflammatory granulomas with SWCNT agglomerates, encased by epithelioid macrophages. In contrast, well-dispersed SWCNTs (D-SWCNTs, mean diameter of 0.69 μm) did not produce granulomas encased by epithelioid macrophages; rather, they induced a more potent interstitial fibrotic response. The latter was also observed to be associated with minimal lung inflammation and macrophage engulfment of D-SWCNTs [23–25]. This suggests that the ability of small D-SWCNT structures to escape macrophage phagocytosis and enter the lung interstitium could be a key determining factor in the relative absence of macrophage-derived lung inflammation and oxidant stress and the enhanced induction of interstitial fibrosis by D-SWCNTs. Because lung fibrosis caused by D-SWCNTs occurs quite rapidly in the absence of sustained inflammatory and oxidative stress responses, traditional *in vitro* screening tests, which are based on cytotoxicity and oxidative stress detection, are generally inadequate for predicting the *in vivo* fibrogenicity of SWCNTs [23–25].

The study described above also revealed that large micrometer-sized agglomerates deposited mainly in the proximal alveolar region, while the small D-SWCNT structures deposited largely in the distal alveoli and rapidly entered the alveolar walls [23]. These data further emphasize the extent to which the bioactivity of a nanomaterial can be affected by the degree to which the nanoparticles are agglomerated, that is, the physical size of the nanoparticle structures as they interact with biological systems. A similar finding was observed with UFCB by Shvedova *et al*. (2007)[26], who reported that intratracheal instillation of well-dispersed CB nanoparticles resulted in an eightfold increase in pulmonary response as compared to agglomerated CB nanoparticles of equal mass burden. Collectively, these studies highlight the pressing need to identify the physicochemical properties of NPs that contribute to their bioactivity in order to adequately screen for their toxicity.

It has been postulated that dissociation of nanoparticle agglomerates may occur *in vivo* and that, following dissociation, smaller individual particles may then elicit differential effects as compared to the agglomerates. Along the same lines, it is thought that the type of material as well as the size of agglomerates determines the translocation and accumulation in exposed animal organs [27, 28]. Electron microscopy studies have confirmed a trend of carbon nanoparticle agglomerates to actually build larger units after deposition in the lungs and uptake in cells, which suggested that an enhanced translocation potential of individual nanoparticles derived from dissociation of those agglomerates should not be expected [29]. This conclusion is in accordance with theoretical considerations presented by Maier *et al.* [30] in a study on TiO_2 nanoparticles, in which the authors concluded that TiO_2 agglomerates do not dissociate following their contact with lung surfactants. They also concluded that the size of the formed agglomerate was expected to remain relatively stable once deposited within the respiratory tract,

and this agglomerate size is likely to influence the resulting biological outcome [30]. However, Porter *et al*. [31] reported that an artificial lung lining fluid is a good dispersant of MWCNTs [31]. This result was confirmed with a pulmonary surfactant by Wang *et al.* [32]. Furthermore, Mercer *et al.* [33, 34] reported that inhaled small agglomerates of MWCNTs appeared to disperse over several months in the lung and that the singlets were translocated to extra-pulmonary organs. This information has been summarized by Castranova *et al.* [35].

6.2.4
Aspect Ratio Considerations

In addition to the type of carbon nanoparticles and their agglomeration state, another key determinant of nanoparticle bioactivity is the aspect ratio. CNTs are high-aspect-ratio nanomaterials (i.e., they are long and thin as opposed to short and thick) and thus have raised concerns that they may cause pulmonary responses similar to asbestos [16]. It is thought that changes in the length or thickness of CNTs may have a large impact on the activity of these particles.

Poland *et al.* [36] found a specific fiber-like effect of MWCNTs when injected intraperitoneally to mice. Each animal received a single injection of 100 $\mu g\ ml^{-1}$ of short or long amosite (asbestos) fibers or of short or long MWCNTs. Compared to the short fibers, long amosite fibers and long MWCNTs, respectively, induced a stronger inflammatory response and larger numbers of inflammatory granulomas [36]. Similarly, a different study found that long MWCNTs induced a more pronounced pro-fibrotic (mRNA expression of matrix metalloproteinase-8 and tissue inhibitor of metalloproteinase-1) and inflammatory (serum level of monocyte chemotactic protein-1) response compared with shorter and more agglomerated MWCNTs. This report also utilized Masson trichrome staining, which revealed epithelial cell hyperplasia upon exposure to the long MWCNTs [37].

A similar pro-fibrogenic effect of nanoparticles was observed with SWCNTs. Manke *et al.* [38] demonstrated that long SWCNTs were significantly more potent than short SWCNTs with respect to their ability to induce reactive oxygen species (ROS), collagen production, and transforming growth factor-beta (TGF-β) release in cultured human lung fibroblasts. The long SWCNTs were also more potent in inducing the fibrogenic and toxic effects *in vivo* when injected into the lungs of mice [38].

6.2.5
Surface Modifications

Surface modifications, such as changes in surface area, charge, coating, or reactivity, can greatly influence the bioactivity and/or toxic potential of carbon nanomaterials. These variations may be unintentional alterations due to differential production processes, or may be manipulated to intentionally alter the properties of nanoparticles. Surface charge and area can affect the cellular uptake of a particle, since it is the surface of the particle that will interact with cells and/or

tissue. This notion has led to the idea that surface area should be considered as a dosing strategy rather than the mass per volume which is commonly used. Indeed, pulmonary responses have been shown to be different with changing the surface area of nanoparticles. A recent study by Shvedova *et al.* (2014) compared the pulmonary responses to SWCNTs by bolus dosing through pharyngeal aspiration and inhalation at 5 h per day for 4 days. Inhalation exposure to SWCNTs (more dispersed and thus greater structure surface) showed significantly greater inflammatory, fibrotic, and genotoxic effects than bolus pharyngeal aspiration (more agglomerated, less structure surface) [39]. The results of this study suggest that long-term pulmonary toxicity of SWCNTs, CNFs, and asbestos may be defined not only by their chemical composition but also by their specific surface area and the type of exposure.

Physical or chemical modifications to the surface of carbon nanoparticles, such as the addition of coatings or via carboxylation or amination (often termed "functionalization" of the NPs), are postulated to alter the biological effects of the NPs, and in some cases are thought to be able to reduce the toxicity of the particles. Continued efforts are going on to address this issue, while several studies have shed light on this approach for the design of carbon nanomaterials. For example, recent findings indicate that atomic layer deposition (ALD) and thin film coating of MWCNTs with Al_2O_3 reduces fibrosis in mice [40]. Similarly, carboxylation of SWCNTs and MWCNTs apparently makes them more vulnerable to oxidative destruction by peroxidases, thereby significantly decreasing their biopersistence and potentially making them less reactive [41, 42]. In addition, functionalization of MWCNTs via carboxylation has been shown to be less inflammatory and fibrogenic than without functionalization in mice exposed to the CNTs by aspiration [43, 44]. The data have also shown that amination of CNTs may lead to more adverse outcomes [43]. Collectively, these studies highlight the extent to which surface modifications may impact the bioactivity of carbon nanoparticles and provide critical insight into the utility of alternative design strategies for nanomaterial manufacturing.

6.3
Fate of Pulmonary Exposed Carbon Nanoparticles (Deposition, Distribution, Translocation, and Clearance)

6.3.1
Deposition and Distribution of Carbon Nanoparticles in the Lung

Deposition of inhaled nanoparticles on the airway walls occurs chiefly via diffusional displacement by the thermal motion of inhaled and exhaled air molecules in contact with the nanoparticles. Importantly, because of their geometry and hydrophobic surface, carbon nanoparticles have a tendency to form agglomerates with a bundle-like structure, thereby increasing in size from the nanoscale to the microscale. In contrast to microparticles, nanoparticles exhibit increased

deposition as their size diminishes, with the deposition (nasal, tracheobronchial, and alveolus) being dependent on the aerodynamic diameter of the particles [45, 46]. Predicted fractional deposition of inhaled particles in the nasopharyngeal, tracheobronchial, and alveolar region of the human respiratory tract during nose breathing has also been reported [45].

Interestingly, yet not surprisingly, inhaled nanoscale and microscale particles end up differentially distributed in the lung. Mercer *et al.* [23] reported that pulmonary-aspirated large agglomerates of SWCNTs (~15 μm in diameter) remained in the alveolar airspaces of the terminal bronchioles and proximal alveoli, while well-dispersed SWCNTs (mean diameter of 0.69 μm) reached the distal alveoli, elicited minimal macrophage engulfment, and entered lung interstitium to induce interstitial fibrosis (Figure 6.2) [23]. Accordingly, it has been demonstrated that inhaled CNTs deposited in the bronchial and alveolar areas, but those deposited in the alveolar region were found to be smaller in size [49].

Pulmonary exposed CNTs can penetrate deep lung tissues, such as the interstitium, or translocate into pleura in a property-dependent manner [33, 47]. Accordingly, an interstitial penetration of nanoparticles and subsequent return onto airway epithelial cells has been reported [50]. In addition, pulmonary exposed MWCNTs have been shown to reach the subpleural area in mice after a single inhalation exposure of 30 mg m^{-3} for 6 h [51]. In this study, the CNTs were found embedded in the subpleural wall and within subpleural macrophages. The number and size of mononuclear cells located on the pleural surface also increased after 1 day of exposure, and subpleural fibrosis was observed 2 and 6 weeks after the exposure. Inhalation of CB nanoparticles or low-dose (1 mg m^{-3}) CNTs did not induce these effects. Other similar studies have also noted the presence of CNTs within the pleura (Figure 6.3), suggesting that the CNTs may have the ability to cause pleural fibrosis or mesothelioma, and highlighting the need for more long-term studies aimed at addressing this issue [33, 47, 51–53].

Mathematical models have been developed in an effort to predict particle deposition in the human airways. The model developed by the International Commission on Radiobiological Protection (ICRP) can be used to compute the proportions, by mass, of inhaled nanoparticles deposited in the airways of an individual breathing through the nose. Nanoparticles 1 nm in diameter are predicted to show ~90% deposition in the nasopharynx, 10% in the tracheobronchial tree, and 0% in the alveolar spaces; the corresponding proportions for 5-nm particles are 30%, 30%, and 30%, respectively, and for 20-nm particles, 15%, 15%, and 50%. With 20-nm particles, the distribution of deposition according to lung surface concentration indicates that alveolar space deposition is 100 times greater than nasopharyngeal deposition and 10 times greater than tracheobronchial deposition [54, 55].

Once deposited in the lungs, the nanoparticles may meet with different fates, in terms of cellular uptake and clearance. As such, endocytosis of nanoparticles has been extensively studied in various cell types. Endocytosis by airway epithelial

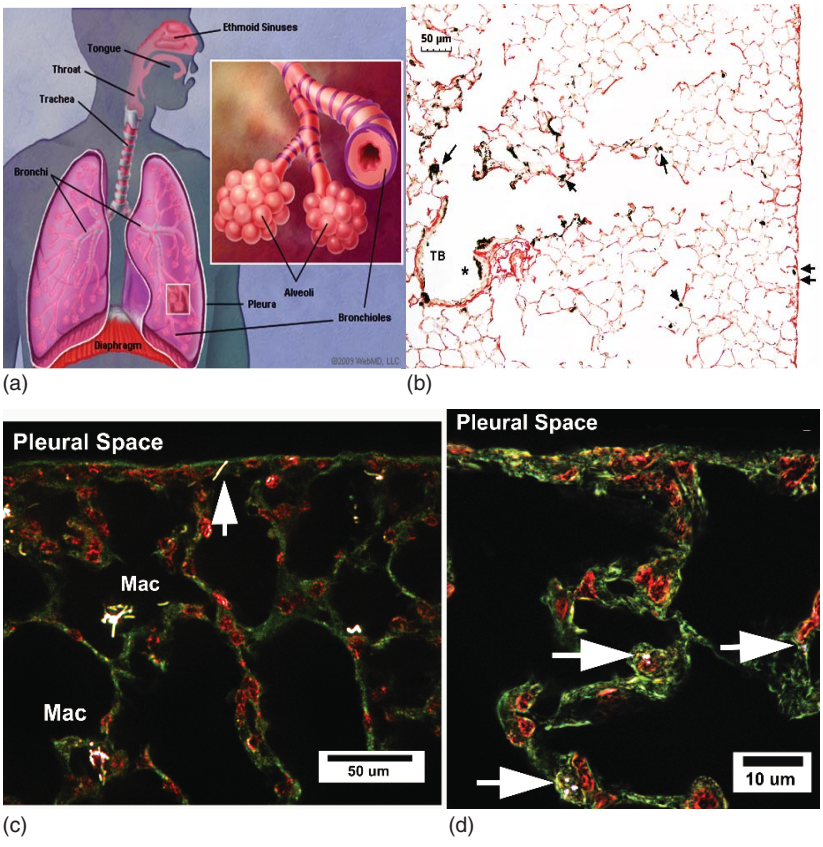

Figure 6.2 Pulmonary exposed MWCNT deposition. (a) Representative image of the lung (http://www.webmd.com/lung). (b) Light micrograph of MWCNT deposition in alveolar region of lungs. Sirius Red-stained micrograph shows the general deposition pattern of MWCNT (arrows) one day after 80 µg per mouse aspiration. A deposit of MWCNT on the epithelium of the terminal bronchiole near the transition between the airways and the alveolar region is indicated by single arrows. Smaller deposits near the subpleural tissue region are indicated by double arrows. Part (b) reprinted from [47]. (c, d) Enhanced dark-field images of the general distribution of CNTs as the bright, white structures in the lungs 7 days after aspiration (40 µg per mouse lung), while nuclei (red) and other tissues (green) produce a significantly duller image. (c) Arrow points to an individual MWCNT penetrating into the mesothelial cell layer forming the boundary between the alveolar tissues and pleural space. While alveolar macrophages are foci for MWCNTs, scattered/submicrometer MWCNT structures can be found in the alveolar interstitium throughout the section. (d) Mouse lung exposed to a highly dispersed preparation of SWCNTs (aspiration 10 µg per mouse lung, 7 days), for comparison. In the case of dispersed SWCNTs, the majority of CNT structures are rapidly incorporated into the alveolar interstitium (arrows). (Reprinted from [48].)

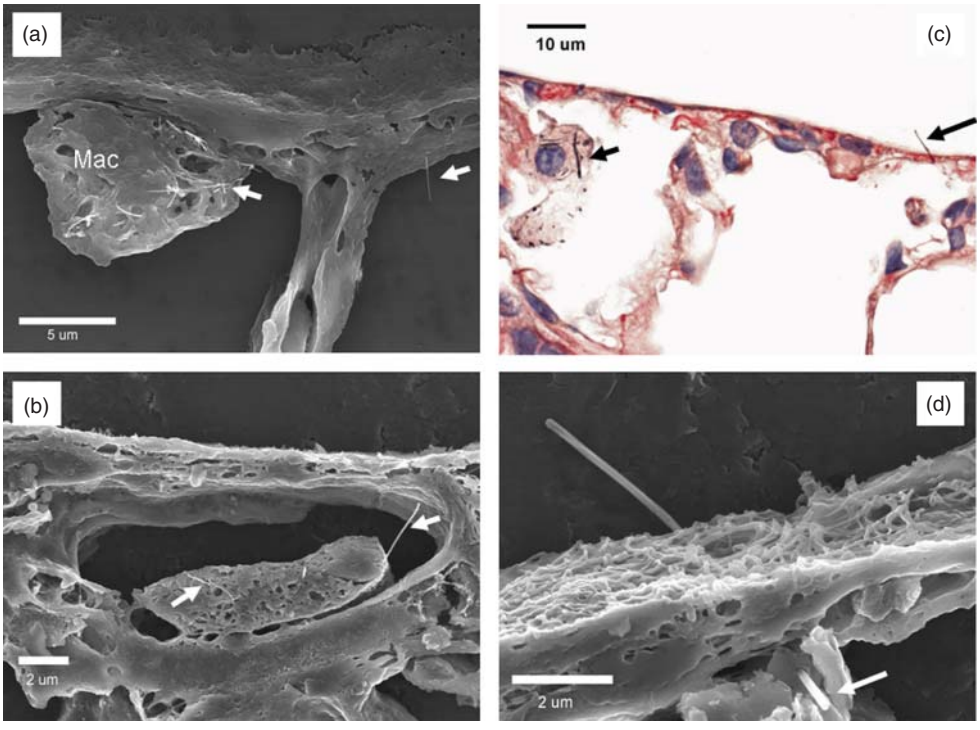

Figure 6.3 (a) Field-effect scanning electron microscopy image depicting an MWCNT-loaded alveolar macrophage and a single MWCNT fiber penetrating the alveolar epithelium into the subpleural tissues (80 μg dose, 28 days post aspiration). (b) Dilated subpleural lymphatic vessel containing a mononuclear inflammatory cell that is penetrated by several MWCNT fibers (80 μg dose, 56-day postaspiration). (c) An MWCNT penetrating the visceral pleura with a MWCNT-loaded alveolar macrophage visible in the left side of the micrograph (80 μg dose, 28 days post aspiration). (d) A single MWCNT penetrating from the subpleural tissue through the visceral pleura into the pleural space (80 μg dose, 56 days post aspiration). (Reprinted from [47].)

cells may occur at all three levels of the airway tree, providing nanoparticles direct entry into the blood and lymph and thereby allowing the particles to translocate to other parts of the body [45, 56, 57].

6.3.2 Translocation of Carbon Nanoparticles

Translocation into the epithelium and interstitium may allow nanoparticles to enter the blood and lymph, and thus distribute throughout the body [34, 50, 56–58]. Consistently, *in vivo* studies have shown effective translocation of ultrafine elemental carbon particles to the liver 1 day after inhalation exposure [57]. Translocation pathways include direct input into the blood compartment

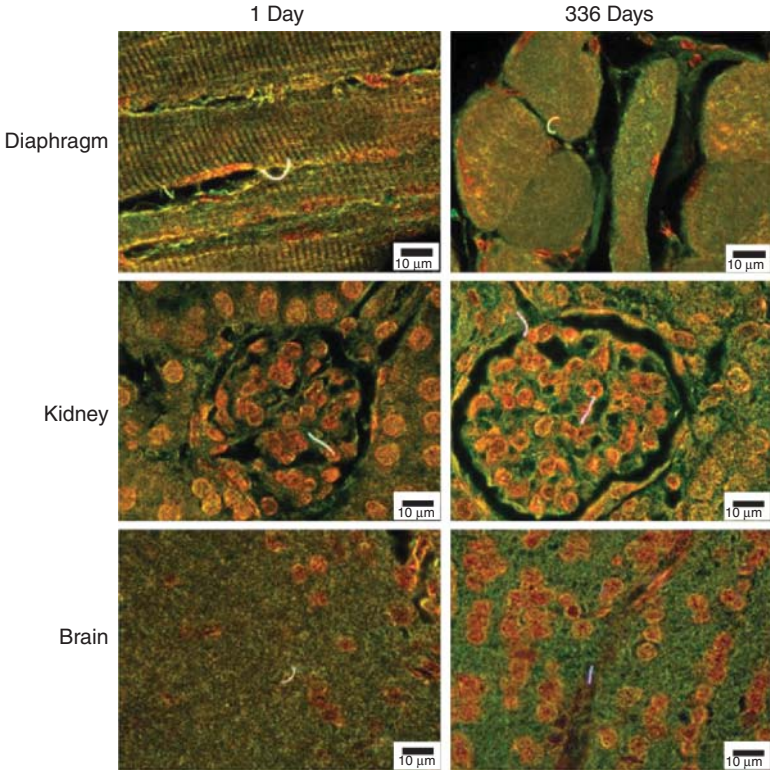

Figure 6.4 Enhanced dark-field images of MWCNT fibers in the diaphragm, kidney, and brain at 1 day and 336 days after inhalation exposure. MWCNT fibers in these figures are bright white, cell nuclei are brownish red, and other tissue elements are green. With rare exceptions, MWCNT fibers detected in extra-pulmonary organs were singlets. Normal (transmitted) light was blended into the fields and contrast-adjusted to make the tissue histology of the organs visible in these photographs. (Reprinted from [34].)

from ultrafine carbon particles deposited throughout the respiratory tract. Mercer *et al*. [33, 34] reported a qualitative study comparing the distribution of pulmonary exposed CNTs from 1 to 336 days after the termination of a 12-day inhalation exposure in order to determine whether there was a significant accumulation of CNTs in systemic tissues over time post exposure. The authors were able to detect the CNTs in lymph nodes, liver, kidney, heart, brain, chest wall, and diaphragm in as early as 1 day post exposure (1.089%) and noted a significant accumulation of CNTs in each of these organs at 336 days post exposure (7.337%), thus demonstrating the ability of the CNTs to translocate and accumulate systemically (Figures 6.4 and 6.5).

The report by Mercer *et al*. (2013) demonstrated the translocation and subsequent accumulation of a significant amount of CNTs within in the lymph nodes of exposed mice [34]. Likewise, a study conducted by Aiso *et al.* [59]

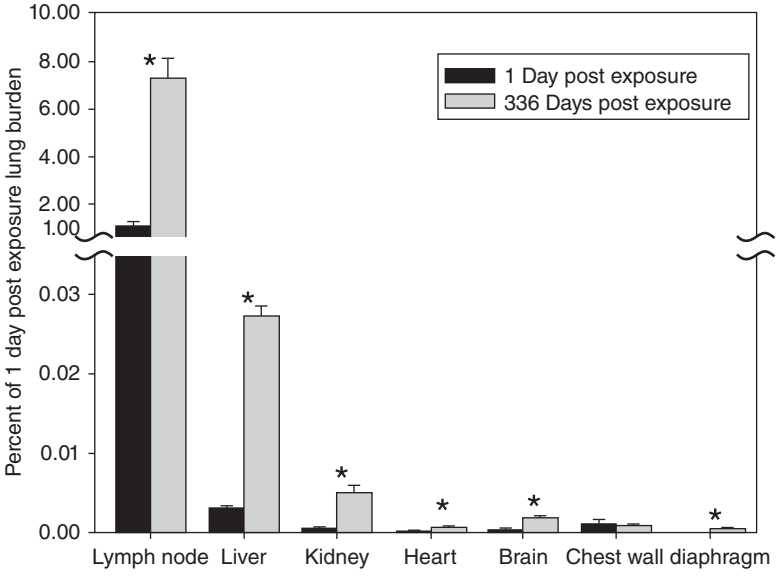

Figure 6.5 Percentage of the lung burden 1 day post exposure detected in tracheobronchial lymph nodes, extra-pulmonary organs, diaphragm, and chest wall. By 336 days post exposure, there was a sevenfold increase in MWCNTs in extra-pulmonary organs and diaphragm, compared to that measured at 1 day post exposure. Categories of extra-pulmonary organs are ordered relative to MWCNT concentration in the respective tissue. Asterisks indicate significant difference between day 1 and 336 days post exposure, $p < 0.05$. (Reprinted from [34].)

using a rat model showed that intratracheal instillation of MWCNTs led to translocation of the nanomaterials to the right and left posterior mediastinal lymph nodes, as well as some accumulation in the parathymic lymph nodes. The deposition of MWCNTs in the lymph nodes was found to increase gradually and dose-dependently with time [59].

Czarny *et al.* [60] reported a quantitative analysis of the tissue biodistribution of MWCNTs as a function of time. In this study, the authors utilized *in situ* ^{14}C-radiolabeled MWCNTs (20 μg per mouse) in combination with radioimaging of organ tissue sections for *ex vivo* electron microscopy analysis at regular intervals up to 1 year post exposure. It was observed that the MWCNTs were cleared slowly from the lungs. Translocation of MWCNTs increased over time, with MWCNTs being observed in numerous organs, notably the white pulp of the spleen and the bone marrow [60]. Another study evaluated the ability of MWCNTs to induce extra-pulmonary toxicities in rats following intratracheal instillation of two different types of MWCNTs into the lungs (0.2, 1, and 5 mg kg^{-1} body weight). Upon histopathological examination, it was found that each of the MWCNTs caused a dose-dependent toxic effect in the liver, including periportal lymphocytic infiltration, ballooning, foamy degeneration, and necrosis at each

time point analyzed post exposure, while examination of the kidney revealed toxicity at the dose of 5 mg kg^{-1} at 1 month post instillation of both MWCNTs [61]. These results further demonstrate the ability of carbon nanoparticles to translocate to other organs and induce potentially toxic effects.

Translocation ability of inhaled nanoparticles also seems to be dependent on the type of particle analyzed as well as the amount of time until examination. In contrast to the aforementioned CNT studies, inhaled ultrafine carbon particles have been shown to be retained in the lung periphery and conducting airways without substantial systemic translocation or accumulation in the liver at 48 h post exposure [56]. In agreement with these findings, another report compared the bioaccumulation of iridium and carbon nanoparticles and found low but significant accumulation of two different sized iridium aggregates in the liver, spleen, kidneys, heart, and brain, as well as within soft tissue and bone. However, the authors observed only a very modest amount of carbon nanoparticle retention within these same organs at 24 h post exposure [28]

6.3.3
Clearance of Carbon Nanomaterials from the Lungs

Particles deposited in the airways are typically cleared by the mucociliary escalator transport that sweeps the particles up to the pharynx where they are subsequently swallowed, phagocytized by macrophages, or translocated through to the lymphatics. The main clearance mechanism of insoluble nanoparticles deposited in the tracheobronchial tree is via the mucocilary escalator and is rapid. Clearance of particles deposited in the alveolar spaces is via macrophage phagocytosis and is slower. The efficacy of this mechanism depends largely on the particle size and shape and whether agglomeration of the particles has occurred. As discussed earlier, several experimental studies in rodents have shown that well-dispersed carbon nanoparticles are poorly cleared by macrophage phagocytosis, the result being substantial accumulation of the CNTs within the alveoli and migration to the alveolar interstitium [23].

Lung retention or clearance of pulmonary-exposed solid particles depends primarily on the particle size and clearance capacity; compared to larger particles having the same chemical composition, inhaled nanoparticles show greater lung retention. After deposition in the lungs, nanoparticles can be cleared through several processes or may be redistributed to secondary target organs such as lymph nodes [34, 59, 62] and pleural sites [47, 51], and to distant organs [34, 63], which could be in a particle size-dependent manner [28]. As early as 1 day post exposure, the content of pulmonary exposed MWCNT fibers in the tracheobronchial lymph nodes was found principally in the form of singlets or a few fibers per MWCNT structure and accounted for 1.08% of the lung burden 1 day post exposure. MWCNT structures in tracheobronchial lymph nodes at 336 days included foci with dense accumulations with the content being substantially increased and equal to 7.34% of the lung burden 1 day post exposure (Figure 6.5, [34]). Deposition of intratracheally instilled MWCNT was greater in

the posterior mediastinal lymph node than in the parathymic lymph node and was dose-dependent [59].

Carbon graphite whiskers (CGWs) were used in a 1-year inhalation study in male Wistar rats, and the biological effects were observed until the 1-year clearance period. Only ~30% of the total deposited CGWs were cleared during the 1-year postexposure period [64]. Several studies have sought to determine the retention time of carbon nanoparticles in the lungs. For example, Oyabu *et al.* [65] used rats that were exposed to well-dispersed MWCNTs for 4 weeks via whole-body inhalation at the exposure concentration of $0.37 \pm 0.18\,\mathrm{mg\,m^{-3}}$. It was noted that ~70% of the exposed MWCNTs were single fibers with the geometric mean diameter and length of 63 nm and 1.1 μm, respectively. As determined by X-ray diffraction and elemental carbon analysis, the amounts of MWCNT deposited in the rat lungs at 3 days post inhalation were calculated to be 68 μg per lung (X-ray diffraction) and 76 μg per lung (elemental carbon analysis). Thus, the calculated deposition fractions were 18% and 20% in each analysis. After 3 months, the amount of retained MWCNT in the lungs sharply decreased with the calculated biological half-times of 51 days and 54 days, respectively [65]. In contrast, SWCNT aspiration studies carried out by Shvedova *et al.* (2014) showed that SWCNTs or CNFs can be seen in the lung at 1 year post exposure, suggesting the slow clearance of these particles from the lung [39]. Therefore, the low clearance rate and repeated exposure of carbon nanoparticles may result in significant pulmonary accumulation. Interestingly, Kagan *et al.* [66] recently demonstrated that SWCNTs may undergo oxidative biodegradation via superoxide/NO* → peroxynitrite-driven oxidative pathways, and thus may facilitate clearance of nanoparticles from the lung as macrophages "digest" the CNTs [66]. Consistently, several other studies have also reported that the process of enzymatic digestion of CNTs that may aid in their clearance from the lung [41, 42, 66]. Although these studies, and others, have shed some light on the mechanisms of clearance and retention of carbon nanomaterials within the lungs, the large number of different types of carbon nanoparticles, as well as the physicochemical properties of these NPs that can affect these processes, make it clear that additional studies are needed to fully understand the biological outcomes of the exposures.

6.4 Carbon Nanomaterial–Induced Lung Responses

6.4.1 Key/Specific Target Lung Cell Types of Pulmonary-Exposed Carbon Nanoparticles

Inflammation occurs as a result of an insult that activates the innate immune system, leading to the release of cytokines and chemokines, which makes inflammatory cells to respond to the insult or injury. These cells usually include neutrophils and macrophages, which can engulf foreign pathogens to aid in their

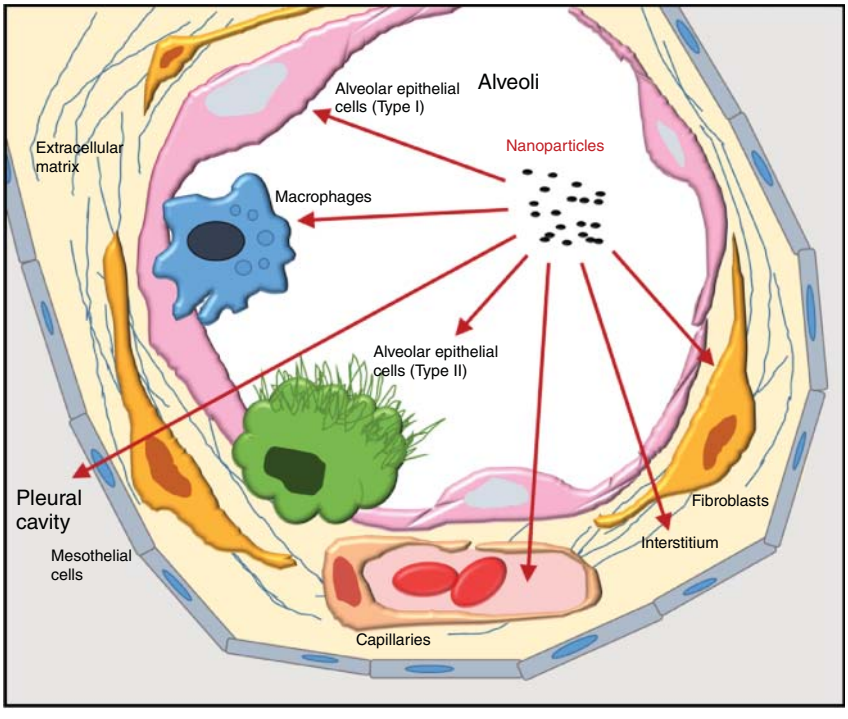

Figure 6.6 Lung cells potentially affected by inhalation of nanoparticles.

clearance. This innate inflammatory response helps to induce activation of the adaptive/humoral response mediated by T cells and B cells, which coordinate the production of antibodies to promote the clearance of foreign pathogens. For carbon nanoparticles, as discussed earlier, the main route of exposure for humans is via inhalation, often resulting in a rapid innate immune response within the lung to recruit phagocytic cells to clear the material. Thus, the major cell types involved in the immune response to these particles generally include alveolar macrophages and, to some degree, neutrophils [62, 67]. Other lung cells are also affected, primarily alveolar epithelial cells, fibroblasts, and possibly pleural mesothelial cells (Figure 6.6). These cells types are able to release various inflammatory mediators, and aberrant stimulation of these cell types is believed to contribute to the development of diseases such as fibrosis or cancer [62, 68].

In terms of cellular interactions with carbon nanoparticles, again, it seems that the particle type and size may play a role. For example, in one study, three different MWCNTs (one short (850 nm) and tangled, and two longer (4 and 5.7 μm) and thicker) were intratracheally instilled into mice and were analyzed for cellular interactions 1, 3, and 28 days after instillation. TEM analysis revealed that all three CNTs were taken up either by a diffusion mechanism or via

endocytosis, and subsequently agglomerated within vesicles in macrophages. However, at 28 days post exposure, the longer and thicker MWCNTs were able to more efficiently escape the vesicular enclosures in macrophages compared to the smaller CNTs, and resulted in more severe eosinophil influx and incidence of eosinophilic crystalline pneumonia [69]. Thus, the target cell types as well as the responses of those cells are likely to differ depending on the characteristics of the nanoparticle.

6.4.2 Lung Inflammation

A large percent of human exposures to respirable carbon nanomaterials is thought to occur as a result of the manufacturing process in an occupational setting, and, as such, several studies have been conducted in an effort to determine whether these working conditions cause lung inflammation or disease. Consistent with this notion, nano-scaled CB particle exposure was found to be the likely cause for reduced lung function and pro-inflammatory cytokine secretion in CB workers, and animals exposed to aerosolized CB particles showed alveolar wall thickening and a significant increase of inflammatory cells in lung tissues after CB exposure [70, 71].

Another study conducted by Lee *et al*. [72] investigated the health effects of MWCNTs in a manufacturer's facility, which included an assessment of the personal and area-specific exposure levels to MWCNTs, as well as exhaled breath condensates (EBCs) and lung function tests from the manufacturing and office workers at the facility. Exposure levels to elemental carbon were found to be $6.2-9.3\,\mathrm{mg\,m^{-3}}$ in the personal samplings and $5.5-7.3\,\mathrm{mg\,m^{-3}}$ in the area samplings. All workers were found to have normal blood chemistry readings as well as normal lung function parameters; however, the EBC analysis revealed increased levels of malondialdehyde (MDA) and 4-hydroxy-2-hexenal (4-HHE), which are markers of oxidative stress and lipid peroxidation, respectively, in the MWCNT manufacturing workers compared to the office workers [72].

Animal models have also been used in an effort to examine the lung inflammatory responses to carbon nanoparticles. Several studies have observed significant lung inflammation and damage at 1 day post MWCNT exposure in rodent models [33, 52]. Interestingly, numerous studies have noted little or transient inflammatory responses but with rapid and persistent interstitial fibrosis or granulomas at the sites of deposition of nanoparticle agglomerates [2, 23, 25, 48, 52, 59, 73, 74]. Similarly, accumulating data also reveal that pulmonary exposure of animals to carbon nanomaterials leads to acute neutrophilic inflammation [24, 75]. Collectively, this would suggest that following exposure to carbon nanoparticles, acute and transient inflammation would primarily serve to recruit macrophages and neutrophils for phagocytosis of the particles, which can ultimately lead to granuloma formation and fibrosis.

Consistently, several studies have observed the formation of granulomas in response to carbon nanomaterials. Warheit *et al*. [76] noted that agglomerated

SWCNTs (with or without metallic residues) induced an inflammatory response with granulomas surrounding the nanotubes, indicating pulmonary toxicity [76]. Similar granulomas were found in rats intratracheally instilled with SWCNTs, although the inflammation resolved within 3 months [23, 25]. Another 90-day study reported granulomatous inflammation, with macrophage and T-cell infiltration, that persisted up to 90 days, and the authors noted a marked elevation in osteopontin, metalloproteinases, and cell adhesion molecules in granulomatous foci, as well as alveolar macrophages from bronchoalveolar lavage [77].

6.4.3 Immune Response

In terms of immune response, in addition to inflammation, CNT exposure may actually enhance allergic asthma induction. For instance, Inoue *et al.* [78] reported that MWCNTs administered intratracheally significantly increased ovalbumin-induced T-lymphocyte proliferation and amplified lung Th_2 cytokines and chemokines as compared with ovalbumin exposure alone [78]. Work by Park *et al*. showed that MWCNT instillation activated alveolar macrophages, resulting in the attraction of immune cells to the BAL fluid. Pro-inflammatory cytokines (IL-1, TNF-α, and IL-6), Th1-type cytokines (IL-12 and IFN-γ), and Th2-type cytokines (IL-4, IL-5, and IL-10) were increased both in BAL fluids and in blood. Differentiation of CD4+ T cell to Th1 cells and Th2 cells were triggered by IL-12 and IL-4, respectively. The elevated numbers of B cells activated by IL-10 were then involved in the production of IgE. This combination of responses may have caused the allergic reactions observed in the mice treated with MWCNTs [79]. Another study determined that exposure of mice to ovalbumin before inhalation of MWCNTs caused significant airway fibrosis in an allergic asthma mouse model, whereas ovalbumin or MWCNTs alone did not significantly increase airway fibrosis in these mice [80].

Similarly, Ronzani *et al*. (2014) investigated the effect of MWCNTs on the immune responses and reported that MWCNT exposure resulted in the aggravation of airway inflammation and remodeling and in increased production of epithelium-derived innate cytokines in a mouse model of asthma. In this study, using a common asthma-causing allergen, namely the house dust mite (HDM), the authors examined common markers of asthma such as the production of the innate cytokines, thymic stromal lymphopoietin (TSLP), IL-25, IL-33, and GM-CSF, as well as the influx of macrophages, eosinophils, and neutrophils, and the production of collagen, transforming growth factor beta 1 (TGF-β1), and mucus. BALB/cByJ mice were exposed by intranasal instillation to HDM + MWCNT and compared with those exposed to HDM alone. The results showed that HDM-treated mice exhibited specific IgG1 in serum and inflammatory cell infiltration as well as increased Th2 cytokine production, mucus hyperproduction, and collagen deposition in the airways when compared to naïve animals. In mice exposed to HDM + MWCNT, the levels of total IgG1, HDM-specific IgG1, IL-13, eotaxin, TARC influx of macrophages, eosinophils, and neutrophils, and production of

collagen, TGF-β1, and mucus were dose-dependently increased compared to those exposed to HDM alone [82]. These results demonstrate that pulmonary exposed MWCNTs increase immune responses in a dose-dependent manner, as well as airway allergic inflammation and remodeling induced by HDM in the mouse.

Overall, there is limited information on pulmonary exposed, carbon nanomaterial–induced systemic immune responses. It is unknown whether CNTs will cause or exacerbate asthma in humans.

6.4.4 Fibrosis

Lung fibrosis has been observed, in varying degrees of severity, in a number of rodent lung models exposed to carbon nanoparticles. Fibrosis is primarily characterized by two main pathological features, that is, excessive accumulation of extracellular matrix proteins such as collagen, and the uncontrolled proliferation of fibroblasts, which together lead to remodeling of the lung architecture [82]. Given the fact that once fibrosis develops there are currently no effective therapeutic treatment options, it is important to consider the fibrogenic potential of all emerging nanotechnologies.

In the case of CNTs, numerous studies have been conducted to determine the fibrogenicity of these nanomaterials. Intratracheal instillation or pharyngeal aspiration of CNT suspensions, which agglomerate into micrometer-sized bundles in aqueous media, stimulates the formation of inflammatory foci known as granulomas within the lung parenchyma. These granulomas, containing fibrotic collagen, have been reported in mice or rats within days of exposure [2, 25, 73, 75, 76]. Interestingly, well-dispersed CNTs resulted in less deposition in the large airways and fewer granulomas. However, more dispersed CNTs exhibited augmented deposition in the deep lung, their migration to the alveolar interstitium, and significantly increased alveolar interstitial fibrosis [23, 25].

Short-term exposure to double-walled CNTs produced dose-dependent pulmonary inflammation, cytotoxicity, and decreased the integrity of blood–gas barrier in the lung, in addition to inducing significant alveolitis and fibrosis in mice at 7 and 56 days post exposure [83]. When considering more long-term effects of carbon nanoparticles, Shvedova *et al.* (2014) recently examined the effects of SWCNTs, CNFs, and asbestos on lung pathology 1 year after a bolus dose of particles via pharyngeal aspiration or through inhalation at 5 h per day for 4 days. The authors could observe substantial levels of particles in the lungs 1 year post exposure, with some in the lymphatic system. Additionally, each of the particles induced chronic bronchopneumonia and lymphadenitis, accompanied by pulmonary fibrosis. On an equal mass basis, SWCNTs were the most fibrogenic of all of the particles tested. Inhalation of SWCNTs was also found to be fibrotic, inflammatory, and genotoxic [39].

Another 13-week study in a rat model used whole-body inhalation to MWCNTs at the concentrations of 0, 0.2, 1, and 5 mg m^{-3} with mass median aerodynamic

diameter of 1.4–1.6 μm, mean width of 94.1–98.0 nm, and mean length of 5.53–6.19 μm, respectively [74]. They observed that inflammatory parameters increased in a concentration-dependent manner from 0.2 mg m^{-3}. Granulomatous changes in the lung were induced at 1 and 5 mg m^{-3} in female rats, and at even a lower dose of 0.2 mg m^{-3} in males. Focal fibrosis of the alveolar wall was observed in both sexes at 1 mg m^{-3} or higher. Moreover, inflammatory infiltration in the visceral pleural and subpleural areas was induced only at 5 mg m^{-3}.

In terms of the mechanism of carbon nanoparticle–induced fibrosis, several theories have been proposed. For example, these bioeffects could be ROS-related. In $ApoE^{-/-}$ transgenic mice, which is a common model for atherosclerosis, examination of the aorta after 7, 28, and 60 days showed mitochondrial DNA damage and oxidative stress after a single intratracheal instillation of SWCNTs [84, 85]. Shvedova *et al*. also recently reported that lipid-derived free radicals contribute to tissue damage induced by SWCNTs, not only in the lungs but also in other organs [86]. Others have postulated, based on the evidence that well-dispersed CNTs can penetrate the alveolar epithelial barrier and enter the interstitium, that carbon nanoparticles may have a direct effect on fibroblasts. Such migration of dispersed SWCNTs or MWCNTs has been reported [23, 33, 34]. As the main producers of collagen, aberrant stimulation of fibroblasts by carbon nanomaterials could induce a fibrotic response. Indeed, *in vitro* analysis using individual lung cell types support the notion that CNTs can directly stimulate fibroblast cell proliferation and collagen production, a hallmark of fibrogenesis [32]. It is also noteworthy, as previously mentioned, that numerous studies have noted little or only transient inflammatory responses to CNTs, but with rapid onset of interstitial fibrosis or granulomas at the sites of nanoparticle deposition [2, 23–25, 48, 52, 59, 73, 74]. This may also support the idea that CNT-induced fibrosis occurs, at least in large part, as a result of the direct stimulation of fibroblasts by these materials without an overt inflammatory response *in vivo* [23, 73].

6.4.5 Genotoxicity

Several studies have observed some degree of genotoxicity in response to carbon nanomaterials, primarily CB. Kyjovska *et al*. [87] reported statistically significant increases in DNA strand breaks in mouse lung BAL cells after a single exposure to CB at the doses of 0.67–6 mg per mouse at 1–28 days post exposure. This DNA damage was found to be primary genotoxicity, which occurred in the absence of inflammation and cell damage, indicating that inflammation is not required for the genotoxic effects of CB [87]. Similarly, another study found that deposition of CB nanoparticles in the lung induced persistent inflammatory and genotoxic effects in mice, not only in the lung but also in other organs such as the liver [88]. Interestingly, this same group found that CB had no effect on cardiac cell gene expression [89]. Collectively, these results suggest that carbon nanoparticles may

induce genotoxicity and highlight the need for additional studies to shed light on this notion.

6.4.6 Cancer

The similarities of CNTs and nanofibers to asbestos in terms of their fiber-like morphology, durability, and high aspect ratio present new challenges to assess, understand, and manage potential adverse health effects caused by human exposure. As discussed throughout this chapter, substantial evidence from mammalian toxicity studies indicates that inhalation exposure to this class of engineered nanoparticles can cause adverse pulmonary effects. Thus, the ability of CNTs to induce cancer has also been the subject of frequent studies.

In the case of CNTs, studies have found that these particles demonstrate carcinogenic characteristics in rodent models. By utilizing a two-stage initiation/promotion protocol *in vivo* to determine carcinogenic potential of CNTs, Sargent *et al*. [68] reported for the first time that some MWCNT exposures, but not vehicle control, promoted the growth and neoplastic progression of initiated lung cells in B6C3F1 mice that received a single intraperitoneal (IP) injection of the initiator methylcholanthrene (MCA, 10 μg g^{-1} BW). IP injection of MCA was followed 1 week later by inhalation of MWCNTs (5 mg m^{-3}, 5 h per day, 5 days per week) or filtered air (controls) for a total of 15 days (MWCNT lung burden of 31.2 μg per mouse approximates feasible human occupational exposures). At 17 months post treatment, 23% of the filtered air controls and 26.5% of the MWCNT-exposed, 51.9% of the MCA-exposed, and 91% of the MCA/MWCNT-exposed mice had lung tumors. Furthermore, 62% of the mice exposed to MCA followed by MWCNT had bronchiolo-alveolar adenocarcinomas compared to 13% of the mice that received filtered air, 22% of the MCA-exposed, or 14% of the MWCNT alone-exposed animals [68]. Consistently, chronic *in vitro* studies using cultured human lung epithelial or mesothelial cells support this finding, with results demonstrating that CNTs can stimulate cell proliferation, migration/invasion, and colony formation, and that SWCNT-transformed human bronchial epithelial cells (BEAS-2B) can form tumors in mice [90].

Other studies have also detected the carcinogenic potential of CNTs. For example, MWCNTs or crocidolite (asbestos) fibers administered as a single intraperitoneal injection in mice induced mesothelioma in 15.8% (3/19) and 31.6% (6/19) of $p53^{+/-}$ animals, respectively [91]. In contrast, no cases of mesothelioma were seen among $p53^{+/-}$ mice exposed to fullerene nanoparticles or unexposed $p53^{+/-}$ mice [68, 91]. Moreover, Shvedova *et al*. [92] reported that exposure to SWCNTs induced recruitment and accumulation of lung-associated, myeloid-derived suppressor cells (MDSC) and MDSC-derived production of

TGF-β, leading to increased tumor burden in the lung. The authors concluded that pulmonary exposure to SWCNTs aids in the formation of a niche that supports lung carcinoma *in vivo* via induction of TGF-β by SWCNT-attracted and presensitized lung-associated MDSC [92]. This group also demonstrated that SWCNTs and CNFs, but not asbestos, increased the incidence of K-ras oncogene mutations in the lung of mice 1 year post exposure; however, no increased lung tumor incidence occurred in this time [39].

As previously mentioned, the similar morphologies of CNTs and asbestos leave many wondering about the potential for CNTs to induce asbestos-like health hazards such as pleural inflammation, fibrosis, and mesothelioma. Length-dependent pathogenicity is a feature of asbestos. A general mechanism for fiber pathogenicity in the pleural cavity is related to the size-restricted clearance mechanisms from the pleural space and the subsequent selective retention of long fibers [93]. This mechanism is independent of chemical composition, other than how chemical composition affects biopersistence, and has been validated by the fact that a number of different fiber types, including asbestos, CNTs, and a number of nanowires, all generate a length-dependent inflammatory response after direct injection into the pleural or peritoneal cavities [36, 94, 95]. The results presented by Murphy *et al*. [94] support a length-dependent pathogenicity of CNTs in the lungs and pleural space following airspace deposition, similar to asbestos. These data support the contention that long CNTs reach the pleura from the airspaces and that they are retained at the parietal pleura and cause inflammation and lesion development. The parietal pleura is the site of origin of mesothelioma, and inflammation is considered to be a process involved in asbestos-induced carcinogenesis. Thus, these data support the assertion that CNTs may pose an asbestos-like mesothelioma hazard [94], indicating that this should be explored in greater detail. Indeed, the study mentioned above demonstrated that MWCNTs administered as a single intraperitoneal injection in mice induced mesothelioma in 15.8% (3/19) and 31.6% (6/19) of $p53^{+/-}$ animals, respectively [68, 91]. The International Agency for Research of Cancer has classified Mitsui-7 MWCNT as class 2B, that is, a possible human carcinogen [96].

Additional studies have been carried out to evaluate the carcinogenicity of other carbon nanomaterials such as CB. Carbon black is widely used in numerous industrial applications, including the production of rubber, tires, paints, toners, and printing inks, and this particle has been classified as a possible human carcinogen (group 2B) by the International Agency for Research on Cancer [96, 97]. In addition, there is evidence for carcinogenicity in rats, together with supporting evidence from human data of structurally related substances, and thus the European Union (EU) criteria for category 2 of carcinogenic substances appear to be fulfilled for bio-durable nanoparticles consisting of matter without known significant specific toxicity [98, 99]. Using rat models, it has been estimated that airborne UFCB concentrations of approximately $0.07-0.3\ \mathrm{mg\ m^{-3}}$ over a lifetime of working conditions are associated with a 0.1% excess risk of lung cancer [100].

6.4.7
Cardiovascular Effects Following Pulmonary Exposure of Carbon Nanomaterials

Induction of the acute-phase response following pulmonary deposition of different kinds of particles, including carbon nanoparticles, is closely linked to risks for cardiovascular diseases, as shown in both epidemiological and animal studies [101]. Blood levels of acute-phase proteins, such as C-reactive protein and serum amyloid A, have been found to be independent predictors of the risk of cardiovascular disease in prospective epidemiological studies [102]. Indeed, inhalation and instillation of numerous nanoparticles, including SWCNTs, MWCNTs, and CB, have been shown to induce pulmonary acute-phase responses [67, 103–109]. In addition, inhalation of MWCNT has been shown to depress the ability of coronary arterioles to respond to dilators [63]. Taken together the studies reviewed herein, it is plausible that exposure to carbon nanoparticles increases the risk of cardiovascular disease.

6.5
Summary

Nanotechnology is a fast growing field that has developed a demand for carbon nanomaterials with novel physicochemical properties for a broad array of applications. Knowledge of their unique bioeffects once exposed to the lung are still limited and critically needed to ensure safe implementation of nanotechnology for utility within the medical field, as well as standards for unintentional pulmonary exposure. Available data from the literature of pertinent pulmonary response studies of carbon nanomaterials suggest that inhaled nano-scaled carbon materials can deposit deep in the lung tissue and distribute into the alveolar interstitium where micrometer-sized particles generally cannot reach. They have also been found in the pleural area, similar to asbestos, and at extra-pulmonary locations but with low translocation rate from the lung. The degree of toxic effects, such as inflammation, lung cell cytotoxicity and genotoxicity, lung fibrosis, and carcinogenic potential, seem to be largely physicochemical property-dependent, highlighting the ever-growing challenge of thoroughly assessing the potential hazards of this expanding area of nanotechnology. A summary of pulmonary toxicology studies for carbonaceous nanoparticles is given in Table 6.1.

Disclaimer

The findings and conclusions in this report are those of the authors and do not necessarily represent the views of the National Institute for Occupational Safety and Health.

Table 6.1 Summary of studies on pulmonary effects of carbon nanomaterials.

Type of carbon nanomaterial	Sources	Animal model	Exposure dose/method	Exposure time	Major findings	References
Carbon black	Evonik Industries, Hanau, Germany	Female BALB/c mice	Single or 8 oropharyngeal aspirations at week 1–3, 5, 7, 9, 11, and 12 using 7 μg Printex 90, 7 μg DQ12 quartz (as a positive control)	2-Day and 3-month post-exposure analysis	Multiple CBNP applications produced: • Reduced lung function • Collagen accumulation • Elevated phospholipid levels in BALF, and a massive infiltration of macrophages • Type II pneumocyte mRNA expression of antioxidative enzymes remained unchanged throughout the subchronic experiment, but showed a significant decrease in interleukin (IL)-6Rα mRNA expression	[70]
SWCNT	CNI, Inc.	C57BL/6J mice	Single pharyngeal aspiration of 0, 10, 20, and 40 μg per mouse	1, 3, 7, 28, and 60 days post-exposure analysis	• Robust but acute inflammation with early onset, yet progressive, fibrosis and granulomas • Interstitial fibrosis and alveolar wall thickening	[23, 25, 32, 110]
SWCNT (effect of length)	Cheap Tubes Inc., Brattleboro, VT, USA	C57BL/6J mice	Single pharyngeal aspiration 40 μg per mouse	90 Days post-exposure analysis	• Long SWCNTs were significantly more potent than short SWCNTs at inducing fibrogenesis	[38]

(*continued overleaf*)

Table 6.1 (*Continued*)

Type of carbon nanomaterial	Sources	Animal model	Exposure dose/method	Exposure time	Major findings	References
MWCNT	Mitsui and Co., Japan	C57BL/6J mice	Single pharyngeal aspiration 0, 10, 40, and 80 μg per mouse lung	1, 7, 28, and 56 Days post-exposure analysis	• Pulmonary inflammation was dose-dependent and peaked at 7 days post exposure • Rapid development of pulmonary fibrosis by 7 days post exposure • Granulomatous inflammation persisted throughout the 56-day post-exposure period • MWCNT can reach the pleura after pulmonary exposure • Lung burden was predominately within alveolar macrophages (~8% delivery to the alveolar septa; and a smaller burden in subpleural tissues) • Average thickness of connective tissue in the alveolar septa increased 45% in the 40 μg and 73% in the 80 μg exposure groups	[48, 52]
MWCNT	Hodogaya Chemical Company (MWNT-7, lot #061220-31)	C57BL/6J	Inhalation 5 mg m^{-3} aerosol for 5 h per day	(Four times per week for 3 weeks, lung burden = 28.1 μg per lung)	• Dose-dependent pulmonary inflammation • Rapid development of pulmonary fibrosis • Transported to the parietal pleura, the respiratory musculature, liver, kidney, heart, and brain in a singlet form and accumulate with time following exposure • The tracheobronchial lymph nodes contain high levels of MWCNT following exposure and further accumulate over nearly a year	[33, 34]

MWCNT	Mitsui and Co., Japan	B6C3F1 mice	Inhalation of 5 mg m^{-3}, 5 h per day, 5 days per week for 15 days (lung burden of 31.2 µg per mouse) 1 week after i.p. initiator methylcholanthrene (10 µg g^{-1} BW; i.p.)	17 months post-treatment analysis	• MWCNT exposures promote the growth and neoplastic progression of initiated lung cells in B6C3F1 mice	[68]
MWCNT	Helix Material Solutions, Inc. (Richardson, TX)	C57BL/6J mice and ovalbumin-sensitized mice	Aerosol (100 mg m^{-3}) or saline aerosol for 6 h	1 and 14 days post-inhalation analysis	• Airway fibrosis which required preexisting inflammation	[80]
Functionalized MWCNT: COOH; PEG; NH_2; sidewall NH_2; PEI-modified	Raw CNTs from Cheap Tubes, Inc., Own modified	C57BL/6 mice	2 mg kg^{-1} Body weight	21 Days	• Fibrogenic effects in the following sequence: Anionic (COOH and PEG) < pristine ≈ neutral < strong cationic (PEI)	[43]
MWCNT: COOH	Nanostructured and Amorphous Materials, Inc., Houston, TX. Own modified MWCNT-COOH	C57BL/6 mice	Single pharyngeal aspiration of 0, 2.5, 10, or 40 µg per mouse	1, 7, and 56 Days post-exposure analysis	• Functionalized COOH significantly reduced inflammation and lung fibrosis	[44]

(*continued overleaf*)

Table 6.1 (*Continued*)

Type of carbon nanomaterial	Sources	Animal model	Exposure dose/method	Exposure time	Major findings	References
Fullerene	Henan University, China	Sprague–Dawley (SD) rats	Intratracheal instillation of 3.7×10^7 Bq ^{99m}Tc-C_{60}(OH)x and $Na^{99m}TcO_4$ in 0.3 ml volume		• Large proportion of the ^{99m}Tc-c060(OH)x was retained in the lung • Transient penetration of the alveolar–capillary barrier by the ^{99m}Tc-c060(OH)x with some translocation into the blood • Uptakes in the liver, bone, and spleen	[12, 111]
Graphene	Cabot	C57BL/6 mice	Single pharyngeal aspiration of 4 or 40 μg three different sized graphene (Gr1, Gr5, or Gr20)/mouse	4 h (day 0), 1, 7, and 28 days postexposure	• Acute inflammation and lung damage • Larger Gr particles appeared to produce more toxicity at the early time points post exposure when compared to controls	[112]

References

1. Oberdorster, G. (2010) *J. Intern. Med.*, **267**, 89.
2. Lam, C.W., James, J.T., McCluskey, R., and Hunter, R.L. (2004) *Toxicol. Sci.*, **77**, 126.
3. Zhang, B.T., Zheng, X., Li, H.F., and Lin, J.M. (2013) *Anal. Chim. Acta*, **784**, 1.
4. Lin, T., Bajpai, V., Ji, T., and Dai, L. (2003) *Aust. J. Chem.*, **56**, 635.
5. Maynard, A.D., Baron, P.A., Foley, M., Shvedova, A.A., Kisin, E.R., and Castranova, V. (2004) *J. Toxicol. Environ. Health A*, **67**, 87.
6. Johnson, D.R., Methner, M.M., Kennedy, A.J., and Steevens, J.A. (2010) *Environ. Health Perspect.*, **118**, 49.
7. Han, J.H., Lee, E.J., Lee, J.H., So, K.P., Lee, Y.H., Bae, G.N., Lee, S.B., Ji, J.H., Cho, M.H., and Yu, I.J. (2008) *Inhalation Toxicol.*, **20**, 741.
8. Methner, M.M. (2008) *J. Occup. Environ. Hyg.*, **5**, D63.
9. Maynard, A. and Kuempel, E.D. (2005) *J. Nanopart. Res.*, **7**, 587.
10. McClellan, R.O. (2000) in *Particle-Lung Interactions*, 1st edn (eds P. Gehr and J. Heyder), Marcel Dekker.
11. Castranova, V. (2011) *J. Occup. Environ. Med./Am. Coll. Occup. Environ. Med.*, **53**, S14.
12. Kumar, V., Kumari, A., Guleria, P., and Yadav, S.K. (2012) *Rev. Environ. Contam. Toxicol.*, **215**, 39.
13. Donaldson, K., Aitken, R., Tran, L., Stone, V., Duffin, R., Forrest, G., and Alexander, A. (2006) *Toxicol. Sci.*, **92**, 5.
14. Xu, J., Alexander, D.B., Futakuchi, M., Numano, T., Fukamachi, K., Suzui, M., Omori, T., Kanno, J., Hirose, A., and Tsuda, H. (2014) *Cancer Sci.*, **105**, 763.
15. Morimoto, Y., Horie, M., Kobayashi, N., Shinohara, N., and Shimada, M. (2013) *Acc. Chem. Res.*, **46**, 770.
16. Pacurari, M., Castranova, V., and Vallyathan, V. (2010) *J. Toxicol. Environ. Health A*, **73**, 378.
17. Rodriguez, N.M., Chambers, A., and Baker, R.T.K. (1995) *Langmuir*, **11**, 3862.
18. Hamilton, R.F. Jr., Wu, Z., Mitra, S., Shaw, P.K., and Holian, A. (2013) *Part. Fibre Toxicol.*, **10**, 57.
19. Donaldson, K. and Tran, C.L. (2002) *Inhalation Toxicol.*, **14**, 5.
20. Tran, C.L., Buchanan, D., Cullen, R.T., Searl, A., Jones, A.D., and Donaldson, K. (2000) *Inhal. Toxicol.*, **12**, 1113.
21. Duffin, R., Tran, C.L., Clouter, A., Brown, D.M., Macnee, W., Stone, V., and Donaldson, K. (2002) *Ann. Occup. Hyg.*, **46**, 242.
22. Poulsen, S.S., Saber, A.T., Williams, A., Andersen, O., Kobler, C., Atluri, R., Pozzebon, M.E., Mucelli, S.P., Simion, M., Rickerby, D., Mortensen, A., Jackson, P., Kyjovska, Z.O., Molhave, K., Jacobsen, N.R., Jensen, K.A., Yauk, C.L., Wallin, H., Halappanavar, S., and Vogel, U. (2015) *Toxicol. Appl. Pharmacol.*, **284**, 16.
23. Mercer, R.R., Scabilloni, J., Wang, L., Kisin, E., Murray, A.R., Schwegler-Berry, D., Shvedova, A.A., and Castranova, V. (2008) *Am. J. Physiol. Lung Cell. Mol. Physiol.*, **294**, L87.
24. Shvedova, A.A., Kisin, E., Murray, A.R., Johnson, V.J., Gorelik, O., Arepalli, S., Hubbs, A.F., Mercer, R.R., Keohavong, P., Sussman, N., Jin, J., Yin, J., Stone, S., Chen, B.T., Deye, G., Maynard, A., Castranova, V., Baron, P.A., and Kagan, V.E. (2008) *Am. J. Physiol. Lung Cell. Mol. Physiol.*, **295**, L552.
25. Shvedova, A.A., Kisin, E.R., Mercer, R., Murray, A.R., Johnson, V.J., Potapovich, A.I., Tyurina, Y.Y., Gorelik, O., Arepalli, S., Schwegler-Berry, D., Hubbs, A.F., Antonini, J., Evans, D.E., Ku, B.K., Ramsey, D., Maynard, A., Kagan, V.E., Castranova, V., and Baron, P. (2005) *Am. J. Physiol. Lung Cell. Mol. Physiol.*, **289**, L698.
26. Shvedova A.A., Sager T., Murray A.R., Kisin E., Porter D.W., Leonard S.S., Schwegler Berry D., Robinson V.A., Castranova V. (2007) Critical issues in the evaluation of possible effects resulting from airborne nanoparticles. Nanotoxicology: Characterization, Dosing and Health Effects. *Monteiro-Riviere*

NA, Tran CL, eds., New York: Informa Healthcare:225–236.
27. Ellinger-Ziegelbauer, H. and Pauluhn, J. (2009) *Toxicology*, **266**, 16.
28. Kreyling, W.G., Semmler-Behnke, M., Seitz, J., Scymczak, W., Wenk, A., Mayer, P., Takenaka, S., and Oberdorster, G. (2009) *Inhalation Toxicol.*, **21** (Suppl. 1), 55.
29. Aijaz, S., Balda, M.S., and Matter, K. (2006) *Int. Rev. Cytol.*, **248**, 261.
30. Maier, M., Hannebauer, B., Holldorff, H., and Albers, P. (2006) *J. Occup. Environ. Med./Am. Coll. Occup. Environ. Med.*, **48**, 1314.
31. Porter, D.W., Sriram, K., Wolfarth, M.G., Jefferson, A., Schwegler-Berry, D., Andrew, M., and Castranova, V. (2008) *Nanotoxicology*, **2**, 144.
32. Wang, L., Mercer, R.R., Rojanasakul, Y., Qiu, A., Lu, Y., Scabilloni, J.F., Wu, N., and Castranova, V. (2010) *J. Toxicol. Environ. Health A*, **73**, 410.
33. Mercer, R.R., Scabilloni, J.F., Hubbs, A.F., Battelli, L.A., McKinney, W., Friend, S., Wolfarth, M.G., Andrew, M., Castranova, V., and Porter, D.W. (2013) *Part. Fibre Toxicol.*, **10**, 33.
34. Mercer, R.R., Scabilloni, J.F., Hubbs, A.F., Wang, L., Battelli, L.A., McKinney, W., Castranova, V., and Porter, D.W. (2013) *Part. Fibre Toxicol.*, **10**, 38.
35. Castranova, V., Porter, D., and Mercer, R. (2015) in *Nanoparticles in the Lung: Environmental Exposure and Drug Delivery* (eds A. Tsuda and P. Gehr), CRC Press.
36. Poland, C.A., Duffin, R., Kinloch, I., Maynard, A., Wallace, W.A., Seaton, A., Stone, V., Brown, S., Macnee, W., and Donaldson, K. (2008) *Nat. Nanotechnol.*, **3**, 423.
37. van Berlo, D., Wilhelmi, V., Boots, A.W., Hullmann, M., Kuhlbusch, T.A., Bast, A., Schins, R.P., and Albrecht, C. (2014) *Arch. Toxicol.*, **88** (9): 1725–37.
38. Manke, A., Luanpitpong, S., Dong, C., Wang, L., He, X., Battelli, L., Derk, R., Stueckle, T.A., Porter, D.W., Sager, T., Gou, H., Dinu, C.Z., Wu, N., Mercer, R.R., and Rojanasakul, Y. (2014) *Int. J. Mol. Sci.*, **15**, 7444.
39. Shvedova, A.A., Yanamala, N., Kisin, E.R., Tkach, A.V., Murray, A.R., Hubbs, A., Chirila, M.M., Keohavong, P., Sycheva, L.P., Kagan, V.E., and Castranova, V. (2014) *Am. J. Physiol. Lung Cell. Mol. Physiol.*, **306**, L170.
40. Taylor, A.J., McClure, C.D., Shipkowski, K.A., Thompson, E.A., Hussain, S., Garantziotis, S., Parsons, G.N., and Bonner, J.C. (2014) *PLoS One*, **9**, e106870.
41. Kotchey, G.P., Zhao, Y., Kagan, V.E., and Star, A. (2013) *Adv. Drug Deliv. Rev.*, **65** (15): 1921–32.
42. Zhao, Y., Allen, B.L., and Star, A. (2011) *J. Phys. Chem. A*, **115**, 9536.
43. Li, R., Wang, X., Ji, Z., Sun, B., Zhang, H., Chang, C.H., Lin, S., Meng, H., Liao, Y.P., Wang, M., Li, Z., Hwang, A.A., Song, T.B., Xu, R., Yang, Y., Zink, J.I., Nel, A.E., and Xia, T. (2013) *ACS Nano*, **7**, 2352.
44. Sager, T.M., Wolfarth, M.W., Andrew, M., Hubbs, A., Friend, S., Chen, T.H., Porter, D.W., Wu, N., Yang, F., Hamilton, R.F., and Holian, A. (2014) *Nanotoxicology*, **8**, 317.
45. Oberdorster, G., Oberdorster, E., and Oberdorster, J. (2005) *Environ. Health Perspect.*, **113**, 823.
46. Takenaka, S., Karg, E., Kreyling, W.G., Lentner, B., Moller, W., Behnke-Semmler, M., Jennen, L., Walch, A., Michalke, B., Schramel, P., Heyder, J., and Schulz, H. (2006) *Inhalation Toxicol.*, **18**, 733.
47. Mercer, R.R., Hubbs, A.F., Scabilloni, J.F., Wang, L., Battelli, L.A., Schwegler-Berry, D., Castranova, V., and Porter, D.W. (2010) *Part. Fibre Toxicol.*, **7**, 28.
48. Mercer, R.R., Hubbs, A.F., Scabilloni, J.F., Wang, L., Battelli, L.A., Friend, S., Castranova, V., and Porter, D.W. (2011) *Part. Fibre Toxicol.*, **8**, 21.
49. Li, J.G., Li, W.X., Xu, J.Y., Cai, X.Q., Liu, R.L., Li, Y.J., Zhao, Q.F., and Li, Q.N. (2007) *Environ. Toxicol.*, **22**(4), 415–21.
50. Semmler-Behnke, M., Takenaka, S., Fertsch, S., Wenk, A., Seitz, J., Mayer, P., Oberdorster, G., and Kreyling, W.G. (2007) *Environ. Health Perspect.*, **115**, 728.
51. Ryman-Rasmussen, J.P., Cesta, M.F., Brody, A.R., Shipley-Phillips, J.K.,

Everitt, J.I., Tewksbury, E.W., Moss, O.R., Wong, B.A., Dodd, D.E., Andersen, M.E., and Bonner, J.C. (2009) *Nat. Nanotechnol.*, **4**, 747.

52. Porter, D.W., Hubbs, A.F., Mercer, R.R., Wu, N., Wolfarth, M.G., Sriram, K., Leonard, S., Battelli, L., Schwegler-Berry, D., Friend, S., Andrew, M., Chen, B.T., Tsuruoka, S., Endo, M., and Castranova, V. (2010) *Toxicology*, **269**, 136.
53. Xu, J., Futakuchi, M., Shimizu, H., Alexander, D.B., Yanagihara, K., Fukamachi, K., Suzui, M., Kanno, J., Hirose, A., Ogata, A., Sakamoto, Y., Nakae, D., Omori, T., and Tsuda, H. (2012) *Cancer Sci.*, **103**, 2045.
54. Andujar, P., Lanone, S., Brochard, P., and Boczkowski, J. (2011) *Rev. Mal. Respir.*, **28**, e66.
55. Oberdorster, G. (2004) First International Symposium on Occupational Health Implications of Nanomaterials, Buxton, Derbyshire, UK, http://www.hsl.gov.uk/media/394200/nanosymrep_final.pdf
56. Moller, W., Felten, K., Sommerer, K., Scheuch, G., Meyer, G., Meyer, P., Haussinger, K., and Kreyling, W.G. (2008) *Am. J. Respir. Crit. Care Med.*, **177**, 426.
57. Oberdorster, G., Sharp, Z., Atudorei, V., Elder, A., Gelein, R., Lunts, A., Kreyling, W., and Cox, C. (2002) *J. Toxicol. Environ. Health A*, **65**, 1531.
58. Nemmar, A., Vanbilloen, H., Hoylaerts, M.F., Hoet, P.H., Verbruggen, A., and Nemery, B. (2001) *Am. J. Respir. Crit. Care Med.*, **164**, 1665.
59. Aiso, S., Kubota, H., Umeda, Y., Kasai, T., Takaya, M., Yamazaki, K., Nagano, K., Sakai, T., Koda, S., and Fukushima, S. (2011) *Ind. Health*, **49**, 215.
60. Czarny, B., Georgin, D., Berthon, F., Plastow, G., Pinault, M., Patriarche, G., Thuleau, A., L'Hermite, M.M., Taran, F., and Dive, V. (2014) *ACS Nano*, **8**, 5715.
61. Reddy, A.R., Krishna, D.R., Reddy, Y.N., and Himabindu, V. (2010) *Toxicol. Mech. Methods*, **20**, 267.
62. Porter, D.W., Hubbs, A.F., Chen, B.T., McKinney, W., Mercer, R.R., Wolfarth, M.G., Battelli, L., Wu, N., Sriram, K., Leonard, S., Andrew, M., Willard, P., Tsuruoka, S., Endo, M., Tsukada, T., Munekane, F., Frazer, D.G., and Castranova, V. (2013) *Nanotoxicology*, **7**, 1179.
63. Stapleton, P.A., Minarchick, V.C., Cumpston, A.M., McKinney, W., Chen, B.T., Sager, T.M., Frazer, D.G., Mercer, R.R., Scabilloni, J., Andrew, M.E., Castranova, V., and Nurkiewicz, T.R. (2012) *Int. J. Mol. Sci.*, **13**, 13781.
64. Ishimatsu, S., Hori, H., Kasai, T., Ogami, A., Morimoto, Y., Oyabu, T., and Tanaka, I. (2009) *Inhalation Toxicol.*, **21**, 668.
65. Oyabu, T., Myojo, T., Morimoto, Y., Ogami, A., Hirohashi, M., Yamamoto, M., Todoroki, M., Mizuguchi, Y., Hashiba, M., Lee, B.W., Shimada, M., Wang, W.N., Uchida, K., Endoh, S., Kobayashi, N., Yamamoto, K., Fujita, K., Mizuno, K., Inada, M., Nakazato, T., Nakanishi, J., and Tanaka, I. (2011) *Inhalation Toxicol.*, **23**, 784.
66. Kagan, V.E., Kapralov, A.A., Croix, C.M.S., Watkins, S.C., Kisin, E.R., Kotchey, G.P., Balasubramanian, K., Vlasova, I.I., Yu, J., Kim, K., Seo, W., Mallampalli, R.K., Star, A., and Shvedova, A.A. (2014) *ACS Nano*, **8**, 5610.
67. Erdely, A., Hulderman, T., Salmen, R., Liston, A., Zeidler-Erdely, P.C., Schwegler-Berry, D., Castranova, V., Koyama, S., Kim, Y.A., Endo, M., and Simeonova, P.P. (2009) *Nano Lett.*, **9**, 36.
68. Sargent, L.M., Porter, D.W., Staska, L.M., Hubbs, A.F., Lowry, D.T., Battelli, L., Siegrist, K.J., Kashon, M.L., Mercer, R.R., Bauer, A.K., Chen, B.T., Salisbury, J.L., Frazer, D., McKinney, W., Andrew, M., Tsuruoka, S., Endo, M., Fluharty, K.L., Castranova, V., and Reynolds, S.H. (2014) *Part. Fibre Toxicol.*, **11**, 3.
69. Kobler, C., Poulsen, S.S., Saber, A.T., Jacobsen, N.R., Wallin, H., Yauk, C.L., Halappanavar, S., Vogel, U., Qvortrup, K., and Molhave, K. (2015) *PLoS One*, **10**, e0116481.
70. Schreiber, N., Strobele, M., Kopf, J., Hochscheid, R., Kotte, E., Weber, P., Hansen, T., Bockhorn, H., and Muller, B. (2013) *J. Toxicol. Environ. Health A*, **76**, 1317.

71. Zhang, R., Dai, Y., Zhang, X., Niu, Y., Meng, T., Li, Y., Duan, H., Bin, P., Ye, M., Jia, X., Shen, M., Yu, S., Yang, X., Gao, W., and Zheng, Y. (2014) *Part. Fibre Toxicol.*, **11**, 73.
72. Lee, J.S., Choi, Y.C., Shin, J.H., Lee, J.H., Lee, Y., Park, S.Y., Baek, J.E., Park, J.D., Ahn, K., and Yu, I.J. (2014) *Nanotoxicology*, 1.
73. Mangum, J.B., Turpin, E.A., Antao-Menezes, A., Cesta, M.F., Bermudez, E., and Bonner, J.C. (2006) *Part. Fibre Toxicol.*, **3**, 15.
74. Kasai, T., Umeda, Y., Ohnishi, M., Kondo, H., Takeuchi, T., Aiso, S., Nishizawa, T., Matsumoto, M., and Fukushima, S. (2014) *Nanotoxicology*, 1.
75. Muller, J., Huaux, F., Moreau, N., Misson, P., Heilier, J.F., Delos, M., Arras, M., Fonseca, A., Nagy, J.B., and Lison, D. (2005) *Toxicol. Appl. Pharmacol.*, **207**, 221.
76. Warheit, D.B., Laurence, B.R., Reed, K.L., Roach, D.H., Reynolds, G.A., and Webb, T.R. (2004) *Toxicol. Sci.*, **77**, 117.
77. Huizar, I., Malur, A., Midgette, Y.A., Kukoly, C., Chen, P., Ke, P.C., Podila, R., Rao, A.M., Wingard, C.J., Dobbs, L., Barna, B.P., Kavuru, M.S., and Thomassen, M.J. (2011) *Am. J. Respir. Cell Mol. Biol.*, **45**, 858.
78. Inoue, K., Koike, E., Yanagisawa, R., Hirano, S., Nishikawa, M., and Takano, H. (2009) *Toxicol. Appl. Pharmacol.*, **237**, 306.
79. Park, E.J., Cho, W.S., Jeong, J., Yi, J., Choi, K., and Park, K. (2009) *Toxicology*, **259**, 113.
80. Ryman-Rasmussen, J.P., Tewksbury, E.W., Moss, O.R., Cesta, M.F., Wong, B.A., and Bonner, J.C. (2009) *Am. J. Respir. Cell Mol. Biol.*, **40**, 349.
81. Ronzani C., Casset A., Pons F. (2014) *Arch Toxicol.*, **88**(2):489–99.
82. Todd, N.W., Luzina, I.G., and Atamas, S.P. (2012) *Fibrogenesis Tissue Repair*, **5**, 11.
83. Sager, T.M., Wolfarth, M.W., Battelli, L.A., Leonard, S.S., Andrew, M., Steinbach, T., Endo, M., Tsuruoka, S., Porter, D.W., and Castranova, V. (2013) *J. Toxicol. Environ. Health A*, **76**, 922.
84. Li, Z., Hulderman, T., Salmen, R., Chapman, R., Leonard, S.S., Young, S.H., Shvedova, A., Luster, M.I., and Simeonova, P.P. (2007) *Environ. Health Perspect.*, **115**, 377.
85. Shvedova, A.A., Kisin, E.R., Murray, A.R., Gorelik, O., Arepalli, S., Castranova, V., Young, S.H., Gao, F., Tyurina, Y.Y., Oury, T.D., and Kagan, V.E. (2007) *Toxicol. Appl. Pharmacol.*, **221**, 339.
86. Shvedova, A.A., Kisin, E.R., Murray, A.R., Mouithys-Mickalad, A., Stadler, K., Mason, R.P., and Kadiiska, M. (2014) *Free Radic. Biol. Med.*, **73**, 154.
87. Kyjovska, Z.O., Jacobsen, N.R., Saber, A.T., Bengtson, S., Jackson, P., Wallin, H., and Vogel, U. (2015) *Environ. Mol. Mutagen.*, **56**, 41.
88. Bourdon, J.A., Saber, A.T., Jacobsen, N.R., Jensen, K.A., Madsen, A.M., Lamson, J.S., Wallin, H., Moller, P., Loft, S., Yauk, C.L., and Vogel, U.B. (2012) *Part. Fibre Toxicol.*, **9**, 5.
89. Bourdon, J.A., Saber, A.T., Jacobsen, N.R., Williams, A., Vogel, U., Wallin, H., Halappanavar, S., and Yauk, C.L. (2013) *Cardiovasc. Toxicol.*, **13**, 406.
90. Wang, L., Luanpitpong, S., Castranova, V., Tse, W., Lu, Y., Pongrakhananon, V., and Rojanasakul, Y. (2011) *Nano Lett.*, **11**, 2796.
91. Takagi, A., Hirose, A., Nishimura, T., Fukumori, N., Ogata, A., Ohashi, N., Kitajima, S., and Kanno, J. (2008) *J. Toxicol. Sci.*, **33**, 105.
92. Shvedova, A.A., Kisin, E.R., Yanamala, N., Tkach, A.V., Gutkin, D.W., Star, A., Shurin, G.V., Kagan, V.E., and Shurin, M.R. (2015) *Cancer Res.*, 15;**75**(8):1615–23.
93. Donaldson, K., Murphy, F.A., Duffin, R., and Poland, C.A. (2010) *Part. Fibre Toxicol.*, **7**, 5.
94. Murphy, F.A., Poland, C.A., Duffin, R., Al-Jamal, K.T., Ali-Boucetta, H., Nunes, A., Byrne, F., Prina-Mello, A., Volkov, Y., Li, S., Mather, S.J., Bianco, A., Prato, M., Macnee, W., Wallace, W.A., Kostarelos, K., and Donaldson, K. (2011) *Am. J. Pathol.*, **178**, 2587.
95. Poland, C.A., Byrne, F., Cho, W.S., Prina-Mello, A., Murphy, F.A., Davies, G.L., Coey, J.M., Gounko, Y., Duffin, R.,

Volkov, Y., and Donaldson, K. (2011) *Nanotoxicology*, **6**, 899.

96. Grosse, Y., Loomis, D., Guyton, K.Z., Lauby-Secretan, B., Ghissassi, E., Bouvard, V., Benbrahim-Tallaa, L., Guha, N., Scoccianti, C., Mattock, H., Straif, K., International Agency for Research on Cancer Monograph Working Group, and International Agency for Reseach on Cancer (2014) *Lancet Oncol.*, **15**(13):1427–8.
97. Baan, R., Straif, K., Grosse, Y., Secretan, B., El Ghissassi, F., Cogliano, V., and WHO International Agency for Research on Cancer Monograph Working Group (2006) *Lancet Oncol.*, **7**, 295.
98. Roller, M. (2009) *Inhal. Toxicol.*, **21** (Suppl. 1), 144.
99. Baan, R.A. (2007) *Inhal. Toxicol.*, **19** (Suppl. 1), 213.
100. Kuempel, E.D., Tran, C.L., Castranova, V., and Bailer, A.J. (2006) *Inhal. Toxicol.*, **18**, 717.
101. Donaldson, K., Duffin, R., Langrish, J.P., Miller, M.R., Mills, N.L., Poland, C.A., Raftis, J., Shah, A., Shaw, C.A., and Newby, D.E. (2013) *Nanomedicine (Lond.)*, **8**, 403.
102. Saber, A.T., Jacobsen, N.R., Jackson, P., Poulsen, S.S., Kyjovska, Z.O., Halappanavar, S., Yauk, C.L., Wallin, H., and Vogel, U. (2014) *Wiley Interdiscip. Rev. Nanomed. Nanobiotechnol.*, **6**, 517.
103. Saber, A.T., Lamson, J.S., Jacobsen, N.R., Ravn-Haren, G., Hougaard, K.S., Nyendi, A.N., Wahlberg, P., Madsen, A.M., Jackson, P., Wallin, H., and Vogel, U. (2013) *PLoS One*, **8**, e69020.
104. Husain, M., Saber, A.T., Guo, C., Jacobsen, N.R., Jensen, K.A., Yauk, C.L., Williams, A., Vogel, U., Wallin, H., and Halappanavar, S. (2013) *Toxicol. Appl. Pharmacol.*, **269**, 250.
105. Saber, A.T., Halappanavar, S., Folkmann, J.K., Bornholdt, J., Boisen, A.M., Moller, P., Williams, A., Yauk, C., Vogel, U., Loft, S., and Wallin, H. (2009) *Part. Fibre Toxicol.*, **6**, 12.
106. Jackson, P., Halappanavar, S., Hougaard, K.S., Williams, A., Madsen, A.M., Lamson, J.S., Andersen, O., Yauk, C., Wallin, H., and Vogel, U. (2013) *Nanotoxicology*, **7**, 85.
107. Jackson, P., Hougaard, K.S., Vogel, U., Wu, D., Casavant, L., Williams, A., Wade, M., Yauk, C.L., Wallin, H., and Halappanavar, S. (2012) *Mutat. Res.*, **745**, 73.
108. Sos Poulsen, S., Jacobsen, N.R., Labib, S., Wu, D., Husain, M., Williams, A., Bogelund, J.P., Andersen, O., Kobler, C., Molhave, K., Kyjovska, Z.O., Saber, A.T., Wallin, H., Yauk, C.L., Vogel, U., and Halappanavar, S. (2013) *PLoS One*, **8**, e80452.
109. Halappanavar, S., Jackson, P., Williams, A., Jensen, K.A., Hougaard, K.S., Vogel, U., Yauk, C.L., and Wallin, H. (2011) *Environ. Mol. Mutagen.*, **52**, 425.
110. Lam, C.W., James, J.T., McCluskey, R., Arepalli, S., and Hunter, R.L. (2006) *Crit. Rev. Toxicol.*, **36**, 189.
111. Xu, J.-Y., Li, Q.-N., Li, J.-G., Ran, T.-C., Wu, S.-W., Song, W.-M., Chen, S.-L., and Li, W.-X. (2007) *Carbon*, **45**, 1865.
112. Roberts, J.R., Kenyon, A., Leonard, S.S., Fix, N.R., Porter, D.W., Sager, T., Wolfarth, M.G., Yingling, B.M., Chaudhuri, I.S., Kyrlidis, A., Bilgesu, S.A., Mercer, R.R., Schwegler-Berry, D., Castranova, V., and Erdely, A. (2013) Toxicologist., **132** (1): 98.

7
Cardiovascular and Hemostatic Effects of Carbon Nanomaterials

Xiaoyong Deng, Cheng Li, Jiajun Wang, and Pan Chen

7.1
Background

Cardiovascular disease (CVD), a broadly used term for all diseases of the cardiovascular system, is the leading cause of death worldwide, being responsible for 3 in every 10 deaths in 2008 [1]. Exposure to small particulate matter in urban air is considered to be a risk factor for CVD. Particulate matter inflicts harmful effects on the cardiovascular system by changing the activity of the fibrinolytic system, giving rise to a procoagulant state, endothelial dysfunction, and cardiac effects [2, 3]. With their unusual chemical and physical characteristics, carbon nanomaterials, including fullerenes, carbon nanotubes (CNTs), and graphene, have extensive applications as the promising materials [4]. However, many studies over the past few years have proven that carbon nanomaterials have potentially hazardous effects on human health [5]. Despite major advances having been made in better understanding the safety profile of carbon nanomaterials, the potential adverse effects arising from their interactions with blood cells as well as the cardiovascular system have been relatively poorly studied. In this chapter, we summarize the breakthroughs and advances related to the hemotoxicity and cardiovascular effects of carbon nanomaterials.

7.2
Carbon Nanotubes

Since their discovery by Iijima in 1991 [6], CNTs have been one of the most promising and carefully studied carbon-based nanomaterials. CNTs are carbon atoms arranged in a crystalline grapheme lattice with a tubular morphology. According to their structural characteristics, CNTs are classified as single-walled carbon nanotubes (SWCNTs) with one layer of sp^2-bound carbon tubular structure, double-walled carbon nanotubes (DWCNTs) with two concentric tubes, and multi-walled carbon nanotubes (MWCNTs) with more than two

Biomedical Applications and Toxicology of Carbon Nanomaterials, First Edition.
Edited by Chunying Chen and Haifang Wang.

layers. CNTs exhibit high tensile strength and unique electrical properties, are durable, and can be functionalized. These properties have found applications in electronics, batteries, stain-resistant fabric, tissue engineering, drug delivery, and so on [7]. Because CNTs can be classified as high-aspect-ratio nanomaterials – similar to fibers – they induce similar adverse health effects [8, 9]. However, over the past decade, despite major advances having been made toward a better understanding of the safety profile of CNTs, their potential adverse effects on the cardiovascular system have been relatively poorly studied [10].

Many studies have indicated that accidental exposure by inhalation or ingestion, via skin or mucosa, could potentially lead to the translocation of CNTs into the bloodstream [11]. On the other hand, many of the proposed biomedical applications of CNTs will require their direct injection into the body via different routes of administration, which will most probably also lead to direct contact with the blood components [12]. The evaluation of the compatibility between nanotubes and blood is considered of great importance given the former's interactions with blood components and the cardiovascular system. Therefore, in order to assess the toxicity of CNTs to the cardiovascular system, it is necessary to jointly review the effects of CNTs on blood cells, complement system, proteins, and cardiovascular cells together, thereby assessing the overall toxicity of CNTs on the human cardiovascular system.

7.2.1 Hemotoxicity of CNTs

7.2.1.1 What Is Hemotoxicity

Usually, the terms "hemotoxicity" and "hemocompatibility" can be used interchangeably. The hemotoxicity of a chemical can be defined as the possible adverse effects in its interaction with blood components, including cells and proteins. In general, when assessing the hemocompatibility of a particular biomaterial, the following parameters can be taken into account: activation of the complement system, blood cell changes, and interaction with processes related to the coagulation system (i.e., platelet activation, coagulation, and thrombosis potential) [13].

The complement system refers to a range of small proteins and factors circulating in the bloodstream. It is part of the innate immune system, and has its function in immune defense. It acts fast, in a nonspecific manner. Once activated, it can remove microorganisms and clear the modified cells such as apoptotic cells [14, 15]. However, the overactivation of the complement system can be linked to pseudo-allergy syndromes observed with nanoparticles used in nanomedicine [16]. Therefore, it is of great importance to investigate the way nanomaterials may interact with the components of the complement system and, eventually, whether this interaction leads to overactivation. Thus, since the mechanism of interaction between nanomaterials and the complement system remains unclear, and since

we do not know whether this interaction can lead to overactivation, more investigations are necessary.

When discussing hemotoxicity, we also include the alteration of blood cells. These can be changes in the number of leukocytes (white blood cells) and reticulocytes (immature red blood cells (RBCs)), cell counts, as well as leukocyte activation (known as the initiation of inflammatory processes) or hemolysis (lysis of erythrocytes or mature RBCs). The above components are the ones we should take in account when hemocompatibility is considered [17]. However, strictly hematologically speaking, the number of leukocytes or their activation is more likely considered as the parameter related to inflammation, and is therefore not directly related to the evaluation of the hemocompatibility of nanomaterials but to their inflammatory profiling.

Thrombosis, according to its definition, is a blood clot (thrombus) formed to stop blood loss in a blood vessel injury [18]. At the end of blood coagulation, a thrombus is formed. In thrombi, there are blood cells (activated platelets) and proteins (coagulation factors). When biomaterials are determined to be thrombogenic, they tend to produce blood clots, which may eventually cause deprivation of the blood supply to vital organs (obstruction of the blood flow) and as a result lead to functional impairment of tissues [19].

7.2.1.2 Complement System

Pristine CNTs are highly hydrophobic nanomaterials because of their aromatic rings of sp^2-bound carbons. Once functionalized, the original hydrophobic surface will be converted into a hydrophilic and/or charged surface, and its surface features (area, charge, hydrophilicity, and chemical features of the appending groups) will interact with the plasma proteins in a completely different manner [20–22]. Salvador-Morales *et al.* were the first to study nanotubes–blood compatibility by using western blot and sodium dodecyl sulfate-polyacrylamide gel electrophoresis (SDS-PAGE) techniques [23]. They demonstrated that, out of the many different proteins in plasma, those binding to the CNT surface were highly selective. Among the few proteins from plasma or serum that were found to bind to nonfunctionalized nanotubes, fibrinogen and apolipoproteins were those that bound in greatest quantity. As to the binding mechanisms of blood proteins, Ge *et al.* studied the interaction between SWCNTs and four major blood proteins, namely bovine fibrinogen, gamma globulin, bovine serum albumin, and transferrin [24]. Their results showed that the $\pi-\pi$ stacking interactions between CNTs and hydrophobic aromatic residues (tryptophan, tyrosine, and phenylalanine residues) played a critical role in determining their adsorption capacity. Moreover, they also concluded that the competitive bindings of blood proteins on the SWCNT surface could greatly alter their cellular interaction pathways and result in much reduced cytotoxicity for these protein-coated SWCNTs, according to their respective adsorption capacity.

Once proteins are adsorbed onto CNTs, complement activation may be triggered; therefore it is important to interrogate in more detail the effect of protein

binding to the complement system. Salvador-Morales *et al.* [23] first demonstrated that both SWCNTs and DWCNTs could activate the complement system via the classical pathway. Many different proteins in the serum samples were tested, but very few of them showed any affinity for the CNTs. C1q proteins were found on the surface of DWCNTs in great quantity. It suggested that the highly selective binding may be responsible for the observed complement activation via the classical pathway. Ling *et al.* [25] confirmed that the activation of the complement system by CNTs was via the classical pathway, which was triggered by the formation of the C1 complex. TEM images showed that MWCNTs bound both the complement component C1q (recognition protein) and the C1s–C1r–C1r–C1s complex (Figure 7.1), while neither DWCNTs nor SWCNTs bound C1q. But despite binding, C1-dependent complement activation was not reported for any of the nanotubes tested [25]. In all, a clear mechanism on such binding and complement activation needs further clarification.

When it comes to the effects of chemical modification of CNTs on the complement system, different groups have provided different results. Salvador-Morales *et al.* [26] investigated the effects of chemical modification of MWCNTs on their complement activation potential. Pristine MWCNTs, MWCNTs modified with 1,8-diamino-octane followed by the covalent attachment of ε-caprolactam or L-alanine, or MWCNTs directly modified with 1-octadecylamine or 1,6-hexadithiol were used. They concluded that modification of the surface characteristics greatly changed the level of activation of the complement system via both the classical pathway and alternative pathways. When comparing the level of activation, chemically modified MWCNTs induced less complement activation than nonmodified MWCNTs. For example, MWNTs functionalized with ε-caprolactam showed >90% reduction in the classical pathway activation compared with unmodified MWCNTs, and this was directly correlated with reduced levels of C1q protein binding and a higher level of factor H (complement activation regulator protein) binding [26].

Poly(ethylene glycol) (PEG), as a commonly used component in nanomaterials (giving them long circulation time), is explored in several studies of the possible effects on complement activation [27–29]. Generally, PEGylation to some degree can limit complement activation, and the extent of activation depends on the PEG conformation, PEG density, and the CNT surface coverage by PEG (full or partial coverage). Hamad *et al.* [27] used pristine SWCNTs coated with PEGylated phospholipid molecules as long-circulating, poly-stabilized CNTs. Their results indicated that complement activation occurred via the lectin pathway rather than the classical pathway and that it depended on the complement component C4. In a recent study by the same group, various carboxylated MWCNTs covalently functionalized with PEG of different chain lengths demonstrated that activation of the complement in human serum occurred in a concentration-dependent manner, irrespective of the PEG chain length (PEG-1000, PEG-1500 or PEG-4000) [29]. In all, when dealing with CNTs clinically, utmost caution and careful monitoring need to be taken because of the possible complement activation.

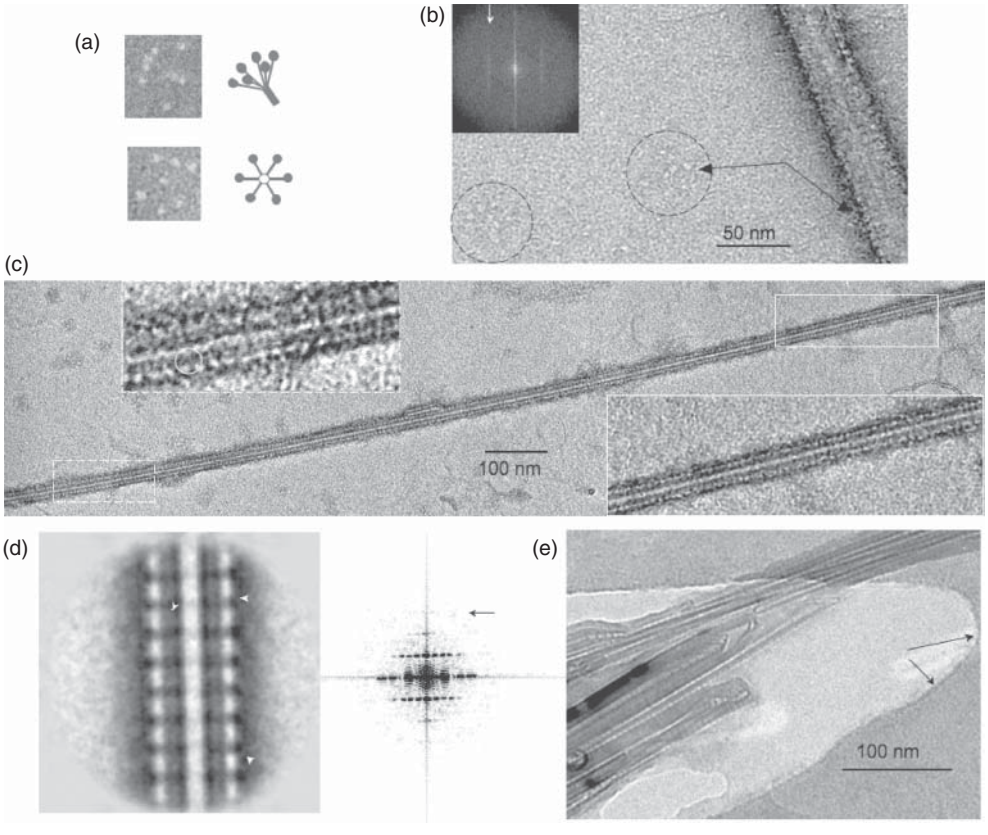

Figure 7.1 Interaction of C1q molecules with MWCNTs. (a) Electron micrographs and schematic representations of side (top) and top (bottom) views of the C1q molecule. (b) Portion of a C1q-covered MWCNT along with free C1q molecules. Inset shows the power spectrum of the covered nanotube with the arrow pointing to a diffraction line at ~1/6 nm. (c) Portion of a MWCNT with organized C1q molecules. Insets show magnified views of the covered nanotube, with the discerned collagen arms circled in the left inset. (d) Averaged view of the C1q organization on the MWCNT in (c) and its power spectrum. White arrowheads point to examples of discerned collagen arms in the image, and the black arrow points to the third diffraction line. (e) Cryo-electron micrograph of an MWCNT bundle embedded in vitrified buffer suspended in a hole of a lacey carbon film. The arrows point to the edge of the carbon film. (Reprinted with permission from [25]. © 2011 American Chemical Society.)

7.2.1.3

Red Blood Cells

Interestingly, when deciding the hemolytic activity of CNTs, different assays reached different conclusions. Donkor *et al.*, the first group to do so, reported that, according to their Raman spectroscopy data, human RBCs did not internalize or oxidize CNTs [30]. In contrast, Sachar and Saxena [31] studied the impact of two types of SWCNTs (pristine and acid-treated) on mouse RBC and

found that the carboxylated SWCNTs could induce hemolysis in a dose- and time-dependent manner, whereas the pristine material did not.

7.2.1.4

Hemostatic System and Coagulation/Thrombosis/Atheroma

In 2005, when Radomski *et al.* [32] evaluated the effects of CNTs on platelet aggregation, they found one possible activity of CNTs in inducing thrombosis. By experimenting on rats in which the carotid artery was chemically damaged in order to induce thrombosis, they demonstrated that SWCNTs induced a higher degree of human platelet aggregation than MWCNTs. Since CNTs in this study were not functionalized – whereas environmental CNTs are usually functionalized – it gives us no reliable information about environmental or occupational toxicology, but it indeed shows us the right direction.

In 2007, Li *et al.* [33] evaluated the formation of atheroma in four groups of $ApoE^{-/-}$ transgenic mice that are susceptible to atherosclerosis and represent a widely used model of human atherosclerosis. By controlling the intake of SWCNTs (or not) and the high fat diet of the mice, they evaluated the size of atheroma formation. The results showed that low amounts of SWCNTs alone (normal diet) did not cause atheroma, but in the group with intake of SWCNTs and on a high fat diet the size of atheroma in carotid artery and in brachiocephalic artery was significantly larger. In the same year, Nemmar *et al.* evaluated whether ground MWCNTs dispersed in saline, containing a dispersing agent (Tween 80, 0.1%), had the ability to accelerate atherosclerosis in mice whose carotid artery was physically damaged by irradiation with green light for 90 s [34]. Mice were first administered with 200 μg of CNTs in saline; after 24 h, the arterial photochemical damage was induced and the rate and extent of thrombus formation at 10-s intervals for 40 min were monitored. The results showed that the thrombus size was significantly higher in MWCNT-instilled mice than in saline-instilled animals. As the experimental model reflects probable human exposure, it may be inferred that, if acutely exposed to large amounts of ground MWCNTs, people with significant arterial damage (e.g., those with advanced atherosclerotic lesions) may develop a thrombus; however, in this study the amount of CNTs was too large to make it worthy of reference.

In 2011, Burke *et al.* [35] studied the interaction of MWCNTs with components of the hemostatic system and the influence of surface modification (covalent chemical functionalization by either carboxylation or amidation) on the MWCNT thrombotic activity. As a result, *in vitro*, both amidated and carboxylated MWCNTs had procoagulant effects, with or without the coating (Figure 7.2). MWCNTs activated platelets *in vitro*, with amidated MWCNTs exhibiting greater platelet activation than carboxylated or pristine MWCNTs. However, contrasting trends were obtained *in vivo*, where functionalization tended to diminish rather than enhance procoagulant activity. In contrast, carboxylated MWCNTS exhibited little procoagulant tendency *in vivo*, eliciting only a mild and transient decrease in platelets. Amidated MWCNTs elicited no statistically significant change in the platelet count. So they concluded that the

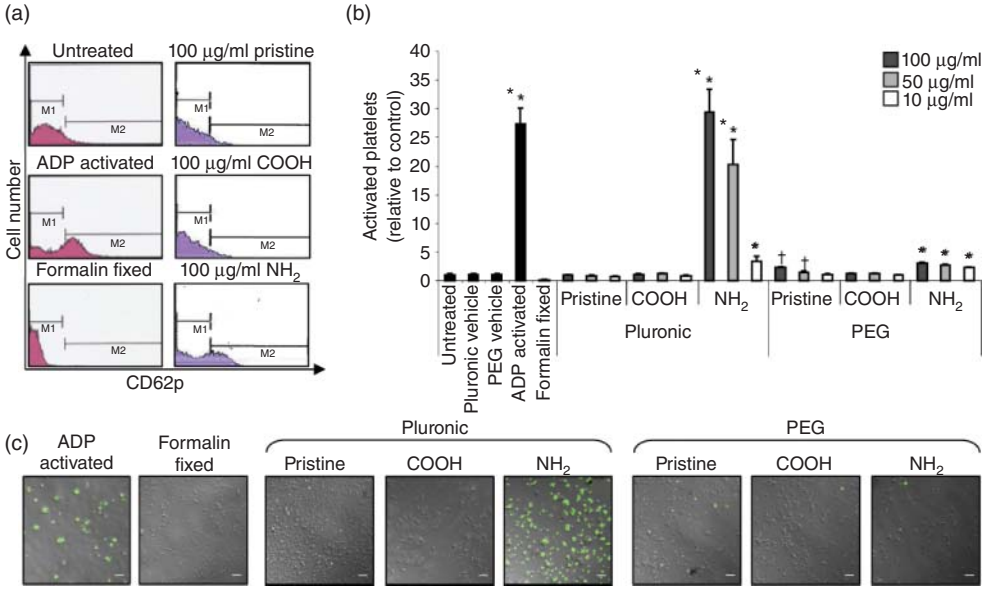

Figure 7.2 MWCNTs differentially activate platelets and induce their aggregation. (a) Representative histograms of control and 100 mg ml^{-1} pluronic F127-coated pristine, carboxylated, and amidated MWCNT treatment conditions. M1 gate delineates the "resting" platelet population, and M2 the "activated" population. (b) Platelet-rich plasma was incubated with MWCNT suspensions at the indicated final concentrations for 30 min prior to fixation and labeling with a FITC-conjugated CD62p antibody. (c) Platelet-rich plasma was incubated with MWCNT suspensions at 100 mg ml^{-1} for 30 min prior to being formalin-fixed and labeled with a FITC-conjugated CD62p antibody. Green fluorescence denotes CD62p expression. Scale bar represents 10 μm. (Reprinted with permission from [35]. © 2011 Elsevier.)

procoagulant tendencies of MWCNTs observed *in vitro* were not necessarily reproduced *in vivo*. Vakhrusheva *et al.* [36] also studied the effects of surface modifications on the thrombogenicity of SWCNTs. Using nanotubes functionalized via carboxylation or covalent PEGylation, or nanotubes coated with human serum albumin, they demonstrated in whole blood that both carboxylated and PEGylated SWCNTs exerted thrombogenic effects, whereas pretreatment of the nanotubes with albumin had a beneficial effect (i.e., reduction in platelet aggregation).

7.2.2
Effects on Cardiovascular System

In the 2007 study by Li *et al.* [33], which was mentioned earlier, the authors decided to figure out whether SWCNTs could cause oxidative damage in the aortic tissue and heart. By using a surrogate biomarker of oxidative stress, namely HO-1 activation, the authors measured the luciferase activities in the tissue

lysates of the aorta and heart of Ho1-luc mice exposed to a single pulmonary challenge with SWCNTs (40 μg) or the vehicle (PBS). After 7 days, they observed significant activation in gene expression in heart homogenates. The activation reverted to normal at day 28. A similar trend was also observed in aortic homogenates. Simeonova *et al.* performed an *in vitro* study to evaluate the ability of raw and purified SWCNTs to induce low density lipoprotein (LDL) oxidation in human aortic endothelial cells [37]. They found that SWCNTs (raw, more than purified) strongly induced LDL oxidation. Oxidized particles are readily taken up by macrophage scavenger receptors, leading to foam cell formation, which is a necessary step in atheroma formation. Thus the ability of SWCNTs to induce LDL oxidation strongly suggests a role of this nanoparticle in the early stages of atherosclerosis. However, in this study, the concentration of the CNTs used was slightly high. Human endothelial aortic cells in fact are not likely to come into contact with such high amounts of CNTs during either occupational or environmental exposure. Raja *et al.* made an interesting discovery in their study [38]. They performed an *in vitro* study on rat aortic smooth muscle cells and challenged the cell cultures with purified and oxidized SWCNTs at concentrations ranging between 10 and 100 μg ml^{-1} for 1–3.5 days. At day 1, they did not find any difference in cell proliferation in comparison to controls; however, at day 3.5, cell proliferation was significantly lower for all SWCNT-containing media in comparison to controls. The response was dose-dependent though nonlinear. Their results showed that in the process of atherosclerosis in humans, there may be a potential toxic effect of CNT exposure.

In 2012, Stapleton *et al.* [39] found that, after the rats were exposed to MWNCTs at the concentration of 5 mg m^{-3} for 5 h, the inhalation of MWCNTs could attenuate vasodilatation response in subepicardial arterioles of the animals. However, the endothelium-independent vasodilation, vasoconstriction, and myogenic response to pressurized vessels were not altered. In the same year, Ge *et al.* [40] used spontaneous hypertensive rats as the model and found that intratracheal instillation of SWCNTs (0.6 mg per rat) could cause a thickening of arterial vessels, toxic responses to the heart, and vascular responses, whereas no unaltered serum levels of C-reactive protein, TNF, ICAM-1, and von Willebrand factor were found.

In 2014, a study by Vesterdal *et al.* showed that, at the intratracheal (i.t.) instillation dose of 0.5 mg kg^{-1} SWCNTs, there was no altered *ex vivo* endothelium-dependent vasodilation in the aorta observed after 2 and 26 h of exposure [41]. Thompson *et al.* [42] also obtained similar results and demonstrated that a single i.t. instillation of MWCNTs (100 μg per rat) affected neither the *ex vivo* endothelial-dependent nor the independent vasorelaxation in coronary arteries. However, a trend toward increased vasoconstriction was found. A recent report has shown that, after the mice were repeatedly exposed to MWCNTs at the dose of 25.6 μg per week for 5 weeks by i.t. instillation, the atherosclerotic plaque area in aorta, pulmonary inflammation, and oxidative stress increased, whereas there were no altered systemic responses on cytokines and 8-isoprostane [43].

7.3 Fullerenes

C_{60}, a type of fullerenes, with a diameter of around 1 nm, was discovered by Kroto *et al.* in 1985 [44]. C_{60} comprises 60 carbon atoms arranged in a stable icosahedron with C5–C5 single bonds forming 12 pentagons and C5–C6 double bonds forming 20 hexagons [45]. Fullerene has attracted much interest because of its unique physicochemical properties. Their cage-like and highly modifiable structure makes them endowed with widespread use, including in materials science, optics, cosmetics, electronics, green energy, and medicine [46].

Although fullerenes were first synthesized in 1985, they might have existed on the earth's environment naturally for thousands of years [47]. With the increasing use of C_{60}, the potential adverse impacts from C_{60} exposure have been investigated by many groups. The *in vitro* cytotoxicity [48], *in vivo* biodistribution [49], biopersistence [50], and adverse pulmonary responses to C_{60} have been widely investigated [51].

7.3.1 Fullerenes' Escape from Lungs into Circulation

Pulmonary exposure is expected to happen in occupations requiring work with raw C_{60} directly. It has been found that C_{60} concentrations in occupational environments reach 23 856–53 119 particles per liter in air [52]. Humans breathe about 360 and 600 l of air per hour, so a short 1-h occupational inhalation exposure can deposit 8 500 000–31 500 000 C_{60} particles into the lungs. Some researchers have found that nanoparticles can be translocated from the lungs into the blood circulation through the air–blood barrier (ABB) [53, 54].

Naota *et al.* [55] examined the translocation pathway of i.t. instilled C_{60} fullerene particles from the lung into the blood circulation in rats. They occasionally found that C_{60} aggregated in the alveolar lumen of the lungs of the exposed animals. Microanatomy showed no obvious signs of inflammation but only an increase in activated hypertrophic macrophages attached to the surface of the alveolar lumen. Furthermore, some of the aggregated C_{60} nanoparticles could adhere to the endothelial cells and RBCs in the alveolar capillaries. It was also demonstrated that C_{60} nanoparticles were immediately confined to the cytoplasm of lymphocyte-like mononuclear cells in the pulmonary lymph nodes. From the electron microscopy images taken at 0 and 5 min after instillation, the RBCs in the capillary lumen of the alveolar wall had C_{60} nanoparticles internalized. This phenomenon was not observed in the lung tissues from control animals. The electron microscopic analysis makes it clear that C_{60} may pass the ABB, resulting in immediate translocation into the systemic circulation.

However, some different results were obtained by other groups. Baker *et al.* [47] compared the transport rate of nanometer-sized (55 nm) and micrometer-sized (930 nm) fullerenes from their respiratory exposure site into the blood circulation but could not detect any fullerenes in the blood following inhalation by rats.

The calculated pulmonary deposition fraction was 14.1% for the C_{60} fullerene nanoparticles, which was much greater than that for the microparticles (9.3%). However, the half-time of clearance from the lungs was similar for both fullerene nanoparticles and microparticles, which suggested that similar elimination processes, such as mucociliary clearance and macrophage uptake, were involved during their removal from the lungs. In another study conducted by Shinohara *et al.*, no C_{60} nanoparticles were found in the organs except the lungs after intratracheal instillation ($3.3\,mg\,kg^{-1}$) and inhalation exposure ($0.12\,mg\,m^{-3}$) in rats, indicating that there was negligible absorption of fullerenes following inhalation [50]. Therefore, whether fullerenes translocate into the systemic circulation from the lungs needs further investigation.

7.3.2 Toxicity of Fullerenes on the Cardiovascular System

Nanoparticles are deposited in the respiratory tract after being inhaled; their small size helps them to be absorbed into cells and transcytosized into the vasculature and lymphatics. Yamawaki *et al.* [56] found that endothelial cells following *in vitro* exposure to C_{60} nanoparticles resulted in internalization by cells, and such nanoparticles showed dose-dependent cytotoxicity. After 10 days of exposure, fullerenes detrimentally affected cell attachment and slowed cell growth. It was therefore speculated that exposure to fullerenes could be a potential risk for CVD ignition or progression. In another study, water-soluble fullerenes were shown to induce Ca^{2+} increase and G1 cell cycle arrest in human umbilical vein endothelial cells, but no cell death was observed, similar to pristine C_{60} [57]. Radomski *et al.* [32] demonstrated that fullerenes are less effective than other nanoparticles in eliciting the aggregation of platelets, suggesting that they are less thrombogenic.

In spite of the various studies on pulmonary and *in vitro* responses to C_{60}, studies of cardiovascular impacts *in vivo* are scarce. Vesterdal *et al.* [58] found that C_{60} could reduce endothelium-dependent vasodilatation in the aortic segments of apolipoprotein E knockout mice, implying that C_{60} may disturb vasomotor balance in the presence of lipid abnormalities and atherosclerosis. In another study, polyvinylpyrrolidone (PVP)-formulated C_{60} was administered intravenously to pregnant and nonpregnant Sprague–Dawley rats, which showed increased vascular tissue contractile response of the main uterine artery through elements of Rho–Rho kinase signaling [59]. Recently, Thompson *et al.* [60] examined cardiovascular detriments through different routes of exposure to C_{60} and described the responses to C_{60} exposure in different sexes. They concluded that i.t. or intravenous (i.v.) exposure to C_{60} at the dose of 28 μg per rat resulted in unique cardiovascular consequences, which might favor heightened coronary resistance and myocardial susceptibility to ischemia/reperfusion (I/R) injury. Figure 7.3 shows the impact of i.t. or i.v. exposure to C_{60} on cardiac I/R injury in male and female rats. Compared to the infarct size following I/R measured in the vehicle groups, myocardial infarction in male rats exposed to C_{60} suspensions expanded to some extent. As for male rats, there were no significant differences

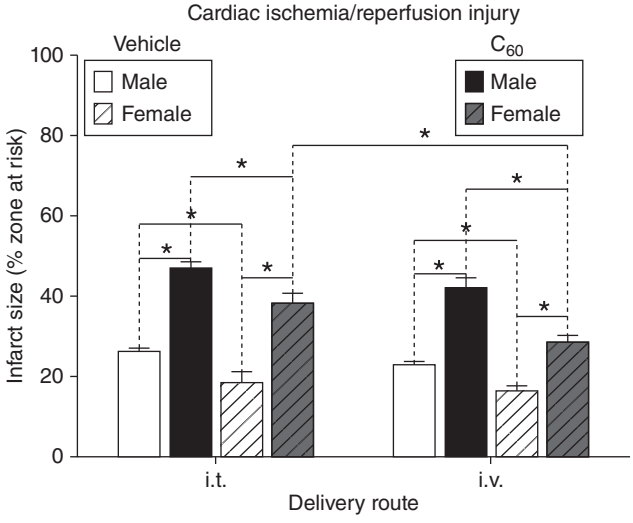

Figure 7.3 Cardiac I/R injury. Male and female rats were subjected to regional cardiac I/R (20/120 min) injury *in situ*, 24 h following intratracheal (i.t.) or intravenous (i.v.) delivery of C_{60} or vehicle. In either case, C_{60} exposure exacerbated myocardial infarction. Within each delivery route, infarct sizes in the male groups were larger than those in the female groups. Between the delivery routes, the females had larger infarctions in response to i.t. C_{60} exposure compared with i.v. exposure. $^*p < 0.05$ by two-way ANOVA, $N = 4–5$. (Reprinted with permission from [60]. © 2014 Oxford University Press.)

between the extent of I/R injury through i.t. or i.v. exposure routes. Female rats also suffered myocardial infarct expansions following I/R in both C_{60} exposed groups, but they did show significantly larger myocardial infarctions following i.t. exposure to C_{60} than i.v. exposure, suggesting that the sex of the animal may influence the biological response to C_{60} exposure. Although exposure to C_{60} appears to represent a risk for cardiovascular disorders, further *in vivo* validations are necessary.

7.4 Graphene-Related Nanomaterials

Graphene is an emerging, novel nanomaterial with a single-atom-thick sheet of hexagonally arrayed, sp^2-bonded carbon atoms, characterized as "the thinnest material in our universe" [61]. Graphene-related nanomaterials offer highly promising advances in biological and medical areas, such as antiviral, bactericidal, and nematocidal agents, disease diagnosis, drug delivery, photothermal therapy, and tissue engineering [62, 63]. With the wide use of graphene-related nanomaterials, the possibility of human exposure to them is greatly increased [64]. This section describes the impacts of graphene-related nanomaterials on the cardiovascular system.

Most of the available literature considers graphene-related nanomaterials to be hemocompatible [65–68]. Hemolysis, platelet activation, and changes in coagulation or hematological markers abnormalities could not be induced by the graphene-related nanomaterials. Yang *et al.* [65] found that i.v. administrated PEGylated graphene oxide (GO) did not cause any hemotoxicity on the treated mice at tested doses as high as 20 mg kg^{-1} in a period of 3 months. All the hematological parameters, including white blood cells, RBCs, hemoglobin, mean corpuscular volume, mean corpuscular hemoglobin, mean corpuscular hemoglobin concentration, platelet count, and mean corpuscular hemoglobin, in the PEGylated GO treated groups remained normal compared to those of the control groups. Zhang *et al.* [66] found that GO had little effect on erythrocyte morphology and membrane integrity at the exposure dose of 10 μg ml^{-1} for 1 and 4 h. Part of the erythrocyte membranes were ruptured and ghost cells were observed at the concentration of 80 μg ml^{-1}. Sasidharan *et al.* [68] found that pristine graphene and acid-oxidized graphene could maintain good blood compatibility with RBCs and platelets, rarely destroying the expression of cytokine (Figure 7.4).

Chowdhury *et al.* [69] investigated the effects of dextran-functionalized graphene (G-Dex) on platelet activation, blood cell hemolysis *in vitro*, and vasoactivity *in vivo*. The results indicated that G-Dex induced a 12–20% increase in the levels of complement proteins at concentrations above 7 mg ml^{-1} but did

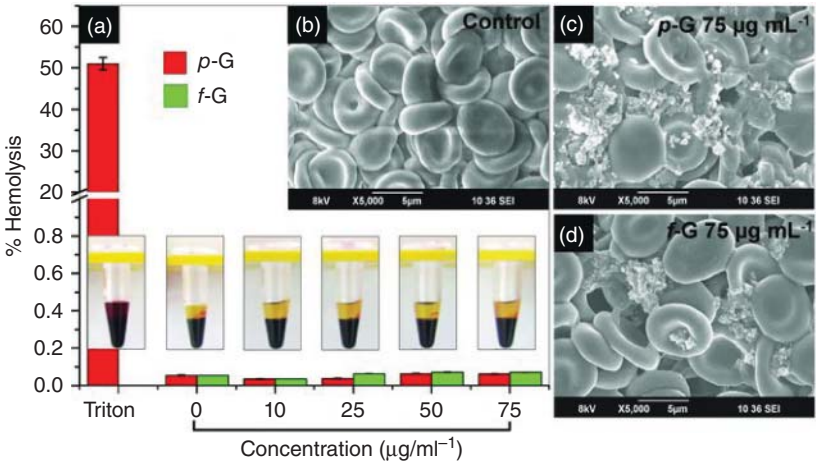

Figure 7.4 (a) Assessment of the hemolytic potential of varying concentrations of whole blood treated with both graphene systems. Inset: Representative optical photographs showing no significant hemoglobin leakage from graphene-treated red blood cells compared to the positive control. (b–d) SEM images showing the normal morphology of (b) untreated, (c) p-G-treated (75 μg ml^{-1}), and (d) f-G-treated (75 μg ml^{-1}) RBCs (p-G, pristine graphene; f-G, carboxyl-functionalized graphene). (Reprinted with permission from [68]. © 2012 John Wiley and Sons.)

not cause platelet activation or blood cell hemolysis. Furthermore, using the hamster cheek pouch *in vivo* model, the initial vasoactivity of G-Dex at concentrations ranging from 1 to 50 mg ml^{-1}, equivalent to the first pass of a bolus injection, was a brief concentration-dependent dilation in arcade and terminal arterioles. Very recently, the same group assessed the *in vitro* effects of graphene (O-GNR) on some of the key hematological and vascular components of the circulatory system. PEG-functionalized O-GNR elicited low concentration-dependent deformation of RBCs, which did not lead to hemolysis, whereas the platelets and complement system were activated by O-GNR at the exposure dose up to 80 μg ml^{-1} [70].

However, on the other hand, Singh *et al.* [71] indicated that GO prepared from Hummer's method induced aggregation of platelets by activating the nonreceptor protein tyrosine kinase of platelets and releasing the element calcium from the cell. When administered intravenously into mouse, GO triggered extensive pulmonary thromboembolism consistent with the pro-thrombotic nature of this nanomaterial, while the considerably less negatively charged reduced GO (RGO) elicited only minor aggregatory response (Figure 7.5). In a later work by the same group, they found amine-functionalized graphene ($G\text{-}NH_2$) was more biocompatible than GO and RGO, which neither demonstrated stimulatory action toward platelets nor induced pulmonary thromboembolism in mice. Furthermore, $G\text{-}NH_2$ was also found to be more hemocompatible than GO, which induced significant hemolysis [72].

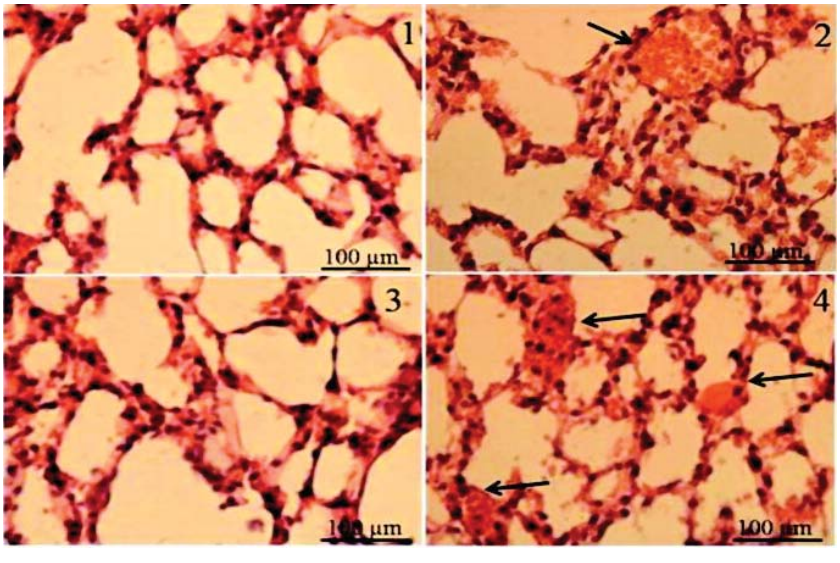

Figure 7.5 Light microscopy of hematoxylin and eosin stained sections of lungs after intravenous injection of mice with normal saline (a), GO (b), RGO (c), and collagen–epinephrine mixture (d). Arrows indicate platelet-rich thrombi occluding lung vessels. (Reprinted with permission from [71]. © 2011 American Chemical Society.)

7.5 Conclusions and Outlook

In this chapter, we tried to provide a concise review of the up-to-date understanding of the hemotoxicty and cardiovascular effects of carbon nanomaterials. In all, the limited amount of studies published warrants more systematic and thorough investigations on these issues. Of all the work mentioned earlier, it seems that the common critical parameters that determine carbon nanomaterials' hemotoxicity along with its cardiovascular effects are their chemical nature of surface modifications, surface charge, and size. Surface characteristics are the major parameter influencing the interaction of these materials with blood components and, therefore, the overall biological impact. The interactions between carbon nanomaterials and the complement system, RBCs, and the hemostatic system may pose one of the greatest challenges to human body including the pulmonary and cardiovascular systems.

However, some conclusions have been reached in the aspect of toxicity of carbon nanomaterials on the cardiovascular system, which hypothesize oxidative stress and inflammatory reaction to be the main mechanisms. Works that focus on how carbon nanoparticles induce cardiovascular toxicity through blood change, function of vessels, and function of cardiac nerve, and so on, are shallow, so the proofs of the biological effect of carbon nanomaterials directly on cardiovascular system are relatively limited and are not mechanically clear. CVD is one of the major human diseases induced by environmental factors, seriously threatening human health and life, so it is very important to devote much more effort to understand the action and mechanism of the cardiovascular system as a result of exposure to carbon nanomaterials.

Acknowledgments

This work was financially supported by the National Natural Science Foundation of China (21371118, 41430644), the China 973 project (2011CB933402), the Program for Innovative Research Team in University (IRT13078), and the Shanghai Science and Technology Committee (13R1414900).

References

1. Franco, M., Cooper, R.S., Bilal, U., and Fuster, V. (2011) Challenges and opportunities for cardiovascular disease prevention. *Am. J. Med.*, **124**, 95–102.
2. Delfino, R.J., Sioutas, C., and Malik, S. (2005) Review potential role of ultrafine particles in associations between airborne particle mass and cardiovascular health. *Environ. Health Perspect.*, **113**, 934–946.
3. Mossman, B.T., Borm, P.J., Castranova, V. *et al.* (2007) Mechanisms of action of inhaled fibers, particles and nanoparticles in lung and cardiovascular diseases. *Part. Fibre Toxicol.*, **4**, 56–60.
4. Jariwala, D., Sangwan, V.K., Lauhon, L.J. *et al.* (2013) Carbon nanomaterials

for electronics, optoelectronics, photovoltaics, and sensing. *Chem. Soc. Rev.*, **42**, 2824–2860.
5. Uo, M., Akasaka, T., Watari, F. *et al.* (2011) Toxicity evaluations of various carbon nanomaterials. *Dent. Mater. J.*, **30**, 245–263.
6. Iijima, S. (1991) Helical microtubules of graphitic carbon. *Nature*, **354**, 56–58.
7. De Volder, M.F., Tawfick, S.H., Baughman, R.H., and Hart, A.J. (2013) Carbon nanotubes: present and future commercial applications. *Science*, **339**, 535–539.
8. Nagai, H. and Toyokuni, S. (2012) Differences and similarities between carbon nanotubes and asbestos fibers during mesothelial carcinogenesis: shedding light on fiber entry mechanism. *Cancer Sci.*, **103**, 1378–1390.
9. Donaldson, K. (2010) Asbestos, carbon nanotubes and the pleural mesothelium: a review of the hypothesis regarding the role of long fibre retention in the parietal pleura, inflammation and mesothelioma. *Part. Fibre Toxicol.*, **7**, 69.
10. Beg, S., Rizwan, M., Sheikh, A.M. *et al.* (2011) Advancement in carbon nanotubes: basics, biomedical applications and toxicity. *J. Pharm. Pharmacol.*, **63**, 141–163.
11. Czarny, B., Georgin, D., Berthon, F. *et al.* (2014) Carbon nanotube translocation to distant organs after pulmonary exposure: insights from in situ ^{14}C-radiolabeling and tissue radioimaging. *ACS Nano*, **8**, 5715–5724.
12. Battigelli, A., Ménard-Moyon, C., Da Ros, T. *et al.* (2013) Endowing carbon nanotubes with biological and biomedical properties by chemical modifications. *Adv. Drug Delivery Rev.*, **65**, 1899–1920.
13. Bussy, C., Methven, L., and Kostarelos, K. (2013) Hemotoxicity of carbon nanotubes. *Adv. Drug Delivery Rev.*, **65**, 2127–2134.
14. Zipfel, P.F. and Skerka, C. (2009) Complement regulators and inhibitory proteins. *Nat. Rev. Immunol.*, **9**, 729–740.
15. Harboe, M., Thorgersen, E.B., and Mollnes, T.E. (2011) Advances in assay of complement function and activation. *Adv. Drug Delivery Rev.*, **63**, 976–987.
16. Szebeni, J., Alving, C.R., Rosivall, L. *et al.* (2007) Animal models of complement-mediated hypersensitivity reactions to liposomes and other lipid-based nanoparticles. *J. Liposome Res.*, **17**, 107–117.
17. Wintrobe, M.M. and Greer, J.P. (2009) *Wintrobe's Clinical Hematology*, vol. 1, Lippincott Williams & Wilkins.
18. Engelmann, B. and Massberg, S. (2013) Thrombosis as an intravascular effector of innate immunity. *Nat. Rev. Immunol.*, **13**, 34–45.
19. Ratner, B.D., Hoffman, A.S., Schoen, F.J., and Lemons, J.E. (2004) *Biomaterials Science: An Introduction to Materials in Medicine*, Academic Press.
20. Bianco, A., Kostarelos, K., Partidos, C.D., and Prato, M. (2005) Biomedical applications of functionalised carbon nanotubes. *Chem. Commun.*, 571–577.
21. Herrero, M.A., Lacerda, L., Bianco, A. *et al.* (2011) Functionalised carbon nanotubes: high biocompatibility with lack of toxicity. *Int. J. Nanotechnol.*, **8**, 885–897.
22. Prato, M., Kostarelos, K., and Bianco, A. (2007) Functionalized carbon nanotubes in drug design and discovery. *Acc. Chem. Res.*, **41**, 60–68.
23. Salvador-Morales, C., Flahaut, E., Sim, E. *et al.* (2006) Complement activation and protein adsorption by carbon nanotubes. *Mol. Immunol.*, **43**, 193–201.
24. Ge, C., Du, J., Zhao, L. *et al.* (2011) Binding of blood proteins to carbon nanotubes reduces cytotoxicity. *Proc. Natl. Acad. Sci. U.S.A.*, **108**, 16968–16973.
25. Ling, W.L., Biro, A., Bally, I. *et al.* (2011) Proteins of the innate immune system crystallize on carbon nanotubes but are not activated. *ACS Nano*, **5**, 730–737.
26. Salvador-Morales, C., Basiuk, E.V., Basiuk, V.A. *et al.* (2008) Effects of covalent functionalization on the biocompatibility characteristics of multiwalled carbon nanotubes. *J. Nanosci. Nanotechnol.*, **8**, 2347–2356.
27. Hamad, I., Hunter, A.C., Rutt, K.J. *et al.* (2008) Complement activation by PEGylated single-walled carbon nanotubes is independent of C1q and alternative

pathway turnover. *Mol. Immunol.*, **45**, 3797–3803.

28. Andersen, A.J., Robinson, J.T., Dai, H. *et al.* (2013) Single-walled carbon nanotube surface control of complement recognition and activation. *ACS Nano*, **7**, 1108–1119.
29. Andersen, A.J., Windschiegl, B., Ilbasmis-Tamer, S. *et al.* (2013) Complement activation by PEG-functionalized multi-walled carbon nanotubes is independent of PEG molecular mass and surface density. *Nanomed. Nanotechnol. Biol. Med.*, **9**, 469–473.
30. Donkor, A.D., Su, Z., Mandal, H.S. *et al.* (2009) Carbon nanotubes inhibit the hemolytic activity of the pore-forming toxin pyolysin. *Nano Res.*, **2**, 517–525.
31. Sachar, S. and Saxena, R.K. (2011) Cytotoxic effect of poly-dispersed single walled carbon nanotubes on erythrocytes in vitro and in vivo. *PLoS One*, **6**, e22032.
32. Radomski, A., Jurasz, P., Alonso-Escolano, D. *et al.* (2005) Nanoparticle-induced platelet aggregation and vascular thrombosis. *Br. J. Pharmacol.*, **146**, 882–893.
33. Li, Z., Hulderman, T., Salmen, R., Chapman, R. *et al.* (2007) Cardiovascular effects of pulmonary exposure to single-wall carbon nanotubes. *Environ. Health Perspect.*, **115**, 377–382.
34. Nemmar, A., Hoet, P., Vandervoort, P. *et al.* (2007) Enhanced peripheral thrombogenicity after lung inflammation is mediated by platelet-leukocyte activation: role of P-selectin. *J. Thromb. Haemost.*, **5**, 1217–1226.
35. Burke, A.R., Singh, R.N., Carroll, D.L. *et al.* (2011) Determinants of the thrombogenic potential of multiwalled carbon nanotubes. *Biomaterials*, **32**, 5970–5978.
36. Vakhrusheva, T.V., Gusev, A.A., Gusev, S.A., and Vlasova, I.I. (2013) Albumin reduces thrombogenic potential of single-walled carbon nanotubes. *Toxicol. Lett.*, **221**, 137–145.
37. Simeonova, P.P. (2007) *Nanotechnology-Toxicological Issues and Environmental Safety and Environmental Safety*, Springer, pp. 53–64.
38. Raja, P.M., Connolley, J., Ganesan, G.P. *et al.* (2007) Impact of carbon nanotube exposure, dosage and aggregation on smooth muscle cells. *Toxicol. Lett.*, **169**, 51–63.
39. Stapleton, P.A., Minarchick, V.C., Cumpston, A.M. *et al.* (2012) Impairment of coronary arteriolar endothelium-dependent dilation after multi-walled carbon nanotube inhalation: a time-course study. *Int. J. Mol. Sci.*, **13**, 13781–13803.
40. Ge, C., Meng, L., Xu, L. *et al.* (2012) Acute pulmonary and moderate cardiovascular responses of spontaneously hypertensive rats after exposure to single-wall carbon nanotubes. *Nanotoxicology*, **6**, 526–542.
41. Vesterdal, L.K., Jantzen, K., Sheykhzade, M. *et al.* (2014) Pulmonary exposure to particles from diesel exhaust, urban dust or single-walled carbon nanotubes and oxidatively damaged DNA and vascular function in apoE-/-mice. *Nanotoxicology*, **8**, 61–71.
42. Thompson, L.C., Frasier, C.R., Sloan, R.C. *et al.* (2014) Pulmonary instillation of multi-walled carbon nanotubes promotes coronary vasoconstriction and exacerbates injury in isolated hearts. *Nanotoxicology*, **8**, 38–49.
43. Cao, Y., Jacobsen, N.R., Danielsen, P.H. *et al.* (2014) Vascular effects of multi-walled carbon nanotubes in dyslipidemic ApoE−/− mice and cultured endothelial cells. *Toxicol. Sci.*, **138**, 104–116.
44. Kroto, H., Heath, J., O'Brien, S. *et al.* (1985) C60: buckminsterfullerene. *Nature*, **318**, 162–163.
45. Krätschmer, W., Lamb, L.D., Fostiropoulos, K., and Huffman, D.R. (1990) C60: a new form of carbon. *Nature*, **347**, 354–358.
46. Dellinger, A., Zhou, Z., Connor, J. *et al.* (2013) Application of fullerenes in nanomedicine: an update. *Nanomedicine*, **8**, 1191–1208.
47. Baker, G.L., Gupta, A., Clark, M.L. *et al.* (2008) Inhalation toxicity and lung toxicokinetics of C60 fullerene nanoparticles and microparticles. *Toxicol. Sci.*, **101**, 122–131.
48. Bunz, H., Plankenhorn, S., and Klein, R. (2012) Effect of buckminsterfullerenes on cells of the innate and adaptive immune system: an in vitro study with human

peripheral blood mononuclear cells. *Int. J. Nanomed.*, **7**, 4571.

49. Kubota, R., Tahara, M., Shimizu, K. *et al.* (2011) Time-dependent variation in the biodistribution of C 60 in rats determined by liquid chromatography–tandem mass spectrometry. *Toxicol. Lett.*, **206**, 172–177.
50. Shinohara, N., Gamo, M., and Nakanishi, J. (2011) Fullerene C60: inhalation hazard assessment and derivation of a period-limited acceptable exposure level. *Toxicol. Sci.*, **123**, 576–589.
51. Ogami, A., Yamamoto, K., Morimoto, Y. *et al.* (2011) Pathological features of rat lung following inhalation and intratracheal instillation of C60 fullerene. *Inhalation Toxicol.*, **23**, 407–416.
52. Johnson, D.R., Methner, M.M., Kennedy, A.J., and Steevens, J.A. (2010) Potential for occupational exposure to engineered carbon-based nanomaterials in environmental laboratory studies. *Environ. Health Perspect.*, **118**, 49–54.
53. Geiser, M., Rothen-Rutishauser, B., Kapp, N. *et al.* (2005) Ultrafine particles cross cellular membranes by nonphagocytic mechanisms in lungs and in cultured cells. *Environ. Health Perspect.*, **113**, 1555–1560.
54. Kreyling, W.G., Semmler-Behnke, M., and Möller, W. (2006) Ultrafine particle-lung interactions: does size matter? *J. Aerosol Med.*, **19**, 74–83.
55. Naota, M., Shimada, A., Morita, T. *et al.* (2009) Translocation pathway of the intratracheally instilled C60 fullerene from the lung into the blood circulation in the mouse: possible association of diffusion and caveolae-mediated pinocytosis. *Toxicol. Pathol.*, **37**, 456–462.
56. Yamawaki, H. and Iwai, N. (2006) Cytotoxicity of water-soluble fullerene in vascular endothelial cells. *Am. J. Physiol., Cell Physiol.*, **290**, C1495–C1502.
57. Gelderman, M.P., Simakova, O., Clogston, J.D. *et al.* (2008) Adverse effects of fullerenes on endothelial cells: fullerenol $C_{60}(OH)_{24}$ induced tissue factor and ICAM-1 membrane expression and apoptosis in vitro. *Int. J. Nanomed.*, **3**, 59.
58. Vesterdal, L.K., Folkmann, J.K., Jacobsen, N.R. *et al.* (2009) Modest vasomotor dysfunction induced by low doses of C60 fullerenes in apolipoprotein E knockout mice with different degree of atherosclerosis. *Part. Fibre Toxicol.*, **6**, 5.
59. Vidanapathirana, A.K., Thompson, L.C., Mann, E.E. *et al.* (2014) PVP formulated fullerene (C60) increases Rho-kinase dependent vascular tissue contractility in pregnant Sprague Dawley rats. *Reprod. Toxicol.*, **49**, 86–100.
60. Thompson, L.C., Urankar, R.N., Holland, N.A. *et al.* (2014) C60 exposure augments cardiac ischemia/reperfusion injury and coronary artery contraction in sprague dawley rats. *Toxicol. Sci.*, **138**, 365–378.
61. Geim, A.K. and MacDonald, A.H. (2007) Graphene: exploring carbon flatland. *Phys. Today*, **60**, 35–41.
62. Shen, H., Zhang, L., Liu, M., and Zhang, Z. (2012) Biomedical applications of graphene. *Theranostics*, **2**, 283.
63. Chung, C., Kim, Y.K., Shin, D. *et al.* (2013) Biomedical applications of graphene and graphene oxide. *Acc. Chem. Res.*, **46**, 2211–2224.
64. Ma, Y., Shen, H., Tu, X., and Zhang, Z. (2014) Assessing in vivo toxicity of graphene materials: current methods and future outlook. *Nanomedicine*, **9**, 1565–1580.
65. Yang, K., Wan, J., Zhang, S. *et al.* (2010) In vivo pharmacokinetics, long-term biodistribution, and toxicology of PEGylated graphene in mice. *ACS Nano*, **5**, 516–522.
66. Zhang, X., Yin, J., Peng, C. *et al.* (2011) Distribution and biocompatibility studies of graphene oxide in mice after intravenous administration. *Carbon*, **49**, 986–995.
67. Dong, X.U., Zhou, N.L., and Shen, J. (2010) Hemocompatibility of carboxylic graphene oxide. *Chem. J. Chin. Univ.*, **31**, 2354–2359.
68. Sasidharan, A., Panchakarla, L.S., Sadanandan, A.R. *et al.* (2012) Hemocompatibility and macrophage response of pristine and functionalized graphene. *Small*, **8**, 1251–1263.

69. Chowdhury, S.M., Kanakia, S., Toussaint, J.D. *et al.* (2013) In vitro hematological and in vivo vasoactivity assessment of dextran functionalized graphene. *Sci. Rep.*, **3**, 2584.

70. Chowdhury, S.M., Fang, J., and Sitharaman, B. (2015) Interaction of graphene nanoribbons with components of the blood vascular system. *Future Sci.* OA, 1, FSO19.

71. Singh, S.K., Singh, M.K., Nayak, M.K. *et al.* (2011) Thrombus inducing property of atomically thin graphene oxide sheets. *ACS Nano*, **5**, 4987–4996.

72. Singh, S.K., Singh, M.K., Kulkarni, P.P. *et al.* (2012) Amine-modified graphene: thrombo-protective safer alternative to graphene oxide for biomedical applications. *ACS Nano*, **6**, 2731–2740.

8
Modulation of the Immune System by Fullerene and Graphene Derivatives

Ligeng Xu and Chunying Chen

8.1
Introduction

Because of their unique physicochemical properties, carbon nanomaterials, including carbon nanotubes, fullerene derivatives, as well as graphene and its derivatives, have shown great potential for applications in the biomedical field, as discussed in detail in Chapter 5. As is well known, the immune system as a defensive barrier plays predominant roles in the protection of the organism against external stimuli and invasion. Undoubtedly, carbon nanomaterials will encounter the immune system after their entry into the organism. Therefore, it is necessary to understand how these materials interact with the immune system, for a comprehensive and accurate understanding of their biological effects. It will also provide invaluable information on their biomedical applications in the future. Because the extensive investigations on the immunological effects of carbon nanotubes have been documented in another chapter, this chapter mainly focuses on the immunological effects of fullerene and graphene derivatives.

8.2
The Immunological Effects of Fullerene and Its Derivatives

As star materials, fullerene and its derivatives have attracted great attention since the former's discovery in 1996 [1]. The biological applications of fullerene and its derivatives have been well documented [2]. However, detailed information about the interactions between fullerene derivatives and immune system still needs to be filled, and there have been only a few dozen related studies in the recent years.

8.2.1
Fullerene Derivatives Can Inhibit Inflammation via Blocking ROS Generation

A number of studies indicate that reactive oxygen species (ROS) serve as an important participant in cell signaling pathways. For instance, ROS can induce

Biomedical Applications and Toxicology of Carbon Nanomaterials, First Edition.
Edited by Chunying Chen and Haifang Wang.

macrophage activation, resulting in the release of cytokines and other inflammatory responses in adipose tissues [3]. As mentioned in Chapter 5, fullerene and its derivatives have shown great potential as antioxidants through inactivating hydroxyl radicals by attaching to double bonds and/or absorbing inside several protons to penetrate the mitochondria [4, 5]. Therefore, it is greatly necessary to explore the interaction between fullerene derivatives and the immune system in this aspect. Since mast cells (MCs) and peripheral blood basophils (PBBs) play critical roles in the initiation and propagation of several inflammatory conditions, especially type I hypersensitivity, Ryan *et al.* [6] systematically investigated the interactions between fullerene derivatives (polyhydroxy- and *N*-ethyl-polyamino-) and both kinds of cells (i.e., MCs and PBBs). They showed that fullerene derivatives could significantly inhibit the IgE-dependent mediator release and the IgE-induced elevation in cytoplasmic ROS levels. The *in vivo* evidence also confirmed the negative effect of fullerene derivatives on allergic responses, including the inhibition of histamine release and decrease in core body temperature. In a subsequent study [7], utilizing the *in vivo* model of phorbol 12-myristate 13-acetate (PMA)-induced inflammation, Dellinger *et al.* also confirmed the negative effect of fullerene derivatives on inflammation. Meanwhile, Roursgaard *et al.* [8] found that pretreatment with polyhydroxylated C_{60} fullerene (fullerenol, 0.01 mg kg^{-1}) could significantly attenuate neutrophilic lung inflammation induced by quartz particles at the dosage of 2.5 mg kg^{-1} partly via blocking ROS-induced inflammation. Another study also evidenced the potential application of water-soluble fullerene as a free-radical scavenger in the treatment of rheumatoid arthritis [9]. In recent years, with improvements in the quality of life, obesity and metabolic syndromes have become worldwide health problems. Increasing pieces of evidence [10–12] have shown that these diseases are greatly correlated with chronic subacute inflammation in adipose tissue and that the interaction between adipocytes and macrophages is the main contributor for the inflammation. Xiao *et al.* [13] found that squalene-dissolved fullerene C_{60} could significantly inhibit the accumulation of intracellular lipid droplets and ROS generation when OP9 preadipocytes were exposed to an adipogenic stimulant (Figure 8.1). Furthermore, it could greatly inhibit macrophage activation and

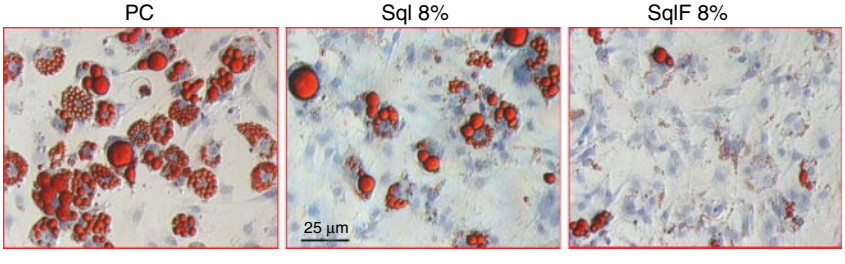

Figure 8.1 Effects of squalane-dissolved fullerene on adipogenesis in OP9 cells. Cells were treated by serum replacement (SR) method with or without Sql or SqlF at 2 days beyond the time of reaching confluence. After further culturing for 5 days, cells were subjected to oil red O staining. (Modified from Ref. [13]. ©2010 Elsevier Ltd.)

lead to low-grade adipogenesis in the OP9–U937 co-culture system. All these pieces of evidence indicate the potential applications of fullerene derivatives in the treatment of ROS-induced inflammatory diseases, metabolic syndrome, and other obesity-related disorders.

8.2.2 Fullerene Derivatives Promote Immune Responses via Modulating Macrophages and/or Antigen Presenting Cells (APCs)

Today, malignant tumors/cancers are still the greatest challenge for the health of humans even with the rapid development of science and technology. It is known that, besides surgery, chemotherapy and radiotherapy are two major strategies for cancer treatment. However, their side effects, such as the induction of lymphopenia and downregulation of the immune system of patients, limit their broad applications in the clinic [14]. Therefore, it is urgently needed to develop effective approaches with low toxicity for cancer treatment and/or chemo or radioprotectors to assist in chemo or radiotherapy.

In 2005, we first reported the antitumor activity of fullerene derivatives – polyhydroxylated metallofullerenols ($Gd@C_{82}(OH)_{22}$) [15]. We showed that tumor growth was greatly inhibited when tumor-bearing mice injected intraperitoneally (i.p.) once a day with $Gd@C_{82}(OH)_{22}$ of high dose (2×10^{-4} mmol kg^{-1}) over 1 week, comparable to that achieved by the cyclophosphamide (CTX, a widely used antineoplastic agent in the clinic) treatment group. Meanwhile, histopathological evaluation indicated that there was lymphocyte infiltration in the tumor tissues in the $Gd@C_{82}(OH)_{22}$ treatment group but not the CTX treatment group (Figure 8.2). Furthermore, a series of results showed that $Gd@C_{82}(OH)_{22}$ was nontoxic to tumor cells and there was low accumulation of this derivative in the tumor tissue. In other words, $Gd@C_{82}(OH)_{22}$ may inhibit the tumor growth via regulating immune responses but not directly damaging tumor cells. In subsequent studies [16, 17], we found that fullerene derivatives, including polyhydroxylated metallofullerenol ($Gd@C_{82}(OH)_{22}$) and fullerenol ($C_{60}(OH)_{20}$), could significantly enhance tumor necrosis factor-alpha (TNF-α)-mediated cellular immunity to inhibit tumor growth (Figure 8.3). To uncover the underlying mechanism, the interactions between macrophages and fullerene derivatives were systematically investigated recently in our lab [18]. Because of their carbon structures, fullerene derivatives' biodistribution and subcellular localizations are difficult to detect. Therefore, in our study, we used synchrotron-based scanning transmission X-ray microscopy (STXM) to evaluate the spatial distribution of $Gd@C_{82}(OH)_{22}$ in macrophages. We found that a large amount of $Gd@C_{82}(OH)_{22}$ was taken up by peritoneal macrophages after peritoneally injected into mice for nearly 1 week and that the derivatives were internalized in a time-dependent manner (Figure 8.4). Meanwhile, siRNA (small interfering RNA) for inflammasome and gene knockout mice assays confirmed that both fullerene derivatives, especially $Gd@C_{82}(OH)_{22}$, could significantly induce interleukin-1β (IL-1β) secretion of peritoneal macrophages

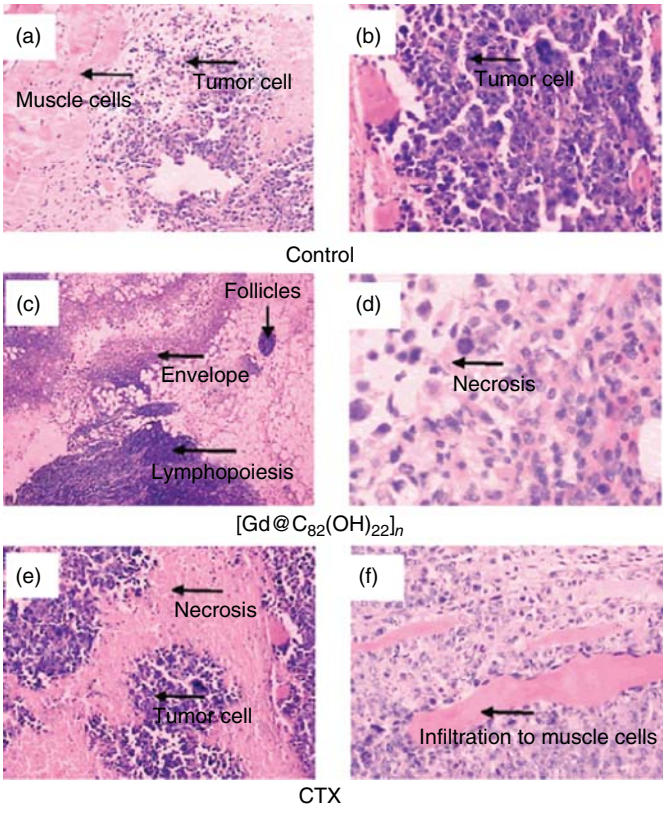

Figure 8.2 Hematoxylin and eosin (H&E) staining of the tumor tissues from the control (a and b), Gd@$C_{82}(OH)_{22}$-treated (c and d), and CTX-treated (e and f) mice. The significant formation of envelopes surrounding the tumor tissue composed of lymphadenoid and fibrosis tissues associated with lymphopoiesis and aggregated (c, arrow) necroses of tumors (d) in the Gd@c082$(OH)_{22}$-treated group are present. Numerous necroses of tumor tissue (e) and visible tumor infiltration to muscle cells (f) are observed. (Original magnification: a, c, and e ×40; b and d ×400, f ×200). (Modified from [15]. © 2005 American Chemical Society.)

through the TLRs/MyD88/NF-κB pathway and NLRP3 inflammasome activation (Figure 8.5). This work may provide us important information for understanding the underlying mechanisms of fullerene derivatives as therapeutic agents in cancer treatment. The study of Yang *et al* [19]. provided sound evidence to confirm our series of works. They found that Gd@$C_{82}(OH)_{22}$ could significantly promote dendritic cell (DC) maturation via upregulating co-stimulatory molecule (CD80, CD86) expression and enhancing the production of multiple cytokines, including IL-1β, IL-6, IL-12, and TNF-α. Furthermore, the proliferation capability of T lymphocytes could be significantly enhanced when mice were intraperitoneally immunized with a mixture of ovalbumin (OVA) and Gd@$C_{82}(OH)_{22}$ compared to treatment with OVA alone. The secretion levels of cellular immunity-related

cytokines (IL-2, IFN-γ) in serum also increased significantly for the group immunized with the mixture. Bunz *et al.* [20] observed that polyhydroxyl- and *N*-ethyl-polyamino- C_{60} could activate cells of the innate immune system such as natural killer cells and macrophages but not interact with T lymphocytes when incubated with peripheral blood mononuclear cells (PBMCs) from healthy subjects. From the above results, it can be concluded that fullerene derivatives, especially the polyhydroxylated ones, may serve as unique therapeutic agents for cancer treatment through modulating the immune system.

Besides serving as immunotherapeutic agents, fullerene derivatives have also shown the potential to be used as protective agents for cancer radiotherapy. Cai *et al.* [21] observed that $C_{60}(OH)_{24}$ pretreatment (daily, 40 mg kg^{-1}, i.p., for 2 weeks) could effectively reduce the radiation-induced mortality of mice without apparent toxicity. Meanwhile, the pretreatment could greatly improve the dysfunctions of T-cell proliferation and mitochondrial function induced by the irradiation. The above sound pieces of evidence demonstrate the promising applications of fullerene derivatives in cancer treatment. However, it is to be noted that all these studies just selected intraperitoneal injection to uncover the interactions between the immune system and fullerene derivatives. As is well known, the exposure route/injection method plays a critical role in the interaction between the nanomaterials and biological systems. Since inhalation exposure is one of the most important routes for humans to come into contact with nanomaterials, Ding *et al.* [22] investigated the effects of fullerene derivatives on the immune system of mice using intratracheal injection. They showed that fullerene derivatives could induce splenic inflammation such as inducing T-cell proliferation and proinflammatory cytokine production (e.g., IL-2, TNF-α) besides inducing pulmonary inflammation at day 6 post administration. Meanwhile, they also found that fullerene derivatives selectively activated $CD11b^+$ cells like macrophages other than T cells or B cells during splenic inflammation.

In addition, prophylactic or therapeutic cancer vaccines have been hot subjects in cancer treatment. However, a vaccine adjuvant, which can enhance the uptake of the antigen and/or modulate immune cells, especially antigen presenting cells (APCs), is essential to improve the immunogenicity of tumor-associated/specific antigens [23]. Considering the modulation by fullerene derivatives of immune cells, especially macrophages and APCs, it can be inferred that fullerene derivatives may show potential application in the development of vaccines for major infectious diseases and cancers. Inspired by the unique self-assembly property of fullerene derivatives, whereby a fullerene molecule of 0.7 nm can form polyanion nanoaggregates with size in the range of 20–100 nm depending on the pH, temperature, ionic strength, and the presence of a relatively high molecular weight dissolved organic acid [16, 24], we hypothesized that polyhydroxylated fullerene derivatives ($C_{60}(OH)_{20}$, fullerenol) could serve as dual-functional adjuvants via encapsulating the antigen during self-assembly and modulating the immune cells to enhance the immunogenicity of the antigen [25]. In this study, a plasmid DNA antigen (Env) for the envelop protein of HIV-1 was selected as model antigen. The results demonstrated the ideal adjuvant activities of fullerenol, such as the

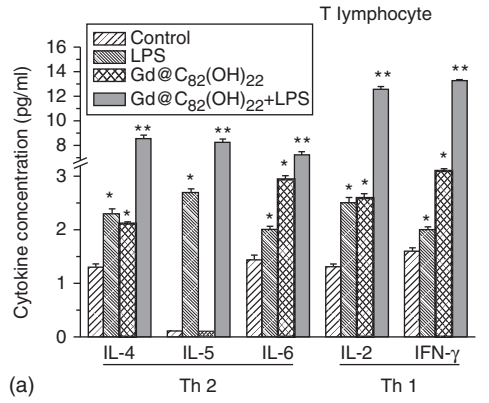
T lymphocyte
Control
LPS
Gd@C82(OH)22
Gd@C82(OH)22+LPS
Cytokine concentration (pg/ml)
IL-4
IL-5
IL-6
IL-2
IFN-γ
Th 2
Th 1
(a)

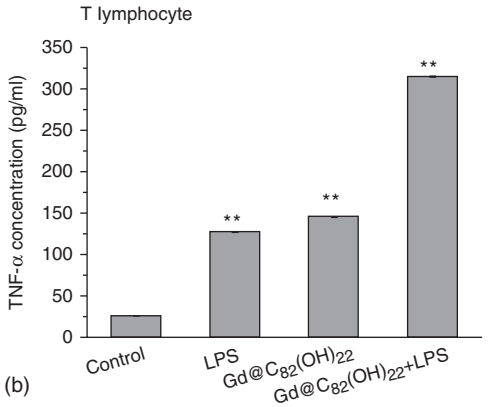
T lymphocyte
TNF-α concentration (pg/ml)
Control
LPS
Gd@C82(OH)22
Gd@C82(OH)22+LPS
(b)

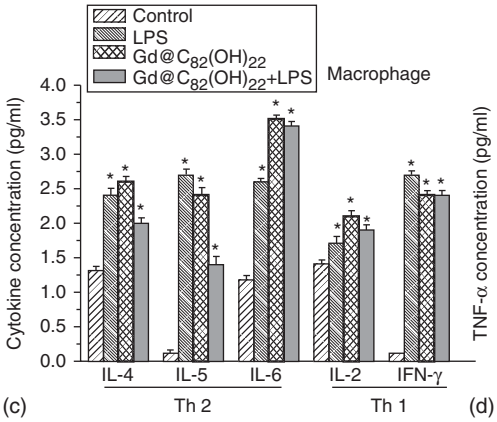
Control
LPS
Gd@C82(OH)22
Gd@C82(OH)22+LPS
Macrophage
Cytokine concentration (pg/ml)
IL-4
IL-5
IL-6
IL-2
IFN-γ
Th 2
Th 1
(c)

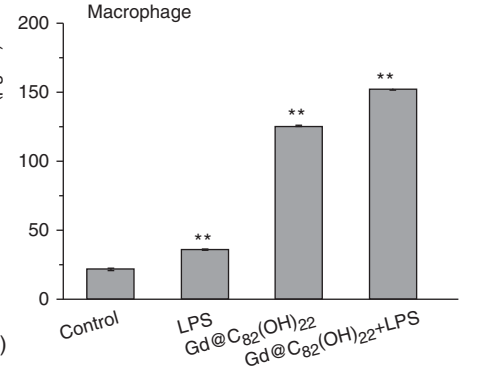
Macrophage
TNF-α concentration (pg/ml)
Control
LPS
Gd@C82(OH)22
Gd@C82(OH)22+LPS
(d)

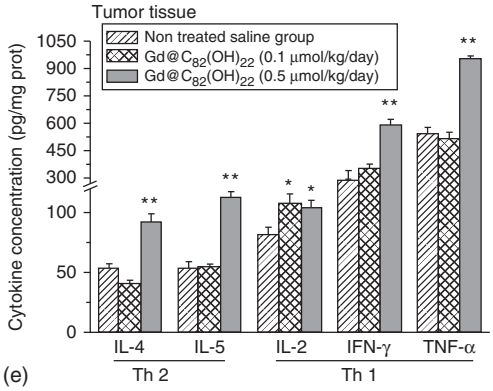
Tumor tissue
Non treated saline group
Gd@C82(OH)22 (0.1 μmol/kg/day)
Gd@C82(OH)22 (0.5 μmol/kg/day)
Cytokine concentration (pg/mg prot)
IL-4
IL-5
IL-2
IFN-γ
TNF-α
Th 2
Th 1
(e)

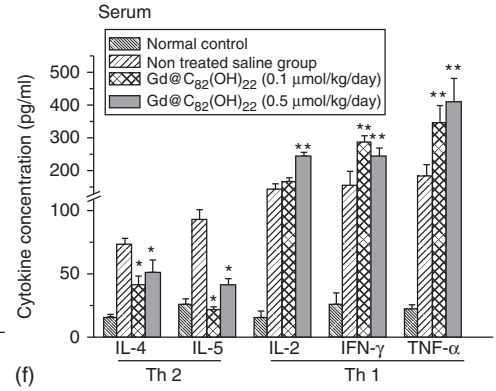
Serum
Normal control
Non treated saline group
Gd@C82(OH)22 (0.1 μmol/kg/day)
Gd@C82(OH)22 (0.5 μmol/kg/day)
Cytokine concentration (pg/ml)
IL-4
IL-5
IL-2
IFN-γ
TNF-α
Th 2
Th 1
(f)

Figure 8.3 $Gd@C_{82}(OH)_{22}$ nanoparticles can directly affect cytokine secretion, and incubation of T lymphocytes and macrophages with $Gd@C_{82}(OH)_{22}$ nanoparticles further affects their capacity to respond to LPS-induced cytokine secretion. LPS (0.1 mg ml^{-1}) was used as a positive control for T-lymphocyte and macrophage activation. Cell culture supernatants were diluted 1:5 and analyzed by flow cytometry using a CBA (cytometric bead array) inflammation kit for quantitative determination of cytokines IL-2, IL-4, IL-5, IL-6 IFN-γ, and TNF-α. Each bar represents the mean of three independent samples. (a) IL-2, IL-4, IL-5, IL-6, and IFN-γ levels of T-cell culture supernatants. (b) TNF-α levels of T-cell culture supernatants. (c) IL-2, IL-4, IL-5, IL-6, and IFN-γ levels of macrophage culture supernatants. (d) TNF-α levels of macrophage culture supernatants. (e) In comparison to the untreated saline group, IFN-γ and TNF-α expression levels in mouse tumor tissues increased markedly in the group treated with 0.5 mmol kg^{-1} day^{-1} $Gd@C_{82}(OH)_{22}$ nanoparticles. (f) IFN-γ, TNF-α, and IL-2 expression levels in mouse serum increased in the $Gd@C_{82}(OH)_{22}$ nanoparticle-treated group, while IL-4 and IL-5 expression levels decreased. Statistical significance (Student's *t*-test) is indicated by $*p < 0.05$, $**p < 0.01$ (compared to untreated cells). (Modified from [16]. © 2009 Elsevier Ltd.)

enhancement of cellular immunity via multiple immunization routes including intramuscular (i.m.), subcutaneous (s.c.), intradermal (i.d.), and intranasal (i.n.) injections and decrease in the required antigen dosage and immunization frequency while maintaining the immune response levels (Figure 8.6). Meanwhile, it could significantly promote the phagocytosis capability of peritoneal macrophages from immunized mice and induce the generation of effector memory $CD8^+$ T cells (T_{EM}), which are of great help for the protection at the early stage of infections. High-throughput screening on toll-like receptor (TLR) signaling pathways and gene knockout mice indicated that fullerenol mainly served as vaccine adjuvant via triggering multiple TLR signaling pathways (e.g., TLR2, TLR4, TLR5, TLR8, TLR9) to activate DC maturation and finally enhanced the immunogenicity of the vaccine antigen (Figure 8.7). Actually, there have been many pieces of clinical evidence to support the great importance of the positive modulations to multiple TLRs on DCs for the generation of robust and long-lived immune responses [26, 27]. For example, the broad range of immune responses elicited by the yellow fever vaccine YF-17D in the clinic [28] are attributed to its activations on multiple TLRs of DCs, including TLR2, TLR7, TLR8, and TLR9 [29]. In addition, immunization of mice with PLGA (poly(lactic-*co*-glycolic acid)) nanoparticles containing antigens plus ligands that signal through TLR4 and TLR7 induces synergistic increases in antigen-specific neutralizing antibodies compared to immunization with nanoparticles containing antigens plus a single TLR ligand [30]. The combined activation of these different receptors results in complementary, synergistic, or antagonistic effects that modulate innate and adaptive immunity [31]. Therefore, fullerenol may be a potential adjuvant candidate for vaccines in the clinic.

However, till now, detailed information on how fullerenol interacts with immune cells, especially DCs, is still lacking. A recent study by Turabekova *et al.* [32] provides us some clues to understand the underlying mechanism of fullerene derivatives. In their study, a computational model was used to analyze

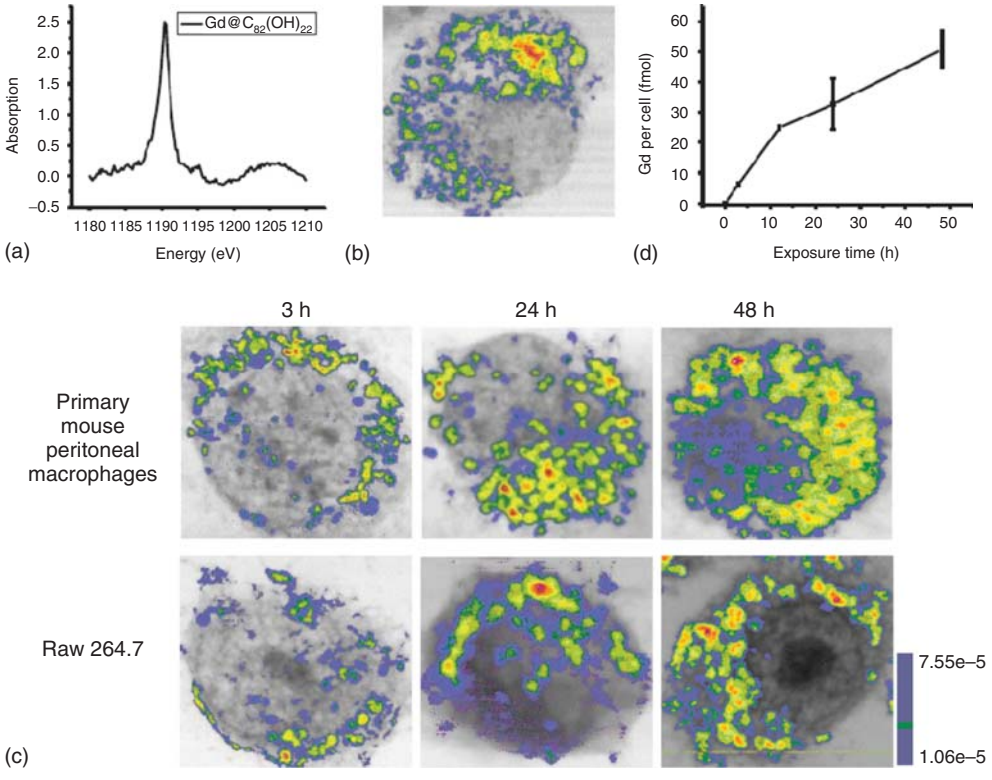

Figure 8.4 Internalization of metallofullerenol by macrophages *in vivo* and *in vitro*. (a) A Gd M-edge NEXAFS (near edge X-ray absorption fine structure) spectrum obtained from Gd@$C_{82}(OH)_{22}$ nanoparticles. (b) Soft X-ray STXM dual-energy contrast images of Gd@$C_{82}(OH)_{22}$ internalized by a primary mouse peritoneal macrophage *in vivo*. (c) Soft X-ray STXM dual-energy contrast images of time-dependent uptake of Gd@$C_{82}(OH)_{22}$ by primary mouse peritoneal macrophages and RAW264.7 cell line *in vitro*. (d) Inductively coupled plasma-mass spectrometry (ICP-MS) quantification of time-dependent uptake in macrophages of primary mouse peritoneal macrophages. (Modified from [18]. © 2014 Wiley-VCH Verlag GmbH & Co. KGaA.)

the interactions of fullerene and carbon nanotubes with the available X-ray structures of TLRs' homo- and hetero-dimer extracellular domains (ECD). They could show that the internal hydrophobic pockets of some TLRs (e.g., TLR1, TLR2, TLR4, and TLR6) might be capable of binding small carbon nanostructures (Figure 8.8).

As summarized in Table 8.1, fullerene derivatives, especially the hydroxylated ones, have shown unique activities to modulate the immune system, such as inhibiting inflammation via blocking the ROS pathway and promoting immunities through activating macrophages and/or APCs. All these pieces of evidence indicate the promising applications of fullerene derivatives in the treatment/prevention of inflammation-related diseases, malignant tumors,

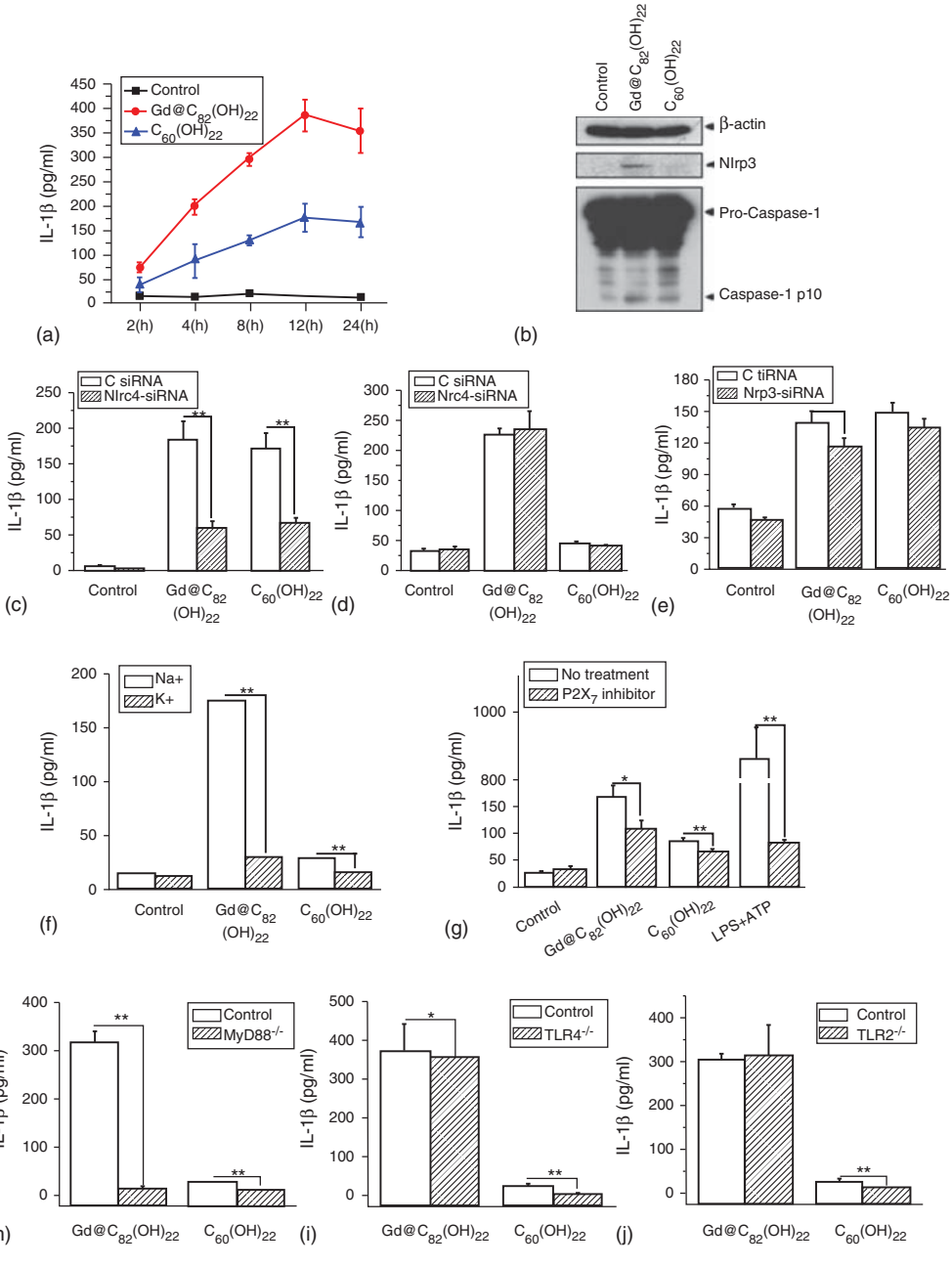
(a)
IL-1β (pg/ml)
Control
Gd@C82(OH)22
C60(OH)22
2(h)
4(h)
8(h)
12(h)
24(h)
(b)
Control
Gd@C82(OH)22
C60(OH)22
β-actin
NIrp3
Pro-Caspase-1
Caspase-1 p10
(c)
C siRNA
NIrc4-siRNA
(d)
C siRNA
Nrc4-siRNA
(e)
C tiRNA
Nrp3-siRNA
(f)
Na+
K+
(g)
No treatment
P2X7 inhibitor
Control
LPS+ATP
(h)
Control
MyD88-/-
(i)
Control
TLR4-/-
(j)
Control
TLR2-/-

Figure 8.5 Essential roles of NLRP3 inflammasome and TLRs/MyD88 pathway for IL-1β secretion during fullerenol exposure in primary mouse peritoneal macrophages. (a) Time dependence of IL-1β secretion by macrophages. (b) Expression level of intracellular NLRP3 inflammasomes and caspase-1 p10 subunit by western blotting. (c, d) IL-1β secretion of macrophages during fullerenol exposure for 6 h after NLRP3/NLRC4 siRNA transfection. (e) IL-18 secretion of macrophages after NLRP3 siRNA transfection. (f, g) IL-1β secretion of macrophages during fullerenol exposure for 6 h after K^+ efflux inhibition and P2X7 receptor inhibition. (h–j) IL-1β secretion of macrophages from MyD88$^{-/-}$, TLR4$^{-/-}$, and TLR2$^{-/-}$ knockout mice. $*p < 0.05$ and $**p < 0.01$ compared to the control group. (Modified from [18]. © 2014 WILEY-VCH Verlag GmbH & Co. KGaA.)

and major infections. Given the crucial roles of multiple parameters such as the physicochemical properties (e.g., size, the number of carbon atoms and functional groups on the surface), dosage, and exposure routes, however, there is still a long way to comprehensively understand the interactions of fullerene derivatives with the immune system and their rational design for the applications of interest. For instance, in a previous study, we observed that, unlike $C_{60}(OH)_{20}$, which could serve as adjuvant via multiple immunization routes, $Gd@C_{82}(OH)_{22}$ could enhance the immunogenicity of DNA antigen only through intramuscular injection (Ligeng Xu, Zhiyun Chen, Ye Liu, Chunying Chen.). Therefore, the interaction between the immune system and other kinds of fullerene derivatives (e.g., carboxyl-, aminated-ones) besides fullerenols needs to be elucidated.

8.3 Immunological Effects of Graphene and Its Derivatives

Graphene, which is the new promising form of carbon [33], is an atomically thick sheet composed of sp^2 carbon atoms arranged in a flat honeycomb structure. However, because of its hydrophobicity, graphene needs to be modified to improve its solubility for potential applications. With various advantages such as high surface area, easy modification, and the fascinating physicochemical and optical properties, graphene derivatives have shown great potential for applications in almost all fields, especially biomedicine [34–38]. Increasing numbers of evidence have demonstrated their good promise as drug/gene delivery systems [39, 40], photothermal agents [41, 42], and theranostic platforms [38, 43, 44]. Before their entry into the clinic, one has to find out how graphene and its derivatives interact with biological systems. There have been many studies focusing on the biodistribution of graphene and its derivatives and their toxicity to the respiratory system (lung), cardiovascular system, brain, liver, and kidney [45–54]. These studies provide much important information for the rational design of graphene derivatives for their applications in the biomedical field. It is noteworthy that, although the immune system plays pivotal roles in the defense and homeostasis of any organism, detailed information is still lacking on the

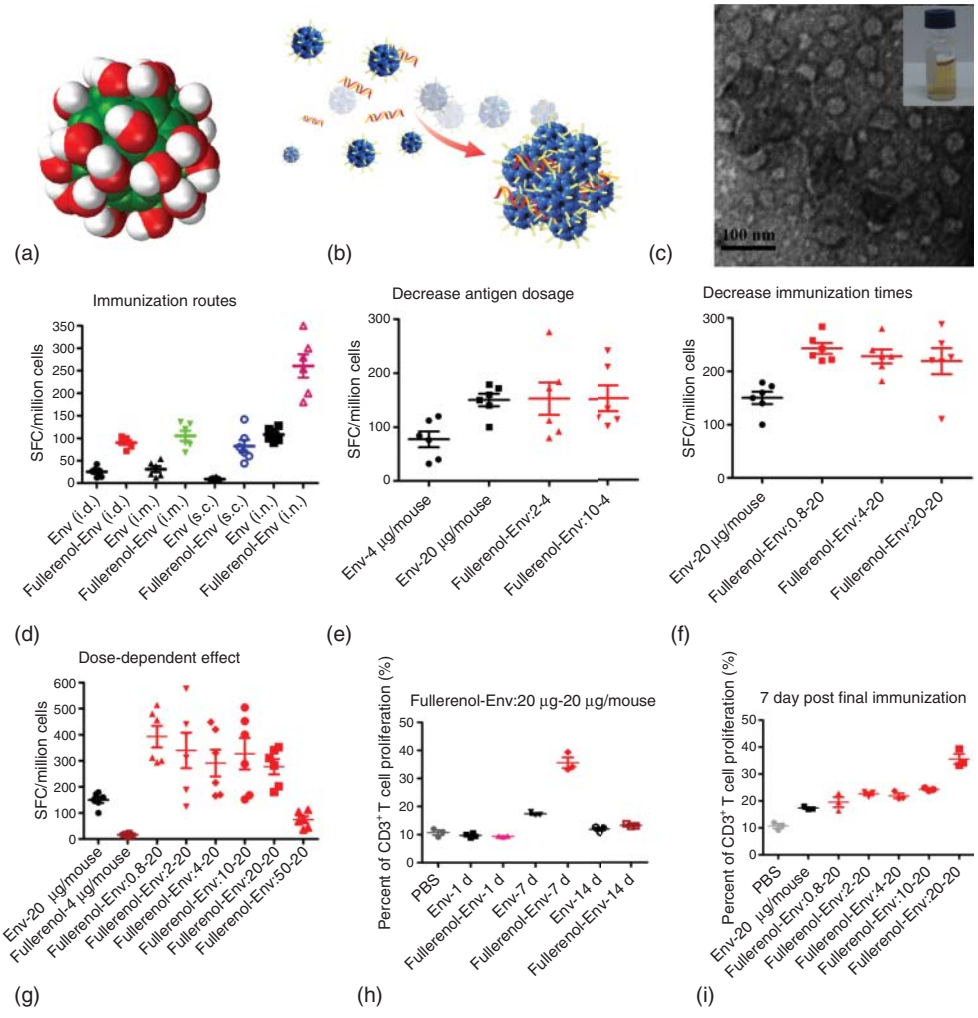

Figure 8.6 (a) Structure of fullerenol. (b) Schematic diagram of HIV Env plasmid DNA encapsulated during the self-assembly of fullerenol. (c) TEM image of Env entrapped by fullerenol. (d–i) Adjuvant properties of fullerenol (d–i). (a) Red balls represent O and white H on the fullerene surface and green balls represent C atoms. (d) Compared to naked Env immunization group, IFN-γ production (immunospot) was significantly enhanced when mice were immunized with the formulation via various immunization routes, including intradermal (i.d.), intramuscular (i.m.), subcutaneous (s.c.), intranasal (i.n.), and intraperitoneal (i.p.) injections. Fullerenol could decrease the antigen dosage (e) and immunization times (f). (g) Fullerenol of different concentrations could significantly enhance IFN-γ production via intradermal injection. (h) T-cell proliferation capability at different time points post third immunization with fullerenol–Env complex (20 μg–20 μg per mouse). (i) Fullerenol–Env complexes at various doses could promote T-cell proliferation capability at day 7 post final immunization. The statistical significance of the data was analyzed by Student's *t*-test; $^{*}p < 0.05$. (Modified from [25]. © 2013 WILEY-VCH Verlag GmbH & Co. KGaA.)

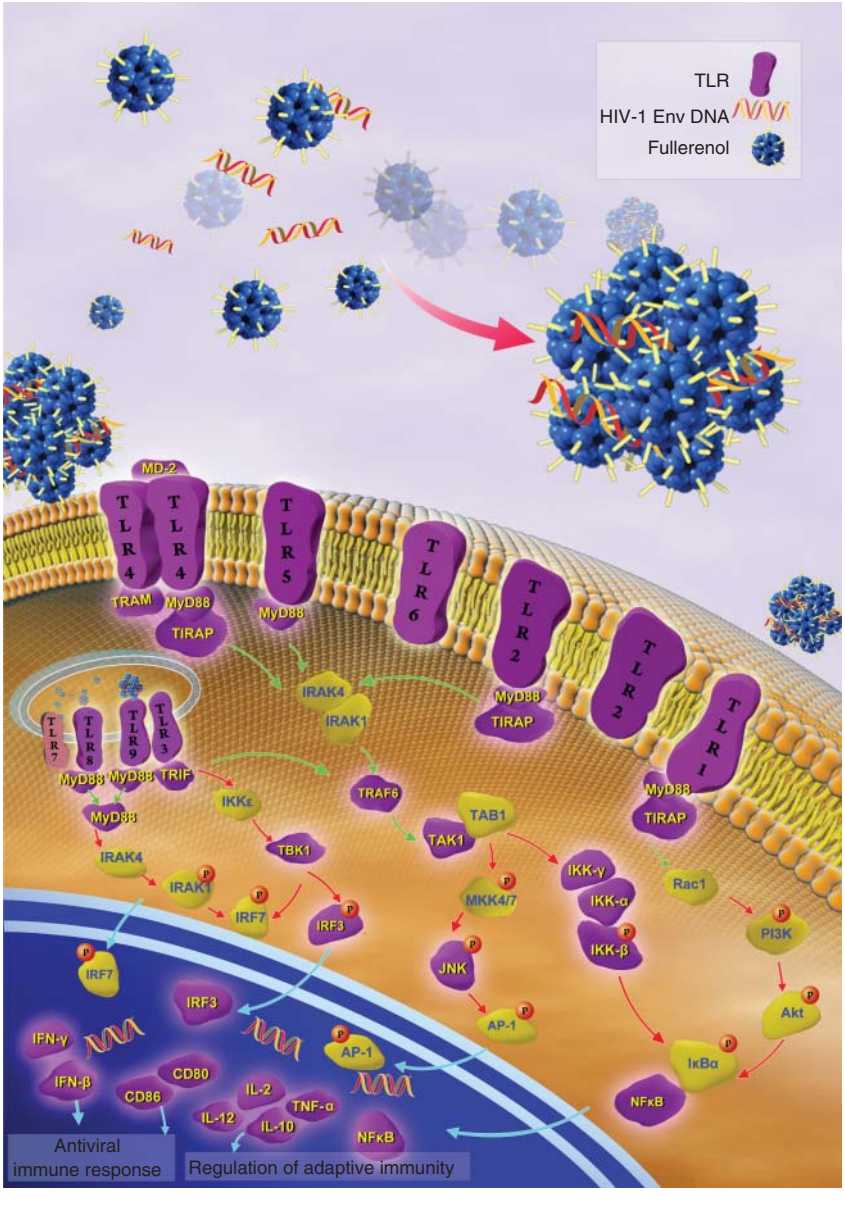

Figure 8.7 Proposed mechanism of fullerenol as a potent adjuvant. The purple modules in the picture indicate that these genes are upregulated significantly. ([25]. © 2013 WILEY-VCH Verlag GmbH & Co. KGaA.)

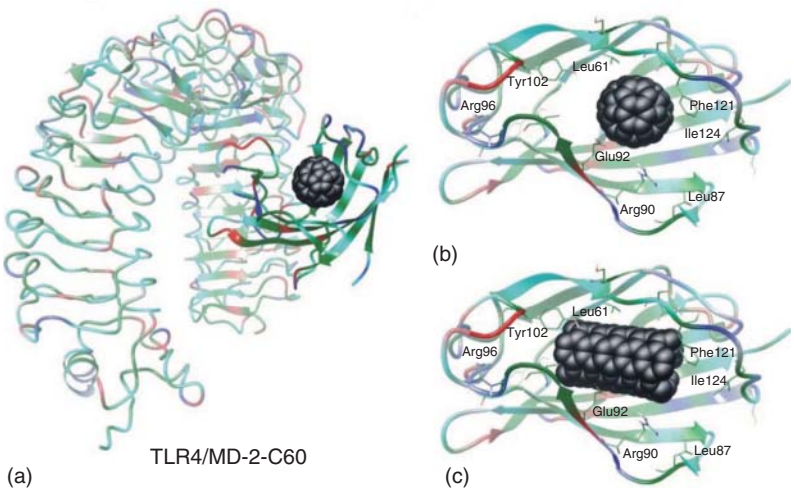

Figure 8.8 Nanostructure-bound TLR4/MD-2 ECD. (a) C_{60} is shown to bind the inner MD-2 hydrophobic pocket in TLR4/MD-2; (b, c) fullerene and the carbon nanotube are both well accommodated in the MD-2 with induced minimal distortion of the entrance residues. (Modified from [32]. © Royal Society of Chemistry.)

interactions between the immune system and graphene derivatives and on how to engineer the interaction for applications of interest. In recent years, more and more researchers have begun to focus their attention to resolve these concerns. However, all current studies mainly focus on the *in vitro* immunological effects of pristine graphene and graphene oxide (GO).

8.3.1
Immunological Effect of Pristine Graphene

Acute toxicity evaluation in our previous study has shown that pristine graphene could induce apparent cytotoxicity in murine RAW264.7 macrophages, such as reducing the MMP and inducing ROS generation [55]. Then it induced cell apoptosis through activating mitogen-activated protein kinase cascades (MAPK, e.g., JNK, ERK, and p38) and tumor growth factor-beta (TGF-β)-related signaling pathways. Meanwhile, subacute toxicity [56] demonstrated that graphene significantly stimulated the secretion of multiple cytokines (e.g., IL-1α, IL-6, IL-10, TNF-α, and GM-CSF) and chemokines (e.g., MCP-1, MIP-1α, MIP-1β, and RANTES) via activating TLRs- and NF-κB signaling pathways. Furthermore, these induced factors could alter the cell morphology via remodeling the actin assembly and attenuate the phagocytosis capability of macrophages. Sasidharan *et al.* [57] observed that the surface chemistry greatly influenced the interactions between graphene and macrophages. They found that pristine graphene (p-G) mainly got attached to the cell membrane, while functionalized graphene (f-G) was localized in the cytosol. p-G showed apparent toxicity to cell viability only

Table 8.1 *In vivo* studies on the interactions between the immune system and fullerene derivatives.

Fullerene derivatives	Injection method and dosage	Results	References
Polyhydroxy C_{60}, *N*-ethyl-polyamino C_{60}	Intravenous injection, 2.5 μg kg^{-1} (mice)	It could suppress the allergic responses via blocking ROS generation	[6]
$C_{60}(OH)_{20\pm2}$	Intratracheal injection, 0.01, 0.1, 1 mg kg^{-1} (mice)	Pretreatment with fullerenol could significantly attenuate lung inflammation induced by quartz particle via blocking ROS generation	[8]
$Gd@C_{82}(OH)_{22}$, $C_{60}(OH)_{20}$	Intraperitoneal injection, 0.76, 0.53 mg kg^{-1}	Both derivatives could induce TNF-α-mediated cellular immunity to inhibit the tumor growth	[16, 17]
$Gd@C_{82}(OH)_{22}$	Intraperitoneal injection, 0.5 mg kg^{-1}	It could induce DC maturation and activate Th1-biased immune response	[19]
$C_{60}(OH)_{24}$	Intraperitoneal injection, 40 mg kg^{-1}	Pretreatment could protect against ionizing-radiation-induced mortality possibly via enhancing immune function, decreasing oxidative damage, and improving mitochondrial function	[21]
Fullerene mixture (C_{60}: 60%, C_{70}: 25%, $<C_{75}$: 15%)	Intratracheal injection, 0.2, 2 mg kg^{-1}	It could selectively induce $CD11b^+$ cells (e.g., macrophages)-mediated splenic inflammation at day 6 post administration	[22]
$C_{60}(OH)_{20}$	Intradermal injection, 0.04, 0.2, 1 mg kg^{-1}	It could serve as vaccine adjuvant mainly via triggering multiple TLR signaling pathways to enhance the immunogenicity of HIV-1 DNA antigen	[25]

when the concentration was above 50 μg ml^{-1} but no damage was done to the integrity of cell membrane (Figure 8.9). Meanwhile, it could induce ROS generation and cell apoptosis compared to those in untreated and f-G treatment groups. The secretion levels of IL-6 and IL-8 also significantly increased when PBMCs were incubated with p-G at high concentration (75 μg ml^{-1}). However, both kinds of graphene showed no effects on the viability and proliferation capability of lymphocytes. Furthermore, they showed excellent compatibility with red blood cells, platelets, and plasma coagulation pathways.

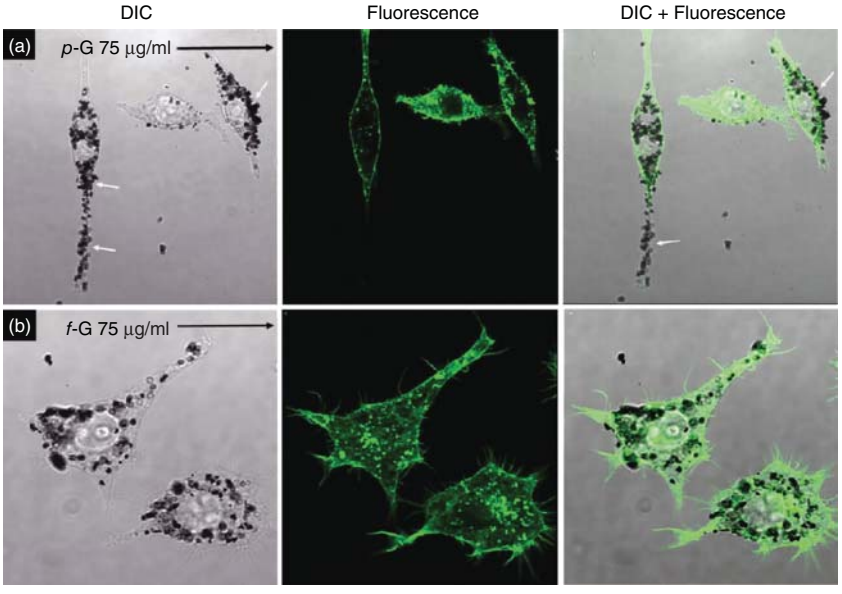

Figure 8.9 Fluorescence confocal microscopy images of (a) p-G (75 μg ml^{-1}) and (b) f-G (75 μg ml^{-1}) treated RAW264.7 cells. F-actin filaments were stained with AlexaFluor 488-conjugated phalloidin. (Modified from [57]. © 2012 WILEY-VCH Verlag GmbH & Co. KGaA.)

8.3.2
Immunological Effects of Graphene Oxide and Its Derivatives

Because of the existence of hydrophilic oxygen-containing functional groups (e.g., hydroxyl, carboxyl, and epoxyl tails) on its surface, GO has greatly improved stability, which makes it possible for its potential applications in the biomedicine field. In recent years, many have reported the immunological effects of GO and its derivatives. As one of the most important immune cells, macrophage is the most commonly used model to explore the immunological effects of nanomaterials. Chen *et al.* [58] observed that GOs of different sizes (i.e., 350 nm, 2.4 μm) could elicit the formation of autophagic vacuoles and activate the autophagic marker proteins Beclin 1 and LC3 in a concentration-dependent manner when macrophages were treated for 24 h (Figure 8.10). Autophagy is a highly conserved process that degrades intracellular components in response to stressful conditions and plays important roles in cell survival, pathogen elimination, and regulation of the immune system [59–61]. To uncover the underlying mechanism, TLR signaling pathways were systematically investigated in this study, because of their close connections with autophagy. It was shown that GO induced autophagy by activating the TLR4 and TLR9 signaling pathways. Meanwhile, GO treatment stimulated the secretions of multiple cytokines, including IL-2, IL-10, IFN-γ, and TNF-α.

Because of the critical roles played by GO's physicochemical properties, it makes great sense to systematically investigate the interaction between immune

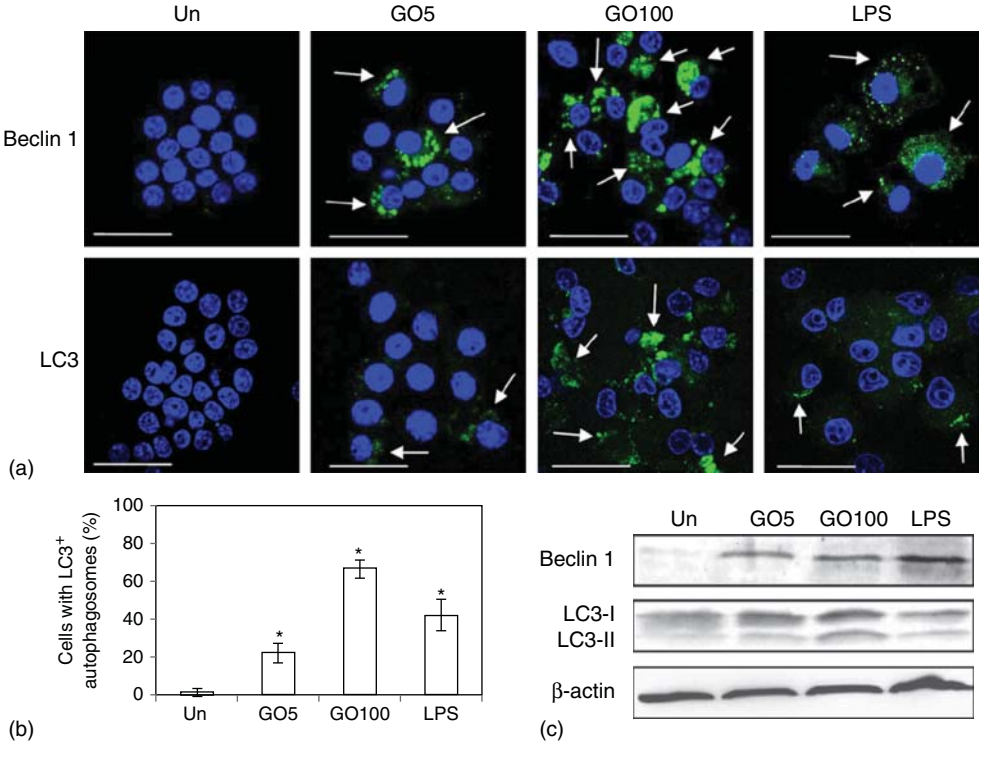

Figure 8.10 GO-induced autophagy in macrophages. (a) Immunofluorescence microscopy for Beclin 1 and LC3. (b) Percentage of cells with $LC3^+$ autophagosomes as determined from quantitative analysis of immunofluorescence microscopic images. (c) Western blot analysis of Beclin 1 and LC3. Scale bar, 100 mm. The number of $LC3^+$ dots was scored on 50–100 cells. $^*p < 0.05$. (Modified from [58]. © 2012 Elsevier Ltd.)

cells and GOs with different sizes and/or surface chemistry. Recently, the effect of size was elucidated by Russier *et al.* [62]. Their results indicated that more GO with smaller size was internalized and that this might lead to more adverse effects on murine peritoneal macrophages, such as decreased cell viability, high ROS generation, and increase of inflammatory cytokines. In their study, the researchers noted that murine peritoneal macrophages were more sensitive to GO than human monocyte-derived macrophages. As for the role of surface chemistry, Qu *et al.* [63] found that three kinds of GO (i.e., GO, aminated GO, and GO-COOH) could induce the necrosis of macrophages (J774A.1 and RAW264.7) by activating the TLR4 signaling pathway. GO could also lead to a large increase of intracellular ROS, alteration of cell morphology, and significant reduction of phagocytosis capability. In this study, all three kinds of GO showed similar size and surface charge in the culture medium. Ding *et al.* [64] reported the immunological effects of GO with different surface modifications on T lymphocytes from PBMCs. Their results showed that p-GO and GO-COOH exhibited similar toxicity to cell viability, DNA damage, and apoptosis of T cells. However,

unlike p-GO, GO-COOH did not induce the ROS generation comparable to the untreated group. It suggested that both materials might show toxicity to T cells via different mechanisms, like ROS-dependent and independent pathways.

As is well known, the homeostasis of the immune system is maintained by the crosstalk among various immune cells. That is to say, it is inaccurate to uncover the immunological effects of graphene derivatives through selecting a single type of immune cells as model. Hence, Zhi *et al.* [65] comprehensively investigated the effect of polyvinylpyrrolidone (PVP, one of commonly used biocompatible polymer materials) coating on the GO interactions with immune cells such as macrophages, DCs, and T lymphocytes, since these cells determine the initiation and regulation of innate and adaptive immunities. Compared to the GO treatment, PVP coating could significantly enhance the mitochondrial metabolism activity of macrophages and greatly reduce the apoptosis of T lymphocytes induced by GO. Both GO and GO-PVP could markedly induce DC maturation and promote the secretion of IL-6. However, GO-PVP showed less effect on the secretion of IL-1β and TNF-α than GO at the same dosage. This indicated that PVP coating greatly improved the biocompatibility of GO to immune cells and that GO-PVP might be a potential vaccine adjuvant in the future. However, a recent work reported the potential activity of GO in boosting DC-based immunotherapy for glioma [66]. It was demonstrated that the toxicity of PBMCs after incubated with DCs pulsed with GO-survivin to target glioma cells (T98G) was significantly enhanced compared to that of DCs pulsed with GO or survivin. In this study, the working concentration of GO (0.1 μg ml^{-1}) was much lower than that used by other researchers.

Undoubtedly, *in vivo* studies are of vital importance for the comprehensive understanding of the interactions between graphene derivatives and the immune system. However, there have been only very few related studies in recent years. Ni *et al.* [67] observed that GO could absorb anti-IL-10 antibody and significantly enhance the $CD8^+$ T-cell-mediated immune response compared to antibody treatment group. As carrier, GO did not influence the bioactivity of anti-IL-10 antibody and could slowly release the antibody in a pH-dependent manner. But the report just mentioned that GO did not induce the secretion of IL-12 in splenocytes. Detailed information between GO and the immune system was unknown. In another study, Shurin *et al.* [68] found that pharyngeal aspiration exposure to GO could greatly attenuate the Th2-biased immune responses in the OVA-induced asthma model and promote Th1-biased immune responses. It induced the recruitment of macrophages in the lung and stimulated the production of mammalian chitinases. Meanwhile, it augmented airway remodeling and hyper-responsiveness. Utilizing *Caenorhabditis elegans* as model, Wu *et al.* [69] confirmed that surface modification such as PEGylation could significantly improve the toxicity of GO.

In our latest study, we systematically investigated the effect of surface chemistry on GO's interaction with dendritic cells and how to engineer GO to serve as a vaccine adjuvant. In this study, GO was modified with different molecules, including polyethylene glycol (PEG) and polyethylenimine (PEI) of different molecular

weights. We could show that the cell viability was more than 90% when treated with GO and GO-PEG at the concentration of 20 μg ml^{-1}. Although free PEI of 42 μg ml^{-1} greatly decreased the viability to 15%, GO-PEG-PEI with comparable PEI content just demonstrated low toxicity to DCs and the cell viability was more than 80%. Meanwhile, the surface chemistry greatly influenced the effects of GO derivatives on DC maturation. It indicated that GO and GO-PEG had no effect on DC maturation. However, GO-PEG-PEI-10 kD demonstrated better effect on DC maturation and IL-12 production than GO-PEG-PEI-1.2 kD, while both derivatives showed similar biocompatibility to DCs. Because of its high toxicity, GO-PEG-PEI-25 kD showed no effect on DC maturation. Moreover, it has been shown that only GO-PEG-PEI-10 kD could greatly induce the upregulation of CD86 and CD80 molecular expressions on the surface of DCs comparable to that of the lipopolysaccharide (LPS) treatment group. The *in vivo* study demonstrated that intradermal injection, among the various routes, might be the optimal route for the adjuvant activity of GO-PEG-PEI to generate cellular immunity (Figure 8.11). Compared to the subcutaneous immunization strategy, T-cell proliferation capability and the secretion level of IFN-γ, TNF-α, and IL-17, which play pivotal roles in the cellular immunity, were significantly enhanced when mice were immunized with GO-PEG-PEI-based vaccine via intradermal injection. Furthermore, multiple pieces of evidence have shown that GO-PEG-PEI served as nanoadjuvant through triggering multiple TLRs and enhancing the cellular uptake of antigen to improve the immunogenicity of the antigen when using the intradermal immunization strategy.

Besides their potential side effects, another great concern is whether nanomaterials can be degraded or eliminated from the organism. Till now, this critical question for carbon nanomaterials has not been addressed because of several existing challenges. The first challenge is the reliable detection of carbon nanomaterials from the background of the complex tissue microenvironment. Secondly, it is difficult to identify the minute chemical and structural changes during biodegradation. Because of GO's high Raman activity, the modifications in vibrational spectral features of graphene caused by the formation of defects, oxidation, and changes in the number of layers can be detected by Raman spectroscopy [70]. Recently, Girish *et al.* [71] optimized a confocal Raman imaging method for three-dimensional (3D) detection of graphene in tissues and reported, for the first time, that graphene could be degraded by macrophages resident in tissues. Considering the Raman spectrum of graphene with the characteristic peak positions at 1360 cm^{-1} (D band), 1585 cm^{-1} (G band), and 2717 cm^{-1} (2D band), the intensity ratio of D (~1350 cm^{-1}) and G (~1580 cm^{-1}) bands (I_D/I_G), the formation of the D' band (~1620 cm^{-1}), and line broadening represented by full width at half-maximum (Γ) were selected as key parameters to determine the defects of graphene at different time points post intravenous injection. A series of experiments indicated that graphene was engulfed by macrophages residing in tissues, such as alveolar macrophages and Kupffer cells. The size of graphene ranged from 200 nm to several micrometers when accumulated in various tissues, such as the lung, liver, spleen, and kidney. Meanwhile, the defects appeared

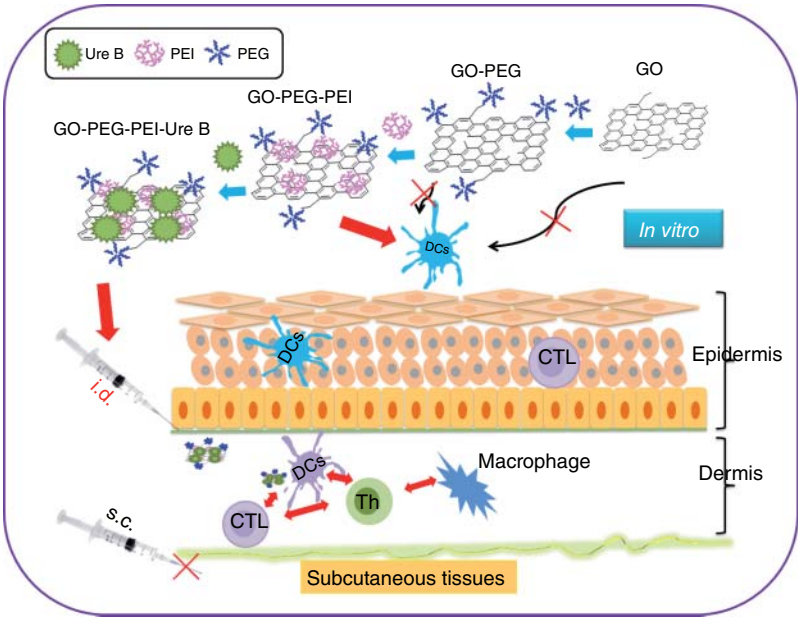

Figure 8.11 Surface chemistry and immunization route greatly influence the potential adjuvant activities of GO derivatives (Ligeng Xu, Jian Xiang, Ye Liu, Zhuang Liu, Rui Peng.).

apparently from day 8 post injection. Furthermore, the intensity of the graphene signal greatly decreased especially toward the edge regions and the 2D band disappeared at 3 months post injection (Figure 8.12). This study provides sound evidence for the potential applications of graphene-based materials in the future.

As summarized in Table 8.2, most existing studies are focused on the immunological effects of pristine graphene and GO *in vitro*. All these pieces of evidence indicate that surface functionalization can be a useful strategy to improve the biocompatibility of graphene derivatives. With appropriate engineering and exposure route, graphene derivatives can show promising applications in the biomedical field. However, there are still many questions to be answered. For instance, detailed information about how physicochemical properties like size, surface charge, and surface chemistry influence graphene derivatives' interaction with the immune system is not available. What is the underlying mechanism of the materials and how to engineer graphene derivatives to generate immune responses for the application of interest are questions that demand answers, which require additional efforts to obtain.

8.4 Perspectives and Outlook

A comprehensive understanding of the interactions between carbon nanomaterials and the immune system can provide very important guidelines for the

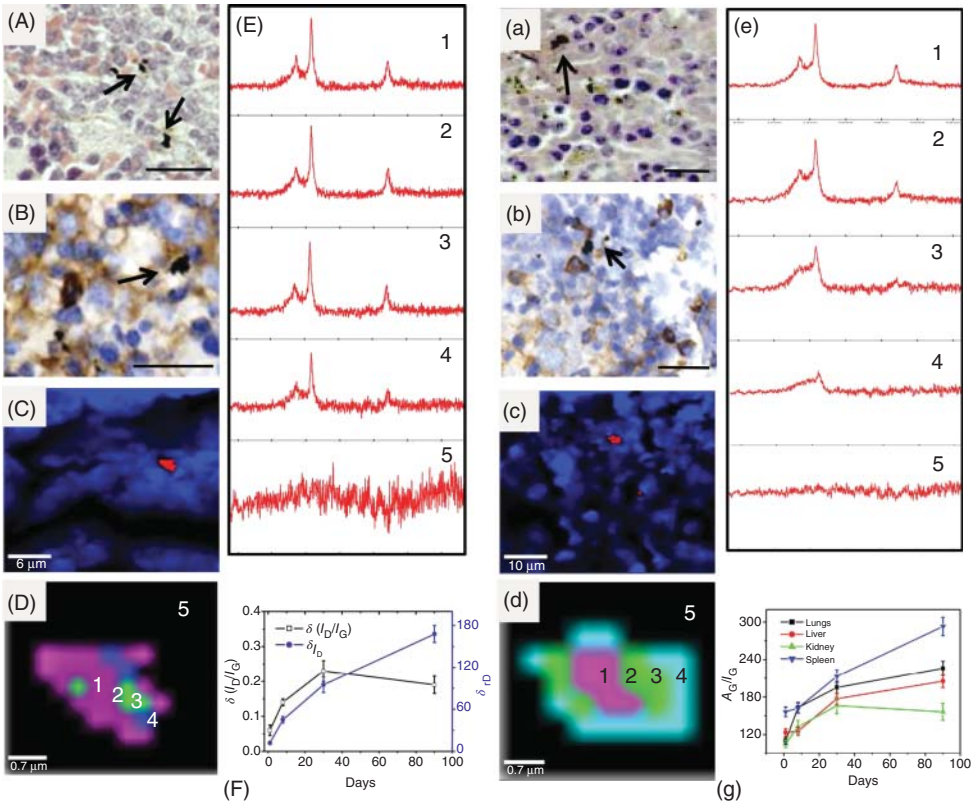

Figure 8.12 Bright-field images, Raman images, and spectral variations of graphene aggregates from 24 h (A–E) and 3 months (a–e) tissue sections. (A, a) H&E stained images of spleen tissue sections, (B, b) Macrophage-specific antibody (CD68)-stained images, (C, c) Raman images of graphene (red) embedded within spleen tissue section obtained by k-means cluster analysis. (D, d) Magnified view of graphene aggregate subjected to secondary cluster analysis showing the subclusters represented in false color code. (E, e) spectrum retrieved from five different points in the graphene aggregates marked as 1, 2, 3, 4, and 5 (1–4 from aggregate, 5 from tissue background), showing the spectral variations related to degradation on 3-month sample. (F) Plot showing the variation in $\delta_{ID/IG}$ and $\delta\Gamma_D$ values from the edges of graphene aggregates in spleen over 3 months. (G) A_G/I_G variation in the edges of graphene aggregates from lung, liver, kidney, and spleen over 3 months. Graphene aggregates are indicated by arrows (error bars in (F) and (G) represents standard deviation from three animals; scale bar – 20 µm). (Modified from [71]. © 2013 WILEY-VCH Verlag GmbH & Co. KGaA.)

rational design of the materials and their potential applications in the biomedical field. Although some important pieces of information have been obtained, the immunological study on fullerene and graphene derivatives is just at the beginning stage and there is a long way to go before we can uncover this mask. From above-mentioned results, several key issues are urgently needed to be addressed: (i) the effects of the physicochemical properties on the carbon nanomaterial

Table 8.2 Recent progress in the immunological effects of graphene derivatives.

Graphene derivatives	Lateral size	Model	Results	References
Pristine graphene	0.5–1 μm	RAW264.7	It could induce the cell apoptosis through activating MAPK and TGF-β-related signaling pathways	[55]
Pristine graphene Carboxyl-, epoxyl-, hydroxyl-graphene	0.2 μm	RAW264.7 PBMCs	Surface modification could significantly reduce the cytotoxicities of *p*-G	[57]
GO	0.35 μm 2.4 μm	RAW264.7	It induced autophagy via activating TLR signaling pathways	[58]
GO	0.13 μm 0.27 μm 1.32 μm	Human monocyte-derived macrophage Murine peritoneal macrophage	GO with smaller size showed more toxicity	[62]
GO, aminated, carboxylated graphene	1–2 μm	J774A.1 RAW264.7 Bone-marrow-derived macrophage	All kinds of materials induced cell necrosis via activating the TLR4 signaling pathway	[63]
GO GO-COOH, GO-PEI	100–300 nm	T cells in PBMC	GO and GO-COOH showed similar cytotoxicity while GO-COOH did not induce ROS generation	[64]
GO GO–PVP	0.5 μm	DCs, T cells, macrophage in PBMC	PVP coating could significantly reduce the toxicity of GO	[65]
GO	20 nm–5 μm	Asthma model of mice	It greatly attenuated the Th2-biased immune responses but augmented the airway remodeling and hyperresponsiveness	[68]
GO GO-PEG	69 nm	*C. elegans*	PEGylation could significantly improve the toxicity of GO	[69]
Graphene	150–220 nm	RAW264.7, mice	It could be degraded by tissue resident macrophages at 3 months postinjection	[71]

interactions with the immune system need to be extensively investigated. For this, standardization of the preparation, modification, and characterization methods for materials is extremely important. Meanwhile, intense cooperation among research groups working in different disciplines around the world will be also very helpful to address this issue within a short time. (ii) The development of models

is another important issue. Compared to other kinds of immune cells, such as natural killer cells and dendritic cells, macrophages are more easily accessed and cultured. Therefore, most existing studies mainly selected macrophages as their model. However, it is undoubtedly inaccurate to uncover the immunological effects of materials by choosing only one type of cells as model. (iii) It is absolutely necessary to adopt other new techniques or methods to evaluate the immunological effects and uncover the underlying mechanisms. For instance, molecular dynamics simulation may give us some clues about how materials interact with the receptor protein on the surface of immune cells. Because of the crosstalk in the immune system, systems biology approaches may be very useful for our understanding the immunological effects of carbon nanomaterials. In summary, with our rapidly growing understanding of the immunological effects and the underlying mechanisms of carbon nanomaterials, the rational design of materials for applications of interest can be realized in the future.

References

1. Kroto, H.W., Heath, J.R., Obrien, S.C. *et al.* (1985) C60: buckminsterfullerene. *Nature*, **318** (6042), 162–163.
2. Bakry, R., Vallant, R.M., Najam-ul-Haq, M. *et al.* (2007) Medicinal applications of fullerenes. *Int. J. Nanomed.*, **2** (4), 639–649.
3. Forman, H.J. and Torres, M. (2002) Reactive oxygen species and cell signaling-Respiratory burst in macrophage signaling. *Am. J. Respir. Crit. Care Med.*, **166** (12), S4–S8.
4. Andrievsky, G.V., Bruskov, V.I., Tykhomyrov, A.A. *et al.* (2009) Peculiarities of the antioxidant and radioprotective effects of hydrated C-60 fullerene nanostuctures in vitro and in vivo. *Free Radical Biol. Med.*, **47** (6), 786–793.
5. Chistyakov, V.A., Smirnova, Y.O., Prazdnova, E.V. *et al.* (2013) Possible mechanisms of fullerene C_{60} antioxidant action. *Biomed Res. Int.*, **2013**, 4.
6. Ryan, J.J., Bateman, H.R., Stover, A. *et al.* (2007) Fullerene nanomaterials inhibit the allergic response. *J. Immunol.*, **179** (1), 665–672.
7. Dellinger, A., Zhou, Z.G., Lenk, R. *et al.* (2009) Fullerene nanomaterials inhibit phorbol myristate acetate-induced inflammation. *Exp. Dermatol.*, **18** (12), 1079–1081.
8. Roursgaard, M., Poulsen, S.S., Kepley, C.L. *et al.* (2008) Polyhydroxylated C60 fullerene (fullerenol) attenuates neutrophilic lung inflammation in mice. *Basic Clin. Pharmacol. Toxicol.*, **103** (4), 386–388.
9. Yudoh, K., Karasawa, R., Masuko, K. *et al.* (2009) Water-soluble fullerene (C60) inhibits the development of arthritis in the rat model of arthritis. *Int. J. Nanomed.*, **4**, 217–225.
10. Hotamisligil, G.S. (2006) Inflammation and metabolic disorders. *Nature*, **444** (7121), 860–867.
11. Kanda, H., Tateya, S., Tamori, Y. *et al.* (2006) MCP-1 contributes to macrophage infiltration into adipose tissue, insulin resistance, and hepatic steatosis in obesity. *J. Clin. Invest.*, **116** (6), 1494–1505.
12. Patsouris, D., Neels, J.G., Fan, W. *et al.* (2009) Glucocorticoids and thiazolidinediones interfere with adipocyte-mediated macrophage chemotaxis and recruitment. *J. Biol. Chem.*, **284** (45), 31223–31235.
13. Xiao, L., Aoshima, H., Saitoh, Y. *et al.* (2010) The effect of squalane-dissolved fullerene-C60 on adipogenesis-accompanied oxidative stress and macrophage activation in a preadipocyte-monocyte co-culture system. *Biomaterials*, **31** (23), 5976–5985.
14. Jordan, J.T., Sun, W., Hussain, S.F. *et al.* (2008) Preferential migration of

regulatory T cells mediated by glioma-secreted chemokines can be blocked with chemotherapy. *Cancer Immunol. Immunother.*, **57** (1), 123–131.

15. Chen, C.Y., Xing, G.M., Wang, J.X. *et al.* (2005) Multihydroxylated $[Gd@C_{82}(OH)_{22}]_n$ nanoparticles: antineoplastic activity of high efficiency and low toxicity. *Nano Lett.*, **5** (10), 2050–2057.
16. Liu, Y., Jiao, F., Qiu, Y. *et al.* (2009) The effect of $Gd@C_{82}(OH)_{22}$ nanoparticles on the release of Th1/Th2 cytokines and induction of TNF-alpha mediated cellular immunity. *Biomaterials*, **30** (23–24), 3934–3945.
17. Liu, Y., Jiao, F., Qiu, Y. *et al.* (2009) Immunostimulatory properties and enhanced TNF-a mediated cellular immunity for tumor therapy by $C_{60}(OH)_{20}$ nanoparticles. *Nanotechnology*, **20** (41), 415102.
18. Chen, Z.Y., Liu, Y., Sun, B.Y. *et al.* (2014) Polyhydroxylated metallofullerenols stimulate IL-1β secretion of macrophage through TLRs/MyD88/NF-κB pathway and NLRP3 inflammasome activation. *Small*, **10** (12), 2362–2372.
19. Yang, D., Zhao, Y.L., Guo, H. *et al.* (2010) $[Gd@C_{82}(OH)_{22}]_n$ nanoparticles induce dendritic cell maturation and activate Th1 immune responses. *ACS Nano*, **4** (2), 1178–1186.
20. Bunz, H., Plankenhorn, S., and Klein, R. (2012) Effect of buckminsterfullerenes on cells of the innate and adaptive immune system: an in vitro study with human peripheral blood mononuclear cells. *Int. J. Nanomed.*, **7**, 4571–4580.
21. Cai, X.Q., Hao, J.J., Zhang, X.Y. *et al.* (2010) The polyhydroxylated fullerene derivative $C_{60}(OH)_{24}$ protects mice from ionizing-radiation-induced immune and mitochondrial dysfunction. *Toxicol. Appl. Pharmacol.*, **243** (1), 27–34.
22. Ding, N., Kunugita, N., Ichinose, T. *et al.* (2011) Intratracheal administration of fullerene nanoparticles activates splenic CD11b(+) cells. *J. Hazard. Mater.*, **194**, 324–330.
23. Li, H., Li, Y., Jiao, J. *et al.* (2011) Alpha-alumina nanoparticles induce efficient autophagy-dependent cross-presentation and potent antitumour response. *Nat. Nanotechnol.*, **6** (10), 645–650.
24. Brant, J.A., Labille, J., Robichaud, C.O. *et al.* (2007) Fullerol cluster formation in aqueous solutions: implications for environmental release. *J. Colloid Interface Sci.*, **314** (1), 281–288.
25. Xu, L.G., Liu, Y., Chen, Z.Y. *et al.* (2013) Morphologically virus-like fullerenol nanoparticles act as the dual-functional nanoadjuvant for HIV-1 vaccine. *Adv. Mater.*, **25** (41), 5928–5936.
26. Kawai, T. and Akira, S. (2010) The role of pattern-recognition receptors in innate immunity: update on Toll-like receptors. *Nat. Immunol.*, **11** (5), 373–384.
27. Pulendran, B. and Ahmed, R. (2006) Translating innate immunity into immunological memory: implications for vaccine development. *Cell*, **124** (4), 849–863.
28. Pulendran, B. (2009) Learning immunology from the yellow fever vaccine: innate immunity to systems vaccinology. *Nat. Rev. Immunol.*, **9** (10), 741–747.
29. Querec, T.D., Akondy, R.S., Lee, E.K. *et al.* (2009) Systems biology approach predicts immunogenicity of the yellow fever vaccine in humans. *Nat. Immunol.*, **10** (1), 116–125.
30. Kasturi, S.P., Skountzou, I., Albrecht, R.A. *et al.* (2011) Programming the magnitude and persistence of antibody responses with innate immunity. *Nature*, **470** (7335), 543–550.
31. Trinchieri, G. and Sher, A. (2007) Cooperation of Toll-like receptor signals in innate immune defence. *Nat. Rev. Immunol.*, **7** (3), 179–190.
32. Turabekova, M., Rasulev, B., Theodore, M. *et al.* (2014) Immunotoxicity of nanoparticles: a computational study suggests that CNTs and C-60 fullerenes might be recognized as pathogens by Toll-like receptors. *Nanoscale*, **6** (7), 3488–3495.
33. Bussy, C., Ali-Boucetta, H., and Kostarelos, K. (2013) Safety considerations for graphene: lessons learnt from carbon nanotubes. *Acc. Chem. Res.*, **46** (3), 692–701.

34. Geim, A.K. and Novoselov, K.S. (2007) The rise of graphene. *Nat. Mater.*, **6** (3), 183–191.
35. Huang, X., Qi, X.Y., Boey, F. *et al.* (2012) Graphene-based composites. *Chem. Soc. Rev.*, **41** (2), 666–686.
36. Loh, K.P., Bao, Q.L., Eda, G. *et al.* (2010) Graphene oxide as a chemically tunable platform for optical applications. *Nat. Chem.*, **2** (12), 1015–1024.
37. Stankovich, S., Dikin, D.A., Dommett, G.H.B. *et al.* (2006) Graphene-based composite materials. *Nature*, **442** (7100), 282–286.
38. Yang, K., Feng, L.Z., Shi, X.Z. *et al.* (2013) Nano-graphene in biomedicine: theranostic applications. *Chem. Soc. Rev.*, **42** (2), 530–547.
39. Feng, L.Z., Yang, X.Z., Shi, X.Z. *et al.* (2013) Polyethylene glycol and polyethylenimine dual-functionalized nano-graphene oxide for photothermally enhanced gene delivery. *Small*, **9** (11), 1989–1997.
40. Zhang, L.M., Xia, J.G., Zhao, Q.H. *et al.* (2010) Functional graphene oxide as a nanocarrier for controlled loading and targeted delivery of mixed anticancer drugs. *Small*, **6** (4), 537–544.
41. Yang, K., Hu, L.L., Ma, X.X. *et al.* (2012) Multimodal imaging guided photothermal therapy using functionalized graphene nanosheets anchored with magnetic nanoparticles. *Adv. Mater.*, **24** (14), 1868–1872.
42. Yang, K., Zhang, S.A., Zhang, G.X. *et al.* (2010) Graphene in mice: ultrahigh in vivo tumor uptake and efficient photothermal therapy. *Nano Lett.*, **10** (9), 3318–3323.
43. He, S.J., Song, B., Li, D. *et al.* (2010) A graphene nanoprobe for rapid, sensitive, and multicolor fluorescent DNA analysis. *Adv. Funct. Mater.*, **20** (3), 453–459.
44. Tang, L.A.L., Wang, J.Z., and Loh, K.P. (2010) Graphene-based SELDI probe with ultrahigh extraction and sensitivity for DNA oligomer. *J. Am. Chem. Soc.*, **132** (32), 10976–10977.
45. Chang, Y.L., Yang, S.T., Liu, J.H. *et al.* (2011) In vitro toxicity evaluation of graphene oxide on A549 cells. *Toxicol. Lett.*, **200** (3), 201–210.
46. Chatterjee, N., Eom, H.J., and Choi, J. (2014) A systems toxicology approach to the surface functionality control of graphene-cell interactions. *Biomaterials*, **35** (4), 1109–1127.
47. Horvath, L., Magrez, A., Burghard, M. *et al.* (2013) Evaluation of the toxicity of graphene derivatives on cells of the lung luminal surface. *Carbon*, **64**, 45–60.
48. Kanakia, S., Toussaint, J.D., Chowdhury, S.M. *et al.* (2014) Dose ranging, expanded acute toxicity and safety pharmacology studies for intravenously administered functionalized graphene nanoparticle formulations. *Biomaterials*, **35** (25), 7022–7031.
49. Li, B., Yang, J.Z., Huang, Q. *et al.* (2013) Biodistribution and pulmonary toxicity of intratracheally instilled graphene oxide in mice. *NPG Asia Mater.*, **5**, e44.
50. Ma, Y.F., Shen, H., Tu, X.L. *et al.* (2014) Assessing in vivo toxicity of graphene materials: current methods and future outlook. *Nanomedicine-UK*, **9** (10), 1565–1580.
51. Sasidharan, A., Panchakarla, L.S., Chandran, P. *et al.* (2011) Differential nano-bio interactions and toxicity effects of pristine versus functionalized graphene. *Nanoscale*, **3** (6), 2461–2464.
52. Wu, Q.L., Yin, L., Li, X. *et al.* (2013) Contributions of altered permeability of intestinal barrier and defecation behavior to toxicity formation from graphene oxide in nematode *Caenorhabditis elegans*. *Nanoscale*, **5** (20), 9934–9943.
53. Yang, K., Wan, J.M., Zhang, S.A. *et al.* (2011) In vivo pharmacokinetics, long-term biodistribution, and toxicology of PEGylated graphene in mice. *ACS Nano*, **5** (1), 516–522.
54. Zhang, W.D., Wang, C., Li, Z.J. *et al.* (2012) Unraveling stress-induced toxicity properties of graphene oxide and the underlying mechanism. *Adv. Mater.*, **24** (39), 5391–5397.
55. Li, Y., Liu, Y., Fu, Y.J. *et al.* (2012) The triggering of apoptosis in macrophages by pristine graphene through the MAPK and TGF-beta signaling pathways. *Biomaterials*, **33** (2), 402–411.
56. Zhou, H.J., Zhao, K., Li, W. *et al.* (2012) The interactions between pristine graphene and macrophages and the

production of cytokines/chemokines via TLR- and NF-kappa B-related signaling pathways. *Biomaterials*, **33** (29), 6933–6942.

57. Sasidharan, A., Panchakarla, L.S., Sadanandan, A.R. *et al.* (2012) Hemocompatibility and macrophage response of pristine and functionalized graphene. *Small*, **8** (8), 1251–1263.
58. Chen, G.Y., Yang, H.J., Lu, C.H. *et al.* (2012) Simultaneous induction of autophagy and toll-like receptor signaling pathways by graphene oxide. *Biomaterials*, **33** (27), 6559–6569.
59. Deretic, V., Saitoh, T., and Akira, S. (2013) Autophagy in infection, inflammation and immunity. *Nat. Rev. Immunol.*, **13** (10), 722–737.
60. Levine, B., Mizushima, N., and Virgin, H.W. (2011) Autophagy in immunity and inflammation. *Nature*, **469** (7330), 323–335.
61. Muenz, C. (2009) Enhancing immunity through autophagy. *Annu. Rev. Immunol.*, **27**, 423–449.
62. Russier, J., Treossi, E., Scarsi, A. *et al.* (2013) Evidencing the mask effect of graphene oxide: a comparative study on primary human and murine phagocytic cells. *Nanoscale*, **5** (22), 11234–11247.
63. Qu, G.B., Liu, S.J., Zhang, S.P. *et al.* (2013) Graphene oxide induces toll-like receptor 4 (TLR4)-dependent necrosis in macrophages. *ACS Nano*, **7** (7), 5732–5745.
64. Ding, Z.J., Zhang, Z.J., Ma, H.W. *et al.* (2014) In vitro hemocompatibility and toxic mechanism of graphene oxide on human peripheral blood T lymphocytes and serum albumin. *ACS Appl. Mater. Interfaces*, **6** (22), 19797–19807.
65. Zhi, X., Fang, H.L., Bao, C.C. *et al.* (2013) The immunotoxicity of graphene oxides and the effect of PVP-coating. *Biomaterials*, **34** (21), 5254–5261.
66. Wang, W., Li, Z.J., Duan, J.H. *et al.* (2014) In vitro enhancement of dendritic cell-mediated anti-glioma immune response by graphene oxide. *Nanoscale Res. Lett.*, **9** (311), 4.
67. Ni, G.Y., Wang, Y.J., Wu, X.L. *et al.* (2012) Graphene oxide absorbed anti-IL10R antibodies enhance LPS induced immune responses in vitro and in vivo. *Immunol. Lett.*, **148** (2), 126–132.
68. Shurin, M.R., Yanamala, N., Kisin, E.R. *et al.* (2014) Graphene oxide attenuates Th2-type immune responses, but augments airway remodeling and hyperresponsiveness in a murine model of asthma. *ACS Nano*, **8** (6), 5585–5599.
69. Wu, Q.L., Zhao, Y.L., Fang, J.P. *et al.* (2014) Immune response is required for the control of in vivo translocation and chronic toxicity of graphene oxide. *Nanoscale*, **6** (11), 5894–5906.
70. Dresselhaus, M.S., Jorio, A., Hofmann, M. *et al.* (2010) Perspectives on carbon nanotubes and graphene Raman spectroscopy. *Nano Lett.*, **10** (3), 751–758.
71. Girish, C.M., Sasidharan, A., Gowd, G.S. *et al.* (2013) Confocal Raman imaging study showing macrophage mediated biodegradation of graphene in vivo. *Adv. Healthcare Mater.*, **2** (11), 1489–1500.

9
Neuro-, Hepato-, and Nephrotoxicity of Carbon-based Nanomaterials

Jia Yao and Yongbin Zhang

9.1
Carbon-based Nanomaterials: Introduction

Historically, carbon-based nanomaterials come from incidences such as volcanoes or combustion; recent advances in nanotechnology enable the mass production of engineered carbon-based nanomaterials. Based on their shape, engineered carbon nanomaterials can be categorized as carbon nanotubes (CNTs), fullerenes, graphenes, and carbon nanoparticles (NPs). As one of the most important types of carbon nanomaterials, CNTs are one-dimensional forms of graphitic material. Depending on the number of graphene sheets formed, CNTs can be further categorized into single-walled carbon nanotubes (SWCNTs), double-walled carbon nanotubes (DWCNTs), and multi-walled carbon nanotubes (MWCNTs) [1]. Normally, the size of SWCNT ranges from 1 to 2 nm in diameter and from 0.05 to 1 μm in length. In contrast, graphene is a two-dimensional, atomic-scale, hexagonal lattice in the form of a flat sheet. Based on the number of layers in the materials, the graphene family includes monolayer graphene and multilayer graphene. As the first engineered carbon-based nanomaterial, fullerene (C_{60}) – also called buckminsterfullerene, or the "Bucky ball" after Richard Buckminster Fuller – is characterized as an allotrope of carbon, which consists of 60 carbon atoms joined together to form a cage-like structure. C_{60} is not water soluble, but it is soluble in aromatic solvents (e.g., toluene or benzene). However, C_{60} can be functionalized (e.g., with –OH, –COOH, or $–NH_2$) to increase its hydrophilicity. The unique physical and chemical properties of carbon-based nanomaterials endow them with great potential for biomedical applications, ranging from early diagnosis, biomedical imaging, and targeted photothermal therapy to drug delivery and tissue engineering [2–4].

Biomedical Applications and Toxicology of Carbon Nanomaterials, First Edition.
Edited by Chunying Chen and Haifang Wang.

9.2 Neurotoxicity of Carbon-based Nanomaterials

The central nervous system (CNS), in particular the brain, is considered as one of the most important systems of the human body. It integrates information and coordinates and influences the activity of other organs in the body. Although the brain accounts for only 2% of the body weight, it consumes 25% of the whole-body glucose for energy production and functioning [5]. The importance of the CNS is further highlighted by the severity of various CNS diseases, such as neurological disorders, psychiatric disorders, and neurodegenerative diseases, as well as the emotional and socioeconomic burden these diseases impose on the patients, their families, and the society. The critical function of the CNS further attests the necessity for the development of CNS therapeutics as well as systematic investigations of materials that may induce potential neurotoxicity. Under physiological conditions, the brain is protected by the blood–brain barrier (BBB) from multiple neurotoxic insults [6, 7]. Nevertheless, pathological changes in the BBB could lead to the influx of neurotoxins into the brain as a result of compromised BBB structure and function. In recent decades, novel materials/carriers, especially nanomaterials, have been developed to cross the BBB or facilitate BBB penetration [8–10]. During the past few decades, the risk for CNS exposure to carbon-based nanomaterials has increased tremendously. Increased mass production of carbon-based nanomaterials can lead to increased occupational exposure, whereas utilization of carbon-based nanomaterials as carriers for drug delivery, particularly to the brain, or for biomedical imaging purposes also inevitably results in increased CNS exposure [11, 12]. Further, previous studies have indicated potential translocation and distribution of carbon-based nanomaterials into the brain with peripheral routes of administration [13].

9.2.1 Blood–Brain Barrier and BBB Penetration by Carbon-based Nanomaterials

Despite the increasing demand for effective therapeutics and diagnostics to treat disorders of the CNS, the development of CNS therapies has been impeded [10]. A major challenge in the development of therapeutics for the CNS is the penetration of the BBB [10, 14]. The BBB is an extended plasma membrane that contains tight junctions between the adjacent endothelial cells of the cerebral capillaries [6, 7]. Unlike noncerebral capillaries, the cerebral endothelium does not have vesicles for macromolecular transport. Astrocyte end-feet cover most (85%) of the cerebral capillary endothelial cells and they also contain a thick basement membrane [15]. Further, endothelial cells at the BBB contain extracellular and intracellular enzymes including peptidases, nucleotidases, monoamine oxidase, and, most importantly, cytochrome P450 enzymes, which offer additional metabolic protection to the brain [16, 17]. The presence of such complex combinations among astrocytes, cerebral capillaries, and basement membrane strongly supports the

BBB function [18, 19] while at the same time raising the challenge for delivery of therapeutics into the brain [10, 20].

For the past two decades, great endeavors have been made to develop effective carriers for BBB penetration. Among the various strategies, nanomaterial-based delivery systems show great promise to improve the uptake and targeted delivery of therapeutics into the brain [9, 10]. Conversely, increased BBB penetration via nanomaterial-based technologies has raised concerns on the potential neurotoxicity associated with the nanomaterials used [21, 22]. In particular, it has been indicated that the olfactory nerve pathway may serve as a portal for NPs to enter into the CNS in humans who are environmentally or occupationally exposed to airborne NPs. De Lorenzo demonstrated that, when silver-coated colloidal gold particles (50 nm) were intranasally administered in squirrel monkeys, the NPs anterogradely moved in the axons of the olfactory nerve to the olfactory bulbs [23]. Olfactory epithelium exposure to manganese, cadmium, nickel, and cobalt nanomaterials could lead to translocation of the nanomaterials to the brain via olfactory neurons [20, 22–25]. Oberdörster *et al.* [26] showed that inhalation of elemental ^{13}C particles of size 36 nm led to a significant and persistent increase in the accumulation of ^{13}C NPs in the olfactory bulb. Nevertheless, Mercer *et al.* demonstrated that 12 days of inhalation exposure to MWCNTs at 5 h per day led to the distribution of MWCNTs in various tissues/organs including the brain [27]. It has been reported that 14-nm carbon black particles might translocate to the olfactory bulb through olfactory neurons, leading to the activation of microglia cells and induction of proinflammatory cytokines and chemokines [28].

Multiple studies have reported that certain carbon nanomaterials are able to penetrate the BBB and enter into the brain. However, to date, in-depth investigations of the neurotoxicity of these nanomaterials are largely scarce. In this section, we will review the current knowledge of the neurotoxicity of carbon-based nanomaterials, including SWCNTs, MWCNT, and fullerene.

9.2.2
Neurotoxicity of Carbon Nanotubes

Previous studies documenting the BBB penetration capability of CNTs have raised concerns of their potential neurotoxicity. To address this issue, multiple *in vitro* studies using either neuronal cell lines or primary neural cultures were performed to evaluate the toxicity of both SWCNTs and MWCNTs. SWCNTs have been demonstrated to decrease cell viability in PC12 neuronal cells in a dose- and time-dependent manner [29]. In addition, the cytotoxic potential of SWCNTs is also dependent on surface coating, such as PEGylation [29, 30]. The surface PEGylation of carbon nanotube altered the surface hydrophobicity of the materials, improved the biocompatibility, decreased the cellular dosages (surface binding or intracellular uptake), thus reduced the cytotoxicity. It is appreciable that the morphology/shape, surface charge, length, diameter, and purity of the materials were characterized using different instrumentation in the study. However, it is possible that the pegylated CNT in this study may not be fully functionalized by

PEG during the synthesis process or could be degraded during storage based on the negative zeta potential data. It is worth noting that complete characterization of the nanomaterials needs to be performed before any biological study in the nanotoxicology field. Mechanistically, the toxicity of SWCNT was associated with activation apoptosis via G2/M phase cell-cycle arrest, decreased mitochondrial membrane potential, decreased activity of antioxidant enzymes, and induction of reactive oxygen species (ROS) [31]. The same group later demonstrated that the antioxidant vitamin E prevented the oxidative stress induced by SWCNT, renormalized mitochondrial membrane potential, and inhibited the activation of the apoptotic pathway [32]. Chen *et al.* [33] demonstrated that MWCNTs inhibit CA1 glutamatergic synaptic transmission in rat hippocampal slices. Using the same model, the same group also reported that MWCNTs inhibited the voltage-gated potassium channels and increased the excitability of hippocampal CA1 neurons [34]. Aside from the neurotoxicity derived directly from CNTs, impurities – in particular metal impurities in CNTs – may also lead to neuronal death. Meng *et al.* [35] reported that a high iron content in MWCNTs led to disruption of the cytoskeletal structure, reduction in cell viability, compromised neuronal differentiation capacity, and dopaminergic phenotype of PC12 cells. We appreciate that the investigators used ICP-MS to validate the metal impurity of the commercial CNT before the toxicological evaluation and found the significant difference in the impurity report from the manufacture. It is crucial that the validation of the physical and chemical properties of the nanomaterials as a good practice before, during, and after the nanotoxicology. Most recently, Bussy *et al.* [36] investigated the region-specific neurotoxic response to various types of MWCNTs using mixed glial cultures derived from different regions of embryonic rat brains, including both frontal cortex and striatum. The authors demonstrated that mixed glia derived from the striatum exhibited greater cytotoxic responses to MWCNTs than those from the frontal cortex and that the increase in cytotoxic sensitivity was due to the increased number of microglia in the striatum.

In addition to the aforementioned i*n vitro* studies, a few *in vivo* studies also indicated the potential toxicity associated with CNTs. Bardi *et al.* [37] reported that stereotactic injection of two functionalized MWCNTs (f-MWCNTs) led to the uptake of the nanotubes in various neural tissue cells, including microglia, astrocytes, and neurons. Both f-MWCNTs led to an acute transient induction of inflammatory cytokine expression, including TNF-α, IL-1β, IL-6, and IL10. Further, there was increased glial activation at the sites of injection, as indicated by a significant increase in the levels of glial fibrillary acidic protein (GFAP) and CD11b (Figure 9.1) [37].

A recent study investigating the impact of PEGylated SWCNTs (PEG-SWCNTs) on the consolidation and retrieval of contextual memory in rats revealed that short-term (30 min) hippocampal infusion of the material led to impaired fear memory retrieval and caused lipid peroxidation in the hippocampus. However, the impairment was transient and was overcome by the mobilization of antioxidant defense mechanisms at 24 h [38]. Further, the impact of PEG-SWCNT occurred at low and intermediate but not high concentration,

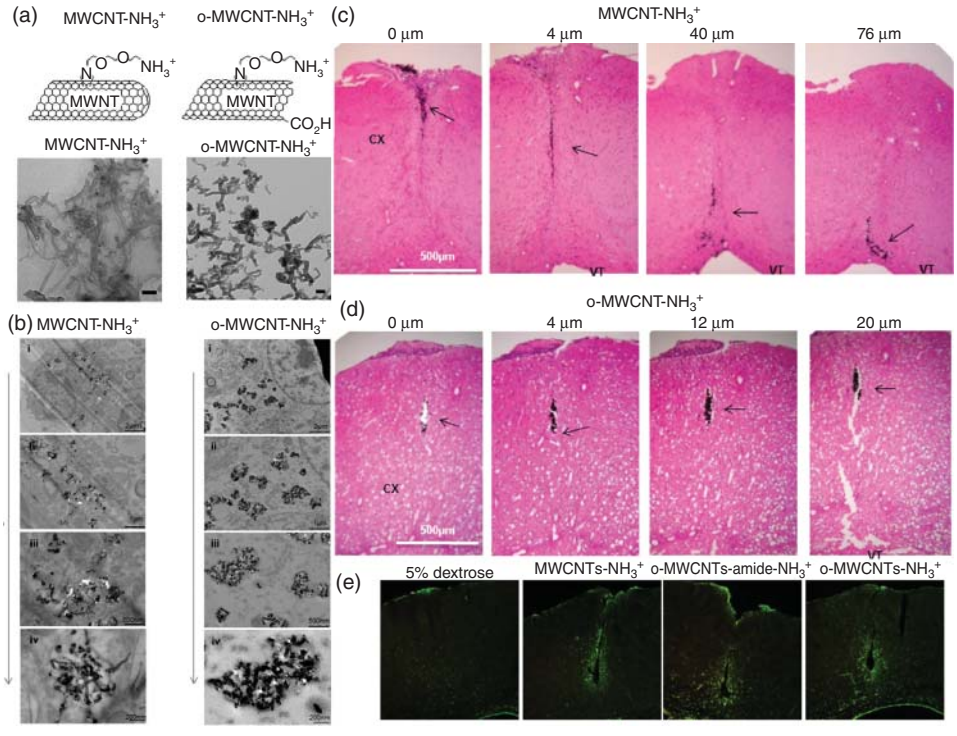

Figure 9.1 Uptake of functionalized MWCNTs by neural tissues and transient induction on neuroinflammatory responses in mouse brain. (a) Chemical structure of functionalized MWCNTs. (b) Cellular uptake of neural cells. (c, d) Parenchymal distribution of MWCNT-NH_3^+ (c) and o-MWCNT-NH_3^+ (d) after stereotactic administration. (e) Transient induction of glial activation after MWCNT injection. (Adapted from [37].)

suggesting that the concentration-dependent increase in the dispersion particle size may affect biological responses [38]. However, the negative zeta potential charge of the PEG-coated materials indicated that the SWCNTs were not fully enveloped by PEG, and the materials may form the aggregates in the dispersion. In addition, there was no clear information of the metal impurity of the nanomaterials, the possible metal impurity might impair the fear memory retrieval and cause lipid peroxidation. Interestingly, a recent study demonstrated that MWCNTs induced brain deformity in the embryo in pregnant $p^{53+/-1}$ C57BL/6J mice without migrating through the BBB, indicating potential genotype-dependent impact of MWCNTs on fetal development [39].

9.2.3
Strategies to Reduce Neurotoxicity of Carbon Nanotubes

Recently, a few studies have looked into strategies to reduce potential neurotoxicity of CNTs by surface modification. It was demonstrated that enveloping

SWCNT molecules with polypyrrole (PPy) could lower the toxicity in rat hippocampal neurons and glial co-culture compared to when using pristine SWCNTs [40]. Another group reported that oxidized MWCNTs (o-MWCNTs) had no impact on the growth rate or viability of PC12 cells during the 24-h experimental period [41]. Similarly, our group demonstrated that PEG-SWCNTs induced less oxidative stress and exhibited less cytotoxicity than pristine SWCNTs in PC12 cells [29]. Avti *et al.* reported that a single bolus intravenous injection of gadolinium nanoparticle-catalyzed SWCNTs solubilized with the amphiphilic polymer PEG-DSPE (PEG-DSPE-Gd-SWCNT) at a potentially non-toxic therapeutic dose (0.5 mg kg^{-1} bw) led to the distribution of nanoparticles in the lung, liver, kidney, spleen, and brain up to 5 days. Further, no inflammation or changes in lipid peroxidation or plasma proinflammatory cytokines were observed, indicating that at a clinically relevant dose PEG-DSPE-Gd-SWCNTs were well tolerated [42]. In addition to surface modification, Ge *et al.* [43] demonstrated the competitive binding of blood proteins on the SWCNT surface and that, based on the adsorption capacity of the SWCNTs, the protein-surface coating could significantly reduce cytotoxicity.

9.2.4 Neurotoxicity of Other Carbon-based Nanomaterials

In addition to CNTs, fullerenes have been of particular interest due to their inhibitory effect against human immunodeficiency virus (HIV) activity via inhibition of an HIV protease essential for the virus's survival [44]. Fullerenes have been demonstrated to interact with biological membranes to elicit antimicrobial action, antitumor activity, enzyme inhibition, DNA photocleavage, and neuroprotective activity via antioxidant activity [45]. Currently, fullerenes are widely used in fuel cells, semiconductors, and product coatings [25]. Compared to that of CNTs, the impact of fullerene on the CNS is less investigated. To date, only a few *in vitro* studies have investigated the impact of fullerenes on neural cells, and those studies primarily focus on the neuroprotective potential of fullerenes. Fullerene C_{60} was demonstrated to protect cultured chromaffin cells against levodopa toxicity [46]. Polyhydroxylated C_{60} fullerenols have been proposed as glutamate receptor antagonists and neuroprotective agents [47]. Fullerene and fullerenols were also demonstrated to protect against a variety of neurotoxic insults, including lead exposure [48], amyloid-β peptides [49], and MPP+/MPTP [50].

In the past decade, graphene and graphene oxide have gained increased interest in neurotherapeutic development. Graphene technology-based biosensors have shown improved accuracy in glucose level detection. Further, because of their unique optical and electromagnetic properties, graphene and graphene oxide have been experimented in novel deep-brain stimulation technology as well as in brain–computer interface and robotic-based neurorehabilitation [51]. However, in contrast to the advancement in the development of graphene for its therapeutic potential, investigations regarding its potential neurotoxicity are largely scarce,

and, to date, there is only very little preclinical data on the neurotoxicity of graphene and graphene oxide [51].

9.3
Hepato and Nephrotoxicity of Carbon-based Nanomaterials

The essential functions of the liver have long been established, which include nutrient homeostasis, filtration of particulates, protein synthesis, bioactivation and detoxification of various metabolites, and production of digestive biochemicals. All these functions could be compromised by acute or chronic exposure to liver-specific or nonspecific toxicants, which will eventually lead to multiple liver-related diseases or even death. The kidneys, also vital organs of the human body, play a principal role in the excretion of metabolic wastes, regulation of electrolyte homeostasis, acid–base balance, hormone secretion, and regulation of blood pressure. Compromised kidney functions, either acute or chronic, can often lead to systemic kidney failure and require routine dialysis or kidney transplantation. Because of their vital physiological functions involved in the metabolism and excretion of molecules, including carbon-based nanomaterials, great efforts have been made to investigate the impact and potential toxicity of carbon-based nanomaterials to the liver and kidney.

9.3.1
Carbon Nanotube Biodistribution in the Liver and Kidney

In the past decade, CNTs have gained significant popularity in biomedical applications, ranging from biomedical imaging for disease diagnosis to drug delivery, tissue engineering, and cancer therapy [12, 52]. To ensure the safety and therapeutic potential of CNTs in clinical applications, it is critical to fully investigate their pharmacological and toxicological profile. To date, there are a few common techniques for toxicokinetic/biodistribution studies of CNTs including radiolabeling of CNTs coupled with quantitative radioactive data collection, MRI/PET/CT-based dynamic *in vivo* imaging analyses, and Raman spectroscopy for the identification of CNT signatures and tissue distribution [53–56]. So far, findings from multiple investigations indicate that the biodistribution of CNTs heavily depends on their physiochemical properties, such as functionalization, surface modification, size, and dispersity (Figure 9.2) [56].

PEGylation is the most commonly used surface modification of CNTs to reduce their uptake in the reticuloendothelial system (RES) and increase their half-life in the circulation [57]. Using ^{13}C-isotope-enriched SWCNTs and isotope mass spectrometry, Yang *et al.* [58] reported that functionalization by covalent PEGylation significantly increased the half-life of SWCNTs in the blood circulation, after intravenous injection, to approximately 15.3 h. One day after injection, 30% of the injected PEG-SWCNTs was retained in the blood circulation, whereas in the case of pristine SWCNTs only 0.2% of the injected

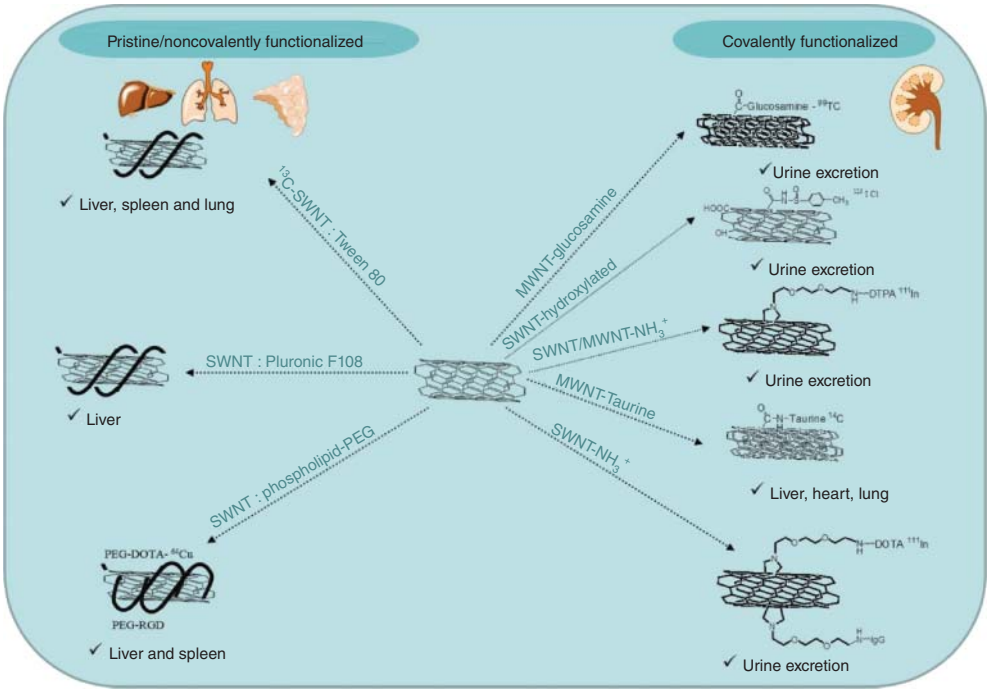

Figure 9.2 Biodistribution of carbon nanotubes based on the nature of functionalization. Pristine/noncovalently functionalized CNTs primarily accumulate in the RES system, whereas covalently functionalized CNTs can be excreted via urine in additional to RES accumulation [56].

dose remained in the blood circulation 1 day post exposure [58]. The authors further reported that, upon injection, covalent PEG-SWCNTs exhibited a rapid distribution ($T_{1/2\alpha} = 20$ min) in blood circulation and tissue and a long half-life in the elimination phase ($T_{1/2\beta} = 22.5$ h) [58]. Increased half-life of PEG-SWCNTs was paralleled by the relatively low hepatic uptake and absence of accumulation in the brain, intestine, or muscle. However, slow clearance from the liver and spleen, but not other organs, was also observed, as a considerable amount was detectable 7 days post exposure [58]. Similarly, Bhirde *et al.* [59] reported that covalent PEG-SWCNT exhibited higher dispersity than pristine SWCNTs. Covalent PEGylation of SWCNT-cisplatin also led to a prolonged half-life in the circulation with no accumulation of PEG-SWCNT in major organs and greater tumor inhibition *in vivo* [59]. In addition to covalent modification, noncovalent PEGylation was also found to increase the half-life of SWCNTs to about 2 h, although significant uptake by the RES was observed [60]. In a subsequent study, the same group used Raman spectroscopy and investigated the biodistribution of multiple noncovalent PEG-SWCNTs at various degrees of surface PEGylation [53, 61]. Consistent with previous findings, they demonstrated that noncovalent PEG-SWCNTs exhibited longer half-life in the circulation. Nanoparticles were

mainly taken up by the RES, and higher PEGylation density was associated with lower RES uptake and more rapid clearance from organs [53]. Prencipe *et al.* [62] increased PEGylation of SWCNTs based on poly(gultamic acid) and poly(maleic anhydride-*alt*-1-octadecene) and demonstrated that increased PEGylation of SWCNTs resulted in high stability in aqueous solutions at various pH values and significantly extended the circulation half-life to 22.1 h coupled with delayed clearance by the RES upon intravenous injection in mice. Campagnolo *et al.* [63] deployed a fluorescently labeled, noncovalent PEG-SWCNT and investigated the biodistribution in pregnant mice and observed localization of fluorescence in major organs, including the liver, lung, brown fat tissue, thymus, pancreas, spleen, and kidney. No brain localization of PEG-SWCNTs was detected, indicating no BBB penetration. Interestingly, PEG-SWCNTs were found in all placentas, both on the maternal and fetal side, but not in the fetus [63].

In addition to PEGylation, other surface modifications were also demonstrated to affect the pharmacokinetic profile and biodistribution of CNTs. Artificial surfactant coating of Pluronic F108 increased SWCNTs' dispersity and extended their blood circulation time. As in the case of PEG-SWCNTs, the liver was the major uptake site with no acute toxicity [64]. In another study, Tween 80-coated SWCNTs were found to accumulate in the liver, lung, and spleen, where the presence of coated SWCNTs was detectable even 4 weeks post injection [65]. Wang *et al.* investigated the biodistribution of hydroxylated SWCNTs and demonstrated that, despite their large molecular weight, the pharmacokinetic profile of hydroxylated SWCNTs was similar to that of small molecules. These nanoparticles were identified in most organs including the stomach, kidney, and bone, and eliminated via urine [66, 67]. Glucosamine-functionalized MWCNTs were shown to easily distribute throughout the entire body after intraperitoneal injection, and nanoparticles were detectable throughout the 24-h study duration [68]. In addition, the major presence in the stomach, urine, and feces at 24 h post injection indicated that the excretion of glucosamine-functionalized MWCNTs was via urine and feces [68]. Taurine ($H_2NCH_2CH_2SO_3H$)-functionalized MWCNTs were found to be taken up by the RES rapidly after intravenous injection. The retention of Taurine-MWCNTs in the liver persisted until 28 days post injection and gradually decreased to 20% of the original exposed dose [69]. The authors also investigated the impact of different routes of administration on Taurine-MWCNT biodistribution, including intravenous injection, oral gavage, and intratracheal instillation. Intravenous injection led to a rapid distribution of Taurine-MWCNTs in the RES but not the brain, stomach, muscle, or bone. The particles eventually accumulated predominantly in the liver and remained there for 28 days. In contrast, Taurine-MWCNTs, when administered intratracheally, mainly accumulated in the lung and were gradually eliminated throughout the 28-day duration, whereas oral gavage administration of Taurine-MWCNTs led to detectable levels only in the stomach, small intestine, large intestine, and feces, with the majority (74%) directly excreted in feces at 12 h post exposure [69]. Functionalization of SWCNT with a chelating molecule, namely diethylenetriaminepentaacetic (DTPA), was also demonstrated to change

its biodistribution after intravenous injection, with no RES retention and rapid clearance from systemic blood circulation via the renal excretion route [70]. The same group later investigated the biodistribution of DTPA-functionalized MWCNTs and revealed primarily localization of the nanoparticles in the kidneys after intravenous injection and similar excretion route via the urine [71]. In a separate study, SWCNTs functionalized with a different chelating molecule 2-(4-isothiocyanatobenzyl)-1,4,7,10-tetraazacyclododecane (DOTA) was reported to accumulate mainly in the kidney, spleen, liver, and bone with rapid blood clearance [72].

Closely associated with functionalization, particle aggregation/agglomeration and dispensability affect CNTs' *in vivo* biodistribution and kinetic profile. Aggregated nanoparticles, including CNT bundles, are more easily recognized by the RES, whereas highly dispersed CNTs would have better pharmacokinetic profiles. As mentioned earlier, functionalization often changes or improves the dispersity of CNTs. In biological or biomedical applications, CNTs are often sonicated in biological solutions such as serum, which could significantly change their pharmacokinetic profile. In fact, it is proposed that various proteins from serum could form a corona coating and compete *in vivo* with the noncovalent coating at CNT's surface. This could lead to desorption and subsequent rapid aggregation in the blood stream (Figure 9.2) [56, 64]. In addition, the length of CNTs affected their biodistribution, likely due to different clearance rates, as longer MWCNTs exhibited stronger retention in the RES organs compared to short MWCNTs [73]. A recent study also investigated the impact of the diameter of f-MWCNTs on their distribution in the organs and demonstrated that narrow MWCNTs with high aspect ratios exhibited enhanced tissue affinity including non-RES tissues (Figure 9.3) [74].

9.3.2
Biodistribution of Other Carbon Nanomaterials

In addition to that of CNTs, *in vivo* biodistribution/toxicokinetics of other carbon nanomaterials have also been investigated but to a lesser extent. The biodistribution and pharmacokinetic profiles of both small size (100–500 nm) and large size (1–5 μm) graphene oxides were investigated by Liu *et al*. After intravenous injection, small-sized graphene oxide mainly accumulated in the liver with sporadic deposition in the lung and spleen. There was no detectable accumulation in the brain, stomach, muscle, bone, or intestine. The distribution and clearance of small-sized graphene oxide was relatively fast, with only 11% of the injected dose remaining in the liver 180 min post injection. In contrast, larger sized graphene oxide mainly accumulated in the lung where 19.1% of the injected dose was retained 180 min post injection [75]. Further, the authors investigated the impact of the injection dose on the biodistribution of small-sized graphene oxide and demonstrated a dose-dependent increase in lung accumulation and a parallel decrease in liver accumulation of the nanoparticles [75]. In another study, the biodistribution profiles of pristine graphene oxide and 1% nonionic Tween

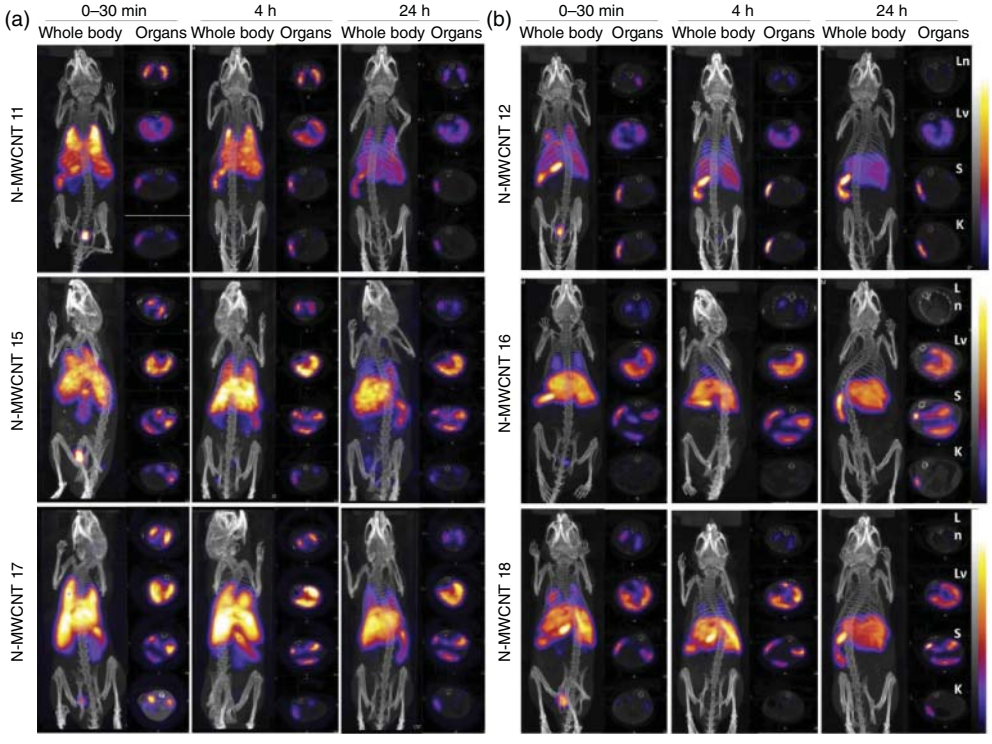

Figure 9.3 Impact of the diameter of functionalized MWCNTs on their biodistribution. Narrow MWCNTs (11, 15, and 17 N-MWCNTs) with high aspect ratio primarily localized to the lung, liver, and spleen, whereas the wide MWCNTs (12, 16, and 18 MWCNTs) were mainly detected only in the liver and spleen [74].

80-coated graphene oxide were compared [35]. Noncoated graphene oxide in phosphate buffered saline (PBS) tended to induce red blood cell aggregation and accumulated mainly in the lungs after intravenous injection, whereas Tween 80-coated graphene oxide did not induce blood cell aggregation and were mainly detected in the liver after injection [35]. Kanakia *et al.* investigated both the short-term (1-day) and long-term (30-day) biodistribution profiles of noncovalently functionalized dextran-coated graphene (GNP-Dex) after intravenous injection at various doses. In the animals treated for 1 day, GNP-DEX nanoparticles were mainly found in the heart and liver with lower levels detected in the lung, kidney, and brain, whereas 30-day-treated animals showed more GNP-Dex in the heart than in other organs. Interestingly, lower doses (25 mg kg^{-1}) of GNP-Dex exhibited higher blood concentration and organ deposition in terms of the percentage of injected dosage in various organs when compared to the medium and high dosages (125 and 250 mg kg^{-1}, respectively). The majority of GNP-Dex was excreted through feces, while only a small fraction was excreted through urine [76]. Yang *et al.* [77] investigated the long-term biodistribution and toxicity of PEGylated graphene nanosheets (NGS-PEG) by radioactive labeling. *In vivo*

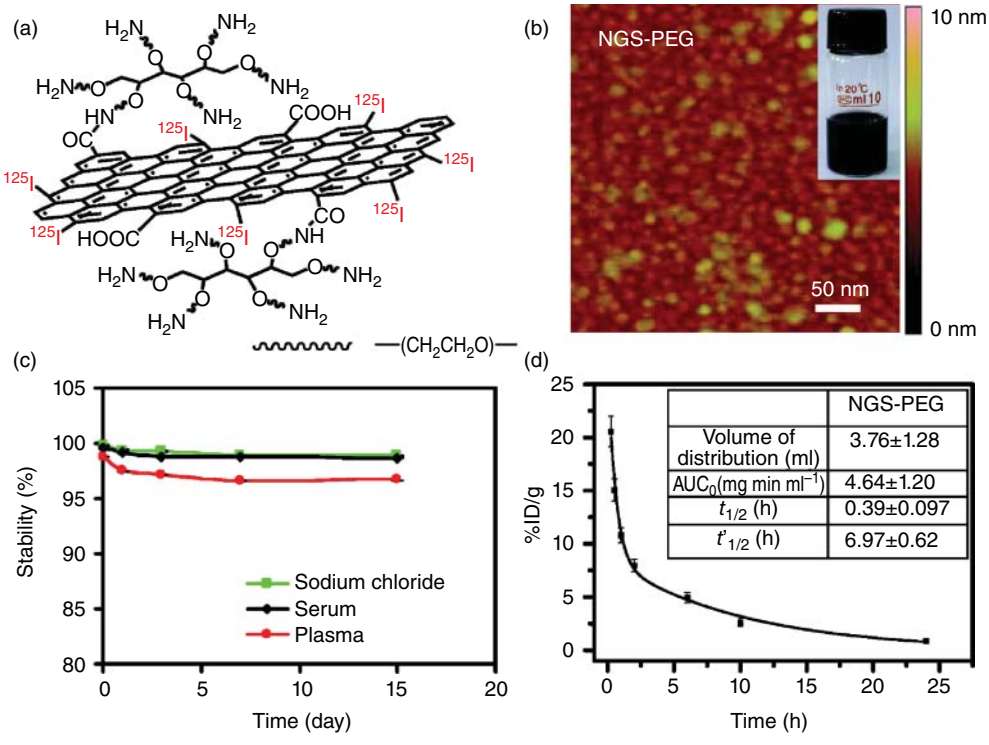

Figure 9.4 NGS functionalized with PEG and the pharmacokinetics of NGS-PEG. (a) A scheme of a graphene sheet with PEG functionalization and ^{125}I labeling. (b) AFM image of NGS-PEG: (inset) a photo of an NGS-PEG solution at a concentration of 0.5 mg ml^{-1}. (c) Radiolabeling stability curve of ^{125}I-NGS-PEG in saline, serum, and mouse plasma at 37 °C. Error bars are based on standard deviations of triplicate measurements. (d) Blood circulation curve of ^{125}I-NGS-PEG. The pharmacokinetics of NGS-PEG followed a two-compartment model. Error bars are based on standard deviations of 4–5 mice per group. (Inset table) Pharmacokinetic data of ^{125}I-NGS-PEG including volume of distribution, AUC, and circulation half-lives [77].

pharmacokinetic analysis indicated a two-compartment model of distribution of NGS-PEG after intravenous injection, with a first and second phase of blood circulation half-lives of 0.39 and 6.97 h, respectively (Figure 9.4). The authors also demonstrated that NGS-PEG, after injection, was initially distributed into many organs within 1 h, but mainly accumulated in the RES, including the liver and spleen, at later time points. Subsequently, NGS-PEG was gradually cleared, likely through both renal and fecal excretion [77]. In a separate study, PEGylation of nano-graphene oxide was demonstrated to reduce RES uptake of the particles after intravenous injection when compared to the pristine oxide [78]. Reduced RES uptake was in parallel with increased half-life of PEGylated graphene oxide in the blood circulation as well as enhanced clearance of aggregated graphene oxide from the liver, lung, and spleen [78]. PEGylation of graphene oxide was also demonstrated to prevent absorption by the digestive system after oral

administration of the compound, and the particles were rapidly excreted [79]. In contrast, intraperitoneal injection of the same PEGylated graphene oxide led to significant accumulation in the RES system with greater RES uptake of the larger sized nanoparticles. These findings indicate that both particle size and the route of administration play critical roles in the biodistribution of graphene oxide nanoparticles.

A few studies also investigated the biodistribution of carbon dots/carbon quantum dots. Huang *et al.* [80] investigated the impact of the administration routes on the biodistribution, clearance, and tumor uptake of photoluminescent carbon dots. The dots primarily accumulated in the kidney for all three routes of administration (intravenous, intramuscular, and subcutaneous) with a small amount in the liver [80]. All three administration routes exhibited rapid absorption into the blood circulation and fast clearance, as shown by minimal signal either at the injection sites or in the kidneys 24 h post injection. Intravenous injection showed the fastest urine clearance rate, followed by intramuscular and then subcutaneous injection [80]. Nurunnabi *et al.* [81] investigated the biodistribution of photoluminescent graphene quantum dots that were functionalized by carboxylation. Graphene quantum dots were found primarily in the liver and heart at the 2-h time point post injection and gradually decreased, whereas the kidney accumulation greatly increased 12 h post injection, indicating that graphene quantum dots were mainly taken up by the RES and excreted through the renal/urine route [81].

9.3.3
Hepatotoxicity of Carbon Nanotubes

To date, multiple studies have investigated the hepatotoxicity of CNTs using various *in vitro* and *in vivo* models. Findings from these studies primarily indicate an oxidative-stress-mediated mechanism of CNT-induced hepatotoxicity. In an *in vitro* liver cell model using the C3A cell line, two MWCNTs were demonstrated to induce oxidative responses in a dose-dependent manner, including increased intracellular ROS levels and decreased cellular glutathione level [82]. Similarly, in HepG2 cells, o-SWCNTs induced oxidative stress, compromised cellular metabolic pathways, protein synthesis, and cytoskeletal systems, and perturbed the cell cycle, whereas oxidized graphene was less cytotoxic [83].

A single dose of oral administration of MWCNTs at both 60 and 120 mg kg^{-1} induced injuries to macrophages, cellular swelling, unspecific inflammation, spot necrosis, and blood coagulation in albino mice at day 14, and the hepatotoxicity remained until the end of the study (day 28) [84]. Similarly, intravenous injection of purified and functionalized MWCNTs and SWCNTs induced a dose-dependent increase in hepatotoxicity in mice, as evidenced by increased ROS levels, increased levels of lipid peroxides, and increased activity of serum aminotransferase and alkaline phosphatase [85, 86]. A 4-week study also reported that oral administration by gavage of SWCNTs at high dose induced inflammatory cell infiltration and hepatic cell adipose degeneration in rat liver. In contrast, two separate studies

reported low toxicity of a single intravenous injection of SWCNTs in mice with no changes in serum immunological indicators (CH 50 level and TNF-α). No apoptosis was observed in major organs including the liver, despite prolonged accumulation in major organs 3 months after injection [87, 88]. The impact of CNTs on the liver, CNS, and some other major organs was also investigated in a mouse study. Ivani *et al* [89]. reported that intraperitoneal injection of MWCNTs at the mating or gestation stage affected neither the reproductive performance of the breeding pairs nor the neurobehavioral or physical parameters of the offspring. However, the absolute weight of certain organ/tissues was decreased in MWCNT-treated group, including the liver, spleen, and thymus, suggesting potential developmental toxicity of CNTs [89].

Multiple factors contribute to the toxicity of CNTs, including their aspect ratio, surface hydrophobicity, metallic impurity, and functionalization. It was reported that in Crandell feline kidney fibroblasts, CNTs of low purity exhibited higher cytotoxicity when compared to those of higher purity [90]. Compared to the pristine MWCNTs, various acid-oxidized, carboxylated CNTs with shorter lengths, hydrophilic surfaces, and high aqueous dispersibility induced significantly less hepatotoxicity (Figure 9.5) [73]. Further, reduction of hepatotoxicity was demonstrated to correlate with the functionalization density and was mechanistically associated with faster clearance and less tissue/organ deposition (Figure 9.5) [73].

PEG functionalization of MWCNTs was also demonstrated to reduce the hepatotoxicity of MWCNTs in mice, although at the dose investigated (60 mg kg^{-1}, i.v. injection) both non-PEGylated and PEGylated MWCNTs activated the TNF-α and NF-κB signaling pathways and induced hepatic inflammatory response, spot necrosis, and mitochondrial destruction even at 60 days post treatment [30]. In contrast, Tang *et al.* [91] reported no differences *in vivo* between control and short, functionalized, PEGylated MWCNTs (PEG-MWCNTs) on inflammatory responses, the coagulation system, hemograms, or vital organ functions, including the liver. The difference in the *in vivo* systematic toxicity of PEG-functionalized CNTs could be dependent on the length and branching structure of PEG chains, as longer and more branched PEG on SWCNTs led to prolonged blood circulation and lower uptake by the RES [53]. A comparative analysis between acid-oxidized MWCNTs (o-MWCNTs) and Tween-80-dispersed MWCNTs (T-MWCNTs) revealed that high doses of the latter induced hepatotoxicity along with increased oxidative damage and altered gene expression involved in cholesterol homeostasis, TNF-α and NF-κB signaling, natural-killer-cell-mediated toxicity, and G protein-coupled receptors (GPCRs), whereas o-MWCNT exhibited less toxicity in mice [92]. Other functionalization approaches, such as using single-stranded DNA (ss-DNA), of MWCNTs were also found to temporarily reduce the oxidative stress and inflammation response in rat liver to 6 h [93]. Studies using various *in vitro* models further confirmed that certain surface modification/functionalization of CNTs reduced CNT cytotoxicity. Using the normal liver cell line L02, Liu *et al.* reported that carboxylation of MWCNTs did not abolish but significantly reduced cytotoxicity by decreasing the activation of mitochondrial-mediated apoptotic pathway [94, 95].

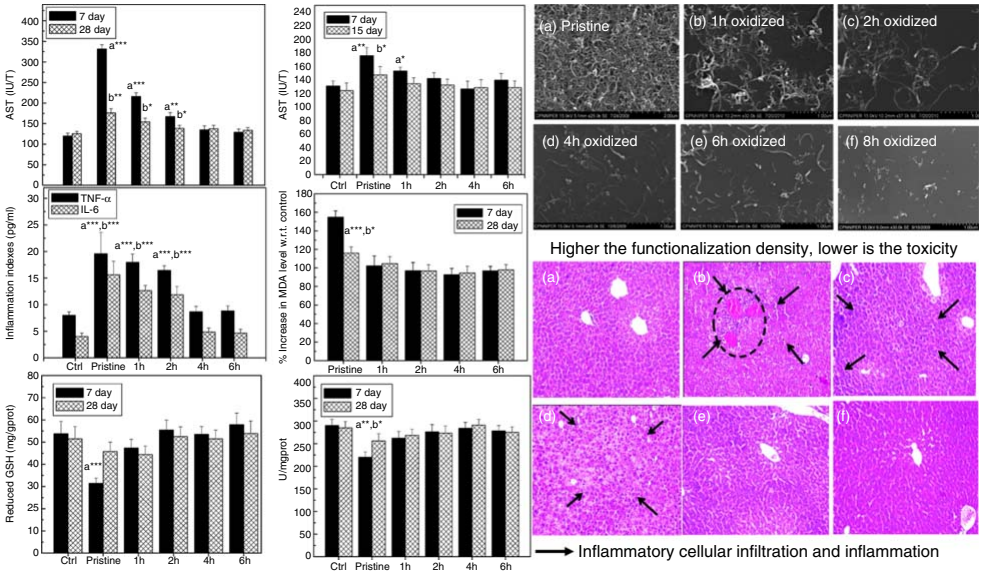

Figure 9.5 Higher carboxylation (functionalization) density leading to faster clearance, less tissue deposition, and reduced hepatotoxicity of carbon nanotubes [73].

9.3.4
Carbon Nanotube Nephrotoxicity/Renal Toxicity

In an *in vitro* human renal cell model, two different MWCNTs together with seven other nanomaterials tested were demonstrated to increase inflammatory IL6 and IL8 production, whereas TNF-α or MCP-1 was not affected [96]. Moreover, MWCNTs were found to induce DNA damage without displaying severe cytotoxicity [96]. Sodium dodecyl sulfate (SDS)-solubilized SWCNTs were also found to induce cell growth inhibition at 8 μg ml^{-1} concentration and activate apoptosis at higher concentrations [97]. Greater toxicity of MWCNTs of 90–150 nm and 60–80 nm was found in the human embryonic kidney cell line HEK293, in which both MWCNTs increased oxidative damage, impaired the mitochondrial function and cell membrane, and led to significant cytotoxicity [98]. In contrast, no toxicity to the kidney or other major organs examined was found in mice treated with either short-length (50–200 nm) MWCNTs or PEG-MWCNTs [91]. Interestingly, various carbon nanomaterials including fullerenes (C_{60}), SWCNTs, and MWCNTs, in particular at lower physiological concentrations, induced decreases in trans-epithelial electrical resistance (TEER) but had no impact on hormone-stimulated ion transport and did not induce cytokine release or cytotoxicity (Figure 9.6) [99]. Similar to hepatotoxicity, the nephrotoxicity and renal clearance/excretion of CNTs is dependent on their aspect ratio, surface hydrophobicity, metallic impurity, and functionalization [73].

9.3.5
Hepatotoxicity and Nephrotoxicity of Other Types of Carbon-based Nanomaterials

Besides CNTs, graphene and fullerene (C_{60}) are two other widely used carbon nanomaterials for bioimaging, biosensing, and other biomedical applications. Fullerene (C_{60}) has been gaining increasing interest in biomedical applications, particularly in cancer therapy. Fullerene C_{60} has been demonstrated to synergize with doxorubicin in tumor inhibition [45]. In a subchronic rodent study, oral administration of fullerene C_{60} did not induce any treatment-related histopathological change and was not detected in the liver, spleen, or kidney at the end of the study, except that the highest dose (1000 mg kg^{-1} day^{-1}) of fullerene led to black feces and black contents of the stomach and large intestine [100]. In contrast, a single oral administration of fullerene C_{60} increased the hepatic level of an oxidative DNA damage marker, namely 8-oxodG [101]. In the same study, mRNA expression of the 8-oxoguanine DNA glycosylase was also found to be upregulated following fullerene C_{60} treatment, but no repair activity was observed [101]. In freshwater *Carassius auratus*, chronic exposure to sublethal fullerene aggregates led to the depletion of glutathione despite the induction of the antioxidant enzymes superoxide dismutase and catalase in the liver [102]. The toxicity of pristine fullerene C_{60} aggregates was also found in multiple *in vitro* and *ex vivo* models, including human

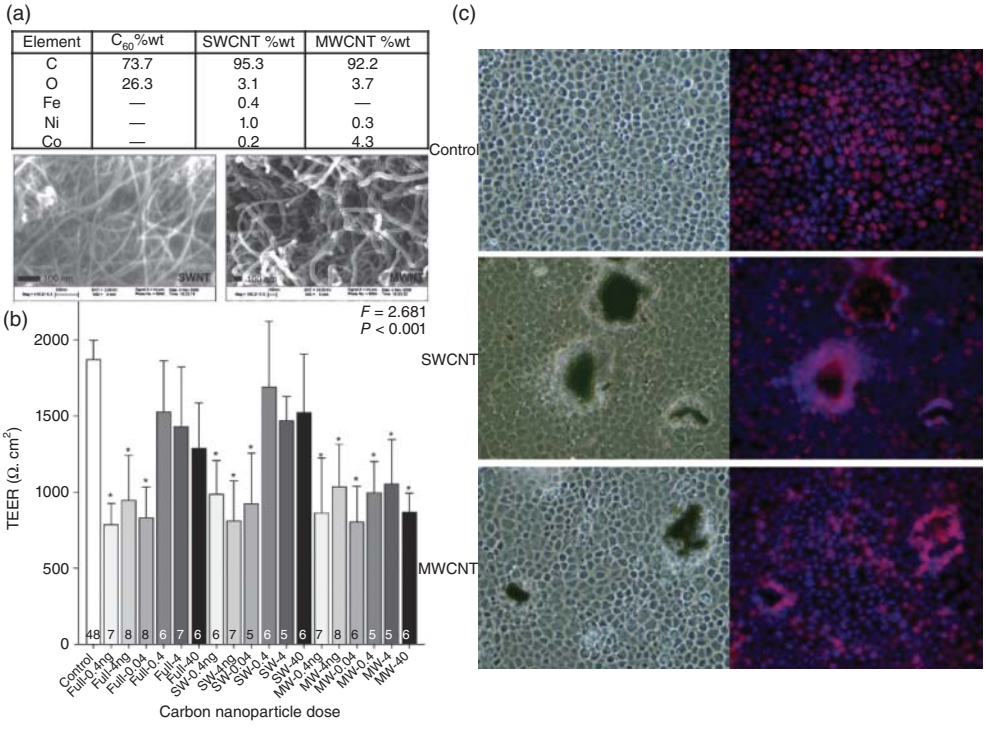

Figure 9.6 Impact of carbon nanotubes on renal epithelial cell structure and function. (a) Elemental analysis of carbon nanotubes. (b) Effect of carbon nanotubes on the trans-epithelial electrical resistance (TEER) of the renal cell line mpkCCD$_{cl4}$. (c) Increased cell proliferation by aggregated carbon nanotubes [99].

liver carcinoma cells (HepG2), human dermal fibroblasts, human neuronal astrocytes, and rat liver microsomes. The cytotoxic mechanisms of aggregated fullerene C_{60} included oxidative damage and peroxidation of the lipid bilayer [103–105].

Currently, multiple fullerene derivatives have been developed to reduce the fullerene C_{60}-associated toxicity. In a rat study, fullerenol C_{60} (OH)24 anion carbon nanoparticles were found to protect against doxorubicin-induced oxidative damage in the kidney, lung, testis, and the heart by acting as an antioxidant [106, 107]. Consistent with this finding, C_{60} (OH)24 was demonstrated to protect mice from ionizing-radiation-induced immune and mitochondrial functions by promoting the antioxidant defense system in the liver and spleen [108]. In a separate study, intravenous injection of hydroxylated fullerene C_{60} (OH)x was found to be largely safe, with only minor and sporadic histopathology changes [109]. The difference in toxicity of fullerene C_{60} and its fullerenol derivatives $C_{60}(OH)_{18-22}$ is likely due to differential partition in lipid membranes and subsequent inhibition of mitochondria [110]. Compared to $C_{60}(OH)_{18-22}$, fullerene C_{60}

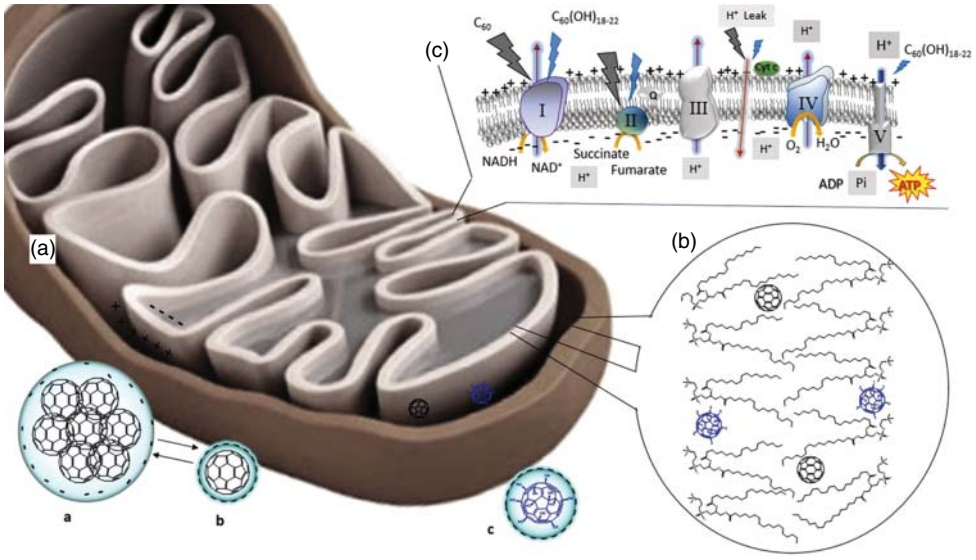

Figure 9.7 Schematic representation of a mitochondrion (A) highlighting some aspects of fullerene–mitochondria interactions. In water phase, large clusters of hydrated C_{60} molecules with a negative surface charge (a) are in equilibrium with free molecules (b), whereas $C_{60}(OH)_{18-22}$ nanoparticles (c) occur mainly as single hydrated molecules, also with a negative surface charge. Functional mitochondria display a transmembrane electric potential across the inner mitochondrial membrane due to proton translocation from the matrix to the intermembrane space. Proton abundance in this mitochondrial compartment may attract the negative fullerene nanoparticles, favoring the partition of the individual fullerene molecules into mitochondrial membranes. (B) The preferential localization of C_{60} and $C_{60}(OH)_{18-22}$ molecules within membrane bilayers, according to fluorescence quenching studies, is shown. (C) The mitochondrial respiratory system is represented, emphasizing the interactions of fullerenes with the complexes *I–V* and the promotion of proton leak (higher in the presence of C_{60} than in the presence of $C_{60}(OH)_{18-22}$ molecules) [111].

localizes in the deeper regions of the lipid bilayer and exhibits greater affinity for dipalmitoylphosphatidylcholine and mitochondrial membrane, which leads to greater inhibition of mitochondrial respiration (Figure 9.7) [111]. In addition to hydroxylation, other modifications can also modify the toxicity of fullerene C_{60}. Polyvinylpyrrolidone (PVP)-wrapped fullerene C_{60} was demonstrated to induce minimal kidney or liver injury in mice even when administered at high oral doses [112].

Graphene and graphene oxide have been increasingly used in various biomedical applications, such as fabrication of biosensors, drug delivery, and cancer targeting [113]. The toxicity of graphene oxide has been mainly attributed to the induction of ROS and subsequent oxidative damage [113]. In addition, it was proposed that the hydrophobicity of graphene could lead to the localization of graphene nanosheets in the hydrophobic interface of contacting proteins

and hence to the disruption of protein–protein interactions [114]. Intravenous injection of nano-sized graphene oxide led to the accumulation of particles in the liver and lung and the loss of body weight [76, 114]. PEG-functionalization has been used to modify the biodistribution of graphene oxide and reduce its toxicity. Compared to pristine graphene oxide, PEG coating significantly reduced the retention of nanoscale graphene oxide in the liver, lung and spleen, promoted clearance, alleviated graphene oxide-induced body weight loss, and reduced injury in the liver and kidney [78]. In mice, intravenous injection of PEGylated graphene led to temporary accumulation in the RES, which was gradually cleared likely via renal and fecal excretion [77]. Subsequent biochemical and histological analysis revealed no overt toxicity at the dose investigated (20 mg kg^{-1}) [77]. In a separate study, PEG-functionalized graphene oxide showed no obvious tissue uptake when administered orally; however, its intraperitoneal injection still led to high accumulation of the particles in the liver and spleen, indicating that in addition to functionalization, the route of administration had a significant impact on the pharmacokinetic and toxicity profiles of graphene oxide [79]. Recently, a new derivative of graphene oxide, namely graphene quantum dots, was developed. Compared to the conventional graphene oxide, graphene quantum dots exhibit less to no cellular toxicity *in vitro* [115]. Further, *in vivo* toxicity analyses indicated that graphene quantum dots induced minimal toxicity in the major organs with faster clearance via kidney, whereas graphene oxide aggregates were present in major organs, including the liver, spleen, and kidney, and induced abnormality [115].

9.4
Points of Consideration for Toxicity Evaluation of Carbon-based Nanomaterials

While the toxicology studies provided valuable information for the safety assessment of carbon nanomaterials, inconsistent findings from these reports can also lead to confusion and add to the difficulty for regulatory agencies as well as the manufacturers to assure the quality, safety, and efficacy of products utilizing nanotechnology. Although such inconsistencies could be partially attributed to the intrinsic variability in the biological systems, many other factors may contribute to or aggravate the disparity in toxicity findings from different studies. As discussed in previous sections, surface functionalization or coating of carbon nanotubes may lead to differential pharmacokinetics and toxicity profiles of carbon nanotubes after systemic exposure. However, technical difficulties to consistently generate and thoroughly characterize surface modification often impeded the validity and reproducibility of toxicity data. Batch-to-batch or lab-to-lab variability in surface modification could lead to differences in toxicity profiles of functionalized carbon nanotubes. Similarly, impurities, in particular trace levels of metal impurity, from carbon nanotube materials or the surfactants utilized for dispersion, may impose artificial toxic effects to biological systems, which may be mistakenly ascribed to carbon nanotubes. Furthermore, the

biological response to carbon nanomaterials is highly dependent on the particle size and/or the dispersion of the nanomaterials of investigation. Dynamic light scattering and electron microscopy are common techniques for particle size measurement. However, each technique has its own limitations and may lead to data in favor of particles of a particular size or artifacts due to sample preparation. Last but not the least, various toxicity evaluation methods used in different studies could lead to different interpretation of the data. Commonly used toxicity assays, such as MTT assay, Trypan blue assay, LDH assay, Caspase assay, and ATP assay, have different mechanisms of detection and utilize different cell death end points for toxicity assessment. Moreover, it has been demonstrated that nanomaterials, including carbon nanotubes, may interfere with specific absorbance-based cell viability assays via adsorption of particular dyes generated in the assay. These approaches will need to be further validated to avoid the potential interference by the carbon nanomaterials in the test systems. The standard test batteries for nanotoxicology are urgently needed in the future.

As discussed earlier, multiple factors could contribute to the inconsistency in toxicity evaluation performed by different research settings. Great attention should be paid to the characterization of the test carbon nanomaterials. Particle size, shape, and dispersity can significantly impact the biodistribution and subsequent toxicity of carbon nanomaterials and, therefore, analyses of these parameters should enlist a compendium of various techniques such as dynamic light scattering, atomic force microscopy, and electron microscopy, to ensure accurate characterization and reliable association between the chemical and physical properties of the carbon nanomaterials and induced biological responses. Furthermore, material impurities and quantification of carbon nanomaterials in biological matrices pose additional challenge for toxicological research of carbon nanomaterials. The impurity of nanomaterials may come from the manufacture process, such as incomplete purification. Qualitative and quantitative identification of impurities, particularly metal impurities, can significantly reduce artificial toxicity that is not intrinsic to the nanomaterials. Raman spectroscopy and ICP-MS are useful techniques to detect and quantify impurities in various nanomaterials. Another critical aspect for consideration is the application and characterization of surface modification to carbon nanomaterials. Surface modification and functionalization is a key determinant for the biodistribution and toxicity of carbon nanomaterials. Reliable functionalization methods and accurate postmodification characterization of surface coating, such as thermogravimetric analysis, are critical for generating reproducible toxicity findings. Points of consideration include the amount of free coating materials, such as PEG, in the solution, the degree of modification to nanomaterials, whether the modification is covalent binding or noncovalent binding, and so on. Last but not the least, priority should be placed to identify proper biological models for toxicity assessment and inclusion of necessary controls. Different biological systems may generate completely different responses to nanomaterials. Nanomaterials can often cause false positive or false negative.

9.5 Summary

Carbon-based nanomaterials, in particular CNTs, graphene, and fullerenes, have exhibited great potential in biomedical applications. In recent years, a number of studies have investigated their potential toxicity to multiple organs, including the nervous system, the liver, and the kidney. Mounting evidence indicates that CNTs and other carbon-based nanomaterials may penetrate the BBB and enter the brain. Similarly, liver and kidney deposition of carbon-based nanomaterials have been observed in many *in vivo* studies with different carbon-based nanomaterials and different routes of administration. In addition, findings from previous toxicological and toxicokinetic researches have indicated that both neurotoxicity and the hepato- and nephrotoxicity are dependent on many parameters, including, but not limited to, the physiochemical properties of the nanomaterials, the functionalization groups, the density as well as the size of functionalization, route of administration, and dosing regimen. These findings highlight the necessity for more systematic and in-depth investigations.

Acknowledgments

We thank the FDA NCTR/ORA Nanotechnology Core Facility and FDA Commissioner's Fellowship Program for supporting this project. The comments and conclusions in this chapter are those of the authors and do not necessarily represent the views of the U.S. Food & Drug Administration.

References

1. Chen, D., Dougherty, C.A., Zhu, K., and Hong, H. (2015) Theranostic applications of carbon nanomaterials in cancer: focus on imaging and cargo delivery. *J. Control. Release*.
2. De Volder, M.F., Tawfick, S.H., Baughman, R.H., and Hart, A.J. (2013) Carbon nanotubes: present and future commercial applications. *Science*, **339**, 535–539.
3. Van Tassel, P.R. (2013) Nanotechnology in medicine: nanofilm biomaterials. *Yale J. Biol. Med.*, **86**, 527–536.
4. Karmakar, A., Bratton, S.M., Dervishi, E., Ghosh, A., Mahmood, M., Xu, Y., Saeed, L.M., Mustafa, T., Casciano, D., Radominska-Pandya, A., and Biris, A.S. (2011) Ethylenediamine functionalized-single-walled nanotube (f-SWNT)-assisted in vitro delivery of the oncogene suppressor p53 gene to breast cancer MCF-7 cells. *Int. J. Nanomedicine*, **6**, 1045–1055.
5. Yao, J., Rettberg, J.R., Klosinski, L.P., Cadenas, E., and Brinton, R.D. (2011) Shift in brain metabolism in late onset Alzheimer's disease: implications for biomarkers and therapeutic interventions. *Mol. Aspects Med.*, **32**, 247–257.
6. Sharma, H.S. (2009) A special section on nanoneuroscience: nanoneurotoxicity and nanoneuroprotection. *J. Nanosci. Nanotechnol.*, **9**, 4992–4995.
7. Bhowmik, A., Khan, R., and Ghosh, M.K. (2015) Blood brain barrier: a challenge for effectual therapy of brain tumors. *Biomed. Res. Int.*, **2015**, 320941.
8. Fu, B.M. (2012) Experimental methods and transport models for drug delivery across the blood-brain barrier. *Curr. Pharm. Biotechnol.*, **13**, 1346–1359.

9. Kreuter, J. (2013) Mechanism of polymeric nanoparticle-based drug transport across the blood-brain barrier (BBB). *J. Microencapsul.*, **30**, 49–54.
10. Hwang, S.R. and Kim, K. (2014) Nano-enabled delivery systems across the blood-brain barrier. *Arch. Pharm. Res.*, **37**, 24–30.
11. Wong, B.S., Yoong, S.L., Jagusiak, A., Panczyk, T., Ho, H.K., Ang, W.H., and Pastorin, G. (2013) Carbon nanotubes for delivery of small molecule drugs. *Adv. Drug Deliv. Rev.*, **65**, 1964–2015.
12. Monaco, A.M. and Giugliano, M. (2014) Carbon-based smart nanomaterials in biomedicine and neuroengineering. *Beilstein J. Nanotechnol.*, **5**, 1849–1863.
13. Zhang, L., Alizadeh, D., and Badie, B. (2010) Carbon nanotube uptake and toxicity in the brain. *Methods Mol. Biol.*, **625**, 55–65.
14. Lu, C.T., Zhao, Y.Z., Wong, H.L., Cai, J., Peng, L., and Tian, X.Q. (2014) Current approaches to enhance CNS delivery of drugs across the brain barriers. *Int. J. Nanomedicine*, **9**, 2241–2257.
15. Kreuter, J., Alyautdin, R.N., Kharkevich, D.A., and Ivanov, A.A. (1995) Passage of peptides through the blood-brain barrier with colloidal polymer particles (nanoparticles). *Brain Res.*, **674**, 171–174.
16. Barlow, C.F. (1964) Clinical aspects of the blood-brain barrier. *Annu. Rev. Med.*, **15**, 187–202.
17. Brito, M.A., Palmela, I., Cardoso, F.L., Sa-Pereira, I., and Brites, D. (2014) Blood-brain barrier and bilirubin: clinical aspects and experimental data. *Arch. Med. Res.*, **45**, 660–676.
18. Lanone, S. and Boczkowski, J. (2006) Biomedical applications and potential health risks of nanomaterials: molecular mechanisms. *Curr. Mol. Med.*, **6**, 651–663.
19. Sharma, H.S., Ali, S.F., Hussain, S.M., Schlager, J.J., and Sharma, A. (2009) Influence of engineered nanoparticles from metals on the blood-brain barrier permeability, cerebral blood flow, brain edema and neurotoxicity. An experimental study in the rat and mice using biochemical and morphological approaches. *J. Nanosci. Nanotechnol.*, **9**, 5055–5072.
20. Migliore, L., Uboldi, C., Di Bucchianico, S., and Coppede, F. (2015) Nanomaterials and neurodegeneration. *Environ. Mol. Mutagen.*, **56**, 149–170.
21. Imam, S.Z., Lantz-McPeak, S.M., Cuevas, E., Rosas-Hernandez, H., Liachenko, S., Zhang, Y., Sarkar, S., Ramu, J., Robinson, B.L., Jones, Y., Gough, B., Paule, M.G., Ali, S.F., and Binienda, Z.K. (2015) Iron oxide nanoparticles induce dopaminergic damage: in vitro pathways and in vivo imaging reveals mechanism of neuronal damage. *Mol. Neurobiol.*
22. Win-Shwe, T.T. and Fujimaki, H. (2011) Nanoparticles and neurotoxicity. *Int. J. Mol. Sci.*, **12**, 6267–6280.
23. Tjalve, H. and Henriksson, J. (1999) Uptake of metals in the brain via olfactory pathways. *Neurotoxicology*, **20**, 181–195.
24. Wu, J., Wang, C., Sun, J., and Xue, Y. (2011) Neurotoxicity of silica nanoparticles: brain localization and dopaminergic neurons damage pathways. *ACS Nano*, **5**, 4476–4489.
25. Karmakar, A., Zhang, Q., and Zhang, Y. (2014) Neurotoxicity of nanoscale materials. *J. Food Drug Anal.*, **22**, 147–160.
26. Oberdorster, G., Sharp, Z., Atudorei, V., Elder, A., Gelein, R., Kreyling, W., and Cox, C. (2004) Translocation of inhaled ultrafine particles to the brain. *Inhal. Toxicol.*, **16**, 437–445.
27. Mercer, R.R., Scabilloni, J.F., Hubbs, A.F., Wang, L., Battelli, L.A., McKinney, W., Castranova, V., and Porter, D.W. (2013) Extrapulmonary transport of MWCNT following inhalation exposure. *Part. Fibre Toxicol.*, **10**, 38.
28. Tin Tin Win, S., Yamamoto, S., Ahmed, S., Kakeyama, M., Kobayashi, T., and Fujimaki, H. (2006) Brain cytokine and chemokine mRNA expression in mice induced by intranasal instillation with ultrafine carbon black. *Toxicol. Lett.*, **163**, 153–160.
29. Zhang, Y., Xu, Y., Li, Z., Chen, T., Lantz, S.M., Howard, P.C., Paule, M.G., Slikker, W. Jr., Watanabe, F., Mustafa,

T., Biris, A.S., and Ali, S.F. (2011) Mechanistic toxicity evaluation of uncoated and PEGylated single-walled carbon nanotubes in neuronal PC12 cells. *ACS Nano*, **5**, 7020–7033.

30. Zhang, D., Deng, X., Ji, Z., Shen, X., Dong, L., Wu, M., Gu, T., and Liu, Y. (2010) Long-term hepatotoxicity of polyethylene-glycol functionalized multi-walled carbon nanotubes in mice. *Nanotechnology*, **21**, 175101.
31. Wang, J., Sun, P., Bao, Y., Liu, J., and An, L. (2011) Cytotoxicity of single-walled carbon nanotubes on PC12 cells. *Toxicol. In Vitro*, **25**, 242–250.
32. Wang, J., Sun, P., Bao, Y., Dou, B., Song, D., and Li, Y. (2012) Vitamin E renders protection to PC12 cells against oxidative damage and apoptosis induced by single-walled carbon nanotubes. *Toxicol. In Vitro*, **26**, 32–41.
33. Chen, T., Yang, J., Zhang, H., Ren, G., Yang, Z., and Zhang, T. (2014) Multi-walled carbon nanotube inhibits CA1 glutamatergic synaptic transmission in rat's hippocampal slices. *Toxicol. Lett.*, **229**, 423–429.
34. Chen, T., Yang, J., Ren, G., Yang, Z., and Zhang, T. (2013) Multi-walled carbon nanotube increases the excitability of hippocampal CA1 neurons through inhibition of potassium channels in rat's brain slices. *Toxicol. Lett.*, **217**, 121–128.
35. Meng, L., Jiang, A., Chen, R., Li, C.Z., Wang, L., Qu, Y., Wang, P., Zhao, Y., and Chen, C. (2013) Inhibitory effects of multiwall carbon nanotubes with high iron impurity on viability and neuronal differentiation in cultured PC12 cells. *Toxicology*, **313**, 49–58.
36. Bussy, C., Al-Jamal, K.T., Boczkowski, J., Lanone, S., Prato, M., Bianco, A., and Kostarelos, K. (2015) Microglia determine brain region-specific neurotoxic responses to chemically functionalized carbon nanotubes. *ACS Nano*.
37. Bardi, G., Nunes, A., Gherardini, L., Bates, K., Al-Jamal, K.T., Gaillard, C., Prato, M., Bianco, A., Pizzorusso, T., and Kostarelos, K. (2013) Functionalized carbon nanotubes in the brain: cellular internalization and neuroinflammatory responses. *PLoS One*, **8**, e80964.
38. Dal Bosco, L., Weber, G.E., Parfitt, G.M., Paese, K., Goncalves, C.O., Serodre, T.M., Furtado, C.A., Santos, A.P., Monserrat, J.M., and Barros, D.M. (2015) PEGylated carbon nanotubes impair retrieval of contextual fear memory and alter oxidative stress parameters in the rat hippocampus. *Biomed. Res. Int.*, **2015**, 104135.
39. Huang, X., Zhang, F., Sun, X., Choi, K.Y., Niu, G., Zhang, G., Guo, J., Lee, S., and Chen, X. (2014) The genotype-dependent influence of functionalized multiwalled carbon nanotubes on fetal development. *Biomaterials*, **35**, 856–865.
40. Hernandez-Ferrer, J., Perez-Bruzon, R.N., Azanza, M.J., Gonzalez, M., Del Moral, R., Anson-Casaos, A., de la Fuente, J.M., Marijuan, P.C., and Martinez, M.T. (2014) Study of neuron survival on polypyrrole-embedded single-walled carbon nanotube substrates for long-term growth conditions. *J. Biomed. Mater. Res. A*, **102**, 4443–4454.
41. Phillips, C.L., Yah, C.S., Iyuke, S.E., Pillay, V., Rumbold, K., and Choonara, Y. (2013) The response effect of pheochromocytoma (PC12) cell lines to oxidized multi-walled carbon nanotubes (o-MWCMTs). *Afr. Health Sci.*, **13**, 947–954.
42. Avti, P.K., Talukdar, Y., Sirotkin, M.V., Shroyer, K.R., and Sitharaman, B. (2013) Toward single-walled carbon nanotube-gadolinium complex as advanced MRI contrast agents: pharmacodynamics and global genomic response in small animals. *J. Biomed. Mater. Res. B Appl. Biomater.*, **101**, 1039–1049.
43. Ge, C., Du, J., Zhao, L., Wang, L., Liu, Y., Li, D., Yang, Y., Zhou, R., Zhao, Y., Chai, Z., and Chen, C. (2011) Binding of blood proteins to carbon nanotubes reduces cytotoxicity. *Proc. Natl. Acad. Sci. U. S. A.*, **108**, 16968–16973.
44. Ibrahim, M., Saleh, N.A., Elshemey, W.M., and Elsayed, A.A. (2012)

Fullerene derivative as anti-HIV protease inhibitor: molecular modeling and QSAR approaches. *Mini Rev. Med. Chem.*, **12**, 447–451.

45. Prylutska, S., Grynyuk, I., Matyshevska, O., Prylutskyy, Y., Evstigneev, M., Scharff, P., and Ritter, U. (2014) C60 fullerene as synergistic agent in tumor-inhibitory Doxorubicin treatment. *Drugs Res. Dev.*, **14**, 333–340.
46. Corona-Morales, A.A., Castell, A., Escobar, A., Drucker-Colin, R., and Zhang, L. (2003) Fullerene C60 and ascorbic acid protect cultured chromaffin cells against levodopa toxicity. *J. Neurosci. Res.*, **71**, 121–126.
47. Jin, H., Chen, W.Q., Tang, X.W., Chiang, L.Y., Yang, C.Y., Schloss, J.V., and Wu, J.Y. (2000) Polyhydroxylated C(60), fullerenols, as glutamate receptor antagonists and neuroprotective agents. *J. Neurosci. Res.*, **62**, 600–607.
48. Chen, T., Li, Y.Y., Zhang, J.L., Xu, B., Lin, Y., Wang, C.X., Guan, W.C., Wang, Y.J., and Xu, S.Q. (2011) Protective effect of C(60) -methionine derivate on lead-exposed human SH-SY5Y neuroblastoma cells. *J. Appl. Toxicol.*, **31**, 255–261.
49. Makarova, E.G., Gordon, R.Y., and Podolski, I.Y. (2012) Fullerene C60 prevents neurotoxicity induced by intrahippocampal microinjection of amyloid-beta peptide. *J. Nanosci. Nanotechnol.*, **12**, 119–126.
50. Lin, A.M., Yang, C.H., Ueng, Y.F., Luh, T.Y., Liu, T.Y., Lay, Y.P., and Ho, L.T. (2004) Differential effects of carboxyfullerene on MPP+/MPTP-induced neurotoxicity. *Neurochem. Int.*, **44**, 99–105.
51. Mattei, T.A. (2014) How graphene is expected to impact neurotherapeutics in the near future. *Expert Rev. Neurother.*, **14**, 845–847.
52. Bartelmess, J., Quinn, S.J., and Giordani, S. (2014) Carbon nanomaterials: multi-functional agents for biomedical fluorescence and Raman imaging. *Chem. Soc. Rev.*
53. Liu, Z., Davis, C., Cai, W., He, L., Chen, X., and Dai, H. (2008) Circulation and long-term fate of functionalized, biocompatible single-walled carbon nanotubes in mice probed by Raman spectroscopy. *Proc. Natl. Acad. Sci. U. S. A.*, **105**, 1410–1415.
54. Al Faraj, A., Cieslar, K., Lacroix, G., Gaillard, S., Canet-Soulas, E., and Cremillieux, Y. (2009) In vivo imaging of carbon nanotube biodistribution using magnetic resonance imaging. *Nano Lett.*, **9**, 1023–1027.
55. Miyawaki, J., Matsumura, S., Yuge, R., Murakami, T., Sato, S., Tomida, A., Tsuruo, T., Ichihashi, T., Fujinami, T., Irie, H., Tsuchida, K., Iijima, S., Shiba, K., and Yudasaka, M. (2009) Biodistribution and ultrastructural localization of single-walled carbon nanohorns determined in vivo with embedded Gd2O3 labels. *ACS Nano*, **3**, 1399–1406.
56. Ali-Boucetta, H. and Kostarelos, K. (2013) Pharmacology of carbon nanotubes: toxicokinetics, excretion and tissue accumulation. *Adv. Drug Deliv. Rev.*, **65**, 2111–2119.
57. Jokerst, J.V., Lobovkina, T., Zare, R.N., and Gambhir, S.S. (2011) Nanoparticle PEGylation for imaging and therapy. *Nanomedicine (Lond.)*, **6**, 715–728.
58. Yang, S.T., Fernando, K.A., Liu, J.H., Wang, J., Sun, H.F., Liu, Y., Chen, M., Huang, Y., Wang, X., Wang, H., and Sun, Y.P. (2008) Covalently PEGylated carbon nanotubes with stealth character in vivo. *Small*, **4**, 940–944.
59. Bhirde, A.A., Patel, S., Sousa, A.A., Patel, V., Molinolo, A.A., Ji, Y., Leapman, R.D., Gutkind, J.S., and Rusling, J.F. (2010) Distribution and clearance of PEG-single-walled carbon nanotube cancer drug delivery vehicles in mice. *Nanomedicine (Lond.)*, **5**, 1535–1546.
60. Liu, Z., Cai, W., He, L., Nakayama, N., Chen, K., Sun, X., Chen, X., and Dai, H. (2007) In vivo biodistribution and highly efficient tumour targeting of carbon nanotubes in mice. *Nat. Nanotechnol.*, **2**, 47–52.
61. Karmakar, A., Iancu, C., Bartos, D.M., Mahmood, M.W., Ghosh, A., Xu, Y., Dervishi, E., Collom, S.L., Khodakovskaya, M., Mustafa, T., Watanabe, F., Biris, A.R., Zhang, Y., Ali, S.F., Casciano, D., Hassen,

S., Nima, Z., and Biris, A.S. (2012) Raman spectroscopy as a detection and analysis tool for in vitro specific targeting of pancreatic cancer cells by EGF-conjugated, single-walled carbon nanotubes. *J. Appl. Toxicol.*, **32**, 365–375.

62. Prencipe, G., Tabakman, S.M., Welsher, K., Liu, Z., Goodwin, A.P., Zhang, L., Henry, J., and Dai, H. (2009) PEG branched polymer for functionalization of nanomaterials with ultralong blood circulation. *J. Am. Chem. Soc.*, **131**, 4783–4787.
63. Campagnolo, L., Massimiani, M., Palmieri, G., Bernardini, R., Sacchetti, C., Bergamaschi, A., Vecchione, L., Magrini, A., Bottini, M., and Pietroiusti, A. (2013) Biodistribution and toxicity of pegylated single wall carbon nanotubes in pregnant mice. *Part. Fibre Toxicol.*, **10**, 21.
64. Cherukuri, P., Gannon, C.J., Leeuw, T.K., Schmidt, H.K., Smalley, R.E., Curley, S.A., and Weisman, R.B. (2006) Mammalian pharmacokinetics of carbon nanotubes using intrinsic near-infrared fluorescence. *Proc. Natl. Acad. Sci. U. S. A.*, **103**, 18882–18886.
65. Sheng-tao Yang, W.G., Lin, Y., Deng, X.-y., Wang, H.-f., Sun, H.-f., Yuan-fang Liu, X.W., Wang, W., Chen, M., Huang, Y.-p., and Sun, Y.-P. (2007) Biodistribution of pristine single-walled carbon nanotubes in vivo. *J. Phys. Chem.*, **111**, 17761–17764.
66. Wang, H., Wang, J., Deng, X., Sun, H., Shi, Z., Gu, Z., Liu, Y., and Zhao, Y. (2004) Biodistribution of carbon single-wall carbon nanotubes in mice. *J. Nanosci. Nanotechnol.*, **4**, 1019–1024.
67. Wang, J., Deng, X.Y., Yang, S.T., Wang, H.F., Zhao, Y.L., and Liu, Y.F. (2008) Rapid translocation and pharmacokinetics of hydroxylated single-walled carbon nanotubes in mice. *Nanotoxicology*, **2**, 28–32.
68. Guo, J., Zhang, X., Li, Q., and Li, W. (2007) Biodistribution of functionalized multiwall carbon nanotubes in mice. *Nucl. Med. Biol.*, **34**, 579–583.
69. Deng, X., Jia, G., Wang, H., Sun, H., Wang, X., Yang, S., Wang, T., and Liu, Y. (2007) Translocation and fate of multi-walled carbon nanotubes in vivo. *Carbon*, **45**, 1419–1424.
70. Singh, R., Pantarotto, D., Lacerda, L., Pastorin, G., Klumpp, C., Prato, M., Bianco, A., and Kostarelos, K. (2006) Tissue biodistribution and blood clearance rates of intravenously administered carbon nanotube radiotracers. *Proc. Natl. Acad. Sci. U. S. A.*, **103**, 3357–3362.
71. Lacerda, L., Soundararajan, A., Singh, R., Pastorin, G., Al-Jamal, K.T., Turton, J., Frederik, P., Herrero, M.A., Bao, S.L.A., Emfietzoglou, D., Mather, S., Phillips, W.T., Prato, M., Bianco, A., Goins, B., and Kostarelos, K. (2008) Dynamic Imaging of functionalized multi-walled carbon nanotube systemic circulation and urinary excretion. *Adv. Mater.*, **20**, 225–230.
72. McDevitt, M.R., Chattopadhyay, D., Kappel, B.J., Jaggi, J.S., Schiffman, S.R., Antczak, C., Njardarson, J.T., Brentjens, R., and Scheinberg, D.A. (2007) Tumor targeting with antibody-functionalized, radiolabeled carbon nanotubes. *J. Nucl. Med.*, **48**, 1180–1189.
73. Jain, S., Thakare, V.S., Das, M., Godugu, C., Jain, A.K., Mathur, R., Chuttani, K., and Mishra, A.K. (2011) Toxicity of multiwalled carbon nanotubes with end defects critically depends on their functionalization density. *Chem. Res. Toxicol.*, **24**, 2028–2039.
74. Wang, J.T., Fabbro, C., Venturelli, E., Menard-Moyon, C., Chaloin, O., Da Ros, T., Methven, L., Nunes, A., Sosabowski, J.K., Mather, S.J., Robinson, M.K., Amadou, J., Prato, M., Bianco, A., Kostarelos, K., and Al-Jamal, K.T. (2014) The relationship between the diameter of chemically-functionalized multi-walled carbon nanotubes and their organ biodistribution profiles in vivo. *Biomaterials*, **35**, 9517–9528.
75. Liu, J.H., Yang, S.T., Wang, H., Chang, Y., Cao, A., and Liu, Y. (2012) Effect of size and dose on the biodistribution of graphene oxide in mice. *Nanomedicine (Lond.)*, **7**, 1801–1812.
76. Kanakia, S., Toussaint, J.D., Mullick Chowdhury, S., Tembulkar, T., Lee, S., Jiang, Y.P., Lin, R.Z., Shroyer,

K.R., Moore, W., and Sitharaman, B. (2014) Dose ranging, expanded acute toxicity and safety pharmacology studies for intravenously administered functionalized graphene nanoparticle formulations. *Biomaterials*, **35**, 7022–7031.

77. Yang, K., Wan, J., Zhang, S., Zhang, Y., Lee, S.T., and Liu, Z. (2011) In vivo pharmacokinetics, long-term biodistribution, and toxicology of PEGylated graphene in mice. *ACS Nano*, **5**, 516–522.
78. Li, B., Zhang, X.Y., Yang, J.Z., Zhang, Y.J., Li, W.X., Fan, C.H., and Huang, Q. (2014) Influence of polyethylene glycol coating on biodistribution and toxicity of nanoscale graphene oxide in mice after intravenous injection. *Int. J. Nanomedicine*, **9**, 4697–4707.
79. Yang, K., Gong, H., Shi, X., Wan, J., Zhang, Y., and Liu, Z. (2013) In vivo biodistribution and toxicology of functionalized nano-graphene oxide in mice after oral and intraperitoneal administration. *Biomaterials*, **34**, 2787–2795.
80. Huang, X., Zhang, F., Zhu, L., Choi, K.Y., Guo, N., Guo, J., Tackett, K., Anilkumar, P., Liu, G., Quan, Q., Choi, H.S., Niu, G., Sun, Y.P., Lee, S., and Chen, X. (2013) Effect of injection routes on the biodistribution, clearance, and tumor uptake of carbon dots. *ACS Nano*, **7**, 5684–5693.
81. Nurunnabi, M., Khatun, Z., Huh, K.M., Park, S.Y., Lee, D.Y., Cho, K.J., and Lee, Y.K. (2013) In vivo biodistribution and toxicology of carboxylated graphene quantum dots. *ACS Nano*, **7**, 6858–6867.
82. Kermanizadeh, A., Gaiser, B.K., Hutchison, G.R., and Stone, V. (2012) An in vitro liver model--assessing oxidative stress and genotoxicity following exposure of hepatocytes to a panel of engineered nanomaterials. *Part. Fibre Toxicol.*, **9**, 28.
83. Yuan, J., Gao, H., Sui, J., Duan, H., Chen, W.N., and Ching, C.B. (2012) Cytotoxicity evaluation of oxidized single-walled carbon nanotubes and graphene oxide on human hepatoma HepG2 cells: an iTRAQ-coupled 2D LC-MS/MS proteome analysis. *Toxicol. Sci.*, **126**, 149–161.
84. Awasthi, K.K., John, P.J., Awasthi, A., and Awasthi, K. (2013) Multi walled carbon nano tubes induced hepatotoxicity in Swiss albino mice. *Micron*, **44**, 359–364.
85. Patlolla, A., McGinnis, B., and Tchounwou, P. (2011) Biochemical and histopathological evaluation of functionalized single-walled carbon nanotubes in Swiss-Webster mice. *J. Appl. Toxicol.*, **31**, 75–83.
86. Patlolla, A.K., Berry, A., and Tchounwou, P.B. (2011) Study of hepatotoxicity and oxidative stress in male Swiss-Webster mice exposed to functionalized multi-walled carbon nanotubes. *Mol. Cell. Biochem.*, **358**, 189–199.
87. Yang, S.T., Wang, X., Jia, G., Gu, Y., Wang, T., Nie, H., Ge, C., Wang, H., and Liu, Y. (2008) Long-term accumulation and low toxicity of single-walled carbon nanotubes in intravenously exposed mice. *Toxicol. Lett.*, **181**, 182–189.
88. Schipper, M.L., Nakayama-Ratchford, N., Davis, C.R., Kam, N.W., Chu, P., Liu, Z., Sun, X., Dai, H., and Gambhir, S.S. (2008) A pilot toxicology study of single-walled carbon nanotubes in a small sample of mice. *Nat. Nanotechnol.*, **3**, 216–221.
89. Ivani, S., Karimi, I., and Tabatabaei, S.R. (2012) Biosafety of multiwalled carbon nanotube in mice: a behavioral toxicological approach. *J. Toxicol. Sci.*, **37**, 1191–1205.
90. Pensabene, V., Vittorio, O., Raffa, V., Menciassi, A., and Dario, P. (2007) Investigation of CNTs interaction with fibroblast cells. Conference Proceeding of the IEEE Engineering in Medicine and Biology Society, 2007, pp. 6621-6624.
91. Tang, S., Tang, Y., Zhong, L., Murat, K., Asan, G., Yu, J., Jian, R., Wang, C., and Zhou, P. (2012) Short- and long-term toxicities of multi-walled carbon nanotubes in vivo and in vitro. *J. Appl. Toxicol.*, **32**, 900–912.
92. Ji, Z., Zhang, D., Li, L., Shen, X., Deng, X., Dong, L., Wu, M., and Liu, Y. (2009)

The hepatotoxicity of multi-walled carbon nanotubes in mice. *Nanotechnology*, **20**, 445101.

93. Clichici, S., Biris, A.R., Tabaran, F., and Filip, A. (2012) Transient oxidative stress and inflammation after intraperitoneal administration of multiwalled carbon nanotubes functionalized with single strand DNA in rats. *Toxicol. Appl. Pharmacol.*, **259**, 281–292.

94. Liu, Z., Dong, X., Song, L., Zhang, H., Liu, L., Zhu, D., Song, C., and Leng, X. (2014) Carboxylation of multiwalled carbon nanotube enhanced its biocompatibility with L02 cells through decreased activation of mitochondrial apoptotic pathway. *J. Biomed. Mater. Res. A*, **102**, 665–673.

95. Vesterdal, L.K., Danielsen, P.H., Folkmann, J.K., Jespersen, L.F., Aguilar-Pelaez, K., Roursgaard, M., Loft, S., and Moller, P. (2014) Accumulation of lipids and oxidatively damaged DNA in hepatocytes exposed to particles. *Toxicol. Appl. Pharmacol.*, **274**, 350–360.

96. Kermanizadeh, A., Vranic, S., Boland, S., Moreau, K., Baeza-Squiban, A., Gaiser, B.K., Andrzejczuk, L.A., and Stone, V. (2013) An in vitro assessment of panel of engineered nanomaterials using a human renal cell line: cytotoxicity, pro-inflammatory response, oxidative stress and genotoxicity. *BMC Nephrol.*, **14**, 96.

97. Nam, C.W., Kang, S.J., Kang, Y.K., and Kwak, M.K. (2011) Cell growth inhibition and apoptosis by SDS-solubilized single-walled carbon nanotubes in normal rat kidney epithelial cells. *Arch. Pharm. Res.*, **34**, 661–669.

98. Reddy, A.R., Reddy, Y.N., Krishna, D.R., and Himabindu, V. (2010) Multi wall carbon nanotubes induce oxidative stress and cytotoxicity in human embryonic kidney (HEK293) cells. *Toxicology*, **272**, 11–16.

99. Blazer-Yost, B.L., Banga, A., Amos, A., Chernoff, E., Lai, X., Li, C., Mitra, S., and Witzmann, F.A. (2011) Effect of carbon nanoparticles on renal epithelial cell structure, barrier function, and protein expression. *Nanotoxicology*, **5**, 354–371.

100. Takahashi, M., Kato, H., Doi, Y., Hagiwara, A., Hirata-Koizumi, M., Ono, A., Kubota, R., Nishimura, T., and Hirose, A. (2012) Sub-acute oral toxicity study with fullerene C60 in rats. *J. Toxicol. Sci.*, **37**, 353–361.

101. Folkmann, J.K., Risom, L., Jacobsen, N.R., Wallin, H., Loft, S., and Moller, P. (2009) Oxidatively damaged DNA in rats exposed by oral gavage to C60 fullerenes and single-walled carbon nanotubes. *Environ. Health Perspect.*, **117**, 703–708.

102. Zhu, X., Zhu, L., Lang, Y., and Chen, Y. (2008) Oxidative stress and growth inhibition in the freshwater fish Carassius auratus induced by chronic exposure to sublethal fullerene aggregates. *Environ. Toxicol. Chem.*, **27**, 1979–1985.

103. Sayes, C.M., Gobin, A.M., Ausman, K.D., Mendez, J., West, J.L., and Colvin, V.L. (2005) Nano-C60 cytotoxicity is due to lipid peroxidation. *Biomaterials*, **26**, 7587–7595.

104. Kamat, J.P., Devasagayam, T.P., Priyadarsini, K.I., Mohan, H., and Mittal, J.P. (1998) Oxidative damage induced by the fullerene C60 on photosensitization in rat liver microsomes. *Chem. Biol. Interact.*, **114**, 145–159.

105. Sera, N., Tokiwa, H., and Miyata, N. (1996) Mutagenicity of the fullerene C60-generated singlet oxygen dependent formation of lipid peroxides. *Carcinogenesis*, **17**, 2163–2169.

106. Injac, R., Perse, M., Boskovic, M., Djordjevic-Milic, V., Djordjevic, A., Hvala, A., Cerar, A., and Strukelj, B. (2008) Cardioprotective effects of fullerenol C(60)(Oh)(24) on a single dose doxorubicin-induced cardiotoxicity in rats with malignant neoplasm. *Technol. Cancer Res. Treat.*, **7**, 15–25.

107. Srdjenovic, B., Milic-Torres, V., Grujic, N., Stankov, K., Djordjevic, A., and Vasovic, V. (2010) Antioxidant properties of fullerenol C60(OH)24 in rat kidneys, testes, and lungs treated with doxorubicin. *Toxicol. Mech. Methods*, **20**, 298–305.

108. Cai, X., Hao, J., Zhang, X., Yu, B., Ren, J., Luo, C., Li, Q., Huang, Q., Shi, X.,

Li, W., and Liu, J. (2010) The polyhydroxylated fullerene derivative C60(OH)24 protects mice from ionizing-radiation-induced immune and mitochondrial dysfunction. *Toxicol. Appl. Pharmacol.*, **243**, 27–34.

109. Monteiro-Riviere, N.A., Linder, K.E., Inman, A.O., Saathoff, J.G., Xia, X.R., and Riviere, J.E. (2012) Lack of hydroxylated fullerene toxicity after intravenous administration to female Sprague-Dawley rats. *J. Toxicol. Environ. Health A*, **75**, 367–373.

110. Nakagawa, Y., Suzuki, T., Ishii, H., Nakae, D., and Ogata, A. (2011) Cytotoxic effects of hydroxylated fullerenes on isolated rat hepatocytes via mitochondrial dysfunction. *Arch. Toxicol.*, **85**, 1429–1440.

111. Santos, S.M., Dinis, A.M., Peixoto, F., Ferreira, L., Jurado, A.S., and Videira, R.A. (2014) Interaction of fullerene nanoparticles with biomembranes: from the partition in lipid membranes to effects on mitochondrial bioenergetics. *Toxicol. Sci.*, **138**, 117–129.

112. Yamashita, K., Yoshioka, Y., Pan, H., Taira, M., Ogura, T., Nagano, T., Aoyama, M., Nagano, K., Abe, Y., Kamada, H., Tsunoda, S.I., Aoshima, H., Nabeshi, H., Yoshikawa, T., and Tsutsumi, Y. (2013) Biochemical and hematologic effects of polyvinylpyrrolidone-wrapped fullerene C60 after oral administration. *Pharmazie*, **68**, 54–57.

113. Perrozzi, F., Prezioso, S., and Ottaviano, L. (2015) Graphene oxide: from fundamentals to applications. *J. Phys. Condens. Matter*, **27**, 013002.

114. Luan, B., Huynh, T., Zhao, L., and Zhou, R. (2014) Potential toxicity of graphene to cell functions via disrupting protein-protein interactions. *ACS Nano*.

115. Chong, Y., Ma, Y., Shen, H., Tu, X., Zhou, X., Xu, J., Dai, J., Fan, S., and Zhang, Z. (2014) The in vitro and in vivo toxicity of graphene quantum dots. *Biomaterials*, **35**, 5041–5048.

10
Genotoxicity and Carcinogenic Potential of Carbon Nanomaterials

Todd A. Stueckle, Linda Sargent, Yon Rojanasakul, and Liying Wang

10.1
Introduction

Engineered carbon nanomaterials (ECNMs) have undergone broad technological developments in fields such as electronics, energy storage, structural materials, cosmetics, environmental remediation, medical diagnostics, and drug delivery [1, 2]. With such widespread incorporation into numerous products and uses, ECNMs' potential human exposure is to be expected during manufacturing, incorporation into other products, use, disposal, and release into the environment [3–5]. Carbon nanotubes (CNTs), a major group of carbon nanomaterials, exhibit a fibrous morphology and biopersistence similar to asbestos, a known human carcinogen, and potentially harbor asbestos-like lung cancer and mesothelioma risks associated with their long-term exposure. Several ECNMs are known to induce irreversible damage to exposed tissue (e.g., fibrosis) in animal models or cause genetic damage (i.e., genotoxicity) upon exposure to sensitive tissues/cells, a key first step at initiating tumorigenesis [6–8]. In addition, ultrafine carbon black (UFCB) and multiwalled carbon nanotubes (MWCNTs) have been identified as potential human carcinogens [9]. It raises urgent occupational, public, and environment safety and health concerns, and therefore a critical need exists to understand specific carbon nanomaterial-induced carcinogenesis potential as well as screen and evaluate methods based on that knowledge.

Lung cancer is the leading cause of cancer-related mortality, and has been largely associated with smoking and environmental carcinogen exposures. With a decrease in the smoking population in developed countries as a result of increased regulations and better control of atmospheric industrial particulates, the incidence of squamous lung carcinoma in the developed countries has seen a decline. However, the rate of adenocarcinoma in these countries has continued to increase, suggesting the rise of unknown environmental factors contributing to such occurrence [10–12]. Outdoor air pollution, a byproduct of anthropogenic activity, is responsible for a significant fraction of ultrafine carbon particulates (PM 2.5), which are considered a human carcinogen [13] and may contribute to

Biomedical Applications and Toxicology of Carbon Nanomaterials, First Edition.
Edited by Chunying Chen and Haifang Wang.

lung adenocarcinoma. Furthermore, exposure to man-made nanomaterials such as ECMNs may contribute to this development.

ECNMs possess novel and unique physicochemical properties that provide technological advantage over conventional materials, but they may also generate unknown health consequences (e.g., carcinogenesis) following their exposure. Assessing the carcinogenic effect of nanomaterials is a huge undertaking due to their rapid growth and great variety of nanomaterials. Guidelines for establishing a material's carcinogenic potential rely on human epidemiological data, confirmed cases in clinical reports, and animal studies. Studies can be qualitative and explorative in nature (i.e., yes or no) or quantitative (i.e., dose–response) to identify the lowest observed and nonobservable effective concentrations (i.e., LOEC and NOEC, respectively). At present, there is no human case of ECNM-induced cancer, and ECNM carcinogenic studies in animal models have only been conducted on a case-by-case basis [14]. These animal studies have used historical data with similar particles (i.e., fine TiO_2 and asbestos fibers) to justify their assessment of nano-sized TiO_2 and MWCNT. Very few engineered nanomaterials (ENMs) have undergone qualitative assessment for their carcinogenic potential (i.e., nano-TiO_2, MWCNT), and no published studies have assessed their quantitative risk through expected exposure routes. The U.S. National Institute for Occupational Safety and Health (NIOSH) is currently conducting dose–response studies with MWCNTs, a known lung cancer and mesothelioma tumor promotor, in a mouse model [15].

With the exponential increase in novel ECNM development, there is an overwhelming and critical need to assess emerging ECNMs for their carcinogenic potential. With very few documented cases of chronic disease in humans linked to prolonged ECNM exposure, the best datasets at present are in sensitive animal models of tumor development and relevant *in vitro* screening models to investigate the unique physicochemical characteristics of ECNMs that can result in specific interactions and detrimental effects in exposed tissues [16].

The *main objective* of this chapter is to provide an overview of ECNM genotoxicity, neoplastic transformation, and tumorigenic potential, and how future ECNM carcinogenesis risk assessment can use current and developing cancer cell biology techniques to quickly screen and assess emerging nanomaterials. Here, we highlight key findings that form the basis of our current understanding of ENM-induced carcinogenesis and raise important issues that need to be addressed in future research. Focus of this chapter is on the pulmonary targets and related pulmonary responses, since the majority of human exposures to ENMs are via inhalation. Secondary effects as a result of ENMs' translocation into other tissues are also discussed. Subsequently, we describe how advances in *in vitro* neoplastic transformation and *in vivo* carcinogenesis models may be employed to screen suspected ENMs for neoplastic transformation and carcinogenic potential. Such information could be used to promote safe-by-design and prevention-by-design strategies that eventually enhance protection for occupational and environmental exposures and for long-term protection of the nanotechnology industry.

10.1.1 Engineered Nanomaterials and Long-Term Disease Risk: An Introduction

Documented or expected exposures to ENMs include occupational (laboratory and industrial raw material synthesis), ENM-enabled product manufacturing, industrial, consumer goods manufacturing, and end-of-life activities including recycling and waste disposal (e.g., incineration). Based on the projected estimates of nanotechnology use, release of ECNMs into the environment is expected [14]. Identified primary routes of ECNM exposure include inhalation as well as dermal and ingestion exposures [17, 18]. Because of their extremely small size and low biodegradable properties, inhaled ECNMs, such as MWCNTs, can deposit and be retained in deep alveolar tissue up to 336 days post exposure [19]. As such, potential long-term health effects such as carcinogenesis might be expected.

Thus far, there is limited evidence for ENM carcinogenesis. However, ENMs, once in contact with biological tissues, can harbor similar responses to their micrometer-sized or bulk counterparts in their ability to induce lung disease. Examples include crystalline silica versus nano-metal oxides and asbestos versus CNTs, which induce similar biological effects, including reactive oxygen species (ROS) generation, inflammation, genotoxicity, and fibrosis [20]. Because of their smaller size and increased reactivity, ENMs are expected to be even more potent and cause unpredictable toxicokinetics (e.g., uptake route) and biological responses. The strongest evidence to date for ENM carcinogenesis is the high-aspect-ratio nanomaterials (HARNs), which suggests that the current fiber pathogenicity paradigm, with some modifications, can give guidance for ENM carcinogenic risk assessment.

At present, no consistent framework exists to screen and assess ENM carcinogenicity. A vast majority of the published literature reports on acute exposure studies in both *in vitro* and *in vivo* systems, with little attention focused on long-term continuous or occasional/repeated exposures in occupational or public health exposure scenarios. In addition, a majority of published ENM toxicology studies report on observed toxicity at doses 10- to 1000-fold greater than the reported or suspected exposure levels [2, 21, 22]. Lack of exposure characterization studies with sensitive ENM analytical detection techniques accounts for part of this lack of appropriate dosing in some toxicological studies. Acute exposure studies have attempted to identify how different physicochemical properties impact toxicology. A percentage of these studies, however, use non-standardized materials, either from commercial supplies or synthesized in-house, with no well-studied control particle to compare across labs and other studies with similar ENMs. The results have been conflicting reports on known initiators and promoters of tumorigenesis, such as genotoxicity, ROS, and inflammation [23]. In addition, no consensus has been reached on the appropriate dose metric. Although mass is an easy and simple metric to use, it is usually not predictive of the effect. Surface area or particle number typically shows increased accuracy and precision in predicting the effect, but these metrics are hard to assess or

impractical for field studies, do not correlate with toxicity for some ENMs (e.g., graphene), or are under-reported in published literature.

A useful screening and prioritization paradigm for ENMs' carcinogenic potential is to conduct systematic studies in assessing model ENMs with different physicochemical characteristics [24]. They should either occur or predicted to occur with high exposure prevalence throughout its life cycle. By linking physicochemical characteristics with known initiation (i.e., genotoxicity) and promotion (i.e., tumorigenesis) effects, these data can then be used in quantitative structure–activity relationship (QSAR)-like predictive models. For example, the International Agency for Research on Cancer (IARC)'s recent establishment of Mitsui #7 MWCNT as a possible carcinogen suggests that the diameter and length may correlate with its tumor-promoting effect [9]. Examples of such strategies in other noncarbon ENMs exist. For example, nano-TiO_2 was found to be a more potent carcinogen than fine TiO_2 [25]. A robust and effective future carcinogenesis assessment framework for ECNM will rely not only on 2 years of dose–response studies [26] but also incorporate standardized genotoxicity tests, early disease screening models, and incorporation of new advances in *in vitro* and tissue culturing models to screen, assess, and predict ECNM carcinogenesis.

10.1.2 Carcinogenesis: A Multistep Process

As molecular and cellular biology tools advance, the tumorigenesis and cancer paradigm continues to evolve. Early studies indicated that DNA damage was an initial hallmark of potential tumor initiation but was not a good predictor since mammalian cells have robust machineries to repair or remove such damage if it occurs. Our current understanding of cancer is that it represents a combination of diseases, each with its own etiology and genomic signatures that rely on multiple factors for its growth and metastasis including interactions with other cell types, epigenetic factors, micro-RNA, and the tumor microenvironment [27]. Here, we aim to give an overview of the current carcinogenesis paradigm to allow toxicologists, biologists, and other researchers evaluating ENMs to understand what types of effects and data should be collected and evaluated. ENM exposures in reported human cases and *in vivo* models and the resulting adverse effects, namely ROS generation, inflammation, and hyperplasia, do suggest that some ENMs may possess carcinogenic potential.

Although advanced-stage cancers have their own unique genotypes and phenotypes, the working carcinogenesis paradigm relies on three broad steps for tumor growth within the human body: *initiation*, *promotion,* and *progression* [28]. A *carcinogen* is defined as a substance, either natural or anthropogenic in origin, which directly or indirectly induces or promotes cancer by damaging DNA or by altering normal cellular metabolic processes. A *genotoxic substance* can initiate tumorigenesis by causing DNA, chromosomal damage, aneuploidy, or mutation. A *co-carcinogen* is not genotoxic and is not tumorigenic, but can either amplify a genotoxic agent's ability to damage DNA, thereby modifying initiation

or enhance the cellular proliferation and altered gene expression associated with tumor promotion. The co-carcinogenic agent must be present at the same time as the carcinogenic agent. A *tumor promotor* is nontumorigenic on its own, but can increase the growth of DNA-damaged cells [29–35].

10.1.2.1

Genotoxicity and Initiation

Genotoxicity describes the property of an agent to damage or alter the genetic information (either DNA or chromosomes) within a cell, which may cause mutations that lead to cancer. Repeated exposure to a genotoxin can initiate carcinogenesis by increasing the mutation frequency resulting in genome instability, which allows changes in programmed cell death and cell survival signaling (Figure 10.1a). Along with DNA damage, nongenotoxic agents can cause epigenetic changes (e.g., DNA methylation) that can serve as initiating events, potentially leading to cancer. Spontaneous errors in replication, not due to genotoxic substance exposure, can lead to mutations and other genetic errors. Mutations greatly influence key regulatory pathways in lung adenocarcinomas

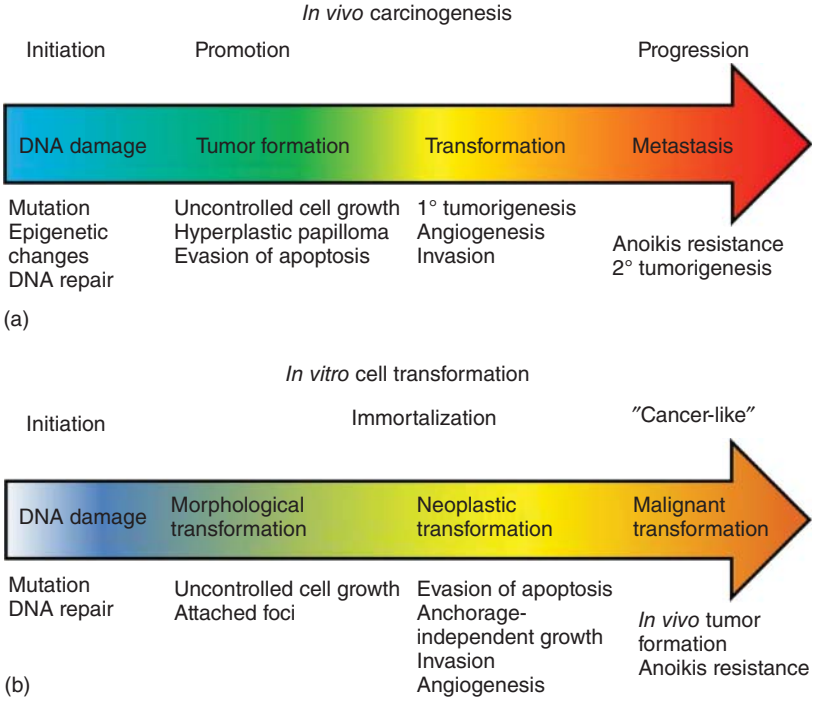

Figure 10.1 Evolution of carcinogenesis with key phenotypes following chromosome damage in mammalian cells. (a) *In vivo* carcinogenesis comprises three major stages, while (b) *in vitro* cell culture transformation assays exhibit initiation and three separate stages of transformation. (Adapted and modified from [36].)

[37]. These mutations typically impact the signaling pathways involved in cell death, proliferation, DNA repair, and cell cycle. Initiation is the first step in the three-stage model of cancer development and is observed in both *in vivo* and *in vitro* models (Figure 10.1a and b). The end product of a tumor-initiating event is the inability to repair DNA damage, genomic instability, and potential survival advantage. However, a cell may still possess DNA repair ability. Since initiation is the result of permanent genetic change, any daughter cells produced from the division of the mutated cell will also carry the mutation [38]. Subsequent mutations and alterations in chromosome number and structure, which can occur during proliferation of a mutated population, can eventually lead to progression of the preneoplastic clone into frank neoplasms [31, 39].

Primary genotoxicity occurs through direct (i.e., DNA adduct) or indirect (i.e., ROS release from damaged mitochondria) mechanisms. Secondary genotoxicity occurs via other cell types interacting with a target cell. The inflammatory response, leukocyte recruitment, and respiratory burst ROS production from macrophages or polymorphonuclear leukocytes are typical and important responses to evaluate.

Numerous particles in the environment are known to induce direct and indirect mutations and oxidative damage of DNA [40]. Many studies report ROS generation from the particle surface itself (e.g., transition metal), interactions with cell components (e.g., altered mitochondrial membrane function), and inflammation response (i.e., neutrophils). Although studies report a dose–response of 8-oxo-7,8-dihydroguanine (8-oxodG) to numerous suspected mutagens, the chosen doses are usually extremely high and are not representative of known oral or inhalation exposures and modeled *in vivo* dose [40]. Depletion of antioxidant defenses (e.g., glutathione, catalase, superoxide dismutase) may also render exposed tissues susceptible to clastogenic DNA damage. Given the numerous direct and indirect genotoxicity modes of action, identifying both genotoxicity and epigenetic modifications to DNA must be a part of future efforts to effectively screen ECNMs for tumor initiation potential.

10.1.2.2 Promotion

Once a cell has been mutated or epigenetically modified by an initiator, it can experience greater sensitivity to the effects of promoters. These compounds promote the proliferation of the mutated cell, giving rise to a large number of preneoplastic or benign daughter cells containing the mutation created by the initiator. Briefly, cells that enter the promotion stage of carcinogenesis usually exhibit the inability to repair DNA damage, avoidance of cell death, enhanced proliferation through self-signals, resistance to tumor suppression factors, replicative immortality, and angiogenesis ability [27]. Clonal expansion of these cells *in vivo* results in the appearance of a papilloma-like tumor. Associated with these changes, late in the promotion phase is a *transformation* that impacts the visual appearance of both a single cell and a mass of cells, which is observable in both *in vitro* and *in vivo* carcinogenesis models. It is a continuous process

that contributes to various steps in the carcinogenic and metastatic processes. *Morphological transformation* relies on numerous cell signaling pathways (e.g., epithelial-to-mesenchymal transition, development signaling pathways) that remodel the neoplastic cell's cytoskeleton, resulting in changes in cell morphology, disorganized patterns in colony growth, and *in vitro* anchorage-independent growth (Figure 10.1) [36, 41]. *Neoplastic transformation* of an *in vitro* cell culture is characterized by the acquisition of most cancer cell hallmarks mentioned above, including invasion and angiogenesis. *Malignant transformation* describes a cell culture that has acquired the tumorigenic ability *in vivo* [36]. A large amount of research findings also support the role of chronic inflammation, inherent reprogramming of cell metabolism, and immune system evasion. Cells experiencing promotion will (i) undergo advancement toward progression and eventual cancer, (ii) continue to grow with no signs of aggression (e.g., benign growth), (iii) persist without further phenotypic advancement or reversal, or (iv) regress [42]. Few chronic ECNM *in vivo* exposures (e.g., MWCNT) show carcinogenesis or continued or arrested hyperplasia [15].

For preneoplastic cells to accelerate their proliferation, escape from tumor suppressor genes and death signaling pathways must occur. Decreased expression or post-transcriptional alterations to p53, p16, check point kinases, and RB1 can result in unregulated, accelerated growth. Conversely, activation of pro-survival signaling, including Ras, MAPK/ERK, Akt, and vascular endothelial growth factor (VEGF) pathways, promotes downstream enhancement of cell proliferation, apoptosis resistance, and angiogenesis. Many of these pro-survival/proliferation pathways are sensitive to changes in ROS/reactive nitrogen species (RNS) balance [43].

In vivo neoplastic growths and neoplastic transformation in cells *in vitro* usually involve not one single morphology or cell type. Rather, there is diverse clonal heterogeneity associated with most neoplasms, consisting of genetically damaged cells that drive and promote growth, while other associated cells experience the influence of these genetically damaged cells [42]. Out of the clonal heterogeneity has arisen the theory of cancer stem cells (CSCs). These cells are thought to have experienced genetic damage that has reversed differentiation and gained stem-cell-like properties including self-renewal, de- and differentiation into stem- and non-stem cell types, aldehyde dehydrogenase (ALDH) overexpression, overactive drug pumps (e.g., ABCG2), and apoptosis resistance signaling, which assist in the promotion and progression of precancerous growth [44].

Research studies routinely depict mixtures of different cell populations with evidence of phenotypic equilibrium within the tumor [45]. As with any other living system, a tumor consists of subpopulations of cells that can undergo population differences over time. Numerous aggressive cancers exhibit a small number of cancer cells with stem-cell-like properties, including the abilities to undergo self-renewal, resistance to death signals, and differentiation into other cell types. CSCs along with other non-stem-like cells exhibit unique surface markers that change over time as the tumor grows, encounters chemotherapeutics, and moves toward metastasis.

Our increased understanding of the tumor microenvironment has greatly impacted the view of cancer as not a single tumor cell type, but rather a unique mixture of primary tumor cells with CSCs, supported by other cell types including cancer-associated fibroblasts, leukocytes, endothelial cells (i.e., angiogenesis), and the extracellular matrix [42]. The broad diversity of heterogeneity, both histological and molecular, implies that cancers grow and evolve through a wide range of phenomena including differences in genetic abnormalities, promotion signaling, interaction with the tumor microenvironment, and epigenetic influences [42].

At present, carcinogenesis is not a simplistic view of one cell type growing to a large mass and metastasizing on its own. Rather, the carcinogenesis process and the resulting aggressive tumor are dependent on the tumor microenvironment: a collection of cancer cells, numerous non-cancer cells that support cancer cell growth, and the extracellular matrix. As our understanding of epigenetics and the tumor microenvironment evolves, the opportunities to develop carcinogenesis screening models early in the developmental process will potentially allow for effective ENM screening and prioritization for long-term carcinogenesis risk assessment studies.

10.1.2.3 Progression

This last stage of carcinogenesis is distinct from the promotion stage. Tumor progression involves more aggressive behaviors of tumor growth away from the site of the primary tumor and includes distinct morphology from preneoplastic hyperplasia, invasion, anoikis resistance, and metastasis (Figure 10.1) [27, 28]. Malignant tumors possess multiple heritable changes over the course of initiation and promotion, which collectively result in aggressive behaviors. It is important to note that several known human carcinogens do not cause initiation or promotion but may act as tumor progressors. A recent study showed that SWCNTs, at the least, have the ability to increase metastatic growth of lung carcinoma [46]. Use of early disease screening assays or models would not detect this phenomenon. ECNM carcinogenesis assessments must evaluate each major step of the carcinogenesis process using appropriate initiation, promotion, and progression models.

10.1.3 Current Knowledge and Challenges in Carcinogenesis Studies

Our understanding of carcinogenesis is continually evolving. This is partially based on key advancements in chemical, biological, and computational technologies that allow rapid development of new tools to study this complex disease. In the past, intracellular research has dominated oncology research in attempts to characterize and understand signaling pathways that control numerous cancer hallmarks. At the DNA regulation and genotoxicity level, evaluating how epigenetics, microRNA, and noncoding RNA influence carcinogenesis will dominate research in the coming years. By identifying additional tumor initiation

mechanisms, genomic biomarkers for early disease detection, screening, and preventive strategies can be developed.

Currently, a transition is under way, shifting from intracellular signaling to investigating carcinogenesis at the extracellular, tissue, and systems-biology levels. Tumor heterogeneity and the different cell types found in the tumor microenvironment may unlock key carcinogenesis mechanisms and identify the preventative targets. Key cell types under study include CSCs, cancer-associated fibroblasts, and several different leukocytes. From these studies, some of the first approved immunotherapies now show promising results in extending patient survival.

Lastly, the role of other health issues, namely environmental pollutants, nutrition, metabolism, and endocrine signaling impacting carcinogenesis, have taken the forefront in evaluating cancer at the systemic or exposome level. Environmental factors along with environmental xenobiotic exposures greatly influence the impact of neoplasm initiation events and the evolution of tumor growth [47, 48]. In addition, occupational exposure to known and suspected carcinogens greatly increases the duration and repeated exposure to documented DNA-damaging initiation agents, thereby greatly escalating the risk of carcinogenesis [48]. Understanding how ECNM exposure impacts the genetic tumor microenvironment and affects long-term health risk is a major challenge over the next few decades. Promising new techniques and models associated with these advances should be utilized in evaluating ECNM carcinogenesis.

10.2
Carbon Nanomaterials: Genotoxicity and Carcinogenic Potential

10.2.1
Physicochemical Properties of ECNMs

Nanotechnology development and research on the effects of ENMs within biological systems have largely focused on how distinct physicochemical properties impact the desired or adverse outcome. Identifying how changes in each property impact ENM bioactivity is the key to developing predictive models for effective and safe-by-design nanotechnology. Genotoxicity and carcinogenesis studies have and should further expand upon this strategy by developing systematic screening assays for each step of the carcinogenesis process.

Certain physicochemical properties of ECNMs such as CNTs, for example, their aerosolizability, biopersistence, and structural similarity to asbestos, which is a Group I human carcinogen [49, 50], may pose asbestos-like lung cancer and mesothelioma risk [20, 51]. According to the major U.S. think tank (RAND Corporation), widespread exposure to asbestos has been described as the worst occupational health disaster in U.S. history and the cost of asbestos-related diseases is expected to exceed $200 billion. Predicting and preventing potential ENM-induced lung cancer has thus become a critical and urgent public health issue.

Size, shape, surface area, surface charges, and agglomeration/dispersion are all physiochemical properties of ECNMs that provide unique and novel technological applications. These same properties, however, can harbor unknown adverse health effects, including chronic diseases such as cancer, as described in this section for each major ECNM discussed. In addition to ECNMs' physicochemical characteristics, particle toxicokinetics (i.e., uptake, biopersistence, elimination/clearance and ultimate fate) must be evaluated since they will determine the internal dose. Translocation within the body away from the primary area of exposure must be considered given ECNMs' small size, surface charge, protein corona, and other physicochemical characteristics (e.g., hydrophobicity) that greatly impact toxicokinetics. Movement of ECNMs into blood circulation or lymphatic system may impact sensitive tissues and organs away from the exposed organs [52]. For example, several studies have reported ECNM presence in the liver, kidney, spleen, and bone marrow following pulmonary or other routes of exposure.

Furthermore, comparative studies within and across classes or groups of ECNMs are vital to identify those physicochemical properties that harbor enhanced genotoxic and cell transformation effects. These types of studies, however, are costly and, at present, do not fully consider vitally needed toxicokinetic and toxicodynamic effects following exposure. For example, a recent study performed a gastrointestinal exposure comparison of diesel exhaust, Printex 90 UFCB, fullerenes, and SWCNT [53]. Both oral instillation to rats and *in vitro* cell culture exposure of diesel exhaust elicited the largest amount of 8-oxodG followed by Printex 90, probably associated with oxidative damage from ROS generation. SWCNT and C60 fullerene showed little effect. Although informative in ranking different ECNMs against a particle exposure with robust literature, this did not report potential uptake differences or the potential role of other xenobiotics [e.g., metals or polyaromatic hydrocarbons (PAHs)] on diesel exhaust effects. Here we highlight recent advances, findings, and short comings in assessing how differences in physicochemical properties impact ECNM carcinogenesis potential.

10.2.2 Ultrafine Carbon Black

Nano-scaled UFCB is widely and primarily used in rubber, plastics, inks, and paints. Occupational exposures usually consist of UFCB with known low levels of sorbed PAHs and metals [54, 55], and therefore its primary physicochemical property leading to adverse effects is its insoluble nature. Ultrafine particles with carbon core from combustion processes are known to cause lung damage following inhalation [56]. At present, carbon black is a Group 2B [57, 58] carcinogen, supported by numerous human epidemiology, *in vivo*, and *in vitro* studies. Its primary basis as a possible human carcinogen is due to elevated rates of lung cancer in workers in the carbon black manufacturing setting, although the available datasets are inconsistent at best. Most *in vivo* data conclude that UFCB is negative for mutagenicity. Prevailing theory for UFCB is indirect genotoxicity via oxidative damage caused by ROS release from infiltrating inflammatory cells.

DNA breaks, oxidized bases, and lipid peroxidation are frequently observed post exposure. Prevailing hypothesis for poorly soluble particles involves particle deposition, uptake via phagocytizing cells, improper clearance, release of pro-inflammatory cytokines and growth factors, inflammation, cell injury and proliferation, ROS release, oxidative damage, and DNA mutation leading to tumorigenesis [58, 59]. Ultrafine carbon particles are routinely found to harbor greater inflammation and ROS generating ability than fine and bulk carbon [60, 61]. Several studies have suggested that ROS [59, 62] generation occurs via direct generation on carbon core or other sorbed ROS-promoting xenobiotics. PAHs are usually tightly bound to the carbon core and pose reduced risk relative to free PAHs [54]. Regardless of other sorbed xenobiotics, long-term *in vivo* exposure studies with pristine carbon black have shown increased tumor incidence above unexposed controls [58].

10.2.2.1 *In Vivo* Studies

Extensive research and description of UFCB deposition, retention, and effects in murine models is available (reviewed by IARC [58]). DNA adducts are not frequently observed above control levels. If they do occur, they are usually particle/cell type-specific [54, 58, 59]. UFCB inhalation results in pro-inflammatory response in rats that is greater than with its fine particle counterpart [63]. A recent low-dose study (7 μg per dose) using multiple aspiration dosing in mice found massive macrophage infiltrate, increased phospholipids, collagen production, and enhanced IL-6 production [64]. Post-exposure chronic inflammation results in oxidized DNA [65, 66]. Additional studies have reported DNA strand breaks in lung and liver tissues following inhalation exposure of UFCB [67–70]. Recent dose–response research at doses below levels known to induce ROS from the inflammatory response indicates that UFCB can damage DNA in the bronchoalveolar lavage (BAL) and lung tissue cells [71]. Although inflammation was not present, low-dose Printex 90 could still generate intracellular ROS in target cells resulting in oxidative damage.

Several long-term inhalation and intratracheal (i.t.) instillation studies have reported that prolonged UFCB exposure causes a positive dose–response tumorigenesis in exposed lung tissue in rats at high doses but not in mice. The majority of these studies reported proliferating cysts with squamous cell morphology following exposure; however, its importance to lung cancer is unclear [58]. Rat lung tumor incidence at 30 months following a 24-month inhalation exposure ranged from 28% to 39% [72]. Conversely, a 9.5-month inhalation exposure study in mice found no difference compared to controls in lung tumor incidence [73]. Two separate groups of rats, exposed for 43 and 86 weeks, displayed 18% and 8% incidence above controls, respectively [74, 75]. The main difference in tumor rate between mice and rats is that mouse models are naturally resistant to particle-induced tumorigenesis [76, 77]. In addition, it has been suggested the rat's response is driven by the "overload phenomenon," where particle number overloads the clearance ability, thus provoking inflammation, excessive ROS,

and lung tumor response [78]. In summary, the size and presence of the carbon core in carbon black are driving factors at moderate to high doses resulting in inflammation and ROS generation. Based on recent evidence of positive direct genotoxicity at doses well below inflammation, long-term inhalation studies should consider the potential absence of a robust inflammatory response in assessing tumorigenesis risk. This would also address issues associated with "overload" in sensitive *in vivo* tumorigenesis models.

10.2.2.2 *In Vitro* Studies

In general, *in vitro* studies suggest that UFCB (e.g., Printex 90) exposure causes ROS generation and is weakly to moderate mutagenic. Acute and subchronic exposure studies with murine cell lines resulted in increased mutation frequency in lacZ and cll transgenes, oxidized purines, strand breaks [79], induction of micronuclei (MN) and cytoskeleton disruption [80], hypoxanthine phosphoribosyltransferase (HPRT) mutations [81], and sister chromatid exchange accompanied by cell transformation [82]. Incubation of epithelial cells with activated neutrophils resulted in oxidative DNA lesions [83]. Human cell line exposures result in strand breaks and oxidative damage, although lung surfactant could mitigate these adverse effects [84, 85]. UFCB with sorbed benzo[a]pyrene (BaP) caused single strand breaks and cell cycle changes, NF-κB and AP-1 activation, and altered p53 phosphorylation [86]. Nanoparticles including urban dust are known to induce single and double strand breaks with subsequent p53 activation, similar to other known carcinogens [87]. The mutation spectrum associated with UFCB exposure suggests an ROS-mediated mechanism [88]. Prolonged UFCB exposure caused dose- and time-dependent proliferation due to stimulation of several ROS-sensitive signaling pathways in human bronchial epithelial cells [89]. A low-dose ($0.02\,\mu g\,cm^{-2}$) 6-month UFCB exposure (Elftex 12) to small airway epithelial cells (SAECs) resulted in slow-growing cells with a pre-senescent transcriptome signature [90].

10.2.3 Carbon Nanotubes

As one of the most promising classes of ECNMs for use in numerous industrial, consumer, and biomedical applications, CNTs are poised for wide production and distribution over the next few decades. Although they possess favorable strength as well as electrical and mechanical properties, they have received some of the most skepticism due to concern regarding their striking similarities to asbestos fibers, a well-established human carcinogen. SWCNTs, double-walled carbon nanotubes (DWCNTs), and multiwalled carbon nanotubes (MWCNTs) possess high aspect ratio (HAR), fiber morphology, high surface area, and limited amount of transition-metal catalysts that contribute to their toxicity in exposed tissues. In addition to these asbestos-like qualities, they vary in their length, width, chirality, structural defect, surface charge, and functionalization, which impact their

toxicokinetics (i.e., protein corona formation and lipid partitioning), tissue distribution, and biopersistence. Upon exposure and deposition in deep airways and terminal bronchioles, CNTs elicit varying degrees of inflammation and ROS generation, resulting in granulomas and fibrosis, all with striking similarity to asbestos (reviewed below). Even though numerous similarities with asbestos exist, some *in vivo* and *in vitro* evidence suggests that CNTs may possess their own unique modes of action for long-term health consequences (i.e., fibrosis and cancer). Assessment of genotoxicity has shown that CNTs can damage DNA *in vitro* and *in vivo* [91]. CNTs disrupt mitosis by interrupting proper centrosome function, and create mono- and poly-polar centrioles, chromosome breaks, mutations, *in vitro* cell transformation, and *in vivo* tumor promotion. Recent IARC review labeled Mitsui #7 MWCNT (Hodogaya, Inc.) as a Group 2B carcinogen (possibly carcinogenic), while other SWCNTs and MWCNTs were placed in Group 3 (not classifiable) due to insufficient evidence [9]. Present research efforts strive to understand those physicochemical properties that influence adverse biological effects (i.e., fibrosis, tumor promotion) to provide information for "safe-by design" and/or "prevention-through-design" strategies for safe technological implementation of these unique ENMs. Here we review studies showing CNT-induced inflammatory and ROS generation, genotoxicity, and carcinogenic potential (Figure 10.2).

10.2.3.1 *In Vivo* Studies

A continuously evolving and published literature details pulmonary toxicological responses to CNTs upon i.t. exposure, pharyngeal aspiration, or inhalation exposure. Upon exposure, CNTs elicit macrophage activation, transient inflammation, neutrophil recruitment, ROS generation, partial clearance, interstitial penetration, biopersistence, epithelial Type II and fibroblast cell proliferation, onset of pulmonary fibrosis, immune suppression, DNA damage, and hyperplasia [17, 22, 92, 93].

Although no clear ENM-driven tumorigenesis mechanism has been described, we highlight those studies that point to potential initiation and promotion mechanisms that drive CNT exposure-associated tumorigenesis. In general, prolonged CNT exposure activates several known and possibly unknown mechanisms that may initiate and promote carcinogenesis. Mechanisms of HAR fiber carcinogenesis include mitotic disruption and DNA breaks, free-radical generation (i.e., ROS and nitric oxide synthase, NOS), stimulation of tumor-promoting cell signaling pathways, and chronic inflammation [17, 92, 94, 95]. It may be decades before ENM-fiber-associated human cancer is observed, if ever. The long latency period between asbestos exposure and mesothelioma development is possibly due to the multiple steps in genetic and cellular changes during carcinogenesis [96].

In consideration of the projected CNT life cycle, the highest risk exposure and the resulting adverse health effects, including potential tumorigenesis, are during CNT manufacturing, handling, and incorporation into other products [5, 22, 92]. Dry CNTs exhibit high dispersion into the air, suggesting that pulmonary

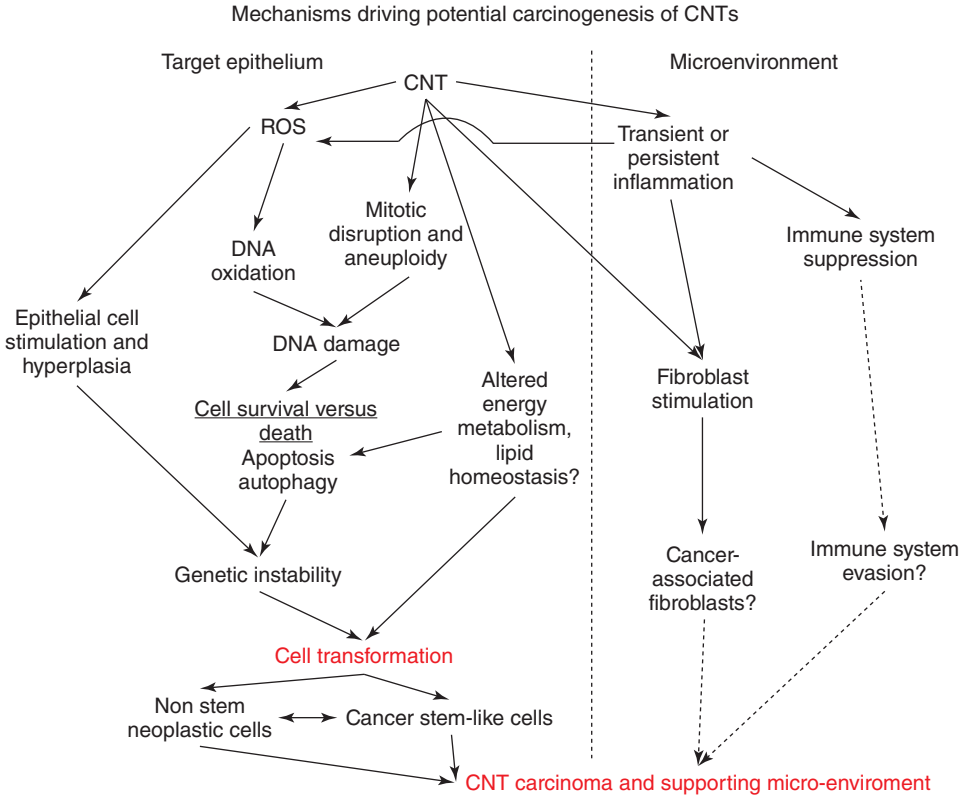

Figure 10.2 Mechanisms driving carbon nanotube carcinogenesis potential.

inhalation and dermal exposures are most likely. Several CNT occupational exposure studies report airborne concentrations and personal breathing zone of worker exposures of >1 μg m^{-3} [21, 97, 98]. Airborne CNT concentrations in several U.S. manufacturing facilities average 10.6 μg m^{-3}, with a majority near the NIOSH-recommended exposure limit of 1 μg m^{-3} [21]. These recent field studies show that ≥75% of airborne CNTs are inhalable, but not respirable [21, 97, 98]. Administration of dispersed CNTs in either pharyngeal aspiration or inhalation exposure to model respirable fraction exposures results in deep lung deposition, primarily in terminal bronchioles and in the bronchiole/alveolar duct (BAD) region [99–101]. Alveolar macrophages, lung epithelial cells, and fibroblast cells are the first group of cells to interact with CNTs with different potential routes of cell uptake and interaction. CNTs interact with cells through either passive diffusion (i.e., random motion) or active uptake (i.e., phagocytosis). Each uptake route has implications for the overall effect and downstream signaling processes, leading to development of potential long-term health consequences.

Passive uptake of CNTs is due to Van der Waals forces and CNT surface–lipid membrane interactions (e.g., hydrophobicity) resulting in CNTs puncturing the

cells and persisting in the cytoplasm of cells. Direct interaction with cytoplasm and cellular structures has several important toxicological consequences for the affected cells. First, sorption and desorption of proteins to and from the protein corona may impact cell signaling and metabolic processes. Second, graphene surface may participate in redox reactions by either sequestering or assisting in the generation of ROS, thereby affecting ROS-sensitive signaling and/or cell damage. Lastly, CNTs show morphology similar to that of microtubules, suggesting that mimicry or interference of microtubule-associated processes may occur. Dinu *et al.* [102] demonstrated that tubulin associates with CNTs and that kinesin activity is impacted in the presence of CNTs. Both SWCNTs and MWCNTs were shown to integrate into the mitotic spindle and centrosome apparatus in human SAECs. Similar to asbestos [103], CNTs are able to disrupt mitosis, causing mono- or poly-polar centrosomes, resulting in chromosome breakage and aneuploidy [6, reviewed later].

Phagocytosis of CNTs can result in complete uptake and compartmentalization of CNTs within phagolysosomes. Several enzymes are capable of breaking down CNTs; however, their occurrence is cell-type-specific and is an extremely slow process. Rigid and long CNTs, however, are unable to undergo complete phagocytosis resulting in "frustrated phagocytosis" [104]. This phenomenon is also observed with asbestos fibers where macrophages are unable to completely engulf the HAR fibers. Phagosome rupture can cause cathespin B release from damaged membrane, activating NRLP3 inflammasome and caspase-1, which in turn activates IL-1β, an important inflammatory cytokine.

Pulmonary exposure to respirable fractions of MWCNTs results in deep penetration, alveolar and interstitial deposition, and extra-pulmonary translocation to subpleura and other sensitive organs. CNTs are known to experience penetration to subpleural tissue [105–108]. At present, it is unclear what adverse health effects inhalable fractions of MWCNT possess [21, 98]. Several reports demonstrated MWCNTs possessing an asbestos-like biopersistence ranging from months to 1 year post exposure [6, 19, 100, 101, 107, 109] and possibly longer. For example, Mitsui #7 MWCNT fate was evaluated in pulmonary and extra-pulmonary tissues at 1 and 336 days after a 12-day whole-body inhalation to 5 mg m^{-3} MWCNTs (49 nm width). At 336 days post exposure, 4.2% of the initial lung burden was found in the airways and 95.8% of the initial lung burden remained in the alveolar region, including 4.8% in the subpleural tissue region [19]. Singlet MWCNT was observed in several extra-pulmonary organs including the chest wall, diaphragm, kidney, and liver. Lymph nodes were especially noted as a significant site of MWCNT accumulation. Notably, tracheobronchial lymph nodes experienced an increase in MWCNT burden going from ~1% at day 1 to 7.3% at day 336 post exposure. A similar increase in extra-pulmonary deposition of MWCNT was observed in the chest wall, other lymph nodes, and organs. In addition, this study suggested that small MWCNT aggregates (>4 fibers) disassociate over time *in vivo*, resulting in persistent singlets that increased 10-fold over the course of the study. These studies highlights the fact that CNTs are not static in tissues once deposited at their primary site of exposure. It appears that through their

biopersistence and novel properties, they exhibit dynamic translocation ability and experience wide systemic distribution and may impact other sensitive areas with known tumor susceptibility. A recent study with ^{14}C-labeled MWCNTs (40 nm width) highlights this fact by finding MWCNTs deposited in spleen, liver, and bone marrow of mice following pulmonary aspiration at an occupationally relevant dose (20 μg bolus ~ 38 working years, Figure 10.3) [110]. Given that liver is sensitive to toxicants and many physiological functions depend on bone

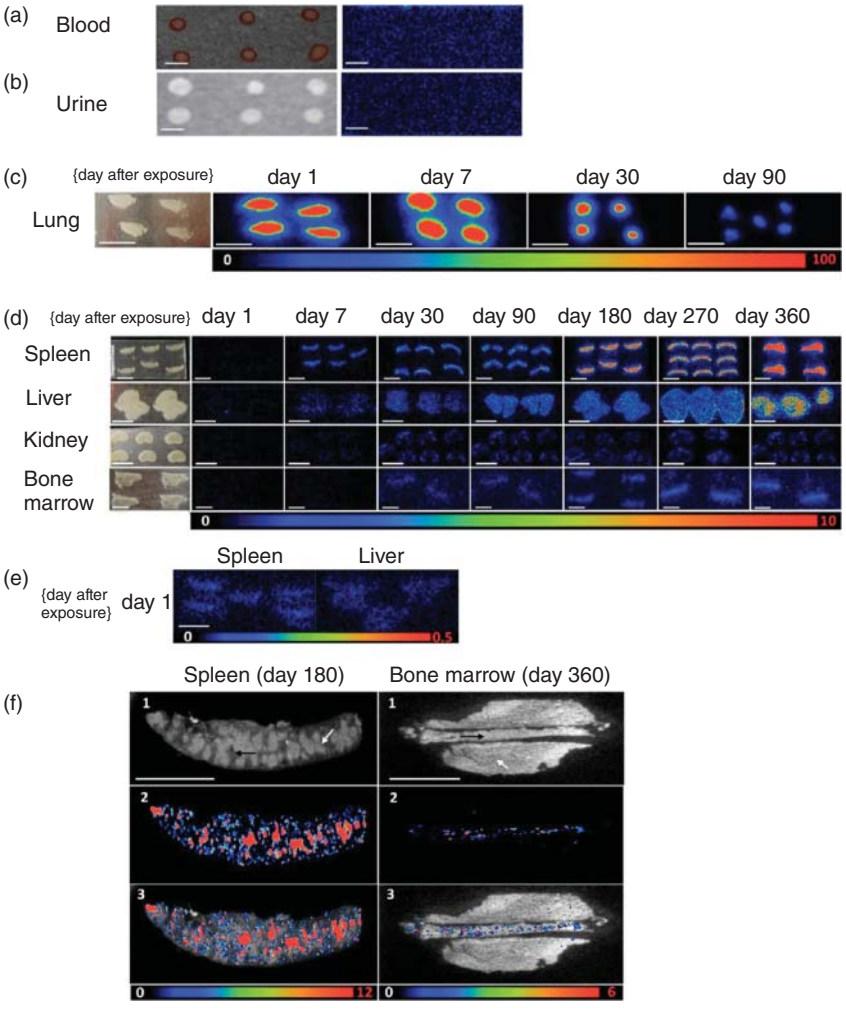

Figure 10.3 Systemic fate of ^{14}C-labeled MWCNTs following 20 μg per lung aspiration exposure in female mice. (a) Following exposure, MWCNTs were found to move out of the lung (b) and into several organs. (c) High-resolution optical (top) and radioimaging (middle) of spleen and bone marrow. (Reprinted with permission from [110]. ©2014 American Chemical Society.)

marrow progenitor cells (e.g., stem and immune cells), this finding is, at least, worrisome. Future studies should evaluate the long-term health effects of CNT deposition and persistence in these sensitive tissues.

SWCNTs, although more difficult to identify, also exhibit this quality with slow degradation over time [111–113]. Alveolar macrophages phagocytose a significant portion of deposited CNTs and move them up the mucus ciliary escalator. It appears, however, that fiber morphology plays a role in macrophage recognition of CNT as a foreign particle. For example, alveolar macrophages only cleared 10% of SWCNTs compared to equal mass dose of well-dispersed MWCNTs [108]. This difference in clearance suggests that lower mass concentrations of SWCNT exposure elicit a response similar to that of higher MWCNT concentrations. The ability of SWCNTs to escape macrophage recognition, phagocytosis, and clearance allows for greater CNT reactivity with epithelium and penetration into the alveolar interstitium and subsequent interaction with lung fibroblasts. How this difference impacts *in vivo* carcinogenesis remains to be evaluated. Regardless, CNTs' ability to penetrate exposed tissue with prolonged biopersistence indicates that chronic CNT exposure at relatively low doses to sensitive tissues harbors increased risk for long-term health risks, potentially including cancer.

Physicochemical factors of CNTs that impact inflammatory and fibrotic effect in exposed lungs include length, width, surface charge, surface functionalization, surface area, dispersion stability, rigidity, and transition-metal content. Similar to asbestos, fiber length and dispersion in single fiber morphology are major factors determining biological responses. For example, well-dispersed SWCNTs and MWCNTs elicit potent inflammatory and fibrotic responses [99, 101, 114, 115], while CNT agglomerates are less reactive and mirror generalized response to large inhaled particles [116].

In early studies evaluating CNT-induced toxicity, several research groups reported data that would support early mechanisms of carcinogenesis. Inhalation exposure of SWCNTs caused a more robust ROS, inflammation, and KRAS mutation response than aspiration exposure using the same material [114]. This mutation is a known factor in increased risk of lung cancer associated with smoking and chemical-induced carcinomas [117]. In addition, several studies evaluating CNT inflammation and fibrosis via whole transcriptome array analyses have identified cancer signatures and known lung cancer prognostic markers in exposed mouse lung tissue [118, 119]. Interestingly, an identified lung cancer gene signature, including Bcl-2 and caveolin-1, has been implicated in CNT *in vitro* cell transformation studies [120, 121]. These genes may play a role in early CNT neoplastic transformation mechanisms. In a follow-up study by Guo *et al.* [122], using the same dataset, a 35-gene signature from MWCNT-exposed mice was able to predict human clinical lung cancer survival rates.

Given CNT's striking similarities to asbestos in subpleural translocation, as well as inflammatory and fibrotic reactions in the lung, recent concern has shifted to a potential for CNT induction of mesothelioma. HAR fiber-associated bioactivities include translocation out of alveoli to mesothelial tissues, biopersistence, epithelial and mesothelial cell injury, and activation of macrophage phagocytosis [123].

Several *in vivo* studies report that translocation of long CNTs from exposed lung to the parietal pleura impart inflammation, mesothelial hyperplasia, granulomatous lesions, and fibrosis [124–127]. The current CNT hypothesis for mesothelial disease closely mirrors that of asbestos in that long fibers tend to become trapped around parietal stomata in attempts to drain to the lymphatic system. This results in penetration, cell damage, and chronic inflammation, all likely key events promoting tumorigenesis [49, 128].

Although CNTs exhibit HAR fiber behavior with striking similarity to asbestos, several studies report deviations of CNT behavior from that of asbestos including lung transport mechanisms, transient inflammation, rapid onset of fibrosis, and prolonged progression of fibrosis in the absence of persistent inflammation [100, 101, 106, 129]. Such differences in both toxicokinetics and toxicodynamics suggest that CNTs possess unique properties, resulting in unknown mechanisms with potential unpredictable effect.

Presently, CNTs are thought to harbor elevated risk of carcinogenesis compared to other ECNMs. Recently, a large number of *in vivo* studies evaluated specific CNTs (most notably Mitsui #7) for neoplastic lesions or tumorigenesis. Overall, based on one report of MWCNT promotion of lung adenocarcinoma [15] and several reports of mesotheliomas following intraperitoneal (i.p.) injection (discussed later), the IARC Working Group concluded that there was sufficient evidence of carcinogenesis of Mitsui #7 in experimental animals. Although the evidence for neoplasia in rats and mice was strong and mechanisms in model systems associated with neoplasia were demonstrated, no neoplastic outcome has been observed in humans. The IARC committee therefore classified the Mitsui #7 MWCNT as a Group 2B carcinogen. Although there were mechanisms of carcinogenesis in experimental models that would be reasonable in humans, the IARC Working Group noted there was no evidence for carcinogenicity in humans. They also cited the lack of systematic and coherent evidence to support generalization to other CNTs [9]. Given no evidence of excess human cancers, short CNT production history (~10 years), and expected latency for detectable HAR fiber-induced tumors, excess cancers may not be observed for another two decades. Rigorous dose–response studies evaluating how key physicochemical properties contribute to CNT lung adenocarcinoma and mesothelioma are urgently needed to form adequate risk assessment and contribute to further "safe-by-design" CNT technology development.

Injection of suspected carcinogens with HAR fiber morphology via i.p. administration is a well-established technique to screen for mesothelioma risk [130]. Several studies using different lengths, widths, morphologies, and dispersibilities of MWCNT have reported that the physicochemical properties of MWCNTs impact their ability to promote HAR fiber-like lesions and mesotheliomas. Four key features of HAR fibers for adverse effects are translocation out of alveoli to mesothelial tissue, biopersistence, epithelial and mesothelial cell injury, and activation of macrophage phagocytosis [123]. In one of the first studies, two short and two long MWCNTs with different fiber thickness were i.p. injected to evaluate inflammation (7-day) and granulomatous lesion (28-day) potential [124]. Long

CNTs (>15 μm) caused asbestos-like inflammation and lesions, while short and tangled CNTs (≪15 μm) showed minimal effect. A study by Muller *et al.* [131] reported that short MWCNTs (<1 μm) did not induce mesothelial tumors following i.p. injection to the peritoneal cavity in male Wistar rats over the course of 2 years. Intrascrotal injections of MWCNTs (Mitsui #7) into male F344 rats caused a robust mesothelioma response, stronger than positive asbestos fiber control, resulting in early death of the majority of animals (37–40 weeks) prior to the 52-week endpoint [132]. Mesotheliomas were noted as aggressive in nature and metastatic in lung tissue.

Injection (i.p.) of MWCNTs (Mitsui #7; 1–20 μm length) results in dose-dependent induction of mesothelioma in p53 heterozygous mice [133, 134]. Doses ranging from 106 to 108 fibers per mouse resulted in 25–95% mesothelioma incidence. Interestingly, in the latter study, the time to tumor onset was dose-independent. All exposed mice exhibited mesothelial hyperplastic lesions, widely considered preneoplastic, with underlying macrophage infiltrate with single MWCNT fibers. This study suggests that frustrated phagocytosis and the resulting inflammation in the mesothelial lining microenvironment promote early tumorigenic events. A significant subset of human population has somewhat faulty p53 behavior, and human cancers possess faulty p53 signaling, so heterozygous p53 models have relevance in carcinogenesis studies [135].

Next, Nagai *et al.* [136] compared thin versus thick MWCNTs using both *in vitro* and *in vivo* models. One month following i.p. injection at low and high doses, thin and crystalline MWCNTs caused fibrosis around most i.p. exposed organs. A 1-year follow-up study found that thin MWCNTs caused mesothelioma that harbored CDKN2A/2B homozygous deletions, a common feature in human and rodent mesothelioma. Thick and tangled MWCNTs were less inflammatory and carcinogenic. *In vitro* exposure studies found that thin, crystalline-like MWCNTs pierced cells and induced cytotoxicity. Two types of mesothelial cells *in vitro* did not experience active MWCNT uptake, while asbestos did associate with these cells. Further investigation found that thin, crystalline MWCNTs passively puncture the plasma and nuclear membranes *in vitro*, leading to their potent cytotoxic effects. The authors systematically ruled out other physicochemical factors contributing to the differences in effect including length, ROS generation, surface area, fiber number, and transition metals. Diameter may be a determining factor for carcinogenesis; however, more systematic evaluations are needed.

A 2-year carcinogenic study in rats was conducted to compare four different MWCNTs to asbestos-induced mesothelioma [137]. A total of 5×10^8 to 5×10^9 CNTs/animal were injected (i.p.) and compared with 108 asbestos fibers/animal. All MWCNTs ranged from 7.9 to 10.2 μm in length and 37 to 85 nm in width. Given their similar lengths, MWCNTs primarily differed on their widths and straight versus curved morphology. Tumor incidence and time to onset was dose- and CNT-particle dependent. Earliest onset was observed in animals exposed to straight MWCNTs with large diameter (85 nm). Curved and narrow width (37 nm) MWCNTs exhibited the longest time to tumor onset. A majority of

MWCNT mesotheliomas were either sarcomatoid or biphasic with high similarities to asbestos-induced mesothelioma. The authors concluded that aspect ratio and curvature of MWCNT appeared to influence mesothelioma potential, although width appeared to contribute to mesothelioma induction potency.

Although i.p. injections provide a model for mesothelioma screening, they do not consider the toxicokinetics and fate in a physiologically relevant exposure (i.e., inhalation). Recent studies have begun to assess the expected exposures, the chronic toxicokinetics of CNTs *in vivo*, and their carcinogenic risk in both lung epithelium and pleural/subpleural mesothelium. Although only a few CNT inhalation studies to date have been conducted, they indicate that CNTs are probably human carcinogens. Sargent *et al.* [15] conducted a classic initiation/promotion evaluation of inhaled MWCNTs' carcinogenic potential by evaluating their ability to affect tumorigenesis in the absence/presence of a well-known DNA-damaging agent and carcinogenic initiator, namely methylcholanthrene (MCA). First, B6C3F1 mice, a National Toxicology Program (NTP) wild-type model, were i.p. exposed to vehicle-only or 10 μg MCA per gram body weight. At 1 week, mice were exposed to filtered air or 5 mg m^{-3} of Mitsui #7 MWCNTs for 15 days, 5 h per day, via whole-body inhalation with a reported lung burden of 31.2 μg per lung. MWCNT-only exposed mice evaluated MWCNT's ability as a complete carcinogen, while MCA+MWCNT evaluated MWCNT's cancer promotion potential. Approximately 52% of MCA-only and 90.5% of MCA+MWCNT mice at 17 months post exposure showed bronchioloalveolar adenomas and adenocarcinomas. Conversely, 26.5% of MWCNT-only and 23% of filtered-air-only exposed mice possessed similar tumors. Interestingly, MWCNT-only exposed mice exhibited focal hyperplasia in lungs characterized by crowded alveolar cells spaced randomly along alveolar septa (Figure 10.4). These foci were termed "focal adenomatous hyperplasia" since atypical hyperplasia is a commonly observed preneoplastic lesion in humans exposed to numerous carcinogens. As expected, singlet and small loose agglomerates of MWCNTs were found in the lung tissue or in subpleural (e.g., diaphragm) tissues (Figure 10.4). Metastasis was observed and potentially contributed to early euthanasia in mice exposed to MCA+MWCNT (Figure 10.5). Nine percent of the MCA+MWCNT mice showed tumors consistent with sarcomatous mesothelioma, as indicated with positive podoplanin and marginal cytokeratin staining (Figure 10.5). Sargent *et al.* [15] concluded that inhaled dispersed Mitsui #7 MWCNT is a lung cancer promoter.

A small pilot study ($n = 6$ per group) performed 100 μg i.t. injection of pristine MWCNT (7 μm long) versus acid-treated MWCNT (0.57 μm long) into C57BL/6 male mice Yu *et al.* 2013 [138]. After 6 months, more potent autophagy accumulation, hyperplastic adenoma, and adenocarcinoma regions response were observed with pristine MWCNT compared to acid-treated MWCNT in exposed mouse lungs.

Xu *et al.* [139] compared MWCNT's and asbestos fiber's ability to induce mesothelial lesions in F344 rats. MWCNT was found to translocate to pleural cavity, resulting in mesothelial hyperplasia following five different i.t. sprayings

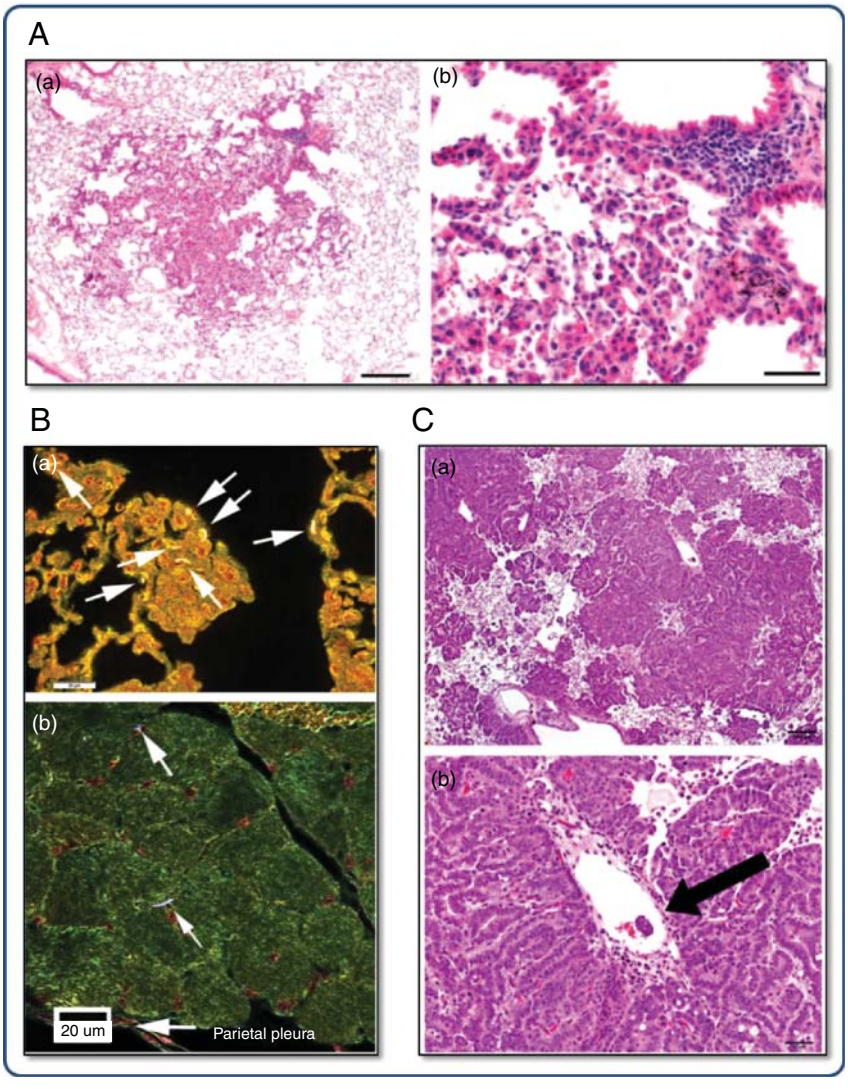

Figure 10.4 Promotion of lung adenocarcinoma and mesothelioma following MWCNT inhalation exposure. (a) MWCNT-only-exposed mice possess regions of focal adematous hyperplasia with unique morphological characteristics. (b) Enhanced dark-field imaging at 17 months post exposure, showing deposited MWCNTs (white arrows) in alveolar (top) and extra-pulmonary (diaphragm) regions. (c) Lung adenocarcinoma (top) and metastatic tumor in pulmonary blood vessel (bottom) in mice exposed to MCA+MWCNT. (Reprinted with permission from [15]. ©2014 Particle and Fibre Toxicology.)

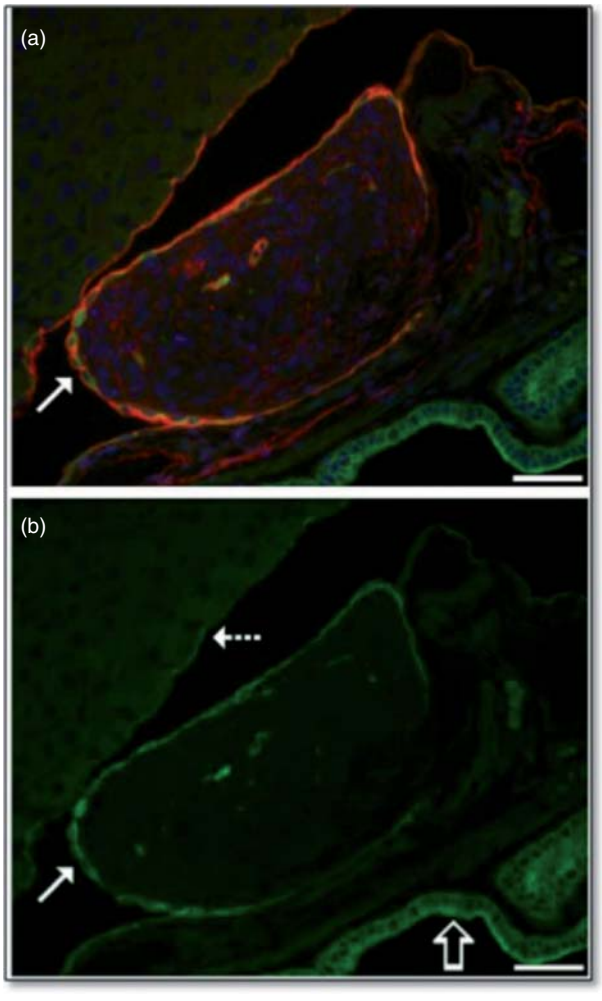

Figure 10.5 Sarcomatous mesothelioma in mice exposed to MCA+MWCNT. Co-staining of (a) podoplanin (red) and (b) cytokeratin (green) identified mesothelioma (white arrow, upper panel) between the gall bladder and liver. (Bottom panel) Cytokeratin staining of mesothelial tissue. (Reprinted with permission from [15]. ©2014 Particle and Fibre Toxicology.)

over 9 days in Fisher rats. MWCNT hyperplastic lesions were associated with macrophage infiltration and inflammation-associated fibrosis. A majority of MWCNTs were found in alveolar macrophages and mediastinal lymph nodes. In addition, pleural macrophages were found to contain MWCNTs, with little to no nanomaterial in mesothelial tissue, thus suggesting that the observed hyperplasia was due to pro-inflammatory signaling. Conditioned medium from MWCNT-exposed macrophages confirmed an inflammation-driven mesothelial cell proliferation *in vitro*.

A follow-up study [127] evaluated the impact of the size and shape of MWCNTs on the fate, fibrosis, and mesothelial proliferation in F344 rats. Long and thick (8 μm) MWCNTs were compared to short, thin, and tangled (3 μm) material using a repeated dosing model comprised of 12 exposures over 24 weeks via transtracheal spray. Total administered MWCNT was 1.625 mg per rat. Long, well-dispersed MWCNTs reached the parietal pleura to induce fibrosis and mesothelial hyperplasia. Long MWCNTs also caused a stronger inflammation response in pleural cavity lavage. Interestingly, the short MWNCTs, which formed small aggregates, caused a more robust inflammation and oxidized DNA in exposed lung tissue than long MWCNTs. This study supports the growing hypothesis that long, thick, and rigid MWCNTs that are well dispersed can translocate to the pleural mesothelium and cause hyperplastic lesions and inflammation, consistent with the preneoplastic etiology observed in asbestos-induced mesothelioma. This study also raises the possibility that particle morphology impacts toxicokinetics and the eventual fate, and can still cause long-term risks in different tissues. Here, although no extra-pulmonary translocation occurred, short and tangled MWCNTs were highly inflammogenic and cytotoxic, in both *in vivo* and *in vitro* models. Although other studies suggest that shorter and tangled CNT exhibit less reactivity [126], it is still important to consider their adverse health effects given that a majority of CNTs in the occupational setting possess a tangled, agglomerated morphology [21].

SWCNTs, because of their single layer of graphene, are more flexible tube structures and can possess numerous morphologies including single fibers, nanoropes, and loose, tangled agglomerates. They do, however, possess significantly greater surface area compared to their DWCNT and MWCNT counterparts. This higher surface area has been implicated in producing greater potency than MWCNTs at equal mass dose. Two published studies with small sample sizes evaluating long-term effects of SWCNT exposure in rats found little tumor evidence after 6 months and 754 days post i.t. instillation [113, 140]. Several recent studies by Shvedova *et al.* [141] and others have suggested that SWCNTs promote carcinogenesis through several mechanisms including genotoxicity, altered cytokine signaling, and yet-undefined mode(s) of action. SWCNTs and carbon nanofibers (CNFs) were compared to asbestos via pharyngeal aspiration to evaluate long-term pulmonary effects, including inflammation, fibrosis, and genotoxicity in C57BL/6 mouse [112]. SWCNT aspiration data were then compared with a 4-day inhalation exposure to evaluate dosimetry. CNF and asbestos fibers were rigid and possessed 2- to 10-fold greater length than flexible SWCNTs. At 1-year post exposure, SWCNTs were still present in exposed lung tissue, primarily as nanoropes, with some detected in lymphatic tissue. SWCNTs were most fibrogenic and produced increases in MN, while CNFs and asbestos exhibited the largest inflammation response. Both SWCNT and CNF, but not asbestos, exposure increased KRAS oncogene mutation frequency. Although no tumors formed in this moderate tumor-resistant model, it is apparent that long, rigid HAR fibers contribute to a greater inflammatory response than the more flexible HAR fibers and that KRAS mutation may be a more common feature of prolonged exposure

to HAR carbon nanomaterials. This study also adds support to the hypothesis that CNT exposure may harbor a unique inflammation-independent mode of action in promoting chronic lung disease (i.e., fibrosis). A distinct CNT mode of action for bronchoalveolar epithelial carcinogenesis has yet to be defined, and is an area for future investigation.

Recently, two studies by Shvedova *et al.* [46] have raised the possibility that CNT exposure modulates immune cells, thus improving the tumor microenvironment and enhancing tumor growth. First, short SWCNTs (230 nm) were aspirated into mice (80 μg) followed by i.v. injection of Lewis lung carcinoma cells. At 21 days post i.v. injection, SWCNT-exposed lungs exhibited a 5-fold increase in weight and a 2.5-fold increase in number and size of lung metastases. Clearly, SWCNT pre-exposure enhanced the recruitment and proliferation of lung metastases. Further examination identified an increased number of recruited myeloid-derived suppressor cells (MDSCs), a cell type known to promote tumor growth, in SWCNT-treated lungs. MDSCs typically are found to suppress the immune response and enhance new blood vessel growth in tumors. Blockage of MDSCs in the mouse lung reduced lung cancer metastases. A second study reviewed the published literature and noted that overexpression of three signaling factors (M-CSF, GM-CSF, and TGF-β) was a common occurrence associated with lung cancer and SWCNT exposure, thus suggesting immune suppression in CNT-exposed lungs. Acute SWCNT aspiration exposure (80 μg) induced recruitment of MDSCs and TGF-β production, which in turn promoted an immunosuppressive microenvironment by suppressing T-cell activation and recruitment [141].

In summary, the length, width, surface functionalization, surface area, crystallinity, dispersion stability all appear to impact CNT toxicokinetics and the resulting genotoxicity and tumorigenesis *in vivo*. Long, straight, and thick MWCNTs appear to pose enhanced risk for mesothelioma due to their deep penetration and translocation ability, resulting in a chronic inflammatory response that drives mesothelial hyperplasia and eventual carcinogenesis. The fact that Mitsui #7 MWCNT agglomerates and similar fibers have the ability to dissociate to singlet fibers over time *in vivo* and systemically disperse [101] is alarming. Tangled MWCNTs typically observed in human occupational settings are potentially less likely to dissociate and translocate, and is an area of current research [21, 98]. NIOSH is currently evaluating carcinogenic dose–response following MWCNT inhalation in the hope of providing data for risk assessment criteria. Although tangled CNTs show little mesothelioma risk and reduced potency compared to well-dispersed fibers, they make up a significant portion of manufactured CNTs, retain some ability to induce a robust inflammatory response in exposed airways similar to other carbon-based particles, and may experience dispersion *in vivo*; therefore, they should not be overlooked as a potential carcinogen. At present, *in vivo* CNT carcinogenesis studies are expanding to consider other important physicochemical properties (e.g., surface functionalization) of these materials, which are projected to experience high manufacturing, wide use, and increased rates of exposure. Tier I *in vitro* genotoxicity/transformation and Tier

II short-term *in vivo* studies are paramount in identifying those properties with potential risk for CNT carcinogenesis.

10.2.3.2 *In Vitro* Studies

There is some evidence *in vitro* that ECNMs, such as CNTs, can gain access to the nucleus and genetic material, which can cause genetic aberrations by a primary mechanism additional to the inflammation or ROS-mediated one. These potential mechanisms require further study [20]. *In vitro* cell models remain and will continue to play a key role in screening novel ENMs for potential toxicity [24]. Recent advances in multicellular models hold vast promise in adding to the battery of available *in vitro* predictive models (reviewed below). Acute exposure to macrophage, epithelial, fibroblast, and endothelial cell results in passive or active uptake, plasma membrane damage, NRLF3 inflammasome activation, inflammatory cytokine release, ROS, proliferation, and enhanced collagen production [51, 142, 143]. Similar to *in vivo* findings, many of the same physicochemical properties of CNTs elicit cytotoxic and subtoxic effects leading to disease onset [144]. Size, surface functionalization, and surface charge impact the uptake route into the cells. COOH, OH, and other negatively charged functional groups repel the negatively charged phospholipid heads of the plasma membrane, thus making direct penetration less likely. Positively charged surfaces, such as N-containing groups, present a positive charge and may be more suitable for direct penetration and membrane disruption [145]. Functional groups and surface coatings may also interact with membrane-bound receptors, which may assist in endosomal uptake or initiate signaling cascades within exposed cells.

ROS generation, inflammation, genotoxicity, and the subsequent downstream signaling pathways and responses are all implicated in the early phases of CNT-associated neoplastic cell behavior and early stage tumor formation. For example, SWCNT exposure to human bronchial epithelial cells resulted in nitric oxide (NO) production, pro-inflammatory cytokine release, and autophagic cell death corresponding to cytoplasm damage and mitochondrial dysfunction [146]. The role of chronic inflammation following MWCNT exposure possibly plays a larger, critical role in mesothelial response, hyperplasia, and CNT tumorigenesis than epithelial cell response. MET5A mesothelial cells directly exposed to a panel of five different MWCNTs did not produce inflammatory cytokines. Rather, cytokines from CNT-exposed macrophages elicited pro-inflammatory cytokines from MET5A cells [128]. Another study reported distinct differences in oxidative responses between neutrophils and macrophages in response to MWCNT versus asbestos fibers. Neutrophils showed no response to MWCNTs, while two types of asbestos fibers elicited ROS and inflammatory responses. Macrophages responded to both particle types with ROS and inflammation [147]. Given the relatively small amount of macrophages in the pleural cavity compared to pulmonary airways, the presence of a positive feedback loop suggests that human mesothelial cells are sensitive to alterations in inflammation.

CNTs are known to cause increased ROS in exposed cells, but also harbor ROS quenching and sequestration ability. Generation or sequestration ability of ROS is most likely material-, impurity-, solution-, and assay-dependent. Residual transition metals from several CNT synthesis methods are known to participate in Fenton-like reactions and can cause greater ROS production than pristine, low-metal-content CNTs [95, 142, 148]. Alternatively, studies have suggested that structural defects and organic surface functional groups with available electrons can donate electrons to reactive radicals [149]. A recent systematic evaluation of MWCNTs in the absence and presence of a lung surfactant showed that MWCNTs, by nature, sequester free oxygen radicals [150]. On a $\mu g\,cm^{-2}$ basis, SWCNTs are more potent inducers of DNA strand breaks than MWCNTs *in vitro*. SWCNT exposure to both normal and malignant mesothelial cells resulted in ROS production, DNA damage, and activation of several signaling pathways including AP-1, NF-κB, p38 MAPK, and Akt, all of which mirror events associated with asbestos-induced mesothelioma [142].

Although ROS generation in exposed tissues is known to occur and cause clastogenic damage, mounting evidence has identified direct genotoxic mechanisms that are ROS independent, echo other HAR fiber disruptions of mitosis, and have large implications for cellular fate. For example, exposure to low-iron-containing MWCNTs induced minimal ROS but DNA damage and apoptosis to both normal and malignant mesothelial cells. ERK and p38 MAPK also experienced enhanced activation [151].

A recent review of the *in vitro* genotoxicity literature identified the mitotic block MN, pH2AX, and comet assays as the most performed mammalian tests for CNT genotoxicity with positive results [152]. A wide range of human and mouse cell lines (e.g., Muta mouse epithelial cells, Balb/c mouse fibroblasts, BEAS-2B epithelial cells, RAW264.7 macrophages, normal human fibroblasts, and A549 cells) all show positive genotoxicity. Early genotoxicity studies employed high-dose CNT exposures with comet assay for hazard identification screening. Most exposures indicated DNA fragmentations with a potential role for oxidative stress damage. High-dose MWCNTs induced 8-nitroguanine lesions on DNA in A549 cells. Inducible nitric oxide synthase (iNOS) was also induced. DNA damage was suppressed by inhibitors of iNOS, NF-κB, actin polymerization, and caveolae-mediated endocytosis, suggesting that uptake and the resulting inflammasome activation contributed to indirect DNA damage via nitrosative DNA damage [153].

A study evaluating both *in vitro* and *in vivo* lung models, however, reported that MWCNTs can induce both clastogenic and aneugenic effects, by using MN and fluorescence *in situ* hybridization (FISH) assays [7]. This suggested that CNTs themselves were either directly interacting with DNA or that CNTs were disrupting chromosome separation during mitosis. With better understanding of occupational exposure levels and potency of CNTs *in vivo*, more recent studies have focused on much lower dose and longer exposure time frames to assess genotoxicity.

CNTs can mimic microtubules *in vitro*, due to its carbon structure, size, and HAR morphology, which interfere with critical microtubule dynamics including proper chromosome separation during mitosis [6]. Dinu *et al.* [102] reported that tubulin can "self-assemble" onto MWCNTs to form tubulin-MWCNT hybrid structures. Alterations in the microtubule structure can impact not only cell division but also intracellular trafficking of proteins, lysosomes, and organelles. Sargent *et al.* [154] showed that high-dose SWCNT (HipCo) exposure caused fragmented centrosomes, multipolar spindles, anaphase bridges, and aneuploidy in two different human lung epithelial cell lines. SWCNTs were found to be associated with chromatin and tubulin, which are known to bind to G–C-rich areas of DNA. Carbon bridges formed during mitosis in SWCNT-exposed cells are reminiscent of asbestos bridges. Asbestos does not typically associate with centrosomes, but CNTs can, possibly due to their durability and flexibility [6]. Intercalation of SWCNTs would induce a DNA morphology change that could interfere with several vital processes including chromatin stability, replication, and transcription.

A follow-up study employing occupationally relevant doses to lung epithelial cells (0.024–24 $\mu g\,cm^{-2}$) of SWCNTs caused similar effects seen in high-dose exposures: fragmented centrosomes, disrupted mitotic spindles, and aneuploidy [155]. Subsequent clonal survival and proliferation assays found that SWCNT-exposed cells experienced increased colony formation and proliferation 7 days post exposure in surviving cells. These studies suggest that SWCNTs can disrupt chromosome integrity and enhance proliferation, which are two early characteristics in the cancer initiation/promotion etiology. Although a majority of cells harboring significant chromosome damage would not survive, it is possible that prolonged exposure would promote the survival of cells with chromosome damage, leading to genetic instability and early stages of carcinogenesis.

Subsequent studies reported similar outcomes for MWCNT exposure with some differences. MWCNTs (25 nm diameter) were found to disrupt cancer cell mitosis via microtubule mimicry [156]. MWCNT exposure (10–20 nm) was shown to cause dose–response (0.024–24 $\mu g\,cm^{-2}$) increases in the frequency of disrupted centrosomes, abnormal monopolar mitotic spindles, and aneuploidy chromosome number in BEAS-2B and primary human SAECs at 24 h (Figure 10.6) [157]. Primary SAECs exhibited decreased viability 72 h post exposure, while low-dose MWCNTs stimulated BEAS-2B cell proliferation. MWCNTs associated with DNA, centrosomes, and microtubules and were observed within the centrosomal structure. At the lowest dose tested, which approximates a 4-week exposure at the OSHA exposure limit, ~40% of the exposed cells exhibited these abnormal phenotypes. Aneuploidy was typically seen in cells with polyploidy, suggesting cytokinesis failure. Primary SAECs exhibited a strong colony-formation ability that was inverse dose-dependent. These worrisome results suggest that those surviving primary cells with genetic damage can expand. Secondly, aneuploidy and centrosome disruption are classically associated with tumor stage [158].

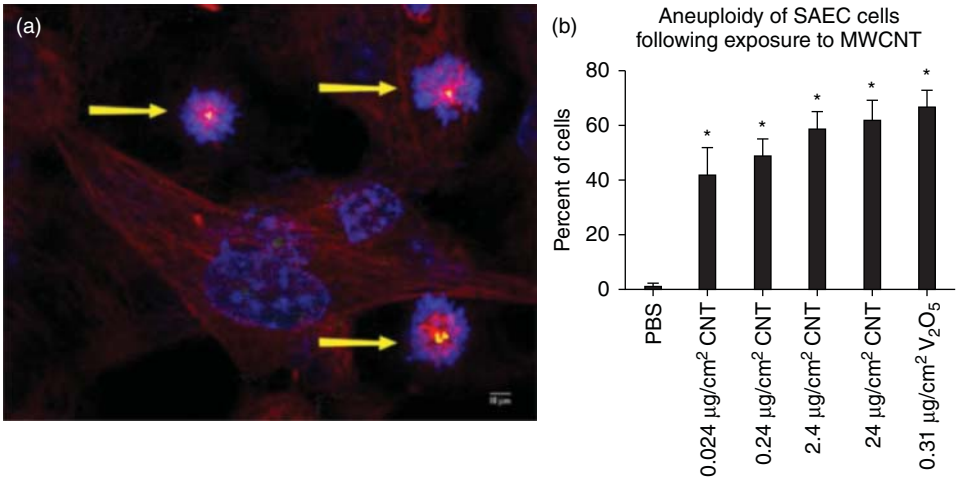

Figure 10.6 Mitotic disruption in MWCNT-exposed human small airway epithelial cells. (a) Monopolar mitotic spindles (yellow arrows) contribute to (b) chromosomal aneuploidy. (Reprinted with permission from [157]. ©2014 Particle and Fibre Toxicology.)

Clearly, CNTs of different physicochemical properties represent a genotoxic hazard to exposed pulmonary tissue. Although hazard clearly exists, very few studies have systematically evaluated specific physicochemical properties and their dose–response that is useful for risk assessment. Most recently, Jackson *et al.* [159] conducted a systematic *in vitro* evaluation of 15 different MWCNTs with different physicochemical properties including diameter, length, and surface functionalization. Although mass doses were high, mouse lung epithelial cells exhibited weak single strand breaks in the comet assay along with ROS and reduced cell proliferation. MWCNTs with large diameter appeared to show greater ability to induce single strand breaks. Studies like this highlight not only how useful systematic studies are but also how important using multiple genotoxicity assays for both direct and indirect genotoxicity can be. In addition, since a majority of *in vitro* and *in vivo* animal studies report positive genotoxic responses, both models should be used in tiered approaches to screen and assess CNT genotoxicity [e.g., 7, p. 159].

In vitro cell transformation studies have long been utilized to quickly screen and assess xenobiotics for genotoxicity and neoplastic transformation potential. Morphological transformation assays with these models are acknowledged as alternative, comparative models to the 2-year *in vivo* carcinogenesis assay [161, 162]. Although simplistic in nature, they possess merit in identifying the underlying molecular and cell mechanisms involved with early steps during carcinogenesis. These studies typically attempt to characterize several cancer hallmarks during promotion, including proliferation, apoptosis/anoikis evasion, anchorage-independent growth, migration, invasion, angiogenesis, and CSCs. The use of neoplastic cell transformation models, coupled with other analysis

platforms, has helped unlock the potential early stage mechanisms associated with tumorigenesis.

Using the Balb/3T3 cell model, Ponti *et al.* [163] evaluated nude and functionalized (–COOH, –OH and $–NH_2$) MWCNTs for cytotoxicity, genotoxicity, and carcinogenesis potential. All MWCNTs possessed short lengths (<1.5 μm) and equal diameters (9.5 nm), which resulted in no observable cyto- or genotoxicity. Surprisingly, they all exhibited increased morphological transformation comparable to asbestos-exposed cells.

Although murine cell line assays are a useful screening tool for morphological transformation, they may harbor inherent differences in behavior compared to human cells in similar tissues. Using human cell lines for morphological and neoplastic transformation coupled with recent technological advances in evaluating genomic signatures and 3D models holds promise for future screening approaches for ENM- and other xenobiotic-associated carcinogenesis. For example, Wang *et al.* [164] found that subchronic, dispersed SWCNT exposure at an occupationally relevant dose ($0.02\,\mu g\,cm^{-2}$) caused malignant transformation, as evidenced by several cancer hallmarks [27] including aggressive proliferation, attachment-independent growth, p53-mediated apoptosis evasion, invasion, angiogenesis, and *in vivo* tumorigenesis in the exposed cells. Decreased p-p53 (Ser15) expression was found to suggest that SWCNTs further destabilize p53 for proteosomal degradation. Similarly, repeated long-term MWCNT exposure to bronchial epithelial cells (BEAS-2B) resulted in oncogenic transformation [165]. Global comparative genomic hybridization identified chromosomal aberration at 2q31–32 near oncogenes HOXD9 and HOXD13, which regulate apoptosis, development, and cell proliferation. Other genes affected are associated with lung cancer, cell cycle, focal adhesion, and MAPK signaling. Conversely, prolonged MWCNT exposure caused increased ROS but had minimal effect on genotoxicity or promotion effect on human lung adenocarcinoma A549 cells [166].

Expansion of these studies [90] performed comparative subchronic HAR fiber exposure ($0.02\,\mu g\,cm^{-2}$) to assess neoplastic transformation potential in human small airway epithelial cells. hTERT-immortalized SAEC cells with known loss of p16 expression after numerous continuous passages are a reasonable model since both asbestos- and CNT-induced mesotheliomas exhibit loss of CDKN2A/2B [136, 167]. After 6 months of exposure, both SWCNTs and MWCNTs caused increased proliferation, soft agar colony formation, migration, invasion, and angiogenesis above UFCB-exposed, asbestos-exposed, and unexposed control cells. Transcriptome profiling found that both SWCNTs and MWCNTs exhibited similar yet unique genome signatures characterized by proliferation, movement, cell death, and development signaling. Cancer-associated signaling was centered on overexpressed MYC, PPARG, COL18A1, PDGFRB, and CASP8. Asbestos-exposed cells, however, displayed a very different and distinct pro-inflammatory transcriptome signature centered on IL-1B, CCL2, and SPI1. Similar to the previous SWCNT-transformed BEAS-2B cells, loss of p-p53 (Ser15) expression was most prevalent in CNT-exposed cells, suggesting that p53 degradation may be a common mechanism in early stage CNT-associated tumorigenesis.

At present, the same group's preliminary analyses to identify CNT-specific *in vitro* gene markers to predict early disease effects *in vivo* [168] have been successful in identifying several genes associated with altered lipid metabolism following MWCNT exposure *in vitro* compared to genomic profiling data in MWCNT-exposed mouse lung [106, 122].

Establishing CNT-transformed cell models with neoplastic or malignant transformation phenotypes, coupled with whole transcriptome signature analysis, has allowed mechanistic studies to evaluate potential carcinogenic modes of action. Results of these studies have identified known signaling pathways and genes that exist in lung cancer, thus suggesting the usefulness of such studies to not only screen ENMs but also potentially use them for early disease biomarker identification. Transcriptome microarray analysis of the SWCNT-transformed BEAS-2B cells identified potential mechanisms for FLIP-mediated apoptosis resistance [169] and oncogenesis including the pAkt/p53/Bcl-2 signaling axis, Ras family cell cycle control, Dsh-mediated Notch1, and downregulated BAX and Noxa [121]. Further studies have identified the role of caveolin-1-mediated CSC induction by CNTs [120, 170]. Side population characterization in SWCNT-transformed bronchial epithelial cells identified CSC-like cells positive for Nanog, SOX2, SOX17, CD24 low/CD133 high, and E-cadherin surface markers. These p53-deficient CSCs possessed self-renewal properties, aggressive cancer behaviors, and *in vivo* tumorigenesis. Furthermore, CSCs were also found in the SWCNT-transformed small airway epithelial cells, suggesting that SWCNT induction of CSCs may be a widespread phenomenon in exposed lung epithelial tissue and that SV40 status does not dictate CSC formation.

Since well-dispersed MWCNT aspiration and inhalation exposure can result in extra-pulmonary translocation and pleural mesothelial exposure [19], similar subchronic neoplastic transformation studies on human mesothelial cells were performed by our group. Continuous subchronic exposure to both SWCNT (HipCo) and MWCNT (Mitsui #7) for 4 months to MET5A cells resulted in neoplastic transformation characterized by enhanced proliferation, cell mobility, and aggressive invasion phenotype [171]. Both sets of CNT-exposed cells exhibited greater cell movement and invasion ability than asbestos-exposed cells. Mechanistic studies, coupled with whole transcriptome profiles, identified distinct CNT invasion signaling pathways which differed substantially from those of asbestos. MMP2 overexpression was important to all three HAR fibers, while PLAU, STAT3, AKT, and VEGFA were specific for CNT-exposed cells. A follow-up dose–response study with SWCNT-exposed mesothelial cells (MET5A and LP-9) identified activated HRAS/ERK, which contributed to cell invasion ability and cortactin overexpression [172].

10.2.4
Fullerenes and Derivatives

Fullerenes (C_{60} or C_{70}) and their water-soluble derivatives (e.g., fullerol) have attracted much attention due to their relatively small size, high surface

area/volume ratio, radical binding capacity, multiple functionalizations, and water solubility [173–175]. Their large diversity mainly rests on the ability to functionalize and/or use solvents to increase hydrophilicity, aqueous dispersion, and manipulation. For example, several manipulative strategies exist to surface-functionalize C60 into water-soluble derivatives, including $C_{60}(OH)_{18}$ and $C_{60}(OH)_{24}$. The sum of all possible forms of fullerenes results in a wide array of potentially benign or toxic behaviors that are not completely understood. Dispersion in air with the resulting inhalation exposure is, at present, restricted to manufacturing and industrial uses of fullerenes and fullerols. At the consumer level, dermal exposure is widely expected as a result of fullerene's presence in a wide variety of cosmetics. Known or expected fullerene exposure levels in an occupational or environmental setting are relatively small compared to other carbon ENMs (e.g., UFCB and CNTs). Exposures during manufacturing range from 36 to 150 $\mu g\,m^{-3}$ for $PM_{2.5}$ while fullerene-specific doses range from 0.0004 to 2 $\mu g\,m^{-3}$ [174, 176].

Similar to other pristine carbon ENMs, as expected, fullerene exhibits ROS scavenging and generation activities [177–180]. Fullerene can exist either as a quencher or as a generator of oxygen radicals. The antioxidant property of fullerene has been aggressively pursued, especially within biomedical applications for disease treatment [reviewed by Johnson *et al*. 4]. Highly dispersed fullerene derivatives and fullerol show enhanced, dose-dependent radical sequestration ability following exposure to known pro-oxidant xenobiotics or therapeutic agents. Photosensitization of C60 generates excited electrons, resulting in singlet or superoxide radicals [179]. Water-soluble fullerenes primarily act as antioxidants partially due to their dispersibility and the resulting high surface area [177]. Anionic, water-soluble fullerenes sequester more superoxide than cationic or pristine fullerenes [178]. In general, both *in vitro* and *in vivo* studies suggest that differences in chemical structure, surface functionalization, dispersion technique, residual solvents, and target cell/tissue all impact the toxicity of fullerene and its derivatives. Toxicity is largely associated with oxidation of sensitive targets, which would dictate an inflammatory and potential genotoxic response.

10.2.4.1 *In Vivo* Studies

Several studies with different pulmonary exposure methods for varying lengths of time reported minimal inflammation response. Both fullerene and fullerol were not toxic in rat lung at 3 months post i.t. exposure [181]. Baker *et al.* [182] reported that nanometer- and micrometer-sized fullerenes caused no significant response following inhalation exposure, with no detection of particles in blood stream, suggesting no or limited translocation out of the lung. No significant inflammation or lung damage was observed during a 4-week inhalation exposure or at 3 months post exposure. A microarray study reported minor inflammation, oxidative stress, and apoptosis response following a 4-week whole-body inhalation in rats [183]. A comparison of i.t. versus inhalation exposure to fullerene in Wistar rats showed no significant induction of neutrophilic inflammation [184]. Conversely, Park *et al.* [185] reported a dose-dependent increase in several

pro-inflammatory cytokines (e.g., IL-1, IL-6, and TNF-α) and minimal cell infiltrate in stained lung tissue sections from 7 to 28 days post i.t. exposure to water-soluble fullerene in ICR male mice. The positive inflammatory response in this study compared to the Sayes *et al.* [181] study may be due to the use of toluene versus tetrahydrofuran dispersant, smaller diameter of the primary particle, and different *in vivo* models. A high dose of fullerol caused an inflammatory response dominated by neutrophils and macrophages. The same study reported that lower doses of fullerol helped in reducing ROS elicited by quartz dust exposure [186]. This finding supports both acellular and *in vitro* studies showing that water-soluble fullerene derivatives quench ROS and raises the possibility that expected low-dose exposures may guard against ROS *in vivo*. Higher doses of well-dispersed particles may break a threshold and elicit an inflammatory response. Jiao *et al.* [187] reported that two different types of functionalized, water-soluble fullerenes provided ROS scavenging ability and reduced lipid peroxidation when exposed to mice with established lung carcinomas. The NTP study found histiocytic infiltration, a shift in inflammatory leukocyte populations, and moderate increases in MCP-1 and IL-1B in both the Wistar rat and B6C3F1 mouse models following a 90-day inhalation fullerene exposure [188, 189].

Fullerene fate studies showed that deposition within the mammalian body following either oral or i.p. injection occurs primarily in the liver, spleen, and lung [190, 191]. It is metabolized or excreted rapidly [190, 192] and might be transported via circulation. Pulmonary exposure studies report relatively short half-lives (26–29 days), BALF macrophages with particles, and little evidence of deep penetration, suggesting adequate clearance for fullerene-exposed lungs [176, 182].

Based on the limited number of published studies, little evidence exists for *in vivo* mammalian genotoxicity. Shinohara *et al.* [176] found little evidence of bone marrow clastogenicity of C_{60} fullerenes in ICR mice following oral exposure. Fullerene was observed to increase 8-oxodG in a gastric exposure to Fischer rats [193]. Increased comet tails and mutation frequencies were reported in gtp transgenic mice in an i.t. exposure at 200 μg per mouse but not at 50 μg per mouse [194]. Single and repeated i.t instillation to male rat lungs resulted in an inflammatory response at 24 h, but no observable DNA damage was found in the comet assay in the collected lung cells [195] which coincided with positive inflammation and no DNA damage response [196]. The positive effect in the Totsuka study could potentially be explained as a generalized response to extremely high levels of particles in the exposed tissue. Although no evidence appeared in the exposed lung tissue, the 90-day NTP inhalation study found significant increases in micronuclei in peripheral blood samples at all tested doses in female B6C3F1 mice, while males experienced no effect [189].

At present, only three published studies have evaluated *in vivo* tumorigenesis. Fullerenes are more probably an anti-carcinogen than a pro-carcinogen, based largely on its radical sequestration properties and bioaccumulation potential in tumor tissue [reviewed by Aschberger *et al*. 174]. Intraperitoneal injection of fullerenes into heterozygous p53 (+/−) mice resulted in minimal adverse tissue

morphology (serosal plaques) with no tumor formation [133]. Liu *et al.* [197] reported that fullerol ($C_{60}(OH_{20})$) exposure reduced Lewis lung carcinoma *in vivo*, possibly due to increased TNF-α levels and elevated T-cell counts that enhanced the ability to eliminate abnormal cells. Conversely, Zogovic *et al.* [198] reported that *in vivo* fullerene exposure to melanoma xenograft tumors promoted tumor growth, while *in vitro* exposure reduced melanoma cell viability. An NTP study has been conducted, but no summary of the results has been reported. At present, no published *in vitro* cell transformation study has been conducted on fullerenes.

10.2.4.2 *In Vitro* Studies

Compared to other carbon ENMs, a decent knowledge base for screening fullerene's *in vitro* genotoxicity exists, most probably due to its perceived small size and wide use in biomedical and cosmetic applications. In general, fullerenes and derivatives show a limited ability to induce genotoxicity compared to other carbon ENMs [174, 196]. If genotoxicity is detected, it usually coincides with ROS-mediated effects associated with photosensitization. Evidence for genotoxicity is given by chromosomal damage, DNA strand breaks, and mutagenicity in multiple human and mouse cell lines. For example, Wang *et al.* [199] found that cyclodextrin-bicapped C60 cleaved DNA under light in presence of NADH. Zhao *et al.* [200] found similar phototoxicity with increased superoxide generation following cyclodextrin-capped pristine and water-soluble fullerene exposure. Studies using the Ames test reported mutagenicity, 8-OHdG adducts, and ROS generation, which correlated with the intensity and duration of light exposure to C_{60} and derivatives [201, 202]. Use of antioxidants reduced genotoxicity in these studies, suggesting indirect genotoxicity via ROS damage. Conversely, no mutagenesis occurred in mouse lung epithelial cells or CHO cells exposed to fullerenol [203]. Rather, fullerenol reduced the micronucleus frequency in these cells. Fullerene at $100\,\mu g\,ml^{-1}$ caused some short-term damage observed in sensitive sites and increased oxidized purines in the comet assay in exposed mouse lung epithelial cells [196], similar to the SWCNT effect.

Although a handful of studies suggest moderate to low genotoxicity, recent studies report on the contrary showing low dose effects. C_{60} exposure to A549 cells caused increased micronuclei at $0.02-200\,\mu g\,ml^{-1}$ [194]. Dose-dependent ONOO production correlated with increased deletion mutations in primary mouse fibroblast cells [204]. Dhawan *et al.* [205] reported that both aqueous and ethanol colloidal fullerenes exhibited genotoxicity in comet assay in exposed human lymphocytes as low as $2\,ng\,ml^{-1}$, most likely due to increased ROS. The authors do acknowledge that the dispersion method has a large impact on the observed genotoxicity. One study reported that chronic exposure at extremely low concentrations ($1-10\,pg\,ml^{-1}$) of water-soluble fullerene elicited a positive micronucleus result along with increased cell proliferation in both normal embryonic kidney and HeLa tumor cells [206]. These low concentrations suggest an ROS-independent mechanism.

In vitro toxicity assessment of fullerenes, water-soluble derivatives, and fullerols have primarily focused on evaluating pulmonary, dermal, macrophage, and hepatic cell responses. Improved hydrophilicity of water-soluble fullerene derivatives, compared to fullerene, appears to reduce the aggregate size, reduce attraction to and interactions with lipid membranes, and reduce cell uptake, thereby reducing cytotoxicity. Improved dispersibility for a material that quenches oxygen radicals can further reduce particle toxicity. For example, a novel β-alanine C_{60} derivative was protective against hydrogen peroxide-induced cell damage [180]. Aggregated pristine fullerene, nanoC_{60}, was more cytotoxic to human fibroblasts and liver carcinoma cells than fullerene derivatives because of superoxide production resulting in lipid peroxidation and cell membrane damage [207]. A follow-up study found that nanoC_{60} elicited ROS-mediated cytotoxicity, lipid peroxidation, and membrane damage responses in several cell lines, with LC_{50} ranging from 2 to 50 ppb [208]. Unlike hydroxylation modification of the fullerene surface, amino acid-functionalized fullerene exposure caused increased production of pro-inflammatory mediators at moderate to high doses in epidermal keratinocytes ($>40\,\mu g\,ml^{-1}$) [209]. Light exposure to some fullerenes causes phototoxicity through the release of singlet oxygen and superoxide [200]. This would suggest potential ROS damage to keratinocytes if workers were exposed. Similarly, exposure to both photosensitized fullerene and $C_{60}(OH)_{18}$ caused ROS and lipid oxidation damage in rat liver microsomes [210]. Interestingly, fullerene toxicity was due to singlet oxygen release, while that of $C_{60}(OH)_{18}$ was due to several radical species resulting in a wider array or lipid and protein oxidation. Conversely, fullerol exposure elicited little response in macrophages (RAW 264.7), but evidence of mitochondrial perturbation via Ca^{2+} ion release was identified [211].

In summary, compared to other ENMs, acute and subchronic fullerene family data suggest low risk for direct genotoxicity or indirect genotoxicity via oxidative stress. The *in vitro* and *in vivo* genotoxicity data, however, are limited. Further research efforts should focus on relevant fullerene and fullerol exposure concentrations, *in vivo* toxicokinetics and translocation, primary and secondary genotoxicity in *in vitro* and animal models, and subchronic and chronic exposure to identified target tissues.

10.2.5
Graphene and Graphene Oxide

The graphene nanomaterial family (GNF; [212]) is expected to experience large-volume and widespread use in nanotechnology fields including medicine, drug delivery, cells, supercapacitors, batteries, and sensors [212–214]. GNF is characterized by graphene sheets, with potentially high surface area, comprised of different lateral widths, edge morphology, number of graphene layers, stiffness, surface functionalization due to oxidation/reduction preparations [pristine vs graphene oxide (GO) vs reduced graphene oxide (rGO)], compact platelets, and well-dispersed graphene sheets. Thermal exfoliation during graphene production

results in dry powders that are respirable, which indicates lung tissue as a primary GNF toxicological target. Surprisingly, little evidence exists in evaluating the GNF for potential genotoxicity and subsequent tumor-associated pathologies when compared to similar nano-sized graphene NMs (i.e., carbon nanotubes) or other weak carcinogenic nano-sized carbon (i.e., carbon black). Similar to CNTs, limited studies suggest that graphene size, surface functionalization, and dispersibility appear to dictate toxicological response. GO, rGO, and organic-coated graphene have received increased attention due to their excellent dispersibility in aqueous solutions for technological manipulation, but they also have shown increased toxicity compared to their pristine counterparts. Several recent detailed reviews on GNF highlight the large nanotechnology potential of these materials, including the biological benefits and consequences of GNF exposure [212, 214–218].

At present, published data indicate that the high surface area, sorption, and catalytic ability of GNF particle surfaces provide dramatic ROS generation or quenching capacity. These qualities are comparable to those of SWCNTs, minus the HAR morphology. At present, it is not clear whether ROS in exposed tissues generated directly from the GFN particle surface or indirectly from cellular sources (e.g., leukocyte inflammation, mitochondria) is a greater risk for DNA oxidative damage. Stacking of monolayer graphene into multilayered graphene (e.g., graphene nanoplatelets) greatly reduces the surface area and alters sheet rigidity/morphology and the potential for altering oxidative/reduction reactions [212, 216]. The bonding between and number of layers in graphene NPs is rarely measured, even though it is thought to directly impact biological effects. Packing of sheets greatly reduces the surface area and should be assessed during characterization since it may lead to conflicting results [212]. Many publications evaluating MWCNTs repeatedly acknowledge that surface area and rigidity, due to the number of graphene layers, has a dramatic impact on particle morphology and toxicity response in exposed tissues. For example, a graphene NP with a fluid shape may experience passive diffusion in cytoplasm, endocytosis, or phagocytosis, while a particle with similar size but rigid morphology may elicit frustrated phagocytosis, inflammation, and ROS generation via recruited leukocytes. Their size ranges from $<10\,\text{nm}$ to $>20\,\mu\text{m}$ in lateral width, which clearly impact the uptake, endosome and lysosome receptor binding, and the potential for frustrated phagocytosis [212]. A few studies suggest the potential for some small-sized graphene with planar morphology to directly interact with DNA. Graphene may bind to single-stranded DNA, during replication or transcription, which could cause DNA damage and failure of genetic inheritance and block specific protein synthesis. It has also been suggested that planar graphene may intercalate into the DNA helix, similar to aromatic compounds [219]. Clearly, systematic studies evaluating the impact of several physicochemical properties on GNF particle toxicokinetics during exposure and in biological tissue, fate, uptake route, direct and indirect genotoxicity, and subchronic effects are warranted.

10.2.5.1

***In Vivo* Studies**

Graphene exposure studies on *in vivo* models have typically used either i.v. injection or i.t. instillation to evaluate GNF particles' fate as well as whole-body or tissue level responses. Most studies report an enhanced inflammation response with little long-term effects, although GNF particles are biopersistent and can exhibit systemic fate. An important study by Duch *et al.* [220] evaluated aggregated graphene, dispersed graphene, and GO following i.t. exposure of 50 μg per mouse. Of note, GO particles displayed uniform, very thin sheets (1 nm thick) while Pluronic-dispersed pristine graphene displayed higher variability in thickness with a mean of ~2.5 nm. GO containing hydroxyl and carbonyl surface groups produced robust and prolonged inflammation with macrophage and neutrophil infiltration followed by severe lung tissue damage. Surprisingly, less GO was found inside phagocytic vesicles than graphene. Enhanced plasma thrombin was specific to GO-exposed mice. GO exposure elevated mitochondrial respiration by lending electrons to the electron transport chain, which enhanced ROS generation. This suggests that ROS generation may partially drive the activation of inflammatory and apoptotic signaling. Conversely, aggregated graphene showed reduced effect, while synthetically dispersed (Pluronic) graphene showed a mild inflammatory response. Interestingly, only GO caused a significant increase in TUNEL positive nuclei *in vivo* and DNA fragmentation in alveolar macrophage exposure experiments *in vitro*. Minimal fibrosis occurred in all three particle exposures compared to control. Intravenous injection of GO into to the tail vein of mice caused significant impacts to lung tissue at 7 and 30 days post exposure [221]. Lung, liver, and spleen were the primary targets of injected GO. GO was found in the lung closely associated with neutrophil and foamy macrophage infiltrates. At 30 days, granulomas containing GO were observed along with interstitial inflammation and thickening of alveolar septa.

Other studies support the idea that well-dispersed pristine graphene causes acute inflammation but with minimal long-term health impacts. A unique inhalation exposure screening study of numerous carbon nanomaterials [222] compared graphene sheets, graphene nanoplatelets, MWCNTs, and carbon black for their *in vivo* cytotoxicity and inflammation response in Wistar rats. Graphene sheets exhibited toxic effects at the highest dose (10 mg m^{-3}), while nanoplatelets and carbon black exhibited little to no toxic response. These responses palled in comparison to MWCNTs', which exhibited responses at ≥0.5 mg m^{-3}.

Graphene nanoplatelets (>5 μm diameter, 1–10 graphene layers) were respirable up to 25 μm diameter in C57Bl6 mice and elicited a robust inflammatory response in the lung (aspiration) and pleural space (i.p. injection) after 1 and 7 days compared to Printex 90 carbon black [223]. Induction of several cytokines (IL-1β, MCP-1, IL-8) and ROS via NADPH oxidase, consistent with NALP3 inflammasome activation, was noted in *in vivo* lung and *in vitro* THP-1 exposures. Frustrated phagocytosis and granulomatous lesions, similar to those reported for different CNTs [106, 125] were also found. Nanoplatelets were found in chest wall pleural tissue with wall thickening at 1 week post injection

and exhibited slower clearance than carbon black via mediastinal lymph nodes. A follow-up report at 6 weeks post aspiration indicated minimal inflammation and oxidative degradation of graphene nanoplatelets in mouse lung tissue [224]. In contrast to CNT exposure, minimal fibrosis or hyperplasia was observed along with no inflammation in the pleural space.

As a follow-up study to the Schinwald studies, a 5-day inhalation exposure to 0.018 and 0.102 mg lung burden using 550-nm-wide stacked graphene platelets found little evidence for lung tissue damage at 28 days post exposure, including no LDH or protein release, with a robust alveolar macrophage phagocytotic response [225]. Interestingly, changes in hemocytometry and blood chemistry were observed in the high-dose group. Only slight alveolar wall thickening was observed. Similar to Schinwald, the authors suspected that the minimal toxicological effect was due to the large width, stacked platelet shape, and low surface area. Expansion of these studies using graphene with different physicochemical properties would greatly assist in identifying property-associated lung disease risk.

Little to no evidence exists in evaluating GNF's *in vivo* genotoxicity following expected exposure scenarios. Based on available *in vitro* data, computational modeling, and *in vivo* data, several potential factors may contribute to GNF's genotoxic potential in exposed tissues. Graphene with small lateral diameter shows the ability to penetrate plasma membrane, are present in cytoplasm, accumulate near nucleus, and minimally penetrate the nucleus. Given their planar morphology, direct interaction with DNA by either direct binding or intercalation in exposed epithelial or fibroblast cells should be evaluated. Large planar graphene is not expected to penetrate deep into tissues but may illicit indirect genotoxicity via ROS generation and oxidative DNA damage.

Although not as reactive in tissue as CNTs, several major lines of evidence support the potential weak carcinogenicity of GNF particles. First, carbon black, a Group 2 carcinogen, possesses similar makeup and *in vivo* fate as GNF particles [222, 224]. Second, given that graphene is more acutely reactive in exposed lung tissue [223], indirect oxidative DNA damage in lung tissue following inflammation over repeated exposure is expected. Recovery periods after a single bolus and several days' inhalation suggest transient inflammation with little fibrosis promotion. Building on this report showing acute inflammation in mouse lungs after 1 day, Schinwald *et al.* [224] reported that pristine GPs showed minimal inflammation in mouse lungs after 6 weeks, even though there was no degradation of GP in lung tissue. It remains to be tested how a prolonged, repeated exposure to GNF particle (i.e., occupational setting) affects the risk for oxidative DNA damage and initiation. GNF particles repeatedly show long biopersistence in exposed tissues, either via i.v. injection or inhalation. At present, it is unclear what types of GNF particles have the potential to either move out of the exposed lung or potentially promote tumorigenesis by stimulating pro-proliferation and other cellular signaling pathways. Interestingly, graphene i.v. injected in the tail vein accumulated in lung tissue [221]. Lastly, use of GNF in biomedical applications involving implants, grafts, and scaffolds may elicit a foreign-body tumor response [212]. These sarcomas

are typically reported following contact with biopersistent materials, regardless of composition, that possess large surface area and smooth surfaces [226] used as implants or grafts. Several types of graphene NMs possess these morphological and surface characteristics [213]. Although not initially identified, inflammatory response followed by ROS and oxidative damage to DNA may be important drivers of tumor progression in foreign-body tumors [227]. It is also may rely on direct contact of preneoplastic cells in contact with a smooth surface and a drop in cell–cell communication, resulting in uncontrolled cell growth [228]. Of interest, a recent study reported the potential involvement of mesenchymal stem cells (MSCs) in foreign-body tumorigenesis [229]. Foreign-body sarcomas usually comprise dense collagen fiber with fibroblast cellular morphology [230] and exhibit late onset [228]. MSCs and MSC-derived cells (i.e., myofibroblasts) currently constitute an intensive area of research as key regulators of interstitial pulmonary fibrotic remodeling [231, 232]. Given that CNT exposure induces stem-like cells, with known MSC markers [233], leading to fibrotic nodules [234], it raises the possibility of a role of MSCs in potential foreign-body tumorigenesis following biopersistent graphene exposure. Clearly, these issues should be addressed in systematic *in vivo* exposure studies using appropriate ROS, biopersistence, and genotoxicity assessment procedures.

10.2.5.2 *In Vitro* Studies

Based on limited *in vitro* data, GNF exposure to established *in vitro* cell models can result in plasma membrane penetration, endocytosis, ROS release or sequestration, and cytotoxicity. Most adverse responses, including apoptosis and cytotoxicity, are reported at high doses. To date, it appears that lateral width and surface functionalization largely dictate both cellular fate and toxic response. Other physicochemical factors that may dictate adverse response include layer number, size, stiffness, and hydrophobicity [212]. Zhang *et al.* [235] compared several-layered graphene to SWCNTs to assess the effect of graphene's shape on cytotoxicity in neuronal cells. Graphene was more potent at reducing metabolic activity at low concentration (0.1 $\mu g\,ml^{-1}$), while SWCNTs produced significantly more LDH and metabolic disruption at higher doses (>1 $\mu g\,ml^{-1}$). ROS generation coincided with caspase 3 activation and apoptosis ($\geq$10 μg GO per milliliter). Exposure of pristine graphene to RAW 264.7 macrophages elicited decreased mitochondrial membrane potential, increased ROS, TGF-β release, and intrinsic Bcl-2-mediated apoptosis pathway activation [236].

Recent computational modeling studies evaluated the impact of graphene sheet size and morphology on cell membrane phospholipid dynamics and potential cytotoxicity. Using bacterial membrane as a model, Tu *et al.* [237] reported that graphene and GO sheet edge can pierce plasma membranes. Sheets also retained the ability to extract phospholipids from the membrane, modify membrane polarization, and enhance cell leakiness. The authors suspect that disruption of the plasma membrane could alter membrane-bound receptor function, resulting in activation of apoptosis. Computational models suggest that size has

an impact on graphene's fate in the cell. Small sheets penetrate cell membranes, medium-sized sheets pierce membrane at certain orientations, and large sheets get absorbed in the membrane [238].

Pristine graphene and GO exhibit greater toxicity to cell models than GNF particles that possess organic coatings or organic polymers. Chang *et al.* [239] evaluated three different size preparations of GO (160–780 nm wide) for uptake, intracellular fate, and ROS generation ability in an alveolar epithelial cell model (A549). GO was not found inside cells, but ROS following exposure did increase due to generation on the GO surface in a cell-free culture medium. Wang *et al.* [221] reported a time-dependent increase in the uptake of GO into lysosomes, mitochondria, and endoplasm of human fibroblasts, albeit at high doses ($>20\,\mu g\,ml^{-1}$). Later time points found GO accumulating around nuclear membrane, with occasional particles inside the nucleus. Another study found that single-layered GO exhibited greater ability than SWCNTs to cause increased cell membrane damage and induction of autophagy, but failure of the autolysosome, resulting in cell death of exposed mouse peritoneal macrophages [240]. A recent report showed that GO triggered an early onset of DNA melting *in vitro* [241].

Hinzmann *et al.* [242] compared pristine GO, rGO, and unaltered GO with graphite and ultra-dispersed detonation diamond in glioblastoma multiforme cells at $50\,\mu g\,ml^{-1}$. Although conducted in a cancer cell line, pristine and reduced GO led to high cytotoxicity compared to other particles. Interestingly, particles showing both high (pristine, rGO) and low cytotoxicity (graphite and ultra-dispersed detonation diamonds) induced DNA damage as seen by positive comet assay. Carboxyl-functionalized graphene improved hydrophilicity, enhanced cell uptake, and reduced cytotoxicity compared to unfunctionalized, hydrophobic graphene [243]. Wang *et al.* [244] examined the effect of different surface charges on GO to cause oxidative stress in lung fibroblast cells. Three types of surface-modified GO were compared to the parent material. Following exposure, ROS in the exposed cells was linked to cytotoxicity. PEG coating was more protective to fibroblasts than PEI coating or unmodified GO. The authors argue that differences in surface charge impacts agglomeration, interaction with plasma membrane, and uptake into cells. Although never assessed in the study, the findings raise the idea that surface coating of GNF may protect cells against ROS-induced oxidative damage to DNA. Similarly, Hu *et al.* [245] reported that the amount of serum in cell culture medium can reduce and minimize GO toxicity as a result of the formation of a thick protein corona.

Next, an interesting, if alarming study of rGO nanoplatelets raises the idea that small nanosized GNF particles at low doses can cause genotoxicity compared to their larger counterparts. Akhavan *et al.* [8] exposed four different sizes (11–3800 nm) of rGO nanoplatelets to human MSCs. The 11-nm rGO nanoplatelets exhibited cytotoxicity as low as $1\,\mu g\,ml^{-1}$, while larger sized platelets showed reduced toxicity. Similarly, the 11-nm platelets caused DNA fragmentation (comet assay) and chromosome aberrations in metaphase assay as low as $0.1\,\mu g\,ml^{-1}$ following a 1-h exposure. Of note, RNA efflux, a marker

for cell membrane damage, was negative across all particles and doses. Although the authors never directly assessed the intracellular location of the nanoplatelets, the study suggests that rGO nanoplatelets are capable of penetrating cell membranes to initiate genotoxicity at low doses while ROS generation may impart indirect oxidative damage at higher doses. Lastly, a comprehensive systems toxicology evaluation of GO versus rGO was conducted to evaluate the impact of hydrophobicity on biological interactions in HepG2 cells [246]. Although both graphene particles displayed similar toxicity endpoints (oxidative stress, DNA damage, and cell death), an omics evaluation along with particle fate analysis identified completely different mechanisms of action. Hydrophilic GO experienced cell uptake, ROS generation via NADPH oxidase, and deregulation of DNA repair and oxidative stress response genes. Signaling analysis revealed TGF-β as a key mediator of toxicological response. rGO, however, got adsorbed to the plasma membrane, thereby generating ROS via direct interactions, activating viral and innate immune response via the Toll-like receptor 4–NF-κB pathway.

Compared to inflammation- and ROS-focused research, very limited data using *in vitro* models exist concerning those physicochemical properties, toxicokinetics factors, and mechanisms associated with GNF particle genotoxicity. Based on GNF's ability to induce inflammation and ROS in exposed cells, indirect genotoxicity via oxidative DNA damage is a distinct possibility [244]; however, this has not been systematically studied to date. A nanomaterial genotoxicity study comparing numerous nanomaterials identified graphene as having comparable, if not more potent, DNA fragmentation ability than other well-studied materials in isolated fibroblast cells [247]. De Marzi *et al.* [248] compared nano-GO (130 nm) to micrometer-sized (1320 nm) GO for DNA damage via comet assay in lung (A549), intestine (Caco2), and kidney (Vero) cells. Nano-GO was more potent at inducing DNA damage than its micrometer counterpart at 10 $\mu g\,ml^{-1}$. At present, GNF's ability to directly damage DNA and chromosome integrity is virtually unknown. Two recent studies, however, raise this possibility. First, exposure to r-GO nanoplatelets caused DNA fragmentation and chromosomal aberrations in human MSCs (0.1 – 1 $\mu g\,ml^{-1}$) at doses far below that exhibited ROS and cytotoxicity (1 – 100 $\mu g\,ml^{-1}$) [8]. Next, a study investigating GO particle's therapeutic ability as a DNA cleavage agent found that GO sheets with bound Cu^{2+} were able to intercalate DNA, resulting in cleavage via hydrolytic and oxidative mechanisms [219]. Other GO-bound metals (Ni^{2+}, Zn^{2+}, Fe^{3+}) also displayed similar ability. Different metals exhibit different affinities for DNA, with often drastic consequences for gene regulation [249]. Carbon nanomaterials, either through synthesis or through environmental release, can sorb different metal ions. This study raises the possibility of direct DNA damage via GNF particle exposure if the particles are successful in moving through the cytoplasm and into the nucleus, especially during cell division. In summary, the size, surface functionalization, platelet structure, and surface morphology can impact direct or indirect genotoxicity (Figure 10.7), but more research is warranted.

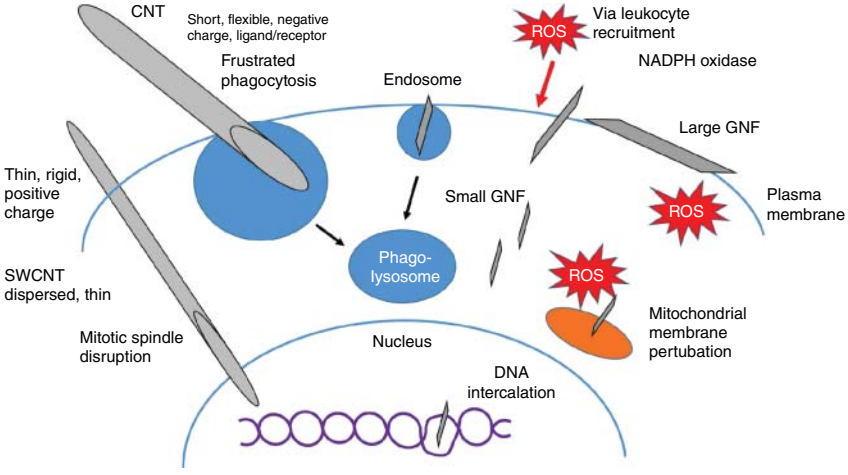

Figure 10.7 Overview of the physicochemical properties of carbon nanotubes' and graphene nanomaterial family's toxicodynamics and genotoxicity potential in target cells and tissues.

10.2.6
Carbon Nanofibers and Other Particles

Given the wide application of ECNMs in various nanotechnological applications, the types of novel ECNMs are expected to expand. In addition, based on the physicochemical properties already identified as posing significant human and environmental health hazards (e.g., pristine and long CNTs), novel second- and third-generation "safe-by-design" ECNMs are already making their way into production (e.g., biodegradable CNTs and coated CNTs). Screening each material is impossible, but through systematic studies of how their physicochemical properties impact genotoxicity and promotion mechanisms, we can effectively screen and prioritize new ECNMs for further *in vivo* testing. Recent work with CNFs compared to CNTs and asbestos shows that this strategy has merit.

CNFs share similar synthesis routes as well as morphological and chemical characteristics with MWCNTs. Their main difference is the orientation of graphene within the fiber structure. CNFs possess graphene in a cupped or stacked orientation, resulting in diameters of 40–200 nm and lengths similar to those of CNTs [22]. Airborne CNFs are known to occur during manufacturing [22, 250, 251].

10.2.6.1
In Vivo Studies

Murray *et al.* [252] evaluated the inflammatory and fibrotic potential of CNFs compared to SWCNTs and asbestos. Particle agglomeration was found to impact granuloma formation and collagen deposition. Well-dispersed CNF and asbestos

fibers did not induce granulomas, while SWCNT agglomerates displayed granulomatous lesions. CNFs showed similar leukocyte recruitment as well as ROS and inflammatory cytokine release compared to other HAR fibers. For all three particle types, effective surface area and mass dose were better predictors of adverse responses compared to other surface area metrics or particle count.

A 90-day inhalation exposure study was conducted on Showa Denko CNF with 5.8 μm mean length [253]. Rats exposed to 2.5 and 25 mg m^{-3} of the material exhibited similar inflammatory responses to CNTs, while the lower dose (0.54 mg m^{-3}) exhibited minimal effect. No fibrosis was found, although fibers persisted at 3 months post exposure, possibly due to deposited lung burden [22].

A 1-year study in mice [112] comparing CNFs to SWCNT and asbestos fibers found no tumor formation. SWCNT exposure caused significant MN and nuclear protrusions. CNF and asbestos exposure resulted in the strongest inflammation response, while SWCNT had the strongest fibrosis response. Increased frequency of KRAS mutations was seen in both CNF- and SWCNT-exposed mice.

10.2.6.2
In Vitro Studies

A few *in vitro* studies have evaluated CNFs for their neoplastic transformation potential. Darne *et al.* [254] conducted a short-term (7-day) *in vitro* neoplastic transformation assessment with 11 carbon fibers of different length and from different stages of production from polyacrylonitrile synthesis using SHE (Syrian Hamster embryo) cells. Electron paramagnetic resonance (EPR) analysis revealed no ROS formation. Subsequently, no morphological transformation compared to chrysotile asbestos positive control was observed. The authors acknowledged that short exposure duration and the high amount of protein serum (20%) in the culture medium potentially contributed to the observed null effect. Large quantities of protein potentially enlarged the protein corona, masked potential carbon binding sites, and reduced toxicity or other stimulatory effects in the exposed cells. A comparative study of CNFs versus SWCNTs and asbestos fibers [255] found that CNF exposure caused greater cytotoxicity than SWCNTs in V79 fibroblasts, while asbestos fibers showed the greatest response. CNFs produced the strongest genomic damage via DNA strand breaks, aneuploidy, and increased micronucleus frequency compared to other fibers. ROS release from exposed macrophages was strongest in CNF- and asbestos-exposed cells.

10.3
Future Challenges in Carbon Nanomaterial Carcinogenesis Risk Assessment

10.3.1
Exposure Characterization and Fate

Effective risk assessment depends on quantitatively measuring exposure concentrations and evaluating the dose–response in both acute and chronic exposure

scenarios in appropriate physiological model systems. A large volume of research has evaluated ECNMs' toxicity in numerous systems, but comparatively, we currently understand very little about exposure concentrations of ECNMs throughout their life cycle (i.e., cradle to grave). The lack of robust analytical sampling and sensitive quantitative detection technologies has proven a big hurdle to assessing ECNMs in environments with large amounts of natural carbon.

The vast majority of ECNM *in vitro* and *in vivo* toxicity studies are single exposures to achieve a modeled tissue burden. Although these models do provide useful data, they do not reflect physiologically relevant exposures (i.e., chronic low to moderate doses) expected either in the occupational or environmental settings. Inhalation chambers for *in vivo* animal models do exist and tend to show larger toxicological effects than equivalent dosing using traditional single-exposure dosing [101]. They are, however, costly and time consuming and typically reserved for either Tier II or Tier III screening [24].

Likewise, tracking of nonbiodegradable ECNMs in exposed tissues, their toxicokinetics, and ultimate fate over extended periods has proven labor intensive in past studies. Recent examples using stable isotope or fluorescent labeling of ECNMs have improved the ability to track their systemic fates in *in vivo* models and have identified new target tissues that should be assessed for adverse outcomes [e.g., 110].

10.3.2 Dosimetry

Researchers engaged in ECNM toxicity studies should first evaluate and justify their use of the chosen dose or dose range based on physiologically and relevant real-world exposure conditions. Past acute studies on ECNMs to measure their dose–response tended to use unrealistic dose ranges that could not be extrapolated to lower doses, which are 100- to 1000-fold lower. For example, noncytotoxic doses of SWCNTs in a fibroblast *in vitro* model showed enhanced proliferation and collagen deposition, which correlated well with the observed *in vivo* effects at the same deposited mass per lung surface area [256].

Currently, the question of which dose metric to use is controversial, which has resulted in a high volume of research. For ECNMs, elemental carbon mass, particle number, and effective surface area have all been proposed. An ideal dose metric should be measurable during exposure (i.e., airborne particles), during deposition/translocation, and at the site of biological effect [62]. Recently, the most useful studies adequately characterized the deposition of ECNMs since this allowed the calculation of the internal dose at the biological receptor [2, 257]. Understanding the toxicokinetics and how they influence internal dose can greatly assist in characterizing dose–response relationships for genotoxicity (or lack thereof), internal cell target, signaling pathway activation, and effects on promotion and progression in appropriate models.

10.3.3 Model Choice

Review of the literature reveals that *in vitro* cell models first established from cancer tissues (e.g., A549) are routinely used in ENM toxicity studies, primarily due to their rapid and robust growth in the laboratory. Although some information about acute toxicity of ENM exposure to these cells is useful, they serve little purpose in ENM exposure-associated neoplastic transformation or tumorigenesis studies. Some *in vivo* studies report no tumor formation following exposure in murine models that have moderate to high resistance to tumorigenesis. Both IARC and OECD have pre-validated *in vitro* cell transformation and murine tumorigenesis models with historical data to support their use on a wide variety of soluble and insoluble organic and metal xenobiotics [258, 259]. The Balb/3T3 and SHE cell lines are pre-validated models for morphological cell transformation upon exposure to known carcinogens [259, 260]. Although these mouse and hamster cell lines show good correlation with their murine *in vivo* model counterparts, they are not human cells. Thus, appropriate human-derived cell lines with a stable genotype should also be used for genotoxicity and early carcinogenic events (i.e., initiation and promotion) to provide adequate screening ability for numerous ENMs. These human cells must be carefully chosen based on the suspected ECNM exposure route, tissue dose, toxicokinetics, and eventual fate within the body [259]. With the advent, incorporation and mainstream use of genome signature profiling and Next Gen sequencing, cell models should represent a healthy phenotype (statistically) to act as an appropriate reference. As confirmed human exposure cases are reported, these models may become refined. It is important to note, however, that few of these models have been used in ENM neoplastic transformation or *in vivo* initiation/promotion studies. Future efforts should be directed toward evaluating how these established models perform in assessing unknown ENM carcinogenic effect with positive control particles (e.g., asbestos) as a measure of effect.

Great advancements have occurred in *in vitro* cell models, with monoculture cell models being quickly phased out as the primary test system. Co-culture with multiple cell types, advancements in immortalization procedures and new cell models, 3D spheroids, 3D tissue sections, microfluidic organ-on-a-chip, numerous extracellular matrix options, and air–liquid interface (ALI) systems are showing great promise in helping to bridge the gap between *in vitro* and *in vivo* exposure/effect model systems [261, 262]. These models are fairly new and relatively untested in assessing carcinogenesis-associated effects. Recent studies have highlighted that multicellular *in vitro* systems are better predictors of *in vivo* effects than a monoculture alone [263] and hold great promise in the near future. Careful design of these multicellular systems, however, needs to be effected to mimic physiological response. For example, several 3D or ALI system with A549 cells and other immune or fibroblast cell lines were employed to assess ECNM toxicity with little ROS, inflammation, or cytotoxic effect, possibly due to the cancer cells' ability to tolerate ECNMs [264, 265]. Use of more sensitive,

noncancerous airway epithelial cells, with underlying fibroblasts, would greatly add value to 3D culture and act as a bridge model between *in vitro* and *in vivo* studies. Future applications of these "bridge models" may have a distinct advantage in that they could be used to (i) predict the *in vivo* effect, (ii) study toxicokinetics in an appropriate 4D system, (iii) isolate and study specific cells via flow cytometry to assist in classifying and characterizing novel mechanisms of tumorigenesis, and (iv) reduce the time and energy needed for *in vivo* models.

10.3.4
Systematic Evaluation of Genotoxicity

Many acute exposure studies, both *in vitro* and *in vivo*, have focused on cytotoxicity and inflammation as major endpoints. The amount of studies focusing on genotoxicity palls in comparison, potentially because of the amount of conflicting results. In order to screen and identify novel ENMs for their carcinogenic potential, a systematic evaluation of numerous ENMs with different physicochemical properties with appropriate exposure models would be necessary, thereby advancing the field dramatically. Pilot studies and examples of such approaches do exist. For example, Watson *et al.* [266] designed a high-throughput comet chip assay to screen numerous ENMs. Development and validation of genotoxicity *in vitro* and *in vivo* assays for ECNMs and other ENMs is currently a major need in the ENM risk assessment framework (see below).

Novel approaches to investigate genotoxicity continue to advance and should be evaluated and potentially implemented into the ECNM toxicity screening framework. Along with the aforementioned high-throughput comet chip assay, genotoxicity studies on single cells, grown in either 2D or 3D formats, can identify and quantify single-cell genotoxicity via DNA fragmentation for use in high-throughput screening of different nanomaterials [248]. This technique could also be used on collected tissues from *in vivo* exposures by labeling a cell with a specific marker of DNA damage and performing single-cell sampling. Single-cell high-throughput polymerase chain reaction (PCR) analysis can further examine the translational impacts of potential DNA damage. Next-generation sequencing may serve as the next high-throughput genotoxicity assay for robust mutation risk assessment. Such strategies, with appropriately designed methods to capture somatic mutations, would capture numerous mutation events, thus potentially removing the use of DNA damage markers and extrapolation from animal models to assess human impact [267].

10.3.5
Role of ROS and Inflammation

Given the long history of transient and/or persistent inflammation and ROS generation following particle exposure, they can be considered strong and robust responses and should not be ignored when evaluating ENMs. Nanomaterials inherently possess high surface-to-volume ratios and particle number per unit mass. Prolonged inflammation and ROS generation can overwhelm DNA repair

mechanisms, leading to inheritance of damaged DNA, genetic instability, and possible promotion of tumorigenesis [268]. In addition, the immune system plays key roles in the promotion and progression of tumorigenesis. With the recent evidence that numerous ENMs (i) elicit DNA damage at doses below known thresholds for induction of inflammation, (ii) possess high reactivity compared to bulk counterparts, and (iii) exhibit potentially different toxicokinetics and fate in exposed tissues than bulk counterparts, future research efforts should evaluate dose–response studies to identify genotoxic, ROS generation, and inflammation thresholds in relation to tumorigenesis thresholds. Systematic studies using several ENMs with different physicochemical properties would provide data for structure/activity models for these three major processes associated with tumorigenesis. These efforts would also evaluate how the immune system responds to (fight or promote) ENM-associated tumorigenesis.

10.4
Assessment of ECNM-Induced Genotoxicity and Carcinogenesis

10.4.1
Recommendations for Screening ENMs for Carcinogenic Potential

1) Characterize, characterize, characterize. A majority of conflicting data in genotoxicity, acute toxicity, and tumorigenesis is largely associated with inadequate physicochemical characterization. Such data is imperative to developing QSAR-like models for ENMs, given the rapid and expansive pace of nanotechnology development.
2) Consider exposure routes and suspected long-term exposure scenario (*dose*). Although somewhat useful as an exploratory, preliminary screen, injections of ENMs into body cavities, usually at high doses, may elicit false positives (e.g., overload) and do not incorporate the toxicokinetics and potential physicochemical changes that an ENM may experience during its uptake and internal distribution routes.
3) Adopt established or fully reported sample preparation and exposure methods.
4) Adequately justify the chosen exposure doses and characterize dosimetry. ENMs behave differently in air, liquid, or tissue. With robust characterization, the ability to model toxicokinetics and eventual internal dose is of utmost importance. Report the mass, surface area, and particle number. Avoid particle overload since this is more likely at lower mass dose due to the particles' high surface areas [269, 200–300 cm^2 in rats]. *In vitro* studies must justify the chosen doses and relate to *in vivo* animal model and expected or known human exposure levels.
5) Evaluate toxicokinetics (i.e., agglomeration, dispersion, and stability) of ENMs both during exposure and once internalized within exposed tissues.
6) Genotoxicity testing should be performed on low-passage, genotypically stable (i.e., p53 status) cell lines that possess low background DNA damage.

Use appropriate nontumorigenic models with either a stable genotype or gene knockdown (p53 +/−) to assess their predisposition for tumorigenesis. *In vitro* cell models from cancers or those sensitive to spontaneous transformation are inappropriate (unless justifiable) for carcinogenesis screening studies.

7) Use two or more genotoxicity tests that cover multiple forms of chromosome/DNA damage.
8) Use multiple particles to assess physicochemical properties, including the source unadulterated or underivatized material to provide structure/activity relationship information.
9) Use literature-established positive control ENMs or ultrafine particles. Well-characterized/studied UFCB, TiO_2, or crystalline silica may serve as a positive control for spherical metal/metal oxide particles. Mitsui #7 MWCNT and/or crocidolite asbestos are excellent choices for fibrous HAR ENMs. This is critical for control banding and tiered assessment approaches.
10) Use multiple doses to identify thresholds (NOEC, LOEC, maximum response); this is required for adequate risk assessment.
11) Use multiple cancer cell phenotype assays at different time points during exposure to characterize the rate of initiation, promotion, and progression of ENM-associated carcinogenesis.
12) Improve upon, assess, and validate multicellular and multidimensional *in vitro* models, CSCs, co-culture, spheroids, 3D tumor microenvironments; refine toxicological strategies; and reduce number of animals used to evaluate long-term health risks. When available, compare and contrast *in vitro* neoplastic transformation with *in vivo* tumorigenesis models. Integration of genotoxicity, cancer cell behavior, and toxicogenomics data from *in vitro* or 3D tissue transformation studies could one day assist in predicting *in vivo* carcinogenesis.
13) Evaluate the effects and mechanisms that support the tumor microenvironment. No ECNM has yet been shown as a complete carcinogen (i.e., initiation, promotion, and progression). A growing body of evidence exists, however, suggesting that carbon ENMs promote or help progress carcinogenesis through either direct interaction with genetically damaged cells (i.e., MWCNTs and UFCB) or indirectly by enhancing the tumor microenvironment (i.e., immunosuppression, extracellular matrix remodeling).
14) Nanotechnology continues to develop at a rapid pace, and carcinogenesis risk research should keep pace with this new development. A small subpopulation of workers is expected to come into contact with raw ECNMs. A majority of ECNM exposures to humans are more likely to occur downstream during ECNM incorporation into composites, product use, and eventual disposal. At present, exposure and toxicological assessment of ECNMs and other ENMs are switching toward life cycle assessment. In addition, second- and third-generation ECNMs continue to enter nanotechnological applications, with improved technology and safe-by-design strategies. Understanding how physicochemical properties of ECNMs

change throughout their life cycle will be imperative to the successful development of safe/prevention-by-design nanotechnologies.

10.4.2 Systematic Screening Paradigm and Workflow for ENM Carcinogenicity Risk Assessment

No documented case of ECNM-exposure-associated tumorigenesis exists. Nevertheless, it is clear that certain physicochemical properties of ECNMs elevate the risks for long-term health impacts and disease, including cancer. Recently, working groups in both the US and EU have proposed strategies to effectively screen ENMs, including ECNMs. Categorization strategies, based on (i) hazard exposure, (ii) ENM's physicochemical properties, and (iii) data from suitable and validated alternative testing strategies (ATS) would aid regulators and industry to prioritize ENMs in qualitative control banding and more quantitative tiered rankings for further costly time- and resource-consuming testing [24, 270–272]. ATS is a proposed approach to perform systematic high-throughput testing on a large number of untested chemicals (e.g., EPA ToxCast) to provide large amounts of data. It relies heavily on numerous *in vitro* assays based on toxicological mechanisms and pathways in an attempt to reduce and refine animal model use. Although the acquired ATS data can be used for understanding ENMs' structure–activity relationships and categorizing the risks, (i) the complexity of *in vivo* systems is lost for assessing both ENM toxicokinetics and dynamics, (ii) time-dependent analysis of disease progression is difficult to perform, (iii) issues exist regarding correct and relevant dosimetry, and (iv) it is necessary to design and implement multifactorial statistical procedures for adequate prediction of *in vivo* response, all of which are major obstacles [24]. Toxicogenomics and *in silico* and systems-biology approaches may allow researchers to overcome these faults. Genome signature profiling has uncovered numerous potentially relevant modes of action for numerous ENMs in both *in vitro* and *in vivo* [90, 145, 273, 274]. Comparative genomic and proteomic studies using multicellular *in vitro* tissue culture with *in vivo* models hold promise as a useful tool in toxicity testing in the near future. Tiered screening approaches using identification of hazard exposures, *in vitro* testing, ATS testing, and 90-day *in vivo* inhalation studies provide avenues to overcome the need to quickly screen and prioritize carbon and other ENMs for chronic disease risk.

Current screening assays for genotoxicity include the Ames test, comet assay, micronucleus assay during cytokinesis block, chromosome aberration, HPRT mutation assay, γ-H2AX expression, 8-hydroxyeoxyguanosine DNA adducts, and so on [275]. Numerous studies have used the comet assay to screen ENMs with conflicting results [276, 277], largely due to the differences in particle preparation, size, crystal structure, and the tested cell types [278]. Based on the great need for systematic genotoxicity assessment of numerous novel ENMs, the comet assay, micronucleus assay, γ-H2AX expression, and 8-hydroxydeoxyguanosine adduct assays provide rapid, high-throughput assay options to capture clastogenic, aneuploidy, and ROS-associated damage of chromosomes. For assessing direct DNA damage across numerous materials, the micronucleus assay has a clear

advantage since it can distinguish between clastogenic and aneuploid damage (with kinetochore staining), and is successfully being implemented in recent high-content/high-throughput imaging platforms. The remaining established assays are usually labor intensive and time consuming, but remain useful in further detailed studies of ENM genotoxicity. 8-Hydroxydeoxyguanosine is typically assayed as a DNA oxidation byproduct, but high baseline levels and nonspecific fluorophore binding are often encountered, resulting in conflicting reports. Even with these shortcomings, there is large evidence showing increased oxidative DNA damage following oral and pulmonary exposure to ECNMs, supported by *in vitro* comet assays [279]. Although these test results are generally accepted, shortcomings in studies still make it difficult to rank either ENMs or their physicochemical properties into meaningful risk groups. Like most assays, with ENMs present in the sample, proper controls with only ENM and no tissue should be used since numerous ENMs have been shown to interact with DNA once other cell structures have been removed (e.g., comet assay) [276]. Secondary tests, in addition to the primary test, should be used to adequately characterize genotoxicity across numerous particles. Nevertheless, current genotoxicity tests provide a sensitive and rapid method to systematically assess ENMs with different physicochemical properties for carcinogenesis initiation risk.

A recent OECD publication reviewed ENM genotoxicity testing strategies that are applicable for ECNMs also [280]. At present, no set guidelines are available for ENM testing. Current hurdles to achieving an effective testing strategy include a robust and adequate testing regime as well as questions as to whether single or a combination of tests should be used and whether certain classes of ENM (like ECNMs) should warrant the development of their own unique set of protocols. At present, a combined testing strategy appears to give adequate genotoxicity characterization *in vitro* [281]. The micronucleus assay (OECD TG 487), using cytochasmin B in the absence of ENM, 24-h ENM exposure, physiologically relevant protein serum levels, and p53-stable cell lines, was cited as a preferable assay at present. The comet assay can characterize both aneugenic and clastogenic DNA damage. The mammalian mutation assay (OECD TG 476) should be used instead of the Ames test since bacteria display strikingly different ENM toxicokinetics.

In vitro testing serves as an appropriate screening strategy, but may not predict *in vivo* effects since several reports show little *in vivo* toxicity although the *in vitro* tests were positive [280]. Toxicokinetics, clearance mechanisms, and inherent variability within an ENM particle class are usually confounding factors that must be characterized, thus dictating that genotoxicity endpoints must be a part of a Tier II short-term *in vivo* toxicity testing strategies. As such, improvements are needed in cell/tissue uptake assessment to identify appropriate dose metrics, low-dose effects, and dispersant effects. Researchers should understand exposure scenarios and base their *in vitro/in vivo* exposures (dose and time) to adequately model potential genotoxicity.

10.5 Concluding Remarks

Accumulated *in vivo* and *in vitro* studies have suggested genotoxicity and carcinogenetic effects of ECNMs, with UFCB and MWCNTs showing human carcinogenic potential, while, currently, an overall understanding of this is lacking. Full characterization of an ECNM's properties appears to lend critical data to understand what drives genotoxicity and promotion. Technological advances in characterizing nanomaterials will help assess their exposure and their fate in the workplace and environment, as well as identify nanomaterials in biological tissues following exposure. Systematic strategies to assess genotoxicity and malignant transformation exist and await incorporation into screening and tiered assessment frameworks. Equal attention should be paid to both genotoxic and non-genotoxic ECNMs since some materials may solely promote or help progress carcinogenesis. As our understanding of carcinogenesis expands (e.g., CSCs, tumor microenvironment), the validation and incorporation of new screening and assay techniques into a comparative model framework can potentially improve cancer risk and keep pace with oncology research and clinical advancements. As the spectrum of ECNMs expands and ECNM-enabled technology use becomes widespread with second- and third-generation materials, the development for rapid and robust assessment for long-term occupational and public health risks is a pressing need. By considering the above recent advancements, it is clear that a multidisciplinary and translational approach must be developed and utilized to improve and mainstream "prevention-by-design" strategies to reduce their carcinogenic potential and safeguard beneficial ECNM nanotechnologies. It is imperative that stakeholders form a consensus on appropriate frameworks to assess the risk and develop ECNM technologies that balance technological benefit and "prevention-by-design" considerations.

Acknowledgments

TAS and LW acknowledge the support of Nanotechnology Research Center (NTRC) through No. ZXFJ. LS is supported by NTRC through No. 011N and NIOSH Intramural Grant No. ZLDA funding. YR acknowledges the support of the National Institute of Health through award No. R01-ES022968 and the National Science Foundation through award No. CBET-1434503. Special thanks are due to Aaron Erdely for his constructive comments on this work.

Disclaimer

The findings and conclusions in this report are those of the authors and do not necessarily represent the views or policy of the National Institute for Occupational Safety and Health. Mention of product name does not constitute an endorsement.

References

1. Zhang, B., Zheng, X., Li, H. *et al.* (2013) Application of carbon-based nanomaterials in sample preparation: a review. *Anal. Chim. Acta*, **784**, 1–17.
2. Oberdorster, G. (2010) Safety assessment for nanotechnology and nanomedicine: concepts of nanotoxicology. *J. Intern. Med.*, **267** (1), 89–105.
3. Maynard, A.D. (2006) Nanotechnology: the next big thing, or much ado about nothing? *Ann. Occup. Hyg.*, **51**, 1–12.
4. Johnson, D.R., Methner, M.M., Kennedy, A.J. *et al.* (2010) Potential for occupational exposure to engineered carbon-based nanomaterials in environmental laboratory studies. *Environ. Health Perspect.*, **118** (1), 49–54.
5. Han, J.H., Lee, E.J., Lee, J.H. *et al.* (2008) Monitoring multiwalled carbon nanotube exposure in carbon nanotube research facility. *Inhalation Toxicol.*, **20** (8), 741–749.
6. Sargent, L.M., Reynolds, S.H., and Castranova, V. (2010) Potential pulmonary effects of engineered carbon nanotubes: in vitro genotoxic effects. *Nanotoxicology*, **4**, 396–408.
7. Muller, J., Decordier, I., Hoet, P.H. *et al.* (2008) Clastogenic and aneugenic effects of multi-wall carbon nanotubes in epithelial cells. *Carcinogenesis*, **29**, 427–433.
8. Akhavan, O., Ghaderi, E., and Akhavan, A. (2012) Size-dependent genotoxicity of graphene nanoplatelets in human stem cells. *Biomaterials*, **33**, 8017–8025.
9. Grosse, Y., Loomis, D., Guyton, K.Z. *et al.* (2014) Carcinogenicity of fluoroedenite, silicon carbibe fibres and whiskers, and carbon nanotubes. *Lancet Oncol.*, **15**, 1427–1428.
10. Dresler, C. (2013) The changing epidemic of lung cancer and occupational and environmental risk factors. *Thorac. Surg. Clin.*, **23**, 113–122.
11. Dey, A., Biswas, D., Saha, S.K. *et al.* (2012) Comparison study of clinicoradiological profile of primary lung cancer cases: an Eastern India experience. *Indian J. Cancer*, **49**, 89–95.
12. Samet, J.M., Avila-Tang, E., Boffetta, P. *et al.* (2009) Lung cancer in never smokers: clinical epidemiology and environmental risk factors. *Clin. Cancer Res.*, **15**, 5626–5645.
13. Loomis, D., Grosse, Y., Lauby-Secretan, B., El Ghissassi, F., Bouvard, V., Benbrahim-Tallaa, L., Guha, N., Baan, R., Mattock, H., Straif, K., and International Agency for Research on Cancer Monograph Working Group IARC (2013) The carcinogenicity of outdoor air pollution. *Lancet Oncol.*, **14**, 1262–1263.
14. Becker, H., Herzberg, F., Schulte, A. *et al.* (2011) The carcinogenic potential of nanomaterials, their release from products and options for regulating them. *Int. J. Hyg. Environ. Health*, **214**, 231–238.
15. Sargent, L.M., Porter, D.W., Staska, L.M. *et al.* (2014) Promotion of lung adenocarcinoma following inhalation exposure to multi-walled carbon nanotubes. *Part. Fibre Toxicol.*, **11**, 3.
16. Nel, A.E., Madler, L., Velegol, D. *et al.* (2009) Understanding biophysicochemical interactions at the nano-bio interface. *Nat. Mater.*, **8**, 543–557.
17. Luanpitpong, S., Wang, L., and Rojanasakul, Y. (2014) The effects of carbon nanotubes on lung and dermal cellular behaviors. *Nanomedicine*, **9**, 895–912.
18. Bergin, I.L. and Witzmann, F.A. (2013) Nanoparticle toxicity by the gastrointestinal route: evidence and knowledge gaps. *Int. J. Biomed. Nanosci. Nanotechnol.*, **3** (1-2), 163.
19. Mercer, R.R., Scabilloni, J.F., Hubbs, A.F. *et al.* (2013) Extrapulmonary transport of MWCNT following inhalation exposure. *Part. Fibre Toxicol.*, **10**, 38.
20. Donaldson, K. and Poland, C.A. (2012) Inhaled nanoparticles and lung cancer – what we can learn from conventional particle toxicology. *Swiss Med. Wkly.*, **142**, w13547.
21. Erdely, A., Dahm, M., Chen, B.T. *et al.* (2013) Carbon nanotube dosimetry:

from workplace exposure assessment to inhalation toxicology. *Part. Fibre Toxicol.*, **10** (1), 53.
22. NIOSH (2013) Occupational exposure to carbon nanotubes and carbon nanofibers, in *Current Intelligence Bulletin*, vol. 65. Centers for Disease Control, United States Department of Human and Health Services.
23. Gonzalez, L., Lison, D., and Kirsch-Volders, M. (2008) Genotoxicity of engineered nanomaterials: a critical review. *Nanotoxicology*, **2**, 252–273.
24. Nel, A.E., Nasser, E., Godwin, H. *et al.* (2013) A multi-stakeholder perspective on the use of alternative test strategies for nanomaterial safety assessment. *ACS Nano*, **7** (8), 6422–6433.
25. Pott, F. and Roller, M. (2005) Carcinogenicity study with nineteen granular dusts in rats. *Eur. J. Oncol.*, **10** (4), 249–281.
26. Fung, V.A., Barrett, J.C., and Huff, J. (1995) The carcinogenic bioassay in perspective: application in identifying human cancer hazards. *Environ. Health Perspect.*, **103**, 680–683.
27. Hanahan, D. and Weinberg, R.A. (2011) Hallmarks of cancer: the next generation. *Cell*, **144**, 646–674.
28. Barrett, J.C. (1993) Mechanisms of multistep carcinogenesis and carcinogen risk assessment. *Environ. Health Perspect.*, **100**, 9–20.
29. Slaga, T.J. (1983) Overview of tumor promotion in animals. *Environ. Health Perspect.*, **50**, 3–14.
30. Gensler, H. and Bowden, G.T. (1984) Influence of 13-cis-retinoic acid on mouse skin tumor initiation and promotion. *Cancer Lett.*, **22**, 71–75.
31. Pitot, H.C., Campbell, H.A., Maronpot, R. *et al.* (1989) Critical parameters in the quantitation of the stages of initiation, promotion, and progression in one model of hepatocarcinogenesis in the rat. *Toxicol. Pathol.*, **17** (4, Pt. 1), 594–611; discussion 611–612.
32. Pitot, H.C. (1993) The molecular biology of carcinogenesis. *Cancer*, **72** (Suppl 3), 962–970.
33. Voight, M.D. (2005) Alcohol in hepatocellular cancer. *Clin. Liver Dis.*, **9**, 151–169.
34. Malkinson, A.M., Koski, K.M., Evans, W.A. *et al.* (1997) Butylated hydroxytoluene exposure is necessary to induce lung tumors in BALB mice treated with 3-methylcholanthrene. *Cancer Res.*, **57**, 2832–2834.
35. Klaassen, C. (2013) *Casarett and Doull's Toxicology*, 8th edn, McGraw-Hill.
36. Combes, R., Balls, M., Curren, R. *et al.* (1999) Cell transformation assays as predictors of human carcinogenicity. *Altern. Lab. Anim.*, **27**, 745–767.
37. Ding, L., Getz, G., Wheeler, D.A. *et al.* (2008) Somatic mutations affect key pathways in lung adenocarcinoma. *Nature*, **455**, 1069–1075.
38. Troll, W. and Wiesner, R. (1985) The role of oxygen radicals as a possible mechanism of tumor promotion. *Annu. Rev. Pharmacol. Toxicol.*, **25**, 509–528.
39. Maslov, A.Y. and Vijg, J. (2009) Genome instability, cancer and aging. *Biochim. Biophys. Acta*, **1790** (10), 963–969.
40. Møller, P., Danielsen, P.H., Jantzen, K. *et al.* (2013) Oxidatively damaged DNA in animals exposed to particles. *Crit. Rev. Toxicol.*, **43**, 96–118.
41. Sato, M., Shames, D.S., and Hasegawa, Y. (2012) Emerging evidence of epithelial-to-mesenchymal transition in lung carcinogenesis. *Respirology*, **17**, 1048–1059.
42. Diaz-Cano, S.J. (2012) Tumor heterogeneity: mechanisms and bases for a reliable application of molecular marker design. *Int. J. Mol. Sci.*, **13**, 1951–2011.
43. Azad, N., Iyer, A.K., Wang, L. *et al.* (2013) Reactive oxygen species-mediated p38 MAPK regulates carbon nanotube-induced fibrogenic and angiogenic responses. *Nanotoxicology*, **7** (2), 157–168.
44. Dalerba, P., Cho, R.W., and Clarke, M.F. (2007) Cancer stem cells: models and concepts. *Annu. Rev. Med.*, **58**, 267–284.
45. Gupta, P.B., Fillmore, C.M., Jiang, G. *et al.* (2011) Stochastic state transitions give rise to phenotypic equilibrium in populations of cancer cells. *Cell*, **146**, 633–644.

46. Shvedova, A.A., Tkach, A.V., Kisin, E.R. *et al.* (2013) Carbon nanotubes enhance metastatic growth of lung carcinoma via upregulation of myeloid-derived suppressor cells. *Small*, **9** (9–10), 1691–1695.
47. Sellers, T.A., Weaver, T.W., Phillips, B. *et al.* (1998) Environmental factors can confound identification of a major gene effect: results from a segregation analysis of a simulated population of lung cancer families. *Genet. Epidemiol.*, **15**, 251–262.
48. Clapp, R.W., Jacobs, M.M., and Loechler, E.L. (2008) Environmental and occupational causes of cancer: new evidence 2005–2007. *Rev. Environ. Health*, **23**, 1–37.
49. Donaldson, K., Aitken, R., Tran, L. *et al.* (2006) Carbon nanotubes: a review of their properties in relation to pulmonary toxicology and workplace safety. *Toxicol. Sci.*, **92**, 5–22.
50. Hussain, M.A., Kabir, M.A., and Sood, A.K. (2009) On the cytotoxicity of carbon nanotubes. *Curr. Sci.*, **96**, 664–673.
51. Pacurari, M., Castranova, V., and Vallyathan, V. (2010) Single- and multi-wall carbon nanotubes versus asbestos: are the carbon nanotubes a new health risk to humans? *J. Toxicol. Environ. Health A*, **73**, 378–395.
52. Oberdorster, G., Oberdorster, E., and Oberdorster, J. (2005) Nanotoxicology: an emerging discipline evolving from studies of ultrafine particles. *Environ. Health Perspect.*, **113**, 823–839.
53. Møller, P., Folkmann, J.K., Danielsen, P.H. *et al.* (2012) Oxidative stress generated damage to DNA by gastrointestinal exposure to insoluble particles. *Curr. Mol. Med.*, **12**, 732–745.
54. Borm, P.J., Cakmak, G., Jermann, E. *et al.* (2005) Formation of PAH-DNA adducts after in vivo and vitro exposure of rats and lung cells to different commercial carbon blacks. *Toxicol. Appl. Pharmacol.*, **205**, 157–167.
55. Oettinger, R., Drumm, K., Knorst, M. *et al.* (1999) Production of reactive oxygen intermediates by human macrophages exposed to soot particles and asbestos fibers and increase in NF-j B p50/p105 mRNA. *Lung*, **177**, 343–354.
56. Harrison, R.M. and Yin, J. (2000) Particulate matter in the atmosphere: which particle properties are important for its effects on health? *Sci. Total Environ.*, **249** (1–3), 85–101.
57. IARC (1996) *IARC Monographs on the Evaluation of Carcinogenic Risks to Humans: Printing Processes and Printing Inks*, Carbon Black and Some Nitro Compounds, vol. 65, IARC, Lyon.
58. IARC (2010) *IARC Monographs on the Evaluation of Carcinogenic Risks to Humans*, Carbon Black, Titanium Dioxide and Talc, vol. 93, IARC, Lyon.
59. Donaldson, K., Tran, L., Jimenez, L.A. *et al.* (2005) Combustion-derived nanoparticles: a review of their toxicology following inhalation exposure. *Part. Fibre Toxicol.*, **2**, 10.
60. Renwick, L.C., Brown, D., Clouter, A. *et al.* (2004) Increased inflammation and altered macrophage chemotactic responses caused by two ultrafine particle types. *Occup. Environ. Med.*, **61**, 442–447.
61. Brown, D.M., Stone, V., Findlay, P. *et al.* (2000) Increased inflammation and intracellular calcium caused by ultrafine carbon black is independent of transition metals or other soluble components. *Occup. Environ. Med.*, **57**, 685–691.
62. Kreyling, W.G., Semmler, M., and Moller, W. (2004) Dosimetry and toxicology of ultrafine particles. *J. Aerosol Med.*, **17**, 140–152.
63. Gilmour, P.S., Ziesenis, A., Morrison, E.R. *et al.* (2004) Pulmonary and systemic effects of short-term inhalation exposure to ultrafine carbon black particles. *Toxicol. Appl. Pharmacol.*, **195**, 35–44.
64. Schreiber, N., Ströbele, M., Kopf, J. *et al.* (2013) Lung alterations following single or multiple low-dose carbon black nanoparticle aspirations in mice. *J. Toxicol. Environ. Health A*, **76**, 1317–1332.
65. Gallagher, J., Sams, R. II,, Inmon, J. *et al.* (2003) Formation of 8-oxo-7,8-dihydro-2′deoxyguanosine in rat lung

DNA following subchronic inhalation of carbon black. *Toxicol. Appl. Pharmacol.*, **190**, 224–231.

66. Bourdon, J.A., Saber, A.T., Jacobsen, N.R. *et al.* (2012) Carbon black nanoparticle instillation induces sustained inflammation and genotoxicity in mouse lung and liver. *Part. Fibre Toxicol.*, **9**, 5.
67. Bourdon, J.A., Halappanavar, S., Saber, A.T. *et al.* (2012) Hepatic and pulmonary toxicogenomic profiles in mice intratracheally instilled with carbon black nanoparticles reveal pulmonary inflammation, acute phase response, and alterations in lipid homeostasis. *Toxicol. Sci.*, **127** (2), 474–484.
68. Saber, A.T., Jacobsen, N.R., Bornholdt, J. *et al.* (2006) Cytokine expression in mice exposed to diesel exhaust particles by inhalation. Role of tumor necrosis factor. *Part. Fibre Toxicol.*, **3**, 4.
69. Jacobsen, N.R., Møller, P., Jensen, K.A. *et al.* (2009) Lung inflammation and genotoxicity following pulmonary exposure to nanoparticles in ApoE-/- mice. *Part. Fibre Toxicol.*, **6**, 2.
70. Jackson, P., Hougaard, K.S., Boisen, A.M. *et al.* (2012) Pulmonary exposure to carbon black by inhalation or instillation in pregnant mice: effects on liver DNA strand breaks in dams and offspring. *Nanotoxicology*, **6**, 486–500.
71. Kyjovska, Z.O., Jacobsen, N.R., Saber, A.T. *et al.* (2015) DNA damage following pulmonary exposure by instillation to low doses of carbon black (Printex 90) nanoparticles in mice. *Environ. Mol. Mutagen.*, **56** (1), 41–49.
72. Nikula, K.J., Snipes, M.B., Barr, E.B. *et al.* (1995) Comparative pulmonary toxicities and carcinogenicities of chronically inhaled diesel exhaust and carbon black in F344 rats. *Fundam. Appl. Toxicol.*, **25**, 80–94.
73. Heinrich, U., Fuhst, R., Rittinghausen, S. *et al.* (1995) Chronic inhalation exposure of Wistar rats and two different strains of mice to diesel engine exhaust, carbon black, and titanium dioxide. *Inhalation Toxicol.*, **7** (4), 533–556.
74. Dungworth, D.L., Mohr, U., Heinrich, U. *et al.* (1994) in *Toxic and Carcinogenic Effects of Solid Particles in the Respiratory Tract* (eds U. Mohr, D.L. Dungworth, J.L. Mauderly, and G. Oberdörster), ILSI Press, Washington, DC, pp. 75–98.
75. Heinrich, U. (1994) in *Toxic and Carcinogenic Effects of Solid Particles in the Respiratory Tract* (eds U. Mohr, D.L. Dungworth, J.L. Mauderly, and G. Oberdörster), ILSI Press, Washington, DC, pp. 57–73.
76. Reeves, A.L., Puro, H.E., Smith, R.G. *et al.* (1971) Experimental asbestos carcinogenesis. *Environ. Res.*, **4**, 496–511.
77. Mauderly, J.L. (1997) Relevance of particle-induced rat lung tumors for assessing lung carcinogenic hazard and human lung cancer risk. *Environ. Health Perspect.*, **105**, 1337–1346.
78. Valberg, P.A. and Watson, A.Y. (1996) Lung-cancer rates in carbon-black workers are discordant with predictions from rat bioassay data. *Regul. Toxicol. Pharm.*, **24**, 155–170.
79. Jacobsen, N.R., Saber, A.T., White, P. *et al.* (2007) Increased mutant frequency by carbon black, but not quartz in the lacZ and cll transgenes of Muta mouse lung epithelial cells. *Environ. Mol. Mutagen.*, **48**, 451–461.
80. Riebe-Imre, M., Aufderheide, M., Gärtner-Hübsch, S. *et al* (1994) in *Toxic and Carcinogenic Effects of Solid Particles in the Respiratory Tract* (eds U. Mohr, D.L. Dungworth, J.L. Mauderly, G. Oberdörster, Jacobsen, *et al.*), ILSI Press, Washington, DC, pp. 519–523.
81. Driscoll, K.E., Deyo, L.C., Carter, J.M. *et al.* (1997) Effects of particle exposure and particle-elicited inflammatory cells on mutation in rat alveolar epithelial cells. *Carcinogenesis*, **18**, 423–430.
82. Kirwin, C.J., LeBlanc, J.V., Thomas, W.C. *et al.* (1981) Evaluation of the genetic activity of industrially produced carbon black. *J. Toxicol. Environ. Health*, **7**, 973–989.
83. Knaapen, A.M., Seiler, F., Schilderman, P.A. *et al.* (1999) Neutrophils cause oxidative DNA damage in alveolar

epithelial cells. *Free Radical Biol. Med.*, **27**, 234–240.

84. Don Porto, C.A., Hoet, P.H., Verschaeve, L. *et al.* (2001) Genotoxic effects of carbon black particles, diesel exhaust particles, and urban air particulates and their extracts on a human alveolar epithelial cell line (A549) and a human monocytic cell line (THP-1). *Environ. Mol. Mutagen.*, **37**, 155–163.
85. Chuang, H.C., Cheng, Y.L., Lei, Y.C. *et al.* (2013) Protective effects of pulmonary epithelial lining fluid on oxidative stress and DNA single-strand breaks caused by ultrafine carbon black, ferrous sulphate and organic extract of diesel exhaust particles. *Toxicol. Appl. Pharmacol.*, **266** (3), 329–334.
86. Mroz, R.M., Schins, R.P., Li, H. *et al.* (2008) Nanoparticle-driven DNA damage mimics irradiation-related carcinogenesis pathways. *Eur. Respir. J.*, **31**, 241–251.
87. Mroz, R.M., Schins, R.P., Li, H. *et al.* (2007) Nanoparticle carbon black driven DNA damage induces growth arrest and AP-1 and NFkappa B DNA binding in lung epithelial A549 cell line. *J. Physiol. Pharmacol.*, **58** (Suppl. 5), 461–470.
88. Jacobsen, N.R., White, P.A., Gingerich, J. *et al.* (2010) Mutation spectrum in FE1-MUTA(TM) Mouse lung epithelial cells exposed to nanoparticulate carbon black. *Environ. Mol. Mutagen.*, **52**, 331–337.
89. Tamaoki, J., Isono, K., Takeyama, K. *et al.* (2004) Ultrafine carbon black particles stimulate proliferation of human airway epithelium via EGF receptor-mediated signaling pathway. *Am. J. Physiol. Lung Cell Mol. Physiol.*, **287**, L1127–L1133.
90. Wang, L., Stueckle, T.A., Mishra, A. *et al.* (2014) Neoplastic-like transformation effect of single-walled and multiwalled carbon nanotubes compared to asbestos on human lung small airway epithelial cells. *Nanotoxicology*, **8**, 485–507.
91. van Berlo, D., Clift, M.J., Albrecht, C. *et al.* (2012) Carbon nanotubes: an insight into the mechanisms of their potential genotoxicity. *Swiss Med. Wkly.*, **5**, 142.
92. Johnston, H.J., Hutchison, G.R., Christensen, F.M. *et al.* (2010) A critical review of the biological mechanisms underlying the in vivo and in vitro toxicity of carbon nanotubes: the contribution of physicochemical characteristics. *Nanotoxicology*, **4**, 207–246.
93. Donaldson, K., Poland, C.A., Murphy, F.A. *et al.* (2013) Pulmonary toxicity of carbon nanotubes and asbestos—similarities and differences. *Adv. Drug Delivery Rev.*, **65** (15), 2078–2086.
94. Sanchez, V.C., Pietruska, J.R., Miselis, N.R. *et al.* (2009) Biopersistence and potential adverse health impacts of fibrous nanomaterials: what have we learned from asbestos? *WIREs Nanomed. Nanobiotechnol.*, **1**, 511–529.
95. Møller, P., Christophersen, D.V., Jensen, D.M. *et al.* (2014) Role of oxidative stress in carbon nanotube-generated health effects. *Arch. Toxicol.*, **88**, 1939–1964.
96. Huncharek, M. (1995) Genetic factors in the ethiology of malignant mesothelioma. *Eur. J. Cancer*, **31A**, 1741–1747.
97. Dahm, M.M., Evans, D.E., Schubauer-Berigan, M.K. *et al.* (2012) Occupational exposure assessment in carbon nanotube and nanofiber primary and secondary manufacturers. *Ann. Occup. Hyg.*, **56** (5), 542–556.
98. Dahm, M.M., Schubauer-Berigan, M.K., Evans, D.E. *et al.* (2015) Carbon nanotube and nanofiber exposure assessments: an analysis of 14 site visits. *Ann. Occup. Hyg.*, **59**, 705–723.
99. Mercer, R.R., Scabilloni, J., Wang, L. *et al.* (2008) Alteration of deposition pattern and pulmonary response as a result of improved dispersion of aspirated single-walled carbon nanotubes in a mouse model. *Am. J. Physiol. Lung Cell Mol. Physiol.*, **294** (1), L87–L97.
100. Mercer, R.R., Hubbs, A.F., Scabilloni, J.F. *et al.* (2010) Distribution and persistence of pleural penetrations by

multi-walled carbon nanotubes. *Part. Fibre Toxicol.*, **7**, 28.

101. Mercer, R.R., Scabilloni, J.F., Hubbs, A.F. *et al.* (2013) Distribution and fibrotic response following inhalation exposure to multi-walled carbon nanotubes. *Part. Fibre Toxicol.*, **10**, 33.

102. Dinu, C.Z., Bale, S.S., Zhu, G. *et al.* (2009) Tubulin encapsulation of carbon nanotubes into functional hybrid assemblies. *Small*, **5**, 310–315.

103. Cortez, B.A., Quassollo, G., Caceres, A. *et al.* (2011) The fate of chrysotile-induced multipolar mitosis and aneuploid population in cultured lung cancer cells. *PLoS One*, **6** (4), e18600.

104. Boyles, M.S., Young, L., Brown, D.M. *et al.* (2015) Multi-walled carbon nanotube induced frustrated phagocytosis, cytotoxicity and pro-inflammatory conditions in macrophages are length dependent and greater than that of asbestos. *Toxicol. in Vitro*, **29**, 1513–1528.

105. Hubbs, A.F., Mercer, R.R., Coad, J.E. *et al.* (2009) Persistent pulmonary inflammation, airway mucous metaplasia and migration of multi-walled carbon nanotubes from the lung after subchronic exposure. *Toxicologist*, **108**, 2193.

106. Porter, D.W., Hubbs, A.F., Mercer, R.R. *et al.* (2010) Mouse pulmonary dose- and time course-responses induced by exposure to multi-walled carbon nanotubes. *Toxicology*, **269**, 136–147.

107. Ryman-Rasmussen, J.P., Cesta, M.F., Brody, A.R. *et al.* (2009) Inhaled carbon nanotubes reach the subpleural tissue in mice. *Nat. Nanotechnol.*, **4**, 747–751.

108. Mercer, R.R., Hubbs, A.F., Scabilloni, J.F. *et al.* (2011) Pulmonary fibrotic response to aspiration of multi-walled carbon nanotubes. *Part. Fibre Toxicol.*, **8**, 21.

109. Porter, D.W., Hubbs, A.F., Chen, B.T. *et al.* (2013) Acute pulmonary dose–responses to inhaled multi-walled carbon nanotubes. *Nanotoxicology*, **7**, 1399.

110. Czarny, B., Georgin, D., Berthon, F. *et al.* (2014) Carbon nanotube translocation to distant organs after pulmonary exposure: insights from in situ (14)C-radiolabeling and tissue radioimaging. *ACS Nano*, **8** (6), 5715–5724.

111. Shvedova, A.A., Kapralov, A.A., Feng, W.H. *et al.* (2012) Impaired clearance and enhanced pulmonary inflammatory/fibrotic response to carbon nanotubes in myeloperoxidase-deficient mice. *PLoS One*, **7** (3), e30923.

112. Shvedova, A.A., Yanamala, N., Kisin, E.R. *et al.* (2014) Long-term effects of carbon containing engineered nanomaterials and asbestos in the lung: one year postexposure comparisons. *Am. J. Physiol. Lung Cell Mol. Physiol.*, **306** (2), L170–L182.

113. Fujita, K., Fukuda, M., Fukui, H. *et al.* (2014) Intratracheal instillation of single-wall carbon nanotubes in the rat lung induces time-dependent changes in gene expression. *Nanotoxicology*, **9**, 1–12.

114. Shvedova, A.A., Kisin, E., Murray, A.R. *et al.* (2008) Inhalation vs. aspiration of single-walled carbon nanotubes in C57BL/6 mice: inflammation, fibrosis, oxidative stress, and mutagenesis. *Am. J. Physiol. Lung Cell Mol. Physiol.*, **295** (4), L552–L565.

115. Manke, A., Luanpitpong, S., Dong, C. *et al.* (2014) Effect of fiber length on carbon nanotube-induced fibrogenesis. *Int. J. Mol. Sci.*, **15** (5), 7444–7461.

116. Pauluhn, J. (2010) Subchronic 13-week inhalation exposure of rats to multi-walled carbon nanotubes: toxic effects are determined by density of agglomerate structures, not fibrillar structures. *Toxicol. Sci.*, **113** (1), 226–242.

117. Jackson, M.A., Lea, I., Rashid, A. *et al.* (2006) Genetic alterations in cancer knowledge system: analysis of gene mutations in mouse and human liver and lung tumors. *Toxicol. Sci.*, **90**, 400–418.

118. Pacurari, M., Qian, Y., Porter, D.W. *et al.* (2011) Multi-walled carbon nanotube-induced gene expression in the mouse lung: association with lung pathology. *Toxicol. Appl. Pharmacol.*, **255**, 18–31.

119. Poulsen, S.S., Jacobsen, N.R., Labib, S. *et al.* (2013) Transcriptomic analysis

reveals novel mechanistic insight into murine biological responses to multi-walled carbon nanotubes in lungs and cultured lung epithelial cells. *PLoS One*, **8**, e80452.

120. Luanpitpong, S., Wang, L., Stueckle, T.A. *et al.* (2014) Caveolin-1 regulates lung cancer stem-like cell induction and p53 inactivation in carbon nanotube-driven tumorigenesis. *Oncotarget*, **5** (11), 3541–3554.

121. Chen, D., Stueckle, T.A., Luanpitpong, S. *et al.* (2015) Gene expression profile of human lung epithelial cells chronically exposed to single walled-carbon nanotubes. *Nanoscale Res. Lett.*, **10**, 12.

122. Guo, N.L., Wan, Y.W., Denvir, J. *et al.* (2012) Multiwalled carbon nanotube-induced gene signatures in the mouse lung: potential predictive value for human lung cancer risk and prognosis. *J. Toxicol. Environ. Health A*, **75**, 1129–1153.

123. Nagai, H. and Toyokuni, S. (2012) Differences and similarities between carbon nanotubes and asbestos fibers during mesothelial carcinogenesis: shedding light on fiber entry mechanism. *Cancer Sci.*, **103**, 1378–1390.

124. Poland, C.A., Duffin, R., Kinloch, I. *et al.* (2008) Carbon nanotubes introduced into the abdominal cavity of mice show asbestos-like pathogenicity in a pilot study. *Nat. Nanotechnol.*, **3** (7), 423–428.

125. Murphy, F.A., Poland, C.A., Duffin, R. *et al.* (2011) Length-dependent retention of carbon nanotubes in the pleural space of mice initiates sustained inflammation and progressive fibrosis on the parietal pleura. *Am. J. Pathol.*, **178** (6), 2587–2600.

126. Murphy, F.A., Poland, C.A., Duffin, R. *et al.* (2013) Length-dependent pleural inflammation and parietal pleural responses after deposition of carbon nanotubes in the pulmonary airspaces of mice. *Nanotoxicology*, **7**, 1157–1167.

127. Xu, J., Alexander, D.B., Futakuchi, M. *et al.* (2014) Size- and shape-dependent pleural translocation, deposition, fibrogenesis, and mesothelial proliferation by multiwalled carbon nanotubes. *Cancer Sci.*, **105** (7), 763–769.

128. Murphy, F.A., Schinwald, A., Poland, C.A. *et al.* (2012) The mechanism of pleural inflammation by long carbon nanotubes: interaction of long fibres with macrophages stimulates them to amplify pro-inflammatory responses in mesothelial cells. *Part. Fibre Toxicol.*, **9**, 8.

129. Shvedova, A.A., Kisin, E.R., Mercer, R. *et al.* (2005) Unusual inflammatory and fibrogenic pulmonary responses to single-walled carbon nanotubes in mice. *Am. J. Physiol. Lung Cell Mol. Physiol.*, **289**, L698–L708.

130. World Health Organizaiton (2002) *IARC Monographs on the Evalution of Carcinogenic Risk to Humans*, Man-Made Vitreous Fibres, vol. 81, IARC, Lyon.

131. Muller, J., Delos, M., Panin, N. *et al.* (2009) Absence of carcinogenic response to multiwall carbon nanotubes in a 2-year bioassay in the peritoneal cavity of the rat. *Toxicol. Sci.*, **110**, 442–448.

132. Sakamoto, Y., Nakae, D., Fukumori, N. *et al.* (2009) Induction of mesothelioma by a single intrascrotal administration of multi-wall carbon nanotube in intact male Fischer 344 rats. *J. Toxicol. Sci.*, **34** (1), 65–76.

133. Takagi, A., Hirose, A., Nishimura, T. *et al.* (2008) Induction of mesothelioma in p53+/- mouse by intraperitoneal application of multi-wall carbon nanotube. *J. Toxicol. Sci.*, **33**, 105–116.

134. Takagi, A., Hirose, A., Futakuchi, M. *et al.* (2012) Dose-dependent mesothelioma induction by intraperitoneal adminstariton of multi-wall carbon nanotubes in p53 heterozygous mice. *Cancer Sci.*, **103**, 1440–1444.

135. Pritchard, J.B., French, J.E., Davis, B.J. *et al.* (2003) The role of transgenic mouse models in carcinogen identification. *Envrion. Health Perspect.*, **111**, 444–454.

136. Nagai, H., Okazaki, Y., Chew, S.H. *et al.* (2011) Diameter and rigidity of multiwalled carbon nanotubes are critical factors in mesothelial injury and carcinogenesis. *Proc. Natl. Acad. Sci. U.S.A.*, **108**, E1330–E1338.

137. Rittinghausen, S., Hackbarth, A., Creutzenberg, O. *et al.* (2014) The carcinogenic effect of various multi-walled carbon nanotubes (MWCNTs) after intraperitoneal injection in rats. *Part. Fibre Toxicol.*, **11**, 59.

138. Yu, K.N., Kim, J.E., Seo, H.W. *et al.* (2013) Differential toxic responses between pristine and functionalized multiwall nanotubes involve induction of autophagy accumulation in murine lung. *J. Toxicol. Environ. Health A*, **76**, 1282–1292.

139. Xu, J., Futakuchi, M., Shimizu, H. *et al.* (2012) Multi-walled carbon nanotubes translocate into the pleural cavity and induce visceral mesothelial proliferation in rats. *Cancer Sci.*, **103** (12), 2045–2050.

140. Kobayashi, N., Naya, M., Mizuno, K. *et al.* (2011) Pulmonary and systemic responses of highly pure and well-dispersed single-wall carbon nanotubes after intratracheal instillation in rats. *Inhalation Toxicol.*, **23** (13), 814–828.

141. Shvedova, A.A., Kisin, E.R., Yanamala, N. *et al.* (2015) MDSC and TGF-β are required for facilitation of tumor growth in the lungs of mice exposed to carbon nanotubes. *Cancer Res.*, **75** (8), 1615–1623.

142. Pacurari, M., Yin, X.J., Zhao, J. *et al.* (2008) Raw single-wall carbon nanotubes induce oxidative stress and activate MAPKs, AP-1, NF-kappaB, and Akt in normal and malignant human mesothelial cells. *Environ. Health Perspect.*, **116** (9), 1211–1217.

143. Azad, N., Rojanasakul, Y., and Vallyathan, V. (2008) Inflammation and lung cancer: roles of reactive oxygen/nitrogen species. *J. Toxicol. Environ. Health B Crit. Rev.*, **11**, 1–15.

144. Aschberger, K., Johnston, H.J., Stone, V. *et al.* (2010) Review of carbon nanotubes toxicity and exposure--appraisal of human health risk assessment based on open literature. *Crit. Rev. Toxicol.*, **40** (9), 759–790.

145. Li, R., Wang, X., Ji, Z. *et al.* (2013) Surface charge and cellular processing of covalently functionalized multiwall carbon nanotubes determine pulmonary toxicity. *ACS Nano*, **7** (3), 2352–2368.

146. Park, E.J., Zahari, N.E., Lee, E.W. *et al.* (2014) SWCNTs induced autophagic cell death in human bronchial epithelial cells. *Toxicol. in Vitro*, **28** (3), 442–450.

147. Funahashi, S., Okazaki, Y., Ito, D. *et al.* (2015) Asbestos and multi-walled carbon nanotubes generate distinct oxidative responses in inflammatory cells. *J. Clin. Biochem. Nutr.*, **56** (2), 111–117.

148. Manke, A., Wang, L., and Rojanasakul, Y. (2013) Pulmonary toxicity and fibrogenic response of carbon nanotubes. *Toxicol. Mech. Methods*, **23**, 196–206.

149. Fenoglio, I., Greco, G., Tornatis, M. *et al.* (2008) Structural defects play a major role in the acute lung toxicity of multiwall carbon nanotubes: physicochemical aspects. *Chem. Res. Toxicol.*, **21** (9), 1690–1697.

150. Tsuruoka, S., Matsumoto, H., Koyama, K. *et al.* (2015) Radical scavenging reaction kinetics with multiwalled carbon nanotubes. *Carbon*, **83**, 232–239.

151. Pacurari, M., Yin, X.J., Ding, M. *et al.* (2008) Oxidative and molecular interactions of multi-wall carbon nanotubes (MWCNT) in normal and malignant human mesothelial cells. *Nanotoxicology*, **2**, 155–170.

152. Toyokuni, S. (2013) Genotoxicity and carcinogenicity risk of carbon nanotubes. *Adv. Drug Delivery Rev.*, **65** (15), 2098–2110.

153. Guo, F., Ma, N., Horibe, Y. *et al.* (2012) Nitrative DNA damage induced by multi-walled carbon nanotube via endocytosis in human lung epithelial cells. *Toxicol. Appl. Pharmacol.*, **260**, 138–192.

154. Sargent, L.M., Shvedova, A.A., Hubbs, A.F. *et al.* (2009) Induction of aneuploidy by single-walled carbon nanotubes. *Environ. Mol. Mutagen.*, **50**, 708–717.

155. Sargent, L.M., Hubbs, A.F., Young, S.H. *et al.* (2012) Single-walled carbon nanotube-induced mitotic disruption. *Mutat. Res.*, **745**, 28–37.

156. Rodriguez-Fernandez, L1., Valiente, R., Gonzalez, J. *et al.* (2012) Multiwalled carbon nanotubes display microtubule biomimetic properties in vivo, enhancing microtubule assembly

and stabilization. *ACS Nano*, **6** (8), 6614–6625.

157. Siegrist, K.J., Reynolds, S.H., Kashon, M.L. *et al.* (2014) Genotoxicity of multi-walled carbon nanotubes at occupationally relevant doses. *Part. Fibre Toxicol.*, **11**, 6.

158. Salisbury, J.L., D'Assoro, A.B., and Lingle, W.L. (2004) Centrosome amplification and the origin of chromosomal instability in breast cancer. *J. Mammary Gland Biol. Neoplasia*, **9**, 275–283.

159. Jackson, P., Kling, K., Jensen, K.A. *et al.* (2015) Characterization of genotoxic response to 15 multiwalled carbon nanotubes with variable physicochemical properties including surface functionalizations in the FE1-Muta(TM) mouse lung epithelial cell line. *Environ. Mol. Mutagen.*, **56**, 183–203.

160. Kato, T., Totsuka, Y., Ishino, K. *et al.* (2013) Genotoxicity of multi-walled carbon nanotubes in both in vitro and in vivo assay systems. *Nanotoxicology*, **7**, 452–461.

161. Balls, M. and Clothier, R. (2010) A FRAME response to the draft report on alternative (non-animal) methods for cosmetics testing: current status and future prospects—2010. *Altern. Lab. Anim.*, **38**, 345–353.

162. Corvi, R., Aardema, M.J., Gribaldo, L. *et al.* (2012) ECVAM prevalidation study on in vitro cell transformation assays: general outline and conclusions of the study. *Mutat. Res.*, **744** (1), 12–19.

163. Ponti, J., Broggi, F., Mariani, V. *et al.* (2013) Morphological transformation induced by multiwalled carbon nanotubes on Balb/3T3 cell model as an in vitro end point of carcinogenic potential. *Nanotoxicology*, **7**, 221–233.

164. Wang, L., Luanpitpong, S., Castranova, V. *et al.* (2011) Carbon nanotubes induce malignant transformation and tumorigenesis of human lung epithelial cells. *Nano Lett.*, **11**, 2796–2803.

165. Wu, P., Yuan, S.S., Ho, C.C. *et al.* (2013) Focal amplification of HOXD-harboring chromosome region is implicated in multiple-walled carbon nanotubes-induced carcinogenicity. *Nano Lett.*, **13**, 4632–4641.

166. Thurnherr, T., Brandenberger, C., Fischer, K. *et al.* (2011) A comparison of acute and long-term effects of industrial multiwalled carbon nanotubes on human lung and immune cells in vitro. *Toxicol. Lett.*, **200**, 176–186.

167. Jean, D., Thomas, E., Manie, E. *et al.* (2011) Syntenic relationships between genomic profiles of fiber-induced murine and human malignant mesothelioma. *Am. J. Pathol.*, **178**, 881–894.

168. Stueckle, T.A., Mishra, A., Derk, R. *et al.* (2013) Identification of novel exposure and lung cancer gene markers for carbon nanotube exposed human lung epithelial cells [abstract]. *Toxicologist*, **426**, 91.

169. Pongrakhananon, V., Luanpitpong, S., Stueckle, T.A. *et al.* (2015) Carbon nanotubes induce apoptosis resistance of human lung epithelial cells through FLICE-inhibitory protein. *Toxicol. Sci.*, **143** (2), 499–511.

170. Luanpitpong, S., Wang, L., Castranova, V. *et al.* (2014) Induction of stem-like cells with malignant properties by chronic exposure of human lung epithelial cells to single-walled carbon nanotubes. *Part. Fibre Toxicol.*, **11**, 22.

171. Lohcharoenkal, W., Wang, L., Stueckle, T.A. *et al.* (2013) Chronic exposure to carbon nanotubes induces invasion of human mesothelial cells through matrix metalloproteinase-2. *ACS Nano*, **7**, 7711–7723.

172. Lohcharoenkal, W., Stueckle, T.A., Wang, L. *et al.* (2014) Role of H-Ras/ERK signaling in carbon nanotube-induced neoplastic transformation of human mesothelial cells. *Front. Physiol.*, **5**, 222.

173. Nielsen, G.D., Roursgaard, M., Jensen, K.A. *et al.* (2008) In vivo biology and toxicology of fullerenes and their derivatives. *Basic Clin. Pharmacol. Toxicol.*, **103**, 197–208.

174. Aschberger, K., Johnston, H.J., Stone, V. *et al.* (2010) Review of fullerene toxicity and exposure-appraisal of a human health risk assessment, based on open literature. *Regul. Toxicol. Pharmacol.*, **58**, 455–473.

175. Johnston, H.J., Hutchison, G.R., Christensen, F.M. *et al.* (2010) The

biological mechanisms and physiochemical characteristics responsible for driving fullerene toxicity. *Toxicol. Sci.*, **114**, 162–182.

176. Shinohara, N., Matsumoto, K., Endoh, S. *et al.* (2009) In vitro and in vivo genotoxicity tests on fullerene C60 nanoparticles. *Toxicol. Lett.*, **191**, 289–296.

177. Takada, H., Kokubo, K., Matsubayashi, K. *et al.* (2006) Antioxidant activity of supramolecular water-soluble fullerenes evaluated by beta-carotene bleaching assay. *Biosci. Biotechnol., Biochem.*, **70**, 3088–3093.

178. Witte, P., Beuerle, F., Hartnagel, U. *et al.* (2007) Water solubility, antioxidant activity and cytochrome C binding of four families of exohedral adducts of C60 and C70. *Org. Biomol. Chem.*, **5**, 3599–3613.

179. Markovic, Z. and Trajkovic, V. (2008) Biomedical potential of the reactive oxygen species generation and quenching by fullerenes (C60). *Biomaterials*, **29**, 3561–3573.

180. Hu, Z., Guan, W., Wang, W. *et al.* (2007) Synthesis of β-alanine C60 derivative and its protective effect on hydrogen peroxide-induced apoptosis in rat pheochromocytoma cells. *Cell Biol. Int.*, **31**, 798–804.

181. Sayes, C.M., Marchione, A.A., Reed, K.L. *et al.* (2007) Comparative pulmonary toxicity assessments of C60 water suspensions in rats: few differences in fullerene toxicity in vivo in contrast to in vitro profiles. *Nano Lett.*, **7** (8), 2399–2406.

182. Baker, G.L., Gupta, A., Clark, M.L. *et al.* (2008) Inhalation toxicity and lung toxicokinetics of C60 fullerene nanoparticles and microparticles. *Toxicol. Sci.*, **101** (1), 122–131.

183. Fujita, K., Morimoto, Y., Ogami, A. *et al.* (2009) Gene expression profiles in rat lung after inhalation exposure to C(60) fullerene particles. *Toxicology*, **258** (1), 47–55.

184. Morimoto, Y., Hirohashi, M., Ogami, A. *et al.* (2010) Inflammogenic effect of well-characterized fullerenes in inhalation and intratracheal instillation studies. *Part. Fibre Toxicol.*, **14** (7), 4.

185. Park, E.J., Kim, H., Kim, Y. *et al.* (2010) Carbon fullerenes (C60s) can induce inflammatory responses in the lung of mice. *Toxicol. Appl. Pharmacol.*, **244** (2), 226–233.

186. Roursgaard, M., Poulsen, S.S., Kepley, C.L. *et al.* (2008) Polyhydroxylated C60 fullerene (fullerenol) attenuates neutrophilic lung inflammation in mice. *Basic Clin. Pharmacol. Toxicol.*, **103**, 386–388.

187. Jiao, F., Qu, Y., Zhou, G. *et al.* (2010) Modulation of oxidative stress by functionalized fullerene materials in the lung tissues of female C57/BL mice with a metastatic Lewis lung carcinoma. *J. Nanosci. Nanotechnol.*, **10**, 8632–8637.

188. NIEHS NTP (2012) NTP Range-Finding Report: Immunotoxicity of C60 Fullerene in Female Wistar Han Rats (CASRNL 99685-96-8), http://ntp.niehs.nih.gov/testing/types/imm/abstract/i20710i20407/index.html (accessed 20 April 2015).

189. NIEHS NTP (2012) NTP Range-Finding Report: Immunotoxicity of C60 Fullerene in Female B6C3F1 Mice (CASRN 99685-96-8), http://ntp.niehs.nih.gov/testing/types/imm/abstract/i20710i20407/index.html (accessed 20 April 2015).

190. Yamago, S., Tokuyama, H., Nakamura, E. *et al.* (1995) In vivo biological behaviour of a water-miscible fullerene: 14C labelling, absorption, distribution, excretion and acute toxicity. *Chem. Biol.*, **2**, 385–389.

191. Bullard-Dillard, R., Creek, K.E., Scrivens, W.A. *et al.* (1996) Tissue sites of uptake of 14C labelled C60. *Bioorg. Chem.*, **24**, 376–385.

192. Gharbi, N., Pressac, M., Hadchouel, M. *et al.* (2005) [60]Fullerene is a powerful antioxidant in vivo with no acute or subacute toxicity. *Nano Lett.*, **5**, 2578–2585.

193. Folkmann, J.K., Risom, L.R., Jacobsen, N.R. *et al.* (2009) Oxidatively damaged DNA in rats exposed by oral gavage to C60 fullerenes and single-walled carbon nanotubes. *Environ. Health Perspect.*, **117**, 703–708.

194. Totsuka, Y., Higuchi, T., Imai, T. *et al.* (2009) Genotoxicity of nano/microparticles in in vitro micronuclei, in vivo comet and mutation assay system. *Part. Fibre Toxicol.*, **6**, 23.
195. Ema, M., Tanaka, J., Kobayashi, N. *et al.* (2012) Genotoxicity evaluation of fullerene C60 nanoparticles in a comet assay using lung cells of intratracheally instilled rats. *Regul. Toxicol. Pharm.*, **62** (3), 419–424.
196. Jacobsen, N.R., Pojana, G., White, P. *et al.* (2008) Genotoxicity, cytotoxicity, and reactive oxygen species induced by single-walled carbon nanotubes and C60 fullerenes in the FE1-Muta™mouse lung epithelial cells. *Environ. Mol. Mutagen.*, **49**, 476–487.
197. Liu, Y., Jiao, F., Qiu, Y. *et al.* (2009) Immunostimulatory properties and enhanced TNF-a mediated cellular immunity for tumor therapy by C60(OH)20 nanoparticles. *Nanotechnology*, **20** (41), 415102.
198. Zogovic, N.S., Nikolic, N.S., Vranjes-Djuric, S.D. *et al.* (2009) Opposite effects on nanocrystalline fullerene (C60) on tumor cell growth in vitro and in vivo and a possible role of immunosuppression in the cancer-promoting activity of C(60). *Biomaterials*, **30** (36), 6940–6946.
199. Wang, D., Sun, L., Liu, W. *et al.* (2009) Photoinduced DNA cleavage by α-, β-, and γ-cyclodextrin- bicapped C60 supramolecular complexes. *Environ. Sci. Technol.*, **43**, 5825–5829.
200. Zhao, B., He, Y.Y., Bilski, P.J. *et al.* (2008) Pristine (C60) and hydroxylated [C60(OH)24] fullerene phototoxicity towards HaCaT keratinocytes: type I vs type II mechanisms. *Chem. Res. Toxicol.*, **21** (5), 1056–1063.
201. Babynin, E.V., Nuretdinov, I.A., Gubskaya, V.P. *et al.* (2002) Study of mutagenic activity of fullerene and some of its derivatives using His+ reversions of salmonella typhimurium as an example. *Russ. J. Genet.*, **38** (4), 453–457.
202. Sera, N., Tokiwa, H., and Miyata, N. (1996) Mutagenicity of the fullerene C60-generated singlet oxygen dependent formation of lipid peroxides. *Carcinogenesis*, **17** (10), 2163–2169.
203. Mrdanović, J., Šolajić, S., Bogdanović, V. *et al.* (2009) Effects of fullerenol C60(OH)24 on the frequency of micronuclei and chromosome aberrations in CHO-K1 cells. *Mutat. Res.*, **680**, 25–30.
204. Xu, A., Chai, Y., Nohmi, T. *et al.* (2009) Genotoxic responses to titanium dioxide nanoparticles and fullerene in gpt delta transgenic MEF cells. *Part. Fibre Toxicol.*, **6**, 3.
205. Dhawan, A., Taurozzi, J.S., Pandey, A.K. *et al.* (2006) Stable colloidal dispersions of C60 fullerenes in water: evidence for genotoxicity. *Environ. Sci. Technol.*, **40**, 7394–7401.
206. Niwa, Y. and Iwai, N. (2006) Genotoxicity in cell lines induced by chronic exposure to water soluble fullerenes using micronucleus test. *Environ. Health Prev. Med.*, **11**, 292–297.
207. Sayes, C.M., Fortner, J.D., Guo, W. *et al.* (2004) The differential cytotoxicity of water-soluble fullerenes. *Nano Lett.*, **4**, 1881–1887.
208. Sayes, C.M., Gobin, A.M., Ausman, K.D. *et al.* (2005) Nano-C60 cytotoxicity is due to lipid peroxidation. *Biomaterials*, **26**, 7587–7595.
209. Rouse, J.G., Yang, J., Barron, A.R. *et al.* (2006) Fullerene-based amino acid nanoparticle interactions with human epidermal keratinocytes. *Toxicol. in Vitro*, **20**, 1313–1320.
210. Kamat, J.P., Devasagayam, T.P.A., Priyadarsini, K.I. *et al.* (2000) Reactive oxygen species mediated membrane damage induced by fullerene derivatives and its possible biological implications. *Toxicology*, **155**, 55–61.
211. Xia, T., Kovochich, M., Brant, J. *et al.* (2006) Comparison of the abilities of ambient and manufactured nanoparticles to induce cellular toxicity according to an oxidative stress paradigm. *Nano Lett.*, **6** (8), 1794–1807.
212. Sanchez, V.C., Jachak, A., Hurt, R.H. *et al.* (2012) Biological interactions of graphene-family nanomaterials: an interdisciplinary review. *Chem. Res. Toxicol.*, **25** (1), 15–34.

213. Soldano, C., Mahmood, A., and Dujardin, E. (2010) Production, properties and potential of graphene. *Carbon*, **48**, 2127–2150.
214. Zhang, Y., Petibone, D., Xu, Y. *et al.* (2014) Toxicity and efficacy of carbon nanotubes and graphene: the utility of carbon-based nanoparticles in nanomedicine. *Drug Metab. Rev.*, **46** (2), 232–246.
215. Guo, X. and Mei, N. (2014) Assessment of the toxic potential of graphene family nanomaterials. *J. Food Drug Anal.*, **22** (1), 105–115.
216. Nezakati, T., Cousins, B.G., and Selfallan, A.M. (2014) Toxicology of chemically modified graphene-based materials for medical application. *Arch. Toxicol.*, **88**, 1987–2012.
217. Seabra, A.B., Paula, A.J., de Lima, R. *et al.* (2014) Nanotoxicity of graphene and graphene oxide. *Chem. Res. Toxicol.*, **27** (2), 159–168.
218. Yang, K., Li, Y., Tan, X. *et al.* (2013) Behavior and toxicity of graphene and its functionalized derivatives in biological systems. *Small*, **9** (9–10), 1492–1503.
219. Ren, H., Wang, C., Zhang, J. *et al.* (2010) Dna cleavage system of nanosized graphene oxide sheets and copper ions. *ACS Nano*, **4**, 7169–7174.
220. Duch, M.C., Budinger, G.R., Liang, Y.T. *et al.* (2011) Minimizing oxidation and stable nanoscale dispersion improves the biocompatibility of graphene in the lung. *Nano Lett.*, **11** (12), 5201–5207.
221. Wang, K., Ruan, J., Song, H. *et al.* (2010) Biocompatibility of graphene oxide. *Nanoscale Res. Lett.*, **6**, 8.
222. Ma-Hock, L., Strauss, V., Treumann, S. *et al.* (2013) Comparative inhalation toxicity of multi-wall carbon nanotubes, graphene, graphite nanoplatelets and low surface carbon black. *Part. Fibre Toxicol.*, **10**, 23.
223. Schinwald, A., Murphy, F.A., Jones, A. *et al.* (2012) Graphene-based nanoplatelets: a new risk to the respiratory system as a consequence of their unusual aerodynamic properties. *ACS Nano*, **6**, 736–746.
224. Schinwald, A., Murphy, F., Askounis, A. *et al.* (2014) Minimal oxidation and inflammogenicity of pristine graphene with residence in the lung. *Nanotoxicology*, **8**, 824–832.
225. Shin, J.H., Han, S.G., Kim, J.K. *et al.* (2015) 5-day repeated inhalation and 28-day post-exposure study of graphene. *Nanotoxicology*, **9** (8), 1023–1031.
226. IARC (1999) *Monographs on the Evaluation of Carcinogenic Risks to Humans*, Surgical Implants and Other Foreign Bodies, vol. 74, International Agency for Research on Cancer/World Health Organization, Lyon.
227. Okada, F. (2007) Beyond foreign-body-induced carcinogenesis: impact of reactive oxygen species derived from inflammatory cells in tumorigenic conversion and tumor progression. *Int. J. Cancer*, **121**, 2364–2372.
228. Kirkpatrick, C.J., Alves, A., Kohler, H. *et al.* (2000) Biomaterial-induced sarcoma: a novel model to study preneoplastic change. *Am. J. Pathol.*, **156**, 1455–1467.
229. Choi, J., Curtis, S.J., Roy, D.M. *et al.* (2010) Local mesenchymal stem/progenitor cells are a preferential target for initiation of adult soft tissue sarcomas associated with p53 and Rb deficiency. *Am. J. Pathol.*, **177**, 2645–2658.
230. Blanchard, K.T., Barthel, C., French, J.E. *et al.* (1999) Transponder-induced sarcoma in the heterozygous p53+/- mouse. *Toxicol. Pathol.*, **27**, 519–527.
231. Bonner, J.C. (2010) Mesenchymal cell survival in airway and intersititial pulmonary fibrosis. *Fibrogenesis Tissue Repair*, **3**, 15.
232. Pierro, M. and Thebaud, B. (2010) Mesenchymal stem cells in chronic lung disease: culprit or savior? *Am. J. Physiol. Lung Cell Mol. Physiol.*, **298**, L732–L734.
233. Marriott, S., Baski, r.R.S., Gaskill, C. *et al.* (2014) ABCG2^{pos} lung mesenchymal stem cells area novel pericyte subpopulation that contributes to fibrotic remodeling. *Am. J. Physiol., Cell Physiol.*, **307**, C684–C698.
234. Luanpitpong, S., Wang, L., Castranova, V. *et al.* (2014) Induction of stem-like cells with fibrogenic properties by

carbon nanotubes and its role in fibrogenesis. *Nano Lett.*, **14** (6), 3110–3116.

235. Zhang, Y., Ali, S.F., Dervishi, E. *et al.* (2010) Cytotoxicity effects of graphene and single-wall carbon nanotubes in neural phaeochromocytoma-dervied PC12 cells. *ACS Nano*, **4**, 3181–3186.

236. Li, Y., Liu, Y., Fu, Y. *et al.* (2012) The triggering of apoptosis in macrophages by pristine graphene through the MAPK and TGF-beta signaling pathways. *Biomaterials*, **33**, 402–411.

237. Tu, Y., Lv, M., Xiu, P. *et al.* (2013) Destructive extraction of phospholipids from Escherichia coli membranes by graphene nanosheets. *Nat. Nanotechnol.*, **8**, 594–601.

238. Dallavalle, M., Calvaresi, M., Bottoni, A. *et al.* (2015) Graphene can wreak havoc with cell membranes. *ACS Appl. Mater. Interfaces*, **7**, 4406–4414.

239. Chang, Y., Yang, S.T., Liu, J.H. *et al.* (2011) In vitro toxicity evaluation of graphene oxide on A549 cells. *Toxicol. Lett.*, **200**, 201–210.

240. Wan, B., Wang, Z.X., Lv, Q.Y. *et al.* (2013) Single-walled carbon nanotubes and graphene oxides induce autophagosome accumulation and lysosome impairment in primarily cultured murine peritoneal macrophages. *Toxicol. Lett.*, **221**, 118–127.

241. Ivask, A., Voelcker, N.H., Seabrook, S.A. *et al.* (2015) DNA melting and genotoxicity induced by silver nanoparticles and graphene. *Chem. Res. Toxicol.*, **28** (5), 1023–1035.

242. Hinzmann, M., Jaworski, S., Kutwin, M. *et al.* (2014) Nanoparticles containing allotropes of carbon have genotoxic effects on glioblastoma multiforme cells. *Int. J. Nanomed.*, **9**, 2409–2417.

243. Sasidharan, A., Panchakarla, L.S., Chandran, P. *et al.* (2011) Differential nano-bio interactions and toxicity effects of pristine versus functionalized graphene. *Nanoscale*, **3**, 2461–2464.

244. Wang, A., Pu, K., Dong, B. *et al.* (2013) Role of surface charge and oxidative stress in cytotoxicity and genotoxicity of graphene oxide towards human lung fibroblast cells. *J. Appl. Toxicol.*, **33** (10), 1156–1164.

245. Hu, W., Peng, C., Lv, M. *et al.* (2011) Protein corona-mediated mitigation of cytotoxicity of graphene oxide. *ACS Nano*, **5**, 3693–3700.

246. Chatterjee, N., Eom, H.J., and Choi, J. (2014) A systems toxicology approach to the surface functionality control of graphene-cell interactions. *Biomaterials*, **35**, 1109–1127.

247. Qiao, Y., An, J., and Ma, L. (2013) Single cell array based assay for in vitro genotoxicity study of nanomaterials. *Anal. Chem.*, **85**, 4107–4112.

248. De Marzi, L., Ottaviano, L., Perrozzi, F. *et al.* (2014) Flake size-dependent cyto and genotoxic evaluation of graphene oxide on in vitro A549, Caco2 and vero cell lines. *J. Biol. Regul. Homeost. Agents*, **28**, 281–289.

249. Ryu, H.W., Lee, D.H., Won, H.R. *et al.* (2015) Influence of toxicologically relevant metals on human epigenetic regulation. *Toxicol. Res.*, **31** (1), 1–9.

250. Methner, M.M., Birch, M.E., Evans, D.E. *et al.* (2007) Identification and characterization of potential sources of worker exposure to carbon nanofibers during polymer composite laboratory operations. *J. Occup. Environ. Hyg.*, **4** (12), D125–D130.

251. Methner, M., Hodson, L., Dames, A. *et al.* (2010) Nanoparticle emission assessment technique (NEAT) for the identification and measurement of potential inhalation exposure to engineered nanomaterials— part B: results from 12 field studies. *J. Occup. Environ. Hyg.*, **7** (3), 163–176.

252. Murray, A.R., Kisin, E.R., Tkach, A.V. *et al.* (2012) Factoring-in agglomeration of carbon nanotubes and nanofibers for better prediction of their toxicity versus asbestos. *Part. Fibre Toxicol.*, **9**, 10.

253. Delorme, M.P., Muro, Y., Arai, T. *et al.* (2012) Ninety-day inhalation toxicity study with a vapor grown carbon nanofiber in rats. *Toxicol. Sci.*, **128** (2), 449–460.

254. Darne, C., Terzetti, F., Coulais, C. *et al.* (2010) In vitro cytotoxicity and transforming potential of industrial carbon dust (fibers and particles) in syrian hamster embryo (SHE) cells. *Ann. Occup. Hyg.*, **54** (5), 532–544.

255. Kisin, E.R., Murray, A.R., Sargent, L. *et al.* (2011) Genotoxicity of carbon nanofibers: are they potentially more or less dangerous than carbon nanotubes or asbestos? *Toxicol. Appl. Pharmacol.*, **252** (1), 1–10.

256. Wang, L., Castranova, V., Mishra, A. *et al.* (2010) Dispersion of single-walled carbon nanotubes by a natural lung surfactant for pulmonary in vitro and in vivo toxicity studies. *Part. Fibre Toxicol.*, **7**, 31.

257. Cohen, J.M., Teeguarden, J.G., and Demokritou, P. (2014) An integrated approach for the in vitro dosimetry of engineered nanomaterials. *Part. Fibre Toxicol.*, **11**, 20.

258. Benigni, R. (2012) Alternatives to the carcinogenicity bioassay for toxicity prediction: are we there yet? *Expert Opin. Drug Metab. Toxicol.*, **8**, 4.

259. Creton, S., Aardema, M.J., Carmichael, P.L. *et al.* (2012) Cell transformation assays for prediction of carcinogenic potential: state of the science and future research needs. *Mutagenesis*, **27**, 93–101.

260. OECD (2007) Detailed review on cell transformation assays for detection of chemical carcinogens, in *OECD Environment, Health and Safety*, Series on Testing and Assessment, vol. 31. OECD, Paris, France, 1–164.

261. Lee, J., Lilly, G.D., Doty, R.C. *et al.* (2009) In vitro toxicity testing of nanoparticles in 3D cell culture. *Small*, **5** (10), 1213–1221.

262. Bhise, N.S., Ribas, J., Manoharan, V. *et al.* (2014) Organ-on-a-chip platforms for studying drug delivery systems. *J. Controlled Release*, **190**, 82–93.

263. Snyder-Talkington, B.N., Dong, C., Zhao, X. *et al.* (2015) Multi-walled carbon nanotube-induced gene expression in vitro: concordance with in vivo studies. *Toxicology*, **328**, 66–74.

264. Endes, C., Schmid, O., Kinnear, C. *et al.* (2014) An in vitro testing strategy towards mimicking the inhalation of high aspect ratio nanoparticles. *Part. Fibre Toxicol.*, **11**, 40.

265. Chortarea, S., Clift, M.J., Vanhecke, D. *et al.* (2015) Repeated exposure to carbon nanotube-based aerosols does not affect the functional properties of a 3D human epithelial airway model. *Nanotoxicology*, **9** (8), 983–993.

266. Watson, C., Ge, J., Cohen, J. *et al.* (2014) High-throughput screening platform for engineered nanoparticle-mediated genotoxicity using CometChip technology. *ACS Nano*, **8**, 2118–2133.

267. Maslov, A.Y., Quispe-Tintaya, W., Gobacheva, T. *et al.* (2015) High-throughput sequencing in mutation detection: a new generation of genotoxicity tests? *Mutat. Res.* doi: 10.1016/j.mrfmmm.2015.03.014

268. Morimoto, Y., Izumi, H., and Kuroda, E. (2014) Significance of persistent inflammation in respiratory disorders induced by nanoparticles. *J. Immunol. Res.*, **2014**, 962871.

269. Tran, C.L., Buchanan, D., Cullen, R.T. *et al.* (2000) Inhalation of poorly soluble particles. II. Influence of particle surface area on inflammation and clearance. *Inhalation Toxicol.*, **12**, 1113–1126.

270. Kumar, A. and Dhawan, A. (2013) Genotoxic and carcinogenic potential of engineered nanoparticles: an update. *Arch. Toxicol.*, **87**, 1883–1900.

271. Godwin, H., Nameth, C., Avery, D. *et al.* (2015) Nanomaterial categorization for assessing risk potential to facilitate regulatory decision-making. *ACS Nano*, **9**, 3409–3417.

272. Nel, A.E. (2013) Implementation of alternative test strategies for the safety assessment of engineered nanomaterials. *J. Intern. Med.*, **274** (6), 561–577.

273. Snyder-Talkington, B., Pacurari, M., Dong, C. *et al.* (2013) Systematic analysis of multiwalled carbon nanotube-induced cellular signaling and gene expression in human small airway epithelial cells. *Toxicol. Sci.*, **133** (1), 79–89.

274. Husain, M., Saber, A.T., Guo, C. *et al.* (2013) Pulmonary instillation of low doses of titanium dioxide nanoparticles in mice leads to particle retention and gene expression changes in the absence of inflammation. *Toxicol. Appl. Pharmacol.*, **269** (3), 250–262.

275. Singh, S., Manshian, B., Jenkins, G.J. *et al.* (2009) Nanogenotoxicology: the DNA damaging potential of engineered nanomaterials. *Biomaterials*, **30**, 3891–3914.

276. Karlsson, H.L. (2010) The comet assay in nanotoxicology research. *Anal. Bioanal. Chem.*, **398**, 651–666.

277. Magdolenova, Z., Collins, A., Kumar, A. *et al.* (2014) Mechanisms of genotoxicity. A review of in vitro and in vivo studies with engineered nanoparticles. *Nanotoxicology*, **8**, 233–278.

278. Møller, P., Jensen, D.M., Christophersen, D.V. *et al.* (2015) Measurement of oxidative damage to DNA in nanomaterial exposed cells and animals. *Environ. Mol. Mutagen.*, **56** (2), 97–110.

279. Møller, P., Hemmingsen, J.G., Jensen, D.M. *et al.* (2015) Applications of the comet assay in particle toxicology: air pollution and engineered nanomaterials exposure. *Mutagenesis*, **30** (1), 67–83.

280. OECD (2014) *Genotoxicity of Manufactured Nanomaterials: Report of the OECD Expert Meeting*, Series on the Safety of Manufactured Nanomaterials, vol. 43. OECD, Paris, France, p. 1–37.

281. Landsiedel, R., Kapp, M.D., Schulz, M. *et al.* (2009) Genotoxicity investigations on nanomaterials: methods, preparation, and characterization of test material, potential artifacts and limitations-many questions, some answers. *Mutat. Res.*, **681**, 241–258.

11
Effect on Reproductive System of Carbon Nanomaterials[1]

Ying Liu and Chunying Chen

11.1
Introduction

Reproductive health is an important aspect of human individual and population growth. It is not only related to human reproduction but significantly affects the population quality and social development. Reproductive toxicity includes damages to organs of adult (female and male) reproductive and endocrine systems, adverse effects on reproductive function, abnormal hormone biosynthesis, and developmental toxicity/teratogenicity of the offspring. Reproductive toxicity is an important part of chemicals' risk evaluation. Since the 1960s, it has been highlighted that human reproduction rate was declining with the changes in industrial production and ecological environment. It is the consensus of academic and industrial circles that reproductive toxicity should be evaluated using more necessary and sufficient research activities.

In the past, reproductive epidemiological study often focused on females. Now, it is apparent that chemicals might affect the reproductive systems of both male and female [1–3]. However, it is quite difficult to evaluate the potential harm of exogenous substances on the reproductive system accurately because of the complexity of the reproductive process, the limitations of extrapolating animal experimental results to humans, and the representation of epidemiological data. The reproductive system is complex, regulated by the endocrine system cooperating with the nervous and immune systems, and maintains its own equilibrium via the hypothalamic–pituitary–gonadal axis controlled by precise positive and negative feedback mechanisms [4]. Xenobiotic interference to the hypothalamic or pituitary function may ultimately impair the reproductive processes, such as spermatogenesis or oogenesis, ejaculation or ovulation, hormone production by Leydig or granulosa cells, and the structure or function of epididymis or fallopian tube [5].

1) This chapter has been partly modified to feature as a Review: Lu, X., Liu, Y., Kong, X., Lobie, P. E., Chen, C., and Zhu, T. (2013) Nanotoxicity: a growing need for study in the endocrine system, Small 9, 1654—1671.

Biomedical Applications and Toxicology of Carbon Nanomaterials, First Edition.
Edited by Chunying Chen and Haifang Wang.

Nanotechnology is a new cutting-edge subject that has been developing since the 1980s. The rapid development of nanotechnology and nanomaterials has brought great challenges to human reproductive health. It is an important and relevant question whether nanomaterials disrupt reproductive health. Carbon nanomaterials, as typical nanomaterials, exhibit physical, chemical, and/or biological characteristics associated with a nanostructure [6], and are used in a variety of areas including advanced materials, electronics, biomedicine, pharmaceuticals, cosmetics, energy, catalysis, environmental detection and monitoring, and so on [7, 8]. With the commercialization of products containing carbon nanomaterials, the potential exposure is likely to increase considerably in the future [6]. Nanomaterials might enter the body through the lungs, skin, or intestinal tract with further translocation to other tissues. And many nanomaterials cannot be effectively eliminated and therefore accumulate in the body for a long time [9, 10]. There is a knowledge gap between the increasing development and use of nanomaterials and the prediction of possible health risks.

In recent years, studies have suggested that some nanomaterials exert adverse effects on different organs, such as the liver, lung, kidney [9, 11], and even the central nervous system [12]. And reproductive toxicity of carbon nanomaterials has been noted as adverse effects of environmental chemicals [13]. It is reported that nanoparticles (NPs) could pass through biological membranes and affect the physiology of any cell in the body [10, 14], with the size, surface, and interface of nanomaterials having a particularly important influence. Unsurprisingly, the possibility of nanoparticles entering biological systems is of great concern because of the possibility of reproductive toxicity. Exposure to nanomaterials may disrupt endocrine functions such as dysregulation of serum sex hormone levels. And nanomaterials may prevent reproduction via various mechanisms.

Here, we summarize and review recent work on the reproductive and developmental effects of carbon nanomaterials, including carbon nanotubes (single-walled carbon nanotubes, (SWCNTs); multi-walled carbon nanotubes MWCNTs), fullerenes (C_{60}, C_{70}, etc.)/fullerene derivatives, graphenes, nanodiamonds, and carbon black (CB), in an attempt to understand the currently identified issues and potentially delineate further required studies in this field.

11.2 Effects of Carbon Nanomaterials on the Reproductive System

Because of the emerging applications of carbon nanomaterials, the potential toxicity of carbon nanomaterials has aroused much attention. For instance, pristine graphene was reported to trigger macrophage apoptosis and stimulate cytokine secretion [15, 16]. However, in another study no evidence of toxicity was detected despite the persistence of SWCNTs within the liver and spleen macrophages for 4 months [17]. Hence, some carbon nanomaterials may possess potential toxicity, while others may not. Adverse effects of carbon nanomaterials on human health often depend on their chemical structure, size, shape, and

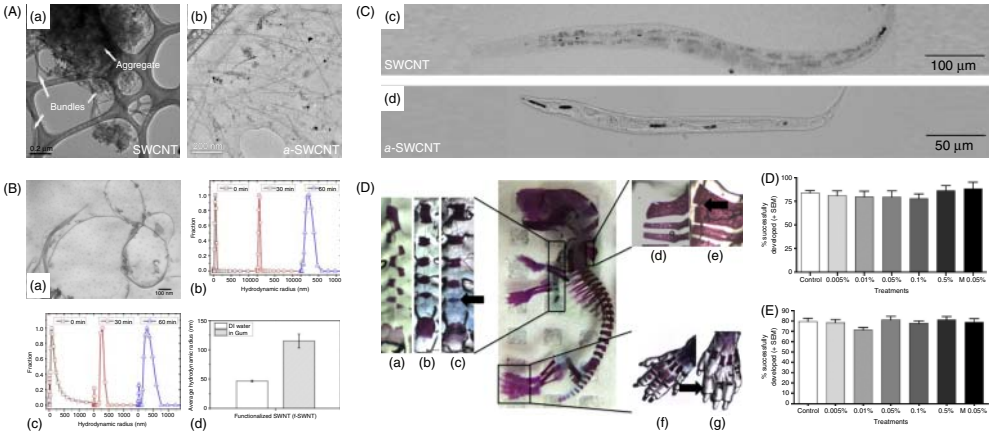

Figure 11.1 Effects of CNTs on the reproductive system. (A) Characterization of SWNCTs and a-SWCNTs. Representative TEM images of SWCNTs (a) and a-SWCNTs (b) dissolved in NGM medium. L1 worms were cultured in NGM medium with SWCNTs (c) or a-SWCNTs (500 mg ml^{-1}) (d) for 48 h and subjected to microscopic observation. Both SWCNTs and a-SWCNTs were observed in the pharynx, intestine lumen, and anus [18]. (B) Representative TEM images showing SWCNTs in 0.5% (w/v) tragacanth gum solution (a). Cluster size distribution of SWCNTs in deionized water (b). Cluster size distribution of SWCNTs in 0.5% tragacanth gum (c). Bar graph showing the average hydrodynamic radii for SWCNTs (d). (C) Skeletal abnormalities observed in CD-1 mouse fetuses (GD 19) following prenatal exposure to 10 mg kg^{-1} SWCNTs. (a) Crankshaft sternebrae (misaligned; 10 mg kg^{-1} SWCNTs); (b) control sternebrae; (c) reduced ossification of sternebrae (10 mg kg^{-1} SWCNTs); (d) control cervical vertebrae; (e) forked cervical vertebrae (10 mg kg^{-1} SWCNTs); (f) control phalanges; (g) reduced ossification of phalanges (10 mg kg^{-1} SWCNTs). Arrows point to skeletal abnormalities. (D) The effect of parental SWCNTs exposure on egg and larval development of Drosophila. (E) The effect of direct exposure of the eggs/larvae to SWCNTs (M: microparticle graphite size control) [19].

agglomeration state, which should be considered for the study of the toxic effects in the reproductive system.

11.2.1 Carbon Nanotubes

Carbon nanotubes (CNTs) are widely used nanomaterials in industry and biomedicine, such as electronics, food packaging, and as drug delivery vehicles. Highly soluble, amide-modified SWCNTs (a-SWCNTs) were efficiently taken up by worms and caused defective embryogenesis (Figure 11.1A) [18]. Only pristine-multiwalled carbon nanotubes (p-MWCNTs) exerted significant reduction in the reproductive capacity of *Caenorhabditis elegans*, while the carboxylated (COOH)-MWCNT was found most cytotoxic and genotoxic among all the surface-functionalized MWCNTs following hydroxylation–oxygenation (O(+)), amination (NH_2), or carboxylation (COOH) of the CNTs. The order of sensitivity was COOH > O(+) > NH_2 > pristine [20]. While hydroxylated CNTs had no

measurable impact on *Drosophila*, a single oral dose of 10 mg kg^{-1} administered to pregnant CD-1 dams during organogenesis significantly increased the number of resorptions and resulted in fetal morphological and skeletal abnormalities (Figure 11.1 B–E and Tables 11.1, 11.2) [19]. Surface functionalization significantly influenced the bioactivity of MWCNTs, which displayed species as well as target-organ specificity. The mechanisms underlying these specific modes of nanomaterial–biological interactions need to be elucidated.

A recent study investigated the effects of water-soluble MWCNTs on the testis. MWCNTs accumulated in the testes 24 h after a single dose (5 mg kg^{-1} per dose). After five doses over 13 days, MWCNTs caused oxidative stress and decreased germinative layer thickness at day 15, but not at days 60 and 90 [21]. Furthermore, the serum levels of the follicle stimulating hormone (FSH), luteinizing hormone (LH), and testosterone, as well as spermatogenesis, were not affected throughout the 90-day period (Figure 11.2A, B). The treated mice continued mating with healthy female mice to produce healthy offspring. Hence, it was concluded that repeated administrations of CNTs in male mice produce reversible testis damage without affecting fertility. However, oxidative stress and alterations in the testes, such as decreased germinative layer thickness and vacuolization of Sertoli cells, have raised concerns because it is possible that these materials may lead to adverse effects on male fertility as a result of accumulated oxidative stress at higher quantities over a longer period.

Another study on the potential embryotoxicity of SWCNTs in mammals provided evidence that CNTs may possess endocrine-disrupting characteristics. The effects of pristine single-walled carbon nanotubes (p-SWCNTs) and oxidized single-walled carbon nanotubes (o-SWCNTs) on the development of the mouse embryo were examined. Figure 11.2C–F shows that after injection at a relatively high dose (30 μg per mouse) at GD 5.5, all SWCNTs induced gross fetal morphological abnormalities: for instance, limbs appeared severely retarded in their development at GD 15.5. In addition, a substantial percentage of SWCNT-exposed mice (ranging from 19% to 31%) presented swollen uteri (at least twice the diameter of a nonpregnant normal uterus) with no developed embryos, a finding not observed in control females and which was interpreted as evidence of early fetal resorption. At lower doses of SWCNTs, the percentage of females with early resorption greatly decreased, but the percentage of mothers with malformed fetuses increased. Further lowering the dosage (0.3 and 0.1 μg per mouse) resulted in no observed miscarriages, but fetuses with gross malformations were still present. Extensive vascular lesions and increased production of reactive oxygen species (ROS) were detected in the placentae of malformed fetuses but not in normal fetuses. Increased ROS levels were likewise detected in malformed fetuses. No increase in ROS production or morphological alterations were observed in maternal tissues. In parallel, o-SWCNT embryotoxicity was evaluated using the embryonic stem cell test, a validated *in vitro* assay developed for predicting embryotoxicity of soluble chemical compounds. The results showed that o-SWCNTs are more toxic to embryonic stem cells than p-SWCNTs. Hence, SWCNT treatment leads reproductive abnormalities [22].

Table 11.1 Assessment of the teratogenic effects of SWCNTs in CD-1 mice exposed prenatally at day 19 [19].

Treatment	Number of litters examined	Mean litter size (±SD)	Mean maternal weight change (g) (±SD)	Number of fetuses examined	Mean fetal weight (g) (±SD)	Mean fetal length (cm) (±SD)	Percentage of total fetuses with gross morphological defects (±SE)	Percentage of total implantations that were resorptions (±SE)	Percentage of total fetuses that were nonviable (±SE)
Control	10	12.3 ± 2.2	26.5 ± 4.6	127	1.39 ± 0.1	2.56 ± 0.1	0	0.8 ± 0.8	0.8 ± 0.8
$10\,mg\,kg^{-1}$	12	11.9 ± 4.1	28.2 ± 5.7	155	1.35 ± 0.1	2.54 ± 0.1	$3.9 \pm 1.5^{*}$	$5.8 \pm 1.8^{*}$	3.2 ± 1.4
$100\,mg\,kg^{-1}$	12	13.1 ± 1.3	29.0 ± 3.6	156	1.37 ± 0.1	2.54 ± 0.1	0	2.5 ± 1.2	0

*Significant difference ($p < 0.05$).

Table 11.2 Skeletal analysis of CD-1 fetuses prenatally exposed to SWCNTs [19].

Treatment	Number of fetuses evaluated	Percent of fetuses with defects (±SE)	Number of defects of type							
			Clavicle	Phalanges of hindlimb	Phalanges of forearm	Sternebrae	Cervical vertebrae	Braincase	Palate	Other
Control	88	8.0 ± 2.9	1	1	0	2	3	0	1	0
10 mg kg^{-1}	122	23.0 ± 3.8*	2	13	8	9	7	0	0	3
100 mg kg^{-1}	124	11.3 ± 2.8	2	0	0	5	4	0	3	1

*Significant difference ($p < 0.05$).

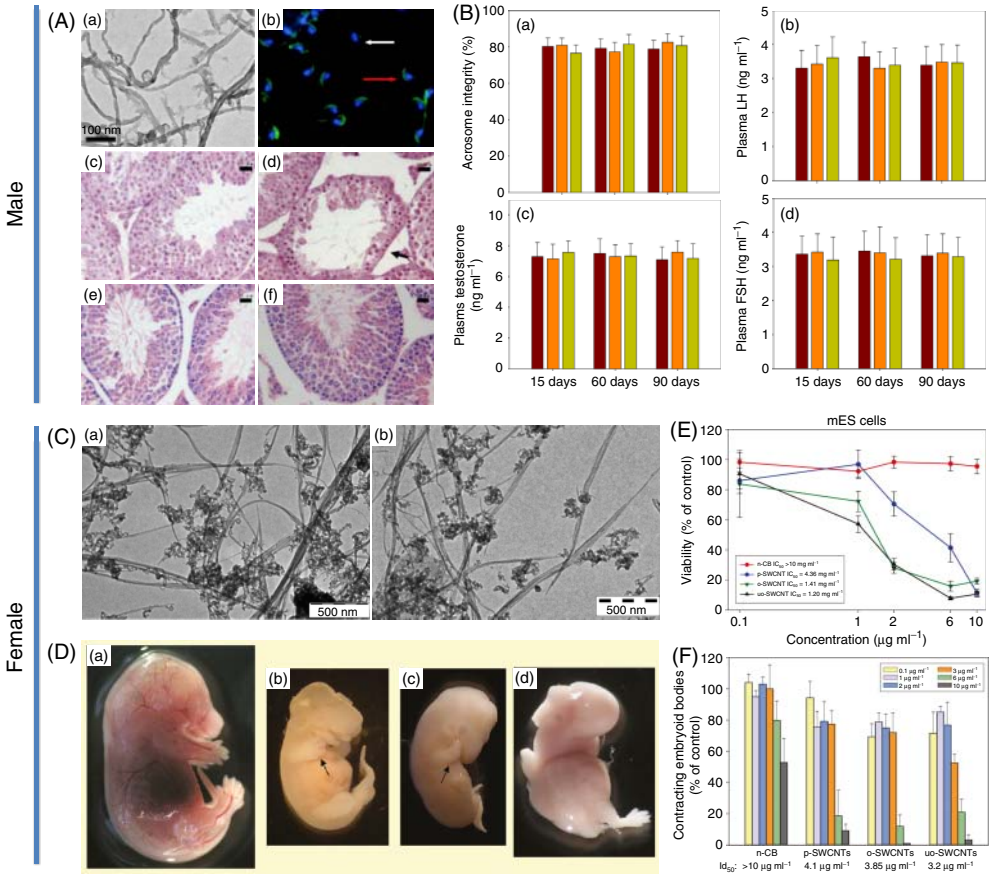

Figure 11.2 Carbon nanotubes induce differential effects on reproductive organs between male mice and female pregnant mice. (A, B) Repeated carbon nanotube administrations in male mice cause reversible testis damage without affecting fertility. (A) The TEM image of MWCNTs (a), the fluorescence image of sperm nuclei and acrosomes labeled with Hoechst 33 258 and FITC–PSA, respectively (b) and histology cross sections of seminiferous tubules from testes of control mice (c) and mice with five doses of MWCNT-COOH treatment at days 15 (d), 60 (e), and 90 (f). Red arrow: an intact acrosome; White arrow: incomplete one. All scale bars are 20 μm. (B) Statistical analysis of acrosome integrity of control and MWCNT-treated mice (a) and ELISA assay to measure LH (b), plasma testosterone (c), and FSH (d) levels in the blood in different groups. (C–F) Low doses of pristine and oxidized SWCNTs affect mammalian embryonic development [21]. (C) TEM images of p-SWCNTs (a) and o-SWCNTs (b). SWCNTs appear organized in bundles of different length. (D) Images refer to 0.3 μg CNT/mouse exposed fetuses, but similar phenotypes were observed at all other effective doses tested. (a) Normal fetus. (b, c) malformed fetuses recovered from p- and o-SWCNT-treated mothers, respectively. Arrows indicate limbs that appear severely retarded in their development. (d) Swollen fetuses missed the crown-rump organization and appeared folded, with swollen abdomen. (E, F) Summary of the EST results. (E) Viability of mES cells in the presence of increasing concentrations of n-CB and SWCNTs was measured using the WST-1 assay. The IC50 values are reported in boxes at the lower left corner. (F) The ID50 for each material is reported at the bottom of the graph. Values are means ± standard error of at least five independent experiments [22].

11.2.2
Fullerene Derivatives

Fullerene is any molecule entirely in the form of a hollow sphere, ellipsoid, or tube. The first fullerene discovered is known as buckminsterfullerene [23]. A number of functionalized fullerene derivatives have been widely investigated in biological applications after the main problem of poor solubility in the cellular environment was solved by chemical or supramolecular approaches [24–28].

Bal *et al.* [29] observed that hydrated C_{60} (C_{60}HyFn) protected the reproductive function in streptozotocin–diabetic male rats. Streptozotocin (STZ) has long been used for generating experimental diabetes in animals, which closely mimics type I diabetes in humans [30]. Because of its toxicity toward β-cells in the pancreatic islets, STZ treatment mainly shows signs of hyperglycemia producing short- and long-term diabetic complications. In their work [29], the authors noticed marked histopathological changes, including degeneration, desquamation, disorganization, and reduction in germinal cells in the control group. Interstitial edema and congestion were also evident in the testes of diabetic rats. C_{60}HyFn treatment resulted in recovery of histopathological changes, such as salvaged apoptosis in testes. Interestingly, whereas the STZ-diabetes group exhibited lowest levels of testosterone and cholesterol, there was no significant difference in the serum between control and C_{60}HyFn groups. In addition, administration of C_{60}HyFn resulted in significant corrective effects. Since testosterone is derived from cholesterol, and administration of C_{60}HyFn resulted in a marked elevation of cholesterol levels (Figure 11.3), it may be suggested that hydrated C_{60} promotes testosterone production by increasing the conversion of cholesterol to testosterone by Leydig cells [29].

Interestingly, another study showed that a highly hydroxylated fullerene (HHF; $C_{60}(OH)_{36}$) also inhibited oxidative stress in adipocytes and adipogenesis-related macrophage activation in adipose tissues. This study implies that HHF might be potentially useful for the therapy of metabolic syndrome and other obesity-related diseases. However, no in-depth study, such as the determination of hormone levels, was performed in this study [31].

11.2.3
Carbon Black Nanoparticles

Carbon black (CB) is a kind of low-solubility particle produced industrially from incomplete thermal decomposition of hydrocarbons. CB particles are complex, with a degenerated graphitic crystallite structure, and high-power electron micrographs clearly show irregular layered graphitic plates [32]. In a study of CB-associated endocrine toxicity, three sizes (14, 56, and 95 nm) of CB were administered intratracheally (0.1 mg per mouse 10 times every week) to male mice, to determine possible adverse effects on reproduction. Serum testosterone levels were significantly elevated in the groups exposed to 14- and 56-nm CB but not in 95-nm CB group. Partial vacuolation of Sertoli

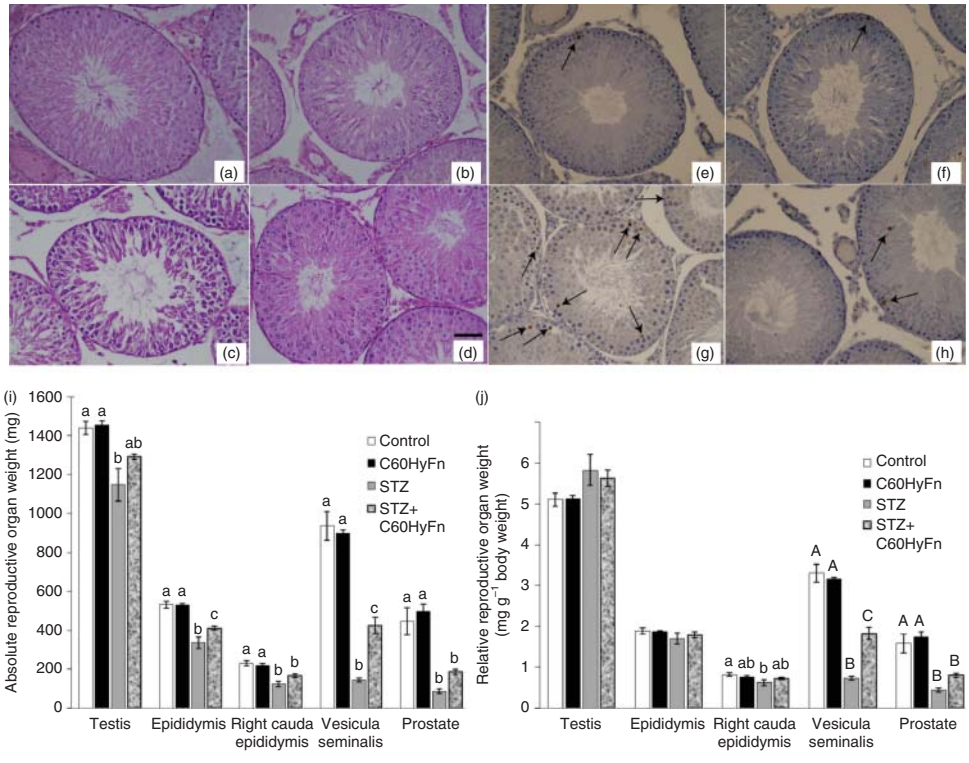

Figure 11.3 Hydrated C_{60} can protect testes from STZ damage and rescue serum hormone levels. (a–d) Histological sections of rat testes. (c) Disorganization, degeneration, and interstitial edema and capillary congestion in STZ-diabetes group compared to normal histological appearance of seminiferous tubules in control group (a) and C_{60}HyFn group (b). (d) Ameliorated histopathological changes observed in STZ-diabetes + C_{60}HyFn group compared to STZ-diabetes group. (e–h) Apoptotic nuclei were occasionally observed in the testis of control by TUNEL assay (e) and C_{60}HyFn-administered rats (f). (i, j) show absolute (i) and relative (j) weights of reproductive organs including testis, epididymis, right cauda epididymis, vesicular seminalis, and prostate [29].

cells (in which testosterone is produced in male animals) was observed in all the CB-exposed groups (14, 56, and 95 nm) [33]. Hence this study provided evidence that CB, a type of carbon-based nanomaterial, does indeed inflict adverse effects on the endocrine system. In contrast, in another study by the same group, 14-nm carbon nanoparticles were administered intravenously (i.v.) to pregnant mice on days 7 and 14 of gestation, and reproductive function of the male offspring was determined at age 5, 10, and 15 weeks after birth. Daily sperm production (DSP) was significantly decreased in fetal CB-exposed mice even at the age of 15 weeks. However, CB administration has no marked effect on the body weight, testicular weight, epididymal weight, or serum testosterone levels in mice exposed *in utero* to carbon NPs compared with mice of the control group [34]. Whether such reduced DSP should lead to impaired infertility is unknown. Thus further

systematic investigations of possible reproductive toxicity induced by carbon NPs are warranted.

11.3 Insights into the Molecular Mechanisms

It is interesting to further discuss and summarize the mechanisms whereby carbon nanomaterials affect reproductive system. Hormone-elicited signaling events involve biosynthesis, storage and secretion, transport to the target cells, recognition by receptor proteins, signal relay and cascades, homeostatic negative feedback loop to reduce hormone levels or functionality, and hormone metabolism [35]. Carbon nanomaterials may disrupt the reproduction and development at all of these stages. We will further discuss the biological mechanisms utilized by different carbon nanomaterials to disturb the reproductive function.

11.3.1 Potential Toxicity to the Female Reproductive System

In a certain sense, female reproductive system is more important and vulnerable than the male system [36]. Because all oocytes are already present in her body before the female individual is born, the number of oocytes is very limited. No extra gametes can be produced after the oocytes are damaged endogenously or exogenously. Also, in addition to providing half of the hereditary material, females also undertake the important mission of converting a fertilized egg to a complete embryo and then to produce a healthy baby. The regular cycle change, which is regulated strictly by the endocrine and nervous systems, is the basic characteristic of the female reproductive system [37].

Ovary is an important steroidogenic endocrine organ of the female and is related to the female reproductive capacity directly. It is currently known that two types of harm can affect a woman's reproductive health. One is the injury to the hypothalamic–pituitary–ovary gonadal axis [38]. The other is direct toxicity to ovary itself [39]. Because of the strict regulation of the female estrous cycle, the hypothalamic–pituitary–ovary gonadal axis has a dominant influence on the differentiation, maturation, and ovulation of the ovarian follicles. Many materials that damage female reproductive health can directly affect the pattern and rhythm of regular estrous cycle [37, 40].

At present, some articles on female reproductive safety and nanomaterials have been reported. Titanium dioxide nanoparticle was found to be toxic to follicular development and oocyte maturation *in vitro* [41]. Calcium phosphate nanoparticles influenced the cell cycle of human ovarian granulosa cells and induced apoptosis [42]. Gold nanoparticles increased the estrogen in rat ovarian granulosa cells [43]. But there are few reports on the effects of carbon nanomaterial exposure to the female reproductive system of mammals. Effects of carbon nanomaterials on the nematode *C. elegans* [44] and benthic organism

Table 11.3 Statistics of abortion rates after exposure to oxidized MWCNTs [48].

Group	Ectroma (colpo-bleeding)	Normal parturition	Average weight change before and after production (g)	Total abortion rate (%)
First o-MWCNTs	7	3	$8.57 \pm 8.95^{*}$	70
First control	1	9	20.73 ± 9.00	10
Second o-MWCNTs	4	6	13.99 ± 9.44	40
Second control	0	10	15.83 ± 4.24	0
Fourth o-MWCNTs	5	5	11.18 ± 5.82	50
Fourth control	3	7	12.72 ± 5.78	30

$^{*}p < 0.05$ compared with the control groups by ANOVA, all data represent means ± s.e.m.

Lumbriculus variegatus (Oligochaeta) [45] have been investigated. Survival, growth, reproduction, and feeding rates were measured to assess possible adverse effects of carbon nanomaterials. Given the limitation of present researches, *in vivo* experiments are of great significance to study the toxicity of nanomaterials to the female reproductive system.

The reproduction rate of *C. elegans* rapidly decreased by the uptake of 100 μg ml^{-1} fullerol nanoparticles [44]. *L. variegatus* was exposed to 10 and 50 mg fullerenes per kilogram sediment dry mass for 28 days. Worm reproduction was not impacted [45]. Reproduction (cocoon numbers) of *Eisenia fetida* was hindered only at very high pristine C_{60} concentrations (5% by weight) [46]. Female C57BL/6J mice were intratracheally instilled with 67 μg MWCNT, and the following day they were co-housed with mature males. A short delay in the delivery of the first litter was observed in the exposed females, which might be caused by lung inflammation due to particle exposure [47]. Oxidized multi-walled carbon nanotubes (o-MWCNTs) inhibited the maternal body weight, decreased the serum progesterone level, and increased the serum estradiol level (Figure 11.4 and Table 11.3) [48].

11.3.2
Potential Toxicity to Male Reproduction of Carbon Nanomaterials

Nearly one-fifth of couples in the world are infertile to different degrees, and the number continues to increase. It is feared that diseases of the reproductive system will become the third major social disease following the cardiovascular diseases and cancer in the future. The number, motility, and morphology of sperm decreased, respectively, by 0.7%, 0.3%, and 2.6% yearly [49]. Male reproductive problem has become a major issue [50]. At present, it is recognized that heavy metals, such as lead [51] and cadmium [52], and some reproductive endocrine hormone disruptors [53] can be hazardous to male reproductive health.

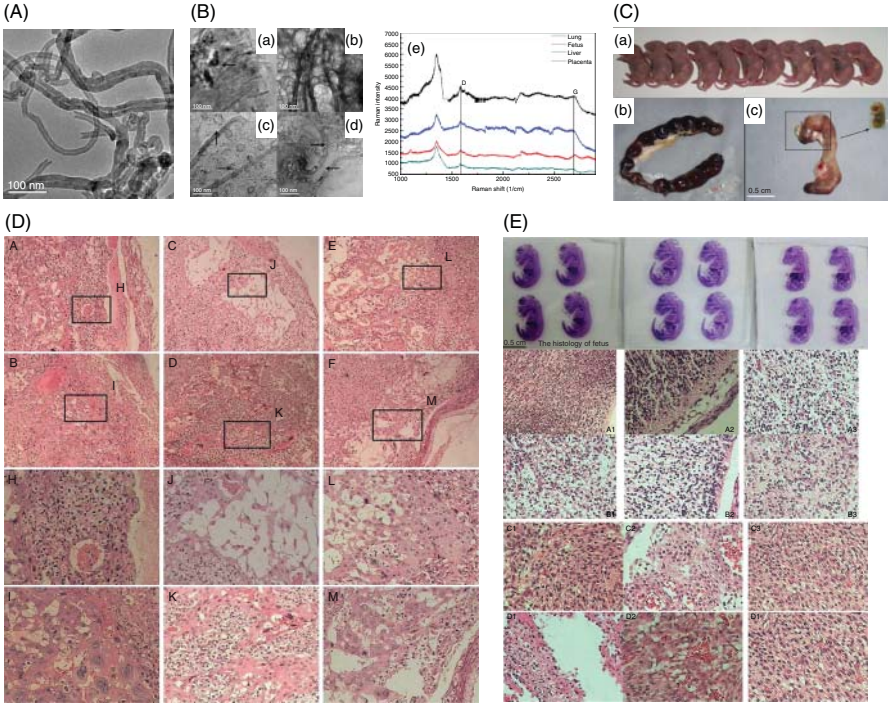

Figure 11.4 Effect of o-MWCNTs on fetal development. (A) TEM of o-MWCNTs. (B) The observed results of o-MWCNTs in TEM and Raman spectrum of tissues digestive solution. a, lung; b, liver; c, foetus; d, placenta. (C) The effect of o-MWCNTs (20 mg kg^{-1} bw) on fetal development after successive exposure to pregnant mice. (a) Fetus of the normal parturition, (b) fetus of abortion for the first pregnant mice, (c) fetus of abortion for the second and fourth pregnant mice. (D) Histology of placenta. (E) Histology of brain and heart of fetus. (A1–A3) Brain tissues for fetus of normal groups of first, second, and fourth pregnancy, respectively. (B1–B3) Brain tissues of fetus of exposure groups of first, second, and fourth pregnancy, respectively. (C1–C3) Heart tissues of fetus of normal groups of first, second, and fourth pregnancy, respectively. (D1–D3) Heart tissues of fetus of exposure groups of first, second, and fourth pregnancy, respectively [48].

Male reproductive toxicity can be caused by several mechanisms, including oxidative damage. Pathological changes of nearly all the male reproductive organs (including testes) are associated with excessive ROS generation [54]. Male sperm membrane is particularly rich in polyunsaturated fatty acids, in which two or more double bonds are very easy to be attacked by ROS. Sperm membrane fluidity will therefore change and sperm motility will become weak or even disappear [55]. Tyrosine, tryptophan, and ornithine in the enzymes related to sperm motility can be nitrated or thiol-oxidized by ROS, which makes these important enzymes to be inhibited and inactivated, affecting sperm movement. The mitochondria of sperms can also be impaired by ROS, which might damage or even kill the sperm, thereby resulting in a decline in male fertility [56].

Reproductive endocrine disorders cause male reproductive toxicity. Reproductive endocrine hormone disruptors affect the hypothalamus–pituitary–testis gonadal axis, which releases luteinizing and follicle-stimulating hormones (LH and FSH) or disrupts Leydig cells to produce testosterone [57, 58]. In addition, endocrine disruptors also damage testicular spermatogenesis directly or indirectly, including spermatogenic cell cytotoxicity and genotoxicity [59]. Damaged blood–testis barrier (BTB) or passage of substances through BTB will affect the normal spermatogenesis ability [60]. And the abnormality of male reproductive organs also affects sperm concentration and sperm motility.

In view of the importance of male reproductive health, and widespread use of nanomaterials, it is of great significance to carry out male reproductive toxicology of nanomaterials. Until 2008, reproductive toxicity of nanomaterials attracted considerable attention [61], but the male reproductive toxicology of nanomaterials was suggested only in 2010 [62]. Carboxyl CNT injection into the tail vein of male mice damaged testis tissue but did not affect the reproductive ability [21]. And nanoparticles such as diesel exhaust particles and CB caused cell toxicity to murine testis-constituent cells [63] and spermatogonial stem cells [64] *in vitro* and damaged mice testis *in vivo* [34]. CB nanoparticles had no direct effect on the induction of oxidative stress, because no effect of CB was found on the expression of HO-1 mRNA in the mouse Leydig cell line TM3 cells at up to 100 g ml^{-1} [63]. However, CB nanoparticles affected the production of steroid hormones in Leydig cells. Steroidogenic acute regulatory (StAR) mRNA expression was increased at 30 g ml^{-1} after incubation for 48 h [63].

11.3.3
Potential Toxicity to Offspring of Carbon Nanomaterials

Several classes of carbon nanomaterials have been shown to have multigenerational impacts once a parental generation has been exposed. Data from the present study indicate that carbon nanomaterials affect F1 and F2 generation after an F0 exposure.

It was demonstrated that carbon nanoparticles can cross the placental barrier and enter the fetus. ^{14}C-labeled C_{60} ($[^{14}C]$ C_{60}) got distributed to the placenta and fetuses of exposed pregnant dams and to the milk and pups of exposed lactating dams [65]. Some research showed no or little toxicity of carbon nanoparticles to dams and their pre- and postnatal offspring. After prenatal exposure to CB, female offspring were raised to maturity and mated with unexposed males. Expanded simple tandem repeat (ESTR) germline mutation rates in the resulting F2 generation were determined from full pedigrees (mother, father, offspring) of F1 female mice. ESTR mutation rates in CB-exposed F2 female offspring were not statistically different from those of F2 female control offspring [66]. MWCNTs were administered to pregnant rats by gavage at 0, 40, 200, and 1000 mg kg^{-1} day^{-1}. Repeated oral doses of MWCNTs during pregnancy induce minimal maternal toxicity and no embryo-fetal toxicity at 1000 mg kg^{-1} day^{-1} in rats [67]. Instillation of a single dose of MWCNT could not induce abnormal behavior and DSP in male

offspring [47]. Maternal particulate exposure of CB did not affect DSP significantly in the F1 generation. F2 offspring, whose fathers were prenatally exposed to CB (Printex90), showed lowered sperm production [68].

However, many carbon nanomaterials showed toxicity to the F1/F2 generation. C_{60}-malonate, SWCNTs, SWCNT-$CONH_2$, and MWCNTs caused a significant decrease in either the survival or reproduction in F1 daphnids; and SWCNT-$CONH_2$ decreased reproduction out to the F2 generation. Carbon nanomaterials have minimal multigenerational impacts based on their size but are highly dependent on the surface chemistry [69]. When pregnant Slc mice were intraperitoneally injected with C_{60} at 25, 50, or 137 mg kg^{-1} on DG 10, C_{60} was incorporated into the concepts and the severely disrupted the function of the yolk sac and embryonic morphogenesis [70]. With intraperitoneal injections of MWCNTs during mating and early pregnancy, MWCNT-treated pups increased depressive and anxious behaviors. The absolute weights of the liver, thymus, and spleen decreased [71]. A single oral dose of hydroxyl-MWCNTs (10 mg kg^{-1}) administered to pregnant CD-1 dams during organogenesis significantly increased the number of resorptions and resulted in morphological and skeletal abnormalities of the fetus [19]. o-MWCNTs narrowed the blood vessel and decreased the number of blood vessels in the placenta. The abortion rates in the first-time, second-time, and fourth-time pregnant mice were 70%, 40%, and 50%, respectively (Figure 11.4) [48]. After the dams were exposed to CB during pregnancy, analysis of newborn's livers by DNA microarrays revealed that female offspring were more sensitive to maternal exposure than male offspring. Cellular signaling, inflammation, cell cycle, and lipid metabolism were among the biological pathways affected in the female offspring. Males, however, responded with subtle changes in metabolism-related genes [72]. When MWCNTs were given intraperitoneally or intratracheally to pregnant ICR mice, various types of malformation were observed. The number of litters having fetuses with external malformation and those having fetuses with skeletal malformations both increased [73]. Respiratory exposure to CB (95 μg kg^{-1}) during middle and late gestation may have allergic or inflammatory effects in the male offspring. CB increased total thymocytes and their immunophenotypes ($CD_4^-CD_8^-$ and $CD_4^+CD_8^+$ cells). CB also increased total lymphocytes, particularly $CD_3^-B_{220}^-$ cells, in the spleen of newborn male offspring, reflecting the stimulation of immature splenocytes. And mRNA expression of genes related to the induction of peripheral tolerance (i.e., thymic Traf6) was upregulated [74].

11.3.4
Impact on the Endocrine Organs and Hormone Biosynthesis/Metabolism

Disruption of endocrine function is associated with adverse health outcomes, including reproductive failure, metabolic syndrome, and some types of cancer. Further investigations are therefore required to obtain a thorough understanding of any potential risk of pathological endocrine disruption from products containing nanomaterials [75]. The reproductive system is regulated by the endocrine

system cooperating with the immune system. Fullerene derivatives were found to have good regulatory effects on immune response [76–79], which might disrupt the reproductive system. Carbon nanomaterials cause direct impairment to the endocrine organs or tissues, which may result in pathological alteration in endocrine cells. These damages will undoubtedly influence endocrine homeostasis. Placentas from malformed fetuses presented apparent alterations in size and vascular organization of the labyrinth layer, characterized by disruption of the radial distribution and arborization of the placental vascular bed. CD31 and Azan–Mallory staining showed much reduced vessel density and branching, as well as aberrant fibrin deposition, reflecting the presence of thrombotic vessels. Neither histological examination nor micro-Raman analysis was able to confirm the presence of SWCNTs in placentae or fetuses from p-SWCNT- and o-SWCNT-treated mothers. However, ROS levels were significantly higher in malformed fetuses but not in maternal tissues such as those of the liver, lung, and spleen. It was presumed that elevated fetal ROS might be responsible for the fetal damage observed [22].

Li *et al.* observed that exposure to low and medium concentrations of nanoparticle-rich diesel (including several kinds of carbon nanomaterials) exhaust significantly increased the mRNA and protein expression of the StAR protein and cytochrome P450 side-chain cleavage (P450scc or CYP11A) in rat testes, which was consistent with the elevated plasma testosterone levels [80]. StAR plays an important role in the enhancement of cholesterol transfer from the outer to the inner mitochondrial membrane [81], while P450scc is essential in the conversion of the transported cholesterol to pregnenolone as well as steroidogenesis, both of which are critically involved in testosterone biosynthesis. The mRNA level of the testicular growth hormone receptor (GHR) increased after exposure to low and medium concentrations of nanoparticle-rich diesel [82]. GH and GH-regulated IGF-I upregulate StAR the expression and steroidogenesis in Leydig cells [83]. P450scc is also upregulated by IGF-I in Leydig cells [84]. Nanoparticle-rich diesel exposure might promote GH signaling and subsequent increases in StAR and P450scc expression levels to increase the plasma testosterone level.

The CYP gene superfamily consists of a large number of genes encoding P450 enzymes, including CYP11A referred to above, which typically catalyze monooxygenase reactions involving molecular oxygen and an equivalent number of electrons. The enzymes are involved in the detoxification of exogenous chemicals such as chemical drugs and the metabolism of endogenous substrates such as steroids, fatty acids, vitamins, and prostanoids. The cytochrome P450 system is expressed in many cells but is especially important in hepatocytes and steroid hormone-producing cells [85]. Carbon nanomaterials may influence CYP450 enzymatic activity. To our knowledge, some members of CYP450 family that are involved in the metabolism of exogenous chemicals also contribute to steroid metabolism; for example, CYP1A plays a role in estrogen metabolism. Hence, the potential interactions between carbon nanomaterials and the CYP450 system requires further investigation.

11.3.5
Others

Many nutrients in breast milk are important to the growth and development of babies. WHO promotes breastfeeding of infants below 2 years of age. Studies have shown that drugs can diffuse passively into the breast milk and then be transferred to the baby [86]. Such drugs can be toxic because of baby's half-grown metabolic function of the liver and renal excretion function [87]. Medication during lactation affects the health of both the mother and the baby, and many drugs are contraindicated for use or to be used with caution [88]. However, with increasing importance of breastfeeding, medication during lactation is also increasing [86]. It was reported that fullerene nanoparticles could cross the placenta and be transmitted to offspring via dam's milk and subsequently systemically absorbed [65]. On the other hand, intravenous exposure to polyvinylpyrrolidone (PVP)-formulated C_{60} (C_{60}/PVP) increased vascular tissue contractility through the elements of Rho–Rho kinase signaling during late stages of pregnancy [89]. It is of great significance to carry out the safety evaluation of materials ingested during lactation.

11.4
Conclusion and Perspectives

Studies of the toxicity of carbon nanomaterials on the reproductive system *in vivo* and *in vitro* were reviewed in this chapter. The adverse effects of carbon nanomaterials on the reproductive system might highly depend on their physicochemical properties and/or on the specific endocrine tissues or cell types they act upon. Carbon nanomaterials influence sex hormone levels and impair the normal functions of the reproductive organs, such as spermatogenesis in males and uterine function in females. There is clear evidence that certain carbon nanomaterials may act as endocrine disruptors. Therefore, possible toxicities of carbon nanomaterials in the various reproductive and endocrine systems warrant future systematic investigation. Because the effects of endocrine modulation may be delayed and long-term features, one should be careful of the profound somatic effects over the lifespan and potential intergenerational effects. We need to establish a rational approach to determine the potential hazards of carbon nanomaterials, which is important to enhance the safety of manufacture and application of engineered carbon nanoproducts.

We have previously proposed that nanotoxicity testing should cover physicochemical characterization of nanomaterials both *in vitro* and *in vivo* [90]. Further multiple parameters such as age, exposure period to nanomaterials, and potential epigenetically mediated intergenerational effects should also be taken into consideration. As more and more nanomaterials are now used in electronic, cosmetic, automotive, and medical products, there is inevitably increased exposure of workers and consumers to such materials. Currently, data on potential endocrine

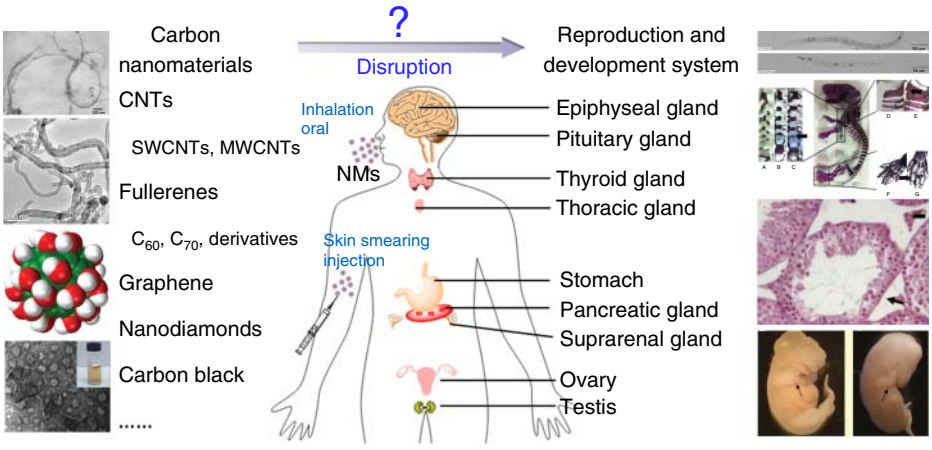

Figure 11.5 Schematic of the interaction between nanomaterials and the reproductive and developmental system [18, 19, 21, 22, 48, 75, 78].

interactions and toxicities are quite limited. Because different animal models are different as far as metabolism, sensitivity, and regulation of the endocrine systems are concerned, it can be questioned whether the current knowledge can be extended to other *in vivo* systems, especially in humans. This question is further confounded by the possible differences in the biodistribution and delivery efficiency of nanomaterials in different models. In addition, the possible combined or synergistic toxicity of nanomaterials and other endocrine disruptors on human health should be critically studied. In summary, further investigation is urgently required to obtain a better understanding of the potential risks to the endocrine function from nanoproducts.

In recent years, there have been some reports on the reproductive toxicity and toxic mechanism of carbon nanomaterials, which provide an important scientific basis for environmental risk assessment of nanomaterials (Figure 11.5 and Table 11.4). However, some problems still need to be studied. (i) There exists an obvious gap in extrapolating the data from animal experiments to human health effects. Most reproductive toxicity data of carbon nanomaterials come from experimental animals, while few researches focus on human reproductive health. And there is often conflict between experimental animal data and epidemiological investigation data. Therefore, it is important to develop translational toxicology and convert the basic toxicology research to the human risk metrics. (ii) Further studies are required to demonstrate the underlying mechanism of reproductive toxicology of carbon nanomaterials. Various toxic responses of carbon nanomaterials are easier to be compared through in-depth study of multiple molecular targets and pathways. Sensitive molecular biomarkers are helpful in evaluating the adverse effects of nanomaterials on humans. For example, the effects of nanomaterials on the neuroendocrine system need to be better understood, because the reproductive process is regulated directly by the neuroendocrine

Table 11.4 Reproductive toxicity of carbon nanomaterials.

Carbon nanomaterials	Characteristics	Animals/cells	Exposure			Findings	References
			Methods	Duration	Concentration		
C_{60}	Purity > 99.9%	Slc mice	Intraperitoneal injection	Single on GD 10	25 – 137 mg kg^{-1}	Deaths of all embryos at 138 mg kg^{-1}; Abnormalities in 50% of embryos at 50 mg kg^{-1}	[70]
$[^{14}C]C_{60}$	>10 nm, Estimated 2 nm in particle size	SD rats	Intravenous injection	Single on DG 15 or LD 8	0.3 mg kg^{-1}	Distribution of C60 to placentae and fetuses of exposed pregnant dams Distribution of C60 to milk and offspring of exposed lactating dams	[65]
C_{60}	Purity > 99.9%	Midbrain cells	Incubation	6 days	10 – 1000 μg ml^{-1}	IC50 for cell differentiation = 430 μg ml^{-1} IC50 for cell proliferation = 470 μg ml^{-1}	[70]
C''_{60}	/	Male rats	Oral (water)	5 weeks	4 μg kg^{-1} per day	Decrease in the no. of apoptotic testicells Alleviate pathological damage after C60 intake in STZ-diabetes mice; reduce diabetes-induced oxidative stress	[29]
Carbon black	Diameter: 14 nm 56 nm 95 nm	Male ICR mice	Intratracheal instillation	10 times at weekly intervals	0.1 mg per mouse	No effect of 14-, 56-, or 95-nm particles on body weight or reproductive organs ↑Serum testosterone levels after instillation of 14- and 56-nm particles ↓DSP after instillation of 14-, 56-, and 90-nm particles	[33]

Carbon black	14 nm in particle size, Printex90	Mouse testis Leydig cell line TM3	Incubation	16, 24, or 48 h	1–1000 μg ml^{-1}	↓Viability of TM3 at 1000 μg ml^{-1} No effect on proliferation of TM3 cells; No changes in HO-1 mRNA expression at up to 100 μg ml^{-1} ↑StAR mRNA expression at 30 μg ml^{-1} for 48 h-incubation	[63]
MWCNT	Diameter: 20–30 nm Length: 0.5–2.0 μm	Male mice	Intravenous injection	Dose five times over 13 days, then test at day 15, 60 and 90	5 mg kg^{-1} per dose	No changes of sex hormones No histopathological change for 90 days	[21]
SWCNT	p-SWCNT *D* (nm):2.37 ± 0.40 *L* (μm): 0.85 ± 0.42 o-SWCNT *D* (nm): 1.58 ± 0.20 *L* (μm): 0.76 ± 0.70	Pregnant mice	Intravenous injection	Dose at 5.5 dpc, then sacrificed at 15.5 dpc	0.1, 0.3, 3 or 30 μg per mouse	A high percentage of early miscarriages and fetal malformations in females exposed to o-SWCNTs Lower percentage exposed to p-SWCNTs	[22]
Nanoparticles in rich diesel exhaust		Pregnant rats and male offspring	Exposure	5 h daily during GD 1–19	NR-DE:148.86 μg m^{-3} F-DE: 3.10 μg m^{-3}	Maybe no effects No significant change in serum concentrations of testosterone, progesterone, corticosterone between different groups	[91]
		Male mice	Exposure	8 Weeks (5 h per day, 5 days per week)	Low (41.73 μg m^{-3}, 8.21×10^5 particles cm^{-3}) High (152.01 μg m^{-3}, 1.80×10^6 particles cm^{-3})	Maybe no effects Exposure to F-DE showed similar results with NR-DE in serum concentrations of testosterone, progesterone, corticosterone	[92]

system. Kisspeptins, the products of *Kiss1* gene acting via the G protein-coupled receptor 54, have recently emerged as essential gatekeepers of puberty onset and fertility. Early exposure to the environmentally relevant estrogen and bisphenol-A can alter the hypothalamic expression of *Kiss1*/kisspeptin in rats and mice. Alterations of endogenous kisspeptin tone induced by inappropriate (early) exposures to environmental compounds with sex steroid activity might be mechanistically relevant for the disruption of puberty onset and gonadotropin secretion later in life [93]. Kisspeptin can be used as a candidate biomarker to evaluate the reproductive toxicity of pollutants, which provides inspiration for the reproductive endocrine toxicity of nanomaterials. (iii) Actually, various environmental pollutants coexist instead of staying alone. Hence, it is important to study the combinational toxicity of different nanomaterials, different homologs of one kind of nanomaterial, and other environmental contaminants (such as heavy metals, bisphenol A, etc.).

Acknowledgments

This work was financially supported by the Ministry of Science and Technology of China (2011CB933401) and the National Science Fund for Distinguished Young Scholars (11425520).

References

1. Olshan, A.F. and Faustman, E.M. (1993) Male-mediated developmental toxicity. *Annu. Rev. Public Health*, **14**, 159–181.
2. Sever, L.E. (1995) Male-mediated developmental toxicity. *Epidemiology*, **6** (6), 573–574.
3. Anderson, D., Schmid, T.E., and Baumgartner, A. (2014) Male-mediated developmental toxicity. *Asian J. Androl.*, **16** (1), 81–88.
4. Di Comite, G., Grazia Sabbadini, M., Corti, A. *et al.* (2007) Conversation galante: how the immune and the neuroendocrine systems talk to each other. *Autoimmun. Rev.*, **7** (1), 23–29.
5. Mattison, D.R., Plowchalk, D.R., Meadows, M.J. *et al.* (1990) Reproductive toxicity: male and female reproductive systems as targets for chemical injury. *Med. Clin. North Am.*, **74** (2), 391–411.
6. Oberdorster, G., Maynard, A., Donaldson, K. *et al.* (2005) Principles for characterizing the potential human health effects from exposure to nanomaterials: elements of a screening strategy. *Part. Fibre Toxicol.*, **2**, 8.
7. Penn, S.G., He, L., and Natan, M.J. (2003) Nanoparticles for bioanalysis. *Curr. Opin. Chem. Biol.*, **7** (5), 609–615.
8. Liu, W.T. (2006) Nanoparticles and their biological and environmental applications. *J. Biosci. Bioeng.*, **102** (1), 1–7.
9. Wang, J., Zhou, G., Chen, C. *et al.* (2007) Acute toxicity and biodistribution of different sized titanium dioxide particles in mice after oral administration. *Toxicol. Lett.*, **168** (2), 176–185.
10. Wang, J., Liu, Y., Jiao, F. *et al.* (2008) Time-dependent translocation and potential impairment on central nervous system by intranasally instilled TiO(2) nanoparticles. *Toxicology*, **254** (1–2), 82–90.
11. Sharma, V., Singh, P., Pandey, A.K. *et al.* (2012) Induction of oxidative stress, DNA damage and apoptosis in mouse liver after sub-acute oral exposure to

zinc oxide nanoparticles. *Mutat. Res.*, **745** (1–2), 84–91.
12. Wang, J., Chen, C., Liu, Y. *et al.* (2008) Potential neurological lesion after nasal instillation of TiO(2) nanoparticles in the anatase and rutile crystal phases. *Toxicol. Lett.*, **183** (1–3), 72–80.
13. Colborn, T., vom Saal, F.S., and Soto, A.M. (1993) Developmental effects of endocrine-disrupting chemicals in wildlife and humans. *Environ. Health Perspect.*, **101** (5), 378–384.
14. Brooking, J., Davis, S.S., and Illum, L. (2001) Transport of nanoparticles across the rat nasal mucosa. *J. Drug Target.*, **9** (4), 267–279.
15. Li, Y., Liu, Y., Fu, Y. *et al.* (2012) The triggering of apoptosis in macrophages by pristine graphene through the MAPK and TGF-beta signaling pathways. *Biomaterials*, **33** (2), 402–411.
16. Zhou, H., Zhao, K., Li, W. *et al.* (2012) The interactions between pristine graphene and macrophages and the production of cytokines/chemokines via TLR- and NF-kappaB-related signaling pathways. *Biomaterials*, **33** (29), 6933–6942.
17. Schipper, M.L., Nakayama-Ratchford, N., Davis, C.R. *et al.* (2008) A pilot toxicology study of single-walled carbon nanotubes in a small sample of mice. *Nat. Nanotechnol.*, **3** (4), 216–221.
18. Chen, P.H., Hsiao, K.M., and Chou, C.C. (2013) Molecular characterization of toxicity mechanism of single-walled carbon nanotubes. *Biomaterials*, **34** (2), 5661–5669.
19. Philbrook, N.A., Walker, V.K., Afrooz, A.R. *et al.* (2011) Investigating the effects of functionalized carbon nanotubes on reproduction and development in Drosophila melanogaster and CD-1 mice. *Reprod. Toxicol.*, **32** (4), 442–448.
20. Chatterjee, N., Yang, J., Kim, H.M. *et al.* (2014) Potential toxicity of differential functionalized multiwalled carbon nanotubes (MWCNT) in human cell line (BEAS2B) and Caenorhabditis elegans. *J. Toxicol. Environ. Health A-Curr. Issues*, **77** (22–24), 1399–1408.
21. Bai, Y., Zhang, Y., Zhang, J. *et al.* (2010) Repeated administrations of carbon nanotubes in male mice cause reversible testis damage without affecting fertility. *Nat. Nanotechnol.*, **5** (9), 683–689.
22. Pietroiusti, A., Massimiani, M., Fenoglio, I. *et al.* (2011) Low doses of pristine and oxidized single-wall carbon nanotubes affect mammalian embryonic development. *ACS Nano*, **5** (6), 4624–4633.
23. Newton, M.D. and Stanton, R.E. (1986) Stability of buckminsterfullerene and related carbon clusters. *J. Am. Chem. Soc.*, **108** (9), 2469–2470.
24. Chen, Z., Ma, L., Liu, Y. *et al.* (2012) Applications of functionalized fullerenes in tumor theranostics. *Theranostics*, **2** (3), 238–250.
25. Chen, Z., Mao, R., and Liu, Y. (2012) Fullerenes for cancer diagnosis and therapy: preparation, biological and clinical perspectives. *Curr. Drug Metab.*, **13** (8), 1035–1045.
26. Liu, Y., Chen, C., Qian, P. *et al.* (2015) Gd-metallofullerenol nanomaterial as non-toxic breast cancer stem cell-specific inhibitor. *Nat. Commun.*, **6**, 5988.
27. Lao, F., Chen, L., Li, W. *et al.* (2009) Fullerene nanoparticles selectively enter oxidation-damaged cerebral microvessel endothelial cells and inhibit JNK-related apoptosis. *ACS Nano*, **3** (11), 3358–3368.
28. Chen, C., Xing, G., Wang, J. *et al.* (2005) Multihydroxylated [Gd@C82(OH)22]n nanoparticles: antineoplastic activity of high efficiency and low toxicity. *Nano Lett.*, **5** (10), 2050–2057.
29. Bal, R., Turk, G., Tuzcu, M. *et al.* (2011) Protective effects of nanostructures of hydrated C(60) fullerene on reproductive function in streptozotocin-diabetic male rats. *Toxicology*, **282** (3), 69–81.
30. Schnedl, W.J., Ferber, S., Johnson, J.H. *et al.* (1994) STZ transport and cytotoxicity. Specific enhancement in GLUT2-expressing cells. *Diabetes*, **43** (11), 1326–1333.
31. Xiao, L., Aoshima, H., Saitoh, Y. *et al.* (2011) Highly hydroxylated fullerene localizes at the cytoskeleton and inhibits oxidative stress in adipocytes and a subcutaneous adipose-tissue equivalent. *Free Radic. Biol. Med.*, **51** (7), 1376–1389.

32. Donaldson, K., Tran, L., Jimenez, L.A. *et al.* (2005) Combustion-derived nanoparticles: a review of their toxicology following inhalation exposure. *Part. Fibre Toxicol.*, **2**, 10.
33. Yoshida, S., Hiyoshi, K., Ichinose, T. *et al.* (2009) Effect of nanoparticles on the male reproductive system of mice. *Int. J. Androl.*, **32** (4), 337–342.
34. Yoshida, S., Hiyoshi, K., Oshio, S. *et al.* (2010) Effects of fetal exposure to carbon nanoparticles on reproductive function in male offspring. *Fertil. Steril.*, **93** (5), 1695–1699.
35. Lacy, P.E. (1975) Endocrine secretory mechanisms. A review. *Am. J. Pathol.*, **79** (1), 170–188.
36. Healy, D.L., Trounson, A.O., and Andersen, A.N. (1994) Female infertility: causes and treatment. *Lancet*, **343** (8912), 1539–1544.
37. McLachlan, J.A., Simpson, E., and Martin, M. (2006) Endocrine disrupters and female reproductive health. *Best Pract. Res. Clin. Endocrinol. Metab.*, **20** (1), 63–75.
38. Nicolopoulou-Stamati, P. and Pitsos, M.A. (2001) The impact of endocrine disrupters on the female reproductive system. *Hum. Reprod. Update*, **7** (3), 323–330.
39. Doerr, J.K., Hooser, S.B., Smith, B.J. *et al.* (1995) Ovarian toxicity of 4-vinylcyclohexene and related olefins in B6C3F1 mice: role of diepoxides. *Chem. Res. Toxicol.*, **8** (7), 963–969.
40. Goldman, J.M., Murr, A.S., and Cooper, R.L. (2007) The rodent estrous cycle: characterization of vaginal cytology and its utility in toxicological studies. *Birth Defects Res. B Dev. Reprod. Toxicol.*, **80** (2), 84–97.
41. Zhao, X., Ze, Y., Gao, G. *et al.* (2013) Nanosized TiO2-induced reproductive system dysfunction and its mechanism in female mice. *PLoS One*, **8** (4), e59378.
42. Liu, X., Qin, D., Cui, Y. *et al.* (2010) The effect of calcium phosphate nanoparticles on hormone production and apoptosis in human granulosa cells. *Reprod. Biol. Endocrinol.*, **8**, 32.
43. Stelzer, R. and Hutz, R.J. (2009) Gold nanoparticles enter rat ovarian granulosa cells and subcellular organelles, and alter in-vitro estrogen accumulation. *J. Reprod. Dev.*, **55** (6), 685–690.
44. Cha, Y.J., Lee, J., and Choi, S.S. (2012) Apoptosis-mediated in vivo toxicity of hydroxylated fullerene nanoparticles in soil nematode Caenorhabditis elegans. *Chemosphere*, **87** (1), 49–54.
45. Pakarinen, K., Petersen, E.J., Leppanen, M.T. *et al.* (2011) Adverse effects of fullerenes (nC60) spiked to sediments on Lumbriculus variegatus (Oligochaeta). *Environ. Pollut.*, **159** (12), 3750–3756.
46. Li, D. and Alvarez, P.J. (2011) Avoidance, weight loss, and cocoon production assessment for Eisenia fetida exposed to C(6)(0) in soil. *Environ. Toxicol. Chem.*, **30** (11), 2542–2545.
47. Hougaard, K.S., Jackson, P., Kyjovska, Z.O. *et al.* (2013) Effects of lung exposure to carbon nanotubes on female fertility and pregnancy. A study in mice. *Reprod. Toxicol.*, **41**, 86–97.
48. Qi, W., Bi, J., Zhang, X. *et al.* (2014) Damaging effects of multi-walled carbon nanotubes on pregnant mice with different pregnancy times. *Sci. Rep.*, **4**, 4352.
49. Carlsen, E., Giwercman, A., Keiding, N. *et al.* (1992) Evidence for decreasing quality of semen during past 50 years. *Br. Med. J.*, **305** (6854), 609–613.
50. Schiffer, C., Muller, A., Egeberg, D.L. *et al.* (2014) Direct action of endocrine disrupting chemicals on human sperm. *EMBO Rep.*, **15** (7), 758–765.
51. Lancranjan, I., Popescu, H.I., Găvănescu, O., Klepsch, I. *et al.* (1975) Reproductive ability of workmen occupationally exposed to lead. *Arch. Environ. Health*, **30** (8), 396–401.
52. Benoff, S., Hurley, I.R., Barcia, M. *et al.* (1997) A potential role for cadmium in the etiology of varicocele-associated infertility. *Fertil. Steril.*, **67** (2), 336–347.
53. Van den Berg, M., Birnbaum, L., Bosveld, A.T. *et al.* (1998) Toxic equivalency factors (TEFs) for PCBs, PCDDs, PCDFs for humans and wildlife. *Environ. Health Perspect.*, **106** (12), 775–792.
54. Saleh, R.A. and Agarwal, A. (2002) Oxidative stress and male infertility: from research bench to clinical practice. *J. Androl.*, **23** (6), 737–752.

55. Tremellen, K. (2008) Oxidative stress and male infertility–a clinical perspective. *Hum. Reprod. Update*, **14** (3), 243–258.
56. Howards, S.S. (1995) Treatment of male infertility. *N. Engl. J. Med.*, **332** (5), 312–317.
57. Sikka, S.C. and Wang, R. (2008) Endocrine disruptors and estrogenic effects on male reproductive axis. *Asian J. Androl.*, **10** (1), 134–145.
58. Phillips, K.P. and Tanphaichitr, N. (2008) Human exposure to endocrine disrupters and semen quality. *J. Toxicol. Environ. Health B Crit. Rev.*, **11** (3–4), 188–220.
59. Petrelli, G. and Mantovani, A. (2002) Environmental risk factors and male fertility and reproduction. *Contraception*, **65** (4), 297–300.
60. Schinkel, A.H., Smit, J.J., van Tellingen, O. *et al.* (1994) Disruption of the mouse mdr1a P-glycoprotein gene leads to a deficiency in the blood-brain barrier and to increased sensitivity to drugs. *Cell*, **77** (4), 491–502.
61. Miyawaki, J., Yudasaka, M., Azami, T. *et al.* (2008) Toxicity of single-walled carbon nanohorns. *ACS Nano*, **2** (2), 213–226.
62. Ema, M., Kobayashi, N., Naya, M. *et al.* (2010) Reproductive and developmental toxicity studies of manufactured nanomaterials. *Reprod. Toxicol.*, **30** (3), 343–352.
63. Komatsu, T., Tabata, M., Kubo-Irie, M. *et al.* (2008) The effects of nanoparticles on mouse testis Leydig cells in vitro. *Toxicol. in Vitro*, **22** (8), 1825–1831.
64. Braydich-Stolle, L., Hussain, S., Schlager, J.J. *et al.* (2005) In vitro cytotoxicity of nanoparticles in mammalian germline stem cells. *Toxicol. Sci.*, **88** (2), 412–419.
65. Sumner, S.C., Fennell, T.R., Snyder, R.W. *et al.* (2010) Distribution of carbon-14 labeled C60 ([14C]C60) in the pregnant and in the lactating dam and the effect of C60 exposure on the biochemical profile of urine. *J. Appl. Toxicol.*, **30** (4), 354–360.
66. Boisen, A.M., Shipley, T., Jackson, P. *et al.* (2013) In utero exposure to nano-sized carbon black (Printex90) does not induce tandem repeat mutations in female murine germ cells. *Reprod. Toxicol.*, **41**, 45–48.
67. Lim, J.H., Kim, S.H., Shin, I.S. *et al.* (2011) Maternal exposure to multi-wall carbon nanotubes does not induce embryo-fetal developmental toxicity in rats. *Birth Defects Res. B Dev. Reprod. Toxicol.*, **92** (1), 69–76.
68. Kyjovska, Z.O., Boisen, A.M., Jackson, P. *et al.* (2013) Daily sperm production: application in studies of prenatal exposure to nanoparticles in mice. *Reprod. Toxicol.*, **36**, 88–97.
69. Arndt, D.A., Chen, J., Moua, M. *et al.* (2014) Multigeneration impacts on Daphnia magna of carbon nanomaterials with differing core structures and functionalizations. *Environ. Toxicol. Chem.*, **33** (3), 541–547.
70. Tsuchiya, T., Oguri, I., Yamakoshi, Y.N. *et al.* (1996) Novel harmful effects of [60]fullerene on mouse embryos in vitro and in vivo. *FEBS Lett.*, **393** (1), 139–145.
71. Ivani, S., Karimi, I., and Tabatabaei, S.R. (2012) Biosafety of multiwalled carbon nanotube in mice: a behavioral toxicological approach. *J. Toxicol. Sci.*, **37** (6), 1191–1205.
72. Jackson, P., Hougaard, K.S., Vogel, U. *et al.* (2012) Exposure of pregnant mice to carbon black by intratracheal instillation: toxicogenomic effects in dams and offspring. *Mutat. Res.*, **745** (1–2), 73–83.
73. Fujitani, T., Ohyama, K., Hirose, A. *et al.* (2012) Teratogenicity of multi-wall carbon nanotube (MWCNT) in ICR mice. *J. Toxicol. Sci.*, **37** (1), 81–89.
74. El-Sayed, Y.S., Shimizu, R., Onoda, A. *et al.* (2015) Carbon black nanoparticle exposure during middle and late fetal development induces immune activation in male offspring mice. *Toxicology*, **327**, 53–61.
75. Lu, X., Liu, Y., Kong, X., Lobie, P.E., Chen, C., and Zhu, T. (2013) Nanotoxicity: a growing need for study in the endocrine system. *Small*, **9** (9–10), 1654–1671.
76. Liu, Y., Jiao, F., Qiu, Y. *et al.* (2009) The effect of Gd@C82(OH)22 nanoparticles on the release of Th1/Th2 cytokines and

induction of TNF-alpha mediated cellular immunity. *Biomaterials*, **30** (23–24), 3934–3945.
77. Liu, Y., Jiao, F., Qiu, Y. *et al.* (2009) Immunostimulatory properties and enhanced TNF- alpha mediated cellular immunity for tumor therapy by C60(OH)20 nanoparticles. *Nanotechnology*, **20** (41), 415102.
78. Xu, L., Liu, Y., Chen, Z. *et al.* (2013) Morphologically virus-like fullerenol nanoparticles act as the dual-functional nanoadjuvant for HIV-1 vaccine. *Adv. Mater.*, **25** (41), 5928–5936.
79. Chen, Z., Liu, Y., Sun, B. *et al.* (2014) Polyhydroxylated metallofullerenols stimulate IL-1beta secretion of macrophage through TLRs/MyD88/NF-kappaB pathway and NLRP(3) inflammasome activation. *Small*, **10** (12), 2362–2372.
80. Li, C., Taneda, S., Taya, K. *et al.* (2009) Effects of inhaled nanoparticle-rich diesel exhaust on regulation of testicular function in adult male rats. *Inhalation Toxicol.*, **21** (10), 803–811.
81. West, L.A., Horvat, R.D., Roess, D.A. *et al.* (2001) Steroidogenic acute regulatory protein and peripheral-type benzodiazepine receptor associate at the mitochondrial membrane. *Endocrinology*, **142** (1), 502–505.
82. Ramdhan, D.H., Ito, Y., Yanagiba, Y. *et al.* (2009) Nanoparticle-rich diesel exhaust may disrupt testosterone biosynthesis and metabolism via growth hormone. *Toxicol. Lett.*, **191** (2–3), 103–108.
83. Kanzaki, M. and Morris, P.L. (1999) Growth hormone regulates steroidogenic acute regulatory protein expression and steroidogenesis in Leydig cell progenitors. *Endocrinology*, **140** (4), 1681–1686.
84. Lin, T., Wang, D., Hu, J. *et al.* (1998) Upregulation of human chorionic gonadotrophin-induced steroidogenic acute regulatory protein by insulin-like growth factor-I in rat Leydig cells. *Endocrine*, **8** (1), 73–78.
85. Ingelman-Sundberg, M. (2004) Human drug metabolising cytochrome P450 enzymes: properties and polymorphisms. *Naunyn-Schmiedeberg's Arch. Pharmacol.*, **369** (1), 89–104.
86. Neville, M.C. (2009) Classic studies of mammary development and milk secretion: 1945–1980. *J. Mammary Gland Biol. Neoplasia*, **14** (3), 193–197.
87. Clark, J.H. and Wilson, W.G. (1981) A 16-day-old breast-fed infant with metabolic acidosis caused by salicylate. *Clin. Pediatr.*, **20** (1), 53–54.
88. Frey, O.R., Scheidt, P., and von Brenndorff, A.I. (1999) Adverse effects in a newborn infant breast-fed by a mother treated with doxepin. *Ann. Pharmacother.*, **33** (6), 690–693.
89. Vidanapathirana, A.K., Thompson, L.C., Mann, E.E. *et al.* (2014) PVP formulated fullerene (C60) increases Rho-kinase dependent vascular tissue contractility in pregnant Sprague Dawley rats. *Reprod. Toxicol.*, **49**, 86–100.
90. Liu, Y., Zhao, Y., Sun, B. *et al.* (2013) Understanding the toxicity of carbon nanotubes. *Acc. Chem. Res.*, **46** (3), 702–713.
91. Li, C., Taneda, S., Taya, K. *et al.* (2009) Effects of in utero exposure to nanoparticle-rich diesel exhaust on testicular function in immature male rats. *Toxicol. Lett.*, **185** (1), 1–8.
92. Li, C., Li, X., Suzuki, A.K. *et al.* (2012) Effects of exposure to nanoparticle-rich diesel exhaust on adrenocortical function in adult male mice. *Toxicol. Lett.*, **209** (3), 277–281.
93. Tena-Sempere, M. (2010) Kisspeptin/GPR54 system as potential target for endocrine disruption of reproductive development and function. *Int. J. Androl.*, **33** (2), 360–368.

12
Immunological Responses Induced by Carbon Nanotubes Exposed to Skin and Gastric and Intestinal System

Haiyan Xu, Jie Meng, Qiang Ma, and Xiaojin Li

12.1
Introduction

Since their discovery, carbon nanotubes (CNTs) have been attracting increasing research and application interests from academics and industries in the biomedical field. Accumulated evidence has demonstrated that CNTs have the ability to deliver therapeutic or detective molecules, such as nucleic acids [1–9], chemotherapeutic agents [10–12], proteins and peptides [13–17] into tissues and organs, and to be used as photoacoustic agents in the molecular imaging [18]. Research has also made it possible for CNTs to be employed in the preparation of prostheses and implants for rehabilitation, biosensors for proteins and enzymes, and supportive materials for tissue growth in tissue engineering [19]. Besides, interactions of CNTs with the immune system have become an important issue in the past decades. The immune system may recognize CNTs as invading foreign particulate matter and mount a multilevel immune response against them, which raises concerns about their safety; meanwhile, the feature of mediating immunological reactions also implies CNTs' promising potential as a novel immunological adjuvant for cancer immune therapies.

With regard to the immunological responses of CNTs, it is necessary to emphasize that the biological effects of CNTs largely depend on their administration routes. It has been reported that the administration of CNTs by intratracheal instillation leads to overt inflammation and fibrosis in the lungs [20–23] and may promote allergic responses in mice [24, 25]. Introduction of long multiwalled carbon nanotubes (MWCNTs) into the abdominal cavity of mice results in inflammation and the formation of granulomas [26]. Contrarily, intravenous administration of single-walled carbon nanotubes (SWCNTs) results in accumulation in the lung, liver, and spleen, exhibiting low toxicity and provoking low-level inflammatory cell infiltration into the lung [27]. Another research group also reported that intravenously administered SWCNTs do not induce obvious toxicity in a pilot study using a small number of mice [28].

Biomedical Applications and Toxicology of Carbon Nanomaterials, First Edition.
Edited by Chunying Chen and Haifang Wang.

Skin and the gastrointestinal system are the first immunological defense line for CNTs administrated through dermal and oral routes, respectively, and, importantly, there are large numbers of immune effector cells in the both systems. In this chapter, we will introduce the biological effects of CNTs exposed through the skin and gastrointestinal system, and will present research progress in utilizing CNT-mediated effects to develop novel technologies against diseases.

12.2
Biological Effects of CNTs by Dermal Exposure

Skin has the highest risk of exposure to nanomaterials. Dermal exposure with CNTs can occur in the manufacturing, handling in laboratories, and using or disposing textile or other products containing CNTs. Therefore, CNTs are environmental challenges to the dermal immune system. Investigations can be divided into two categories: (i) *in vitro* assessment with dermal-related cell lines, or (ii) *in vivo* studies in animal models.

12.2.1
In Vitro Assessment in Dermal-Related Cell Lines

There are multiple kinds of cells that are being used in studies of skin exposure to CNTs, including mainly keratinocytes, dermal fibroblast cells, mast cells, and reconstructed epidermises. Acute effects of CNTs on dermal cells are summarized in Table 12.1.

The nanotoxicology of CNTs is closely related to their dispersing behaviors in biological fluids. In cell culture media, for instance, hydrophobic CNTs assemble into micrometer-sized agglomerates bound by Van der Waals forces. In order to expose cells to the finest suspended CNTs, much effort has been made to increase CNTs' dispersion using concentrated acids with sonication and/or amphiphilic agents [34–36]. Nevertheless, the dispersion status of treated CNTs varies largely in different laboratories even when similar treatments are employed, which may lead to differences in the biological effects observed, because cells might react differently to individualized particles and to large agglomerates of the same compound, as supported by recent evidence [37]. Vankoningsloo *et al.* [29] investigated the cytotoxicity of MWCNTs in different agglomeration states with three kinds of skin-related cell lines, namely (i) immortalized human keratinocytes (IHK), expressing telomerase and lacking a functional cyclin-dependent kinase inhibitor $p16^{INK4a}$, while retaining their full differentiation potential; (ii) SZ95 sebocytes, isolated from a human sebaceous gland and keeping the main phenotypic and functional features of sebocytes, even after immortalization with the simian virus SV-40 large T antigen; and (iii) reconstructed human epidermises (RHE), reconstructed as a model closer to reality, engineered *in vitro* with keratinocytes pooled from different human donors. Results showed that water-suspended MWCNTs, as micrometer-sized agglomerates, were not harmful to

Table 12.1 Skin-related cell lines and biological effects of CNTs.

Cells	CNTs	Effects	References
Immortalized human keratinocytes (IHK)	MWCNTs (water-suspended agglomerates)	Minor toxic effects after a short exposure (24–48 h)	[29]
		Increased levels of reactive oxygen species; secretion of IL-8, IL-6, and C–C motif ligand 3	[30]
	MWCNTs (mild sonication)	Increased cytotoxicity	[29]
	MWCNTs (sonication with the addition of dispersive agents hydroxypropylcellulose or Pluronic F108)	Without cytotoxic effects	[29]
		No pro-inflammatory effects	[30]
SV-40 immortalized sebocytes SZ95	MWCNTs (water-suspended agglomerates)	No cytotoxic effects	[29]
		No pro-inflammatory effects	[30]
	MWCNTs (mild sonication)	No cytotoxic effects	[29]
		No pro-inflammatory effects	[30]
	MWCNTs (sonication with the addition of dispersive agents)	No cytotoxic effects	[29]
		No pro-inflammatory effects	[30]
In vitro reconstructed epidermises	MWCNTs (water-suspended agglomerates)	No cytotoxic effects	[29]
		No pro-inflammatory effects	[30]
	MWCNTs (mild sonication)	No cytotoxic effects	[29]
		No pro-inflammatory effects	[30]
	MWCNTs (sonication with the addition of dispersive agents)	No cytotoxic effects	[29]
		No pro-inflammatory effects	[30]
Dermal fibroblast cells (NHDF)	MWCNTs (40, 200, and 400 $\mu g\,ml^{-1}$)	Dose-dependent cytotoxicity through genomic DNA damage and programmed cell death	[31]
Dermal fibroblasts and NIH 3T3 murine fibroblasts	MWCNTs (1, 5, 10, 20, 50, 100 $\mu g\,ml^{-1}$)	Dose-dependent cytotoxicity; arrest cell cycle in G1 phase; downregulate adhesion-related genes level; cytoskeleton damage and disturbance of actin stress fibers; inhibit cell spreading, adhesion, migration, and wound-healing ability	[32]
Mast cells	SWCNTs	Suppress pro-inflammatory function through inhibiting antigen-induced signaling pathways and degranulation responses	[33]

skin cells, except for minor effects in keratinocytes after a short exposure of 24–48 h. When treated with mild sonication, the agglomeration of CNTs slightly decreased, but the cytotoxicity increased on keratinocytes. Researchers also observed that the addition of some surfactants, such as hydroxypropylcellulose or Pluronic F108, improved MWCNTs' dispersion and masked the harmful effects of sonicated nanotubes. These results indicate that CNTs induced cytotoxicity in keratinocytes, particularly when they were sonicated before cell incubations. However, the cytotoxic effects of raw and sonicated CNTs could be prevented in presence of dispersive agents. But, no cytotoxic effects were observed in SZ95 sebocytes or *in vitro* reconstructed epidermal tissues, suggesting the cornified layer is an efficient barrier against MWCNTs.

Patlolla *et al.* [31] conducted a study on the toxicity of MWCNTs at 40, 200, and 400 μg ml^{-1} on dermal fibroblast cells and found dose-dependent cytotoxicity with MWCNTs through genomic DNA damage and programmed cell death. Another study investigated the influence of MWCNTs on the cellular behavior of dermal fibroblasts and NIH 3T3 murine fibroblasts [32]. Besides inducing dose-dependent cytotoxicity, MWCNTs arrested the cell cycle in the G1 phase, indicating inhibition of DNA synthesis. The presence of MWCNTs also down-regulated the expression level of adhesion-related genes, and simultaneously caused cytoskeleton damage and disturbance of actin stress fibers, thereby inducing dramatically adverse effects on the cells' physiological functions such as cell spreading, adhesion, migration, and wound-healing ability. Therefore CNTs indeed can be very toxic at sufficiently high concentrations from environmental and occupational exposure, and careful monitoring of toxicity studies is essential for risk assessment.

In addition, CNTs are involved in the pro-inflammatory process, but the effects are cells-type-dependent *in vitro*. Vankoningsloo *et al.* [30] investigated the pro-inflammatory effects of MWCNTs in different dispersion states (from water-suspended raw agglomerates to isolated entities obtained by sonication in the presence of the dispersive agents hydroxypropylcellulose and Pluronic F108) on human N-hTERT telomerase-immortalized keratinocytes, SV-40 immortalized sebocytes SZ95, and *in vitro* reconstructed epidermises. It was found that, contrary to individualized MWCNTs, agglomerated particles increased the intracellular levels of reactive oxygen species as well as the expression and secretion of various cytokines, such as interleukin-8, interleukin-6, and C–C motif ligand 3 in N-hTERT cells. By contrast, the pro-inflammatory effects of MWCNTs were not observed in SZ95 cells and *in vitro* reconstructed epidermal tissues, as assessed by transcript level and secretion of interleukin-1α and interleukin-8, used as specific markers for skin irritation and sensitization.

Mast cells (MCs) are pro-inflammatory immunocytes that reside at the interfaces with the environment, and are sources of pro-inflammatory mediators (histamine, serotonin, matrix-active proteases, eicosanoids, prostanoids, cytokines, and chemokines), which are released in a calcium-dependent manner following immunological challenge or physicochemical stimulation. Umemoto *et al.* reported that unmodified SWCNTs, which share geometry with C-60

fullerenes, suppress mast cell-driven inflammatory responses [33]. It would seem paradoxical since CNTs are widely regarded as having the capacity to initiate macrophage-based inflammation and act pro-fibrotically [38]. Mast cells recognize unmodified SWCNTs by remodeling the plasma membrane, disaggregating the cortical actin cytoskeleton, and relocalizing clathrin in the contact zone. Clathrin was also identified as a component of an affinity-purified "interactome" isolated from MC using an SWCNT affinity matrix for mast cell lysates. Via this novel recognition mechanism, SWCNTs inhibit antigen-induced signaling pathways, such as calcium mobilization, FCεRI-induced phosphorylation of the syk kinase, PLCγ1, the ERK, and AKT kinases and AMP kinases α and β, and the pro-inflammatory degranulation responses, thus suppressing MC pro-inflammatory function. Nevertheless, it is still controversial whether CNTs are pro-inflammatory or anti-inflammatory, and further study should focus on the inflammatory effect of different CNTs on immunocytes.

12.2.2 *In Vivo* Studies on the Responses Elicited by Skin Exposed with CNTs

It should be noted that results *in vivo* show low toxicity, which is different from those obtained *in vitro*. Kishore *et al.* [39] assessed the dermal and ocular irritation potential with two different sizes of MWCNTs *in vivo*. The results of acute eye irritation toxicity studies in rabbits demonstrated reversible conjunctival redness and discharge and exhibited minimal concern, while acute dermal irritation studies indicated that MWCNTs of two sizes were nonirritant to the skin of rabbits. Then, Ema *et al.* conducted a further *in vivo* study, during which two products composed of SWCNTs and two products composed of MWCNTs were tested regarding acute dermal and acute eye irritation using rabbits and skin sensitization using guinea pigs [40]. The concentrations of MWCNTs in the substances were the maximum allowable for administration. The two products of SWCNTs and one of the products of MWCNTs were not irritants to the skin or eyes. The other product of MWCNTs caused very slight erythema at 24 h, but not at 72 h, after patch removal in the dermal irritation experiments, and conjunctival redness and blood vessel hyperemia at 1 h, but not at 24 h, in eye irritation experiments. These findings show that one product of MWCNTs is a very weak acute irritant to the skin and eyes. No products of SWCNTs and MWCNTs exhibited skin-sensitization effects. The existing *in vivo* results that CNTs did not cause skin toxicity as severe as they did in the cell lines are possibly attributed to the performance of skin as a barrier. The CNTs are exposed to the complete skin instead of individual cells. When skin-related cells incorporate with a matric to form complete skin tissue, a barrier is constructed, which has much stronger resistant functions to the CNT exposure than individual cells. Nevertheless, the knowledge about the toxicological effects of CNTs is still limited. Further information is needed to clarify the potential for irritation and sensitization, given the complex nature of CNTs.

12.3
Immunological Reactions Elicited by Subcutaneous Administration of MWCNTs

Anatomically, the skin is composed of three primary layers: epidermis, dermis, and subcutis (also known as the hypodermis or subcutaneous layer), and the subcutis is the innermost layer of the skin. It is crucial to figure out the effects of CNT exposure through the subcutis because there are plenty of immune cells in the subcutaneous layer, particularly phagocytes. From the viewpoint of immune therapy or immune protection, vaccines are usually administrated through subcutaneous injection. Hence, in this section, we will introduce the immunological reactions elicited by MWCNTs injected subcutaneously into healthy BALB/c mice, mainly on the basis of our previous work.

12.3.1
Preparation and Characterization of Multiwalled Carbon Nanotubes for Uses in Studies

In our studies, pristine MWCNTs with a purity of >95%, diameter of 20–30 nm, and average length of 2, 30, and 50 μm were purchased from Chengdu Organic Chemicals Co. Ltd. (Chengdu, China). The as-received products were treated by an oxidation/purification procedure, allowing various oxygen-containing groups to be introduced on the surface. Meanwhile, the MWCNTs became shorter. For one example [41], the as-received product of 50 μm in length was suspended in a 3:1 mixture of concentrated H_2SO_4/HNO_3 and sonicated with a probe at 540 W for 90 s. The resulting mixture was then diluted with large amounts of distilled water and filtered through a polycarbonate filter membrane of 2 μm pore (Millipore). The filtrate was rinsed thoroughly until neutral and then dried completely at 50 °C in a vacuum. The oxidized product could be well dispersed in water with a short sonication step to afford a stable aqueous solution of 0.3 mg ml^{-1} suitable for injections. The pH value of the solution was 6.5, which was the same as that of filtered distilled water. The MWCNTs could also be dispersed well in the cell culture medium, and were stable for at least 2 weeks without changing the characteristic UV–vis–NIR spectrum of the culture medium. The tube-like structure of MWCNTs was well kept, and most of the tubes ranged 0.5–2.0 μm in length and had an average diameter of 20–30 nm, the average length being about 900 nm. When measured by dynamic light scattering (DLS) spectroscopy, the MWCNTs showed a symmetric size distribution with an apparent hydrodynamic radius of 140 nm. X-ray photoelectron spectroscopy (XPS) showed that the C 1s spectrum of MWCNTs could be resolved into five characteristic peaks. The binding energies of 284.7, 286.4, 288.3, 289.9, and 291.6 eV were attributed to C–C, C–O, C═O, O═C–O, and $\pi-\pi^*$ bonds, respectively. Pristine MWCNTs contained about 1.5% of carboxylic group, which was due to the manufacturing process. For the oxygen-containing carbon species, the amount of carboxylic carbon dramatically increased to nearly 3 times that of pristine ones, whereas the other species showed mild increases. Fourier transform infrared (FTIR) spectroscopy showed that the spectrum of pristine MWCNTs was featureless,

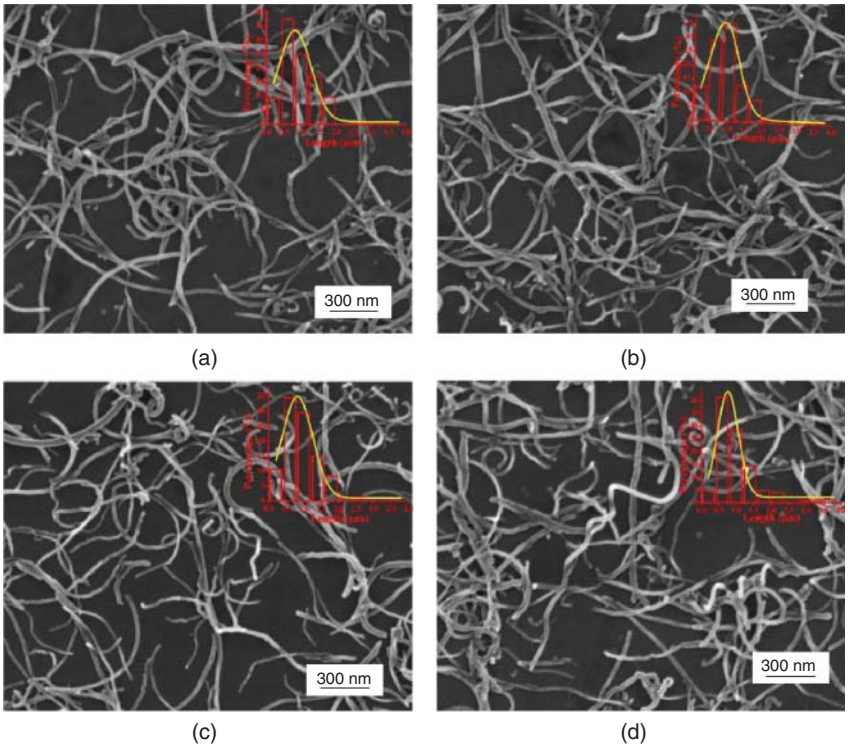

Figure 12.1 SEM images for oxidized MWCNTs in different oxidation degrees: (a) MWCNT-O_1, (b) MWCNT-O_2, (c) MWCNT-O_3, and (d) MWCNT-O_4. The oxidation degree increases from O_1 to O_4 [41].

with extremely low infrared absorption intensities, while MWCNTs presented a different FTIR spectrum: the infrared peaks could be assigned as follows: the peak at 1715 cm^{-1} was assigned to the C=O stretching mode of the –COOH groups on the oxidized MWCNTs, and the peak at 1570 cm^{-1} to the C=C graphitic stretching mode of the MWCNTs. These demonstrated that carboxylic groups were introduced into the oxidized MWCNTs (Figures 12.1 and 12.2).

12.3.2
Distribution of Subcutaneously Injected Carbon Nanotubes

In the *in vivo* studies, the first question was where CNTs accumulates after being injected subcutaneously. To answer this question, we injected 0.1 mg MWCNTs into the subcutis of healthy mice and sacrificed the animals on day 2, 7, 30, 60, and 90 post injection (P.I.). The subcutaneous tissue surrounding the injection site, lymph nodes, and organs were excised and processed for H&E staining [42]. It is interesting to observe that the tissue in the injection site was black at 1 h and even on day 90 after injection. As seen from the H&E stained samples, there were large

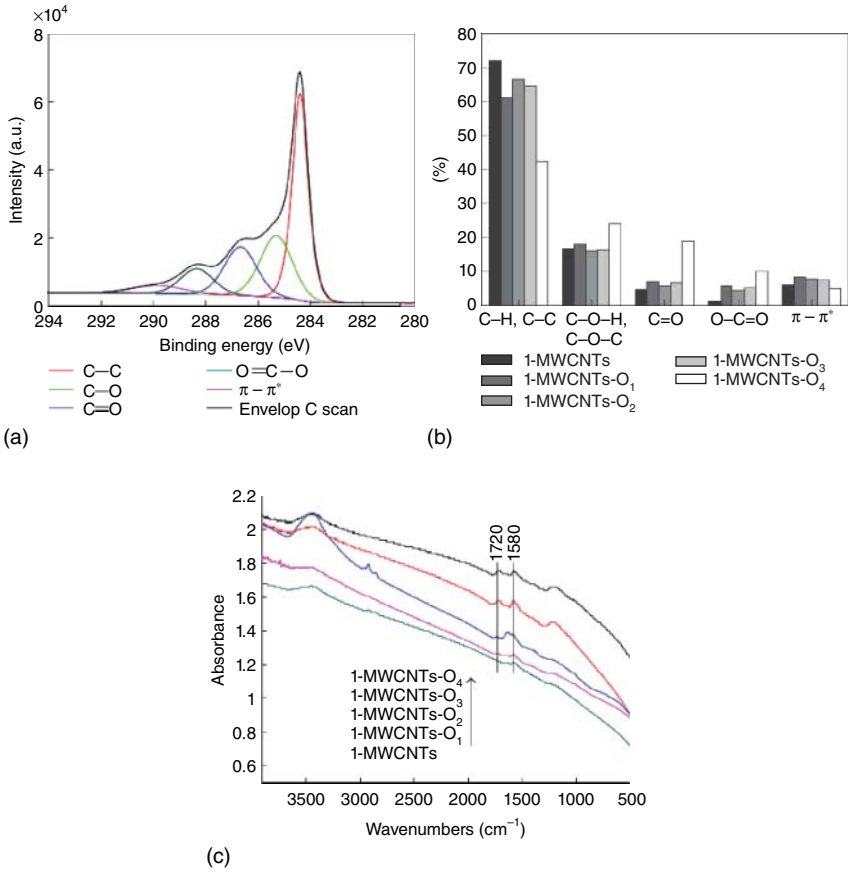

Figure 12.2 Surface chemistry of oxidized MWCNTs dispersed in aqueous solution. (a) XPS spectra of MWCNT-O_4. (b) Relative amounts of various oxygen species. (c) FTIR spectrum of MWCNTs with different oxidation degrees. The oxidation degree increases from O_1 to O_4 [41].

amounts of MWCNTs aggregating in the injection site, much of which was taken up by cells, making the cells black. But, no obvious acute inflammation or appreciable necrosis was seen in the subcutis around the injection site at the testing time points. On comparing the black color of the subcutis between 1 h and 90 days post injection, the color showed slight variation during the experimental period, implying that majority of the aggregating MWCNTs stayed around the injection site for more than 90 days. Although oxidized MWCNTs are stable in water because of the expelling of surface charge, they are likely to aggregate in phosphate buffered saline (PBS) buffer or in a saline medium because salt ions in these solutions affect the interactions between water molecules and MWCNTs. Therefore, the possible reason why many CNTs aggregated in the subcutaneous tissue is surface charge variation when CNTs encountered the physiological environment, because the

existing salts ions in the subcutaneous tissue can neutralize the surface charges of MWCNTs, resulting in their aggregation.

Then we asked what kinds of cell took up the CNTs. In subcutaneous tissue, there are plenty of phagocytic cells, and macrophages are the number one phagocyte because they are sentinel cells of the innate immune system and have a significant influence on the overall development of the body's immune response. In normal physiological conditions, macrophages are responsible for engulfing and clearing invading foreign particles or pathogens. Macrophages are larger than lymphocytes and have irregular shapes, unlike the latter which are round. Based on the morphology of the "black" cells, they were likely macrophage cells. By staining the tissue sections with the antibody against the macrophage membrane glycoprotein F4/80, it was confirmed that the "black" cells engulfing MWCNTs were mostly macrophages, evidenced by the brown-colored staining of the cells with the antibody.

In addition to the subcutaneous tissue, axillary lymph nodes of mice that received the MWCNTs through subcutaneous injection also exhibited black color, suggesting that the subcutaneously injected MWCNTs migrated from the injection site to the nearest skin-draining lymph nodes. These partially axillary lymph nodes remained black 90 days after the injection of MWCNTs, implying that some of the nanoparticles could stay in the lymph nodes for at least 3 months. Results from the analysis of H&E images showed that in the axillary lymph nodes excised 30 days after injection, scattered aggregation of MWCNTs were seen clearly, which were mainly accumulated in the subcapsular sinuses that are macrophage-rich regions of the lymph nodes. The MWCNTs moved gradually from subcapsular sinuses to the cortex region and medullary region over time. On day 30 post injection, only a small amount of MWCNTs were observed in the cortical sinuses, and 60 days after injection, more obvious aggregation of MWCNT could be observed in the cortex region while some MWCNTs appeared in the medullary region. Ninety days after injection, the number of MWCNTs in the cortex was observably less than that 60 days post injection, but the aggregates were larger in size. As it has been demonstrated that there were large numbers of macrophage cells engulfing MWCNTs in the injection site, we inferred that a part of MWCNTs were engulfed and carried into the lymph nodes by macrophage cells via the lymph ducts.

In the tumor-bearing mice, similar to the situation in the healthy mice, subcutaneously injected MWCNTs were observed only in the subcutaneous tissue around the injection site and lymph nodes, but not entering into the tumor tissue, which was shown either by anatomic photography or in sample slides of H&E staining. Even when injected into the subcutaneous tissue very close to the tumor, MWCNTs were not likely to diffuse into the tumor mass; instead, they were taken up by macrophages around the tumor [43]. It was thus clear that there are two zones surrounding the tumor mass. The zone immediately surrounding the tumor tissue consisted of numerous lymphocytes. Outside of the lymphocyte zone was an area consisting of numerous black cells expressing macrophage-specific glycoprotein F4/80. There have been some reports in the literature that CNTs entered the tumor

cells through different routes of administration. For example, Liu *et al.* reported that PEGylated SWCNTs showed high tumor accumulation when administrated intravenously due to their relatively long blood circulation times and low uptake by the reticuloendothelial system (RES) [44]. Murakami *et al.* [10] delivered SWCNTs adsorbed with PEG-doxorubicin into the tumor mass through intratumor injections. But, by the administration of subcutaneous injection, MWCNTs do not accumulate in the tumors mass. It is noticeable that there was no obvious accumulation of MWCNTs in organs of mice that received the injection subcutaneously. Representative histological images showed that no appreciable MWCNTs were observed in the liver, kidney, spleen, and heart of mice 2, 7, 30, 60, and 90 days after injection of 1 mg of MWCNT, suggesting that subcutaneously administrated MWCNTs mainly accumulated in the subcutaneous tissue around the injection site and in the lymph nodes in tumor-bearing mice.

In order to further indentify whether subcutaneously injected MWCNTs accumulated in the organs, a sensitive probe to track subcutaneously administrated MWCNTs is necessary. Basically, there are three ways to track CNTs *in vitro* or *in vivo*: (i) Radioactive labeling, which is widely used as a pharmacokinetic tool. For example, yttrium-86 and indium-111 were conjugated to CNTs [45], but there were potential safety issues though radioactive signals are sensitive. (ii) Raman spectroscopy is another effective method [46], but it is not applicable for the application in biological systems. (iii) The third method is fluorescent labeling using quantum dots [47] and chemical fluorophores. However, severe or even total fluorescent quenching occurs when fluorophores attach directly to the surface of CNTs, no matter whether they are noncovalently or covalently bound. Both energy-transfer and electron-transfer processes are considered to be major deactivation pathways for excited fluorophores on CNT surfaces [48–50]. To prevent this from happening, polyethylene glycol (PEG) chains have often been used as a spacer to connect fluorophores and CNTs [51]. This, however, might affect the bio-behavior of CNTs. For instance, CNTs are easily engulfed by phagocytes, especially macrophages, but PEGylation may help them to avoid phagocytosis by macrophages [52].

Porphyrin and its derivatives present intense fluorescence in the range 590–800 nm [53], making them widely investigated for electron-transfer study [54] and used as a photodynamic therapy agent to treat cancer [55], whereas in the spectral window the absorbance of biosystems is low. In our study, a novel fluorescent conjugate of MWCNTs and 5-(4-aminophenyl)-10,15,20-triphenylporphyrin (MWCNT–Pr) was synthesized for tracking CNTs in tissues [56]. Importantly, the porphyrin molecule has single amino group, allowing it to react with one CNT instead of several CNTs at the same time.

Comparing the FTIR spectra of MWCNT–Pr and MWCNTs, the peak at 1715 cm^{-1} disappeared in the latter, which is attributed to the carboxyl group of MWCNTs. In the meantime, a new peak due to the amide bond appeared at 1685 cm^{-1}, indicating that the amino porphyrin was covalently attached to the surface of MWCNTs through such a bond. The porphyrin density on the CNTs was estimated using X-ray photoelectron spectroscopy (XPS) analysis.

The nitrogen atom percentage was 1.55%, that of carbon 88.15%, and that of oxygen 10.3%. According to the molecular formula of porphyrin ($C_{44}H_{31}N_5$), the density of porphyrin getting attached to the surface of oxidized MWCNTs was 250 carbons per attached porphyrin unit.

The conjugate MWCNT – Pr had an excitation spectrum similar to that of free porphyrin and showed strong absorption peaks at 420 and 530 nm (monitoring wavelength was 700 nm). When excited at 420 nm, there were two main emission peaks of porphyrin and MWCNT – Pr at 670 and 730 nm, respectively, while the oxidized MWCNTs alone did not display any background fluorescence across the whole spectral window. Although a certain degree of fluorescent quenching existed in the conjugate, the fluorescent intensity of MWCNT – Pr was strong enough to make the oxidized MWCNTs visible.

In our *in vitro* studies, 420 nm was used as the excitation wavelength in *ex vivo* or *in vitro* experiments, because it resulted in stronger fluorescent emission. We, therefore, examined the fluorescent spectrum of tissue homogenates of mice that received subcutaneous injection of MWCNT – Pr. As very little background fluorescent emission was detected from the homogenates of control mice in all harvested tissues, we could conclude that the fluorescent emissions of the tested homogenates around 660 and 720 nm mainly came from the conjugate 3 months post subcutaneous injection.

By this method, we detected fluorescent spectra in the homogenates of the liver and kidney of mice that received subcutaneous injection of MWCNT – Pr. It was noted that the fluorescent intensity increased in the liver and lung during the experimental period (Figure 12.3). This may be indicative of a dynamic metabolic process of MWCNT – Pr in mice, accumulating first in the reticular endothelial system (RES) and then gradually metabolizing out, as the liver is the main organ of the metabolic RES. The increasing fluorescent intensity after 3 months post injection implied that there was a slight accumulation of MWCNT – Pr in the liver when MWCNTs were administrated through a subcutaneous local (nonvenous) exposure. Minimal fluorescent emissions were observed in the heart, lung, spleen, and kidney, indicating no obvious accumulation of oxidized MWCNTs.

For *in vivo* imaging experiments, fluorescent images of organs and tissues were acquired from the mice that received subcutaneous injection of MWCNT – Pr *ex vivo* because the fluorescence was not strong enough to penetrate deep tissues. An aqueous solution of MWCNT – Pr 0.5 ml (1 mg ml^{-1}) was injected into CD-ICR mice subcutaneously. The kidney, heart, liver, lung, spleen, and subcutaneous connective mucosa were harvested, and the fluorescent images were acquired at 1 h, 7 days, and 130 days post injection. Fluorescence could be observed clearly in the subcutaneous connective mucosa and liver even after 130 days after injection, while very little and no obvious fluorescence was observed in the lung and spleen/heart, respectively (Figure 12.4). Taken together, the above results show that subcutaneously administrated MWCNTs mainly accumulated in the subcutaneous tissue for more than 3 months, some MWCNTs migrated into the lymph nodes, while only a very small part entered the liver and lung. Based on these results, the administrated MWCNTs can be expected not to enter the blood

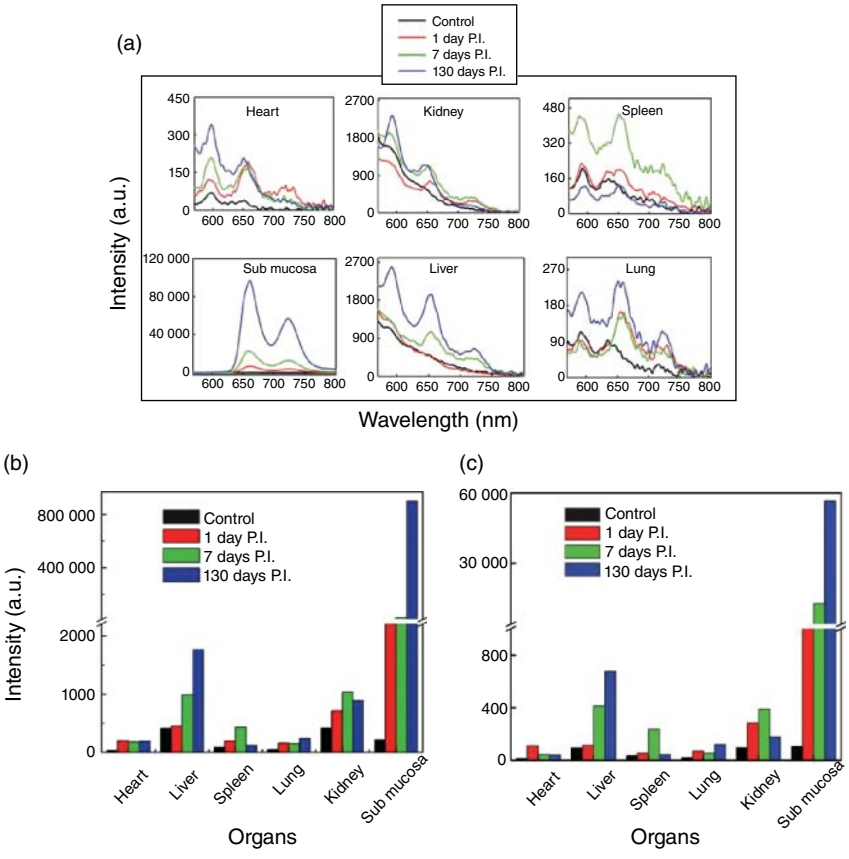

Figure 12.3 Biodistribution of MWCNT–Pr in mice throughout the experimental period. (a) Fluorescent spectra of WCNT-Pr in various organs and tissues of mice at different time points. (b, c) Histograms of peak values of the emission spectra. Note that "sub-mucosa" means subcutaneous connective mucosa. Excitation wavelength was 420 nm; emission peaks were around 660 and 720 nm [56].

circulation in a large way and accumulate in major organs. Differently, SWCNTs administrated by vein mainly accumulated in the liver, lung, and spleen [27].

The accumulation of MWCNTs in the auxiliary lymph nodes has the following implications to immune therapies. First, as there are plenty of lymphocytes in the lymph nodes, CNTs entering into the lymph nodes may act as a novel adjuvant to stimulate the lymphocytes, thereby elevating the immune activity of the cells. Second, lymph nodes are one of the major sites of cancer metastasis. The ability of MWCNTs to migrate to and accumulate in the lymph nodes makes them potential candidates of delivery systems targeting tumor cells and/or immune cells in the lymph nodes. As for the long-term accumulation of MWCNTs in the lymph nodes, we have demonstrated that MWCNTs in the lymph nodes migrate from the subcapsular sinus to the cortical sinus and then to the medullary region over

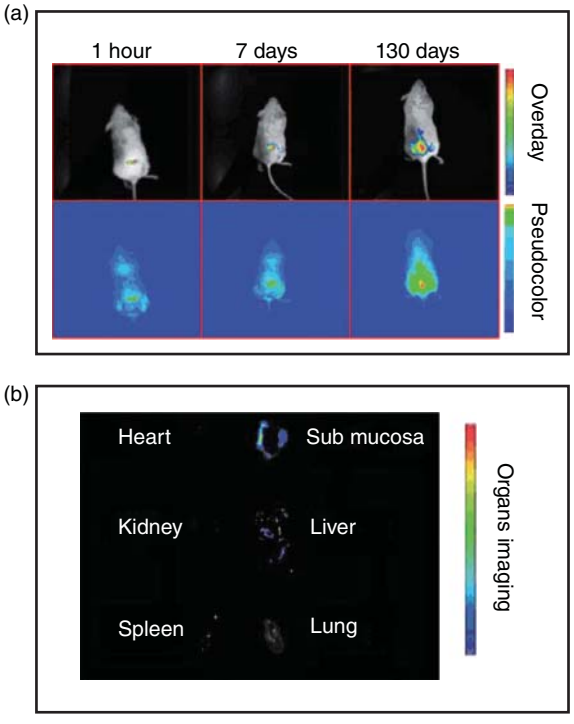

Figure 12.4 (a) Typical *in vivo* fluorescence images of MWCNT–Pr injected subcutaneously into the back of mouse. The mouse was imaged at multiple time points after injection. (b) Fluorescent images showing the *ex vivo* biodistribution of MWCNT–Pr 130 days post injection [56].

time, suggesting that the MWCNTs in the lymph nodes move out of the nodes at a slow rate and may eventually get out of them.

12.3.3
Immunological Responses Induced by Subcutaneously Injected MWCNTs

From pathological observations [42], slight fibrosis occurred in the subcutaneous tissue around the injection site of MWCNTs. Fiber-like substance in pink color and a small number of lymphocytes could be identified, indicative of a low level of inflammation. In the liver and kidney, short-term inflammatory reactions were observed: For mice scarified on day 2, post MWCNT injection, hepatocytes in the liver were slightly pale stained and swollen with few inflammatory cells and sinusoids with congestion. Vessels in the glomeruli of the kidney showed congestion and perivascular edema. But, on day 7 post MWCNTs injection, the hepatocytes almost reversed to normal morphology; the edema of the kidney was also reduced. The tissues collected on day 30 and 60 post injection exhibited normal histology, and no obvious signs of immune reactions such as tissue degeneration, necrosis, or

fibrosis were observed. The weights of organs in the MWCNT-administered and control groups on days 2, 7, 30, 60, and 90 post injection showed no significant differences. However, larger gaps between the cells and lighter staining of the cells in the liver could be seen on day 90 after MWCNT injection, suggesting that subcutaenous injection of MWCNTs has a minor influence on the histology of the liver.

12.3.3.1

Macrophages Responses Exerted by MWCNTs

Based on pathological analysis, we hypothesized that macrophages play crucial roles in response to the MWCNTs because subcutaneously residing macrophages are the first immune population encountered by MWCNTs and can largely engulf them. Macrophages were originally believed to be solely pro-inflammatory and destructive phagocytes. Their major functions are to phagocytose particulate matter and clear invading substances. Upon their activation, macrophages influence many processes of the innate and adaptive immune response, including inflammation, defense against infection, proliferation of antigen-specific T and B cells, and regulation of differentiated function of T and B cells. In addition, in recent years macrophages have been recognized as one of targeting cells in therapies for inflammation-related diseases such as cancer and atherosclerosis [57]. Since the 1990s, macrophages are believed to have ability to convert to a pro-healing phenotype [58] when they encounter other signals such as IL-4, IL-10 or IL-3, necessary for angiogenesis, wound healing, and tumor growth [59]. These macrophages are referred to as "alternatively activated" and named as "M2" to distinguish them from pro-inflammatory "M1" macrophages. Importantly, tumor-associated macrophages (TAMs) are widely believed to belong to the class of M2 macrophages, and are demonstrated as promoting angiogenesis [60]. Therefore, macrophages have many faces in biological systems and can be activated in different ways and thus take on different functions, depending what stimulating signals they receive from their microenvironments.

In the literature, CNTs are mainly reported as a toxic stimulus to macrophages, initiating macrophage-based inflammation and resulting in the fibrosis formation. For example, CNTs were found to stimulate macrophages to produce pro-inflammatory cytokines such as IL-1β, IL-6, INF-γ, and TNF-α through activating the NF-κB signaling pathway or inflammasome formation, thereby promoting inflammation and resulting in fibrosis in the lung [61–67]. But, it should be noticed that in most of the studies there has been a lack of a positive control such as lipopolysaccharide (LPS) treatment, and therefore it is not fair to conclude that CNTs exert significant levels of proinflammatory responses, according to the existing data; additionally, usually several typical inflammatory cytokines were examined instead of a complete profile. However, some research groups have reported that, in some cases, CNTs failed to induce strong inflammatory responses [68–70]. These conflicting cues imply that macrophage cells may be activated by CNTs with a mixed activation profile, instead of simple proinflammation or immune suppression.

We examined whether MWCNTs could modulate macrophages' phenotypes and functions, using cytokine array, ELISA assay, transwell assay, confocal microscopy, and reactive oxygen species (ROS) examination, taking LPS treatment as positive control and a combination of IL-4, IL-10, and IL-13 as negative control [71]. When macrophage cells were incubated with the MWCNT-containing culture medium, their function of phagocytosis was initiated. The cells engulfed a large amount of MWCNTs and became MWCNT-activated macrophages (named MWCNT-RAW). Accompanied with the phagocytosis were macrophages' cytoskeleton changes, leading to the variation of cell morphology. Naïve macrophages (named as con-RAW) displayed transparent cytoplasm without filopodia, and the F-actin (red fluorescence) was mainly diffused in the cytoplasm. LPS-treated macrophages (named as LPS-RAW) displayed the F-actin distribution throughout the whole cells; differently, the F-actin was restrained in the elongated filopoda and around the nucleus of MWCNT-RAW, suggesting that MWCNT-RAW has an activation status different from that induced by LPS.

Actually, macrophages can show an activation spectrum according to stimulating signals they receive. M1 and M2 represent the two extremes in the activation spectrum: M1 macrophages promote inflammatory reactions and antitumoral responses, while M2 macrophages regulate immunological responses and enhance wound healing [72]. By detecting surface markers of macrophages upon MWCNT exposure, we can learn about the phenotypes of the macrophages. We chose following surface markers: polyspecific receptor (CD14), a complex of toll-like receptor 4 and myeloid differentiation factor 2 (TLR4/MD2), CD11b, mannose receptor (MR, or named as CD206), and the main histocompatible complex II (MHCII).

CD14 is expressed predominantly on the surface of monocytes and macrophages, presenting invading substance to the complex of TLR4/MD2 and further signaling inside the cell. It was shown that MWCNTs upregulate CD14 level significantly while downregulate the TLR4/MD2 level in a concentration-dependent manner, suggesting that MWCNTs induced TLR4 endocytosis [73] and resulted in the downregulation of TLR4/MD2. CD11b is a pattern recognition receptor, capable of recognizing and binding to many molecules found on the surface of invading bacteria or foreign cells. MWCNTs induced a concentration-dependent rising level of CD11b, indicating that the phagocytosis of macrophages was initiated. During phagocytosis, foreign substances or antigens are processed into peptides in the cell and delivered to the surface of the cell with MHCII, facilitating antigen presentation. However, the level of MHCII was not upregulated by MWCNTs, implying that macrophage cells not taking MWCNTs as a dangerous exogenous antigen. In contrast to MHCII, CD206, one of the markers indicating alternative activation for macrophages [73, 74], was elevated significantly by MWCNTs. Taken together, these mean that MWCNTs were internalized largely by macrophages and activated macrophages in a specific way that is different either from the classical activation way or from the alternative activation way.

Phenotypes determine the function of cells. As expected, macrophages were activated classically by LPS treatment; most of the pro-inflammatory cytokines were significantly upregulated. On the contrary, macrophages did not produce significant pro-inflammatory cytokines upon the IL treatment. Differently, the levels of many pro-inflammatory cytokines did not increase significantly by MWCNT exposure compared to that by LPS. For example, typical pro-inflammatory cytokines such as IL-1α, IL-1β, IL-6, IL-12p70, IL-17, TNF-α, MCP-1, granulocyte colony-stimulating factor (G-CSF), granulocyte-macrophage colony-stimulating factor (GM-CSF), and C5a were elevated little upon the MWCNTs exposure [71]. Consistent with our above observation, other researchers also reported that both short (220 nm) and long (800 nm) MWCNTs activated human monocytes significantly lower than microbial lipopeptide and LPS, and no activity appeared following the variation in the length of CNTs [69]. But, it is striking that macrophage inflammatory protein-1 alpha (MIP-1α) and MIP-2 and tissue inhibitor of metalloproteinases 1 (TIMP-1) were upregulated significantly by MWCNT exposure: the level of MIP-1α was twice that induced by LPS; the level of MIP-2 was comparable to that induced by LPS; and the level of TIMP-1 was about 6 times that induced by LPS. The signature of MWCNT-mediated macrophage activation is clearly different from that of LPS-mediated or IL-mediated activation.

MIP-1α and MIP-2 belong to a superfamily of small proteins. The role of MIPs is to recruit naïve macrophages and lymphocytes. We applied a transwell assay to verify whether MWCNTs initiated the recruitment function of macrophages [71]. Naïve macrophages were added in the upper chamber, and MWCNT-containing cell culture medium was added in the bottom chamber. Significant migration of naïve macrophages was observed until 24 h of incubation, which was strongly dependent on the incubation time. A large number of macrophages migrated into the lower chamber containing MWCNTs, while little migrated into the control medium. Results from western blot assay verified the incubation-time-dependent elevation in MIP-1α and MIP-2 production for MWCNT-RAW. When the antibody of MIP-1α or MIP-2 was supplemented in the MWCNT-containing culture medium in the lower chamber, 30% or 50% of the migration of macrophages was inhibited, respectively.

According to these results, we infer that macrophages simultaneously migrating into the lower chamber engulf MWCNTs in the culture medium and produce recruiting-related cytokines subsequently. It is time consuming to accumulate MIP-1α and MIP-2 sufficiently to attract naïve macrophages in the upper chamber to migrate into the lower chamber. The newly formed MWCNT-RAW secrete MIP-1α and MIP-2 to attract naïve macrophage cells toward to the MWCNT-RAW, allowing MIP-1α and MIP-2 to accumulate gradually to form a feedback loop of recruiting naïve macrophages. In this case, MWCNT-RAW acts as a core of attracting naïve macrophage cells but not as a source inducing severe inflammations. Similar to with above mechanism, the concentration-dependent effect of MWCNTs was also observed [71].

The results that MWCNT-RAW exhibits constant level of MHCII and elevated level of CD206 and produce high amount of TIMP-1 imply that MWCNT-RAW may act like M2 supporting tissue repair. We then examined the secretion of matrix metalloprotein 9 (MMP-9) and VEGF for MWCNT-RAW, both of which are typical factors to promote the fusion of blood vessels [75]. Results show that MWCNT-RAW secreted MMP-9 and VEGF depending on the concentration of MWCNTs. It is known that the endogenous inhibitor TIMP-1 regulates the activity of MMP-9. The synthesis of MMP-9 and TIMP-1 are under the control of the same transcription factors, and MMP-9 and TIMP-1 reach a balance to control physiological processes including migration, angiogenesis, and wound healing [76]. MWCNT-RAW significantly produced TIMP-1 and MMP-9, allowing MWCNT-RAW in a balanced function of tissue degradation and formation. The secretion feature of MWCNT-RAW can explain why subcutaneously injected MWCNTs did not cause severe tissue injury in the subcutis, lymph nodes, and liver. Another research group reported that CNTs induced moderate cell infiltration and cytokine production (TNF-α, IL-β), which were much lower than that of LPS, while the concentration of MIP-1α in BAL fluid significantly increased by about 32.2-fold at 24 h after instillation of 4 mg kg^{-1} SWCNT compared to the vehicle control [77].

It is also interesting that the level of MHCII was kept constant for MWCNT-RAW; meanwhile, most pro-inflammatory cytokines in the array were mildly upregulated except for several recruitment-related cytokines, suggesting that macrophages do not regard MWCNTs as a hazard like LPS. Meanwhile, the CD206 level was elevated significantly, along with the secretion of MMP-9 and VEGF. Both MMP-9 and VEGF are closely associated with wound healing through promoting angiogenesis. From these data, the following conclusions can be made: (i) MWCNT-RAW is partially activated in the classical way and partially in the alternative way, showing a CNT-mediated specific activation signature. (ii) MWCNT-RAW has double faces; it combines the functions of M1 and M2, playing M1 function to secrete recruiting-related cytokines to recruit naïve macrophages, and playing M2 function to produce MMP-9 and VEGF that have the potential for angiogenesis. These results imply a better biocompatibility of CNTs than that of many other inorganic and metal nanomaterials.

12.3.3.2 MWCNTs Attract Naïve Monocyte Macrophages Through Activating Macrophages in the Subcutis

The MWCNT-mediated activation of macrophages has implications in eliciting immune responses in healthy mice. According to above results, the question emerges: do MWCNTs attract naïve macrophages to their aggregation site? Or are there new macrophages from the circulating blood coming to the injection site?

In order to identify the origin of macrophages in the injection subcutis tissue, we utilized ultrasmall paramagnetic iron oxide (USPIO) nanoparticles as an indicator of the variation of macrophages in the tissues, because iron oxide nanoparticles can show blue color by Perl's blue staining [78]. USPIO

nanoparticles are a type of contrast agent for magnetic resonance imaging (MRI) because of their specificity for macrophages, and usually used for MRI of lymph nodes [79]. After intravenous injection, USPIO nanoparticles are taken up by monocytes in the blood and differentiate to tissue macrophages. Meanwhile, USPIO can enter the interstitial space from blood vessels directly and be intracellularly trapped in tissue macrophages. Those macrophages containing USPIO can be visualized in tissue by Perl's blue staining. Therefore, the blue area and iron content in the tissues can indicate the macrophages recruited from circulating blood. Figure 12.5 presents histological observations of mice that received subcutis injection of USPIO intravenously after subcutaneous administration of MWCNTs injection or the same volume of water for 1 week. Figure 12.5a and c are the subcutis sections stained by H&E, showing that the subcutaneously injected MWCNTs were aggregated in the subcutis and taken up by resident macrophages. Interestingly, in Perl's blue-stained sections, there were many blue-stained cells in the subcutis around the MWCNTs aggregation (Figure 12.5b), while no obvious "blue" cells could be seen in the control subcutis where no MWCNTs were injected (Figure 12.5d). According to the characteristics of USPIO mentioned above, it is inferred that those blue cells were

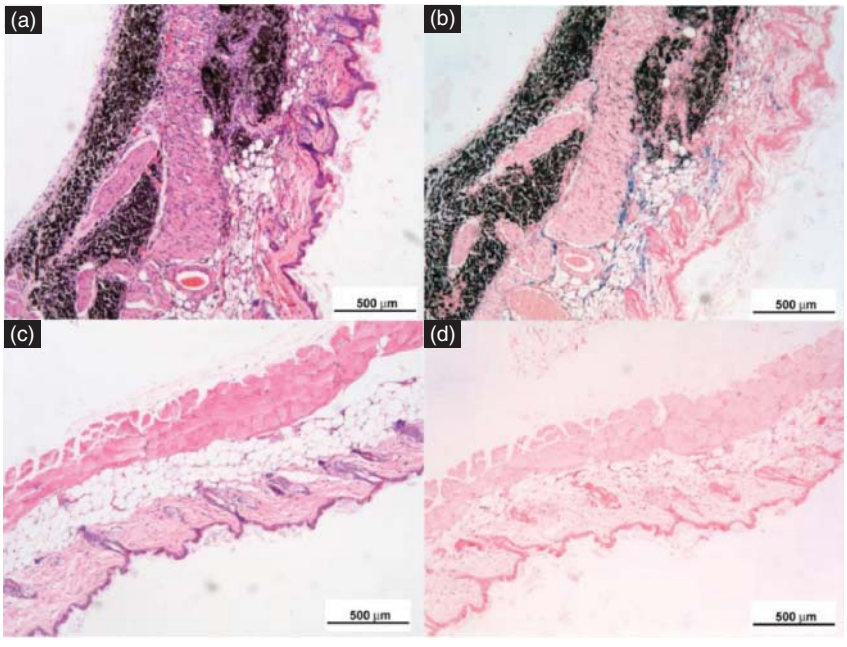

Figure 12.5 Histological observations of subcutis around subcutaneously injected o-MWCNT or water by H&E and Perl's blue staining. (a, b) Subcutis tissues stained by H&E and by Perl's blue around the injection site of o-MWCNT injection. (c, d) Subcutis tissues stained by H&E and by Perl's blue around the injection site of control [78].

new macrophages attracted by aggregated MWCNTs from the interstitial space and/or circulating blood, indicating macrophages taking up MWCNTs attracted naïve macrophages constantly during the experimental period. This is consistent with results of MWCNTs initiating macrophage recruitment function. It is clearly shown that subcutaneously injected MWCNTs not only initiate resident macrophages in the subcutis around the injection site but also induce activated resident macrophages to recruit naïve macrophages.

12.3.3.3

Subcutaneously Injected MWCNTs Induce Complement Activation

The complement system is comprised of more than 30 serum proteins and cell-surface receptors that interact to recognize, opsonize, and clear or kill invading microorganisms, and alter host cells and other foreign materials; therefore it is a major component of the innate immune system. The activation of the complement is organized into three separate pathways: the classical, lectin, and alternative pathways, all of which converge at the third complement component (C3). C3 is enzymatically cleaved into C3a and C3b, which are deposited on the surface of cells or microbes. This process, in turn, leads to the cleavage of C5 and the release of C5a, which act to recruit immune cells to the site of inflammation. Therefore, consumption of C3 and production of C5a are indicative of complement activation. After being injected for 2 days, MWCNTs induced the C3 level to decrease significantly in the serum, indicating that C3 consumption and the complement system were activated. Further decreasing of C3 was observed 7 days post injection. After 30 days post injection, C3 in the serum returned to the normal level. Meanwhile, the levels of C5a displayed an increasing trend, and then went down to the normal level. Although the levels of C3 and C5a varied over time, we found no statistically significant differences between mice that received different doses of MWCNTs, suggesting that no obvious concentration dependence exists [42].

Complement activation by systemically administered drugs is responsible for some tissue injury and hypersensitivity (allergic) reactions and anaphylaxis, which is a life-threatening condition [80]. Additionally, high levels of complement activation are known to generate inflammatory responses and promote the formation of granulomas. Our histological analyses showed that only a minor inflammatory reaction was produced at the injection site, and no granulomas were observed over time. The dynamic variation in the levels of C3 and C5a in the serum induced by subcutaneously administrated MWCNTs indicates that this route of administration induces only short-term complement activation, because the levels of these complement proteins return to normal levels 1 week after injection. Therefore, subcutaneous administration of MWCNT is relatively safe compared to other methods of administration such as intravenous injection, inhalation, and so on. Complement activation can enhance macrophage phagocytosis, and therefore macrophages can engulf more MWCNTs, which in turn is likely to promote macrophages to secrete more MIPs and VEGF and MMP9.

12.3.3.4

Subcutaneously Injected MWCNTs Elevate Pro-inflammatory Cytokines in the Blood

Cytokines are part of an extracellular signaling network that controls every function of innate and specific immune response such as inflammation, defense against virus infection, proliferation of specific T and B cell clones, and regulation of their differentiated function. The different cytokines fall into a number of categories, including interferons (IFNs), interleukins (ILs), colony-stimulating factors (CSFs), chemokines, and others such as transforming growth factor-beta (TGF-β) as well as tumor necrosis factors TNF-α and TNF-β. Pro-inflammatory cytokines are mainly produced by immune effector cells including lymphocytes, macrophages, and neutrophils.

To analyze the cytokine profiles in the serum of the mice that were injected with MWCNTs, we employed a cytokine array to detect the relative expression levels of 40 different inflammatory cytokines 2 and 7 days post injection [42]. Among the 40 cytokines tested, 19 were clearly upregulated by more than twofold 2 days after injection with MWCNTs. Among these, interleukin (IL)-17 was the most significantly up regulated, as indicated by its 5.41-fold increase in expression in the MWCNTs group; I-TAC, IL-1β, and IFN-γ exhibited more than threefold increase in expression, and IL-1α, IL-2, IL-3, IL-6, IL-10, IL-13, CD30L, G-CSF, GM-CSF, KC, leptin, MIG, TIMP-2, and TNF-α were modestly upregulated, as shown by a twofold increase in their expression. Seven days after injection of MWCNTs, most of the cytokines returned to almost normal levels, with only slight variations, when compared to the levels of the control group. Analysis of the cytokine array indicated that the MWCNTs induce inflammatory responses within 2 days after injection. This is consistent with a previous report [31], in which cytokines in the blood, including IL-1, IL-6, and IL-10, reached their highest levels before the third day after a single intratracheal instillation of nanotubes. It is important to note that, here, the inflammatory response in mice apparently disappeared, and the cytokine levels returned to normal 7 days after the injection of MWCNTs.

We consider that the elevated pro-inflammatory cytokines are due mainly to the interaction of MWCNTs with subcutaneous resident and naïve macrophages and lymphocytes recruited by MWCNTs that are engulfed by macrophages. Because there are no antigens as targets for those stimulated macrophages and lymphocytes, the innate immune responses are not able to initiate specific immune reactions. In this case, although macrophages engulfing MWCNTs kept on attracting naïve macrophages to take up aggregated MWCNTs, the innate inflammatory reactions eventually turned to a low level over time. Researchers in other groups observed the length dependence of pro-inflammatory responses induced by MWCNTs upon the human acute monocytic leukemia cell line THP-1 *in vitro* and the response in subcutaneous tissue *in vivo*. They used 220- and 825-nm-long MWCNTs and found that the degree of inflammatory responses in subcutaneous tissue in rats around the short MWCNTs was small in comparison with that around the long MWCNTs. However, no severe inflammatory responses such as necrosis, degeneration, or neutrophil infiltration *in vivo* was observed around both the MWCNTs examined throughout the experimental period [69].

Carcinogenicity is another important factor of MWCNTs that should be evaluated with respect to their applications. Researchers have performed a carcinogenicity test by implanting MWCNTs into the subcutaneous tissue of rasH2 mice, using the carbon black present in black tattoo ink as a reference material for safety. They reported that the rasH2 mice did not develop neoplasms after being injected with MWCNTs; instead, MWCNTs showed lower carcinogenicity than carbon black. Such evaluations should facilitate the clinical application and development of CNTs for use in important medical fields [81]. Altogether, our and others' results indicate that subcutaneous injection of MWCNTs induces pro-inflammatory responses to certain degrees in the short term, which, however, do not reach serious levels, suggesting that this route of administration is safer than systemic administration of CNTs.

12.4 Immunological Responses Induced by Subcutaneous Administration of MWCNTs in Tumor-Bearing Mice

Cancer is a generic term that encompasses a group of disease characterized by an uncontrolled proliferation of cells. There are over 200 different types of cancer, each of which derives its name according to the type of tissue the cell originates in. There are currently many therapies in clinical use. The significance of immunotherapy as an adjuvant anticancer treatment has been well recognized [82–84].

As described above, MWCNTs stimulate the innate immune system, and thereby possess inherent adjuvant properties, which has implications in cancer immune therapy. Cancer cells often develop immune tolerance and immune escape mechanisms [85, 86]. Meanwhile, tumor-specific antigens have not been identified yet for most cancers. Hence, in order to mount an anticancer immune reaction, a cancer adjuvant should be used to rescue and increase immune responses against tumors in immunocompromised patients, with acceptable profiles of toxicity and safety.

Adjuvants currently investigated in immunotherapies mainly include tumor cell vaccines (TCVs) made of inactivated cancer cells, dendritic cells (DC) that have been exposed to tumor antigens, and cytokines that modulate the immune function [87–89]. Although these techniques have achieved various degrees of success, the efficacy of immunotherapy generally needs additional improvement [90, 91]. Currently, various candidates such as Bacillus Calmette-Guerin (BCG), heat shock protein (HSP), Detox, Montanide, QS-21, CpG oligonucleotide (CpG ODN), alum, very small size proteoliposomes (VSSP), polylactic acid (PLA) nanoparticles, chitosan nanoparticles, and dendrimers are being investigated [92]. It has been recognized that an adjuvant for cancer vaccines needs to be more potent, but they may be more toxic and even induce autoimmune reactions. Given the immune stimulant features of CNTs, it will be of great interest to evaluate whether CNTs can be applied as a novel adjuvant to improve antitumor responses in tumor-bearing mice.

12.4.1 MWCNTs Induce Systematic Immune Responses in Tumor-Bearing Mice

In tumor-bearing mice, tumor self-antigens exist in multiple forms, such as tumor cells, debris of dead cells, molecules secreted by tumor cells, and so on. Hence, we investigated whether MWCNTs could induce specific immunological responses in a tumor-bearing mice model via their local administration through subcutaneous injection to stimulate the immune system. We also explored the possibility of utilizing the immune responses to modify the rate of tumor progression [43].

After subcutaneous injection of MWCNTs, the volume of tumor in mice in the control and MWCNTs groups was measured every 3 days and the inhibition rate for each mouse was calculated to examine whether the subcutaneously injected MWCNTs affected the tumor progression in mice. When plotted in terms of their natural logarithm, the mean tumor volume of the MWCNTs group had a trend to decrease after the second injection of MWCNTs, while that of the control group kept increasing. In the experimental period, a number of tumor-bearing mice in the MWCNTs group showed tumor regression, and even the clearing off of the tumor, while in others the tumor growth progressed, making the standard deviation for the mean tumor volume of natural logarithm at each time point increase over time. The difference in tumor volume variation between the MWCNTs group and tumor control group was significant within the eight time points ($^{**}P = 0.001$), as calculated by multivariate analysis of variance (MANOVA). In addition, the tumor volume of the mice subcutaneously injected with MWCNTs very near the tumor mass did not show any obvious difference in comparison with those injected with MWCNTs in the neck.

At the end of the experimental period, tumor tissues were removed from the mice and fixed for histological observations. The tumor tissue of the MWCNT group was heavily surrounded by lymphocytes; some of these lymphocytes were even infiltrating into the surrounding tumor mass. At the edges of the tumors tissue, caseous necrosis was observed, in which dead tumor cells formed an amorphous proteinaceous mass. Differently, tumor cells in the control group showed marked variation in the size and shape of their nuclei, indicating heavy proliferation, hyperchromatism, and numerous mitoses. Histological observations were also performed with the liver, kidney, and spleen of mice in the MWCNTs group when the experiment was terminated. It could be seen that there were no appreciable MWCNTs in these organs. Additionally, tissues in the liver, kidney, and spleen basically remained normal without any signs of fibrinosis and necrosis as well as granuloma formation. According to these observations, we concluded that subcutaneous administration of MWCNTs could induce systematic immune responses in tumor-bearing mice, and therefore it is one of the administration options to boost the general antitumor immune activity.

12.4.2 MWCNTs Upregulate Multiple Pro-inflammatory Cytokines in the Blood

To understand the mechanism of the above effect, we examined the serum cytokine production of the MWCNTs group and the tumor control group. Many

cytokines, such as IFN-γ, ILs, and TNF-α, have been proven to be relevant to enhance immune functions of T cells, B cells, and macrophages, and have been used in cancer therapy at different stages [93]. In our study, a mouse protein cytokine array was performed with serum samples of mice to detect the levels of 40 cytokines [43]. We noticed that 2 days after subcutaneous injection, the level of the 40 cytokines were unchanged in comparison to that of the control, suggesting that the immune system was suppressed because of the existence of the tumor.. On day 7 post injection, most of the cytokines were clearly upregulated in the MWCNTs group compared to those of the control group. Our results indicated that 19 cytokines were most notably upregulated (variation > 50%), including G-CSF, GM-CSF, IFN-γ, and eight interleukins (ILs); 14 cytokines were modestly upregulated (variation > 20%), including 6 ILs and tumor necrosis factor-alpha (TNF-α). Among those inflammatory cytokines, interferon-γ (IFN-γ), IL-1, IL-6, and IL-12 are widely considered to have functions against tumor cells. Meanwhile, regulatory cytokines such as IL-4 and IL-10 are also upregulated, which suggests two points: (i) A balance between inflammatory and regulatory responses exists, avoiding severe injury due to strong immune reactions elicited by MWCNTs. (ii) MWCNTs may induce both cellular and hormonal responses.

As we have demonstrated, MWCNTs can be carried by macrophages into lymph nodes where plenty of lymphocytes stay; meanwhile, MWCNTs aggregating in the subcutis are taken up by macrophages, inducing them to secrete cytokines to attract naïve macrophages and lymphocytes. Both ways allow lymphocytes to interact with MWCNTs directly. Therefore, the elevated pro-inflammatory cytokines in the blood should be contributed by lymphocytes and macrophages.

12.4.3
MWCMTs Mediate Cytotoxicity of Lymphocytes

Beside cytokine production, we also evaluated whether MWCNTs could trigger cytotoxicity through affecting the function of lymphocytes. The effects of MWCNTs on lymphocyte-mediated cytotoxicity on multiple human cell lines were assessed. Moreover, the influence of MWCNTs on the proliferation of lymphocytes, the production of IFN-γ and TNF-α by lymphocytes, and the activation of NF-κB was examined in order to demonstrate the mechanisms of CNT-induced immune cytotoxicity [92].

It is interesting that MWCNTs at low concentration ($0.001 - 0.1\,\mathrm{mg\,ml^{-1}}$) enhanced the immune-mediated cytotoxicity against multiple types of human cells *in vitro* but did not cause obvious cell death or apoptosis directly. In addition, MWCNTs increased the secretion of cytokines signaling the activation of lymphocytes, including IFN-γ and TNF-α, but failed to trigger a proliferation of the lymphocytes. Furthermore, MWCNTs upregulated the NF-κB expression in immune cells, and the blockage of the NF-κB pathway reduced the CNT-induced cytotoxicity by lymphocytes. These results suggest that CNTs may potentially trigger an indirect cytotoxicity through enhancing the function of lymphocytes.

12.4.4 MWCNTs Induce Complement Activation

Besides the upregulation of inflammatory cytokines in the blood serum, on day 7 after the subcutaneous injection of MWCNTs, complement activation occurred as well. Nanoparticle-induced complement activation may result in altered biodistribution in the form of rapid clearance from the systemic circulation via complement receptor-mediated phagocytosis by mononuclear cells. In addition to its primary role in nonspecific pathogen clearance, complement activation was proven to be important in supporting cell-mediated immunity through enhancement of B-cell responses to antigen and the promotion of the activation of dendritic cells and T cells [80]. Therefore, complement activation is important in antitumor activities of the body; both cellular immunity and antibody immunity are complement-dependent. Accompanying the increase in inflammatory cytokines, on the seventh day after second injection of MWCNTs, serum C3 level for the MWCNTs group dropped significantly compared to the control group. It is interesting to note that C3 level is related to the tumor dimension. Mice with tumor inhibition rates >50% displayed lower C3 levels than those with tumor inhibition rates <50% [43]. This suggests that subcutaneously injected MWCNTs activate the complement system of tumor-bearing mice, and the significant complement activation induced by MWCNTs influences the progression of tumor growth.

12.4.5 MWCNTs Attract Monocyte-Macrophages to Affect the Microenvironment of Tumor Mass

Besides boosting immune responses of tumor-bearing mice against tumor cells, MWCNTs can affect the tumor microenvironment. Tumor development and antitumor mechanisms of the host are critical issues with enormous complexity and challenges. As is known, aggressive or metastatic tumor cells can produce attractants to draw macrophages into the tumor microenvironment and then educate them to promote tumor progression [94]. These TAMs are in the alternate M2 activation state and exhibit characteristics of both wound-healing macrophages and regulatory macrophages, and produce cytokines and growth factors that can help tumor growth. Extensive research has demonstrated that macrophages in the tumor microenvironment are closely associated with the development and progression of a variety of tumors, such as breast cancer [95, 96], prostate cancer [97], glioma [98], lymphoma [99], bladder cancer [100], lung cancer [101], cervical cancer [102], and melanoma [103]. For these reasons, antitumor activities of the immune cells in the tumor-bearing hosts are at very low levels, thus allowing most tumor cells to escape the immune system [104]. In the development of immune suppression, macrophages play crucial roles to tumor microenvironments.

It has been recognized that macrophages within the tumor microenvironment are derived from peripheral blood monocytes recruited into the tumor, rather than

from local tissue macrophages [105]. Our results show that on intravenous injection of USPIO and stained with Perl's blue, the tumor mass of mice shows blue areas (Figure 12.6a); meanwhile, blue color also appears in the subcutis where MWCNTs aggregated, indicating that monocyte-macrophages are attracted to the MWCNTs. Then we asked whether the subcutaneously injected MWCNTs can compete with the tumor mass to attract macrophages, reducing the number of macrophages in the tumor microenvironment. Observation in Perl's blue-stained tissue sections (Figure 12.6b,c) shows that there are many blue cells in the tumor margin. Compared to control (tumor-bearing mice that did not receive MWCNTs), the tumor tissue of the MWCNTs group has less blue areas. This observation was proven by the result of inductively coupled plasma-mass spectrometry (ICP-MS) analysis (Figure 12.6d), showing less iron in the tumor mass of MWCNTs group. The blue cells in the tumor margin were macrophages expressing F4/80 (Figure 12.6e). These results indicate that monocyte-macrophages are recruited by the tumor mass. Because of the competing attraction from subcutaneous MWCNTs, fewer monocyte-macrophages were recruited into the tumor mass of the MWCNTs group compared to that of the control group.

Tumor-associated macrophages play the role of supporting angiogenesis in the tumor microenvironment to promote tumor metastasis [94, 106]. Hence, fewer macrophages migrating to the tumor would lead to the formation of fewer neovascular structures. Histological observation shows that more vascular structures exist around the tumor mass of the control group than that of the MWCNT group by statistically counting the vessel density in five randomly selected areas in three sections for each group. Immunohistological staining of vascular endothelium cells with anti-CD31 antibody showed that CD31 in the MWCNTs group was less than that in the control group.

It is reasonable to infer that the attraction of MWCNTs to monocyte-macrophages contributes to the inhibition of tumor progression. In the mouse breast tumor 4T1 model, which is highly metastatic to lung, tumor cells in the control group show features of heavy proliferation, indicated by marked variation in the size and shape of their nuclei, with hyperchromatism and numerous mitoses; on the contrary, tumor cells in the MWCNTs group exhibit shrunken nuclei and many pores appearing in the tumor mass. Additionally, metastatic lesions were observed in the control group, while no obvious metastasis was observed in the lung of the MWCNTs group. These results suggest that subcutaneously injected MWCNTs have an inhibitory effect on lung metastasis by affecting the tumor microenvironment as well as stimulating lymphocytes of mice.

In summary, subcutaneously injected MWCNTs can function as an immunostimulatory adjuvant in tumor-bearing mice. By initiating macrophage activation, MWCNTs induce complement system activation significantly, elevate the pro-inflammatory cytokine level in the blood, and mediate cytotoxicity of lymphocytes. All these responses increase the activity of the host immune system and inhibit the progression of tumor growth, suggesting MWCNTs' potential as a new class of adjuvants in antitumor immune therapies. The clinical implications,

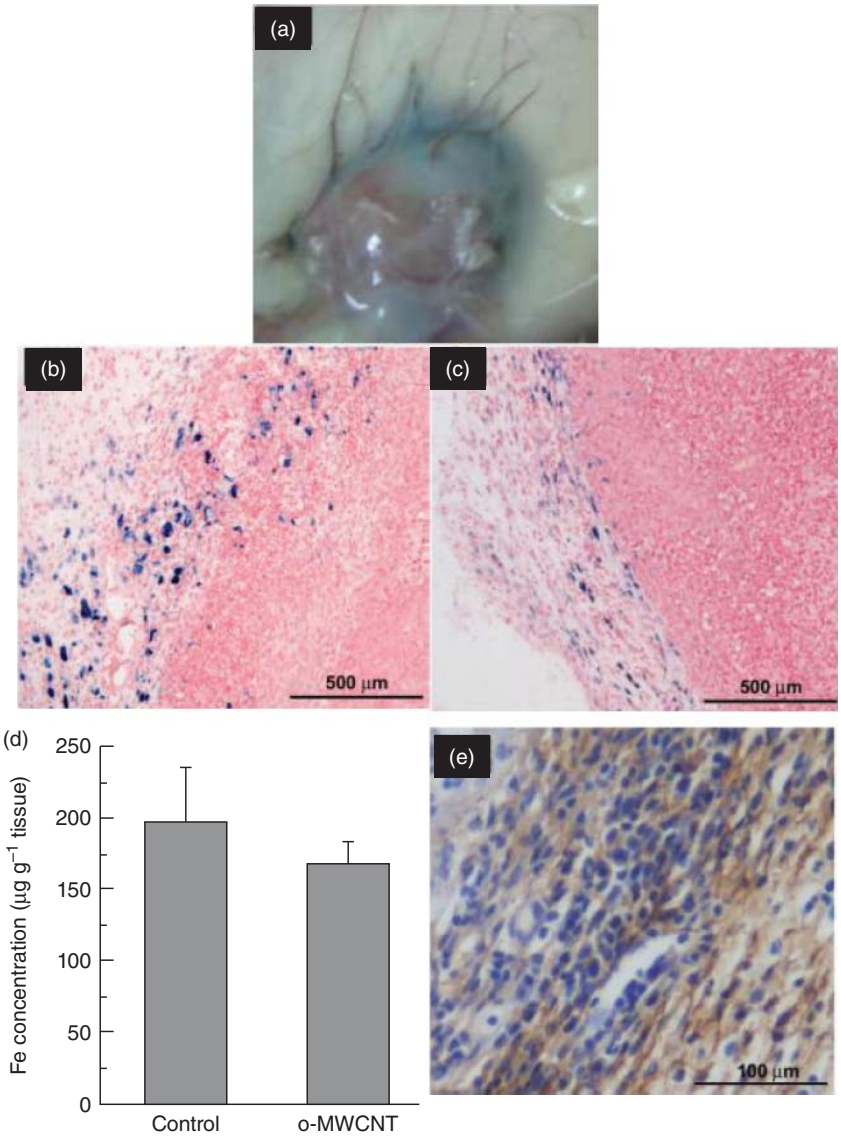

Figure 12.6 Subcutaneous injection of MWCNTs reduces macrophages in the tumor microenvironment. (a) Anatomical morphology of tumor mass stained by Perl's blue. (b) Histological analysis of tumor tissue stained with Perl's blue of control mouse. (c) Histological analysis of tumor tissue stained with Perl's blue of MWCNT- injected mouse. (d) ICP-MS analysis of iron concentration in tumor mass of the control and MWCNT-injected mice ($n = 3$). (e) Immunohistochemical staining of macrophage in the tumor tissue sections with anti-F4/80 [78].

safety evaluations of MWCNTs, and underlying mechanisms require further investigation.

12.5 CNTs as Antigen Delivery System to Enhance Immune Responses Against Tumors

While chemotherapy faces the issues of accumulative toxicity and drug resistance, antitumor immunotherapy usually has few adverse effects, good patient tolerance, and the potential to significantly improve the prognosis [107]. Active specific immunotherapies (vaccines) take advantage of the ability of the immune system to recognize and react with foreign antigens. An effective tumor vaccine must induce a potent immune response, either at the cellular level, stimulating cytotoxic T cells that target and destroy tumor cells, or at hormonal level, through stimulation of the production of neutralizing antibodies that promote opsonization and consequent tumor clearance. However, in case of cancer vaccines, the antigens typically are not foreign, but overexpressed self-antigens on the surface of or inside the tumor cells [108]. Tumor self-antigens are generally poorly immunogenic, and the host bearing the tumor either does not recognize the antigen or is tolerant to it [109]. Conjugation of antigenic epitopes to particulate scaffolds is believed to have the ability to improve immune responses and the responses are most improved when the particles are on the nanoscale [110].

The physiochemical properties of CNTs encompass flexible surface chemistry, a variety of structure morphologies, and enhanced transport ability across the cell lipid bilayer [111]. One area of particular interest is CNTs' role in modulating immunological functions. Prior study has revealed that viral peptides conjugated to CNTs can elicit strong anti-peptide antibody responses in mice with no detectable cross-reactivity to the CNTs [112]. It is also reported that functionalized CNTs are noncytotoxic to immune cells [113]. These properties are attractive for the design of immunotherapeutic platforms. In this section, we review the research progress of CNTs as immunotherapeutic platforms for antigen delivery in oncology immunotherapy.

The attachment of proteins and peptides to the outer surface of CNTs can be realized through either covalent or noncovalent bonding. Noncovalent functionalization includes hydrophobic, $\pi-\pi$ stacking, and electrostatic interactions. Covalent attachment of biomolecules on the surface of CNTs can proceed directly on the carbon surface or via the introduction of defects [114]. The development of fluorination [115], nucleophilic substitution [116], electrophilic addition [117], and cycloaddition [118] reactions directly on the surface of CNTs has been previously demonstrated, enabling covalent attachment of biomolecules to the surface of CNTs.

One of the tumor self-antigens is the tumor lysate protein, containing multiple kinds of tumor proteins. Unlike tumor-specific antigens that are rare and difficult to obtain, tumor lysates are readily obtainable and have been investigated in antitumor immunotherapy studies with promising results [119, 120]. In our study, H22

liver cancer cells were lysed and the tumor lysate proteins (H22P) were extracted. In order to conjugate H22P to CNTs, an oxidation/sonication procedure was used to introduce sufficient carboxyl groups to the CNTs for solubilization and subsequent protein conjugation [15]. The tube-like structure of the CNTs was well kept, with average length of 500–800 nm and a average diameter of 20–30 nm. The H22P cells were then covalently conjugated to the oxidized CNTs to prepare the conjugate, CNT–H22P. In the immune therapy experiment, in addition to the tumor control, the treatment of TCV was also set as a control. BALB/c mice inoculated with H22 tumor cells subcutaneously were divided into four groups and given subcutaneous injection of CNT-H22P+TCV, CNT+TCV, H22P+TCV, and TCV only. In the experimental period, lymphocytes separated from the group of CNT-H22P+TCV showed significantly higher cytotoxicity against H22 cells compared to lymphocytes from the other treatment groups, and eventually reached a final cure rate of 54.2%, which was significantly higher than that of the other groups. The cure rates of the TCV+H22P and the TCV+CNT groups were 37.5% and 45.6%, respectively. Histological studies with the tumor tissue showed that it was heavily infiltrated with small lymphocytes, with obvious tumor necrosis, suggesting that it is the immune mechanism that plays the role in the cure of H22 cancer. All cured animals successfully rejected the newly inoculated tumor, but failed to gain sufficient immunity against the EMT cancer (another kind of cancer breast cell). The immune reaction of the spleen lymphocytes against the H22 cells was significantly higher than that against the EMT cells, suggesting that the previously developed antitumor immunity was relatively tumor-specific against the H22 cancer cells. This study first shows that conjugating the tumor lysate protein to CNTs can elevate the specific antitumor immune response and enhance the cancer cure rate of a TCV immunotherapy in mice.

Antigen presentation is a process crucial to mount an immune response against foreign antigens or tumor antigens. Professional antigen presenting cells (APCs), such as DCs or macrophages, will take up a source of antigen, degrade it, and present it to T cells [121]. As an excellent protein carrier, CNTs can bring tumor antigens into APCs of the immune system more efficiently. Sun *et al.* prepared a conjugate of MWCNTs and human cancer cell MCF7 lysates (CNT-TumorP) to investigate whether the conjugates influence the uptake of tumor antigen by human DCs and the capacity of DCs to induce anticancer cytotoxicity *in vitro*. Two groups of DCs were separately co-incubated with tumor cell lysates (TumorP) and CNT-TumorP (with a loading rate of ~4 mg protein per mg of MWCNTs). Their results showed that the uptake of tumor lysates by DCs was significantly enhanced when the lysates were conjugated to CNTs. Although CNTs or CNT-TumorP did not show a significant influence on the DCs' maturation process, DCs pretreated with CNT-TumorP induced in human lymphocytes higher antitumor cytotoxicity, suggesting that CNT-TumorP enhanced the function of DCs to induce anticancer response in lymphocytes and implying that CNT-based nanotechnology may have a prospective role in the development of more efficacious DC-based anticancer immunotherapy [122].

Dendritic cells present the antigen to T cells by the surface complexes MHC class I or class II. While MHC class I induces a more cytotoxic $CD8^+$ T cell response, MHC class II shifts the immune response to helper $CD4^+$ T cells, which promotes an antibody-based response. Pantarotto *et al.* [112] covalently linked a neutralizing B-cell epitope from the foot-and-mouth disease virus (FMDV) to mono- and bis-derivatized CNTs. Their results showed that the antigen epitope was appropriately presented after conjugation to CNTs. Moreover, the peptide-CNT conjugate elicited strong anti-peptide responses in mice, with no detectable cross-reactivity to the CNTs. The peptide alone with a conventional adjuvant in BALB/c mice is not immunogenic. The amount of antigen loading played a great role in the specific immune response, and the mono-conjugated CNT-peptide elicited virus-neutralizing antibody responses in all mice, which were significantly higher than those induced by the bi-conjugate. Villa *et al.* [113] studied the feasibility of using SWCNTs as antigen carriers to improve the immune responses to peptides that were weak immunogens. Wilm's tumor (WT1) protein is upregulated in many human leukemia and cancers. Several vaccines have been developed directed at this protein and are under human clinical trials. A 19-amino acid peptide named WT1 peptide 427 derived from WT1 protein has high binding affinity across multiple human HLA-DR haplotypes and induces human CD4 T-cell responses. But the peptide has a poor binding affinity to BALB/c mouse MHC class II molecules. Researchers prepared a conjugate SWNT-WT1Pep427, which was purified and added to immature DCs. SWNT-WT1Pep427 was rapidly internalized and accumulated by DCs. Human $CD4^+$ T cells' response to SWNT-WT1Pep427 was comparable to that achieved with the peptide alone *in vitro*. However, SWNT-WT1Pep427 significantly increased the peptide-specific IgG response when vaccination was performed in mice. SWCNTs may facilitate the trafficking and delivery of the antigens, inducing a tissue depot effect. Another possibility is that conjugation to SWCNTs redirects the immune response to WT1Pep427 toward a Th2 response. A previous study indicated that nanoparticulate vaccines are able to shift response from Th1 to Th2 with increasing particle size [123]. Additionally, solubilized SWCNTs alone were nontoxic *in vitro* and did not induce antibody responses *in vivo*. These results demonstrated that SWNTs are able to serve as antigen carriers for delivery into APCs to induce hormonal immune responses against weak tumor antigens.

As mentioned earlier, CNTs may activate MHC class I receptors, which would induce a cytotoxic, Th1-biased cell response, characterized by the production of cytokines such as IFN-γ, TNF-α, and IL-12. Although pristine CNTs do not induce a $CD8^+$ T-cell response, there is indirect evidence that functionalized, conjugated SWCNTs and MWCNTs give rise to such responses. It has been shown that both prophylactic and therapeutic strategies were highly effective when employing CNTs as delivery system for an anticancer vaccine formulation [124]. In the study, both NY-ESO-1 (cancer testis antigen) and CpG oligonucleotides (CpG-ODNs) were attached noncovalently to oxidized MWCNTs. The conjugates were rapidly internalized into DCs both *in vitro* and *in vivo* without affecting cellular viability. The conjugates were more effective in stimulating the

host immune system. The antigen specificity is effective on the response of $CD8^+$ T lymphocytes to tumor cells. The increase in the T-cell response resulted in greater protection and prolonged survival of mice challenged with a syngeneic, transgenic, melanoma-expressing NY-ESO-1. Moreover, the vaccination of conjugates was found to be able to delay tumor growth in B16-NY-ESO-1-bearing mice. Similar results were found with CT-26, a colon carcinoma cell line expressing NY-ESO-1. Therefore, MWCNT-based vaccination not only inhibited the tumor growth in anticancer treatments but also delayed the tumor progression in the cancer prevention.

In summary, CNTs can be used as a tumor antigen platform to present tumor antigens at high density, triggering enhanced cellular response, stimulating cytotoxic T cells and hormonal responses, which specifically target tumor cells, delaying tumor growth, and prolonging survival. Nevertheless, using CNTs in antitumor immunotherapeutic applications is still at an early stage, though much progress has been made in understanding how CNTs generally interact with cells and tissues *in vitro* and *in vivo*.

12.6 Immunological Responses of Gastric and Intestinal Systems Exposed to Carbon Nanotubes

Researches have shown that it is inevitable for humans to be exposed with nanoparticles, and the gastric and intestinal system is one of the major exposure paths. There are three major ways for CNTs to enter the gastrointestinal tract. The first is by ingestion, which can occur from unintentional hand-to-mouth transfer of materials or as a consequence of swallowing inhaled material following mucociliary clearance, because CNTs are being manufactured and applied in various industries. The second one is while exploring nanoparticles as gastrointestinal delivery systems for therapeutics. The third route is through CNTs ingested into the gastrointestinal tract through drinking water contaminated with CNTs [125, 126].

Except for gases, all necessary nutrients for the body are absorbed in the gastrointestinal tract. However, the gastrointestinal tract does not come into contact with the ingested materials directly. The whole surface of the gastrointestinal tract serves as a complex barrier. Following ingestion, there are four different pathways by which nanoparticles can translocate into and across the gastrointestinal mucosa [127]:

(i) Nanoparticles generally in the <50 – 100 nm diameter range can be endocytosed by epithelial cells. (ii) Nanoparticles can be taken up through the M-cell-rich layer of Peyer's patches. This is the quintessential pathway for gut particle uptake, especially for nanoparticles (200 – 500 nm). (iii) It is possible through persorption: passage through "gaps" at the villous tip following loss of enterocytes to the gut lumen. Small and large nanoparticles potentially access this route. (iv) Under certain conditions, it is possible for very small nanoparticles to gain access to the

gastrointestinal tissue via paracellular transcytosis across tight junctions of the epithelial cell layer.

Overall, the literature reporting the effects of CNTs on the gastric intestinal system *in vitro* and *in vivo* is very limited. Caco-2 cell is one cell line that is widely used, displaying many of the properties that characterize enterocytes, such as apical microvilli, basolateral basement membrane, and glycogen. The cell monolayers also display tight junctions and electrical resistance. Clark *et al.* [128] reported that exposure to pristine or oxidized MWCNTs at 50 $\mu g\,ml^{-1}$ for 24 h, with or without natural organic matter, did not markedly affect Caco-2 cell's viability assessed using lactate dehydrogenase (LDH) assay and propidium iodide staining assay. It is striking to see that Caco-2 cells did not take up either type of MWCNTs by ultrastructural analysis, through some damage to microvilli co-localized with the MWCNT was revealed. In contrast, pristine and oxidized MWCNTs were taken up by the mouse macrophage cell line RAW 264.7. Jos *et al.* [129] evaluated the cytotoxicity of SWCNTs functionalized with carboxylic acid on differentiated and nondifferentiated Caco-2 cells. Cells were exposed to concentrations between 5 and 1000 $mg\,ml^{-1}$ CNTs, and toxic effects were studied after 24 h of exposure. The neutral red (NR) uptake, protein content (PT), a tetrazolium salt (MTS) metabolization, LDH leakage, and cell viability by means of the trypan blue exclusion test (TBET) as biomarkers were assessed; a morphological study was performed as well. NR and MTS results showed a concentration-dependent trend with an inhibitory response from 100 $mg\,ml^{-1}$ CNTs, together with an increase in LDH leakage. TBET resulted in an 80% reduction at higher concentrations, and finally PT was only modified at higher concentrations. Hence, it was suggested that SWCNTs had cytotoxic effects on the Caco-2 cells. Importantly, cytotoxic effects on the Caco-2 cells with differentiated cultures showed a higher sensitivity.

As for genotoxicity of CNTs, only a few studies have been published. Folkmann *et al.* [130] investigated the effect of a single oral administration of C60 fullerenes and SWCNTs in Fisher 344 rats. They measured the level of oxidative damage to DNA as the premutagenic 8-oxo-7,8-dihydro-2′-deoxyguanosine (8-oxodG) in the colon mucosa, liver, and lung, and investigated the regulation of DNA repair systems toward 8-oxodG in the liver and lung tissue of rats after intragastric administration of pristine C60 fullerenes or SWCNTs (0.064 or 0.64 $mg\,kg^{-1}$ body weight) suspended in saline solution or corn oil. They found that both doses of SWCNTs increased the levels of 8-oxodG in liver and lung, but no effects were seen on 8-oxodG in colon mucosa. Suspension of particles in saline solution or corn oil yielded a similar extent of genotoxicity, whereas corn oil per se generated more genotoxicity than the particles. These results indicate that oral exposure to low doses of SWCNT is associated with elevated levels of 8-oxodG in the liver and lung, which is caused by a direct genotoxic ability rather than through inhibition of the DNA repair system. Several hypotheses were proposed to account for the genotoxic effects of SWCNTs, including the formation of adduct and/or damage at the level of DNA or chromosomes [131]. The possible mechanisms may involve the interaction of CNTs to biomolecules, especially to molecules with similar dimensions such as DNA [132].

Matsumoto *et al.* [133] reported their *in vivo* studies of CNTs through the gastrointestinal route. The researchers found no toxicological effects in SD rats that received acute or repeated oral administration of SWCNTs or MWCNTs. In an acute experiment, they used three female Crl:CD (SD) rats/group dosed with SWCNTs or MWCNTs four times by gavage at a total of 50 or 200 mg kg^{-1} bw (four equally divided doses at 1-h intervals). Acute oral doses of SWCNTs and MWCNTs caused neither death nor toxicological effects, and thus the oral LD50 values for SWCNTs and MWCNTs were considered to be greater than 50 and 200 mg kg^{-1} bw, respectively. In repeated experiments, 5 or 10 Crl:CD(SD) rats/sex were dosed with SWCNTs once daily by gavage at the dose of 0 (control), 0.125, 1.25, or 12.5 mg kg^{-1} bw per day for 28 days with a 14-day recovery period (0 and 12.5 mg kg^{-1} bw per day groups). Six or 12 Crl:CD(SD) rats/sex were dosed with MWCNTs once daily by gavage at a dose of 0 (control), 0.5, 5.0, or 50 mg kg^{-1} bw per day for 28 days with a 14-day recovery period (0 and 50 mg kg^{-1} bw per day groups). The results showed no toxicological effects.

However, another group reported contradictory results. Golokhvast *et al.* [134] reported that oral adminstration of the MWCNTs caused hyperpermeability of the gastrointestina tissue, hyperemia in renal vascular glomeruli, increased the size of Malpighian bodies, and shifted the red to white pulp ratio toward to the predominance of white pulp in spleen in CBA mice. They found mast cells migrating to the lamina propria after 1 day of oral administration. On day 3, MWCNTs were found in the deep layers and were detected not only in the epitheliocyte cytoplasm but in the nuclei as well. This was paralleled by the reduction of nucleus basophilia. On days 3–6, the mucosal epitheliocytes of various gastrointestinal compartments contained nanotubes diffusely scattered in the cytoplasm; nanotubes were also identified in the epitheliocyte nuclei. No pathological changes in the kidneys or filtration barrier reaction to MWCNTs were detected in intact mice and in mice after 1 and 2 days of the challenge, but 3 days later, analysis of biopsy specimens from the kidney showed hyperemia in vascular glomeruli. The vascular glomerular cells and macula densa were basophilic. The tubular wall in the renal cortical parenchyma had normal structure on day 3, but starting from day 4, nuclear and cytoplasmic basophilia increased, which could indicate strained function of the filtration system. The nuclei acquired a flat shape, and by day 6 became oval; the nuclear/cytoplasmic proportion increased significantly. Infiltration by erythrocytes occurred in regions adjacent to the tubules. Lymphoid tissue was seen in the renal parenchyma and connective tissue; follicles were forming, with reactive zones identified in some of them. Solitary neutrophils were identified among lymphocytes in the lymphoid tissue.

On day 6, in addition to changes in the gastrointestinal mucosal barrier structures, the lymphoid follicles in the mucosal lamina propria were enlarged. In the spleen, the red to white pulp ratio in experimental mice shifted toward predominance of the white pulp, and Malpighian bodies increased in size after 6 days of observation. Mast cells appearing in the lamina propria of small intestinal microvillous mucosa could result from the reaction with oral MWCNTs. The histophysiology of mast cells suggested that they were involved in the attraction

of macrophages (by means of production of appropriate cytokines) and induced (by secreting local homeostasis regulators) changes in the microcirculatory vascular lumen permeability for nanoparticle elimination through the portal vein system into the liver for detoxification.

Nevertheless, no MWCNTs were identified in the renal structures. The cell reaction in the macula densa of the distal tubular wall manifested by more intense basophilia, and hypertrophy was an indirect evidence of their effects on the water–salt metabolism in mice. Therefore, generalized reaction of the immune system to oral administration of CNTs is believed to realize at the expense of hypertrophy of lymphoid structures in the lamina propria of the gastrointestinal mucosa, follicle hypertrophy in the renal capsule and parenchyma, and Malpighian body hypertrophy in the splenic white pulp. It was hypothesized that lymphoid tissue hypertrophy in the gastrointestinal wall and spleen resulted from induction of the immune response by epitheliocytes contaminated with CNTs, with subsequent antigen presentation by effector immunocytes and their migration.

The conflicting biological effects of MWCNTs from the two groups strongly suggest careful comparisons of the materials and animals used in the studies. The results imply that MWCNTs may exert different toxicological responses in Crl:CD(SD)rats and CBA mice. Moreover, it is crucial to characterize MWCNTs because the variation of physical parameters may greatly affect their biological effects, which has been demonstrated by numerous investigations. It is to be noted that the MWCNTs tested by the two groups were purchased from different companies and with different physical parameters: for instance, Matsumoto *et al.* [133] used MWCNTs with an average diameter of 18–20 nm, while Golokhvast *et al.* [134] used MWCNTs with an average diameter of 30 nm. However, the average length of MWCNTs used in the studies was not given in either paper. In summary, immunological effects of CNTs exposed through gastric and intestinal system are crucial, but a large gap still exists in relevant knowledge, and therefore more and deeper investigations are needed.

References

1. Mintzer, M.A. and Simanek, E.E. (2009) Nonviral vectors for gene delivery. *Chem. Rev.*, **109** (2), 259–302.
2. Lacerda, L., Bianco, A., Prato, M., and Kostarelos, K. (2008) Carbon nanotube cell translocation and delivery of nucleic acids in vitro and in vivo. *J. Mater. Chem.*, **18** (1), 17–22.
3. Podesta, J.E., Al-Jamal, K.T., Herrero, M.A. *et al.* (2009) Antitumor activity and prolonged survival by carbon-nanotube-mediated therapeutic siRNA silencing in a human lung xenograft model. *Small*, **5** (10), 1176–1185.
4. Liu, Z., Winters, M., Holodniy, M., and Dai, H. (2007) siRNA delivery into human T cells and primary cells with carbon-nanotube transporters. *Angew. Chem. Int. Ed.*, **46** (12), 2023–2027.
5. Singh, R., Pantarotto, D., McCarthy, D. *et al.* (2005) Binding and condensation of plasmid DNA onto functionalized carbon nanotubes: toward the construction of nanotube-based gene delivery vectors. *J. Am. Chem. Soc.*, **127** (12), 4388–4396.
6. Kam, N.W., Liu, Z., and Dai, H. (2005) Functionalization of carbon nanotubes

via cleavable disulfide bonds for efficient intracellular delivery of siRNA and potent gene silencing. *J. Am. Chem. Soc.*, **127** (36), 12492–12493.
7. Yeh, I.C. and Hummer, G. (2004) Nucleic acid transport through carbon nanotube membranes. *Proc. Natl. Acad. Sci. U.S.A.*, **101** (33), 12177–12182.
8. Pantarotto, D., Singh, R., McCarthy, D. *et al.* (2004) Functionalized carbon nanotubes for plasmid DNA gene delivery. *Angew. Chem. Int. Ed.*, **43** (39), 5242–5246.
9. Zhang, Z., Yang, X., Zhang, Y. *et al.* (2006) Delivery of telomerase reverse transcriptase small interfering RNA in complex with positively charged single-walled carbon nanotubes suppresses tumor growth. *Clin. Cancer Res.*, **12** (16), 4933–4939.
10. Murakami, T., Sawada, H., Tamura, G. *et al.* (2008) Water-dispersed single-wall carbon nanohorns as drug carriers for local cancer chemotherapy. *Nanomedicine (Lond.)*, **3** (4), 453–463.
11. Liu, Z., Chen, K., Davis, C. *et al.* (2008) Drug delivery with carbon nanotubes for in vivo cancer treatment. *Cancer Res.*, **68** (16), 6652–6660.
12. Dhar, S., Liu, Z., Thomale, J. *et al.* (2008) Targeted single-wall carbon nanotube-mediated Pt(IV) prodrug delivery using folate as a homing device. *J. Am. Chem. Soc.*, **130** (34), 11467–11476.
13. Kam, N.W. and Dai, H. (2005) Carbon nanotubes as intracellular protein transporters: generality and biological functionality. *J. Am. Chem. Soc.*, **127** (16), 6021–6026.
14. Shi Kam, N.W., Jessop, T.C., Wender, P.A., and Dai, H. (2004) Nanotube molecular transporters: internalization of carbon nanotube-protein conjugates into Mammalian cells. *J. Am. Chem. Soc.*, **126** (22), 6850–6851.
15. Meng, J., Meng, J., Duan, J. *et al.* (2008) Carbon nanotubes conjugated to tumor lysate protein enhance the efficacy of an antitumor immunotherapy. *Small*, **4** (9), 1364–1370.
16. Pantarotto, D., Briand, J.P., Prato, M., and Bianco, A. (2004) Translocation of bioactive peptides across cell membranes by carbon nanotubes. *Chem. Commun. (Camb.)*, **7** (1), 16–17.
17. Pantarotto, D., Partidos, C.D., Graff, R. *et al.* (2003) Synthesis, structural characterization, and immunological properties of carbon nanotubes functionalized with peptides. *J. Am. Chem. Soc.*, **125** (20), 6160–6164.
18. De la Zerda, A., Zavaleta, C., Keren, S. *et al.* (2008) Carbon nanotubes as photoacoustic molecular imaging agents in living mice. *Nat. Nanotechnol.*, **3** (9), 557–562.
19. Fiorito, S., Serafino, A., Andreola, F., and Bernier, P. (2006) Effects of fullerenes and single-wa ll carbon nanotubes on murine and human macrophages. *Carbon*, **44** (6), 1100–1105.
20. Warheit, D.B., Laurence, B.R., Reed, K.L. *et al.* (2004) Comparative pulmonary toxicity assessment of single-wall carbon nanotubes in rats. *Toxicol. Sci.*, **77** (1), 117–125.
21. Mitchell, L.A., Gao, J., Wal, R.V. *et al.* (2007) Pulmonary and systemic immune response to inhaled multiwalled carbon nanotubes. *Toxicol. Sci.*, **100** (1), 203–214.
22. Mitchell, L.A., Lauer, F.T., Burchiel, S.W., and McDonald, J.D. (2009) Mechanisms for how inhaled multiwalled carbon nanotubes suppress systemic immune function in mice. *Nat. Nanotechnol.*, **4** (7), 451–456.
23. Muller, J., Huaux, F., Fonseca, A. *et al.* (2008) Structural defects play a major role in the acute lung toxicity of multiwall carbon nanotubes: toxicological aspects. *Chem. Res. Toxicol.*, **21** (9), 1698–1705.
24. Journeay, W.S., Suri, S.S., Moralez, J.G. *et al.* (2008) Rosette nanotubes show low acute pulmonary toxicity in vivo. *Int. J. Nanomed.*, **3** (3), 373–383.
25. Nygaard, U.C., Hansen, J.S., Samuelsen, M. *et al.* (2009) Single-walled and multi-walled carbon nanotubes promote allergic immune responses in mice. *Toxicol. Sci.*, **109** (1), 113–123.
26. Poland, C.A., Duffin, R., Kinloch, I. *et al.* (2008) Carbon nanotubes introduced into the abdominal cavity of

mice show asbestos-like pathogenicity in a pilot study. *Nat. Nanotechnol.*, **3** (7), 423–428.
27. Yang, S.T., Wang, X., Jia, G. *et al.* (2008) Long-term accumulation and low toxicity of single-walled carbon nanotubes in intravenously exposed mice. *Toxicol. Lett.*, **181** (3), 182–189.
28. Schipper, M.L., Nakayama-Ratchford, N., Davis, C.R. *et al.* (2008) A pilot toxicology study of single-walled carbon nanotubes in a small sample of mice. *Nat. Nanotechnol.*, **3** (4), 216–221.
29. Vankoningsloo, S., Piret, J.P., Saout, C. *et al.* (2010) Cytotoxicity of multiwalled carbon nanotubes in three skin cellular models: effects of sonication, dispersive agents and corneous layer of reconstructed epidermis. *Nanotoxicology*, **4** (1), 84–97.
30. Vankoningsloo, S., Piret, J.P., Saout, C. *et al.* (2012) Pro-inflammatory effects of different MWCNTs dispersions in p16(INK4A)-deficient telomerase-expressing human keratinocytes but not in human SV-40 immortalized sebocytes. *Nanotoxicology*, **6** (1), 77–93.
31. Patlolla, A., Patlolla, B., and Tchounwou, P. (2010) Evaluation of cell viability, DNA damage, and cell death in normal human dermal fibroblast cells induced by functionalized multiwalled carbon nanotube. *Mol. Cell. Biochem.*, **338** (1–2), 225–232.
32. Zhang, Y., Wang, B., Meng, X. *et al.* (2011) Influences of acid-treated multiwalled carbon nanotubes on fibroblasts: proliferation, adhesion, migration, and wound healing. *Ann. Biomed. Eng.*, **39** (1), 414–426.
33. Umemoto, E.Y., Speck, M., Shimoda, L.M. *et al.* (2014) Single-walled carbon nanotube exposure induces membrane rearrangement and suppression of receptor-mediated signalling pathways in model mast cells. *Toxicol. Lett.*, **229** (1), 198–209.
34. Furtado, C.A., Kim, U.J., Gutierrez, H.R. *et al.* (2004) Debundling and dissolution of single-walled carbon nanotubes in amide solvents. *J. Am. Chem. Soc.*, **126** (19), 6095–6105.
35. Monteiro-Riviere, N.A., Inman, A.O., Wang, Y.Y., and Nemanich, R.J. (2005) Surfactant effects on carbon nanotube interactions with human keratinocytes. *Nanomedicine*, **1** (4), 293–299.
36. Rastogi, R., Kaushal, R., Tripathi, S.K. *et al.* (2008) Comparative study of carbon nanotube dispersion using surfactants. *J. Colloid Interface Sci.*, **328** (2), 421–428.
37. Wick, P., Manser, P., Limbach, L.K. *et al.* (2007) The degree and kind of agglomeration affect carbon nanotube cytotoxicity. *Toxicol. Lett.*, **168** (2), 121–131.
38. Ali-Boucetta, H., Nunes, A., Sainz, R. *et al.* (2013) Asbestos-like pathogenicity of long carbon nanotubes alleviated by chemical functionalization. *Angew. Chem. Int. Ed.*, **52** (8), 2274–2278.
39. Kishore, A.S., Surekha, P., and Murthy, P.B. (2009) Assessment of the dermal and ocular irritation potential of multiwalled carbon nanotubes by using in vitro and in vivo methods. *Toxicol. Lett.*, **191** (2–3), 268–274.
40. Ema, M., Matsuda, A., Kobayashi, N. *et al.* (2011) Evaluation of dermal and eye irritation and skin sensitization due to carbon nanotubes. *Regul. Toxicol. Pharm.*, **61** (3), 276–281.
41. Cheng, X., Zhong, J., Meng, J. *et al.* (2011) Characterization of multiwalled carbon nanotubes dispersing in water and association with biological effects. *J. Nanomater.* 2011 (1), 90–110
42. Meng, J., Yang, M., Jia, F. *et al.* (2011) Immune responses of BALB/c mice to subcutaneously injected multi-walled carbon nanotubes. *Nanotoxicology*, **5** (4), 583–591.
43. Meng, J., Yang, M., Jia, F. *et al.* (2010) Subcutaneous injection of water-soluble multi-walled carbon nanotubes in tumor-bearing mice boosts the host immune activity. *Nanotechnology*, **21** (14), 145104.
44. Liu, Z., Cai, W., He, L. *et al.* (2007) In vivo biodistribution and highly efficient tumour targeting of carbon nanotubes in mice. *Nat. Nanotechnol.*, **2** (1), 47–52.
45. McDevitt, M.R., Chattopadhyay, D., Jaggi, J.S. *et al.* (2007) PET imaging of soluble yttrium-86-labeled carbon

nanotubes in mice. *PLoS One*, **2** (9), e907.

46. Cherukuri, P., Gannon, C.J., Leeuw, T.K. *et al.* (2006) Mammalian pharmacokinetics of carbon nanotubes using intrinsic near-infrared fluorescence. *Proc. Natl. Acad. Sci. U.S.A.*, **103** (50), 18882–18886.
47. Guo, Y., Shi, D.L., Cho, H.S. *et al.* (2008) In vivo imaging and drug storage by quantum-dot-conjugated carbon nanotubes. *Adv. Funct. Mater.*, **18**, 2489–2497.
48. Didenko, V.V. and Baskin, D.S. (2006) Horseradish peroxidase-driven fluorescent labeling of nanotubes with quantum dots. *Biotechniques*, **40** (3), 295–296, 298, 300–302.
49. Yang, R., Tang, Z., Yan, J. *et al.* (2008) Noncovalent assembly of carbon nanotubes and single-stranded DNA: an effective sensing platform for probing biomolecular interactions. *Anal. Chem.*, **80** (19), 7408–7413.
50. Yang, R., Jin, J., Chen, Y. *et al.* (2008) Carbon nanotube-quenched fluorescent oligonucleotides: probes that fluoresce upon hybridization. *J. Am. Chem. Soc.*, **130** (26), 8351–8358.
51. Cheng, J., Fernando, K.A., Veca, L.M. *et al.* (2008) Reversible accumulation of PEGylated single-walled carbon nanotubes in the mammalian nucleus. *ACS Nano*, **2** (10), 2085–2094.
52. Liu, Z., Davis, C., Cai, W. *et al.* (2008) Circulation and long-term fate of functionalized, biocompatible single-walled carbon nanotubes in mice probed by Raman spectroscopy. *Proc. Natl. Acad. Sci. U.S.A.*, **105** (5), 1410–1415.
53. Schneckenburger, H., Lang, M., Kollner, T. *et al.* (1989) Fluorescence spectra and microscopic imaging of porphyrins in single cells and tissues. *Lasers Med. Sci.*, **4**, 159.
54. D'Souza, F., Chitta, R., Sandanayaka, A.S. *et al.* (2007) Self-assembled single-walled carbon nanotube: zinc-porphyrin hybrids through ammonium ion-crown ether interaction: construction and electron transfer. *Chemistry*, **13** (29), 8277–8284.
55. el-Far, M.A. and Pimstone, N.R. (1986) Selective in vivo tumor localization of uroporphyrin isomer I in mouse mammary carcinoma: superiority over other porphyrins in a comparative study. *Cancer Res.*, **46** (9), 4390–4394.
56. Jia, F., Wu, L., Meng, J. *et al.* (2009) Preparation, characterization and fluorescent imaging of multi-walled carbon nanotube–porphyrin conjugate. *J. Mater. Chem.*, **19** (47), 8950–8957.
57. Wynn, T.A., Chawla, A., and Pollard, J.W. (2013) Macrophage biology in development, homeostasis and disease. *Nature*, **496**, 445–455.
58. Stein, M., Keshav, S., Harris, N., and Gordon, S. (1992) Interleukin 4 potently enhances murine macrophage mannose receptor activity: a marker of alternative immunologic macrophage activation. *J. Exp. Med.*, **176** (1), 287–292.
59. Wang, Z., Cui, Y., Wang, J. *et al.* (2014) The effect of thick fibers and large pores of electrospun poly(ε-caprolactone) vascular grafts on macrophage polarization and arterial regeneration. *Biomaterials*, **35** (22), 5700–5710.
60. Spiller, K.L., Anfang, R.R., Spiller, K.J. *et al.* (2014) The role of macrophage phenotype in vascularization of tissue engineering scaffolds. *Biomaterials*, **35** (15), 4477–4488.
61. Zhu, Z., Wang, C., Chen, S. *et al.* (2011) Carbon nanotubes enhance cytotoxicity mediated by human lymphocytes in vitro. *PLoS One*, **6** (6), e21073.
62. Qu, C., Wang, L.X., He, J. *et al.* (2012) Carbon nanotubes provoke inflammation by inducing the pro-inflammatory genes IL-1β and IL- 6. *Gene*, **493** (1), 9–12.
63. Manna, S.K., Sarkar, S., Barr, J. *et al.* (2005) Single-walled carbon nanotube induces oxidative stress and activates nuclear transcription factor-kappaB in human keratinocytes. *Nano Lett.*, **5** (9), 1676–1684.
64. He, X., Young, S.H., Schwegler-Berry, D. *et al.* (2011) Multiwalled carbon nanotubes induce a fibrogenic response by stimulating reactive oxygen species production, activating NF-κB

signaling, and promoting fibroblasttomyofibroblast transformation. *Chem. Res. Toxicol.*, **24** (12), 2237–2248.
65. Yang, M., Flavin, K., Kopf, I. *et al.* (2013) Functionalization of carbon nanoparticles modulates inflammatory cell recruitment and NLRP3 inflammasome activation. *Small*, **9** (24), 4194–4206.
66. Hamilton, R.F. Jr., Buford, M., Xiang, C. *et al.* (2012) NLRP3 inflammasome activation in murine alveolar macrophages and related lung pathology is associated with MWCNT nickel contamination. *Inhalation Toxicol.*, **24** (14), 995–1008.
67. Hussain, S., Sangtian, S., Anderson, S.M. *et al.* (2014) Inflammasome activation in airway eepithelial cells after multiwalled carbon nanotube exposure mediates a profibrotic response in lung fibroblasts. *Part. Fibre Toxicol.*, **11**, 28.
68. Shvedova, A.A., Kisin, E.R., Mercer, R. *et al.* (2005) Unusual Inflammatory and fibrogenic pulmonary responses to single-walled carbon nanotubes in mice. *Am. J. Physiol. Lung Cell. Mol. Physiol.*, **289** (5), L698–L708.
69. Sato, Y., Yokoyama, A., Shibata, K. *et al.* (2005) Influence of length on cytotoxicity of multi-walled carbon nanotubes against human acute monocytic leukemia cell line THP-1 in vitro and subcutaneous tissue of rats in vivo. *Mol. Biosyst.*, **1** (2), 176–182.
70. Bellucci, S., Chiaretti, M., Cucina, A. *et al.* (2009) Multiwalled carbon nanotube buckypaper: toxicology and biological effects in vitro and in vivo. *Nanomedicine (Lond.)*, **4** (5), 531–540.
71. Meng, J., Li, X., Wang, C. *et al.* (2015) Carbon nanotubes activate macrophages into a M1/M2 mixed status: recruiting naïve macrophages and supporting angiogenesis. *ACS Appl. Mater. Interfaces*, **7** (5), 3180–3188.
72. Mosser, D.M. and Edwards, J.P. (2008) Exploring the full spectrum of macrophage activation. *Nat. Rev. Immunol.*, **8** (12), 958–969.
73. Zanoni, I., Ostuni, R., Marek, L.R. *et al.* (2011) CD14 controls the LPS-induced endocytosis of toll-like receptor 4. *Cell*, **147** (4), 868–880.
74. Luo, Y., Zhou, H., Krueger, J. *et al.* (2006) Targeting tumor-associated macrophages as a novel strategy against breast cancer. *J. Clin. Invest.*, **116** (8), 2132–2141.
75. Mehra, N.K., Mishra, V., and Jain, N.K. (2014) A review of ligand tethered surface engineered carbon nanotubes. *Biomaterials*, **35**, 1267–1283.
76. Hassan, F., Ren, D., Zhang, W., and Gu, X.X. (2012) Role of c-Jun N-terminal protein kinase 1/2(JNK1/2) in macrophage-mediated MMP-9 production in response to Moraxella catarrhalis lipooligosaccharide (LOS). *PLoS One*, **7** (5), e37912.
77. Inoue, K., Takano, H., Koike, E. *et al* (2008) Effects of pulmonary exposure to carbon nanotubes on lung and systemic inflammation with coagulatory disturbance induced by lipopolysaccharide in mice. *Exp. Biol. Med. (Maywood)*, **233**, 1583–1590.
78. Yang, M., Meng, J., Cheng, X. *et al.* (2012) Multiwalled carbon nanotubes interact with macrophages and influence tumor progression and metastasis. *Theranostics*, **2** (3), 258–270.
79. Neuwelt, E.A., Várallyay, P., Bagó, A.G. *et al.* (2004) Imaging of iron oxide nanoparticles by MR and light microscopy in patients with malignant brain tumours. *Neuropathol. Appl. Neurobiol.*, **30** (5), 456–471.
80. Dobrovolskaia, M.A., Aggarwal, P., Hall, J.B., and McNeil, S.E. (2008) Preclinical studies to understand nanoparticles interaction with the immune system and its potential effects on nanoparticles biodistribution. *Mol. Pharm.*, **5** (4), 487–495.
81. Takanashi, S., Hara, K., Aoki, K. *et al.* (2012) Carcinogenicity evaluation for the application of carbon nanotubes as biomaterials in rasH2 mice. *Sci. Rep.*, **2**, 498.
82. Vermorken, J.B., Claessen, A.M., van Tinteren, H. *et al.* (1999) Active specific immunotherapy for stage II and stage III human colon cancer: a randomised trial. *Lancet*, **353** (9150), 345–350.
83. Rosenberg, S.A. (2001) Progress in human tumour immunology and

immunotherapy. *Nature*, **411** (6835), 380–384.
84. Takayama, T., Sekine, T., Makuuchi, M. *et al.* (2000) Adoptive immunotherapy to lower postsurgical recurrence rates of hepatocellular carcinoma: a randomised trial. *Lancet*, **356** (9232), 802–807.
85. Chatterjee, M., Draghici, S., and Tainsky, M.A. (2006) Immunotheranostics: breaking tolerance in immunotherapy using tumor autoantigens identified on protein microarrays. *Curr. Opin. Drug Discovery Dev.*, **9** (3), 380–385.
86. Muller, A.J. and Scherle, P.A. (2006) Targeting the mechanisms of tumoral immune tolerance with small-molecule inhibitors. *Nat. Rev. Cancer*, **6** (8), 613–625.
87. Copier, J. and Dalgleish, A. (2006) Overview of tumor cell-based vaccines. *Int. Rev. Immunol.*, **25** (5–6), 297–319.
88. Banchereau, J., Schuler-Thurner, B., Palucka, A.K., and Schuler, G. (2001) Dendritic cells as vectors for therapy. *Cell*, **106** (3), 271–274.
89. Yang, J.C. and Childs, R. (2006) Immunotherapy for renal cell cancer. *J. Clin. Oncol.*, **24** (35), 5576–5583.
90. Emens, L.A. (2006) Roadmap to a better therapeutic tumor vaccine. *Int. Rev. Immunol.*, **25** (5–6), 415–443.
91. Figdor, C.G., de Vries, I.J., Lesterhuis, W.J., and Melief, C.J. (2004) Dendritic cell immunotherapy: mapping the way. *Nat. Med.*, **10** (5), 475–480.
92. Sun, Z., Liu, Z., Meng, J. *et al.* (2011) Carbon nanotubes enhance cytotoxicity mediated by human lymphocytes in vitro. *PLoS One*, **6**, e21073.
93. Dranoff, G. (2004) Cytokines in cancer pathogenesis and cancer therapy. *Nat. Rev. Cancer*, **4** (1), 11–22.
94. Pollard, J.W. (2004) Tumour-educated macrophages promote tumour progression and metastasis. *Nat. Rev. Cancer*, **4** (1), 71–78.
95. Yu, J.L. and Rak, J.W. (2003) Host microenvironment in breast cancer development: inflammatory and immune cells in tumour angio-genesis and arteriogenesis. *Breast Cancer Res.*, **5** (2), 83–88.
96. Luo, Y.P., Zhou, H., Krueger, J. *et al.* (2010) Knockdown of Fra-1 in RAW macrophages by siRNA downregulates IL-6 and Stat3, decreases the release of pro-angiogenesis factors and inhibits migration and invasion of 4T1 breast cancer cells. *Oncogene*, **29** (5), 662–673.
97. Josson, S., Matsuoka, Y., Chung, L.W. *et al.* (2010) Tumor-stroma coevolution in prostate cancer progression and metastasis. *Semin. Cell Dev. Biol.*, **21** (1), 26–32.
98. Watters, J.J., Schartner, J.M., and Badie, B. (2005) Microglia function in brain tumors. *J. Neurosci. Res.*, **81** (3), 447–455.
99. Aldinucci, D., Gloghini, A., Pinto, A. *et al.* (2010) The classical Hodgkin's lymphoma microenvironment and its role in promoting tumour growth and immune escape. *J. Pathol.*, **221** (3), 248–263.
100. Takayama, H., Nishimura, K., Tsujimura, A. *et al.* (2009) Increased infiltration of tumor associated macrophages is associated with poor prognosis of bladder carcinoma in situ after intravesical bacil-lus Calmette-Guerin instillation. *J. Urol.*, **181** (4), 1894–1900.
101. Wang, R., Zhang, J., Chen, S. *et al.* (2011) Tumor-associated macrophages provide a suitable microenvironment for non-small lung cancer invasion and progression. *Lung Cancer*, **74** (2), 188–196.
102. Utrera-Barillas, D., Castro-Manrreza, M., Castellanos, E. *et al.* (2010) The role of macrophages and mast cells in lymph angiogenesis and angiogenesis in cervical carcinogenesis. *Exp. Mol. Pathol.*, **89** (2), 190–196.
103. Hussein, M.R. (2006) Tumour-associated macrophages and melanoma tumourigenesis: integrating the complexity. *Int. J. Exp. Pathol.*, **87** (3), 163–176.
104. Chaudhuri, D., Suriano, R., Mittelman, A., and Tiwari, R.K. (2009) Targeting the immune system in cancer. *Curr. Pharm. Biotechnol.*, **10** (2), 166–184.
105. Shih, J.Y., Yuan, A., Chen, J.J., and Yang, P.C. (2006) Tumor-associated

macrophage: its role in cancer invasion and metastasis. *J. Cancer Mol.*, **2** (3), 101–106.

106. Chen, J.J., Lin, Y.C., Yao, P.L. *et al.* (2005) Tumor-associated macrophages: the double-edged sword in cancer progression. *J. Clin. Oncol.*, **23** (5), 953–964.

107. Dumortier, H., Lacotte, S., Pastorin, G. *et al.* (2006) Functionalized carbon nanotubes are non-cytotoxic and preserve the functionality of primary immune cells. *Nano Lett.*, **6** (7), 1522–1528.

108. Farkas, A.M. and Finn, O.J. (2010) Vaccines based on abnormal self-antigens as tumor-associated antigens: immune regulation. *Semin. Immunol.*, **22** (3), 125–131.

109. Houghton, A.N. and Guevara-Patiño, J.A. (2004) Immune recognition of self in immunity against cancer. *J. Clin. Invest.*, **114** (4), 468–471.

110. Fifis, T., Gamvrellis, A., Crimeen-Irwin, B. *et al.* (2004) Size-dependent immunogenicity: therapeutic and protective properties of nano-vaccines against tumors. *J. Immunol.*, **173** (5), 3148–3154.

111. Sahoo, N.G., Bao, H., Pan, Y. *et al.* (2011) Functionalized carbon nanomaterials as nanocarriers for loading and delivery of a poorly water-soluble anticancer drug: a comparative study. *Chem. Commun. (Camb.)*, **47** (18), 5235–5237.

112. Pantarotto, D., Partidos, C.D., Hoebeke, J. *et al.* (2003) Immunization with peptide-functionalized carbon nanotubes enhances virus-specific neutralizing antibody responses. *Chem. Biol.*, **10** (10), 961–966.

113. Villa, C.H., Dao, T., Ahearn, I. *et al.* (2003) Single-walled carbon nanotubes deliver peptide antigen into dendritic cells and enhance IgG responses to tumor-associated antigens. *ACS Nano*, **5** (7), 5300–5311.

114. Niyogi, S., Hamon, M.A., Hu, H. *et al.* (2002) Chemistry of single-walled carbon nanotubes. *Acc. Chem. Res.*, **35** (12), 1105–1113.

115. Khabashesku, V.N., Billups, W.E., and Margrave, J.L. (2002) Fluorination of single-wall carbon nanotubes and subsequent derivatization reactions. *Acc. Chem. Res.*, **35** (12), 1087–1095.

116. Stevens, J.L., Huang, A.Y., Peng, H. *et al.* (2003) Sidewall amino-functionalization of single-walled carbon nanotubes through fluorination and subsequent reactions with terminal diamines. *Nano Lett.*, **3** (3), 331–336.

117. Xu, Y., Wang, X., Tian, R. *et al.* (2008) Microwave-induced electrophilic addition of single-walled carbon nanotubes with alkylhalides. *Appl. Surf. Sci.*, **254** (8), 2431–2435.

118. Georgakilas, V., Kordatos, K., Prato, M. *et al.* (2002) Organic functionalization of carbon nanotubes. *J. Am. Chem. Soc.*, **124** (5), 760–761.

119. Sosman, J.A. and Sondak, V.K. (2003) Melacine: an allogeneic melanoma tumor cell lysate vaccine. *Expert Rev. Vaccines*, **2** (3), 353–368.

120. Yu, J.S., Liu, G., Ying, H. *et al.* (2004) Vaccination with tumor lysate-pulsed dendritic cells elicits antigen-specific, cytotoxic T-cells in patients with malignant glioma. *Cancer Res.*, **64** (14), 4973–4979.

121. Yanofsky, V.R., Mitsui, H., Felsen, D., and Carucci, J.A. (2013) Un*derstanding dendritic cell*s **a**nd their role in cutaneous carcinoma and cancer immunotherapy. *Clin. Dev. Immunol.*, **2013**, 624123.

122. Sun, Z., Wang, W., Meng, J. *et al.* (2010) Multi-walled carbon nanotubes conjugated to tumor protein enhance the uptake of tumor antigens by human dendritic cells in vitro. *Cell Res.*, **20** (10), 1170–1173.

123. Mottram, P.L., Leong, D., Crimeen-Irwin, B. *et al.* (2007) Type 1 and 2 immunity following vaccination is influenced by nanoparticle size: formulation of a model vaccine for respiratory syncytial virus. *Mol. Pharm.*, **4** (1), 73–84.

124. de Faria, P.C., dos Santos, L.I., Coelho, J.P. *et al.* (2014) Oxidized multiwalled carbon nanotubes as antigen delivery system to promote superior CD8(+) T cell response and protection against cancer. *Nano Lett.*, **14** (9), 5458–5470.

125. Simate, G.S., Iyuke, S.E., Ndlovu, S. *et al.* (2012) Human health effects of residual carbon nanotubes and traditional water treatment chemicals in drinking water. *Environ. Int.*, **39** (1), 38–49.
126. Upadhyayula, V.K., Deng, S., Mitchell, M.C., and Smith, G.B. (2009) Application of carbon nanotube technology for removal of contaminants in drinking water: a review. *Sci. Total Environ.*, **408** (1), 1–13.
127. Powell, J.J., Faria, N., Thomas-McKay, E., and Pele, L.C. (2010) Origin and fate of dietary nanoparticles and microparticles in the gastrointestinal tract. *J. Autoimmun.*, **34** (3), J226–J233.
128. Clark, K.A., O'Driscoll, C., Cooke, C.A. *et al.* (2012) Evaluation of the interactions between multiwalled carbon nanotubes and Caco-2 cells. *J. Toxicol. Environ. Health A*, **75** (1), 25–35.
129. Jos, A., Pichardo, S., Puerto, M. *et al.* (2009) Cytotoxicity of carboxylic acid functionalized single wall carbon nanotubes on the human intestinal cell line Caco-2. *Toxicol. In Vitro*, **23** (8), 1491–1496.
130. Folkmann, J.K., Risom, L., Jacobsen, N.R. *et al.* (2009) Oxidatively damaged DNA in rats exposed by oral gavage to C60 fullerenes and single-walled carbon nanotubes. *Environ. Health Perspect.*, **117** (5), 703–708.
131. Patlolla, A., Knighten, B., and Tchounwou, P. (2010) Multi-walled carbon nanotubes induce cytotoxicity, genotoxicity and apoptosis in normal human dermal fibroblast cells. *Ethn. Dis.*, **20** (1, Suppl. 1), S1-65–S1-72.
132. Li, S., He, P., Dong, J. *et al.* (2005) DNA-directed self-assembling of carbon nanotubes. *J. Am. Chem. Soc.*, **127** (1), 14–15.
133. Matsumoto, M., Serizawa, H., Sunaga, M. *et al.* (2012) No toxicological effects on acute and repeated oral gavage doses of single-wall or multi-wall carbon nanotube in rats. *J. Toxicol. Sci.*, **37** (3), 463–474.
134. Golokhvast, K.S., Chaika, V.V., Kuznetsov, L.V. *et al.* (2013) Effects of multiwalled carbon nanotubes received orally during 6 days on the gastrointestinal tract. *Bull. Exp. Biol. Med.*, **155** (6), 788–792.

13
Modulation of Immune System by Carbon Nanotubes

Marit Ilves and Harri Alenius

13.1
Immune System

Our body is protected from infectious agents, called pathogens, and harmful substances by a variety of cells and molecules that together form an inbuilt system called the immune system. The cells of the immune system are found as resident cells in different tissues, circulating in blood stream and residing in the lymph nodes. Such wide distribution of immune cells spreading throughout the body ensures a fast response when pathogens enter our body.

Immune system can be divided into innate and adaptive. Innate, nonadaptive responses are rapid and unspecific, taking place within minutes or hours after encountering a pathogen and hence form the earliest barriers to an infection. If a pathogen can breach the innate immunity defense mechanisms, an adaptive immune response is activated where antigen-specific effector cells that target the specific microorganism and memory cells providing long-lasting immunity against re-exposure to the same pathogen are generated. Hence in contrast to innate immunity response, adaptive immune reactions are pathogen-specific, occur days later, and result in the development of immunological memory.

Innate and adaptive immunity reactions are mediated by leukocytes that derive from the hematopoietic stem cells. These stem cells give rise to immediate progenitors, myeloid and lymphoid cells, that have more limited developmental potential. Most of the cells of innate immunity originate from a common myeloid precursor, while cells of the adaptive immune system (adaptive lymphocytes) and innate lymphoid cells (ILCs) of the innate immunity arise from a common lymphoid progenitor. Every type of leucocytes has an important role to fulfill in immune response, and these reactions are dependent on each other [1].

Complement is a sophisticated innate immune surveillance system that provides the first line of defense against pathogens and altered host cells. It is a complex system involving many soluble proteins and membrane-expressed receptors and regulators that function on the cell surface, in blood, and in tissues. The complement system is activated by structural changes in recognition

Biomedical Applications and Toxicology of Carbon Nanomaterials, First Edition.
Edited by Chunying Chen and Haifang Wang.

molecular complexes when danger signals are detected. The following cascade of enzymatic reactions is strictly regulated to ensure that the complement is activated only at certain locations where defense against pathogens is required, thus excluding damage to the host tissue. Complement proteins help immune cells by opsonizing foreign matter and triggering inflammatory reactions. Their action leads to phagocytosis of the pathogen and ultimately results in the stimulation of adaptive immune response [2, 3].

13.1.1 Innate Immunity Cells and Their Main Functions

In a healthy organism, the microorganisms that are exposed daily are encountered and neutralized by innate immunity cells within minutes or hours. Innate immunity cells are divided into several cell types. These include monocytes and macrophages, polymorphonuclear leukocytes, mast cells (MCs), ILCs, and dendritic cells (DCs).

Macrophages are relatively long-lived resident cells present in almost all tissues and act as a first-line defense against pathogens that have passed the physical and chemical barriers of the body. They are the mature form of monocytes, which function in blood and migrate into tissues where they differentiate. Monocytes and macrophages are one type of phagocytes in the immune system; they recognize, engulf, and kill microorganisms upon first encounter but are also responsible for disposing pathogens and damaged cells that are targeted during an adaptive immunity response.

Polymorphonuclear leukocytes are divided into three subclasses: neutrophils, eosinophils, and basophils. They are also called granulocytes because of the granules located in their cytoplasm. They are short-lived cells, circulating only in blood under normal conditions, but they migrate rapidly into the tissue to reinforce macrophages during inflammation. Similar to macrophages, neutrophils also have phagocytic ability. They are able to take up a variety of pathogens and neutralize them in intracellular vesicles by degradative enzymes and other substances stored in their cytoplasmic granules. In contract to macrophages, neutrophils die after one round of phagocytosis. The role of eosinophils is less understood. Their granules consist of enzymes and toxic proteins that are released upon cell activation. Eosinophils are relevant in the defense against parasites that are too large to be ingested by macrophages and neutrophils. They have also been found to take part in allergic inflammatory reactions, but their effects are rather damaging than protective in such responses [1]. Basophils will not be included in this chapter because of the lack of information of CNT-induced effects on this cell type. Eosinophils will be described in more detail in the context of allergy and asthma.

ILCs are innate lymphocytes that are relatively rare in comparison to adaptive lymphocytes in the lymphatic system, but the barrier surfaces of the body, such as the skin, lung, and intestine, are rich in them [4–6]. ILCs rapidly respond to cytokine and microbial signals and are potent innate cellular sources of multiple pro-inflammatory and immunoregulatory cytokines. Furthermore, ILCs are

important in modulating adaptive immunity. The first ILC subset discovered were natural killer (NK) cells whose task is to detect and kill infected and abnormal cells [1, 6, 7].

Mast cells circulate in the bloodstream in an immature form but undergo final differentiation when entering tissues. They are found in many tissues of the body, particularly in parts that are close to external environment and therefore take part in the early recognition of pathogens. Upon activation, they release a variety of preformed mediators present in their cytoplasmic granules. Mast cells take part in defense against parasites, but they are also important immune cells that orchestrate allergic reactions linking innate and adaptive immunity [8]. Mast cells will be described in more detail in the context of allergy and asthma.

Dendritic cells such as macrophages and neutrophils are phagocytic cells. However, dendritic cells are important because they create a bridge between innate and adaptive immunity. The main function of these cells is activation of T lymphocytes. Upon capturing and uptake of pathogens, dendritic cells display the pathogen antigens on the cell surface on major histocompatibility complex (MHC) I or MHC II molecules. This allows T cells to recognize the presented antigens through T-cell receptors (TCRs). Because of this function, dendritic cells are also called antigen-presenting cells (APCs) [1].

13.1.2 Adaptive Immunity Cells and Their Main Functions

Adaptive immunity is responsible for antigen-specific immune responses. The cells of the adaptive immune system are T cells and B cells, which recognize antigens through TCRs or B-cell receptors (BCRs), respectively. APCs activate and functionalize T and B cells to eliminate evading pathogens [9]. T and B cells may also be activated by the pathogens themselves without APC involvement. To eliminate invading pathogens successfully, interactions between innate and adaptive immunity are required. Even if the adaptive immune reactions are more specific toward specific antigens, innate immunity still determines the nature of adaptive T- and B-cell response [9].

T cells mature in the thymus and are the major effector cells in cell-mediated immunity, as T cells are activated by APCs to create adaptive immune response. T cells are classified as cytotoxic T (Tc) cells, regulatory T (Treg) cells and T helper (Th) cells, separated by different cell surface markers. Tc cells express the $CD8^+$ surface marker and recognize antigens bound in the MHC I molecule, whereas Treg and Th cells express $CD4^+$ on their surface and recognize antigens bound in MHC II molecules. Tc cells destroy, for example, virus-infected cells by secreting effector molecules and are activated by APCs and, in some cases, by Th cells. Treg cells suppress immune response by secreting transforming growth factor (TGF)-β and interleukin (IL)-10 or direct cell–cell contact with, for example, Tc cells. On the other hand, Th cells activate macrophages, B cells, and neutrophils to strengthen adaptive immune response [1]. Th cells are divided into different subclasses based on the cytokines produced during the acting phase (Figure 13.1).

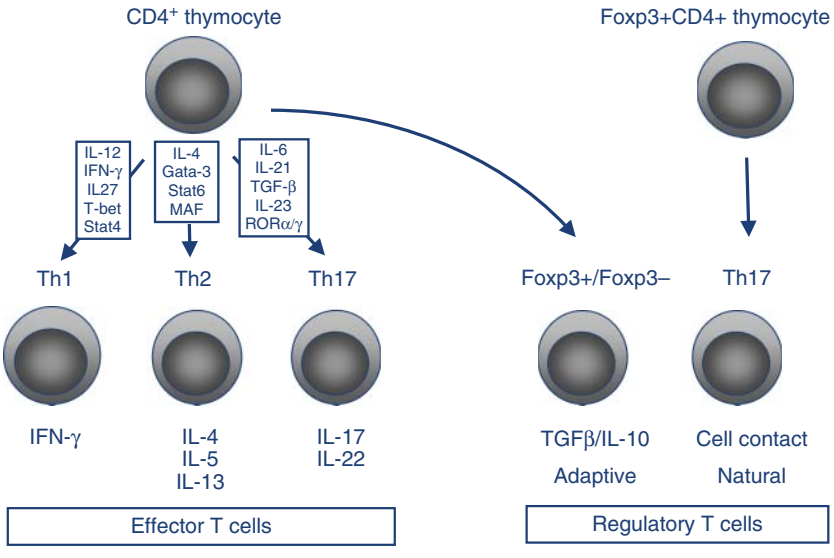

Figure 13.1 Differentiation of the most important T-helper cell subpopulations.

The differentiation of T cells into different lineages of response type is a complex process depending on multiple factors, such as the dose and type of antigen. Also, T memory cells are generated during the first contact with the antigen. They are responsible of immunological memory, producing rapid immune response when challenged with a known antibody.

B cells mature in the bone marrow and act in the humoral immunity by producing antibodies that have a role in pathogen elimination by binding them. This leads to the neutralization of pathogens or their removal by phagocytic cells such as macrophages. A sophisticated communication between T cells or other cell types such as dendritic cells and B cells leads to B cell differentiation into antibody-producing plasma cells or memory B cells, providing fast and effective removal of a pathogen after the later entry of the same pathogen into the body [9]. B cells produce antibodies (Ab) of different isotypes: IgA, IgD, IgE, IgG, and IgM, and the different isotypes have different functions in the adaptive immune response. IgG is the most potent isotype secreted in humans, opsonizing pathogens, which are then ingested by phagocytes, whereas IgE has an important function in the pathomechanism of allergy.

13.2 Carbon Nanotubes (CNTs) and Innate Immunity

CNT, as all engineered nanomaterials (ENMs), may enter the body via different exposure routes, such as respiratory, dermal, gastrointestinal, and intravenous [10]. Depending on the exposure scenario, the routes are often divided into

unintentional and intentional. Exposure to CNT via respiratory, dermal, and gastrointestinal routes may occur unintentionally in an occupational environment. Accidental exposure to CNT may take place during synthesis and, especially, in postproduction processes such as pouring, packaging, storing, and transporting. On the other hand, intentional dermal and gastrointestinal exposures occur when using ENM-containing consumer products. Intravenous exposure is the only intentional exposure route that takes place during administration of drugs in which ENMs can be used as carries of therapeutic agents [11].

Although immunomodulatory effects may occur in response to CNTs upon every type of exposure, inhalation is envisaged as the most relevant route to investigate. This is due to the spike-like shape and high aspect ratio of CNT fibers that resemble the characteristics of asbestos, which is known to cause pathological changes in the lungs. Lungs are one of the most vulnerable targets for ENMs also because of their anatomy. Once the materials enter the lungs, they are in direct contact with immune cells and can potentially activate the immune system and cause significant health effects. Therefore, a great majority of toxicity research on CNTs *in vitro* and *in vivo* has been carried out in cell models and in mammalian systems with a focus on respiratory system exposures, and for this reason [11] most examples in this chapter originate from such studies.

13.2.1 Complement Activation

Complement proteins opsonize pathogens and induce inflammatory responses, thereby helping immune cells to fight against infection [2, 3]. The complement system activation can be triggered via three distinct pathways – classical pathways (CP), lectin pathways (LP), and alternative pathways (AP). Initiation of each pathway leads to a common terminal pathway. The most important component of complement is C3, which at the end of all pathways is cleaved into functionally active parts, namely an inflammation mediator C3a and an opsonin C3b. CP induction happens when C1q binds to antigen–immunoglobulin complexes or pattern recognition molecules on the surface of the pathogen. These components together form a specific complex, where Cq1 undergoes a conformational change leading to activation of serine proteases C1r and C1s. Further reactions allow the formation of C3 convertases near the binding site of the C1 complex. LP uses proteins that resemble C1q for triggering the complement cascade. Mannose-binding lectin (MBL) binds specifically to sugars that are often expressed by pathogens and dying cells. MBL forms a complex with serine proteases MASP-1 and MASP-2. Upon binding to target surface, MASP-2 is activated and eventually causes the formation of C3 convertase [2]. AP is a permanently active and dominant complement pathway in healthy conditions. Unlike CP, AP can proceed without the presence of a specific antibody. The pathway can be activated by spontaneous transformation of C3 into C3 (H_2O). The latter binds the plasma protein factor B and is cleaved by factor D, resulting in a fluid-phase C3 convertase. The convertases can activate many more C3 molecules by cleaving them into C3a and C3b units [1].

To date, there is evidence that several complement proteins bind onto CNTs and are able to trigger the activation of complement system pathways and even the entire complement system [12–15]. Salvador-Morales *et al*. demonstrated that single-walled carbon nanotubes (SWCNTs) and double-walled carbon nanotubes (DWCNTs) stimulate the complement system via the classical pathway. Moreover, DWCNTs were able to activate also the alternative pathway. They detected a very selective binding of C1q onto the surface of both materials [15]. Organized binding of C1 components C1q and C1s–C1r–C1r–C1s on DWCNTs and multi-walled carbon nanotubes (MWCNTs) was also observed in another study; however, the C1 complex was not activated by CNT [16]. In contrast, human serum albumin-coated SWCNTs were shown to activate the complement system via C1q-mediated classical and alternative pathways [12]. To study whether surface coating of CNTs could affect complement activation, the authors functionalized the SWCNTs with methoxypoly(ethylene glycol)-based amphiphilines that improve CNT dispersibility. They found that, depending on amphiphilic structure, the functionalized SWCNTs trigger the lectin pathway activation instead [12]. Poly(ethylene glycol) (PEG) functionalization is another method used for ENMs, which confers their stabilization and prolonged circulation profiles in blood stream [17]. Andersen *et al*. tested different PEG-functionalized carboxylated MWCNT to find out whether PEG coating of various chain lengths has an influence on complement system activation but found that all the tested versions of PEGylated MWCNT activated the complement system equally [13]. Pondman *et al*. have provided evidence for CNT-induced complement activation up to C3 and C5, suggesting that the whole complement cascade becomes activated. Moreover, they found that opsonization of CNTs increases their uptake by U937 cells. Further investigation of cytokine production levels showed decreased mRNA expression of pro-inflammatory cytokines and elevation of anti-inflammatory cytokines in U937 cells and human monocytes [14]. The data reported by Pondman *et al*. indicate that complement activation triggered by the tested CNTs might induce cellular influx and phagocytosis but does not lead to pro-inflammatory immune response.

13.2.2 Macrophages

Macrophages that have phagocytic and pattern recognition abilities represent the first line defense against pathogens and foreign material in blood circulation and many tissues [1]. Therefore, these cells are often used as an *in vitro* model to mimic the first responses taking place upon CNT exposure.

Particle internalization by phagocytic cells serves as a defense process to remove potentially harmful agents. It has been shown on other cell types that CNT fibers enter the cell's tip first, but the exact mechanism how CNTs are taken up by the cells is unclear [18]. It is likely that material internalization by macrophages takes place in a similar way. Interaction between a CNT fiber and a cell begins with membrane contact, adhesion, and uptake. This process is dependent on several

factors such as material composition, size, shape, surface charge and coating, biocorona, and aggregation status [19]. Macrophages engulf ENMs by several mechanisms, but for particles in size range of CNTs, the uptake of a fiber might happen either by diffusion through the plasma membrane or by phagocytosis [20]. Phagocytosis is an active process where the particle is at first surrounded by the phagocyte membrane and then taken up in a membrane-enclosed vesicle called phagosome or endocytic vacuole. The phagosome content becomes then acidic and degrades the fiber. Phagocytes have also membrane-enclosed granules called lysosomes that contain hydrolytic enzymes which contribute to neutralization process by fusing into phagosomes and generating a phagolysosome in which the components of lysosomes are released to deactivate the danger [1].

It has been noted that the optimal particle size for phagocytosis by alveolar macrophages is 3–6 μm [21]. However, macrophages whose size is ~20 μm in diameter [22] attempt to engulf all thin fibers regardless of their length. This results in a situation where rigid CNT fibers that are longer than the size of the phagocytes are not fully internalized. Such an incomplete process is called frustrated phagocytosis [23] and can lead to the release of lysosomal contents onto the cell surface, thereby causing tissue injury and inflammation. Even if macrophages are able to successfully internalize shorter fibers, there is a possibility that the fibers, depending on their rigidness, can rupture phagolysosomes, which results in the release of lysosomal content in the cytoplasm and subsequent activation of pro-inflammatory cytokine pathways [24, 25].

Macrophages have been shown to form foreign-body giant cells (FBGCs) in response to long, needle-like MWCNTs in mice (Figure 13.2) [23, 26]. Of all

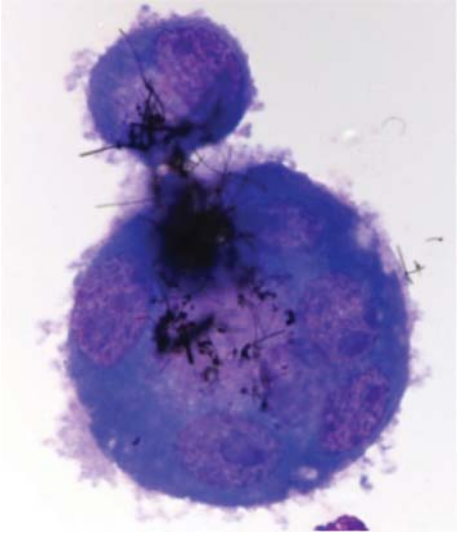

Figure 13.2 Macrophages engulfing MWCNT and undergoing frustrated phagocytosis and formation of FBGC. (from [26], © 2014 BioMed Central Ltd.)

ENMs, CNTs alone have been associated with this phenomenon. FBGCs, which result upon the fusion of macrophages in response to large foreign material [27], are recognized as the pathological hallmark of several diseases, including granulomatous diseases [27]. It has been suggested that frustrated phagocytosis is a driving force for such multinucleation. Fusion of cells in response to large particles could be seen as combining phagocytic forces of macrophages that are individually ineffective to completely uptake the material, or that such multinucleation might have an isolation function to protect host tissues from further damage and adverse effects of chronic inflammatory response [28, 29].

The production of reactive oxygen species (ROS) upon exposure of cells to particulate matter is considered a major contributor to ENM's toxicity [30]. Mechanistically, the induction of ROS generation can occur at different levels. Some types of CNTs have been shown to cause ROS production in particle preparations by themselves, that is, abiologically, by their intrinsic chemical reactivity [31, 32]. In addition, metal impurities in the materials, such as iron that is commonly used as a catalyst for the synthesis of CNTs, can contribute to formation of ROS [33]. CNTs could trigger ROS generation also during the interaction of particles with other cellular structures that are involved in the catalysis of biological redox processes [19]. For example, macrophages produce ROS from a variety of sources. They generate and release ROS upon phagocytosis, where ROS participate in neutralizing the infectious agents or foreign material [34]. In addition, the mitochondrial electron transport chain contains several redox centers that may release electrons to oxygen, constituting the primary source of oxygen radicals in most tissues [35]. CNT fibers could worsen such processes by directly influencing, for example, mitochondria and cause enhancement of ROS production. As a consequence of cell exposure to CNTs, the materials affect, via ROS formation, cellular signaling cascades that control inflammatory processes and cell death [36, 37].

The defense systems of innate immunity are effective in combating pathogens and foreign matter using a small number of receptors to recognize non-self material. The detection of microbial motifs called pathogen-associated molecular patterns (PAMPs) takes place by pattern-recognition receptors (PRRs), which are expressed by macrophages but also by other immune cells such as monocytes, dendritic cells, neutrophils, as well as cells of the adaptive immune system. Among others, PRRs include the membrane-bound Toll-like receptors (TLRs), which scan the extracellular environment and endosomal compartments for PAMPs. The result of PAMP recognition by PRRs depends upon the nature of both the responding cell and the invading microbe. However, signal transduction from these receptors converges on a common set of signaling modules, often including the activation of the NF-κB and AP-1 transcription factors that drive pro-inflammatory cytokine/chemokine such as pro-IL-1β, tumor necrosis factor (TNF), and IL-6 production [25]. Transcription and release of these cytokines has been seen in RAW 264.7 mouse macrophages [38].

It has not been shown to date how CNT-loaded macrophages behave in response to pathogen exposure *in vitro*. Upon recognition of bacteria and viruses, CNT-loaded cells may possibly obtain loss of defense and scavenging functions,

which might result in reduced immunological fitness and the inability to process pathogens. However, Shvedova *et al*. [39] observed that SWCNT-treated mice inoculated by pharyngeal aspiration with *Listeria monocytogenes* had functional respiratory deficiencies and slower bacterial clearance from the lungs compared to control mice.

13.2.3
Activation of Inflammasome Complex and IL-1β Secretion

It has been shown that, upon uptake of certain type of CNTs, the enhanced ROS production and lysosomal rupture induces the release of bioactive mediators, finally leading to inflammation [40]. One of the most well-studied CNT-triggered pathways is the IL-1 signaling pathway [24, 40]. However, the processing and secretion of IL-1 family cytokines is more strictly controlled compared to many other macrophage-derived cytokines. The IL-1 family cytokine, Il-1β, needs two stimuli to become biologically active. The first signal happens through the detection of pro-inflammatory signals, such as lipopolysaccharide (LPS) or TNF, that activate the NF-κB transcription factor and allow IL-1β promoter activation [25]. It leads to the production of the precursor pro-IL-1β, which is an inactive form of the cytokine. The second stimulus involves the assembly of the inflammasome complex, and results eventually in the cleavage of pro-IL-1β and release of the biologically active, mature IL-1β. The NLRP3 inflammasome is the most important activator of IL-1β and can be activated by PAMP as well as danger-associated molecular patterns (DAMPs).

Long and needle-like MWCNTs have been shown to have the ability to activate the NLRP3 complex [24]. Palomäki *et al*. [24] demonstrated that long and needle-like MWCNT-induced NLRP3 inflammasome activation depended on ROS production, cathepsin B activity (indicative or lysosomal rupture), and P2X7 receptor (indicative of activation of the adenosine triphosphate (ATP) gating cation channel) (Figure 13.3). Furthermore, NLRP3 inflammasome has been identified as a critical player in aluminum hydroxide- and aluminum phosphate-mediated adjuvant effects. As a result, the inflammasome has been considered to play a role in the development of adaptive immunity. Better knowledge on the roles of inflammasome in adaptive immunity will provide a deeper understanding on the material's adjuvant effect and will facilitate the development of new vaccines [40].

However, to date, it has not been reported whether CNTs are able to induce pro-IL-1β transcription, activation of the first part of the pathway. Instead, as mentioned above, LPS, which is an endotoxin found in cell walls of Gram-negative bacteria, is a PAMP that primes macrophages to produce the premature form of IL-1β, and therefore it has been emphasized how important the purity of the tested CNT should be. In realistic conditions, CNT exposure could possibly worsen the inflammation in individuals with a pre-existing infection. However, it remains questionable whether the co-exposure to these agents could cause inflammation upon inhalation of CNTs that have bound microbial endotoxins on their surface from air.

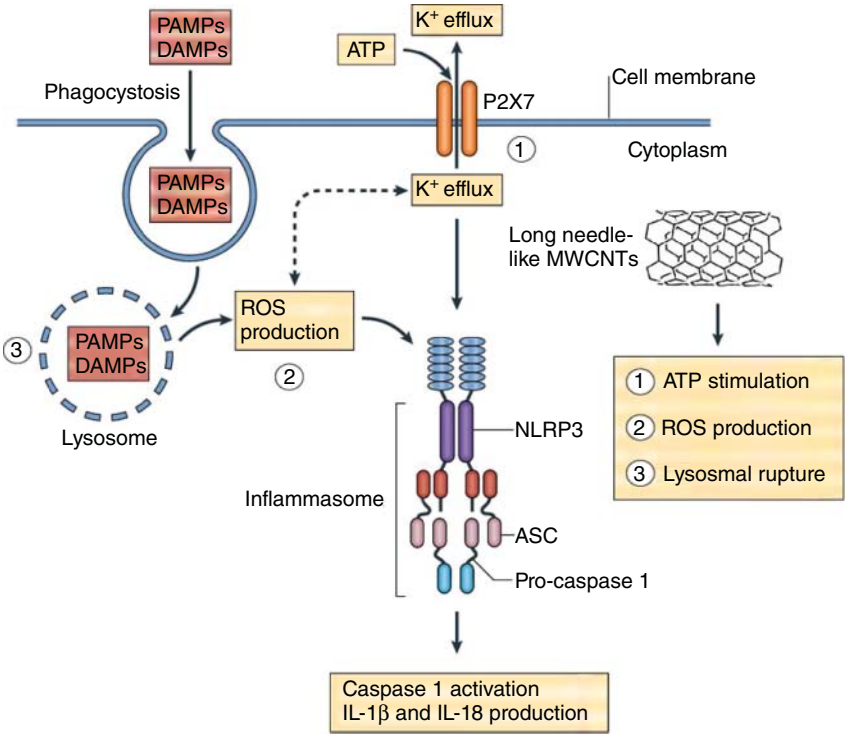

Figure 13.3 Possibleactivation routes of NLRP3 inflammasome by long, needle-like MWCNTs in the study by Palomäki *et al.* [24]. They demonstrated that P2X7 ATP channel (1), ROS production (2), and lysosome rupture (3) actively participate in NLRP3 inflammasome activation and release of bioactive IL-1β from LPS-primed macrophages after the stimulation with such MWCNTs. (Modified from [42], © 2010 Macmillan Publishers Limited.)

13.2.4
Neutrophils

Neutrophils are professional killers of the immune system. They are the most abundant white blood cells, and during inflammation they are the first cells recruited within hours to the inflammatory site from the blood steam. They are activated by several bacterial- and host-derived signals, including the classical chemoattractants and cytokines TNF and IL-1β, which are released by resident tissue cells such as macrophages upon recognition of foreign threat. Upon activation, neutrophils adhere firmly to the blood vessel walls and migrate through the endothelium into underlying tissues. Within the inflamed tissue, neutrophils follow chemotactic gradients toward the target [43]. To date, there have been numerous studies reporting the recruitment of neutrophils during the acute phase of the inflammation upon inhalation, pharyngeal aspiration, or intratracheal intstillation of SWCNTs, DWCNTs, or MWCNTs in rats or mice

[39, 44–47]. Increase in the number of neutrophils in bronchoalveolar lavage (BAL) fluid has been detected as early as 4 h after the administration of CNTs [44].

During the migration of neutrophils, chemoattractants bind to their respective receptors on neutrophils and initiate a signaling cascade that eventually leads to the assembly of the oxidative burst machinery, a classical sign of neutrophil activation. Neutrophils as macrophages express a variety of PRRs including TLR, and once they have reached their target, their activation culminates in killing processes of phagocytosis, degranulation, and NETosis (process of setting neutrophil extracellular traps, NETs) [43].

Neutrophilic granules contain an enzyme called myeloperoxidase (MPO) that is critical in the oxidative burst. Kagan *et al.* [48] have shown that, on incubation with human myeloperoxidase (hMPO), H_2O_2, and NaCl, carboxylated SWCNTs underwent morphological changes including a decrease in size and an increase in defects, and the SWCNTs degraded over time because the suspension turned translucent in the test tube. When neutrophil activation proceeds, their MPO-containing granules are mobilized and fused into the plasma membrane or phagosome. Such fusion is also important, as it enables the assembly of the NADPH oxidase complex, which initiates the reactive oxygen cascade by the generation of superoxide radicals and eventually forming hydrogen peroxide. This allows MPO, upon degranulation into the phagosome, react with hydrogen peroxide and produce different reactive species, including hypochlorous acid, which is the major product of MPO in phagosome [43]. Kagan *et al.* [48] demonstrated that, upon neutrophil activation by a chemoattractant and simultaneous degranulation by cytochalasin B, engulfed, IgG-functionalized nanotubes underwent 100% degradation. They furthermore confirmed that both hMPO and NADPH oxidase were necessary for the biodegradation.

NETosis is an active form of neutrophilic cell death during which decondensed chromatin is released into extracellular space, creating a mesh-like structure called NET. NETs are equipped with antimicrobial peptides and MPOs that normally reside within the neutrophil granules, and their formation is tightly linked to the ROS production by neutrophil NADPH oxidase [49]. Farrera *et al.* [50] have shown that oxidized SWCNTs are bound in NETs of PMA-stimulated primary human neutrophils. They furthermore demonstrated that the material undergoes biodegradation in purified NETs and that the process is MPO-dependent.

MPO-dependent clearance of SWCNTs has been reported also *in vivo* [51]. Investigating the biodegradability of SWCNT by neutrophils in MPO-deficient and wild-type mice, the authors found that clearance of the material from the lungs of MPO-deficient mice after pharyngeal aspiration was notably less effective than in wild-type controls, whereas the fibrotic inflammatory response was more robust than in wild-type mice.

Improved knowledge about the biodegradation of CNTs by MPO has provided support for using CNTs as nanocarriers for drugs. Seo *et al.* [52] have demonstrated that cytostatic and cytotoxic effects of doxorubicin, a drug used in cancer chemotherapy, but not the SWCNT-carried drug, on cancer cell lines were diminished in the presence of MPO-induced oxidative conditions created

by tumor-activated myeloid regulatory cells. These data reveal that nanocarriers are useful in protecting the drugs against oxidative biodegradation since they may serve as a scavenger for the oxidant and reactive intermediate species that are generated by the MPO cycle.

Taken together, neutrophils are important players of the innate immune system, as they are capable of peroxidase-dependent degradation of CNT, thus underscoring the important role of these cells in the defense against foreign intrusion.

13.2.5
Innate Lymphoid Cells (ILCs)

ILCs were first identified on the basis of their ability to promote rapid and essential innate immune responses to different classes of pathogens, in part by modulating local epithelial cell, myeloid cell, or granulocyte responses [4, 5, 53]. Therefore, they play an important part in orchestrating acute inflammation. However, they also have various other functions because, in addition to promoting early inflammatory reactions, they also take part in tissue repair, resolution of inflammation, and elicitation of chronic inflammation. There are several subtypes of ILCs, which have been divided into three groups based on their activation and the cytokines that each members of the subgroup express [4, 5, 53]. Group 1 ILCs respond to IL-12 and produce cytokines including interferon (IFN)-γ and TNF. Conventional NK cells are a subset of ILC1. Group 2 ILCs (ILC2) respond to the cytokines IL-25, IL-33, and TSLP, and they produce the cytokines IL-4, IL-5, IL-9, and IL-13. The healthy lung and skin of mice and humans seem to be rich in ILC2. Group 3 ILCs respond to IL-1β, IL-6, and IL-23 and produce the effector cytokines IL-17 and/or IL-22 [4–6, 53].

There is very limited knowledge about the effects of CNTs on ILCs. Delogu *et al*. [54] investigated the uptake of pristine and functionalized MWCNTs by NK cells, as well as the viability and activation of these cells in response to these materials. They evaluated the morphology of NK cells and found that their size did not change notably after MWCNT exposure, indicating that the cells that do not have phagocytic ability indeed did not take up the material. They also found that the tested materials did not decrease the cell viability. However, they found that NK cells were activated by the materials regardless of their functionalization, as they measured higher expression of surface markers CD69 and CD161 on CNT-treated cells compared to controls. The role of ILCs and associated cytokines in the context of allergy and asthma development will be discussed in Section 13.4.

13.2.6
Dendritic Cells

Most of the existing literature related to CNT exposure and dendritic cells is in the field of nanomedicine. CNT materials are useful for many therapeutic and drug-delivery application due to their ability to act as transporters of proteins and peptides across cell membrane.

In a study by Yang *et al*. [55], SWCNTs were shown as potential carriers for small interfering ribonucleic acid (siRNA) transport to phagocytic cells including dendritic cells. siRNAs mediate ribonucleic acid interference (RNAi), which is a beneficial method to study the functional outcome of gene silencing and is used for therapeutic intervention strategies [56]. Sun *et al*. [57] demonstrated that MWCNTs carrying tumor protein can increase the uptake of tumor antigen by human dendritic cells and promote the ability dendritic cells to activate anticancer response *in vitro*. Villa *et al*. [58] showed similarly that SWCNTs loaded with a tumor-epitope-bearing protein were immediately taken up into dendritic cells by micropinocytosis and subsequent binding into MHC II complexes.

13.3
CNTs and Adaptive Immunity

Nanomaterials may enter the body and encounter the immune system either via administration for biomedical application or unintentionally, for example, as a result of occupational exposure. Therefore, it is of fundamental importance to understand how different types of nanomaterials interact with immune cells and which kinds of health effects are induced. Adaptive immunity enables an immune defense with high specificity and also provides memory. In most cases, we wish for tolerance toward nanoparticles to ensure that they are recognized as harmless and no immune response is mounted. However, the potential of some nanoparticles to break tolerance and to induce strong immune reactions makes them interesting for medical applications. Understanding the responsible mechanisms is the key to the further advance of nanomedicine. In addition, adaptive immune mechanisms constantly evaluate whether nanoparticles are dangerous, which is also the central question of nanosafety research.

13.3.1
The Effects of CNTs on Vaccine Delivery and Immunotherapy

At present, vaccines still face difficulties for application worldwide because of their modest efficacy. CNTs as carriers or immunoregulators are promising candidates for optimizing the efficacy of vaccines [59]. The physiochemical properties of carbon nanomaterials, including CNTs, encompass flexible surface chemistry and a variety of structural morphologies. It is also easy to chemically or biologically modify the nanomaterial surface (Figure 13.4) [60]. Important requirements for successful biomaterial-based immunotherapeutics and vaccines involve efficient proliferation of antigen-specific effector cells, enhanced defense against pathogens, and successful immunization with minimal parenteral administration. In this context, CNTs are an attractive platform since they can be used to present the antigen at a high density, thus triggering enhanced cellular response [59]. Additionally, the ability of certain types of CNTs to translocate easily through the lipid bilayer provides advantage for priming a cellular immune

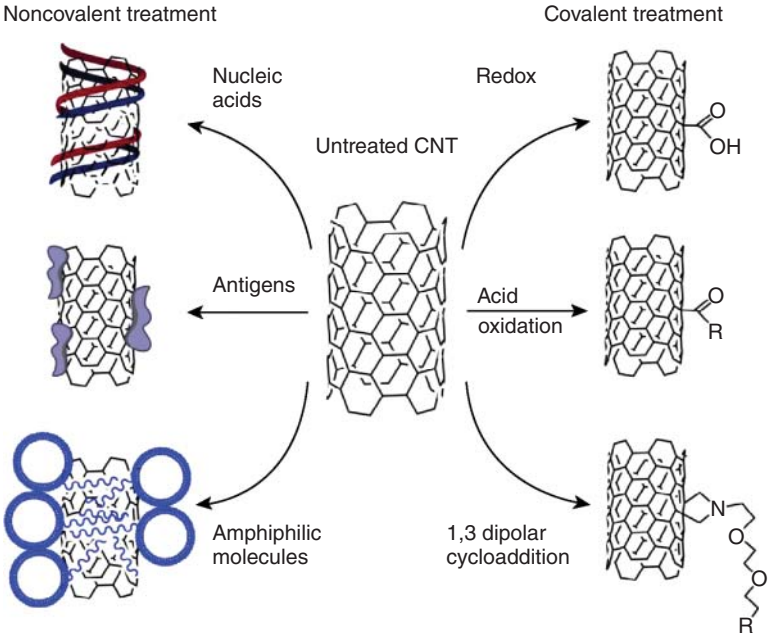

Figure 13.4 General functionalization strategies for the application of CNTs for immune modulation (reviewed in [59]). CNT chemistry can be tailored using noncovalent or covalent functionalization of their surface. Covalent strategies involve direct and stable linkage of various chemical groups on the CNT's surface, and noncovalent methods involve the adsorption of various biomolecules. Covalent treatments can be followed by additional functionalization, including the use of noncovalent methods. (Reproduced with permission from [59], © 2014 Elsevier Ltd.)

response. Ultimately, CNTs could have the potential to facilitate antigen adjuvancy, delivery, and presentation into a single, versatile biomaterial [59]. However, there are still some obstacles to be overcome for the application of nanomaterials. For example, bindings between nanomaterials and proteins *in vivo* would not only change both the shapes and sizes of the nanomaterials but also might mask surface modifications of the materials when they are delivered into the body. This might change the initial regulatory functions of these materials and trigger unpredictable and unwanted complications [60].

Fadel *et al.* [61] demonstrated that anti-CD3 adsorbed onto SWCNT bundles stimulated T cells more effectively than equivalent concentrations of soluble anti-CD3. Stimulation by antibody adsorbed onto SWCNTs was significantly higher than onto other high-surface-area materials (activated carbon, polystyrene, and C60 nanoparticles). Antibody stimuli adsorbed onto SWCNT bundles represent a novel tool for efficient activation of lymphocytes, potentially useful for clinical immunotherapy [61, 62]. Villa *et al.* investigated the feasibility of SWCNTs as antigen carriers to improve humoral immune responses to peptides that are weak immunogens, which is a typical characteristic of human tumor antigens [58]. They

used novel, spectrally quantifiable chemical approaches to covalently attach large numbers of the Wilm's tumor protein (WT1) peptide onto solubilized SCWNT scaffolds. Peptide–SCWNT constructs were rapidly internalized into dendritic cells and macrophages *in vitro* in a dose-dependent manner. Immunization of BALB/c mice with the SCWNT–peptide constructs mixed with immunological adjuvant induced specific IgG responses against the peptide, while the peptide alone or peptide mixed with the adjuvant did not induce such a response [58]. A similar approach was also used by Faria *et al.* [63]. They used a synthetic hybrid supramolecule comprising CNTs as the delivery system for the cancer testis antigen (NY-ESO-1). The CNT constructs were rapidly internalized into dendritic cells, both *in vitro* and *in vivo*, and served as an intracellular antigen depot. In contrast to the study by Villa *et al.* [58], in which strong antigen-specific humoral immune response was elicited, the construct favored the induction of strong $CD4^+$ T-cell- as well as $CD8^+$ T-cell-mediated immune responses against the NY-ESO-1. Moreover, the vaccination significantly delayed the tumor development and prolonged the mice's survival. The groups of Bianco and Gennaro demonstrated that functionalized CNTs conjugated with amphotericin B (an antifungal drug) could achieve an antifungal activity comparable to, or better than, amphotericin B alone in T-cell lines [64]. These studies highlight the potential application of CNTs as a vaccine or drug delivery system to provide superior immunogenicity and potentially stronger protection against diseases.

In view of the broad potential biomedical applications of CNTs in modulating the immune system, current knowledge is restricted mainly to exploring some activation markers and cytokines. However, Pescatori *et al.* [65] reported genome-wide Affymetrix microarray studies on Jurkat T-cell line and a monocytic THP-1 cell line, representative of adaptive and innate immunity, respectively. They treated the two cell lines with four types of functionalized MWCMTs, which differed in terms of functionalization and diameter. None of the CNT preparations induced cytotoxicity, and the overall effect on cell metabolism was negligible. However, they found a cell-specific action on THP-1 monocytes for three types of CNTs, which specifically enhanced the innate immunity activation mechanisms. The authors speculated the future perspectives for their application also as immunotherapeutic agents and/or vaccine adjuvants [65].

13.3.2
Utilization of CNT Scaffolds in the Expanding and Modulation of Immune Cells

Clinical translation of cell therapies requires strategies that can manufacture cells efficiently and economically. One promising way to reproducibly expand T cells (e.g., for cancer therapy) is by attaching the stimuli for T cells onto artificial substrates with high surface area. In an elegant study by Fadel *et al*. [66], antigens were attached to bundled CNTs and this complex was combined with polymer nanoparticles containing magnetite and the T-cell growth factor IL-2 (Figure 13.5). This novel composite was found to be an efficient and useful platform for generating large numbers of cytotoxic T cells for cancer immunotherapy.

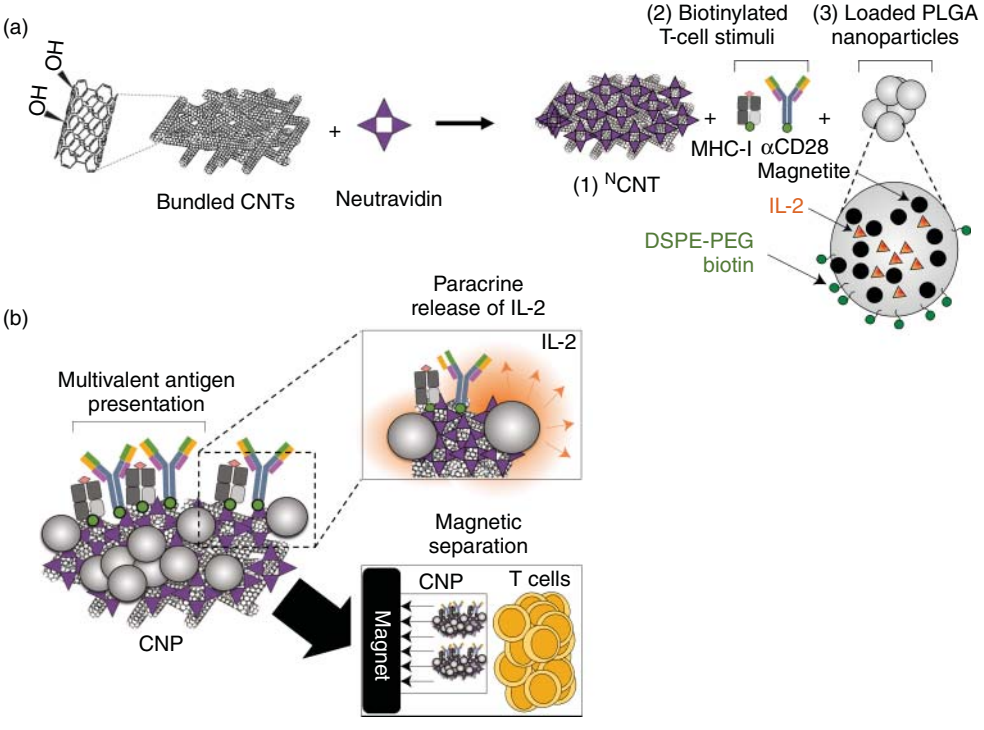

Figure 13.5 Design of CNPs in the study by Fadel *et al.* [66]. Schematics describing the combination of multivalent antigen presentation, paracrine delivery of cytokine, and T-cell enrichment capabilities into CNPs. (a) Schematic showing bundled CNTs binding neutravidin to present biotinylated T-cell stimuli and PLGA nanoparticles encapsulating magnetite and IL-2. (b) Schematic highlighting three properties of the engineered CNP platform: multivalent antigen presentation, paracrine release of IL-2, and magnetic separation of CNPs from T cells. (Modified from [66], © 2014 Macmillan Publishers Limited.)

The composite system provides several advantages to engineer optimal antigen presentation using different T-cell antigens (e.g., peptide/MHC complexes and antibodies). In addition to efficient antigen presentation, biodegradable polymeric nanoparticles can be encapsulated with the cytokine of interest. The CNT antigen-presentation system offers the potential for enhancing the proliferation and function of T cells to a level that would require at least 1000-fold less soluble IL-2 compared to conventional culture conditions. Finally, magnetic separation via magnetite co-encapsulated in the particles enables easy isolation and enrichment of activated T cells for adoptive transfer. The CNT composite system presented may offer greater stability and thus a more economical way to generate T cells for use than relying on live cells [66].

Nanotechnologies are increasingly used in tissue engineering strategies to improve the interface between artificial scaffolds and cells. Crucial to the exploitation of artificial scaffolds in organ repair is to investigate the immune

system response to nanoscale three-dimensional architectures, enabling the sustenance of tissue growth. To explore the potential of future tissue engineering constructs and to assess their immune modulatory action, Aldinucci *et al.* [67] evaluated CNTs' interactions with human DCs. They incorporated DC cultures to CNTs and demonstrated that DCs, when interfaced to CNTs, exhibited a lower immunogenic profile. These results suggest that altering the topographical and physical features of growth surfaces holds the potential to tune immune reaction modulation. It can be anticipated that different substrates are able to instruct cell responses by different mechanisms, which involve cytoskeleton modification with consequent alteration of immune function. It has been shown that MWCNTs can be incorporated into constructs to produce neural interfaces with high interfacial areas, conductivity, and electrochemical stability [68]. The authors suggest investigation in this framework of DCs' phenotypic/functional shift when interfaced to MWCNTs. This approach may hold the potential to predict the immune response toward electrodes and provide a valuable tool to tackle a key challenge in engineering neural implants [67].

13.3.3
Immunosuppressive Effects of CNTs

Several researchers have reported that nanotubes cause pulmonary inflammation following intratracheal instillation [69]. In contrast, Mitchell *et al.* [70] found that inhaled MWNTs did not induce notable pulmonary effects. However, inhaled MWCNTs caused systemic immunosuppression 14 days after the exposure. Immunosuppression was characterized by reduced T-cell-dependent antibody response as well as T-cells' proliferative ability in presence of mitogen. Assessment of nonspecific NK cell activity showed decreased NK cell function [70]. In their further studies, they demonstrated that CNT-induced immune suppression involved the activation of cyclooxygenase enzymes in the spleen in response to a signal from the lungs [71]. Spleen cells from exposed animals partially recovered their immune function when treated with ibuprofen, a drug that blocks the formation of cyclooxygenase enzymes. Knockout mice without cyclooxygenase enzymes were not affected when exposed to MWCNTs, further confirming the importance of this enzyme in immune suppression. Proteins from the lungs of exposed mice suppressed the immune function of spleen cells from normal mice but not those from knockout mice. Findings suggest that signals from the lung can activate signals in the spleen to suppress the immune function of exposed mice [71]. Murray *et al.* also demonstrated by aspiration exposure approach that, in addition to CNT-induced pulmonary inflammatory and fibrogenic responses, systemic suppression of immunity was elicited, as documented by decreased proliferation of splenic T cells *ex vivo* on day 28 post exposure [72]. These results emphasize that airway exposure to CNTs can induce various types of effects including pulmonary inflammation but also suppression of systemic immune response. Differences in the effects are likely due to differences in the exposure system and the type of CNTs applied.

13.4
The Effect of CNTs in Allergy and Asthma

The great majority of studies exploring the potential pathogenic effects of ENMs have been conducted in study settings mimicking the effects in healthy individuals, but only part of the world's population can be categorized into this group. A significant proportion of the population has impaired health conditions (such as allergy and asthma) that are believed to make these individuals more susceptible to additional health risks from particulate exposure.

In this section, the effects of exposure to CNT on asthma and allergy are discussed. We explore studies with naïve mice mimicking responses in healthy individuals. In addition, we review studies in which mice are already sensitized to protein or chemical allergens, thus mimicking scenario in which individuals have pulmonary disease or underlying immune condition.

13.4.1
Allergic Reactions and Their Immunological Mechanisms

Allergic reactions (hypersensitivity reactions) are the result of exaggerated and inappropriate immune reactions that are triggered by substances which are normally innocuous to the host. Allergic reactions are most commonly classified as immediate hypersensitivity reactions (or anaphylactic reactions) that involve IgE-mediated release of inflammatory mediators from mast cells, and as delayed reactions in which the immune system's response typically occurs 1–2 days after the antigenic exposure [1]. Delayed reactions are mediated by T cells and monocytes/macrophages rather than by antibodies, and are often called cell-mediated immunity.

Allergic immune response is initiated by a sensitization phase in which allergen exposure together with epithelial insults results in the activation of airway epithelial cells and internalization of allergens by immature DCs (Figure 13.6). Secretion of pro-inflammatory cytokines from the activated airway epithelium induces DC maturation and enhances expression of homing molecules for draining lymph nodes. Adaptive immune responses will take a place in draining lymph node in which proliferation of allergen-specific Th2 cells and production of allergen-specific IgE antibodies by B cells take place. Circulating IgE antibodies bind to the high-affinity IgE receptors on the surface of mast cells in the tissue (Figure 13.6). Repeated encounter with the same allergen results in immediate hypersensitivity symptoms.

Immediate hypersensitivity reactions manifest clinically as allergic asthma, allergic rhinitis, food allergy, and atopic dermatitis. Early acute-phase allergic reactions are mediated by the release of preperformed and newly synthesized inflammatory mediators such as histamine, tryptase, or proteoglycans from mast cells (Figure 13.6), which cause clinical symptoms like vasodilatation, mucus secretion, increased vascular permeability, and increased smooth muscle contraction [1]. This signaling cascade is triggered by the binding of IgE on

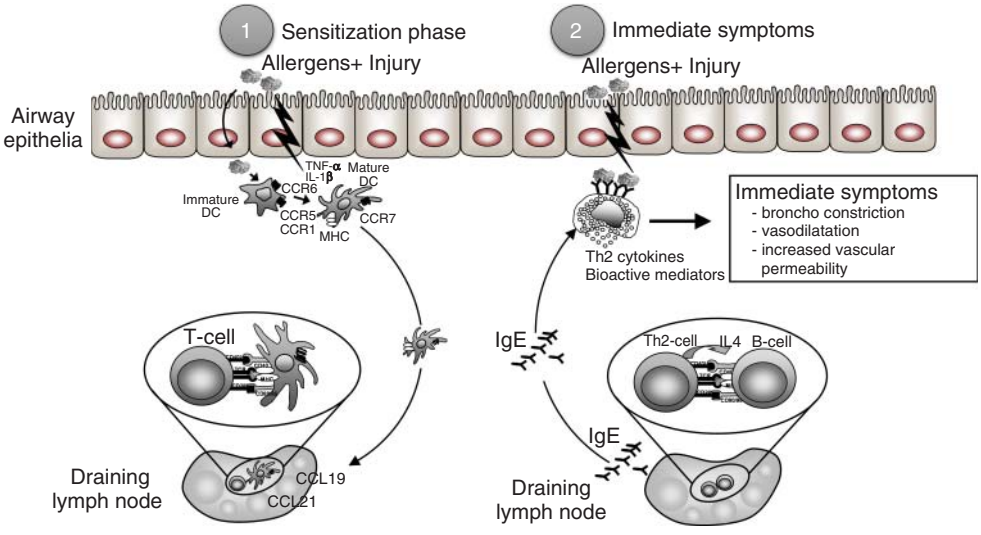

Figure 13.6 Immunological mechanisms of allergen sensitization and immediate hypersensitivity symptoms.

high-affinity FcεRI receptors on mast cells, and occurs within minutes of allergen exposure (Figure 13.6). The late-phase reaction occurs about 6–24 h after the encounter with allergen.

Late-phase reactions are caused by enhanced synthesis and release of inflammatory mediators such as prostaglandins, leukotrienes, chemokines, and cytokines such as IL-5 and IL-13 from the activated mast cells [73] (Figure 13.7). In response to early phase mediators, endothelial cells express several adhesion molecules (vascular cell adhesion molecules, VCAMs), which in turn alter the avidity and expression of the counter-ligands on leukocytes (selectins and integrins). Interactions between these adhesion molecules results in the activation and recruitment of leukocytes, which move from the blood to the site of inflammation [1]. This may eventually lead to a chronic allergic inflammation and in mucosal damage through the effects of fibroblasts, vascular endothelial cells, and tissue remodeling [1] (Figure 13.7).

13.4.2 Asthma

Asthma is a chronic inflammatory disorder of the lungs that is characterized by recurrent episodes of airflow obstruction, bronchial inflammation, mucus hypersecretion, and airway hyper-responsiveness (AHR) [74]. The most general form of asthma is allergic asthma resulting from airway inflammation triggered by an environmental allergen. Other forms of asthma are nonallergic asthma, where the cause of airway inflammation is unclear, and mixed-type asthma with a combination of allergic and nonallergic factors. The most popular paradigm

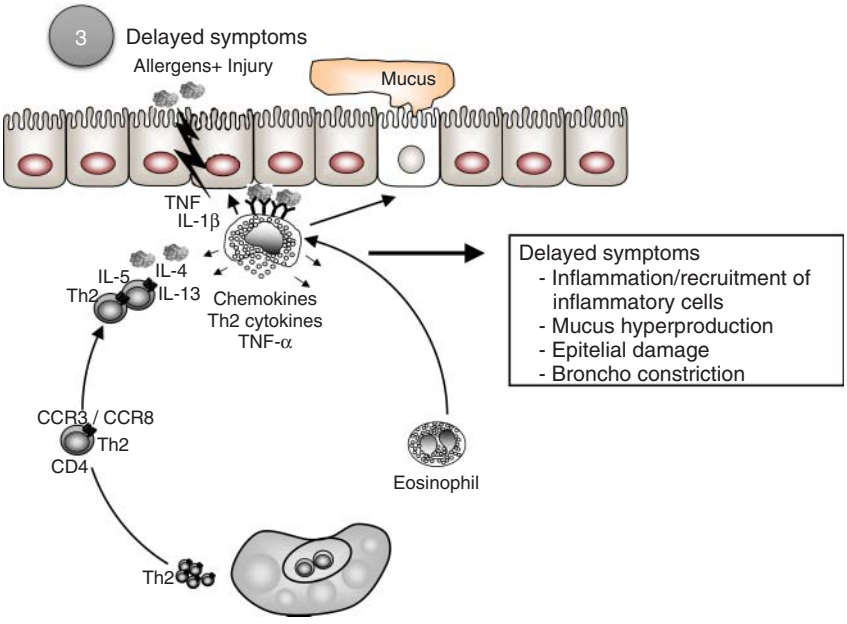

Figure 13.7 Immunological mechanisms of delayed-type symptoms.

regarding asthma pathogenesis involves allergen-specific $CD4^+$ T helper (Th2) cells, which are thought to be present in the lungs of nearly all patients with asthma [75]. In genetically predisposed individuals, primary exposure to an allergen leads to the activation of Th2 lymphocytes, which produce cytokines such as IL-4, IL-5, and IL-13 and stimulate IgE production from B cells [1]. Later on, antigen exposure causes immediate release of biologically active mediators (histamine, leukotrienes) via mast cell degranulation with resulting extensive vascular leakage, airway smooth muscle constriction, mucus hypersecretion, eosinophil inflammation, and enhanced airway hyper-reactivity.

Mast cells are important contributors both in the initiation of asthma with release of acute-phase mediators and also in the later stages in the production of a variety of inflammatory cytokines [73]. Persistent inflammation lasting for years can eventually lead to irreversible structural changes, such as airway smooth muscle hypertrophy and hyperplasia, thickening of airway mucosa, and increased vascularity hyperplasia of goblet cells, with the development of fibrosis [74]. Although the classical Th1/Th2 paradigm explains many features of asthma, evidence suggests that Th2 cells alone may not be sufficient for the development of all types of asthma. For example, cytokines such as IFN-γ and IL-17 are frequently found in the lungs of patients with severe asthma and with patients with corticosteroid-resistant asthma [74]. Also, the degree of pulmonary inflammation does not always correlate with the severity of asthma and, in some forms of asthma, neutrophils instead of eosinophils predominate in the airways [74].

13.4.3
Allergic Pulmonary Inflammation Induced by Airway Exposure to CNTs

Park *et al.* [76] investigated pulmonary inflammation and humoral immune responses after intratracheal instillation of MWCNTs in mice. Pro-inflammatory Th2 and Th1 cytokines were increased in a dose-dependent manner, both in BAL and in blood after installation. Moreover, distribution of B cells in the spleen and blood were significantly increased, together with elevated levels of IgE in BAL and blood. The authors suggested that MWCNTs may induce allergic responses through B-cell activation and production of IgE [76]. It should be noted, however, that although some features of allergic inflammation could be identified, cellular and cytokine profiles were not typical for Th2-dominated response; characteristic features of allergic airway inflammation such as eosinophilia and goblet cell hyperplasia could not be observed [74]. In a study by Hsieh *et al.* [77], a single intratracheal instillation of SWCNTs induced airway hyperreactivity and airflow obstruction as well as granulomatous changes in the lung parenchyma that persisted from 7 days to 6 months after exposure. Transcriptomic analysis showed that SWCNT exposure upregulated cathepsin K, matrix proteinase 12 (MMP12), chemokines (CCL2, CCL3), and several macrophage receptors. Although classical signs of allergic inflammation were not found, results suggest that exposure to SWCNT may cause irreversible obstructive airway disease. Toxicogenomics approach suggests a role for MMP12 and cathepsin K in the pathobiology of lung injury [77].

Exposure to CNTs, especially in the occupational context, happens mainly by inhalation. Although the inhalation exposure method is the closest to real-life scenarios, the number of such studies is very limited. In the study by Rydman *et al.* [26], healthy mice were exposed by inhalation exposure to two types of MWCNTs, rigid rod-like and flexible tangled particles. A short-term 4-day inhalation of the rod-like CNTs induced novel innate-immunity-mediated allergic-like airway inflammation. Marked eosinophilia was accompanied by mucus hypersecretion, AHR, and the expression of Th2-type cytokines. Exploration of the early events by transcriptomics analysis revealed that a single 4-h inhalation exposure to rod-shaped CNTs, but not to tangled CNTs, causes a radical upregulation of the genes involved in innate immunity and cytokine/chemokine pathways. Mast cells were found to partially regulate the inflammation caused by rod-like CNTs, but also alveolar macrophages play an important role in the early stages [26]. This study demonstrates that, in addition to the previously described asbestos-associated pathologies, inhalation of rod-like CNTs is able to induce a novel innate-immunity-mediated asthma-like airway inflammation. The study also highlights marked dissimilarities in the ability of different CNT to impact health [26].

Pulmonary-deposited CNTs are likely cleared slowly from the lung, but there is limited information on how CNTs interact with the lung tissue over time. Rydman *et al.* [44] investigated the difference between two different CNTs (long tangled, and long rod-like CNT) and crocidolite asbestos in inducing

inflammatory reactions in mice after a single pharyngeal aspiration exposure. To explore the functional role of a major inflammatory cytokine IL-1β, they utilized etanercept (TNF inhibitor) and anakinra (IL-1 receptor antagonist) as antagonists as well as IL1R$^{-/-}$ mice. Results showed that rod-like CNT-induced inflammation drastically changed over time: starting from neutrophilic pulmonary inflammation at 4–16 h and then changing to pulmonary eosinophilia that peaked at 7 days after the exposure [44]. After 28 days, pulmonary goblet cell hyperplasia and Charcot–Leyden-like crystals containing acidophilic macrophages were observed especially in rod-like CNT-exposed mice. IL-1R$^{-/-}$ mice and antagonist-treated mice exhibited a significant decrease in neutrophilia at 16 h. However, rod-like CNT-induced Th2-type inflammation, as evidenced by the expression of IL-13 and mucus production, was unaffected in IL-1R$^{-/-}$ mice at 28 days. These results demonstrate that IL-1R interaction regulates mainly neutrophilic inflammation in the acute inflammatory response but this interaction is not critical for Th2-dominated allergic-type response observed 1 month after the exposure to rod-like CNTs. Køibler *et al.* [78] examined the effects of exposure to three different MWCNTs by intratracheal instillation. Their results [78] revealed that two types of MWCNTs had very similar pattern of cellular interactions in lung tissue, with the longer and thicker CNTs resulting in more severe effects in terms of eosinophil influx and induction of crystalline bodies in the cytosol of alveolar macrophages, as was seen also in the study of Rydman *et al.* [44].

13.4.4
Modulation of Allergen-Induced Airway Inflammation by Exposure to CNTs

Versatile approaches and models have been used to induce allergic airway inflammation in rodents. Ovalbumin (OVA) allergen-induced experimental asthma is likely the most widely studied asthma model worldwide. Intraperitoneal immunization with OVA (together with aluminum hydroxide as an adjuvant) followed by OVA inhalation/aspiration induces a robust, allergic pulmonary inflammation and airway hyper-responsiveness in mice. There are also several variations in which sensitization is done by repeated intranasal or intratracheal administration with OVA, but without the adjuvant. Moreover, several allergen types have been used in addition to OVA to induce Th2-type allergic immune response, including house dust mite (HDM) extract.

Nygaard *et al.* [79] investigated whether SWCNTs and MWCNTs have the capacity to promote allergic responses in OVA-immunized mice. Mice were exposed intranasally to SWCNTs, MWCNTs, as well as ultrafine carbon black particles (ufCBPs) during sensitization with the OVA. Five days after an intranasal OVA booster, OVA-specific IgE, IgG1, and IgG2a antibodies in serum and the numbers of inflammatory cells and cytokine levels in BAL were determined. Results demonstrated that both SWCNTs and MWCNTs together with OVA strongly increased serum levels of OVA-specific IgE, the number of eosinophils in BAL, and the secretion of Th2-associated cytokines in the draining lymph nodes [79]. Inoue *et al.* also examined the effects of MWCNTs [80] and SWCNTs [81] by

repeated intranasal exposure with and without OVA allergen. Repeated exposure to MWCNTs and SWCNTs aggravated allergen-induced airway inflammation characterized by the infiltration of eosinophils, neutrophils, and mononuclear cells in the lung, and an increase in the number of goblet cells in the bronchial epithelium. MWCNTs exhibited adjuvant activity for allergen-specific IgG1 and IgE. MWCNTs significantly increased OVA-specific T-cell proliferation. Also, these studies revealed the ability of both MWCNTs and SWCNTs to potentiate allergen-induced airway inflammation [80, 81]. In an interesting study by Li *et al.* [82], repeated intratracheal administration with OVA was used to sensitize Wistar rats and to induce asthma-like airway inflammation. The results showed that exposure to SWCNTs exacerbated OVA-induced allergic asthma and that this exacerbation was counteracted by concurrent administration of vitamin E. It was concluded that elimination of ROS, downregulation of Th2 responses, reduced Ig production, and the relief of allergic asthma symptoms were explained by the antagonistic effects of vitamin E [82].

Ryman-Rasmussen explored the effects of MWCNT inhalation in a mice model of OVA-induced allergic asthma [83]. Normal and OVA-sensitized mice were exposed to an MWCNT aerosol ($100\,mg\,m^{-3}$) or saline aerosol for 6 h. The inhaled MWCNTs were distributed throughout the lung and were found in macrophages by light microscopy, but they were also evident in epithelial cells by electron microscopy. Significant airway fibrosis was observed at 14 days in mice that received a combination of OVA and MWCNT, but not in mice that received OVA or MWCNT only. OVA-sensitized mice that did not inhale MWCNTs had elevated levels IL-13 and TGF-β1 in the lung lavage fluid, but not platelet-derived growth factor (PDGF)-AA. In contrast, unsensitized mice that inhaled MWCNTs had elevated PDGF-AA, but not increased levels of TGF-β1 and IL-13. This suggested that airway fibrosis resulting from combined OVA sensitization and MWCNT inhalation requires PDGF, a potent fibroblast mitogen, and TGF-β1, which stimulates collagen production [83]. These findings suggest that individuals with pre-existing allergic inflammation may be susceptible to airway fibrosis from inhaled MWCNTs. Although the results are highly interesting, real-life relevance of these results should be interpreted with caution because of the excessive concentration of MWCNTs used for inhalation exposure.

Protein exposure usually induces Th2-type immune response, which is typical for allergic inflammation. However, people are sensitized also to several chemicals, especially in the occupational context. Depending on the physicochemical nature of the chemicals, exposure time, and frequency, chemical-induced Th2, Th1, or irritant response can be elicited. Staal *et al.* studied MWCNT responses by using high-IgE-responding brown Norway rats with trimellitic anhydride (TMA)-induced respiratory allergy [84]. The rats were exposed 2 days per week over a 3.5-week period to MWCNTs. At the end of the exposure period, the allergic animals were rechallenged with TMA. Histopathological examination of the respiratory tract showed agglomerated/aggregated MWCNTs in the lungs and in the lung-draining lymph nodes. Large MWCNT agglomerates were found in granulomas in the allergic rats, suggesting decreased macrophage clearance

in these animals. In allergic rats, MWCNT exposure decreased serum IgE levels and the number of lymphocytes in BAL lavage. It was concluded that MWCNTs did not aggravate the acute allergic reaction but modulated the allergy-associated immune responses [84].

13.4.5 CNT in the Context of Mast Cells and Eosinophils

Exposure to CNTs can occur via the respiratory, gastrointestinal, or dermal route. MCs reside at these interfaces with the environment. Mast cells are central effectors in immediate hypersensitivity reactions. After encountering an allergen, IgE-sensitized mast cells release a broad panel of bioactive mediators and Th2-type cytokines (e.g., IL-4, IL-5, IL-13) in order to initiate and promote airway inflammation, but mast cells are important contributors also in the later stages of allergy and asthma [73]. Umemoto *et al.* [85] explored the effects of SWCNTs on mast cell signaling pathways as well as phenotype and pro-inflammatory function. It was observed that exposure with SWCNTs suppressed antigen-induced signaling pathways and pro-inflammatory degranulation responses. Mast cells recognize SWCNTs by remodeling the plasma membrane, disaggregating the cortical actin cytoskeleton, and relocalizing clathrin. These data suggest the ability of SWCNTs to suppress mast cell pro-inflammatory function via a novel recognition mechanism [85].

Pulmonary eosinophilia is the hallmark of allergic asthma. Eosinophil peroxidase (EPO) is one of the major oxidant-producing enzymes during inflammatory states in the human lung. It has been described that exposure to CNTs induces acute pulmonary eosinophilia and release of EPO into inflammatory foci in the lungs of exposed mice [86]. Andón *et al.* [87] reasoned that EPO released from eosinophils under physiologically relevant conditions could play an important role in the biodegradation of CNTs. They found that biodegradation of SWCNTs is higher in the presence of sodium bromide, but neither EPO alone nor H_2O_2 alone caused the degradation of nanotubes. Molecular modeling revealed two binding sites for SWCNT on EPO: one located at the proximal side (same side as the catalytic site) and the other on the distal side of EPO. The oxidized groups on SWCNTs in both cases are stabilized by electrostatic interactions with positively charged residues. Biodegradation of SWCNT can also be executed in an *ex vivo* culture system using primary murine eosinophils stimulated to undergo degranulation. Thus, human EPO in *in vitro* and *ex vivo* activated eosinophils mediate biodegradation of SWCNTs: an observation that is relevant to pulmonary responses to these materials [87].

13.4.6 Role of IL-33 Pathway in CNT-Induced Allergic Responses

IL-33 (IL-1F11) is a cytokine that belongs to the IL-1 family and is linked to Th2-type immune responses [88]. IL-33 is expressed by cells of barrier tissues (e.g., skin,

gut, and lung) and is known to activate naive and Th2 lymphocytes, mast cells, and eosinophils to produce Th2-type cytokines. Chang *et al.* [53] reported in a mouse model that influenza induced airway hyper-reactivity (AHR), a classical feature of asthma, independently of adaptive immunity involvement. Instead, influenza infection induced AHR through a previously unknown pathway that required the IL-13–IL-33 axis and cells of the non-T-cell, non-B-cell innate lymphoid type called "natural helper cells". Infection with influenza A virus, which activates the NLRP3 inflammasome [25], resulted in much more production of IL-33 by alveolar macrophages, which in turn activated helper cells producing substantial IL-13, which is one of the key cytokines in IgE class switching, mucus secretion, and allergy development.

Beamer *et al.* [89] tested the hypothesis that instillation of MWCNTs impaired pulmonary function in mice because of the development of IL-33-dependent Th2-associated inflammation. MWCNT exposure resulted in elevated levels of IL-33 in the lavage fluid (likely originating from airway epithelial cells), enhanced AHR, eosinophil recruitment, and production of Th2-associated cytokines and chemokines. Moreover, these events were dependent on IL-13 signaling and the IL-33/ST2 axis, but independent of T and B cells [89]. Finally, MWCNT exposure resulted in the recruitment of ILCs. Their study suggests that MWCNTs induce epithelial damage, which results in the release of IL-33, which in turn promotes ILC recruitment and the development of IL-13-dependent inflammatory response. Ronzani *et al.* [90] investigated the effect of MWCNTs on systemic immune response and airway inflammation and remodeling induced by HDM, which is the most frequent allergen associated with asthma. Mice exposed to HDM exhibited specific IgG1 in serum and inflammatory cell infiltration as well as increased Th2 cytokine production, mucus hyperproduction, and collagen deposition in the airways when compared to naïve animals. Levels of total IgG1 and HDM-specific IgG1, influx of eosinophils and neutrophils, production of collagen, TGF-β1, and mucus, as well as levels of IL-13, eotaxin, and TARC were dose-dependently increased in mice exposed to HDM + MWCNT compared to HDM alone. These effects were associated with an increased production of the allergy-promoting cytokines TSLP, IL-25, IL-33, and granulocyte macrophage colony-stimulating factor (GM-CSF) in the airways. This study shows that MWCNTs increase, in a dose-dependent manner, systemic immune response as well as airway allergic inflammation and remodeling induced by HDM. Data suggest also a role for airway epithelium and innate cytokines in these effects [90].

Rydman *et al.* [26] explored the role of ILCs and early expression of Th2 cytokines and IL-33 in a rod-like CNT-induced inflammation. They measured LC2 markers IL-25 and ROR-α in both isolated BAL cells and lung tissue, but found no upregulation in their expression in response to rod-like CNT inhalation exposure. However, the pro-allergic IL-33, which promotes the activation of mast cells, was expressed by isolated alveolar tissue. On the contrary, no significant induction of IL-13 and IL-4 was observed from the isolated BAL cells after a 4-h exposure to rod-like CNTs, suggesting that the alveolar macrophages do not

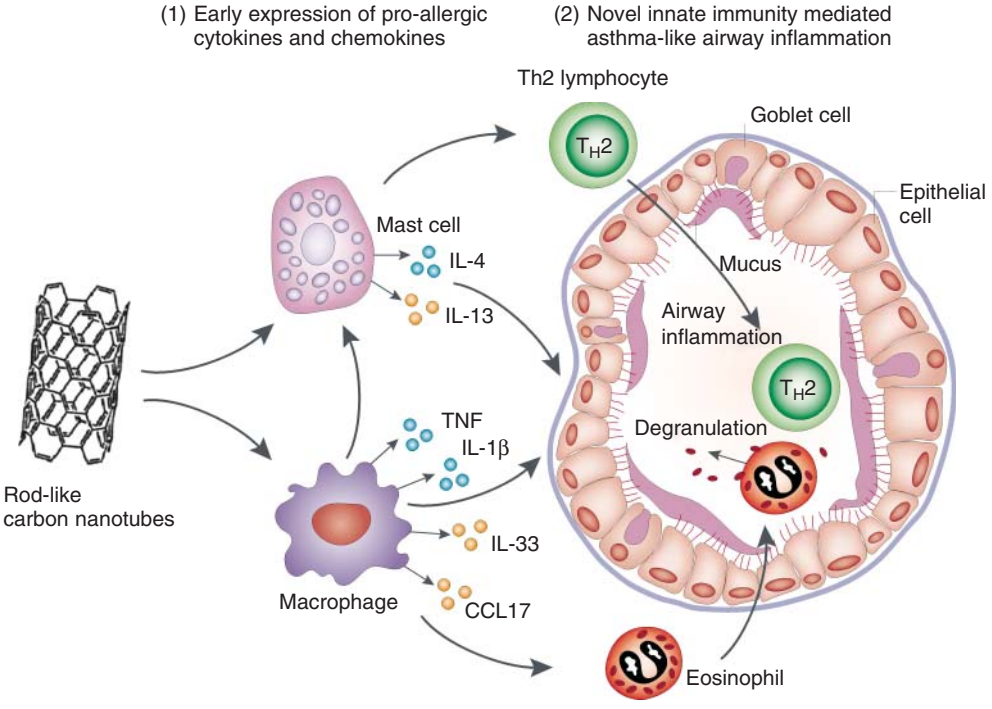

Figure 13.8 The study by Rydman *et al.* [26]. The authors concluded that inhalation exposure to rod-like MWCNT results in rapid induction of IL-4 and IL-13 from mast cells and pro-inflammatory (TNF and IL-1β) and pro-allergic cytokines and chemokines (IL-33 and CCL17) from alveolar macrophages. In the context of repeated CNT exposure, this in turn results in the recruitment of eosinophils and Th2 cells, finally leading to full-blown allergic innate-immunity-mediated airway inflammation, mucus hypersecretion, and airway hyper-reactivity. (Modified from [91]. © 2002 Macmillan Magazines Ltd.)

synthetize these Th2 cytokines at the early stages. Expression of IL-13 and IL-4 was significantly decreased in MC-deficient mice, suggesting that MCs are likely an early source of these Th2 cytokines in rod-like CNT-induced inflammation. The authors [83] concluded that the early events of MWCNT-induced Th2-type responses most likely include the activation of mast cells by IL-33 derived at least partially from lung macrophages (Figure 13.8). Their results demonstrate that rod-like CNT-activated alveolar macrophages are an important source of not only pro-inflammatory but also allergy-promoting cytokines.

13.5 Conclusions and Future Prospects

Interactions between CNTs and the immune system are highly desirable when CNTs are engineered to carry known molecules modulating the activity of

immune cells. The use of nanoparticles that have unique immunological properties, determined by their size, shape, charge, porosity, and hydrophobicity, will enable researchers to customize immune responses in new and innovative ways (reviewed in [92]). Improved and faster immune-mediated protection against invading pathogens could be achieved through the utilization of nanoparticle composites in which the unique combinations of antigens are bound to the nanomaterial scaffold. In addition to antigen coupling, nanoparticles could be combined with various type biomolecules (such as cytokines and co-stimulatory ligands) to fine-tune the immune system into the desired direction – either to stimulate or to inhibit the immune response in a selective manner. By introducing selected components of microbial pattern recognition systems in the context of weak antigens, one could induce T- and B-cell mediated responses to antigens that normally do not activate easily the immune system. It is also possible that "suppressive nanoparticles" could be given to patients with specific autoimmune diseases in order to prevent disease development. The application of nanotechnology in immunology open diverse possibilities to improve upon current strategies for the prevention or treatment of the human diseases (reviewed in [92]).

In addition to these beneficial effects, CNTs can induce undesirable effects such as cytotoxicity, inflammation, genotoxicity, and even cancer. More research is required to fully understand their complex interactions, but it is obvious that the exposure to CNTs can significantly influence the immune system. However, because of the existence of numerous types of CNTs, immune responses vary greatly depending on the physicochemical characteristics of these CNTs. Indeed, the physicochemical characteristics of CNT such as their length, purity, aggregation state, and surface properties directly affect the way the immune system detects them. Unintentional exposure to harmful CNTs in occupational settings may occur and lead to deleterious immune system events or other malignancies, which remain major concerns [10]. Intrinsic immunostimulatory or inhibitory properties of CNTs must be taken into account in the evaluation of their potential use for biomedical applications, consumer product manufacture, and nanotechnology in general.

Because of the unique interactions of CNTs with the immune system and the potential for these materials to act as adjuvants, it is likely that these materials may also contribute or promote the development of allergic diseases such as asthma, dermatitis, rhinitis, and others [93]. IgE is a key mediator of allergic disease, in which mast cells and basophils are primed to respond to allergens. A few studies in animal models have begun to identify changes in IgE levels associated with CNT exposure [76, 79–81]. Interestingly, activation of novel innate-immune type of allergic airway inflammation has been described after the inhalation exposure to rod-like CNTs but not to tangled CNTs [26]. Moreover, a few studies have also described exacerbation of allergen-induced airway inflammation after inhalation exposure to CNTs [58, 62, 82, 83, 89, 94]. Despite the few reports related to the development or exacerbation of allergic inflammation and asthma, there is still a significant lack of knowledge to understand the risk of allergic diseases resulting

from CNT exposures. On the other hand, innovative use of functionalized CNTs may also open avenues to treat allergic diseases efficiently.

The field of nanotechnology will continue to provide remarkable insights into the nature of the immune response. The application of nanotechnology in immunology might also give rise to new strategies for the prevention or the treatment of human diseases. However, evidence also exits that exposure to certain CNTs has the capacity to induce severe adverse effects, implying the need for further research and great caution before introducing such products into the market.

References

1. Murphy, K., Travers, P., Walport, M., and Janeway, C. (2012) *Janeway's Immunobiology*, 8th edn, Garland Science, New York, p. xix, 868 pp.
2. Merle, N.S., Church, S.E., Fremeaux-Bacchi, V., and Roumenina, L.T. (2015) Complement system part I – Molecular mechanisms of activation and regulation. *Front. immunol.*, **6**, 262.
3. Merle, N.S., Noe, R., Halbwachs-Mecarelli, L., Fremeaux-Bacchi, V., and Roumenina, L.T. (2015) Complement system part II: role in immunity. *Front. immunol.*, **6**, 257.
4. Brestoff, J.R., Kim, B.S., Saenz, S.A. *et al.* (2015) Group 2 innate lymphoid cells promote beiging of white adipose tissue and limit obesity. *Nature*, **519** (7542), 242–246.
5. Hepworth, M.R., Fung, T.C., Masur, S.H. *et al.* (2015) Immune tolerance. Group 3 innate lymphoid cells mediate intestinal selection of commensal bacteria-specific CD4(+) T cells. *Science*, **348** (6238), 1031–1035.
6. Sonnenberg, G.F. and Artis, D. (2015) Innate lymphoid cells in the initiation, regulation and resolution of inflammation. *Nat. Med.*, **21** (7), 698–708.
7. Artis, D. and Spits, H. (2015) The biology of innate lymphoid cells. *Nature*, **517** (7534), 293–301.
8. Urb, M. and Sheppard, D.C. (2012) The role of mast cells in the defence against pathogens. *PLoS Pathog.*, **8** (4), e1002619.
9. Bonilla, F.A. and Oettgen, H.C. (2010) Adaptive immunity. *J. Allergy Clin. Immunol.*, **125** (2, Suppl. 2), S33–S40.
10. Dumortier, H. (2013) When carbon nanotubes encounter the immune system: desirable and undesirable effects. *Adv. Drug Deliv. Rev.*, **65** (15), 2120–2126.
11. Oberdorster, G., Oberdorster, E., and Oberdorster, J. (2005) Nanotoxicology: an emerging discipline evolving from studies of ultrafine particles. *Environ. Health Perspect.*, **113** (7), 823–839.
12. Andersen, A.J., Robinson, J.T., Dai, H. *et al.* (2013) Single-walled carbon nanotube surface control of complement recognition and activation. *ACS Nano*, **7** (2), 1108–1119.
13. Andersen, A.J., Windschiegl, B., Ilbasmis-Tamer, S. *et al.* (2013) Complement activation by PEG-functionalized multi-walled carbon nanotubes is independent of PEG molecular mass and surface density. *Nanomedicine*, **9** (4), 469–473.
14. Pondman, K.M., Sobik, M., Nayak, A. *et al.* (2014) Complement activation by carbon nanotubes and its influence on the phagocytosis and cytokine response by macrophages. *Nanomedicine*, **10** (6), 1287–1299.
15. Salvador-Morales, C., Flahaut, E., Sim, E. *et al.* (2006) Complement activation and protein adsorption by carbon nanotubes. *Mol. Immunol.*, **43** (3), 193–201.
16. Ling, W.L., Biro, A., Bally, I. *et al.* (2011) Proteins of the innate immune system crystallize on carbon nanotubes but are not activated. *ACS Nano*, **5** (2), 730–737.

17. Moghimi, S.M., Andersen, A.J., Hashemi, S.H. *et al.* (2010) Complement activation cascade triggered by PEG-PL engineered nanomedicines and carbon nanotubes: the challenges ahead. *J. Control. Release*, **146** (2), 175–181.
18. Shi, X., von dem Bussche, A., Hurt, R.H., Kane, A.B., and Gao, H. (2011) Cell entry of one-dimensional nanomaterials occurs by tip recognition and rotation. *Nat. Nanotechnol.*, **6** (11), 714–719.
19. Unfried, K., Sydlik, U., Bierhals, K., Weissenberg, A., and Abel, J. (2008) Carbon nanoparticle-induced lung epithelial cell proliferation is mediated by receptor-dependent Akt activation. *Am. J. Physiol. Lung Cell. Mol. Physiol.*, **294** (2), L358–L367.
20. Krug, H.F. and Wick, P. (2011) Nanotoxicology: an interdisciplinary challenge. *Angew. Chem. Int. Ed.*, **50** (6), 1260–1278.
21. Frohlich, E. (2015) Value of phagocyte function screening for immunotoxicity of nanoparticles in vivo. *Int. J. Nanomed.*, **10**, 3761–3778.
22. Krombach, F., Munzing, S., Allmeling, A.M. *et al.* (1997) Cell size of alveolar macrophages: an interspecies comparison. *Environ. Health Perspect.*, **105** (Suppl. 5), 1261–1263.
23. Poland, C.A., Duffin, R., Kinloch, I. *et al.* (2008) Carbon nanotubes introduced into the abdominal cavity of mice show asbestos-like pathogenicity in a pilot study. *Nat. Nanotechnol.*, **3** (7), 423–428.
24. Palomaki, J., Valimaki, E., Sund, J. *et al.* (2011) Long, needle-like carbon nanotubes and asbestos activate the NLRP3 inflammasome through a similar mechanism. *ACS Nano*, **5** (9), 6861–6870.
25. Schroder, K. and Tschopp, J. (2010) The inflammasomes. *Cell*, **140** (6), 821–832.
26. Rydman, E.M., Ilves, M., Koivisto, A.J. *et al.* (2014) Inhalation of rod-like carbon nanotubes causes unconventional allergic airway inflammation. *Part. Fibre Toxicol.*, **11**, 48.
27. Helming, L. and Gordon, S. (2009) Molecular mediators of macrophage fusion. *Trends Cell Biol.*, **19** (10), 514–522.
28. McNally, A.K. and Anderson, J.M. (2011) Foreign body-type multinucleated giant cells induced by interleukin-4 express select lymphocyte co-stimulatory molecules and are phenotypically distinct from osteoclasts and dendritic cells. *Exp. Mol. Pathol.*, **91** (3), 673–681.
29. McNally, A.K. and Anderson, J.M. (2011) Macrophage fusion and multinucleated giant cells of inflammation. *Adv. Exp. Med. Biol.*, **713**, 97–111.
30. Nel, A., Xia, T., Madler, L., and Li, N. (2006) Toxic potential of materials at the nanolevel. *Science*, **311** (5761), 622–627.
31. Chen, C.Y. and Jafvert, C.T. (2010) Photoreactivity of carboxylated single-walled carbon nanotubes in sunlight: reactive oxygen species production in water. *Environ. Sci. Technol.*, **44** (17), 6674–6679.
32. Hsieh, H.S., Wu, R., and Jafvert, C.T. (2014) Light-independent reactive oxygen species (ROS) formation through electron transfer from carboxylated single-walled carbon nanotubes in water. *Environ. Sci. Technol.*, **48** (19), 11330–11336.
33. Aldieri, E., Fenoglio, I., Cesano, F. *et al.* (2013) The role of iron impurities in the toxic effects exerted by short multiwalled carbon nanotubes (MWCNT) in murine alveolar macrophages. *J. Toxicol. Environ. Health A*, **76** (18), 1056–1071.
34. Forman, H.J. and Torres, M. (2001) Redox signaling in macrophages. *Mol. Aspects Med.*, **22** (4–5), 189–216.
35. Turrens, J.F. (2003) Mitochondrial formation of reactive oxygen species. *J. Physiol.*, **552**(Pt. 2), 335–344.
36. Funahashi, S., Okazaki, Y., Ito, D. *et al.* (2015) Asbestos and multi-walled carbon nanotubes generate distinct oxidative responses in inflammatory cells. *J. Clin. Biochem. Nutr.*, **56** (2), 111–117.
37. Sweeney, S., Grandolfo, D., Ruenraroengsak, P., and Tetley, T.D. (2015) Functional consequences for primary human alveolar macrophages following treatment with long, but not short, multiwalled carbon nanotubes. *Int. J. Nanomed.*, **10**, 3115–3129.
38. Zhang, T., Tang, M., Kong, L. *et al.* (2012) Comparison of cytotoxic and inflammatory responses of pristine

and functionalized multi-walled carbon nanotubes in RAW 264.7 mouse macrophages. *J. Hazard. Mater.*, **219-220**, 203–212.

39. Shvedova, A.A., Kisin, E.R., Mercer, R. *et al.* (2005) Unusual inflammatory and fibrogenic pulmonary responses to single-walled carbon nanotubes in mice. *Am. J. Physiol. Lung Cell. Mol. Physiol.*, **289** (5), L698–L708.
40. Sun, B., Wang, X., Ji, Z., Li, R., and Xia, T. (2013) NLRP3 inflammasome activation induced by engineered nanomaterials. *Small*, **9** (9–10), 1595–1607.
41. Eisenbarth, S.C., Colegio, O.R., O'Connor, W., Sutterwala, F.S., and Flavell, R.A. (2008) Crucial role for the Nalp3 inflammasome in the immunostimulatory properties of aluminium adjuvants. *Nature*, **453** (7198), 1122–1126.
42. Tschopp, J. and Schroder, K. (2010) NLRP3 inflammasome activation: the convergence of multiple signalling pathways on ROS production? *Nat. Rev. Immunol.*, **10** (3), 210–215.
43. Amulic, B., Cazalet, C., Hayes, G.L., Metzler, K.D., and Zychlinsky, A. (2012) Neutrophil function: from mechanisms to disease. *Annu. Rev. Immunol.*, **30**, 459–489.
44. Rydman, E.M., Ilves, M., Vanhala, E. *et al.* (2015) A single aspiration of rod-like carbon nanotubes induces asbestos-like pulmonary inflammation mediated in part by the IL-1R. *Toxicol. Sci.* 2015 Sep., **147** (1), 140–55.
45. Sager, T.M., Wolfarth, M.W., Andrew, M. *et al.* (2014) Effect of multi-walled carbon nanotube surface modification on bioactivity in the C57BL/6 mouse model. *Nanotoxicology*, **8** (3), 317–327.
46. Shvedova, A.A., Fabisiak, J.P., Kisin, E.R. *et al.* (2008) Sequential exposure to carbon nanotubes and bacteria enhances pulmonary inflammation and infectivity. *Am. J. Respir. Cell Mol. Biol.*, **38** (5), 579–590.
47. Tian, F., Habel, N.C., Yin, R. *et al.* (2013) Pulmonary DWCNT exposure causes sustained local and low-level systemic inflammatory changes in mice. *Eur. J. Pharm. Biopharm.*, **84** (2), 412–420.
48. Kagan, V.E., Konduru, N.V., Feng, W. *et al.* (2010) Carbon nanotubes degraded by neutrophil myeloperoxidase induce less pulmonary inflammation. *Nat. Nanotechnol.*, **5** (5), 354–359.
49. Amulic, B. and Hayes, G. (2011) Neutrophil extracellular traps. *Curr. Biol.*, **21** (9), R297–R298.
50. Farrera, C., Bhattacharya, K., Lazzaretto, B. *et al.* (2014) Extracellular entrapment and degradation of single-walled carbon nanotubes. *Nanoscale*, **6** (12), 6974–6983.
51. Shvedova, A.A., Kapralov, A.A., Feng, W.H. *et al.* (2012) Impaired clearance and enhanced pulmonary inflammatory/fibrotic response to carbon nanotubes in myeloperoxidase-deficient mice. *PLoS One*, **7** (3), e30923.
52. Seo, W., Kapralov, A.A., Shurin, G.V. *et al.* (2015) Payload drug vs. nanocarrier biodegradation by myeloperoxidase- and peroxynitrite-mediated oxidations: pharmacokinetic implications. *Nanoscale*, **7** (19), 8689–8694.
53. Chang, Y.J., Kim, H.Y., Albacker, L.A. *et al.* (2011) Innate lymphoid cells mediate influenza-induced airway hyper-reactivity independently of adaptive immunity. *Nat. Immunol.*, **12** (7), 631–638.
54. Delogu, L.G., Venturelli, E., Manetti, R. *et al.* (2012) Ex vivo impact of functionalized carbon nanotubes on human immune cells. *Nanomedicine*, **7** (2), 231–243.
55. Yang, R., Yang, X., Zhang, Z. *et al.* (2006) Single-walled carbon nanotubes-mediated in vivo and in vitro delivery of siRNA into antigen-presenting cells. *Gene Ther.*, **13** (24), 1714–1723.
56. Guo, H., Ingolia, N.T., Weissman, J.S., and Bartel, D.P. (2010) Mammalian microRNAs predominantly act to decrease target mRNA levels. *Nature*, **466** (7308), 835–840.
57. Sun, Z., Wang, W., Meng, J. *et al.* (2010) Multi-walled carbon nanotubes conjugated to tumor protein enhance the uptake of tumor antigens by human dendritic cells in vitro. *Cell Res.*, **20** (10), 1170–1173.

58. Villa, C.H., Dao, T., Ahearn, I. *et al.* (2011) Single-walled carbon nanotubes deliver peptide antigen into dendritic cells and enhance IgG responses to tumor-associated antigens. *ACS Nano*, **5** (7), 5300–5311.
59. Fadel, T.R. and Fahmy, T.M. (2014) Immunotherapy applications of carbon nanotubes: from design to safe applications. *Trends Biotechnol.*, **32** (4), 198–209.
60. Liu, Y., Xu, Y., Tian, Y. *et al.* (2014) Functional nanomaterials can optimize the efficacy of vaccines. *Small*, **10** (22), 4505–4520.
61. Fadel, T.R., Steenblock, E.R., Stern, E. *et al.* (2008) Enhanced cellular activation with single walled carbon nanotube bundles presenting antibody stimuli. *Nano Lett.*, **8** (7), 2070–2076.
62. Fadel, T.R., Look, M., Staffier, P.A. *et al.* (2010) Clustering of stimuli on single-walled carbon nanotube bundles enhances cellular activation. *Langmuir*, **26** (8), 5645–5654.
63. de Faria, P.C., dos Santos, L.I., Coelho, J.P. *et al.* (2014) Oxidized multiwalled carbon nanotubes as antigen delivery system to promote superior CD8(+) T cell response and protection against cancer. *Nano Lett.*, **14** (9), 5458–5470.
64. Benincasa, M., Pacor, S., Wu, W. *et al.* (2011) Antifungal activity of amphotericin B conjugated to carbon nanotubes. *ACS Nano*, **5** (1), 199–208.
65. Pescatori, M., Bedognetti, D., Venturelli, E. *et al.* (2013) Functionalized carbon nanotubes as immunomodulator systems. *Biomaterials*, **34** (18), 4395–4403.
66. Fadel, T.R., Sharp, F.A., Vudattu, N. *et al.* (2014) A carbon nanotube-polymer composite for T-cell therapy. *Nat. Nanotechnol.*, **9** (8), 639–647.
67. Aldinucci, A., Turco, A., Biagioli, T. *et al.* (2013) Carbon nanotube scaffolds instruct human dendritic cells: modulating immune responses by contacts at the nanoscale. *Nano Lett.*, **13** (12), 6098–6105.
68. Keefer, E.W., Botterman, B.R., Romero, M.I., Rossi, A.F., and Gross, G.W. (2008) Carbon nanotube coating improves neuronal recordings. *Nat. Nanotechnol.*, **3** (7), 434–439.
69. Murray, A.R., Kisin, E., Leonard, S.S. *et al.* (2009) Oxidative stress and inflammatory response in dermal toxicity of single-walled carbon nanotubes. *Toxicology*, **257** (3), 161–171.
70. Mitchell, L.A., Gao, J., Wal, R.V. *et al.* (2007) Pulmonary and systemic immune response to inhaled multiwalled carbon nanotubes. *Toxicol. Sci.*, **100** (1), 203–214.
71. Mitchell, L.A., Lauer, F.T., Burchiel, S.W., and McDonald, J.D. (2009) Mechanisms for how inhaled multiwalled carbon nanotubes suppress systemic immune function in mice. *Nat. Nanotechnol.*, **4** (7), 451–456.
72. Murray, A.R., Kisin, E.R., Tkach, A.V. *et al.* (2012) Factoring-in agglomeration of carbon nanotubes and nanofibers for better prediction of their toxicity versus asbestos. *Part. Fibre Toxicol.*, **9**, 10.
73. Galli, S.J., Tsai, M., and Piliponsky, A.M. (2008) The development of allergic inflammation. *Nature*, **454** (7203), 445–454.
74. Fanta, C.H. (2009) Asthma. *N. Engl. J. Med.*, **360** (10), 1002–1014.
75. Lloyd, C.M. and Hessel, E.M. (2010) Functions of T cells in asthma: more than just T(H)2 cells. *Nat. Rev. Immunol.*, **10** (12), 838–848.
76. Park, E.J., Cho, W.S., Jeong, J. *et al.* (2009) Pro-inflammatory and potential allergic responses resulting from B cell activation in mice treated with multi-walled carbon nanotubes by intratracheal instillation. *Toxicology*, **259** (3), 113–121.
77. Hsieh, W.Y., Chou, C.C., Ho, C.C. *et al.* (2012) Single-walled carbon nanotubes induce airway hyperreactivity and parenchymal injury in mice. *Am. J. Respir. Cell Mol. Biol.*, **46** (2), 257–267.
78. Kobler, C., Poulsen, S.S., Saber, A.T. *et al.* (2015) Time-dependent subcellular distribution and effects of carbon nanotubes in lungs of mice. *PLoS One*, **10** (1), e0116481.
79. Nygaard, U.C., Hansen, J.S., Samuelsen, M. *et al.* (2009) Single-walled and multiwalled carbon nanotubes promote allergic immune responses in mice. *Toxicol. Sci.*, **109** (1), 113–123.

80. Inoue, K., Koike, E., Yanagisawa, R. *et al.* (2009) Effects of multi-walled carbon nanotubes on a murine allergic airway inflammation model. *Toxicol. Appl. Pharmacol.*, **237** (3), 306–316.

81. Inoue, K., Yanagisawa, R., Koike, E., Nishikawa, M., and Takano, H. (2010) Repeated pulmonary exposure to single-walled carbon nanotubes exacerbates allergic inflammation of the airway: possible role of oxidative stress. *Free Radic. Biol. Med.*, **48** (7), 924–934.

82. Li, J., Li, L., Chen, H. *et al.* (2014) Application of vitamin E to antagonize SWCNTs-induced exacerbation of allergic asthma. *Sci. Rep.*, **4**, 4275.

83. Ryman-Rasmussen, J.P., Tewksbury, E.W., Moss, O.R. *et al.* (2009) Inhaled multiwalled carbon nanotubes potentiate airway fibrosis in murine allergic asthma. *Am. J. Respir. Cell Mol. Biol.*, **40** (3), 349–358.

84. Staal, Y.C., van Triel, J.J., Maarschalkerweerd, T.V. *et al.* (2014) Inhaled multiwalled carbon nanotubes modulate the immune response of trimellitic anhydride-induced chemical respiratory allergy in brown Norway rats. *Toxicol. Pathol.*, **42** (7), 1130–1142.

85. Umemoto, E.Y., Speck, M., Shimoda, L.M. *et al.* (2014) Single-walled carbon nanotube exposure induces membrane rearrangement and suppression of receptor-mediated signalling pathways in model mast cells. *Toxicol. Lett.*, **229** (1), 198–209.

86. Girtsman, T.A., Beamer, C.A., Wu, N., Buford, M., and Holian, A. (2014) IL-1R signalling is critical for regulation of multi-walled carbon nanotubes-induced acute lung inflammation in C57Bl/6 mice. *Nanotoxicology*, **8** (1), 17–27.

87. Andon, F.T., Kapralov, A.A., Yanamala, N. *et al.* (2013) Biodegradation of single-walled carbon nanotubes by eosinophil peroxidase. *Small*, **9** (16), 2721–2729, 2720.

88. Liew, F.Y., Pitman, N.I., and McInnes, I.B. (2010) Disease-associated functions of IL-33: the new kid in the IL-1 family. *Nat. Rev. Immunol.*, **10** (2), 103–110.

89. Beamer, C.A., Girtsman, T.A., Seaver, B.P. *et al.* (2013) IL-33 mediates multi-walled carbon nanotube (MWCNT)-induced airway hyper-reactivity via the mobilization of innate helper cells in the lung. *Nanotoxicology*, **7** (6), 1070–1081.

90. Ronzani, C., Casset, A., and Pons, F. (2014) Exposure to multi-walled carbon nanotubes results in aggravation of airway inflammation and remodeling and in increased production of epithelium-derived innate cytokines in a mouse model of asthma. *Arch. Toxicol.*, **88** (2), 489–499.

91. Gern, J.E. and Busse, W.W. (2002) Relationship of viral infections to wheezing illnesses and asthma. *Nat. Rev. Immunol.*, **2** (2), 132–138.

92. Smith, D.M., Simon, J.K., and Baker, J.R. Jr., (2013) Applications of nanotechnology for immunology. *Nat. Rev. Immunol.*, **13** (8), 592–605.

93. Shannahan, J.H. and Brown, J.M. (2014) Engineered nanomaterial exposure and the risk of allergic disease. *Curr. Opin. Allergy Clin. Immunol.*, **14** (2), 95–99.

94. Orecchioni, M., Bedognetti, D., Sgarrella, F. *et al.* (2014) Impact of carbon nanotubes and graphene on immune cells. *J. Transl. Med.*, **12**, 138.

14
Carbon Dots: Synthesis, Bioimaging, and Biosafety Assessment

Jie Wang and Yao He

14.1
Introduction

14.1.1
Synthesis and Fabrication of C-dots

To date, there exist a large number of elegant works involving the development of nanomaterials featuring well-defined structures and the required functionality. For example, metal (e.g., silver and gold) nanostructures (e.g., nanoparticles, nanorods, and nanoshells) [1], fluorescent semiconductor II–VI quantum dots (QDs) [2], silicon nanostructures (e.g., silicon nanoparticles (SiNPs) and nanowires) [3], carbon-based nanostructures (e.g., carbon nanotubes, graphene, and carbon dots (C-dots)) [4], and magnetic nanoparticles (e.g., Fe_3O_4 nanoparticles) [5] have been arousing intense attention of researcher. Among them, C-dots, considered the most important zero-dimensional carbon nanostructures, are of particular interest due to their numerous attractive merits, including size- and wavelength-dependent luminescence emission, resistance to photobleaching, ease of bioconjugation, and so forth. A consensus has been reached that, for wide-ranging applications, high-quality C-dots are required to be prepared at low cost, easily, and in large scale.. To date, several representative strategies have been developed for meeting such demands. As far as 2004, Xu *et al.* for the first time noticed an unknown fluorescent carbon nanomaterial when they purified single-walled carbon nanotubes (SWCNTs) prepared from arc-discharge soot [6]. By oxidizing arc soot with 3.3 M HNO_3 and extracting the sediment thus obtained, they obtained a stable black suspension, which was then separated by gel electrophoresis into SWCNTs, producing C-dots emitting green-blue, yellow, and orange colors under the excitation of 366 nm. Since then, the attractive properties of C-dots has been arousing the interest of more and more scientists, and correspondingly a variety of high-efficacy physical and chemical methods have been introduced to prepare fluorescent C-dots in the past decade, including microwave-assisted methods, hydrothermal carbonization, electrochemical

Biomedical Applications and Toxicology of Carbon Nanomaterials, First Edition.
Edited by Chunying Chen and Haifang Wang.

oxidization, chemical oxidation, ultrosonication, plasma treatment, laser ablation, supported and thermal routes, and so on. Typically, in 2006, Sun *et al.* [7] developed the laser-ablation method for the production of C-dots. In this method, a kind of carbon target, prepared by hot-pressing a mixture of graphite powder and cement, was first ablated by a Q-switched Nd:YAG laser (1064 nm, 10 Hz) in a flow of argon gas carrying water vapor at 900 °C and 75 kPa. Afterward, the treated carbon target was further heated at reflux in 2.6 M HNO_3 for up to 12 h to yield C-dots featuring strong fluorescence. In the following years, soot derived from the combustion of unscented candles or natural gas burners have also been explored as elegant and simple sources of C-dots [8]. For example, in order to synthesize C-dots, Mao and colleagues collected soot by placing a piece of aluminum foil or a glass plate atop a burning candle, mixing the soot with 5 M HNO_3, and then refluxing it for 12 h to oxidize the particle surfaces, and, eventually producing the C-dots with sizes of <2 nm through centrifugation or dialysis and further polyacrylamide gel electrophoresis (PAGE) fractionation [8]. Pang and colleagues synthesized fluorescent C-dots by electrochemically oxidizing a graphitic column electrode at 3 V against a saturated calomel electrode with a Pt wire counter-electrode in 0.1 M NaH_2PO_4 aqueous solution [9]. Apart from the top-down method mentioned above, bottom-up methods can also provide C-dots using carbonaceous molecular precursors. In 2008, Giannelis and colleagues employed a one-step thermal decomposition (calcining the precursor at 300 °C for 2 h) of low-temperature-melting molecular precursors (ammonium citrate salt or 4-aminoantipyrine (4AAP)) to form surface-passivated C-dots [10], whose geometry and physical properties could be precisely engineered and controlled. In 2009, Yang's group employed a facile microwave pyrolysis approach for preparing the C-dots, in which an aqueous solution containing PEG200 and a saccharide (e.g., glucose, fructose) was heated in a 500-W microwave oven for 2–10 min to produce C-dots with controllable emission wavelengths [11]. In the same year, Li and colleagues utilized surfactant (F127)-modified silica spheres as supports to localize the growth of C-dots during high-temperature treatment (900 °C in argon for 2 h) [12]. In this case, carboxy groups could be readily introduced on the C-dot surface by refluxing in 3 M HNO_3 for 24 h, followed by surface passivation with PEG1500N. Note that, for all these mentioned methods, necessary surface modification is required to enable the C-dots to exhibit superior photoluminescent properties, stability, and biocompatibility, which generally involves relatively complicated and additional procedures. Therefore, more facile and green synthetic methods requiring accessible and cheaper carbon sources (e.g., protein and small-molecular carbohydrates) have been extensively developed in recent years. Examples include, but are not limited to, natural silk, bovine serum albumin (BSA), hair fiber and gelatin, glycerol, chitosan, and sucrose [13]. In addition, food products [14] (e.g., caramels, honey, and sweet pepper) and biomass (e.g., grass, plant leaves, and paper ash) have also been exploited as diverse reaction precursors for the synthesis of C-dots. In order to use all these sources to prepare C-dots, the most frequently selected methods are microwave-assisted and hydrothermal strategies because of their simultaneous,

homogeneous, and fast heating, simple manipulation, low energy consumption, and good selectivity, leading to highly photoluminescent C-dots without the need for further functionalization or passivation. Details concerning the synthesis of carbon dots will be discussed in Section 14.2.

14.1.2 Bioimaging of C-dots

One of the most important biological imaging techniques is fluorescence imaging (bioimaging) because of its superior accessibility to sensitive, rapid, and noninvasive observation of biological systems. For fluorescence bioimaging applications, biological fluorescent probes are the essential tools, allowing the tracking of biological targets, observation of cellular morphology and behaviors, and so forth [2, 15]. Fluorescent proteins and organic dyes, recognized as conventional fluorescent bioprobes, have been widely utilized for myriad bioimaging studies since the last century. However, bioimaging in real time and over a long term is limited to some extent by their intrinsic photobleaching charactristic. Through rapid advances in nanotechnology, nanomaterials featuring attractive optical features (e.g., strong fluorescence coupled with anti-photobleaching property) have been intensively fabricated in the past two decades, providing an attractive means of designing novel, high-quality biological nanoprobes. Among them, II–VI semiconductor quantum dot (e.g., CdSe/ZnS QD)-based fluorescent probes have been widely utilized for bioimaging applications [2, 15] since Alivisatos and Nie's group, for the first time, demonstrated their merits in 1998 [2]. Notably, taking advantages of their robust photostability, QD-based nanoprobes have been demonstrated to be suitable for long-term and real-time fluorescence bioimaging. Nevertheless, safety concerns due to the heavy metals used in II–VI QDs [16, 83, 84] still remain to be fully resolved to date, and thus fuel continuous search for novel nanomaterial-based bioprobes featuring favorable biocompatibility and superior optical properties.

To address this issue, several kinds of low- or nontoxic nanomaterials have been extensively explored as novel, biocompatible fluorescent bioprobes in recent years. In particular, fluorescent SiNPs featuring favorable biocompatibility along with unique optical properties (including high fluorescence and robust photostability) have been found valuable for bioimaging applications [17]. Similar to SiNPs, C-dots have been attracting widespread interest in their own right, both being composed of biocompatible elements without toxic heavy metals. Moreover, the carbonaceous quantum dots feature a variety of favorable properties, such as ease of bioconjugation, resistance to photobleaching, as well as size- and wavelength-dependent luminescence emission. As C-dots possess these key merits for bioimaging applications without arousing intrinsic toxicity, they have been considered as fascinating alternatives to II-VI QDs. As a result, the past decade has witnessed extensive investigations on C-dots, which were extensively investigated as a novel kind of fluorescent nanoprobes by making use of their excellent optical merits and good biocompatibility for bioimaging applications.

Correspondingly, representative progress made in the fabrication of C-dots and their use for bioimaging will be, respectively, illustrated in a detailed way in Sections 2 and 3, respectively.

14.1.3 Biosafety Assessment of C-dots

Until now, a large amount of nanomaterials have been used in a wide variety of commercial applications [18], exposing humans to increasingly more risks derived from nanomaterials, resulting in the appearance of the concept of nanotoxicology [19], and making the biosafety assessment of nanomaterials to be a vital precondition for practical applications.

Owing to their unique optical advantages as described above, carbon dots have shown great potential for myriad biological and biomedical applications. As such, the evaluation of C-dot-related biosafety turns out to be very essential. Although carbon is believed to be a kind of non- or low-toxic material, it is fundamental to carry out comprehensive and reliable biological safety assessment on the nanomaterials. There have been a series of pioneering studies exploring the *in vitro* and *in vivo* behaviors of carbon dots, including cell viability, biodegradability, biodistribution in the organs, and pharmacokinetics, which substantiated the favorable biocompatibility of carbon dots. For instance, in 2009, Sun and colleagues conducted trypan blue and methylthiazolyldiphenyl-tetrazolium bromide (MTT) assays to study the *in vitro* cytotoxicity of C-dots passivated by PEG1500N [20]. In their experiment, human breast cancer MCF-7 and human colorectal adenocarcinoma HT-29 cells co-cultured with C-dots at the concentration of 0.1 mg ml^{-1} exhibited more than 80% cell viability rate. And in 2011, Tao *et al.* [21] investigated the *in vivo* cytotoxicity of C-dots derived from MWCNTs, SWCNTs, and graphite via mixed-acid treatment methods in female BALB/c mice. They found that neither death nor significant body weight drop was observed in the mice injected with C-dots at the dose of 20 mg kg^{-1} over 3 months, meaning that C-dots exerted no obvious toxic influence on the mice.

Nevertheless, some controversial issues still exist among the abundant investigations on the biosafety of carbon dots for a wide range of applications remaining to be dealt with in the future. For example, in 2014, in contrast to the demonstration by Huang *et al.* [22] that diverse injection routes could influence the biodistribution and clearance of C-dots in major organs and tissues, Zhang and colleagues claimed that the biodistribution and clearance of graphene quantum dots functionalized by poly(ethylene glycol) (GQD-PEG), which were prepared through a modified oxidative cutting method [23], were independent of the administration route. Furthermore, in the latter experiment, graphene quantum dots (GQDs) mainly accumulated in kidney, which was also different from the observations in other studies. According to Lee and colleagues [24], GQDs could be found in most organs such as the liver, kidneys, lung, and spleen. In independent experiments, Hahn and colleagues [25], Liu and colleagues [21], and Chen and colleagues [22] found that polymer-coated carbon dots could be mainly cleared out through

liver (into bile) and kidneys (into urine); additionally, the particles could be totally cleared in 24 h, independent of the way in which the polymer-coated carbon dots were injected. In short, based on most of the exploration on the biosafety of carbon dots, their quick clearance and feeble dispersion in the organs render them extraordinarily biocompatible. We will demonstrate these in detail in Section 14.4.

14.2 Synthetic Strategies

There are two representative types of approaches to prepare C-dots, namely top-down and bottom-up. Microwave-assisted methods, hydrothermal carbonization, electrochemical synthesis, chemical oxidation, ultrasonication-assisted strategy, plasma treatment, and laser ablation method are classified as top-down methods, in which the C-dots are synthesized or "broken off" from a larger-sized carbon structure. On the contrary, in the bottom-up approaches (e.g., combustion/thermal and supported synthetic), the C-dots are derived from molecular precursors. Specifically, their surfaces are oxidized and further purified through centrifugation, dialysis, electrophoresis, or other separation techniques. In this section, several typical synthetic strategies will be illustrated in a detailed way.

14.2.1 Microwave-Assisted Methods

Microwave chemistry has received considerable attention in the last decade, and its scope has essentially been established. Although initially both thermal and non-thermal microwave dielectric heating effects have been claimed, it seems to be generally accepted that a different temperature regime due to microwave dielectric heating is the main contributing factor to any acceleration observed, which can be caused by either a faster initial heating rate or the occurrence of local spots with higher temperatures. Therefore, the microwave-assisted method features several attractive properties, such as prompt startup, easy heat control (on and off), prompt and homogeneous heating, and so forth, making it widely utilized in the production of C-dots in the past several years.

In 2012, Li *et al.* prepared greenish-yellow luminescent GQDs that showed a quantum yield (QY) value of 11.7% via cleaving graphene oxide (GO) under acid conditions assisted by microwave irradiation [26]. Note that the cleaving and reduction processes can be completed at the same time under microwave treatment without adding a reducing agent. When the gGQDs were further reduced with $NaBH_4$, the QY value of the GQDs further increased to 22.9%. Meanwhile, Tang *et al.* developed a kind of microwave-assisted hydrothermal method for the synthesis of highly luminescent GQDs derived from glucose [27]. The prepared GQDs possessed the largest emission energy of 4.1 eV, with an average diameter as small as 1.65 nm (five layers) and a QY value of 7–11%. Note that the emission wavelength of this GQDs had no relation to the size of

the GQDs but was dependent on their surface states between the π* band and π energy level, formed by the functional groups (C–OH, C═O, C–O–C, C–H) on the surface of the GQDs. A surface state emissive trap will dominate the emission if a certain excitation wavelength excites the GQDs; instead, another related surface state emissive trap will become dominant in the GQD's emission if the excitation wavelength changes, resulting in the excitation-wavelength dependence of GQDs.

Also in the same year, Qu *et al.* reported a simple, low-cost, one-step microwave method to prepare water-soluble luminescent C-dots, and applied them as a novel biocompatible fluorescent ink [28]. In their experiment, a transparent solution containing citric acid and urea was heated in a domestic 750-W microwave oven for 4–5 min. During this process, the color of the solution changed from colorless to brown and finally to dark brown, indicating the formation of C-dots. The aqueous solution of C-dots featured a broad absorption spectrum with peaks centered at 270, 340, and 405 nm, representing the typical absorptions of an aromatic pi system and implying extended conjugation in the C-dot structure. The aqueous solution of the C-dots exhibited excitation-wavelength-dependent photoluminescence (PL) properties with serial emission peaks ranging from 440 (blue) to 570 nm (yellow) upon excitation from 340 to 500 nm. Among them, the strongest fluorescence emission band occurred at 540 nm under 420 nm excitation, yielding a QY value of 14%.

Very recently, Wang *et al.* introduced an easy and green method for one-pot and large-scale synthesis of fluorescent C-dots (Figure 14.1) to take advantages of unique merits of microwave irradiation (e.g., homogeneous heating and uniform product formation, accelerated reaction rate, and enhanced reaction selectivity) [29]. The prepared C-dots featured a wide range of excellent optical characteristics including strong fluorescence (quantum yield: 16%) and excitation-wavelength-dependent PL. Notably, this strategy is suitable for producing C-dots in large quantities in a rapid manner (e.g., 0.3 g C-dots/25 min).

The above achievements suggest microwave-assisted technique as an economical and green method suitable for the facile and high-volume synthesis of fluorescent C-dots. In particular, taking advantage of the fast heating and the subsequent significant enhancement in reaction rates, the C-dots can be derived from a carbon precursor solution within minutes and for large quantity production, which cannot be performed under traditional reflux and hydrothermal treatments. As a result, the microwave-assisted method is currently being considered as a very feasible and promising fabrication technique for the preparation of C-dots.

14.2.2 Hydrothermal Carbonization

As a traditional soft chemical preparation route, the hydrothermal synthesis route has aroused extensive attention because of its inexpensive apparatus, simple manipulation, low energy consumption, and good selectivity. Being based on the water system, the hydrothermal synthesis route is regarded as one of the

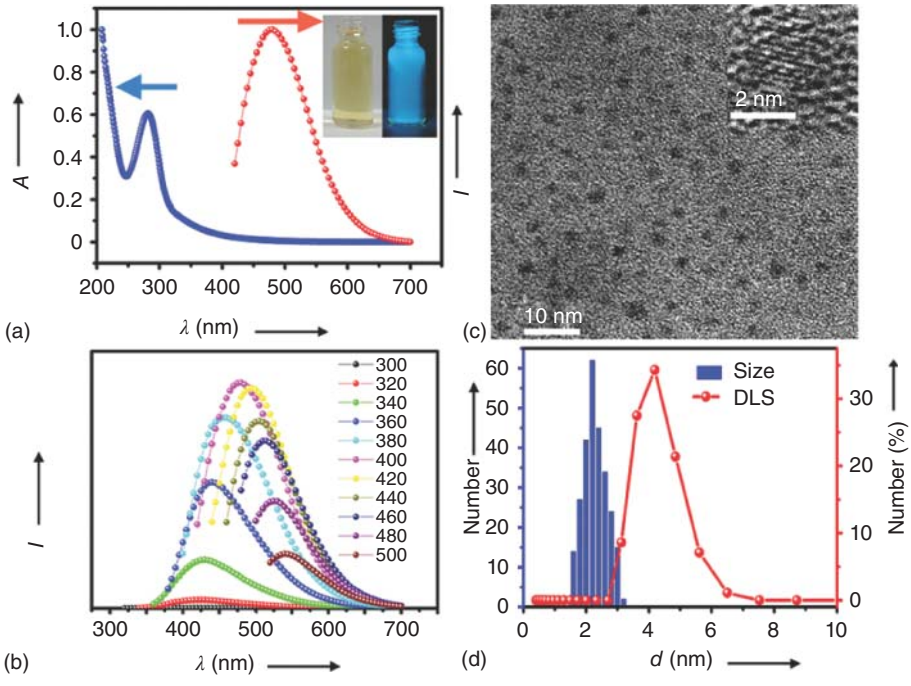

Figure 14.1 (a) Absorption and photoluminescence (UV-PL) spectra of the C-dots (inset: digital photographs of the prepared C-dot aqueous sample in ambient conditions (left) and under UV irradiation (right)). (b) Excitation-wavelength-dependent PL spectra of C-dots. (c) TEM image of the C-dots; scale bar: 10 nm (inset: an HRTEM image of the C-dots; scale bar: 5 nm). (d) Size distribution pattern of C-dots as determined by TEM and DLS of the prepared C-dots in aqueous solution.

simplest, most cost effective, and environmentally benign methods, and has been extensively exploited for rapidly preparing carbon nanodots in recent years.

In 2010, Pan *et al.* [30] presented a novel and simple hydrothermal approach to cut the graphene sheets (GSs) into surface-functionalized GQDs with an average diameter of 9.6 nm. The functionalized GQDs featured bright blue PL, hardly observed in GSs and graphene nanoribbons (GNRs) because of their large lateral sizes. The GSs were oxidized by concentrated H_2SO_4 and HNO_3 prior to the hydrothermal treatment. Then a series of distinct changes occurred, including a reduction in the (002) spacing to 0.343 nm, changes in the Fourier transform infrared (FTIR) and C 1s X-ray photoelectron spectroscopy (XPS) spectra, and deoxidization during the hydrothermal process. In addition, the size of the GSs was reduced markedly, and ultrafine GQDs were isolated by a dialysis process. Another notable change concerned the optical properties of the oxidized GSs and the GQDs dispersed in water. The oxidized GSs showed no detectable PL, while the GQDs emitted bright blue luminescence (PLQY: 6.9%) and exhibited an excitation-dependent PL behavior.

In 2012, Liu *et al.* successfully prepared water-soluble, nitrogen-doped, carbon-rich, photoluminescent polymer nanodots (PPNDs) by using hydrothermal treatment of grass. After the grass was treated at 180 °C, a yellow dispersion was formed [31]. Transmission electron microscopy (TEM) image of the PPNDs revealed that the nanodots, with diameters ranging from 3 to 5 nm, were well separated from each other. The XPS spectrum showed three peaks at 284.0, 400.0, and 530.6 eV, which were attributed to C 1s, N 1s, and O 1s, respectively. The NMR spectrum further confirmed the structure of the carbon nanodots belonging to a coumarin-type dye structure. In addition, according to elemental analysis, the composition of the nanodots was C 41.54 wt%, H 4.18 wt%, N 4.23 wt%, and O (calculated) 50.05 wt%. In effect, these experimental results showed that these dots were nitrogen-doped, carbon-rich polymer nanodots that differed much from the carbon dots (CDs) reported earlier.

In 2013, Zhu *et al.* [32] succeeded in preparing C-dots using a hydrothermal method, which showed extremely strong PL with a notably high PLQY value of 80%. In this case, citric acid and ethylenediamine were condensed first, whereupon polymer-like C-dots were formed, which were then carbonized to yield the C-dots (Figure 14.2a). TEM images of the C-dots are shown in Figure 14.2b, which establishes that the C-dots with an average diameter of 2–6 nm possess a uniform dispersion without obvious aggregation. Furthermore, as seen in the high-resolution TEM image, a majority of particles showed an amorphous structure without any lattices; only a small number of particles showed well-resolved lattice fringes, consistent with the XRD characterization (Figure 14.2c). It is worth noting that this method is a easy and high-output strategy for the fabrication of

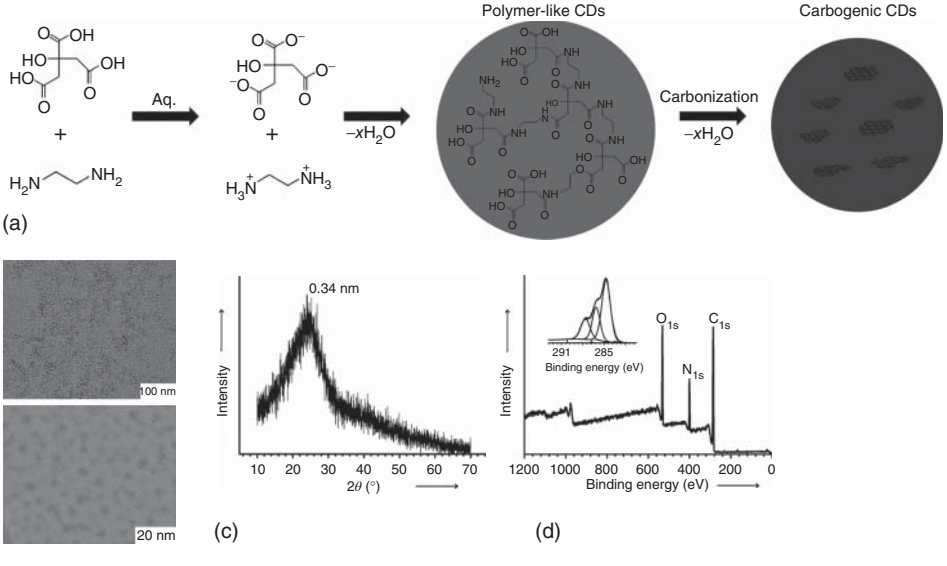

Figure 14.2 (a) Synthetic route using citric acid and ethylenediamine: from ionization to condensation, polymerization, and carbonization. (b) TEM (upper) and high-resolution TEM (lower) images of the C-dots. (c) XRD pattern and (d) XPS of C-dots.

C-dots, and potentially ideal for industrial-scale production (yield is about 58%). In addition, the QY, which is as high as ~80%, is the best recorded for any fluorescent carbon-based materials and is nearly comparable with that of fluorescent dyes.

Also in 2013, Li *et al.* reported a simple hydrothermal treatment of cocoon silk for preparing water-soluble, nitrogen-doped, photoluminescent polymer-like, carbonaceous nanospheres (CNSs) in the aqueous phase, without the requirement of additives (e.g., salts, acids, or bases) [33]. When treated at 200 °C hydrothermally, the cocoon silk was transformed into a yellow dispersion of the CNSs. Substantiated by TEM, dynamic light scattering (DLS), XPS, and other methods, the as-prepared CNSs featured a uniform morphology, with an average size of ~70 nm, abundant oxygen and nitrogen functional groups, excellent fluorescent properties with a QY of ~38%, and robust stability.

Without doubt, as a direct and efficient thermal route, hydrothermal carbonization is one of the most popular methods for the production of functional nanomaterials. For preparing C-dots, hydrothermal carbonization is especially attractive thanks to its ease, high effectiveness, and inexpensiveness. Among the approaches mentioned above, hydrothermal treatment of many carbon sources must lead to the formation of C-dots with a series of attributes in an effective way. Consequently, there is tremendous need for the development of new hydrothermal methods using diverse precursors to produce functional C-dots with versatile and desirable properties.

14.2.3
Electrochemical Synthesis

Electrochemical methods have been extensively used to prepare noble metal (e.g., Au and Ag) nanoparticles, semiconductor quantum dots, and even clusters for a long time, since these methods enable precise control of the synthesis of nanoparticles by optimizing the electrode potential and current density. Thanks to the low cost, easy manipulation, and high output, electrochemical methods are advantageous to produce C-dots. In addition, electrochemical methods allow the investigators to monitor the size of C-dots and provide them with the possibility to perform large scale (using large area electrodes) synthesis.

Li *et al.*, in 2012, introduced a facile electrochemical approach to prepare luminescent and electrocatalytically active nitrogen-doped graphene quantum dots (N-GQDs) that possessed abundant oxygen-containing functional groups [34]. In order to introduce N atoms into the as-prepared GQDs to synthesize N-GQDs, they used N-containing tetrabutylammonium perchlorate (TBAP) in the presence of acetonitrile as the electrolyte. Using cyclic voltammogram (CV) scanning over a potential window of ±3.0 V, which was high enough to drive the electrolyte ions into the graphene layers and oxidize the C–C bonds in the graphene sheets, the N-GQDs could be constantly prepared. By increasing the number of scan cycles, the newly produced N-GQDs were dispersed in the electrolyte solution, with the color of the solution changing from colorless to yellow. The physical and/or chemical defects along the starting filtration-formed graphene film supplied

a large amount of active sites with preferential electrochemical oxidation at the defect sites, which brought about breakage of the graphene film into tiny graphene dots. The resultant N-GQDs featuring an N/C atomic ratio of ~4.3% possessed blue luminescence. The relative atomic force microscopy (AFM) image showed a typical topographic height of 1–2.5 nm, which indicated that most of the N-GQDs were made of ~1–5 graphene layers.

According to Bao *et al.* [35], the preparation of C-dots could be accomplished by electrochemically etching a bundle of carbon fibers (CFs) at a constant potential in acetonitrile consisting of 0.1 M TBAP for several hours. TEM images of C-dots acquired at different potentials demonstrated that the resultant C-dots featured a spherical shape and were uniform and monodisperse. Furthermore, high-resolution TEM (HR-TEM) images showed that for each type of typical C-dot, the lattice spacing of the C-dots, which should be attributed to the (002) facet of graphite, was ~3.25 Å. In addition, the authors speculated that surface oxidation would bring surface defects to C-dots and that different surface defects could introduce different emission sites onto C-dots, leading to different emission spectra. They further added trace water into the acetonitrile to enhance the oxidation ability and applied a potential of 2.5 V to produce C-dots. The optimal emission wavelength of the as-prepared C-dots reached about 500 nm (Figure 14.3a), which produced green colored light (Figure 14.3b) under the excitation of a UV lamp.

Shinde and Pillai introduced a two-step solution process to electrochemically transform multiwalled carbon nanotubes (MWCNTs) into GQDs in 2013 [36]. In particular, after reduction at −1 V for 2 h, sustained oxidation of the MWCNTs was performed in propylene carbonate-containing $LiClO_4$ as supporting electrolyte at 1 V for 15 h at 90 °C. Each step generated discrete spherical GQD particles with tunable sizes, which was presumably attributed to the lateral unzipping, unlike the longitudinal unzipping of CNTs to produce GNRs. For acquiring monodispersed GQDs (3 ± 0.3 nm), they further performed post-synthetic size separation strategies through density-gradient ultracentrifugation as well as dialysis. After functionalization by dodecyl amine, these GQDs, which were easily soluble in organic solvents such as dichloromethane (DCM), were used for further experiments.

In 2014, Wang *et al.* presented an electrochemical approach (Figure 14.4) to synthesize C-dots of fair quality with high yields (~55%) using cheap and nontoxic organic precursors, such as glycine under alkaline conditions in an aqueous medium instead of an organic solvent [37]. Additionally, the whole process was accomplished in 2 h by applying a potential of 10 V, which meant that they required less energy than needed by other reported methods.

As mentioned above, we know that carbon-based materials such as graphite and MWCNTs have widespread use as the working electrode for the electrochemical preparation of C-dots, adopting high redox potential from ±1.5 to ±3 V, which is high enough to oxidize either the C–C bonds or water to generate hydroxyl and oxygen radicals that serve as an electrochemical "scissors" during the oxidative cleavage reaction. In addition, the potential cycling is able to lead the supporting electrolyte (BF_4^- or TBA^+ ions) to intercalate into the carbon anode, which can

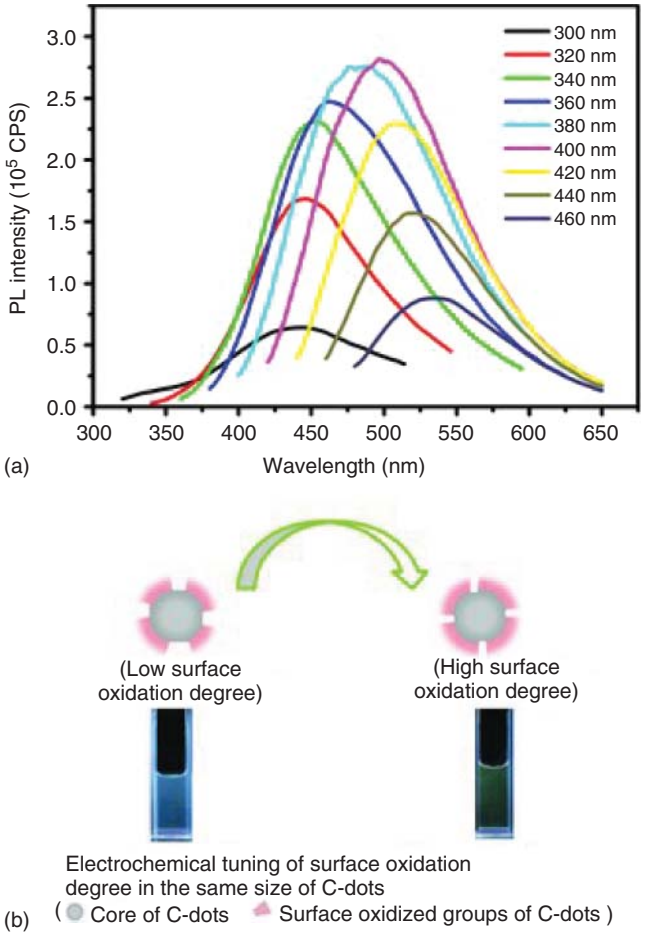

Figure 14.3 (a) Photoluminescence spectra of C-dots obtained at 2.5 V with electrolyte containing trace water. The excitation wavelength ranged from 300 to 460 nm with 20 nm increments, as indicated. (b) Illustration of emission from C-dots along with the variation of surface oxidation degree.

result in the depolarization and expansion of the carbon anode. In short, it is the interplay between anodic oxidation and anion intercalation that brings about the exfoliation of the carbon anode and the production of C-dots. Therefore, the electrochemical method is efficient and advantageous to prepare carbon dots owing to its low cost and facile manipulation.

14.2.4 Chemical Oxidation

Chemical oxidation has been widely used by many research groups to prepare carbon nanoparticles because this method has been proven to be a convenient

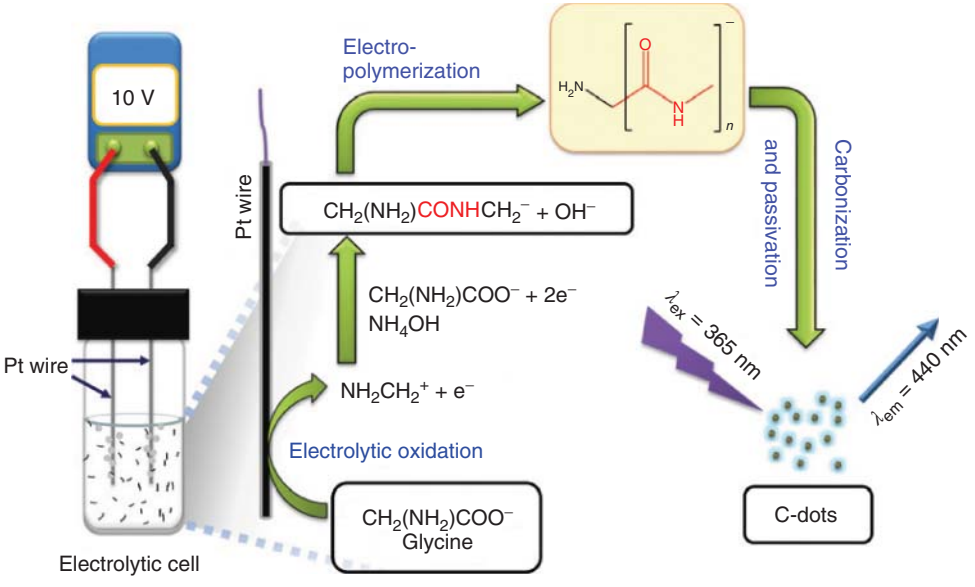

Figure 14.4 Preparation of C-dots from glycine through electroxidation, electropolymerization, carbonization, and passivation.

and effective way to produce C-dots with favorable fluorescence QY without elaborate apparatus and complicated procedure, which is even easy to scale-up. Furthermore, it is nonselective from the point of view of cutting the aromatic carbon framework smaller, and it is especially the case for precisely controlling the morphology and size distribution of carbon dots. To date, there have been many efforts to synthesize a series of carbon precursors for the chemical oxidation method.

In 2012, Fang *et al.* introduced an ingenious method to keep the carbon components small by incorporating hollows during the carbonation reaction, which were referred to as hollow fluorescent carbon nanoparticles (HFCNs) [38]. The cross-linked HFCNs emitting green luminescence could be rapidly synthesized by just adding acetic acid (AC), water, and diphosphorus pentoxide (P_2O_5) together, of which AC played the role of both the polar solvent and the carbon precursor (Figure 14.5). HFCNs were thus formed spontaneously by making use of self-generated heat, which had small oxygen-containing graphite domains, enabling them to emit green luminescence. It is worth noting that solid fluorescent carbon nanoparticles (SFCNs), which were obtained by just reducing the released heat, took a critical part as a benchmark toward HFCNs.

In the same year, an easy and large-scale synthesis of GQDs was demonstrated by Peng *et al.*, which consisted of acid treatment of pitch-based carbon fibers [39]. The as-synthesized GQDs were highly soluble in water and other polar organic solvents such as dimethylformamide (DMF) and dimethyl sulfoxide (DMSO). The TEM image of the fiber-derived GQDs (prepared at 120 °C) showed a narrow

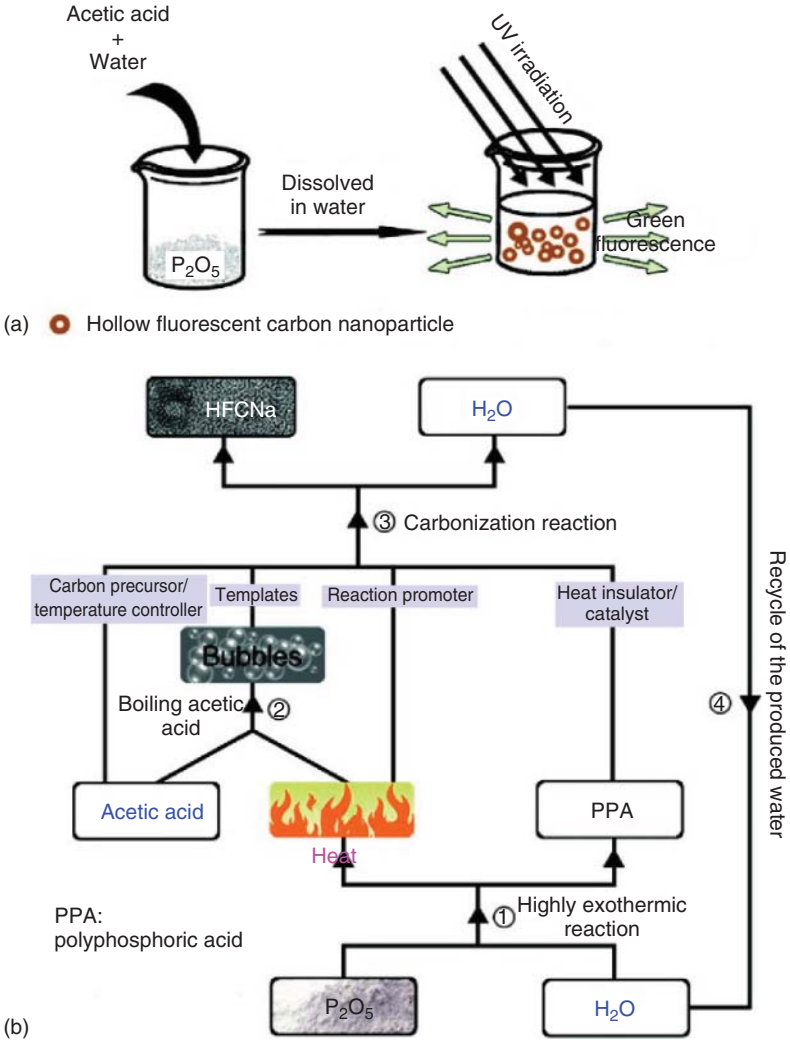

Figure 14.5 (a) Synthetic method and (b) reaction process yielding the HFCNs.

size distribution between 1 and 4 nm, and the HR-TEM image showed high crystallinity of the GQDs, with a lattice parameter of 0.242 nm ((1120) lattice fringes of graphene). The topographic morphology of GQDs was indicated in the AFM image, from which it could be concluded the heights of GQDs were between 0.4 and 2 nm, corresponding to 1–3 graphene layers. Significantly, the PL from these CF-derived GQDs could be controlled by just selecting differente reaction temperatures because temperature could effectively tune the size of GQDs.

After two years, in 2014, Li *et al.* reported a simple, energy-efficient synthesis method to produce green luminescent C-dots that was energy, material, and labor efficient [40]. Mixing the saccharide and basic solutions, meaning simply leaving them alone for a relatively short period and then dialyzing, was the only step needed to prepare C-dots, which could be obtained without acidic catalysts, external heating, or additional energy input. Although a series of saccharide and base source materials were experimented with in this work, the consideration was focused on a fructose/sodium hydroxide combination because this combination could indicate the real-time detection of C-dots formation, which was extremely hard especially when complex apparatus and high temperatures were utilized in the production process. It is worth pointing out that this method had many advantages, such as increased energy efficiency (i.e., room temperature and pressure used), the use of renewable precursor materials (e.g., the saccharides), and real-time analysis during synthesis.

Chemical oxidation is not only effective but also convenient for large-scale production of carbon dots in the absence of sophisticated equipment, making it possible for widespread implementation of the synthesis of C-dots. In fact, after a mixed acid treatment of a carbon resource, the carbon dots thus obtained could be stored at room temperature for a long time (even for a year) without showing any precipitates. In short, this method is extremely advantageous for the production of C-dots on a large scale owing to its obvious superiority of simplicity, energy, material, and labor efficiency, and low cost.

14.2.5
Ultrosonication

Alternating low-pressure and high-pressure waves would be generated in a liquid by ultrasound, resulting in both the formation and collapse of small bubbles, which create high-speed impinging liquid jets, deagglomeration, and strong hydrodynamic shear forces. Because of acoustic cavitation, ultrasonic irradiation creates various physical and chemical effects that lead to unique interactions between energy and matter [41]. To date, several pathways have been introduced for the modification of fluorescent C-dots by ultrasonication [42].

In 2012, Zhuo *et al.* proposed a novel acid-assisted ultrasonic strategy to synthesize GQDs using graphene as the starting material [43]. After ultrasonic treatment, ultrasmall particles with monodispersed diameters of 3–5 nm were formed, as indicated in the TEM images (Figure 14.6). Raman spectroscopy of the GQDs, which presented the G band at 1589 cm^{-1} and D band at 1331 cm^{-1}, substantiated the character of the as-prepared GQDs. UV–vis absorption spectrum of GQDs in water displayed an absorption band at ~300 nm. As indicated in the photograph of the as-produced GQDs illuminated under UV light (365 nm), the bright blue PL of GQDs was so strong that it was easily seen by the naked eye. Furthermore, the GQDs exhibited an extraordinary excitation-independent PL behavior and also upconversion PL properties, which were utilized in complex photocatalysts (rutile TiO_2/GQD and anatase TiO_2/GQD systems).

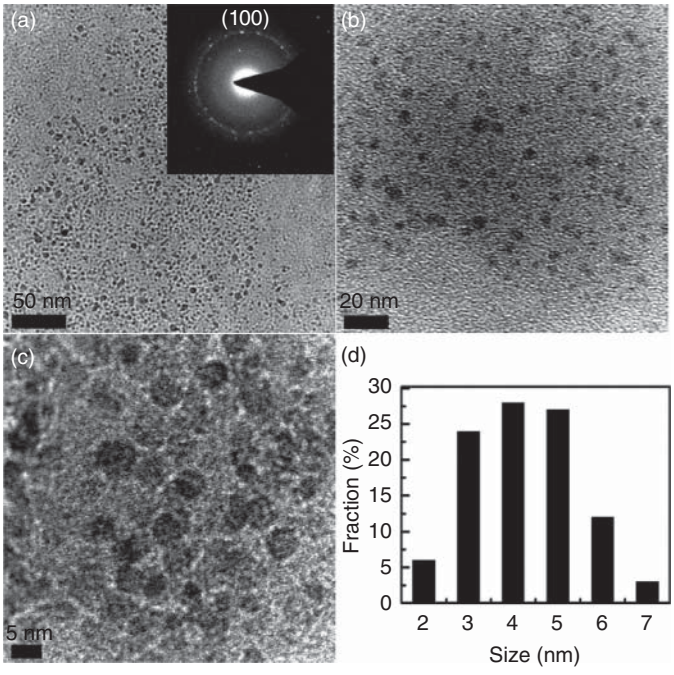

Figure 14.6 (a–c) TEM images of as-prepared GQDs with different magnification. (d) Size distribution of GQDs. The inset in (a) is the selected area electron diffraction (SAED) pattern of GQDs.

In 2013, Ye *et al.* [44] obtained GQDs by sonicating bituminous coal, coke, and anthracite in concentrated sulfuric acid and nitric acid, followed by heat treatment at 100 or 120 °C for 24 h. In contrast to pure sp^2-carbon structures, the crystalline carbon of the coal structure can be more easily oxidatively displaced, leading to nanometer-sized GQDs possessing amorphous carbon attached to the edges. It is worth noting that what they developed was an easy approach to make various nanometer-sized GQDs from different types of coal. They confirmed that the unique structure of coal was beneficial for preparing GQDs, which could result in novel discoveries in coal chemistry.

In 2015, Zhu *et al.* [45] prepared GQDs with only graphene oxide and $KMnO_4$ using a one-step synthesis using ultrasonication, which were then applied in the label-free, simple, and fast fluorescence assay of alkaline phosphatase (ALP). According to the HR-TEM images, GQDs thus produced were uniform and of high crystallinity, and had an average lateral diameter of 3.0 nm with a narrow size distribution. As revealed in the AFM image, most of the GQDs had few graphene layers with a height profile within the narrow range of 0.7–3 nm and the resultant GQDs consisted of mainly single- or double-layered GQDs. XPS measurements, IR analysis, and Raman spectroscopy were also used to prove the composition of GQDs, which confirmed the abundant presence of oxygen-containing groups that made the GQDs soluble in water. The GQDs exhibited

excitation-dependent PL behavior, and the maximum emission intensity was at 470 nm when excited at 380 nm, with a QY of ~27.8% at pH 7, which was higher than earlier reported values. Zhu *et al.* ascribed the comparatively satisfactory QY to the high crystallinity of GQDs and the presence of functional groups on their surface [45].

In conclusion, by taking advantage of the cavitation and vibration effects, the reaction medium can be rapidly and uniformly heated during the ultrasonication synthesis process, so the reaction time can be considerably shortened while the product yields and purities can be significantly enhanced [46].

14.2.6 Plasma Treatment

From the point of view of industrial production, plasma treatment has many potential advantages. First of all, the process is nonpolluting, so waste handling does not arise. Furthermore, the reaction times are very short, providing an efficient heating method. Following that, because of the minimal structural damage to the materials, the surface chemistry can be manipulated in a desired way by adjusting the plasma conditions including the time, atmosphere, pressure, and power. As a result, this oxidation method is regarded as an attractive alternative for the preparation of carbon dots.

In 2012, Wang *et al.* [47] introduced the fabrication of egg-derived fluorescent CDs and their application as "inks" for luminescent patterns using inkjet or silk-screen printing. They selected chicken eggs as the starting material because the resultant product could maintain low toxicity and affordability. As shown in Figure 14.7, before being used, the egg was separated into egg white and egg yolk by using an egg separator. A glass dish full of egg white or yolk was set between two quartz slides (height = 1.5 cm) of the plasma generator, which utilized low-temperature plasma with high energy, inherently charged particles (electrons or cations), and excited neutral species to generate an active chemical environment to synthesize nanostructures. Following that, intense and uniform plasma beams originating from the upper electrode (voltage = 50 V, current = 2.4 A) irradiated the egg samples for 3 min. They could obtain dark black products, which the authors called CD_{pew} and CD_{pey} for the plasma-treated egg white and yolk, respectively, with a yield of ~5.96%. Elemental analysis indicated an increase in the carbon content of the products (62.42% for CD_{pey} and 56.75% for CD_{pew}) when compared with that of the starting material (57.55% for egg yolk and 43.50% for egg white), which substantiated carbonization occurring during the plasma treatment. Notably, when irradiated with UV light ($\lambda_{ex} = 302$ nm), solutions of CD_{pew} and CD_{pey} emitted bright blue fluorescence.

In 2014, by taking advantage of a thermal plasma jet, Kim *et al.* demonstrated a size-controllable and low-cost GQD fabrication strategy [48]. By injecting a great deal of ethylene gas (2.5 l min^{-1}), acting as carbon source, constantly into an Ar plasma, a carbon atomic beam was generated, which was then flowed through a carbon tube attached to the anode and then dispersed into a chamber. GQDs were

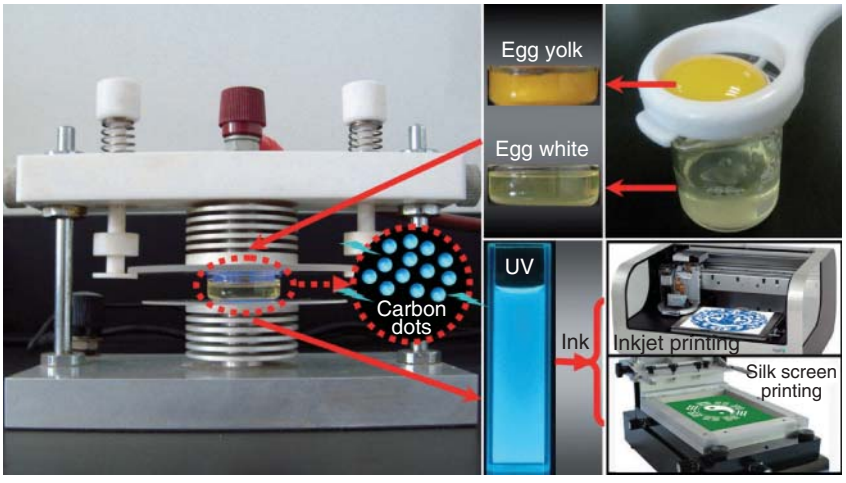

Figure 14.7 Digital photographs of plasma-induced fabrication of egg-derived C-dots and their application as fluorescent carbon inks. Egg white or yolk, after a few minutes of plasma treatment under ambient conditions, was transformed into well-defined C-dots with bright blue emission under UV light. The C-dot solutions can also be used as inks for making luminescent patterns by inkjet or silk-screen printing.

produced by a gas-phase collision reaction while flowing through the attached carbon tube, and yielding 4 g GQDs per hour. The as-prepared GQDs were characterized by a fairly monodispersed size distribution, the average size of which was tunable by changing the length of the attached carbon tube.

Although surface modification of the carbon nanoparticle via plasma activation has been largely reported, not much attention has been paid to the chemical modification of carbon nanodots by plasma treatment, which is an effective tool to attach functional groups onto the surface of carbon nanodots.

14.2.7
Laser Ablation Methods

Laser ablation/irradiation in liquid (LAL) is a simple and "green" strategy that is generally operated in water or organic liquids under ambient conditions. Recently, there has been rapidly growing interest in the fabrication and modification of a wide range of nanomaterials in liquids based on laser irradiation because of its wide versatility, reduced formation of byproducts in the process, simpler precursors, absence of catalysts, environmental sustainability, and low cost. Undoubtedly, laser ablation in liquids is greatly advantageous in acquiring carbon dots in terms of the possibility of scaling up the preparation process to the industrial level.

In 2006, using argon as carrier gas in the presence of water vapor, Sun *et al.* [7] produced carbon dots through laser ablation of a carbon target. To begin with,

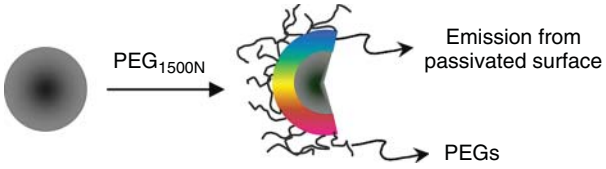

Figure 14.8 Scheme of carbon dots with PEG1500N species attached to the surface.

the carbon target was prepared by hot-pressing a mixture of graphite powder and cement, followed by stepwise baking, curing, and annealing in an argon flow. They used a Q-switched Nd:YAG laser (1064 nm, 10 Hz) to ablate the carbon target in a flow of argon gas with water vapor (through a water bubbler) at 900 °C and 75 kPa. As indicated by electron microscopy analyses, the as-prepared sample was mainly made of nanoscale carbon particles in aggregates of a variety of sizes. Almost no PL from the sample and its aqueous suspension could be detected. After treatment by refluxing for up to 12 h in an aqueous nitric acid solution (up to 2.6 M), there was still no detectable PL. Surface passivation by attaching simple organic species to the acid-treated carbon particles (Figure 14.8) resulted in bright luminescence emissions.

Russo *et al.* [49] prepared either PG or GQDs by femtosecond laser ablation of highly oriented pyrolytic graphite (HOPG) in water, which was a novel, scalable, and green method. GQDs displaying dimensions of ~2–5 nm was found to be dispersed in the solution, while PG showing a pore dimension of 20 nm floated at the water–air interface. The femtosecond ablation of HOPG resulted in the exfoliation of graphene layers, which were further oxidized to GO layers through femtosecond laser-induced breakdown of water. The sp^3 carbon atoms in the GO layers reacted simultaneously with O_2 in a way that was comparable to what occurred in the coal gasification process. As a result, CO and CO_2 molecules were produced, and carbon vacancies were created, leading to the formation of nanopores and PG.

According to the results reported, LAL is a facile, "clean," and rapid synthesis method of carbon dots, which is based on the strong ability of laser to ablate the carbon resource. This method is much superior owing to the ambient temperature and pressure conditions needed to prepare carbon dots, whereas other methods may not be able to give carbon dots under the same ambient conditions. Moreover, considering the one-step and one-pot fabrication of carbon dots, the LAL method possesses significant advantages. The main disadvantage of LAL is its low productivity, in spite of which gram-scale production can be realized by adjusting the ablation and liquid media parameters.

14.2.8 Supported Methods

In the past a few decades, support strategies have been widely used in the production of a variety of nanomaterials by both hard and soft templates that are able

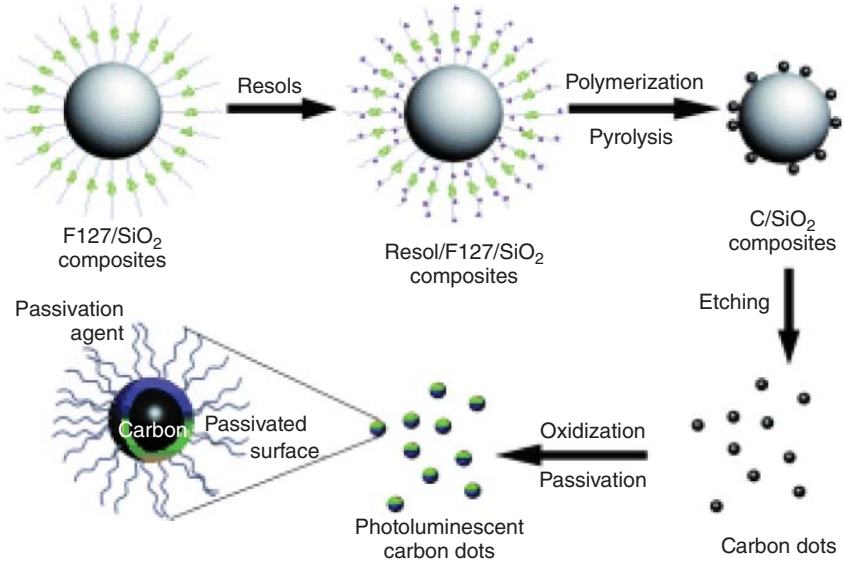

Figure 14.9 Processing diagram for the synthesis of multicolor photoluminescent C-dots.

to serve as nanoreactors with confined spaces to construct nanostructures of the desired morphology. Accordingly, when utilized for the construction of carbon dots, the support helps localizing the growth of C-dots via blocking nanoparticle agglomeration when treated under high temperature, leading to the yield of C-dots possessing a narrow size distribution and well-defined morphology.

In 2009, Li and colleagues applied surfactant-modified silica spheres as support (Figure 14.9), which localize the growth of C-dots by preventing nanoparticle agglomeration when treated at high temperature [12]. To begin with, composites were produced by functionalizing silica spheres with F127, an amphiphilic triblock copolymer. The F127/SiO_2 composites were thus formed, which were then introduced to carbon precursor resols (phenol/formaldehyde resins, MW < 500). Next, the F127/SiO_2 composites were polymerized. The F127 surfactant phase, serving as an anchor for the adsorption of resols through hydrogen bonding, was very crucial as it led to polymerization occurring on the shell of the SiO_2 sphere rather than inside the solution. C-dot/SiO_2 composites were obtained by further heating the composite to 900 °C in argon for 2 h. Subsequently, the silica spheres were cleared after treatment using 2 M NaOH solution. The C-dots thus released, all of which led to amorphous (possessing both sp^2 and sp^3 hybrids) material with 1.5–2.5 nm in size and 90.3% C, 1.4% H, and 8.3% O (wt%) in composition. By refluxing in 3 M HNO_3 for 24 h, carboxy groups were introduced on the C-dot surface, which could be validated by FTIR spectra after neutralization and dialysis. Finally, C-dots were produced whose λ_{ex}-dependent broadband PL emission ranged from 400 to 580 nm after surface passivation by ultrasonication with PEG1500N, which went through thermal treatment at 120 °C for 72 h.

A facile one-pot method to prepare highly luminescent GQDs using reverse micelles as nanoreactors and sugar as precursor was presented by Kwon *et al.* in 2012 [50]. First, an aqueous solution of glucose (the water phase) was emulsified in decane (the oil phase) in the presence of bis(2-ethylhexyl) sulfosuccinate sodium salt (AOT, the surfactant) to form water-in-oil reverse micelles, inside which condensation polymerization between glucose molecules was induced by heat to form oligosaccharides. After this process, the transparent solution changed from colorless to orange. Instantly, owing to the water evaporation, the micelles reached a key supersaturation situation, so carbonization took place by intermolecular dehydration of the oligosaccharides derived from the mentioned steps. This condition was so harsh that it decreased the AOT–water bonding to destroy the micelles at the same time; however, AOT would then be attached to the surface of GQDs by adhering to the hydroxyl groups on GQDs to block undesirable aggregation. The resultant GQDs were briefly passivated by excess hexadecylamine (HDA), which resulted in a homogeneous dark brown solution. As the size of the micelles could be tailored by the water–surfactant molar ratio, GQDs produced by this method were characterized by size tunability and narrow size distribution, even in the absence of any size separation process. In addition, the GQDs exhibited size-dependent optical properties and high quantum yields of maximum 35% when excited at 360 nm. Undesirable aggregation between reactants was blocked by the micelles, with the benefits of not only high product yield but also large-scale production.

14.2.9 Thermal Routes

Mild pyrolysis of molecular precursors, as a popular kind of bottom-up synthetic approach, is straightforward, employing simple and cheap carbon source and always proceeding in a single step, providing surface-functionalized nanoparticles that are able to disperse in aqueous or organic solvents owing to their surface functionality. By taking advantage of the pyrolysis treatment, several works of significance have been carried out.

In 2007, Mao and colleagues demonstrated a strategy to prepare C-dots using a combustion–oxidation method [8]. In order to collect soot, Mao and colleagues placed a piece of aluminum foil or a glass plate above a burning candle. After mixing with 5 M HNO_3, the collected soot was subsequently refluxed for 12 h to oxidize the particle surface. After cooling down to room temperature, the as-prepared C-dots (<2 nm) were collected by centrifugation and dialysis and further subjected to PAGE fractionation; they were found to be ~1 nm in height, as determined by AFM.

And in 2014, Liu *et al.* easily prepared C-dots by making use of hair, a raw material that is not only natural but also nontoxic, as the precursor by a one-step pyrolysis treatment [51]. Specifically, hair was directly thermally decomposed under a nitrogen atmosphere at 300 °C for 2 h at a heating rate of 5 °C min^{-1},

generating a dark brown product that was ground to finer powder in a mortar after cooling down to room temperature. Following that, 0.01 g of the powder was ultrasonically dispersed in water for 20 min and the suspension was centrifuged at 14 000 rpm for 10 min to clear the nonfluorescent deposit. The as-made transparent brown supernatant was further filtered with an ultrafiltration membrane (200 nm) three times to remove the impurities and larger particles before characterization, which resulted in bright blue fluorescence (quantum yield: 17%) under UV light irradiation. The functional groups on the surface of C-dots enabled these nanomaterials to disperse in water and most polar organic solvents easily and endowed them with excellent compatibility with polymer matrices including poly(methyl methacrylate) and polyvinylpyrrolidone.

Hence, the thermal route is a highly effective and attractive means to prepare carbon dots. It is able to directly result in surface-passivated C-dots whose surface characteristics can be precisely engineered. Moreover, by selecting the carbon source and surface modifier carefully, it is possible to have better control of both the geometry and a variety of physical characteristic of the C-dots.

In short, there have been enormous efforts devoted to developing efficient preparation strategies for making carbon dots, all of which can be categorized as top-down and bottom-up methods. Methods such as microwave-assisted synthesis, hydrothermal carbonization, electrochemical synthesis, chemical oxidation, ultrasonication, plasma treatment, and laser-ablation can be termed as the top-down routes where carbon dots are prepared or "broken off" from the cleavage of carbonaceous materials. Bottom-up routes include thermal routes, supported methods, and so forth, in which the carbon dots are derived from molecular precursors. The advantages of top-down routes are obvious, such as the availability of abundant raw materials as well as the possibility of large-scale production and simple operation. Most importantly, a large number of oxygen-containing functional groups of the carbon dots thus obtained are available at the edge, rendering them soluble in water or organic phase and making it easy for functionalization and passivation. Admittedly, a number of disadvantages also exist, which include the requirement of special equipment, low yield, damage to the aromatic carbon framework, and the nonselective chemical cutting process that blocks precise control over the morphology and the size distribution of the products. Contrarily, the bottom-up methods enable us to easily control the molecular size, shape, and, thus, the properties of carbon dots; but complex synthetic procedures and special organic precursors that are not easily accessible are always involved in these bottom-up methods, leading to carbon dots of poor solubility and strong tendency of aggregation, which block their further applications. The past years have witnessed tremendous efforts devoted to elaborate designs of carbon dots characterized by fascinating optical/biocompatible/dispersible properties, which have offered exciting opportunities for myriad biological and biomedical applications.

14.3
C-Dots-based Fluorescent Probes for Bioimaging Applications

14.3.1
Fluorescent Probes for Bioimaging Applications

Fluorescence imaging techniques are being increasingly used by many scientists thanks to their distinctive benefits such as the availability of biocompatible imaging agents, maneuverable instruments, and high temporal resolution with good sensitivity [52]. Undoubtedly, fluorescence imaging has taken a significant step from basic life science research to clinical applications since it is noninvasive, rapid, highly sensitive, and inexpensive. For creating precise representation of biological objects and/or processes, a series of state-of-the-art imaging technologies have been developed in order to enhance the resolution of optical imaging, including stimulated emission depletion (STED) microscopy, stochastic optical reconstruction microscopy (STORM), photoactivated localization microscopy (PALM), and total internal reflection fluorescence microscopy (TIRFM), all of which possess greater sensitivity and higher resolution. However, although these technologies are advantageous when utilized to observe cellular structures, for visualizing dynamic events occurring in a live cell, there is another factor that requires further improvement, that is, temporal resolution. Fluorescent probes with high brightness and photostability are in great need for all imaging modalities. As is well known, fluorescent probes are fundamental for bioimaging applications, such as labeling the targeted molecules, investigating *in vitro* and *in vivo* behaviors of chemical and biological species, diagnosing disease, and many others. It is agreed that the fluorescent probe determines the quality of fluorescence imaging to a great extent. As a result, fluorescent probes of high quality are basically essential, which are expected to be highly fluorescent, water dispersible, chemically and photostable, and biocompatible.

In order to gain a favorable signal output, a wide range of fluorescent probes based on various kinds of molecules and colloidal nanoparticles have been investigated. Specifically, the small molecules (e.g., fluorescent proteins and organic dyes) feature outstanding biocompatibility and relatively small sizes, which are more appropriate for intracellular target labeling [53]. Consequently, from the last century until now, fluorescent proteins and organic dyes, serving as well-established fluorescent bioprobes, have been widely used for biological and biomedical research. However, their serious photobleaching has severely limited their applications, especially for long-term bioimaging [54].

In contrast to the fluorescent proteins and organic dyes, inorganic quantum dots possess excellent photostability with narrow emission and broad photoexcitation spectra, high fluorescence, and size-tunable emission wavelengths, all of which make them ideal for multiplex imaging over long periods [55]. Their only disadvantage is that most II–VI QDs contain heavy metal ions (e.g., Cd^{2+}, Te^{2-}, etc.), which poses major safety concerns [16, 56], despite a series of strategies of surface modification (e.g., ZnS shell/silica/polymer coating) being available that

reduce the toxicity to some extent. It is worth noting that upconverting nanophosphors (UCNPs), composed of lanthanide-doped nanocrystals, can convert several near-infrared (NIR) photons into one visible light photon through energy transfer processes, which are resistant to photobleaching when compared to fluorescent proteins and organic dyes. With the advantages of minimal auto-fluorescence (background noise), low toxicity, high quantum yields, sharp absorption and emission lines, and long life times, UCNPs are opening new doors to a next generation of potential bioimaging modalities, as the utilization of NIR excitation leads to deep-penetration imaging [57].

SiNPs have recently been shown to be biodegradable and can be easily excreted from the body via renal clearance [17, 58]. With no detectable toxicity *in vivo*, fluorescent SiNPs are characterized by favorable biocompatibility and their unique optical properties, namely high fluorescence and robust photostability. Fluorescent SiNPs have been also extensively investigated as a new kind of high-quality nanoprobes for bioimaging applications.

Meanwhile, there is another new generation of promising probes inspiring great interest owing to their long fluorescence lifetimes, extended far-red emission (600–800 nm), excellent photostability (i.e., no photobleaching and no photoblinking), and ease in surface functionalization: that is, fluorescent nanodiamond (FNDs) containing negatively charged nitrogen-vacancy centers (N-V centers) as fluorophores [59].

Similar to its popular cousins, namely the nanodiamonds, the carbon nanodot as the nearest form of nanocarbon is attracting worldwide interests in its own right. Compared to the well-studied II–VI QD-based fluorescent nanoprobes (e.g., CdTe and related core–shell nanoparticles), fluorescent C-dots, which are made of biocompatible carbon element without toxic heavy metals, are considered as a fascinating alternative. These carbonaceous quantum dots contain a number of favorable characteristics of traditional semiconductor-based quantum dots, including ease of bioconjugation, resistance to photobleaching, size- and wavelength-dependent luminescence emission, and absence of intrinsic toxicity [60]. Therefore, in the past decade, C-dots have been intensively explored as a novel kind of fluorescent nanoprobes by taking advantage of their unique optical properties and favorable biocompatibility, and have been widely used for *in vitro* and *in vivo* bioimaging applications, which will be illustrated in detail in this section.

14.3.2
In Vitro Imaging

Sun and colleagues, for the first time, utilized C-dots for bioimaging applications [20, 61]. They indicated the possibility of C-dots functionalized with poly(propionylethyleneimine-*co*-ethyleneimine) (PPEI-EI) for two-photon luminescence microscopy using human breast cancer MCF-7 cells as a cellular model. When incubated with C-dots for 2 h at room temperature, the cells showed bright green luminescence in both the cell membrane and cytoplasm regions after

being washed to remove any extracellular C-dots and observing by a fluorescence microscope with the excitation of 800 nm. Their work has inspired scientists worldwide to utilize carbon dots as fluorescent probes in bioimaging.

In 2014, Kong *et al.* [62] synthesized fluorescent carbon nanodots by refluxing PEG, which exhibited excellent biocompatibility, strong photoluminescence, and stable fluorescence properties even when exposed to different temperatures, ionic strengths, and times. Additionally, the fluorescent carbon nanodots were able to label the cell nucleus alone, without staining any other parts in the cell, enabling both efficient organelle selection and accurate subcellular localization of the fluorescent probes (Figure 14.10). Hence, it is reasonable to consider fluorescent carbon nanodots as an ideal target in cellular imaging rather than commercially available dyes.

Despite the fundamental advantages of carbon dots for bioimaging applications, including a broad possibility for surface functionalization, strong PL, multicolor emission, and excellent biocompatibility, there are limited reports

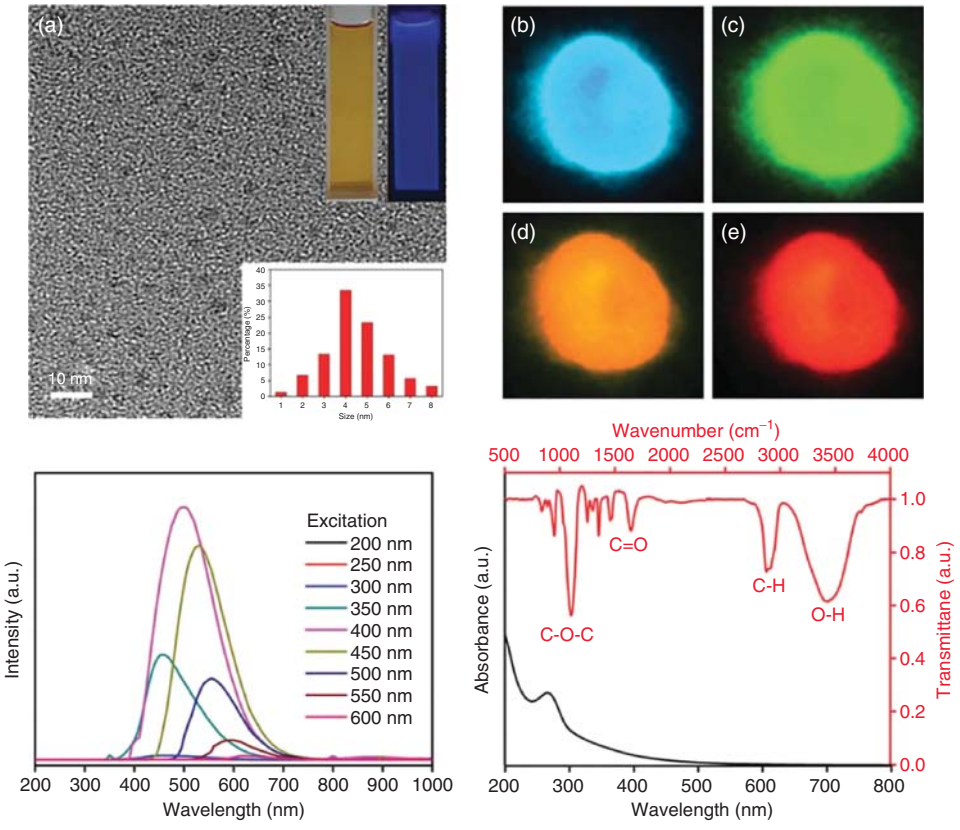

Figure 14.10 Comparison of the HeLa cells stained with (a) fluorescent C-dots (FCDs) and (b) Hoechst dye. HeLa cells stained with Hoechst dye show void regions (marked by red circles). Scale bar: 10 μm.

concerning super-resolution imaging with C-dots. Very recently, Leménager *et al.* successfully employed STED microscopy to observe carbon dots in cells with a resolution down to 30 nm, achieving a more than sixfold improvement of the spatial resolution in both fixed and living cells compared to conventional confocal microscopy [63]. In this case, they produced the carbon nanoparticles by laser ablation of a carbon target, and passivated them with diamine-terminated oligomeric (PEG) $H_2NCH_2(CH_2CH_2O)_nCH_2CH_2CH_2NH_2$ (average *n*: 35, PEG1500N). Notably, the successful application of C-dots for high-resolution STED imaging would open a wide range of applications and provide more possibilities in life sciences.

GQDs could also be employed in bioimaging as a new member of the group of carbon dots, which began to arouse extensive interests since Zhu *et al.* [64a] successfully used them for bioimaging for the first time in 2011. In this work, they prepared strongly green photoluminescent GQDs on a large scale by a one-step solvothermal route with graphene oxide serving as carbon source, which could be dissolved in water and most polar organic solvents without further chemical modifications. Because of their low cytotoxicity, stable photoluminescence, excellent solubility and biocompatibility, GQDs are particularly suitable for bioimaging. Similar to carbon nanodots, GQDs exhibits excitation-dependent PL behavior, leading to various visible results: when excited at 488 nm, green-yellow emission is observed, and when excited at 405 nm, bright blue color is observed. Moreover, in 2012, Zhu *et al.* [64b] successfully employed GQDs for two-photon luminescence microscopy using the as-prepared green luminescent GQDs, m-GQDs, and r-GQDs with different oxidation degrees and surface modification by a two-step solvothermal and separation method, all of which possessed upconversion properties. In Figure 14.11, a bright green or blue area inside MC3T3 cells under near-IR excitation (808 nm) can be seen, which indicates successful translocation of GQDs through the cell membrane. Additionally, even though there was no further bioconjugation, all three kinds of GQDs could penetrate living cells. Furthermore, these GQDs featured high photostability: that is, under continuous excitation over 20 min, no obvious reduction in PL brightness was observed. Thus, these GQDs can act as powerful tools in upconversion bioimaging with little harm to living cells or tissue.

Then in 2013, Liu *et al.* synthesized N-GQDs by a facile solvothermal method using DMF as both the solvent and the nitrogen source, and systematically investigated two-photon-induced fluorescence using human cervical carcinoma HeLa cells. They were able to significantly extend the fundamental two-photon imaging depth limit in scattering tissues [65]. On incubation with the N-GQD (50 μg ml^{-1} DMEM high glucose) at 37 °C for 2 h, the living HeLa cells became brightly illuminated when excited at 800 nm (with a low laser power of 1 mW and average power density of 13 W cm^{-2}), providing a high-contrast fluorescence image of green N-GQDs distributed around each nucleus. This indicated the capability of N-GQD to label both the cell membrane and the cytoplasm of HeLa cells with negligible disturbance of the nucleus. Furthermore, using an NIR laser as the excitation source, the N-GQDs could be imaged with high resolution and

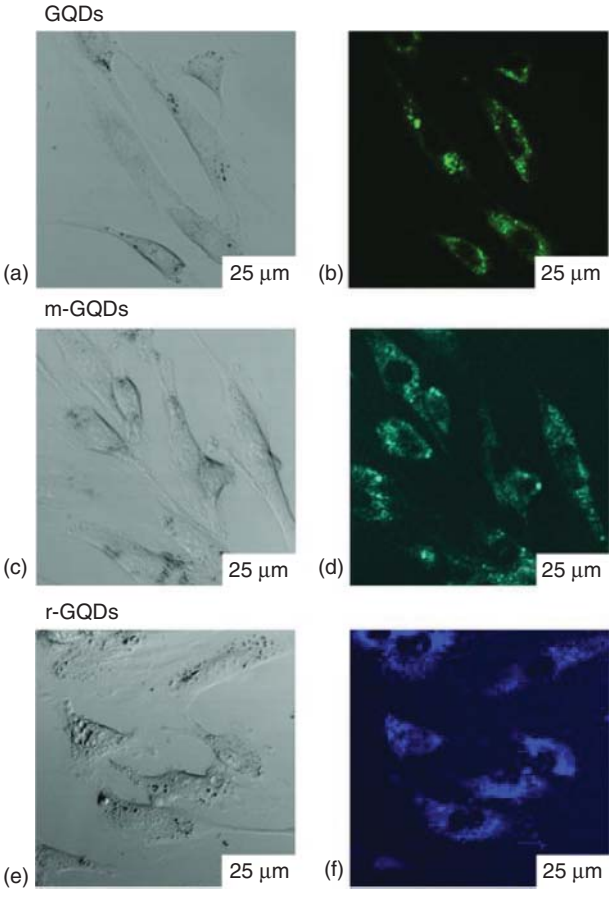

Figure 14.11 Upconversion cellular imaging of GQDs. The washed cells were imaged under bright field (a, c, e) and 808 nm excitation (b, d, f). The detection wavelength was in the 490–550 nm range for GQDs, 450–500 nm for m-GQDs, and 420–460 nm for r-GQDs.

high signal-to-noise ratio at depths ranging from 0 to 1300 μm in the tissue phantom, even at the depth of 1800 μm. N-GQDs could also be easily identified with appreciable two-photon fluorescence signal. In contrast, the maximum penetration depth of OPFI (a kind of organic dye) was only 400 μm because of the strong scattering and refraction of the visible excitation light in the turbid tissue phantom. Thus, with high two-photon absorption cross section (48 000 GM) and little photobleaching and photothermal effects under repeated femtosecond NIR laser irradiation, the N-GQDs prepared by a one-pot solvothermal approach using DMF as solvent and nitrogen source are powerful tools for bioimaging.

The bioimaging of carbon dots becomes more meaningful when they are useful in bioanalyzing also simultaneously by taking advantage of their PL. For instance, in 2012, Tian and colleagues demonstrated a ratiometric strategy to sense Cu^{2+} *in vitro* (Figure 14.12A) by integrating C-dots that were

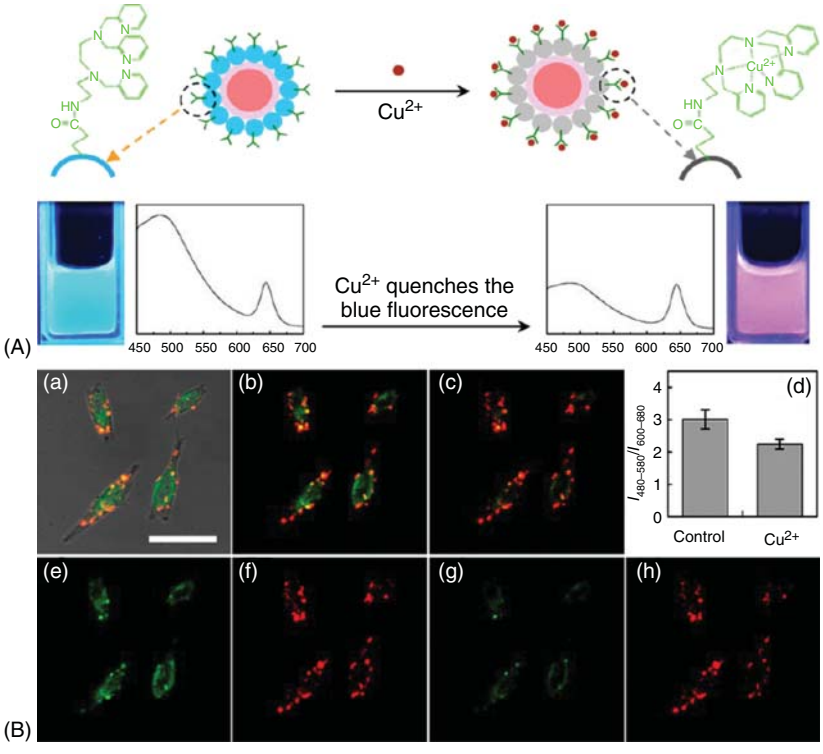

Figure 14.12 (A) Schematic illustration of the dual-emission fluorescent sensing of Cu^{2+} based on CdSe@C–TPEA nanohybrid. (B) (a) Overlay of bright-field and fluorescence images of HeLa cells incubated with CdSe@C–TPEA. (b, c) Confocal fluorescence images of HeLa cells (b) before and (c) after the exogenous Cu^{2+} source treatment. (d) Bar graph representing the integrated intensity from 480 to 580 nm over the integrated fluorescence intensity from 600 to 680 nm. Values are the mean ratio generated from the intensity from three randomly selected fields in both channel. (e, g) Confocal fluorescence images obtained from the 480–580 nm channel before and after the exogenous Cu^{2+} source treatment, while (f, h) are from the 600–680 channel. Scale bar: 25 μm.

coated with a specific organic molecule *N*-(2-aminoethyl)-*N*,*N*,*N*′tris(pyridin-2ylmethyl)ethane-1,2-diamine (AE-TPEA) and CdSe/ZnS QDs [66]. The fluorescent probe could detect Cu^{2+} in concentrations ranging from 5 to 200 μM at physiological pH. After uptake, as indicated in Figure 14.12B, the nanoparticles resided in diverse intracellular compartments: when treated by an exogenous Cu^{2+} source, the fluorescence emission color of the probe turned from green-yellow to red (only CdSe/ZnS QDs emits). The results suggested that by making use of the bioimaging, C-dot-based dual-emission hybrid sensors can offer great promise for the investigation of fundamental biological processes.

Additionally, Tian and colleagues [67] also introduced a type of C-dot-based probes for two-photon bioimaging in both live cells and deep tissues. As can be seen in Figure 14.13, the fluorescent intensity exhibited good linearity with pH

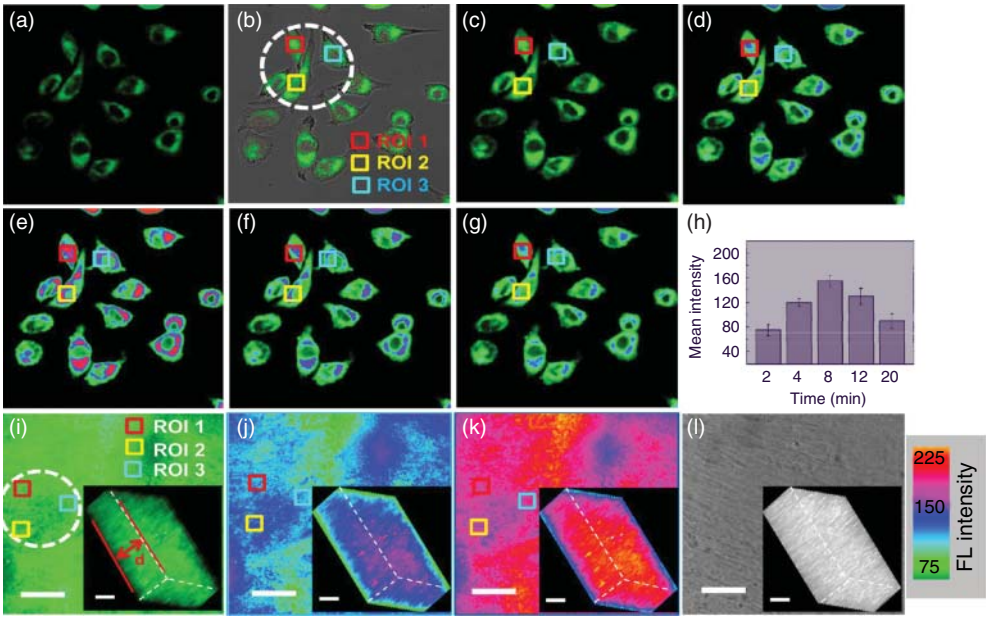

Figure 14.13 (a–g) Na^+–H^+ exchange-dependent two-photon confocal fluorescence images of A549 cells. (a) Two-photon confocal fluorescence. (b) Overlapped images of A549 cells incubated with C-dots–TPY probe. (c–e) Whole visual field of ouabain-treated A549 cells suspended in choline CH_3SO_3-Ringer's solution for (c) 2, (d) 4, and (e) 8 min. (f, g) Na^+-dependent realkalinization of ouabain-treated A549 cells by adding $NaCH_3SO_3$ on top of the choline CH_3SO_3-Ringer's solution for another (f) 4 and (g) 8 min. (h) Mean fluorescence intensity induced by Na^+–H^+ exchange of A549 cells. Data represent the mean fluorescence intensity of distinct fields (inset ROI 1–3). (i–l) Two-photon confocal fluorescence and bright-field images of C-dots–TPY probe in A549 lung cancer cells tissue slice upon pH changes from 7.8 (i, inset), to 7.1 (j, inset), and then to 6.4 (k, inset). (i–k) Two-photon confocal fluorescence and (l) bright-field images at a depth of 150 μm. (i–k, inset) 3D two-photon confocal fluorescence and (l, inset) bright-field images accumulated along the *z*-direction at depth of 65–185 μm. Scale bars: 60 μm.

from 6.0 to 8.5, satisfying the requirement of pH variation in *in vivo* sensing. The images of real-time cytosolic pH changes were derived from A549 cells and LCC tumor cells upon Na^+–K^+ exchanges. Additionally, the 3D two-photon confocal fluorescence imaging along the *z*-direction indicated that the C-dot–TPY probe was able to monitor pH gradients at 65–185 μm depth in living tissues using two-photon microscopy.

14.3.3 *In Vivo* Imaging

Besides relatively abundant reports relating to C-dot-based bioprobes for *in vitro* bioimaging, there have been several pioneering studies concerning *in*

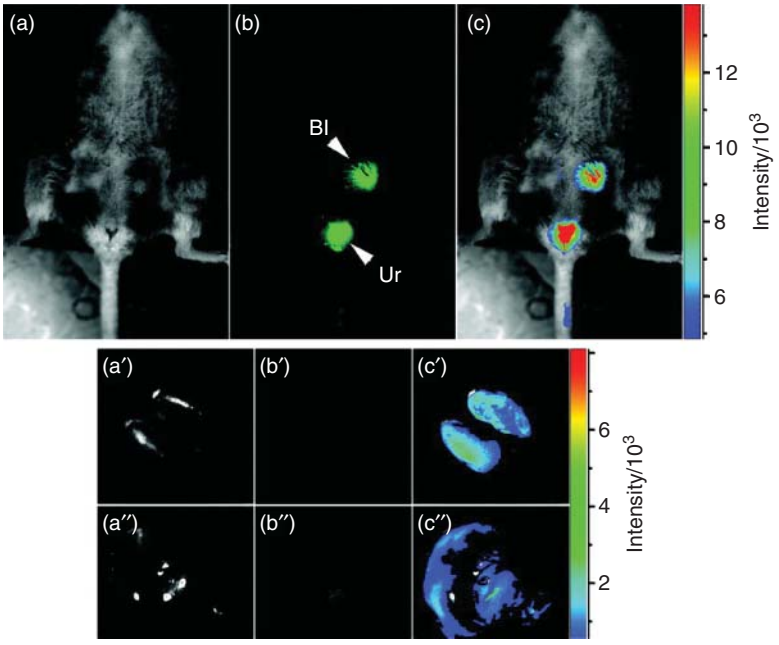

Figure 14.14 Intravenous injection: (a) bright field, (b) as-detected fluorescence (Bl: bladder and Ur: urine), and (c) color-coded images. The same order for the images of the dissected kidneys (lower left) and liver (lower right).

vivo bioimaging in the past several years. In 2009, by hot-pressing a mixture of graphite powder and cement, Yang *et al.* synthesized C-dots via laser ablation (using a Q-switched Nd:YAG laser emitting at 1064 nm, 10 Hz) with PEG diamine surface passivation [61]. For whole-body circulation, a C-dot solution (440 μg in 200 μl) was intravenously injected into mice, after which the abdomen was shaved for fluorescence detection of the dots trapped in organs during the circulation. As indicated in Figure 14.14, only emissions from the bladder area were observed, and bright fluorescence in the urine became visible in the image after 3 h, indicating primarily urine excretion for the intravenously injected C-dots.

In 2012, Tao *et al.* [21] prepared carbon nanodots from carbon nanotubes and graphite by a mixed-acid treatment, with which *in vivo* fluorescence bioimaging was then conducted. Using a series of excitation wavelengths (e.g., 455, 523, 595, 605, 635, 661, and 704 nm) and differentiating the background autofluorescence (green) by spectral unmixing, the subcutaneously injected spots (red) exhibited bright fluorescence images (Figure 14.15), among which those taken under longer wavelength excitation (595 nm and beyond) presented much better signal-to-background separation as the tissue autofluorescence background decreased at longer wavelengths. Also, no noticeable toxicity of the C-dots was found in the treated animals, thereby showing that C-dots hold outstanding potential in biomedical imaging application as optical nanoprobes.

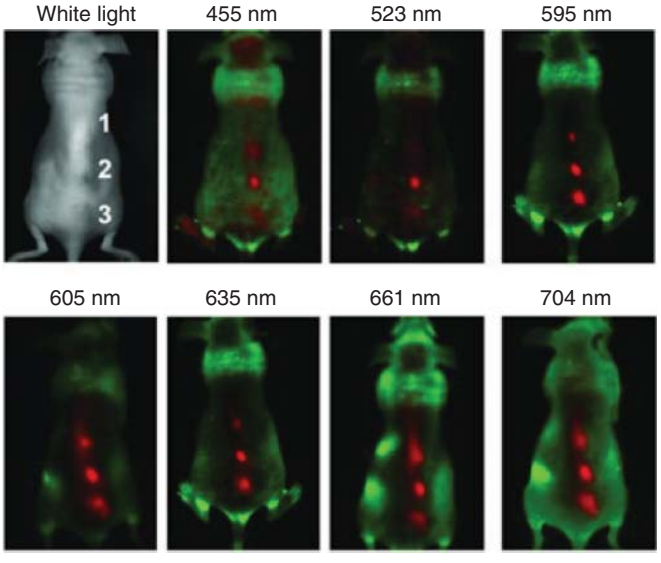

Figure 14.15 *In vivo* fluorescence imaging. *In vivo* fluorescence images of a CND-injected mouse. The images were taken under various excitation wavelengths (455, 523, 595, 605, 635, 661, and 704 nm). Red and green represent fluorescent signals of CNDs and tissue autofluorescence, respectively. (Reprinted with permission from [21]. © 2012 Wiley-VCH.)

C-dots prepared from green carbon sources, such as milk, present high great promise for *in vivo* bioimaging owing to their favorable photoluminescent properties. As a proof of concept in bioimaging applications, Wang *et al.* applied C-dots that were synthesized from milk by microwave-assisted methods to both *in vitro* and *in vivo* bioimaging [29]. In their work, HeLa cells were stained with C-dots with distinct blue, green, and red colors under 405, 488, and 543 nm excitation, respectively, showing that most of the C-dots were distributed in the cell membrane and cytoplasmic areas, as evidenced by the strong fluorescence there, which was in marked contrast to the feeble fluorescent signals of C-dots located in the cell nucleus (Figure 14.16a–d). As for the *in vivo* bioimaging, female nude mice bearing U87 MG human glioblastoma tumors were intratumorally injected with C-dots and then imaged by the Maestro *in vivo* imaging system (CRi Inc.). Significantly, tumor tissues distributed with the C-dots displayed strong and spectrally resolved signals, suggesting the potential application of *in vivo* imaging using the prepared C-dots (Figure 14.16e–h).

Similarly, the C-dots synthesized from tire soot - which can be found everywhere – are also very promising for *in vivo* bioimaging [68]. Ko *et al.* derived fluorescent C-dots (referred to as tC-dots) from tire soot by mixing the materials collected from the combustion of several tire pieces with nitric acid, and then demonstrated NIR fluorescence of the tC-dots using C6 (a rat glioma cell line) cells for *in vitro* and *in vivo* bioimaging. As shown in Figure 14.17a, confocal

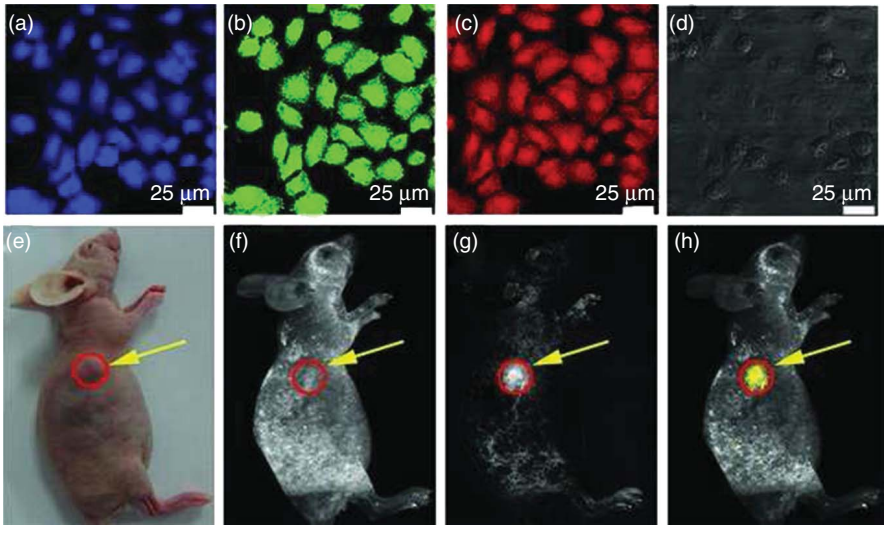

Figure 14.16 (a–d) Laser scanning confocal microscopy images of the C-dot-labeled HeLa cells: (a) $\lambda_{excitation} = 405$ nm; emission bandpass: 420–480 nm; (b) $\lambda_{excitation} = 488$ nm; emission bandpass: 500–580 nm; (c) $\lambda_{excitation} = 543$ nm; emissionband pass: 580–660 nm, and (d) bright-field (scale bar = 25 μm). (e–h) Fluorescence images of a U87 MG tumor-bearing mouse after intratumoral injection of C-dots. (e) Bright-field, (f) the autofluorescence of the mouse, (g) fluorescence of C-dots (with excitation at 455 nm, emission at 500–650 nm, and exposure time 200 ms), and (h) merged images.

microscopy analysis substantiated that the tC-dots were able to easily enter C6 cells even in the absence of any further functionalization on the surface of the tC-dots. The C6 cells with and without uptake of the tC-dots were then subcutaneously implanted into the right thigh and the left thigh of a nude mice, respectively. As indicated in Figure 14.17b, *in vivo* images of the subcutaneously injected C6 cells bearing tC-dots were acquired with a series of excitation wavelengths (430, 465, 500, 535, 570, 605, 640, 675, and 710). Obviously, the fluorescence intensity diminished at longer excitation wavelengths (Figure 14.17b), but relatively strong fluorescence signal could be obtained differentiated from the background at emission wavelengths of 660, 700, 740 and 800 nm. Because of their NIR properties, tC-dots were particularly advantageous for high-resolution *in vivo* imaging.

It is worth noting that C-dots can also be applied for *in vivo* tumor therapy. For example, in 2012, Huang *et al*. [69] rationally designed and prepared multifunctional chlorin e6-conjugated C-dots (C-dots-Ce6) that could be employed for imaging-guided therapy, as the light-triggered theranostics for simultaneous enhanced-photosensitizer fluorescence detection (PFD) and photodynamic therapy (PDT). Typically, PEG-coated C-dots (C-dots-NH_2), terminated with amine groups, were then covalently bound with Ce6 using a modified EDC–NHS reaction. As the fluorescence emission of C-dots (450–650 nm) overlaps with the absorption of Ce6, the latter can be excited by the fluorescence emission of

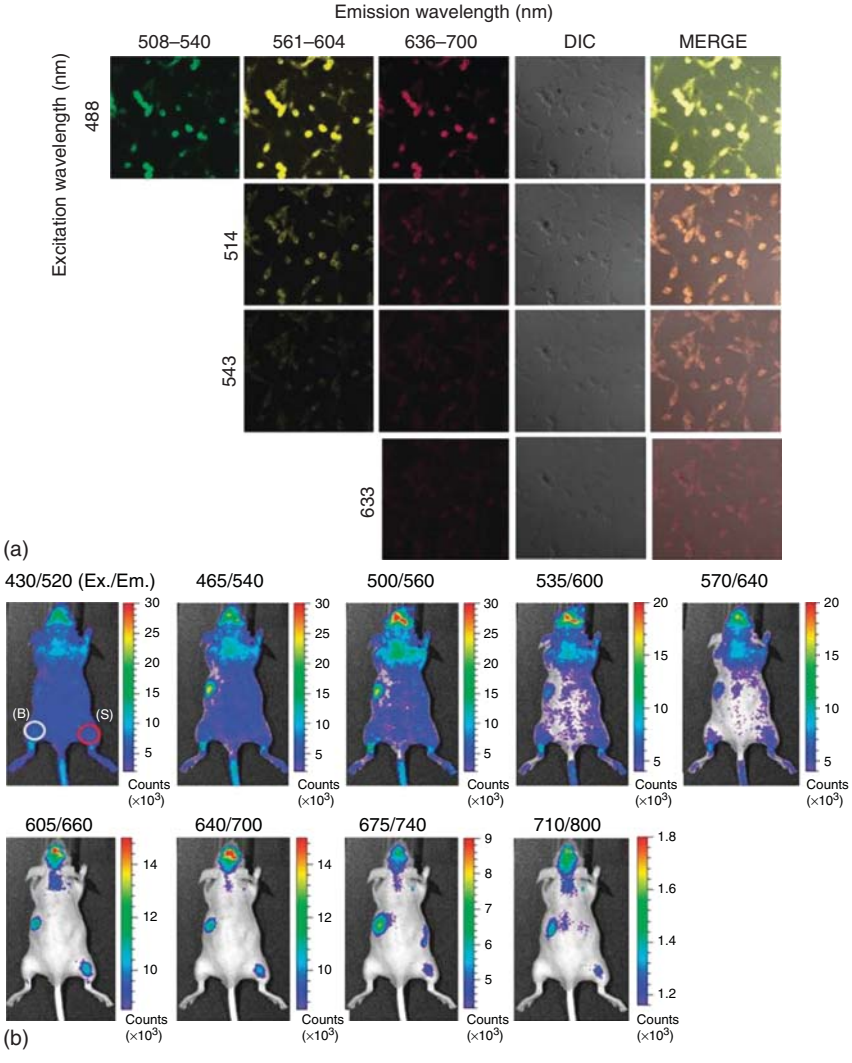

Figure 14.17 (a) Confocal microscopy image of the tC-dots in C6 cells with excitation at 488 (first row), 514 (second row), 543 (third row), and 633 nm (fourth row) and 508–580 (first column), 561–593 (second column), and 636–700 nm (third column) of the emission filter. DIC shows the bright field image of cellular morphology. (b) *In vivo* fluorescence imaging of C6 cells bearing the tC-dots. C6 cells with and without incubation of 200 mg ml^{-1} of tC-dots were subcutaneously implanted into the right thigh (indicated by a red circle and an S) and the left thigh (indicated by a white circle and a B) of a nude mice ($n = 3$).

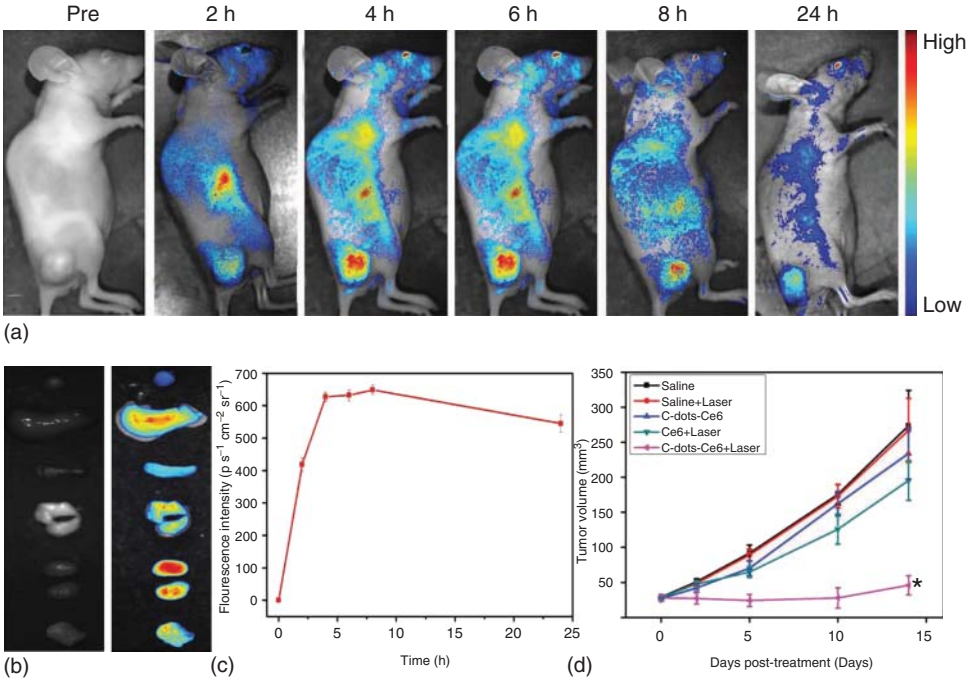

Figure 14.18 (a) Real-time *in vivo* NIR fluorescence images after intravenous injection of C-dots–Ce6 in nude mice at different time points. (b) *Ex vivo* images of mice tissues (from top to bottom: heart, liver, spleen, lung, kidneys, tumor). (c) Average fluorescence intensities from the tumor area at 24 h post injection ($n = 5$). (d) MGC803 tumor growth curves after various treatments ($n = 5$; $P < 0.05$ for other groups versus C-dots–Ce6 + laser group).

C-dots indirectly. The viability of MGC803 cells gradually dropped when the drug concentration increased. More importantly, C-dots-Ce6 featured much stronger PDT effect than Ce6 alone, indicating that C-dots-Ce6 was superior to the conventional formulation. Furthermore, they probed the capability of C-dots-Ce6 for fluorescence imaging-guided PDT. When nude mice with subcutaneous MGC803 gastric cancer xenograft were injected intravenously with C-dots-Ce6 (5 μmol equivalent of Ce6/kg body weight), as shown in Figure 14.18a, the tumor area exhibited significant fluorescence due to the C-dots-Ce6. We can also obtain the tissue/organ distribution (Figure 14.18b) after 24h by harvesting the organs of the mice injected with C-dots-Ce6. Measuring Ce6 fluorescence intensity of tumor, C-dots-Ce6 accumulation in tumor can be acquired, as shown in Figure 14.18c, which reached a plateau after 8 h postinjection. Within 8 h post injection, the tumor area was then treated with a 671-nm laser (100 mWcm$_{-2}$) for 10 min, and the C-dots-Ce6-injected mice showed partial tumor regression (Figure 14.18d). These results indicated that C-dots-Ce6 possessed wonderful imaging and tumor-homing capability without compromising the photodynamic efficacy, which was appropriate for simultaneous PFD and PDT of tumor in *vivo*.

14.3.4 Conclusion

We presented the recent representative achievements of C-dot-based nanoprobes for bioimaging applications. Although the application of C-dots as a kind of nanomaterial for bioimaging has been proven only recently , it has caught worldwide attention owing to their easy preparation, fascinating photophysical properties, excellent stability, low toxicity, and versatile surface chemistry. Hence, these kinds of C-dot-based bioprobes are highly suitable for both long-term and real-time *in vitro* and *in vivo* imaging applications, by featuring bright and stable fluorescent signals for direct and long-time visualization of biological labeling. Actually, the versatility of C-dots offer enormous possibilities in a wide range of *in vitro* and *in vivo* imaging applications including real-time cell tracking, high-resolution multiplexed vascular imaging, intraoperative image guidance, and so forth. Furthermore, recent improvements in the design and fabrication of C-dot probes along with the potential virtue of this technology have changed the focus from the preparation of single-component probes to the fabrication of hybrid nanostructures composed of multiple targeting, imaging, and therapeutic modules. For instance, when integrated with drugs or nucleic acid therapeutics, C-dots can act as traceable delivery vehicles. Generally speaking, C-dots can be applied as universal scaffolds for the attachment of extra components and targeting ligands because of their large surface area and modular surface chemistry. In order to expand C-dots functionality, it is very important to design C-dot-based multifunctional nano-devices promising to integrate the imaging, drug loading, and even sensing capacities within a single nanoparticle. However, existing C-dot probes are not ideal enough, leaving much room for the advancement of novel engineering for the functional surface of C-dots.

14.4 Toxicity Assessment

To date, nanomaterials have been employed in a wide range of commercial products [18], leading to more and more environmental and human exposure to such materials. Therefore, the concept of nanotoxicology has emerged [19], and biosafety assessment of nanomaterials has become a fundamental requirement for their practical applications. Specifically, it was shown that titanium dioxide nanoparticles utilized in sunscreens could cause brain damage in mice [70]; carbon nanotubes can be potentially harmful to cells by exerting asbestos-like effects on the cells, and soot particles may adversely influence human health [71] in spite of possessing the biocompatibility of bulk carbon. For a variety of nanomaterial-based biomedical applications, deliberate, direct ingestion or injection of nanomaterials [72–74] is involved, so the toxicity of the nanomaterials should be taken into account seriously. Recently, the biosafety assessment of carbon nanodots has been reviewed in the literature [75–77].

As discussed in previous sections, C-dots have great potential for use in a variety of biological and biomedical applications with favorable properties, such as strong photoluminescence and robust stability, but biocompatibility of C-dots still remains a key concern for further biological applications, particularly in live cells, tissues, and animals. It is worth pointing out that, although carbon is credited with biocompatibility, it is still important to perform systematic and reliable biosafety assessment of carbon dots before employing them in practical applications. The past few years have witnessed pioneering work conducted to investigate *in vitro* and *in vivo* behaviors (e.g., cellular viability, biodistribution, pharmacokinetics, etc.) of not only raw C-dots but also passivated ones. On the whole, it is the surface passivation molecules, which possess negligible cytotoxicity even at high concentrations, such as PEG and PPEI-EI, that are beneficial for C-dot functionalization for biological applications. As for the molecules exhibiting more obvious cytotoxic effect, for instance branched polyethyleneimine (BPEI), the corresponding C-dots should be still applicable *in vivo* when their concentrations are kept low enough or the incubation time is short enough. These primary results demonstrated favorable biocompatibility of carbon dots while some studies addressed possible safety concerns on the basis of research of detectable *in vitro* and *in vivo* toxicity caused by carbon dots. In this section, we will take C-dots as models to present recent investigations involving C-dot-induced toxic effect, and hope this outline of the pioneering work can serve as the starting points for risk assessment of carbon dots.

14.4.1 *In Vitro* Toxicity Assessment

Along with the potential of C-dots for bioimaging, as mentioned earlier, their toxicity has been arousing increasing attention. To date, a series of systemic toxicity studies have been performed, demonstrating that C-dots possess low toxicity. For example, in 2009, Sun and colleagues investigated the *in vitro* cytotoxicity of C-dots synthesized through laser ablation and surface passivation with PEG1500N [61]. The human breast cancer MCF-7 and human colorectal adenocarcinoma HT-29 cells were co-cultured with the C-dots, and then trypan blue and MTT assays of the cells were carried out to determine cell mortality, proliferation, and viability. The results suggested >80% cell viability for C-dot concentrations up to 0.1 mg ml^{-1}.

Then in 2011, Tao *et al.* [21] tested the *in vitro* cytotoxicity of C-dots prepared from mixed-acid treatment of MWCNTs, SWCNTs, and graphite using the human kidney embryonic 293T cell line. With these materials serving as the carbon source, the C-dots produced without any further functionalization exhibited no significant reduction in cell viability after adding various concentrations of C-dots to the cells cultured in 96-well plates and incubated for 24 h. They further performed a standard assay to evaluate the cell viabilities even when the concentration of C-dots was ultrahigh (up to 0.5 mg ml^{-1}), demonstrating that the C-dots produced by this mixed-acid treatment method from MWCNTs, SWCNTs, and graphite were not obviously toxic *in vitro* (Figure 14.19).

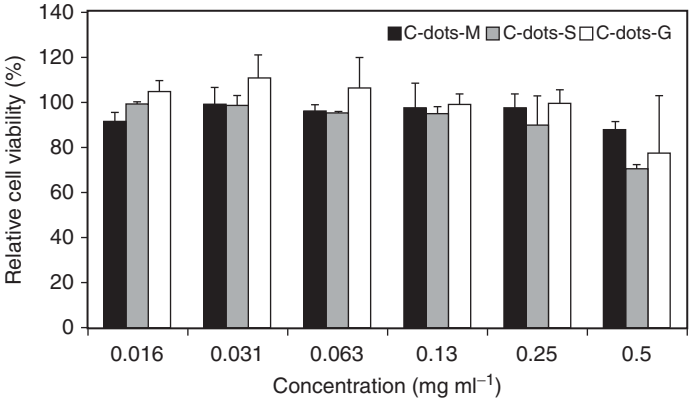

Figure 14.19 Relative viabilities of 293T cells (normalized to the untreated control) after being incubated with C-dots at various concentrations for 24 h. Error bars are based on standard deviations of triplicated samples.

What if the C-dots are prepared from other commercial, accessible, and common materials? In 2013, Ko *et al.* [68] obtained fluorescent C-dots from tire soot (designated as tC-dots) by means of an oxidative acid treatment with nitric acid and studied the cellular viability of the dots in C6 cells. Various concentrations (0, 20, 40, 100, 200, and 400 mg ml^{-1}) of the tC-dots were added to the C6 cells, which showed no noticeable toxicity to the C6 cells. Also, confocal microscopy analysis suggested that the tC-dots were able to easily enter into C6 cells without any further functionalization on the surface of the dots.

As C-dots prepared from tire soot showed no significant reduction in the cellular viability, it is likely that C-dots produced from green carbon sources also would present little toxicity. In 2015, Wang *et al.* [29] tested the *in vitro* cytotoxicity of C-dots produced from milk by microwave-assisted synthesis using human glioblastoma (U87 MG) cell line. A variety of concentrations of such C-dots were added to the cells cultured in 96-well plates and incubated for 24, 48, and 72 h, following which a standard assay was performed to assess the cell viabilities. No significant reduction in cell viability was seen after even adding C-dots of ultrahigh concentrations of up to 300 μg ml^{-1}, which suggested that the C-dots produced from the green precursor (milk) assisted by microwave irradiation were not toxic *in vitro*.

However, not all C-dots prepared from green carbon source possess are nontoxic to cells. For example, C-dots prepared from green tea, according to Chang and colleagues [78a], would negatively influence the growth efficiency of human breast cancer (MDA-MB-231) cells. In their work in 2013, although they studied the inhibitive effect of C-dots on cancer cells *in vitro*, the underlying molecular mechanism of such inhibition remains unclear. So in 2014, they further conducted a more systemic investigation on the suppression efficiency of C-dots on the growth of cancer cells. In that study, they prepared photoluminescent C-dots from ginger by the hydrothermal method, and found that the dots exhibited extremely high suppression efficiency on the growth of human hepatocellular

carcinoma (HepG2) cells and presented low toxicity to normal mammary epithelial (MCF-10A) cells and mouse liver (FL83B) cells [78b]. They conducted surface-assisted laser desorption/ionization time-of-flight mass spectrometry (SA-LDITOF-MS), western blot, and imaging cytometry analysis to investigate the biological activities and the toxic effects of the C-dots on human lung cancer (A549) cells, human breast cancer (MDA-MB-231) cells, human cervical cancer (HeLa) cells, and human hepatocellular carcinoma (HepG2) cells, and found that the inhibition efficiency of C-dots on HepG2 cells was more selective than on the others. Figure 14.20a shows the dose-dependent *in vitro* cytotoxicity of C-dots on the five cell lines (96-well plates) for 24 h, revealing that C-dots have higher inhibition efficiency on hepatocellular carcinoma cells (HepG2) than on the other kinds of cancer cells. Reactive oxygen species (ROS) levels, an important mediator of the programmed cell death pathway in HepG2 cells, were increased notably by significantly taking up C-dots, but remained almost the same in the other cells. Moreover, western blot results showed an increased expression of p53 only in the HepG2 cell line after 24 h of treatment with C-dots, which indicated DNA damage, hypoxia, and ROS-induced apoptosis, Figure 14.20b further proves that the increased ROS level can be attributed to the death of HepG2 cells through apoptosis. The influence of the C-dots (1.11 mg ml^{-1}) on the cell-cycle phases and apoptosis of HepG2 cells is shown in Figure 14.20c, supporting the C-dot-caused apoptosis of HepG2 cells.

Since Zhu *et al.* [30, 34, 64a, 79] first applied GQDs for *in vitro* bioimaging, the toxicity of GQDs has aroused increasing worldwide attention. Previous reports demonstrated that both the oxygenous groups and small size of GQDs lead to their fine biocompatibility.

Taking the GQDs prepared by Zhu *et al.* [32] as example, the GQDs were prepared by the one-step solvothermal method and the cell viability tests were carried out on MG-63 (human osteosarcoma) cells using the MTT assay. It was shown that adding up to 400 mg of GQDs to 150 ml^{-1} of the culture medium (10^4 cells) did not impact the cell activity significantly, which indicated that GQDs induced no noticeable toxicity at the cellular level.

Then in 2013, Nurunnabi *et al.* [24] tested the toxicity of GQDs using the lactate dehydrogenase (LDH) release profile and MTT assay. GQDs were prepared by acidic oxidation of carbon fibers during ultrasonication, which were then cultured with diverse cell lines (KB, MDA-MB231, and A549) in order to observe the LDH release profile. Specifically, if the cell membrane was damaged, intracellular LDH molecules should leak out, so the LDH levels in the culture medium can present cell membrane integrity, which can be used to test cytotoxicity. In the above work, the amount of LDH release from KB cells was higher compared to that from MDA-MB231, A549, and Madin–Darby canine kidney (MDCK) epithelial cells (Figure 14.21), which should be ascribed to the fact that KB cells were incorporated GQDs into subcellular vesicles avidly while MDA-MB231 and A549 cells did not efficiently take up the dots.

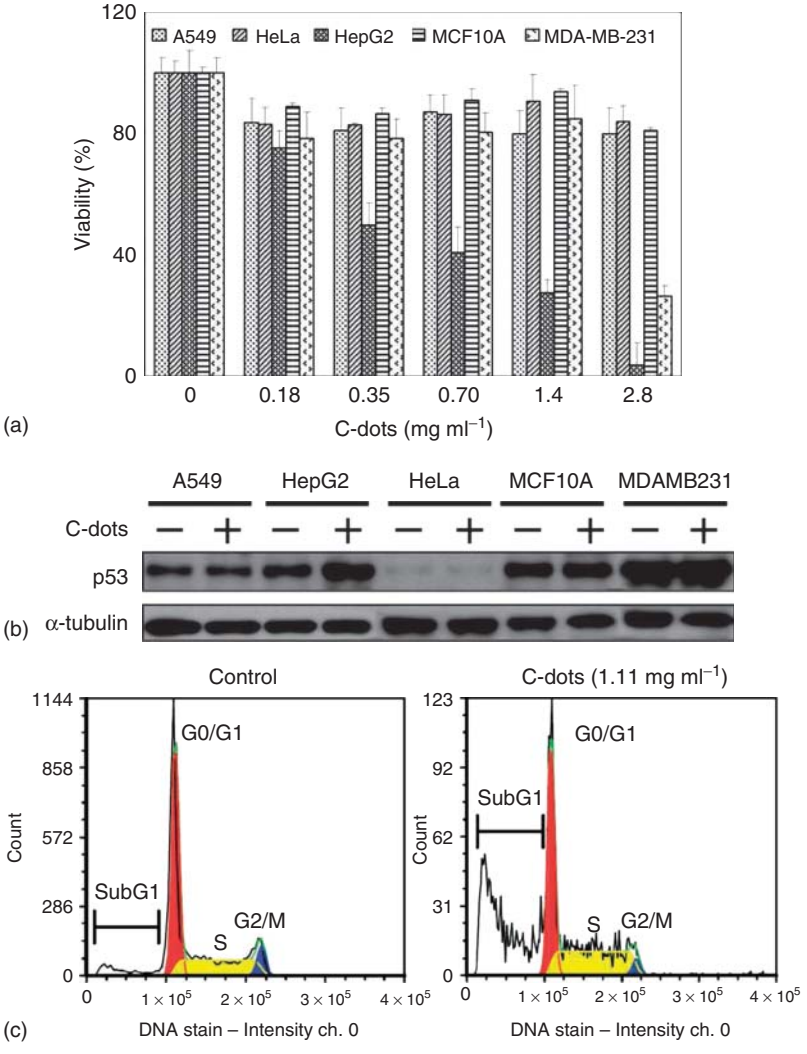

Figure 14.20 (a) Viability of five cell lines (A549, HeLa, HepG2, MCF10A, and MDA-MB-231) after C-dot (0–2.8 mg ml^{-1}) treatment for 24 h. (b) p53 protein expression of the five cell lines without (–) and with 1.11 mg ml^{-1} C-dots (+) treatment for 24 h. (c) Cell cycle distributions of HepG2 cells without (control) and with 1.11 mg ml^{-1} C-dot treatment for 24 h.

Furthermore, as indicated in Figure 14.21, Nurunnabi *et al.* also performed an *in vitro* cytotoxicity study for different cancer cell lines including KB, MDA-MB231, A549, and MDCK cells at a series of concentrations of GQDs (50, 100, 250, and 500 μg ml^{-1}) for 24 h by MTT colorimetric assay, which showed that the GQDs did not cause noticeable toxicity since the cell viability was more than 80% even when exposed to GQDs of a relatively high concentration (500 μg m^{-1}) (Figure 14.21). Notably, the cell viability of MDA-MB231 and A549 cells was

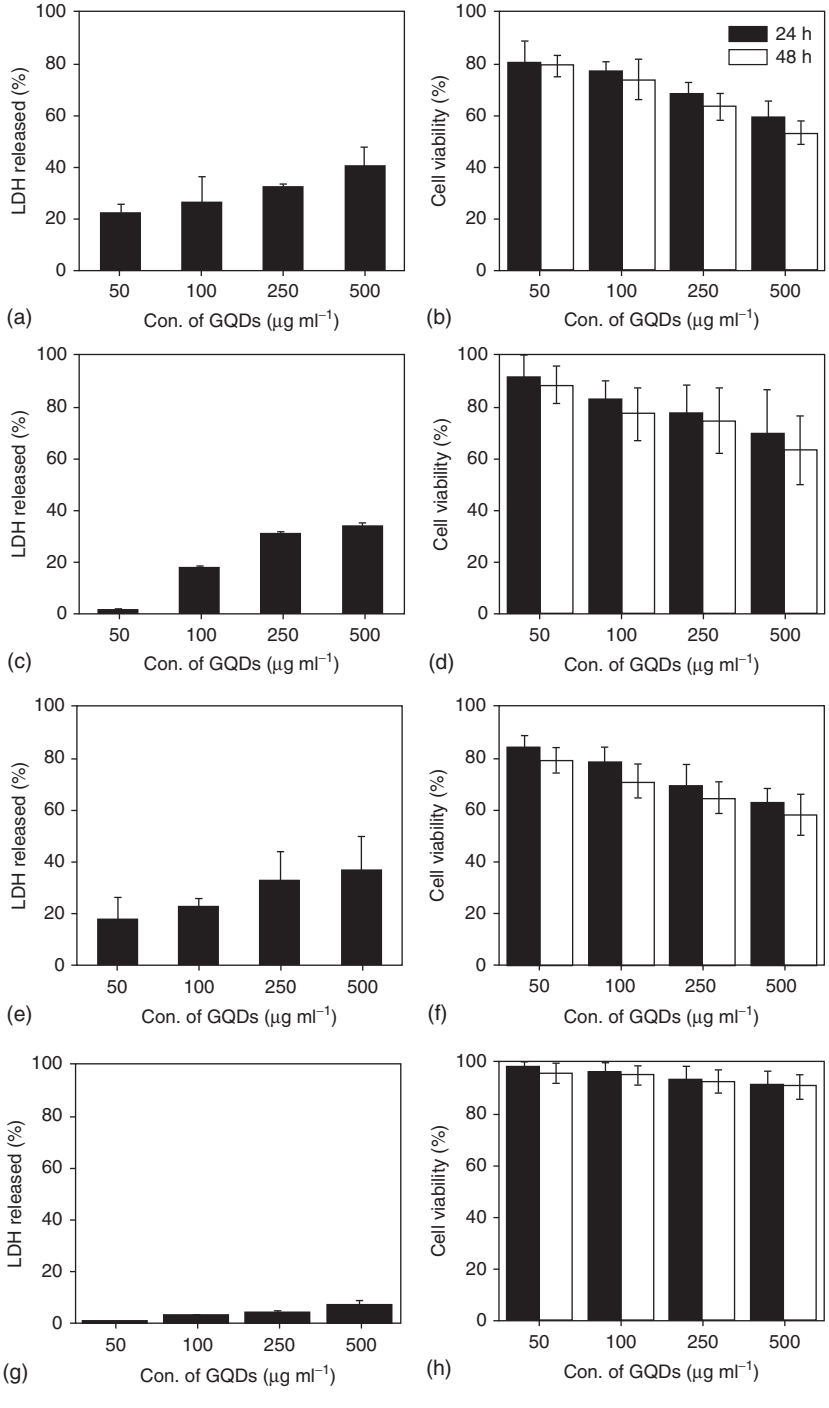
LDH released (%)
Cell viability (%)
24 h
48 h
Con. of GQDs (μg ml−1)
(a)
(b)
(c)
(d)
(e)
(f)
(g)
(h)

Figure 14.21 *In vitro* cytotoxicity test. Lactate dehydrogenase (LDH) release study and MTT assay of KB (a and b), MDA-MB231 (c and d), A549 cancer cells (e and f), and MDCK normal cells (g and h) treated with carboxylated GQDs. The graphs show that the cell viability of the GQD-treated MDCK cell is more than 90%. LDH release of the GQD-treated MDCK cell is lower than that of the cancer cells. Data represent mean (SEM ($n = 6$); $p < 0.05$, one-way ANOVA).

even higher than that of KB cells under the same conditions (concentration, duration, and incubation time). On the basis of the MTT assay and LDH release test results, the authors concluded that breast cancer cells (MDA-MB231) and human epithelial cancer cells (A549) were less sensitive to GQDs when compared with human epidermal cancer cells. As for MDCK cells, after treatment with the GQDs, they presented low amounts of LDH release (below 4%) and high cell viability (above 95%), showing that the nonspecific GQD nanoparticles did not exhibit any potential toxicity. In addition, from these results it can be concluded that carboxylated GQDs may not be taken up by normal cells and thus exerted no appreciable toxicity. As a result, GQDs showed relatively low toxicity and high cell viability as evidenced by MTT assay and LDH release profile.

In 2014, Chong *et al.* [23] further performed more systemic investigations concerning the toxicity of GQDs by employing various cellular assays (WST-1, cell apoptosis, LDH, ROS) to analyze the effect of GQDs on the cells; the dots were obtained via a modified oxidative cutting method. To begin with, WST-1 assay proved little toxicity of GQD-PEG to HeLa cells and A549 cells as the level of succinate dehydrogenase was changed. As shown in Figure 14.22a, more than 95% of HeLa cells were alive after 24 h of incubation with GQD-PEG, even when exposed to GQD concentrations of up to 160 mg ml^{-1}; in the case of A549 cells, a similar phenomenon could be observed and GQD-PEG exhibited ~85% cell viability when the GQD concentration reached 640 mg ml^{-1}. Furthermore, immunochemistry experiments for apoptosis and necrosis also indicated negligible negative effects of GQD on the cells. Figure 14.22b shows that even at the concentration of 160 mg/ml^{-1}, GQDs did not lead to any apoptosis or necrosis of HeLa cells, apoptosis levels of which had no correlation with the dose of the GQD. This is different from the result of the Yang group (as mentioned above) [64a], who demonstrated negligible toxicity of GQD (80–90% of cell viability at low dose) in several cell lines, but matched well with low toxicity of hyaluronic acid derivatives of carbon dots at low concentrations [25]. Although the low cytotoxicity is likely due to the PEGylation or the inherent properties of the GQD sample, the good biocompatibility of GQDs should be ascribed to their high oxygen content (36%), as bare GQD sample exhibited low toxicity in their experiment. LDH assay and ROS production were employed to further investigate the cytotoxicity of GQD-PEG. As indicated in Figure 14.22c,d, GQDs presented comparable LDH release and ROS level to the control group despite the fact that graphene and graphene oxide negatively influenced cell oxidative stress [80] and membrane integrity [81] in general, suggesting that the no noticeable cytotoxicity of GQD should be possibly attributed to the abundant oxygen content of GQD.

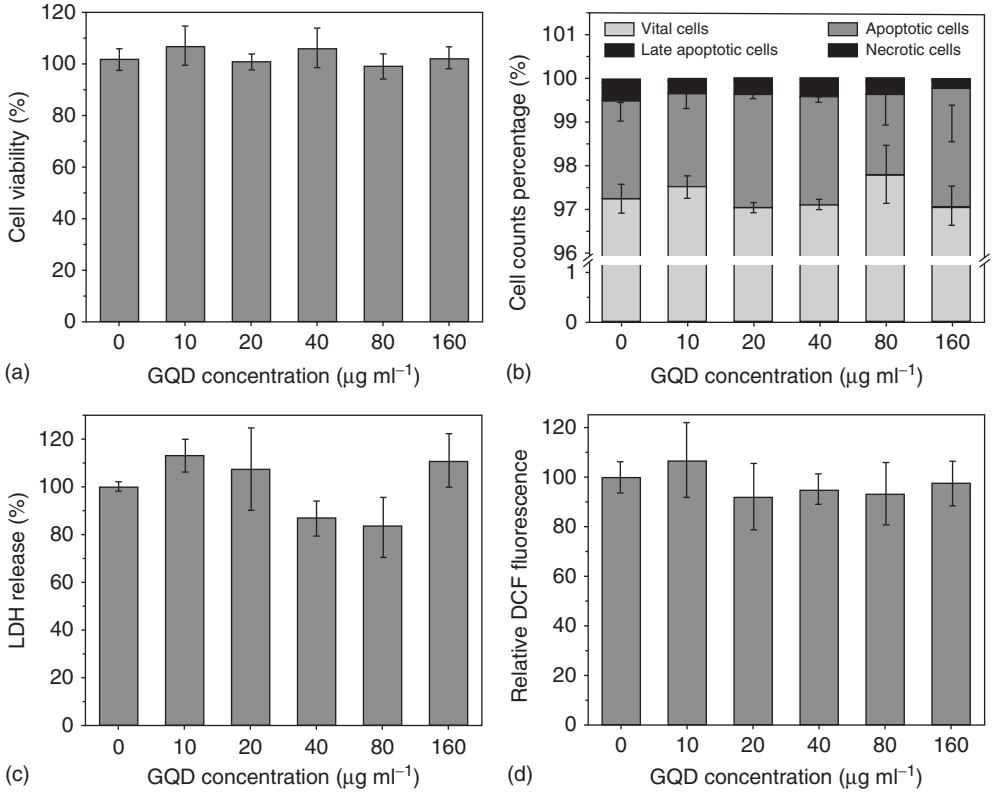

Figure 14.22 Results from (a) WST-1 assay, (b) cell apoptosis and necrosis, (c) LDH assay, and (d) ROS generation of GQD, all suggesting no obvious toxicity of GQD-PEG to HeLa cells at GQD concentration as high as 160 mg ml^{-1}. Values represent mean ± SE, $n = 3$.

GQDs also exhibited feeble cytotoxicity to stem cells, which was essential to assess the suitability of GQDs for stem cell tracking, as was demonstrated by Shang *et al.* [82] in 2014. They prepared GQDs from a highly pure graphite rod by the electrochemical method, which were taken up by human neural stem cells (hNSCs) in a concentration- and time-dependent manner via the endocytosis mechanism while exerting little effect on the proliferation, metabolic activity, and differentiation potential of hNSCs. Therefore, these data show that GQDs have the potential to track stem cells and also render them promising candidates for biomedical applications.

14.4.2 *In Vivo* Toxicity Assessment

In order to apply carbon dots for clinical applications, it is important to study their disposition and fate in the body. Thus, besides the above *in vitro* toxicity

assessment, there have been several pioneering studies to investigate the *in vivo* toxicity of carbon dots.

In 2009, Sun and colleagues conducted *in vivo* studies of C-dots passivated with PEG1500N using CD-1 mice, which were divided into three groups and intravenously injected either 8 or 40 mg of C-dots or 0.9% NaCl aqueous solution (nontoxic control) [61]. After 1, 7, and 28 days, blood and organ samples of all these mice were taken for *in vivo* toxicological assays, showing no adverse clinical signs as seen by the similar levels of hepatic indicators, kidney function, uric acid, blood urea nitrogen (BUN), and creatinine (CRE) of the mice with or without treatment of C-dots. In addition, the harvested organs of the treated mice also exhibited similarly with the untreated ones, as demonstrated by the absence of any necrosis. Even though the C-dots were found to be accumulated in the liver and spleen more than in other organs, they produced no organ damage. Hence, all results indicated the nontoxicity of C-dots at least for the exposure levels and times utilized here.

Furthermore, in 2011, Tao *et al.* [21] systematically studied the *in vivo* toxicology of C-dots made from MWCNTs on female BALB/c mice, which was prepared from MWCNTs via mixed-acid treatment. Over 3 months, no noticeable toxic side effect was found in the mice injected with C-dots at the dose of 20 mg kg^{-1}. Specifically, neither death nor any significant body weight drop was observed in the treatment group. By sacrificing the mice (five mice per group) administrated with C-dots (20 mg kg^{-1}, unlabeled) at 1, 7, 20, 40, and 90 days post injection, several kinds of experiment were performed. According to the results of blood biochemistry and hematology analysis, the blood levels of liver function markers such as alanine aminotransferase (ALT), aspartate aminotransferase (AST), ALP, and the ratio of albumin (ALB) and globulin (A/G) of C-dot-M treated mice were all similar to those of the control group (age-matched control, five mice per group) administrated at day 3, 40, and 90 for blood collection, indicating that no apparent hepatic toxicity was caused by C-dot administration; the blood urea level, serving as an indicator of kidney functions, was also consistent with that of untreated mice. For hematological assessment, the fundamental hematology markers in the C-dot-treated mice at various post-injection times, including white blood cells (WBC), red blood cells, hemoglobin (Hb), mean corpuscular volume, mean corpuscular hemoglobin, mean corpuscular hemoglobin concentration, platelet count (PLT), and mean corpuscular hemoglobin, were examined, which agreed well with those of the untreated mice within the reference normal ranges. Careful necropsy was carried out, and no noticeable organ damage was present. They harvested the main organs such as liver, spleen, kidney, and heart of treated and untreated mice groups, which were sliced for hematoxylin and eosin (H&E) staining (Figure 14.23), and found no obvious histopathological abnormality or lesion. In conclusion, these results proved that C-dots injected at the dose of 20 mg kg^{-1} were not obviously toxic to the administrated animals.

In 2012, Qu *et al.* [28] derived water-soluble luminescent C-dots from citric acid and urea by a one-step microwave synthesis route. Following that, toxicity studies of the C-dots were performed with both plants and animals. Specifically,

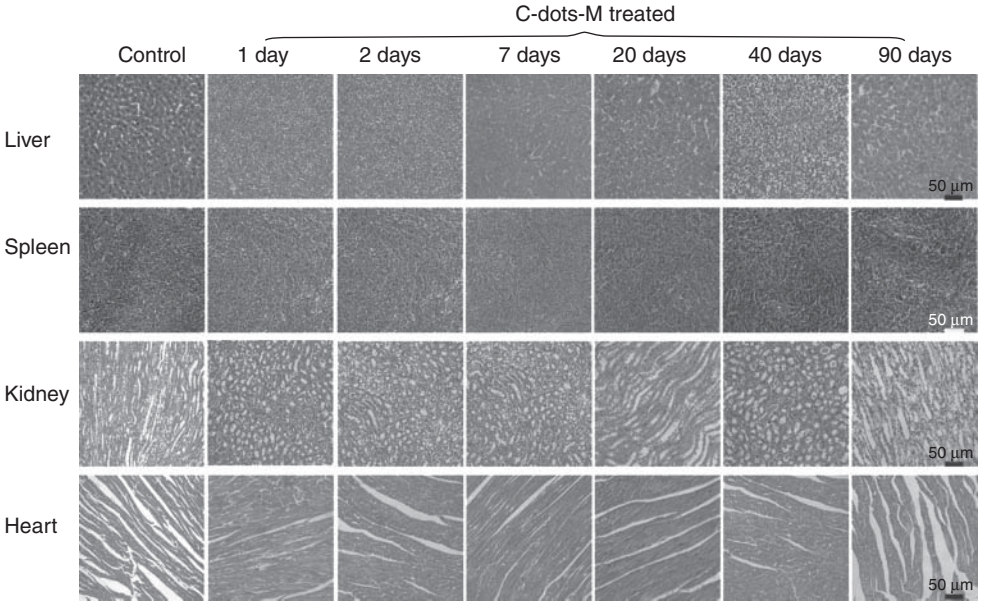

Figure 14.23 Representative H&E stained images of major organs, including the liver, spleen, and kidney, collected from the control untreated mice and the C-dot-M-injected ($20\,mg\,kg^{-1}$) mice at various time points post injection. No noticeable abnormality or lesion was observed in organs of C-dot-treated mice.

bean sprouts could grow well in an aqueous solution of C-dots ($1.5\,mg\,ml^{-1}$), showing excitation-wavelength-dependent fluorescence (Figure 14.24a), which strongly suggested that C-dots were able to permeate throughout the plant cells but not to block the growth of the plant. Ten mice were fed the aqueous solution of C-dots ($0.7\,mg\,ml^{-1}$) along an otherwise normal food intake for 5 weeks, after which all the mice survived with no symptom of anorexia, such as hair loss, scabs, vomiting, or diarrhea. And all these mice exhibited no violent or lethargic behavior over the 5-week period, and all their activities were similar to those of the mice in the control group, which were given normal food and water. Furthermore, the urine of mice that were given the aqueous solution of C-dots presented excitation-wavelength-dependent fluorescence phenomena, whereas blood derived from the ophthalmic artery of each of these mice featured no excitation-wavelength-dependent fluorescence, indicating that the C-dots could get through the urinary tract. More importantly, the test mice were given normal water for the following four weeks, after which the PL spectra of their urine returned to normal, just similar to the control group, proving that C-dots, in fact, possessed low or zero toxicity to not only plants but also animals.

Furthermore, in 2013, Huang *et al.* [22] claimed that, even though different injection routes led to different clearance rates, C-dots exhibited no significant toxicity *in vivo* after injected into the animal model via all possible routes. They investigated the effect of three injection routes (intravenous (i.v.),

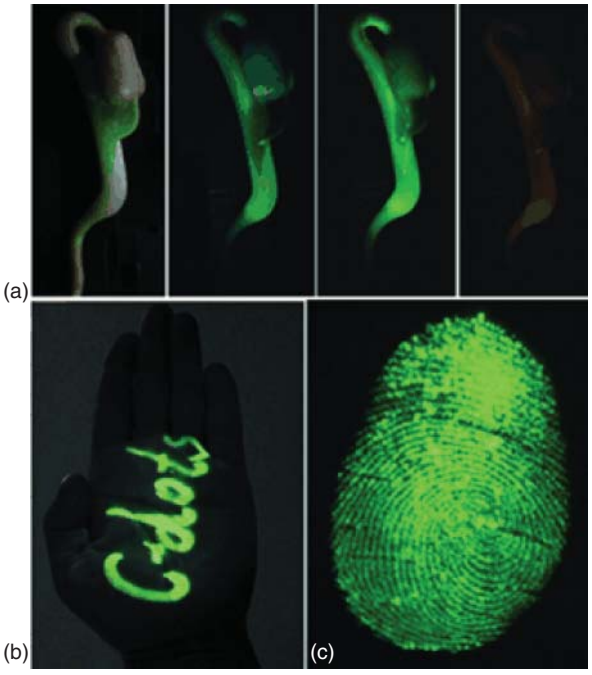

Figure 14.24 (a) (Left to right) Optical and fluorescent images of a bean sprout grown with C-dot aqueous solution (1.5 mg ml^{-1}) under daylight, 340 nm excitation (BA 395 nm), 420 nm excitation (BA 450 nm), and 500 nm excitation (BA 550 nm). (b) C-dot-marked fluorescent characters on human skin captured under 420 nm excitation (BA 450 nm). (c) C-dot-formed fluorescent fingerprint on commercially available filter paper captured under 420 nm excitation (BA 450 nm).

subcutaneous (s.c.), and intramuscular (i.m.)) on the fate of C-dots *in vivo* and demonstrated that C-dots can be efficiently and rapidly excreted from the body by all these routes, in spite of the different clearance rate (intravenous > intramuscular > subcutaneous). They synthesized C-dots via laser ablation of a carbon target in the presence of water vapor with argon, which were passivated by diamine-terminated oligomeric PEG and subsequently coupled with the NIR dye ZW800, showing low retention in the reticuloendothelial system (RES) and high tumor-to-background contrast. Specifically, ZW800-labeled C-dots (C-dot-ZW800) were mainly cleared through the kidneys (into urine) rather than the liver and spleen without notable accumulation at the injection sites over time (Figure 14.25), satisfying the need for clinical translation. Additionally, due to the presence of different biological barriers, different injection routes led to different blood clearance patterns and urine accumulation rates, following the order i.v. > i.m. > s.c., which in turn resulted in decreased tumor retention, enabling researchers to control the *in vivo* behaviors of C-dots, including the circulation time, major organ accumulation, and passive tumor targeting by the injection routes.

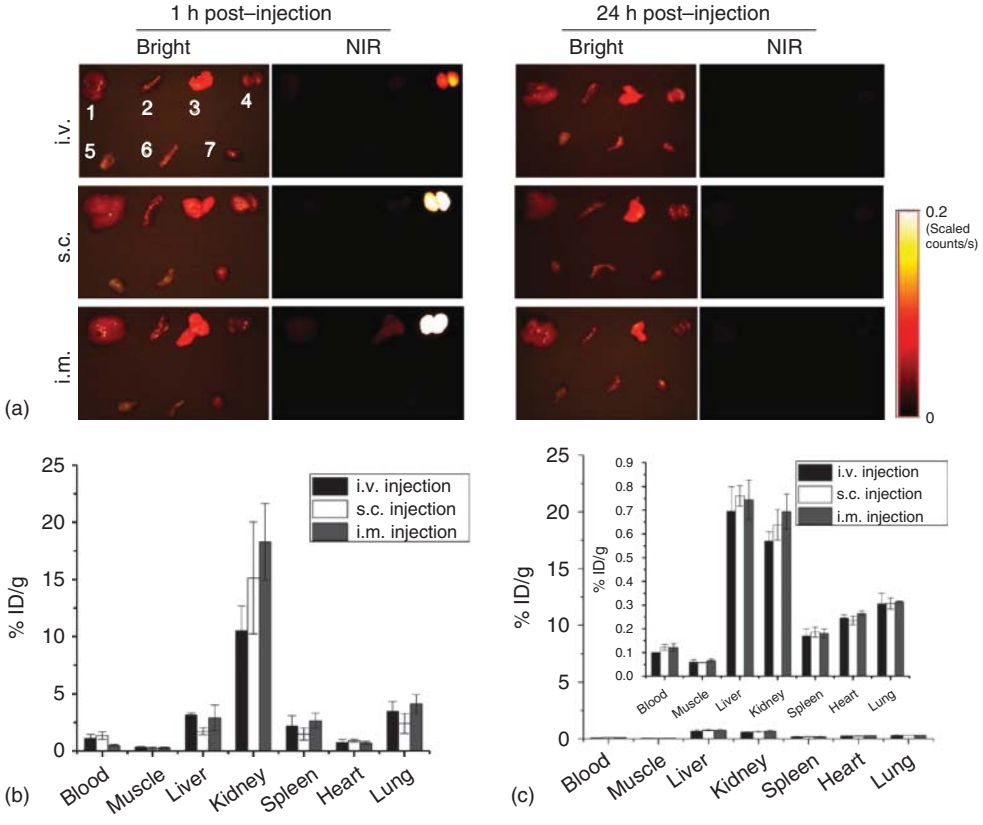

Figure 14.25 Biodistribution of particles after three injection routes. (A) *Ex vivo* imaging of biodistribution of C-dot particles. After injection of particles, the major organs and tissues were harvested from BALB/C mice at the indicated time points, and subsequently the bright-field and NIR images were acquired using a Maestro imaging system. Left: 1 h post injection (top, i.v.; middle, s.c.; bottom, i.m.); right: 24 h post injection (top, i.v.; middle, s.c.; bottom, i.m.). Bright field: 1, liver; 2, spleen; 3, lung; 4, kidneys; 5, muscle; 6, intestine; 7, heart. (b, c) Quantification of the biodistribution of ^{64}Cu-labeled C-dots via three injection routes at 1 h (b) and 24 h (c) time points. At 1 and 24 h post injection of ^{64}Cu-C-dots, the mice were euthanized, and major organs and tissues including blood, muscle, liver, kidneys, spleen, heart, and lung were harvested and measured by gamma counting.

Then in 2013, Nurunnabi *et al.* [24], for the first time, performed a long-term *in vivo* study of GQDs and claimed that no acute toxicity or morphological changes were noted at the tested exposure levels. The GQDs were prepared from carbon fibers after treating them sulfuric acid, which mainly accumulated in the liver, spleen, lung, kidney, and tumor sites after i.v. injection, showing no appreciable toxicity to the treated animals as indicated by complete blood count, serum biochemical analysis, and histological evaluation results. Specifically, they selected the indicative markers including Hb, WBC, hematocrit (HCT), and PLT for the

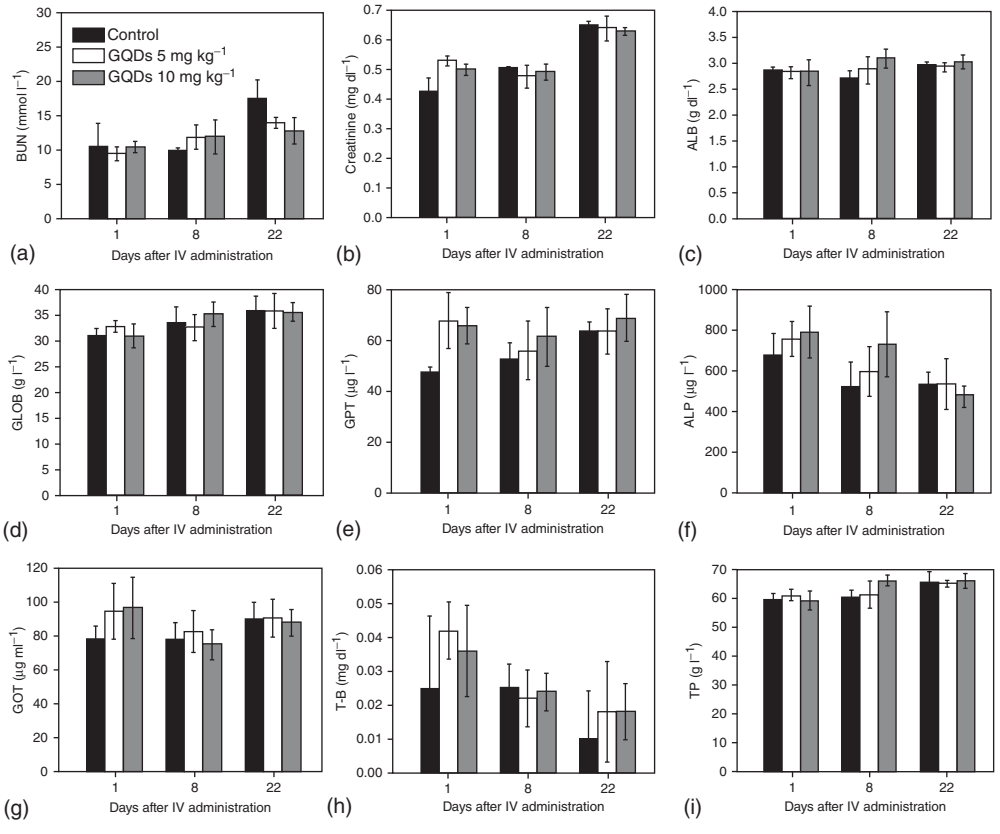

Figure 14.26 Serum biochemistry results from rats treated with the carboxylated GQDs. (a–i) Results showing mean SEM ($n = 6$) of (a) BUN, (b) CRE, (c) ALB, (d) GLOB, (e) GTP, (f) ALP, (g) GOT, (h) TB, and (i) TP. Control means the serum samples of rats treated with saline ($p < 0.05$, one-way ANOVA).

hematology study, finding that all these values of treated mice were within normal levels, similar to the control group.

For serum biochemistry study, BUN and CRE, both of which are the indicators of kidney function, were also normal (Figure 14.26a,b) and similar to those of control animals. Besides that, there was no sign of liver injury (Figure 14.26c–i) after measuring the seven important hepatic indicators: albumin (ALB), globulin (GLOB), glutamic pyruvate transaminase (GTP), ALP, glutamic oxaloacetic transaminase (GOT), total bilirubin (TB), all of which were within normal ranges and were similar to values for control animals. In histological analysis, which can provide a detailed microscopic assessment and histological evaluation of tissue interactions, no apparent histopathological abnormalities or lesions were seen in the heart, kidney and spleen, and the H&E staining images of these organs were similar to those of untreated animals. Admittedly, moderate pathological changes were shown in the liver and lungs when administrated a higher dose (10 mg kg^{-1})

of the carboxylated GQD nanoparticle. But there were no signs of inflammatory response in the liver samples, no pulmonary fibrosis in the lung samples, and no pathological changes in the heart, lung, kidney, liver, or spleen. The glomerulus structure in the kidney section could not be easily observed, and necrosis could not be seen in any of the histological samples analyzed. The fluctuations of body weights monitored every other day were no more than those of the control group. As a result, few could disagree with the fact that the GQDs exerted no adverse effects to the treated mice, with obvious organ damage or lesions, after 21 days of i.v. injection of 5 or 10 mg kg^{-1} dose of GQDs, rendering the GQDs promising for biological applications.

In 2014, Zhang and colleagues [23, 80] prepared GQD samples through a modified oxidative cutting method, which was attached with Cy7 (a kind of NIR fluorescent dyes) and was then intravenously or intraperitoneally injected into BALB/c (200 ml of 1.5 mg ml^{-1} GQDs solution). Different from Huang *et al.* [22], who claimed that biodistribution and clearance of C-dots in major organs and tissues should be influenced by the diverse injection routes, Zhang and colleagues found that GQD-PEG distributions were independent of administration routes after harvesting the organs and tissues of mice sacrificed post 1, 4, 12, 24, and 48 h and calculating the Cy7 fluorescence intensity of the organs for a semiquantitative biodistribution analysis. In other words, as indicated in Figure 14.27, GQD-PEG mainly accumulated in the kidneys and tumor sites, and GQD-PEG was excreted from the kidneys soon. Note that these results – that GQDs were dominantly present in kidney – were also contrary to those while using carbon dots in other studies. For instance, Lee and colleagues [24] insisted that GQDs could be found in most organs including the liver, kidneys, lung, and spleen, and Hahn and colleagues [25], Liu and colleagues [21] and Chen and colleagues [22], in separate experiments, concluded that polymer-coated carbon dots were predominantly cleared out through liver (into bile) and kidneys (into urine). Moreover, the particles could be totally cleared in 24 h, especially in the first hour no matter how the polymer-coated carbon dots were injected. In contrast, in Zhang's work [23], strong fluorescence of GQD could be observed in urine while not in RES. According to Zhang *et al.* [23], the difference was due to the smaller size and higher oxygen content of GQDs. Additionally, there was consistently strong Cy7 fluorescence in the tumor, which indicated the accumulation of GQD-PEG due to the enhanced permeability and retention (EPR) effect. In summary, the quick clearance in kidneys and feeble dispersion in the other organs endowed GQD-PEG with excellent biocompatibility.

14.4.3 Conclusion

In this section, we reviewed the biosafety assessment of carbon dots prepared by various methods, and showed that cytotoxicity of carbon dots is highly dependent on the cell lines, properties of carbon dots (e.g., diameter, surface ligands,

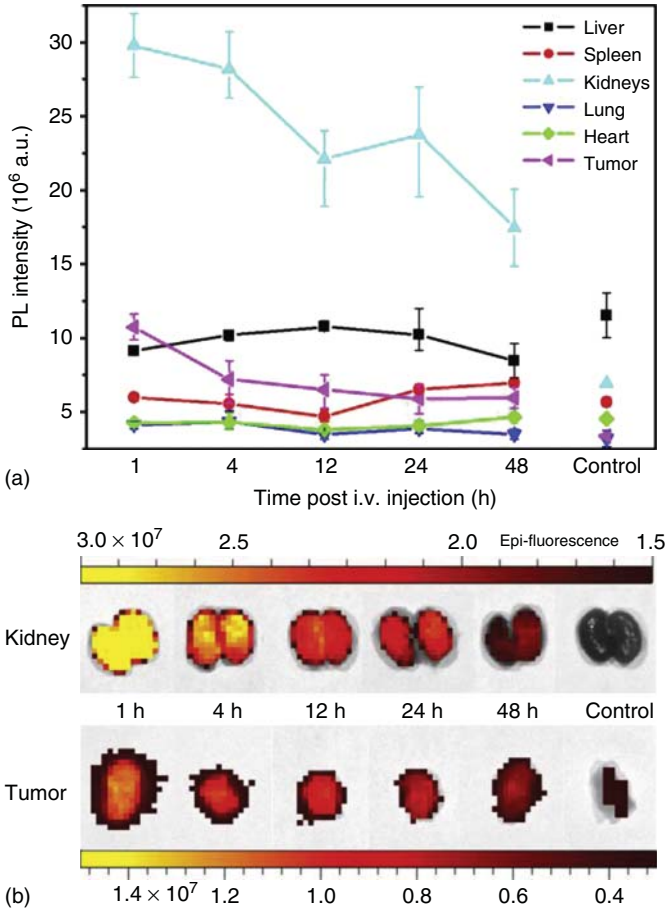

Figure 14.27 (a) PL intensities of livers (black), spleens (red), kidneys (cyan), lungs (blue), hearts (green), and tumors (purple) indicate the GQD concentrations in these organs collected at various time points from mice i.v. injected with GQD-PEG–Cy7. (b) Photographs of kidneys and tumors under NIR illumination clearly showing the changes of GQD concentration in these organs. Values represent mean ± SE, $n = 3$.

etc.), and the incubation conditions (e.g., incubation time and carbon dot concentration). Note that, according to the *in vivo* experiment, carbon dots can be readily cleared out of the mice through the renal route, so carbon dots with no detectable toxicity *in vivo* are able to serve as novel biodegradable nanomaterials. Even though some other kinds of carbon dots were seen to get dispersed in other organs besides the kidney, there were no signs of inflammatory response in the liver samples, no pulmonary fibrosis in the lung samples, and no pathological changes in the heart, lung, kidney, liver, or spleen, indicating the biocompatibility of carbon dots. Furthermore, different injection routes, when applied to carbon dots prepared by Huang *et al*. [22], resulted in different clearance rates, and C-dots

exhibited no apparent toxicity *in vivo* after injected via all the possible routes. But this theory cannot agree well with the experimental results obtained by Zhang *et al* [23]. who claimed that GQD-PEG dispersion was independent of the administration routes and cleared out from kidneys soon, which exhibited no significant toxicity *in vivo*. Such inconsistent results are possibly due to the diverse properties of carbon dots, including their surface chemistry, component, morphology, and so forth. Therefore, more elaborate investigations are still needed to further deal with these issues, which must be highly beneficial for C-dot-based biological and biomedical applications.

14.5 Perspectives

In this chapter, we reviewed the synthetic approaches, bioimaging applications, and toxicity assessment *in vitro* and *in vivo* of C-dots. Owing to their oxygen groups, pronounced quantum confinement, and edge effects, carbon dots undoubtedly possess excellent chemical stability, fascinating optical properties, and biocompatibility/nontoxicity, which have inspired extensive research interest. Despite the above-mentioned representative references involving C-dots published in recent years, there is still considerable room for the development of carbon dots, as there are still some urgent issues remaining to be solved: for example, the lack of methods for accurately controlling the surface group, the unequivocal PL mechanism, the narrow spectral coverage and the deficiencies in tuning their optical properties, and the relatively low product yield and quantum yield. From the view of point of the development tracks of graphene, C-dots, and even semiconductor quantum dots, we speculate the future perspectives on carbon nanodots as follows.

14.5.1 Unequivocal PL Mechanism

In spite of the large efforts spent on this issue, there is no unequivocal and comprehensive understanding of the optical properties of carbon dots as agreed to by most scientists. Carbon dots prepared through diverse methods by different research groups possess different characteristics, including size, shape, surface structure, edge effects, and so forth. The mechanism of carbon dots' PL has been demonstrated to derive from the combination of or competition between the factors mentioned; the fact is that few can indicate a detailed PL mechanism, and the current mechanisms always result in confusing results since in diverse cases different C-dots work in distinct ways. Hence, a more comprehensive and more detailed understanding of the optical properties of carbon dots is really needed, especially for those who want prepare carbon dots with expected and desirable properties.

14.5.2 Expanding the Spectral Coverage

Until now, most C-dots exhibit blue to yellow emission upon excitation. Despite the NIR PL spectrum obtained by Tao *et al.* [21], who synthesized C-dots via mixed-acid treatment of carbon nanotubes, the narrow spectral coverage is not able to satisfy the requirement of some applications such as, for example, multicolor imaging. As a result, expanding the spectral coverage of C-dots to all visible wavelengths and even NIR by size control, oxidation degree variation, surface modification and doping need to be explored; if successful, carbon dots will play a more fundamental role in future investigations, undoubtedly.

14.5.3 QY Improvement

Also challenging is the QY improvement. In fact, the QYs of carbon dots reported to date are mostly ~20%, which is far lower than that of semiconductor QDs (QYs: ~60–80%). Fortunately, surface passivation is able to notably enhance the QY of C-dots. In 2009, Tian and colleagues produced C-dots from natural gas soot with the QY significantly increased from 0.43% to 36.7–60.1% through the formation of carbon–metal nanocomposites [8]; in 2013, Zhu *et al.* [32] prepared C-dots with QY as high as 80% by condensing citric acid and ethylenediamine via hydrothermal treatment. Consequently, different passivation routes should be developed to improve the QY, via two-step or *in situ* modifications and others. It is worth pointing out that, with the achievement of uniform size, shape, and edge, multicolor PL emission, and high QY, carbon dots will attain greater potential in biomedical applications such as bioimaging, biosensors, and drug and gene delivery, among others.

14.5.4 Bioimaging

Because of their easy preparation, fascinating photophysical properties, excellent stability, and low toxicity, C-dots have aroused considerable attention as a relatively new nanomaterial for bioimaging without a long history. By further surface functionalization C-dots can be rendered to have high QY, good biocompatibility, and long-term stability, all of which are beneficial for *in vitro* and *in vivo* bioimaging. As thus, undoubtedly, C-dots have been promising alternatives for quantitative detection, high-resolution fluorescent imaging, and real-time tracking of molecules besides the popular II–VI semiconductor quantum dots, SiNPs, FNDs, and so forth. In fact, the excellent characteristics of C-dots have brought flexibility to a series of *in vivo* bioimaging applications, including high-resolution multiplexed vascular imaging, intraoperative image guidance, real-time cell tracking, as well as specific interaction with biomolecules and cells. Furthermore, the

attractive advantages of this technology have made the design of hybrid nanostructures composed of multiple targeting, imaging, and therapeutic modules more worthwhile than the synthesis of single-component probes. Owing to their large surface area, C-dots can be exploited as universal scaffolds to attach extra components and targeting ligands to combine the benefits of multiple imaging modalities and incorporate imaging, drug loading, and sensing capacities within a single nanoparticle. However, plenty of room exists for their development, and a great deal of effort is still needed to design more versatile and multifunctional C-dot-based nanoprobes.

14.5.5 Toxicity Assessment

Although benign biocompatibility is attributed to carbon, systematic and reliable *in vitro* and *in vivo* biosafety assessment of carbon-based nanomaterials such as carbon dots still needs to be performed. Only by comprehensively carrying out systematic risk assessment of carbon nanotechnology in a reliable way can carbon dots serve as a useful and usable platform for a wide range of biological and biomedical applications. From the work so far, we can conclude that the cytotoxicity of carbon dots is influenced by the cell lines, properties of carbon dots, and incubation conditions. As revealed by *in vivo* experiments, carbon dots can be easily cleared out of mice. Therefore, as seen from their small toxicity in *in vitro* and *in vivo* bioassay experiments, carbon dots are promising to be exploited as a novel kind of biocompatible nanomaterials, raising great hope for their myriad applications in the biological and biomedical fields.

References

1. (a) Murphy, C.J., Thompson, L.B., Chernak, D.J., Yang, J.A., Sivapalan, S.T., Boulos, S.P., Huang, J., Alkilany, A.M., and Sisco, P.N. (2011) Gold nanorod crystal growth: from seed-mediated synthesis to nanoscale sculpting. *Curr. Opin. Colloid Interface Sci.*, **16**, 128–134; (b) Dreaden, E.C., Alkilany, A.M., Huang, X., Murphy, C.J., and El-Sayed, M.A. (2012) The golden age: gold nanoparticles for biomedicine. *Chem. Soc. Rev.*, **41**, 2740–2779; (c) Chen, J.Y., McLellan, J.M., Siekkinen, A., Xiong, Y., Li, Z.Y., and Xia, Y. (2006) Facile synthesis of gold–silver nanocages with controllable pores on the surface. *J. Am. Chem. Soc.*, **128**, 14776–14777.
2. (a) Bruchez, M., Moronne, M., Gin, P., Weiss, S., and Alivisatos, A.P. (1998) Semiconductor nanocrystals as fluorescent biological labels. *Science*, **281**, 2013–2016; (b) Chan, W.C. and Nie, S. (1998) Quantum dot bioconjugates for ultrasensitive nonisotopic detection. *Science*, **281**, 2016–2018; (c) Medintz, I.L., Uyeda, H.T., Goldman, E.R., and Mattoussi, H. (2005) Quantum dot bioconjugates for imaging, labelling and sensing. *Nat. Mater.*, **4**, 435–446; (d) Michalet, X., Pinaud, F., Bentolila, L., Tsay, J., Doose, S., Li, J., Sundaresan, G., Wu, A., Gambhir, S., and Weiss, S. (2005) Quantum dots for live cells, in vivo imaging, and diagnostics. *Science*, **307**, 538–544.
3. (a) Grom, G.F., Lockwood, D.J., McCaffrey, J.P., Labbe, H.J., Fauchet, P.M., White, B., Diener, J., Kovalev, D., Koch, F., and Tsybeskov, L. (2000)

Ordering and self-organization in nanocrystalline silicon. *Nature*, **407**, 358–361; (b) Pavesi, L., Dal Negro, L., Mazzoleni, C., Franzo, G., and Priolo, F. (2000) Optical gain in silicon nanocrystals. *Nature*, **408**, 440–444; (c) Ma, D., Lee, C., Au, F., Tong, S., and Lee, S. (2003) Small-diameter silicon nanowire surfaces. *Science*, **299**, 1874–1877.

4. (a) Kostarelos, K., Bianco, A., and Prato, M. (2009) Promises, facts and challenges for carbon nanotubes in imaging and therapeutics. *Nat. Nanotechnol.*, **4**, 627–633; (b) Chung, C., Kim, Y.K., Shin, D., Ryoo, S.R., Hong, B.H., and Min, D.H. (2013) Biomedical applications of graphene and graphene oxide. *Acc. Chem. Res.*, **46**, 2211–2224; (c) Zhu, Y., Murali, S., Cai, W., Li, X., Suk, J.W., Potts, J.R., and Ruoff, R.S. (2010) Graphene and graphene oxide: synthesis, properties, and applications. *Adv. Mater.*, **22**, 3906–3924.
5. Laurent, S., Forge, D., Port, M., Roch, A., Robic, C., Vander Elst, L., and Muller, R.N. (2008) Magnetic iron oxide nanoparticles: synthesis, stabilization, vectorization, physicochemical characterizations, and biological applications. *Chem. Rev.*, **108**, 2064–2110.
6. Xu, X.Y., Ray, R., Gu, Y.L., Ploehn, H.J., Gearheart, L., Raker, K., and Scrivens, W.A. (2004) Electrophoretic analysis and purification of fluorescent single-walled carbon nanotube fragments. *J. Am. Chem. Soc.*, **126**, 12736–12737.
7. Sun, Y.P., Zhou, B., Lin, Y., Wang, W., Fernando, K.A.S., Pathak, P., Meziani, M.J., Harruff, B.A., Wang, X., Wang, H.F., Luo, P.J.G., Yang, H., Kose, M.E., Chen, B.L., Veca, L.M., and Xie, S.Y. (2006) Quantum-sized carbon dots for bright and colorful photoluminescence. *J. Am. Chem. Soc.*, **128**, 7756–7757.
8. (a) Liu, H.P., Ye, T., and Mao, C.D. (2007) Fluorescent carbon nanoparticles derived from candle soot. *Angew. Chem. Int. Ed.*, **46**, 6473–6475; (b) Ray, S.C., Saha, A., Jana, N.R., and Sarkar, R. (2009) Fluorescent carbon nanoparticles: synthesis, characterization, and bioimaging application. *J. Phys. Chem. C*, **113**, 18546–18551; (c) Tian, L., Ghosh, D., Chen, W., Pradhan, S., Chang, X., and Chen, S. (2009) Nanosized carbon particles from natural gas soot. *Chem. Mater.*, **21**, 2803–2809.
9. Zhao, Q.L., Zhang, Z.L., Huang, B.H., Peng, J., Zhang, M., and Pang, D.W. (2008) Facile preparation of low cytotoxicity fluorescent carbon nanocrystals by electrooxidation of graphite. *Chem. Commun.*, **44**, 5116–5118.
10. Bourlinos, A.B., Stassinopoulos, A., Anglos, D., Zboril, R., Karakassides, M., and Giannelis, E.P. (2008) Surface functionalized carbogenic quantum dots. *Small*, **4**, 455–458.
11. Zhu, H., Wang, X.L., Li, Y.L., Wang, Z.J., Yang, F., and Yang, X.R. (2009) Microwave synthesis of fluorescent carbon nanoparticles with electrochemiluminescence properties. *Chem. Commun.*, **45**, 5118–5120.
12. Liu, R.L., Wu, D.Q., Liu, S.H., Koynov, K., Knoll, W., and Li, Q. (2009) An aqueous route to multicolor photoluminescent carbon dots using silica spheres as carriers. *Angew. Chem. Int. Ed.*, **48**, 4598–4601.
13. (a) Wu, Z.L., Zhang, P., Gao, M.X., Liu, C.F., Wang, W., Leng, F., and Huang, C.Z. (2013) One-pot hydrothermal synthesis of highly luminescent nitrogen-doped amphoteric carbon dots for bioimaging from Bombyx mori silk–natural proteins. *J. Mater. Chem. B*, **1**, 2868–2873; (b) Wang, Q., Huang, X., Long, Y., Wang, X., Zhang, H., Zhu, R., Liang, L., Teng, P., and Zheng, H. (2013) Hollow luminescent carbon dots for drug delivery. *Carbon*, **59**, 192–199; (c) Sun, D., Ban, R., Zhang, P.H., Wu, G.H., Zhang, J.R., and Zhu, J.J. (2013) Hair fiber as a precursor for synthesizing of sulfur-and nitrogen-co-doped carbon dots with tunable luminescence properties. *Carbon*, **64**, 424–434; (d) Liang, Q., Ma, W., Shi, Y., Li, Z., and Yang, X. (2013) Easy synthesis of highly fluorescent carbon quantum dots from gelatin and their luminescent properties and applications. *Carbon*, **60**, 421–428; (e) Lai, C.W., Hsiao, Y.H., Peng, Y.K., and Chou, P.T. (2012) Facile synthesis of highly emissive carbon dots from pyrolysis of glycerol; gram scale production of carbon dots/mSiO_2 for cell imaging

and drug release. *J. Mater. Chem.*, **22**, 14403–14409; (f) Liu, C., Zhang, P., Zhai, X., Tian, F., Li, W., Yang, J., Liu, Y., Wang, H., Wang, W., and Liu, W. (2012) Nano-carrier for gene delivery and bioimaging based on carbon dots with PEI-passivation enhanced fluorescence. *Biomaterials*, **33**, 3604–3613; (g) Yang, Y.H., Cui, J.H., Zheng, M.T., Hu, C.F., Tan, S.Z., Xiao, Y., Yang, Q., and Liu, Y.L. (2012) One-step synthesis of amino-functionalized fluorescent carbon nanoparticles by hydrothermal carbonization of chitosan. *Chem. Commun.*, **48**, 380–382; (h) Chen, B., Li, F., Li, S., Weng, W., Guo, H., Guo, T., Zhang, X., Chen, Y., Huang, T., Hong, X., You, S., Lin, Y., Zeng, K., and Chen, S. (2013) Large scale synthesis of photoluminescent carbon nanodots and their application for bioimaging. *Nanoscale*, **5**, 1967–1971.

14. (a) Palashuddin Sk, M., Jaiswal, A., Paul, A., Ghosh, S.S., and Chattopadhyay, A. (2012) Presence of amorphous carbon nanoparticles in food caramels. *Sci. Rep.*, **2**, 383–387; (b) Wu, L., Luderer, M., Yang, X., Swain, C., Zhang, H., Nelson, K., Stacy, A.J., Shen, B., Lanza, G.M., and Pan, D. (2013) Surface passivation of carbon nanoparticles with branched macromolecules influences near infrared bioimaging. *Theranostics*, **3**, 677–686; (c) Yin, B., Deng, J., Peng, X., Long, Q., Zhao, J., Lu, Q., Chen, Q., Li, H., Tang, H., Zhang, Y., and Yao, S. (2013) Green synthesis of carbon dots with down-and up-conversion fluorescent properties for sensitive detection of hypochlorite with a dual-readout assay. *Analyst*, **138**, 6551–6557; (d) Krysmann, M.J., Kelarakis, A., and Giannelis, E.P. (2012) Photoluminescent carbogenic nanoparticles directly derived from crude biomass. *Green Chem.*, **14**, 3141–3145; (e) Zhu, L., Yin, Y., Wang, C.F., and Chen, S. (2013) Plant leaf-derived fluorescent carbon dots for sensing, patterning and coding. *J. Mater. Chem. C*, **1**, 4925–4932; (f) Wei, J., Shen, J., Zhang, X., Guo, S., Pan, J., Hou, X., Zhang, H., Wang, L., and Feng, B. (2013) Simple one-step synthesis of water-soluble fluorescent carbon dots derived from paper ash. *RSC Adv.*, **3**, 13119–13122.

15. Gao, X., Cui, Y., Levenson, R.M., Chung, L.M.K., and Nie, S. (2004) *In vivo* cancer targeting and imaging with semiconductor quantum dots. *Nat. Biotechnol.*, **22**, 969–976.

16. Su, Y.Y., He, H., Lu, H.T., Sai, L.M., Li, Q.N., Li, W.X., Wang, L.H., Shen, P.P., Huang, Q., and Fan, C.H. (2009) The cytotoxicity of cadmium based, aqueous phase–synthesized, quantum dots and its modulation by surface coating. *Biomaterials*, **30**, 19–25.

17. (a) He, Y. and Su, Y.Y. (2014) *Silicon Nano-Biotechnology*, Springer, Berlin; (b) Park, J.H., Gu, L., Von Maltzahn, G., Ruoslahti, E., Bhatia, S.N., and Sailor, M.J. (2009) Biodegradable luminescent porous silicon nanoparticles for *in vivo* applications. *Nat. Mater.*, **8**, 331–336.

18. Sharifi, S., Behzadi, S., Laurent, S., Forrest, M.L., Stroeve, P., and Mahmoudi, M. (2012) Toxicity of nanomaterials. *Chem. Soc. Rev.*, **41**, 2323–2343.

19. Elsaesser, A. and Howard, C.V. (2012) Toxicology of nanoparticles. *Adv. Drug Delivery Rev.*, **64**, 129–137.

20. Yang, S.T., Wang, X., Wang, H.F., Lu, F.S., Luo, P.G., Cao, L., Meziani, M.J., Liu, J.H., Liu, Y.F., Chen, M., Huang, Y.P., and Sun, Y.P. (2009) Carbon dots as nontoxic and high-performance fluorescence imaging agents. *J. Phys. Chem. C*, **113**, 18110–18114.

21. Tao, H.Q., Yang, K., Ma, Z., Wan, J.M., Zhang, Y.J., Kang, Z.H., and Liu, Z. (2011) *In vivo* NIR fluorescence imaging, biodistribution, and toxicology of photoluminescent carbon dots produced from carbon nanotubes and graphite. *Small*, **8**, 281–290.

22. Huang, X., Zhang, F., Zhu, L., Choi, K.Y., Guo, N., Guo, J., Tackett, K., Anilkumar, P., Liu, G., Quan, Q., Choi, H.S., Niu, G., Sun, Y.P., Lee, S., and Chen, X.Y. (2013) Effect of injection routes on the biodistribution, clearance, and tumor uptake of carbon dots. *ACS Nano*, **7**, 5684–5693.

23. Chong, Y., Maa, Y.F., Shen, H., Tu, X.L., Zhou, X., Xu, J.Y., Dai, J.W., Fan, S.J., and Zhang, Z.J. (2014) The in vitro and

in vivo toxicity of graphene quantum dots. *Biomaterials*, **35**, 5041–5048.

24. (a) Nurunnabi, M., Khatun, Z., Huh, K.M., Park, S.Y., Lee, D.Y., Cho, K.J., and Lee, Y.K. (2013) *In vivo* biodistribution and toxicology of carboxylated graphene quantum dots. *ACS Nano*, **7**, 6858–6867; (b) Nurunnabi, M., Khatun, Z., Nafiujjaman, M., Lee, D.G., and Lee, Y.K. (2013) Surface coating of graphene quantum dots using mussel-inspired polydopamine for biomedical optical imaging. *ACS Appl. Mater. Interfaces*, **5**, 8246–8253.
25. Goh, E.J., Kim, K.S., Kim, Y.R., Jung, H.S., Beack, S., Kong, W.H., Scarcelli, G., Yun, S.H., and Hahn, S.K. (2012) Bioimaging of hyaluronic acid derivatives using nanosized carbon dots. *Biomacromolecules*, **13**, 2554–2561.
26. Li, L.L., Ji, J., Fei, R., Wang, C.Z., Lu, Q., Zhang, J.R., Jiang, L.P., and Zhu, J.J. (2012) A facile microwave avenue to electrochemiluminescent two-color graphene quantum dots. *Adv. Funct. Mater.*, **22**, 2971–2979.
27. Tang, L.B., Ji, R.B., Cao, X.K., Lin, J.Y., Jiang, H.X., Li, X.M., Teng, K.S., Luk, C.M., Zeng, S.J., Hao, J.H., and Lau, S.P. (2012) Deep ultraviolet photoluminescence of water-soluble self-passivated graphene quantum dots. *ACS Nano*, **6**, 5102–5110.
28. Qu, S.N., Wang, X.Y., Lu, Q.P., Liu, X.Y., and Wang, L.J. (2012) A biocompatible fluorescent ink based on water-soluble luminescent carbon nanodots. *Angew. Chem. Int. Ed.*, **51**, 12215–12218.
29. Wang, J., Peng, F., Lu, Y.M., Zhong, Y.L., Wang, S.Y., Ji, X.Y., Zhou, Y.F., Yang, L., Xu, M.F., Su, Y.Y., Liao, L.S., and He, Y. (2015) Large-scale green synthesis of fluorescent carbon nanodots and their use in optics applications. *Adv. Opt. Mater.*, **3**, 103–111.
30. Pan, D.Y., Zhang, J.C., Li, Z., and Wu, M.H. (2010) Hydrothermal route for cutting graphene sheets into blue-luminescent graphene quantum dots. *Adv. Mater.*, **22**, 734–738.
31. Liu, S., Tian, J.Q., Wang, L., Zhang, Y.W., Qin, X.Y., Luo, Y.L., Asiri, A.M., Al-Youbi, A.O., and Sun, X.P. (2012) Hydrothermal treatment of grass: a low-cost, green route to nitrogen-doped, carbon-rich, photoluminescent polymer nanodots as an effective fluorescent sensing platform for label-free detection of Cu(II) ions. *Adv. Mater.*, **24**, 2037–2041.
32. (a) Zhu, S.J., Meng, Q.N., Wang, L., Zhang, J.H., Song, Y.B., Jin, H., Zhang, K., Sun, H.C., Wang, H.Y., and Yang, B. (2013) Highly photoluminescent carbon dots for multicolor patterning, sensors, and bioimaging. *Angew. Chem. Int. Ed.*, **52**, 3953–3957; (b) Song, Y.B., Zhu, S.J., Xiang, S.Y., Zhao, X.H., Zhang, J.H., Zhang, H., Fu, Y., and Yang, B. (2014) Investigation into the fluorescence quenching behaviors and applications of carbon dots. *Nanoscale*, **6**, 4676–4682.
33. Li, W., Zhang, Z.H., Kong, B., Feng, S.S., Wang, J.X., Wang, L.Z., Yang, J.P., Zhang, F., Wu, P.Y., and Zhao, D.Y. (2013) Simple and green synthesis of nitrogen-doped photoluminescent carbonaceous nanospheres for bioimaging. *Angew. Chem. Int. Ed.*, **52**, 8151–8155.
34. Li, Y., Zhao, Y., Cheng, H., Hu, Y., Shi, G., Dai, L., and Qu, L. (2012) Nitrogen-doped graphene quantum dots with oxygen-rich functional groups. *J. Am. Chem. Soc.*, **134**, 15–18.
35. Bao, L., Zhang, Z.L., Tian, Z.Q., Zhang, L., Liu, C., Lin, Y., Qi, B.P., and Pang, D.W. (2011) Electrochemical tuning of luminescent carbon nanodots: from preparation to luminescence mechanism. *Adv. Mater.*, **23**, 5801–5806.
36. Shinde, D.B. and Pillai, V.K. (2013) Electrochemical resolution of multiple redox events for graphene quantum dots. *Angew. Chem. Int. Ed.*, **52**, 2482–2485.
37. Wang, C.I., Wu, W.C., Periasamya, A.P., and Chang, H.T. (2014) Electrochemical synthesis of photoluminescent carbon nanodots from glycine for highly sensitive detection of hemoglobin. *Green Chem.*, **16**, 2509–2514.
38. Fang, Y.X., Guo, S.J., Li, D., Zhu, C.Z., Ren, W., Dong, S.J., and Wang, E.K. (2012) Easy synthesis and imaging applications of cross-linked green fluorescent hollow carbon nanoparticles. *ACS Nano*, **6**, 400–409.

39. Peng, J., Gao, W., Gupta, B.P.K., Liu, Z., Romero-Aburto, R., Ge, L.H., Song, L., Alemany, L.B., Zhan, X.B., Gao, G.H., Vithayathil, S.A., Kaipparettu, B.A., Marti, A.A., Hayashi, T., Zhu, J.J., and Ajayan, P.M. (2012) Graphene quantum dots derived from carbon fibers. *Nano Lett.*, **12**, 844–849.
40. Li, Y.S., Zhong, X.X., Rider, A.E., Furmand, S.A., and Ostrikov, K.K. (2014) Fast, energy-efficient synthesis of luminescent carbon quantum dots. *Green Chem.*, **16**, 2566–2570.
41. (a) Bendicho, C., Calle, I.D.L., Pena, F., Costas, M., Cabaleiro, N., and Lavilla, I. (2012) Ultrasound-assisted pretreatment of solid samples in the context of green analytical chemistry. *TrAC, Trends Anal. Chem.*, **31**, 50–60; (b) Capelo-Martínez, J.L. (2009) *Ultrasound in Chemistry*, Wiley-VCH Verlag GmbH, Weinheim.
42. (a) Li, H.T., He, X.D., Liu, Y., Huang, H., Lian, S., Lee, S.T., and Kang, Z.H. (2011) One-step ultrasonic synthesis of water-soluble carbon nanoparticles with excellent photoluminescent properties. *Carbon*, **49**, 605–609; (b) Li, H.T., He, X.D., Liu, Y., Yu, H., Kang, Z.H., and Lee, S.T. (2011) Synthesis of fluorescent carbon nanoparticles directly from active carbon via a one-step ultrasonic treatment. *Mater. Res. Bull.*, **46**, 147–151; (c) Ma, Z., Ming, H., Huang, H., Liu, Y., and Kang, Z. (2012) One-step ultrasonic synthesis of fluorescent N-doped carbon dots from glucose and their visible-light sensitive photocatalytic ability. *New J. Chem.*, **36**, 861–864.
43. Zhuo, S., Shao, M., and Lee, S.T. (2012) Upconversion and downconversion fluorescent graphene quantum dots: ultrasonic preparation and photocatalysis. *ACS Nano*, **6**, 1059–1064.
44. Ye, R.Q., Xiang, C.S., Lin, J., Peng, Z.W., Huang, K.W., Yan, Z., Cook, N.P., Samuel, E.L.G., Hwang, C.C., Ruan, G.D., Ceriotti, G., Raji, A.R.O., Martı, A.A., and Tour, J.M. (2013) Coal as an abundant source of graphene quantum dots. *Nat. Commun.*, **4**, 2943–2948.
45. Zhu, Y.H., Wang, G.F., Jiang, H., Chena, L., and Zhang, X.J. (2015) One-step ultrasonic synthesis of graphene quantum dots with high quantum yield and their application in sensing alkaline phosphatase. *Chem. Commun.*, **51**, 948–951.
46. Doicrycz, S.J. and Suslick, K. (1990) Interparticle collisions driven by ultrasound. *Science*, **247**, 1067–1069.
47. Wang, J., Wang, C.F., and Chen, S. (2012) Amphiphilic egg-derived carbon dots: rapid plasma fabrication, pyrolysis process, and multicolor printing patterns. *Angew. Chem. Int. Ed.*, **51**, 9297–9301.
48. Kim, J.H. and Suh, J.S. (2014) Size-controllable and low-cost fabrication of graphene quantum dots using thermal plasma jet. *ACS Nano*, **8**, 4190–4196.
49. Russo, P., Hu, A.M., Compagnini, G., Duley, W.W., and Zhou, N.Y. (2014) Femtosecond laser ablation of highly oriented pyrolytic graphite: a green route for large-scale production of porous graphene and graphene quantum dots. *Nanoscale*, **6**, 2381–2389.
50. Kwon, W. and Rhee, S.W. (2012) Facile synthesis of graphitic carbon quantum dots with size tunability and uniformity using reverse micelles. *Chem. Commun.*, **48**, 5256–5258.
51. Liu, S.S., Wang, C.F., Li, C.X., Wang, J., Mao, L.H., and Chen, S. (2014) Hair-derived carbon dots toward versatile multidimensional fluorescent materials. *J. Mater. Chem. C*, **2**, 6477–6483.
52. (a) Leblond, F., Davis, S.C., Valdés, P.A., and Poque, B.W. (2010) Pre-clinical whole-body fluorescence imaging: Review of instruments, methods and applications. *J. Photochem. Photobiol., B*, **98**, 77–94; (b) Kondepati, V.R., Heise, H.M., and Backhaus, J. (2008) Recent applications of near-infrared spectroscopy in cancer diagnosis and therapy. *J. Anal. Bioanal. Chem.*, **390**, 125–139; (c) Kircher, M.F., Gambhir, S.S., and Grimm, J. (2011) Noninvasive cell-tracking methods. *Nat. Rev. Clin. Oncol.*, **8**, 677–688.
53. (a) Tsien, R.Y. (1998) The green fluorescent protein. *Annu. Rev. Biochem.*, **67**, 509–544; (b) van de Linde, S., Heilemann, M., and Sauer, M. (2012) Live-cell super-resolution imaging with synthetic fluorophores. *Annu. Rev. Phys. Chem.*, **63**, 519–540.

54. Jaiswal, J.K., Mattoussi, H., Mauro, J.M., and Simon, S.M. (2002) Long-term multiple color imaging of live cells using quantum dot bioconjugates. *Nat. Biotechnol.*, **21**, 47–51.
55. (a) He, Y., Lu, H.T., Su, Y.Y., Sai, L.M., Hu, M., and Fan, C.H. (2011) Ultra-photostable, non-cytotoxic, and highly fluorescent quantum nanospheres for long-term, high-specificity cell imaging. *Biomaterials*, **32**, 2133–2140; (b) He, Y., Lu, H.T., Sai, L.M., Su, Y.Y., Hu, M., Fan, C.H., Huang, W., and Wang, L.H. (2008) Microwave synthesis of water-dispersed CdTe/CdS/ZnS core-shell-shell quantum dots with excellent photostability and biocompatibility. *Adv. Mater.*, **20**, 3416–3421; (c) He, Y., Zhong, Y.L., Su, Y.Y., Lu, Y.M., Jiang, Z.Y., Peng, F., Xu, T.T., Su, S., Huang, Q., Fan, C.H., and Lee, S.T. (2011) Water-dispersed near-infrared-emitting quantum dots of ultrasmall sizes for in vitro and in vivo imaging. *Angew. Chem. Int. Ed.*, **50**, 5695–5698; (d) Lu, Y.M., Su, Y.Y., Zhou, Y.F., Wang, J., Peng, F., Zhong, Y.L., and He, Y. (2013) In vivo behavior of near infrared-emitting quantum dots. *Biomaterials*, **34**, 4302–4308; (e) Wang, J., Lu, Y.M., Peng, F., Zhong, Y.L., Zhou, Y.F., Jiang, X.X., Su, Y.Y., and He, Y. (2013) Photostable water-dispersible NIR-emitting CdTe/CdS/ZnS core–shell–shell quantum dots for high-resolution tumor targeting. *Biomaterials*, **34**, 9509–9518.
56. (a) Derfus, A.M., Chan, W.C.W., and Bhatia, S.N. (2004) Probing the cytotoxicity of semiconductor quantum dots. *Nano Lett.*, **4**, 11–18; (b) Kirchner, C., Liedl, T., Kudera, S., Pellegrino, T., Munoz-Javier, A., Gaub, H.E., Stolzle, S., Fertig, N., and Parak, W.J. (2005) Cytotoxicity of colloidal CdSe and CdSe/ZnS nanoparticles. *Nano Lett.*, **5**, 331–338; (c) Jan, E., Byrne, S.J., Cuddihy, M., Davies, A.M., Volkov, Y., Gun'ko, Y.K., and Kotov, N.A. (2008) High-content screening as a universal tool for fingerprinting of cytotoxicity of nanoparticles. *ACS Nano*, **2**, 928–938; (d) Hauck, T.S., Anderson, R.E., Fischer, H.C., Newbigging, S., and Chan, W.C.W. (2010) In vivo quantum dot toxicity assessment. *Small*, **6**, 138–144; (e) Su, Y.Y., Hu, M., Fan, C.H., He, Y., Li, Q., Li, W., Wang, L.H., Shen, P., and Huang, Q. (2010) The cytotoxicity of CdTe quantum dots and the relative contributions from released cadmium ions and nanoparticle properties. *Biomaterials*, **31**, 4829–4834; (f) Chen, N., He, Y., Su, Y.Y., Li, X.M., Huang, Q., Wang, H.F., Zhang, X.Z., Tai, R.Z., and Fan, C.H. (2012) The cytotoxicity of cadmium-based quantum dots. *Biomaterials*, **33**, 1238–1244.
57. Wang, F. and Liu, X. (2009) Recent advances in the chemistry of lanthanide-doped upconversion nanocrystals. *Chem. Soc. Rev.*, **38**, 976–989.
58. Godin, B., Gu, J., Serda, R.E., Bhavane, R., Tasciotti, E., Chiappini, C., Liu, X., Tanaka, T., Decuzzi, P., and Ferrari, M. (2010) Tailoring the degradation kinetics of mesoporous silicon structures through PEGylation. *J. Biomed. Mater. Res. Part A*, **94**, 1236–1243.
59. Mochalin, V.N., Shenderova, O., and Ho, D. (2011) The properties and applications of nanodiamonds. *Nat. Nanotechnol.*, **7**, 11–23.
60. Baker, S.N. and Baker, G.A. (2010) Luminescent carbon nanodots: emergent nanolights. *Angew. Chem. Int. Ed.*, **49**, 6726–6744.
61. Yang, S.T., Cao, L., Luo, P.G., Lu, F.S., Wang, X., Wang, H.F., Meziani, M.J., Liu, Y.F., Qi, G., and Sun, Y.P. (2009) Carbon dots for optical imaging in vivo. *J. Am. Chem. Soc.*, **131**, 11308–11309.
62. Kong, W.Q., Liu, R.H., Li, H., Liu, J., Huang, H., Liu, Y., and Kang, Z.H. (2014) High-bright fluorescent carbon dots and their application in selective nucleoli staining. *J. Mater. Chem. B*, **2**, 5077–5082.
63. Leménager, G., Luca, E.D., Sun, Y.P., and Pomp, P.P. (2014) Super-resolution fluorescence imaging of biocompatible carbon dots. *Nanoscale*, **6**, 8617–8623.
64. (a) Zhu, S.J., Zhang, J.H., Qiao, C., Tang, S.J., Li, Y., Yuan, W., Li, B., Tian, L., Liu, F., Hu, R., Gao, H., Wei, H., Zhang, H., Sun, H., and Yang, B. (2011) Strongly green-photoluminescent graphene quantum dots for bioimaging applications. *Chem. Commun.*, **47**, 6858–6860;

(b) Zhu, S.J., Zhang, J.H., Tang, S.J., Qiao, C., Wang, L., Wang, H., Liu, X., Li, B., Li, Y., Yu, W., Wang, X., Sun, H., and Yang, B. (2012) Surface chemistry routes to modulate the photoluminescence of graphene quantum dots: from fluorescence mechanism to up-conversion bioimaging applications. *Adv. Funct. Mater.*, **22**, 4732–4740.

65. Liu, Q., Guo, B.D., Rao, Z.Y., Zhang, B.H., and Gong, J.R. (2013) Strong two-photon-induced fluorescence from photostable, biocompatible nitrogen-doped graphene quantum dots for cellular and deep-tissue imaging. *Nano Lett.*, **13**, 2436–2441.
66. Zhu, A., Qu, Q., Shao, X., Kong, B., and Tian, Y. (2012) Carbon-dot-based dual-emission nanohybrid produces a ratiometric fluorescent sensor for in vivo imaging of cellular copper ions. *Angew. Chem. Int. Ed.*, **51**, 7185–7189.
67. Kong, B., Zhu, A., Ding, C., Zhao, X., Li, B., and Tian, Y. (2012) Carbon dot-based inorganic–organic nanosystem for two-photon imaging and biosensing of pH variation in living cells and tissues. *Adv. Mater.*, **24**, 5844–5848.
68. Ko, H.Y., Chang, Y.W., Paramasivam, G., Jeong, M.S., Cho, S.J., and Kim, S. (2013) *In vivo* imaging of tumour bearing near-infrared fluorescence-emitting carbon nanodots derived from tire soot. *Chem. Commun.*, **49**, 10290.
69. Huang, P., Lin, J., Wang, X.S., Wang, Z., Zhang, C.L., He, M., Wang, K., Chen, F., Li, Z.M., Shen, G.X., Cui, D.X., and Chen, X.Y. (2012) Light-triggered theranostics based on photosensitizer-conjugated carbon dots for simultaneous enhanced fluorescence imaging and photodynamic therapy. *Adv. Mater.*, **24**, 5104–5110.
70. Long, T.C., Saleh, N., Tilton, B.D., Lowry, G.V., and Veronesi, B. (2006) Titanium dioxide (P25) produces reactive oxygen species in immortalized brain microglia (BV2): implications for nanoparticle neurotoxicity. *Environ. Sci. Technol.*, **40**, 4346–4352.
71. Donaldson, K., Tran, L., Jimenez, L.A., Duffin, R., Newby, D.E., Mills, N., MacNee, W., and Stone, V. (2005) Combustion-derived nanoparticles: a review of their toxicology following inhalation exposure. *Part. Fibre Toxicol.*, **2**, 10.
72. Lewinski, N., Colvin, V., and Drezek, R. (2008) Cytotoxicity of nanoparticles. *Small*, **4**, 26–49.
73. Fadeel, B. and Garcia-Bennett, A.E. (2010) Better safe than sorry: understanding the toxicological properties of inorganic nanoparticles manufactured for biomedical applications. *Adv. Drug Delivery Rev.*, **62**, 362–374.
74. Aillon, K.L., Xie, Y., El-Gendy, N., Berkland, C.J., and Forrest, M.L. (2009) Effects of nanomaterial physicochemical properties on in vivo toxicity. *Adv. Drug Delivery Rev.*, **61**, 457–466.
75. Lu, Y.M., Zhong, Y.L., Wang, J., Su, Y.Y., Peng, F., Zhou, Y.F., Jiang, X.X., and He, Y. (2013) Aqueous synthesized near-infrared-emitting quantum dots for RGD-based *in vivo* active tumour targeting. *Nanotechnology*, **24**, 135101.
76. Winnik, F.M. and Maysinger, D. (2012) Quantum dot cytotoxicity and ways to reduce it. *Acc. Chem. Res.*, **46**, 672–680.
77. Andón, F.T. and Fadeel, B. (2013) Programmed cell death: molecular mechanisms and implications for safety assessment of nanomaterials. *Acc. Chem. Res.*, **46**, 733–742.
78. (a) Hsu, P.C., Chen, P.C., Ou, C.M., Chang, H.Y., and Chang, H.T. (2013) Extremely high inhibition activity of photoluminescent carbon nanodots toward cancer cells. *J. Mater. Chem. B*, **1**, 1774–1781; (b) Li, C.L., Ou, C.M., Huang, C.C., Wu, W.C., Chen, Y.P., Lin, T.E., Ho, L.C., Wang, C.W., Shi, C.C., Zhou, H.C., Lee, Y.C., Tzeng, W.F., Chiou, T.J., Chu, S.T., Cangm, J., and Chang, H.T. (2014) Carbon dots prepared from ginger exhibiting efficient inhibition of human hepatocellular carcinoma cells. *J. Mater. Chem. B*, **2**, 4564–4571.
79. Li, Y., Hu, Y., Zhao, Y., Shi, G., Deng, L., Hou, Y., and Qu, L. (2011) An electrochemical avenue to green-luminescent graphene quantum dots as potential electron-acceptors for photovoltaics. *Adv. Mater.*, **23**, 776–780.
80. Chang, Y., Yang, S.T., Liu, J.H., Dong, E., Wang, Y., Cao, A., Liu, Y.F., and Wang,

H.F. (2011) In vitro toxicity evaluation of graphene oxide on A549 cells. *Toxicol. Lett.*, **200**, 201–210.

81. (a) Li, Y., Yuan, H., von dem Bussche, A., Creighton, M., Hurt, R.H., Kane, A.B., and Gao, H.J. (2013) Graphene microsheets enter cells through spontaneous membrane penetration at edge asperities and corner sites. *Proc. Natl. Acad. Sci. U.S.A.*, **110**, 12295–12300; (b) Tu, Y., Lv, M., Xiu, P., Huynh, T., Zhang, M., Castelli, M., Liu, Z.R., Huang, Q., Fan, C.H., Fang, H.P., and Zhou, R.H. (2013) Destructive extraction of phospholipids from Escherichia coli membranes by graphene nanosheets. *Nat. Nanotechnol.*, **8**, 594–601; (c) Wang, A., Pu, K., Dong, B., Liu, Y., Zhang, L., Zhang, Z., Duan, W., and Zhu, Y.M. (2013) Role of surface charge and oxidative stress in cytotoxicity and genotoxicity of graphene oxide towards human lung fibroblast cells. *J. Appl. Toxicol.*, **33**, 1156–1164.

82. Shang, W.H., Zhang, X.Y., Zhang, M., Fan, Z.T., Sun, Y., Han, M., and Fan, L.Z. (2014) Quantitative and real-time effects of carbon quantum dots on single living HeLa cell membrane permeability. *Nanoscale*, **6**, 5116–5120.

83. Yong, K.T., Indrajit, R., Hong, D., Bergey, E.J., and Prasad, P.N. (2009) Biocompatible near-infrared quantum dots as ultrasensitive probes for long-term in vivo imaging applications. *Small*, **5**, 1997–2004.

84. Chauhan, V.P., Popovic, Z., Chen, O., Cui, J., Fukumura, D., Bawendi, M.G., and Jain, R.K. (2011) Fluorescent nanorods and nanospheres for real-time in vivo probing of nanoparticle shape-dependent tumor penetration. *Angew. Chem. Int. Ed.*, **50**, 11417–11420.

15
Transport in the Environment and Ecotoxicity of Carbon Nanomaterials

Yingying Xu and Chunying Chen

15.1
Introduction

Carbon nanomaterials have become the most common nanoproducts according to "The Nanotechnology Consumer Products Inventory." The production, use, and disposal of carbon nanomaterials will inevitably lead to their release into the atmosphere, surface water, soil, and groundwater [1]. Carbon nanomaterials can enter the environment through intentional or unintentional releases. When they enter the environment, nanoparticles may transform physically and chemically by, for example, oxidation, photochemical transformation, dissolution and precipitation, adsorption, and biodegradation. The transport and fate of the released nanoparticles in the environment can eventually affect their ecotoxicity [2].

Ecotoxicity deals with how chemicals affect the environment and the organisms living in it. With increasing attention paid to the potential environmental risks of nanomaterials, Kahru and Dubourguier named the next decade of ecotoxicology as "the (eco)toxicogenomical and nano(eco)toxicological 2010s" [3]. The ecotoxicity of carbon nanomaterials has been investigated in both aqueous and terrestrial species. Studies indicate that carbon nanomaterials can enter the food chain and stress the ecological system.

Many possible mechanisms for the ecotoxicity of carbon nanomaterials have been proposed, which include damage to membrane integrity, protein destabilization and oxidation, cell damage via reactive oxygen species (ROS), and release of metal ions [2]. The ecotoxicity of carbon nanomaterials can be influenced by their intrinsic physicochemical properties such as shape, surface area, surface chemistry, charge, and aggregation. When nanomaterials are released into the environment, some environmental factors may also influence their toxicity, such as pH, ionic strength, and the presence of natural organic matter (NOM). In this chapter, we review the fate and transformation of carbon nanomaterials including fullerene, carbon nanotubes (CNTs), and graphene in the environment. We will also discuss the ecotoxicity of carbon nanomaterials to microorganisms, animals, and plants.

Biomedical Applications and Toxicology of Carbon Nanomaterials, First Edition.
Edited by Chunying Chen and Haifang Wang.

15.2
Transport of Carbon Nanomaterials in the Environment

15.2.1
Entry of Carbon Nanomaterials into the Environment

With increase in the production of carbon nanomaterials, their release into the environment and their potential ecotoxicity effects have been increasing concerns. However, nanoparticles can be modified by the components in the environment, which can change their physicochemical properties, such as the size, surface charge, and reactivity. Therefore, it is first necessary to determine the transport and transformation of nanomaterials in the environment.

Carbon nanomaterials can enter the environment through intentional releases or unintentional releases such as atmospheric emissions and waste streams from production facilities. Intentional release of nanomaterials includes their use to remediate contaminated soils or groundwater [4]. Moreover, carbon nanomaterials contained in various products enter the environment in proportion to their use [5]. The emitted carbon nanomaterials will ultimately deposit on land and surface water bodies. The deposited particles may further contaminate the soil and migrate into groundwater. If they are not eliminated by wastewater treatment processes, carbon nanomaterials may flow directly into natural waters from domestic and industrial wastewater [6]. Carbon nanoparticles may be released into the atmosphere by manufacturing facilities or consumer products during their use [7–9]. The major cross-media transport of carbon nanomaterials in the environment might be through deposition from the atmosphere to the surface [10]. It is also possible to be suspended from aqueous and terrestrial systems by waves, bubbles, and wind. Nanoparticles in wastewater effluents, direct discharges, or accidental spillages can be transported to aquatic systems by wind or rainwater runoff.

15.2.2
Fate and Transformation in the Environment

Carbon nanomaterials released into the environment will interact with the environmental media such as water, soil, light, and microorganisms, and undergo physical and chemical transformations (Figure 15.1). These interactions may change the physicochemical properties, agglomeration, and mobility of the nanomaterials, which further affect their ecotoxicological effects. Several important alteration and transformation processes can act on engineered carbon nanomaterials, such as oxidation, photochemical transformation, dissolution and precipitation, adsorption, and biodegradation.

15.2.2.1
Oxidation

Oxidation is an important process that determines the environmental effects of carbon nanomaterials, because it could increase their solubility in aqueous

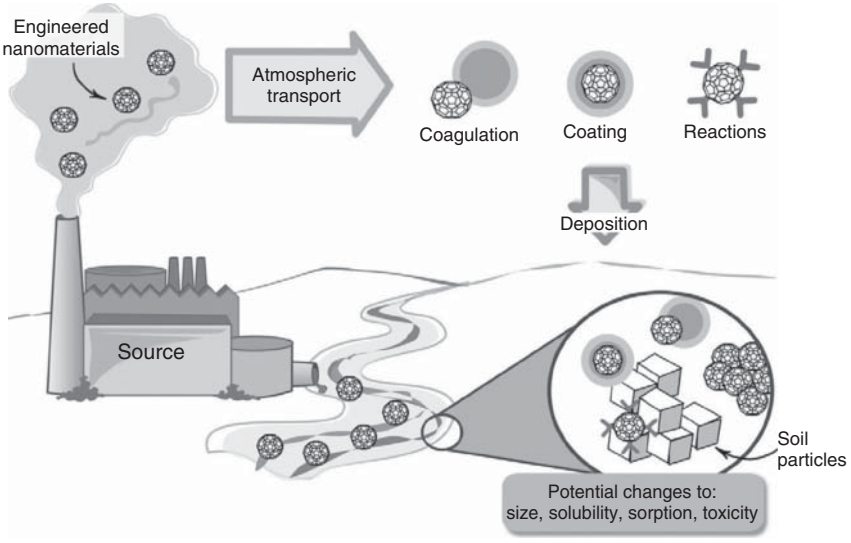

Figure 15.1 Fate and transformation of carbon nanomaterials in the environment, depicted here by C_{60} fullerene. The nanoparticles may be discharged directly to a natural waterway, or may deposit after having been emitted into the atmosphere. A variety of atmospheric transformations may occur between emission and deposition. These transformations could alter the physicochemical properties and further ecotoxicological effects. (Adapted with permission from [10]. ©2010 American Society of Agronomy, Crop Science Society of America, and Soil Science Society of America.)

solutions. Evidence suggests that carbon nanomaterials may be oxidized by hydroxyl radicals, ozone, and other oxidants, which lead to the formation of oxides, hydroxyls, carboxylic acid, and other functionalities [11]. The oxidation reaction can make the nanoparticles more hydrophilic. Carbon nanomaterials can be oxidized under harsh conditions such as strong acid or involving an organic solvent. However, similar reactions are difficult in the natural environment. Carbonaceous nanoparticles in the natural environment will be present in aqueous solutions or in the atmosphere but not in organic solvents.

Fullerenes exhibit higher oxidation reactivity than CNTs and graphene. The oxidation reaction of fullerene can occur under mild conditions and generate functional groups containing oxygen. Hamano *et al.* reported the oxidation of C_{60} by cytochrome *P450* chemical model systems in 1995 [12]. A simulated P450 enzymatic reaction system was constructed by using tetraphenylporphine iron (III) chloride and tetraphenylporphine manganese(III) chloride as catalysts and iodobenzene oxide as oxidizing agent. This system can oxidize C_{60} to 1,2-C_{60} epoxy. This reaction might be one of the biological transformation patterns of fullerene, since the P450 enzyme is an important detoxification enzyme in many organisms. Extended mixing in water can make fullerenes and its aggregates negatively charged and introduce hydroxyl groups [13–15]. The hydrated form the fullerene (hydroxylated fullerenes) is also called fullerenol. Kokubo *et al.* [16] obtained water-soluble fullerenol by heating H_2O_2 in the presence of Fe(II).

This Fenton reaction can generate OH radicals, which is responsible for C_{60} oxidation. Fullerene can also be oxidized by dissolved ozone in the aqueous phase. Aqueous C_{60} colloids can be oxidized readily on exposure to an O_2/O_3 gas stream. Product analyses indicate highly oxidized fullerene with an average of nearly 29 oxygen additions per molecule, arranged in repeating hydroxyl and hemiketal (R–O–C–OH) functionalities [17].

CNTs can be oxidized by free radicals such as Fenton's reagent and ozone. Fenton's reagent is effective in introducing carboxyl and hydroxyl groups on the surface of CNTs [18]. Oxidation of single-walled carbon nanotubes (SWCNTs) with ozone can generate ester and quinone groups [19]. Further studies indicate the formation of hydroxyl and carboxyl groups on the surface of CNTs by ozone oxidation [20]. Aqueous solutions of SWCNTs exposed to 5% ozone results in the formation of hydroxyl, carbonyl, and carboxyl groups, as well as increased particle stability in solution, decreased particle diameter, and increased zeta potential [21]. Carbonyl and epoxide groups could also be formed on SWCNT sidewalls [22]. Cataldo *et al.* reported that O_3 exposure leads to the formation of a variety of ketonic groups on multiwalled carbon nanotubes (MWCNTs) [23].

Graphene is also chemically inert and difficult to be oxidized. Oxidation of graphene needs highly reactive oxidizing reagents. Similar to that of CNTs, oxidation of graphene in the natural environment is difficult. However, oxidation may occur in some special environments, such as in free-radical reaction, which is one of the main ways of graphene covalent reaction. For instance, Liu *et al.* [24] demonstrated a photochemical reaction between graphene and benzoyl peroxide under light irradiation. Photoexcited graphene can transfer an electron to benzoyl peroxide and induce it to decompose to a phenyl radical, which further introduces spatially localized defects into the graphene basal plane. The oxidation process of carbon nanoparticles occurring in the atmosphere may result in the formation of oxygen-containing groups on the surface, which can further affect their fate in the environment and ecotoxicity.

15.2.2.2 Photochemical Transformation

It has been demonstrated that carbon nanomaterials can undergo direct or indirect photochemical transformation in both water and air. In the photochemical transformation, incident light can induce excitation of carbon nanomaterials and generate free radicals [25]. Photochemical processes may alter the interaction of carbon nanomaterials with the environmental components.

Fullerenes have been found to be susceptible to photolysis in laboratory studies and possibly in the natural aqueous environment. In 1991, Arbogast *et al.* [26] first reported the photochemical behavior of C_{60}. They found that C_{60} dissolved in the organic solvent benzene could generate singlet oxygen ($^1O_2$) under the laser irradiation, and put forward the possibility that C_{60} released into the environment may cause adverse effects to the organisms under light irradiation. Subsequently, Taylor *et al.* [27] confirmed the photochemical degradation of C_{60} in nonpolar organic solvents. Polarity products were produced in the photochemical process.

Lee *et al.* [28, 29] reported that exposure of C_{60} to UV light could produce ROS (OH, $^1O_2$ and $O_2\bullet^-$) in the aqueous phase. Hou and Jafvert characterized the products formed when aqueous C_{60} clusters (nC_{60}) were exposed to natural sunlight. Exposing aqueous C_{60} to sunlight and 300–400 nm lamplight resulted in the production of water-soluble products containing vinyl ether and carbonyl or carboxyl groups, as well as decrease in colloid size and loss of solution color [30]. Aggregation of fullerenes in the aqueous phase reduces the photolysis rate significantly, since oxygen plays an important role in the photochemical process [31]. Therefore, this transformation may be less significant in natural waters. However, in the atmosphere, photolysis may be important for C_{60} aerosols, since aggregation is less likely under typical conditions.

Similar to C_{60}, CNTs contains large delocalized π-bonds. In theory, CNTs also have strong absorption ability and may also undergo photolysis. Savage *et al.* [32] found that MWCNTs film could undergo light-induced oxidation under 240 nm light irradiation. The film reacted with oxygen and generated singlet oxygen. SWCNTs dispersed in an aqueous solution containing certain surfactants became hydroxylated under light irradiation at 254 nm [33]. ROS may be involved in this transformation, since the introduction of molecular oxygen as a radical scavenger suppressed the hydroxylation. MWCNTs can also be oxidized and give ether, epoxy, and carbonate moieties when exposed to UV radiation [34]. Chen and Jafvert [35] studied the photochemical transformation of carboxylated SWCNTs colloidal suspension and detected the generation of ROS . They pointed out that the agglomeration state and surface functional groups of CNTs had a significant impact on the singlet oxygen generation.

15.2.2.3 Dissolution and Precipitation

Carbon nanomaterials may contain certain metal impurities during their synthesis process. These metal impurities can release individual ions that are soluble in water. The solubility of unfunctionalized carbon nanomaterials in water is extremely low because of their highly hydrophobic nature [36]. Aqueous solutions of C_{60} colloids can be prepared by extended mechanical stirring of C_{60} in water [14]. Labille *et al.* [37] reported that fullerene colloids prepared via mechanical stirring consisted of highly polydisperse colloids of diameters 20–500 nm, with both angular and rounded colloid morphologies. Therefore, C_{60} colloids formed in natural aqueous systems might also be polydisperse in size with varying morphologies. Hydroxyl groups can be formed in the surface of fullerene colloids, which can increase the hydrophilicity of fullerene. Labille *et al.* [15] suggested that the formation of hydroxyl groups may also occur in the natural aqueous environment. Hydrophilic functionalized C_{60} fullerenes can also form colloids by extended stirring in water, and these colloids may be more stable in the natural environment due to their hydrophilic functional groups [38].

Unfunctionalized CNTs are very hydrophobic and insoluble in all organic solvents and aqueous solutions [36, 39]. Various hydrophilic functionalizations

have been explored to improve their solubility in water, including noncovalent and covalent ones [40–42]. CNTs can be functionalized with hydrophilic groups by a variety of acids [43]. Oxygen-containing functional groups grafted onto the CNTs surface can promote their colloidal stability, which further influence their fate and transport in aqueous environments.

The agglomeration and dispersion of carbon nanomaterials are affected by the physicochemical conditions of the aqueous environment such as ionic strength and surfactants. Simulation studies indicate that the aggregate size of colloidal C_{60} increases with the increase in ionic strength [44]. Therefore, C_{60} colloids can be destroyed and precipitation can be formed in an electrolyte solution with high concentration. This phenomenon validated the electrostatic stabilization mechanism of the C_{60} colloid, that is, the stability of C_{60} colloid mainly depends on the repulsion between the double electron layers [45]. Studies indicated that stable colloidal solutions of SWCNTs by acid treatment could also form aggregates with the increase of electrolyte concentration [46]. Surfactants in the aqueous environment are beneficial to the dispersion of carbon nanomaterials. Fullerene C_{60} can disperse stably in the micelles formed in the surfactant Triton X-100, in which fullerene molecules exist in the hydrophobic core of the micelles [47]. Anionic, cationic, and non-ionic surfactants can all help CNTs to be suspended stably in aqueous solutions. The surfactant can increase the surface area of CNTs and make them more easily dispersed in the aqueous solution [48].

15.2.2.4 Adsorption

Carbon nanomaterials adsorb dissolved NOMs when enter into the environment. NOMs widely exist in the natural aqueous environment. Interaction between carbon nanomaterials and NOMs may affect their surface properties and, further, their transportation in the environment. Adsorption of NOMs can occur by means of van der Waals attraction, electrostatic interaction, or chemical bonding. Proteins, humic acid, fulvic acid, and tannic acid can weaken the aggregation and settlement of C_{60} colloids, which is due to the steric hindrance and charge stabilization effect [47]. It is reported that the presence of NOMs in an aqueous system can affect the stability, size, and morphology of C_{60} colloid [49]. Chen and Elimelech found that humic acid could affect the properties of C_{60} colloids, and the influence could differ depending on the electrolytic composition of the solution [50].

Dissolved NOMs can improve the stability and migration of CNTs solution. Chappell *et al*. [51] reported that humic substances could stabilize CNTs in aqueous solution, resulting in a reduced average particle diameter and polydisperse particle population. The chemical structure of NOMs influences the stabilizing effect of CNTs. Generally, NOMs containing hydrophobic groups exert increased stabilizing effect compared hydrophilic NOMs [51, 52]. The dissolved NOM can more efficiently stabilize MWCNTs in an aqueous solution compared to the common industrial surfactant sodium dodecyl sulfate [53]. Other NOMs such as

tannic acid, protein, polysaccharides, and other polymers can also increase the solubility of CNTs in aqueous solution through noncovalent absorption [54, 55].

15.2.2.5

Biodegradation

Biodegradation of carbon nanomaterials is a major concern in the evaluation of their ecotoxicity. Researchers have studied the biodegradation of fullerenes and CNTs. There is only one report on the biodegradation of hydroxylated fullerene by two white rot basidiomycete fungi (*Phlebia tremellosa and Trametes versicolor*) [56]. Fullerenol was incubated with the fungi for 32 weeks. Both kinds of fungi were able to bleach and oxidize fullerenol to CO_2 and incorporate it into fungal biomass. It provide evidence that if fullerenol is released to the environment it will have a great likelihood of being chemically altered by white rot fungi, though further study is needed to determine the chemical structures of the bleached fullerenol products.

Biodegradation of CNTs by enzymes has been reported involving plant-derived horseradish peroxidase (HRP) and animal-derived neutrophil myeloperoxidase (MPO). Allen *et al*. [57, 58] first reported the degradation of carboxylated SWCNTs through enzymatic catalysis with HRP and investigated the degradation pathways. Degradation of the nanotube structure was observed by incubating carboxylated SWCNTs with HRP and low concentrations of H_2O_2 (~40 μM) at 4 °C over 12 weeks under static conditions (Figure 15.2) [57]. However, pristine SWCNTs showed no degradation with HRP incubation, because the strong hydrophobicity of pristine SWCNTs hinders their binding to the active site of HRP [58]. Degradation of MWCNTs by HRP is similar to that of SWCNTs [59]. Oxidized MWCNTs (o-MWCNTs) and MWCNTs doped with nitrogen atoms show good degradation performance, while the pristine MWCNTs cannot be degraded under the same condition. Another enzyme that degrades CNTs is MPO, a human neutrophil enzyme. Kagan *et al*. [60] reported that the biodegradation of SWCNTs catalyzed by MPO was intermediated by the oxidation of

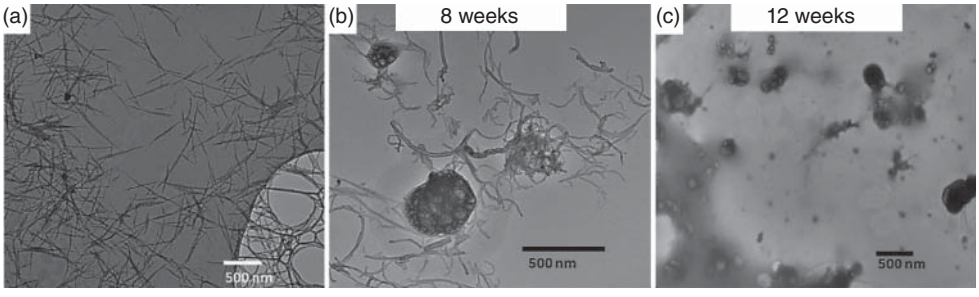

Figure 15.2 TEM tracks the biodegradation of SWCNTs incubated with HRP and H_2O_2 in different times. (a) Control. (b) At week 8, length decrease is seen with some globular material. (c) At week 12, mostly globular material is present. (Reprinted with permission from [57]. ©2008 American Chemical Society.)

hypochlorite and reactive radical. Shvedova *et al*. [61] compared the clearance and pulmonary inflammatory/fibrotic response of SWCNTs in wild-type mice and MPO knockout mice. Their results showed that oxidation and clearance of SWCNTs from the lungs of MPO-deficient mice was markedly less effective whereas the inflammatory response was more robust than in wild-type mice. This study provides *in vivo* evidence that MPO plays an important role in the degradation of SWCNTs.

15.3 Ecotoxicity of Fullerene

15.3.1 Effect of Fullerene on Microorganisms

Microorganisms play an important role in the ecological balance. Inhibition effects of fullerene on the growth of microorganisms have been reported, including bacteria, virus, and fungi. The antibacterial activities of fullerenes have been investigated for water-soluble fullerene derivatives [62–64] and water suspensions of fullerene (nC_{60}) [65].

C_{60} aqueous solution exhibits inhibitory effect to both bacteria gram-negative *Escherichia coli* and gram-positive *Bacillus subtilis* at relatively low concentrations, which is indicated by lack of growth and decreased aerobic respiration rates [44, 65]. In low-salt media, nC_{60} associated with both the bacteria, while nC_{60} tended to aggregate in a high-salt medium. Therefore, solutions with higher salt content reduced or eliminated the antimicrobial properties of nC_{60} [65]. Three kinds C_{60} suspension prepared by different methods were further compared. All suspensions exhibited relatively strong antibacterial activity toward *B. subtilis*, and the suspension containing smaller C_{60} aggregates exhibited greater antibacterial activity. Mechanistic study of the antibacterial activity of nC_{60} indicated neither ROS production nor ROS-mediated damage. Additionally, nC_{60} could interfere with the colorimetric assays for ROS production and result in false positives. The authors therefore concluded that the antibacterial activity of nC_{60} is not due to ROS-mediated damage, but nC_{60} behaves as an oxidant and exerts ROS-independent oxidative stress [66]. A follow-up study found that this ROS-independent oxidative stress was evidenced by protein oxidation, changes in cell membrane potential, and interruption of cellular respiration. This mechanism is mediated by direct contact between the nanoparticle and the bacterial cell, and differs from previously reported ROS-involved nanomaterial antibacterial mechanisms [67]. One study investigated the influence of nC_{60} on a soil microbial community. Soils were treated with an aqueous suspension of C_{60} and incubated for up to 180 days. The results indicated that the introduction of fullerene had little impact on the structure and function of the soil microbial community and microbial processes [68].

The antiviral activities of fullerene C_{60} have also been investigated. A number of studies reported that fullerene has effect on anti-HIV-1 due to its distinct molecular structure. Friedman *et al*. [69] found that C_{60} could interact with the active site of the HIV-1 protease and had a competitive inhibition to HIV protease. Further researches confirmed the anti-HIV effect of C_{60} [70–72]. Käsermann and Kempf demonstrated that the fullerene C_{60} could be used to mediate the photodynamic inactivation of enveloped viruses such as the Semliki Forest virus (SFV) and vesicular stomatitis virus (VSV) and that this viral inactivation was oxygen-dependent [73]. Photodynamic inactivation of the influenza virus with C_{60} suspension in allantoic fluid was also reported [74]. Lin *et al*. reported that the regioisomer of carboxyfullerene derivatives with C3 symmetry could inactivate the dengue-2 virus without light when the dose of the C3 isomer was increased to 40 μM. The results indicated that C3 isomer blocked viral replication at the attachment and penetration stages, which suggested that a direct interaction between the C3 isomer and the virion was required for inactivation [75].

15.3.2
Effect of Fullerene on Animals

15.3.2.1
Effect of Fullerene on Invertebrates

Daphnia magna is a widely used model organism for ecotoxicity research. *D. magna* is forms vital connection in the food chain between the algae that they consume and fish that consume them in the aqueous environment. Therefore, understanding the toxic response of *D. magna* to nanomaterials is imperative and important.

Lovern *et al*. [76] investigated the acute toxicity of C_{60} to *D. magna*. The median lethal concentration (LC50), lowest-observable-effect concentration (LOEC), and no-observable-effect concentration (NOEC) were determined. Results indicated that exposure to filtered C_{60} caused an increase in mortality with increasing concentration. The LC50 for filtered C_{60} was only 460 ppb, and complete mortality was achieved at 880 ppb. Oberdörster *et al*. investigated the sublethal effects of fullerene exposure to *D. magna*. Results showed that C_{60} aqueous solution could cause mortality, although LC50 concentrations could not be calculated due to lack of acute toxicity at up to 35 ppm. Uptake of nC_{60} occurred at 48 h of exposure, and sublethal effects including mortality, delays in molting, and reduced ability to produce offspring were observed [77]. A comparison study investigated the differences in acute toxicity to *D. magna* between tetrahydrofuran (THF)-solubilized and water-stirred nC_{60}. Results showed that the LC50 at 48 h for THF-nC_{60} was at least one order of magnitude less (0.8 ppm) than that for water-stirred nC_{60} (>35 ppm) [78]. They also investigated the sublethal effects of aqueous C_{60} on the *Hyalella azteca* and a marine harpacticoid copepod. No significant toxic effects were observed for both bentonic organisms, probably because the amount of nC_{60} available for this study was limited [78].

15.3.2.2

Effect of Fullerene on Vertebrates

Oberdörster first reported the toxicity of C_{60} water suspension in an aquatic species, namely largemouth bass [79]. Significant lipid peroxidation in the brain of largemouth bass was found after 48 h of exposure to nC_{60}, and glutathione (GSH) was marginally depleted in gills of fish. This is the first study indicating that fullerenes can cause oxidative damage and depletion of GSH *in vivo* in an aquatic species. The author speculated that fullerene may be transported to the brain via the olfactory neuron, since it had been reported that other nanoparticles could be selectively transported to the brain in this way [80]. To exclude the effect of THF introduced during the preparation of nC_{60}, Zhu *et al*. compared the toxicity of THF-solubilized and water-stirred nC_{60} to adult male fathead minnow (FHM, *Pimephales promelas*). FHMs were exposed to either 0.5 ppm of THF- or water-stirred-nC_{60} for 48 h. THF-nC_{60}-exposed fish showed 100% mortality between 6 and 18 h, while fish exposed to the water-stirred nC_{60} showed no obvious physical effects after 48 h. However, water-stirred-nC_{60} elevated lipid peroxidation (LPO) in the brain, significantly increased LPO in the gill, and expression of CYP2 family isozymes in the liver [78]. Additional study on FHMs and Japanese medaka *Oryzias latipes* indicated that the peroxisomal lipid transport protein PMP70 was significantly reduced in FHMs but not medaka exposed to nC_{60}. The results indicated potential changes in acyl-CoA pathways [78].

15.3.3

Effect of Fullerene on Plants

15.3.3.1

Effect of Fullerene on Algae

Algae play an integral role in the ecological system, and can be considered as the bottom of the aquatic food chain. Therefore, any population changes of algae will heavily affect the ecological balance of water. The toxicity of fullerene on algae has been reported, and adverse effects have been observed.

Luo investigated the effects of fullerene C_{60} on *Chlamydomonas reinhardtii*, a species of green algae. The bioaccumulation of nanoparticles from the algae to the *D. magna* was also evaluated since *C. reinhardtii* is a natural food of *D. magna*. Results indicated that the effects of C_{60} were greatest in the long term. The population of algae treated with 10 ppm of C_{60} was unable to recover within a 20-day period. The population of algae in the flask treated with 10 ppm C_{60} was less than one-half of the original population in the flask, and the population was unable to recover within a 20-day period. Additionally, the coloration of the algae changed from a deep green to more of yellow or yellow-green after C_{60} exposure. Bioaccumulation test indicated that C_{60} could transfer from the algae to the *D. magna*, primarily through water but also through the algae [81].

Blaise *et al*. [82] reported that fullerene C_{60} appeared less toxic than the other nanomaterials including SWCNTs, which were highly toxic for algae even at concentrations less than 5 mg l^{-1}. Baun *et al*. [83] studied the potential of

fullerene nanoparticles as contaminant carriers in aqueous systems with the algae *Pseudokirchneriella subcapitata*. Four common environmental contaminants (atrazine, methyl parathion, pentachlorophenol (PCP), and phenanthrene) were used as model compounds to investigate the influence of C_{60} aggregates on the toxicity and bioaccumulation of environmentally relevant contaminants. They found 85% sorption for phenanthrene to C_{60} aggregates, and 10% sorption for atrazine, methyl parathion, and PCP. The addition of C_{60} to the aqueous solution of phenanthrene increased its toxicity, while no enhanced bioaccumulation of phenanthrene was observed in the presence of C_{60}. These results indicated that phenanthrene sorbed to C_{60}-aggregates contributed to the overall toxicity to algae.

15.3.3.2

Effect of Fullerene on Higher Plants

Lin *et al*. [84] provided the first evidence on the uptake, accumulation, and generational transmission of NOM-suspended fullerene C_{70} in rice plants, the staple food crops of over half the world's population. Black aggregates were observed in the seeds and roots, and less frequently in stems and leaves of the first generation of plants treated by NOM-suspended C_{70} in the plants. C_{70} aggregates were also found in the vascular system of the stem, which may due to the transportation of these black aggregates along with water and nutrients through the xylem (Figure 15.3).

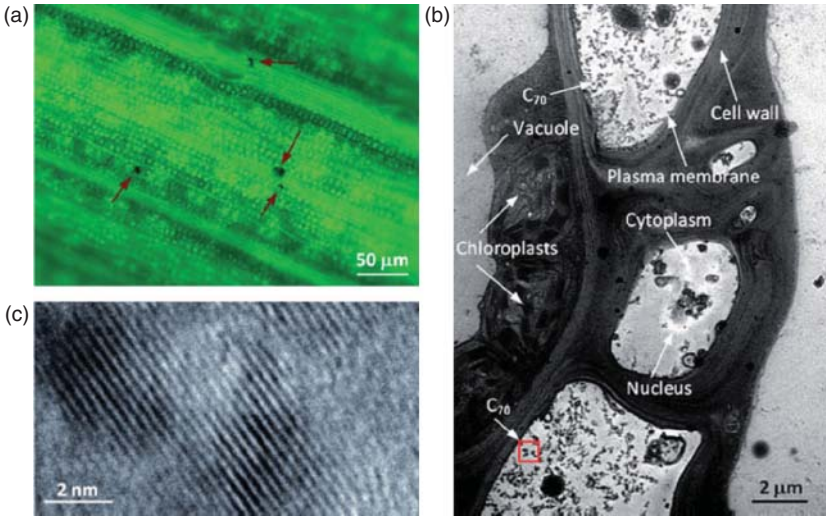

Figure 15.3 (a) Bright-field image of a leaf from a second-generation plant, where C_{70} aggregates (indicated by arrows) appear mostly in or near the vascular system. (b) TEM image of C_{70} aggregates in the leaf cells of a 2-week-old rice plant. Arrows indicate plant cell walls and other organelles. (c) Higher magnification TEM image of the C_{70} aggregates in (b) (red square). The lattice spacing of the C_{70} particles was 0.257 nm determined by fast Fourier transform (FFT) analysis of the TEM image. (Reprinted with permission from [84]. ©2009 Wiley-VCH Verlag GmbH & Co. KGaA, Weinheim.)

15.4
Ecotoxicity of Carbon Nanotubes (CNTs)

15.4.1
Effect of CNTs on Microorganisms

After release into the environment, CNTs may cause damage to microorganisms living in water and soil and on solid surfaces. Antimicrobial activity of CNTs has been extensively investigated. On the basis of the reported studies, it was suggested that SWCNTs are more toxic than MWCNTs. The size and surface characteristics of CNTs significantly influence their microbial toxicity. Additionally, CNTs that are well dispersed, negatively charged, and with higher metal content exhibit higher toxicity than agglomerated, positively charged, and pure CNTs [85]. Also, microbial toxicity is influenced by external environmental factors such as the presence of NOMs.

Efficient antimicrobial activity of SWCNTs was reported on both suspended and deposited bacteria, and SWCNTs coatings could significantly reduce biofilm formation. Kang *et al*. [86] reported that highly purified SWCNTs exhibit strong antimicrobial activity. The possible mechanism was supposed to be cell membrane damage resulting from direct contact between SWCNTs and bacteria (Figure 15.4). Direct SWCNT–bacteria contact can result in membrane perturbation and the release of intracellular contents, and further cause cell death. Liu *et al*. [87] found that well-dispersed SWCNTs were more toxic than agglomerates to bacteria. Individually dispersed SWCNTs can be visualized as moving "nano darts," which constantly attack the bacteria and cause cell death. Therefore, increasing the dispersity of SWCNTs can improve their antibacterial efficiency. Surface functionalization also influences the aggregation of CNTs and the antibacterial activity further. Arias *et al*. [88] reported that SWCNTs functionalized with OH– or COOH– exhibited extremely strong antimicrobial activity to both gram-positive and gram-negative bacterial cells, while SWCNTs functionalized with NH_2 exhibited antimicrobial activity only at higher concentrations.

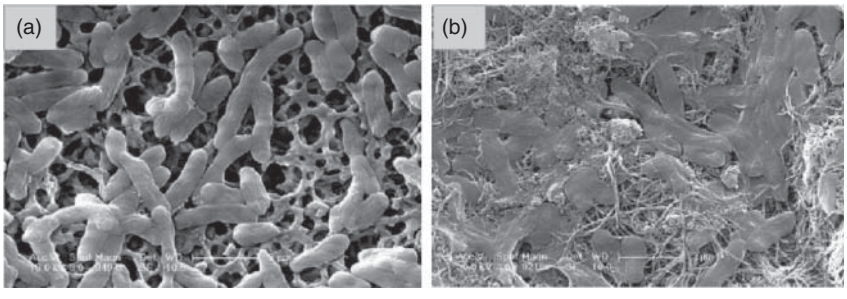

Figure 15.4 Scanning electron microscopy (SEM) images of *Escherichia coli* incubated (a) without or (b) with SWCNTs for 60 min. (Reprinted with permission from [86]. ©2007 American Chemical Society.)

Yang *et al*. [89] investigated the length effect of SWCNTs on their antimicrobial activity to bacterial cells. They found that longer SWCNTs exhibited stronger antimicrobial activity at same weight concentration. Electronic structure is also a key factor regulating antimicrobial activity of SWCNTs. Vecitis *et al*. reported that increasing the fraction of metallic SWCNTs led to increased antibacterial activity to *E. coli.* Increased oxidative stress was observed with increasing fraction of metallic SWCNTs. The authors therefore proposed a three-step antimicrobial mechanism of SWCNTs: initial SWCNT–bacteria contact, perturbation of the cell membrane, and further electronic structure-dependent bacterial oxidation [90]. Environmental NOMs can modify the surface of SWCNTs and may affect their antibacterial activity. Kang *et al*. reported that elevated concentration of NOMs reduced the attachment of bacteria on SWCNTs aggregates, possibly by reducing SWCNT–cell interactions [91]. SWCNTs also influence biofilm formation. Rodrigues and Elimelech [92] reported that SWCNTs could contact with bacterial cells prior to biofilm maturation and inhibit their growth at the initial stage of the film formation. Biofilm formation was significantly affected on SWCNT-deposited surfaces.

MWCNTs are reported to be less toxic to bacteria than SWCNTs [88]. The reduced toxicity of MWCNTs may be caused by less tight interactions between bacteria and MWCNT due to the higher inherent rigidity and possibly smaller van der Waals' forces on the MWCNT surface. Thin and shorter MWCNTs exhibit higher antibacterial activity than thicker and longer ones, which might be due to greater membrane interaction with bacteria [93, 94]. Similar to SWCNTs, when MWCNTs are uncapped, debundled, and dispersed in solution, the toxicity increased [95].

Several mechanisms for antimicrobial action of CNTs have been proposed. First is through membrane integrity disruption induced by electrostatic interaction between bacteria and CNTs, as well as oxidation of the membrane. Second is through ROS-induced DNA damage or protein inactivation leading to cell death or apoptosis. Third is by impurity toxicity elicited by release metal ions [89, 96, 97].

15.4.2
Effect of CNTs on Animals

15.4.2.1
Effect of CNTs on Invertebrates

Most toxicological studies of CNTs on invertebrates are focused on aquatic species, including fresh water, estuarine, and marine invertebrates. Only a few terrestrial invertebrate species were reported with regard to the toxic effects of CNTs, including earthworm and the fruit fly.

The interactions between *D. magna* and water-soluble, lysophosphatidylcholine (LPC)-coated SWCNTs was reported by Roberts *et al.* They showed that biomodification of SWCNTs occurred through digestion of the lipid coating (Figure 15.5). The modification significantly altered the physical properties such as solubility of the nanotubes in freshwater [98]. The toxicity of SWCNTs and MWCNTs to

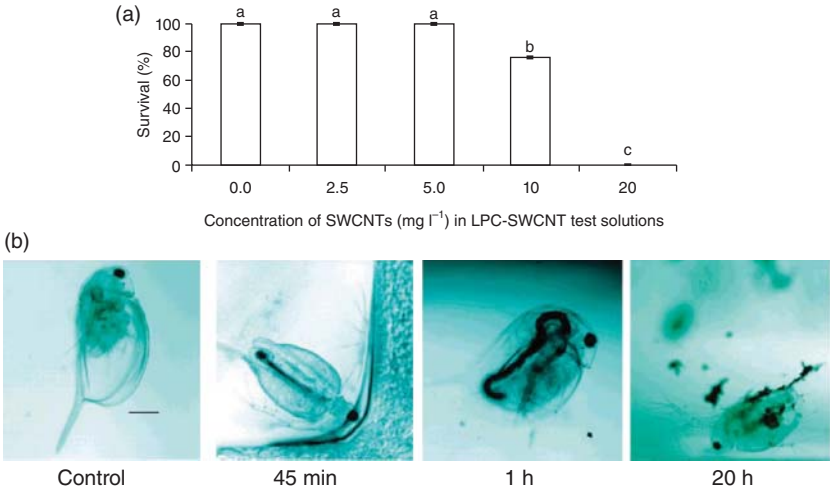

Figure 15.5 (a) Survival rate of *Daphnia magna* exposed to LPC-coated SWCNTs (LPC-SWCNTs) in a static renewal test. (b) Time course micrographs of *D. magna* exposed to 5 mg l^{-1} of LPC-SWCNTs. (Adapted with permission from [98]. ©2007 American Chemical Society.)

D. magna was reported by Zhu *et al*. [99]. The immobilization and mortality of *D. magna* exposed to CNTs were studied with different time durations. SWCNTs induced 48-h immobilization at EC50 of 1.3 mg l^{-1} and mortality at LC50 of 2.4 mg l^{-1}, which are significantly lower than those for MWCNTs, whose EC50 and LC50 to *D. magna* were 8.723 mg l^{-1} and 22.751 mg l^{-1}, respectively. These results indicated that *D. magna* was more susceptible to SWCNTs than MWCNTs. Acute toxicity of a mixture of copper and LPC-modified SWCNTs to *D. magna* was evaluated [100]. The toxicity of a mixture of SWCNTs and Cu was additive, and the addition of LPC-SWCNTs with nontoxic concentration enhanced the uptake and toxicity of copper. Increased accumulation of Cu was found upon addition of LPC-SWCNTs.

Kim *et al*. reported the immobilization and mortality of *D. magna* in the presence of MWCNTs. MWCNTs stabilized in NOMs were shown to have low acute ecotoxicity to *D. magna*. They did not induce in *D. magna* 48-h mortality even at 20 mg l^{-1}, while prolonged exposure for 96 h induced mortality at LC50 of 2.5 mg l^{-1} [101]. Similar results were obtained by Edgington and colleagues. They found that MWCNTs resuspended in NOMs induced *D. magna* 96-h mortality at LC50 of 2–4 mg l^{-1}, depending on the NOM type. Polyethylenimine (PEI) coatings could enhance the stability of MWCNTs in aqueous solutions, and therefore increase MWCNTs' toxicity [102]. Alloy and Roberts [103] evaluated the influence of MWCNTs on reproductive function of *D. magna*. By exposure for 21 days to MWCNT stabilized by NOM, 45% reduction in reproductive means was observed at an LOEC 0.24 mg l^{-1}.

The above studies all used single species for tests in the laboratory, which lacks ecological realism. Velzeboer *et al*. [104] first studied the effects of MWCNT-contaminated sediments on a benthic macroinvertebrate community. The sediment was taken from an unpolluted site, cleaned from invertebrates, and mixed with increasing levels of MWCNTs. Then the sediment was returned to the original unpolluted site for three months of exposure. Results indicated that the numbers of individual taxa increased with increasing MWCNT concentration. No significant effect of MWCNT addition on biodiversity was observed. This study showed an opposite effect of MWCNTs compared to other laboratory studies. It is speculated that the subtoxic concentrations of CNTs possess a slight stimulatory effect by upregulation of repair mechanisms, a paradigm observed for other pollutants [105].

15.4.2.2

Effect of CNTs on Vertebrates

Fish was the main pelagic vertebrate for toxicity studies of nanomaterials. The target organs for studying nanomaterial toxicity in fish may include gills, gut, liver, and brain [106, 107]. Acute and chronic toxicity of CNTs have been assessed with aquatic vertebrates. Cheng *et al*. [108] studied the effect of SWCNTs on developing zebrafish (*Danio rerio*) embryos. Exposure to SWCNTs induced a significant hatching delay in zebrafish embryos at concentrations >120 mg l^{-1}. However, embryonic development was unaffected (NOEC 360 mg l^{-1}).

The toxicity of MWCNTs to zebrafish embryos was also assessed. Phenotypic defects in zebrafish embryo were observed at an LOEC 60 μg l^{-1}. At high concentrations, MWCNTs significantly delayed hatching and mortality. Microinjection of 5 ng MWCNTs to eight-cell stage zebrafish embryos induced similar harmful effects to the aquatic MWCNTs exposures. In another study, microinjection of 2 ng MWCNTs to zebrafish embryos at the one-cell stage did not induce mortality or abnormal development up to the second generation, while a significant reduction of survival rates of the second generation was observed [109]. Immune response by accumulating circulating white blood cells at the trunk region was observed in the early stages of the first generation.

Both size and dispersion can influence the toxicity of CNTs to fish. When MWCNTs were cut by sonication in acid, the produced shorter CNTs induced severe developmental toxicity, while the longer CNTs did not affect the embryos [110]. Double-walled carbon nanotubes (DWCNTs) formed smaller aggregates in the sea water after sonication compared to stirring [111]. After exposure the fry of medaka fish *Oryzias melastigma* to two kinds of DWCNT suspension, medaka growth was reduced with LOEC of stirred DWCNTs 10-fold higher than sonicated DWCNTs.

Toxicity of CNTs to fish after full development has also been investigated. Smith *et al*. [112] studied effects of SWCNTs in an older fish, juvenile rainbow trout *Oncorhynchus mykiss*. SWCNTs induced dose-dependent systemic toxicity in *O. mykiss*, including respiratory toxicity, neurotoxicity, and hepatotoxicity. However, no oxidative stress or hematological changes were observed in the

treated fish. Dietary exposure of 500 mg kg^{-1} SWCNTs to *O. mykiss* for 6 weeks did not result in obvious toxicity (weight, hematological alternations, metal accumulation, oxidative injury, or pathology). However, lipid peroxidation, indicated by a transient elevation of thiobarbituric acid reactive substances in the brain, was observed after the SWCNT exposure [113]. Therefore, the toxicity of CNTs is significantly affected by the exposure route.

15.4.3
Effect of CNTs on Plants

15.4.3.1
Effect of CNTs on Algae

At present, phytotoxicity studies of carbon nanomaterials are mostly focused on aquatic algae, while the toxicity to higher plants is less studied.

Similar to the case of bacteria, toxic effects of CNTs in algae are mostly driven by a direct contact with the surface. Schwab *et al.* [114] studied the toxicological effects of pristine and oxidized CNTs on two fresh-water green algae *Chlorella vulgaris* and *P. subcapitata*. The growth of both algae was inhibited, and the EC50 value of agglomerated CNTs was much higher than that of well-dispersed CNTs. However, the photosynthetic activity was not affected. Growth inhibition was possibly mediated by CNT shading and the formation of algae–CNT agglomerates. This suggests that the inhibition effect was mainly caused by indirect effects including reduced availability of light and different growth conditions caused by the locally elevated algal concentration inside of CNT agglomerates. NOM dispersion of CNTs may reduce the growth inhibition to algae. Youn *et al.* [115] investigated growth inhibition of *P. subcapitata* exposed to SWCNTs dispersed in gum arabic (GA) with different concentrations. After 4 days of exposure to SWCNTs, algal growth was inhibited at LOEC of 0.25 mg l^{-1} in the presence of 0.023% (v/v) GA; however, the observed toxicity disappeared when GA concentrations were increased to levels ≥0.046%. During a 14-day long-term exposure, *P. subcapitata* could easily recover from the initial growth inhibition, which indicated the possibility of GA to mitigate the toxicity of SWCNTs.

MWCNTs can also inhibit algal growth of *C. vulgaris*. Long *et al.* [116] exposed *C. vulgaris* to MWCNTs of diameter 10, 20–40, and 60–100 nm for 96 h, and found that growth was inhibited at EC50 41.0, 12.7, and 12.4 mg l^{-1}, respectively. However, the toxicity was lower under dark conditions. The contribution of metal catalyst residues in the MWCNTs to the algal growth inhibition was negligible, as was the contribution from the MWCNTs' adsorption of nutrient elements. The algal toxicity of MWCNTs was mainly due to the combined effects of oxidative stress, agglomeration, physical interactions, and shading effects. Algal growth inhibition by DWCNTs was reported with the marine diatom *Thalassiosira pseudonana* [117]. It was found that the sonicated double-walled carbon nanotubes (so-DWCNTs) were more toxic than the stirred double-walled carbon nanotubes (st-DWCNTs). The median aggregation size of so-DWCNTs was much smaller than that of st-DWCNTs. These findings indicated that the

dispersion method and the size of aggregations should be considered in DWCNT toxicity testing. Wei *et al*. [118] reported the toxicity of carboxylated MWCNTs to the marine algae *Dunaliella tertiolecta*. Lag in the growth phase, oxidative stress, and photosynthesis inhibition were observed after MWCNT exposure. However, when the MWCNT suspension was filtered through a 0.2-μm filter and the large aggregates were removed, all the above observed effects disappeared. This indicated that the toxic effects mainly originated from the large MWCNTs aggregates.

15.4.3.2

Effect of CNTs on Higher Plants

Compared to those in animals, researches on the toxic effects of carbon nanomaterials on plants is very limited. The phytotoxicity of carbon nanomaterials seems less obvious than the toxicity to animals. This may be due to the protection effect of the cell wall outside the plant cell membrane, which serves as a barrier for nanoparticles. The few studies report no effects or effects at relatively high doses of CNTs to the plants [119]. Lin and Xing [93] investigated the effects of MWCNTs on seed germination and root growth of six higher plant species (radish, rape, ryegrass, lettuce, corn, and cucumber). The seeds were soaked and germinated for 5 days in 2000 mg l^{-1} MWCNTs, and no significant effect was observed on seed germination or root growth. MWCNTs dispersed in 25% Hoagland medium exhibited assay-dependent phytotoxicity to *Cucurbita pepo* (zucchini). No effective on germination and root elongation, but reduced plant biomass, was observed for the MWCNT-exposed seeds [94]. Begum *et al*. [120] reported the phytotoxicity of MWCNTs to a selected plant species. Seven crop species (lettuce, rice, cucumber, spinach, lady's finger, chili, and soja) were exposed and phytotoxicity was evaluated. After 15 days of hydroponic culture, phytotoxicity including the root and shoot lengths, cell death, and electrolyte leakage was observed for spinach, lettuce, rice and cucumber at 1000 and 2000 mg l^{-1} MWCNTs, while lady's finger, chili, and soja did not respond to the exposure at NOEC 2000 mg l^{-1}. In a follow-up study, MWCNTs were tested with the most sensitive species identified, namely spinach [121]. Growth inhibition and cell death, as well as adverse effects on root and leaf morphology, were observed. Mechanistic studies suggested that the primary mechanism of the MWCNTs' toxicity was oxidative stress.

Functionalization of CNTs may affect their phytotoxicity. Cañas *et al*. [122] compared the effects of nonfunctionalized and poly-3-aminobenzenesulfonic acid-functionalized SWCNTs on the root elongation of six crop species (cabbage, carrot, cucumber, lettuce, onion, and tomato) (Figure 15.6). Results indicated that root elongation was more affected by nonfunctionalized SWCNTs. Nonfunctionalized SWCNTs inhibited root elongation in tomato and enhanced root elongation in onion and cucumber, while functionalized nanotubes inhibited root elongation in lettuce. In this study, both enhancing and inhibitory effects (at low and high dose, respectively) were observed, and the phytotoxicity effects of the same CNTs were plant-selective.

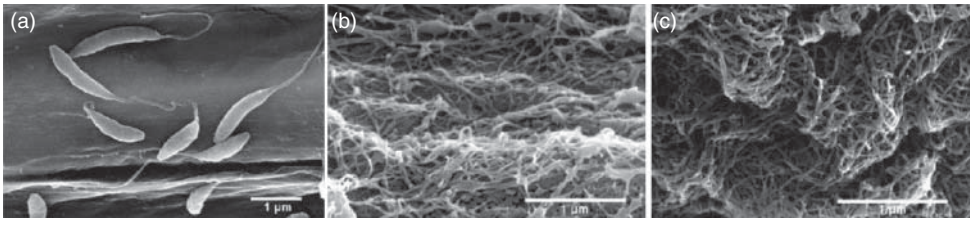

Figure 15.6 SEM images of the secondary roots of cucumber exposed to (a) control, (b) nonfunctionalized SWCNTs, and (c) functionalized SWCNTs. (Reprinted with permission from [122]. ©2008 SETAC.)

However, Mondal *et al*. observed a beneficial role of MWCNTs on mustard plant growth [123]. Low concentrations of oxidized o-MWCNTs exhibited positive effects on seed germination rate and plant as compared to nonoxidized as well as high concentration o-MWCNT-treated seeds. Their results indicated that o-MWCNTs can increase the moisture content of seeds and the water absorption machinery of root tissues. High concentration of MWCNTs is harmful to both plant growth and biomass production. Khodakovskaya *et al*. [124] also reported the positive effects of MWCNTs on plant growth and gene expression. MWCNTs upregulated the stress-related genes and the water-channel genes in tomato. Similar results were obtained by Villagarcia *et al*. [125]. They observed that well-dispersed MWCNTs increased plant growth in tomato. The production of tomato water channel protein was activated in plants exposed to functionalized MWCNTs that were well dispersed, while the agglomerated pristine MWCNTs had no effect.

The phytotoxicity of CNTs is contradictory as seen from the above results. Some studies suggest that CNTs in low doses can penetrate into the roots and seeds and stimulate plant growth, while others do not observe this effect or report phytotoxicity at high doses. This may due to the difference in the physicochemical properties of the CNTs used. Potential mechanisms for both the stimulation and inhibition effects on plants need to be investigated.

15.5 Ecotoxicity of Graphene

Compared to those of fullerene and CNTs, fewer studies have been reported on the ecotoxicity of graphene. It has been documented that graphene exhibits toxic effects to bacteria, mammalian cells, animals, and plants. The antibacterial activity of graphene has been reported for both gram-positive and gram-negative bacteria. Akhavan and Ghaderi [126] constructed graphene nanowalls and investigated their bacterial toxicity. By measuring the efflux of cytoplasmic materials of the bacteria, they found that the cell membrane damage of the bacteria was mainly caused by direct contact of the bacteria with the extremely sharp edges of

the nanowalls. Therefore, the gram-negative *E. coli* bacteria were more resistant to the cell membrane damage caused by the nanowalls than the gram-positive *S. aureus*, because *E. coli* has an outer membrane while *S. aureus* does not have one. Similar results of antibacterial activity of graphene oxide and reduced graphene oxide on *E. coli.* were reported by Hu *et al*. [127]. Metabolic activity of the bacterial cells was reduced to ~70% and 13% at concentrations of 20 and 85 mg ml^{-1}, respectively. Also, a similar mechanism of the antibacterial activity was proposed, that is, contact of graphene and the cell membrane, resulting in the loss of membrane integrity. Liu *et al*. [128] compared the antibacterial activity of four types of graphene-based materials, namely graphite, graphite oxide, graphene oxide, and reduced graphene oxide, toward *E. coli*. Their results indicated that, under similar concentration, graphene oxide dispersion showed the highest antibacterial activity, followed by reduced graphene oxide, graphite, and graphite oxide. Disruption of the cell membrane by direct contact with graphene nanosheets was confirmed by scanning electron microscopy (SEM). All the four kinds of materials can oxidize glutathione, which serves as a redox-state mediator in bacteria. The authors therefore concluded that the antimicrobial actions resulted from both membrane disruption and oxidation stress.

The ecotoxicity of two kinds of pristine graphene nanoparticles was investigated in model marine organisms [129]. Inhibition of bioluminescence of bioluminescent bacterium *Vibrio fischeri* and growth of the unicellular algae *D. tertiolecta* were observed. However, no acute toxicity was observed with respect to the crustacean *Artemia salina*. Significant increase of catalase and glutathione peroxidase activities, as well as lipid peroxidation of membranes, was observed in graphene-treated *A. salina.* Guo *et al*. [130] investigated the biological uptake and depuration of ^{14}C-labeled graphene by *D. magna*. The graphene concentration in the organism was nearly 1% of the organism's dry mass after exposure for 24 h to a 250 μg l^{-1} solution of graphene. The depuration results indicated that roughly constant body burdens were reached after elimination for 24 h in clean, artificial freshwater. Adding algae and humic acid to water during the depuration period led to the release of a significant fraction (>90%) of the accumulated graphene. And a very small amount of graphene could be transferred to the next generation of neonates.

One study reported the toxic effects of graphene on terrestrial plant species. Begum *et al*. [131] investigated the phytotoxic effects of graphene on four plant species, namely cabbage, tomato, red spinach, and lettuce. Their results showed significant toxic effect of graphene on cabbage, tomato, and red spinach, but no clear toxic effect for lettuce. The effects of graphene on root and shoot growth, biomass, shape, cell death, and ROS production were analyzed. Graphene significantly inhibited plant growth and biomass compared to a control after 20 days of exposure. A concentration-dependent increase in ROS production and visible symptoms of necrotic lesions were observed, indicating graphene-induced adverse effects on cabbage, tomato, and red spinach mediated by oxidative stress necrosis.

15.6 Conclusion and Perspectives

In this chapter, we reviewed the transport and transformation of carbon nanomaterials, including fullerene, CNTs, and graphene, in the environment, as well as the ecotoxicity of these carbon nanomaterials to aqueous and terrestrial species. With the increase in production of carbon nanomaterials, there will be a corresponding increase release of nanoparticles into the environment. Humans can be influenced by nanoparticles either directly through exposure to air, soil, and water, or indirectly by consuming plants or animals that have accumulated nanoparticles. After the particles are released into the environment, physical and chemical transformation can occur to change the intrinsic properties of carbon nanomaterials. The fate and transformation processes may introduce many uncertainties into their ecological risk assessments.

Several points should be considered for the ecotoxicity study of carbon nanomaterials. First, characterization and quantitation of carbon nanomaterials is a prerequisite for their ecotoxicity testing, which include evaluating the starting materials, nanoparticle characteristics during ecotoxicity tests, and the extent to which the nanoparticles are altered during the test. Analytical methods will be required to detect carbon nanomaterials in a range of environmental media, especially complex matrices such as biosolids and biological tissues. Second, during the ecotoxicity test, potential artifacts may exist due to the released chemicals from carbon nanomaterials (such as heavy metals from CNT catalysts) or dispersing agents used to make the nanoparticles stable in solution (such as THF in fullerene suspension). Third, methods are required to analyze carbon nanomaterials in biological tissues to assess potential bioaccumulation or biomagnification. Finally, long-term low-exposure tests focused on chronic endpoints are needed. Only very few studies have investigated the chronic endpoints of carbon nanomaterials. And the observed effects are generally at concentrations higher than environmental concentrations. Therefore, it is necessary to conduct ecotoxicity tests at environmental concentration.

Acknowledgments

This work was financially supported by the Ministry of Science and Technology of China (2011CB933401) and the National Science Fund for Distinguished Young Scholars (11425520).

References

1. Aschberger, K., Micheletti, C., Sokull-Kluttgen, B., and Christensen, F.M. (2011) Analysis of currently available data for characterising the risk of engineered nanomaterials to the environment and human health – lessons learned from four case studies. *Environ. Int.*, **37** (6), 1143 – 1156.

2. Klaine, S.J., Alvarez, P.J., Batley, G.E. *et al.* (2008) Nanomaterials in the environment: behavior, fate, bioavailability, and effects. *Environ. Toxicol. Chem.*, **27** (9), 1825–1851.
3. Kahru, A. and Dubourguier, H.C. (2010) From ecotoxicology to nanoecotoxicology. *Toxicology*, **269** (2–3), 105–119.
4. Wei-xian Zhang, D.W.E. (2006) Applications of iron nanoparticles for groundwater remediation. *Remediation J.*, **16** (2), 7–21.
5. Biswas, P. and Wu, C.Y. (2005) Nanoparticles and the environment. *J. Air Waste Manage. Assoc.*, **55** (6), 708–746.
6. Bakry, R., Vallant, R.M., Najam-Ul-Haq, M. *et al.* (2007) Medicinal applications of fullerenes. *Int. J. Nanomed.*, **2** (4), 639–649.
7. Nowack, B. and Bucheli, T.D. (2007) Occurrence, behavior and effects of nanoparticles in the environment. *Environ. Pollut.*, **150** (1), 5–22.
8. Navarro, E., Baun, A., Behra, R. *et al.* (2008) Environmental behavior and ecotoxicity of engineered nanoparticles to algae, plants, and fungi. *Ecotoxicology*, **17** (5), 372–386.
9. Yeganeh, B., Kull, C.M., Hull, M.S., and Marr, L.C. (2008) Characterization of airborne particles during production of carbonaceous nanomaterials. *Environ. Sci. Technol.*, **42** (12), 4600–4606.
10. Tiwari, A.J. and Marr, L.C. (2010) The role of atmospheric transformations in determining environmental impacts of carbonaceous nanoparticles. *J. Environ. Qual.*, **39** (6), 1883–1895.
11. Jimenez, J.L., Canagaratna, M.R., Donahue, N.M. *et al.* (2009) Evolution of organic aerosols in the atmosphere. *Science*, **326** (5959), 1525–1529.
12. Hamano, T., Mashino, T., and Hirobe, M. (1995) Oxidation of [60]fullerene by cytochrome-P450 chemical-models. *J. Chem. Soc., Chem. Commun.*, (15), 1537–1538.
13. Brant, J.A., Labille, J., Bottero, J.Y., and Wiesner, M.R. (2006) Characterizing the impact of preparation method on fullerene cluster structure and chemistry. *Langmuir*, **22** (8), 3878–3885.
14. Duncan, L.K., Jinschek, J.R., and Vikesland, P.J. (2008) C(60) colloid formation in aqueous systems: effects of preparation method on size, structure, and surface, charge. *Environ. Sci. Technol.*, **42** (1), 173–178.
15. Labille, J., Masion, A., Ziarelli, F. *et al.* (2009) Hydration and dispersion of C-60 in aqueous systems: the nature of water-fullerene interactions. *Langmuir*, **25** (19), 11232–11235.
16. Kokubo, K., Matsubayashi, K., Tategaki, H., Takada, H., and Oshima, T. (2008) Facile synthesis of highly water-soluble fullerenes more than half-covered by hydroxyl groups. *ACS Nano*, **2** (2), 327–333.
17. Fortner, J.D., Kim, D.I., Boyd, A.M. *et al.* (2007) Reaction of water-stable C60 aggregates with ozone. *Environ. Sci. Technol.*, **41** (21), 7497–7502.
18. Escobar, M., Goyanes, S., Corcuera, M.A. *et al.* (2009) Purification and functionalization of carbon nanotubes by classical and advanced oxidation processes. *J. Nanosci. Nanotechnol.*, **9** (10), 6228–6233.
19. Mawhinney, D.B., Naumenko, V., Kuznetsova, A. *et al.* (2000) Infrared spectral evidence for the etching of carbon nanotubes: ozone oxidation at 298 K. *J. Am. Chem. Soc.*, **122** (10), 2383–2384.
20. Mawhinney, D.B. and Yates, J.T. (2001) FTIR study of the oxidation of amorphous carbon by ozone at 300 K – Direct COOH formation. *Carbon*, **39** (8), 1167–1173.
21. Li, M.H., Boggs, M., Beebe, T.P., and Huang, C.P. (2008) Oxidation of single-walled carbon nanotubes in dilute aqueous solutions by ozone as affected by ultrasound. *Carbon*, **46** (3), 466–475.
22. Simmons, J.M., Nichols, B.M., Baker, S.E. *et al.* (2006) Effect of ozone oxidation on single-walled carbon nanotubes. *J. Phys. Chem. B*, **110** (14), 7113–7118.
23. Cataldo, F. (2007) Ozone reaction with carbon nanostructures. 1: reaction between solid C60 and C70 fullerenes and ozone. *J. Nanosci. Nanotechnol.*, **7** (4–5), 1439–1445.

24. Liu, H.T., Ryu, S.M., Chen, Z.Y. *et al.* (2009) Photochemical reactivity of graphene. *J. Am. Chem. Soc.*, **131** (47), 17099–17101.
25. Brunet, L., Lyon, D.Y., Hotze, E.M., Alvarez, P.J., and Wiesner, M.R. (2009) Comparative photoactivity and antibacterial properties of C60 fullerenes and titanium dioxide nanoparticles. *Environ. Sci. Technol.*, **43** (12), 4355–4360.
26. Arbogast, J.W., Darmanyan, A.P., Foote, C.S. *et al.* (1991) Photophysical properties of C60. *J. Phys. Chem.*, **95** (1), 11–12.
27. Taylor, R., Parsons, J.P., Avent, A.G. *et al.* (1991) Degradation of C60 by light. *Nature*, **351** (6324), 277.
28. Lee, J., Fortner, J.D., Hughes, J.B., and Kim, J.H. (2007) Photochemical production of reactive oxygen species by C60 in the aqueous phase during UV irradiation. *Environ. Sci. Technol.*, **41** (7), 2529–2535.
29. Lee, J. and Kim, J.H. (2008) Effect of encapsulating agents on dispersion status and photochemical reactivity of C60 in the aqueous phase. *Environ. Sci. Technol.*, **42** (5), 1552–1557.
30. Hou, W.C. and Jafvert, C.T. (2009) Photochemical transformation of aqueous C-60 clusters in sunlight. *Environ. Sci. Technol.*, **43** (2), 362–367.
31. Lee, J., Yamakoshi, Y., Hughes, J.B., and Kim, J.H. (2008) Mechanism of C-60 photoreactivity in water: fate of triplet state and radical anion and production of reactive oxygen species. *Environ. Sci. Technol.*, **42** (9), 3459–3464.
32. Savage, T., Bhattacharya, S., Sadanadan, B. *et al.* (2003) Photoinduced oxidation of carbon nanotubes. *J. Phys.: Condens. Matter*, **15** (35), 5915–5921.
33. Alvarez, N.T., Kittrell, C., Schmidt, H.K. *et al.* (2008) Selective photochemical functionalization of surfactant-dispersed single wall carbon nanotubes in water. *J. Am. Chem. Soc.*, **130** (43), 14227–14233.
34. Parekh, B., Debies, T., Knight, P., Santhanam, K.S.V., and Takacs, G.A. (2006) Surface functionalization of multiwalled carbon nanotubes with UV and vacuum UV photo-oxidation. *J. Adhes. Sci. Technol.*, **20** (16), 1833–1846.
35. Chen, C.Y. and Jafvert, C.T. (2010) Photoreactivity of carboxylated single-walled carbon nanotubes in sunlight: reactive oxygen species production in water. *Environ. Sci. Technol.*, **44** (17), 6674–6679.
36. Tasis, D., Tagmatarchis, N., Bianco, A., and Prato, M. (2006) Chemistry of carbon nanotubes. *Chem. Rev.*, **106** (3), 1105–1136.
37. Labille, J., Brant, J., Villieras, F. *et al.* (2006) Affinity of C60 fullerenes with water. *Fullerenes Nanotubes Carbon Nanostruct.*, **14** (2–3), 307–314.
38. Bouchard, D., Ma, X., and Issacson, C. (2009) Colloidal properties of aqueous fullerenes: isoelectric points and aggregation kinetics of C-60 and C-60 derivatives. *Environ. Sci. Technol.*, **43** (17), 6597–6603.
39. Saito, R. and Kataura, H. (2001) Optical properties and Raman spectroscopy of carbon nanotubes, in *Carbon Nanotubes*, Topics in Applied Physics, vol. **80**, Springer, pp. 213–246.
40. Fernando, K.A.S., Lin, Y., and Sun, Y.P. (2004) High aqueous solubility of functionalized single-walled carbon nanotubes. *Langmuir*, **20** (11), 4777–4778.
41. Zeng, L.L., Zhang, L., and Barron, A.R. (2005) Tailoring aqueous solubility of functionalized single-wall carbon nanotubes over a wide pH range through substituent chain length. *Nano Lett.*, **5** (10), 2001–2004.
42. Tagmatarchis, N. and Prato, M. (2005) Carbon-based materials: from fullerene nanostructures to functionalized carbon nanotubes. *Pure Appl. Chem.*, **77** (10), 1675–1684.
43. Smith, B., Wepasnick, K., Schrote, K.E. *et al.* (2009) Influence of surface oxides on the colloidal stability of multi-walled carbon nanotubes: a structure-property relationship. *Langmuir*, **25** (17), 9767–9776.
44. Fortner, J.D., Lyon, D.Y., Sayes, C.M. *et al.* (2005) C-60 in water: nanocrystal formation and microbial response. *Environ. Sci. Technol.*, **39** (11), 4307–4316.
45. Brant, J., Lecoanet, H., and Wiesner, M.R. (2005) Aggregation and deposition characteristics of fullerene

nanoparticles in aqueous systems. *J. Nanopart. Res.*, **7** (4–5), 545–553.
46. Sano, M., Okamura, J., and Shinkai, S. (2001) Colloidal nature of single-walled carbon nanotubes in electrolyte solution: the Schulze-Hardy rule. *Langmuir*, **17** (22), 7172–7173.
47. Espinasse, B., Hotze, E.M., and Wiesner, M.R. (2007) Transport and retention of colloidal aggregates of C60 in porous media: effects of organic macromolecules, ionic composition, and preparation method. *Environ. Sci. Technol.*, **41** (21), 7396–7402.
48. Moore, V.C., Strano, M.S., Haroz, E.H. *et al.* (2003) Individually suspended single-walled carbon nanotubes in various surfactants. *Nano Lett.*, **3** (10), 1379–1382.
49. Xie, B., Xu, Z.H., Guo, W.H., and Li, Q.L. (2008) Impact of natural organic matter on the physicochemical properties of aqueous C-60 nanoparticles. *Environ. Sci. Technol.*, **42** (8), 2853–2859.
50. Chen, K.L. and Elimelech, M. (2007) Influence of humic acid on the aggregation kinetics of fullerene (C-60) nanoparticles in monovalent and divalent electrolyte solutions. *J. Colloid Interface Sci.*, **309** (1), 126–134.
51. Chappell, M.A., George, A.J., Dontsova, K.M. *et al.* (2009) Surfactive stabilization of multi-walled carbon nanotube dispersions with dissolved humic substances. *Environ. Pollut.*, **157** (4), 1081–1087.
52. Yang, K. and Xing, B.S. (2009) Adsorption of fulvic acid by carbon nanotubes from water. *Environ. Pollut.*, **157** (4), 1095–1100.
53. Hyung, H., Fortner, J.D., Hughes, J.B., and Kim, J.H. (2007) Natural organic matter stabilizes carbon nanotubes in the aqueous phase. *Environ. Sci. Technol.*, **41** (1), 179–184.
54. Wang, X.L., Lu, J.L., and Xing, B.S. (2008) Sorption of organic contaminants by carbon nanotubes: influence of adsorbed organic matter. *Environ. Sci. Technol.*, **42** (9), 3207–3212.
55. Lin, D.H. and Xing, B.S. (2008) Tannic acid adsorption and its role for stabilizing carbon nanotube suspensions. *Environ. Sci. Technol.*, **42** (16), 5917–5923.
56. Schreiner, K.M., Filley, T.R., Blanchette, R.A. *et al.* (2009) White-rot basidiomycete-mediated decomposition of C60 fullerol. *Environ. Sci. Technol.*, **43** (9), 3162–3168.
57. Allen, B.L., Kichambare, P.D., Gou, P. *et al.* (2008) Biodegradation of single-walled carbon nanotubes through enzymatic catalysis. *Nano Lett.*, **8** (11), 3899–3903.
58. Allen, B.L., Kotchey, G.P., Chen, Y.N. *et al.* (2009) Mechanistic investigations of horseradish peroxidase-catalyzed degradation of single-walled carbon nanotubes. *J. Am. Chem. Soc.*, **131** (47), 17194–17205.
59. Zhao, Y., Allen, B.L., and Star, A. (2011) Enzymatic degradation of multiwalled carbon nanotubes. *J. Phys. Chem. A*, **115** (34), 9536–9544.
60. Kagan, V.E., Konduru, N.V., Feng, W.H. *et al.* (2010) Carbon nanotubes degraded by neutrophil myeloperoxidase induce less pulmonary inflammation. *Nat. Nanotechnol.*, **5** (5), 354–359.
61. Shvedova, A.A., Kapralov, A.A., Feng, W.H. *et al.* (2012) Impaired clearance and enhanced pulmonary inflammatory/fibrotic response to carbon nanotubes in myeloperoxidase-deficient mice. *PLoS One*, **7** (3), e30923.
62. Bosi, S., Da Ros, T., Castellano, S., Banfi, E., and Prato, M. (2000) Antimycobacterial activity of ionic fullerene derivatives. *Bioorg. Med. Chem. Lett.*, **10** (10), 1043–1045.
63. Tsao, N., Wu, C.M., Hsu, H.P. *et al.* (2001) Inhibition of the increased permeability of blood-brain barrier in Escherichia coli-induced meningitis by carboxyfullerene. *Fullerene Sci. Technol.*, **9** (3), 307–320.
64. Tsao, N., Luh, T.Y., Chou, C.K. *et al.* (2001) Inhibition of group A streptococcus infection by carboxyfullerene. *Antimicrob. Agents Chemother.*, **45** (6), 1788–1793.
65. Lyon, D.Y., Fortner, J.D., Sayes, C.M., Colvin, V.L., and Hughe, J.B. (2005)

Bacterial cell association and antimicrobial activity of a C60 water suspension. *Environ. Toxicol. Chem.*, **24** (11), 2757–2762.

66. Lyon, D.Y., Brunet, L., Hinkal, G.W., Wiesner, M.R., and Alvarez, P.J.J. (2008) Antibacterial activity of fullerene water suspensions (nC(60)) is not due to ROS-mediated damage. *Nano Lett.*, **8** (5), 1539–1543.
67. Lyon, D.Y. and Alvarez, P.J.J. (2008) Fullerene water suspension (nC(60)) exerts antibacterial effects via ROS-independent protein oxidation. *Environ. Sci. Technol.*, **42** (21), 8127–8132.
68. Tong, Z., Bischoff, M., Nies, L., Applegate, B., and Turco, R.F. (2007) Impact of fullerene (C60) on a soil microbial community. *Environ. Sci. Technol.*, **41** (8), 2985–2991.
69. Friedman, S.H., Decamp, D.L., Sijbesma, R.P. *et al.* (1993) Inhibition of the Hiv-1 protease by fullerene derivatives – Model-building studies and experimental-verification. *J. Am. Chem. Soc.*, **115** (15), 6506–6509.
70. Marchesan, S., Da Ros, T., Spalluto, G., Balzarini, J., and Prato, M. (2005) Anti-HIV properties of cationic fullerene derivatives. *Bioorg. Med. Chem. Lett.*, **15** (15), 3615–3618.
71. Bosi, S., Da Ros, T., Spalluto, G., Balzarini, J., and Prato, M. (2003) Synthesis and anti-HIV properties of new water-soluble bis-functionalized[60]fullerene derivatives. *Bioorg. Med. Chem. Lett.*, **13** (24), 4437–4440.
72. Mashino, T., Shimotohno, K., Ikegami, N. *et al.* (2005) Human immunodeficiency virus-reverse transcriptase inhibition and hepatitis C virus RNA-dependent RNA polymerase inhibition activities of fullerene derivatives. *Bioorg. Med. Chem. Lett.*, **15** (4), 1107–1109.
73. Kasermann, F. and Kempf, C. (1997) Photodynamic inactivation of enveloped viruses by buckminsterfullerene. *Antiviral Res.*, **34** (1), 65–70.
74. Zarubaev, V.V., Belousova, I.M., Kiselev, O.I. *et al.* (2007) Photodynamic inactivation of influenza virus with fullerene C-60 suspension in allantoic fluid. *Photodiagn. Photodyn. Ther.*, **4** (1), 31–35.
75. Lin, Y.L., Lei, H.Y., Wen, Y.Y. *et al.* (2000) Light-independent inactivation of dengue-2 virus by carboxyfullerene C3 isomer. *Virology*, **275** (2), 258–262.
76. Lovern, S.B. and Klaper, R. (2006) Daphnia magna mortality when exposed to titanium dioxide and fullerene (C-60) nanoparticles. *Environ. Toxicol. Chem.*, **25** (4), 1132–1137.
77. Oberdorster, E., Zhu, S.Q., Blickley, T.M., McClellan-Green, P., and Haasch, M.L. (2006) Ecotoxicology of carbon-based engineered nanoparticles: effects of fullerene (C-60) on aquatic organisms. *Carbon*, **44** (6), 1112–1120.
78. Zhu, S.Q., Oberdorster, E., and Haasch, M.L. (2006) Toxicity of an engineered nanoparticle (fullerene, C-60) in two aquatic species, Daphnia and fathead minnow. *Mar. Environ. Res.*, **62**, S5–S9.
79. Oberdorster, E. (2004) Manufactured nanomaterials (fullerenes, C60) induce oxidative stress in the brain of juvenile largemouth bass. *Environ. Health Perspect.*, **112** (10), 1058–1062.
80. Oberdorster, G., Sharp, Z., Atudorei, V. *et al.* (2004) Translocation of inhaled ultrafine particles to the brain. *Inhalation Toxicol.*, **16** (6–7), 437–445.
81. Luo, J. (2007) Toxicity and bioaccumulation of nanomaterial in aquatic species. *J. U.S. SJWP*, **2**, 1.
82. Blaise, C., Gagne, F., Ferard, J.F., and Eullaffroy, P. (2008) Ecotoxicity of selected nano-materials to aquatic organisms. *Environ. Toxicol.*, **23** (5), 591–598.
83. Baun, A., Sorensen, S.N., Rasmussen, R.F., Hartmann, N.B., and Koch, C.B. (2008) Toxicity and bioaccumulation of xenobiotic organic compounds in the presence of aqueous suspensions of aggregates of nano-C-60. *Aquat. Toxicol.*, **86** (3), 379–387.
84. Lin, S., Reppert, J., Hu, Q. *et al.* (2009) Uptake, translocation, and transmission of carbon nanomaterials in rice plants. *Small*, **5** (10), 1128–1132.
85. Jackson, P., Jacobsen, N.R., Baun, A. *et al.* (2013) Bioaccumulation and ecotoxicity of carbon nanotubes. *Chem. Cent. J.*, **7**, 154.

86. Kang, S., Pinault, M., Pfefferle, L.D., and Elimelech, M. (2007) Single-walled carbon nanotubes exhibit strong antimicrobial activity. *Langmuir*, **23** (17), 8670–8673.
87. Liu, S.B., Wei, L., Hao, L. *et al.* (2009) Sharper and faster "nano darts" kill more bacteria: a study of antibacterial activity of individually dispersed pristine single-walled carbon nanotube. *ACS Nano*, **3** (12), 3891–3902.
88. Arias, L.R. and Yang, L.J. (2009) Inactivation of bacterial pathogens by carbon nanotubes in suspensions. *Langmuir*, **25** (5), 3003–3012.
89. Yang, C.N., Mamouni, J., Tang, Y.A., and Yang, L.J. (2010) Antimicrobial activity of single-walled carbon nanotubes: length effect. *Langmuir*, **26** (20), 16013–16019.
90. Vecitis, C.D., Zodrow, K.R., Kang, S., and Elimelech, M. (2010) Electronic-structure-dependent bacterial cytotoxicity of single-walled carbon nanotubes. *ACS Nano*, **4** (9), 5471–5479.
91. Kang, S., Mauter, M.S., and Elimelech, M. (2009) Microbial cytotoxicity of carbon-based nanomaterials: implications for river water and wastewater effluent. *Environ. Sci. Technol.*, **43** (7), 2648–2653.
92. Rodrigues, D.F. and Elimelech, M. (2010) Toxic effects of single-walled carbon nanotubes in the development of E. coli biofilm. *Environ. Sci. Technol.*, **44** (12), 4583–4589.
93. Lin, D. and Xing, B. (2007) Phytotoxicity of nanoparticles: inhibition of seed germination and root growth. *Environ. Pollut.*, **150** (2), 243–250.
94. Stampoulis, D., Sinha, S.K., and White, J.C. (2009) Assay-dependent phytotoxicity of nanoparticles to plants. *Environ. Sci. Technol.*, **43** (24), 9473–9479.
95. Kang, S., Mauter, M.S., and Elimelech, M. (2008) Physicochemical determinants of multiwalled carbon nanotube bacterial cytotoxicity. *Environ. Sci. Technol.*, **42** (19), 7528–7534.
96. Liu, X.Y., Vinson, D., Abt, D., Hurt, R.H., and Rand, D.M. (2009) Differential toxicity of carbon nanomaterials in Drosophila: larval dietary uptake is benign, but adult exposure causes locomotor impairment and mortality. *Environ. Sci. Technol.*, **43** (16), 6357–6363.
97. Musee, N., Thwala, M., and Nota, N. (2011) The antibacterial effects of engineered nanomaterials: implications for wastewater treatment plants. *J. Environ. Monit.*, **13** (5), 1164–1183.
98. Roberts, A.P., Mount, A.S., Seda, B. *et al.* (2007) In vivo biomodification of lipid-coated carbon nanotubes by Daphnia magna. *Environ. Sci. Technol.*, **41** (8), 3025–3029.
99. Zhu, X.S., Zhu, L., Chen, Y.S., and Tian, S.Y. (2009) Acute toxicities of six manufactured nanomaterial suspensions to Daphnia magna. *J. Nanopart. Res.*, **11** (1), 67–75.
100. Kim, K.T., Klaine, S.J., Lin, S.J., Ke, P.C., and Kim, S.D. (2010) Acute toxicity of a mixture of copper and single-walled carbon nanotubes to Daphnia magna. *Environ. Toxicol. Chem.*, **29** (1), 122–126.
101. Kim, K.T., Edgington, A.J., Klaine, S.J., Cho, J.W., and Kim, S.D. (2009) Influence of multiwalled carbon nanotubes dispersed in natural organic matter on speciation and bioavailability of copper. *Environ. Sci. Technol.*, **43** (23), 8979–8984.
102. Petersen, E.J., Pinto, R.A., Mai, D.J., Landrum, P.F., and Weber, W.J. (2011) Influence of polyethyleneimine graftings of multi-walled carbon nanotubes on their accumulation and elimination by and toxicity to Daphnia magna. *Environ. Sci. Technol.*, **45** (3), 1133–1138.
103. Alloy, M.M. and Roberts, A.P. (2011) Effects of suspended multi-walled carbon nanotubes on daphnid growth and reproduction. *Ecotoxicol. Environ. Saf.*, **74** (7), 1839–1843.
104. Velzeboer, I., Kupryianchyk, D., Peeters, E.T.H.M., and Koelmans, A.A. (2011) Community effects of carbon nanotubes in aquatic sediments. *Environ. Int.*, **37** (6), 1126–1130.
105. Calabrese, E.J. (2005) Paradigm lost, paradigm found: the re-emergence of hormesis as a fundamental dose response model in the toxicological sciences. *Environ. Pollut.*, **138** (3), 378–411.

106. Handy, R.D., Henry, T.B., Scown, T.M., Johnston, B.D., and Tyler, C.R. (2008) Manufactured nanoparticles: their uptake and effects on fish-a mechanistic analysis. *Ecotoxicology*, **17** (5), 396–409.

107. Handy, R.D., Al-Bairuty, G., Al-Jubory, A. *et al.* (2011) Effects of manufactured nanomaterials on fishes: a target organ and body systems physiology approach. *J. Fish Biol.*, **79** (4), 821–853.

108. Cheng, J.P., Flahaut, E., and Cheng, S.H. (2007) Effect of carbon nanotubes on developing zebrafish (Danio rerio) embryos. *Environ. Toxicol. Chem.*, **26** (4), 708–716.

109. Cheng, J.P., Chan, C.M., Veca, L.M. *et al.* (2009) Acute and long-term effects after single loading of functionalized multi-walled carbon nanotubes into zebrafish (Danio rerio). *Toxicol. Appl. Pharmacol.*, **235** (2), 216–225.

110. Cheng, J.P. and Cheng, S.H. (2012) Influence of carbon nanotube length on toxicity to zebrafish embryos. *Int. J. Nanomed.*, **7**, 3731–3739.

111. Kowk, K.W.H., Leung, K.M.Y., Flahaut, E., Cheng, J.P., and Cheng, S.H. (2010) Chronic toxicity of double-walled carbon nanotubes to three marine organisms: influence of different dispersion methods. *Nanomedicine*, **5** (6), 951–961.

112. Smith, C.J., Shaw, B.J., and Handy, R.D. (2007) Toxicity of single walled carbon nanotubes to rainbow trout, (Oncorhynchus mykiss): respiratory toxicity, organ pathologies, and other physiological effects. *Aquat. Toxicol.*, **82** (2), 94–109.

113. Fraser, T.W.K., Reinardy, H.C., Shaw, B.J., Henry, T.B., and Handy, R.D. (2011) Dietary toxicity of single-walled carbon nanotubes and fullerenes (C-60) in rainbow trout (Oncorhynchus mykiss). *Nanotoxicology*, **5** (1), 98–108.

114. Schwab, F., Bucheli, T.D., Lukhele, L.P. *et al.* (2011) Are carbon nanotube effects on green algae caused by shading and agglomeration? *Environ. Sci. Technol.*, **45** (14), 6136–6144.

115. Youn, S., Wang, R., Gao, J. *et al.* (2012) Mitigation of the impact of single-walled carbon nanotubes on a freshwater green algae: Pseudokirchneriella subcapitata. *Nanotoxicology*, **6** (2), 161–172.

116. Long, Z., Ji, J., Yang, K., Lin, D., and Wu, F. (2012) Systematic and quantitative investigation of the mechanism of carbon nanotubes' toxicity toward algae. *Environ. Sci. Technol.*, **46** (15), 8458–8466.

117. Kwok, K.W., Leung, K.M., Flahaut, E., Cheng, J., and Cheng, S.H. (2010) Chronic toxicity of double-walled carbon nanotubes to three marine organisms: influence of different dispersion methods. *Nanomedicine (Lond)*, **5** (6), 951–961.

118. Wei, L., Thakkar, M., Chen, Y. *et al.* (2010) Cytotoxicity effects of water dispersible oxidized multiwalled carbon nanotubes on marine alga, Dunaliella tertiolecta. *Aquat. Toxicol.*, **100** (2), 194–201.

119. Miralles, P., Church, T.L., and Harris, A.T. (2012) Toxicity, uptake, and translocation of engineered nanomaterials in vascular plants. *Environ. Sci. Technol.*, **46** (17), 9224–9239.

120. Begum, P., Ikhtiari, R., Fugetsu, B. *et al.* (2012) Phytotoxicity of multi-walled carbon nanotubes assessed by selected plant species in the seedling stage. *Appl. Surf. Sci.*, **262**, 120–124.

121. Begum, P. and Fugetsu, B. (2012) Phytotoxicity of multi-walled carbon nanotubes on red spinach (Amaranthus tricolor L) and the role of ascorbic acid as an antioxidant. *J. Hazard. Mater.*, **243**, 212–222.

122. Canas, J.E., Long, M.Q., Nations, S. *et al.* (2008) Effects of functionalized and nonfunctionalized single-walled carbon nanotubes on root elongation of select crop species. *Environ. Toxicol. Chem.*, **27** (9), 1922–1931.

123. Mondal, A., Basu, R., Das, S., and Nandy, P. (2011) Beneficial role of carbon nanotubes on mustard plant growth: an agricultural prospect. *J. Nanopart. Res.*, **13** (10), 4519–4528.

124. Khodakovskaya, M.V., de Silva, K., Nedosekin, D.A. *et al.* (2011) Complex genetic, photothermal, and photoacoustic analysis of nanoparticle-plant

interactions. *Proc. Natl. Acad. Sci. U.S.A.*, **108** (3), 1028–1033.

125. Villagarcia, H., Dervishi, E., de Silva, K., Biris, A.S., and Khodakovskaya, M.V. (2012) Surface chemistry of carbon nanotubes impacts the growth and expression of water channel protein in tomato plants. *Small*, **8** (15), 2328–2334.

126. Akhavan, O. and Ghaderi, E. (2010) Toxicity of graphene and graphene oxide nanowalls against bacteria. *ACS Nano*, **4** (10), 5731–5736.

127. Hu, W.B., Peng, C., Luo, W.J. *et al.* (2010) Graphene-based antibacterial paper. *ACS Nano*, **4** (7), 4317–4323.

128. Liu, S.B., Zeng, T.H., Hofmann, M. *et al.* (2011) Antibacterial activity of graphite, graphite oxide, graphene oxide, and reduced graphene oxide: membrane and oxidative stress. *ACS Nano*, **5** (9), 6971–6980.

129. Pretti, C., Oliva, M., Di Pietro, R. *et al.* (2014) Ecotoxicity of pristine graphene to marine organisms. *Ecotoxicol. Environ. Saf.*, **101**, 138–145.

130. Guo, X.K., Dong, S.P., Petersen, E.J. *et al.* (2013) Biological uptake and depuration of radio-labeled graphene by Daphnia magna. *Environ. Sci. Technol.*, **47** (21), 12524–12531.

131. Begum, P., Ikhtiari, R., and Fugetsu, B. (2011) Graphene phytotoxicity in the seedling stage of cabbage, tomato, red spinach, and lettuce. *Carbon*, **49** (12), 3907–3919.

16
Exposure Scenarios in the Workplace and Risk Assessment of Carbon Nanomaterials

Rui Chen and Chunying Chen

16.1
Introduction

16.1.1
Background

Nanotechnology is one of the fastest growing and most promising technologies with booming development since the early 2000s. There are tremendous production requirements on the carbon nanomaterials because of their new and often beneficial properties. However, adverse effects and toxicity could result from these novel properties that their bulk material counterparts do not have. Their increased production will ultimately lead to more possibilities of occupational exposure. Carbon nanomaterials are biopersistent materials. Because of their small particle size, they may be systemically translocated in biological organisms after exposure and persist for a long period without being eliminated by phagocytosis of macrophages [1–3]. Worker safety is an important issue in nanotechnology. While the workers are the first to be influenced by the advancement of nanotechnology, their working environment provides the first opportunity to develop and implement responsible practices.

16.1.2
Exposure Routes and Exposure Scenarios

Synthesis of carbon nanomaterials contains gas-phase processes, which leads to high concentrations of airborne manufactured nanoparticles. Other occupational settings, such as handling and packaging of the produced material and routine cleaning and maintenance of apparatus, present similar situations. For occupational exposure to carbon nanomaterials, the most probable and easiest route for nanoparticles to enter the human body is via inhalation compared to other possible routes, that is, dermal contact, ingestion, and injection. Inhalation exposure to carbon nanomaterials by humans in the workplace is the scenario that is paid the most attention in this chapter.

Biomedical Applications and Toxicology of Carbon Nanomaterials, First Edition.
Edited by Chunying Chen and Haifang Wang.

16.1.3 Exposure Metrics

There are at least three metrics related to exposure monitoring in the work place. They are (i) mass concentration [mg m^{-3}], (ii) number concentration [particles m^{-3}], and (iii) surface area concentration [m^2 m^{-3}]. Mass concentration is the conventional metric for monitoring particulate matter and constitutes the basis for current regulations. However, number concentration and surface area concentration are two important metrics especially for nanoparticle monitoring because of their low mass compared to the larger particles. They increase exponentially when particle size decreases to less than 100 nm for particles of the same mass concentration, which renders nanoparticles more biologically active [4]. Further, it has been shown that health effects arising from exposure to nanoparticles may better correlate with the surface area rather than with mass concentration [5]. However, the basic toxicological mechanisms of human exposure to nanoparticles are not fully understood. Therefore, it is not possible to find a single metric to suit all nanomaterials or all exposure scenarios. Metrics related to characteristics such as matching to the health effects of concern, reasonable and applicable in the measurement, and sensitive enough to differentiate with the background should be selected in exposure monitoring. For example, the mass concentration of elemental carbon (EC) had been recommended as the occupational exposure limit (OEL) of carbon nanotubes (CNTs). However, the mass concentrations of EC and even the total respirable dust still do not specifically represent the quantities of CNTs. Researchers usually use the P/B ratio (process to background ratio) to relatively evaluate the impact of specific investigated processes from the background. To date, there is only one method that is specifically linked to CNTs exposure. Hedmer *et al.* recommended filter-based methods with electron microscopy (EM) analysis for risk evaluation in occupational exposure [6]. However, CNTs could be highly toxic not only because of their length but also the related catalyst metal particles [7]. Further, there are obvious shortcomings in this method because it is offline, time consuming, and laborious, and lacks a valid protocol. Until now there is no agreement on the criteria or metrics for field exposure monitoring, which makes it difficult to compare exposure data from different studies.

16.1.4 Occupation Exposure Limit for Carbon Nanomaterials

Similar to there being no agreement on the metrics, there is no consensus on OEL related to carbon nanomaterials until now. As an alternative, benchmark levels of particle number concentrations recommended by the German Institute for Occupational Safety and Health (IFA) could be used for carbon nanomaterial particle release monitoring (Table 16.1). This recommended OEL is based on the findings that the surface of nanoparticles contributes to their toxicity and hazard [9, 10]. Nanomaterials are divided into four groups in terms of their size, form, biopersistence, and density. The number concentration of this OEL

Table 16.1 Nano reference values (NRVs) of nanomaterials.

	Description	Density	NRV (8-h TWA)	Examples
1	Rigid, biopersistent nanofibers for which effects similar to those of asbestos are not excluded	—	0.01 fibers cm^{-3}	SWCNT or MWCNT or metal oxide fibers for which asbestos-like effects are not excluded
2	Biopersistent granular nanomaterial in the range of 1 and 100 nm	>6000 kg m^{-3}	20 000 particles cm^{-3}	Ag, Au, CeO_2, CoO, Fe, Fe_xO_y, La, Pb, Sb_2O_5, SnO_2
3	Biopersistent granular and fiber form nanomaterials in the range of 1–100 nm	<6000 kg m^{-3}	40 000 particles cm^{-3}	Al_2O_3, SiO_2, TiN, TiO_2, ZnO, nanoclay, carbon black, C_{60}, dendrimers, polystyrene. Nanofibers with no asbestos-like effects
4	Nonbiopersistent nanomaterial in the range of 1 and 100 nm	—	Applicable OEL	Fats, NaCl

Source: Reproduced with permission from [8].

was established corresponding to a mass concentration of 0.1 mg m^{-3} for a supposed sphere-like shape of nanomaterials with diameter less than 100 nm. Fullerenes and graphene belong to the defined low-density group. The OEL of CNTs was set by the number of 0.01 fibers cm^{-3} for the reason that they may exhibit asbestos-like effects.

The U.S. National Institute for Occupational Safety and Health (NIOSH) proposes a recommended OEL of 1 μg m^{-3} elemental carbon as a respirable mass 8-h time-weighted average (TWA) concentration, which is based on a quantitative assessment of the risk using the animal studies with sufficient dose–response data (NIOSH Publication Number 2013-145). The OELs of CNTs from NIOSH and IFA are based on different metrics, namely mass or number concentration, and they could not be compared because of various characters of CNTs under different exposure scenarios. However, OELs were defined with a high level of stringency based on present knowledge, typically from the extrapolation of animal data to the human situation by using appropriate assessment factors. They are expected to reduce the risks of adverse effects, for example, pulmonary inflammation and fibrosis. However, because of some residual risk at the OEL and uncertainty concerning chronic health effects, including whether some types of CNTs may be carcinogenic, continued efforts should be made to reduce exposures as much as possible.

16.1.5 Strategy for Exposure Assessment of Carbon Nanomaterials

If there is no particle release, there is no occupational exposure and there is no risk for the workers. The knowledge and control of the exposure are critical in risk

assessment and management. To meet these requirements, exposure assessment can be used either for the characterization of the particles released or for providing data for evaluating the effectiveness of the control measures implemented. For the exposure assessment to be repeatable and their results comparable, a reasonable and applicable strategy/protocol is absolutely required, even though there are too many variants in application situations. Based on the knowledge and published data on nanoparticle assessment, a strategy for carbon nanomaterial assessment is provided (Figure 16.1). In general, occupational exposure assessment is performed

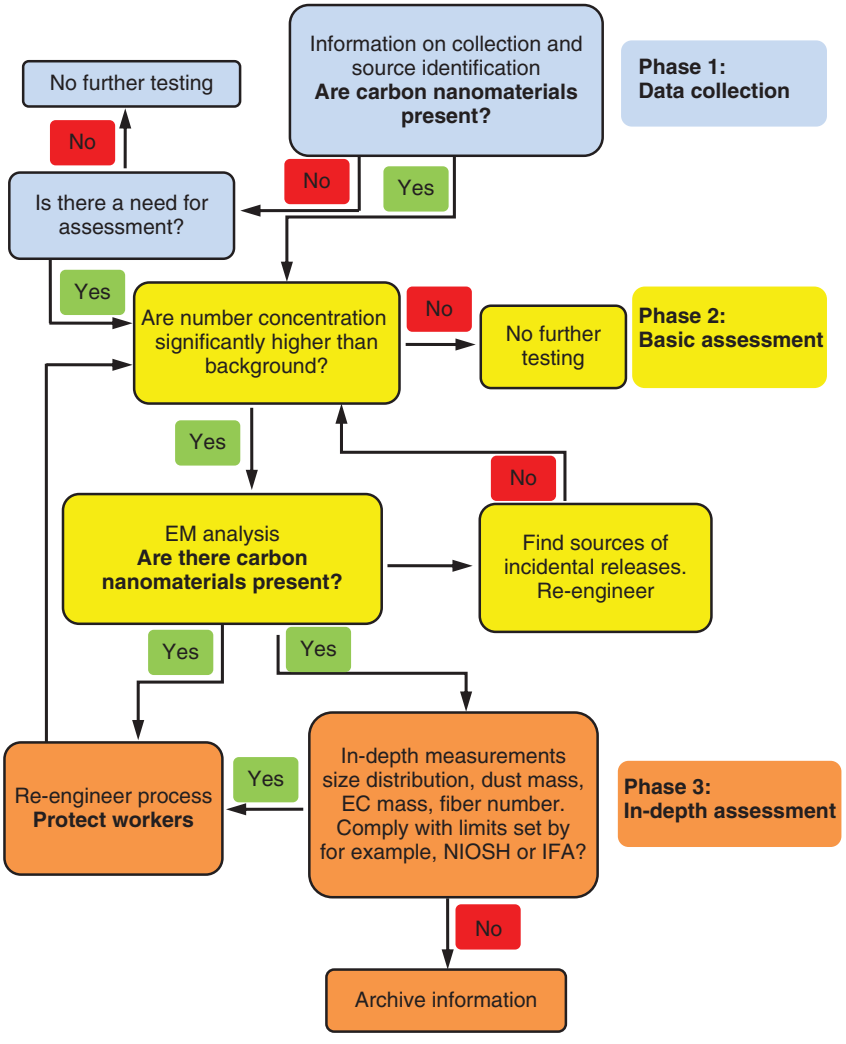

Figure 16.1 Summary of the recommended strategy for exposure assessment of carbon nanomaterials. Strategy was edited according to the final report of the MARINA 7 program and other related contributions [11, 12].

by a tiered approach: start with the basics and continue to more advanced assessment if nanoparticles are detected. The first step is to collect primary information and confirm whether we indeed work with nanomaterials and to see if potential exposure can be excluded. The second step is to take particle number concentration measurements and EM analysis at suspected emission sources. The EC mass concentration of carbon nanomaterials could be measured according to the NIOSH-recommended Method 5040. A transmission electron microscope (TEM) equipped with an energy-dispersive X-ray (EDX) analysis attachment can help distinguish the presence of carbon nanomaterials from other collected aerosol particles. Further, the background, ventilation and protective equipment, number of workers, and frequency of exposure should be addressed. If the presence of particles is confirmed by the basic assessment, a more advanced exposure assessment is carried out in step 3. This assessment includes the determination of the particle size distributions, dust mass, and EC mass on area or personal breathing zone (PBZ) samples, fiber number concentration, surface area concentration, and EM analysis.

16.2 Potential Exposure in the Workplace

16.2.1 Carbon Nanotubes

CNTs are a form of carbon, which are similar in structure to graphene but elongated to form long and thin cylinders. CNTs are usually defined by their special characteristics including the shape, dimension, chemical composition, and surface functionalization. CNTs with a single wall and multiple walls are termed single-walled carbon nanotubes (SWCNTs) and multiwalled carbon nanotubes (MWCNTs), respectively. They may be termed as "raw" CNTs, which contain residual metal catalysts, or "purified" CNTs, from which most of the metal catalysts have been removed. They also can be defined as long CNTs or short CNTs by their dimension, or aligned CNTs, entangled CNTs, or bundled CNTs by their shape [13]. It was estimated that the production capacity of carbon nanotubes was at least 1000 tons/year in 2012, and their commercial market is expected to show a steady increase in the coming decade [14]. High-volume production means increased possibility of occupational exposure in various production or processing steps. Previous data indicate that airborne exposures to CNTs may occur during the transfer, weighing, blending, and mixing of the bulk powders, and during the cutting and drilling of CNT composite materials.

Traditionally, exposure assessment methods of CNTs have focused on the collection of samples for the total gravimetric mass (GM) of all particles or indirectly estimated mass specific to CNTs. The exposure metrics can be described as total GM, mass of elemental carbon fraction, or number concentration at the PBZ, as shown in the exposure concentration summary in Table 16.2. Maynard *et al*.

Table 16.2 Studies with detectable personal breathing zone (PBZ) mass concentrations.

Type of samples collected	PBZ mass concentrations	References
Estimated inhalable mass ($\mu g\,m^{-3}$)	0.7–53	[15]
Total gravimetric mass ($\mu g\,m^{-3}$)	N.D.–430	[16]
Total gravimetric mass ($\mu g\,m^{-3}$)	7.8–320.8	[17]
Total carbon – inhalable size fraction ($\mu g\,m^{-3}$)	64–1094	[18]
Elemental carbon – inhalable size fraction ($\mu g\,m^{-3}$)	N.D.–38	[19]
Elemental carbon – inhalable size fraction ($\mu g\,m^{-3}$)	N.D.–7.86	[20]
Elemental carbon – respirable size fraction ($\mu g\,m^{-3}$)	45–80	[21]
Total particle number concentration (number cm^{-3}, P/B)	4000–7000, ≈1	[22]
Total particle number concentration (number cm^{-3}, P/B)	<2000, ≈1	[23]
Total gravimetric mass (PM_{10}, $\mu g\,m^{-3}$)	800–2400	[24]
Fiber concentration (fibers cm^{-3})	0.2	[24]
Fiber concentration (fibers cm^{-3})	1.9	[25]
Total gravimetric mass of sanding process ($\mu g\,m^{-3}$, P/B)	0.2–21.4, 0.66–24.4	[26]
P/B ratio from total particle number concentration in sanding process	1.04	[26]
Weighting process, total gravimetric mass ($\mu g\,m^{-3}$, P/B)	N.D.–0.03, 1.79	[26]
P/B ratio from total particle number concentration in sanding process	1.06	[26]
Elemental carbon – respirable size fraction ($\mu g\,m^{-3}$), from 14 sites	0.02–2.94	[27]
Fiber concentration (fibers cm^{-3})	0.017–0.06	[28]
Elemental carbon – inhalable size fraction ($\mu g\,m^{-3}$)	6.2–9.3	[29]
Respirable dust mass ($\mu g\,m^{-3}$)	73–93	[6]
Elemental carbon – respirable size fraction ($\mu g\,m^{-3}$)	0.08–7.4	[6]
Fiber concentration (fibers cm^{-3})	0.04–2.0	[6]

N.D., nondetectable samples; P/B, process to background ratio.

assessed the SWCNT exposures in a laboratory-based study and during the handling (e.g., furnace removal, powder transfer, cleaning) of unrefined material at four small-scale SWCNT manufacturing facilities [15]. The mass concentrations of SWCNT exposure were estimated to range from 0.7 to 53 $\mu g\,m^{-3}$ (area samples) in the absence of exposure controls. The aerosolized SWCNTs were agglomerated with sizes typically larger than 1 μm. Han *et al.* found the total particulate concentrations before any control ranging from 0.21 to 0.43 $mg\,m^{-3}$, which then decreased to an undetectable level after implementing control measures. MWCNTs represented only a fraction of this total dust. The number of MWCNTs in the samples obtained from the MWCNT blending laboratory ranged from 172.9 to 193.6 tubes cm^{-3} before the control measures, which decreased to 0.018–0.05 tubes cm^{-3} after introduction of protective measures [16]. Another study on seven CNT-handling workplaces found the total GM concentrations from PBZ measurements ranging from 7.8 to 320.8 $\mu g\,m^{-3}$ [17]. It was shown that processing steps such as opening the chemical vapor deposition (CVD) cover and catalyst preparation presented high chances of nanoparticle release, followed by spraying, CNT preparation, ultrasonic dispersion, and wafer

heating. The occupational exposure in all these operation processes could be effectively controlled by measures such as engineering control.

Bello *et al.* [22] measured the airborne particle concentrations of MWCNTs during production. A real-time fast-mobility particle sizer (FMPS) and a condensation particle counter (CPC) were used to monitor the particle number concentrations throughout the CNT production. No increase in the total airborne particle concentration was reported during the CNT handling processes. No detectable quantity of MWCNTs was observed by EM detection. However, this study did not provide enough information on the differentiation between the background and the manufactured nanoparticles. The total particle number concentration of indoor environment measured by CPC3007 (10 – 1 μm) usually varies between 2000 and 10 000 particles cm^{-3} without ventilation control [30]. This value was between 4000 and 7000 particles cm^{-3} in Bello's study [22]. The background aerosol particles originate from various natural and anthropogenic sources such as forest fires, traffic, combustion sources, and so on. However, the particles released from CNT production are mostly elemental carbon and metal particles from the catalyst. Their morphology and chemical composition differ from those of manufactured nanoparticles. In order to assess the exposure to manufactured nanoparticles, we need to discriminate between particles from various sources. A preliminary monitoring focused on the CNT handling processes including laser labeling on CNT films after growth on silicon substrate and the rolling detach procedure of CNTs from the silicon substrate was implemented in a clean CNT manufacturing facility. The two CNT handling procedures showed obvious particle release to the environment at the low background level of aerosol. Further, an undetectable level was logged in the PBZ sites of workers, which means ventilation resulted in quick cleaning of the released particles in this factory. In a high aerosol background environment, it could be supposed the released nanoparticles are still chemically present in the aerosol even though they are scavenged by background particles in the absence of ventilation or other engineering control.

Tsai *et al.* [23] determined the airborne particle and CNT release in a laboratory setting, in which various types of CNTs were produced using CVD. Particle concentrations of the background level were determined to assist in quantifying the release of CNTs during their synthesis and handling. Particle measurements inside a fume hood during the synthesis of SWCNTs were found to peak at 4×10^6 to 1×10^7 particles cm^{-3} with an average particle diameter of 50 nm, whereas the concentration levels at PBZ sites of workers near the fume hood were considerably lower (<2000 particles cm^{-3}). Recently, several studies have utilized methodologies to measure the chemical-specific mass of elemental carbon as a marker for CNT exposure. NIOSH has recommended Method 5040 as a standard method to quantify the occupational exposure of CNTs. Methner *et al.* [18, 19] conducted emission and exposure assessment studies at different sites where engineered nanomaterials were produced or used by this recommended method. In CNT- and carbon nanofiber (CNF)-related sites, few detectable exposures occurred during short-duration tasks at SWCNT or CNF downstream user facilities [19].

PBZ samples were collected and analyzed for EC. The highest PBZ concentration (38 μg m^{-3}) occurred during the harvesting of SWCNTs from the reactor. Most of the collected samples showed evidence of SWCNT or CNF exposure by EM, although EC concentrations were undetectable. Birch *et al.* found that the elemental carbon concentrations of respirable size fraction ranged from 45 to 80 μg m^{-3} in a large CNF production facility, which was equal to 96–170 times that outdoors [21]. Dahm *et al.* compared the exposure patterns between primary producers and secondary manufactures of MWCNT, SWCNT, and CNF materials [20]. The elemental concentration ranged from undetectable to 7.86 μg m^{-3} for the inhalable size fractions. The concentrations of PBZ samples from two secondary manufacturing facilities handing dry powder were found to be generally higher than all samples from surveyed primary producing factories. Similarly, microscopy-based evidences showed CNTs/CNFs were found at all sites, with the highest CNT/CNF structure counts in samples collected at secondary manufacturing sites. Recently, Dahm *et al.* [27] reported their new investigation data on the industrywide exposure assessment among U.S. CNT and CNF manufacturers and users. Respirable EC PBZ concentrations ranged from 0.02 to 2.94 μg m^{-3} with a geometric mean of 0.34 μg m^{-3} and an 8-h TWA of 0.16 μg m^{-3}. PBZ samples at the inhalable size fraction for EC ranged from 0.01 to 79.57 μg m^{-3} with a GM of 1.21 μg m^{-3}. PBZ samples analyzed by TEM showed concentrations ranging from 0.0001 to 1.613 CNT or CNF structures per cubic centimeters with a GM of 0.008 and an 8-h TWA concentration of 0.003. The most common CNT structure sizes were found to be larger agglomerates in the 2–5 μm range as well as agglomerates >5 μm. A statistically significant correlation was observed between the inhalable samples for the mass of EC and structure counts by TEM (Spearman $\rho = 0.39$, $P < 0.0001$). This industrywide survey revealed that EC PBZ and area TWA samples were below the NIOSH recommended exposure limit (REL), 96% were <1 μg m^{-3} at the respirable size fraction), while 30% of the inhalable PBZ EC samples were found to be >1 μg m^{-3}. They suggested that EC monitoring (both respirable and inhalable size fractions) and TEM should be implemented in future work.

Machining of composite materials containing CNTs is another important scenario that offers the possibility of occupational exposure. Until now, the particle release from cutting, drilling, and sanding on CNT composites has been reported [24–26]. Fiber concentrations were determined by the NIOSH Method 7400 in these studies. Particle release was found to increase with the thickness (or number of plies) of the composite sample during the cutting process. Surface area concentration was used to evaluate the airborne exposures to nanoscale particles and fibers during cutting CNT composites [24]. This is the only study in which surface area concentrations are reported. Measurements were made of the airborne concentrations at the source and in the breathing zone of workers (Table 16.3).

In drilling, high-speed drilling on dry samples and larger drills produce higher number concentrations (Table 16.2). The emissions arising from both cutting and drilling could be greatly reduced by using lubricants in the machining processes. Higher input energies (e.g., higher drilling rpms, larger drill bits) and longer drill times associated with thicker composites generally produced

Table 16.3 Airborne concentrations in the processes of cutting CNT composite.

Composite	Arithmetic mean (SEM) of total number concentration (number cm^{-3})		Arithmetic mean surface area (μm^2 cm^{-3}) by size range (fraction of the total surface area)			
	FMPS	APS	$d \leq 0.1\,\mu m$	$0.1 < d \leq 1.0\,\mu m$	$1 < d \leq 10\,\mu m$	$10 < d \leq 20\,\mu m$
Background	4.82×10^3 (0.63×10^4)	11.4 (0.08)	286 (0.26)	340 (0.29)	642 (0.44)	10 (0.00)
Wet cutting of base carbon	9.4×10^4 (0.28×10^4)	47.6 (2.0)	12 580 (0.11)	99 373 (0.85)	4 077 (0.04)	68 (0.00)
Source, dry cutting						
Base – alumina	1.48×10^5 (3.7×10^4)	135.2 (4.8)	6 367 (0.10)	4 429 (0.06)	65 551 (0.83)	863 (0.01)
CNT – alumina	0.38×10^5 (0.13×10^4)	285.3 (19.1)	1 118 (0.01)	17 046 (0.14)	214 506 (0.84)	2 281 (0.01)
Base – carbon	2.83×10^5 (9.5×10^4)	1 003.8 (33.5)	6 914 (0.02)	35 056 (0.09)	411 140 (0.89)	3 944 (0.01)
CNT – carbon	2.94×10^5 (1.7×10^4)	867.1 (52.2)	7 809 (0.04)	40 898 (0.25)	339 971 (0.71)	4 386 (0.01)
PBZ, dry cutting						
Base – alumina	0.88×10^5 (0.51×10^4)	72.2 (4.6)	3 102 (0.13)	4 053 (0.16)	24 768 (0.71)	44 (0.00)
CNT – alumina	0.28×10^5 (0.69×10^3)	62.2 (4.6)	711 (0.04)	10 517 (0.29)	33 374 (0.67)	54 (0.00)
Base – carbon	3.19×10^5 (1.12×10^4)	777.5 (26.1)	7 311 (0.03)	32 487 (0.12)	270 961 (0.85)	1 769 (0.00)
CNT – carbon	1.53×10^5 (0.77×10^4)	215.7 (11.5)	4 150 (0.05)	30 917 (0.34)	79 899 (0.61)	544 (0.00)

APS, aerodynamic particle sizer; FMPS, fast-mobility particle sizer.
Source: Reproduced with permission from [24].

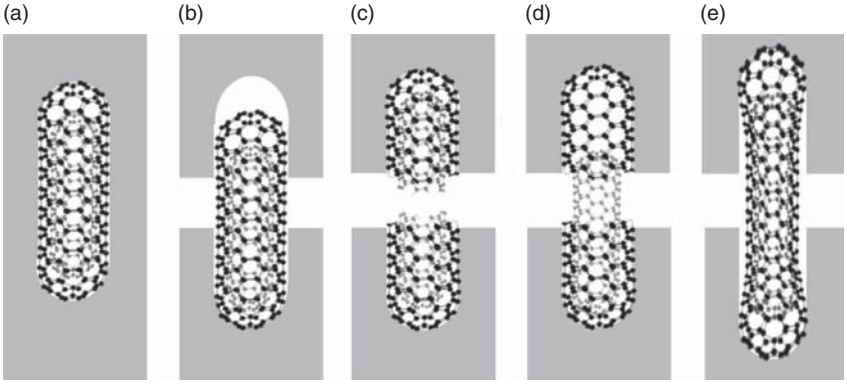

Figure 16.2 Schematic description of possible fracture mechanisms of CNTs. (a) Initial state of the CNT. (b) Pull-out caused by CNT/matrix debonding in case of weak interfacial adhesion. (c) Rupture of CNT – strong interfacial adhesion in combination with extensive and fast local deformation. (d) Telescopic pull-out fracture of the outer layer due to strong interfacial bonding and pull-out of the inner tube. (e) Bridging and partial debonding of the interface local bonding to the matrix enabling crack bridging and interfacial failure in the nonbonded regions. (Reprinted with permission from [31].)

higher exposures, and the drilling of CNT-based composites generated a higher amount of nanofibers than while cutting CNT-based composites. In the case of sanding, the PBZ nanoparticle number concentrations were negligible compared to background concentrations in all tested conditions including without local exhaust ventilation, in a fume hood, and in a biological safety cabinet. TEM data showed that the particles generated during sanding were micrometer-sized with protruding CNTs and were very different from bulk, agglomerated CNTs of the same size. Gojny *et al*. [31] schematically described possible processes and mechanisms, explaining the physical deformation of CNTs in composite materials. Tubes in these materials are generally thought to have a bridging role. As illustrated in Figure 16.2, the initial situation of CNTs in an ideal case is complete impregnation and isolation embedded in the matrix. In case of a crack, various fracture outcomes can occur depending on the interfacial adhesion and the mechanical properties of the CNTs.

In summary, a range of methods and measurement metrics (number mass and surface area concentrations) have been used in attempts to quantify the exposure of CNTs in workplace. The measurement of EC is a more specific and sensitive marker of exposure, which provides a more realistic workplace exposure concentration when compared to gravimetric sampling and number concentration counting. There is rather limited data of CNT exposure at the present evaluation stage. Most studies showed some evidence of elevated levels in particle release, usually combined with morphology evidences of the released fibers or "fiber-like" particulates. Most exposures seemed to be linked with worst case scenarios, such as absent, defective, or disabled control systems.

16.2.2
Fullerenes, Metallofullerenes, and Graphenes

Fullerenes are carbon allotropes composed entirely of carbon, in the form of a hollow sphere, ellipsoid, or tube. One of the representative fullerenes, the C_{60} fullerene, is a remarkably stable compound with a form like a soccer ball, with a diameter about 0.7 nm and a molecular weight of 720 g mol^{-1} [32]. Fullerenes are considered nanomaterials, although they may agglomerate as crystals with sizes much larger than 100 nm. An individual fullerene molecule has a cage-like structure with a hollow inside the structure that is capable of trapping various metals. Metallofullerenes are used to represent a series of combined structures, such as lanthanum-containing fullerene ($La@C_{82}$) or gadolinium-containing fullerene ($Gd@C_{82}$) [33, 34]. Surface modifications are often carried out to make fullerenes hydrophilic, such as Gd-metallofullerenol [$Gd@C_{82}(OH)_{22}$]. The different physicochemical characters of various fullerenes determine their potential toxicity during human exposure. It is generally accepted that the fullerene production quantity is of small scale, ~10 tons per year by 2012 estimates, but it is expected to show a steady growth in the next decade [14].

The commercial manufacturing of fullerenes is carried out under a closed reaction chamber under vacuum conditions. Possible particle exposure may occur only after the synthesis process when the reaction chamber is opened. The possible occupational exposure can happen in procedures such as dust collection, product weighing and packaging, and routine equipment maintenance and cleaning [35]. Fujitani *et al.* [35] measured the physicochemical properties, number concentrations, and number and size distributions of aerosols in a fullerene factory in Japan. At this facility, mixed fullerene was extracted by a solvent from soot generated by the combustion of hydrocarbon–oxygen mixtures. The mixed fullerenes produced included C_{60}, C_{70}, and other higher fullerenes. Fullerenes are produced in a closed system to minimize the potential for exposure during production. After the drying process, the fullerene is transported to and kept in a storage tank until it is removed and bagged. The transportation, weighing, and bagging procedures cause the leakage of coarse particles (diameter > 1 μm) of fullerene. SEM examination has revealed that the coarse particles emitted during bagging and/or weighing were aggregates/agglomerates of fullerenes (Figure 16.3). It was estimated the highest possible concentration applied in the exposure assessment was 2.0 μg m^{-3} for micrometer-sized particles (>2000 nm), and 0.004 μg m^{-3} for nanometer-sized particles (<50 nm) [35]. As a comparison, Shinohara *et al.* [36] provided similar low-level exposure data of the C_{60} air concentrations monitored at a metal-containing fullerene manufacturing site (Table 16.4).

Yeganeh *et al.* [37] characterized airborne particle concentrations during the production of fullerenes in a commercial nanotechnology facility. They measured inhalable fine particle mass concentrations ($PM_{2.5}$) and submicrometer size distributions at three locations inside the facility: inside the fume hood where nanomaterials were produced, just outside the fume hood, and in the background. Three activities were assessed as "arc reaction," "sweeping," and "vacuuming." The

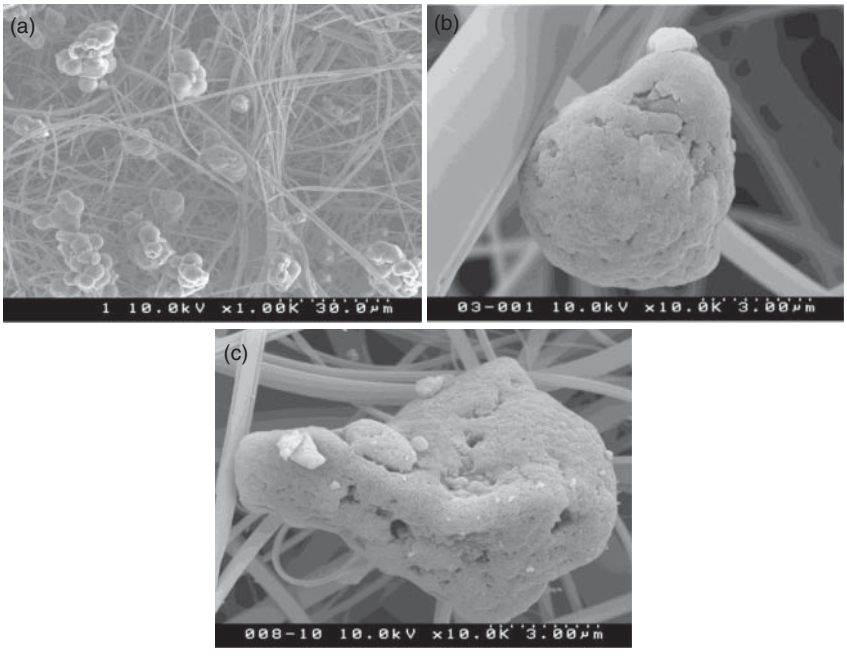

Figure 16.3 (a) SEM images of released fullerene particles during the agitation process. (b) Bagging process in a fullerene factory. (Reprinted with permission from [35].)

Table 16.4 Air concentration of C_{60} captured as particles at the manufacturing site of metal-containing fullerene.

Particle diameter (nm)	Air concentration (µg m^{-3})				
	Beside synthesis device			Beside weighing equipment	
	Work hours (6 h × 3 days)	During handling operation (30 min)	During synthesis (2 h)	Work hours (6 h × 3 days)	During handling operation (30 min)
<250	0.0023	0.064	No measurement	0.00083	0.014
250–500	0.0014	Data lost		0.00065	0.0040
500–1 000	0.0038	0.11		0.0029	0.0028
1 000–2 500	0.0040	0.056		0.0032	N.D.
2 500–10 000	0.0092	0.080		0.0049	0.025
All particles		0.22	0.0045		No measurement
(including > 10 000)	0.13	0.66	0.0069	0.040	

N.D., below the limit of detection.
Source: Reproduced with permission from [36].

monitoring data was assessed by comparison with outdoor measurements. The average $PM_{2.5}$ and particle number concentrations were not significantly different inside and outside the facility. The $PM_{2.5}$ mass concentration ranged from 50 to 125 $\mu g\, m^{-3}$ but it seemed to vary with the activities. However, large short-term increases in $PM_{2.5}$ and particle number concentrations were associated with physical handling of nanomaterials and other production activities ("including drilling and cutting of graphite and metal"). In many cases, an increase in the number of sub-100-nm particles accounted for most of the increase in the total number concentrations. Based on the measurements in this study, the engineering controls at the facility appear to be effective in limiting exposure to nanomaterials. In summary, only two studies were identified as relevant to occupational exposure to fullerenes, both describing production activities. A range of methods and measurement metrics (particle number and mass concentration) have been used in an attempt to quantify exposure. Both studies showed some evidences of elevated exposures usually caused by handling of the fullerene product.

Graphene, made up of two-dimensional hexagonal lattices, is the basic structural element of CNTs and fullerenes. Most applications and research have focused on its derivative, graphene oxide (GO), which is characterized by a high density of functional groups. To date, there is a paucity of published information and data concerning exposure to GO/graphene in working place. It may be due to the following reasons: (i) It has lower toxicity when compared to other carbon nanomaterials, for example, CNTs [38–40]. (ii) GO is reported to be an auto-degrading material on the time scale of months, with an aqueous degradation pathway resulting in the formation of humic acid, which is a benign end product and may be easily cleared from the body [41]. Even so, a cautious attitude should be taken with these carbon nanomaterials. More information and data on occupational, consumer, and environmental exposure are urgently needed to support effective risk assessment and characterization.

16.3
Exposure Risk Assessment and Engineering Control

16.3.1
Risk Assessment Strategy on Carbon Nanomaterials

The risk assessment structure on nanomaterials has been well described by Tsuji *et al.* [12]. In the risk assessment framework of carbon nanomaterials, the first step is to characterize the nanomaterial itself, which is given in Chapter 1. Then, the interaction, distribution, metabolism, excretion, and associated toxicity of carbon nanomaterials with organisms at the *in vitro*/*in vivo* levels were thoroughly discussed as a main part in this book. Further, assessment of the particle release in workplace is an important step in our understanding of the hazards associated with carbon nanomaterials. It provides information about workplace exposures, the types and nature of carbon nanomaterials when released in the workplace, and

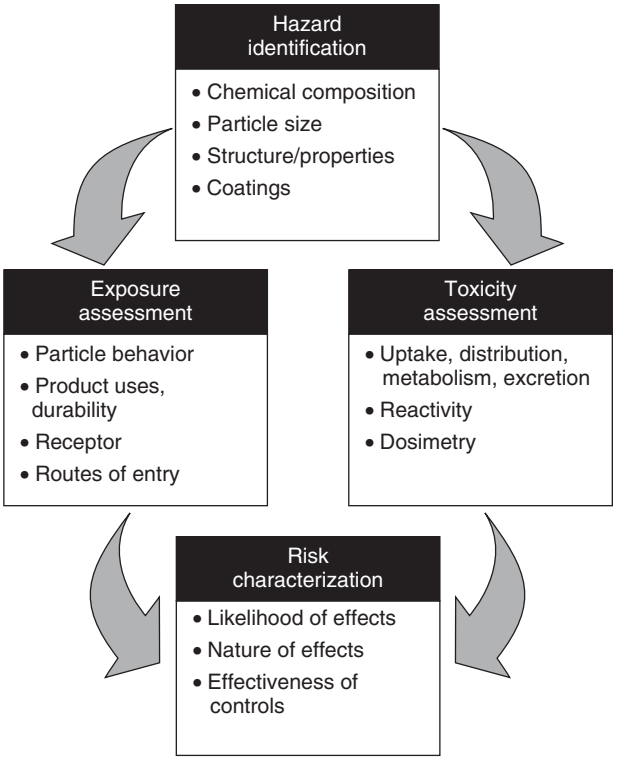

Figure 16.4 Risk assessment framework for nanomaterials. (Reprinted with permission from [12].)

how that compares with the toxicity study in this book. Finally, risk assessments are carried out following both a quantitative and a qualitative approach based on the identified information (Figure 16.4). Based on the limited exposure monitoring data of carbon nanomaterials, most particle release scenarios are associated with physical handling of carbon nanomaterials and other processing activities on material composites. Further, the actual occupational exposure at the working site is considered lower than the estimated levels with the use of engineering control/protective measures; however, the estimation obtained should be applied in the risk assessment as a worst case.

In an occupational setting, exposure to carbon nanomaterials, for example, fullerenes, graphenes, and CNTs, can in principle occur for workers at all phases of the material life cycle. The potential toxicology relating to the exposure comprises respiratory effects during their manufacture and handling of the dry powder, including recovery, packaging, transport, and storage. Also of concern are operations, manufacturing, and during the incorporation of high-aspect-ratio CNTs into products, for example, nanocomposites, and possibly during the downstream handling and manipulating of these products, for example, cutting and drilling. The downstream handling of powder materials contributed to

the worst case, as seen from the reviewed publications (Table 16.2). In these circumstances, the exposure quantities of materials will typically be much larger and even higher than the recommended OELs. Apart from this, there is obvious shortage of occupational exposure information for effective risk assessment. Most published exposure scenarios are generally likely to be able to identify the hazards associated with production and handling of carbon nanomaterials. The main gaps comprise nanomaterial characterization, standardized detection methods, nanomaterial fate, dynamics of particle release, and the effective dosage assessment of human exposure. These uncertainties require additional work for the risk assessment of carbon nanomaterials.

16.3.2 Inhalation Exposure Assessment Method

Risk assessments based on the PBZ samples were implemented in most published exposure scenarios. However, there is a lack of correlation to occupational exposures in workers due to paucity of human exposure assessment data. As an alternative, risk assessments could be done by estimating the exposure quantities from the data of realistic workplace exposure scenarios. This alternative method provides a quantitative comparison of the exposures on human and animals (mice or rats), based on lung doses that are estimated by accounting for the differences in the routes of exposure and particle size characteristics and by normalizing to either the mass or alveolar surface area of the lungs in each species. Then, the risk estimation can be achieved by assuming similar significant toxic effects that would take place in humans and animals for a high corresponding dose and a low dose to serve as a no observable effect level.

The pulmonary toxicity is mostly related to the pulmonary alveolar region, including toxicity, inflammation, and interstitial fibrosis in the lung. The multipath particle deposition model (MPPD, Applied Research Associates, Inc., USA) was used to estimate the particle deposition in the lung [42–45]. Particle characteristic input values used in MPPD include the mass median aerodynamic diameter (MMAD), geometric standard deviation (GSD), and density. The default breathing rates and parameters were automatically decided for different species. The deposition ratios can be calculated by this software based on the specified parameters of the used particles. Therefore, alveolar deposition is calculated as follows:

Human alveolar deposition (mg) = exposure concentration ($mg\,m^{-3}$) × duration (h/day × day per week × week) × minute ventilation ($l\,min^{-1}$) × 0.001 $m^3\,l^{-1}$ × 60 $min\,h^{-1}$ × alveolar deposition fraction.

Then, the lung dose estimates in different species are normalized by the lung alveolar surface area to estimate the equivalent dose as follows:

Human deposition/human alveolar surface area = mouse deposition/mouse alveolar surface area = rat deposition/rat alveolar surface area.

The average alveolar surface area assumed for human is 102 m^2, for mice 0.055 m^2, and for rat 0.4 m^2.

16.3.3 Exposure Controls

Exposure hazards in the workplace and toxicity development of human exposure force effective exposure control. The appropriate risk management practices generally are compulsorily required in the workplace involving carbon nanomaterials. Exposure control methods consist of two parts: engineering control and personal protective equipment (PPE), for example, enclosure of exposure sources or ventilation for the former, and facemask or protective clothing of the latter. Nanoparticles have a quick diffusion character and will float in the air for a considerably long time. Here, engineering control systems are designed for use to control airborne nanoparticles as gas rather than as particulate challenges. The PPE provides isolation between nanoparticles and the human body. However, few studies have focused on investigating the effectiveness of common types of exposure controls used to reduce workplace exposures. For example, glove depositions of CNTs in working place were quantified, but no assessment of the protection was done across the range of possible exposure concentrations and job tasks [15, 46]. Exposure control techniques such as well-designed ventilation systems and source enclosures that isolate the generation source from the workers have been shown to be effective for controlling the release of airborne nanoparticles [27, 35]. One research showed the fume hood with traditional constant flow may not be completely effective in controlling nanoparticle exposures, but a newly designed air-curtain hood gives high and effective protection [47]. The evaluation of engineering controls and the effectives of PPE should be intensified considering the future expected high-volume production of carbon nanomaterials. Therefore, it is suggested to evaluate workplace exposures and the protection effectiveness of the exposure controls using the above-mentioned OELs from IFA or NIOSH by well-controlled procedures. Generally, several issues should be considered for exposure control and occupational health protection in the carbon-nanomaterial-related working places: (i) forced ventilation systems should be compulsorily used; (ii) workers should be mandated to wear PPE, such as special clothing, facemask, and gloves; (iii) workers should be made aware of the adverse health effects in the case of exposure; and (iv) workers should be made to undergo regular medical check-ups, especially for the adverse effects that were thoroughly discussed in this book.

In summary, exposure control for nanoparticles is unlikely to be highly dependent on the composition of material since the primary process of both collection and dispersion is diffusion, which is largely a function of the physical size. Most of the exposure studies have shown that exposure occurs only where the exposure control systems are defective or have been deliberately deactivated. In a general sense, the methods used appear to work if they have been properly maintained. Lots of additional data and information are required for evaluating the occupational safety and health concerns of working with carbon nanomaterials: (i) research and development of improved sampling and analytical methods for measuring airborne exposures to carbon nanomaterials; (ii) determination of the effectiveness of engineering controls according to REL/OELs, for example,

1 μg m^{-3} from NIOSH; (iii) determination of the effectiveness of high efficiency particulate air (HEPA) filters in an exhaust ventilation system for removing released carbon nanomaterials; and (iv) validation of the protective functions of gloves and other PPE in preventing exposure from carbon nanomaterials.

16.4 Summary and Outlook

This chapter provided an overview of the exposure scenarios of carbon nanomaterials in the workplace. One of the essential steps to link toxicity evaluation and the risk assessment is to know and identify the exposure potential in the place where there is a high chance of exposure, namely the working environment. To date, knowledge on occupational exposure of carbon nanomaterials is not sufficient to make conclusive decisions on their risks. Preliminary conclusions of the risk estimation can be carried out only on a case-by-case basis. It might be possible to fulfill this task after more valid data become available from different exposure scenarios. Improvement in the understanding of the risks to human health will enable a safer development of nanotechnology in the future. However, there are many challenges ahead that must be overcome, which include the uncertainty surrounding the choice of the most appropriate exposure metric (e.g., particle size, number, mass, surface area, etc.), the lack of relevant protocols (e.g., strategy, validated apparatus, risk estimation models, etc.), and the time and expense needed for detailed occupational exposure assessment studies. The complexities of occupational assessment of carbon nanomaterials require more delicate analysis and design. Further, high-efficiency approaches, such as grouping or tiered exposure assessment methods, are essential to ensure that human risk assessments can be carried out both efficiently and comprehensively. With increasing applications of carbon nanomaterials, it is clear that we must pay much more attention to their adverse potentials and seek solutions beyond the state of the art for sustainable development.

Acknowledgments

We acknowledge the support from the Ministry of Science and Technology of China (2011CB933401), the National Natural Science Foundation of China (21477029 and 21277080), and the National Science Fund for Distinguished Young Scholars (11425520).

References

1. Liu, Y., Zhao, Y., Sun, B. *et al.* (2013) Understanding the toxicity of carbon nanotubes. *Acc. Chem. Res.*, **46** (3), 702–713.
2. Meng, L., Chen, R., Jiang, A. *et al.* (2013) Short multiwall carbon nanotubes promote neuronal differentiation of PC12 cells via up-regulation of the

neurotrophin signaling pathway. *Small*, **9** (9–10), 1786–1798.
3. Jiao, F., Liu, Y., Qu, Y. *et al.* (2010) Studies on anti-tumor and antimetastatic activities of fullerenol in a mouse breast cancer model. *Carbon*, **48** (8), 2231–2243.
4. Oberdorster, G., Oberdorster, E., and Oberdorster, J. (2005) Nanotoxicology: an emerging discipline evolving from studies of ultrafine particles. *Environ. Health Perspect.*, **113** (7), 823–839.
5. Braakhuis, H.M., Cassee, F.R., Fokkens, P.H. *et al.* (2015) Identification of the appropriate dose metric for pulmonary inflammation of silver nanoparticles in an inhalation toxicity study. *Nanotoxicology*, **23**, 1–11.
6. Hedmer, M., Isaxon, C., Nilsson, P.T. *et al.* (2014) Exposure and emission measurements during production, purification, and functionalization of arc-discharge-produced multi-walled carbon nanotubes. *Ann. Occup. Hyg.*, **58** (3), 355–379.
7. Meng, L., Jiang, A., Chen, R. *et al.* (2013) Inhibitory effects of multiwall carbon nanotubes with high iron impurity on viability and neuronal differentiation in cultured PC12 cells. *Toxicology*, **313** (1), 49–58.
8. Van Broekhuizen, P., Van Broekhuizen, F., Cornelissen, R. *et al.* (2012) Workplace exposure to nanoparticles and the application of provisional nanoreference values in times of uncertain risks. *J. Nanopart. Res.*, **14** (4), 1–25.
9. Nalwa, H.S. and Zhao, Y. (eds) (2007) *Nanotoxicology*, American Scientific Publishers.
10. Chen, R. and Chen, C. (2012) *Nanotoxicity*, in *The Nanobiotechnology Handbook* (ed Y.B. Xie), Taylor & Francis, Abingdon, pp. 599–620.
11. OECD (2009) Emission Assessment for Identification of Sources and Release of Airborne Manufactured Nanomaterials in the Workplace: Compilation of Existing Guidance, http://www.oecd.org/science/nanosafety/43289645.pdf (accessed June 2015).
12. Tsuji, J.S., Maynard, A.D., Howard, P.C. *et al.* (2006) Research strategies for safety evaluation of nanomaterials, part IV: risk assessment of nanoparticles. *Toxicol. Sci.*, **89** (1), 42–50.
13. Chen, R., Zhang, L., Ge, C. *et al.* (2015) Subchronic toxicity and cardiovascular responses in spontaneously hypertensive rats after exposure to multiwalled carbon nanotubes by intratracheal instillation. *Chem. Res. Toxicol.*, **28** (3), 440–450.
14. Piccinno, F., Gottschalk, F., Seeger, S. *et al.* (2012) Industrial production quantities and uses of ten engineered nanomaterials in Europe and the world. *J. Nanopart. Res.*, **14** (9), 1–11.
15. Maynard, A.D., Baron, P.A., Foley, M. *et al.* (2004) Exposure to carbon nanotube material: aerosol release during the handling of unrefined single-walled carbon nanotube material. *J. Toxicol. Environ. Health A*, **67** (1), 87–107.
16. Han, J.H., Lee, E.J., Lee, J.H. *et al.* (2008) Monitoring multiwalled carbon nanotube exposure in carbon nanotube research facility. *Inhalation Toxicol.*, **20** (8), 741–749.
17. Lee, J.H., Lee, S.B., Bae, G.N. *et al.* (2010) Exposure assessment of carbon nanotube manufacturing workplaces. *Inhalation Toxicol.*, **22** (5), 369–381.
18. Methner, M., Hodson, L., Dames, A. *et al.* (2010) Nanoparticle Emission Assessment Technique (NEAT) for the identification and measurement of potential inhalation exposure to engineered nanomaterials--Part B: results from 12 field studies. *J. Occup. Environ. Hyg.*, **7** (3), 163–176.
19. Methner, M., Beaucham, C., Crawford, C. *et al.* (2012) Field application of the Nanoparticle Emission Assessment Technique (NEAT): task-based air monitoring during the processing of engineered nanomaterials (ENM) at four facilities. *J. Occup. Environ. Hyg.*, **9** (9), 543–555.
20. Dahm, M.M., Evans, D.E., Schubauer-Berigan, M.K. *et al.* (2012) Occupational exposure assessment in carbon nanotube and nanofiber primary and secondary manufacturers. *Ann. Occup. Hyg.*, **56** (5), 542–556.
21. Birch, M.E., Ku, B.K., Evans, D.E. *et al.* (2011) Exposure and emissions monitoring during carbon nanofiber production--Part I: elemental carbon and

iron-soot aerosols. *Ann. Occup. Hyg.*, **55** (9), 1016–1036.

22. Bello, D., Hart, A.J., Ahn, K. *et al.* (2008) Particle exposure levels during CVD growth and subsequent handling of vertically-aligned carbon nanotube films. *Carbon*, **46** (6), 974–977.
23. Tsai, S.-J., Hofmann, M., Hallock, M. *et al.* (2009) Characterization and evaluation of nanoparticle release during the synthesis of single-walled and multiwalled carbon nanotubes by chemical vapor deposition. *Environ. Sci. Technol.*, **43** (15), 6017–6023.
24. Bello, D., Wardle, B.L., Yamamoto, N. *et al.* (2009) Exposure to nanoscale particles and fibers during machining of hybrid advanced composites containing carbon nanotubes. *J. Nanopart. Res.*, **11** (1), 231–249.
25. Bello, D., Wardle, B.L., Zhang, J. *et al.* (2010) Characterization of exposures to nanoscale particles and fibers during solid core drilling of hybrid carbon nanotube advanced composites. *Int. J. Occup. Environ. Health*, **16** (4), 434–450.
26. Cena, L.G. and Peters, T.M. (2011) Characterization and control of airborne particles emitted during production of epoxy/carbon nanotube nanocomposites. *J. Occup. Environ. Hyg.*, **8** (2), 86–92.
27. Dahm, M.M., Schubauer-Berigan, M.K., Evans, D.E. *et al.* (2015) Carbon nanotube and nanofiber exposure assessments: an analysis of 14 site visits. *Ann. Occup. Hyg.*, **59** (6), 705–723
28. Fonseca, A.S., Viitanen, A.K., Koivisto, A.J. *et al.* (2014) Characterization of exposure to carbon nanotubes in an industrial setting. *Ann. Occup. Hyg.*, **59** (5), 586–599.
29. Lee, J.S., Choi, Y.C., Shin, J.H. *et al.* (2014) Health surveillance study of workers who manufacture multi-walled carbon nanotubes. *Nanotoxicology*, **14**, 1–10.
30. Chen, R., Shi, X., Bai, R. *et al.* (2015) Airborne nanoparticle pollution in a wire electrical discharge machining workshop and potential health risks. *Aerosol Air Qual. Res.*, **15** (1), 284–294.
31. Gojny, F.H., Wichmann, M.H., Fiedler, B. *et al.* (2005) Influence of different carbon nanotubes on the mechanical properties of epoxy matrix composites–a comparative study. *Compos. Sci. Technol.*, **65** (15), 2300–2313.
32. Kroto, H.W., Allaf, A.W., and Balm, S.P. (1991) C_{60}: Buckminsterfullerene. *Chem. Rev.*, **91** (6), 1213–1235.
33. Liu, Y., Chen, C., Qian, P. *et al.* (2015) Gd-metallofullerenol nanomaterial as non-toxic breast cancer stem cell-specific inhibitor. *Nat. Commun.*, **6**, 5988.
34. Chai, Y., Guo, T., Jin, C. *et al.* (1991) Fullerenes with metals inside. *J. Phys. Chem. A*, **95** (20), 7564–7568.
35. Fujitani, Y., Kobayashi, T., Arashidani, K. *et al.* (2008) Measurement of the physical properties of aerosols in a fullerene factory for inhalation exposure assessment. *J. Occup. Environ. Hyg.*, **5** (6), 380–389.
36. Shinohara, N., Matsumoto, T., Gamo, M. *et al.* (2009) Is lipid peroxidation induced by the aqueous suspension of fullerene c60 nanoparticles in the brains of cyprinus carpio? *Environ. Sci. Technol.*, **43** (3), 948–953.
37. Yeganeh, B., Kull, C.M., Hull, M.S. *et al.* (2008) Characterization of airborne particles during production of carbonaceous nanomaterials. *Environ. Sci. Technol.*, **42** (12), 4600–4606.
38. Sydlik, S.A., Jhunjhunwala, S., Webber, M.J. *et al.* (2015) In vivo compatibility of graphene oxide with differing oxidation States. *ACS Nano*, **9** (4), 3866–3874.
39. Seabra, A.B., Paula, A.J., De Lima, R. *et al.* (2014) Nanotoxicity of graphene and graphene oxide. *Chem. Res. Toxicol.*, **27** (2), 159–168.
40. Yan, L., Zhao, F., Li, S. *et al.* (2011) Low-toxic and safe nanomaterials by surface-chemical design, carbon nanotubes, fullerenes, metallofullerenes, and graphenes. *Nanoscale*, **3** (2), 362–382.
41. Dimiev, A.M., Alemany, L.B., and Tour, J.M. (2013) Graphene oxide. Origin of acidity, its instability in water, and a new dynamic structural model. *ACS Nano*, **7** (1), 576–588.

42. Anjilvel, S. and Asgharian, B. (1995) A multiple-path model of particle deposition in the rat lung. *Fundam. Appl. Toxicol.*, **28** (1), 41–50.
43. Chen, R., Huo, L., Shi, X. *et al.* (2014) Endoplasmic reticulum stress induced by zinc oxide nanoparticles is an earlier biomarker for nanotoxicological evaluation. *ACS Nano*, **8** (3), 2562–2574.
44. Huo, L., Chen, R., Zhao, L. *et al.* (2015) Silver nanoparticles activate endoplasmic reticulum stress signaling pathway in cell and mouse models: the role in toxicity evaluation. *Biomaterials*, **61**, 307–315.
45. Erdely, A., Dahm, M., Chen, B.T. *et al.* (2013) Carbon nanotube dosimetry: from workplace exposure assessment to inhalation toxicology. *Part. Fibre Toxicol.*, **10** (1), 53.
46. Takaya, M., Ono-Ogasawara, M., Shinohara, Y. *et al.* (2012) Evaluation of exposure risk in the weaving process of MWCNT-coated yarn with real-time particle concentration measurements and characterization of dust particles. *Ind. Health*, **50** (2), 147–155.
47. Tsai, S.J., Huang, R.F., and Ellenbecker, M.J. (2010) Airborne nanoparticle exposures while using constant-flow, constant-velocity, and air-curtain-isolated fume hoods. *Ann. Occup. Hyg.*, **54** (1), 78–87.

Index

Biomedical Applications and Toxicology of Carbon Nanomaterials, First Edition.
Edited by Chunying Chen and Haifang Wang.

g

h

WILEY END USER LICENSE AGREEMENT

Go to www.wiley.com/go/eula to access Wiley’s ebook EULA.